



**18th International Conference on
Sustainable Energy Technologies**

20-22 August 2019 - Kuala Lumpur - Malaysia

Sustainable Energy Towards the New Revolution

**Conference Proceedings
Volume 3**



University of
Nottingham
UK | CHINA | MALAYSIA



UNIVERSITI SAINS MALAYSIA



Proceedings of the
**18th International Conference on
Sustainable Energy Technologies**
SET 2019
20-22 August 2019
Kuala Lumpur, Malaysia

Volume 3

Edited by
Professor Saffa Riffat, Dr Yuehong Su,
Professor Norli Ismail and Dr Mardiana Idayu Ahmad

*SET 2019 Admin Support
Department of Architecture and the Built Environment
Faculty of Engineering, University of Nottingham*

© 2019 Copyright University of Nottingham & WSSET

The contents of each paper are the sole responsibility of its author(s); authors were responsible to ensure that permissions were obtained as appropriate for the material presented in their articles, and that they complied with antiplagiarism policies.

Reference to a conference paper:

To cite a paper published in these conference proceedings, please substitute the highlighted sections of the reference below with the details of the article you are referring to:

Author(s) Surname, Author(s) Initial(s), 2019. 'Title of paper'. In: Riffat, Su, Ismail, Ahmad. ed., **Sustainable Energy Towards the New Revolution**: Proceedings of the 18th International Conference on Sustainable Energy Technologies, 20-22 August 2019, Kuala Lumpur, Malaysia. University of Nottingham: Buildings, Energy & Environment Research Group. Volume X, pp XX-XX. Available from: nottingham-repository.worktribe.com/ [Last access date].

ISBN-13: 9780853583318

Version: 10.02.2020

Foreword

The 18th International Conference on Sustainable Energy Technologies was a significant international academic event in the domain of world sustainable energy technologies with a theme of '*Sustainable Energy Towards the New Revolution*'. The conference aimed to provide a forum for the exchange of latest technical information, the dissemination of up-to-date research results, and the presentation of major topics including sustainable energy, low carbon technologies, eco-cities, energy security and environmental policy.

Held from August 20th – 22nd 2019 in Kuala Lumpur, Malaysia, the conference was a collaboration between the World Society of Sustainable Energy Technologies (WSSET), the Universiti Sains Malaysia and University of Nottingham. World-renowned experts and scholars in the area, representatives of prominent enterprises and universities attended to discuss new developments and achievements in the field, as well as promoting academic exchange, application of scientific results, university-industry collaboration and government-industry collaboration.

The papers contained in these proceedings focus on topics such as Energy Storage for the Age of Renewables; Research, Innovation and Commercialisation in Sustainable Energy Technologies; Integrating Planning & Policy, Architecture, Engineering & Economics; Energy and Environment; Engineering Thermo-physics; and Systemic Change for Cities.

About 230 delegates from 30 countries attended SET2019; nearly 400 abstracts were received and 190 papers have been published in the conference proceedings. The proceedings have therefore been divided into three volumes. I hope you enjoy as much as I did the breadth of work you will find in these proceedings.

We would like to thank all participating authors for their contributions to both the conference and to the publishing of this book. We are also indebted to our international scientific committee for their advice and seemingly endless review of papers. We would also like to thank unreservedly Celia Berry, Zeny Amante-Roberts, Dr Mardiana Idayu Ahmad and Professor Dr Norli Ismail for their tireless efforts in making SET2019 one of the most successful conferences we have held. Also a huge thanks to our sponsors First Solar, PCM Products Ltd and Professor Terry Payne.

Professor Saffa Riffat
Chair in Sustainable Energy Technologies
President of the World Society of Sustainable Energy Technologies
Fellow of the European Academy of Sciences
SET 2019 Chairman

CONTENTS

Paper Number	Title	Page
#251:	Towards an electric revolution: a review on vehicle-to-grid, smart charging and user behaviour	1
#254:	Tracking architectural sustainable development in Thailand	10
#259:	Fabrication and testing of a low cost passive solar dryer	21
#260:	Experimental study of a building integrated solar water heater	29
#262:	Optimal design of structured packing column for cryogenic air separation with particle swarm optimisation algorithm	37
#263:	A study on the thermal and living environment of the slice room in Korea during winter season	46
#265:	Sizing and simulating the performance of a standalone solar water pumping and pasteurisation system for remote Egyptian oases	53
#267:	Computational fluid dynamics investigation of the thermal effectiveness of an oscillating air jet from a cassette split type air conditioner	64
#270:	Static and dynamic forecasting of solar radiation: a comparative study	74
#273:	Performance modelling and validation on the co-gasification of coal and sawdust pellet in research-scale downdraft reactor	87
#274:	Development of biomass-fired micro-scale CHP system with modified Rankine cycle (RC)	99
#276:	Performance analysis of the concentrator with flap-wind turbine combination	109
#278:	Influence of a deflector on a self-starting speed and power performance of a two-bladed Savonius hydrokinetic turbine	116
#280:	Effect of 3D morphological distribution of cities on urban heat island formation: A GIS approach	127
#281:	Experimental research on heat transfer and pressure drop characteristics of R410a within an asymmetric plate evaporator	138
#283:	Adoption of energy efficient buildings with improvement of their windows' aesthetic features	149
#284:	Experimental measurements of straw drying using flue gases	159
#285:	Insight into the dynamics and performance of vertical-axis turbines with pitch optimisation	169
#286:	Dynamic simulations of ground-coupled heat pumps using high-resolution analytical models	180
#287:	Assessing the harmful effects of domestic fuelwood burning on air quality in residential areas within communities: a case study of Kaduna state	190
#290:	Vehicle-induced pressure on divider in isolate and tandem	197
#294:	A review on green and sustainable technology in protecting honey bees against <i>Varroa destructor</i>	204
#298:	Can west-facing PV panels help the grid during the sunset?	216
#301:	Thermal performance assessment of solar box cookers with propolis based latent heat storage and low-cost booster reflectors	231
#304:	An exciting opportunity for Zeolite-A/Bentonite adsorbent design as molecular sieve in fuel grade ethanol production through adsorptive distillation	240
#306:	The indoor climate monitoring using Zigbee wireless network for building thermal comfort application	250
#308:	Energy-economic analysis of a small-scale hybrid trigeneration system including biomass-fired steam cycle and wind turbine	257
#312:	The implementation of micro hydro power at Diwak River, Semarang, Central Java, Indonesia	268
#319:	CFD-based analysis of a battery module with cylindrical lithium cells for automotive	274
#320:	Performance investigation of roof mounted cross axis wind turbine	285
#323:	CFD analysis on operative temperature prediction inside an office equipped with a fan-coil air conditioning system	295
#328:	A case study of a small wind turbine integrated with the building of AGH Centre of Energy, Krakow	304
#329:	A comprehensive numerical simulation of a sustainable power and heat generation cycle using CO ₂	314
#333:	Trends on sustainability in Saudi building industry: advances and challenges	324
#334:	Dosimetric and performance analysis of <i>Rhizophora</i> spp. particleboards as phantom material for SPECT/CT imaging	336
#338:	Thermal performance of a novel thermoelectric refrigerator with a water to air heat exchanger and SiO ₂ , TiO ₂ and Al ₂ O ₃ nanofluids	344
#340:	Microwave air heater: experimental investigation of a green heat transfer approach in helical coil	353
#341:	3-D simulation of submicron particle filtration on an elliptical fibrous surface	360
#342:	The study on the heat transfer characteristics of the double U-tube pipes underground	372
#343:	Experimental studies of a new design of biogas burner for gas-fired wall-mounted boilers	380
#344:	Synthesis of carbon nanotube-MgO composite by chemical vapour deposition for thermal energy storage	391
#345:	Study on controllable electrical nucleation of sodium acetate phase-change material based on anode surface powder-embedded treatment	398
#348:	Energy performance of venetian blinds in south-oriented residential spaces in Cairo	405
#352:	The city of emergence: Urban design strategies for Sejong Smart City	416

#353: Comparison of cascade PCM storage with single-phase sensible or latent heat storage for solar thermal energy	423
#354: Courtyard buildings in desert climates: are they energy efficient when air-conditioned?	434
#355: Regulatory and policy framework for the uptake of renewable energy in the United Kingdom	445
#356: Emission analysis for 1.6lL turbocharged CamPro engine using electric turbocompounding as exhaust energy recovery	455
#357: Global energy transition: A review of status and future challenges	462
#358: Experimental study on thermal performance of novel trapezoidal reactor	472
#361: Stimulation of continuous variable transmission (CVT) gear box with Single Input Rule Modules (SIRMs) connected fuzzy based actuator for wind energy harvesting.....	483
#363: Thermoregulation techniques in honey bees' (Apis Mellifera) beehive microclimate and its similarities to our buildings.....	493
#372: Numerical simulation on flow characteristics of falling film outside the horizontal tube in low counter-current air flow.....	501
#373: Numerical study on heat transfer of supercritical water in different sub-channels.....	510
#375: Study on the migration and degradation of organic compounds in coal-gasification wastewater with a novel treatment.....	520
#376: Developing an integrated Building Information Management (BIM) guideline for educational campuses facility management:	532
#377: Bioenergy contributions to the renewable energy technology mix: research incursion in South Africa	540
#378: Chemo-physical and thermal properties of sugarcane bagasse fractions (fibre and pith) technique.....	549
#379: Sustainable waste management by Sri Lankan entrepreneurs	558
#380: Laboratory testing for the vacuum glazing, double glazing and single glazing	569
#381: The impact of shading devices on the visual comfort and energy consumption of office rooms	580
#383: Quality improvement of syngas from gasification process of palm kernels using NiO/CaO catalysts on ceramic supporters coupled with biochar absorber from agricultural residues.....	592
#384: Recovery of malic acid using trioctylamine in 1-decanol: equilibrium studies by response surface methodology using Box Behkhen optimisation technique	601

#251: Towards an electric revolution: a review on vehicle-to-grid, smart charging and user behaviour

Julie WALDRON¹, Lucelia RODRIGUES², Mark GILLOTT³, Sophie NAYLOR⁴, Rob SHIPMAN⁵

¹ University of Nottingham, NG7 2RD University Park, Nottingham, UK, julie.waldron@nottingham.ac.uk

² University of Nottingham, NG7 2RD University Park, Nottingham, UK, lucelia.rodrigues@nottingham.ac.uk

³ University of Nottingham, NG7 2RD University Park, Nottingham, UK, mark.gillott@nottingham.ac.uk

⁴ University of Nottingham, NG7 2RD University Park, Nottingham, UK, sophie.naylor@nottingham.ac.uk

⁵ University of Nottingham, NG7 2RD University Park, Nottingham, UK, rob.shipman@nottingham.ac.uk

According to the Intergovernmental Panel on Climate Change in their Special Report on Global warming, it is clear that there is a need of a rapid change in all aspects of society to achieve limiting global warming to 1.5°C. The transport sector alone is currently responsible for 20.5% of the global emissions. Therefore, the transport sector is exploring new technologies and business models to make a transition to electric vehicles. This paper presents a review of the last decade on vehicle-to-grid (V2G), the advantages and barriers of this technology and the support V2G can give for the transition to electric mobility. The future scenarios for vehicle-to-grid are discussed, including the application of user behaviour analyses, data management and real-world demonstrators such as EV-elocity. This paper highlights the relevance of adopting V2G to integrate different vectors of the transport system and the energy infrastructure to generate environmental, social and economic benefits.

Keywords: electric vehicles; smart charging; vehicle to grid; renewable energy; clean transport; human behaviour

1. INTRODUCTION

Climate change is one of the biggest concerns of humanity as forecasts are currently showing risk of irreversible damages to the planet and human health. The Intergovernmental Panel on Climate Change in their Special Report on Global warming stated that a rapid change in all aspects of society is necessary in order to achieve limiting global warming to 1.5°C (Allen et al., 2018). The transport sector alone is currently responsible for 20.5% of the global emissions (The World Bank, 2019) and the adoption of clean transport technologies had become a steadfast alternative to reduce those emissions (Li et al., 2018). However, the problem has more factors to be considered as the mass production and large adoption of electric vehicles (EVs) will bring new challenges, such as the coordination of vehicles and the energy infrastructure (Letendre and Kempton, 2002), the integration of renewable sources to energy storage on EVs, the democratisation of the energy transactions and the prevention of energy shortage (Sortomme and El-Sharkawi, 2011).

In 2002, Letendre and Kempton pinpointed the relevance of looking at two different but compatible energy conversion systems: vehicles and the energy grid. According to the authors' forecasts, in 2050 electric vehicles could provide 20% of the energy required by the energy grid. The integration of these two systems occur with the 'Vehicle-to-Grid' or V2G, which refers to the capability of an electric vehicle to feed into the electric grid (Letendre and Kempton, 2002). The bidirectional characteristic of V2G allows the reversal of electric energy stored in EVs batteries. This two-way communication system works by charging and discharging the energy according to the demand (Zheng, 2019). Therefore, V2G can provide several ancillary services such as extra power for peak load demand, spinning reserves and regulation of the system (Lopes et al., 2011), as well as storage of renewables, which can be erratic, unpredictable and geographically determined (Yaqoot et al., 2016).

According to the Department for Business, Energy & Industrial Strategy (2018), renewable energy generated from photovoltaics and wind in the UK increased from 5,288 GWh in 2007 to 61,529 GWh in 2017. However, these sources are intermittent and dependant on weather variations, and this aspect has been reported as an important obstacle for its inclusion in the energy systems (Yaqoot et al., 2016). Therefore, energy storage systems are required as they can compensate the system by storing the renewables and sending it to the grid on demand, whilst providing flexibility, reliability and stability to the system (Parra et al., 2017; Sardi et al., 2017).

Ofgem (2019) stated that the rapid fall in the cost of EV batteries *"means that EVs may soon be as cheap to consume as conventional vehicles"* (p. 2) which will increase their use, and in consequence will bring implications to the energy system. Therefore, integrating electric mobility with the energy grid has become crucial to unlock storage capacity of renewable energy and the future demand that vehicles will bring to the grid. It is however observed that the academic production and studies regarding vehicle-to-grid have been conducted mainly during the last decade and it would be of interest to determine what are the main drivers that impulse research in this field. Therefore, this paper presents an overview on the last decade of vehicle-to-grid developments, the advantages and barriers to integrate this system reported by other authors, and future scenarios integrating behavioural analysis in real-world demonstrators.

2. LITERATURE REVIEW OF THE LAST DECADE OF V2G

A literature search of articles was conducted in the databases ScienceDirect and Scopus using common terms referring to vehicle-to-grid: "vehicle to grid", "vehicle-to-grid" and "V2G". The search was limited to publications in the last decade 2009-2019 which included the referred terms in the title, abstract or author-specified keywords. The number of papers published by year are presented in Figure 1.

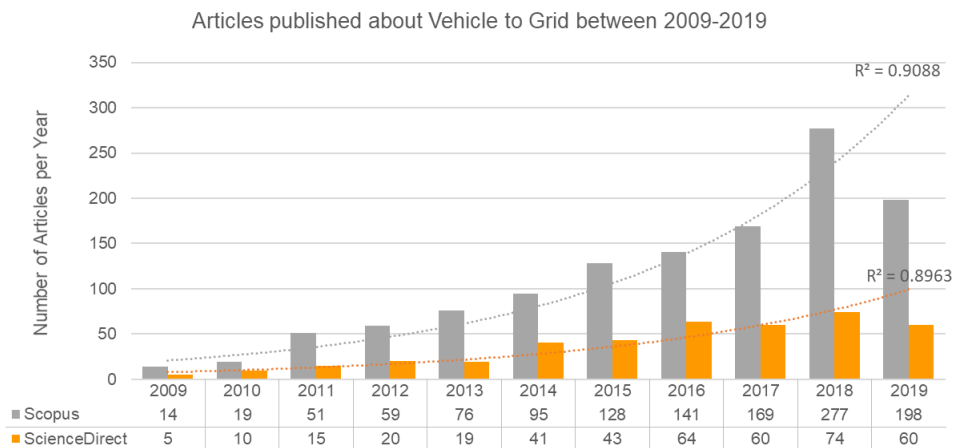


Figure 1: Number of articles published in Scopus and ScienceDirect between 2009 and 2019 about V2G

The number of publications about V2G presented a growth over the last decade. Taking into account the number of publications made until July 2019, the trend line is projecting that the number of papers will continue to increase as it has done during the past 10 years, achieving nearly 300 publication in Scopus and 50 publications in ScienceDirect by the end of 2019 (Scopus $R^2=.91$ and ScienceDirect $R^2=.90$). It is interesting to observe that in 2009, only 14 papers were published about V2G in Scopus and 5 papers in ScienceDirect, as the earliest publications on V2G date from 2002.

According to H. Sekyung et al. (2010) the first publications on V2G were mainly focused on how to connect the batteries to the grid (this refers to the earliest publication in the field conducted by Kempton et al., 2001 and Tomić and Kempton, 2007) and the fundamentals of load leveling, regulation and reserve (Pang et al., 2012). Later on, in 2010, other aspects such as the characteristics of the aggregator performance and the algorithms to control energy exchanges started to be developed using simulated scenarios (H. Sekyung et al., 2010; Lopes et al., 2011). By this time, the unpredictability brought by the users' behaviour was identified, as this prevented the business models to be successfully developed. One of the authors addressed this concern and proposed a possible solution by stating that: "It is mandatory that drivers actively notify the expected departure time upon plugging in. A driver would sign on a contract that he or she would keep the vehicle connected to the grid for certain amount of time in return of incentives such as a life time battery warranty" (H. Sekyung et al., 2010, p. 66), nevertheless, restricting the flexible use of the vehicles could affect the adoption of the technology.

Other challenges were also highlighted regarding the creation of a communication infrastructure to allow: i) the integration between the aggregator and the grid, and ii) the data management as this system required high frequency of data exchange due to its fluctuation (Guille and Gross, 2009).

A study conducted by Saber and Venayagamoorthy (2011) demonstrated the importance of integrating renewable sources of energy to the vehicle to grid system. In this study, the authors compared two simulated scenarios: the first one consisted in a conventional generation of energy where the EVs were charged using load-leveling optimisation, and the second one consisted in a smart grid model where the EVs were charged from renewable energy sources. The authors reported that the model integrating renewables presented significantly better performance in the reduction of greenhouse emissions. However, this model required a higher initial investment in the infrastructure to generate renewable energy.

One of the main strengths of vehicle to grid is the expansion on the energy storage capacity to integrate renewable sources. This is achieved by storing the surplus of energy generated by renewables and selling it on demand to the energy grid. However, this bidirectional charging and discharging of the battery have been generating concerns over the battery degradation and performance (Taiebat and Xu, 2019; Zheng et al., 2019). A study conducted by Peterson et al. (2010) regarding the degradation of lithium-ion battery concluded that several thousand driving days charging and discharging (driving/V2G) cause less than 10% of capacity loss regardless of the amount of V2G support used; however, intermittent modes of V2G could lead to rapid capacity fade.

3. ADOPTION OF VEHICLE-TO-GRID TECHNOLOGIES

Despite the relevance of integrating V2G to the energy infrastructure envisaged by several authors in the early 2000s (Brooks, 2002; Kempton et al., 2001; Kempton and Tomić, 2005a, 2005b), its application did not become a popular topic until more recent years. Some of the main barriers to adopt V2G, reported from 2010, were: i) the costs of the infrastructure to produce renewables (Saber and Venayagamoorthy, 2011), ii) the high costs of the EVs (Sortomme and El-Sharkawi, 2011), and iii) the technology development required (Guille and Gross, 2009; Sortomme and El-Sharkawi, 2011). In order to understand the evolution of the different systems involved in vehicle to grid, here is presented a comparison between the energy generated from renewables in the UK and the number of ultra-low emission vehicles licensed in the UK in the last years. The Digest of United Kingdom Energy Statistics presents the data regarding the renewable resources used to generate electricity and heat in the UK from 2007 to 2017 (BEIS, 2018). The data was filtered to include only the contribution made by solar photovoltaics and wind sources. A growth on the renewables since 2007 is observed. The contribution from wind sources increased from nearly 5,000 GWh in 2007 to 50,000 GWh in 2017 and the contribution of solar sources have been increasing since 2012.

Similarly, Figure 3 presents the data of ultra-low emission vehicles registered in the UK between 2010 and 2019. An important growth is observed in the acquisition of electric vehicles over the last decade, with an important acceleration between 2015 and 2019. This results show a similar pattern to the trends presented on Figures Figure 1 and Figure 2, where the publications regarding V2G and the energy generated by renewable sources also presented a continuous increase over the last 10 years.

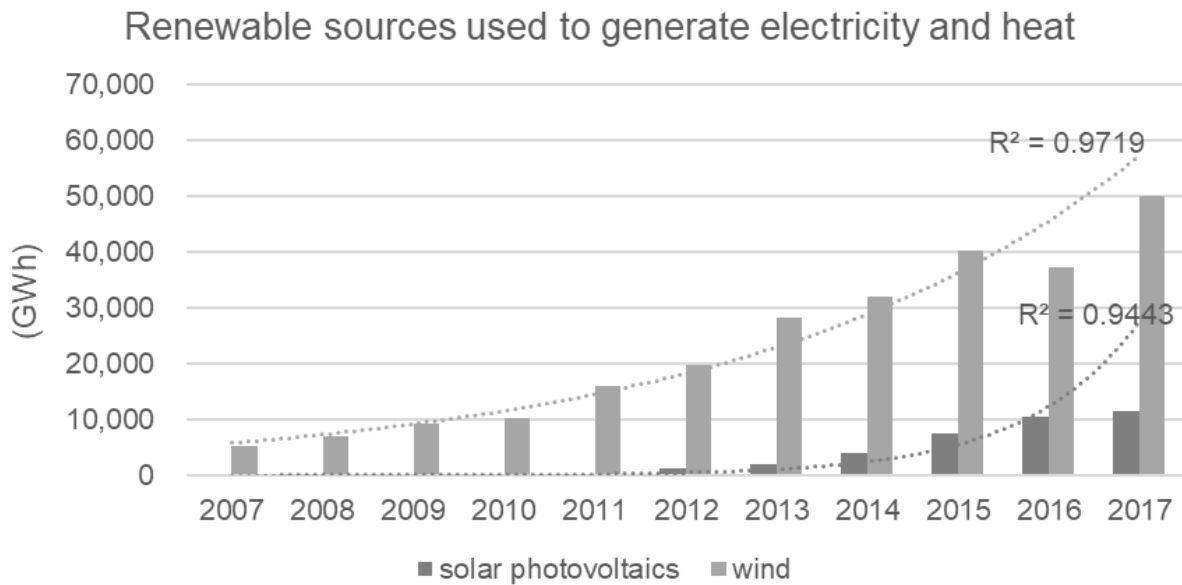


Figure 2: Electricity and heat generated by renewable sources 2007 – 2017. Data source: BEIS, 2017

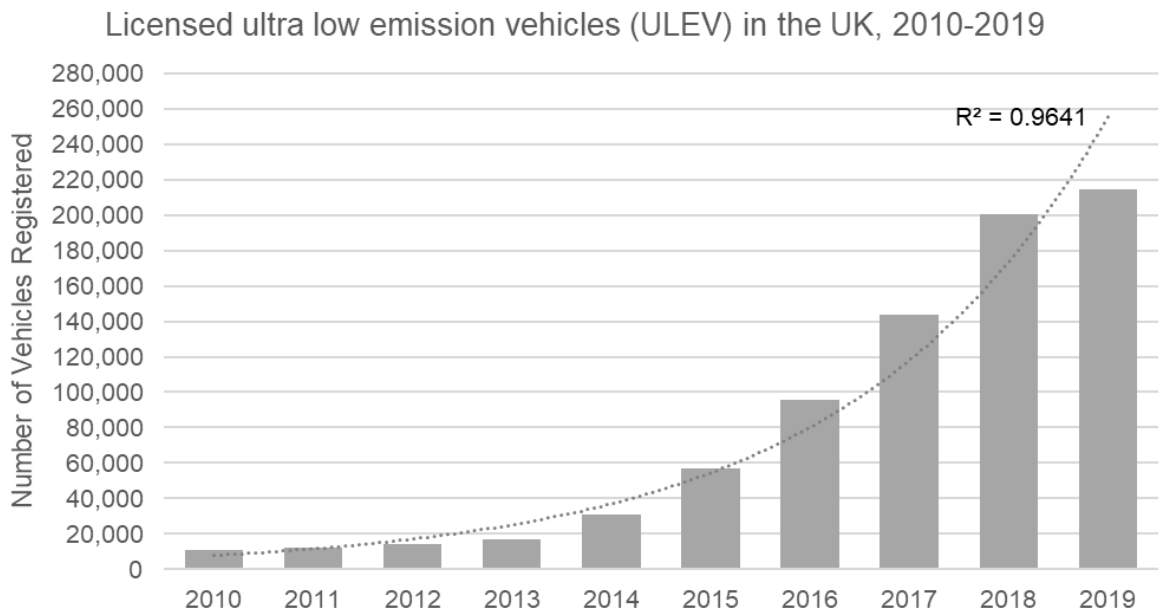


Figure 3: Ultra-low Emission Vehicles registered in the UK between 2010 and 2019

According to Küfeoglu et al. (2019), there are three trends that are currently enabling the bi-directional power flow to occur: i) the increasing uptake of electric vehicles, ii) the increased development and performance of vehicle batteries, and iii) the shift towards renewable energy. This combined development of EVs, energy storage and renewable energy can provide a revolution of the way we generate, store, manage and consume energy.

4. ADVANTAGES, BARRIERS AND CHALLENGES OF V2G

As mentioned in the introduction, one of the main benefits of V2G is that it can support the energy grid by regulating the peak demand, load shifting at distribution level and regulation of the system (Guille and Gross, 2009; Lopes et al., 2011). The bidirectional charging and discharging allows providing spinning reserve, frequency regulation, prevent overloading of lines and transformers, decrease the energy costs and charging costs, and also provides other ancillary services for power grid (Taiebat and Xu, 2019; Zheng et al., 2019).

From the user perspective, the benefits of V2G are related to economic incentives generated by selling the energy to the grid. This could represent a reduction of the life cycle cost of the vehicle by providing revenue (Taiebat and Xu, 2019). It also produces an optimisation on the price of electricity, as the price-based charge can achieve reductions up to 10% of the charging costs and possibilities of achieving more saving with dynamic prices, which

could be available in different business models (Iacobucci et al., 2019; Taiebat and Xu, 2019). Some authors reported different types of incentives, such as life time battery warranty (H. Sekyung et al., 2010, p. 66) or commodities, services, information or money (Guille and Gross, 2009).

Vehicle-to-grid can also provide a better management of electricity resources (Taiebat and Xu, 2019). It offers the possibility to absorb the surplus energy valley before the EVs batteries are charged (Zheng et al., 2019) and it could reduce the system costs in V2G optimised transport networks (Iacobucci et al., 2018; Taiebat and Xu, 2019). Moreover, V2G and smart charging solutions are key to integrate variable renewable sources, such as wind and solar by coordinated charging strategies (Lopes et al., 2011; Zheng et al., 2019). According to Pfeifer et al (2019), renewable energy sources are frequently generating excess of power that requires to be stored. To address this issue, V2G can provide fast response storage with minimal impact on infrastructure costs when the vehicles are stationary. As a result of the capability to store renewables, V2G has the potential to make a significant contribution on the reduction of greenhouse emissions (Saber and Venayagamoorthy, 2011).

On the other hand, some of the barriers reported are: the anxiety among the challenges presented by implementing the V2G technology, concerns over battery performance and degradation (Taiebat and Xu, 2019; Zheng et al., 2019), lack of scientific consensus and uncertainties (Taiebat and Xu, 2019) and the fact that cost/benefit of combined models such as wireless charging, shared electric vehicles and V2G is still unknown (Taiebat and Xu, 2019). According to Zheng et al. (2019), uncoordinated charging modes of electric vehicles can increase power loss, elevate load peaks, affect the grid frequency, overload the lines and transformers, increase electricity costs for power companies and increase charging costs for EV users.

The reported uncertainties are the main challenges V2G projects will be facing over the coming years. As reported by Lopes et al. (2011), a new infrastructure will be required including charging stations, fast charging opportunities, battery swapping stations, domestic and public individual charging points and life cycle analysis of vehicle batteries. Moreover, an adequate market operation considering the patterns of the grid is also needed (Lopes et al., 2011).

5. HUMAN BEHAVIOUR AND DATA MANAGEMENT

It is clear from the breadth of study in this field that V2G applications have a range of challenges to meet before wide-scale application is possible. However, many V2G studies focus only on the technical side of these challenges. Only 2.1% of papers published in the field sampled by Sovacool et al. (2018) addressed user behaviours and routines, with 1.1% addressing range anxiety adoption issues. Despite a relative lack of attention, user behaviours and routines remain a key component in whether V2G will be viable in application.

User-centred challenges in V2G applications can include the social (attitudes towards the technology, socioeconomic factors in technology adoption) and the practical (vehicle availability for V2G events, user predictability, behavioural incentives). In particular, analysis of user routines and vehicle use patterns can provide key evidence for V2G application. For example, in the simulation of vehicle battery availability for V2G, behavioural patterns can be used to assess the economic feasibility of V2G over the longer term (Gough et al., 2017). In the work of Metz and Doetsch (2012), it was found that domestic vehicles were spending a combined 81% of time on average available for grid support if able to charge at both home and work locations. It has been shown that the patterns of vehicle use, state of charge on arrival and desired state of charge on departure can significantly affect the impact that V2G services could have on load management in different building types (Kuang et al., 2017). Usage patterns can also inform the planning of public charging infrastructure (Morrissey et al., 2016).

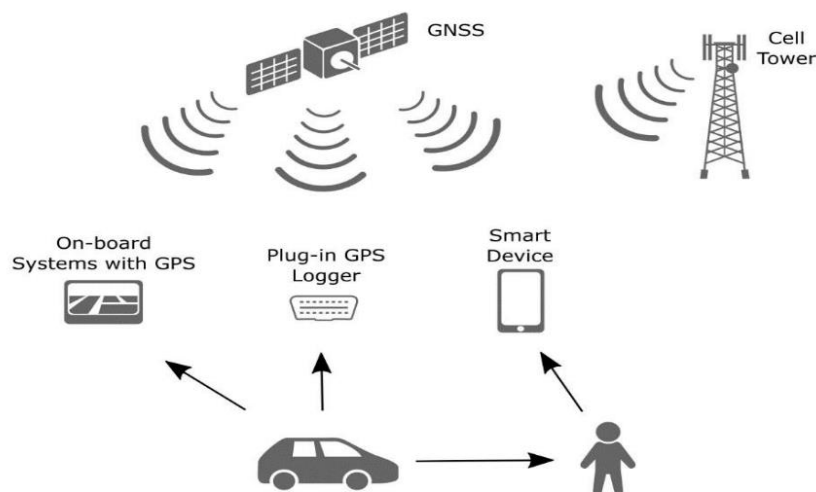


Figure 4: Vehicle tracking data collection

While it is clear that user behaviours can have a significant impact on V2G application, solutions that seek to track user behaviours and routines encounter additional challenges around data collection. Vehicle mobility data requires some knowledge of location, traditionally from standalone GPS receivers that can be installed in vehicles. Increasingly, alternative data sources are becoming available, including on-board vehicle navigation/tracking systems and personal smart devices as shown in Figure 4. Mobility data can also be extracted without explicit knowledge of GPS co-ordinates as discussed in (Naylor et al., 2019). This is particularly useful to minimise risks related to data protection and privacy.

6. FUTURE SCENARIOS FOR V2G

Other authors referred several possibilities to connect electric vehicles to provide power services, such as: vehicle to home (V2H), vehicle to vehicle (V2V), vehicle to load (V2L) or vehicle to everything (V2X) which refers to the vehicle acting as independent clusters of generation (Rodríguez-Licea et al., 2019). According to Pang et al. (2012), vehicle-to-grid can take a long penetration time into the market as it is reported to produce significant revenue mainly in large-scale scenarios. Therefore, vehicle to building (V2B) was also identified as an option to attract early adopters of electric vehicles to “export electrical power from a vehicle battery into a building connected to the distribution system to support loads” (Pang et al., 2012, p. 474).

Several deployment scenarios will need to be studied taking into account multiple variables like the type of vehicles (fleet or individual), the technology used (electric, hybrid, or fuel cell), the owners’ behaviour, the traffic patterns, the places where cars are parked and connected to the grid, the type of connection between the EV and the network, as well as the grid control architecture (Lopes et al., 2011).

6.1. Real-world Demonstrator: EV-elocity

One of the challenges of vehicle-to-grid is the lack of real-world scenarios to gather data and test the viability of the technology and the business models. The literature review conducted showed that the benefits of V2G have been widely explored using modelling techniques and forecasting different scenarios. However, the deployment of vehicle-to-grid infrastructure has only occurred recently. As suggested by Taiebat and Xu (2019), there is lack of scientific consensus regarding the benefits of EVs adoption, particularly in determining the environmental benefits that this technology can generate. Currently, the attention has been focused in the operation and optimisation of the EV system, so there has not been quantitative analysis using real-world travel demand data, and this extends also to the V2G systems (Taiebat and Xu, 2019).

As part of the funding call “Innovation in vehicle-to-grid (V2G) systems: real-world demonstrators” (Innovation Funding Services, 2017), EV-elocity is a research and development project conducting real-world demonstrators that will support the uptake of electric vehicles through helping consumers to monetise their investment using vehicle-to-grid innovation (EV-elocity, 2018). This project is exploring new technologies, encouraging behaviour change and developing business models that will enable the sharing of the value V2G can bring to the grid, local and regional business and the consumer.

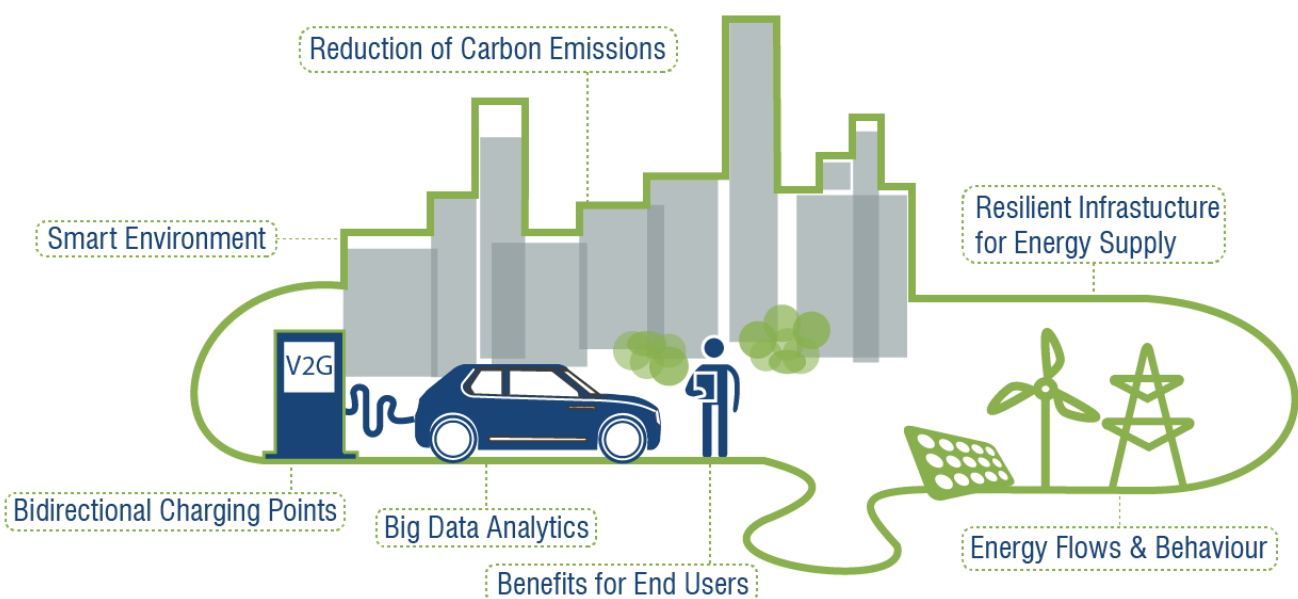


Figure 5: Benefits of vehicle-to-grid and smart charging

In alignment with the advantages of V2G reported by other authors in Section 4, EV-elocity proposal will impact fundamental features of the vehicle-to-grid technology on various aspects: 1) Economic: by enhancing the business model to uptake electric vehicles through the provision of a new revenue source for the owners and helping to reduce the cost of energy, 2) Social: by increasing infrastructure resilience and security of the energy supply, increasing a wider participation by proposing sustainable life-styles and encouraging behaviour change by raising awareness of energy related issues, and 3) Environmental: by reducing carbon emissions from transport through increasing electric vehicle usage, optimising the energy system by providing energy on demand from the bi-directional charging, and increasing the energy storage capacity to integrate renewable sources to the energy grid (EV-elocity, 2018).

7. CONCLUSIONS

According to the review of the last decade of V2G, the importance of supporting the transition to electric mobility has been highlighted by various authors, as the transport sector is currently responsible for 20.5% of the global carbon emissions. This complex transition will need to consider the coordination of the transport and energy infrastructure. One of the risks envisaged by other authors regarding the transition to electric mobility is the overload of the energy system due to the simultaneous charge of electric vehicles. Therefore, a dynamic system where the EVs are contributing to the grid by storing renewable energy is required.

Early studies on V2G from 2002 pointed the possibilities that electric vehicles could bring to the energy system. Nevertheless, the relevance of deploying this technology started to appear from 2012, when the market of renewables and electric vehicle batteries started to accelerate.

A similar increasing trend has been reported over the last decade between: i) the articles published about V2G, ii) the market of low emission vehicles, and iii) the production of energy from renewables. This correlation suggests a maturity of the transport system and the energy infrastructure to integrate V2G.

Several studies reported the advantages of V2G and smart charging technologies in terms of economic, social and environmental benefits. Moreover, V2G can support the energy grid by regulating the peak demand and offering ancillary services. From the user perspective, V2G can provide different incentives that can promote the switch from internal combustion engine (ICE) to electric vehicles (e.g. economic and environmental). With regards to the energy grid, V2G can help to increase the storage capacity of the energy system allowing the generation and use of intermittent renewable sources and with low impact in infrastructure costs.

In order to implement vehicle-to-grid and smart charging successfully, some challenges which have been identified must be overcome. Amongst these are: the anxiety caused by the implementation taking into account concerns over the economic and environmental incentives of electric vehicles and vehicle-to-grid. There are also challenges in integrating algorithms based on user behaviour analysis to create a flexible and resilient charging infrastructure.

In the future scenarios of V2G and smart charging, real-world demonstrator projects such as EV-elocity are required to provide further real-world data regarding the economic, social and environmental benefits. This type of research and development projects will support the transition to electric mobility by developing products, services and knowledge of future V2G infrastructure.

8. ACKNOWLEDGEMENTS

This paper is an outcome of the research activities of the project EV-elocity funded by the Office for Low Emissions Vehicles (OLEV), the Department for Business, Energy and Industrial Strategy (BEIS) and facilitated by Innovate UK. The partners of this project are: A.T. Kearney, Brixworth Technology, Cenex, Honda, Ecar, Forward Utility, The University of Nottingham, The University of Warwick, Leeds City Council, Nottingham City Council and Peel Land & Property.

9. REFERENCES

Allen, M., Babiker, M., Chen, Y., Taylor, M., Tschakert Australia, P., Waisman, H., Warren, R., Zhai, P., Zickfeld, K., Zhai, P., Pörtner, H., Roberts, D., Skea, J., Shukla, P., Pirani, A., Moufouma-Okia, W., Péan, C., Pidcock, R., Connors, S., Matthews, J., Chen, Y., Zhou, X., Gomis, M., Lonnoy, E., Maycock, T., Tignor, M., Waterfield, T., 2018. IPCC, 2018: Summary for Policymakers. In: Global Warming of 1.5°C. An IPCC Special Report on the impacts of global warming of 1.5°C above pre-industrial levels and related global greenhouse gas emission pathways, in the context of strengthening the global, World Meteorological Organization. Geneva.

BEIS, D. for B.E. & I.S., 2018. Digest of United Kingdom Energy Statistics (DUKES).

Brooks, A.N., 2002. Vehicle-to-Grid Demonstration Project: Grid Regulation Ancillary Service with a Battery Electric Vehicle.

EV-elocity, 2018. EV-elocity Project | vehicle-to-grid (V2G) innovation with electric vehicles [WWW Document]. URL <https://www.ev-elocity.com/> (accessed 8.7.19).

Gough, R., Dickerson, C., Rowley, P., Walsh, C., 2017. Vehicle-to-grid feasibility: A techno-economic analysis of EV-based energy storage. *Appl. Energy* 192, 12–23. <https://doi.org/10.1016/j.apenergy.2017.01.102>

Guille, C., Gross, G., 2009. A conceptual framework for the vehicle-to-grid (V2G) implementation. *Energy Policy* 37, 4379–4390. <https://doi.org/10.1016/j.enpol.2009.05.053>

H. Sekyung, H. Soohye, K. Sezaki, 2010. Development of an Optimal Vehicle-to-Grid Aggregator for Frequency Regulation. *IEEE Trans. Smart Grid* 1, 65–72. <https://doi.org/10.1109/TSG.2010.2045163>

Iacobucci, R., McLellan, B., Tezuka, T., 2019. Optimization of shared autonomous electric vehicles operations with charge scheduling and vehicle-to-grid. *Transp. Res. Part C Emerg. Technol.* 100, 34–52. <https://doi.org/10.1016/j.trc.2019.01.011>

Iacobucci, R., McLellan, B., Tezuka, T., 2018. Modeling shared autonomous electric vehicles: Potential for transport and power grid integration. *Energy* 158, 148–163. <https://doi.org/10.1016/j.energy.2018.06.024>

Innovation Funding Services, 2017. Competition Overview - Innovation Funding Service [WWW Document]. URL <https://apply-for-innovation-funding.service.gov.uk/competition/29/overview> (accessed 8.7.19).

Kempton, W., Tomić, J., 2005a. Vehicle-to-grid power implementation: From stabilizing the grid to supporting large-scale renewable energy. *J. Power Sources* 144, 280–294. <https://doi.org/10.1016/j.jpowsour.2004.12.022>

Kempton, W., Tomić, J., 2005b. Vehicle-to-grid power fundamentals: Calculating capacity and net revenue. *J. Power Sources* 144, 268–279. <https://doi.org/10.1016/j.jpowsour.2004.12.025>

Kempton, W., Tomic, J., Letendre, S., 2001. Vehicle-to-Grid Power: Battery, Hybrid, and Fuel Cell Vehicles as Resources for Distributed Electric Power in California Publication Date.

Kuang, Y., Chen, Y., Hu, M., Yang, D., 2017. Influence analysis of driver behavior and building category on economic performance of electric vehicle to grid and building integration. *Appl. Energy* 207, 427–437. <https://doi.org/10.1016/j.apenergy.2017.07.006>

Küfeoğlu, S., Melchiorre, D.A., Kotilainen, K., 2019. Understanding tariff designs and consumer behaviour to employ electric vehicles for secondary purposes in the United Kingdom. *Electr. J.* 32, 1–6. <https://doi.org/10.1016/j.tej.2019.05.011>

Letendre, S.E., Kempton, W., 2002. The V2G concept: a new for model power? Connecting utility infrastructure and automobiles. *Public Util. Fortn.*

Li, L., Dababneh, F., Zhao, J., 2018. Cost-effective supply chain for electric vehicle battery remanufacturing. *Appl. Energy* 226, 277–286. <https://doi.org/10.1016/j.apenergy.2018.05.115>

Lopes, J.A.P., Soares, F.J., Almeida, P.M.R., 2011. Integration of Electric Vehicles in the Electric Utility Systems. *Proc. IEEE* 99. <https://doi.org/10.5772/16587>

Metz, M., Doetsch, C., 2012. Electric vehicles as flexible loads - A simulation approach using empirical mobility data. *Energy* 48, 369–374. <https://doi.org/10.1016/j.energy.2012.04.014>

Morrissey, P., Weldon, P., O'Mahony, M., 2016. Future standard and fast charging infrastructure planning: An analysis of electric vehicle charging behaviour. *Energy Policy* 89, 257–270. <https://doi.org/10.1016/j.enpol.2015.12.001>

Naylor, S., Pinchin, J., Gough, R., Gillott, M., 2019. Vehicle Availability Profiling from Diverse Data Sources. *IEEE Int. Conf. Pervasive Comput. Commun. Work.* 171–176.

- Office of Gas and Electricity Markets, 2019. Future Insights Series - Implication on the transition to Electric Vehicles.
- Pang, C., Dutta, P., Kezunovic, M., 2012. BEVs/PHEVs as dispersed energy storage for V2B uses in the smart grid. *IEEE Trans. Smart Grid* 3, 473–482. <https://doi.org/10.1109/TSG.2011.2172228>
- Parra, D., Swierczynski, M., Stroe, D.I., Norman, S.A., Abdon, A., Worlitschek, J., O'Doherty, T., Rodrigues, L., Gillott, M., Zhang, X., Bauer, C., Patel, M.K., 2017. An interdisciplinary review of energy storage for communities: Challenges and perspectives. *Renew. Sustain. Energy Rev.* 79, 730–749. <https://doi.org/10.1016/j.rser.2017.05.003>
- Peterson, S.B., Apt, J., Whitacre, J.F., 2010. Lithium-ion battery cell degradation resulting from realistic vehicle and vehicle-to-grid utilization. *J. Power Sources* 195, 2385–2392. <https://doi.org/10.1016/j.jpowsour.2009.10.010>
- Rodríguez-Licea, M.A., Perez-Pinal, F.J., Soriano-Sánchez, A.G., Vázquez-López, J.A., 2019. Noninvasive vehicle-to-load energy management strategy to prevent li-ion batteries premature degradation. *Math. Probl. Eng.* 2019. <https://doi.org/10.1155/2019/8430685>
- Saber, A.Y., Venayagamoorthy, G.K., 2011. Plug-in vehicles and renewable energy sources for cost and emission reductions. *IEEE Trans. Ind. Electron.* 58, 1229–1238. <https://doi.org/10.1109/TIE.2010.2047828>
- Sardi, J., Mithulananthan, N., Gallagher, M., Hung, D.Q., 2017. Multiple community energy storage planning in distribution networks using a cost-benefit analysis. *Appl. Energy* 190, 453–463. <https://doi.org/10.1016/j.apenergy.2016.12.144>
- Sortomme, E., El-Sharkawi, M.A., 2011. Optimal charging strategies for unidirectional vehicle-to-grid. *IEEE Trans. Smart Grid* 2, 119–126. <https://doi.org/10.1109/TSG.2010.2090910>
- Sovacool, B.K., Noel, L., Axsen, J., Kempton, W., 2018. The neglected social dimensions to a vehicle-to-grid (V2G) transition: A critical and systematic review. *Environ. Res. Lett.* 13. <https://doi.org/10.1088/1748-9326/aa9c6d>
- Taiebat, M., Xu, M., 2019. Synergies of four emerging technologies for accelerated adoption of electric vehicles: Shared mobility, wireless charging, vehicle-to-grid, and vehicle automation. *J. Clean. Prod.* 230, 794–797. <https://doi.org/10.1016/j.jclepro.2019.05.142>
- The World Bank, 2019. CO2 emissions from transport (% of total fuel combustion) | Data [WWW Document]. URL <https://data.worldbank.org/indicator/en.co2.tran.zs?end=2014&start=1960&view=chart> (accessed 7.4.19).
- Tomić, J., Kempton, W., 2007. Using fleets of electric-drive vehicles for grid support. *J. Power Sources* 168, 459–468. <https://doi.org/10.1016/j.jpowsour.2007.03.010>
- Yaqoot, M., Diwan, P., Kandpal, T.C., 2016. Review of barriers to the dissemination of decentralized renewable energy systems. *Renew. Sustain. Energy Rev.* 58, 477–490. <https://doi.org/10.1016/j.rser.2015.12.224>
- Zheng, Y., Niu, S., Shang, Y., Shao, Z., Jian, L., 2019. Integrating plug-in electric vehicles into power grids: A comprehensive review on power interaction mode, scheduling methodology and mathematical foundation. *Renew. Sustain. Energy Rev.* <https://doi.org/10.1016/j.rser.2019.05.059>

#254: Tracking architectural sustainable development in Thailand

A professional architects' perspective

Sumavalee CHINDAPOL¹

¹ Building Innovation and Management Research Center, Faculty of Architecture, Chiang Mai University, 239, Huaykaew Road, Suthep, Muang, Chiang Mai, sumavalee.ch@cmu.ac.th

Green architectural concept development has become a root principle in project concern for over two decades. The aim of this study is to track sustainable development in Thailand's architectural scholars. The research method was to define sustainable green development by reviewing literature, finding a remarkable case study of the design approach and interviewing the designers. There have been several movements driving sustainable design approach. After the financial crisis in 1997, the overall economic status was frozen for at least three years and the real estate business had also been so for five years. Each wave of design approach had brought new ideas and collaborated with new partners in the architectural field. The first green development started in 2003 due to the first active green building approach, driven by an insulated house idea. The second wave occurred from the country's energy policy and the global green building evaluation approach. Many green criteria emerged in Thailand along with the Energy Conservation Act B.E. 2535. Over a decade, Thailand was overwhelmed with the green building assessment. The third wave was a new paradigm of sufficient economy concept applied to the vernacular architectural design concept. It was an argument towards the former wave that would form the green criteria from the international standard which was a sustainable solution. Then, the fourth wave was to integrate a high energy efficiency building to a healthy occupant, following the Sustainable Development Gold's United Nation approach. The fifth wave has been shifting along with sustainable journey in Thailand. It is a use of new technology for saving energy and being friendly to the environment. Smart city is the next sustainable trend. The Ministry of Energy in Thailand and the Thai Green Building Institute (TGBI) have supported Smart cities – Clean Energy campaign. The top 7 sustainable cities won a 10 Million Baht for development. The winners are NIDA Smart Compact City, CMU Smart city Clean Energy, CU Smart City, Thammasat Smart City, Whizdom 101, Khonkaen Smart City and Baan Chang Smart City. A major contribution of the study was learning from the past to improve the better future sustainable approach.

Keywords: sustainable; architecture; development; Thailand

1. INTRODUCTION

Thailand is in a tropical climate. Vernacular Thai architecture has been designed with harmony and uniting with nature in mind. Local materials are commonly used in the design such as wood. It is expected to be repaired since it cannot last forever in the hot and humid climates, but it can also be found around the neighbourhood.

The most obvious characteristic of vernacular Thai architecture is the roof. Long eaves and a steep roof is necessary for running off heavy rain in the monsoon season, protecting the indoor from flooding. Steep roofs also helps the wind keep buildings well ventilated. The platform of the house is elevated on pillars to reduce humidity from the soil and mitigate the flooding effect. Space under the platform is used for agricultural storage or animal husbandry (Horayangkura, et al., 2017).

Thailand experienced the financial crisis in 1997. During 1985-1996, the Thai economy grew very well, booming like bubbles, particularly asset businesses. When finance companies collapsed, real asset businesses were affected significantly. Thailand needed to receive a rescue package from the International Monetary Fund (IMF). Most businesses were frozen, including the asset. Thailand's economy had recovered by 2001 and real estate businesses started to be re-activated. The first real estate projects were housing and they were designed simply at first. Sustainability had not been a consideration at that time yet.

This study has tracked sustainability in architectural construction and professional knowledge in Thailand. It aims to discover the Thailand sustainable development trend over four decades. Methodology is separated into two parts of professional development and reviewing the design strategies. The first part was conducted by in-depth interviews. There were over 10 experts to conclude five case studies representing five green movements. The second part was to summarise from a green idea to green approach and from sustainable trend to sustainable strategies compared to the UN 17 SDG approach (UN, 2018). Sustainable Development Goal's from United Nation has 17 items launched in 2018 entitled, the 2030 Agenda for Sustainable Development (UN knowledge platform, 2016). Architectural case studies have involved eight items, including 3) Good Health & Well-being, 4) Quality Education, 6) Clean Water & Sanitation, 7) Affordable & Clean Energy, 9) Industry Innovation & Infrastructure, 11) Sustainable Cities & Communities, 12) Responsible Consumption & Production, and 13) Climate Action.

2. GREEN WAVES DEVELOPMENT: ARCHITECTURAL PROFESSION

Thailand has had several movements driving sustainable design approach. Before the financial crisis in 1997, architectural and real estate businesses were extravagant. Green architecture had not been defined yet, although a few projects could be identified as having a green approach such as Wat Mahajedikaew (the million bottles temple) in 1990, the 1st Energy Conservation Promotion Act B.E. 2535 (1995) and Roong Aroon School (holistic resources management) built in 1997 (see Figure 1). After the financial crisis in 1997, the overall economic status froze for at least 3 years and the real estate business had similarly been stagnant for 5 years (Horayangkura, V., et. al, 2017). Each wave occasion had brought new ideas to the architectural field and seen collaborations with new partners. The first green development started in 2003 due to the first active green building approach in Thailand. The second wave occurred from the country's energy policy. The third wave was a new paradigm of sufficient economy concept applied to the architectural design concept. The fourth wave was to integrate a high energy efficiency building to a healthy occupant. The fifth wave has been moving with the sustainable journey in Thailand. It is a use of new technology for saving energy and being friendly to the environment.

The most significant wave was driven by Dr. Soontorn Boonyatikan's green projects (Boonyatikan, S. 2002). It was the very first step claiming to be green architecture. The Bio-Solar House was the first official project in Thailand claiming energy saving from building (see Figure 1). Many active cooling techniques were applied in the house such as thick insulation roof and wall, solar PV cell on the steep roof, long eaves. The cooling techniques were integrated in a public scale project. Shinawatra University (case study 1) was built and received many energy awards at that time such as ASHRAE Regional Technology Award and ASEAN Energy Award. Although many architects' firms and real estate business had still not completely recovered from the financial crisis, Dr. Soontorn brought the new green idea for Thailand's architectural concept.

The second movement happened when the Ministry of Energy launched the Energy Conservation Promotion Act (No.2) B.E. 2550 in 2007. It was implemented on all large building. The move challenged all architects and engineers in Thailand to be more positive on energy conservation. The TGBI (Thai Green Building Institute) was founded to develop the sustainable design guidelines for new buildings. It was at the same time as the LEED approached to Thailand. LEED criteria were adopted and applied in the TREES rating system (Thai's Rating of Energy and Environmental Sustainability) for hot and humid climate of Thailand. Unfortunately, the tool took several years to develop. During that time, many projects were applied and certified for LEED. 144 buildings in Thailand have been LEED certified since then. The first official LEED building in Thailand is K-Bank office at Paholyotin. It received a gold level from the existing building. The first official LEED platinum building is Park Ventures – case study 2 (Palmer & Turner, 2011).

The third wave occurred when “Sufficiency Economy” philosophy was adopted in construction projects. The sufficiency economy was created by His Majesty the King Rama IX and officially published in 2008. It was meant originally for sustainable agriculture, but it has been applied to most fields, including sustainable architecture (Panyaden International School, 2012). The passive design, being considerate with local weather and using local materials were the key. In addition, during the active high-tech approach, there were many questions raised asking why Thai architectures needed to use high-tech and expensive solution to be sustainable, while they could be sustainable with local wisdom gained over a hundred years. Passive design techniques were integrated for cooling spaces. Local materials from neighbourhood were used as a construction material such as wood, brick and bamboo (Markus Roselleb, interviewed on 11th February 2016). For example, Kantana Studio is a showcase of local load bearing wall brick architecture as same as the traditional style but in a new arrangement. The holistic approach could also be adapted to all processes of building construction and operation. Roong Aroon School is the very first example of combining holistic learning process from waste management to lessons. Panyaden International School adapted the holistic approach not only within the learning process but with the construction process. Waste from agriculture becomes a construction material in an adobe wall of the school.



Figure 1: Five decades green design approach development in Thailand

The fourth wave is not only about energy conservation in buildings, but it is also about healthy lifestyle buildings. Sick building syndrome has been an issue for employees for a long time. It contributes to less productive performance of the overall office outcome. Healthy buildings make employees feel happier and healthier. Sustainable projects cannot maintain their sustainability and environmentally friendly status unless the occupants also have sustainable lifestyles. A building with a pocket garden or a small gym has become the standard. The office building with a jogging track, a bicycle lane and surrounded by a large park has become a privilege. Office buildings in Bangkok have started adapting this concept in several ways. The Unilever office in Bangkok uses an open plan office. The responses from employee have been encouraging since they feel more active, energetic and healthier. The SCG 100th Year Building provides a jogging lane and a bike lane within the building (Jakkasin Noiraipoom, interviewed on 3rd May 2016).

The fifth wave involves the experimental use of advanced technology in building projects. It was not an entirely new concept since it had appeared previously in Thai construction. For example, in 1985 K-Bank headquarter office at Ratburana used ice-storage system with the cooling system to reduce energy consumption during the peak hours (see Figure 1). It was one of the advanced energy conservation techniques in the 1980s. During the energy crisis in the 2000s, Ministry of Energy was targeted to use 20% of its electrical energy from renewable energy replacing 100% energy from fossil fuel by 2024 (Energy Conservation Promotion Act (No.2) B.E. 2550, 2007). Solar power was a wise choice of renewable energy, but it was very expensive and almost unaffordable even for the large building. Only a few high-rise buildings installed solar PV cell in the 2000s such as Energy Complex, the Office at Central World and Sathorn Square.

Nowadays, Solar energy has also become commonly used since technologies for energy conservation have become affordable, including solar cell and high efficient cooling system. Many domestic suppliers can produce their own innovation, so their products were ready to use and required simple maintenance, including smart devices for monitoring, detecting, even thinking. The current state-of-the-art technology is the use of new energy sources like hydrogen. Phi Suea House claims to be the first house in the world using hydrogen power. The buildings can be a stand-alone – off-grid - since it consumes only water and solar energy without any electric power supply.

3. RESULTS: ARCHITECTURAL DESIGN CASE STUDIES

3.1. Shinawatra University – representing the first wave

Shinawatra University (SIU) is an international university in Thailand. The bachelor's, master's and doctoral degree programs are in four schools and one institute: School of Management, School of Science and Technology, School of Nursing (bachelor's degree only), School of Liberal Arts (post-graduate degrees) and the Institute of Public Administration and Governance. The project floor area is 81,440 m² on a 48,000 m² site area. It cost 950 Million Baht (equivalent to AUD\$41.8 Million in 2002) and was completed in 2002. The project was designed by Dr. Soontorn Boonyatikan (Personal Representative Department, 2017, see Figure 2 – left).

Key sustainability strategy of Shinawatra University is that it was the very first official project concerning about sustainability in Thailand. Its original concept was proposed by Dr. Soontorn Boonyatikan in 2000. The building itself is not only energy conservation by the insulated wall and hi-efficient glass, it also reuses the waste energy from the classroom to the other area. Water resource helps reducing water temperature before using in the air conditioning system (Boonyatikan, 2002).

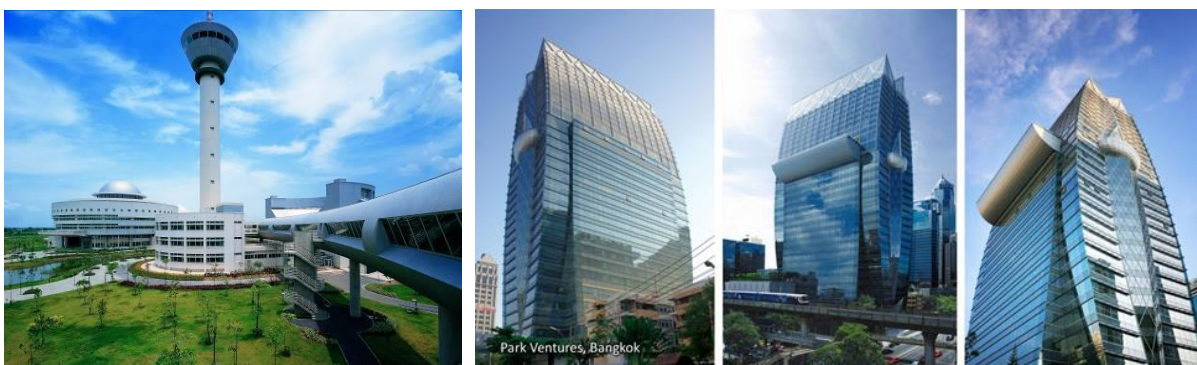


Figure 2: Shinawatra University (left) and Park Ventures (right)
Sources: Left - PR department (2017); Right: Univentures (2013)

3.2. Park Ventures: the Ecoplex – representing the second wave

Park Ventures is a mix-use commercial building consisting of A-grade offices and a 6-star hotel, “Okura”, at the top with total 81,440 m² floor area on 9,000 m² site area. The construction cost approximately 5,000 million Baht (equivalent to AUD\$150 Million in 2012). The project was completed in February 2010 and designed by Palmer and Turners (Thailand) Ltd. (see Figure 1).

Key sustainability strategies are most significant and Park Ventures was the first LEED Platinum building in Thailand in 2012 (see Figure 2 - right). The eco-complex building results from 25% green areas, 63% water resource reduction and 25% energy conservation. Green design strategies also include high quality technologies during the operations such as hi-speed elevator, personal IEQ control and Building Automatic System (BAS). There were several awards for the project, including ASEAN Energy Awards 2013 (1st runner-up Energy Efficient Building - New and Existing category), Thailand Energy Awards 2013-2014, and ASIA PACIFIC Awards 2011, Best Mixed-Use Architecture of Asia Pacific, and of Thailand. The design process was developed based on LEED Platinum approach from the beginning (Na-Ranong, 2012). The design and energy consultant teams negotiated for a compromised option.

Design development is for ultimate eco-friendly design concept proposed requires compromising between marketing a regional landmark and green design (Na-Ranong, 2012). The building shape represents the respect by Thai greeting gesture and the diamond pattern on the top of the building is simplified from a lotus to represent hospitality with warm welcome. Although the building form is beneficial for the energy conservation, the 100% view does not play the same role. Longitudinal elevation of the building is designed to face north-south orientation to acquire less heat. The low-E double glassing is also the essential technique for energy consumption approach. LEED Platinum. Energy consumption design and eco materials requirement were the most difficult method during the pre-construction process. Back in 2010, ‘LEED’ as green rating assessment was very new in Thailand. To receive “Platinum” level from LEED was a great challenge. The building is required to present better energy efficiency than the minimum requirement as in the base-case set by ASHRAE which was already above average green building standard in Thailand. The air-conditioning system requires high energy efficiency and non-CFC refrigerator. Eco-friendly construction-finishing materials and furniture were also hardly released in Thailand in 2010. Such HVAC system and most certified green materials and eco-friendly furniture were imported from oversea. The challenge effected on the point of the use of local material. Consequently, the additional construction cost was proposed to achieve the challenge (Norachai Akrapipatkul, interviewed on 24th April 2016).

Key lessons are 1) Eco-friendly design requires collaboration between owners, architects, engineers, and consultants from the pre-construction period; 2) High performance energy efficiency not only requires high technology and innovative systems, but also accomplishes by a great maintenance plan; 3) To achieve 100% working area virtual comfort, the design needs to compromise between natural light, scenery view and heat conduction through windows; 4) Eco-friendly materials and low-VOC furniture were used following LEED Platinum requirement, even though they were imported from oversea; and 5) The design and construction cost were increased to achieve LEED Platinum certification.

3.3. Panyaden International School – representing the third wave

The Panyaden International primary school project has 375 students and is located in Chiang Mai, Thailand. The buildings were built from rammed earth, adobe bricks, clay and treated bamboo. The project size is 5,000 m² floor area on approximately 3,000 m² site area at the initiated period, costing over 100 Million Baht (equivalent to AUD\$3.13 Million in 2012) and completed in April 2012. The project was designed by 24H Architecture (2012) and Chiangmai Life Construction (CLC), Co., Ltd. (2012)

The key sustainable strategy was that it was built using sustainable and environmentally-friendly ideas which were adopted from architectural design through to curriculum and resource management. The entire school has been built from local earth and local bamboo which was naturally treated. The main lesson of the curriculum is how to live an environmentally mindful life with a low carbon footprint. The campus consumes energy only for lighting and fans on some days in summer. Their awards are ‘Grand Award in the Overall Category’; ‘Gold Award for sustainable at the 2012 design for Asia awards, Business of Design Week, Hong Kong’; and ‘IDEA-TOPS Award for Green Architecture, International Space Design Award 2017, Shenzhen’ (Chiangmai Life Construction, 2012).

Strategy 1: Holistic environmentally-friendly concept. Most of the construction materials in the buildings are from nature and waste. The rammed earth is made from cement and local clay. Adobe is made from clay, dried rice straw and other agricultural waste in the school. Roof material is treated bamboo, which was cut and left several months before treating to remove sugar from the bamboo membrane. Glass windows framed by recycled local hardwood, glass bottles and washing machine windows bring natural light into the classrooms. Cupboards and shelves are all integrated in an adobe wall curving around the sanitary block. Strategy 2: Energy efficiency. Main buildings have three classrooms. Passive cooling design techniques are used for thermal comfort. Long eaves are

designed to reduce direct heat and glare through the classrooms. They also shield the classrooms' corridors around the building from rain. A light weight bamboo roof structure is a local wisdom for the ASEAN region. Strategy 3: Comfort approach. All classroom buildings are rammed earth wall with adobe finishing. The 30 cm thick wall is a great insulator for both thermal and acoustic comfort. During summer and winter, rammed earth walls are efficiently use their high thermal mass effect. This evens out daily temperature variations and alleviates the need for air conditioning and heating. During a learning session, a mass wall insulates noise disruption between classrooms. Additionally, the bamboo roof structure installed on the top of the 2.5 m rammed earth wall is separated from the mass wall. It allows ventilation through the top of the classroom, both across and along-side of the building. This technique can remove heat collected in the space from the classroom level (24H architecture, 2012).



Figure 3: Panyaden International School Hall – 1st hall damaged by flood in 2017 (left) and gymnasium hall (right)
Sources: Left – the Author, 24 April 2016; Right - Chiangmai Life Construction (2012)

The school's design and construction process consisted of an informal arrangement of pavilions (salas), organized along pathways inspired by the shape of the tropical antler horn fern. This original design has since evolved organically to its final form which is still in keeping with its original purpose of creating buildings from earth's elements and shapes that are an ode to nature's beauty. The classroom pavilions have load-bearing walls from rammed earth, dividing the building into 3 classrooms. The outer walls are made of adobe. The bearing-wall is a base of the bamboo roof. The curved contours of the bamboo roof structure mirror the mountains at the horizon of the site (Markus Roselleb, interviewed on 11th February 2016).

Post construction, the school has inspired so many projects. During the construction, the owner had become the expert for bamboo construction, forming Chiangmai Life Construction (CLC) firm (Chiangmai Life Construction, 2012). Many local architects and builders have been inspired and adopted the advanced passive cooling techniques in their vernacular projects. Energy consumption during operation is very low since only lighting system is a main energy consumption.

However, adobe wall is built from clay which could be softened by water. The school site is located in the valley next to the mountain, similar to Chiangmai city. Even so, it had never flooded but during the rainy season in 2017, the site was flooded. Many adobe walls were damaged and the school was closed for 6 months for renovation.

Key lessons of holistic sustainable concepts has been presented integrally from architectural design to children's activities in the school curriculum. Local materials have been used sustainably with new construction techniques in a new form. High performance energy efficiency is achieved by using passive design techniques, including incorporating local wisdom. The multipurpose pavilion type is used for common functions such as the assembly hall and the canteen. Columns consist of bamboo bundles reaching up to the bamboo canopy from their stone foundations give a feeling of walking through a majestic bamboo forest.

Other pavilions designed and created by the local team (playground, around the swimming pool, Buddha pavilion etc) resemble birds or leaves – elements found in nature and in daily Thai life (such as the paper umbrellas made in Chiang Mai). The entire school has been built from local earth and local bamboo that has been naturally treated to withstand the elements. Organic vegetables and rice will be grown on school property. The students will be the ambassadors to introduce green living into the lives of their communities. In addition to the Thai and native English-speaking teachers, they will be supervised by experts in various arts, creativity as well as traditional wisdom such as local agricultural methods, specialists in tropical forest plants, cloth weaving and northern cuisine etc. Panyaden School aims to deliver a holistic education that integrates Buddhist principles and green awareness with the highly regarded, International Primary Curriculum (Panyaden International School, 2012).

3.4. SCG 100th Years – the fifth wave

The SCG Company's headquarters office building, 74,605 m² construction area across 2 buildings, consist of a 22-story office building and 10-story seminar function building. Total landscape area was 25,000 m² and total cost was 3,300 Million Baht (equivalent to AUD\$111 Million in 2013), completed in 2013 and designed by Design 103. International Ltd (SCG 2013).

Key sustainability strategies are 'eco-friendly design' as the main concept. All SCG advanced eco-friendly materials are used in the building to be a role model in sustainability. The building is high performance with high efficiency techniques in energy controlling, air-conditioning, and water systems with 32.45% energy conservation and 60% water supply reduction. Healthy-lifestyle function is also provided in the building, including more than 50% green space of all open space area. It was awarded several honours such as 'LEED Platinum certification in Design and Construction' in 2014; 'Asia Pacific Property Awards 2015 "Highly Commended" Commercial High-Rise Architecture, Thailand'; 'ASEAN Energy Awards' 2015 - 1st Runner-up: Green Building; 'Thailand Energy Awards' 2015 - Excellence in New and Existing Building Category and Green Building Category; and 'BCI Asia Top 10 Architects Awards' 2013 – Thailand (SCG, 2013).

During construction, SCG found that there were several issues the company should develop to be holistically sustainable. One of the issues is SCG does not have contraction business. For example, SCG has started developing some new construction products for the whole eco house style. 'SCG heim' is a house with ultimate healthy living. The users shall get 4 main concepts: healthy live without dust, fungi and bacteria; absolute relaxation with thermal and sound insulated system; highest safety and confidence; and lifetime worry free with 6 times free check-up during 20 years (Anont Bukkanasuta, interviewed on 29th April 2016)

First strategy is energy efficiency. The building envelope is designed for energy saving. With 25 W/sq.m overall thermal transfer value (OTTV), the building consumes 32.45% energy conservation compared to the ASHRAE standard. The 84 kW solar PV cell can produce 99,000 kWh/ year energy, equivalent to 1.83% of overall energy consumption. Second strategy is Eco-materials. SCG, as the biggest construction material supplier in Thailand, used as many own eco-products as possible from 100 available 'SCG eco-value' products, consequently more than 80% of construction materials were locally-sourced. More than 50% of wooden materials are from the forest management certification products, certified by the Forest Stewardship Council (FSC). Waste from construction process can be recycled in the SCG eco-product. Therefore, the waste can be reduced by up to 90%. Strategy 3: Eco-life quality. The building is environmentally-friendly designed for occupants. CO₂ is maintained lower than 600 ppm at all time from the automatic air to air exchanger system to provide healthy air in the working space. It is 30% better quality than the ASHRAE 62.1-2007 standard. Strategy 4: Water resources management. Water resources are used to maximum benefit through water-saving toilet equipment. The sanitary system is designed for 33% water utility reduction, using 100% water saving eco-value sanitary wares, such as a 2.5/4 litres toilet and water sensing faucet. Recycled wastewater is reused in the toilet and for 100% of landscape watering. Strategy 5: Smart innovative system. Destination Control Elevator is installed in the building using regenerative elevator drive technique to reduce energy used in elevator's moving. It is connected to the building security through the flap gate personal control system (Praput Ponglaohapan, 2014).

Post-construction, some building performance aspects have been better than expected. For example, water supply used during operation shows a 75% reduction which is approximately 15% better than expectation in 2014. Overall personal transportation is also lower than expected since there are several convenient options such as train and bike. Transportation is not necessary anymore for meetings due to video conference communication. It not only saves energy, but most importantly saves time in Bangkok's traffic congestion (Jakkasin Noirairoom, 2015).

Key lessons of this project are 1) Eco-materials used, the building is the successful case for using local eco commercial products. The recycled waste management is also excellent. 90% of construction waste materials had been recycled for another process. Although it is a different green approach from Panyaden, the goal for sustainability is similar. 2) Eco living. SCG has received many socially responsible awards. It is not surprising when several healthy functions are provided in the buildings (see Figure 4). However, the daily eco lifestyle has not been confirmed holistically yet. All exercise functions are still outdoor. 3) Lifelong learning company. SCG is very open-minded to learn new things. SCG 100th year was the company's first construction management project. They had to control many sub-contractors to meet the standard and installation quality. Although the company still insists it does not cover contract business, it has started developing new eco-products to complete the whole large project since then (Anont Bukkanasuta, interviewed on 29th April 2016).



Figure 4: SCG 100th Year building (left), landscape design for healthy lifestyle (top right) and solar roof top (bottom right)
Sources: TK-Studio (2013).

3.5. Phi Suea House Project – the Sixth wave

It is the world's first solar and hydrogen powered multi-house residence, totalling 27,424 m², with 744 m² main house living space, 55 m² main kitchen with 138 m² wood terrace, 25m long swimming pool, and 903 m³ water reserve tank. The project is a private house designed by CNX Construction Ltd, completed in January 2016. Construction costs are not known due to confidentiality reasons. Phi Suea House adopted high technology for high efficiency. It is the first project in the world that combines solar energy and Hydrogen energy storage together. The stand-alone project can be 100% off-grid. Most of the time, the project can produce electricity to the grid (Cowan, V. and Berow, E. R., 2016).



Section shown South facing solar cell

Figure 5: Phi-Suea House's orientation design (left), Phi-Suea House with solar roof (middle), Phi-Suea House's Hydrogen battery system (top right) and the underground cooling water system for Hydrogen energy management process (bottom right)

Sources: Cowan, V. and Berow, E. R. (2016).

The design process was developed from the lowest energy demand and ecological footprint, designed with sustainability and functional design. They believe that it is the answer to energy needs of the future, and is the solution to storing energy in the most effective and ecological way (see Figure 1 & 5). Green energy approach: The system is the ultimate green energy storage, ideally suited for residential buildings in remote locations. Its modular concept can be adapted to numerous different situations, where complete independence from the grid is desired. Eco design development: the motivation is purely philanthropic: "Everyone should do something to live in a better world. Our family is now doing our part – leaving the world a greener place while gaining and sharing knowledge. This is without a doubt worth all efforts. We aim to have the lowest ecological footprint possible – especially as a foreigner in another country." (Jan-Justus Schmidt, interviewed on 28th April 2016).

Construction process: The biggest challenge of the project was the quality of the construction. The contractor, CNX construction, was hired for the project. They were formed in 2014 to meet the German standard required by the owner. All local staff and labour were required to train and learn about the German construction standards and understand how to meet the standards. Some construction techniques were tested on-site before installation. For example, several techniques were tested to finish the perfect flat wall. The 6-meter high sliding door in the main house is very heavy and its frame and frame roller required replacement for an aeroplane standard.

High efficiency technologies of the project include PV INSTALLED: 86 kW, average daily power production: 326.8 kWh, solar panels installed: 287 panels (128x 315W, 75 x 330W, 84 x 250W), estimated energy demand: 6000 kWh monthly, peak load during the day: 30kW, hot water - integrated into the solar panel roof (no electricity needed), hybrid energy storage - hydrogen / battery with 2x 2000Ah lead-acid battery banks, 96kWh (48kWh at 50% DOD) nominal capacity per battery bank, 8kW electrolyser maximum power demand, maximum 2000 litres/hr Hydrogen gas production rate with 90,000 litres of H₂ at 30 bar of Hydrogen Energy Storage capacity. The fuel cell power output is between 4kW and 130kWh at full storage (Schmidt, J.-J., 2017).

Key lessons for this project were that to initiate the innovation required a huge effort from both the initiator and staff, high-end technology required a well-thought-out plan and considerable budget to be successful. High performance energy efficiency not only requires high technology and innovative systems, but must also be met with a great management plan for construction and operation.

4. CONCLUSION AND KNOWLEDGE GAPS

Thailand has seen several occasions using many sustainable techniques with most building types. However, the big challenge of sustainability is religious buildings and government buildings. Even the energy conservation act and any promotion of green labels are not applicable for these buildings. Although most religious buildings in Thailand are Buddhism pavilion consuming almost zero energy, the government buildings do not. Only a large or a mega project would agree to be a sustainable building. Government buildings cover a variety of scales including Subdistrict – District - Provincial Administrative Organisation, K-12 school classroom, university buildings, up to the whole Ministry.

The opportunity in this situation is the government subsidisation. Sustainability is not only a trend; it has become a task for national and SDG's UN (UN knowledge platform, 2016) driven strategies. The government has started supporting and subsidising the sustainable project. For example, the office of Electricity Generating Authority of Thailand as a public-private partnership has developed a sustainable building, receiving LEED-gold in 2010. The Provincial Electricity Authority projects have also been moving forward for sustainability. Smart city and Thailand 4.0 policies have been subsidised in many projects in 2018. The Thailand smart city clean energy competition was launched in 2017 and awarded to top seven-smart city protocol from over 30 components. The Ministry of Energy has supported 10 million Baht (equivalent to \$US) per city for developing their infrastructure development (DEPA, 2016). A bigger change and a better future for sustainability in Thailand shall be more significant in a near future.

Table 1: Case studies comparison of the green movement in Thailand

Green movement	Project [year]	Significant factor	Strategies	Energy efficiency	SDG,s
1 st wave	Shinawatra University (SIU) [2002]	The 1 st official project concerning about sustainability in Thailand	• Reuses cool air from the classroom to chill the corridor.	N/A	• 4,6,7,12,13
2 nd wave	<ul style="list-style-type: none"> • Park Ventures [2012] [LEED-Platinum 2010] • Energy Complex Building [LEED-Platinum 2014] 	<ul style="list-style-type: none"> • The 1st LEED platinum in Thailand • The 2nd LEED platinum 	<ul style="list-style-type: none"> • Follow LEED Platinum criteria, both projects need to be at least 25% saving energy 	<ul style="list-style-type: none"> • 25% green area • 63% water resource reduction • 25% energy conservation. 	• 6,7,11,13

Green movement	Project [year]	Significant factor	Strategies	Energy efficiency	SDG,s
3 rd wave	Panyaden International School	Comprehensive sustainable and environmentally friendly idea, including physical environment and curriculum.	<ul style="list-style-type: none"> Holistic environmentally friendly concept with local materials (bamboo and adobe wall) No air-conditioner 	<ul style="list-style-type: none"> Almost zero electricity consumption (only consumed for lighting and fans in summer) 	• 3,4,11,12
4 th wave	SCG 100 th Years	Holistic 'Eco-friendly design'	<ul style="list-style-type: none"> Eco materials used more than 80% of construction materials were from local. >50% of wooden materials are from the forest management certification products, certified by the Forest Stewardship Council (FSC). 	<ul style="list-style-type: none"> 32% energy conservation compared to the ASHRAE standard. The 84 kW solar PV cell can produce 99,00 kWh/year energy equivalent to 1.83% of overall energy consumption 	• 3,6,7,11,12,13
5 th wave	Phi Suea House Project	The world's first solar and hydrogen powered multi-house residence	<ul style="list-style-type: none"> The lowest energy demand and ecological footprint A stand-alone prototype in term of electricity consumption without external grid electricity 	<ul style="list-style-type: none"> PV INSTALLED: 86 kW, average daily power production: 326.8 kWh Solar panels installed: 287 panels (128x 315W, 75x 330W, 84 x 250W) estimated energy demand: 6000 kWh monthly, 	• 9,12,13

5. SCOPE AND LIMITATION

Many sustainable projects in Thailand were contacted, but not all of them replied nor agreed to participate. These five projects are the best sustainable showcase with agreement among all available information. In some cases, plans of the building were not consented to be published for privacy reason.

6. ACKNOWLEDGEMENT

This study had conducted the in-depth interview from several key speakers. The following names and affiliation would be appreciated on behalf of the author.

- Shinawatra University – Information and Social Communication Unit, Shinawatra University.
- Park Ventures - Mr. Norachai Akrapipatkul, Corporate Communication at Univenture Ltd. And Palmer and Turners (Thailand) Ltd.
- Panyaden International School - Markus Roselieb, M.D., Chiangmai Life Construction, Co. Ltd.
- SCG 100th Year head quarter office – Mr. Anont Buknasuta and Ms. Nantana Onteanchai, Siam Cement Group PCL and SCG 100th year building.
- Phi Suea House - Mr. Sebastian-Justus Schmidt, Initiator, Project Owner. Mr. Jan-Justus Schmidt, Project Lead, Energy Storage and Automation, CNX Construction Co., Ltd. and Mr. Karn Nattapong, Managing Director, CNX Construction Co., Ltd.

7. REFERENCES

Boonyatikan, S. 2002. Energy Conservation Building, in Energy report series 38: Building Features. Bangkok: Ministry of Energy.

Chiangmai Life Construction. 2012. Panyaden School Assembly & Indoor Sports Hall, retrieved on 3rd December 2018 at <https://www.bamboo-earth-architecture-construction.com/>

Cowan, V. and Berow, E. R., 2016. Phi Suea House Project: Solar Hydrogen Multi-house Residence, Media Coverage Report, Chiangmai: CNX Construction

DEPA. 2016. Thailand smart city, Department of Digital Economic Promotion Agency, Ministry of Digital Economy and Society.

Energy Conservation Promotion Act B.E. 2535. 1995., Department of Alternative Energy Development and Energy Conservation, Ministry of Energy.

Energy Conservation Promotion Act (No.2) B.E. 2550. 2007. Department of Alternative Energy Development and Energy Conservation, Ministry of Energy.

Horayangkura, V., et. al, 2017. In *Revealing Modern Thai Architectural Identity*. Bangkok: Thammasat University Publisher and Thailand Research.

Jakkasin Noiraipoom, 2015. SCG 100th year building, *ASA Journal*, issue 05, 20-25.

Na-Ranong, O. (editor-at-large). 2012. *Park Ventures' Documentary Book*, Bangkok: Univentures Public Company Limited, pp 44-72.

P-Landscape, 2013. Gallery, Mixed-use, Park Ventures and Okura Hotel, Bangkok, retrieved on 3rd December 2018 at <http://www.plandscape.com/work/highlight>

Palmer&Turner, 2011. Mixed-use, Park Ventures, Bangkok, retrieved on 3 December 2018 at <http://www.p-t-group.com/park-ventures1.html>

Panyaden International School, 2012. Campus, Green architecture, Retrieved on 3rd December 2018 at <https://www.panyaden.ac.th/>

Personal Representative Department. 2017. Semi-structure interviewed, Shinawatra University. Interviewed on 2 February 2018.

Praput Ponglaohapan, 2014. SCG 100th year: The building with technology and LEED, in MITR 45th year. Retrieved on 3rd December 2018 at <https://www.mitr.com/mitr-article.php?cid=167&hl=th>

Schmidt, J.-J. 2017. Phi Suea House Project: World's First Solar and Hydrogen Powered Multi-House Residence, International High-Performance Built Environment Conference – A Sustainable Built Environment Conference 2016 Series (SBE16), iHBE 2016, *Procedia Engineering*, Volume 180, pp 183-197.

SCG, 2013. *SCG 100 years of Innovations for Sustainability*, 1st edition, Bangkok: Sirivatana Interprint.

TK-Studio, 2013. Library, Corporate, SCG 100 year, retrieved on 3rd December 2018 at <http://www.tkstudio.co.th/library/18>

UN knowledge platform. (2016). *Sustainable Development Goals. The 2030 Agenda for Sustainable, United Development of Economic and Social Affairs*, United Nation.

Univentures, 2013. *Park Venture: the Ecoplex on Witthayu*. Bangkok: Univenture, retrieved on 3 December 2018 at <http://www.park-ventures.com/home/>

24H architecture, 2012. Panyaden School, natrified architecture, learn, retrieved on 3rd December 2018 at <http://www.natrified.nl/learn/panyaden-school/>

#259: Fabrication and testing of a low cost passive solar dryer

Mohsin KHAN¹, Namrata SENGAR², Sunita MAHAVAR³

^{1,3} Department of Physics, University of Rajasthan, Jaipur 302004 India, mkmohsin850@gmail.com, smjpr1986@gmail.com

² Department of Pure and Applied Physics, University of Kota, Kota 324005, India, namrata@uok.ac.in

Solar energy is a renewable and sustainable source of power for many low to high thermal applications viz. water heating, cooking, drying, power generation, cooling etc. Worldwide, the energy consumption of agriculture drying industries is considerably high but could be reduced through prudent use of solar energy, particularly in countries blessed with abundant solar energy throughout the year like India. The conventional drying process using fossil fuels has a negative impact on the environment and it is expensive too while the solar dryer is much cheaper with no harmful effects on the environment. It is estimated that removing moisture from food from 80% to 10% can prevent product wastage and growth of bacteria, yeast, mold and enzymes. Considering the importance of agriculture drying, a solar dryer was made and tested. This paper presents fabrication details and experimental study of solar dryer for its application of ginger drying. The designed system was installed and tested at the Department of Pure and Applied Physics, University of Kota. The solar dryer was a cabinet type dryer having a base of 63.5cm x 134cm. Three major sets of experiments were carried out to study the performance parameters of the system. Temperature variations at various sections in the device were measured on a number of days. In the first experiment specific amount of ginger were dried and studied. The comparative studies of open sun drying and in the solar dryer were carried out in the second experiment. The full load capacity test was done as a third set of experiments. The solar dryer, fabricated with locally available materials (plywood, G.I. sheet, polystyrene sheet) was an economically affordable system for domestic industries with the drying capacity of 5 kg of agriculture products. The thermal efficiency of a full load system was found to be 29.1%. An experimental study showed that, on the first day, 45% of moisture was removed in the dryer while only 7.06% moisture was removed in open sun drying. The maximum drying rate was recorded on the first day of full load conditions i.e. 0.318 kg/h.

Keywords: solar energy; solar drying; ginger drying; thermal efficiency

1. INTRODUCTION

The world's population is increasing at an increasingly fast rate and demand for food is increasing continuously. With developments in agricultural technology, production of food is expanding to meet the demand (Islam et al, 2019). One of the problems faced by farmers is the post-harvest damage of the agriculture product due to moisture present in it. Moist conditions helps bacteria, yeast and mould to grow and damage the agriculture products. Solar drying is used to overcome such problems. Solar drying is a process for the preservation of food and it also adds higher value to the products. A solar dryer can achieve this result by supplying heat and reducing the relative humidity of the air (Srisittipokakun et al, 2012). The solar dryer is a device that is used to dry the agriculture products and eliminate product wastage. The drying involves the extracting of moisture from the product by heating. Drying is a dual process of (i) transferring heat to the product from the heating source (ii) transferring moisture from the inner part of the product to its surface and then evaporation to the surrounding air. In solar drying, the air flow can be generated by either natural or forced-convection. The process that occurs at the surface of the product is a simple evaporation. Through solar dryers a controlled drying process can be executed, and it also prevents the product from outer damage by animal, birds, insects, dust and rain which is a limitation of natural open-air drying.

The solar-energy drying systems can be classified as: (i) direct or integral type (ii) indirect or distributed type and (iii) mixed type of solar dryer. Indirect type solar dryers may be of two types: passive dryers (natural circulation) and active dryers (forced circulation). In passive dryers air is heated and circulated through the material naturally by buoyant force or as a result of wind pressure or a combination of both. In the forced circulation mode, heated air is circulated through the material using motorized fans or pumps (Mahavar, 2015). For last five decades different authors have developed different type of solar dryers. Fudholi (Fudholi et al, 2010) have presented a good review on construction of solar dryers. Ekechukwua and Norton (Ekechukwua & Norton, 1999) have presented a comprehensive review of the various designs, details of construction and operational principles of the wide variety of practically-realized designs of solar-energy drying systems reported previously. On the basis of type of dryer, drying item and efficiency of system a short review has been done and it is summarized in Table 1. The component details of a few system are presented in Table 2.

Table 1: Various type of dryers

Reference	Dryer (Type)	Food Product	Temperature (°C)	Efficiency (%)
Ayala et al, 2014	Hybrid dryer	Pineapple	50.8	9.3 – 14
Banout et al, 2011	Double pass solar dryer (Direct, forced convection)	Red chillies	54.5	15.22
Bennamoun et al, 2003	Solar batch dryer (Indirect, forced convection)	Onion	50	-
Bolaji, 2005	Solar air collector for crop drying (Indirect)	Maize	57 - 64	21 – 36
Eke et al, 2013	Small scale solar dryer (Direct, natural convection)	Tomato, okra, carrot	49.9 – 52.29	21.8 (tomato) 21.18 (carrot) 24.95 (okra)
Hamdaniet al, 2018	Hybrid solar-biomass dryer	Fishery	50	-
Islam et al, 2019	Induced, attic, natural	Apple, Banana, pineapple, Guava	-	-
Janjai et al, 2011	Solar greenhouse dryer (Direct)	Chilli, coffee, banana	60	-
Janjai et al, 2008	Roof –integrated solar dryer (Indirect, forced convection)	Rosella flower, chilli	70	-
Jairaja et al, 2009	Cabinet dryer, staircase dryer, glass roof dryer, foldable dryer, hybrid dryer	Grapes	-	-
Musembi et al, 2016	Updraft solar dryer (Indirect solar dryer)	Red apples	53.5	17.89
Ozuomba et al, 2013	Absorption solar dryer (Direct)	-	59	22.8
Shamekhi-Amiri et al, 2018	Indirect solar dryer	Lemon balm leaves	38 - 68	15 -52
Srisittipokakun et al, 2012	Parabolic-shaped solar tunnel dryer (Direct, forced convection)	Andrographispaniculata.	35 - 75	-

Table 2: Component details of different systems

Author	Food product	Absorber material	Insulation material	Dimension (cm ³)	Total Cost
Banout et al, 2011	Red chillies	G.I. sheet	Styrofoam	150x65x60	2700 USD (190000 INR)
Mwithiga & Kigo, 2006	Coffee	Mild steel	Block Board	100x80x30	-
Ozuomba et al, 2013	-	Aluminium sheet/ black leather	Wood	-	-

Table 1 reveals that the temperature found in these studies were in the range of 35 -75 °C and efficiencies in the range of 9.3 – 52%. It also concludes there are not many studies available concerning ginger drying. The component studied presented in Table 2 suggest a use of locally available material for designing the dryer.

Therefore, in the present work a low cost solar dryer for small domestic industries with easily available, low cost and scrap materials for ginger drying was fabricated and tested. The design of the system is not very different from the conventional system but the use of GI sheet as absorber, plywood as casing, polystyrene as insulation and single glass glazing reduced the cost of solar dryer considerably. The designed system was economically affordable for use in small domestic industries.

2. PASSIVE SOLAR DRYER

2.1 Fabrication details

The solar dryer was fabricated with locally available materials (plywood, G.I. sheet, polystyrene sheet etc.). It was a cabinet-type passive dryer having a base area of 63.5 x 134 cm². The side walls were inclined at 24° angles and the inclined wall length was 117cm. At the back side there was a chamber 110 x 21 x 27cm³ big on which a chimney (of PVC pipe) was fitted. The working of the solar dryer was as follow: the fresh outside air entered through the four air holes at the front of the system and was heated during its passage to the cabinet. The heated air rose through the drying trays in the drying chamber and left the chamber at the top through the exhaust chimney. For easy transportation of the device, 6 wheels were attached at the bottom providing ease in operation of the dryer. Inside the system two trays were inserted on which the food products were placed for drying. The dimensions of each tray were 56 x 51 cm². As these were made of wire mesh with a gap of 10mm between those, it limited the maximum load capacity to around 2.5 kg, so the load capacity of the device was about 5kg. Other details of system are summarised in Table 3. The dryer is shown in Figures 1 and 2.

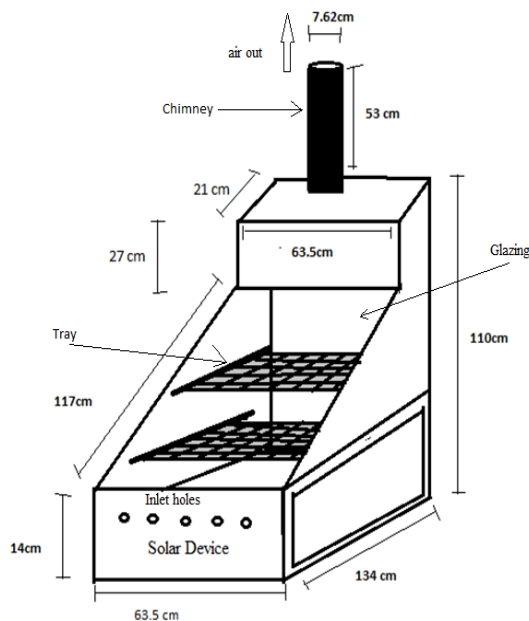


Figure 1: Schematic diagram of Solar Dryer system



Figure 2: Experimental set-up of the Passive Solar Dryer

Table 3: Various component details of system

S. No.	Parameters	Details
1.	Casing	
	(i) Dimension	134 x 110 x 63.5 cm ³
	(ii) Material	Plywood, GI sheet
	(iii) Thickness	1.2 cm (plywood), 0.064 cm/0.051 cm (GI sheet)
2.	Glaze	
	(i) No. Of Glaze	1
	(ii) Material	Extra clear glass
	(iii) Thickness	0.5 cm
3.	Insulation	
	(i) Material	Polystyrene sheet
	(ii) Thickness	2.6 cm
4.	Collector	
	(i) Material	GI sheet
	(ii) Dimension	0.064 cm width, 134 x 63.5 cm ²
5.	Chimney	
	(i) Material	PVC pipe
	(ii) Dimension	2.54 cm dia, 91.4 cm length

2.2 Thermal performance parameters

Thermal performance parameters were measured and computed for the present system (Sain, 2013). Here some parameters were used to carry out the study of the dryer. Efficiency of any device is very crucial to calculate. Moreover other studies like bone dry weight, specific energy consumption, moisture content of product, drying rate of dryer and dehydration ratio were calculated. Parameters used for these calculations are given in Table 4 while the results of these calculations are shown in Table 5 in a later section.

Table 4: Various thermal performance parameters

S. No.	Parameter	Equation
1.	Total quantity of water in product, M_{tw}	$W_g \times \left[\frac{M_i}{100} \right]$
2.	Bone dry weight of material, W_{bdm}	$W_g \times \left[1 - \left(\frac{M_i}{100} \right) \right]$
3.	Thermal Efficiency η	$\left[\frac{m_v L}{I_{av} A_{in} t} \right] \times 100$
4.	Specific energy consumption S	$\left[\frac{I_{av} A_{in} t}{m_v L} \right] \times \frac{1}{1000}$
5.	Moisture content	$M.C.(wb) \% = \left[\frac{(W_1 - W_2)}{W_1} \right] \times 100$ $M.C.(db) \% = \left[\frac{(W_1 - W_2)}{W_2} \right] \times 100$
6.	Drying rate(R)	$\frac{\Delta w}{\Delta t}$
7.	Dehydration ratio (R_d)	$\frac{w_1}{w_2}$

Nomenclature

A_{in}	Effective area of collector, (m^2)	T_{ch}	Temperature of air coming out of chimney, ($^{\circ}C$)
db	Dry basis	t	Time in second
I_{av}	Average solar radiation, (kW/m^2)	W_g	Weight of material, (kg)
L	Latent heat of water (for moisture) ,2230 J	w_1	Weight of sample before drying, (kg)
M_i	Initial moisture content, (%)	w_2	Weight of sample after drying, (kg)
m_v	Mass of moisture evaporated, (kg)	$W_{b,dm}$	Bone dry mass, (kg)
PSD	Passive solar dryer	wb	Wet basis
S	Specific energy consumption, (kJ/kg)	Δw	Weight loss of sample in a time period
T_a	Ambient temperature, ($^{\circ}C$)	Δt	Time period (h)
T_s	Surface temperature, ($^{\circ}C$)	η	Thermal efficiency, (%)
T_i	Temperature inside the HSD, ($^{\circ}C$)		

3. EXPERIMENTAL STUDY OF SOLAR DRYER

3.1 Setup

The solar dryer was fabricated and tested at the Department of Pure and Applied Physics, University of Kota (25.11° N, 75.82° E). To measure the temperature at various positions (surface of dryer, inside the dryer and at the exit of the chimney) thermocouples and a K-type thermometer of accuracy of $\pm(0.5\% \pm 1^{\circ}C)$ HTC company were used. Every hour, the temperature was recorded. The ambient temperature was measured using mercury thermometer. Solar insolation (W/m^2) was measured by using pyranometer (KIPP & ZONEN CMP3. company). An electronic weigh machine was used to measure the weight of the product. This was manufactured by KERRO and the model number was BL25000. The experimental set-up is shown below in Figure 3.



Figure 3: Ginger drying in Solar Dryer

3.2 Thermal profile

In the fabricated passive dryer Ginger was used as the drying item. Before being put into the dryer, the product was washed properly using water to remove the adhered dirt and then cleaned by cotton cloth smoothly. The thermal performance of the system was measured under two load conditions (i) with 1.5 kg and (ii) with 5 kg (full load). In the first experiment 1.5 kg of drying product was placed inside the dryer and at the same time, the same amount of product was placed for open sun drying. The temperature profile of PSD on the first day is shown in Figure 4 under 1.5 kg load condition. In another experiment, a full load study of the dryer was done with an amount of 5kg of ginger. Figure 5 depicts the temperature profile of solar dryer with full load i.e. 5kg on the first drying day. Figures 6 and 7 shows the temperature profile of the dryer's inner surface on successive drying days of food load with 1.5kg and 5kg of ginger respectively. The weight difference measured after drying of food products on different days is given in Table 5.

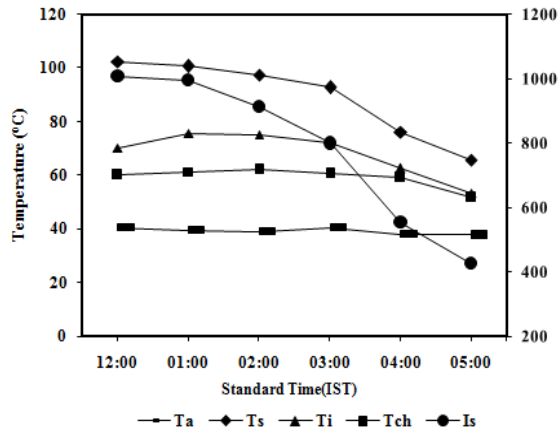


Figure 4: Thermal profile of solar dryer with 1.5 kg Ginger. (T_a , T_s , T_i and T_{ch} are ambient, surface, inside air and outgoing air temperatures, respectively, I_s is solar insolation, 30/03/2017)

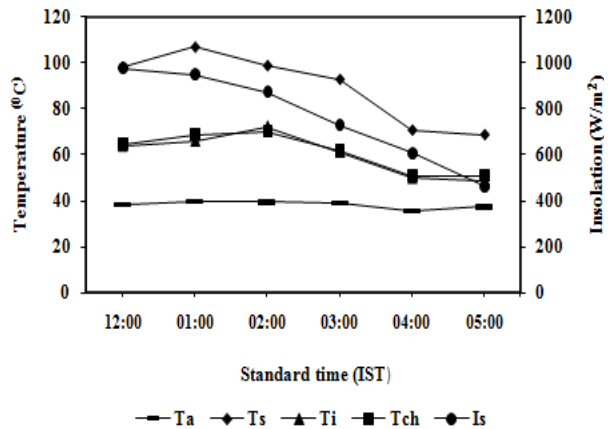


Figure 5: Thermal profile of solar dryer with 5.0 kg Ginger. (T_a , T_s , T_i and T_{ch} are ambient, surface, inside air and outgoing air temperatures, respectively, I_s is solar insolation, 05/04/2017)

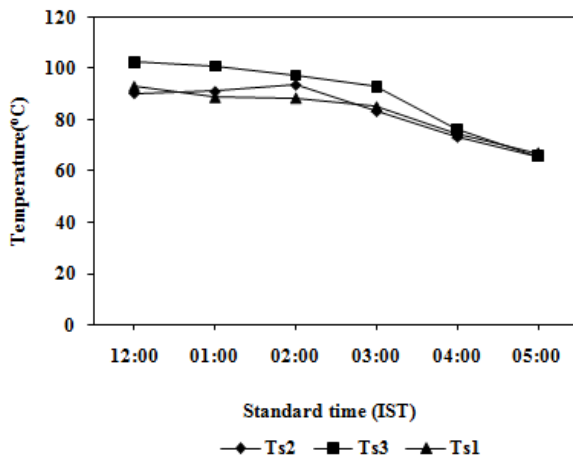


Figure 6: Temperature variation of inner surface of solar dryer (1.5 kg Ginger load) on successive drying days with Indian standard time. (T_{si} is surface temperature, subscript represents number of days, 30/03/2017 to 01/04/2017)

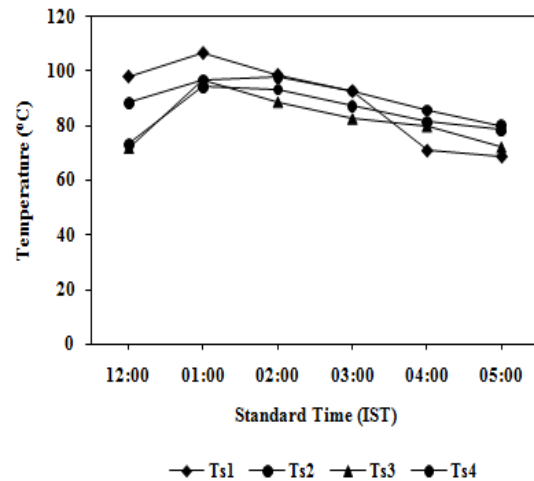


Figure 7: Temperature variation of inner surface of solar dryer (5 kg Ginger load) on successive drying days with Indian standard time. (T_{si} is surface temperature, subscript represents number of days, 05/04/2017 to 08/05/2017).

Table 5: Drying weight on successive drying days with different load condition

No. of days	Load amount in Passive Solar Dryer (kg)		Load amount in open sun drying (kg)
	1.5 kg	5.0 kg	
1	0.825	3.40	1.39
2	0.505	2.23	1.14
3	0.240	1.57	0.920
4	-	0.98	

4. RESULTS AND DISCUSSION

From Figures 4 and 5, the maximum surface temperatures of the PSD were observed to be 100°C and 110°C with 1.5 kg and 5 kg load, respectively. The inside air temperature remained around 70°C in both experiments. The maximum temperature of outlet air was found 70.2°C at the chimney exit in both experiments. Figures 6 and 7 show that in successive drying the surface temperatures remained around 100°C which is enough to sustain a good drying rate. The decrease in weight is reported in Table 5. The full drying of 1.5 kg load occurred in 3 days

while in open air drying the weight of Ginger remained 0.920 kg after 3 days. In four days successive drying for 20 hrs, the full load 5 kg of Ginger was dried to 0.980 kg. The maximum drying rate was 0.318 kg/h on the first day of full load, this rate decreases on successive days. The different parameters presented in Table 4 are computed using the thermal profiles of section 3. These are mentioned in Table 6. The thermal efficiency for the full load condition was observed in the range of 29.11%. Thermal efficiency can be varied according to the product as the above study has been done on fresh ginger without slicing it. The component costs of PSD are given in Table 7. The cost of the device was maintained to a minimum. The approximate cost of the dryer was INR 8610. The dryer was economic for small domestic industries due to its low cost. The materials used in the dryer have low cost and were easy availability on the market eg the G.I sheet, commercial plywood, PVC pipe etc. Insulation (Polystyrene sheet) used were retrieved from scrap and had no cost. As for the project's future aspects, some additions and study will be ongoing to use the device as a solar cooker too. The main focus is to modify it into a hybrid device so that can be use as solar dryer, solar cooker and as a solar water heater.

Table 6: Various thermal performance parameters

Parameters	Total quantity of product (in grams)	Total quantity of water in product (in grams)	Bone dry weight of material, W_{pdm} (in grams)	Thermal Efficiency η , %	Specific energy consumption, S (kJ/kg)	Moisture content, %	Drying rate (kg/h)	Dehydration ratio
Exp. 1	1500	1260	240	24.13	9.35	84	0.084	6.4
Exp. 2	5000	4020	980	29.11	7.75	80.4	0.201	5.1

Table 7: Cost of different components of PSD

S. No.	Item	Quantity	Rate (INR/quantity)	Approx. cost in INR
1.	GI sheet	30 kg	100	3000
2.	Plywood	40 sq. feet	90	3600
3.	Extra clear glass	10 feet	100	1000
4.	Wheels (6 wheel drive)	6 numbers	60	360
5.	PVC pipe	5 feet	10	50
6.	Transportation	-	-	500
7.	Polystyrene sheet	50 sq. feet	0	0
8.	Miscellaneous			100
Total cost				8610

5. CONCLUSION

Drying is one of the oldest methods using solar energy where products such as vegetables, fruits, fish, and meat are dried by direct exposure to the sun. This method is economical for large scale drying because of cheaper operating costs compared to the drying machine. A passive solar dryer was fabricated and tested for Ginger drying. According to full load test, drying of ginger could be done into 4 days. The thermal efficiency of full load system was obtained to be 29.1%. Experimental study shows that 45% of moisture was removed in the dryer while only 7.06% moisture was removed in open sun drying on the first day. The maximum drying rate was recorded on the first day of full load condition. i.e. 0.318 kg/h. The fabricated dryer is also economic for small domestic industries.

ACKNOWLEDGEMENT

Authors are thankful to University of Kota to provide Experimental facility.

6. REFERENCES

Ayala, D.G., Calderón-Topete, Á. 2014. Pineapple drying using a new solar hybrid dryer, Energy Procedia 57, 1642 – 1650

- Bolaji, B.O. 2005. Development and Performance evaluation of a box type Absorber solar air collector for crop drying. *Journal of food technology*, 3 (4), 595-600.
- Banout, J., Ehla, P., Havlik, J., Lojka, B., Polesny, Z., Verner, V. 2011. Design and performance evaluation of a Double-pass solar dryer for drying of red chilli (*Capsicum annum L.*). *Solar Energy*, 85, 506–515.
- Bennamoun, L., Belhamri, A. 2003. Design and simulation of a solar dryer for agriculture products.. *Journal of Food Engineering*, 59, 259–266.
- Eke, Akachukwu, b. 2013. Development of Small Scale Direct Mode Natural Convection Solar Dryer for Tomato, Okra and Carrot. *International Journal of Engineering and Technology* Volume 3 No. 2.
- Ekechukwua, O.V., Norton, B. 1999. Review of solar-energy drying systems II: an overview of solar drying technology. *Energy Conversion & Management*, 40, 615-655.
- Fudholi, A., Sopian, K., Ruslan, M.H., Alghoul, M.A., Sulaiman, M.Y. 2010. Review of solar dryer for agricultural and marine products. *Renewable and Sustainable Energy Reviews*, 14, 1-30.
- Hamdani, Rizal, T.A., Muhammad, Z. 2018. Fabrication and testing of hybrid solar-biomass dryer for drying fish. Case study in thermal engineering, 12, 489-496.
- Islam, M.,Islam,Md.,Tusar,M.,Limon, A. H. 2019. Effect of cover design on moisture removal rate of a cabinet type solar dryer for food drying application. *Energy procedia*, 160, 769-776.
- Janjai, S., Intawee, P., Kaewkiew, j., Sritus, C., Khamvongsa, v. 2011. A large scale solar greenhouse dryer using polycarbonate cover: Modelling and testing in a tropical environment of Lao people's Democratic Republic. *Renewable energy*, 36, 1053-1062.
- Jairaja, K.S., Singhb, S.P., Srikanta, K. 2009. A review of solar dryers developed for grape drying. *Solar Energy*, 83, 1698–1712.
- Janjai, S., Srisittipokakun, N., Bala, B.K. 2008. Experimental and Modelling Performance of a roof-integrated solar drying systemfor drying herbs and spices. *Energy*, 33, 91-103.
- Mahavar S. 2015. Review of Materials Used in Various Solar Thermal Appliances. *Solar Engineering-I (Applications)* Vol. 5 Ch.6. Editors: Dr. Sri Sivakumar,Dr. Umesh Chandra Sharma &Dr. Ram Prasad, Studium Press LLC, USA.
- Musembia, M. N., Kiptoob, K. S., Yuichic, N. 2016. Design and Analysis of Solar Dryer for Mid-Latitude Region. *Energy Procedia*, 100, 98 – 110.
- Mwithiga. G., Kigo. S. N., 2006. Performance of a solar dryer with limited sun tracking capability. *Journal of Food engineering*, 247-252.
- Ozuomba, J. O., Okonkwo, N. A., Uzor, B.C., Uba, J. I. 2013. Fabrication and characterization of a direct absorption solar dryer. *Advances in Applied Science Research*, 4(3), 186-194.
- Srisittipokakun,N.,Kirdsiria, K., Kaewkhao, J.2012. Solar drying of *Andrographispaniculata* using a parabolic-shaped solar tunnel dryer. *Procedia Engineering*, 32, 839 – 846.
- Shamekhi-Amiria,S.,Tahereh B. Gorjia, B., Gorji-Bandpya,M.,Jahanshahi., Md. 2018.Drying behaviour of lemon balm leaves in an indirect double-passpacked bed forced convection solar dryer system. Case study in thermal engineering, 12, 677-686.
- Sain. P. 2013. Design and development of a natural convection type solar dryer with thermal storage. A Dissertation submitted in partial fulfilment for the award of the Degree of Master of Technology in Renewable energy, Rajasthan Technical University.

#260: Experimental study of a building integrated solar water heater

Sunita MAHAVAR¹, Ankit GOYAL²

¹Department of Physics, University of Rajasthan, Jaipur 302004, India, smjpr1986@gmail.com

²Department of Physics, University of Rajasthan, Jaipur 302004, India, ankit17goyal@gmail.com

Solar thermal technologies have a special relevance for countries which have a scarcity of conventional fuel resources but have good solar potential i.e. radiation about 4.5-6 kWh/m²/day with an average of 280 clear days. A judicious use of solar energy for water heating and cooking can cut down conventional fuel consumption and can solve the problems related to economy, ecology, environment, air pollution global warming and public health arising due to currently-used fuel. Among various solar thermal appliances solar water heating systems have reached technical maturity and are used in many countries. But still domestic solar water heaters are not in the range of purchasing capacity of the mass population of developing countries like India. It is estimated in different studies that building integrated solar thermal systems have become 40% less expensive than conventional solar thermal installations. Therefore, this present study focused on the development of building an integrated solar thermal system. An experimental study of a building integrated solar water heater has been performed and presented in this paper. Due to building integration, water heating systems are highly weather resistant. The experiments were conducted at the University of Rajasthan, Jaipur, over a number of days. In these experiments, the solar radiation intensity (I_s) on a horizontal surface was measured using a pyranometer and temperature of inlet (T_{in}), outlet (T_{out}) and ambient (T_a) were measured through temperature data logger. The measurements of temperatures were carried out on clear sunny days for the duration of 10:00 to 14:00 Indian Standard Time (IST) with single and double poly (methyl methacrylate) (PMMA) glaze sheet. The maximum outlet water temperature obtained was 74°C in open and closed loop testing. The poly (methyl methacrylate) (PMMA) as glaze is found to be the promising option to increase efficiency and durability of solar water heater.

Keywords: Solar thermal system; building integrated; water heater; glaze

1. INTRODUCTION

The solar energy is an important alternative energy source which provide clean and green energy. It can be considered as a blessing for the countries having good solar potential i.e. radiation about 4.5-6 kWh/m²/day with average 280 clear days (Mahavar et al, 2015a). In all nations, a major share of total energy consumption is utilised by the household sector for water heating and cooking purpose. This household energy consumption is expected to increase in the future along with the economic growth and changes in lifestyles of the citizens of the developing nations (Mahavar et al, 2012, Mahavar et al, 2015b, Sukhatme, 2007, Mahavar et al, 2011). A well-designed solar water heater can overcome water heating fuel consumption problems. It can collect, store and utilise the solar radiation to heat the water using flat plate collector. The basic components of solar water heater (SWH) are: collector (absorber tray), water storage tank, insulation, transparent cover (glaze) and connecting pipes.

It can be used as an open and closed loop system. In a close-coupled SWH system the storage tank is horizontally mounted above the solar collectors on the roof and the hot water naturally rises into the tank through thermosyphon flow (Sukhatme, 2007, Mahavar et al, 2011). Different types of solar water heaters have been developed and tested by several researchers. Some of the references are mentioned here (Shariah et al, 1999, Li et al, 2007, Garnier et al, 2009, Changa et al, 2008, Han et al, 2010, Hossainb et al, 2011, Helal et al, 2011, Souliotis et al, 2013). Effects of thermal conductivity of the absorber plate on the performance of a solar water heater has been analysed by Shariah (Shariah et al, 1999). An experimental set-up is introduced and analysed by Li et al. for a direct expansion solar assisted heat pump water heater (DX-SAHPWH) (Li et al, 2007). An analysis of the temperature stratification inside an Integrated Collector Storage Solar Water Heater (ICS-SWH) was carried out by Garnier (Garnier et al, 2009). Changa (Changa et al, 2008) and Han (Han et al, 2010) have presented future aspects, possibilities and benefits associated with economic, environmental and social life through the use of solar water heaters in Taiwan and China, respectively. A review of solar water heater collectors and thermal energy performance of circulating pipes has been presented by Hossainb (Hossainb et al, 2011). An integrated collector storage (ICS) consisting of a single cylindrical horizontal tank placed in a reflector composed of three parabolic branches has designed and geometric characteristics have been determined by Helal (Helal et al, 2011). Souliotis (Souliotis et al, 2013) have designed, constructed and experimentally studied three Integrated Collector Storage Solar Water Heaters (ICSSWH) in comparison to a Flat Plate Thermosiphonic Unit (FPTU). Domestic hot water usage (DHW) accounts for a significant share of energy consumption in different types of buildings (Fuentes et al, 2018).

Hafiz (Hafiz, 2018) estimated that if an IECC standardised building is integrated with a passive solar water heating system to meet the water heating load then the use of solar water heating system shows 76% reduction in energy consumption as compared to the electric water heater. A number of solar water heater systems have been developed by many authors and several experimental studies have been performed for the thermal and components performance analysis (Pandy et al, 2017, Mohsen et al, 2009). The building integrated solar thermal collectors developed by Pugsley et al. aim to reduce costs of solar water heating systems by utilising polymer materials and offsetting costs of conventional roofing construction components (Pugsley et al, 2019). Good glaze and insulation materials are also vital for good thermal performance of a SWH, a significant work has also been done in testing of different glaze and insulation materials in water heater. Kaushika and Reddy (Kaushika & Reddy, 1999) have conducted the experimental study of transparent insulation materials cover systems for integrated-collector-storage solar water heaters. The top surface of the tank is transparently insulated with TIM cover to reduce the heat losses. Kumar & Rosen (Kumar & Rosen, 2010) have also tested the thermal performance of integrated collector storage solar water heater with corrugated absorber surface. Taheri (Taheri et al, 2013) have designed and tested a compact solar water heater. Transparent double glass (one 4 mm and other 6 mm thick) were used as cover; air gap between those was 4.5 mm. A comparative study of insulation materials for solar water storage system has also been done by Chaurasia (Chaurasia, 1992). The detailed literature review reveals that the most well-known building integration of solar energy applications is building integrated photovoltaic (BIPV), and yet, the concept of building integrated solar water heater is not tested much, only a few works has been done in this direction (Pugsley et al, 2019; Buonomano et al, 2019). Therefore, the present work aims for design development of a building integrated solar water heater and its component testing. The thermal performance of a solar flat collector depends on its component materials. In our previous work, we have tested different glaze materials in context of solar cooker (Mahavar et al, 2011, Mahavar et al, 2012) and have recommended (poly (methyl methacrylate) PMMA as suitable glaze option in solar thermal appliances. In this work, we have tested PMMA for solar water heater. This paper includes fabrication detail, characterisation test and testing of PMMA as glaze material for the building integrated solar water heater. The replacement of glaze material from glass to PMMA has significantly improve the thermal performance besides removing the main drawback of fragility in solar water heaters.

2. EXPERIMENTAL STUDY

2.1. Fabrication details

The fabricated building integrated solar water heater is shown in the Figure 1. This system is developed and installed at solar energy research laboratory (SERL), University of Rajasthan, Jaipur (26.92°N, 75.87°E). This system consists of water storage tank, solar thermal collector, connecting pipes, valves. The system components and dimensions are mentioned in Table 1.

2.2. Transparent cover (glaze) material

Different glazing sheets (poly (methyl methacrylate)) (PMMA), Glass, and Polycarbonate (PC) have been theoretically studied in our previous work for the solar thermal systems. Those are studied on the following properties given in Table 2. This property indicates that PMMA can be suitable glaze material for solar water heater along the feature of non-fragility and can significantly increase thermal performance due to low extinction coefficient and refractive index. Hence, PMMA as single and double glaze are tested.

Table 1: Components details of building integrated solar water heater (BISWH)

S. No	Parameters	Details
Solar collector		
1.	Casing (i) Dimension (ii) Material (iii) Thickness (iv) Inclination (tilt angle)	144x140x37 cm ³ (outer), 122x112x23 cm ³ (inner) RCC, tile bricks and cement 11 cm (upper and lower walls), 14 cm (side walls) 45° (facing due south)
2.	Absorber tray (i) Dimension (ii) Shape	110x100x 6 cm ³ (aperture) Trapezoidal
3.	Collector tube (i) Shape (ii) Diameter (iii) Length (iv) Material (v) Coating	Spiral 1.15 cm 15.24 m Copper (both) Black matt paint (both)
4.	Glaze (i) No. of glaze (ii) Material (iii) Thickness (iv) Spacing between glaze	1 and 2 PMMA 2.75 mm 10 mm (double)
5.	Insulation (i) Material (ii) Thickness	Mineral wool 6 cm (bottom and all sides)
6.	Storage tank (i) Shape (ii) Dimension(outer) (iii) Material (iv) Insulation thickness (v) Storage capacity	Cylindrical 0.45 m (diameter), 0.66 m height Stainless Steel 0.04 (Mineral wool) 62 litre



Figure 1: The building integrated solar water heater (BISWH)

Table 2: Properties of glaze materials (Mahavar et al, 2015, Mahavar et al, 2012)

S.No	Attributes	Glass (Plane)	PMMA	PC
1.	Refractive Index	1.52	1.49	1.58
2.	Extinction coefficient (m^{-1})	15	0.05	0.05
3.	Thermal expansion ($10^{-6}/K$)	5 – 9 at 20°C	50 – 90 at 23°C	65 - 70 at 23°C
4.	Thermal conductivity (W/m.K)	0.90 - 0.93	0.17 - 0.19	0.19 - 0.22
5.	Fragile	Yes	No	No
6.	Density (kg/m^3)	2500– 2800	1170– 1200	1200– 1220
7.	Upper service temperature (°C)	110-250	115-130	85-145
8.	Scratch resistance	Good	Average	Average
9.	Weather-ability	Good	Average	Average
10.	Cost (INR/m ²)	485	915	1830

2.3. Experimental set-up and measurements:

The experimental studies have been conducted at the Solar Energy Research Laboratory (SERL), University of Rajasthan, Jaipur (26.92°N, 75.87°E). During the experiments the water inlet and outlet temperatures are recorded by 85XX+ Masibas data logger (0.1°C least count, sensor type K of range (-10°C to 600 °C) and weather parameters (solar insolation (I_s), ambient temperature (T_a), wind speed etc.) are measured by weather station (Virtual pvt. Ltd) installed at SERL. Tests are conducted with double PMMA glaze for close loop with storage tank and for open loop without storage tank. Thermal profiles are presented in Figures 2 and 3. The open loop test is also conducted for single PMMA glaze as shown in Figure 3. The thermal profile shown in Figure 2 are compared with the experiment observation of single glass glaze reported by (Sengar, 2007, Marwal, 2012) and is shown Figure 4. In closed loop water was allowed to circulate through the storage tank as shown in Figure 2. To see the direct effect of glazing in closed heating water was not circulated in the water heater (12:00 IST to 14:00 IST), both inlet and outlet valves were closed and only water inside the copper tube was heated Figure 5. For the duration 10:00 IST to 12:00 IST the water temperatures are measured for open cycle.

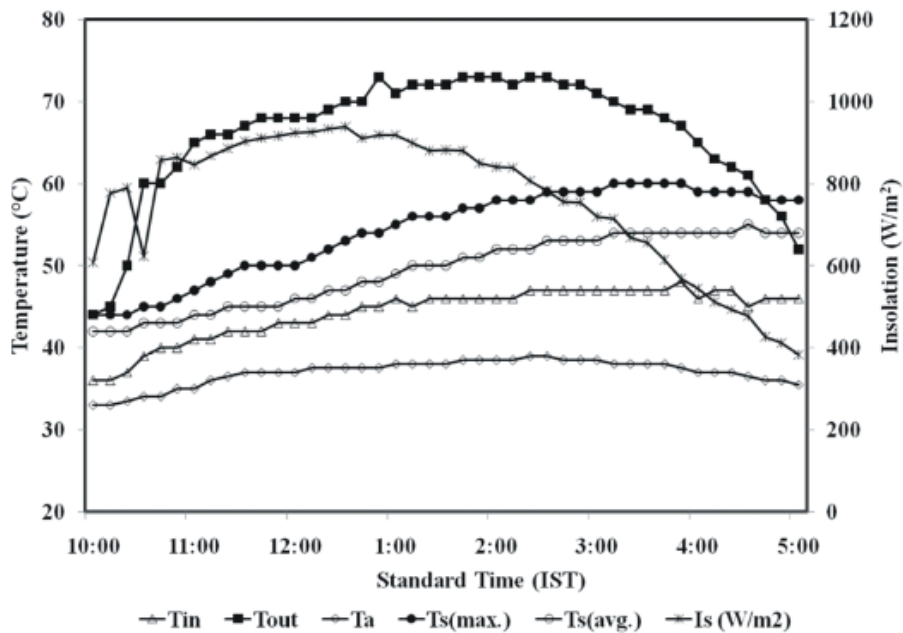


Figure 2: Thermal profile of BISWH (close loop) on 21 June 2017 with PMMA double glaze (T_a , T_{in} , T_{out} and T_s are ambient, inlet water, output water and storage tank water temperatures, I_s is solar insolation)

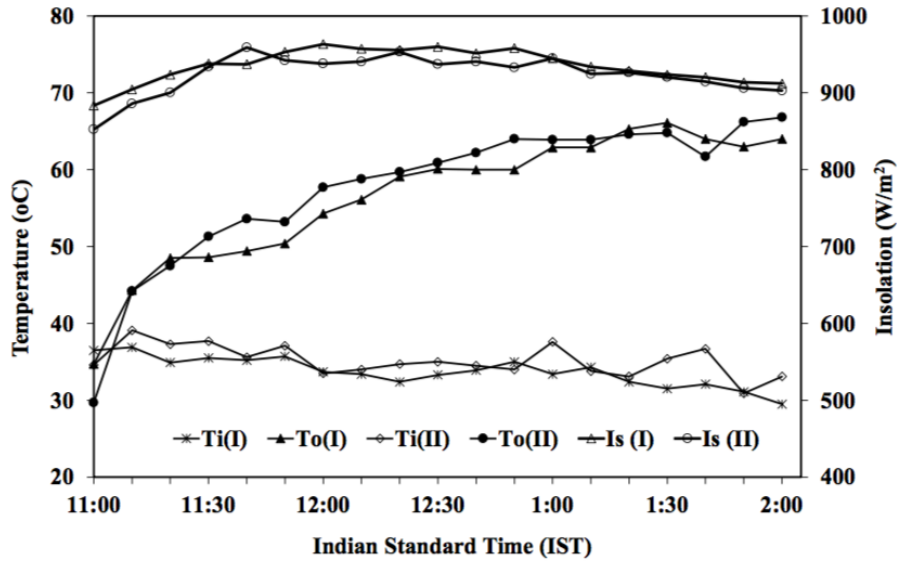


Figure 3: Thermal profile of BISWH (open loop) on 10 May 2019 (double glaze II) and on 22 April 2019 (single glaze I). (T_i and T_o are inlet and output water temperature and I_s is solar insolation).

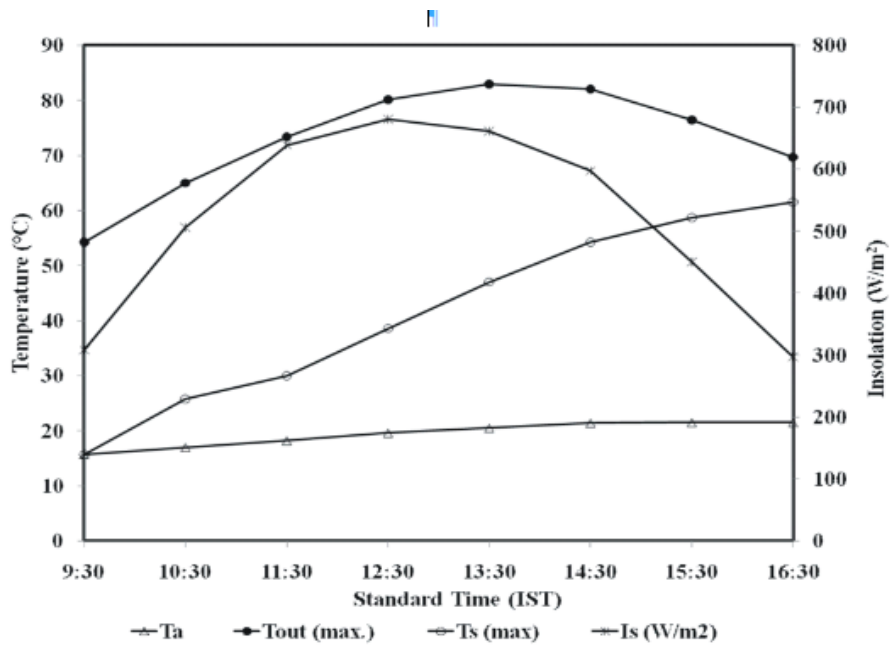


Figure 4: Thermal profile of BISWH (close loop) on 21 Dec. 2006 with single glass glaze (T_a , T_{out} and T_s are ambient, output water and storage tank water temperatures, I_s is solar insolation) (Sengar, 2007, Marwal, 2012).

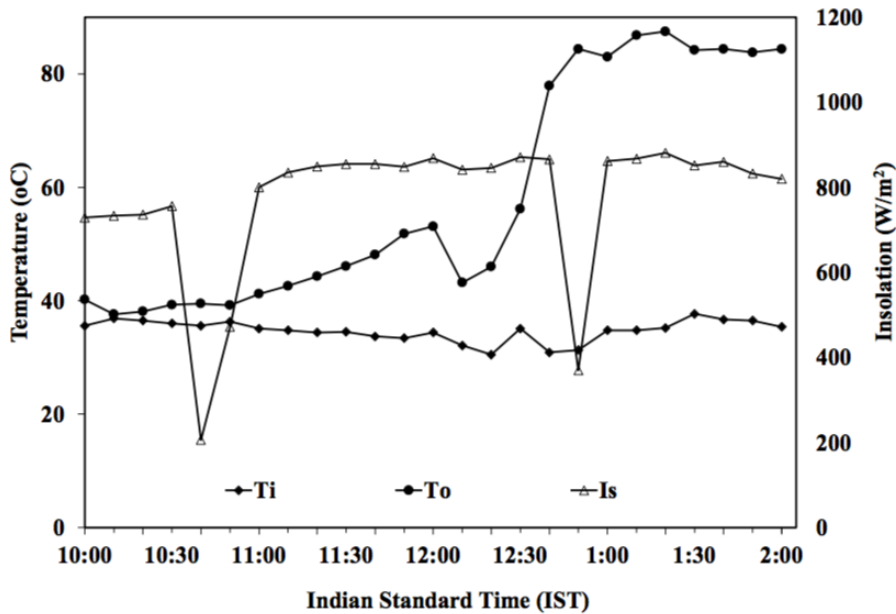


Figure 5: Thermal profile of BISWH (close heating) on 4 June 2019 with PMMA double glaze (T_{in} and T_{out} are the inlet and outlet water temperatures, I_s is solar insolation).

3. RESULTS AND DISCUSSION

The experimental studies are conducted in the year 2017 and 2019. The representative experimental observations for close loop cycle are plotted for PMMA double and single glaze. It can be observed from Figure 2, that the maximum outlet water temperature is about 74°C around 2:00 IST and storage tank temperature reaches around 60°C around 4:00 IST. The system thermal performance has also been studied by Marwal (Marwal, 2012) with single glass glaze which is shown in Figure 4. A comparison of Figure 2 with Figure 4 reveals that outlet temperature remained comparable with PMMA double glaze and the higher temperature (65°C) is sustained for longer duration in PMMA glaze. Although components of system (glaze, insulation, storage tank etc.) have been changed yet the casing is same. It indicates building material casing makes the system good weather resistance and increases the durability. Thermal profile with PMMA glaze is found to be nearly equal to the single glass glaze. A comparison between thermal profiles of single and double PMMA sheets are also depicted in Figure 3. The figure shows that although experiments are performed on different days yet as the insolation values are reasonably close throughout the experiments and the inlet water temperatures are also similar, so, these conditions provide equal weather condition to compare the thermal performances. The double PMMA sheet temperature is slightly higher than single PMMA which might be due to slightly higher insolation. During observation it was found that single sheet got effected due to temperature rise (70°C) and minor bending is observed in single sheets. So, close loop test was not conducted with single PMMA sheet. In order to test temperature effects on double PMMA sheet, test is conducted in close heating without circulation of water as it causes high collector temperature. It is shown in Figure 5. This figure indicates that the maximum outlet temperature is around 85°C, yet no bending and distortion are observed in PMMA glazes.

Hence, in building integrated water heater systems PMMA glaze can be used as alternative of glass glaze with good thermal performance. It has advantage of non-fragility which prevents sudden damages caused by climate or manual rough handling.

4. CONCLUSION

It is estimated in different studies that building integrated solar thermal system has been 40% less expensive than conventional solar thermal installations. Therefore, the present work is also directed for development of building integrated solar thermal system. The system is fabricated and tested for open and close loop cycles. In solar water heater fragility of glaze is a major limitation to popularise its use. Considering this, tests have been conducted with PMMA single and double glazes. The performance of PMMA glaze is found to be comparable to glass glaze. It is also observed that double PMMA is also durable, sufficient temperature resistant and easy to use due to light weight and non-fragility.

5. ACKNOWLEDGEMENT

Authors are thankful to UGC (New Delhi), DST (New Delhi) and SERB (New Delhi) to provide financial and other assistant to conduct experimental studies. Sincere, thanks to Dr. Vikas Marwal and Dr. Namerta Sengar for their positive concern to use their experimental data for comparison.

6. REFERENCES

Buonomano, A., Forzano, C., Kalogirou, S. A., Palombo, A. 2019. Building-façade integrated solar thermal collectors: Energy-economic performance and indoor comfort simulation model of a water based prototype for heating, cooling, and DHW production. *Renewable Energy*, 137, 20-36.

Changa, K. C., Leeb, T. S., Linc, W. M., Chungb, K. M., 2008. Outlook for solar water heaters in Taiwan. *Energy Policy*, 36, 66–72.

Chaurasia, P. B. L. 1992. Comparative study of insulating materials in solar water storage systems. *Energy Convers Manage*, 33, 7-12.

Fuentes, E., Arce, L., Salom, J. 2018. A review of domestic hot water consumption profiles for application in systems and buildings energy performance analysis. *Renewable and Sustainable Energy Reviews*, 81, 1530-47.

Garnier, C., Currie, J., Muneer, T. 2009. Integrated collector storage solar water heater: Temperature stratification. *Applied Energy*, 86, 1465–1469.

Hafiz, M. 2018. The potential of energy savings and the prospects of cleaner energy production by solar energy integration in the residential buildings of Saudi Arabia, *Journal of Cleaner Production*

Han, J., Mol, A. P. J., Lu, Y. 2010. Solar water heaters in China: A new day dawning. *College of Energy Policy*, 38, 383–391.

Helal, O., Chaouachi, B., Gabsi, S. 2011. Design and thermal performance of an ICS solar water heater based on three parabolic sections. *Solar Energy*, 85, 2421–2432.

Hossainb, M. S., Saidura, R., Fayazb, H., Rahimb, N. A., Islama, M. R., Ahameda, J. U., Rahmanb, M. M. 2011. Review on solar water heater collector and thermal energy performance of circulating pipe. *Renewable and Sustainable Energy Reviews*, 15, 3801–3812.

Kaushika, N. D., & Reddy, K. S. 1992. Thermal design and field experiment of transparent honeycomb insulated integrated-collector-storage solar water heater. *Appl Therm Eng.*, 19, 145-61.

Kumar, R., Rosen, M. A. 2010. Thermal performance of integrated collector storage solar water heater with corrugated absorber surface. *Appl Therm Eng.*, 30, 1764-68.

Li, Y. W., Wang, R. Z., Wu, J. Y., Xu, Y. X. 2007. Experimental performance analysis on a direct-expansion solar-assisted heat pump water heater. *Applied Thermal Engineering*, 27, 2858–2868.

Mahavar, S. 2011. Modelling, development and testing of improved components for specific purpose solar thermal appliances. Thesis submitted to University of Rajasthan, Jaipur, India, 2011.

Mahavar, S., Sengar, N., Rajawat, P., Verma, M., and Dashora, P. 2012. Design development and performance studies of a novel Single Family Solar Cooker., *Renewable Energy*, 47, 67-76.

Mahavar, S., Rajawat, P., Marwal, V. K., Punia, R. C., Dashora, P. 2012. Modeling and on-field testing of a Solar Rice Cooker, *Energy*, 49, 404-412.

Mahavar, S., Verma, M., Rajawat, P., Sengar, N., Dashora, P. 2013. Novel solar cookers: suitable for single families. *International Journal of Sustainable Energy*, 32(6), 574-586.

Mahavar, S., Rajawat, P., Punia, R. C., Verma, M., Dashora, P. 2015a. Evaluating the optimum load range for box-type solar cookers. *Renewable Energy*, 74, 187-194.

Mahavar, S. 2015b. Review of Materials Used in Various Solar Thermal Appliances. Solar Engineering-I (Applications) Vol. 5 Ch.6. Editors: Dr. Sri Sivakumar, Dr. Umesh Chandra Sharma & Dr. Ram Prasad, Studium Press LLC, USA.

Marwal, V. 2012. Study of solar radiation and novel building material housing flat-plate solar collector for hybrid applications. Thesis submitted to University of Rajasthan, Jaipur, India.

Mohsen, M. S., Al-Ghandoor, A., Al-Hinti I. 2009. Thermal analysis of compact solar water heater under local climatic conditions. International Communications in Heat and Mass Transfer, 36, 962-968.

Pugsley, A., Zacharopoulos, A., Smyth, M., Mondol, J., 2019. Performance evaluation of the energy polycarbonate and asphalt carbon nanotube solar water heating collectors for building integration. Renewable Energy.

Pandya, H., Behura, A. K. 2017. Experimental study of V-through solar water heater for tilt angle and glass transmissivity. Energy Procedia, 109, 377-84.

Reddy, K. S., & Kaushika N. D. 1999. Comparative study of transparent insulation materials cover systems for integrated-collector-storage solar water heaters. Solar Energy Materials & Solar Cells, 58, 431-46.

Sengar, N. 2007. Utilization of solar energy in low grade energy applications. Thesis submitted to University of Rajasthan, Jaipur, India.

Shariah, A. M., Rousana, A., Rousanb, K. K., Ahmada, A. A. 1999 Effect of thermal conductivity of absorber plate on the performance of a solar water heater. Applied Thermal Engineering, 19, 733-41.

Souliotis, M., Chemisana, D., Caouris, Y. G., Tripanagnostopoulos Y. 2013. Experimental study of integrated collector storage solar water heaters. Renewable Energy, 50, 1083-1094.

Sukhatme, S. P. 2007. Solar energy: Principles of thermal collection and storage. New Delhi: Tata McGraw-Hill Book Co.

Taheri, Y., Ziapour, B. M., Alimardani, K. 2013. Study of an efficient compact solar water heater. Energy Convers Manage, 70, 187-93.

#262: Optimal design of structured packing column for cryogenic air separation with particle swarm optimisation algorithm

Bin WANG¹, Shanshan SHI², Shunhao WANG³, Limin QIU⁴, Xiaobin ZHANG⁵

¹ Institute of Refrigeration and Cryogenics, School of Energy Engineering, Zhejiang University, 310027 Hangzhou China, binw@zju.edu.cn

² Institute of Refrigeration and Cryogenics, School of Energy Engineering, Zhejiang University, 310027 Hangzhou China, shishanshan@zju.edu.cn

³ Institute of Refrigeration and Cryogenics, School of Energy Engineering, Zhejiang University, 310027 Hangzhou China, wangshzju@126.com

⁴ Institute of Refrigeration and Cryogenics, School of Energy Engineering, Zhejiang University, 310027 Hangzhou China, limin.qiu@zju.edu.cn

⁵ Institute of Refrigeration and Cryogenics, School of Energy Engineering, Zhejiang University, 310027 Hangzhou China, zhangxb@zju.edu.cn

Large scale cryogenic air separation is currently the most efficient and cost-effective approach to produce high-purity air products. Structured packing columns (SPC) are widely focused and applied due to their characteristics of high efficiency and energy saving in the cryogenic distillation process. The main aims of the design of SPC are to reduce energy consumption and initial investment, while its optimal design is a highly nonlinear and multivariable problem. The coexistence of real variables and integer variables, such as the flow rates and the positions of materials at the inlets/outlets, makes the optimisation become a typical mixed integer nonlinear programming (MINLP) problem. The purpose of this paper is to study the optimal design for the cryogenic SPC using the particle swarm optimisation (PSO) algorithm. With the basis of original research, a modified PSO for handling the MINLP problem (MI-PSO) is proposed. A multi-objective optimal design for the SPC in cryogenic air separation unit with the capacity of 17000 Nm³/h, based on the FORTRAN compiler, is investigated. The multiple inlets/outlets of the model are validated by the limited available measurements, while the calculated distributions of the component molar fraction, temperature, pressure and flow rates along the column are compared with those from the Rate-based module of Aspen plus simulation. By MI-PSO algorithm, the total exergy loss reduces 36.3% and the main condenser heat load decreases 5.4% after optimisation.

Keywords: optimal design; particle swarm optimisation; structured packing column; cryogenic air separation

1. INTRODUCTION

The air separation unit (ASU) is a key foundation for several major industries, including electronics, metallurgy, petroleum refining and chemical engineering (Pattison, 2014). Compared to the other two common air separation methods, pressure swing adsorption (a purity of 98 to 99.5 vol%) and membrane separation (a purity of less than 98 vol%), cryogenic distillation is still an irreplaceable technique for obtaining high purity gases and liquid on a large scale at present. The distillation process takes place in the distillation column and its energy consumption in the cryogenic ASU is the largest (Aneesh, 2016 & Rizk, 2012). Ebrahimi et al. analysed the exergy destruction on a two columns cryogenic ASU, and the results show that the compression and distillation units occupied 34.48 and 52.89 percent of total exergy destruction, respectively (Ebrahimi, 2015). Therefore, the optimal design of cryogenic distillation columns has received a significant attention, with the main goal of reducing energy consumption and initial investment (Zhu, 2010).

The structured packing column (SPC) is an intricate system with many factors coupling and interacting with each other. Commercial simulation software, such as Aspen plus, used by industrial users and researchers is often of a “black box” type from which derivatives cannot be directly obtained and available for optimisation studies (Cao, 2017). Although the sensitivity analysis in software can help explore the influence of single factor on the optimisation goal, it is unavailable to consider the coupling effects of the various factors. Rizk et al. achieved the optimisations of geometrical structures and operating parameters for three types of columns with sensitivity analysis, which were not the rigorous optimal solutions (Rizk, 2012). With a suitable optimisation method for optimal design of SPC, one can save lots of manpower, material and other costs.

Optimisation algorithms can be roughly divided into two categories: deterministic and heuristic methods, in which the methods based on metaheuristic population are very suitable for solving nonlinear programming problems (Luo, 2007). Among these stochastic optimisation algorithms, compared with the simulated annealing (SA) and genetic algorithm (GA), the particle swarm optimisation (PSO) is computationally faster and needs fewer user-specified parameters (Khan, 2013). Hence, it is focused by the researchers and widely used for optimisation processes, such as transportation network design (Babazadeh, 2011), assembly line design (Kuo, 2011), system identification (Lu, 2016), image segmentation (Tian, 2018) and chemical engineering problems in past several years. Lazzús developed a method to simulate the vapor-liquid phase change process based on PSO, and two activity coefficient models (UNIQUAC and NRTL) were successfully optimised (Lazzús, 2010). Sudibyo et al. proposed a modified PSO, annealing-particle swarm optimisation (SA-PSO), and effectively controlled the temperature of the trays in the MTBE reactive distillation column (Sudibyo, 2015). Cao et al. applied the PSO to achieve the optimal control of the nitrogen operational liquefier in the ASU, and proved that adjusting different operation set-points could reduce the energy consumption (Cao, 2017). Jia et al. optimised the flow rates and the stage numbers of thermally coupled dividing wall column (DWC) different sections by using the PSO (Jia, 2017). Hamed et al. used the PSO to optimise the parameters of various nitrogen-methane separation processes with the objective of energy consumption minimisation, and the results showed that a single-column process needed more energy to perform the separation compared to other configurations (Hamed, 2018). However, it is by present rarely reported on the optimisation of the SPC in cryogenic ASU with the PSO.

Currently, control equations modelling and optimisation based on rigid mechanism model have become an internationally approved mainstream direction of technology. These optimisation propositions often have the characteristics of many equations, high dimensions and strong nonlinearity, making it difficult to be solved and stored, such as the optimal design of SPC in cryogenic ASU based on the non-equilibrium model. The various factors, such as the flow rates and positions of materials at the inlets/outlets, make it a typical mixed integer nonlinear programming (MINLP) problem (Shokrian, 2014) with inequality constraints, significantly increasing the difficulty of optimisation. This paper provides a modified PSO for handling MINLP (MI-PSO). With the basis of a FORTRAN calculation program that has been successfully validated to model a steady-state cryogenic air separation process, the multi-objective optimal design for the SPC of an actual cryogenic ASU with capacity of 17000 Nm³/h is mainly carried out.

2. THE MI-PSO ALGORITHM

The mathematical model of the general mixed integer nonlinear programming (MINLP) problem is as follows:

Equation 1: Mixed integer nonlinear programming (MINLP) problem

$$\begin{aligned} & \min f(x, y) \\ & \text{s. t. } \begin{cases} g_l(x, y) \leq 0, & l = 1, 2, \dots, L \\ x \in R^n; y \in Z^m \end{cases} \end{aligned}$$

Where:

- $f(x, y)$ = objective function
- $g_l(x, y)$ = inequality constraints function

From Equation (1), there are two types of variables to be optimised, the real variables and the integer variables. In regard to the real variables, the particle swarm optimisation (PSO) introduced by Shi and Eberhart is able to handle (Shi, 1998). Each particle is indicated by its traveling velocity and position. After each travel, the position is updated by adding the velocity vector to the current position.

$$\text{Equation 2: Particle position update equation} \quad x_i(t+1) = x_i(t) + v_i(t+1)$$

Where:

- t = time instant
- x = particle position
- v = particle velocity
- $i = i_{th}$ particle ($i=1,2,\dots,N$, N = number of particles)
- $x_i(t)$ = i_{th} particle's position at time t
- $v_i(t+1)$ = new velocity at time $t+1$

$$\text{Equation 3: Particle velocity update equation} \quad v_i(t+1) = \omega(t)v_i(t) + c_1r_1(pbest_i(t) - x_i(t)) + c_2r_2(gbest(t) - x_i(t))$$

$$\text{Equation 4: best positions for } i_{th} \text{ particle} \quad pbest_i(t+1) = \begin{cases} pbest_i(t), & \text{if } f(x_i(t+1)) \geq f(pbest_i(t)) \\ x_i(t+1), & \text{if } f(x_i(t+1)) \leq f(pbest_i(t)) \end{cases}$$

$$\text{Equation 5: best positions for all particle} \quad gbest(t) = \min\{f(pbest_1(t)), f(pbest_2(t)), \dots, f(pbest_N(t))\}$$

$$\text{Equation 6: inertia weight function} \quad \omega(t) = (\omega_1 - \omega_2) \times \frac{T-t}{T} + \omega_2$$

Where:

- c_1 = personal acceleration factor
- c_2 = global acceleration factor
- r_1 and r_2 = random number in the range $[0,1]$
- $pbest_i(t)$ and $gbest(t)$ = best positions reached at time t for i_{th} particle and all particles, respectively
- $\omega(t)$ = inertia weight function
- ω_1 and ω_2 = start value and end value, respectively
- T = the max time instant

As for integer variables, the method of updating particles' position and its corresponding velocity must be modified. Equation (3) shows that the new velocity depends on original velocity, the best position of i_{th} particle and the best position of all particles. So, we can give a random integer from the range $[l_i(t), u_i(t)]$ as a new velocity. The formulas of $l_i(t)$ and $u_i(t)$ are given, which are both related to $v_i(t)$, $pbest_i(t)$ and $gbest(t)$:

$$\text{Equation 7: If } pbest_i(t) > x_i(t) \text{ and } gbest(t) > x_i(t) \text{ then} \quad \begin{cases} l_i(t) = v_i(t) \\ u_i(t) = v_i(t) + c_1(pbest_i(t) - x_i(t)) + c_2(gbest(t) - x_i(t)) \end{cases}$$

$$\text{Equation 8: If } pbest_i(t) < x_i(t) \text{ and } gbest(t) < x_i(t) \text{ then} \quad \begin{cases} l_i(t) = v_i(t) + c_1(pbest_i(t) - x_i(t)) + c_2(gbest(t) - x_i(t)) \\ u_i(t) = v_i(t) \end{cases}$$

$$\text{Equation 9: If } pbest_i(t) > x_i(t) \text{ and } gbest(t) < x_i(t) \text{ then} \quad \begin{cases} l_i(t) = v_i(t) + c_2(gbest(t) - x_i(t)) \\ u_i(t) = v_i(t) + c_1(pbest_i(t) - x_i(t)) \end{cases}$$

$$\text{Equation 10: If } pbest_i(t) < x_i(t) \text{ and } gbest(t) > x_i(t) \text{ then} \quad \begin{cases} l_i(t) = v_i(t) + c_1(pbest_i(t) - x_i(t)) \\ u_i(t) = v_i(t) + c_2(gbest(t) - x_i(t)) \end{cases}$$

Above, Equations (2) to (10) are the MI-PSO control equations. Comparing with the classical PSO, the MI-PSO can handle MINLP to achieve optimisation of both real variables and integer variables.

3. PROCESS DESCRIPTION

3.1. Distillation calculation program

In previous literature, the present authors have implemented and solved a non-equilibrium model (NEM) for cryogenic distillation calculation by program coded in FORTRAN language. With a practical structured packing column (SPC) of a cryogenic air separation unit (ASU) made by Hangzhou Hangyang Co. Ltd with capacity of 17000 Nm³/h as an application (Figure 1), the distributions of the component molar fraction, temperature and flow rates along the column were simulated (Figures 2 to 5). Table 1 gives specific parameters of materials at the inlets and outlets of the SPC. The more details of NEM, solution strategy and verification process are described by us in the literature (Wang, 2019).

Figures 2 to 4 indicate that the distributions of the molar fraction and temperature show the “singularity”, which stands for the large exergy loss and energy consumption. Table 2 gives N₂ molar fraction difference between feed materials and fluids corresponding to the same stage at the inlets, and the results show that there are obvious differences for these four materials, waste LN₂ in, rich O₂ liquid air in, expanded air in and Liquid air return. The unavoidable flow mutations, shown in Figure5, will amplify the effect of molar fraction difference, leading to produce singularity.

Hence, this paper continues to take the 17000Nm³/h of SPC in cryogenic ASU as an actual example. With the basis of cryogenic distillation calculation program, the researches of applying the MI-PSO to achieve multi-objective optimal design are carried out.

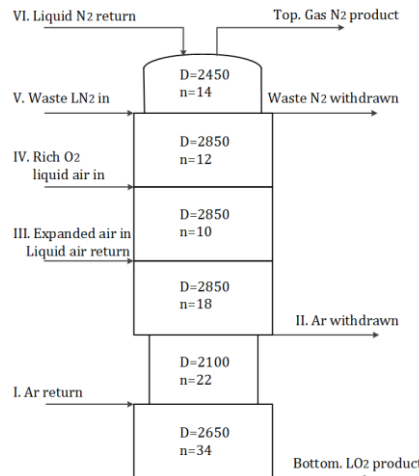


Figure 1: Parameters of the SPC

Table 2: Measured data of the materials at the inlets and outlets in 17000 Nm³/h ASU

	Stage	Phase	Temperature /K	Pressure /kPa	x_{N_2}	x_{O_2}	Flow rate /Nm ³ ·h ⁻¹
N ₂ product	1	V	79.3	126.7	0.999922	0.00005	17010
LN ₂ return	1	L	79.3	126.7	0.999838	0.000005	22198 #
Waste N ₂ withdrawn	3 #	V	81	130.1	0.934	0.054	47083 #
Waste LN ₂ in	15 #	L	80.7	126.7	0.813	0.175	17373 #
Rich O ₂ liquid air in	27 #	L	82.6	129.6	0.6125	0.3732	5822 #
Expanded air in	36 #	V	83.9	129.5	0.782	0.209	9069 #
Liquid air return	37 #	L	86.2	127.9	0.615	0.371	22334 #
Ar withdrawn	55 #	V	92.4	129.9	0.000159	0.936841	18805 #
Ar return	77 #	L	92.3	129.8	0.000046	0.937288	18102 #
LO ₂ product	111	L	92.8	132.2	0	0.99765	12002

Notes: The superscript # stands for the parameter to be optimised. All of these data come from Hangzhou Hangyang Co. Ltd, China. ($x_{O_2} + x_{N_2} + x_{Ar} = 1$)

Table 3: N_2 molar fraction difference between feed materials and fluids at the inlets

Inlet	N_2 molar fraction	
	Feed materials	Fluids
1	0.999838	0.9839
15	0.813	0.7859
27	0.6125	0.5597
36	0.782	0.5006
37	0.615	0.4484
77	0.000046	0.0000243

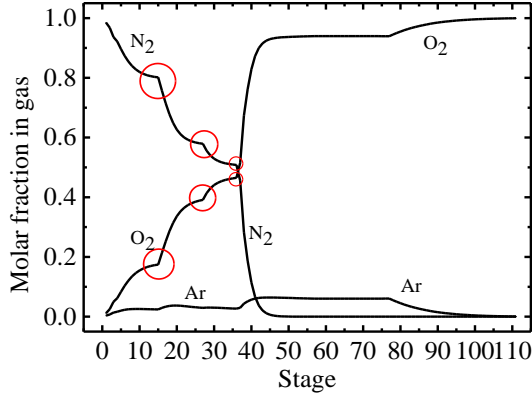


Figure 2: Molar fraction distributions in gas phase

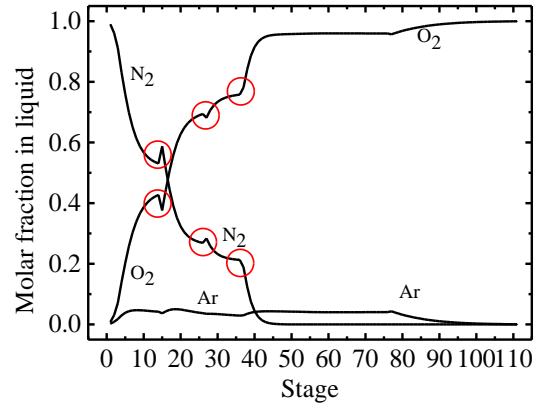


Figure 3: Molar fraction distributions in liquid phase

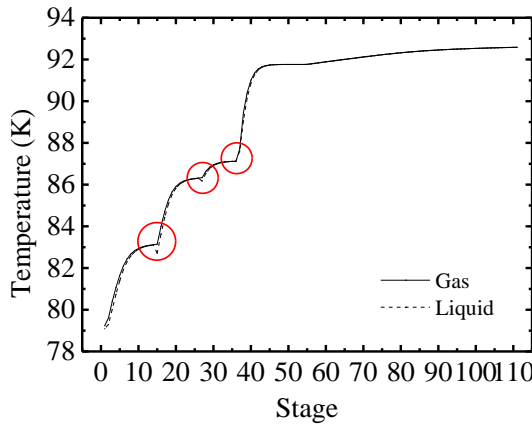


Figure 4: Temperature distributions in gas and liquid phases

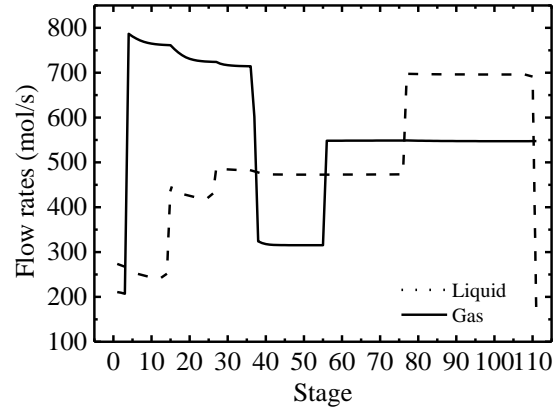


Figure 5: Flow rate distributions in gas and liquid phases

3.2. Formulation of optimisation goal

The materials flow rates and positions at the inlets and outlets, the parameters with the superscript # in Table 1, are two types of variables to be optimised. The weighted sum value minimisation of the total exergy loss and main condenser heat load is used as the fitness function and expressed as:

$$\min[Ex(x_1, x_2, \dots, x_8, y_1, y_2, \dots, y_7) + \kappa Q(x_1, x_2, \dots, x_8, y_1, y_2, \dots, y_7)]$$

Equation 11: Weighted sum value minimisation

$$s. t. \begin{cases} x_{1min} \leq x_1 \leq x_{1max} \\ x_{2min} \leq x_2 \leq x_{2max} \\ \dots \\ y_{7min} \leq y_7 \leq y_{7max} \\ x_1, x_2, \dots, x_8 \in R \\ y_1, y_2, \dots, y_7 \in Z \end{cases}$$

Where:

- Ex = total exergy loss (kW)
- Q = main condenser heat load (kW)
- κ = additional weight
- x_1, x_2, \dots, x_8 = flow rates variables
- y_1, y_2, \dots, y_7 = positions variables

In order to guarantee convergence of calculations, Table 3 listed the upper and lower limits of the variables values. Equation (11) is a fitness function with inequality constraints. By introducing a penalty function (Mellal, 2015 & Panda, 2016), it can be transferred as an unconstrained problem:

Equation 12: control equation of multi-objective minimisation optimisation problem

$$\min \left[\begin{array}{l} Ex(x_1, x_2, \dots, x_8, y_1, y_2, \dots, y_7) + \kappa Q(x_1, x_2, \dots, x_8, y_1, y_2, \dots, y_7) \\ + 10^8 \times \left\{ \begin{array}{l} \sum_{l=1}^8 [\max\{0, (x_l - x_{lmax}), (x_{lmin} - x_l)\}]^2 \\ + \sum_{k=1}^7 [\max\{0, (y_k - y_{kmax}), (y_{kmin} - y_k)\}]^2 \end{array} \right\} \end{array} \right]$$

s. t. $\begin{cases} x_1, x_2, \dots, x_8 \in R \\ y_1, y_2, \dots, y_7 \in Z \end{cases}$

Equation (12) is the control equation of the 15-dimension nonlinear multi-objective minimisation optimisation problem.

Table 4: The upper and lower limits of the variables values

Variable	Lower limit	Upper limit
x_1 (LN ₂ return)	21100	23300
x_2 (Waste N ₂ withdrawn)	44700	49400
x_3 (Waste LN ₂ in)	16300	18100
x_4 (Rich O ₂ liquid air in)	5500	6200
x_5 (Expanded air in)	8600	9600
x_6 (Liquid air return)	21200	23500
x_7 (Ar withdrawn)	17800	19800
x_8 (Ar return)	17200	19000
y_1 (Waste N ₂ withdrawn)	2	8
y_2 (Waste LN ₂ in)	10	20
y_3 (Rich O ₂ liquid air in)	22	32
y_4 (Expanded air in)	31	41
y_5 (Liquid air return)	32	42
y_6 (Ar withdrawn)	50	60
y_7 (Ar return)	72	82

Combining Equations (2) to (12), the MI-PSO algorithm is programmed by FORTRAN compiler. Table 4 and Table 5 show the MI-PSO programming process and user-specified parameters, respectively. The termination condition is that iteration reaches the max time instant (T) or the fitness function value has no change after 30 consecutive iterations (Hamed, 2018).

Table 5: MI-PSO programming process

Pseudocode of applying MI-PSO to optimise the SPC	
1.	Begin
2.	Randomly initialise particle swarm in search space based on Table 3
3.	Round for each position variable
4.	While (the problem is not convergent)
5.	Calculate fitness of the particle swarm by Equation (12)
6.	Update the inertia weight by Equation (6)
7.	for n=1 to N (number of particles)
8.	Find p_{best} by Equation (4)
9.	Find g_{best} by Equation (5)
10.	for d=1 to D (number of variables)
11.	if $d \leq 8$ (flow rates variable)
12.	Update the velocity by Equation (3) and position by Equation (2)
13.	Else if
14.	Update the velocity by Equations (7) to (10) and position by Equation (2)
15.	next d
16.	next n
17.	next iteration until convergence
18.	End

Table 6: The user-specified parameters of MI-PSO and fitness function

User-specified parameters	Value
Number of particles (N)	25
Max time instant (T)	200
Personal acceleration factor (c_1)	1.7
Global acceleration factor (c_2)	1.7
Start inertia weight (ω_1)	1.1
End inertia weight (ω_2)	0.5
Additional weight (κ)	1.0

4. OPTIMISATION RESULTS

The convergence process of the optimisation algorithm is shown in Figure 6. The fitness function value decreases considerably in the first 25 iterations, and it doesn't basically change after that. Figures 7 to 9 give the exergy loss, molar fraction in gas and liquid phases distributions in the SPC with original and optimised configuration. The results show that the singularities are almost disappeared and exergy loss distribution gets an improvement after optimisation. The optimum solution of the variables and goals is shown in Table 6, which indicates that both two optimisation goals are optimised. Comparing the optimised column with the original one, the total exergy loss reduces 36.3% and the main condenser heat load decreases 5.4%.

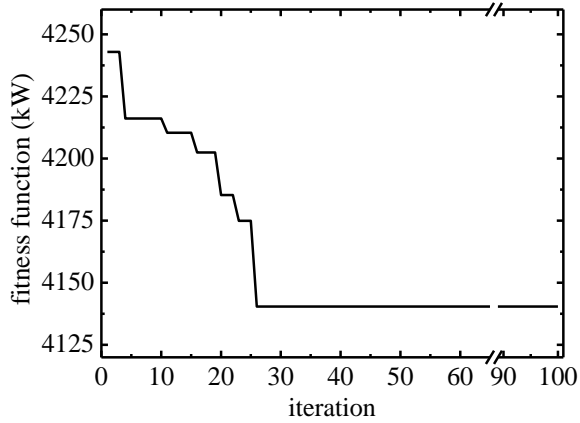


Figure 6: Iteration process of the optimisation algorithm

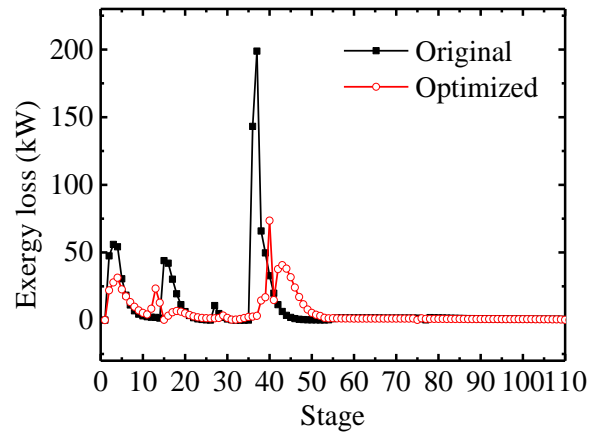


Figure 7: Exergy loss distributions with original and optimised

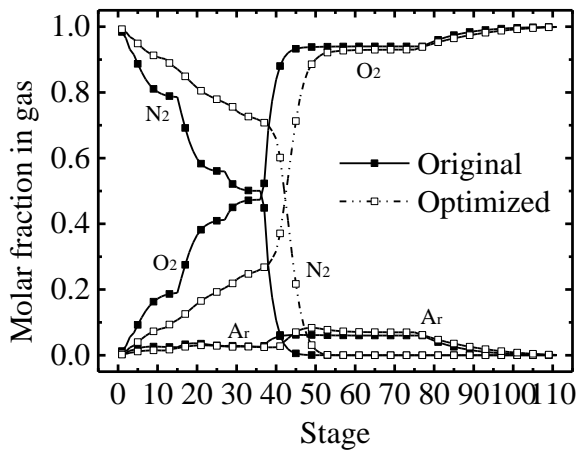


Figure 8: Molar fraction distributions in gas phase

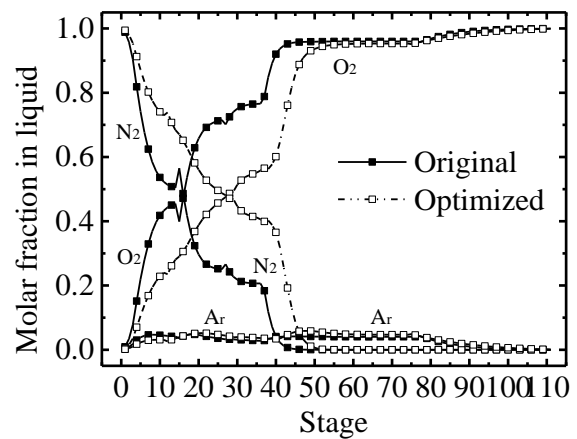


Figure 9: Molar fraction distributions in liquid phase

Table 7: The optimum solution of the 17000Nm³/h SPC in cryogenic ASU

	Materials	Original configuration	Optimised configuration
Positions of materials at the inlets/outlets	LN ₂ return	1	1
	Waste N ₂ withdrawn	3	3
	Waste LN ₂ in	15	12
	Rich O ₂ liquid air in	27	29
	Expanded air in	36	40
	Liquid air return	37	41
	Ar withdrawn	55	52
	Ar return	77	75
Flow rates of materials at the inlets/outlets (Nm ³ /h)	LN ₂ return	22198	21449
	Waste N ₂ withdrawn	47083	44750
	Waste LN ₂ in	17373	17356
	Rich O ₂ liquid air in	5822	6038
	Expanded air in	9069	9436
	Liquid air return	22334	23411
	Ar withdrawn	18805	18389
	Ar return	18102	17287
Main condenser heat load (kW)		3688.6	3490.8
Total exergy loss (kW)		1019.3	649.5

5. CONCLUSIONS

This paper proposes a modified particle swarm optimisation (MI-PSO), suitable for the mixed integer nonlinear programming (MINLP) problem, especially the optimal design of structured packing column (SPC). Based on already established and solved FORTRAN cryogenic distillation calculation program, an optimal design for a 17000 Nm³/h of SPC in cryogenic air separation unit with two objective functions is investigated. MI-PSO is applied to optimise the materials flow rates and positions at the inlets and outlets of SPC sections. After optimisation, the total exergy loss reduces 36.3% and the main condenser heat load decreases 5.4%.

6. ACKNOWLEDGEMENTS

This work was supported by the National key R&D plan of China (2017YFB0603702) and the Nature and Science Foundation of China (No. 51576169; 51636007).

7. REFERENCES

- Babazadeh, A., Poorzahedy, H., Nikoosokhan, S., 2011. Application of particle swarm optimization to transportation network design problem. *Journal of King Saud University-Science*, 23, 293-300.
- Ebrahimi, A., Meratizaman, M., Reyhani, H.A., Pourali, O., Amidpour, M. 2015. Energetic, exergetic and economic assessment of oxygen production from two columns cryogenic air separation unit. *Energy*, 90, 1298-1316.
- Panda, A., Pani, S. 2016. A Symbiotic Organisms Search algorithm with adaptive penalty function to solve multi-objective constrained optimization problems. *Applied Soft Computing*, 46, 344-360.
- Wang, B., Zhou, R., Yu, L., Qiu, L.M., Zhi, X.Q., Zhang, X.B. 2019. Evaluation of mass transfer correlations applying to cryogenic distillation process with non-equilibrium model. *Cryogenics*, 97, 22-30.
- Tian, D.P., Shi, Z.Z. 2018. MPSO: Modified particle swarm optimization and its applications. *Swarm and Evolutionary Computation*, 41, 49-68.
- Hamed, H., Karimi, I.A., Gundersen, T. 2018. Optimal cryogenic processes for nitrogen rejection from natural gas. *Computers and Chemical Engineering*, 112, 101-111.
- Lazzús, J.A. 2010. Optimization of activity coefficient models to describe vapor-liquid equilibrium of (alcohol + water) mixtures using a particle swarm algorithm. *Computers and Mathematics with Applications*, 60, 2260-2269.
- Rizk, J., Nemer, M., Clodic, D. 2012. A real column design exergy optimization of a cryogenic air separation unit. *Energy*, 37, 417-429.

- Lu, J.S., Xie, W.D., Zhou, H.B. 2016. Combined fitness function based particle swarm optimization algorithm for system identification. *Computers & Industrial Engineering*, 95, 122-134.
- Mellal, M.A., Williams, E.J. 2015. Cuckoo optimization algorithm with penalty function for combined heat and power economic dispatch problem. *Energy*, 93, 1711-1718.
- Shokrian, M., High, K.A. 2014. Application of a multi objective multi-leader particle swarm optimization algorithm on NLP and MINLP problems. *Computers and Chemical Engineering*, 60, 57-75.
- Khan, M.S., Lee, M. 2013. Design optimization of single mixed refrigerant natural gas liquefaction process using the particle swarm paradigm with nonlinear constraints. *Energy*, 49, 146-155.
- Pattison, R.C., Baldea, M. 2014. Optimal design of air separation plants with variable electricity pricing. the 8th International Conference on Foundations of Computer-Aided Process Design, 393-398.
- Kuo, R.J., Yang, C.Y. 2011. Simulation optimization using particle swarm optimization algorithm with application to assembly line design. *Applied Soft Computing*, 11, 605-613.
- Jia, S.K., Qian, X., Yuan, X.G. 2017. Optimal design for dividing wall column using support vector machine and particle swarm optimization. *Chemical Engineering Research and Design*, 125, 422-432.
- Sudibyo, Mirat and et al., 2015. MIMO neural wiener based model predictive control (NWMPC) for MTBE reactive distillation using simulated annealing-particle swarm optimization (SA-PSO). 12th International Symposium on Process Systems Engineering and 25th European Symposium on Computer Aided Process Engineering, 1631-1636.
- Aneesh, V., Antouy, R., Paramasivan, G., Selvaraju, N. 2016. Distillation technology and need of simultaneous design and control: A review. *Chemical Engineering and Processing: Process Intensification*, 104, 223-224.
- Cao, Y., Cerrillo, J.F., Swartz, C.L.E. 2017. Practical optimization for cost reduction of a liquefier in an industrial air separation plant. *Computers and Chemical Engineering*, 99, 13-20.
- Shi, Y.H., Eberhart, R.C. 1998. A modified particle swarm optimizer. Proceedings of IEEE International Conference on Evolutionary Computation, Piscataway, New Jersey: IEEE Press, 69-73.
- Luo, Y., Yuan, X., Liu, Y. 2007. An improved PSO algorithm for solving non-convex NLP/MINLP problems with equality constraints. *Computers and Chemical Engineering*, 31(3), 153-162.
- Zhu, Y., Legg, S., Laird, CD. 2010. Optimal design of cryogenic air separation columns under uncertainty. *Computers and Chemical Engineering*, 34, 1377-1384.

#263: A study on the thermal and living environment of the slice room in Korea during winter season

Wontaek RYU¹, Woo-Seung YUN², Hyuncheol SEO³, Won-Hwa HONG⁴

¹ Kyungpook National University, 41566, Daegu, South Korea, dbdnjsxor97@live.com

² Kyungpook National University, 41566, Daegu, South Korea, bmqwe011@gmail.com

³ Kyungpook National University, 41566, Daegu, South Korea, notsools@gmail.com

⁴ Kyungpook National University, 41566, Daegu, South Korea, hongwh@knu.ac.kr

The slice room is a typical type of housing for the energy poverty in Korea. The resident of a slice room has a personal space with an average size of 4 square metres and a shared toilet and a washroom. A mechanical system for maintaining indoor air quality and thermal environment is not normally installed. Therefore, common residents in slice rooms cannot guarantee an acceptable living environment. Energy poverty and housing welfare are global issues. To establish a policy for housing welfare and energy poverty, collecting base data is essential. In this study, the results of the survey and analysis on the living and thermal environment of residents in slice rooms are presented. Interviews and field surveys were conducted for 35 households. Measurement instruments was installed in 29 households to collect indoor air quality and thermal environment data. Deep-interviews were conducted to investigate the living and thermal environment of the households. We collected residents' personal information, room stay-time, comfort sensation vote in indoor environments, income and energy cost burden. The field surveys were conducted to derive architectural characteristics of the slice rooms. Insulation, structural materials and building locations were collected. Indoor air quality was monitored by DIY sensor. Internet of Things (IoT) based data acquirer is designed to not disturb the daily life of the residents. The measuring factors were indoor dry-bulb temperature, relative humidity, black bulb temperature, air velocity, CO₂, PM 2.5, occupancy (PIR). The results of the investigation show that the average indoor temperature inside the room was 15.7°C (±4.7°C). The measured IAQ was analysed and compared with the standard and recommendation. The indoor air quality mostly cannot meet the recommendation especially during cooking and when smoking inside. Predicted mean vote was calculated based on the thermal environment data. Most residents have been living in an unpleasant environment due to energy cost.

Keywords: slice room; indoor air quality; thermal comfort; winter season

1. INTRODUCTION

A slice room is a typical type of housing for energy poverty in Korea. The resident in slice room has personal space with an average size of 4 square meters and a shared toilet and a washroom (The Academy of Korean Studies, 2001). There is no place to accommodate the poor, so the government is in a level of management only. This is the lowest residential area for the poor to live in, and it has begun to emerge with the homeless who have risen sharply since the Korea financial crisis (IMF) in 1997 (Ha, 2000). Most residents of slice rooms do not use air conditioning or boilers because of energy costs. Therefore, it is impossible to guarantee a healthy thermal environment. The Korean government is conducting energy welfare projects for the socially underprivileged (Korea Energy Economics Institute, 2015), however, as these are focused on energy fuel supply and energy cost reduction, it is hard to improve the residential environment (Park, 2018). Most studies of slice rooms are aimed at slice room residents, so investigation of the environment of the slice room is needed. Therefore, in this paper, we visited slice rooms in D city in the winter season and conducted deep-interviews. An Internet of Things (IoT) data acquirer was installed to measure the indoor environment factor, like air temperature, relative humidity, black bulb temperature, air velocity, and PM2.5.

2. THEORETICAL BACKGROUND

Previous research has been reviewed for the investigation of the slice room. The research on the slice room in Korea began in earnest in the 2000s (Ha, 2000). According to the 'Slice room study', the reason why the slice room occurred in Korea is as follows: in 1997, the Korean financial crisis (IMF) led to a surge in the number of homeless people and the need for homeless people to live in cheap places. So they started to live in a slice room at a cheap price. The problem that arises is that the house has been illegally remodelled and used. It has been remodelled to an inappropriate housing environment. As the slice room emerged as a social problem, research was carried out in various fields. Kang (2017) analysed the elderly residing in the slice room. Chae (2008) analysed residence status and studied support measures. However, most of the studies on slice rooms were conducted on the slice room resident rather than their environment (Park, 2018). Most of the advance research in Korea were limited to studies on slice room residents. They have been illegally remodelled and cannot guarantee a proper living environment. There have been no detailed studies on the living environment of the slice room. This needs to be investigated. The preliminary field study was conducted during the summer season. Slice room residents cook and smoke indoors and there has been concern about indoor environmental pollution (Lim, 2015). Because of low outside temperature, ventilation is rarely performed in the winter season. Indoor pollution is hard to be solved. Therefore, in this study, we visited the slice room in winter and conducted deep-interviews and installed the IoT data acquirer to measure the thermal environment and PM2.5 inside the slice room.

3. FIELD STUDY

The slice room case study was located in Daegu city in Korea. About 80 residents were living in nine houses. Most slice rooms consist of a single room in a single-family house, and there are no private toilets or kitchens. Sometimes there is no window. Due to space constraints, conventional measuring devices could not be used. So we used the IoT device. The factors that IoT device can measure are shown in Table 1. Deep-interviews were conducted with a total of 35 residents. Among them, 29 residents who agreed to install the equipment was measured for temperature, and 19 residents were measured for PM 2.5.

Table 1: Measuring Factor

Factor	Part name	Measuring method	Accuracy
Air Temperature & Humidity	Sht31-D	IC	$\pm 0.3(^{\circ}\text{C})$, $\pm 2(\%)$
PM2.5	SPS30	laser scattering	(0 to 100 $\mu\text{g}/\text{m}^3 \pm 10 \mu\text{g}/\text{m}^3$) (100 to 1,000 $\mu\text{g}/\text{m}^3 \pm 10\%$)

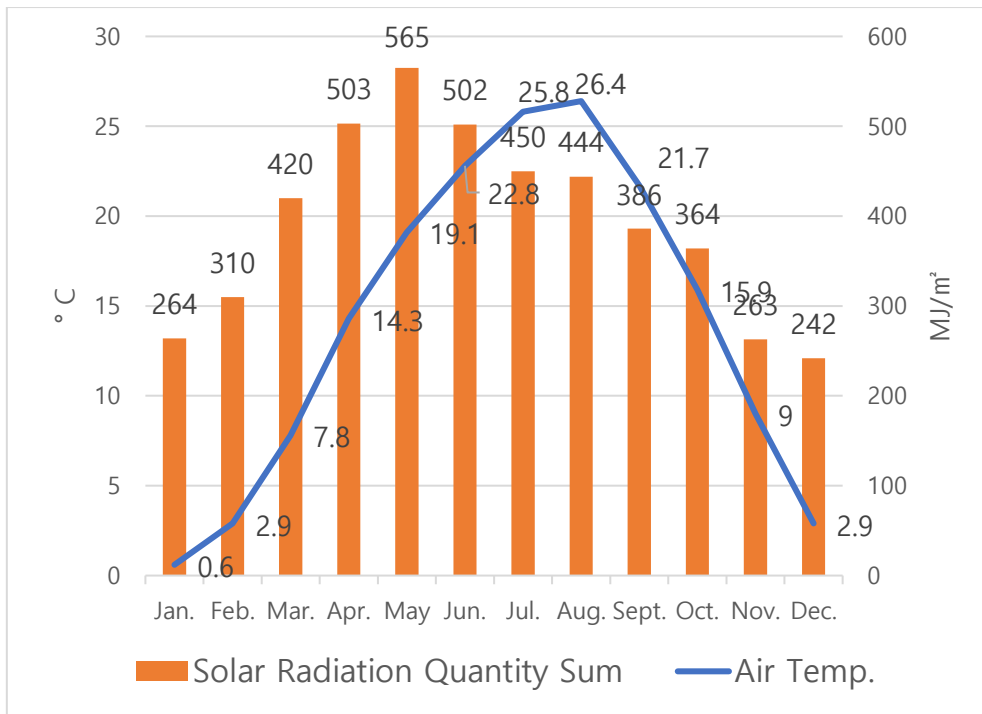


Figure 10: D city's Climatological Standard Normals

4. THERMAL AND LIVING ENVIRONMENT OF THE SLICE ROOM

The information of the resident residing in the slice room is shown in the table below.

Table 2: slice room resident information

Sex		Age	Average length of residence	Job			Average annual income (\$)	Monthly rental fee (\$)
Male	Female	56.8±9.5	7.0±7.5	Full-time	Daily employees	Unemployed	9,261.24 ± 509.08	125.53 ± 13.57
34	1			2	19	14		

The residents of the slice room were mostly male. The average annual income was \$9,261, but the monthly income was unstable due to a large number of daily employees. The average monthly rent was 125 dollars, with individual rents varying by 10 to 20 dollars depending on the presence of windows and the size of the room. Except for the 18 places using the main heating equipment, there was no heating equipment or it was not used because of energy costs. Some of the places where the heating equipment is being used were using energy sources (briquettes) from government welfare. 19 of the 35 residents lived in the slice room for financial reasons and were living outside the workplace due to distance from the workplace and living environment. 19 people had respiratory problems due to the cold environment. 26 residents included utility charges in the monthly rent. 9 residents were paying 20.36 ± 5.94 dollars.

4.1. The lived experience

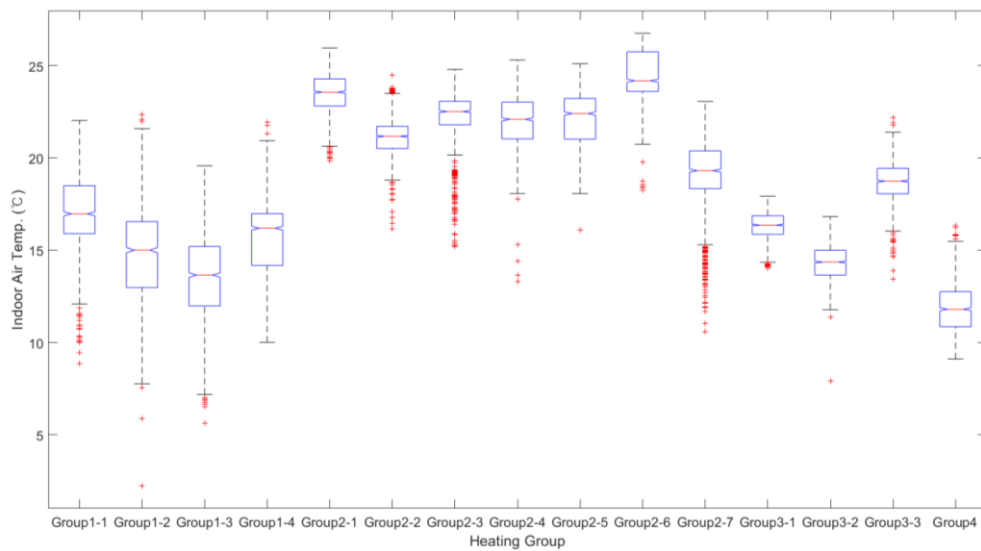


Figure 2: Heating Group

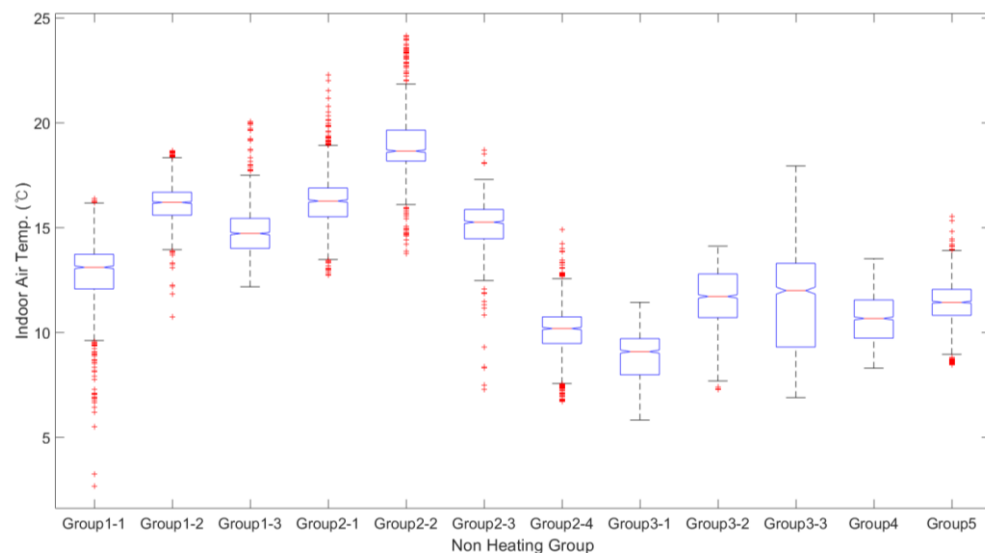


Figure 3: Non Heating Group

The indoor temperature distribution of the slice room are classed according to whether the heating device is operated or not. It is shown in Figures 2 and 3. Slice rooms in the same building were classed as the same group. In the heating group, the average temperature distribution was $18.6 \pm 3.8^\circ\text{C}$, but in the non-heating group, it was $13.3 \pm 2.8^\circ\text{C}$. Groups 1, 2 and 4 of the heating group used briquet boilers and Group 3 used night-time electric boilers. Most resident had a median value of 15 degrees or more, and Group 2 had a median value of 20 degrees or more. In the case of slice rooms located in the same building, the temperature distribution was similar, and the temperature distribution was different according to the characteristics of the building where each slice room was located. Groups 1 and 3 of the non-heating group were not equipped with boilers. Groups 2, 4, and 5 were equipped with briquettes or oil boilers but were not operating due to energy costs. Most of the groups where boilers were not installed had a median value of fewer than 15 degrees. However, Group 2 showed a higher median than other groups, which is considered to be a characteristic of the building. In the case of Group 2, non-heating residents were caught between the heating areas. The room temperature was significantly affected by the presence of main heating equipment and the building where the slice room was located.

4.2. Indoor environment quality

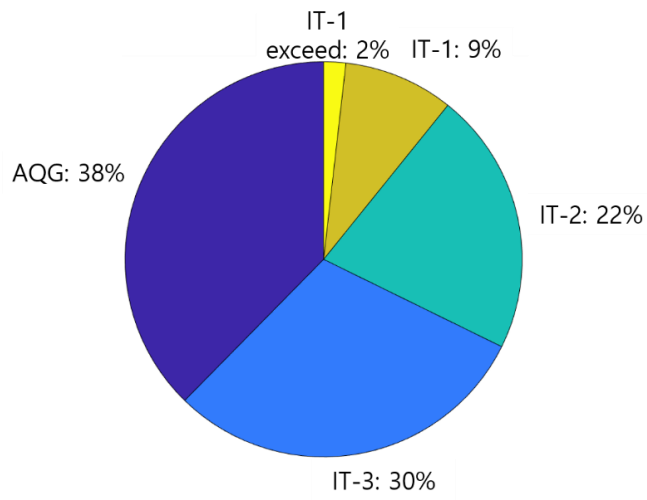


Figure 4: Korea meteorological administration Measurements PM 2.5

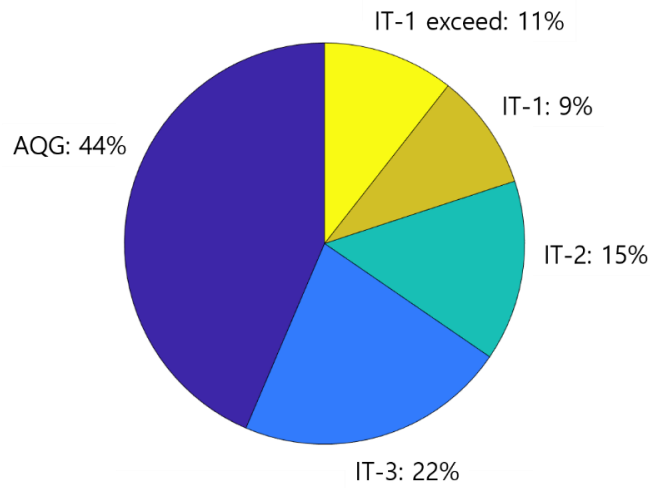


Figure 5: Non Smoking Group

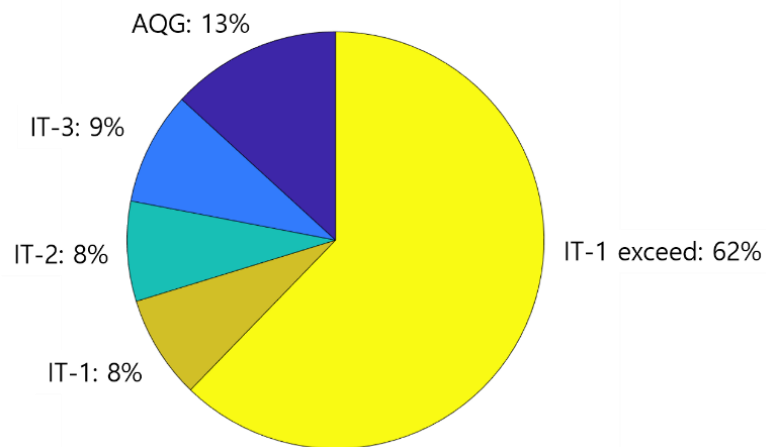


Figure 6: Smoking Group

Table 3: WHO Air quality guideline and interim targets for PM: 24-hour mean (WHO, 2005)

24-hour mean level	PM2.5	Basis for the selected level
WHO interim target 1 (IT-1)	75	Based on published risk coefficients from multicentre studies and meta-analyses (about 5% increase in short-term mortality over AQG)
WHO interim target 2 (IT-2)	50	Based on published risk coefficients from multicentre studies and meta-analyses (about 2.5% increase in short-term mortality over AQG)
WHO interim target 3 (IT-3)	37.5	About 1.2% increase in short-term mortality over AQG
WHO air quality guidelines (AQG)	25	Based on relation between 24-hour and annual PM levels

IT-3 (37 and 50 ppm), IT-1 (50 and 75 ppm), IT-1 exceed (exceeding 75 ppm), and AQG (0 and 25 ppm) were categorized. The atmosphere PM2.5 level was measured at a measuring station of Korea Meteorological Administration, which was 1.3 km away from the slice room. Figure 4 shows the average PM2.5 for one hour from February 13, 2019 to February 21, 2019, according to the WHO guideline. Slice room residents were divided into two groups as smokers and non-smokers. The PM2.5 in indoor air was classified according to the WHO guidelines and shown in Figures 5 and 6. Of 19 residents, 13 were smokers and 6 were non-smokers. For the non-smoking group, IT-1 and IT-1 exceed increase to 20%, higher than atmospheric levels. However, AQG and IT-3 accounted for a total of 66%, similar to atmospheric levels. The smoker group showed a 62% increase in IT-1 exceed, indicating a significant increase in the PM2.5 level during smoking. Considering that little ventilation occurs due to the cold outside temperatures in winter, PM2.5 was a health threat level.

5. CONCLUSIONS

This study was conducted in order to collect data on the slice rooms used by the poor in Korea. The experiment was carried out over three weeks from January 25, 2019, to February 15, 2019. We conducted a deep-interview on 35 residents. Measurements were taken at 25 residents agreed to equipment installation and PM2.5 measured at 19 residents. Residents were found to live on average for more than 7 years in slice rooms, but the variance was even. Most residents were found to have an unstable monthly income. Financial reasons led to residents residing in the slice room. The temperature was measured for 25 residents and classified into the heating group and non-heating group. The heating group showed an average temperature distribution of $18.6 \pm 3.8^\circ\text{C}$, which was higher than that of the non-heating group at $13.3 \pm 2.8^\circ\text{C}$. PM2.5 was classified into 5 sections according to WHO guidelines. In the case of the smoking group, IT-1 exceed exceeded 62% of the total, and the number of PM2.5 due to indoor smoking increased significantly. This is a level that threatens the health of the residents. Ventilation was poor so PM2.5 did not drop to normal levels. Most of the residents in the slice room were living in a poor environment. Room temperature in winter was different depending on heating and building. This is considered to be the difference according to the characteristics of the building. In the case of PM2.5, the air quality of the smoker group was bad. Therefore, a proper ventilation plan is required. In future research, we plan to conduct a field study for the summer season. We will evaluate the living environment of the slice room by using the collected slice room, indoor temperature, and indoor PM 2.5 concentration.

6. ACKNOWLEDGEMENT

This work was supported by National Research Foundation of Korea (NRF) grants funded by the Korean government (MSIP, South Korea) (No.2019R1A2C3002219)

7. REFERENCES

Chae, M. J., 2008. A Study on Analysis of Dwelling Condition of Urban Substandard Housing District and Plan of Supporting Habitability, Chung-Ang University, Masters dissertation.

Ha, S. K., 2000. Korea center for city and environment research

Kang, J. H., 2017. Research on spatial design for senior citizens living alone in Slice Rooms. *Korea Institute of Spatial Design*, 43, 35-45.

Korea Energy Economics Institute, 2015. Preliminary research for development of energy welfare policy and performance evaluation

Lim, J. H., 2015. Current Status of Indoor Air Pollutants According to the Product Type and Operation Condition of Cooking Appliances in Residential Buildings. *The Society of Living Environment System, Korea*, 22 (1), 11-22.

Park, Y. Y., 2018. A Study on the Korean Research Trends Analysis of 'Jjokbang'. *The Korean Housing Association*, 30(2), 414-417

The Academy of Korean Studies, 2001. Slice room. Encyclopaedia of Korean Culture

WHO, 2005. Air Quality Guidelines, Global Updates 2005. *World Health Organization*

#265: Sizing and simulating the performance of a standalone solar water pumping and pasteurisation system for remote Egyptian oases

Ahmed YOUSSEF¹, Ahmed HESHAM², Omar AHMED³, Omar TAREK⁴, Mark MAGED⁵, Muhammed A. HASSAN⁶, Adel KHALIL⁷

Mechanical Power Engineering Department, Faculty of Engineering, Cairo University, Giza 12613, Egypt

¹ ayayaya2851996@gmail.com

² mido12619966@gmail.com

³ eng.omar.ismail96@gmail.com

⁴ omartareq477@gmail.com

⁵ markmaged12@gmail.com

⁶ mhd.zidan17@cu.edu.eg

⁷ khalila2@asme.org

The aim of this study is to develop the concept, size, and analyse the performance of a proposed standalone solar power-driven system for pumping groundwater at remote communities of the Egyptian oases to be used in irrigation, and pasteurising a fraction of pumped water for domestic use (domestic hot water as well as cold water). A transient model is built on TRNSYS® for simulating the key variables of the pasteuriser throughout the year with predetermined loads. El-Kharga oasis, located in the Egyptian part of the Sahara Desert, has been considered as a case study. Glazed flat plate collectors and poly-crystalline PV's has been optimised to a tilt angle of 27 degrees (oriented due South) and a feedwater heat exchanger has been used to warm up the feedwater while cooling half of the pasteurised water. The results provided here are based on a community of 40 single-family houses; each family of 5 people. A preliminary cost analysis showed that the proposed system is more efficient than a traditional electricity-driven system.

Keywords: solar energy; water pasteurisation; PV-pumping.

1. INTRODUCTION

Water is the most important factor for sustainable life and the shortage of clean water is one of the most challenging issues facing the world right now. Access to a sustainable water supply is essential for irrigation, industry, and power generation. It is the most influential factor for determining the quality of living, especially in developing communities. Clean water resources, e.g. rivers, are sufficient for the current worldwide population. However, they are not evenly distributed causing a significant shortage of direct supply in many locations around the world. Hence, many communities are relying on groundwater pumping systems (Aliyu *et al.*, 2018). Locations where those systems are utilised are typically far from the country's industrial clusters or major cities. Therefore, it is usually a time-consuming process to connect those communities to the local electric power grid, which limits the expansion of those communities. This makes solar power-driven systems an attractive option for providing both water and energy requirements considering the strong relationship between the availability of intense solar radiation and water demand (Meah, Ula and Barrett, 2008). Meanwhile, the quality of groundwater is not necessarily appropriate for drinking and irrigation. In that case, it must be treated first. Among many solar energy technologies that can be used for such systems, solar photovoltaic water pumping (SPVWP) turned out to be the most cost-efficient one, which is reflected by the wide adaptation of such technology in many locations around the world nowadays (Allouhi *et al.*, 2019).

SPVWP systems are one of the main topics extensively investigated in solar energy research nowadays. For instance, Benghanem *et al.* (Benghanem, Daffallah and Almohammed, 2018) proposed a nonlinear model for predicting the flowrate of SPVWP systems as a function of the corresponding solar irradiance for different locations in Saudi Arabia. Pali and Vadhera (Pali and Vadhera, 2019) developed an analytical model of a novel solar photovoltaic power generation system whose output power is unaffected by the availability of solar radiation. The system consists of a submersible pump, a pico-hydro turbine-generator, and a pumped-hydro energy storage system, and it doesn't require the use of charge controllers, batteries, transformers, or inverters. Meunier *et al.* (Meunier *et al.*, 2019) developed and validated a model for simulating the performance of SPVWP systems used for producing domestic water at off-grid rural communities in Sub-Saharan African countries. Renu *et al.* (Renu *et al.*, 2017) investigated the effect of solar irradiance and ambient temperature variations on the output water flow rate of SPVWP systems. The authors also investigated the optimal performance of these systems using the height of water tables and pump's operating points. Tiwari and Kalamkar (Tiwari and Kalamkar, 2018) performed experimental work on an artificial well to investigate the effect of the head and the solar irradiance on the overall system efficiency. Ali (Ali, 2018) performed an extensive economic evaluation using levelised energy cost (LEC) to highlight the optimal solar power-driven irrigation system for Sudan. The study included parabolic trough, concentrating dish, and photovoltaic-driven pumps, and it was found that the later technology is the most economic efficiency one for the weather conditions, design parameters, and interest and inflation rates in Sudan. Yahyaoui *et al.* (Ali, 2018) optimised the area of PV arrays, the capacity of batteries, and the volume of the storage tank for SPVWP systems in North Tunisia given the monthly average meteorological data and the amount of water for fulfilling irrigation water requirements in that location.

As stated earlier, the quality of groundwater may necessitate a treatment process before it is being used for domestic purposes, or even for irrigation. Water pasteurisation is the process of heating water to a level sufficient for microbiological decontamination of water. For locations with high-quality groundwater, this process, alongside with pre-filtration, is sufficient for producing water safe for drinking and domestic use. Some research efforts have been made recently to design reliable and automated solar power-driven pasteurisers. For instance, Da Silva *et al.* (Carielo da Silva, Tiba and Calazans, 2016) designed a small-scale self-driven solar pasteuriser that is able to produce up to 30 l/day of pure water using a programmed temperature controller. Dobrowsky *et al.* (Dobrowsky *et al.*, 2015) investigated the possibility of using a closed-loop solar water heating system (evacuated tube collectors) to reduce the microbiological contamination of rainwater. For temperatures above 72°C, heterotrophic bacteria, *Escherichia coli*, and total coliforms were found below the detection limit, while *Yersinia spp.*, *Legionella spp.* and *Pseudomonas spp.*, have been detected in the water tank at the same temperature level. Abraham *et al.* (Abraham, Plourde and Minkowycz, 2015) found that using a simple concentrated solar power system consisting of a parabolic collector, a heat exchanger, and an automated valve can be used as a continuous flow pasteurisation system with complete inactivation of pathogens. Bigoni *et al.* (Bigoni *et al.*, 2014) also used a small-scale parabolic trough collector in a pasteuriser that is able to produce a maximum of 66 l/day while being stable in reducing the content of *Escherichia coli* bacteria at a pasteurisation temperature of 87°C. Manfrida *et al.* (Manfrida, Petela and Rossi, 2017) developed a new concept of a natural-circulation water disinfection (by pasteurisation) system that is able to produce 40 to 80 kg/day/m² of collector area, depending on the location. Monteagudo *et al.* (Monteagudo *et al.*, 2017) designed and tested a passive annular continuous-flow compound parabolic concentrator coupled with a pasteurisation system for the dual function of water disinfection and chemical decontamination. A thermostatic valve set at a temperature of 80°C was used in the pasteuriser and it was found that the chemical decontamination increases as the water residence time in the concentrator increases. Finally, Rossi *et al.* (Rossi *et al.*, 2019) performed a life cycle assessment and exergo-environmental analysis on natural circulation and thermostatic valve pasteurisation systems. Their results demonstrated the superiority of the first type of systems regarding environmental sustainability.

In this paper, a novel hybrid solar power-driven system is proposed to serve irrigation water, domestic consumption water (cold and hot), as well as electric power for small and remote villages/communities in the Egyptian oases for sustainable living and agriculture. The main components of the system are sized, and the water pasteurisation unit is simulated to determine its performance throughout the year. This is a preliminary numerical investigation to study the feasibility and the anticipated performance of the system. Energetic analysis has been performed and the water temperature levels were taken as an indicator of the microbiological contamination/decontamination in the system. As justified later, the quality of water in the studied location is high-enough for direct domestic and irrigation consumption. Therefore, there is no need for chemical treatment or desalination of water; only a low-cost sand filtration is necessary for domestic consumption, which is the common practice in those locations. To the best of authors' knowledge, the exact configuration of the system has not been proposed or investigated before.

2. MATERIALS AND METHODS

2.1. Studied location

The Egyptian Western Desert (West of the Nile river) is a part of the well-known Sahara Desert of North Africa. It is characterised by harsh subtropical climate with surplus of solar radiation, high ambient temperature, low relative humidity, and low rainfall. The desert is almost inhabitant except for five oases cantered around regions of abundant groundwater and wide cultivatable lands. These oases are Siwa, Bahariya, Farafra, Dakhla, and Kharga (see Figure 1). The soil salinity is relatively high for some oases, like Siwa, while being very low in others, like Dakhla and Kharga. One remark about Egyptian oases is the style of living, where people tend to live in small village/communities (near cultivated lands) rather than crowded cities. Therefore, each oasis has one or two cities and tens of small villages (Figure 1 Figure), making the proposed system very attractive for sustainable living and agriculture.

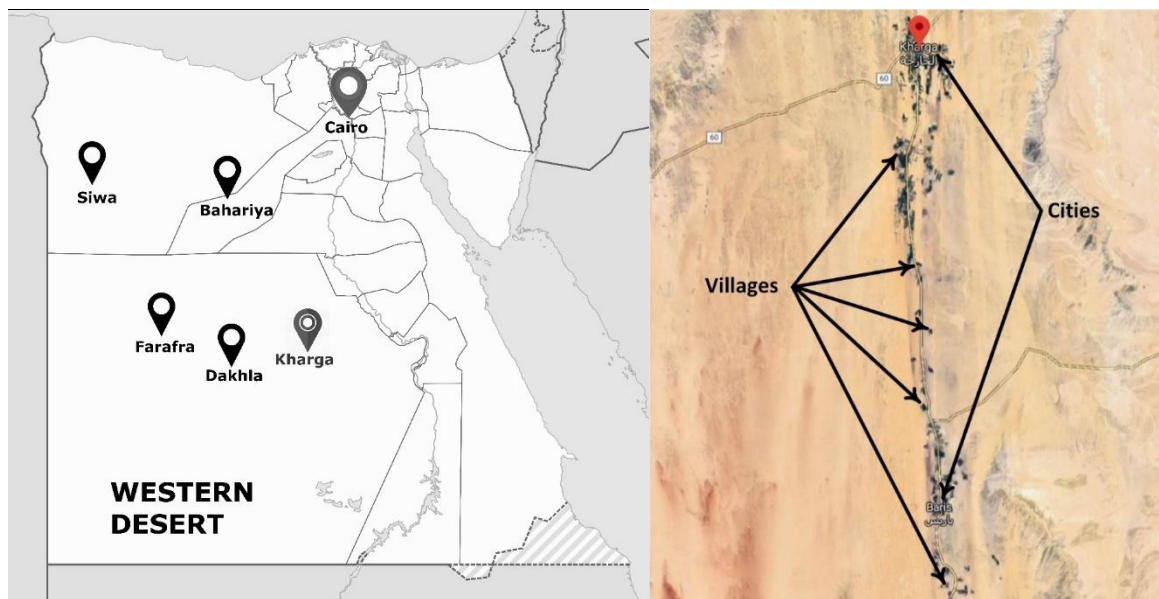


Figure 1: A map showing the locations of Egyptian oases (left) and a satellite image of Kharga Oasis (right).

The studied location in this paper is Kharga oasis, located at a latitude of $25^{\circ}26'$, a longitude of $30^{\circ}32'$, with an average elevation of 32 m. It has been selected here for some favourable characteristics such as low head of groundwater, relatively low groundwater salinity, wide cultivatable lands with soil that is easy to excavate, and few numbers of hills (mostly flat ground). Meteorological data of the city is obtained from the Meteonorm® database packaged in the simulation software TRNSYS® 16.0. Figure 2 shows the variation of the global horizontal solar irradiance as well as the ambient temperature (the two most influential meteorological parameters on the performance of both photovoltaic "PV" panels and flat plate collectors "FPCs") throughout the year. The oasis is located within the sunbelt and the abundant solar irradiance, illustrated in the figure, is favourable for both water pumping and heating applications. The extensive tests performed by Jahin and Gaber (Jahin and Gaber, 2011) on many groundwater wells in the selected oasis showed that the quality of water is safe for irrigation and drinking with total dissolved solids (TDS) number between 227 and 636 mg/l (average of 440 mg/l). Thus, the exclusion of a water chemical treatment or desalination unit is justified.

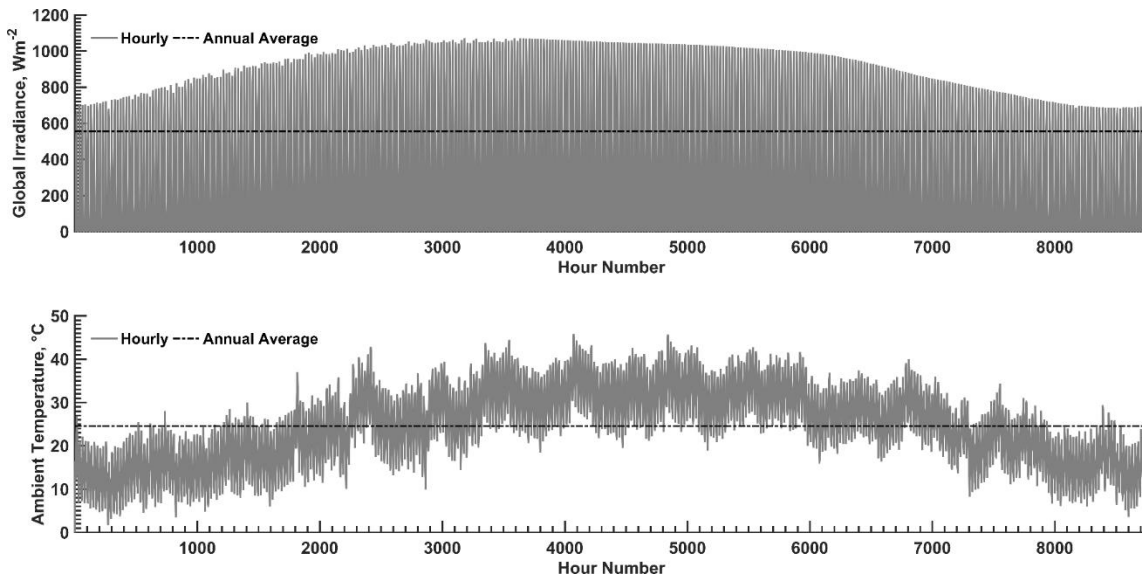


Figure 2: Variation of hourly global solar irradiance and ambient temperature at Kharga oasis.

2.2. Concept development

The layout of the proposed system is shown in Figure 3. A submersible pump is driven by PV panels to pump the groundwater out of the well. The pumped water is then stored in a large variable volume storage tank for delayed use during night. Stored water flows from the storage tank to both the cultivated lands (for agricultural use) and the water treatment unit (for domestic consumption). The fraction of pumped water drawn to the water treatment unit is determined by the daily consumption of all family houses and it has the priority to be served first. Meanwhile, the remaining fraction (irrigation water) depends on the daily number of sunshine hours, i.e. it varies from a day to another depending on the output of the PV system. The feed water (to the pasteurisation unit) goes through a filtration unit first to get rid of any impurities such as sand particles (this unit has not been sized here). Then, it gets treated in the pasteurisation unit and served to the family houses in the forms of cold water (e.g. for drinking) and hot water (e.g. for bathing and dish washing). The PV panels are sized to provide enough electric power for pumping the groundwater as well as for driving the electric appliances in the family houses.

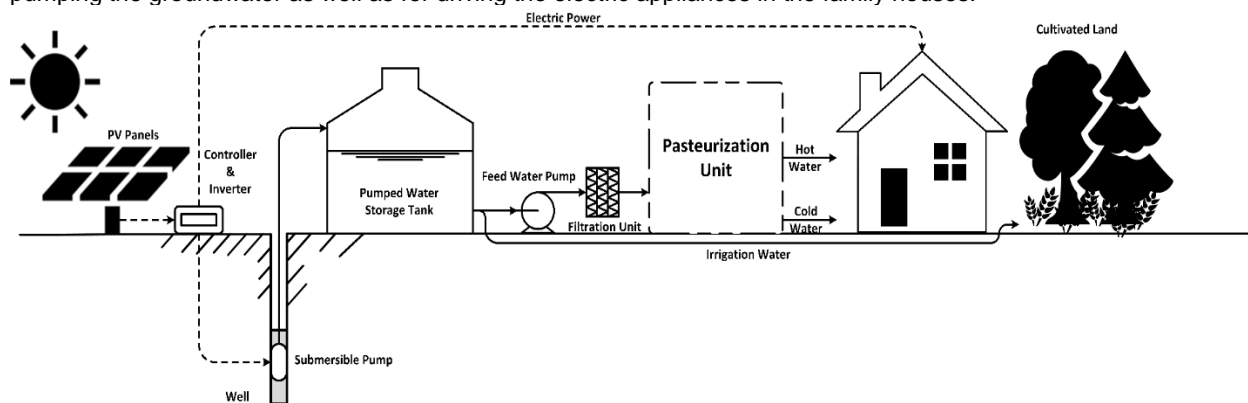


Figure 3: Layout of the hybrid system.

A P&I diagram of the pasteurisation unit is shown in Figure 4. Simply, a heat exchanger (HEX) is used to preheat the feed water before entering the thermal energy storage (TES) tank using the hot water extracted from the top of the tank. The heated water is divided into two equal fraction using a simple flow divider. The first part is served directly to the family houses as domestic hot water, and a controllable backup heater can be used during nights or times of solar irradiance shortage. The other part is the one used to preheat the feed water, while being cooled to the temperature level of direct drinking water. On the other hand, a heat transfer fluid is circulated in a closed loop by flowing from the bottom of the tank to a circulation pump, heated in the flat plate collectors, and collected back to the top of the TES tank. A temperature differential controller is used to control the operation of the single-speed pump (on/off) depending on the temperature levels in the collectors and the TES. Some necessary auxiliary components are shown in the figure for enhancing the reliability of the system.

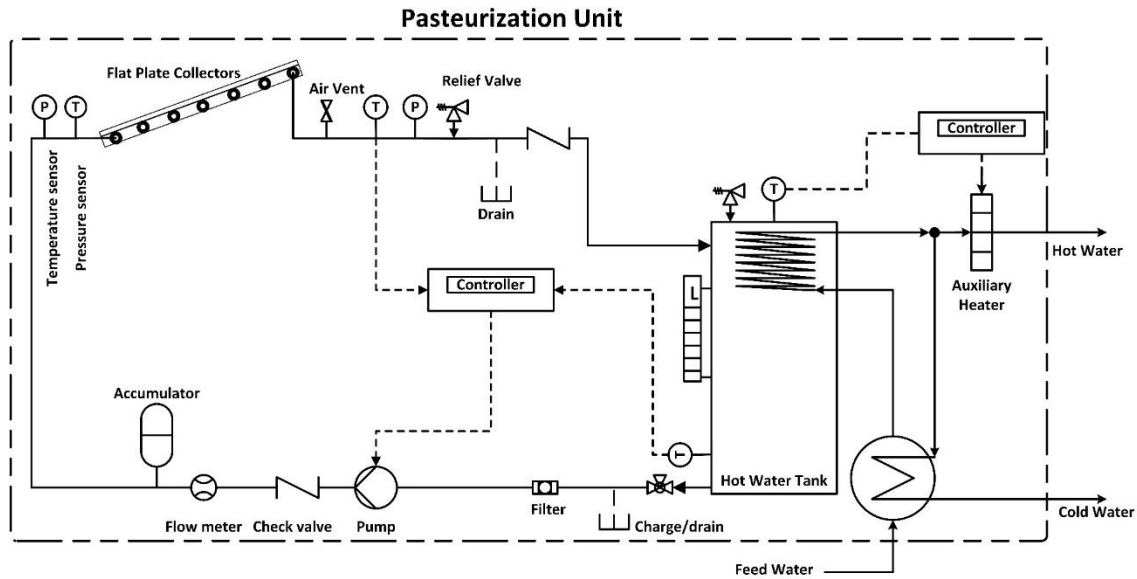


Figure 4: P&I diagram of the solar-driven pasteurisation unit.

2.3. System sizing

The system is sized based on a community of 40 family houses, each of five individuals. The first step of sizing the system is to determine the daily domestic water requirements. Accurate estimation of domestic hot water consumption is a time consuming and usually infeasible process due to the high variations of human behaviour in consuming water. A common approach in sizing solar domestic hot water systems is using the average numbers recommended by practical guides based on long-term research (Fuentes, Arce and Salom, 2018). According to (German Solar Energy Society, 2010), typical consumption of hot water per person is 20-30 l/day (low consumption), 30-50 l/day (medium consumption), or 50-70 l/day (high consumption). Here, a low consumption value of 25 l/day/person is used in sizing the system. According to the WHO (World Health Organization), a minimum amount of 50 l/day/person is required for sustainable living in the studied location based on the assumption of intermediate access scenario (water supply covers drinking, hand washing, laundry, and bathing, with low impact on people's health) (World Health Organization, 1994). Therefore, an additional 25 l/day/person of cold water is added to the system load. The total amount of water needs to be pasteurised first before divided into hot- and cold-water supplies.

The heat transfer fluid (HTF) flowing in the solar loop is a water-ethylene glycol (60:40) mixture with a density and a specific heat capacity of 1041 kg/m³ and 3.726 kJ/kg.K. The HTF is selected for some favourable characteristics such as low freezing point (to avoid freezing during cold desert nights due to nocturnal cooling effects), and high boiling point (during periods of intense solar irradiance and low consumption). FPCs are used for harnessing the solar irradiance. These collectors have been chosen for their simplicity, low maintenance costs, availability in the local market, and lower sensitivity to dust accumulation in desert locations, compared to other collectors that can be used to heat the HTF to the same temperature level. The FPCs have been set at optimal tilt and azimuth angles of 27° (fixed throughout the year) and 0° (due south). The required area of the FPCs has been determined following the procedure described in (German Solar Energy Society, 2010). According to this guide, a solar fraction (SF) of 0.8 or higher can be considered for tropical climates. Here a value of 0.95 has been taken. A code, developed using Engineering Equation Solver (EES), has been used to determine the design overall system efficiency (η_s) by estimating the useful heat gain and the thermal losses throughout the system; the resulting value was 53%. The design stored heat equals 243,455 kWh/year based on a temperature difference of 57.5°C between the design supply temperature (80°C) and the average temperature of water drawn from the mains (22.5°C).

The final sizing parameter is the total annual solar irradiation (E_g) per unit area, which is 2124 kWh/m²/year for the studied location (Wold Bank Group, 2016). Thus, the required area can be determined as $A_c = (SF \cdot Q_c) / (E_g \cdot \eta_s) \sim 220 \text{ m}^2$ (330 FPCs with gross area of 2 m²). To limit the temperature difference throughout each collector to a maximum of 10°C, the FPCs have been arranged in 110 arrays (each of three FPCs in series). The efficiency curve of the FPCs is defined by the following parameters: a_0 (intercept factor) = 0.8, a_1 (efficiency slope) = 3.6 W/m².K, and a_2 (efficiency curvature) = 0.014 W/m².K². The external heat exchanger (HEX) is designed based on the aforementioned design temperatures and a required cold-water outlet temperature of 28°C (to decrease in the supply lines to the normal tap water temperature, e.g. 24°C). Using the logarithmic-mean temperature difference method and the appropriate heat transfer correlations for a shell-and-tube HEX, an overall heat transfer coefficient (UA) value of 3746 W/K is used. The circulation pump is used for circulating the HTF throughout the solar loop

during durations of intense solar irradiance (9:00 am to 3:00 pm). It is selected based on a flow rate of 8.29 m³/h and a head of 3 m, only to overcome the head losses through the closed loop. A single-stage centrifugal in-line pump (Grundfos TP 80-40/4) is used in the simulation. The diameter of the piping system in this loop is 3" and the velocity in pipes is limited to 0.5 m/s. A simple temperature differential controller is used to control the pump with upper and lower dead band temperature differences of 10 and 8°C, accordingly. On the other hand, the submersible pump is supposed to draw the total daily demand of domestic as well as irrigation water from the well. The pump is selected based on a flow rate of 150 m³/day and a total head of 75 m (these numbers have been obtained from local irrigation and agricultural experts in Kharga for artesian aquifers). This head covers the static head difference between the suction point of the pump and the tank water level (70 m) as well as the head losses through the piping system (3 m). The selected pump is a multi-stage submersible pump of model Grundfos 85s100-9.

A wooden hydraulic storage tank is used for storing pumped water for night irrigation. Its volume is 150 m³ considering 10 m³ for domestic water and 140 m³ for irrigation water. A wooden tank was found relatively cheaper, with good corrosion resistance, long-life expectancy and low maintenance cost (though, a concrete storage tank may be considered). As for the TES tank, a volume of 10 m³ is required to store the domestic water demand of a single day. A stainless-steel tank (high corrosion resistance) with 1" mineral wool insulation is proposed. The tank has an aspect ratio of 2.5 (i.e. height of 4.4 m and diameter of 1.75 m) to maximise the thermal stratification (better charging/discharging efficiency) and to minimise the inlet temperature to the collectors (higher FPCs' thermal efficiency). The submersible pump requires a power of 11 HP (8 KW) and a voltage of 380 V (3 phase). Meanwhile, the circulating pump has a power 0.323 HP (0.2375 KW) and a voltage of 220 V (1 phase). An inverter of model GD100-011G-4-PV has been selected for its availability in the local market and suitability for those design parameters. Based on these design data and using the polycrystalline PV panels SunTech STP330 (relatively less expensive, while being popular in the local market), the PV farm was designed as 17 parallel arrays, with each array consisting of 5 panels in series.

2.4. Numerical simulation

TNSYS® is a transient simulation software that is widely used in research and commercial renewable energy, power generation, and HVAC applications, among others. It has a modular structure, where different modules (called types) of already validated models are connected and numerical information propagates at each time step through the flow diagram from input modules, such as weather data modules, to output modules, such as plotters, integrators, and printers. The information flow diagram of the TRNSYS code is illustrated in Figure 5 for the pasteurisation unit. The weather data module (Type 109) is used to acquire the METEONORM® data, namely: the global irradiance on tilted surface (based on the designated collector angles), the ambient temperature, and the wind speed, to be used in modelling the performance of FPCs. Meanwhile, a forcing function (Type 14h) is used to define the operation period of the pump. All types selected to model the components are highlighted in the figure, and online plotters and printers are used to obtain the simulation results for further processing. Additional input parameters used in the simulation are shown in Table 1. The simulation is carried on for the whole year with a time step of 20 minutes.

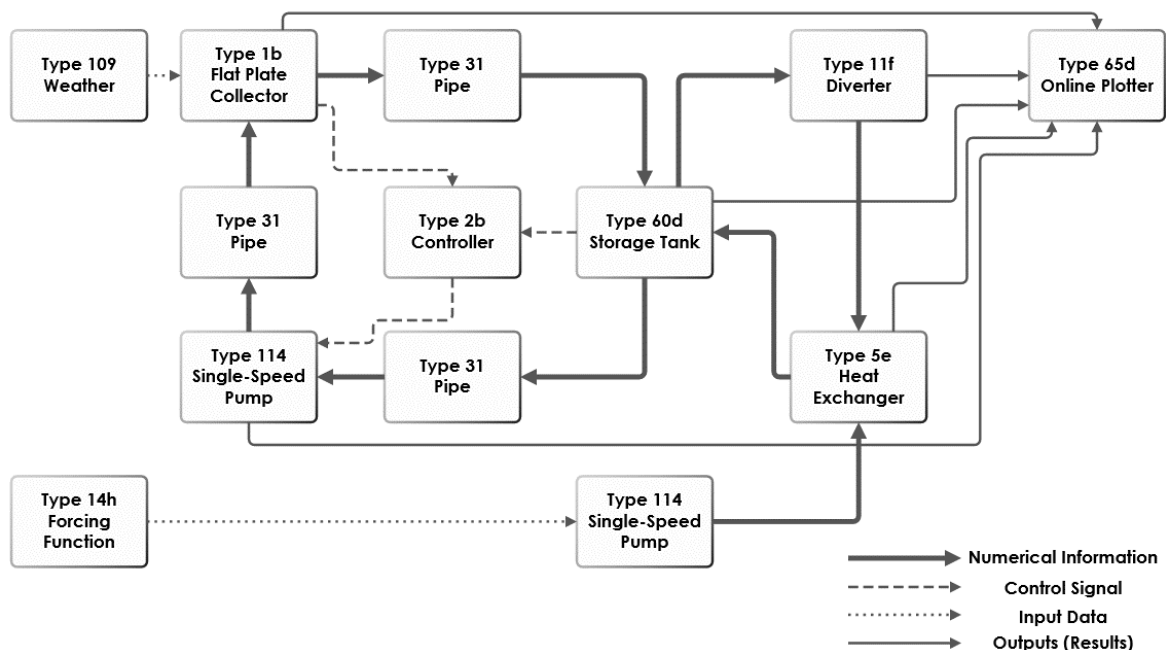


Figure 5: Flow diagram of the TRNSYS code.

Table 1: Additional inputs of the TRNSYS model.

Parameter	Value	Unit
Piping heat loss coefficient	0.04	W/m ² .K
Tank heat loss coefficient	0.04	W/m ² .K
Water specific heat	4.18	KJ/kg.K
Water density	1000	Kg/m ³
Height of auxiliary heater inside the tank	2	m
Height of thermostat inside the tank	3	m
Set point temperature of the tank	80	°C
Glycol fraction	0.4	-
Internal heat exchanger pipe inlet diameter	0.0254	m
No of fines per meter	0 (smooth surface internal HEX)	-
Total surface area of internal heat exchanger	11.98	m ²
Heat exchanger length	139.2	m
Heat exchanger wall conductivity	111	W/m ² .K

3. RESULTS AND DISCUSSION

3.1. Performance evaluation

This section briefly describes the preliminary simulation results. As shown in Figure 6, the outlet temperatures of the FPCs are high enough to decontaminate the water in the thermal energy storage tank. The FPCs' outlet temperature has an average of 56.6°C, which is within the operating temperature range of these collectors. However, during sunny days, the outlet temperature at the end of the loop can reach up to 180°C, which indicate a serious stagnation problem during these days. As stated before, the FPCs have been selected due to their local availability in the market. However, the simulation results indicate that alternative collectors that have better thermal characteristics at such elevated temperature range, e.g. evacuated-tube or CPC collectors, may be more appropriate for this system. The figure also shows that the inlet temperature to the solar field (from the TES tank) is relatively high (not very suitable for FPCs). On the other hand, Figure 7 shows the variations in the mean and inlet temperatures of the TES tank. The TES's annual average temperature is about 73°C, even with the short diurnal operation duration of the pasteurisation unit and the high time thermal losses, keeping the water temperature at a safe level above contamination temperatures. The inlet temperature of to the TES (from the feedwater HEX) is ranging from 20°C and 50°C, indicating a high potential of this HEX in reducing the required energy from the FPCs.

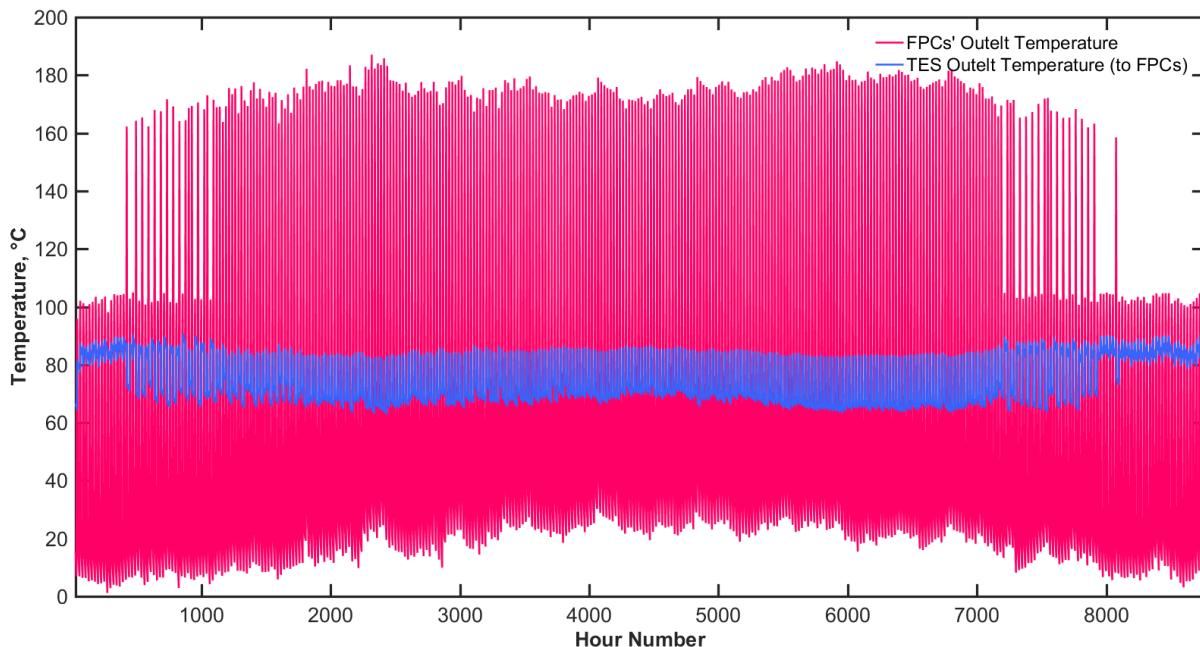


Figure 6: Variation of the inlet and outlet temperatures of the FPCs loop.

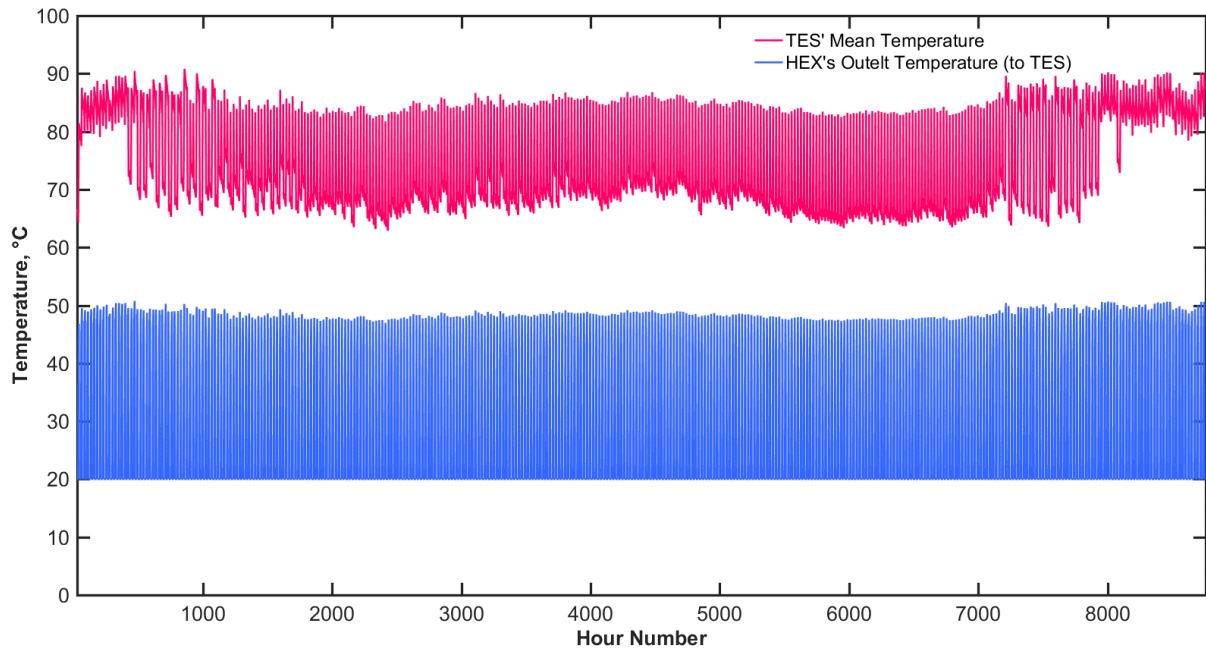


Figure 7: Variation of the TES' inlet and mean temperatures.

3.2. Economic evaluation

The lifetime of the flat plate solar water is the longest compared to electric or gas heaters; it can reach up to 25 years. Here, its salvage value (SV) is being calculated using the straight-line method for an estimated annual depreciation rate (d) of 3%. No obvious maintenance cost can be considered except that the magnesium rod, which costs 40 L.E. (2.41 USD)/piece and should be replaced annually. Associated gas heater running cost for both insolation shortage and tank losses is 4500 L.E. (270.6 USD)/year. After analysing the machining processes, man hours, and the average labour salary required for manufacturing one unit of the solar water heater, an average labour cost of 5% of the whole system price is considered. A full detailed price list of the whole solar water heater components is shown in Table 2. The total solar water heater initial cost (P) equals 3701802 L.E. (222618 USD). The annual depreciation charge (Dt) = $P \cdot d = 3701802 \cdot 0.03 = 111054$ L.E. (6678.5 USD)/year. For an inflation rate of 5%, and a compound bank profit of 10.5%, the effective interest rate is determined as $0.105 + 0.05 + 0.05 \cdot 0.105 = 16\%$. On the other hand, there is the annual profit of the cultivated crops. Typical feddan consumes 5 m^3 , which means a total cultivated area of 27 feddans. This is based on the traditional method of irrigation (surface irrigation). If a modern conservative method (e.g. drip or sprinkler irrigation) is used, even wider lands can be irrigated. Typical crops planted in the targeted location are potatoes, barley, and beans (by enquiring a field expert). However, barley is used for fertilising the land, yet it covers its expenses without profit.

Potatoes are planted in winter with a yield of 18 tons/feddan. The expenses are covered by 10 tons, the profit can be estimated as 8 tons only, and it is sold with a rate of 4000 L.E./ton. Beans are planted in summer and the feddan provides 3 tons, the yield is 1 ton /feddan, sold at a rate of 18000 L.E. (1082.5 USD)/feddan. Based on the assumed interest and inflation rates, the salvage value is estimated as 925452 L.E. (56654.6 USD). The equivalent uniform annual costs (EUAC) of payments and profit are estimated as 611928 (36800 USD) and 738072 L.E. (44386 USD)/year, accordingly. Finally, the costs of the proposed system are compared to a standard electric system. The electricity cost for the highest electricity consumption section (<1000KW) is 2 L.E. (0.12 USD)/kWh. The required energy for the main heat exchanger (TES tank) per year = 243455 kWh. The submersible pump is supposed to operate 6 hr/day and its power consumption is 8.1 kW. For consumption taxes of 25%, the EUAC value for an electric system is 652920 L.E. (39265.1 USD)/year. Therefore, it can be seen that the proposed system, beside its lower environmental impact, is more cost-efficient compared to the electricity-driven system (summary of the results is provided in Table 3). This is based on the assumption that the studied community is already connected to the national electric grid. If an electricity line is to be extended to the targeted location, the proposed system is expected to be even more superior.

Table 2: Detailed costs of the system.

#	Item	Specifications/Model	Price	Quantity	Total cost (L.E.)
1	PV panels	Polycrystalline SunTech STP330	6.3 L.E./W	95	197505
2	Submersible pump controller & inverter	Invet Good drive GD100-011G-4-PV	10500 L.E./unit	1	10500
3	Submersible pump	85S100-9 Grundfos	6100 L.E./unit	1	61000
4	Storage tank	Stainless steel	1675 L.E./ m ³	10 m ³	16750
5	Feed water pump	TP 80-40/4 RUUE Grundfos	30000L.E./unit	1	30000
6	Filtration unit	Integrated underground water filter system	8000 L.E./unit	1	8000
7	Flat plate collectors	3 covers	10000 L.E./unit	330	3300000
8	Circulating pump	Grundfos TP 80-40/4	30000 L.E./unit	1	30000
9	Hot water tank	Buffer tank	110 L.E./ ft ³	1227.2 ft ³	134000
10	Feed-water heat exchanger	Shell and tube HEX	50 L.E./ ft ³	500 ft ³	25000
11	Auxiliary heater	Gas heater	2000 L.E./unit	1	2000
12	Relief valve	Automatic	335 L.E./unit	1	335
13	Check valve	Hydraulic	400 L.E./unit	2	800
14	Flow meter	Digital	500 L.E./unit	500	500
15	Pressure sensor	GPT200 RS485 HART	420L.E./unit	2	840
16	Temperature sensor	E-type	210 L.E./unit	4	840
17	Air vent	-	300 L.E./unit	1	300
18	Accumulator	Hydraulic press.	800 L.E./unit	1	800
19	Filter	Simple type	2500 L.E./unit	1	2500
20	Circulation pump controllers	Invet Good Drive	1300 L.E./unit	2	2600
21	Pipes (3 inch)	PVDF Thermo plastic	43.3 L.E./kg	200 m	8660
	Pipes (3 inch)	Brass	380 L.E./6 m	31 m	1963.33
	Pipes (1.25 inch)	Brass	180 L.E./6 m	220 m	6600
22	Fittings/elbows	PVDF	30 L.E.	4	120
23	Pipe insulation	Mineral wool	36 L.E./piece (130 cm * 120 cm)	25	900
24	Circulating pump controller & inverter	Invet Good Drive	2300 L.E.	1	2300
25	Tank insulation	Mineral wool	36 L.E./piece (130 cm * 120 cm)	17	612
26	Water glycol	-	16.75 L.E.	661 kg	11100
Total equipment/material cost				3525525.33 (212017 USD)	
Total labour cost				176276.3 (10600.85 USD)	
Total project cost				3701802 (222617.91 USD)	

Table 3: summary of the economic analysis.

EUAC	Solar Power-Driven system	Traditional Electrical System
Paid L.E. (USD)/year	611923 (36799.65)	662920 (39866.49)
Profit L.E. (USD)/year	738072 (44385.96)	687080 (41319.42)
Payback period	5 years	6 years

4. CONCLUSION

This study is an investigation of a hybrid system for producing electricity, irrigation water, and domestic water for remote oases in the Egyptian desert. The concept of the system has been developed and preliminary sizing, simulation, and cost analysis have been introduced. Preliminary results show a great potential of the concept and economic superiority compared to traditional electricity-driven systems. However, it was found that the FPCs may not be the optimal choice as the heating collectors due to the elevated temperature levels. This may be remedied via a reliable stagnation control or by using alternative collectors. Using an automated valve to control the flow out of the TES based on predetermined set temperatures (to ensure the decontamination of water) is another way for enhancing the system's operation. Future work includes: 1- detailed design of a low-cost filtration unit, 2- extending the PV area to account for the domestic electricity consumption in the family houses based on accurate estimation of the household consumption, 3- incorporating the SPVWP system in the simulation to monitor all system's key

parameters simultaneously, and 4- investigating the possibility of extending the operation time of the pasteurisation unit to night time.

5. REFERENCES

Abraham, J. P., Plourde, B. D. and Minkowycz, W. J. (2015) 'Continuous flow solar thermal pasteurization of drinking water: Methods, devices, microbiology, and analysis', *Renewable Energy*. Elsevier Ltd, 81, pp. 795–803. doi: 10.1016/j.renene.2015.03.086.

Ali, B. (2018) 'Comparative assessment of the feasibility for solar irrigation pumps in Sudan', *Renewable and Sustainable Energy Reviews*. Elsevier Ltd, 81(August 2017), pp. 413–420. doi: 10.1016/j.rser.2017.08.008.

Aliyu, M. *et al.* (2018) 'A review of solar-powered water pumping systems', *Renewable and Sustainable Energy Reviews*. Elsevier Ltd, 87(March 2017), pp. 61–76. doi: 10.1016/j.rser.2018.02.010.

Allouhi, A. *et al.* (2019) 'PV water pumping systems for domestic uses in remote areas: Sizing process, simulation and economic evaluation', *Renewable Energy*. Elsevier Ltd, 132, pp. 798–812. doi: 10.1016/j.renene.2018.08.019.

Benghanem, M., Daffallah, K. O. and Almohammed, A. (2018) 'Estimation of daily flow rate of photovoltaic water pumping systems using solar radiation data', *Results in Physics*. The Authors, 8, pp. 949–954. doi: 10.1016/j.rinp.2018.01.022.

Bigoni, R. *et al.* (2014) 'Solar water disinfection by a Parabolic Trough Concentrator (PTC): Flow-cytometric analysis of bacterial inactivation', *Journal of Cleaner Production*. Elsevier Ltd, 67, pp. 62–71. doi: 10.1016/j.jclepro.2013.12.014.

Cariello da Silva, G., Tiba, C. and Calazans, G. M. T. (2016) 'Solar pasteurizer for the microbiological decontamination of water', *Renewable Energy*. Elsevier Ltd, 87, pp. 711–719. doi: 10.1016/j.renene.2015.11.012.

Dobrowsky, P. H. *et al.* (2015) 'Efficiency of a closed-coupled solar pasteurization system in treating roof harvested rainwater', *Science of the Total Environment*. Elsevier B.V., 536, pp. 206–214. doi: 10.1016/j.scitotenv.2015.06.126.

Fuentes, E., Arce, L. and Salom, J. (2018) 'A review of domestic hot water consumption profiles for application in systems and buildings energy performance analysis', *Renewable and Sustainable Energy Reviews*. Elsevier Ltd, 81(April 2017), pp. 1530–1547. doi: 10.1016/j.rser.2017.05.229.

German Solar Energy Society (2010) *Planning and installing solar thermal systems: A guide for installers, architects and engineers*. 2nd ed. London: Earthscan. doi: 10.4324/9781849775120.

Jahin, H. S. and Gaber, S. E. (2011) 'Study of groundwater quality in El-Kharga Oasis, Western Desert, Egypt.', *Asian Journal of Water, Environment and Pollution*, 8(4), pp. 1–7. Available at: <http://iospress.metapress.com/content/401k371551x11312/fulltext.html>.

Manfrida, G., Petela, K. and Rossi, F. (2017) 'Natural circulation solar thermal system for water disinfection', *Energy*. Elsevier Ltd, 141, pp. 1204–1214. doi: 10.1016/j.energy.2017.09.132.

Meah, K., Ula, S. and Barrett, S. (2008) 'Solar photovoltaic water pumping-opportunities and challenges', *Renewable and Sustainable Energy Reviews*, 12(4), pp. 1162–1175. doi: 10.1016/j.rser.2006.10.020.

Meunier, S. *et al.* (2019) 'A validated model of a photovoltaic water pumping system for off-grid rural communities', *Applied Energy*. Elsevier, 241(February), pp. 580–591. doi: 10.1016/j.apenergy.2019.03.035.

Monteagudo, J. M. *et al.* (2017) 'A novel combined solar pasteurizer/TiO₂ continuous-flow reactor for decontamination and disinfection of drinking water', *Chemosphere*, 168, pp. 1447–1456. doi: 10.1016/j.chemosphere.2016.11.142.

Pali, B. S. and Vadhera, S. (2019) 'A novel solar photovoltaic system with pumped-water storage for continuous power at constant voltage', *Energy Conversion and Management*. Elsevier, 181(December 2018), pp. 133–142. doi: 10.1016/j.enconman.2018.12.004.

Renu *et al.* (2017) 'Optimum sizing and performance modeling of Solar Photovoltaic (SPV) water pumps for different climatic conditions', *Solar Energy*. Elsevier Ltd, 155, pp. 1326–1338. doi: 10.1016/j.solener.2017.07.058.

Rossi, F. *et al.* (2019) 'Environmental impact analysis applied to solar pasteurization systems', *Journal of Cleaner Production*. Elsevier Ltd, 212(August 2017), pp. 1368–1380. doi: 10.1016/j.jclepro.2018.12.020.

Tiwari, A. K. and Kalamkar, V. R. (2018) 'Effects of total head and solar radiation on the performance of solar water pumping system', *Renewable Energy*. Elsevier Ltd, 118, pp. 919–927. doi: 10.1016/j.renene.2017.11.004.

World Bank Group (2016) *Global Solar Atlas*. Available at: <https://globalsolaratlas.info/> (Accessed: 13 June 2019).

World Health Organization (1994) *Guidelines for drinking-water quality [electronic resource]: incorporating first addendum. Vol. 1, Recommendations. – 3rd ed., Society*. Geneva. doi: 10.1111/j.1462-2920.2010.02199.x.

#267: Computational fluid dynamics investigation of the thermal effectiveness of an oscillating air jet from a cassette split type air conditioner

Yunqing FAN

Living environment systems laboratory, Mitsubishi Electric Corporation, 2478501, Kamakura, Kanagawa, Japan, Fan.Yunqing@ak.MitsubishiElectric.co.jp

A comfortable healthy indoor environment has become a major concern since people spend about 90% of their time in the indoor environment on average. Thermal uniformity in the indoor environment is not only about thermal comfort with high indoor environment quality, but it is also advantageous to assess diffusive performance of the air conditioner.

The purpose of this study is to qualitatively investigate the thermal effectiveness of an oscillating air jet generated by side-to-side swing-type louvers (air delivery device) which are mounted inside a cassette split type air conditioner to provide the thermal uniformity. The impact of air supply control strategies such as louvers' movement type, time interval, and swing angle, on indoor thermal environment were evaluated by Computation Fluid Dynamic (CFD) numerical simulation. A full-scale field experiment for validation is conducted in the environment chamber. The simulated result matches the experimental data well and verifies the feasibility of the proposed control method.

In this study, the temperature performance was evaluated by: (i) average temperature difference and standard deviation (RMS) at represent sections; (ii) temperature utilisation coefficient for energy efficiency; (iii) air draught rate (DR%) on the face to determine the local discomfort due to cold draught in heating mode. The oscillating airflow as generated by the side-to-side swing deliver louvers mounted inside a cassette split type air conditioner could shorten warming time in heating conditions. In addition, the high temperature area is sign of the circle generates from diffusive type oscillating (louvers swing angle $\pm 40^\circ$) airflow. The supply air provides even temperature at each representative section compared to the conventional straight type airflow.

The operation optimisation on the louvers' movement parameters significantly improves the thermal uniformity, with a temperature difference reduction of 34% and draught rates on the face ranged 0-35% at 1.2m height horizontal section. The temperature utilisation coefficient varied in accordance with the louver's directions, however, relatively poor temperature utilisation coefficients are occurred at the corners under straight type airflow.

Keywords: air conditioner; side-to-side swing; oscillating air jet; CFD; thermal effectiveness

1. INTRODUCTION

A comfortable healthy indoor environment has become a major concern since people spend an average of 90% of their time in the indoor environment (Brasche and Bischof 2005). A total of 40%-50% of world energy is used by buildings in order to maintain thermal comfort using heating, ventilation and air conditioning (HVAC) systems (Lombard et al. 2008). Statistics show that commercial buildings take up to 39% of the total CO₂ emission while residential houses account for 32% in Tokyo (Shibuya and Croxford 2016). More than 40% of this is taken up by HVAC system. The Japanese Ministry of Economy has set stringent targets to reduce greenhouse gas emissions by 26% by 2030 from 2010 levels and 50% by 2050 (Strategy for energy conservation of Japan, 2016). One of the key solutions to decrease the energy consumption of HVAC systems is to improve the thermal performance of air distribution systems. Cao (2014) and Melikov (2016) pointed out that such systems are responsible for indoor thermal comfort and air environmental quality which significantly affects the health and productivity of occupants.

Fan and Ito (2012, 2014) noted that temperature stratifies, especially in heating mode, in the vertical direction and apparently degraded the occupants' thermal sensation, and comfort levels varied depending on their location in the space as a result of insufficient air mixing throughout the whole space. As mentioned in previous investigations, thermal stratification often occurred in large open-plan office buildings and storage facilities especially in winter seasons (Rhee et al. 2015), buoyancy-driven ventilated spaces including displacement (Gilani and Montazeri 2016), under-floor air distribution (UFAD) (Xue and Chen 2014) and stratum ventilation systems (Tian, Lin and Wang 2011). In the viewpoint of local personal comfort, discomfort and complaints typically triggered by draught or low temperature are often attributed to inappropriate airflow design. In addition, vertical air temperature difference can be increased when indoor supply air temperature had a large difference with the room air temperature, and which would result in the local discomfort and the deterioration of indoor environmental quality conditioning. Therefore, to deliver air evenly throughout every corner in any space and to decrease the horizontal and vertical temperature difference has become the key issues for current airflow delivery design.

In this paper, the thermal performance of an oscillating airflow generated by side-to-side swing type louvers (air delivery device) which are mounted inside a cassette split type air conditioner to provide the thermal uniformity is qualitatively investigated. The thermal performance was evaluated by: (i) average temperature difference and standard deviation (root mean square error) at representative sections; (ii) temperature utilisation coefficient for energy efficiency; (iii) air draught rate (DR%) on the face to determine the local discomfort due to cold draught in heating mode.

2. METHODOLOGY

2.1. Oscillating jet air supply device

Driven by concerns for building energy-efficiency, new and retrofitted buildings apparently preferred to use energy-efficient cassette split or multi type package air conditioning (PAC) systems, especially in Japanese office. Hence, the thermal performance of an oscillating air jet generated from cassette split type air conditioner was studied here. The side-to-side swing deliver louvers created by Mitsubishi Electric Corporation (SlimZR series PLP-U160ELR) were installed inside the air supply opening as shown in Figure 1. To provide the oscillating jet, louvers were set to swing -40° to $+40^\circ$ consecutively. Each louver was controlled by unique motor correspondingly to facilitate a simultaneous and synchronous swapping direction. Consequently 360 degree even jet flow can be provided by a clock wise and/or anti-clock wise movement of these 4 side-to-side swing louvers.

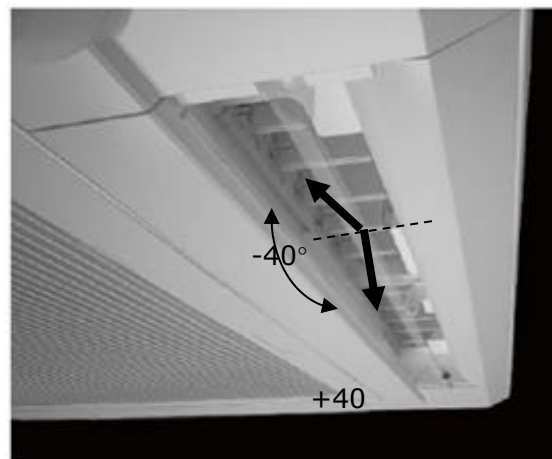


Figure 11: Schematic of side-to-side swing louver in the supply opening

2.2. CFD numerical simulation

In this study, FlowDesigner18 was adopted as commercial CFD tool to construct the physical model, generate the mesh and calculate the thermal environment. The airflow pattern in the target space was analysed using a standard k-ε turbulence model with a generalised logarithmic type wall function. Reynolds averaged Navier-Stokes (RANS) modelling was recommended by Zhang and Chen (2007) in indoor air assessment because it provides good results with the least amount of computing time compared with large eddy simulation and direct numerical simulation.

Equation 13: The transport equations for turbulent kinetic energy
$$\frac{\partial k}{\partial t} + \frac{\partial k U_j}{\partial x_j} = \frac{\partial}{\partial x_j} \left[\left(\nu + \frac{\nu_t}{\sigma_k} \right) \frac{\partial k}{\partial x_j} \right] + P_k + G_k - \varepsilon$$

Equation 2: The transport equations for dissipation rate
$$\frac{\partial \varepsilon}{\partial t} + \frac{\partial \varepsilon U_j}{\partial x_j} = \frac{\partial}{\partial x_j} \left[\left(\nu + \frac{\nu_t}{\sigma_\varepsilon} \right) \frac{\partial \varepsilon}{\partial x_j} \right] + \frac{\varepsilon}{k} \cdot [C_{\varepsilon 1} \cdot (P_k + C_{\varepsilon 3} G_k) - C_{\varepsilon 2} \cdot \varepsilon]$$

Equation 3: Production term P for turbulent kinetic energy
$$P_k = -\overline{u_i u_j} \frac{\partial U_i}{\partial x_j} \approx 2\nu_t S_{ij} S_{ij}$$

Equation 4: Buoyancy production term for turbulent kinetic energy
$$G_k = -\beta g_i \overline{u_i \theta} \approx \beta g_i \frac{\nu_t}{\sigma_\theta} \frac{\partial \Theta}{\partial x_i}$$

Equation 5: The transport equation of the relevant parameters, e.g., temperature, humidity et al.
$$\frac{\partial \Phi}{\partial t} + \frac{\partial \overline{U_i \Phi}}{\partial x_i} = \frac{\partial}{\partial x_i} \cdot \left(\left(\Gamma + \frac{\mu_t}{\sigma_i} \right) \frac{\partial \Phi}{\partial x_i} \right) + S_\Phi$$

Where:

- $\overline{U_i}$ = ensemble averaged air velocity vector (m/s)
- Φ = target scalar
- Γ = molecular diffusion coefficient of the scalar in air (m²/s)
- μ_t = turbulent viscosity (m²/s)
- σ_i = Turbulent Schmidt number
- S_Φ = source term

The SIMPLE (Semi-Implicit method for pressure linked equation) algorithm was applied to couple the pressure and velocity calculations. The standard interpolation scheme was adopted for pressure, and the QUICK scheme was used for all the other variables. The buoyancy model which employed the Boussinesq approximation was integrated. Unsteady state with one second time-step and three dimensional analyses were conducted in this study. Boundary conditions are shown in Table 1. In addition, louver movement patterns which were defined as confluent type (CASE1) diffusive type (CASE2) and conventional straight type (CASE3) are shown in Figure 2. In this study, louver movement patterns were investigated to analyse the thermal performances quantitatively.

Table 8: Boundary condition of CFD simulation

Analysis Condition	Unsteady state	
Turbulence model	Standard k-ε turbulent model	
Total mesh number	2,917,075 (structured)	
Algorithm	SIMPLE	
scheme	QUICK	
Time step	1s	
AC	SA	$Q_{inAC} = 24\text{m}^3/\text{min}$ $k_{in} = 3/2 \times (0.1 U_{in})^2$, $\varepsilon_{in} = (C_\mu^{3/4} k_{in}^{3/2}) / l_{in}$, $l_{in} = 0.1 L_0$
	RA	$Q_{inAC} = 24\text{m}^3/\text{min}$ $U_{out} = k_{out} = \varepsilon_{out} = \text{link with SA}$
Wall surface	Velocity: generalised log law	

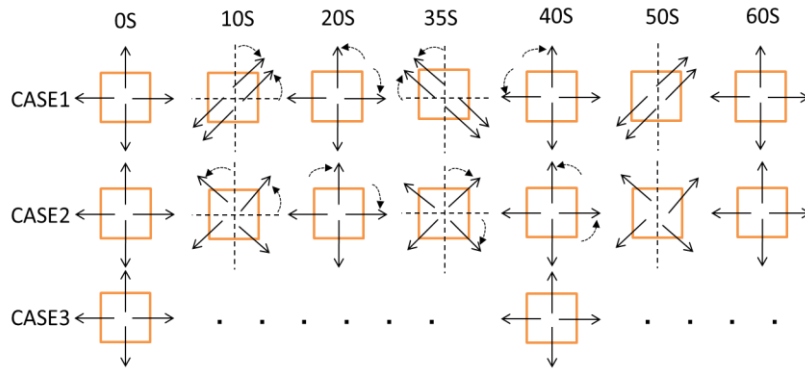


Figure 2: Louvers movement patterns (Swing period 40s)

2.3. Experimental setups

Full scale field testing was conducted in the environmental chamber with high thermal insulated. The initial indoor temperatures were obtained by a constant air volume air conditioning system. Solar heat gain, ventilation heat gain, inner heat generation were ignored in this field test. A cassette split type air conditioner was mounted in the centre of the ceiling (Figure 3). In order to obtain thermal distribution data throughout the space, air temperature was measured every 5 seconds through T-type thermocouples arrays; a total of 637 points (13(L) × 7(W) × 7(H)) were included in the analysis of thermal uniformity in the whole space. Local air temperatures were measured at the height of 0.1, 0.4, 0.8, 1.2, 1.6, 2.0, and 2.4 m, respectively. Therefore, 91 temperature sensors at horizontal locations were evenly distributed at each height.

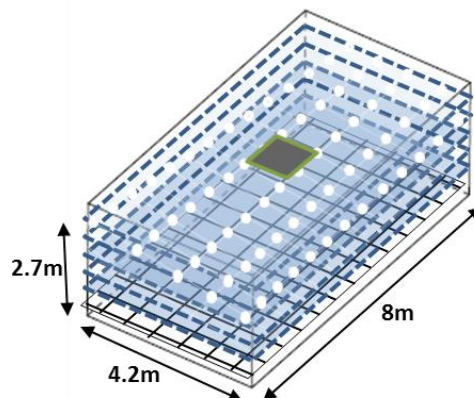


Figure 3: Environmental chamber geometry and temperature sensor layout

Table 2 summarises the field testing measurement conditions. Supply airflow rate Q was $24\text{m}^3/\text{min}$ and the velocity in the centre of the supply inlet varied at about $2.25\text{m/s} \sim 2.5\text{m/s}$. The setting temperature was 26°C in heating mode and a temperature difference between the supply and room mean air was kept at 15°C approximately to ensure the inverter compressor operated at the maximum value.

Table 2: Field testing conditions

Outdoor temperature	10°C (constant)
Initial room temperature	9°C
Setting temperature	26°C
Airflow rate	$Q = 24\text{m}^3/\text{min}$
Air supply Velocity	$2.2\sim 2.5\text{m/s}$
Supply air type	Straight type airflow
Measurement time	Longer than 1 hour to reach steady state condition

3. EVALUATION METHOD

3.1. Average temperature and its standard deviation

Equation 6: Average value and its standard deviation, root mean square(RMS) error at representative section

$$x = \frac{1}{N} \sum_{i=1}^N x_i \quad RMS = \sqrt{\frac{1}{N} \sum_{i=1}^N (x_i - x)^2}$$

Where:

x = average value

N = Number of sample data

x_i = local value

3.2. Temperature utilisation coefficient for energy efficiency

Equation 7: Temperature utilisation coefficient for energy efficiency

$$\eta = \frac{T_{SA} - T_i}{T_{SA} - T_{RA}}$$

Where:

T_{SA} = Supply air temperature (°C)

T_{RA} = Return air temperature (°C)

T_i = local air temperature (°C)

3.3. Prediction of the draught rate on the face

A draught is defined as an unwanted local cooling of the skin caused by air movement. The most widely used draught model was introduced by Fanger and Melikov et al. (1988) and was written as Equation (8). In addition, Wu and Li et al. (2017) created Equation (9) to obtain a suitable draught model for personal air supply while wearing winter clothing.

Equation 8: Quantity of draught rate

$$DR\% = 3.143(34 - T_i)(v - 0.05)^{0.625} + 3.369 v T_u(34 - T_i)(v - 0.05)^{0.625}$$

Equation 9: Draught rate model on face

$$DR\% (\text{face}) = 0.635(V_{\text{face}} - 0.05)^{3.19}(28 - T_i), R^2 = 0.9$$

Where:

DR = draught rate (%)

T_i = local air temperature (°C)

v = local air velocity (m/s)

T_u = turbulent intensity (%)

R^2 = coefficient of determination

4. RESULTS AND DISCUSSIONS

4.1. Validation of the CFD model

With the same setup as that of the full scale field testing, the predicted temperatures from the CFD simulations are compared with the experimental measurement data on the steady state condition. Figure 4 shows the comparison between numerically simulated and experimentally measured temperature profiles of three representative sensor lines in the middle vertical section. The sample A and C lines are 1.2m away from the indoor unit. In general, the predicted temperature distribution profiles present similar variation patterns as those of the experimental measurements as shown in Figure 4.

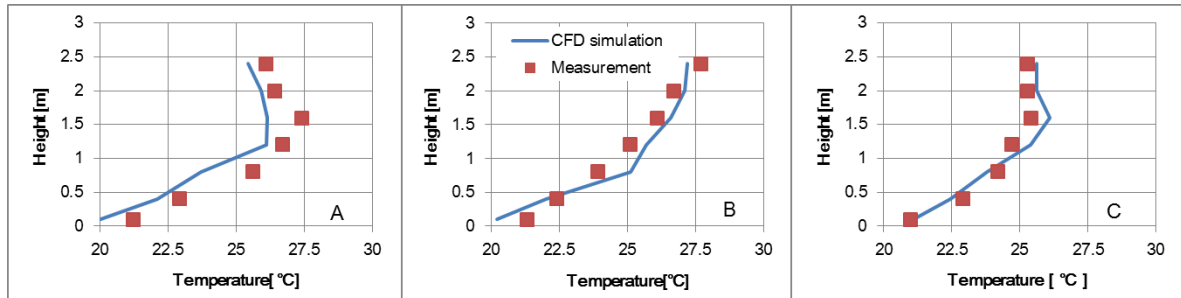
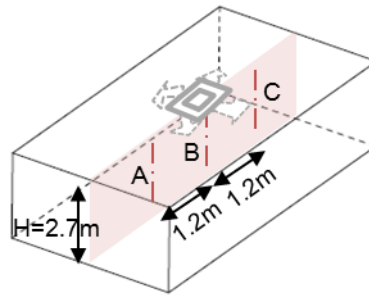


Figure 4: Comparisons of CFD predicted temperature profiles with experimental measurements

4.2. Comparison among louver swing types

In order to investigate the thermal performance of an oscillating airflow generated by side-to-side swing type louvers and to optimise the louver movement pattern, three types of louver movement patterns are compared respectively: confluent type (CASE1); diffusive type (CASE2); conventional straight type (CASE3). As shown in Figure 5, CASE1 with the confluent airflow supply that provides by the neighbouring supply opening can provide relatively higher average temperature at each height of the room. CASE2 was able to provide the highest average temperature profile of occupied zone. The RMS at the representative horizontal section (1.2m height) indicates that CASE2 with diffusive airflow supply has the most even temperature distribution. The vertical air temperature difference (ΔT) between head and ankle levels is limited to less than 3°C among all cases. As summarised in Table 3, the temperature difference of CASE2 was reduced by 34% compared to CASE3 at 1.2m horizontal section. In addition, temperature differences are close, within 0.3°C at the vertical direction among all the cases. Apparently, CASE3 has the poorest vertical temperature profile at the occupied zone (0.5m~1.4m height above the domain floor surface).

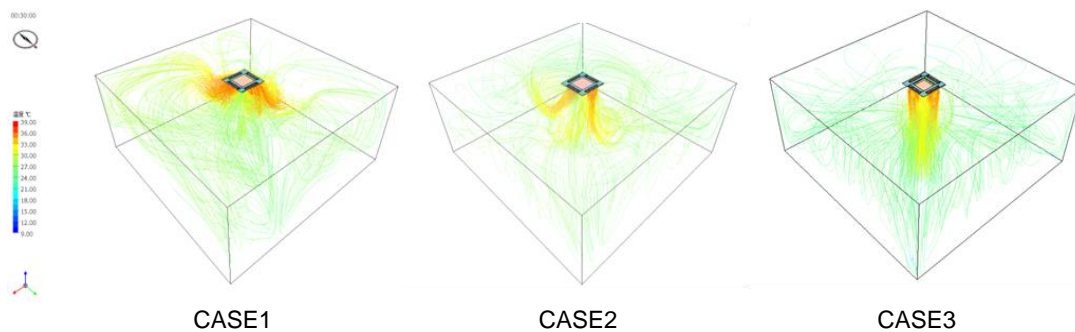


Figure 5: Airflow distribution profile comparisons among confluent type (CASE1) diffusive type (CASE2) and conventional straight type (CASE3) air supply.

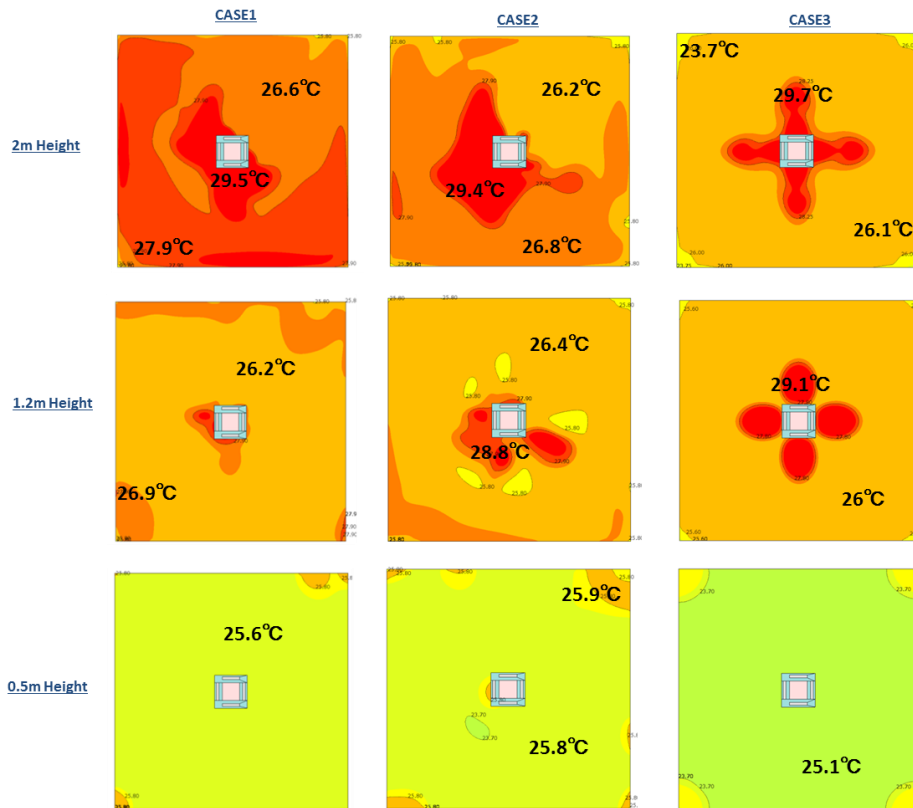


Figure 6: The temperature distribution at representative horizontal sections (0.5m / 1.2m / 2m height)

Table 3: Summary of thermal parameters

	Average temperature / RMS at 1.2m height [°C]	Horizontal temperature difference at 1.2m height [°C]	Vertical temperature difference in occupied zone [°C]	Average temperature difference in occupied zone [°C]
CASE 1	26.7 / 0.86	2.8	2.3	26.1
CASE 2	26.6 / 0.78	2.4	2.2	26.3
CASE 3	26.5 / 1.26	3.6	2.5	25.8

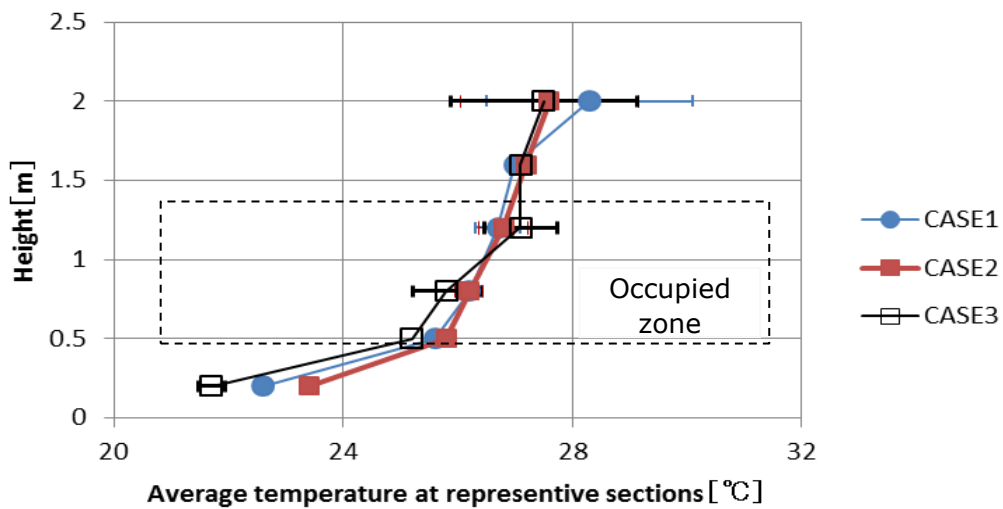


Figure 7: Comparison of the average temperature of representative horizontal sections

4.3. Comparison of temperature utilisation coefficient

The temperature utilisation coefficient was defined by Equation (7). The temperature utilisation coefficient was proportional to the local thermal efficiency. As illustrated in Figure 8, eight representative points selected at 1.2m height above the domain floor, 1.2m away from the centre of cassette type air conditioner indoor unit. The temperature utilisation coefficient varied in accordance with the louver's directions as shown in the Table 4. CASE1 has relatively high temperature utilisation coefficient at the corner direction due to the confluent airflow, while CASE2 shows apparently even temperature utilisation coefficient at each representative point. The sign of circle high temperature airflow was generated from the diffusive type oscillating airflow. CASE3 indicates that high temperature utilisation coefficient only occurred in the centre line of each air supply opening. Apparently, poor temperature utilisation coefficients occurred at the corners. The average temperature utilisation coefficients are nearly the same at the selected horizontal section (1.2m height) among all cases.

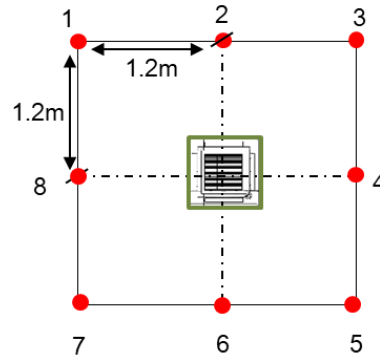


Figure 8: The representative temperature points at representative horizontal sections (1.2m height)

Table 4: Summary of temperature utilisation coefficient at each representative point

Points	CASE1	CASE2	CASE3
1	118%	108%	<u>95%</u>
2	110%	103%	117%
3	105%	109%	<u>99%</u>
4	103%	106%	119%
5	102%	119%	<u>94%</u>
6	<u>97%</u>	105%	112%
7	109%	100%	<u>95%</u>
8	108%	<u>99%</u>	113%

4.4. Comparison of draught rate at the face

Draught, which was a function of local air temperature and air velocity, was defined as unwanted local cooling of the skin caused by air movement. The 1.2m high horizontal section was selected as the face level of a sedentary person. The prediction results of air velocity distribution and temperature distribution at 1.2m height horizontal section were utilised for Draught Rate regressions. The maximum draught rate of each are summarised in Table 5. As regressed by Equation (9), the results indicate the actual draught rates at the face ranged between 0%-45% in CASE1 and CASE3, and between 0%-35% in CASE2. The diffusive type oscillating airflow (CASE2) provides lower draught rate on average compared to the straight type airflow. The results also indicate that louver movements reduce the momentum of straight airflow from the supply opening, and thus the draught rate is decreased accordingly.

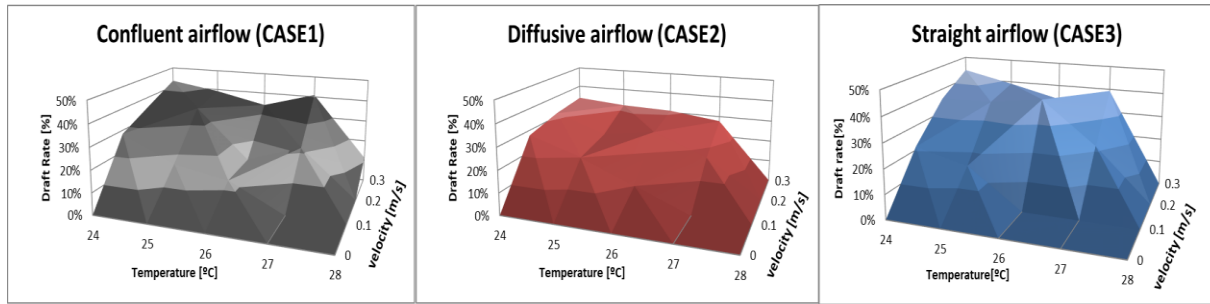


Figure 9: Comparison of the draught rate at the face level (1.2m height)

Table 5: Maximum draught rates at the face of each case

CASE1	CASE2	CASE3
41.6%	33.6%	44.1%

5. CONCLUSIONS

In this study, thermal uniformity, air diffusion performance, temperature utilisation coefficient, and draught rate at the face are investigated by comparing the conventional straight type airflow with two types of oscillating airflows, confluent type and diffusive type. The CFD result is then applied to determine the appropriate air supply control strategies.

A full scale field testing were conducted in environmental chamber with fixed geometry in order to investigate and evaluate the performance of side-to-side swing louvers mounted in a cassette split type air conditioner. The simulated results agreed well the experimental data.

The results indicated that oscillating airflow has a larger mean temperature at each representative height and a smaller temperature difference in the occupied zone as well as the whole space, compared to conventional straight type airflow. The operation optimisation on the louvers' movement significantly improved the thermal uniformity, with a temperature difference reduction of 34% and draught rates on the face ranged 0-35% at 1.2m horizontal section.

The temperature utilisation coefficient varied in accordance with the louvers' directions, however, average temperature utilisation coefficient were nearly the same at the selected horizontal section. Relatively poor temperature utilisation coefficients occurred at the corners under straight type airflow. Therefore, it is possible to regard the oscillating airflow provided better indoor thermal environment. Moreover, the oscillating airflow is successful in providing the acceptable thermal uniformity, higher thermal effectiveness compared to conventional straight airflow.

6. ACKNOWLEDGEMENT

Field testing of this research was supported by Mitsubishi Electric Corporation Shizuoka Works.

7. REFERENCES

Brasche S, Bischof W. 2005. Daily time spent indoors in German homes – Baseline data for the assessment of indoor exposure of German occupants. *International Journal of Hygiene and Environmental Health*, 208(4), 247-253.

Cao G, Awbi HB, Yao R, Fan YQ, et al. 2014. A review of the performance of different ventilation and airflow distribution systems in buildings. *Building and environment*, 73,171-186.

Fan YQ, Ito K. 2012. Energy consumption analysis intended for real office space with energy recovery ventilator by integrating BES and CFD approaches. *Building and Environment*, 52, 57-67.

- Fan YQ, Kameishi K, Onishi S, Ito K. 2014. Field-based study on the energy-saving effects of CO₂ demand controlled ventilation in an office with application of energy recovery ventilators. *Energy and Buildings*, 68,412-422.
- Fanger PO, Melikov AK, Hanzawa H, Ring J. 1988. Air turbulence and sensation of drought. *Energy and Buildings*, 1221-1239.
- Gilani S, Montazeri H, Blocken B. 2016. CFD simulation of stratified indoor environment in displacement ventilation: Validation and sensitivity analysis. *Building and Environment*, 95,299–313.
- Lombard LP, Ortiz J, Pout C. 2008. A review on buildings energy consumption information. *Energy and Buildings*, 40, 394–398.
- Melikov A.K. 2016. Advanced air distribution: improving health and comfort while reducing energy use. *Indoor Air*, 26 (1), 112-124
- Mr.Slim indoor unit optional device. <http://www.mitsubishielectric.co.jp/news/2018/pdf/0130.pdf> (accessed on May. 30, 2019).(in Japanese)
- Rhee KN, Shin MS, Choi SH. 2015. Thermal uniformity in an open plan room with an active chilled beam system and conventional air distribution systems. *Energy and Buildings*, 93,236-248.
- Shibuya T, Croxford B. 2016. The effect of climate change on office building energy consumption in Japan. *Energy and Buildings*, 117,149-159.
- Strategy for energy conservation of Japan 2016. Ministry of Economy, Trade and Industry.
- Tian L, Lin Z, Wang Q. 2011. Experimental investigation of thermal and ventilation performances of stratum ventilation. *Building and Environment*, 46, 1309-1320.
- Wu Y, Liu H, Li BZ, Chen Y, et.al. 2017. Thermal comfort criteria for personal air supply in aircraft cabins in winter. *Building and Environment*, 125, 373–382.
- Xue Y, Chen Q. 2014. Influence of floor plenum on energy performance of buildings with UFAD systems. *Energy and Buildings*, 79,74-83.
- Zhang Z, Zhang W, Zhai ZJ and Chen Q. 2007. Evaluation of various turbulence models in predicting airflow and turbulence in enclosed environments by CFD: Part 2 —comparison with experimental data from literature. *HVAC & R Research*; 13(6):871-886.

#270: Static and dynamic forecasting of solar radiation: a comparative study

Muhammed A. HASSAN¹, Adel KHALIL², Sayed KASEB³, Mahmoud A. KASSEM⁴

¹ Mechanical Power Engineering Department, Faculty of Engineering, Cairo University, Giza 12613, Egypt.
mhd.zidan17@cu.edu.eg

² Mechanical Power Engineering Department, Faculty of Engineering, Cairo University, Giza 12613, Egypt.
khalila2@asme.org

³ Mechanical Power Engineering Department, Faculty of Engineering, Cairo University, Giza 12613, Egypt.
kaseb@cu.edu.eg

⁴ Mechanical Power Engineering Department, Faculty of Engineering, Cairo University, Giza 12613, Egypt.
mahmoudkassem2@gmail.com

The ever-growing global interest in renewable energies and the need to integrate their power generation systems into local electric grids necessitate powerful forecasting tools for estimating the future values of the resources. Motivated by the lack of such studies, this article investigates the potential of dynamic artificial neural networks (ANNs) in global solar irradiation forecasting compared to the well-established static modelling approach. The adopted networks are focused time delay network (FTD), nonlinear autoregressive network (NAR), and nonlinear autoregressive network with exogenous inputs (NARX), as well as the newly suggested distributed time delay network (DTD) and layer recurrent network (LRN), while the static multilayer perceptron network (MLP) was considered as a reference. Long-term high-resolution data of the ener-MENA Network Project of three MENA locations, namely: Adrar (Algeria), Ma'an (Jordan), and Zagora (Morocco), have been used for developing the models. It was found that except for LRN, all dynamic algorithms have lower prediction accuracy in sunshine-based modelling compared to MLP. Meanwhile, most of the dynamic models have the same or significantly better performances in independent and temperature-based modelling. Although dynamic ANNs are slow to train and cost extensive to optimize, they are generally less sensitive to the sky clearness index and have more stable performances when new data are introduced in the forecasting phase.

Keywords: Solar radiation, forecasting, time series, static neural networks, dynamic neural networks

1. INTRODUCTION

The problem of predicting the ground-level solar radiation is quite old and has a massive number of research works, especially during the last two decades, motivated by the unavailability of such ground measurements at most of locations around the world. With the recent achievements in the advanced solar thermal and power generation systems, accurate forecasting models are required for efficient grid integration of these systems to predict the anticipated output power (Hassan, Khalil, Kaseb and M.A. Kassem, 2017). The old practices in this field, however, did not consider the time-series methods as the standard approach. Instead, simple empirical regression-based correlations have been used (Besharat, Dehghan and Faghih, 2013). Consequently, there are two approaches to estimate solar radiation, namely: function approximation and time-series approaches. In function approximation modelling, the solar radiation component is determined using a simple equation or a complex static algorithm that typically correlates the radiation component to some meteorological, climatological or geographic parameters, without considering the order of data points. For time-series modelling, the global irradiation is determined using its past values using simple time series analysis methods or dynamic machine learning algorithms, where the order of observations is vital (Badescu, 2008). Since most solar radiation modelling research has been focused on the first type, the reader is referred to the following articles for reviews on modelling the global solar irradiation based on the measurements of sunshine hours, (Yao *et al.*, 2018), ambient temperature (Gouda *et al.*, 2019), combinations of different meteorological variables (Rao K, Premalatha and Naveen, 2018), or even without measured inputs (Gouda *et al.*, 2019). Some corresponding static data-driven algorithms that have been developed using the same types of inputs can be found in (Ghimire *et al.*, 2019) for artificial neural networks (ANNs), (Meenal and Selvakumar, 2018) for support vector machines, (Torres-Barrán, Alonso and Dorransoro, 2019) for regression trees, (Hassan, Khalil, Kaseb and M. A. Kassem, 2017) for ensemble methods, (Zang *et al.*, 2019) for neuro-fuzzy inference systems (ANFIS).

For comprehensive reviews of such algorithms and their implementations in solar radiation modelling, the reader is invited to read the following articles (Voyant *et al.*, 2017; Zang *et al.*, 2019). This article is dedicated to time series modelling using artificial neural networks. Such networks are called dynamic networks, which means that they use the historical values of solar radiation for making forecasts. Therefore, they differ from static ANNs that rely only on the static correlations between the exogenous input(s) and the output of the network. The ANNs are considered here since they are the most established algorithms in renewable energy fields and due to the availability of many toolboxes and software that can be used by engineers to develop forecasting tools (Voyant *et al.*, 2017). Very few studies, however, have been dedicated to modelling the solar radiation using dynamic ANNs, or to evaluate the applicability and potential of these algorithms. Wu and Chan (Wu and Chan, 2012) compared the performances of ARIMA and focused time delay neural network (FTD) in modelling the monthly average solar irradiance over Singapore using a dataset of a single year. It was found the FTD algorithm is more accurate but less stable than ARIMA. In another study (Wu and Chan, 2011), the same authors demonstrated the merits of hybridizing the autoregressive moving average (ARMA) method and the FTD algorithm for forecasting the hourly global irradiance. Another dynamic ANN, namely the nonlinear autoregressive neural network with exogenous input (NARX), has been adopted by Piri and Kisi (Piri and Kisi, 2015) to develop global irradiation models for two stations in Iran. The authors found that NARX is significantly more accurate than the corresponding meteorological-based empirical correlations but slightly less accurate than the ANFIS algorithm with Gaussian membership function.

Gairaa *et al.* (Gairaa *et al.*, 2016) investigated the performances of the ARMA method, the nonlinear autoregressive neural network (NAR), as well as a hybrid ARMA-NAR model in modelling the global solar irradiation over different locations in Algeria. The authors found that while the hybrid model offers a slight improvement over the NAR-based model. In (Benmouiza and Cheknane, 2016), the authors replaced the k-means algorithm with the ARMA method and showed that the hybrid ARMA-NAR model outperforms its base-learners (ARMA and NAR) in making short-term forecasts. Azimi *et al.* (Azimi, Ghayekhloo and Ghofrani, 2016) proposed another global irradiance forecasting framework by hybridizing a transformation-based K-means algorithm with the static multi-layer perceptron (MLP) neural network to obtain future values for several time horizons. Alzahrani *et al.* (Alzahrani, Kimball and Dagli, 2014) showed that the NARX network can outperform the traditional linear regression models in forecasting the hourly global irradiance, especially when the cloud cover data are considered. Bouzgoua (Bouzgou, 2014) forecasted the global irradiance together with the wind speed, in different horizons, using the extreme learning machine (ELM) algorithm. Hussain and AIAlili (Hussain and AIAlili, 2017) studied four different ANN algorithms, namely MLP, NARX, ANFIS and generalized regression neural network (GRNN), in forecasting the global horizontal irradiation using temperature, relative humidity, wind speed, and sunshine duration. In another study (Hussain and AIAlili, 2016), the authors applied the Morlet wavelet analysis to measured and simulated time series for MLP-, ANFIS-, and NARX-based models. It was found that such analysis results in better performance in case of the NARX network. Ahmad *et al.* (Ahmad, Anderson and Lie, 2015) showed that the NARX network outperforms the corresponding MLP, ARMA and persistence models in making 24-hours-ahead forecasts of the global irradiance in New Zealand. Di Piazza *et al.* (Di Piazza, Di Piazza and Vitale, 2016) adopted the NARX network for making 8 to 24-hours-ahead forecasts of the global solar irradiance using temperature-based models. Yadav and Behera (Yadav and Behera, 2014) proposed a wavelet-based recurrent neural network model for forecasting the global irradiance in 7-days-ahead horizon using several meteorological inputs. Kashyap *et al.* (Kashyap, Bansal and Sao, 2015) found that the Elman neural network outperforms all other adopted static ANNs in modelling the global solar irradiance.

After reviewing the relevant solar radiation modelling studies, it was apparent that ANN-based dynamic forecasting algorithms have been rarely investigated, compared to static ANN algorithms. This work is providing the first and most comprehensive study of dynamic neural networks in solar radiation forecasting. Another contribution of the study is introducing novel algorithms that have never been used for forecasting solar radiation such as the distributed time-delay network (DTD) and the fully layer-recurrent network (LRN).

2. THEORETICAL BACKGROUND

2.1. Multilayer perceptron neural network

The multilayer perceptron (MLP, Figure 1a) is the most popular ANN architecture, with wide adaptation in many scientific fields. A typical MLP architecture consists of the network's inputs, one or more hidden layers, and an output layer. Each hidden layer is consisted of some computational elements, called neurons, while the output layer typically has a single neuron. Each neuron is connected with all neurons of the preceding layer and the following layer with adaptable weights and biases. The output of the neuron is the summation of the weighted inputs (the model's inputs or the preceding layer's outputs, multiplied by the corresponding weights) and the neuron's bias. Using mathematical notation and given a training set $G = \{X_i, Y_i\}_{i=1}^n$ with input (X) and output (Y) pairs of n observations, the output (a) of the u^{th} neuron in the v^{th} layer (a_u^v) is expressed as $a_u^v = \psi(W S) = \psi(\sum_{j=1}^J W_{j-u}^v a_j^{v-1} + b_u^v)$, where J is the number of neurons in the preceding layer ($1 \leq j \leq J$), W_{j-u}^v is the weight assigned to the connection between the j^{th} neuron in the $(v-1)^{\text{th}}$ layer and the u^{th} neuron in the v^{th} layer, while b_u^v is the bias associated with the u^{th} neuron. The transfer (or activation) function (ψ) is typically a non-linear function in the hidden layers and a linear one in the output layer. The tangential-sigmoid (ψ_1) and pure-linear (ψ_2) functions used here are defined as $\psi_1(W S) = \frac{2}{1+e^{-2 W S}} + 1$, and $\psi_2(W S) = W S$, where $W S$ is the input weighted summation. The outputs of the neurons propagate forwardly towards the output layer, where the estimated output is determined and compared to the target value to obtain the error estimate, which is introduced later to a training algorithm in order to generate the backpropagation error signals that update the old values of weights and biases (learning process). The training process continues until the stopping criterion is met (Samarasinghe, 2006).

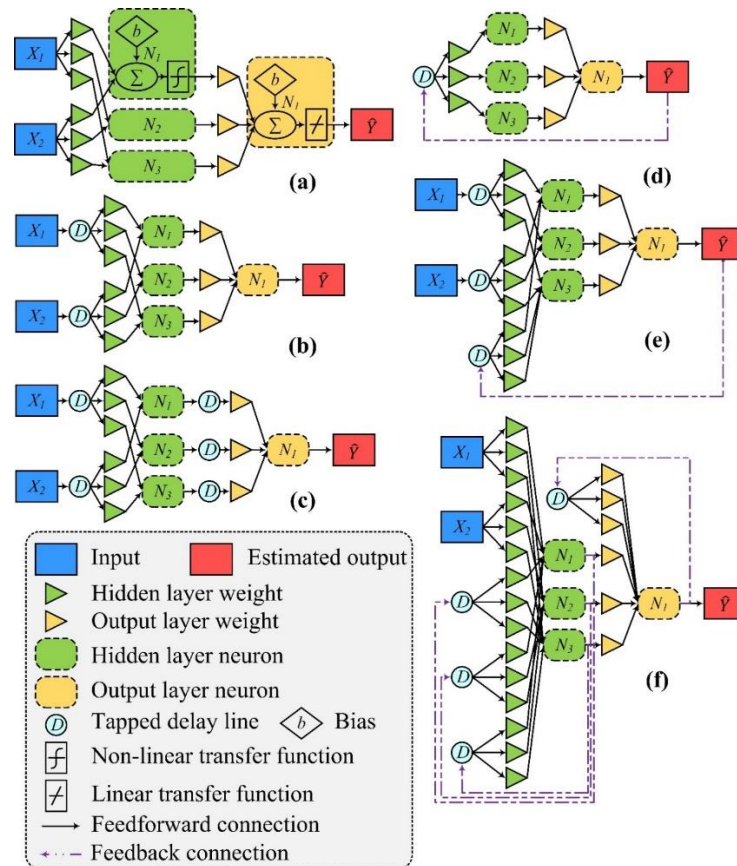


Figure 1: Typical architectures of the adopted ANN algorithms: (a) MLP, (b) FTD, (c) DTD, (d) NAR, (e) NARX, and (f) LRN.

2.2. Time delay neural networks

Dynamic neural networks are those networks with feedback signals and/or input time delays. This means that the network's output is dependent not only on the current values of inputs, but also on the networks' past inputs, outputs, or states. Therefore, the dynamic ANNs have a finite dynamic response that makes them a typical choice for forecasting purposes. Dynamic ANNs can be classified to feedforward-dynamic networks (also known as time delay neural networks, TDNNs) and recurrent (or feedback) neural networks (RNNs). In TDNNs, the time is embedded externally in the form of short-memory filters, called tapped delay lines (TDLs). Meanwhile, the dynamic effect occurs in the RNNs due to the feedback signals (Samarasinghe, 2006). The first dynamic network adopted here is the focused time delay network (FTD), which is one of the simplest dynamic ANN networks, as shown in Figure 1b. This network is a TDNN with an architecture that is similar to that of the MLP, but instead of introducing a single value of each input at each epoch, the network has a TDL associated with the inputs in order to introduce the past values of each independent variable. Hence, the output of the network can be represented as $Y^{t+1} = f(X_1^t, X_1^{t-1}, X_1^{t-2}, \dots, X_1^{t-k_{x_1}}, X_2^t, X_2^{t-1}, X_2^{t-2}, \dots, X_p^{t-k_{x_p}})$, where f is a nonlinear function of the network's arguments that maps the past observations to the next outcome, X_p is an explanatory variable, P is the number of explanatory variables ($1 \leq p \leq P$), t is the time step index, and k_{x_p} is the size of the delay-line memory for the input X_p . The other TDNN adopted here is the distributed time delay network (DTD), shown in Figure 1c. This is also a TDNN with similar architecture to the FTD network, but with TDLs associated with the inputs as well as the hidden neurons' outputs, which, typically, enables the network to have a longer time response (Samarasinghe, 2006).

2.3. Recurrent neural networks

Three types of RNNs are adopted here, namely: the non-linear autoregressive network (NAR), the nonlinear autoregressive neural network with exogenous input (NARX), and the layer recurrent network (LRN). The NAR network (Figure 1d) has feedback signals from the output layer carrying the historical output values to be used for estimating the future value. Hence, the output of the network can be expressed as $Y^{t+1} = f(Y^t, Y^{t-1}, Y^{t-2}, \dots, Y^{t-k_y})$, where k_y is the length of the TDL assigned to the output. Since the feedback signal (network's output) is also the network's input (after being delayed), the time delays can be viewed as input delays (IDs) or feedback delays (FDs). The NARX network (Figure 1e) can be viewed as an extension to the NAR network. This network uses the current and past values of the modelled variable as well as the current and past values of some exogenous variables to predict the future values of the modelled variable. Hence, the network also has some TDLs on the exogenous inputs. The output of the network can be expressed as $Y^{t+1} = f(X_1^t, X_1^{t-1}, X_1^{t-2}, \dots, X_p^{t-k_{x_p}}, Y^t, Y^{t-1}, Y^{t-2}, \dots, Y^{t-k_y})$. The final RNN considered here is the layer recurrent network (LRN), shown in Figure 1f. This network does not have input TDLs. Instead, it has the feedback signals from all layers. This means that the output signals of each layer (the inputs are not considered as a layer) are associated with TDLs to introduce their current and past states for predicting future values. In this paper, fully recurrent networks are developed instead of having the feedback signals only from the hidden layers (Elman network) or from the output layer (Jordan network) (Samarasinghe, 2006).

3. DATA AND METHODOLOGY

3.1. Studied locations and collected data

Three locations in three different MENA countries with different climate conditions, have been considered, namely: Adrar (Algeria), Ma'an (Jordan), and Zagora (Morocco) (Figure 2). Adrar station is located at 27.880°N, 0.274°W, with an elevation of 262 m. The station is equipped with a two-axis sun-tracking unit (SOLYS-2), on top of which the radiation sensors are mounted. A first-class CHP1 pyrheliometer is used for measuring the normal irradiance, while two secondary standard CMP21 pyranometers are used for measuring the horizontal global and diffuse irradiances (with a shadow-ball assembly for diffuse irradiance measurements). Other installed sensors include the CS-215 probe (for temperature and relative humidity measurements), NRG-40C anemometer, NRG-200P wind vane, and Setra-278 barometric pressure sensor. Ma'an station is located at 30.172°N, 35.818°E, with an elevation of 1012 m, and has the same installed sensors as those of Adrar. Zagora station is located at 30.272°N, 5.852°W, with an elevation of 783 m. The same meteorological sensors are used in this station. However, the irradiance components are measured using an RSP-4G rotating shadowband irradiometer.



Figure 2: A map showing the three studied locations.

3.2. Irradiation models

Different dynamic models have been developed, using the aforementioned algorithms, and compared to the well-established multilayer perceptron feedforward backpropagation neural network as a reference static network. Table 1 provides a list of all developed models for each station, alongside with their exogenous inputs. Except for the endogenous NAR algorithm, all algorithms have been used to develop three types of models, according to the exogenous variables, namely: sunshine-based models, temperature-based models, and independent models. Models' inputs can be calculated as follows

$$\text{Equation 1:} \quad H_o = \left(\frac{24+3600+I_{sc}}{\pi} \right) \left(1 + 0.033 \cos\left(\frac{360 N}{365}\right) \right) (\cos \delta \cos \varphi \sin \omega_{ss} + \frac{\pi \omega_{ss}}{180} \sin \delta \sin \varphi),$$

$$\text{Equation 2:} \quad SF = \frac{S}{S_o} = \frac{15 S}{2 \cos^{-1}(-\tan \varphi \tan \delta)},$$

$$\text{Equation 3:} \quad \delta T = T_{max} - T_{min},$$

where H_o is the horizontal extra-terrestrial daily irradiation ($\text{MJ/m}^2 \cdot \text{day}$), SF is the solar fraction, δT is the maximum daily temperature difference ($^{\circ}\text{C}$, I_{sc} is the solar constant ($= 1367 \text{ W/m}^2$), N is the day number ($= 1$ for January 1st), δ is the solar declination angle ($^{\circ}$), φ is the latitude angle ($^{\circ}$), ω_{ss} is the sunset hour angle ($^{\circ}$), S and S_o are the actual and the astronomical totals of sunshine hours, while T_{max} and T_{min} are the maximum and minimum daily temperatures ($^{\circ}\text{C}$). More details on these parameters can be found in (Badescu, 2008).

3.3. Computation procedure and evaluation method

A detailed illustration of the procedure followed to develop both static and dynamic models is shown in Figure 3. First, the solar-meteorological data files for Adrar (September 27, 2012, to December 31, 2016), Ma'an (January 11, 2011, to December 31, 2016), and Zagora (May 31, 2013, to December 31, 2016) are imported to the main computational environment (MATLAB R2016a®). Then, the time/date stamps, as well as the geographical coordinates, are used to calculate the solar time, solar angles, and the extra-terrestrial irradiation values. Meanwhile, the direct irradiance measurements are used to calculate the sunshine fraction, since the actual sunshine duration is defined as the total daily hours during which the pyrheliometer's signal is above the threshold of 120 W/m^2 (Badescu, 2008).

Table 1: A list of all developed models. IDs: input delays, FDs: feedback delays.

Model Name	Algorithm	Exogenous Inputs	Optimized Features
MLP1	MLP	H_o, SF	
MLP2	MLP	$H_o, \delta T$	Number of neurons (5:5:200)
MLP3	MLP	H_o	
NAR	NAR	-	Number of neurons (5:5:200)
LRN1	LRN	H_o, SF	
LRN2	LRN	$H_o, \delta T$	
LRN3	LRN	H_o	Number of FDs (1:1:10)
NARX1	NARX	H_o, SF	Number of neurons (5:5:200)
NARX2	NARX	$H_o, \delta T$	
NARX3	NARX	H_o	Number of FDs (1:1:10)
			Number of IDs (1:1:10)

Model Name	Algorithm	Exogenous Inputs	Optimized Features
FTD1	FTD	H_o, SF	Number of neurons (5:5:200)
FTD2	FTD	$H_o, \delta T$	
FTD3	FTD	H_o	
DTD1	DTD	H_o, SF	Number of IDs (1:1:10)
DTD2	DTD	$H_o, \delta T$	
DTD3	DTD	H_o	

A data filtering procedure, described in details in (Hassan, Khalil, Kaseb and M.A. Kassem, 2017), has been applied to the instantaneous raw data (minute-by-minute observations) to eliminate suspicious and irrelevant observations. Eventually, this pre-processing procedure leaves 1554, 2179, and 1303 valid daily observations at Adrar, Ma'an, and Zagora, accordingly. The data matrix is then divided into three sub-matrices for training, validating and testing the models, with size fractions of approximately 0.7, 0.15 and 0.15, accordingly. The station, algorithm, and model type are selected and a preliminary structure of the network is generated using the minimum number of neurons and delays, as shown in Table 1. Afterward, initial values of all weights and biases are randomly generated and the input-target pairs are introduced to the algorithm sequentially. The estimated output of the model is continuously compared to the targeted output and the training process is repeated until one of the stopping criteria is met (basically, when the predetermined minimum error or gradient is met, or when the maximum number of epochs is reached). When the model is fully trained, the final weights, biases, and states are used, alongside with the validation dataset, to evaluate the model's performance. The validation error estimate is determined and saved, and the whole process (for the same model) is repeated with other structural features until all considered architectures are tried. As shown in Table 1, the range of neurons' numbers is set to [5,200] with a step of 5 neurons, while the range of delays' numbers (input and/or feedback delays) is set to [1,10] with a step of one delay.

For sake of simplifying the optimization process, some structural features have been fixed, such as the training function (Levenberg-Marquardt algorithm), the number of hidden layers (single hidden layer), and the type of transfer functions (tangent-sigmoid functions in the hidden layers, and pure-linear functions in the output layers). Altering these features was found of minor impact on the overall performance of the networks in a former study (Hassan, 2017) provided that the fixed types/numbers are adequate. In addition, the length of the TDL (i.e. the number of past values, on which the current value is dependent) was assumed the same for all neurons/inputs in each step of the optimization loop, in order to reduce the computational costs of this procedure. In the case of NARX algorithm, however, the numbers of IDs and FDs were optimized separately in two nested loops. As soon as the optimization loop ends, the saved values of the validation mean square error (MSE) are used to select the best architecture of the model. Then, the selected network is tested using the independent test subset and all results are saved and printed. Quantitative error measures include the mean bias error (MBE), the mean absolute percentage error (MAPE), the root mean square error (RMSE), the relative root mean square error (RRMSE), and the coefficient of determination (R^2).

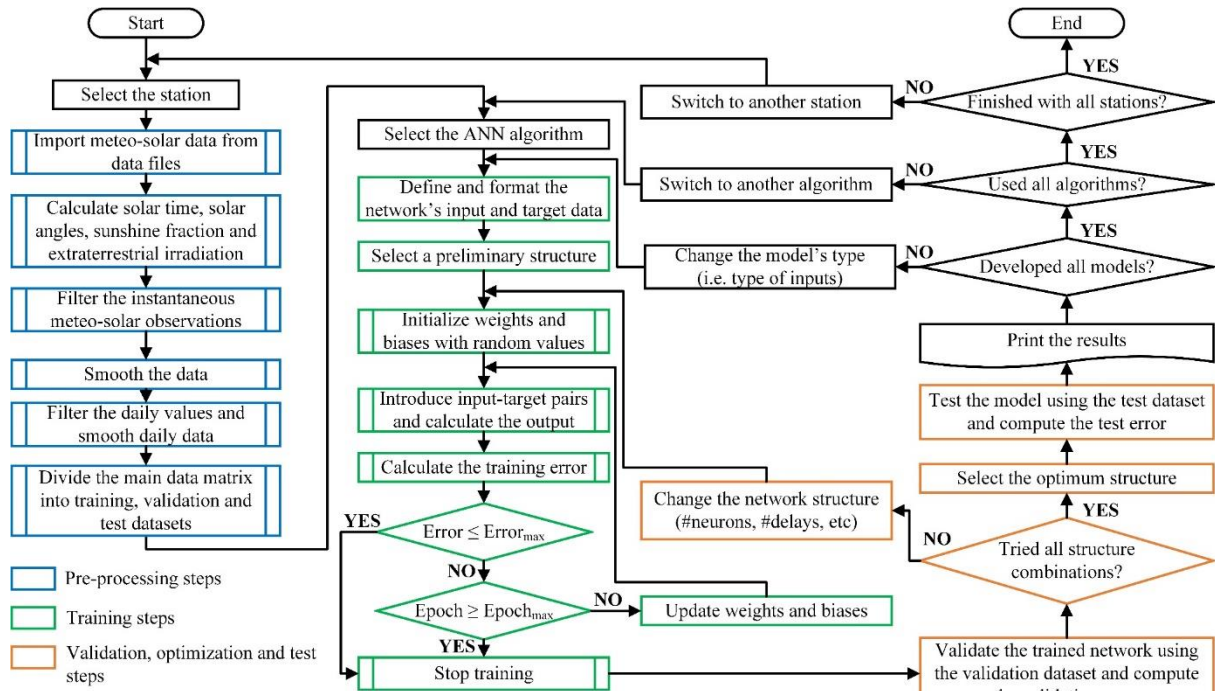


Figure 3: Computation procedure for developing both static and dynamic models.

4. RESULTS AND DISCUSSION

4.1. Performance evaluation

Tables 2-4 provide the optimized structural features of both static and dynamic models, as well as their main performance indicators (MBE, RMSE, and R^2) during the training, validation and independent test phases for the three stations. In these tables, best values are shown in bold, while the results of models that failed to adapt to introduced data are underlined. The validation results are used here for evaluating the prediction accuracy of the models, while the independent test error measures will be used in the next section for evaluating the stability of the models.

Table 2: Optimal structure and performance indicators for static and dynamic models of Adrar. Best values are shown in bold.

Model	Structure			Training			Validation			Test		
	#Neurons	#IDs	#FDs	MBE	RMSE	R^2	MBE	RMSE	R^2	MBE	RMSE	R^2
MLP1	40			0.000	1.041	0.974	-0.001	0.973	0.980	-0.003	1.235	0.969
MLP2	20			-0.001	2.420	0.868	-0.007	2.218	0.888	-0.005	2.500	0.851
MLP3	10			-0.002	3.132	0.780	-0.011	2.688	0.847	-0.006	3.142	0.739
NAR	80		4	0.607	3.643	0.696	-0.346	2.804	0.814	-0.373	3.213	0.776
NARX1	35	5	2	0.525	3.392	0.739	0.943	2.355	0.863	0.599	3.302	0.753
NARX2	15	2	2	-0.062	3.671	0.694	-0.596	2.172	0.896	0.264	2.732	0.824
NARX3	5	3	2	-0.147	3.195	0.773	-0.285	2.421	0.858	-0.139	2.451	0.852
LRN1	15		2	-0.047	0.778	0.983	-0.094	0.875	0.977	0.339	0.822	0.991
LRN2	15		4	-0.070	1.956	0.891	-0.206	1.858	0.898	0.231	1.604	0.964
LRN3	5		2	0.053	2.965	0.750	0.310	2.964	0.740	-0.337	2.843	0.888
FTD1	10	2		0.347	2.564	0.851	-0.472	1.828	0.918	-0.252	1.926	0.918
FTD2	30	3		-0.058	3.157	0.766	-0.636	2.437	0.867	-0.243	2.705	0.850
FTD3	15	5		-0.016	3.466	0.719	0.127	2.688	0.837	-0.789	3.448	0.749
DTD1	10	3		0.090	3.213	0.768	-0.574	2.794	0.813	0.268	3.212	0.763
DTD2	45	2		0.399	3.256	0.763	-0.845	2.439	0.847	1.166	3.883	0.662
DTD3	20	3		-0.055	3.436	0.726	-0.616	2.969	0.798	-0.038	3.363	0.763

For Adrar station (Table 2), the best models, with highest prediction accuracy, are MLP1 and LRN1, with a slight superiority for the later one (validation RMSE of 0.875 MJ/m².day). The dynamic model (LRN1) also shows superior performances in the training and test phases. Based on the expected RMSE values for global irradiation models (Li *et al.*, 2013), the LRN1 model provides excellent forecasting accuracy as well as reliable performance (the reliability is indicated by the stable performances in the three phases, i.e. no overfitting). The MLP1 model, on the other hand, shows the lowest MBE as compared to all other models (validation MBE of -0.001 MJ/m².day); the same holds true for the two other locations. When comparing the static MLP models to the dynamic models, some general remarks can be made. For instance, the sunshine-based MLP model (MLP1) shows better accuracy as compared to the corresponding dynamic models, except for the LRN1 model, as stated before. However, both static and dynamic models have the same accuracy level when the ambient temperature is considered as the exogenous input. The best models here are LRN2 and NARX2 (both are RNNs), with validation RMSEs of 1.858 and 2.172 MJ/m².day, accordingly. As for the independent models, the accuracy of the dynamic models is either equal to or less than that of the static model MLP3. Models LRN3 and DTD3 have lower accuracy, while models NARX3 and FTD3 have equivalent or slightly better accuracy. The NAR model is an endogenous model. Though, it can be viewed as an independent model in the sense that it does not require any meteorological parameters. The results show that it has very good estimations, considering its relative simplicity, with an accuracy that is better than those of models LRN3 and NARX3. Figure 4 illustrates the performances of all developed models for Adrar using goodness-of-fit plots.

Table 3: Optimal structure and performance indicators for static and dynamic models of Ma'an. Best values are shown in bold, while results of successively trained models are underlined.

Model	Structure			Training			Validation			Test		
	#Neurons	#IDs	#FDs	MBE	RMSE	R^2	MBE	RMSE	R^2	MBE	RMSE	R^2
MLP1	20			0.000	1.083	0.976	-0.002	1.041	0.978	0.000	1.067	0.979
MLP2	25			-0.001	2.333	0.890	-0.004	1.892	0.921	-0.004	2.255	0.901
MLP3	15			-0.001	2.568	0.867	-0.005	2.103	0.904	-0.003	2.607	0.866
NAR	85		2	0.183	3.042	0.817	-0.346	2.511	0.862	0.170	2.983	0.806
NARX1	5	2	2	-0.184	2.665	0.857	-0.138	2.383	0.885	-0.350	2.667	0.847
NARX2	40	3	2	0.170	3.047	0.810	0.143	2.570	0.872	-0.223	2.782	0.837
NARX3	20	4	4	0.357	2.542	0.872	-1.161	2.057	0.907	0.574	2.817	0.829
LRN1	25		4	-0.037	1.116	0.974	0.244	1.073	0.978	0.003	1.434	0.958
LRN2	15		4	-0.123	2.266	0.893	0.400	2.505	0.883	0.161	2.666	0.855
LRN3	15		2	-0.099	2.179	0.901	0.064	2.438	0.889	0.219	2.264	0.896
FTD1	55	6		<u>-0.060</u>	<u>4.944</u>	<u>0.507</u>	<u>0.133</u>	<u>4.597</u>	<u>0.541</u>	<u>-0.664</u>	<u>5.038</u>	<u>0.490</u>
FTD2	5	3		<u>0.083</u>	<u>6.007</u>	<u>0.269</u>	<u>0.977</u>	<u>5.857</u>	<u>0.321</u>	<u>1.349</u>	<u>6.189</u>	<u>0.175</u>

Model	Structure			Training			Validation			Test		
	#Neurons	#IDs	#FDs	MBE	RMSE	R ²	MBE	RMSE	R ²	MBE	RMSE	R ²
FTD3	20	5		0.087	2.589	0.866	-0.729	2.129	0.895	0.153	2.505	0.875
DTD1	45	6		0.357	2.631	0.861	-0.881	2.146	0.893	0.026	2.610	0.867
DTD2	15	6		0.168	2.554	0.864	-0.631	2.231	0.898	0.118	2.653	0.872
DTD3	5	3		0.147	2.670	0.854	-0.746	2.092	0.911	0.237	2.558	0.871

Table 4: Optimal structure and performance indicators for static and dynamic models of Zagora. Best values are shown in bold, while results of successively trained models are underlined.

Model	Structure			Training			Validation			Test		
	#Neurons	#IDs	#FDs	MBE	RMSE	R ²	MBE	RMSE	R ²	MBE	RMSE	R ²
MLP1	30			0.000	1.234	0.960	-0.004	1.310	0.958	-0.006	1.918	0.913
MLP2	10			-0.002	2.642	0.820	-0.004	2.456	0.854	-0.013	2.574	0.836
MLP3	60			-0.002	3.172	0.749	-0.008	2.881	0.779	-0.011	3.144	0.735
NAR	40		2	-0.660	3.555	0.677	0.825	3.024	0.746	-0.218	3.431	0.722
NARX1	35	2	2	0.431	3.150	0.757	-0.022	2.466	0.806	-0.133	3.205	0.743
NARX2	15	2	2	-0.125	3.443	0.696	-0.534	2.947	0.791	-0.785	3.877	0.605
NARX3	30	4	2	-0.285	3.108	0.755	-0.180	2.480	0.829	-0.970	3.296	0.741
LRN1	25		4	-0.135	1.516	0.943	-0.072	1.448	0.939	-0.273	2.285	0.873
LRN2	25		3	0.167	2.695	0.819	-0.203	2.781	0.775	-1.239	3.601	0.685
LRN3	5		4	0.538	2.896	0.791	0.500	2.875	0.759	-0.009	3.054	0.774
FTD1	65	6		<u>-0.188</u>	<u>5.479</u>	<u>0.237</u>	<u>0.079</u>	<u>5.013</u>	<u>0.308</u>	<u>-0.208</u>	<u>5.912</u>	<u>0.159</u>
FTD2	5	6		<u>-0.522</u>	<u>6.039</u>	<u>0.096</u>	<u>0.367</u>	<u>5.502</u>	<u>0.157</u>	<u>-0.264</u>	<u>5.869</u>	<u>0.078</u>
FTD3	15	3		-0.019	3.180	0.748	-0.554	2.730	0.791	0.158	3.510	0.687
DTD1	20	4		-0.575	3.213	0.733	-0.584	2.903	0.791	1.846	3.841	0.641
DTD2	15	4		0.225	3.469	0.696	-0.811	2.974	0.773	-0.870	3.021	0.757
DTD3	50	2		0.235	3.320	0.722	-0.989	2.892	0.779	0.156	3.282	0.724

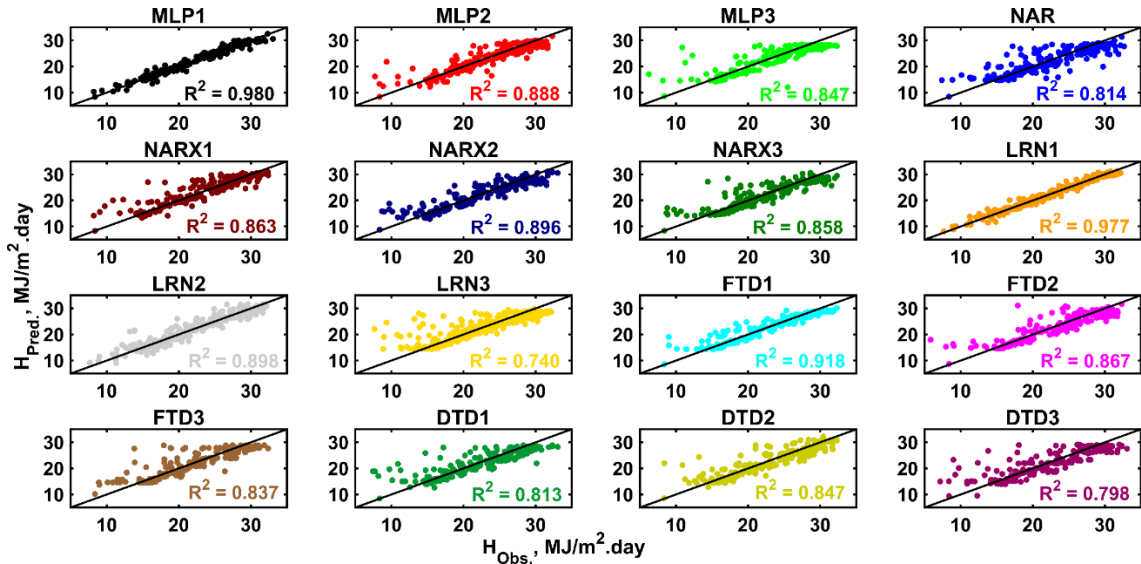


Figure 4: Goodness of fit plots of all developed models for Adrar (validation dataset).

Ma'an station has clearer skies during the year, with fewer partially cloudy days than Adrar. This results in some changes in the relative performances of dynamic models as compared to the static models, as illustrated in Table 1. For this location, the sunshine-based MLP model (MLP1) shows the best performance in the three development phases, based on all statistical measures, with the lowest validation MBE and RMSE values (-0.002 and 1.041 MJ/m².day, respectively) and the highest coefficient of determination (97.8%). This static model has only a slight improvement in the prediction accuracy over the LRN1 model, which has validation MBE, RMSE and R² values of 0.244 MJ/m².day, 1.073 MJ/m².day, and 97.8%, respectively. On the other hand, the FTD sunshine-based model (FTD1) cannot adapt to the current climate conditions. This is not due to overfitting (since the training error measures are also unacceptable) but due to their failure in finding the global minima (they stuck in local minima). More details on this issue can be found in (Izenman, 2008). Therefore, the FTD network is not recommended for forecasting solar radiation based on the sunshine hours. The same situation happens for the temperature-based models, where the performance of the MLP network (MLP2) surpasses those of all dynamic models, with an RMSE of 1.892 MJ/m².day, and, also, the FTD model (FTD2) fails again to simulate the temperature-global irradiation relationship. Nevertheless, the FTD has a reasonable performance when used to forecast the global irradiation independently (model FTD3), with a validation RMSE of 2.092 MJ/m².day. It can also be noticed that the DTD3 and NARX3 models slightly outperform the MLP3 model. Finally, the NAR model has the lowest coefficient of determination (R²=0.862). The sunshine- and temperature-based models for Zagora behave almost the same way

as those for Ma'an. Again, models MLP1 and MLP2 outperform all corresponding sunshine- and temperature-based dynamic models, with RMSEs of 1.310 and 2.456 MJ/m².day, accordingly. Meanwhile, the independent NARX model (NARX3) has a significantly better performance than those of MLP3 and all other independent dynamic models. Finally, the NAR model has a modest performance as compared to all other successfully trained models of all types, with a validation RMSE of 3.024 MJ/m².day.

Figure 5 provides a brief demonstration of the performances of all models during the three phases of development based on the relative error measures (MAPE and RRMSE). Each model is represented by a single point on RRMSE-MAPE axes. By comparing the results of the models at the three locations, it can be noticed that most of the ANN models perform better at Ma'an station, which has a clearer sky while having the worst performances at Zagora that has some total overcast days and more partial overcast days during a typical year. Moreover, it can be noticed that while the static models are significantly better in modelling the solar radiation using the sunshine data than all dynamic models (except for LRN-based models), they have comparable performances in temperature-based modelling and lower performances when no such meteorological data are available. The LRN algorithm offers excellent estimations for the two first types of models while having the lowest prediction accuracy in case of independent models.

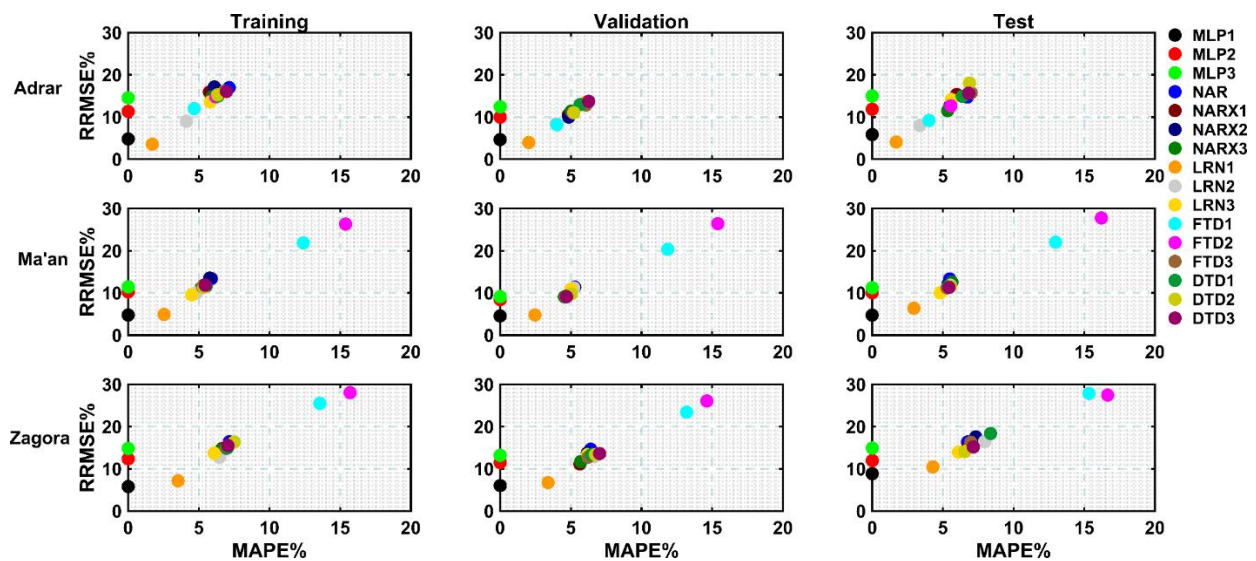


Figure 5: Scatter plots showing the overall performances of all developed model in the training, validation and test phases.

The NARX and DTD algorithms behave in a different manner since they have relatively better performances in forecasting solar radiation independently. The FTD algorithm should be avoided since it cannot easily conform to the input-output correlations of sunshine- and temperature-based models at all locations. Besides, it provides moderate accuracies for independent forecasting. Finally, the NAR algorithm, due to being an endogenous learner, has a prediction accuracy comparable to those of independent models. As shown in the figure, all MLP models have almost-zero relative bias errors. However, bias error measures are less important than random error measures for investigating the true performance of the models since the RMSE (or RRMSE) assigns higher weights to large deviations from measured data by squaring the errors before averaging. Based on the RRMSE, it can be noticed that MLP1 and LRN1 have significantly lower random error values, while almost all other models are clustered in one region. Figure 6 shows different time-series plots for all sunshine-based models at the three locations during some typical summer and winter days. The figure further highlights the capability of the MLP and LRN algorithms in capturing the short-term variations of global irradiation.

4.2. Stability

This section aims to shed some light on another criterion that is rarely discussed in the relevant literature, which is the stability of the forecasting algorithms. A stable model would provide the same level of errors during the training, validation, and test phases. If the validation error is significantly higher than the training/fitting error, that would indicate an overfitting problem. If the test error is significantly higher than the validation error that would indicate that the model is incapable of generalizing to new data in the forecasting process. The stability of the model is more important in case of inherently unstable algorithms such as the ANNs, while less important in case of simple empirical correlations or inherently stable algorithms such as SVMs (Izenman, 2008).

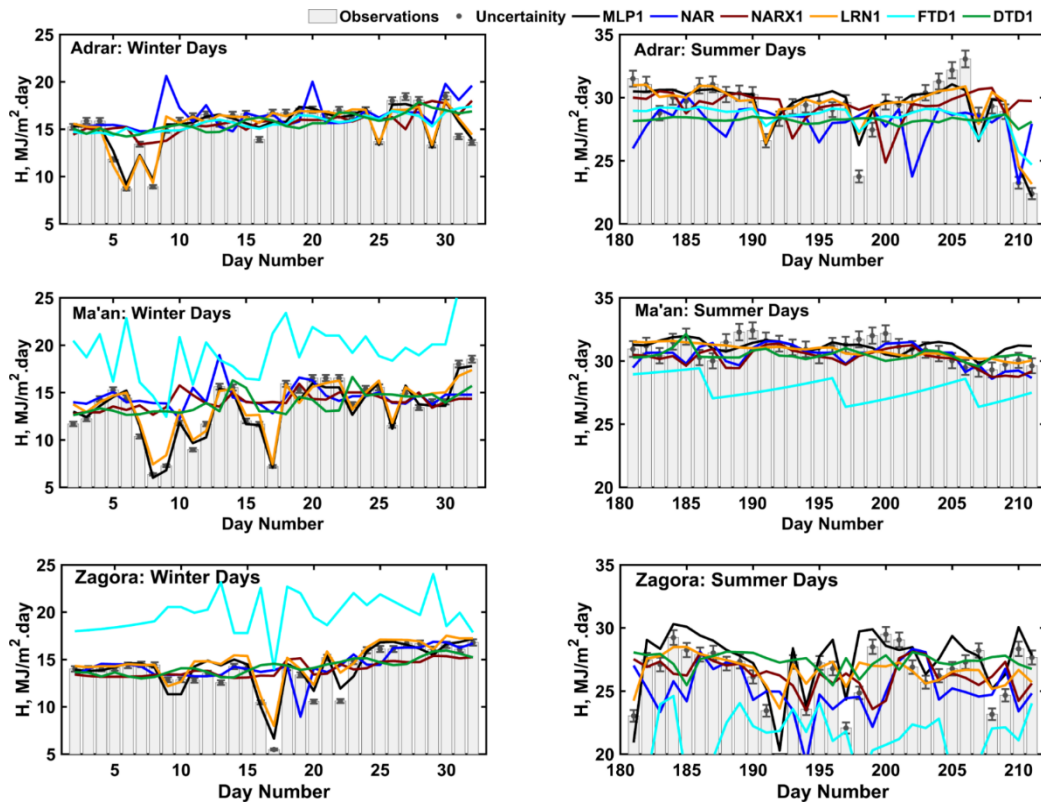


Figure 6: Time-series plots showing the variations of measured and estimated values of global irradiation during typical winter and summer days for endogenous and sunshine-based models.

In Figure 7, the horizontal axis represents the percentage difference between training and validation RMSEs, while the vertical axis represents the percentage difference between validation and test RMSEs. Therefore, the x- and y-axis values may be used to check the model for overfitting and instability issues. Stable models are represented by points in the lower left corner of the figure, where the RMSE values decrease continuously through the training, validation and test phases. As seen in the figure, most of the models have negative values on the x-axis, indicating that they are not overfitting, thanks to the optimization procedure. However, they have positive values on the y-axis, indicating that the error estimates increase when they are used to predict future values. For Adrar, the most stable models are LRN2, LRN3, and NARX3. Meanwhile, model LRN1 shows a less common behaviour as it overfits in the validation stage but adapts well to the test dataset. At Ma'an, model MLP1 shows a relatively stable behaviour, model LRN3 behaves the same way as model LRN1 at Adrar, while models NARX3 and LRN1 are relatively unstable. Model LRN2, on the other hand, shows considerable overfitting and instability issues.

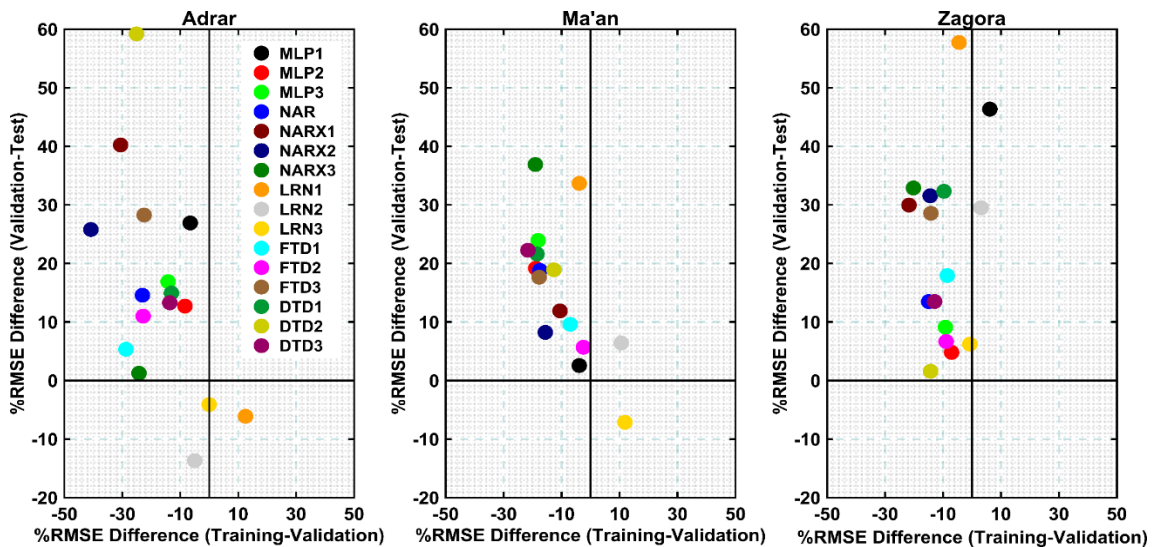


Figure 7: Scatter plots demonstrating the stability characteristics of the developed models, where the percentage increase of the RMSE in the validation phase is plotted against that of the test phase.

For Zagora station, models MLP1, LRN1, LRN2, NARX1, NARX2, NARX3, FTD3, and DTD1 show relatively unstable performances, with slight overfitting corresponding to models MLP1 and LRN2. The figure may suggest that the static models are less stable than the dynamic TDNNs as well as the simple NAR network, but slightly more stable than the dynamic RNNs. However, Figure 8 elaborates the stability of the networks furthermore by showing the training curves of MLP (static), LRN (RNN) and DTD (TDNN) models at Adrar. In this figure, the validation errors of the static models tend to increase again after reaching the minima as the training process goes on, while the validation errors of the dynamic models become more stable as the training process continues. The figure also shows that even when the MLP models provide considerably lower validation errors, the test errors are equal to or higher than those of the dynamic models.

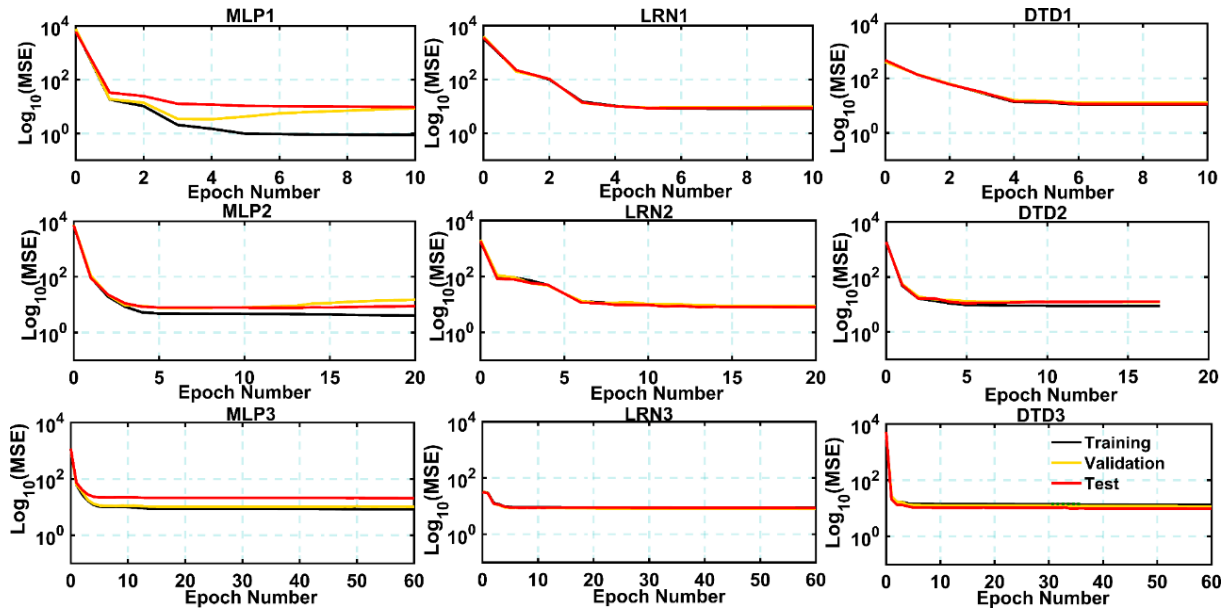


Figure 8: Training curves of MLP, LRN and DTD models (Adrar). MSE: mean square error.

5. CONCLUSION

This work aimed to provide an extensive evaluation of the dynamic neural networks in solar radiation forecasting. It was found that the prediction accuracy offered by the dynamic models highly depends on the algorithm used and the type of inputs. The LRN provides the same level of errors as the MLP, or even lower, except when used to model the global irradiation independently. The NARX and DTD networks show average performances for sunshine- and temperature-based models, while having superior performances for independent modelling. The FTD network was found unstable, at least for the studied locations, except when used for modelling the solar irradiation independently, where it provides good forecasts. Finally, the NAR network always offers modest levels of accuracy due to its simplicity and endogenous nature. The dynamic ANNs, though, have some favourable characteristics such as their less tendency to overfitting, better performances when low-class inputs are used, and their stability at clear-sky locations. On the other hand, they are slower to train and optimize. However, once trained, their computational costs during the forecasting process are almost the same as in the static networks. It is recommended to examine the potential of dynamic ANNs for other climates, especially heavy-sky climates, or in shorter forecasting horizons, e.g. for estimating the hourly global irradiance. Besides, it is recommended to hybridize the dynamic models (especially LRN) with other algorithms such as the support vector regression algorithm, which typically as accurate as static ANNs while being more stable, to develop a superior model that benefits from the merits of its base models.

6. NOMENCLATURE

ANN	Artificial neural networks	NARX	Nonlinear autoregressive network with exogenous input
ARIMA	Autoregressive integrated moving average method	R^2	Coefficient of determination
DTD	Distributed time delay network	RMSE	Root mean square error
FTD	Focused time delay network	RNN	Recurrent neural network
H	Global horizontal irradiation, MJ/m ² .day	RRMSE	Relative root mean square error
H_0	Extraterrestrial horizontal irradiation, MJ/m ² .day	SF	Sunshine fraction
k	Time lag	t	time
LRN	Layer recurrent network	TDNN	Time delay neural network

MAPE	Mean absolute percentage error	TDL	Tapped delay line
MBE	Mean bias error	X	Explanatory variable
MLP	Multilayer perceptron network	Y	Target output
N	Day number	\hat{Y}	Estimated output
NAR	Nonlinear autoregressive network	δT	Daily temperature range, °C

7. ACKNOWLEDGEMENT

The authors would like to express their deep gratitude to the Institute of Solar Research and the German Aerospace Centre (DLR) for the scientific and financial support. The authors sincerely appreciate the efforts made by the other local partners of the ener-MENA project in collecting the data used in this study.

8. REFERENCES

- Ahmad, A., Anderson, T. N. and Lie, T. T. (2015) 'Hourly global solar irradiation forecasting for New Zealand', *Solar Energy*. Elsevier Ltd, 122, pp. 1398–1408.
- Alzahrani, A., Kimball, J. W. and Dagli, C. (2014) 'Predicting solar irradiance using time series neural networks', *Procedia Computer Science*. Elsevier Masson SAS, 36(C), pp. 623–628.
- Azimi, R., Ghayekhloo, M. and Ghofrani, M. (2016) 'A hybrid method based on a new clustering technique and multilayer perceptron neural networks for hourly solar radiation forecasting', *Energy Conversion and Management*. Elsevier Ltd, 118, pp. 331–344.
- Badescu, V. (ed.) (2008) *Modeling Solar Radiation at the Earth's Surface: Recent Advances*. 1st edn. Verlag: Springer-Verlag Berlin Heidelberg.
- Benmouiza, K. and Cheknane, A. (2016) 'Small-scale solar radiation forecasting using ARMA and nonlinear autoregressive neural network models', *Theoretical and Applied Climatology*, 124(3–4), pp. 945–958.
- Besharat, F., Dehghan, A. A. and Faghih, A. R. (2013) 'Empirical models for estimating global solar radiation: A review and case study', *Renewable and Sustainable Energy Reviews*. Elsevier, 21, pp. 798–821.
- Bouzgou, H. (2014) 'A fast and accurate model for forecasting wind speed and solar radiation time series based on extreme learning machines and principal components analysis', *Journal of Renewable and Sustainable Energy*, 6(1).
- Gairaa, K. et al. (2016) 'Estimation of the daily global solar radiation based on Box-Jenkins and ANN models: A combined approach', *Renewable and Sustainable Energy Reviews*. Elsevier, 57, pp. 238–249.
- Ghimire, S. et al. (2019) 'Global solar radiation prediction by ANN integrated with European Centre for medium range weather forecast fields in solar rich cities of Queensland Australia', *Journal of Cleaner Production*. Elsevier Ltd, 216, pp. 288–310.
- Gouda, S. G. et al. (2019) 'Model selection for accurate daily global solar radiation prediction in China', *Journal of Cleaner Production*. Elsevier Ltd, 221, pp. 132–144.
- Hassan, M. A., Khalil, A., Kaseb, S. and Kassem, M. A. (2017) 'Exploring the potential of tree-based ensemble methods in solar radiation modeling', *Applied Energy*.
- Hassan, M. A., Khalil, A., Kaseb, S. and Kassem, M.A. (2017) 'Independent models for estimation of daily global solar radiation: A review and a case study', *Renewable and Sustainable Energy Reviews*. Elsevier Ltd, 82(July 2017), pp. 1565–1575.
- Hassan, M. A. (2017) *Solar radiation modeling using advanced statistical and machine learning techniques*. Cairo University.
- Hussain, S. and AlAlili, A. (2016) 'A new approach for model validation in solar radiation using wavelet, phase and frequency coherence analysis', *Applied Energy*. Elsevier Ltd, 164, pp. 639–649.
- Hussain, S. and AlAlili, A. (2017) 'A hybrid solar radiation modeling approach using wavelet multiresolution analysis and artificial neural networks', *Applied Energy*. Elsevier, 208(August), pp. 540–550.

- Izenman, A. (2008) *Modern Multivariate Statistical Techniques: Regression, Classification, and Manifold Learning*. 1st edn. New York: Springer.
- Kashyap, Y., Bansal, A. and Sao, A. K. (2015) 'Solar radiation forecasting with multiple parameters neural networks', *Renewable and Sustainable Energy Reviews*. Elsevier, 49, pp. 825–835.
- Li, M. F. et al. (2013) 'General models for estimating daily global solar radiation for different solar radiation zones in mainland China', *Energy Conversion and Management*. Elsevier Ltd, 70, pp. 139–148.
- Meenal, R. and Selvakumar, A. I. (2018) 'Assessment of SVM, empirical and ANN based solar radiation prediction models with most influencing input parameters', *Renewable Energy*. Elsevier Ltd, 121, pp. 324–343.
- Di Piazza, A., Di Piazza, M. C. and Vitale, G. (2016) 'Solar and wind forecasting by NARX neural networks', *Renewable Energy and Environmental Sustainability*, 1, p. 39.
- Piri, J. and Kisi, O. (2015) 'Modelling solar radiation reached to the Earth using ANFIS, NN-ARX, and empirical models (Case studies: Zahedan and Bojnurd stations)', *Journal of Atmospheric and Solar-Terrestrial Physics*. Elsevier, 123, pp. 39–47.
- Rao K, D. V. S. K., Premalatha, M. and Naveen, C. (2018) 'Analysis of different combinations of meteorological parameters in predicting the horizontal global solar radiation with ANN approach: A case study', *Renewable and Sustainable Energy Reviews*. Elsevier Ltd, 91(March), pp. 248–258.
- Samarasinghe, S. (2006) *Neural Networks for Applied Sciences and Engineering: From Fundamentals to Complex Pattern Recognition*. 1st edn. New York: Auerbach Publications.
- Torres-Barrán, A., Alonso, Á. and Dorronsoro, J. R. (2019) 'Regression tree ensembles for wind energy and solar radiation prediction', *Neurocomputing*, 326–327, pp. 151–160.
- Voyant, C. et al. (2017) 'Machine learning methods for solar radiation forecasting: A review', *Renewable Energy*. Elsevier Ltd, 105, pp. 569–582.
- Wu, J. and Chan, C. K. (2011) 'Prediction of hourly solar radiation using a novel hybrid model of ARMA and TDNN', *Solar Energy*, 85(5), pp. 808–817.
- Wu, J. and Chan, C. K. (2012) 'The prediction of monthly average solar radiation with TDNN and ARIMA', in *11th International Conference on Machine Learning and Applications, ICMLA*. Boca Raton, Florida, pp. 469–474.
- Yadav, A. P. and Behera, L. (2014) *Solar radiation forecasting using neural networks and wavelet transform*, IFAC Proceedings Volumes (IFAC-PapersOnline). IFAC.
- Yao, W. et al. (2018) 'A new correlation between global solar radiation and the quality of sunshine duration in China', *Energy Conversion and Management*. Elsevier, 164, pp. 579–587.
- Zang, H. et al. (2019) 'Estimation and validation of daily global solar radiation by day of the year-based models for different climates in China', *Renewable Energy*. Elsevier Ltd, 135, pp. 984–1003.

#273: Performance modelling and validation on the co-gasification of coal and sawdust pellet in research-scale downdraft reactor

Fatin Zafirah MANSUR¹, Che Ku Mohamad Faizal Che Ku YAHYA², Samson Mekbib ATNAW³, Shaharin Anwar SULAIMAN⁴

¹Energy and Environmental, Faculty of Engineering Technology, Universiti Malaysia Pahang, 26300, Gambang, Pahang, zafirahmj8@gmail.com

²Energy and Environmental, Faculty of Engineering Technology, Universiti Malaysia Pahang, 26300, Gambang, Pahang, mfaizal@ump.edu.my

³College of Electrical and Mechanical Engineering, Addis Ababa Science and Technology University, Ethiopia, samson.mekbib@aastu.edu.et

⁴Department of Mechanical Engineering, Universiti Teknologi Petronas, 32610, Bandar Seri Iskandar, Perak, shaharin@utp.edu.my

Co-gasification of fossil fuel with biomass is considered a very promising clean energy option in reducing greenhouse gas emissions and non-renewable energy dependency. The main objective of this research was to develop a simple and reliable model as a preliminary tool to evaluate the performance of co-gasification of sub-bituminous coal with densified biomass (sawdust pellet). The simulation model was validated experimentally to ascertain the performance parameters. The model, which included the minimization of the Gibbs free energy, was simulated using Aspen Plus as the modelling tool. Experimental investigations were carried out under controlled conditions of the electrically-driven externally-heated fixed bed downdraft gasifier in the Biomass laboratory in the Department of Mechanical Engineering, Universiti Teknologi Petronas. The operating parameter of the biomass blending ratio, gasification temperature and equivalence ratio (ER_{air}) on the co-gasification performance parameter were analysed. Three performance parameters, calorific value of the syngas (CV_{syngas}), syngas yield (Y_{syngas}) and gasification efficiency (η_{GE}), were studied. The experimental works of the co-gasification took place with air, at the various sawdust pellet blending ratios of 0, 25, 50, 75, 100% w/w, in a gasification temperature ranging from 650 to 850°C, and various air equivalence ratios ranging from 0.1 to 0.4 and under atmospheric pressure.

The increase of the biomass blending ratio denoted a decrease of the calorific value (CV_{syngas}), syngas yield (Y_{syngas}) and gasification efficiency (η_{GE}). On the contrary, effects of the gasification temperature at the various blending ratios exhibited an increase for all the performance parameters. In addition, ER_{air} resulted in the decline of the syngas yield (Y_{syngas}), the calorific value of the syngas (CV_{syngas}) and gasification efficiency (η_{GE}).

Meanwhile, as the ER_{air} increased, the syngas yield (Y_{syngas}) also increased. Furthermore, it was found out the result obtained from the developed model agreed well with the experimental data conducted in replicate. Thus, the model was validated and considered reliable for predicting the co-gasification performance parameter on the coal and sawdust pellet.

Keywords: co-gasification; coal; wood pellet; Aspen Plus; performance

1. INTRODUCTION

Coal, the third primary energy resources after natural gas and crude oil, accounted for about 16k tonnes of oil equivalent (toe) of the total primary energy supply in Malaysia, and was predicted to increase by 23% over the year in Malaysia (Energy Commission, 2016). Apart from the issue of depletion of fossil fuels reserves, the primary concern of the usage of coal is the production of greenhouse gas emissions and other toxic gases such as CO₂ and NO_x eventually causing global warming and acid rain (Alauddin *et al.*, 2010). Thus, it has heightened the need to search for promising solutions that are renewable, environmentally friendly, sustainable, economical and lessen the current environmental issues. Recent research has proven that co-utilization of coal and biomass was a development of sustainable bioenergy network between a renewable and non-renewable resource, especially in co-gasification to produce syngas and electricity in a sustainable manner (Paiman *et al.*, 2018). Co-gasification technology aids in potentially reducing the exploitation of conventional coal resources, assists in lowering greenhouse gases (GHG) emissions, but also boosts the overall gasification process efficiency (Ali *et al.*, 2016). It has been discovered that the co-gasification of these two fuels exhibited synergism reaction that reduced GHG emissions without reducing the energy content of the product gas (Ciferno and Marano, 2002). Furthermore, biomass characterization and the percentage mixture of biomass with coal plays an essential role as it is directly associated with the fuel gas composition. The co-gasification process between biomass and fossil fuels significantly reduces the carbon footprint on the environment and enhances the H₂/CO ratio in the produced syngas, which is essential in liquid fuel synthesis. Another crucial point, it has been discovered that the inorganic matter present in biomass functions as a catalyst for coal gasification (Satyam Naidu, Aghalayam and Jayanti, 2016). Thus, production of superior gas quality by using coal-biomass blends at different operating conditions and temperatures and ER_{air} have gained interest among researchers (Sarker, 2016). A number of research projects on co-gasification of the various blending ratio of biomass with coal have been conducted with the results indicating that blending coal with biomass eventually enhances the gasification beyond levels that were possible by gasifying these feedstocks alone (Valdés *et al.*, 2016). Most of the studies were focused on the raw biomass co-gasified with coal; however, the co-gasification on the pre-treated biomass, especially pelletization, is still lacking. Dafnomilis *et al.* (2018) expressed the opinion that the pre-treatment of biomass in the form of pelletized or otherwise densified resulted in better fuel operability in terms of handling, transportation, storage, and feeding compared than raw biomass. Gasification of pellet fuel has been widely applied in commercial gasification resulting in syngas composition being much more stable by maintaining a more steady and efficient gasification; the uniform shape and density of the pellet fuels aids in smooth feeding by making less of a biomass bridge and gasification reaction (Yoon *et al.*, 2012). It has been discovered by a number of researchers that the co-gasification of biomass pellets/coal resulted in a promising efficient production of syngas. Although pelletized biomass has been utilized as a co-feed in gasification or combustion systems, the reason for the improvement in the efficiency of the pelletized case gasification is not apparent (Pradhan, Mahajani and Arora, 2018). The development of a fuel-flexible gasification in the pellet form co-gasified with coal remains a challenge, and the field requires further attention. Hence, this study attempts to simulate a co-gasification model of the downdraft fixed bed gasifier with the application of the Aspen Plus® software environment.

Much research has been conducted in modelling the downdraft gasification on various feedstocks either using agricultural residue or forestry residue. This is due to the application of software serving as an alternative to minimize experimental costs and time (Monir *et al.*, 2018). Able to simulate the gasifier by breaking gasification into the drying zone, the pyrolysis zone, the oxidation zone and the reduction zone as well as considering the heat and mass transfer in the model, this tool is capable of predicting gasification performance effectively. Subsequently, the performance of a gasifier system at the different operating and design parameters which can be validated from the optimal model allows designers to speculate the effects of parameters even without any further experimental data (Ismail and El-Salam, 2017). Keche *et al.* (2015) built the developed model with the different biomass fuels in an atmospheric fixed bed reactor to investigate the syngas composition. A model developed by Gao *et al.* (2017) investigated the production of H₂ from the co-gasification of coal and biomass in the presence of CaO as a sorbent. Co-gasification of the charcoal with EFB was developed by Monir *et al.* (2018) that found out that the highest mole fraction of H₂ and CO occurred at a temperature of 975°C and pressure of 35 bar. Ali *et al.* (2016) developed a simulation model of the rice-husk and coal that indicated the model capable of serving as a reliable benchmark for revamping an existing Egyptian natural gas-based power plant. Kuo and Wu (2015) designed the co-gasification of coal with pre-treated biomass, which was the torrefied woody biomass as a substitution to the raw woody biomass. The simulation noted that the utilization of the torrefied woody biomass significantly improved syngas yield. Meanwhile, according to the power generation's view, the co-gasification of coal and torrefied biomass resulted in an optimal input condition in terms of power generation and system efficiency. As far as the authors are aware, there is still limited modelling of co-gasification of coal with pre-treated biomass, especially densified biomass using the Aspen Plus® software.

The objective of this study was to investigate the co-gasification of sub-bituminous coal (CL) with sawdust pellet (SP) by modelling and simulate a kinetic free equilibrium model of fixed-bed downdraft gasifier in Aspen Plus®. The sawdust pellet (SP) blending ratio, gasification temperature and air equivalence ratio were varied to predict the calorific value of the syngas (CV_{syngas}), syngas yield (Y_{syngas}) and gasification efficiency (η_{GE}). Furthermore, the results obtained from the experimental measurement were used to verify the simulation result obtained from

the developed model. The results acquired through this study will serve for preliminary investigation on gasification performance of the pre-treated biomass co-gasified with coal.

2. METHODOLOGY

2.1. Aspen Plus simulation model

In modelling the co-gasification process, a kinetic free equilibrium model is developed using Aspen Plus® software (ver. 8.6). The major chemical reactions that occurred in the gasifier are listed in Table 1 (Kuo and Wu, 2015). The co-gasification process was divided into three sub-systems to form a downdraft gasifier system. The drying sub-system minimized the moisture content of the feed before being fed into the next reactor. The second sub-system aided in decomposing the feed into volatile components and char. Moreover, the FOTRAN statement will be included to specify the yield distribution for each conventional components. Next, the RGibbs sub-system simulated the partial oxidation and gasification process by minimizing Gibbs free energy. In carrying out the modelling, some assumptions were made. The assumptions applied in the model were:

- The process occurred in a steady state with kinetic free and the residence time was not considered.
- Atmospheric pressure was assumed in all sub-system.
- Air was introduced in the RGibbs to enhance the co-gasification process at ambient temperature and pressure.
- The gasification agent mixed homogenous and reacted with feed instantly in the reactor.
- All sulphur was produced in the H₂S form; meanwhile no oxide of nitrogen was formed as only NH₃ was produced.
- Tars were assumed to be negligible in the syngas.

The gases involved were in compliance with the Peng-Robinson equation of state with Boston-Mathias alpha function (PR-BM) to estimate all physical properties of the conventional and non-conventional components at the multiple phase in the gasification process (Yu *et al.*, 2015)

Table 1: Chemical reactions that occur in gasifier.

Reaction number	Reaction name	Reaction equation
1	Combustion reaction	$C + O_2 \rightarrow CO_2$
2	Bourdouard reaction	$C + CO_2 \leftrightarrow 2CO$
3	Water gas shift reaction	$C + H_2O \rightarrow CO + H_2$
4	Water gas shift reaction	$CO + H_2O \rightarrow CO_2 + H_2$
5	Methanation reaction	$C + 2H_2 \leftrightarrow CH_4$
6	Methanation reaction	$2C + 2H_2O \rightarrow CH_4 + CO$
7	NH ₃ formation reaction	$0.5N_2 + 1.5 H_2 \rightarrow NH_3$
8	H ₂ S formation reaction	$H_2 + S \rightarrow H_2S$

2.2. Model development

The simulation model flowsheet used in the developed model is shown in Figure 1. Firstly, the stream of feed consisted of a mixture of sawdust pellet and coal, with a ratio blend of 0, 25, 50, 75, 100% w/w, respectively was fed into the system. The sawdust pellet blending ratio was defined as the mass ratio of sawdust pellet to the total of biomass and coal, therefore, 0, 100% of sawdust pellet blending ratio refers to the pure coal and pure sawdust pellet, respectively. The feed stream was passed through all blocks with different reaction temperatures. The feedstock was specified as a non-conventional component in Aspen Plus and was defined by their ultimate and proximate analysis present in Table 2. In addition, Table 3 provides the operation model that was used in this study. The drying process that removed the residual moisture in the feed was simulated in the 'RStoic' block by including the FOTRAN statement in the calculator block to control the drying operation. After drying, the feed decomposed into its constituent components (C, H, O, S and N) by specifying yield distribution in the block 'RYield'. The feed needed to decompose as the 'RGibbs' block cannot calculate the feed due to its non-conventional components. In the 'RYield' block, the yield distribution of the feed was specified by FOTRAN statement in a calculator block into its components. The total yield of volatiles was assumed to be equal to the volatile content of the parent fuel by taking into account the proximate analysis of the fuel. The co-gasification process was simulated in 'RGibbs' block by minimizing the Gibbs free energy assuming the complete chemical equilibrium calculations. The gasifying agent, which was air, was introduced into the block where partial oxidation and gasification reactions took place. Furthermore, the 'RGibbs' block was capable of calculating the syngas composition as it can generate light gases such as CO, CO₂, H₂, H₂O, N₂, CH₄, and H₂S. H₂S in the gases were considered negligible due to the lower content of sulphur in the fuel. In addition, considering that only NH₃ formed in the gasifier without any formation nitrogen oxide has already been used by other researchers (Schuster *et al.*, 2001). The outlet stream of the 'RGibbs' passed through the 'Sep' block to separate gases from ash according to the specified splits fractions as desired. The 'Sep' in the Aspen Plus model was simulated for the functioning in ash separation from the syngas.

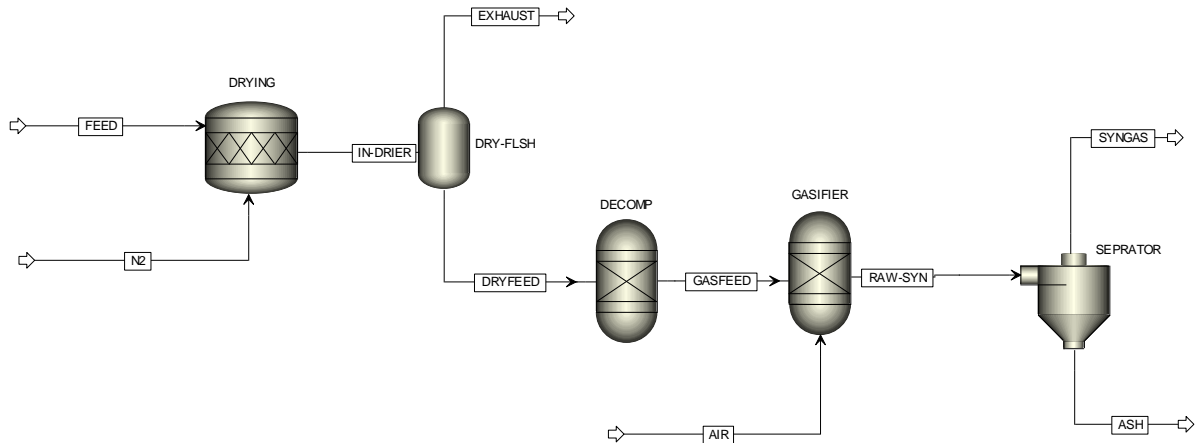


Figure 1: ASPEN Plus simulation model of co-gasification on coal with WP.

Table 2: Proximate, ultimate and calorific value of the coal and WP

Components	Coal	Sawdust
Proximate analysis (wt %)		
Moisture content	8.18	9.19
Volatile matter	39.79	79.00
Fixed carbon	33.81	10.16
Ash content	18.22	1.65
Ultimate analysis (wt %)		
Carbon (C)	52.58	44.28
Hydrogen (H)	5.90	6.09
Nitrogen (N)	1.49	1.05
Sulphur (S)	1.14	0.28
Oxygen (O)	38.90	48.62
Calorific value (MJ/kg)	20.19 ± 0.082	17.46 ± 0.085

Table 3: List of ASPEN Plus unit operation model.

Aspen Plus Model	Operation	Description	Function
RStoic	Drying	Conversion reactor with known stoichiometry	Reduce the moisture content of the wet feed
RYield	Decomposed	Yield reactor with known products yield	Decomposed non-conventional feed into its element constituents applying FOTRAN statement
RGibbs	Gasifier	Multiphase chemical equilibrium reactor (non-stoichiometry)	Models gas-phase chemical equilibrium and aids in calculating the syngas composition by minimizing Gibbs free energy
Sep	Separator	Split a stream into two stream or more by specifying split fractions	Separates gas from ash

2.3. Model verification

In order to demonstrate the validity of the proposed model, the experimental measurement of co-gasification of coal with SP was carried out in a lab-scale electrical downdraft gasifier, as shown in Figure 2. The system was custom-fabricated and located in the Biomass laboratory under the Department of Mechanical Engineering of Universiti Teknologi Petronas, Malaysia. The reactor was a cylindrical tube made up of stainless steel class SS316 consisting of an internal diameter of 80mm and 500mm long. The gasifier was positioned vertically as a function in a free-fall, gravity-fed reactor. About 100g of the feed was then loaded into the gasifier with the different mixture ratio of SP at 0, 25, 50, 75, 100% w/w. The electrical downdraft gasifier was heated with a WATLOW 240V, 1300W ceramic-embedded radiant tube heater with a maximum heating temperature of 1000°C on continuous duty. Furthermore, the operating temperature varied from 650°C to 850°C and was measured by an external PID controller coupled with a K-type thermocouple mounted on the gasifier reactor. Meanwhile, a stainless steel grate was held at the centre inside the gasifier acting as the feedstock holder and also as the reactor bed where the thermal conversions took place. Air as an oxidizing agent was distributed in the gasifier by the compressed air through a 5mm welded connection situated slightly below the top of the gasifier and controlled by a rotameter. The equivalent ratio of air fixed at 0.20, 0.25 and 0.30 were varied using the airflow rate from 2 L/min - 4L/min. The gasifier had two threaded openings at the top and bottom for the feedstock loading and for ash removal and cleaning access respectively. Gases flowed to the bottom of the reactor, certifying a downdraft fixed bed

configuration (Susastriawan, Saptoadi and Purnomo, 2017). The gases then flowed to a gas conditioning unit before entering the online gas analyzer for gas composition measurement.

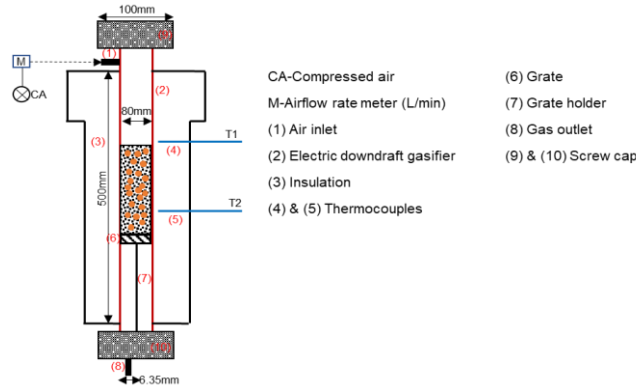


Figure 2: Schematic diagram of laboratory scale electrical downdraft gasifier used for the model validation.

The developed simulation model for co-gasification of coal and SP was used to perform the sensitivity analysis. The effect of the sawdust pellet (SP) blending ratio, gasification temperature and air equivalence ratio (ER) on each syngas composition, the calorific value of the syngas (CV_{syngas}), syngas yield (Y_{syngas}) and gasification efficiency (η_{GE}) was investigated. The calorific value of the syngas (CV_{syngas}) was calculated as it was an important output parameter that defined the quality of syngas produced from gasification in terms of energy content per unit volume or mass. The calorific value of the syngas (CV_{syngas}) was calculated by taking into account the volume percentage of combustible gas components in the syngas (CO , H_2 and CH_4) produced from the co-gasification experiment with their specific calorific value obtained from the US National Renewable Energy Laboratory (NREL) in the unit of MJ/Nm^3 as per standard value (Basu, 2010b). The equation is expressed in Equation 1 Equation.

Equation 1: Calorific value of the syngas (CV_{syngas}). $CV_{syngas} = (V_{CO} \times 12.63) + (V_{CH_4} \times 39.82) + (V_{H_2} \times 12.74)$

Where:

- CV_{syngas} = calorific value of the syngas (MJ/Nm^3)
- V = volumetric percentage for each of CO , CH_4 and H_2 obtained from online gas analyzer measurements (%)

Meanwhile, the syngas yield (Y_{syngas}) in the unit for each experiment took into account the volume of syngas produced per unit mass of feedstock consumed in the gasifier by considering the nitrogen balance method that was proposed and applied by several authors (Atnaw, Sulaiman and Yusup, 2011). It was applied by taking into account the continuous exposures of the high temperatures as well as the tar depositions in the measuring equipment causing the inaccuracy of the reading. The calculated value is given in Equation 2.

Equation 2: The syngas yield (Y_{syngas}) from the co-gasification of coal and SP. $Y_{syngas} = \frac{Q_a \times 79\%}{m_{feed} \times N_2}$

Where:

- Y_{syngas} = syngas yield (Nm^3/kg)
- Q_a = volume flow rate of air (Nm^3/h)
- m_{feed} = mass flow rate of the feedstock in the gasifier system (kg/h)
- $N_2\%$ = volumetric percentage of N_2 in the dry fuel gas

Furthermore, the gasification efficiency (η_{GE}) can be calculated either from the cold gas efficiency or hot gas efficiency (Kumar et al., 2014). It is possible to define the cold gas efficiency as the ratio between the chemical energy leaving the system associated with the cold and tar-free syngas and the chemical energy entering the system related to the biomass (Inayat et al., 2016). Thus, the gasification efficiency was calculated by considering the specific gas production and the energy content of the biomass. The gasification efficiency (η_{GE}) was calculated using Equation 3.

Equation 3: The gasification efficiency from the co-gasification of coal and SP.

$$\eta_{GE} = \frac{CV_{syngas} \times Y_{syngas}}{CV_{feed}} \times 100$$

Where:

- η_{GE} = gasification efficiency (%)
- CV_{syngas} = calorific value of the syngas (MJ/Nm³)
- CV_{feed} = calorific value of the feed (MJ/kg)
- Y_{syngas} = syngas yield (Nm³/kg)

The comparison between the predicted data from the simulation model and the experimental data for the co-gasification of coal and SP were discussed on the gasification performance in term of CV_{syngas} , Y_{syngas} and η_{GE} . In addition, the root mean square error (RMSE) was calculated using Equation 4 for each gasification performance at different gasification conditions to measure the error between simulation and experimental.

Equation 4: Calculation of RSME at every gasification performance.

$$RMSE = \sqrt{\frac{\sum_{i=1}^n (P_i - O_i)^2}{n}}$$

Where:

- P = predicted value
- = observed value
- n = number of dataset

3. RESULTS AND DISCUSSION

A sensitivity analysis was performed in the GASIFIER block by varying the gasification temperature and airflow parameter at different sawdust pellet blending ratios. This was to investigate the effect of sawdust pellet blending ratio, gasification temperature and air equivalence ratio on the gasification performance. In ASPEN Plus, this tool helped in determining the gasification performance on the varying input parameters. Table 4 shows the input parameters of the temperature and airflow applied in the model.

Table 4: Variable set in the GASIFIER block of the model.

Variable	Type	Block/stream	Variable	Unit	Limits	Increment
Temperature	Block-var	GASIFIER	TEMP	°C	600-1000	50
Air flow	Stream-var	AIR	MASS-FLOW	kg/hr	0.1-0.4	0.025

3.1. Effect of sawdust pellet blending ratio

Figures 3 (a), (b) and (c) present the effect of the sawdust pellet at blending ratio of 0, 25, 50, 75, 100% w/w on the CV_{syngas} , Y_{syngas} and η_{GE} , respectively. The gasification temperature and the ER_{air} was fixed at 750°C and 0.25, respectively. It can be seen that all the gasification performance increased with the increasing of the sawdust pellet blending ratio from 0 to 50%. The range of the CV_{syngas} , Y_{syngas} and η_{GE} calculated were 3.00 – 6.00 MJ/Nm³, 1.00 – 2.00 Nm³/kg and 25% - 37%, respectively. It was found that the maximum value of the CV_{syngas} , Y_{syngas} and η_{GE} from the simulation was calculated at 5.78 MJ/Nm³, 2.00 Nm³/kg and 37%, respectively that occur at 50% of the sawdust blending ratio. However, as the amount of the sawdust pellet blending ratio increased to 75%, all of the gasification performance dropped down by an average of 30%. A similar trend was found by Seo *et al.* (2010) who noted that increasing the Y_{syngas} at all temperatures together with an increase in biomass ratio was due to the transfer of hydrogen radicals in biomass to coal that resulted in higher decomposition of coal. The suggested minimum blend of 40% pine chips to 60% Sabero refuse coal with the value of 1.78 Nm³/kg by Pan *et al.* (2000) was quite similar to those for the highest yield of syngas obtained from this study when assessing influence of the biomass blending ratio on the Y_{syngas} . In term of the RSME value, both of the CV_{syngas} and Y_{syngas} were in the range of the 0 to 1.60, being relatively low and generally well aligned with the experimental result. Hence, this denoted that the purpose model was validated and reliable. In contrast, the RSME value of the η_{GE} was in the range of 0 to 21, in which the highest was recorded at 50% of the sawdust pellet blending ratio. This deviation might be due to the equilibrium condition that was applied in the gasification model that eliminated insignificant reaction between the coal and biomass (Ghassemi and Shahsavan-markadeh, 2014).

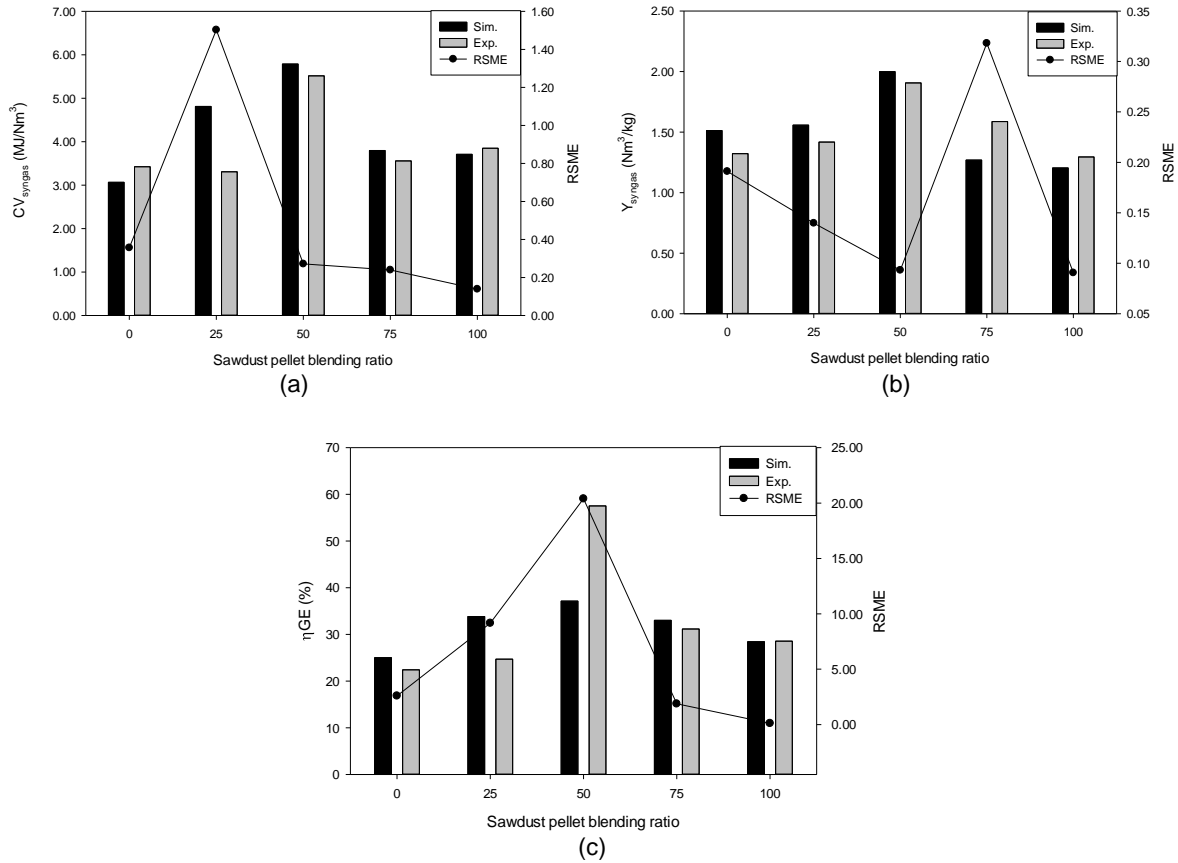


Figure 3: Effect of the sawdust pellet blending ratio with calculated RMSE value on (a) CV_{syngas} (b) Y_{syngas} and (c) η_{GE} at gasification temperature and E_{air} fixed at 750°C and 0.25.

3.2. Effect of gasification temperature

The influence of the gasification temperature from 650 to 850°C on various sawdust pellet blending ratio with the ER_{air} fixed at 0.25 on the gasification performance is illustrated in Figure 4. Figures 4(a), (c) and (e) show the CV_{syngas} , Y_{syngas} and η_{GE} as a function of gasification temperature, respectively. Meanwhile, the RSME value for every gasification performance in terms of CV_{syngas} , Y_{syngas} and η_{GE} are illustrated in Figures 4(b), (d) and (f), respectively. Altogether, it can be seen that the gasification temperature at the various sawdust pellet blending ratio exhibited an increase for all the performance parameters. The range of the CV_{syngas} was from 2.00 to 6.00 MJ/Nm³, and Y_{syngas} ranged from 1.00 to 2.00 Nm³/kg. Furthermore, η_{GE} ranged from 18% to 37%. The maximum of each of the gasification performances occurred at 50% of the sawdust pellet blending ratio. It can be concluded that the optimum blending ratio for the sawdust pellet with coal was 50%. A study conducted by Masnadi *et al.* (2014) assessed that the increase of the CV_{syngas} was associated with higher gasification temperatures resulting in the endothermic gasification reactions (Adeyemi *et al.* 2017). Complementary to this higher gasification temperature, there were more heat losses of the system and eventually the gasification process on the syngas production was improved. Meanwhile, increasing the gasification temperature enhanced the release of gaseous products from the pyrolysis, steam reforming, gasification and cracking reactions inside the gasifier and contributed to the high total amount of Y_{syngas} (Patel and Narnaware, 2018). These results were also recognised by several researchers who attributed the influence of temperature on Y_{syngas} in co-gasification (Fermoso *et al.*, 2009). Considering the rising of the gasification temperature improved the endothermic char reactions in the gasifier, it can be concluded that the increase of the Y_{syngas} was expected due to the increasing concentration of gaseous product (Ahmed *et al.* 2015). It was seen that the increase of η_{GE} as the gasification temperature increased was mainly due to the rise in CV_{syngas} . As previously mentioned, the lower RSME value indicated the least error between simulation and experimental. It can be seen from the RSME value for each the gasification performance parameter against the gasification temperature was lower than 20. Consequently, the model was suitable to serve as a preliminary for the co-gasification of coal with pellets.

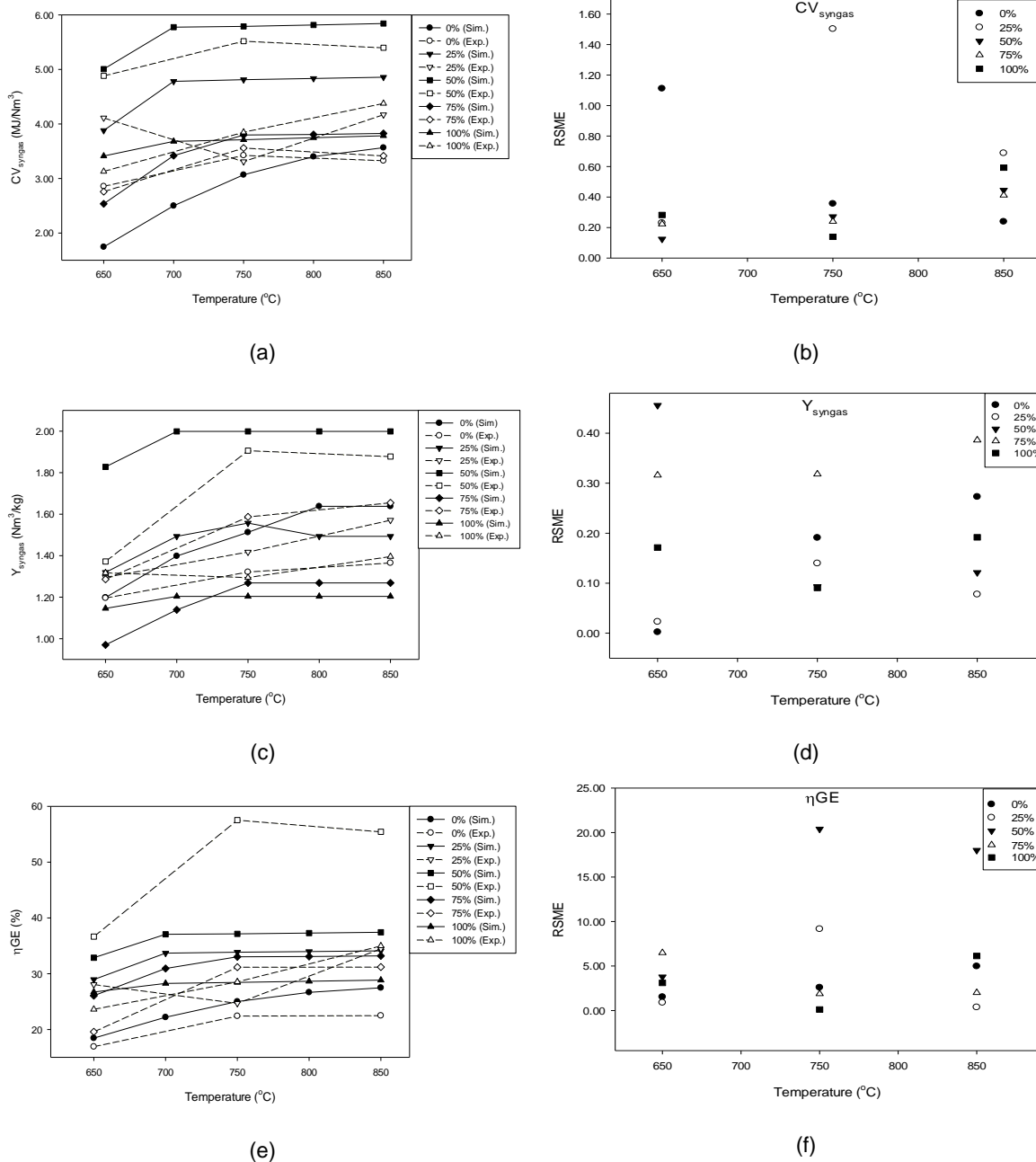


Figure 4: Gasification temperature at ER_{air} of 0.25 influence on (a) CV_{syngas} (c) Y_{syngas} and (e) η_{GE} with the respectively calculated RSME (b), (d) and (f).

3.3. Effect of air equivalence ratio

CV_{syngas} , Y_{syngas} and η_{GE} plot are presented in Figures 5 (a), (c) and (e), respectively for co-gasification of sawdust pellets at various blending ratio testing at gasification temperature fixed at 750°C. It can be seen that the CV_{syngas} and η_{GE} gradually decreased as the ER_{air} increased to 0.4. The CV_{syngas} and η_{GE} ranged from 1.6 to 8.4 MJ/Nm³ and 14% to 51%, respectively. Both of the highest quantities of CV_{syngas} were recorded at pure sawdust pellet achieved at 8.369 MJ/Nm³ and 51%, respectively. This can be predicted as the nature of the pellet form enhanced the energy density per unit volume, uniformity and defined structure of fuels thus possessed higher stability without depending on the critical variation of time (Yoon *et al.*, 2012). In addition, for other feeds, increasing the ER_{air} contributed to the higher airflow rate resulting in the lower heating values for syngas and significantly reduced the gasification process efficiency (Azargohar *et al.*, 2015; Valdés *et al.*, 2016). This was believed to occur due to the ER_{air} being related to the airflow rate, therefore increasing the airflow rate resulted in the shorter residence time of the feed to undergo reactions (Basu, 2010; Yan *et al.*, 2018). Inversely, increasing the ER_{air} value, the value of the Y_{syngas} also increased. Upadhyay *et al.* (2019) stated that the total Y_{syngas} was mainly associated with the fuel and air consumption rates. The study conducted on the co-gasification of lignite and sawdust briquette found that the

higher gas yield reached at 2.99 Nm³/kg obtained a high ER_{air} of 0.386. Commonly, it has been stated that for effective downdraft gasification, the ER should be between 0.2-0.4 (Basu, 2010). For the RSME value, as previously described, the RSME value for both for the CV_{syngas} and Y_{syngas} were lower, ranging from 0 to 2.3. The RSME value for η_{GE} ranged from 0 to 32 which is quite high, and was calculated at 50% of the sawdust pellet blending ratio. This might be due to the kinetic reaction taking place in the gasifier during the experimental measurement.

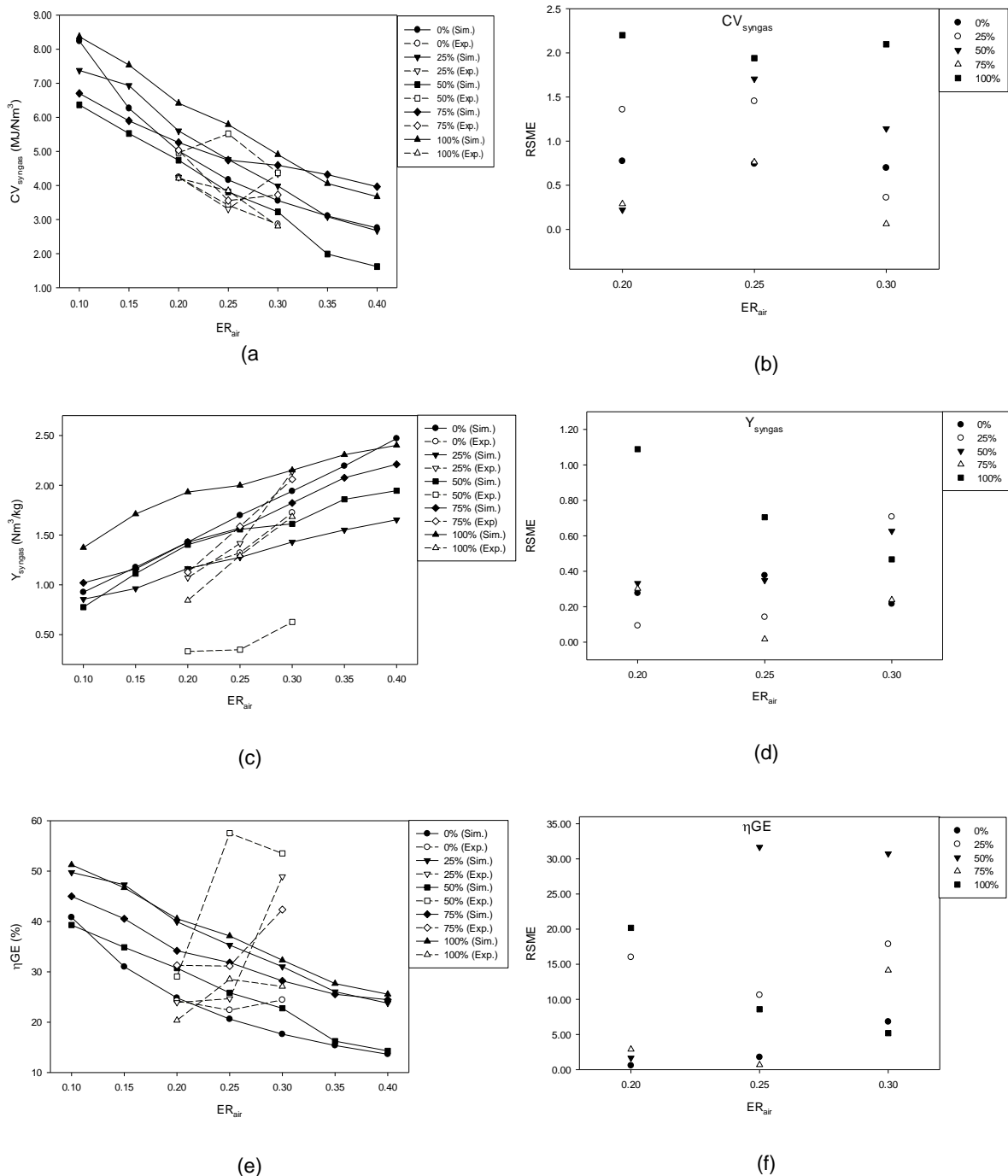


Figure 5: Influence of ER_{air} at the various sawdust pellet blending ratio from 0, 25, 50, 75, 100% w/w at gasification temperature 750 °C on the (a) CV_{syngas} (c) Y_{syngas} and (e) η_{GE} with the respectively calculated RSME (b), (d) and (f)

4. CONCLUSION

Simulation modelling on the co-gasification of coal and sawdust pellets was developed using the Aspen Plus software. The effect of the sawdust pellet blending ratio, gasification temperature and E_{air} on the gasification

performance were investigated. The results show that 50% of the sawdust pellet blending ratio in the co-gasification possessed the maximum CV_{syngas} , Y_{syngas} , and η_{GE} at 5.84 MJ/Nm³, 2.00 Nm³/kg and 37%, respectively. Increasing of gasification temperature also increased the gasification performance of the co-gasification. The effect of the ER_{air} on the gasification performance was also studied. The sensitivity results indicated that the higher ER_{air} contributed to the lower value of the CV_{syngas} and η_{GE} that occurred at 50% of the sawdust pellet blending ratio. The data obtained from the simulation model was validated with the experimental measurement by calculated the RSME value. The RSME showed the relatively low value of CV_{syngas} and Y_{syngas} indicating that the proposed model could be adopted to measure the gasification performance. In contrast, the RSME value on the η_{GE} was quite high due to the equilibrium state assumed in the model. Hence, in future work on co-gasification of other types of sawdust pellet with coal, the same model could be used to carry out studies of the gasification performance in terms of CV_{syngas} and Y_{syngas} . To improve the model, the kinetic reaction between the sawdust pellet and coal needs to be taken into consideration and be simulated in the model.

5. ACKNOWLEDGEMENTS

This project was funded by the Ministry of Higher Education Malaysia and Universiti Malaysia Pahang through the FRGS/1/2014/TK06/UMP/02/6 and PGRS190394, respectively. The authors would also like thanks Universiti Teknologi Petronas for providing full facilities and assistance during the research work.

6. REFERENCES

- Adeyemi, I., Janajreh, I., Arink, T. and Ghenai, C. (2017) 'Gasification behavior of coal and woody biomass: Validation and parametrical study', *Applied Energy*. Elsevier Ltd, 185, pp. 1007–1018.
- Ahmed, A. M. A., Salmiaton, A., Choong, T. S. Y. and Wan Azlina, W. A. K. G. (2015) 'Review of kinetic and equilibrium concepts for biomass tar modeling by using Aspen Plus', *Renewable and Sustainable Energy Reviews*, 52, pp. 1623–1644.
- Alauddin, Z. A. B. Z., Lahijani, P., Mohammadi, M. and Mohamed, A. R. (2010) 'Gasification of Lignocellulosic Biomass in Fluidized Beds for Renewable Energy Development: A Review', *Renewable and Sustainable Energy Reviews*. Elsevier Ltd, 14(9), pp. 2852–2862.
- Ali, D. A., Gadalia, M. A., Abdelaziz, O. Y. and Ashour, F. H. (2016) 'Modelling of coal-biomass blends gasification and power plant revamp alternatives in Egypt's natural gas sector', *Chemical Engineering Transactions*, 52, pp. 49–54.
- Atnaw, S. M., Sulaiman, S. A. and Yusup, S. (2011) 'Downdraft Gasification of Oil Palm Fronds', *Trends in Applied Science Research*, 6(9), pp. 1006–1018.
- Azargohar, R., Gerspacher, R., Dalai, A. K. and Peng, D. Y. (2015) 'Co-gasification of petroleum coke with lignite coal using fluidized bed gasifier', *Fuel Processing Technology*, 134, pp. 310–316.
- Basu, P. (2010a) *Biomass Gasification and Pyrolysis: Practical Design and Theory*. Kidlington, Oxford: Academic Press.
- Basu, P. (2010b) *Biomass Gasification and Pyrolysis Handbook*.
- Ciferno, J. P. and Marano, J. J. (2002) *Benchmarking Biomass Gasification Technologies for Fuels, Chemicals and Hydrogen Production*, US Department of Energy. National Energy. Available at: <http://seca.doe.gov/technologies/coalpower/gasification/pubs/pdf/BMassGasFinal.pdf>.
- Dafnomilis, I., Lodewijks G., Junginger, M and Schott D. I. (2018) 'Evaluation of wood pellet handling in import terminals', *Biomass and Bioenergy*. Elsevier Ltd, 117(March), pp. 10–23.
- Energy Commission (2016) *Malaysia Energy Statistics Handbook 2016*. Putrajaya.
- Fermoso, J., Arias, B., Plaza, M. G., Pevida, C., Rubiera, F., Pis, J. J., Garcia-Pena, F. and Casero, P. (2009) 'High-pressure co-gasification of coal with biomass and petroleum coke', *Fuel Processing Technology*. Elsevier B.V., 90(7–8), pp. 926–932.

- Gao, W., Yan, L., Tahmoures, M. and Safdar, A. M. A. (2017) 'Hydrogen production from co-gasification of coal and biomass in the presence of CaO as a sorbent', *Chemical Engineering and Technology*, pp. 1–13.
- Ghassemi, H. and Shahsavan-markadeh, R. (2014) 'Effects of Various Operational Parameters on Biomass Gasification Process; A Modified Equilibrium Model', *Energy Conversion and Management*. Elsevier Ltd, 79, pp. 18–24.
- Inayat, M., Sulaiman, S. A., Kumar, A. and Guangul, F. M. (2016) 'Effect of Fuel Particle Size and Blending Ratio on Syngas Production and Performance of Co-gasification', *Journal of Mechanical Engineering and Sciences (JMES)*, 10(2), pp. 2188–2200.
- Ismail, T. M. and El-Salam, M. A. (2017) 'Parametric Studies on Biomass Gasification Process on Updraft Gasifier High Temperature Air Gasification', *Applied Thermal Engineering*. Elsevier Ltd, 112, pp. 1460–1473.
- Keche, A. J., Gaddale, A. P. R. and Tated, R. G. (2015) 'Simulation of biomass gasification in downdraft gasifier for different biomass fuels using ASPEN PLUS', *Clean Technologies and Environmental Policy*, 17(2), pp. 465–473.
- Kumar, A., Sharma, A. and Bhandari, P. (2014) 'Biomass Gasification and Syngas Utilization', in Lijun, W. (ed.) *Sustainable Bioenergy Production*. CRC Press.
- Kuo, P.-C. and Wu, W. (2015) 'Design of co-gasification from coal and biomass combined heat and power generation system', *Energy Procedia*. Elsevier B.V., 75, pp. 1120–1125.
- Masnadi-Shirazi, M. S. (2014) *Biomass/fossil fuel co-gasification with and without integrated CO₂ capture*. The University of British Columbia. Available at: <https://circle.ubc.ca/handle/2429/46917>.
- Monir, M. U., Aziz, A. A., Kristanti, R. A. and Yousuf, A. (2018) 'Co-gasification of empty fruit bunch in a downdraft reactor: A pilot scale approach', *Bioresource Technology Reports*. Elsevier Ltd, 1, pp. 39–49.
- Paiman, M. E. S., Hamzah, N. S., Idris, S. S., Rahman, N. A. and Ismail, K. (2018) 'Synergistic Effect of Co-utilization of Coal and Biomass Char: An Overview', *IOP Conference Series: Materials Science and Engineering*, 358(1).
- Pan, Y. G., Velo, E., Roca, X., Manya, J. J. and Puigjaner, L. (2000) 'Fluidized-bed co-gasification of residual biomass/poor coal blends for fuel gas production', *Fuel*, 79(11), pp. 1317–1326.
- Patel, B. and Narnaware, S. (2018) 'Co-gasification of coal / biomass blends and effects of parameter variation on the performance of gasifier : A Review', (1), pp. 94–100.
- Pradhan, P., Mahajani, S. M. and Arora, A. (2018) 'Production and utilization of fuel pellets from biomass: A review', *Fuel Processing Technology*. Elsevier, 181(September), pp. 215–232.
- Sarker, S. (2016) *Thermochemical Gasification of Local Lignocellulosic Biomass via Fixed-Bed and Fluidized-Bed Reactors*. University of Agder.
- Satyam Naidu, V., Aghalayam, P. and Jayanti, S. (2016) 'Synergetic and inhibition effects in carbon dioxide gasification of blends of coals and biomass fuels of Indian origin', *Bioresource Technology*. Elsevier Ltd, 209, pp. 157–165.
- Schuster, G., Löffler, G., Weighl, K. and Hofbauer, H. (2001) 'Biomass Steam Gasification - An Extensive Parametric Modeling Study', *Bioresource Technology*, 77(1), pp. 71–79.
- Seo, M. W., Goo, J. H., Kim, S. D., Lee, S. H. and Choi, Y. C. (2010) 'Gasification characteristics of coal/biomass blend in a dual circulating fluidized bed reactor', *Energy and Fuels*, 24(5), pp. 3108–3118.
- Susastriawan, A. A. P., Saptoadi, H. and Purnomo (2017) 'Small-Scale Downdraft Gasifiers for Biomass Gasification: A Review', *Renewable and Sustainable Energy Reviews*, 76(March), pp. 989–1003.

Upadhyay, D. S., Sakhiya, A. K., Panchal, K., Patel, A. H. and Patel, R. N. (2019) 'Effect of equivalence ratio on the performance of the downdraft gasifier-An experimental and modelling approach', *Energy*. Elsevier Ltd, 168, pp. 833–846.

Valdés, C. F., Chejne, F., Marrugo, G., Macias, R. J., Gomez, C. A., Montoya, J. I., Londono, C. A., Cruz, J. D. L. and Arenas, E. (2016) 'Co-gasification of sub-bituminous coal with palm kernel shell in fluidized bed coupled to a ceramic industry process', *Applied Thermal Engineering*, 107, pp. 1201–1209.

Yan, L., Cao, Y., Li, X. and He, B. (2018) 'Characterization of a dual fluidized bed gasifier with blended biomass/coal as feedstock', *Bioresource Technology*, 254(January), pp. 97–106.

Yoon, S. J., Son, Y. I., Kim, Y. K. and Lee, J. G. (2012) 'Gasification and power generation characteristics of rice husk and rice husk pellet using a downdraft fixed-bed gasifier', *Renewable Energy*. Elsevier Ltd, 42, pp. 163–167.

Yu, M. M., Masnadi, M. S., Grace, J. R., Bi, X. T., Lim, C. J. and Li, Y. (2015) 'Co-gasification of biosolids with biomass: Thermogravimetric analysis and pilot scale study in a bubbling fluidized bed reactor', *Bioresource Technology*. Elsevier Ltd, 175, pp. 51–58.

#274: Development of biomass-fired micro-scale CHP system with modified Rankine cycle (RC)

Krzysztof SORNEK¹, Mariusz FILIPOWICZ²

¹ AGH University of Science and Technology, Faculty of Energy and Fuels, Department of Sustainable Energy Development, Mickiewicza Av. 30, 30-059 Krakow, Poland, krzysztof.sornek@agh.edu.pl

² AGH University of Science and Technology, Faculty of Energy and Fuels, Department of Sustainable Energy Development, Mickiewicza Av. 30, 30-059 Krakow, Poland, mariusz.filipowicz@agh.edu.pl

Nowadays, many research activities are devoted to the development of renewable energy-based micro cogeneration systems dedicated to domestic, commercial, and agricultural sectors. This paper illustrates the prototype micro CHP system developed at the AGH UST in Krakow. The system is powered by a 100 kW_{th} biomass-fired batch boiler and operates according to a modified Rankine Cycle. Steam is generated and superheated in two shell and tube heat exchangers (working as evaporator and superheater, respectively) and powers a steam engine. Next, it is condensed in another one shell and tube heat exchanger (i.e. condenser). The condensate is pumped to a degasser and finally – to an evaporator. Electricity is generated in a power generator connected to the steam engine.

Operation of the proposed micro CHP system is controlled by a specially developed control and measurement system recording the following parameters: temperature, pressure, and medium flow (in the boiler, oil circuit, steam/condensate circuit, and cooling water circuit) and the following parameters are continuously adjusting during the system works: pump power, air fan power, steam valve opening, and the level of power taken from the power generator.

During presented tests, selected parameters in oil and steam-condensate circuits were analysed, including: (i) oil temperature and boiler power variations in case of single and continuous combustion processes, (ii) oil, condensate, and steam temperature variations in the evaporator and superheater, (iii) steam pressure variations and steam flow variations in the steam bus, (iv) voltage current and power generated in the power generator.

Actual configuration of the developed system allows for power generation only at a level of ~1,15 kW_{el}. Such a low value results, e.g. from the limitations in maximum oil temperature, not optimised evaporator heat exchange surface, large pipe capacity, and low power generator capacity. These limitations were discussed and guidelines for further improvements of the system were elaborated.

Keywords: CHP; micro cogeneration; renewable energy sources; biomass; Rankine Cycle

1. INTRODUCTION

Combined heat and power (CHP) systems, also known as cogeneration systems, generate heat and electricity in one technological process. CHP systems are an important alternative for conventional energy systems from the standpoint of reducing primary energy consumption, increasing energy efficiency and reducing greenhouse gas emissions to the atmosphere.

The worldwide developing CHP technologies are mostly powered by fossil fuels, including natural gas and oil. Among the units powered with energy from renewable sources, the most promising are devices based on the use of biomass energy, solar energy and fuel cells (Thilak Raj et al., 2011). Depending on the power installed, CHP systems may be classified as micro scale systems (with a maximum capacity below 50 kW_e), small scale systems (with an installed capacity below 1 MW_e) and others (Directive 2009/28/EC). The use of micro scale (on-site) CHP systems may improve energy security of buildings (in terms of technical reliability and independence from changes in energy prices), and reduce buildings' operating costs (no fees for using external electric network) (Ferrara et al., 2013).

In biomass powered micro scale applications, the most popular fuels are: wood and waste from its processing, straw, plants from energy crops and agricultural products. The most important biomass properties from the standpoint of energy generation are: calorific value, moisture content, ash content, volatile parts content and bulk density of the fuel. The selection of fuel depends also on the local availability of biomass, as well as expected investment and operating costs. Environmental aspects are also important. In comparison to conventional fuels (coal, oil or natural gas), the biomass caloric value is lower. On the other hand, wide availability of biomass, low cost of energy generation and quite neutral impact on the environment make that the use of biomass is more and more popular (Sornek et al., 2014).

Biomass may be converted to electricity in the process of its gasification and combustion. Technologies based on biomass gasification are characterized by higher efficiency and possibility of usage a wide range of biomass fuels, however they require higher financial investments comparing to combustion based ones (there are currently not widely available on the market) (Rentizelas et al., 2009; Dong et al., 2009).

In practice, two main combined heat and power generation technologies are considered in the view of biomass utilization (both in the way of gasifying and combustion): the internal combustion piston engines and turbine-based cogeneration plants with a steam/vapour turbine working on a simple Rankine Cycle (RC) or Organic Rankine Cycle (ORC). An Organic Rankine Cycle is a commonly used due to its numerous advantages, including lower costs and maintenance requirements. Other combined heat and power (CHP) technologies, such as those based on gas turbines, Stirling engines, and fuel cells, are still in the development phase. Additionally, thermoelectric generators are currently slowly being introduced for domestic heating appliances, such as stoves (Borsukiewicz-Gozdur et al., 2014; Sornek et al., 2016; Sornek et al., 2019).

There are many worldwide studies in the field on the use of biomass-based technologies for combined heat and power generation in the micro scale (Hawkes et al., 2007; Qiu and Hayden, 2012; Alanne and Saari, 2004; Colonna et al., 2015). The most popularly analysed are systems with steam turbines work according to the organic Rankine cycle (ORC) and Stirling engines (Karellas et al., 2008; Pei et al., 2011). Significantly fewer works are devoted to systems working in the Clausius-Rankine cycle and other technologies.

The example of the ORC system using a biomass boiler as a heat source was studied by Liu et al. This system was characterized by an electricity output of 2 kW_e, and electrical efficiency 7.5-13.5% (Liu et al., 2011). Another example is an experimental ORC system based on a 50 kW_{th} pellet-fired boiler. In this case, the maximum electrical power was observed at a level of 860 W_e (Qiu et al., 2012). On the other hand, three variants of the ORC based CHP plant fuelled with sawmill waste have been analysed by Borsukiewicz-Gozdur et al. A 250 kW_{th} boiler was used as a heat source and generated power varied from 25 to 70 kW_e (Borsukiewicz-Gozdur et al., 2014). Besides performance analysis of micro scale CHP systems, many studies have been performed, including e.g. analysis of the dedicated constructions of turbines (Klonowicz et al., 2014) and heat exchangers (Wajs et al., 2018). Worldwide literature contains not only experimental works, but also investigations based on dynamic simulations (Calise et al., 2014), including simulations devoted to hybrid biomass-solar CHP systems (Di Fraia et al., 2018).

This paper shows the experimental tests of the prototypical micro scale CHP system with a 100 kW_{th} biomass-fired batch boiler. This system was developed at AGH University of Science and Technology and it is based on modified Rankine Cycle operation. Previously conducted tests have shown the high potential of the boiler application as a heat source for combined heat and power generation (Sornek and Filipowicz, 2019). On the other hand, it is the second approach to extend the functionality of a batch boiler with a power generation system – the first one was based on the use of a 180 kW_{th} straw-fired batch boiler equipped with additional heat exchanger located after the second combustion chamber (Sornek and Filipowicz, 2016).

2. EXPERIMENTAL RIG

The Rankine cycle is a thermal cycle used in classic steam power plants. The steam is generated in a steam boiler and used in a steam turbine that drives a power generator. Classic steam power plants are an example of condensing power plants (there are equipped with condenser used to condense vapour after passing through the steam turbine). The configuration of the classical steam power plants cannot be directly scaled to micro scale CHP units. Therefore, authors proposed a prototypical design of micro cogeneration system based on the modified Rankine cycle operation (see Figure 1). This system uses a superheated steam as a working fluid to obtain a higher efficiency compared to cycle with saturated steam. A piston steam engine is used as an expander (replacing steam turbine typically used in systems operate with classic Rankine cycle).

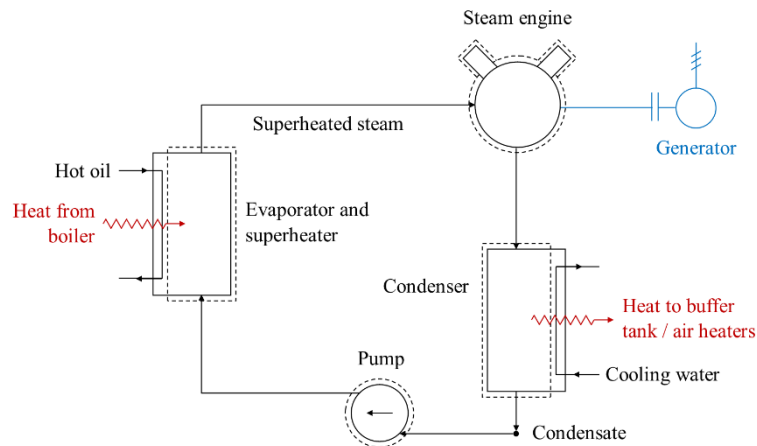


Figure 12: General scheme of the modified Rankine cycle

Configuration of the developed prototypical system includes three main circuits: oil circuit, steam/condensate circuit and cooling water circuit. In the oil circuit, oil is heated up in a 100 kW_{th} biomass-fired batch boiler. The boiler has an oil jacket (replacing typically used water jacket) and a dedicated fuel feeder providing continuous fuel combustion process (see Figure 2). The operation of the boiler is based on counter flow combustion system, which allows to burn the fuel with efficiency ca. 80% and CO emission is lower than 1250 mg/m³ (Kristensen and Kristensen, 2004).

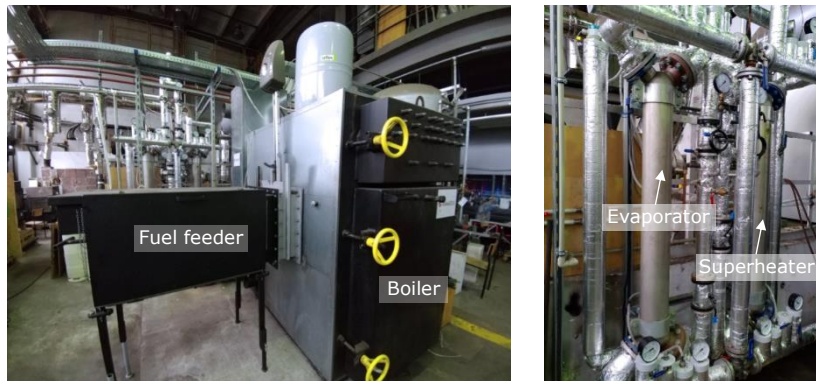


Figure 2: Boiler with fuel feeder (on the left picture) and evaporator and superheater (on the right picture)

Thermal oil heated up in the boiler is transferred to shell and tube heat exchangers, connected in series, and operate respectively as an evaporator and superheater. Oil circuit is equipped also in an emergency/cooling oil-to-water plate heat exchanger, which work only in time, when oil temperature is too high. The general scheme of the oil circuit was shown in Figure 3.

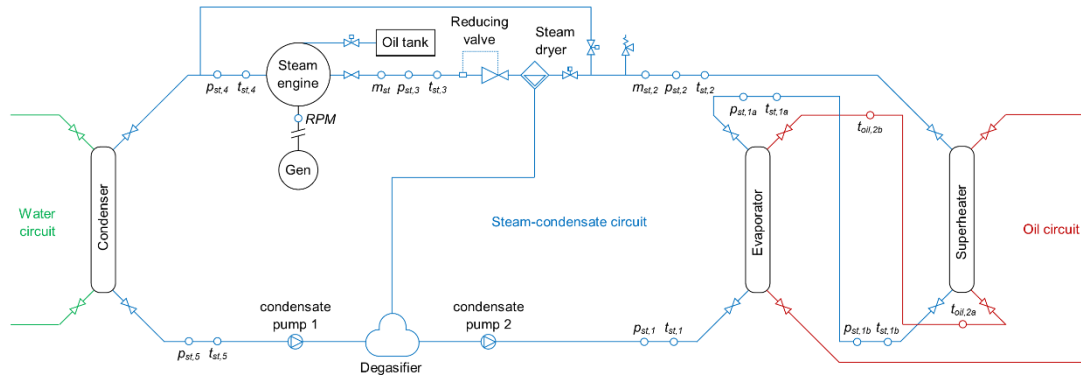


Figure 3: The general scheme of the oil circuit

Steam generated in the evaporator is then superheated in the superheater and conditioned in steam dryer and reducing valve. After that process, the steam got to the 20-horsepower, 2-cylinder, double-acting steam engine. Partially expanded steam is condensed in shell and tube heat exchanger (condenser). Water is then pumped to the degasser and finally – to the evaporator. Steam engine is connected with power generator. The power is currently consumed by electric load equipped with 20 bulbs with total power of 2 kW_e. The main components of steam/condensate circuit are shown in Figure 4.



Figure 4: The main components of the steam-condensate circuit

The simplified scheme of the steam/condensate circuit is shown in Figure 5. This scheme includes only these components, which are important from the standpoint of studies included in this paper (shut-off valves, vents, elbows, etc. were omitted). The heat taken from the condenser is used to heat up the water, which is then pumped to buffer tank or to two air heaters.

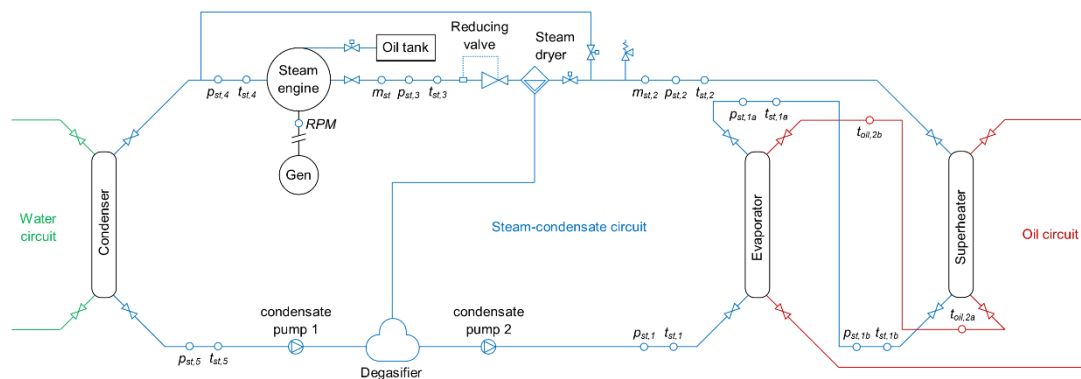


Figure 5: The simplified scheme of the steam-condensate circuit

The operation of the developed installation is controlled by a dedicated automation system with WAGO PFC200 PLC controller. The following parameters are controlled: inlet air flow, flue gas flow, oil flow, condensate flow and cooling water flow (via inverters connected with fans and pumps). Moreover, several data were measured: temperature, pressure and flow of the flue gas, oil, steam, condensate and cooling water as well as current and voltage generated in the power generator. All controlled and measured parameters were available via CoDeSys software using especially developed visualization.

3. RESULTS AND DISCUSSION

The main goal of conducted tests was to determine operation parameters of the developed CHP system. At the beginning two fuel feeding scenarios were compared: combustion of single fuel input (according to original way of boiler's functionality) and continuous combustion of fuel (boiler equipped with especially developed fuel feeder). Next, the selected parameters of the oil and steam/condensate circuits were considered, including variations in oil temperature, variations in power transferred from boiler to oil, variations in steam temperature, pressure and flow, as well as variations in voltage, current and power generated in the power generator. The analysis of obtained results allowed to discuss limitations and elaborate guidelines for further improvements of the system.

During analysed single combustion process four rectangular straw bales with total weight 39.2 kg and moisture content lower than 10% were burned. In case of continuous combustion process, the initial input was also four bales, but the next bales were successively added. Each load matched as "input x" represents one bale weighted ca. 7.8 kg. Totally 108.1 kg of straw was burned, including 37.9 kg of initializing fuel input. The input of the additional bales was realized by a fuel feeder in time, when flue gas temperature at the outlet from the boiler dropped below 270°C. It can be observed, that time shift between two inputs was typically 9-10 minutes (in case of fuel inputs 1-7), while for two last inputs it increased to 14-15 minutes. It was connected with the fact, that upper temperature of the hot oil was achieved.

3.1. Oil temperature and boiler's power in case of single and continuous straw combustion

The variations in the oil temperature at the outlet from the boiler (t_{oil}) in two analysed cases were shown in Figure 6. Taking into account time from the beginning of combustion process up to point, when oil temperature dropped below 100°C, significant difference in the maximum and average temperature levels is observed. The maximum and average oil temperature in case of single combustion process was respectively 154.1°C and 115.3°C, while in case of continuous combustion process these values were 221.9°C and 168.5°C. Temperature fluctuations were slight due to the high thermal inertia of the boiler. Time, when oil temperature was higher than 200°C was ca. 1 h in case of continuous combustion process.

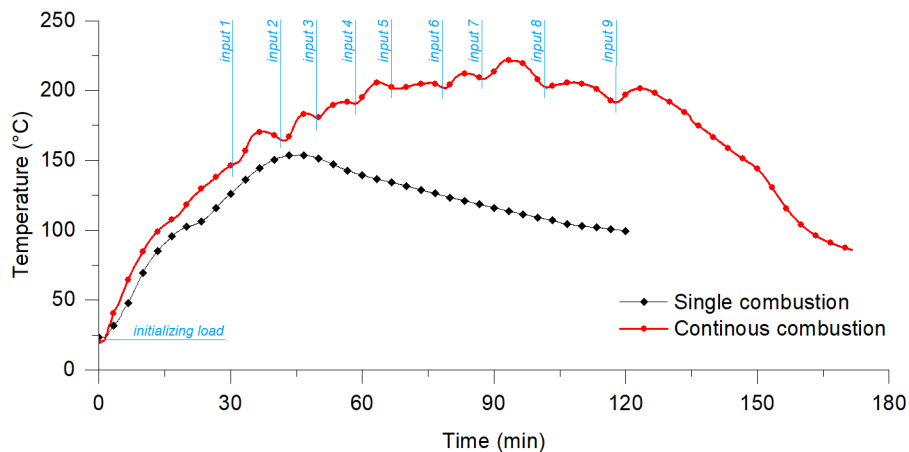


Figure 6: The variations in the oil temperature at the outlet from boiler in case of single and continuous combustion processes

As a consequence of temperature difference, significant difference in the boiler's power were observed during single and continuous combustion process. The average boiler's power in the time, when emergency/cooling heat exchanger was switched-off, was 19.2 kW_{th} (for single combustion process) and 67.0 kW_{th} (for continuous combustion process). Taking into account typical straw caloric value (4.2 kWh/kg), the efficiency of the conversion chemical energy to the heat transferred to the oil may be calculated. In case of the single combustion process it was ca. 12%, while in case of the continuous combustion process – ca. 33.1% (in time, when emergency/cooling heat exchanger was switched-off). These values do not correspond to the efficiency of the boiler, because the amount of heat transferred from oil to the water (via emergency/cooling heat exchanger) and heat losses from the boiler to the environment are not included. The variations in the boiler's power are shown in Figure 7.

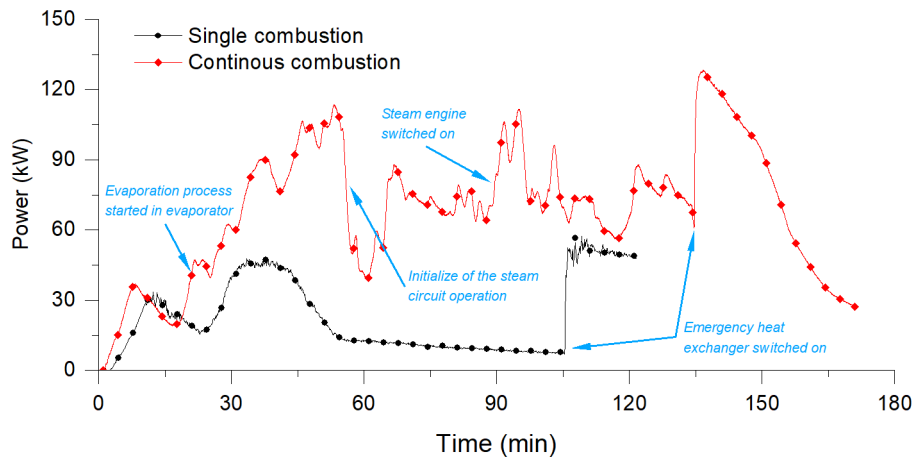


Figure 7: The variations in the power transferred from boiler to oil in case of single and continuous combustion processes

Such a low amount of heat transferred to the oil in the first case results e.g. with thermal losses for heating the cold boiler. On the other hand, the variations in the power transferred from boiler to oil, observed in the second case, result not only from oil temperature, but there are also connected with the actual operating parameters of the steam/condensate circuit (discussed in the further part of the paper). In general, the significant reduction of the boiler's power in 58 minute of continuous combustion process was connected with the initialize of the steam circuit operation. On the other, the significant increase in the boiler's power in 135 minute resulted from switch-on of the emergency/cooling (oil to water) heat exchanger.

3.2. Analysis of the selected steam parameters

Analysis of the selected steam parameters was carried out only for continuous combustion process. The most important steam parameters from the standpoint of power generation are pressure, temperature and flow. The variations in the steam temperature at the outlet from superheater (and corresponding oil temperature at the inlet to superheater and at the outlet from evaporator) were shown in Figure 8. The condensate (steam) flown in counter flow to the oil. The process of evaporation was initialized in 20 minute (when steam temperature achieved level 100°C) and in the next 35 minutes fluctuations in the steam temperature were observed. These fluctuations resulted from the fact, that saturated steam was condensing in the pipe section between evaporator and superheater and water was flown into superheater. Steam superheating process was stabilized in 60 minute (oil temperature at the inlet to superheater was then 190°C, while steam temperature at the outlet from superheater – 175°C. Generally, between 60 and 135 minute difference in the oil temperature at the inlet to the superheater and the steam temperature at the outlet from the superheater was ca. 15.1 K. On the other hand, the average oil temperature decrease in the superheater and the evaporator was total ca. 53.7 K and the average temperature increase of water in evaporator and then steam in superheater was total ca. 140.6 K (in the corresponding time). The energy transferred from oil to water and steam from the beginning of the process up to 135 minute was ca. 150.7 kW_{th}.

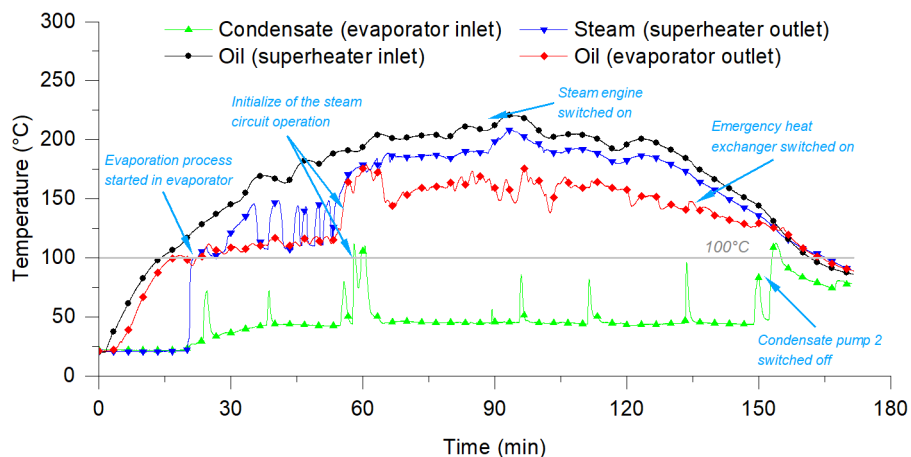


Figure 8: Oil, condensate and steam temperature distribution in the evaporator and superheater

The highest level of the steam pressure was measured at the outlet from superheater. In the initial part of evaporating process, reducing valve was closed. It was switched-on when steam pressure achieved a level of 8 bars (in 62 minute), what caused significant decrease in the steam pressure and increase in steam flow. Between

62 and 88 minute steam circulated in the circuit composed of evaporator, superheater, treatment station, moisture separator, reducing valve, condenser and degasser (steam engine was cut-off). The increase in pressure after 78 minute was connected with the decrease in steam flow (realized by partially closing reducing valve). Steam engine was switched-on in 90 minute, what resulted in the fluctuations in the steam pressure. At the same time, reducing valve was set to 50%, while in the further phase this setting was changing from 25 to 60% (so fluctuations in the steam flow were observed). The reducing valve was used to control steam pressure and flow (what directly impacted on the steam engine's rotation speed). In general, the difference between steam pressure at the outlet from superheater and at the inlet to the steam engine varied between 2.5 – 3 bars and was caused by partial expansion of steam in steam bus (including pipes, reducing valve and other steam equipment). The variations in steam pressure and flow were shown in Figure 9.

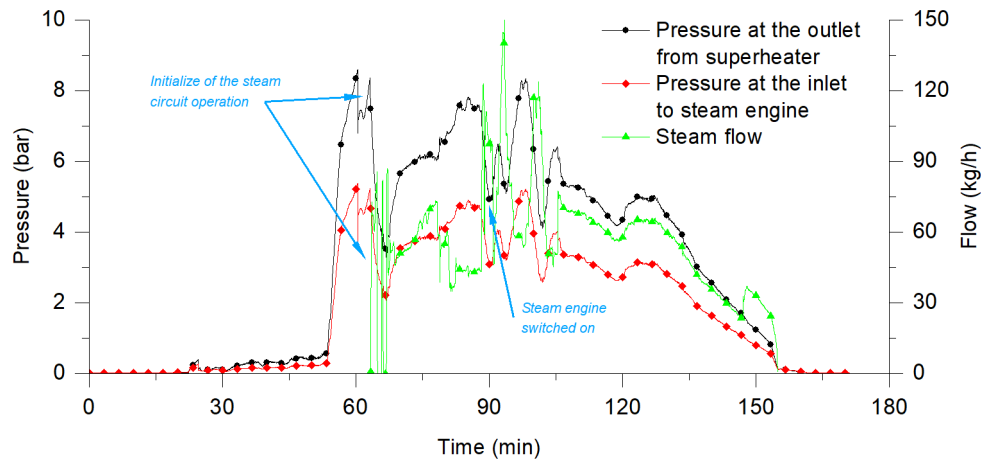


Figure 9: Steam pressure at the outlet from superheater and inlet to the steam engine as well as steam flow in the steam bus

Power generated in the power generator resulted from the actual steam pressure and flow as well as from the set of electric load (the set of electric load was constant over the time in the analysed process). Steam parameters affected on the engine's rotation speed and consequently on the generated voltage. As a result, same variations in the current and power were noted, as was shown in Figure 10. The maximum power level of 825 W_e was recorded in 93 minute (while current was 3.2 A and voltage was 250 V. On the other hand, between 90 and 135 minute generated power was higher than 500 W_e . It should be noted, that maximum power point tracker (MPPT) was not used during presented tests.

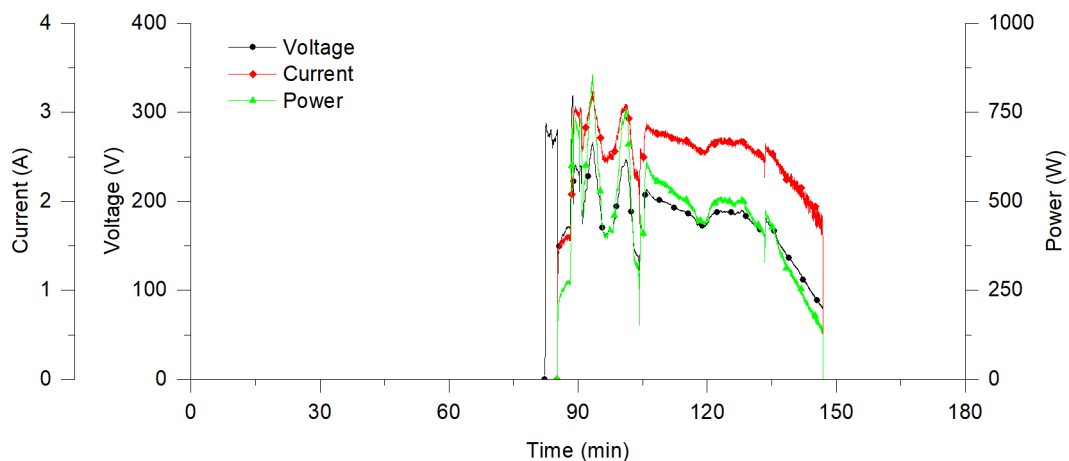


Figure 10: The variations in voltage, current and power generated in the power generator

The relationship between generated power and steam pressure and flow is clearly shown in Figure 11. In time, when electric power achieved the highest level equal 825 W (without maximum power tracking), steam flow was ca. 145 kg/h and steam pressure was ca. 4.2 bars.

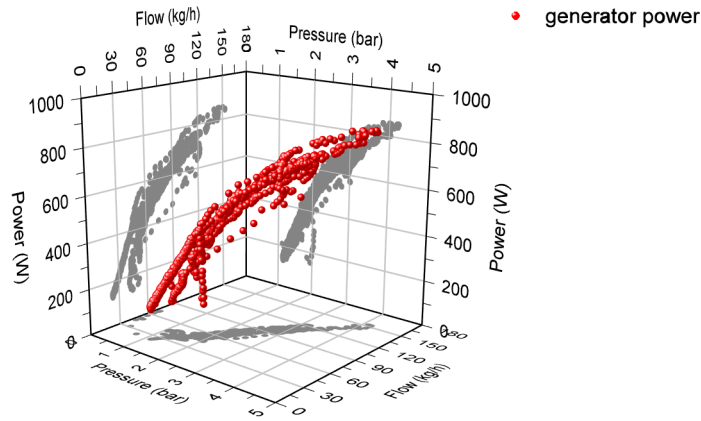


Figure 11: The relationship between generated power, steam pressure and steam flow

Taking into account another one similar continuous combustion process (special run focused on determine I-V and P-V characteristics) the I-V and P-V characteristic of the steam engine-generator were determined (see Figure 12). Presented characteristics were determined for different values of steam pressure at the inlet to the steam engine (shown in figure). Average value of the steam flow ranged from 108.6 to 112.1 kg/h in each case. During this process, maximum power point tracking was realized manually by changing the set of electric load from 0 to 2 kW_e. The maximum power was ~1.15 kW_e and was reached when steam pressure at the inlet to the steam engine was ca. 3.9 bars and steam flow was ca. 137.7 kg/h.

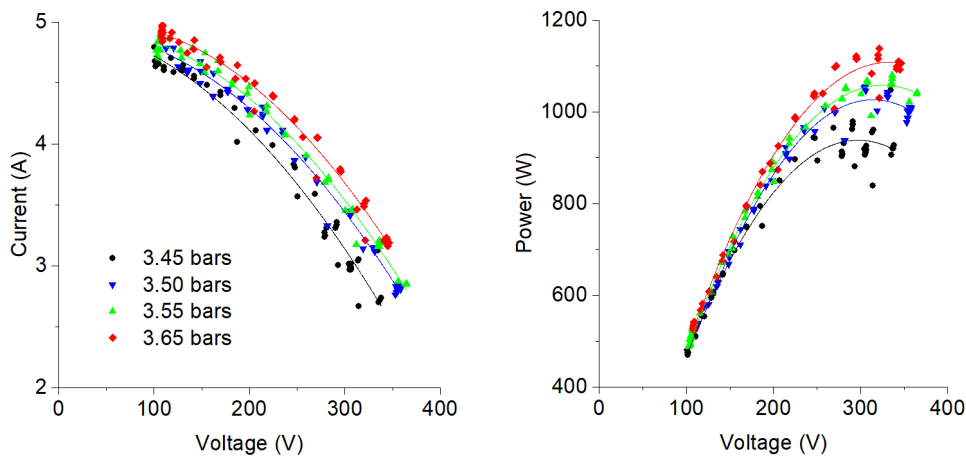


Figure 12: Characteristic of the steam engine and generator: I-V (on the left diagram) and P-V (on the right diagram)

It may be noted, that power 1.15 kW_e was achieved in a time, when thermal power generated in boiler was at a level of ~110 kW_{th}. Consequently, the share of electricity generation in the total energy generation in the analysed system was only 1.05%. On the other hand, the average value of the generated power was significantly lower. Such a low power resulted mainly from very low steam pressure, what was a consequence of limitations in oil and steam temperature. Other limitations were caused also by steam bus and power generator's construction (including e.g. insufficient evaporator heat exchange surface, large pipe capacity, and low power generator capacity).

3.3. Guidelines for further improvements

Actual version of the developed CHP system is not optimized. To achieve higher level of power generation some modifications in the system structure are required. First of all, the heat exchange surface in the evaporator should be extended. It may be realized e.g. by connecting existing shell and tube heat exchangers in parallel (both exchangers should operate as evaporators) and adding another one heat exchanger connected in series (working as superheater). Further improvement should be connected with the length and dimension of pipes in the steam bus. Pipes should have lower diameter to provide higher speed of the steam, less water condensation and higher steam pressure (due to lower volume of the pipes). The other one activity should be focused on replacement of the power generator – currently used one has only 1.5 kW_e of installed power. Introducing all of above mentioned improvements and additionally increasing hot oil temperature, it will be possible to reach ca. 10 kW_e (this value was estimated based on preliminary dynamic simulation using TRNSYS software). Therefore, the optimized project of the CHP system was developed. The optimized version of the system includes compacted structure of the

installation – all important elements are close to each other, piping length is strongly reduced and an engine with high-and-low pressure cylinders are recommended.

4. CONCLUSION

Prototypical CHP installation with biomass-fired boiler and modified Rankine Cycle was characterized and tested. Results obtained so far are promising, but many further works should be done to achieve an efficient system operation. Analysing results it may be noted that:

- continuous combustion process is required to provide sufficient hot oil temperature (i.e. higher than 200°C) – in case of single combustion of 4 straw bales temperature at a level only of 150°C was observed;
- the average power transferred from boiler to oil in the time, when emergency/cooling heat exchanger was switched-off, was 3.5 times higher in case of continuous combustion process compared to single combustion process;
- the processes of steam generation and superheating started in 20 minute, but significant fluctuations of steam parameters continued up to 60 minute. Steam parameters, sufficient to switch on steam engine, was achieved in 90 minute;
- the energy transferred from oil to water and steam from the beginning of the process up to 135 minute was ca. 150.7 kW_{th};
- the maximum power in case of operation without maximum power tracking was 825 W_e, while the maximum power was ~1.15 kW_e when maximum power tracking was using (the share of electricity generation in the total energy generation in the analysed system was only 1.05%);
- the limitations of such a low value of electricity generated in the system were discussed and some guidelines for further improvements were listed.

5. ACKNOWLEDGEMENTS

The work has been completed as part of the statutory activities of the Faculty of Energy and Fuels at the AGH UST in Krakow (no. 16.16.210.476), using the data obtained during the fulfilment of the project entitled: “BioORC: Construction of cogeneration system with small to medium size biomass boilers”.

6. REFERENCES

- Alanne, K., Saari, A., 2004. *Sustainable small-scale CHP technologies for buildings: the basis for multi-perspective decision-making*. Renewable and Sustainable Energy Reviews, 8, 401–31.
- Borsukiewicz-Gozdur, A., Wiśniewski S., Mocarski S., Bańkowski M., 2014. *ORC power plant for electricity production from forest and agriculture biomass*. Energy Conversion and Management, 87, 1180-1185.
- Calise, F., Capuozzo, C., Carotenuto, A., Vanoli, L., 2014. *Thermoeconomic analysis and off-design performance of an organic Rankine cycle powered by medium-temperature heat sources*. Energy, 103, 595-609.
- Colonna, P., Casati, E., Trapp, C., Mathijssen, T., Larjola, J., Turunen-Saaresti, T., et al., 2015. *Organic Rankine Cycle power systems: from the concept to current technology, applications, and an outlook to the future*. Journal of Engineering for Gas Turbines and Power, 137, 100801.
- Di Fraia, S., Figaj, R.D., Massarotti, N., Vanoli, L., 2018. *An integrated system for sewage sludge drying through solar energy and a combined heat and power unit fuelled by biogas*, Energy Conversion and Management, 171, 587-603.
- Directive 2009/28/EC of the European Parliament and of the Council of 23 April 2009 on the promotion of the use of energy from renewable sources and amending and subsequently repealing Directives 2001/77/EC and 2003/30/EC.
- Dong, L., Liu, H., Riffat S., 2009. *Development of small-scale and micro-scale biomass-fuelled CHP systems – A literature review*. Applied Thermal Engineering, 29, 2119–2126.
- Ferrara, G., Manfreda, G., Pescioni, A., 2013. *Model of a small steam engine for renewable domestic CHP (combined heat and power) system*. Energy, 58, 78-85.

- Hawkes, A.D., Leach, M.A., 2007. *Cost-effective operating strategy for residential microcombined heat and power*. Energy, 32, 711-723.
- Karellas, S., Schuster, A., 2008. *Supercritical fluid parameters in organic Rankine cycle applications*. International Journal of Thermodynamics, 11(3), 101–108.
- Klonowicz, P., Borsukiewicz-Gozdur, A., Hanausek, P., Kryłłowicz, W., Bruggemann, D., 2014. *Design and performance measurements of an organic vapour turbine*. Applied Thermal Engineering, 63, 297-303.
- Kristensen, E.F., Kristensen, J.F., 2004. *Development and test of small-scale batch-fired straw boilers in Denmark*. Biomass and Bioenergy, 26, 561-569.
- Liu, H., Shao, Y., Li, J., 2011. *A biomass-fired micro-scale CHP system with organic Rankine cycle (ORC) - Thermodynamic modelling studies*, Biomass and Bioenergy, 35, 3985-3994.
- Pei, G., Li, J., Li, Y., Wang, D., Ji, J., 2011. *Construction and dynamic test of a small-scale organic rankine cycle*. Energy, 36, 3215–3223.
- Qiu, G., Shao, Y., Jinxing, L., Liu, H., Riffat, S.B., 2012. *Experimental investigation of a biomass-fired ORC-based micro-CHP for domestic applications*. Fuel, 96, 374-382.
- Qiu, K., Hayden, A.C.S., 2012. *Integrated thermoelectric and organic Rankine cycles for micro-CHP systems*. Applied Energy, 97, 667-672.
- Rentizelas, A., Karellas, S., Kakaras, E., Tatsiopoulou, I., 2009. *Comparative techno-economic analysis of ORC and gasification for bioenergy applications*. Energy Conversion and Management, 50, 674–681.
- Sornek, K., Filipowicz, M., 2016. *A study of the applicability of a straw-fired batch boiler as a heat source for a small-scale cogeneration unit*. Chemical and Process Engineering, 37(4), 503-515.
- Sornek, K., Filipowicz, M., 2019. *Study of the operation of straw-fired boiler dedicated to steam generation for micro-cogeneration system*. IOP Conference Series: Earth and Environmental Science, 214(1), 012108.
- Sornek, K., Filipowicz, M., Rzepka, K., 2016. *The development of a thermoelectric power generator dedicated to stove-fireplaces with heat accumulation systems*, Energy Conversion and Management, 125, 185-193.
- Sornek, K., Filipowicz, M., Zoladek, M., Kot, R., Mikrut, M., 2019. *Comparative analysis of selected thermoelectric generators operating with wood-fired stove*. Energy, 166, 1303-1313.
- Sornek, K., Szubel, M., Goryl, W., Bożek, E., Filipowicz, M., 2014. *Possibilities of generation and use of energy from biomass* (in Polish). Przemysł chemiczny, 93 (12), 2071-2076.
- Thilak Raj, N., Iniyar, S., Goic, R., 2011. *A review of renewable energy based cogeneration technologies*. Renewable and Sustainable Energy Reviews, 15, 3640-3648.
- Wajs, J., Mikielwicz, D., Jakubowska, B., 2018. *Performance of the domestic micro ORC equipped with the shell-and-tube condenser with minichannels*. Energy, 157, 853-861.

#276: Performance analysis of the concentrator with flap-wind turbine combination

Emre KOC¹, Tahir YAVUZ²

¹ Department of Mechanical Engineering, Baskent University, 06790, Etimesgut, Ankara, Turkey, ekoc@baskent.edu.tr

² Department of Mechanical Engineering, Baskent University, 06790, Etimesgut, Ankara, Turkey, tyavuz@baskent.edu.tr

Wind energy is a renewable energy resource that can be used to ensure energy sustainability without causing environmental pollution. In this context, many studies have been conducted on how to acquire more energy from the wind. One of the approaches to maximise the wind turbine is to increase the wind speed at the turbine. In order to achieve this, a concentrator is added around the turbine, called the turbine-concentrator system. The concentrator creates a low pressure zone behind the turbine and consequently increases wind speed at the wind turbine zone in the concentrator. Optimization analysis of the combinations of the wind turbine and concentrator leading to the maximum free wind speed increase has been carried out. In the optimization analysis, the Response Surface Method with 2D CFD analysis is applied. Using optimum geometric parameters, the performance analysis of the wind turbine-concentrator combinations is determined by the 3D CFD analysis. It is seen that turbine performance can be significantly improved by using a concentrator. The concentrator increases the power output by a factor of about 2.5. Thus, the concentrator provides more power generation from the wind turbine and also can be used to generate energy in regions with poor wind statistics.

Keywords: horizontal axis wind turbine; concentrator; flap; 3D CFD analysis

1. INTRODUCTION

Global scientific research and studies on renewable energy sources have increased in recent years and a huge research fund has been provided to researchers. It is known that renewable energies make a positive contribution to economic life and the environment of countries. Also, renewable energy is able to be seen as an opportunity to reduce energy dependence on fossil fuel exporting countries. Therefore, countries are focused on renewable energies, mainly on wind and solar energies.

Wind energy, which is a clean and renewable source of electricity, is an energy that can be easily and quickly converted into electrical energy. It is the fastest progression of renewable energy technologies. Also hydrokinetic energy systems, which is another renewable energy source, has similar working principles to wind energy systems.

In the literature, there are many studies looking at mechanisms to accelerate the approaching flow to the wind turbine. A concentrator can be used to increase the flow speed through the rotor and consequently capturing wind energy in a more efficient way (Gilbert & Foreman, 1983; Igra, 1981). There are two types of concentrator: the flanged type and the airfoil type structure surrounding the rotor. A flanged-type concentrator, as shown in Figure 1, generates a large separation region behind the concentrator and consequently increases wind speed at the wind turbine zone (Ohya et al., 2008).

Matsushima et al. (Matsushima et al., 2006) experimentally demonstrated that a wind turbine enclosed by a small-capacity flanged concentrator produces 2.4 times more energy than the turbine without a flanged concentrator. Toshimitsu et al. (Toshimitsu et al., 2008) studied the performance of a wind turbine placed in a barrel with a flanged emitter using the Particle Image Velocity (PIV) technique and concluded that the wind power ratio was found to be about 2.6 times higher. Similar studies on flanged concentrators were carried out by different authors (Ohya & Karasudani, 2010; Kosasih & Tondelli, 2012; Wang et al., 2015; Zahaby et al., 2017). They investigated concentrator performance with changing geometric parameters such as flange height, concentrator angle etc.

In the airfoil shaped concentrator, as shown in Figure 2, the mass flow rate increases through the rotor by the lift effect of the airfoil (Frankovic & Vrsalovic, 2001; Shives & Crawford, 2011). Also, by adding a flap or slot behind the airfoil-shaped concentrator, a large concentrator exit area can be obtained without flow separation providing more mass flow rate inside the concentrator (Phillips et al., 2002; Phillips, 2003).

In all the works in the literature, the concentrator was considered without the wind turbine and the performance of the concentrator was given. As the turbine creates a blockage effect in the concentrator and, consequently, the performance of the concentrator with and without the turbine are not the same. Therefore, the combinations of the concentrator and turbine have to be considered in the performance analysis of the system.



Figure 1: Flanged type concentrator

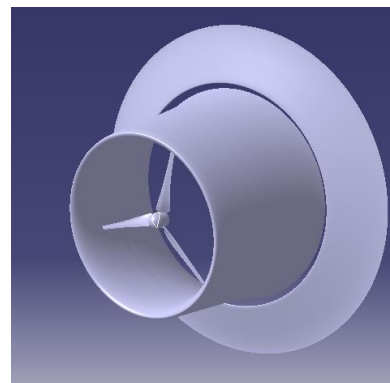


Figure 2: Airfoil type concentrator

In this study, the airfoil type concentrator with flap is chosen. In the performance analysis the combination of the wind turbine and concentrator is considered. The airfoil type concentrator-wind turbine performance depends on the dimensions of the geometry, airfoil shape and the position of the flap with respect to the main part of concentrator. As the interactions between the design parameters are very important, the interactions between parameters have to be considered in the performance analysis of the concentrator-wind turbine combination. In the optimization analysis the Response Surface Method with 2D CFD analysis is used to obtain optimum parameters leading maximum flow speed increase at the turbine zone. After the optimization analysis, the 3D CFD analysis is applied to the system to get the performance of the system with and without concentrator.

2. METHODOLOGY

2.1. Geometry of concentrator-wind turbine combination

The SG 6043 airfoil, which has a high lift coefficient, was chosen for both the main concentrator and flap (Giguere & Selig, 1998). The concentrator geometry with flap is given in Figure. 3. The geometric parameters considered in the optimization analysis are; x/c_1 , y/c_1 , c_1/D , c_2/c_1 , α , and δ . D is the rotor diameter of the wind turbine and x , y and δ define the position of the flap with respect to the main airfoil. All optimum geometric parameters are obtained as a function of the rotor diameter of the turbine, D .

In the verification analysis, the experimental work by Karlsen (Karlsen, 2009) is used. In this work the NREL S826 blade profile was applied. Also this profile has been chosen in some numerical and experimental studies in the literature (Krogstad & Lund, 2012; Anik et al., 2014; Adaramola & Krogstad, 2011). Therefore the NREL blade profile for the wind turbine was chosen in the verification analysis. The rotor diameter was chosen to be about 0.9m.

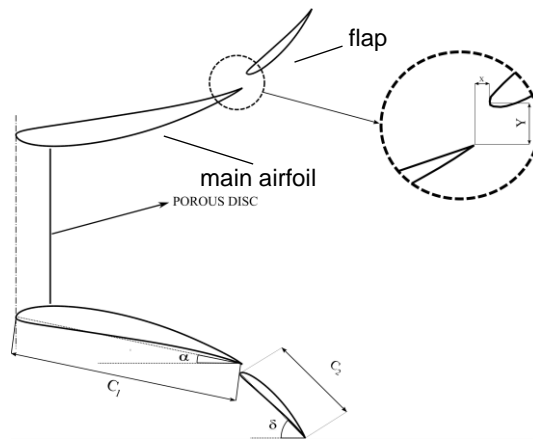


Figure 3: Geometry and parameters of the concentrator with flap

The porous disc represented turbine was located at the narrowest cross-section of the concentrator with flap in optimization analysis. The optimum values of the geometric parameters were obtained after the optimization studies with 2D CFD analyses and Response Surface Method. More details on the optimization procedure are given by Koc and Yavuz (Koc & Yavuz, 2019).

2.2. CFD analysis

A commercial CFD solver ANSYS-FLUENT was used to solve RANS equations for a steady flow. The k- ω turbulence model was chosen as its ability to model boundary layer separation in adverse pressure gradients. Green-Gauss cell-based discretization method was chosen as a solver in the CFD analyses. Also, the second-order scheme was used for the discretization.

The verification study was carried out with a turbine without concentrator by referring experimental work (Karlsen, 2009). The computational domain used for the computations is shown in Figure 4. The computational domain had dimensions of $2D$ in radial direction and $11D$ in axial direction. Flow field around the turbine was assumed to be rotationally periodic. This reduced the number of cells by one-third. A cylindrical domain was placed around the rotor and the Moving Reference Frame model was used to give rotor rotation.

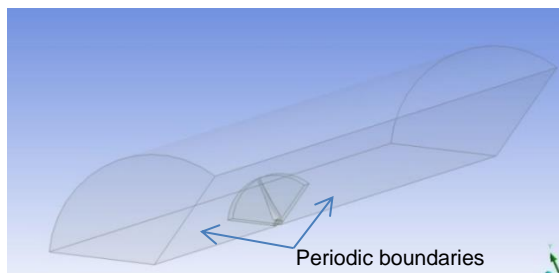


Figure 4: CFD domain of the bare turbine

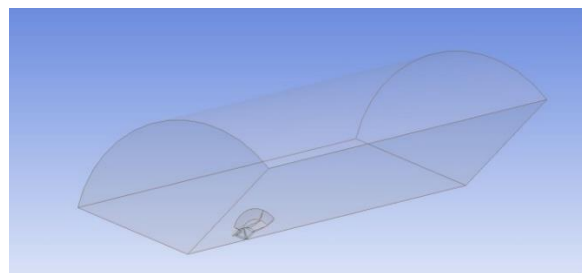


Figure 5: CFD domain of the wind turbine-concentrator combination

In the mathematical modeling of the wind turbine-concentrator combination, a large computational domain (10D in radial and 20D in axial directions) was chosen to avoid wall effect, as shown in Figure 5. The boundary conditions were: velocity inlet (10 m/s), pressure outlet, periodic boundaries and wall. An inflation layer was used in the boundary layer region for capturing velocity gradient. The first layer distance from blade surface was set to be 0.005 mm to keep the value of the y^+ below 5.

Different torque values were obtained as a function of tip speed ratio, $\lambda = \omega R/U$ where ω was the angular velocity of the rotor and U was the inlet flow speed (10 m/s). $C_p - \text{TSR}$ graph is obtained.

Equation 1: Power coefficient

$$C_p = \frac{T\omega}{\frac{1}{2}\rho U_\infty^3 A}$$

Where:

- T = torque (Nm)
- ω = angular velocity of the turbine (rad/s)
- ρ = density of the air (kg/m^3)
- U_∞ = free stream velocity (10 m/s)
- A = turbine area

Equation 2: Tip speed ratio

$$\lambda = \frac{\omega R}{U_\infty}$$

Where:

- R = blade radius (0.45 m)

3. RESULTS AND DISCUSSIONS

The results of the verification analysis of the wind turbine without concentrator are given in Figure 6. The results show that the CFD results were lower than the experimental data (Karlsen, 2009). It shows that, depending on the tip speed ratio, the difference between the CFD and experimental data was about six percent. This indicates that the CFD methodology was correctly constructed. The difference can be due to the error on the velocity measurements and taken the average value of the experimental data.

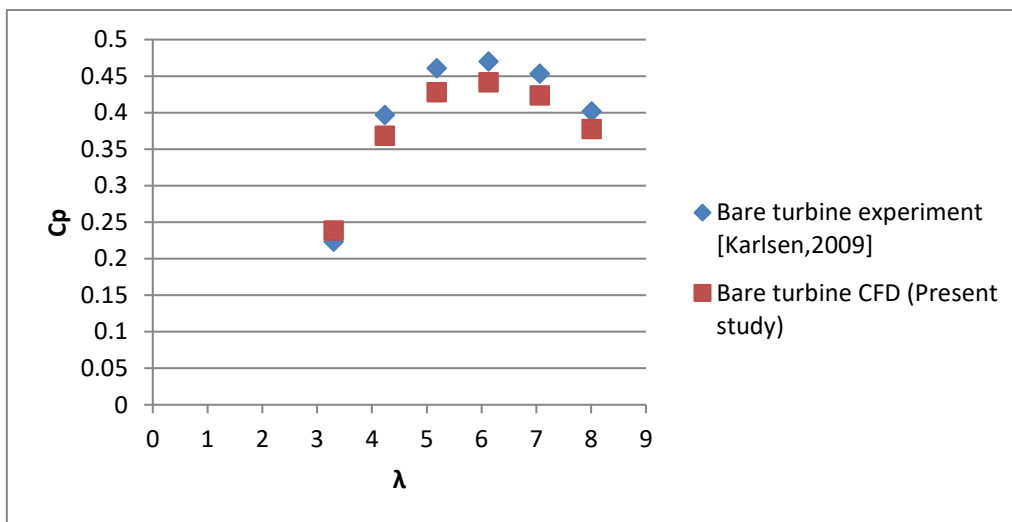


Figure 6: Results of the verification analysis

The optimum parameters leading maximum flow speed increase at the turbine zone in the concentrator were obtained to be 5% (x/c_1), 2% (y/c_1), 10.2° (α), 0.4 (c_2/c_1) and 75° (δ). The analysis shows that the flow speed increases linearly with the length of the concentrator as reported in the literature (Ohya et al., 2008; Venters et al., 2017). Therefore, the ratio of the c_1/D is taken to be 1 in the performance analysis ($c_1=D=0.9\text{m}$). Consequently, knowing the rotor diameter of the wind turbine gives all optimum geometric parameters of concentrator leading maximum free wind speed increase.

Using the optimum geometric parameters of the wind turbine-concentrator combinations, the performance analysis of the system were determined by the 3D CFD analysis. Figure 7 shows the concentrator effects on the power

coefficient or efficiency of the system. The value of the C_p was obtained as 0.44 for bare turbine and 1.11 for wind turbine –concentrator combination at the tip speed ratio of approximately $\lambda \approx 6$. Bear in mind that, in the definition of the power coefficient, the free wind speed, 10 m/s, was taken into account. The power coefficient increases by 2.5 times compared to bare turbine. The power coefficient is higher for all other tip speed ratios for the wind turbine with concentrator than the bare turbine.

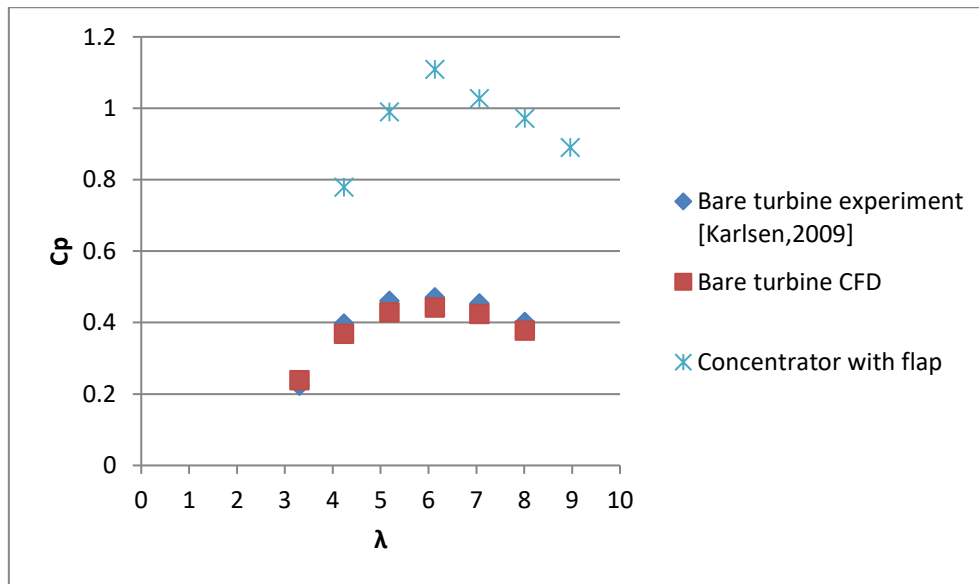


Figure 7: Variation of the power coefficient with tip speed ratio for wind turbine with and without concentrator

The pressure distributions on the surface of the wind turbine blade without and with the concentrator obtained at the speed ratio $\lambda = 6.1$ are shown in Figure 8 and 9 respectively. Comparing pressure levels in suction and pressure sides of the blade, the suction side pressure was lower and the pressure side is higher for the case of the wind turbine with concentrator. This situation led to more torque from the turbine with concentrator.

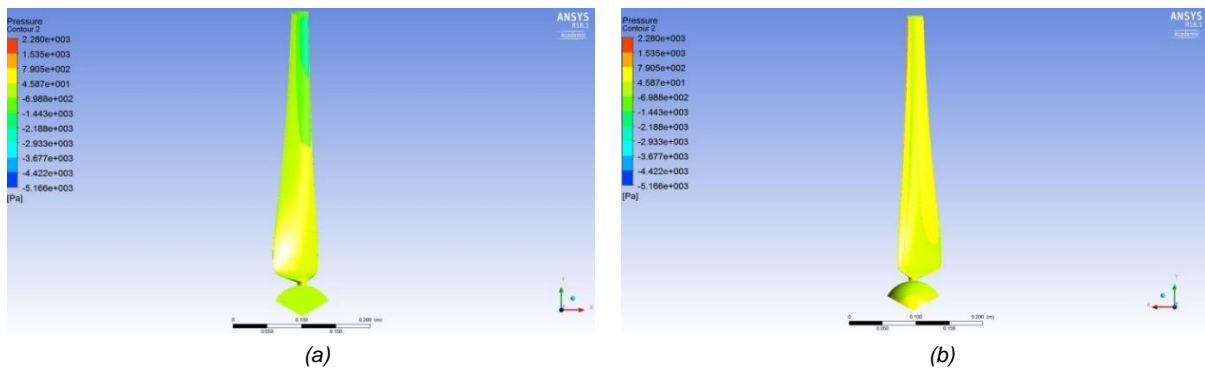


Figure 8: Pressure distribution of the bare turbine, (a) suction (b) pressure sides, $\lambda = 6.1$

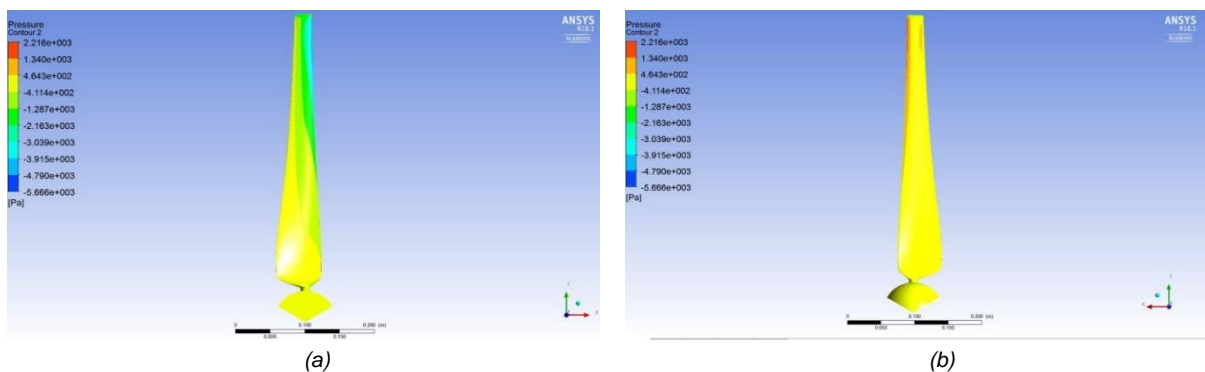


Figure 9: Pressure distribution of the turbine with concentrator, (a) suction (b) pressure sides, $\lambda = 6.1$

Local pressure distributions around the turbine for both cases are given in Figure 10 and Figure 11. As it is seen, the local pressure difference is higher for the concentrator case between the front and back of the turbine blade. For the bare turbine blade, the pressure reached 168.2 Pa and -1713 Pa in front and behind the blade, while it reached the values of 290 Pa and -2366 Pa for the wind turbine with concentrator.

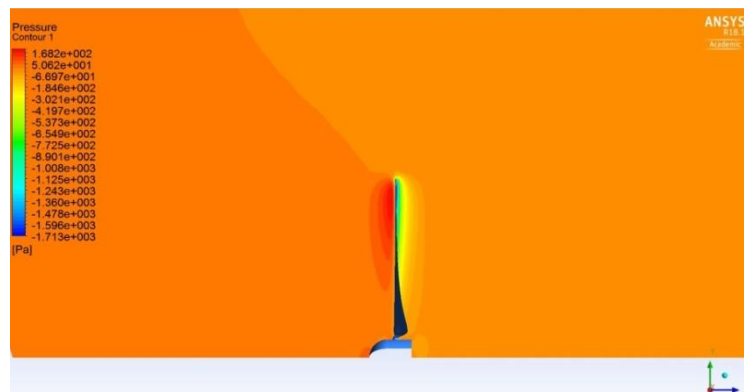


Figure 10: Local pressure distribution around bare turbine, $\lambda = 6.1$

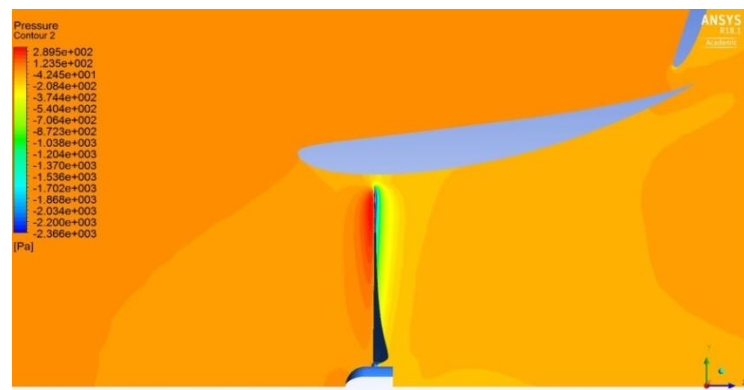


Figure 11: Local pressure distribution around the turbine with concentrator, $\lambda = 6.1$

4. CONCLUSION

The optimization analysis of the combinations of the wind turbine and concentrator leading to maximum flow speed increase at the zone of the wind turbine in the concentrator was considered. An airfoil type concentrator with flap is chosen and the porous disc model was used to represent the wind turbine in the concentrator for optimization studies. The Response Surface Method with the 2D CFD analysis was applied in the optimization analysis.

Conclusions drawn from the study were;

- The location of the flap with respect to the main concentrator played an important role on the flow speed increase.
- The optimum geometric parameters leading to the maximum flow speed increase in the concentrator were 5% (x/c_1), 2% (y/c_1), 10.2° (α), 0.4 (c_2/c_1) and 75° (δ).
- Knowing the diameter of the wind turbine rotor gave all optimum geometric parameters of the concentrator leading the maximum flow speed increase in the concentrator.
- The concentrator increased the power output by a factor about 2.5.
- Due to the increasing flow speed at the zone of the wind turbine in the concentrator, the wind turbine with concentrator can be used to produce more energy from the wind and also it can be used to produce energy in areas with poor wind statistics.

5. REFERENCES

Anik, E., Abdulrahim, A., Ostovan, Y., Mercan, B., Mercan, B., Uzol, O., 2014. Active control of the tip vortex: an experimental investigation on the performance characteristics of a model turbine. *TORQUE 2014 Conference*.

- Adaramola, M.S., Krogstad, P.A., 2011. Experimental investigation of the wake effects on wind turbine performance. *Renewable Energy*, 36, 2078-2086.
- Frankovic, B., and Vrsalovic, I., 2001. New high profitable wind turbines. *Renewable Energy*, vol. 24(3-4), pp. 491-499.
- Giguère, P. and Selig, M. S., 1998. New airfoils for small horizontal axis wind turbines. *J. Sol. Energy Eng.*, vol. 120, no. 2, pp. 108.
- Gilbert, B. L. and Foreman, K., 1983. Experiments with a concentrator- augmented model wind turbine. *J. Energy Resour. Technol.*, vol. 105, pp. 46-53.
- Igra, O., 1981. Research and development for shrouded wind turbines. *Energy Conversion and Management*, vol. 21(1), pp. 13 - 48.
- Karlsen, J.A., 2009. Performance Calculations for a Model Turbine. Master Thesis, Norwegian University of Science and Technology.
- Koc, E., Yavuz, T., 2019. Effect of flap on the wind turbine-concentrator combination. *International Journal of Renewable Energy Research*, vol. 9, no. 2, pp. 551-560.
- Kosasih, B. and Tondelli, A., 2012. Experimental study of shrouded micro-wind turbine. *Procedia Engineering*, vol. 49, pp. 92-98.
- Krogstad, P.A, Lund, J.A., 2012. An experimental and numerical study of the performance of a model turbine. *Wind Energy*, 15, 443-457.
- Matsushima, T., Takagi, S., and Muroyama, S., 2006. Characteristics of a highly efficient propeller type small wind turbine with a concentrator. *Renew. Energy*, vol. 31(9), pp. 1343-1354.
- Ohya, Y. and Karasudani, T., 2010. A shrouded wind turbine generating high output power with wind-lens technology. *Energies*, vol. 3, pp. 634-649.
- Ohya, Y., Karasudani, T., Sakurai, A., ichi Abe, K. and Inoue M., 2008. Development of a shrouded wind turbine with a flanged concentrator. *J. Wind Eng. Ind. Aerodyn.*, vol. 96(5), pp. 524-539.
- Phillips, D., Richards P. and Flay R., 2002. CFD modelling and the development of the diffuser augmented wind turbine. *Wind Struct.*, vol. 5, pp. 267-276.
- Phillips, D., 2003. An investigation on diffuser augmented wind turbine design", PhD thesis, The University of Auckland, Auckland, New Zealand.
- Toshimitsu, K., Nishikawa, K., Haruki, W., Oono, S., Takao, M., and Ohya, Y., 2008. PIV measurements of flows around the wind turbines with a flanged-concentrator shroud. *J. Therm. Sci.*, vol. 17, pp. 375-380.
- Shives, M. and Crawford, C., 2011. Developing an Empirical Model for Ducted Tidal Turbine Performance Using Numerical Simulation Results. *Proc. Inst. Mech. Eng., Part A*, vol. 226(1), pp. 112-125.
- Venters, R., Helenbrook, B.T., Visser, K.D., 2017. Ducted wind turbine optimization. *Journal of Solar Energy Engineering*, 140, 011005- 011005-8.
- Wang, W., Matsubara, T., Hu, J., Odahara, S., Nagai, T., Karasutani, T., Ohya, Y., 2015. Experimental investigation into the influence of the flanged concentrator on the dynamic behavior of CFRP blade of a shrouded wind turbine. *Renew. Energy*, vol. 78, pp. 386-397.
- Zahaby, A. M., Kabeel, A. E., Elsayed, S. S., and Obiaa, M. F., 2017. CFD analysis of flow fields for shrouded wind turbine's concentrator model with different flange angles. *Alexandria Eng. J.*, vol. 56, no. 1, pp. 171-179.

#278: Influence of a deflector on a self-starting speed and power performance of a two-bladed Savonius hydrokinetic turbine

Mohd Badrul SALLEH, Noorfazreena M.KAMARUDDIN*, Zulfaa MOHAMED-KASSIM, Elmi ABU BAKAR

School of Aerospace Engineering, Universiti Sains Malaysia, 14300 Nibong Tebal, Pulau Pinang, MALAYSIA
*Corresponding author: fazreena@usm.my

The aim of this study is to investigate the self-starting speed and power performance of a 2-bladed Savonius rotor turbine for hydrokinetic application with the presence of a deflector. Experiments were performed in a closed-circuit wind tunnel under two cases: with and without a deflector. First, the self-starting speed of the turbine was characterised at different rotor angles for various deflector angles ranging from 30° to 120° where the coefficient of the static torque was also acquired. Based on the self-starting speed of the turbine, the power performance, in terms of coefficients of power and torque, were acquired and compared. The study found that the deflector reduced the self-starting speed of the turbine with the highest reduction, which occurred when the deflector was configured at 90°. At this optimal deflector angle, the lowest self-starting speed of the turbine was found to be 5.1 m/s air flow speed (equivalent to 0.29 m/s water flow speed) where it had reduced by 38.55%, relative to the baseline case. Moreover, the turbine exhibited the highest coefficients of static torque for all the deflector angles considered in this study. Besides, the coefficient of power had significantly improved by 84.62%, and the range of tip speed ratio also increased which indicated the capability of the turbine to generate more power. With the presence of a deflector, the returning blade was blocked from the incoming flow, thus reducing the negative torque on the blade that opposed the turbine's rotational motion. The comparisons of the turbines' performance indicated that the turbine with a deflector operating under low flow rate condition was capable of generating a marginally more substantial amount of power compared to the turbine with no deflector, which operated under a high flow rate. This study demonstrated the effectiveness of the deflector to improve the operating range and performance of the Savonius turbine under low water flow speed condition for hydrokinetic application without deteriorating the turbine performance. Therefore, it can be suitably adopted for low load applications to provide sustainable electrical power, especially in remote areas with extensive river networks such as those found in Malaysia.

Keywords: deflector; Savonius turbine; self-starting speed; power performance; sustainable; hydrokinetic

1. INTRODUCTION

Hydrokinetic turbine (HKT) is one of the hydropower-based technologies that offers a sustainable and environmentally friendly production of electrical power. The turbine generates electricity by directly extracting the kinetic energy of free-flowing rivers. Hence, it can omit the requirement for the construction of a water reservoir which can pose negative impacts on the environment and the nearby settlement (William and Jain, 2011, Tanbhir et al., 2011). The working principle of the turbine is similar to a wind turbine, but as water is about 800 times denser than air, the HKT can generate more power under the same flow rate input (Vermaak et al., 2014). Moreover, it offers good predictability, in terms of the direction and velocity of the incoming water, in comparison to the wind turbine (Kusakana and Vermaak, 2013).

There are various types of HKT which can be categorized into the horizontal axis and vertical axis turbines (Kumar and Saini, 2016). Amongst the various types of HKT, the vertical axis Savonius HKT is considered to be the most suitable turbine for a low load and low-cost power production system, especially for remote areas application. Geometrically, this turbine has a far simpler design compared to the other types of turbine. Hence, it can offer a relatively low operation, development and maintenance costs (Kumar and Sarkar, 2016). Besides, the turbine has lower noise, high static torque and can perform better under shallow and limited water flow rate condition (Akwa et al., 2012). Therefore, this type of turbine is suitable for river current application to provide a green and sustainable low electrical power, especially to remote area communities in developing countries such as Malaysia.

The Savonius turbine was invented by a Finnish engineer, Sigurd Savonius in 1925 (Ushiyama and Nagai, 1988). It works based on the drag force difference between advancing and returning blades. Due to the difference of blade shape with respect to the incoming flow, the advancing blade experiences greater drag force than the returning blade creating a net positive torque that drives the turbine (Kamoji et al., 2008). The drag force on the returning blade generates negative torque that opposes the rotational motion of the turbine. Thus, some of the energy will be lost while overcoming this torque. As a result, the turbine suffers low efficiency in comparison to other types of turbines, which is a major drawback for the Savonius turbine (Behrouzi et al., 2016).

Due to this fact, various studies have been conducted over the past years to improve the performance of the Savonius turbine through numerical and experimental studies. It is found that an augmentation technique by using flat deflectors can significantly improve the turbine's performance. The presence of flat deflectors positioned at the upstream of the turbine block deflected the incoming flow from impinging on the returning blade, hence reducing the drag force exerted on that blade which will eventually improve the power output (Alom and Saha, 2018, Kerikous and Thévenin, 2019). For instance, Ogawa and Yoshida (1986) performed wind tunnel experiments on the Savonius rotor with a flat deflector at different deflector angles ranging from 0° to 75° . The results showed an improvement in the coefficient of power, C_p by 27% at 30° deflector angle where the maximum coefficient of power is $C_{p_{max}} = 0.212$. Then, Mohamed et al. (2010) optimised the configuration of a flat deflector upstream of the returning blade of two-bladed and three-bladed Savonius turbines through a numerical study. At the optimised deflector configuration, the performances of the two-bladed and three-blade turbines had improved by 27.3% and 27.5%, respectively. On the other hand, Iio et al. (2011) used a flat deflector to improve the C_p of a Savonius turbine with an in-plane axis. From the experimental study, they found that the $C_{p_{max}} = 0.47$ can be achieved by the turbine without any flat deflector, with an improvement of 80% relative to the turbine.

Golecha et al. (2011) conducted an experimental study to investigate the effect of a single flat deflector configuration on the performance of a modified Savonius turbine for an HKT application. Eight different deflector configurations, positioned upstream of the returning blade were tested. It was found that the highest improvement of C_p by 50% can be achieved by the turbine when the deflector was configured at a deflector angle, $\delta = 101^\circ$, where the $C_{p_{max}} = 0.21$ at a tip speed ratio of 0.82. Then, based on the optimised returning blade deflector configuration, Golecha et al. (2012) added another flat deflector upstream of the advancing blade. At the optimised advancing blade deflector angle of 50° , the $C_{p_{max}}$ of the turbine was significantly increased to 0.35 at a tip speed ratio of 1.08 with 150% improvement relative to the performance of the turbine without any deflector.

Altan and Atilgan (2010) also adopted two deflector plates concept to reduce the negative torque that opposed the turbine rotational motion and hence improve the coefficient of power. They used two deflectors known as curtains that could significantly improve the turbine's performance where the highest $C_{p_{max}}$ of 0.38 was obtained when the advancing and returning curtains were configured at 15° and 45° , respectively. On the other hand, Roy et al. (2014) employed two flat deflectors upstream of the turbine that acted as a concentrator such that a major portion of the incoming flow was being directed towards the concave surface of the advancing blade. Based on the wind tunnel experiment, the $C_{p_{max}}$ of 0.32 (with 47.5% improvement) was exhibited by the turbine when the advancing and returning blade deflector angles were set at 40° and 10° , respectively.

Based on the previous studies, it was proven that the use of deflectors could significantly improve the Savonius turbine performance in terms of the coefficient of power, which was the main concern associated with the turbine.

Although the self-starting capability of the turbine was less critical in comparison to its power performance, it is rather fundamental to investigate the effect of a deflector on the self-starting speed of the turbine so that its power loss and operating range can be improved. Since the deflector reduces the negative torque that opposes the turbine's rotational motion, the self-starting capability of the turbine can be improved with the use of a deflector where a lower incoming flow speed would be sufficient for the turbine to self-start. Wong et al. (2017) stated that the use of augmentation technique such as a deflector could increase the incoming flow speed, thus allowing the turbine to operate under low flow speed conditions without losing its performance. Therefore, it is of significance to investigate the effect of the deflector on the self-starting speed of the turbine and its corresponding power performance.

In the present study, the self-starting speed and power performance of a two-bladed Savonius HKT with the presence of a deflector were experimentally studied in a closed-circuit wind tunnel. First, the self-starting speed of the turbine was characterised at various rotor angles for two cases, i.e. without and with a deflector. In this study, the self-starting speeds of the turbine were investigated at a particular rotor angle which corresponded with the minimum airflow speeds at which the turbine started to self-rotate. Based on these speeds, the equivalent water flow speeds were calculated using the Reynolds number similarity approach. In order to further understand the self-starting capability of the turbine, the coefficient of static torque was acquired for all the tested rotor angles. Then, the power performance of the turbine, in terms of coefficient of power and coefficient of torque for both cases, were acquired and compared under a similar incoming flow speed. The practicality of the deflector for low water flow applications was further demonstrated by comparing the coefficient of the power curves obtained under different flow rate conditions.

2. SAVONIUS TURBINE WITH A DEFLECTOR

2.1. Turbine model

In this study, a conventional two-bladed Savonius turbine with a central shaft had been considered for experimental tests. The height of the turbine was $H = 0.09$ m and its diameter was $D = 0.14$ m. Hence, the turbine had an aspect ratio, $AR = 0.64$. The blades of the turbine had a semi-circular profile with a diameter, $d = 0.075$ m, made of 1 mm thick aluminium sheet. Each blade was attached to the central shaft of 0.01 m in diameter, made of aluminium rod. The blades were oriented at 180° apart from each other, as shown in Figure 1. The turbine had no end plates that covered the top and bottom edge of the blades. The blade with a concave side facing the freestream was described as the advancing blade whereas the blade with a convex side facing the freestream direction was called the returning blade. The configuration of the advancing blade with respect the freestream direction was used to determine the rotor angle, θ .

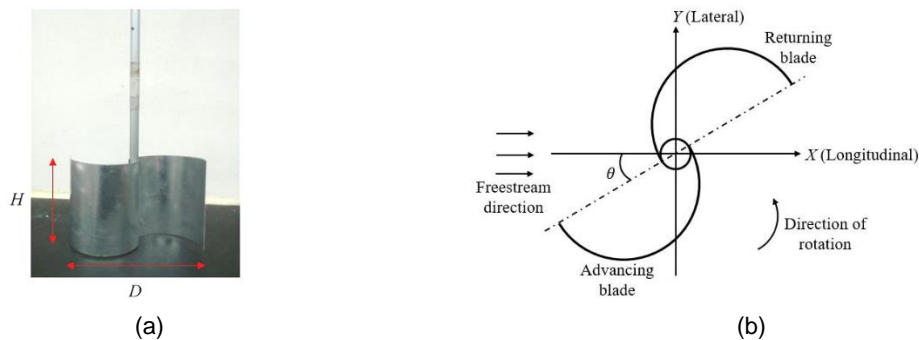


Figure 1: Savonius turbine model (a) front view of the turbine model and (b) the schematic diagram (top view)

2.2. Flat deflector

In order to investigate the effect of deflector on the self-starting speed and power performance of the Savonius turbine model, a flat deflector made of clear acrylic plate is placed upstream of the returning blade of the turbine. The deflector has a dimension of 0.255 m height \times 0.15 m width \times 0.008 m thick. Figure 2 shows the configuration of the flat deflector where the longitudinal distance between the central shaft of the turbine and the nearest edge of the deflector is fixed at 0.145 m. In this study, four different deflector angles, $\delta = 30^\circ, 60^\circ, 90^\circ,$ and 120° have been considered where the deflector angle is defined as the angle between the flat deflector and the freestream direction.

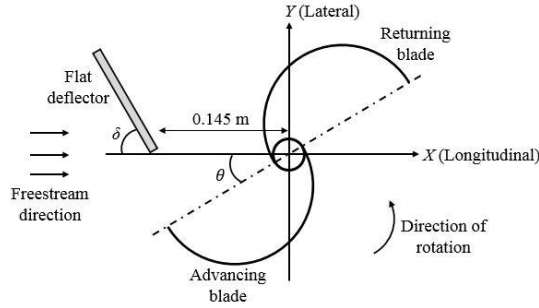


Figure 2: Configuration of the flat deflector in the experimental setup (top view)

3. METHODOLOGY

3.1. Experimental setup

The experiment was conducted in a closed-circuit wind tunnel having a rectangular test section of 1.8 m length \times 0.8 m height \times 1.0 m width with a turbulent intensity inside the test section of about 0.1%. The two-bladed Savonius turbine is placed in the middle of the test section where the longitudinal distance between the test section inlet and centre of the turbine is 0.9 m, as shown in Figure 3. The shaft of the turbine is held by a bearing located on top of the test section. The bearing is sprayed with a commercially available WD 40 lubricant at the beginning of the experiment to reduce friction. A pulley is mounted on the top end of the central shaft as part of the Prony brake dynamometer setup for torque measurement which will be discussed in the next section.

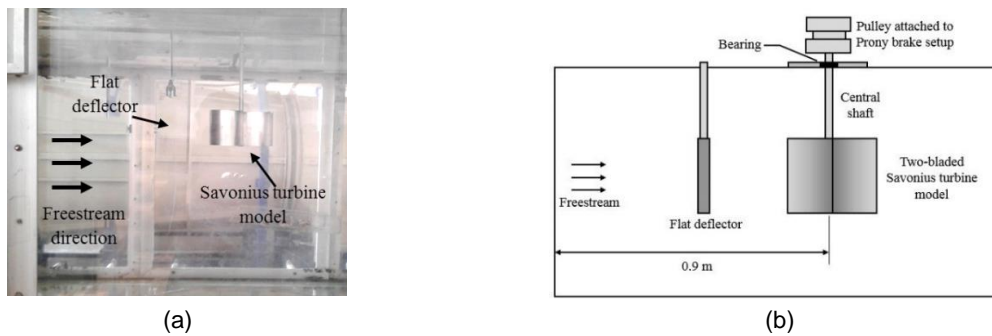


Figure 3: Experimental setup (a) inside the test section (side view) and (b) the schematic diagram (side view)

3.2. Torque measurement

The power performance of the Savonius turbine model is obtained and analysed by acquiring the torque generated by the turbine. The generated torque is acquired using a Prony brake dynamometer setup on top of the test section, as depicted in Figure 4. The setup consists of two load cells ($\pm 0.02\%$ full-scale accuracy), and a non-contact digital tachometer ($\pm 0.05\%$ full-scale accuracy) used to measure the applied load and rotational speed of the turbine in revolution per minute (RPM) respectively. In order to acquire the dynamic torque, the turbine is gradually loaded by tightening the traction belt around the pulley until the rotational speed of the turbine is reduced at certain RPM. In this study, the dynamic torque is acquired at various RPMs where the applied loads and rotational speeds of the turbine are used to calculate the turbine's dynamic torque and coefficient of power.

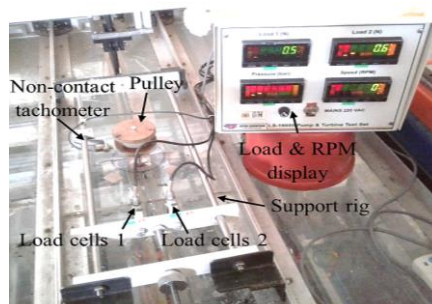


Figure 4: Prony brake setup on top of the test section for torque measurement

3.3. Data reduction

The Reynolds numbers, Re of the freestream inside the wind tunnel and water channel based on the diameter of the Savonius turbine model are given by Equation 1 and Equation 2, respectively.

Equation 1: Freestream Reynolds number inside the wind tunnel $Re_{WT} = \frac{\rho_a U_a D}{\mu_a}$

Equation 2: Freestream Reynolds number inside the water channel $Re_{WC} = \frac{\rho_w U_w D}{\mu_w}$

Where:

- Re_{WT} = freestream Reynolds number inside the wind tunnel
- Re_{WC} = freestream Reynolds number inside the water channel
- ρ_a = density of air (kg/m³)
- ρ_w = density of water (kg/m³)
- U_a = air flow speed (m/s)
- U_w = water flow speed (m/s)
- D = diameter of the Savonius turbine model
- μ_a = dynamic viscosity of air (kg/ms)
- μ_w = dynamic viscosity of water (kg/ms)

In this study, the freestream Reynolds number inside the wind tunnel, Re_{WT} was used to obtain equivalent water flow speeds, U_w that correspond to the self-starting speeds of the Savonius turbine as it operates in a water channel by means of the Reynolds number similarity approach given by Equation 3.

Equation 3: Reynolds number similarity $Re_{WT} = Re_{WC}$

The power performance of the Savonius turbine was analysed in terms of coefficient of power, C_p which depicts the efficiency of the turbine to extract power from the incoming airflow and it is given by Equation 4 as follows (Talukdar et al., 2018).

Equation 4: Coefficient of power $C_p = \frac{P_{out}}{P_{in}}$

Where :

- C_p = coefficient of power
- P_{out} = power generated by the turbine (W)
- P_{in} = power available in the incoming airflow (W)

P_{in} and P_{out} can be expressed in Equation 5 and Equation 6 respectively.

Equation 5: Power available in the incoming airflow $P_{in} = \frac{1}{2} \rho_a H D V_a^3$

Equation 6: Power generated by the turbine $P_{out} = T \omega$

Where:

- T = dynamic torque generated by the turbine (Nm)
- ω = angular speed of the turbine (rad/s)

The generated dynamic torque can be obtained based on the applied load acquired by the Prony brake dynamometer setup, and it is given by Equation 7.

Equation 7: Dynamic torque generated by the turbine

$$T = (F_1 - F_2)r_p$$

Where:

- F_1 = applied load acquired by load cell 1 (N)
- F_2 = applied load acquired by load cell 2 (N)
- r_p = radius of the pulley (m)

Whereas the angular speed of the turbine can be calculated based on the rotational speed, *RPM* of the turbine acquired by the non-contact tachometer which is expressed by Equation 8.

Equation 8: Angular velocity of the turbine

$$\omega = \frac{2\pi}{60} \times RPM$$

The ability of the turbine to generate power can be indicated by the coefficient of the torque, C_T and it is given by Equation 9. Usually the variations C_T and C_p are plotted against the tip speed ratio, λ given by Equation 10. Having Equation 9 and Equation 10, the C_p can be expressed in terms of C_T and λ given by Equation 11.

Equation 9: Coefficient of torque

$$C_T = \frac{4T}{\rho_a H D^2 V_a^2}$$

Equation 10: Tip speed ratio

$$\lambda = \frac{\omega D}{2V_a}$$

Equation 11: Relationship between C_p , C_T , and λ

$$C_p = C_T \lambda$$

On the other hand, the ability of the turbine to self-start can be indicated by the coefficient of the static torque, C_{TS} given by Equation 12.

Equation 12: Coefficient of static torque

$$C_{TS} = \frac{4T_s}{\rho_a H D^2 V_a^2}$$

Where:

- T_s = static torque generated by the turbine (Nm)

The static torque can be acquired by configuring the turbine blade in static condition at various initial rotor angles, θ .

4. RESULTS AND DISCUSSION

The effect of a deflector on the self-starting speed and power performance the two-bladed Savonius turbine model were analysed based on the wind tunnel experiments. First, the experiment was conducted by characterising the self-starting speeds of the turbine with respect to various deflector angles. In this experiment, the turbine was initially configured at various rotor angles, ranging from 0° to 180°. At each rotor angle, the air flow speed inside the test section was gradually increased until the turbine self-started. The air flow speed at which the turbine started to rotate is defined as the self-starting speed of the turbine at a particular rotor angle. By using the Reynolds number similarity approach, an equivalent water flow speed was then obtained to ensure that the flow was dynamically similar in both conditions. In addition, the coefficient of static torque was acquired at all the rotor angles tested for the various deflector angles. Then, the experiment was conducted by acquiring the dynamic torque generated by the turbine to obtain the power performance. The dynamic torque was acquired at the air flow speed, which corresponded to the highest self-starting speed of the turbine without any flat deflector. At the air flow speed, the turbine was able to sustain its rotational motion at a greater revolution to ensure measurability of the dynamic torque. For each analysis, the experiment was first performed on the turbine with no deflector case, followed by an experiment on a turbine with a deflector case.

4.1. Effect of deflector on the self-starting speed

Figure 5 shows the experimental results of the effect of deflector on the self-starting speed of the two-bladed Savonius turbine model. Overall, the self-starting speeds of the turbine varied with respect to the rotor angle and this trend can be observed for the no deflector case as well as with a deflector case. For both cases, the lowest and highest self-starting speeds were obtained when the turbine was initially configured at $\theta = 30^\circ$ and 150° respectively. At $\theta = 30^\circ$, the advancing blade was exposed and impinged by the incoming flow earlier than the returning blade. Hence, the advancing blade experiences a drag force that has caused the turbine to rotate before a negative torque was generated on the returning blade and vice versa when the turbine was configured at $\theta = 180^\circ$. Therefore, even at low air velocity, there was sufficient drag force that had been exerted on the advancing blade to generate a positive torque that drives the turbine at $\theta = 30^\circ$. For the turbine with no deflector case, the lowest and highest self-starting speed were 8.3 m/s (equivalent water flow speed of 0.48 m/s) and 14.6 m/s (equivalent water flow speed of 0.84 m/s), respectively. With the presence of a deflector upstream of the returning blade, it was found that the self-starting speeds of the turbine were lower than that of the turbine with no deflector case. Deflector angle, $\delta = 90^\circ$ was found to be the optimal deflector angle where the turbine exhibits the largest reduction in the self-starting speed at all rotor angles. The lowest self-starting speed which occurs at $\theta = 30^\circ$ was 5.1 m/s (equivalent to the water flow speed of 0.29 m/s) whereas the highest self-starting speed occurs at $\theta = 150^\circ$ was 8.4 m/s (equivalent to the water flow speed of 0.48 m/s). According to Table 1, these self-starting speeds have been reduced by 38.55% and 42.47% respectively, relative to the no deflector case. A significant reduction in the self-starting speed of the turbine at $\delta = 90^\circ$ was because, at this configuration, the flat deflector effectively deflected the incoming flow from impinging on the returning blade hence reducing the drag force exerted on that blade. Consequently, it reduced the negative torque on the returning blade that opposes the rotational motion of the turbine. Therefore, the turbine was able to self-start even at lower air flow speed which consequently increases the operating range of the turbine.

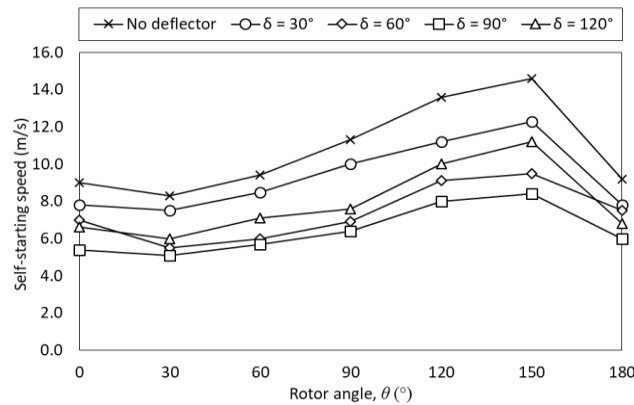


Figure 13: Variations of self-starting speed against rotor angle of the turbine for various deflector angles

Table 9: Reduction of self-starting speed (%) with the presence of a flat deflector relative to no deflector case

Rotor angle, θ ($^\circ$)	Deflector angle, δ ($^\circ$)			
	30 $^\circ$	60 $^\circ$	90 $^\circ$	120 $^\circ$
0 $^\circ$	13.33%	22.22%	40.00%	26.67%
30 $^\circ$	9.64%	33.73%	38.55%	27.71%
60 $^\circ$	9.57%	36.17%	39.36%	24.47%
90 $^\circ$	11.50%	38.94%	43.36%	32.74%
120 $^\circ$	17.65%	33.09%	41.18%	26.47%
150 $^\circ$	15.75%	34.93%	42.47%	23.29%
180 $^\circ$	18.48%	18.48%	34.78%	26.09%

By analysing the coefficient of static torque, C_{TS} of the turbine, as shown in Figure 6, it was found that the highest and lowest C_{TS} mostly occurred at $\theta = 30^\circ$ and 150° respectively. This explains the ability of the turbine to self-start at lower air velocity when the rotor was initially configured at $\theta = 30^\circ$. Large positive C_{TS} indicates that the turbine has a good self-starting capability. With the presence of a flat deflector, the C_{TS} of the turbine was higher than the

no deflector case. A significant increment of C_{TS} at $\theta = 30^\circ$ can be observed for $\delta = 90^\circ$ and due to this fact, the turbine has the lowest self-starting speed for all deflector angles tested in this study. The use of the deflector increases the self-starting capability of the turbine and consequently improves the working range of the turbine where it allows the turbine to operate under low flow rate condition.

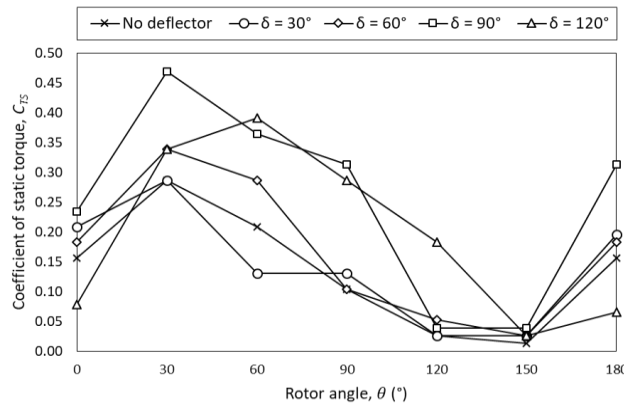


Figure 6: Variations of the coefficient of static torque against rotor angle of the turbine for various deflector angles

4.2. Effect of deflector on the power performance

The power performance of the turbine was analysed in terms of coefficient of power, C_p and coefficient of torque, C_T with respect to various deflector angles at air flow speed, $U = 14.6$ m/s (equivalent water flow speed of 0.45 m/s). This operating condition corresponded to a $Re = 1.32 \times 10^5$ which was a typical flow speed for hydrokinetic application (Patel et al., 2016). Figure 7 and Figure 8 show the variation of C_p and C_T of the turbine for various deflector angles respectively. With the presence of a deflector, the C_p of the turbine was higher than the turbine with no deflector case where $\delta = 90^\circ$ resulted in the highest C_p curve against the tip speed ratio. The maximum coefficient of power C_{Pmax} for the turbine with no deflector case was 0.013, but it has increased to 0.024 when the flat deflector was configured at $\delta = 90^\circ$ with a significant improvement of 84.62% relative to the turbine with no deflector case. In addition, it was also found that the range of the tip speed ratio, λ for both the C_p and C_T curves increases with the presence of a deflector which was similar to the results found by Golecha et al. (2011). The largest maximum tip speed ratio, λ_{max} can be observed at $\delta = 90^\circ$ and it was followed by $\delta = 60^\circ$, 120° , and 30° . The increment of λ indicates that the turbine was rotating at a higher angular velocity, ω as the negative torque that opposes the turbine's rotational motion was reduced and hence more power can be generated by the turbine. Table 2 lists the C_{Pmax} , C_T and λ that correspond to the C_{Pmax} , as well as C_{Pmax} improvement and λ_{max} for all the deflector angles.

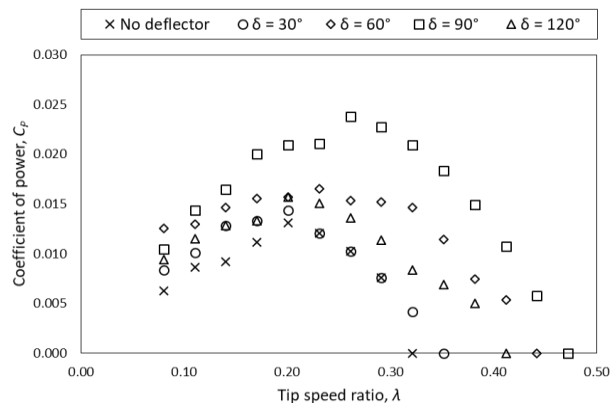


Figure 7: Variations of the coefficient of power against tip speed ratio of the turbine for various deflector angles

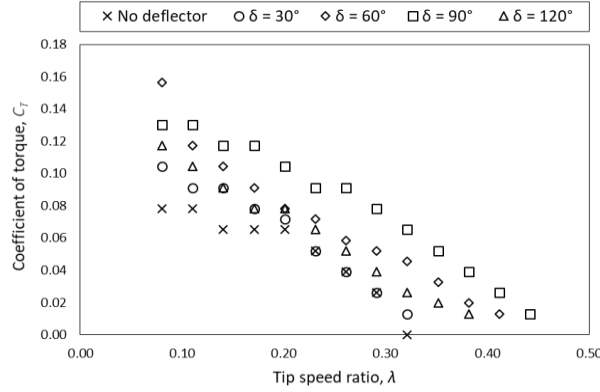


Figure 8: Variations of the coefficient of torque against the tip speed ratio of the turbine for various deflector angles

Table 2: Power performance of the turbine with respect to various deflector angles

Deflector angle, δ ($^{\circ}$)	C_{Pmax}	C_T at C_{Pmax}	λ at C_{Pmax}	λ_{max}	Improvement of C_{Pmax} (%)
No deflector	0.013	0.065	0.20	0.32	-
30 $^{\circ}$	0.014	0.070	0.20	0.35	7.69%
60 $^{\circ}$	0.017	0.081	0.23	0.44	30.77%
90 $^{\circ}$	0.024	0.091	0.26	0.47	84.62%
120 $^{\circ}$	0.016	0.080	0.20	0.41	23.08%

In order to demonstrate the practicality of a flat deflector, the C_p of the turbine with no deflector was compared with the C_p of the turbine with a flat deflector configured at $\delta = 90^{\circ}$. The C_p for the case of $\delta = 90^{\circ}$ was obtained at an air flow speed of 8.4 m/s which corresponded with the highest self-starting speed of the rotor for that case. It was found that the C_{Pmax} of the turbine for the case of $\delta = 90^{\circ}$ was marginally larger (i.e., 0.016) than the no deflector case (i.e. 0.014) although the air velocity was 0.58 slower than the no deflector case. It meant that even under low flow speed, the turbine with a deflector was able to generate a similar or even larger amount of power as it was operating under a high flow speed with no deflector. The result highlighted the practicality of the flat deflector to be augmented into the Savonius hydrokinetic turbine for low water flow speed applications without compromising the power performance of the turbine.

5. CONCLUSION

In this paper, an experimental study to investigate the effect of a deflector on the self-starting speed and power performance of a two-bladed Savonius hydrokinetic turbine (HKT) was conducted. The self-starting speeds of the rotors at different rotor angle, θ with respect to deflector angle, δ were characterised in a closed-circuit wind tunnel. Based on the results obtained, the equivalent water velocities that corresponded to the self-starting speeds of the turbine in the water channel were calculated using the Reynolds number similarity approach to ensure that the flow would be dynamically similar in both conditions. The lowest and highest self-starting speeds of the turbine with no deflector case and with a deflector case were found to be at $\theta = 30^{\circ}$ and 150° . With the presence of a deflector, however, the self-starting speeds of the turbine at all the initially configured rotor angles were reduced with an optimal reduction occurred when $\delta = 90^{\circ}$. At this deflector angle, the lowest self-starting speed of the turbine was 5.1 m/s (equivalent to the water flow speed of 0.29 m/s) where it was reduced by 38.55%, relative to the no deflector case. The turbine exhibited the highest coefficient of static torque curve in comparison to other deflector configurations. In terms of power performance, the coefficient of power, C_p curves increased with the presence of a deflector. A significant improvement of the maximum coefficient of power, C_{Pmax} by 84.62% was obtained at the optimal deflector angle of $\delta = 90^{\circ}$. The tip speed ratio range also increased indicating the capability of the turbine to generate more power. Under a lower air flow speed, the turbine with optimal deflector was able to generate a comparable amount of power as the turbine with no deflector operated under a higher flow velocity. The experimental results demonstrate the effectiveness of a flat deflector in improving the self-starting capability and power performance of the Savonius HKT. Therefore, it can be considered as the most practical and reliable augmentation technique to be adopted for low water flow speed applications with a vast river network in providing a low cost and sustainable electrical power, particularly to the communities residing in remote areas of developing countries.

6. ACKNOWLEDGEMENT

The authors would like to acknowledge the financial support from Universiti Sains Malaysia under the Bridging Grant (304.PAERO.6316309).

7. REFERENCES

- Akwa JV, Vielmo HA, Petry AP, 2012. A review on the performance of Savonius wind turbines. *Renewable and Sustainable Energy Review*, 16 (5), 3054–64. <https://doi.org/10.1016/j.rser.2012.02.056>
- Alom N, Saha UK, 2018. Four decades of research into the augmentation techniques of Savonius wind turbine rotor. *Journal of Energy Resources Technology*, 140, 1-14. <https://doi.org/10.1115/1.4038785>
- Altan BD, Atilgan M, 2010. The use of curtain design to increase the performance level of a Savonius wind rotors. *Renewable Energy*, 4, 821-29. <https://doi.org/10.1016/j.renene.2009.08.025>
- Golecha K, Eldho TI, Prabhu SV, 2011. Influence of the deflector on the performance of modified Savonius water turbine. *Applied Energy*, 88, 3207-17. <https://doi.org/10.1016/j.apenergy.2011.03.025>
- Golecha K, Eldho TI, Prabhu SV, 2012. Performance study of modified Savonius water turbine with two deflector plates. *International Journal of Rotating Machinery*, 140, 1-11. <http://dx.doi.org/10.1155/2012/679247>
- Iio S, Katayama Y, Uchiyama F, Sato E, Ikeda T, 2011. Influence of setting condition on characteristics of Savonius hydraulic turbine with a shield plate. *Journal of Thermal Science*, 20 (3), 224-28.
- Kamoji MA, Kadare SB, Prabhu SV, 2008. Experimental investigations on single stage, two stage and three stage conventional Savonius rotor. *International Journal of Energy Research*, 32, 877-95. <https://doi.org/10.1002/er.1399>
- Kamoji MA, Kadare SB, Prabhu SV, 2009. Experimental investigations on single stage modified Savonius rotor. *Applied Energy*, 86, 1064–73. <https://doi.org/10.1016/j.apenergy.2008.09.019>
- Kerikous E, Thevenin D, 2019. Optimal shape of thick blades for a hydraulic Savonius turbine. *Renewable Energy*, 134, 629-638. <https://doi.org/10.1016/j.renene.2018.11.037>
- Kumar A, Saini RP, 2016. Performance parameters of a Savonius type hydrokinetic turbine - a review. *Renewable and Sustainable Energy Review*, 64, 289-310. <https://doi.org/10.1016/j.rser.2016.06.005>
- Kumar D, Sarkar S, 2016. A review on the technology, performance, design optimization, reliability, techno-economics and environmental impacts of hydrokinetic energy conversion systems. *Renewable and Sustainable Energy Review*, 58, 796-813. <https://doi.org/10.1016/j.rser.2015.12.247>
- Kusakana K, Vermaak HJ, 2013. Hydrokinetic power generation for rural electricity supply: case of South Africa. *Renewable Energy*, 55, 467-73. <https://doi.org/10.1016/j.renene.2012.12.051>
- Mohamed MH, Janiga G, Pap E, Thevenin D, 2010. Optimization of Savonius turbine using obstacle shielding the returning blade. *Renewable Energy*, 88, 2618-26. <https://doi.org/10.1016/j.renene.2010.04.007>
- Ogawa T, Yoshida H, 1986. The effects of a deflecting plate and rotor end plates. *Bulletin JSME*, 29 (253), 2115-21. <https://doi.org/10.1299/jsme1958.29.2115>
- Patel V, Bhat G, Eldho TI, Prabhu SV, 2016. Influence of overlap ratio and aspect ratio on the performance of Savonius hydrokinetic turbine. *International Journal of Energy Research*, 1-16. <https://doi.org/10.1002/er.3670>
- Roy S, Mukherjee P, Sha UK, 2014. Aerodynamic performance evaluation of a novel Savonius-style wind turbine under an oriented jet. Gas Turbine India Conference. India: Proceeding of ASME 2014 2014. <https://doi.org/10.1115/GTINDIA2014-8152>
- Talukdar PK, Sardar A, Kulkarni V, Saha UK, 2018. Parametric analysis of model Savonius hydrokinetic turbines through experimental and computational investigations. *Energy Conversion Management*, 158, 36-49. <https://doi.org/10.1016/j.enconman.2017.12.011>

Tanbhir H, Nawshad UA, Islam N, Sina I, Syfullah K, Raiyan R, 2011. Micro hydropower: promising solution for off-grid renewable energy source. *International Journal of Science and Engineering Research*, 2 (12), 1-5.

Ushiyama I, Nagai H, 1988. Optimum design configurations and performance of Savonius rotors. *Wind Engineering*, 12 (1), 59–75.

Vermaak HJ, Kusakana K, Koko SP, 2014. Status of micro-hydrokinetic river technology in rural applications: a review of literature. *Renewable and Sustainable Energy Reviews*, 29, 625-633. <http://dx.doi.org/10.1016/j.rser.2013.08.066>

Williams GG, Jain P, 2011. Renewable energy strategies. Sustain: a Journal of Environmental and Sustainability issues. *The Kentucky Institute of Environment and Sustainable Development*, 23, 29–42.

Wong KH, Chong WT, Sukiman NL, Poh SC, Shiah Y-C, Wang C-T, 2017. Performance enhancements on vertical axis wind turbines using flow augmentation systems: a review. *Renewable and Sustainable Energy Reviews*, 73, 904-21. <https://doi.org/10.1016/j.rser.2017.01.160>

#280: Effect of 3D morphological distribution of cities on urban heat island formation: A GIS approach

Victor EQUERE¹, Parham MIRZAEI², Saffa RIFFAT³

¹ Department of Architecture and Built Environment, Faculty of Engineering, University of Nottingham, NG7 2RD, University Park, Nottingham, UNITED KINGDOM, Victor.Equere@nottingham.ac.uk

² Department of Architecture and Built Environment, Faculty of Engineering, University of Nottingham, NG7 2RD, University Park, UNITED KINGDOM, Parham.mirzaei_ahranjani@nottingham.ac.uk

³ Department of Architecture and Built Environment, Faculty of Engineering, University of Nottingham, NG7 2RD, University Park, Nottingham, UNITED KINGDOM, Saffa.riffat@nottingham.ac.uk

The impact of the urban heat island (UHI) on the health of urban residents, energy consumption, as well as outdoor air quality has become increasingly significant in cities. Despite multiple recent studies on developing UHI predictive models, the impact of vertical morphological parameters on the UHI formation is barely investigated. The current work investigates the extent of vertical morphological components' impact on the UHI intensity in urban areas and proposes a novel vertical urban morphological parameter defined as elevation index. Using remote-sensing satellite images, and a Geographical Information System (GIS) based approach, both horizontal and vertical morphological components of San-Francisco, as the case study city, were studied for 20 of its representative built up areas. High-resolution geometrical data of these areas were then correlated with the land surface temperature (LST) of those areas. Linear and nonlinear regression analysis revealed that the newly proposed elevation index has a significant impact on representing of the UHI behaviour with a coefficient of determination factor (R^2) of 0.88. The model was then successfully validated against the UHI prediction of five new areas not being used for the training purposes. The impact of elevation morphology on UHI intensity was seen to be significant, especially at areas with a significant elevation variation.

Keywords: urban heat island; predictive tool; regression; remote-sensing; GIS

1. INTRODUCTION

Urban Heat Island (UHI) has a significant impact on health of urban residents (Mavrogianni, 2012), energy consumption (Polydoros and Cartalis, 2015), as well as air quality (Liu and Weng, 2012). The UHI research has shown that the urban morphological composition such as increased impervious land cover, geometry of street canyons, reduced sky visibility are the main key players, impacting on the energy balance, wind speed, and long-wave radiation, and resulting in the elevation of temperature in cities (Mirzaei et al., 2015, Oke, 1982).

Numerous studies have given attention to improve techniques in studying of the UHI (Mirzaei and Haghighat, 2010, Mirzaei et al., 2015). In view of this, the thermal remote-sensing method have been widely adopted to investigate morphological impact on UHI intensity of a region, because of its performance in large scale morphology data acquisition (Li et al., 2018, Streutker, 2003). To extract morphological information from the remotely-sensed spatial images, several indices have been developed to aid in mapping these features. Some examples include UMBAs and ISDD (Meng et al., 2018), UTFVI (Ahmed, 2018), NDBal, NDVI, NDWI and NDBI (Chen et al., 2006). Nonetheless, it suffice to say that remote sensing retrieved indices are still limited in generating the elevation information, which are also fundamental in explaining the UHI effect (Mirzaei and Haghighat, 2010).

To include the vertical spatial distribution to the account, several studies during the last decade such as (Benediktsson et al., 2007, Keqi et al., 2003) proposed to benefit from the emergence of topographic airborne LiDAR data for land cover classification. Airborne LiDAR refers to laser profiling and scanning system for bathymetric and topographic applications, which gained commercially prominence in mid- 1990s (Yan et al., 2015). Unlike the 2D planimetric remote-sensing data, the explicit LiDAR data point cloud accounts for the elevation aspect of a surveyed area as it describes the 3D topographic profile of the Earth surface (Wang, 2013). Airborne LiDAR survey is widely adopted for spatial data classifications because of its accuracy in object recognition (Germaine, 2011). Despite the mentioned advantages of LiDAR technique in generating digital 3D city model, issues such as expense and rigorous process involved in obtaining permits from local authorities have made this technique still an unsuitable one to provide vertical explanations of the UHI. As another alternative, many recent studies have taken advantage of innovative 3D city modelling Geographical Information System tools to overcome the difficulty associated with the large scale digital 3D model production.

GIS is a framework for gathering, managing and analysis geographical data to enable visualisation and to provide more information on a specific area. Based on this framework, 3D city model tools served as an interface to combine user inputted 2D spatial data set with the elevation information to generate 3D models. Such tools have become very useful in 3D city related studies especially if they are tailored for the built environment studies (Li et al., 2016, Stoter et al., 2013), or the UHI ones, e.g. (Nakata-Osaki et al., 2018) adopted a GIS based approach to generate 3D building models for extraction of the urban geometry parameter coupled with Oke's model to determine the maximum UHI intensity, although the vegetation impact and large scale implementation of the case study were main drawbacks to this approach. Despite this, there is still a need to explore approaches suitable for large scale elevation data extraction, to compliment the limitation of satellite based UHI approaches on the elevation information extraction, so as to improve the application of the UHI intensity explanation in large scale studies.

This paper aims to explore the extent of vertical morphology components impact on the UHI intensity in urban areas by defining a novel index called the elevation index, and furthermore to propose a UHI predictive model that account for both horizontal (Landsat derived) and vertical (elevation) morphological components of a case study city. For this purpose, LST data obtained from 20 study areas in San-Francisco city was firstly used as the UHI indicator. Esri 3D city engine, Landsat images and Google Earth were then used to retrieve both the horizontal and vertical morphology parameters in order to explain the spatial distribution of the LST across the studied regions. A multi-linear regression and a multi-nonlinear regression analysis were employed based on these parameters to develop couple of predictive UHI LST models. Furthermore, the predictive models were validated using five new areas, not being initially used in the training process of them.

2. GEOGRAPHICAL INFORMATION OF THE STUDY AREA

The city of San Francisco is the cultural, financial and commercial hub of Northern California. According to (U.S.CensusBureau, 2017). It is located on the West Coast of the United States at the north end of the San Francisco Peninsula and has a latitude and longitude of 37 ° 47'N; 122 ° 25'W, respectively. Its landmass is estimated at about 46.89 square miles (121.4 km²). According to the Koppen climate classification, San Francisco has a warm-summer Mediterranean climate with moist mild winters and dry summers (GoldenGateWeatherServices, 2009).

2.1. Study domain and measured parameters

San Francisco was chosen for this study because of a free access to available 3D building dimension data to be used for the geometry construction using Esri City engine satellite database. The 20 study areas, denoted with the symbol A1-A20 as shown in Figure 1, were selected based on two parameters, including area classification and LST distribution. For the purpose of this study, the entire city was classed into four categories based on the occupancy/use of buildings as described in Table 1. The 20 study areas were selected in such a way that all the four outlined areas has an even number of representative.



Figure 1: Aerial map of San Francisco and locations of study areas (GoogleEarth, 2019).

Table 1: Description of the four areas classification adopted in this study.

Class	Description	Study areas	Colour	Areas
Industrial	This area comprises of industrial buildings e.g. warehouses, factories, etc.	A7, A12, A13, A16, A20	Blue	A1, A6, A9, A14, A19
Commercial	This is an area with most buildings used for commercial purposes e.g. offices, schools, etc.	A3, A5, A8, A11, A17	Orange	A2, A3, A5, A10, A13
Residential	This class comprises of areas with mostly residential buildings.	A2, A4, A9, A10, A15	Red	A7, A12, A16, A18, A20
Recreation	This area comprises of open space areas such as recreation spaces, play grounds, parks, etc.	A1, A6, A14, 18, 19	Yellow	A4, A8, A11, A15, A17

The second criteria for selecting 20 study areas was justified based on the LST distribution. Four predominant colours (Red, Yellow, Orange, and Blue) used to represent varying degrees of LST as shown in Figure 2. Thus, the study areas were selected to evenly capture all these colour groups, so as to explain the variation in temperature across these areas. The area classification according to colours is shown in Table 1. Five more areas were randomly selected to be later used in testing the performance of the proposed model in the LST prediction. These areas are referred as trial areas in this study and are denoted with the symbol TA1-TA5. Details of these five areas are given in Table 2. Each area has a dimension of 300m × 300m chosen to correspond with the downloaded satellite image resolution as depicted in Figure 2.

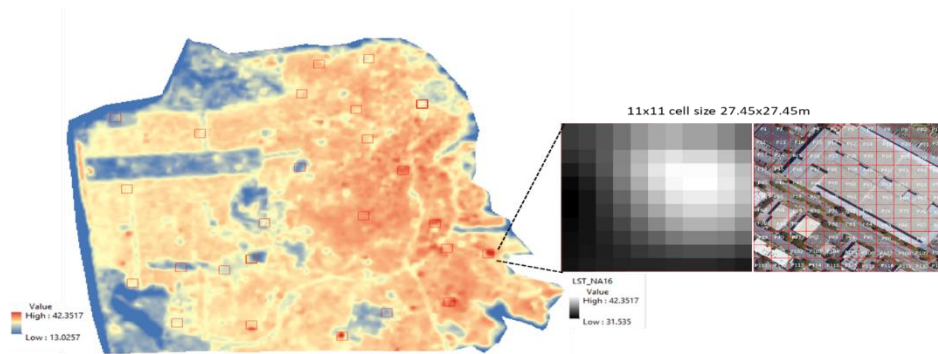


Figure 2: Land surface temperature distribution for the city, showing illustration of cell division to correspond with the pixel resolution of output LST image for A16.

Table 2: Description of new areas for model validation.

Label	Colour	Area
TA1	Orange	Commercial
TA2	Blue	Recreation
TA3	Orange	Recreation/residential
TA4	Yellow	Residential
TA5	Red	Commercial

3. METHODOLOGY

The flowchart illustrated in Figure 3 highlights the stages involved in development of the UHI predictive model as well as the necessary input datasets leading to the LST prediction equation.

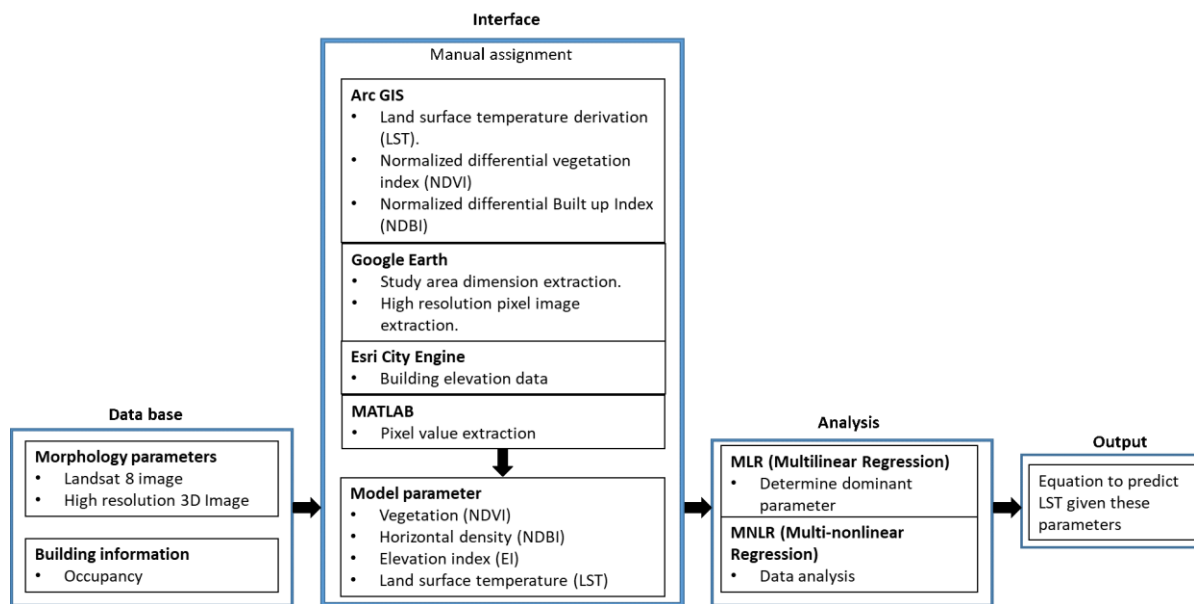


Figure 3: Flowchart of the proposed predictive model.

3.1. Input data

a) *Satellite images*: The Landsat 8 OLI_TIRS suit for the city of San-Francisco, California, U.S.A acquired on 01-06-2018, at 18:44:51.9199550Z, was used. This satellite data was corrected to account for the atmospheric inferences and positional errors (Roy et al., 2014), and then was used to derive the LST, NDBI and NDVI of the selected areas. It is noteworthy to mention that TIRS bands were acquired at 100m resolution though they were resampled to 30m resolution in the delivered data product (Landsat.usgs.gov, 2014).

b) *High-resolution 3D image*: This study obtained a high-resolution georeferenced 3D image on the study area from Google Earth and a 3D building image with all dimensions from the Esri City engine satellite database (EsriCityengine, 2019).

c) *Occupancy*: The occupancy information for the study areas was necessary to class each area according to predominant activities in the region. This information was obtained from Google Earth by activating the places option, which gives information on the building use at each location.

3.2. Parameter retrieval

a) *Land surface temperature (LST)*: The satellite image had to be geo-processed using the Split-Window algorithms to retrieve the LST for 20 areas being studied. This algorithm has been proven effective in LST retrieval from Landsat 8 suits and the procedure has been outlined by (Son et al., 2017).

b) *NDVI*: NDVI is a vegetation index used to map vegetation presence in satellite images. In this study, ArcGIS 10.4 was used to obtain NDVI of the selected areas as depicted in Figure 4.

c) *Normalised differential built-up index (NDBI)*: The NDBI has been widely used (He et al., 2010, Zha et al., 2003) to map built up areas and barren ground automatically from satellite images. The NDBI distribution for San Francisco is presented in Figure 4.

3.3. Morphology parameters mapping

Each study area was subdivided into cells of 30 x 30 to correspond with the pixel sizing of the Landsat processed image files, however due to the thickness of each dividing line, an actual grid of 11 x 11 cells of 27.45m x 27.45m dimension is obtained. The morphology is extracted from each cell, which corresponds with a pixel as illustrated in Figure 5 and described as follows:

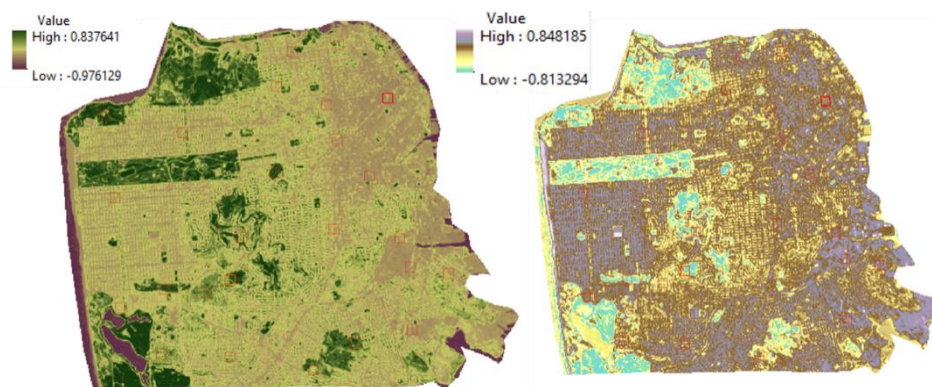


Figure 4: NDVI and NDBI distribution for San Francisco

a) *LST, NDBI and NDVI pixel value extraction*

The pixel values for LST, NDBI and NDVI was extracted using the grayscale image pixel value extraction procedure provided by (Mathworks.com, 2014). A normally distribution is assumed, hence 95% of the values represented in the mean calculation. This process was repeated for all 20 study areas and also the additional 5 areas used for the validation study of the predicting model.

b) *Elevation index (EI)*

The EI is the proposed parameter to represent the vertical density (building and tree heights) in each study area. The procedure for deriving the EI is comprised of three major steps, which are explained in the following section.

Step 1: Building and tree height: The height of the highest elevation feature (tree/building) was adopted as the cell height for each cell, while the flat surfaces like roads or open fields are assumed to have a height value of 0. To extract the building height, the Esri city engine software interface was used to access the building dimensions satellite data set for the study area as illustrated in Figure 5. The tree height was obtained by using google earth pro software to access the high-resolution 3D image of the area and estimate the tree height by observation, using the nearby building heights as bench marks. Three classes of tree heights were developed for ease of representation, including T1 (5m height), T2 (7m height) and T3 (11m height).

Step 2: Normalised elevation: Normalising was necessary to reduce the margin of variance among cell heights and also to set the EI values in a range of 0 and 1 to correspond with the rest of the model variables (NDVI and NDBI).

Firstly, the value distribution was adjusted to account for 99.7% of the data, and normalisation method was adopted using Equation 1:

$$\text{Equation 1: Elevation value normalisation. } Vi = ((Vi - Min_a) / (Max_a - Min_a)) \times (New\ Max - New\ Min) + New\ Min$$

Where:

- V_i = pixel value
- Min_a and Max_a = minimum and maximum height value of entire study area, respectively
- New Max is set to 1
- New Min is set to 0

Step 3 Calculation of EI index: The value for EI for each study area was calculated as the average normalised elevation value for each study area.

3.4. Data analysis

The data was analysed using a multi-linear regression (MLR) method, which explain the relationship between the dependent variable Y and several independent variables, assuming a linear relationship between them as expressed in Equation 2:

$$\text{Equation 2: Multilinear regression. } Y = \alpha + \beta_1 X_1 + \dots + \beta_k X_k$$

Where:

- α = intercept,
- β = slope or coefficient and
- k = number of observations

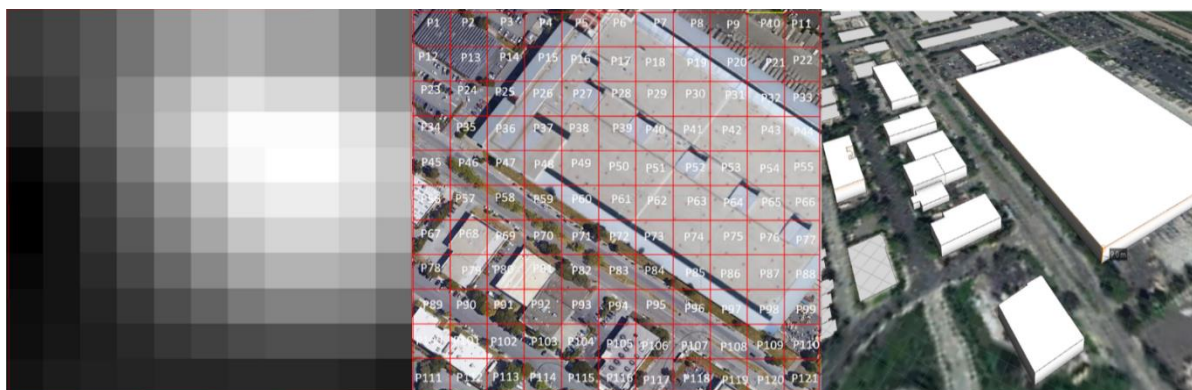


Figure 5: Illustration of corresponding area grid cells and pixel distribution and building dimension extraction interface on Esri 3D city engine, for A16.

For this study, the LST is the dependent variable (Y) while NDVI (vegetation), NDBI (horizontal density eg. Built up spaces), and EI (building/tree heights) are constituted as the independent variables. The 95% confidence level was adopted in analysing both the input and output parameters. Further analysis was conducted using the multi-nonlinear regression method, which assumes the nonlinearity of the relationship between the dependent variable Y and independent variables, and is expressed as Equation 3:

$$\text{Equation 3: Multi-nonlinear regression. } Y = \alpha + \beta_1 X_i + \beta_2 X_j + \beta_3 X_i^2 + \beta_3 X_j^2 + \dots + \beta_k X_i X_j$$

4. RESULTS

The proposed new parameter elevation index (EI) is used to assess the impact of the vertical morphology component in remote sensing based UHI study. From Figure 6, and Figure 7, we observe that Recreational areas (A1, A6, A14, A18, A19), all had lower LSTs due to their relatively high NDVI, low NDBI. However, A18 is seen to have a higher LST, because of the artificial grass covering the area. All commercial areas (A3, A5, A8, A11, A17), showed relatively high NDBIs and EI with relatively low NDVI, because of more built up areas and high rise buildings with very little vegetation, which reflects in their high LST values. Industrial areas (A7, A12, A13, A16, A20), has

the highest LST values, due to its higher NDBI values as most of it are factory buildings and tared drive ways, the EI on these areas are quite low, since there are not many tall trees or buildings in this area. A very low NDVI is observed here as well, because of the abundant artificial land covering in these areas.

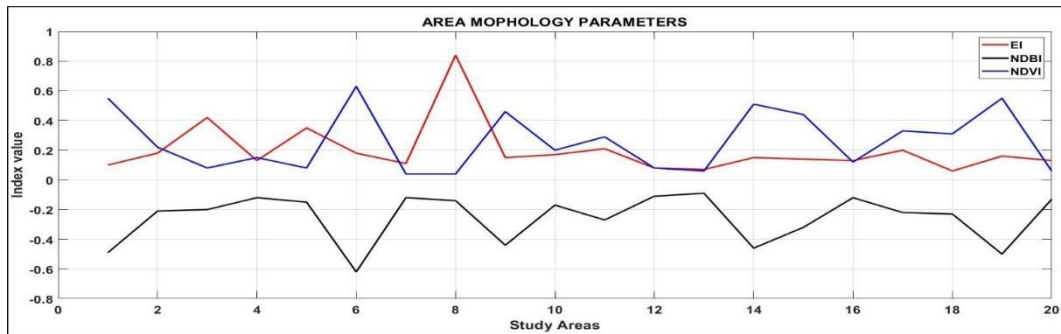


Figure 6: Area morphology index data

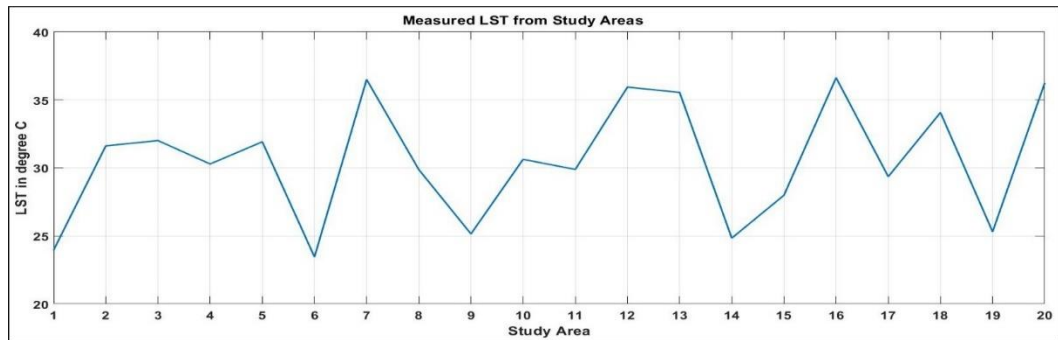


Figure 7: LST distribution graph across the 20 study areas

The residential areas (A2, A4, A9, A10, A15), are seen to have a relatively modest LST values, as it tends to have complimenting amount of vegetation (NDVI), with the built up area (NDBI) and a relatively homogenous elevation height in terms of buildings and tress throughout the region. Table 3 shows the area data for each five new areas chosen for the model validation.

Table 3: Model morphology parameters for model testing areas.

Area	NDBI	EI	NDVI	LST
TA1	-0.15	0.12	0.12	32.84
TA2	-0.27	0.17	0.31	28.56
TA3	-0.17	0.06	0.24	32.32
TA4	-0.13	0.13	0.18	32.23
TA5	-0.13	0.15	0.12	35.21

Figure 8 shows a fairly negative correlation trend between the EI and the LST, which qualified its inclusion in the proposed predictive model presented in this study. The NDBI, shows a positive correlation trend with LST, in agreement with a number of studies (Ahmed, 2018, Son et al., 2017). The NDVI, is seen to demonstrate a negative correlation with the LST. This agrees with the many similar findings in literature such as (Lima Alves and Lopes, 2017).

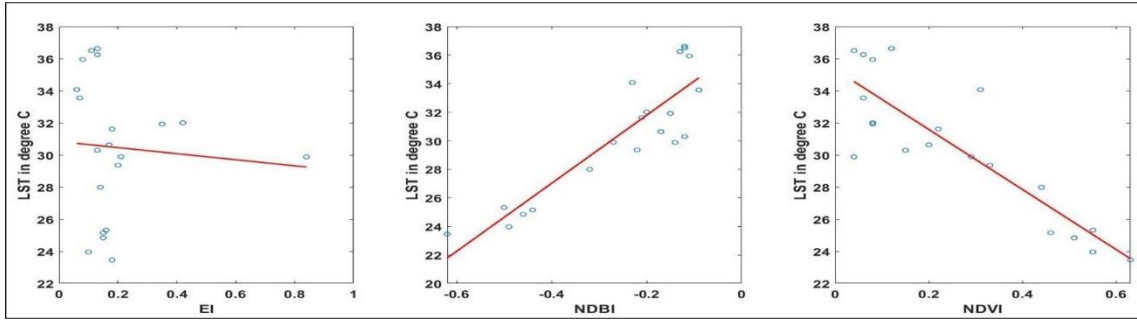


Figure 8: Scatter plot showing the correlation trend between the independent variables (NDBI, NDVI and EI) and the dependent variable LST.

4.1. Regression analysis

A series of regression analysis is conducted to develop a suitable predictive model. An MLR analysis firstly correlating the two satellite based horizontal parameters (NDBI and NDVI) with the LST is conducted. The second MLR analysis is conducted to correlate the new proposed EI alongside the NDBI and NDVI, with the LST. Then lastly a MNLR analysis was conducted to correlate EI, NDBI and NDVI, with the LST, essentially to determine if the relationship between the dependent and independent variables are more linear or non-linear so as to improve the predictive ability of the proposed model.

Table 4: Performance comparison between all the models considered.

Statistical Parameter	MLR W/O EI	MLR with EI	MNLR with EI
statistical significance	1.9×10^{-6}	1.8×10^{-7}	2.4×10^{-5}
R ²	0.79	0.88	0.88
R ² Adjusted	0.76	0.85	0.83
RMSE	4.40	2.74	3.20

The statistical information presented in Table 4, shows that the model with the new proposed EI is more statistically significant than the model without EI, because the model with EI explains the impact of both the vertical and horizontal morphology aspects on the dependent variable (LST), as opposed to only the horizontal impact, explained by the model without EI. Furthermore, R² and R² adjusted, which indicate prediction accuracy and statistical significance of newly added parameter respectively. The RMSE which represents the degree of variance between predicted and observed LST is significantly lower in the model with EI. The table also shows that the MNLR analysis cannot significantly improve the MLR model as R² remains the same while the RMSE increases. Also, the statistical significance measure of the MNLR model is seen to be lower than the MLR one. The performance graph of each model is presented in Figure 9.

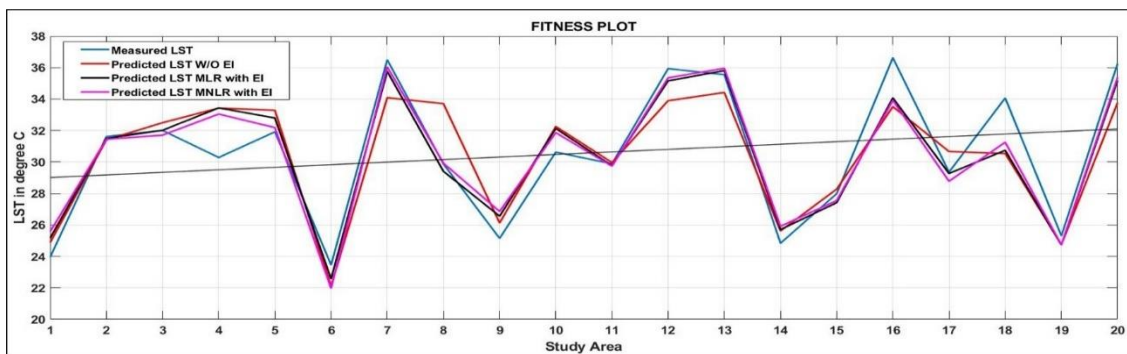


Figure 9: Fitness plot, showing a comparison between the predicted dependent variable of each model and the actual LST.

For the industrial areas (A7, A12, A13, A16 and A20), it is observed that the model without the EI performs the worst, and thus demonstrates the models weak LST predicting ability in areas of dominant elevation features, the model accuracy improves for A13, possibly because this area's EI value is lower than the rest, hence, its impact might have been negligible. The models with EI, performed overall better than the base model in the commercial area (A3, A5, A8, A11 and A17), where elevation features (high rise buildings) are dominant, which demonstrates the strength of the new model in accounting for elevation features to improve its predictive performance. The based model without the EI performed better than the models with EI in the residential areas (A2, A4, A9, A10, and A15), this can be related to the very negligible height variations between elevation features in these areas, especially building heights, hence, the effect of EI is negligible. However both new and base models performed poorly in

Areas 4 and 10. This is because although these areas are residential, nearly half of the entire area is a large unbuilt space occupied by trees, which can be considered by the model as a mix of recreational and residential area, hence the poor performance. The model without EI perform better in the Recreational areas (A1, A6, A14, A18, A19), possibly due to the low presence of elevation features in these areas, as most of it is an open grass lands or sport pitches. Although, all models performed poorly in Area 8, possibly due to the effect of the artificial covering over the surface which resulted in elevated LST, hence, the model is weak in explaining the LST causative factor as the causes of LST in this area is peculiar to it.

4.2. Predictive model

From the MLR analysis the P value for the parameters are as follows; NDVI (0.023), NDBI (0.75) and EI (0.0040). From these values, the new proposed EI is seen to be most significant morphology parameter, followed by the NDVI and lastly the NDBI. Hence the equation for the model used for the proposed equation is given as Equation 4.

$$\text{Equation 4: Proposed LST prediction equation. } LST = 37.76 - 8.66 (EI) + 2.90 (NDBI) - 18.67 (NDVI)$$

This model is validated by comparing the model predicted with the measured LST for five new areas as shown in Figure 10. From Figure 10, the model without the EI performed better in Trial Area 1 which is a commercial area, possibly due to the large sport pitch covered with artificial materials that intensify the LST, hence the model is unable to explain this as a function EI. However, the model with EI performed is seen to be better in areas 3 and 4, which are residential areas, this is possibly due to the negligible height variance between buildings in these regions thereby making the model consider the area's EI as one homogenous shape, hence the ease in predicting the temperature spread across the areas. Trial areas 2 (Recreational) and areas 1 and 5 (commercial); can easily be described as areas with more height variance, which could have limited the models performance in its LST prediction. Also, the fact that the LST used in this study was acquired by Landsat on 01-06-2018, at 18:44:51 could also explain the variance as this does not reflect the daily average performance of each area.

5. CONCLUSION

It can be concluded that, Vertical morphology features impact significantly on UHI formation and intensity, as the new proposed elevation parameter (EI) showed a statistical significant P value in the regression analysis. Also the integration of EI to the conventional 2D satellite based morphology parameter model, significantly improves its predictive performance. Although, the model without EI, tend to perform better than the models with EI in areas of low elevation features. The relationship between the considered morphology parameters and the LST are linear as the MLR performed better overall in its predictive ability in comparison to the MNLR. The EI and NDVI have a negative correlation with the LST, while the NDBI demonstrates a positive correlation with the LST.

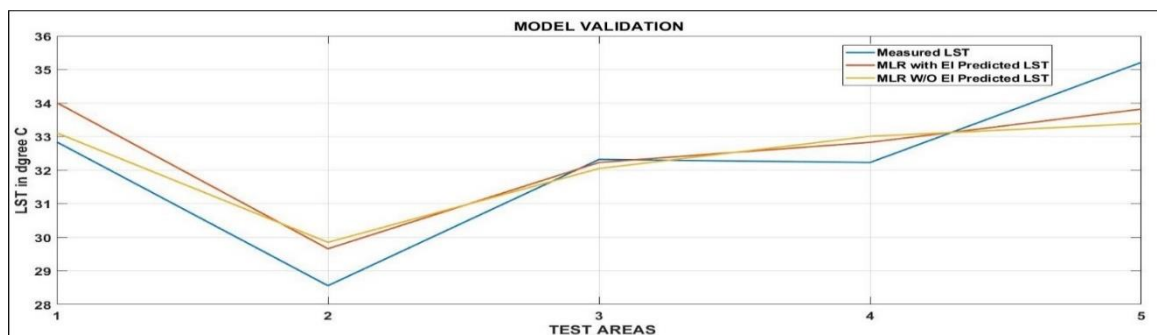


Figure 10: Model testing result, showing model performance in LST prediction.

6. REFERENCES

Ahmed, S. 2018. Assessment of urban heat islands and impact of climate change on socioeconomic over Suez Governorate using remote sensing and GIS techniques. *The Egyptian Journal of Remote Sensing and Space Science*, 21, 15-25.

Benediktsson, J. A., Chanussot, J. & Fauvel, M. Multiple Classifier Systems in Remote Sensing: From Basics to Recent Developments. 2007 Berlin, Heidelberg. Springer Berlin Heidelberg, 501-512.

Chen, X.-L., Zhao, H.-M., Li, P.-X. & Yin, Z.-Y. 2006. Remote sensing image-based analysis of the relationship between urban heat island and land use/cover changes. *Remote Sensing of Environment*, 104, 133-146.

EsriCityEngine. 2019. *Build a city in five steps* [Online]. Available: <https://www.esri.com/en-us/arcgis/products/esri-cityengine/overview> [Accessed 21st June 2019].

Germaine, K. A. 2011. Delineation of Impervious Surface from Multispectral Imagery and Lidar Incorporating Knowledge Based Expert System Rules. *Photogrammetric engineering and remote sensing*, v. 77, pp. 75-85-2011 v.77 no.1.

GoldenGateWeatherServices. 2009. *Climate of San Francisco Narrative* [Online]. Available: <https://www.ggweather.com/sf/narrative.html> [Accessed 8th November 2018].

GoogleEarth. 2019. *San Francisco*.

He, C., Shi, P., Xie, D. & Zhao, Y. 2010. Improving the normalized difference built-up index to map urban built-up areas using a semiautomatic segmentation approach. *Remote Sensing Letters*, 1, 213-221.

Keqi, Z., Shu-Ching, C., Whitman, D., Mei-Ling, S., Jianhua, Y. & Chengcui, Z. 2003. A progressive morphological filter for removing nonground measurements from airborne LIDAR data. *IEEE Transactions on Geoscience and Remote Sensing*, 41, 872-882.

Landsat.USGS.Gov. 2014. *What are the band designations for the Landsat satellites* [Online]. U.S. Geological Survey. Available: <https://landsat.usgs.gov/what-are-band-designations-landsat-satellites> [Accessed 2 November 2018].

Li, H., Zhou, Y., Li, X., Meng, L., Wang, X., Wu, S. & Sodoudi, S. 2018. A new method to quantify surface urban heat island intensity. *Science of The Total Environment*, 624, 262-272.

Li, Z., Quan, S. J. & Yang, P. P.-J. 2016. Energy performance simulation for planning a low carbon neighborhood urban district: A case study in the city of Macau. *Habitat International*, 53, 206-214.

Lima Alves, E. & Lopes, A. 2017. The Urban Heat Island Effect and the Role of Vegetation to Address the Negative Impacts of Local Climate Changes in a Small Brazilian City. *Atmosphere*, 8, 18.

Liu, H. & Weng, Q. 2012. Enhancing temporal resolution of satellite imagery for public health studies: A case study of West Nile Virus outbreak in Los Angeles in 2007. *Remote Sensing of Environment*, 117, 57-71.

Mathworks.com. 2014. *how to extract the value pixel valu from image? - MATLAB Answers - MATLAB Central* [Online]. Available: <https://www.mathworks.com/matlabcentral/answers/151779-how-to-extract-the-value-pixel-valu-from-image> [Accessed].

Mavrogianni, A., Wilkinson, P., Davies, M., Biddulph, P. & Oikonomou, E. 2012. Building characteristics as determinants of propensity to high indoor summer temperatures in London dwellings. *Building and Environment*, 55, 117-130.

Meng, Q., Zhang, L., Sun, Z., Meng, F., Wang, L. & Sun, Y. 2018. Characterizing spatial and temporal trends of surface urban heat island effect in an urban main built-up area: A 12-year case study in Beijing, China. *Remote Sensing of Environment*, 204, 826-837.

Mirzaei, P. A. & Haghighat, F. 2010. Approaches to study Urban Heat Island – Abilities and limitations. *Building and Environment*, 45, 2192-2201.

Mirzaei, P. A., Olsthoorn, D., Torjan, M. & Haghighat, F. 2015. Urban neighborhood characteristics influence on a building indoor environment. *Sustainable Cities and Society*, 19, 403-413.

Nakata-Osaki, C. M., Souza, L. C. L. & Rodrigues, D. S. 2018. THIS – Tool for Heat Island Simulation: A GIS extension model to calculate urban heat island intensity based on urban geometry. *Computers, Environment and Urban Systems*, 67, 157-168.

Oke, T. 1982. The energetic basis of urban heat island. *Quarterly Journal of the Royal Meteorological Society*, 108, 1-24.

Polydoros, A. & Cartalis, C. 2015. Use of Earth Observation based indices for the monitoring of built-up area features and dynamics in support of urban energy studies. *Energy and Buildings*, 98, 92-99.

Roy, D. P., Wulder, M. A., Loveland, T. R., C.E. W., Allen, R. G., Anderson, M. C., Helder, D., Irons, J. R., Johnson, D. M., Kennedy, R., Scambos, T. A., Schaaf, C. B., Schott, J. R., Sheng, Y., Vermote, E. F., Belward, A. S., Bindschadler, R., Cohen, W. B., Gao, F., Hipple, J. D., Hostert, P., Huntington, J., Justice, C. O., Kilic, A., Kovalskyy, V., Lee, Z. P., Lyburner, L., Masek, J. G., Mccorkel, J., Shuai, Y., Trezza, R., Vogelmann, J., Wynne, R. H. & Zhu, Z. 2014. Landsat-8: Science and product vision for terrestrial global change research. *Remote Sensing of Environment*, 145, 154-172.

Son, N.-T., Chen, C.-F., Chen, C.-R., Thanh, B.-X. & Vuong, T.-H. 2017. Assessment of urbanization and urban heat islands in Ho Chi Minh City, Vietnam using Landsat data. *Sustainable Cities and Society*, 30, 150-161.

Stoter, J., Van Den Brink, L., Beetz, J., Ledoux, H., Reuvers, M., Janssen, P., Penninga, F., Vosselman, G. & Oude Elberink, S. 2013. Three-dimensional modeling with national coverage: case of The Netherlands. *Geo-spatial Information Science*, 16, 267-276.

Streutker, D. R. 2003. Satellite-measured growth of the urban heat island of Houston, Texas. *Remote Sensing of Environment*, 85, 282-289.

U.S.CensusBureau. 2017. *QuickFacts: San Francisco County, California; UNITED STATES* [Online]. United States of America: United States Department of Commerce. Available: <https://www.census.gov/quickfacts/fact/table/sanfranciscocountycalifornia,US/PST045217> [Accessed 08 November 2018].

Wang, R. 2013. 3D building modeling using images and LiDAR: a review. *International Journal of Image and Data Fusion*, 4, 273-292.

Yan, W. Y., Shaker, A. & El-Ashmawy, N. 2015. Urban land cover classification using airborne LiDAR data: A review. *Remote Sensing of Environment*, 158, 295-310.

Zha, Y., Gao, J. & Ni, S. 2003. Use of normalized difference built-up index in automatically mapping urban areas from TM imagery. *International Journal of Remote Sensing*, 24, 583-594.

#281: Experimental research on heat transfer and pressure drop characteristics of R410a within an asymmetric plate evaporator

Yang LI¹, Shaozhi ZHANG², Yiyang XU³, Ruihua DONG⁴

¹ Institute of Refrigeration and Cryogenics, School of Energy Engineering, Zhejiang University, 310027 Hangzhou China, 1831923654@qq.com

² Institute of Refrigeration and Cryogenics, School of Energy Engineering, Zhejiang University, 310027 Hangzhou China, enezsz@zju.edu.cn

³ Huadong Engineering Corporation Limited, Power Construction Corporation of China, 310014 Hangzhou China, 458968041@qq.com

⁴ Institute of Refrigeration and Cryogenics, School of Energy Engineering, Zhejiang University, 310027 Hangzhou China, 895220868@qq.com

Conventional plate heat exchangers (PHE) have identical channel geometries on both hot and cold sides. This kind of symmetrical PHE cannot perform well in situations of evaporative heat transfer because the fluid flow rates on both sides are unbalanced. Asymmetric PHE provides channels of different cross-sectional flow areas to achieve balanced flow, which makes the pressure drops on both sides closer and leads to the enhancement of heat transfer. In this paper, experiments were carried out to study the heat transfer and pressure drop characteristics of an asymmetric plate evaporator (APE) with R410a as refrigerant and ethylene glycol (EG) solution as secondary refrigerant. For comparison, a conventional plate evaporator (CPE) was also tested under the same conditions. The operating conditions of the experiments are as follows: evaporation temperature, -2 - 8°C ; inlet temperature of EG solution, 8 - 24°C ; volume flow rate of EG solution, 30 - $80\text{ L}\cdot\text{min}^{-1}$; R410a mass flux, 13 - $44\text{ kg}\cdot\text{m}^{-2}\cdot\text{s}^{-1}$; heat flux, 4 - $13\text{ kW}\cdot\text{m}^{-2}$. The results imply that the APE has better heat transfer performance, the energy density of which is about 20%-40% higher than that of CPE. It means that the APE can make the size of heat exchanger smaller and reduce the charge of the refrigerant when the same heat duty is achieved. Through in-depth analysis, the R410a heat transfer coefficient of APE is estimated to be around 27% higher than that of CPE under the same Reynolds number, which demonstrates that the unequal depth corrugated structure of APE is beneficial for heat transfer. Moreover, the fanning friction factor of R410a in APE is lower than that in CPE under the same equivalent Reynolds number, which is mainly due to the smaller corrugation pressing depths of APE.

Keywords: plate evaporator; asymmetric; heat transfer; pressure drop; performance

1. INTRODUCTION

Plate heat exchangers (PHE) are widely used in industrial applications and air-conditioning systems compared with shell-and-tube heat exchangers due to its significant advantages such as extremely high heat transfer rates, flexibility of flow arrangements, ease to clean maintaining hygiene and small footprint (Wang, 2007). Conventional PHE have identical channel geometries on both hot and cold sides. This symmetrical geometry is very effective when both fluids have the same duty requirement and pressure drop. But typical applications in today's marketplace involve unequal flow rates with varying duty requirements for the hot and cold fluids (Chang, 2008 & Lee, 2013). Besides, in situations where fluids have different viscosities or when one fluid is easy to scale, it is necessary that the more viscous of the fluids has as little resistance to flow as possible, or that the impurity fluid is provided with wider channels to flow through. When the conditions are such, both fluids can never be totally optimised with symmetrical channels, and the exchanger will not be the most economical.

The proposal of the asymmetric PHE is one way to deal with such asymmetric conditions. The asymmetric PHE has channels with different structures on hot and cold sides and the characteristics of the channels are also different. Through matching the volume of the cold and hot side channels with the fluid flow rates, the pressure drop on both sides will be more balanced and the heat transfer efficiency may be improved. For the design of asymmetric plates, there are several patented inventions (Wang, 1992 & Dahlgren, 1998 & Ulf Vestergren 2001 & Dahlgren 2010). Wang et al. proposed a new type of plate, in which the sinusoidal waveform with alternating amplitudes was taken as the basic waveform, and the asymmetric heat transfer channel was obtained by the reverse or forward stacking of adjacent plates (Wang, 1992). Dahlgren et al. proposed an asymmetric PHE with a wide fluid range, which realised the asymmetry and high adaptability of the heat exchanger by adjusting the distance between plates with bolts (Dahlgren, 1998). In addition, some researches on the heat transfer and pressure drop characteristics of asymmetric PHE are available (Focke, 1985 & Utraiainen, 2002 & Kim, 2013). Focke carried out a study on the "asymmetrically corrugated" plate type heat exchangers, which have channels of different cross-sectional flow area. It was found that these asymmetric profiles have a lower heat transfer rates compared to the conventional sinusoidal symmetric surfaces. When the pressure drop requirement differs, however, these geometries can be advantageous (Focke, 1985). Kim et al. investigated the asymmetric PHE of different geometry by the numerical study. The results indicated that the effect of the asymmetric profile is highly sensitive to the given operating conditions and the designs (Kim, 2013).

Based on the advantages of asymmetric PHE, it's easy to think of applying it to the two-phase flow, such as evaporators or condensers, where one fluid has much higher flow rate than the other. A similar experimental investigation is available by Lee et al. (Lee, 2013). In this investigation, the resistance and heat transfer correlations of a new type of asymmetric heat exchanger was studied when it worked as an evaporator, and it showed that the asymmetric profiles were significantly superior to the symmetric profiles. However, the heat exchanger adopted in the study is not a kind of PHE in the general sense. To conclusion, the existing researches mainly focus on the single-phase flow, no studies on two-phase heat transfer in asymmetric PHE are available. In actual, even if the two-phase flow characteristics in conventional PHE, only a few experimental works are found (Hsieh, 2002 & Han, 2003 & Rossato, 2016 & Djordjevic, 2008 & Muhammad, 2017). Hsieh et al. studied the saturated flow boiling heat transfer and pressure drop of refrigerant R410A in a vertical plate heat exchanger, and three impact factor: heat flux, refrigerant mass flux and refrigerant pressure were studied in depth (Hsieh, 2002). Han et al. performed flow boiling experiments with the refrigerants R410a and R22 in PHEs with different chevron angles. The results demonstrate that larger chevron angle creates stronger turbulence and more abrupt changes of the flow path, which intensifies the heat transfer (Han, 2003). Rossato et al. presented measurements of heat transfer coefficient obtained during flow boiling of R32 inside a brazed PHE and compared the experimental data to the previous studies (Rossato, 2016).

Due to the lacking of research on the asymmetric PHE under two-phase flow conditions, the present work aims to provide a preliminary exploration of the thermal and hydraulic performance of an asymmetric plate evaporator (APE) by experiment. The APE adopted in this study is made by alternately stacking the equal depth corrugated plate and unequal depth corrugated plate. R410a and ethylene glycol (EG) solution are selected as working fluids. For performance assessment, the asymmetric plate evaporator is compared with the conventional plate evaporator (CPE) under a series of working conditions.

2. EXPERIMENTAL SETUP

2.1. Tested plate evaporator

Figure 1(a) presents a schematic of the chevron plate and its main geometrical parameters. The cross-section profiles of the symmetric and asymmetric plate heat exchangers are shown in Figure 1(b). Based on the conventional sinusoidal profile, if the corrugation depth (b_1) is same for adjoining plates, the cross-section area of the channel on two sides will be identical, if one plate has unequal corrugation depth (b_1 , b_2), by means of alternately stacking the equal depth corrugated plate and unequal depth corrugated plate, the cross-section area

of the channel on two sides will be different. Because the ratio of the depth of high corrugation to the depth of low corrugation can be changed, the design flexibility can be achieved easily. The geometrical parameter values of APE and CPE adopted in this experiment are shown in Table 1 and Table 2.

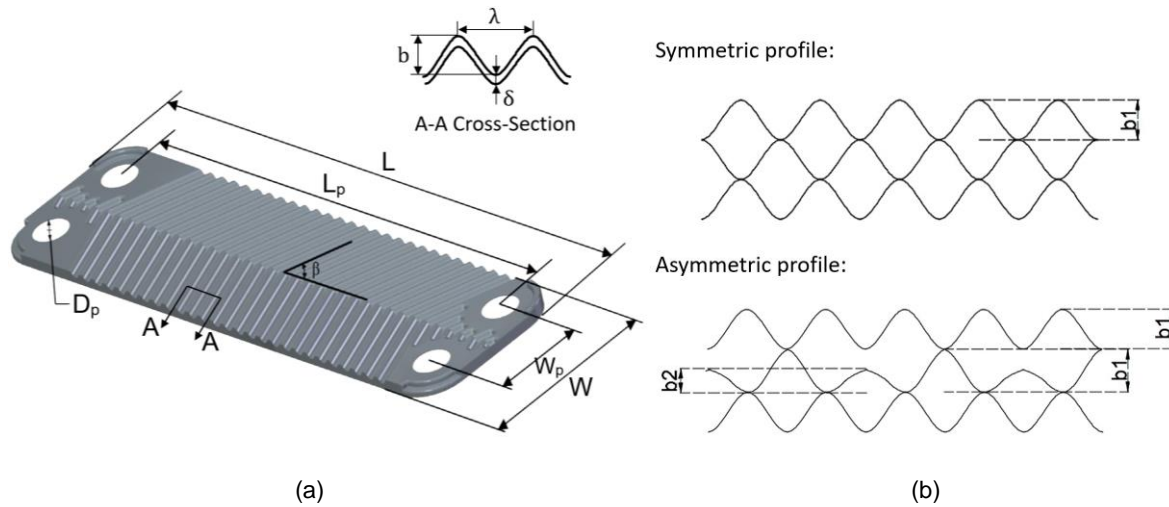


Figure 1: Drawing of the chevron plate prototype and the related geometrical parameters

Table 1: The same geometrical data of the two types of plate evaporators

Parameters	Value
Plate length (L), mm	525
Plate width (W), mm	107
Longitudinal distance between ports (L_p), mm	466
Lateral distance between ports (W_p), mm	50
Port diameter (D_p), mm	34
Chevron angle (β), °	65
Plate thickness (δ), mm	0.4
Corrugation pitch (λ), mm	7
Corrugation depth (b_1, b_2), mm	2, 1
Heat transfer area (projected area), (A_{hi}), m ²	0.5
Number of hot side channels	15
Number of cold side channels	14

Table 2: The different geometrical data of the two types of plate evaporators

Parameters	Value of APE		Value of CPE
	wide channel	narrow channel	
Equivalent diameter (D_{eq}), mm	4.75	3.65	4.2
Cross sectional area of single channel (A_c), mm ²	237	162	206
Volume for single channel (V), cm ³	139	107	128

2.2. Test facility

Figure 2 shows a schematic of the experimental system, which consists of two loops: the EG solution (hot-side) loop and the R410a (cold-side) loop. The concentration of EG solution is 80 wt%. For EG solution loop, a 9 kW electrical heater, a tank, a pump, a magnetic flow meter, a triple valve and one side of the test plate evaporator are included. And the R410a loop contains the other side of the test plate evaporator, a compressor (BOCK, 15 kW), an air cooled condenser, a mass flow meter, an expansive valve and so on. The test plate evaporator has a counter flow arrangement with R410a flowing through the channels upwardly and EG solution flowing downwardly. For the APE, R410a flows through the narrow channels due to its smaller mass flow rate.

There are three types of measuring instruments in our experimental setup: temperature sensor, pressure transducer, and flow meter. The PT-100 thermometers are mounted at the inlet and outlet of the test plate evaporator to calculate the heat supplied to the evaporator. The differential and absolute pressures are measured with micro pressure transducers, which are placed near the port of two streams. The Micro-motion Coriolis type flow meter is applied to measure the mass flow rate of the R410a. And the volume flow rate of the EG solution is measured by magnetic flow meter (YOKOGAWA, AXF025G). A summary of the accuracies of the measured parameters is listed in Table 3.

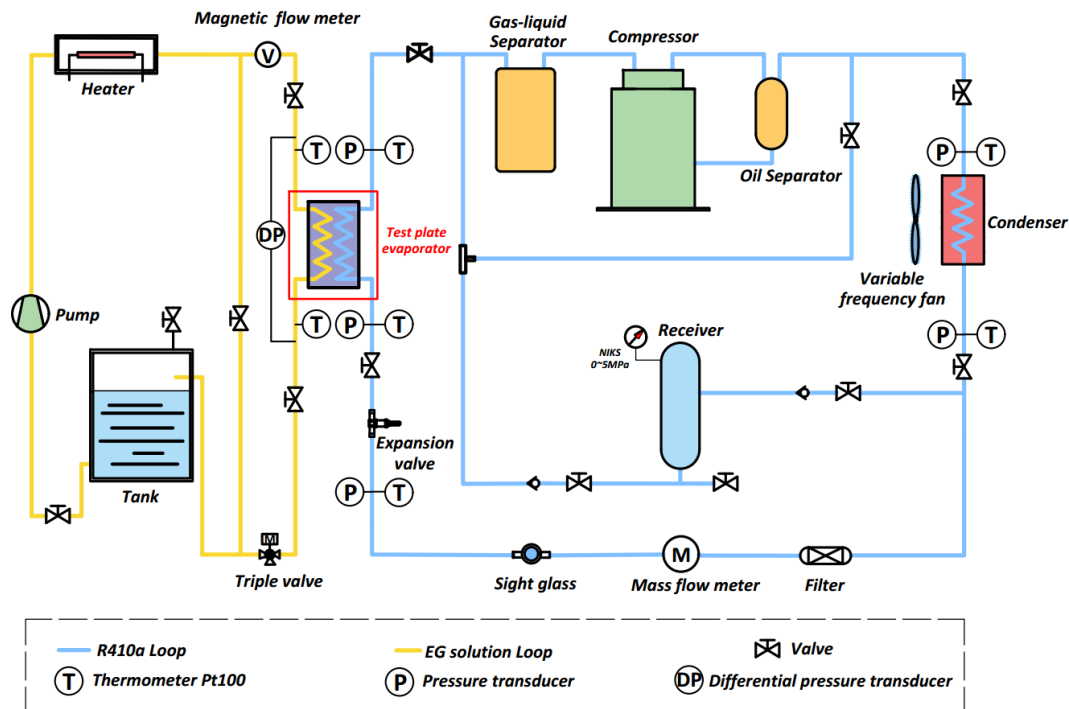


Figure 2: Schematic diagram of the test system

Table 3: Summary of the measured parameters accuracy

Measured Parameters	Type of sensor	Range	Accuracy
Fluid temperature	PT-100 thermometer	-50-500 (°C)	±0.1 K
Absolute pressure	Pressure transducer	0-5 (MPa)	±0.2%
Differential pressure	Pressure transducer	0-200 (kPa)	±0.25%
Mass flow rate of R410a	Coriolis flow meter	0-0.378 (kg/s)	±0.2%
Volume flow rate of EG solution	Magnetic flow meter	0-17.671 (m ³ /h)	±0.2%

2.3. Experimental procedure

The performance of different types of plate evaporators was tested under various operating conditions. During the tests, the condensation pressure and condenser outlet subcooling were set as constant values so that the inlet enthalpy of R410a in the evaporator was constant under the assumption of isenthalpic throttling in the expansion valve. And the speed of the compressor was adjusted to guarantee a certain superheat degree of R410a at the evaporator outlet. Three main parameters were changed in a certain step to achieve different working conditions: evaporation temperature, EG solution inlet temperature and EG solution flow rate. The change of evaporation temperature depended on the opening degree of the expansion valve whereas the change of EG solution flow rate depended on the opening degree of the triple valve, and the EG solution temperature was controlled by the input power of electrical heater. Therefore, the R410a mass flux and the heat flux were changed indirectly. The detailed operating conditions of the experiment are shown in Table 4.

During the experiment, the system could be controlled automatically and the measured data was collected by a commercial software. A range between 60 and 90 min was allowed to reach statistically the steady state condition. Then, the data acquisition system started to record data after 30 min of stability. The energy balance deviation between hot-side and cold-side for 60 measurements of all plate evaporator is within ±5%.

Table 4: Operating conditions of the experiment

Parameters	As constant	As variable
Condensation temperature [°C]	45	/
Condenser outlet subcooling [°C]	5	/
Evaporation temperature [°C]	2	-2 - 8
Evaporator outlet superheat [°C]	5	/
EG solution inlet temperature [°C]	16	8-24
EG solution volume flow rate [L/min]	50	30 - 80
R410a mass flux [kg·m ⁻² ·s ⁻¹]	/	13 - 44
Heat flux [kW·m ⁻²]	/	4 - 13
Number of test cases per plate evaporator	20	/

3. DATA REDUCTION

In order to investigate the heat transfer and pressure drop characteristics of the plate evaporator, the overall heat transfer coefficient, the heat transfer coefficients and friction factors of R410a must be determined from the measured values of the temperature and pressure.

3.1. Heat transfer coefficient

Based on energy balance, the R410a side heat transfer rate equals to the EG solution side heat transfer rate.

Equation 1: Heat balance equation.
$$Q = Q_h = Q_c = \rho_h \cdot \dot{V}_h \cdot c_{p,h} \cdot (T_{h,i} - T_{h,o})$$

Where:

- Q_h/Q_c = heat transfer rate of hot/cold side (W)
- ρ_h = density of the EG solution (kg m^{-3})
- \dot{V}_h = volume flow rate of the EG solution ($\text{m}^3 \text{s}^{-1}$)
- $c_{p,h}$ = specific heat capacity of the EG solution ($\text{J kg}^{-1}\text{K}^{-1}$)
- $T_{h,i}/T_{h,o}$ = inlet/outlet temperature of the EG solution ($^{\circ}\text{C}$)

The overall heat transfer coefficient was calculated by the following equation:

Equation 2: Heat transfer equation.
$$U = \frac{Q}{A_{ht} \cdot \Delta T_{LMTD}}$$

Where:

- U = overall heat transfer coefficient ($\text{W m}^{-2} \text{K}^{-1}$)
- A_{ht} = effective heat transfer area (m^2)
- ΔT_{LMTD} = logarithmic mean temperature difference ($^{\circ}\text{C}$)

When there is flow boiling as well as superheating, the logarithmic mean temperature difference (LMTD) is given by Equations 3 to 7:

Equation 3: LMTD under flow boiling as well as superheating.
$$\Delta T_{LMTD} = Q / (Q_{tp} / \Delta T_{tp} + Q_{sh} / \Delta T_{sh})$$

Equation 4: Heat transfer rate in two-phase zone.
$$Q_{tp} = \dot{m}_h c_{p,h} (T_{h,t} - T_{h,o})$$

Equation 5: Heat transfer rate in superheating zone.
$$Q_{sh} = \dot{m}_h c_{p,h} (T_{h,i} - T_{h,t})$$

Equation 6: LMTD in two-phase zone.
$$\Delta T_{tp} = \frac{T_{h,t} - T_{h,o}}{\ln[(T_{h,t} - T_{sat}) / (T_{h,o} - T_{sat})]}$$

Equation 7: LMTD in superheating zone.
$$\Delta T_{sh} = \frac{(T_{h,i} - T_{c,o}) - (T_{h,t} - T_{sat})}{\ln[(T_{h,i} - T_{c,o}) / (T_{h,t} - T_{sat})]}$$

Where:

- \dot{m}_h = mass flow rate of the EG solution (kg s^{-1})
- T_{sat} = evaporation temperature of R410a ($^{\circ}\text{C}$)
- $T_{c,o}$ = outlet temperature of R410a ($^{\circ}\text{C}$)

The temperature of hot side fluid corresponding to turning point of refrigerant between the two-phase zone and the superheating zone is given by the following equation:

Equation 8: Turning point temperature of the EG solution.
$$T_{h,t} = T_{h,i} - [\dot{m}_c c_{p,c,g} (T_{c,o} - T_{sat}) / (\rho_h \dot{V}_h c_{p,h})]$$

Where:

- \dot{m}_c = mass flow rate of R410a (kg s^{-1})
- $c_{p,c,g}$ = specific heat capacity of R410a in superheating zone ($\text{J kg}^{-1}\text{K}^{-1}$)

Once the overall heat transfer coefficient has been obtained, the saturated flow boiling heat transfer coefficient of R410a side is evaluated from the following equation:

Equation 9: Calculation of heat transfer coefficient of R410a.
$$\frac{1}{h_c} = \frac{1}{U} - \frac{1}{h_h} - \frac{\delta}{k_w}$$

Where:

- h_c = convective heat transfer coefficient of R410a ($W m^{-2} K^{-1}$)
- h_h = convective heat transfer coefficient of the EG solution ($W m^{-2} K^{-1}$)
- δ = plate thickness (m)
- k_w = thermal conductivity ($W m^{-1} K^{-1}$)

The EG solution heat transfer coefficient is calculated by the correlations proposed by Yang, which is suitable for high Prandtl number fluids (Yang, 2017).

3.2. Pressure drop

The total pressure drop between the inlet and outlet of the R410a side consists of four components: static pressure drop due to the vertical configuration of heat exchangers, pressure drop due to acceleration of the refrigerant, pressure drop due to inlet/outlet manifolds and frictional pressure drop through the main core of plate channel. The frictional pressure drop accounts for the main part and can be obtained by removing other pressure loss factors from this total pressure drop.

Equation 10: Calculation of frictional pressure drop.
$$\Delta P_f = \Delta P_{total} - \Delta P_{static} - \Delta P_{momentum} - \Delta P_{port}$$

Equation 11: Calculation of static pressure drop.
$$\Delta P_{static} = g \cdot \rho_{c,m} \cdot L_p$$

Equation 12: Mean density of R410a in the two-phase zone.
$$\rho_{c,m} = \left(\frac{x_m}{\rho_v} + \frac{1-x_m}{\rho_l} \right)^{-1}$$

Equation 13: Calculation of acceleration pressure drop.
$$\Delta P_{momentum} = G^2 \cdot (1/\rho_v - 1/\rho_l) \cdot \Delta x$$

Equation 14: Calculation of port pressure drop.
$$\Delta P_{port} = 0.75 \left[\frac{G_{port}^2}{2\rho_i} + \frac{G_{port}^2}{2\rho_o} \right]$$

Where:

- g = acceleration of gravity ($m s^{-2}$)
- L_p = effective channel length (m)
- x_m = mean vapour quality of R410a in the two-phase zone
- Δx = vapour quality difference between the inlet and outlet of the channel
- ρ_v/ρ_l = vapour/liquid phase density of R410a in the two-phase zone ($kg m^{-3}$)
- ρ_i/ρ_o = density of R410a in the inlet/outlet port ($kg m^{-3}$)
- G = mass flux of R410a ($kg m^{-2} s^{-1}$)
- G_{port} = mass flux of R410a in the port ($kg m^{-2} s^{-1}$)

Finally, the two-phase friction factor for evaporation of refrigerant is given by the following equation:

Equation 15: Fanning friction factor formula.
$$f = \frac{\Delta P_f D_{eq} \rho_m}{2 L_p G^2}$$

Where:

D_{eq} = equivalent diameter of cold side channel (m)

3.3. Uncertainty analysis

The experimental uncertainty analysis has been performed in agreement with the guidelines provided (JCGM, 2008). In order to get the uncertainty of indirect measurements the law of error propagation is used, given by the following equation:

Equation 16: Uncertainty transfer formula.

$$\pm \varepsilon_F = \sqrt{\sum_i \left(\frac{\partial F}{\partial x_i}\right)^2 \varepsilon_{x_i}^2}$$

Where:

- x_i = measured value, as in present case temperature, pressure, mass flow meter, and heat exchanger geometrical measurements
- F = parameter or factor for which the uncertainty is being calculated
- ε = uncertainty in the measured valued as specified by the manufacturer

4. RESULT AND DISCUSSION

Table 5 summarises the uncertainty of the final results calculated from the measured parameters. As mentioned above, the change of working conditions is realised by varying three parameters: EG solution inlet temperature, EG solution volume flow rate and evaporation temperature, then R410a mass flux and heat flux will change within a certain range consequently. The following results are selected to illustrate the boiling heat transfer and pressure drop characteristics of R410A in APE and CPE respectively.

Table 5: Estimated uncertainty of the final results

Calculated parameters	Range	Accuracy
Logarithmic mean temperature difference	4-16.2 (°C)	±1.3-5.1%
Heat duty	6.3-18.7 (kW)	±2.2-5.2%
Overall heat transfer coefficient	667-1206 (W·m ⁻² ·K ⁻¹)	±2.7-7.4%
R410a flow boiling heat transfer coefficient	860-2230 (W·m ⁻² ·K ⁻¹)	±5.6-18.7%
Friction pressure drop	6.6-21.4 (kPa)	±0.8-4.2%
R410a friction factor	1.9-4.6	±2.4-9.6%

4.1. Boiling heat transfer

Figures 3 to 5 show the energy density for two plate evaporators as EG solution inlet temperature, EG solution volume flow rate and evaporation temperature change, respectively. The energy density is defined as a heat duty per unit volume of the heat exchanger (Dae, 2017). The curves in the figures intuitively indicate that energy density increases as the inlet temperature and volume flow rate of EG solution increases, but decreases as the evaporation temperature rises. It's easy to understand that the temperature difference driving heat transfer increases as the EG solution inlet temperature increases and the evaporation temperature decreases, thus the heat duty improves. As for EG solution volume flow rate, it mainly influences the convective heat transfer coefficient of the hot side, when it increases, the overall heat transfer coefficient also increases.

By Comparing two plate evaporators, it can be found that the energy density of APE is around 20%-40% higher than that of CPE, which reflects the higher heat transfer efficiency of APE. For one thing, the use of APE can reduce the size of the heat exchanger compared with CPE when equal heat duty is achieved, thus saving the space and cost. For another, the charge of refrigerant in APE can be reduced, especially for some harmful refrigerants. Therefore, the application of APE is of great significance for maintaining safety, saving energy and protecting the environment.

The results about energy density obtained above is an overall performance of PHE, more in-depth analysis is needed. There are two possible reasons to explain the advantage of the APE in heat transfer performance. The first one is that the APE matches the volume of the channels with the flow rate of the fluids, making the flow velocity and convective heat transfer coefficient of both fluids more balanced, which is analogy with single-phase flow. For single-phase flow, the formula of the convective heat transfer coefficient in the flow path on both sides is very close, on general, similar flow velocity or mass flux of hot and cold side fluids means more balanced convective heat transfer coefficient, therefore, the overall heat transfer coefficient will increase when the flow rate of fluids does not change. However, evaporative heat transfer is more complicated and it's difficult to find an optimal point to match the asymmetry of PHE with the fluid conditions.

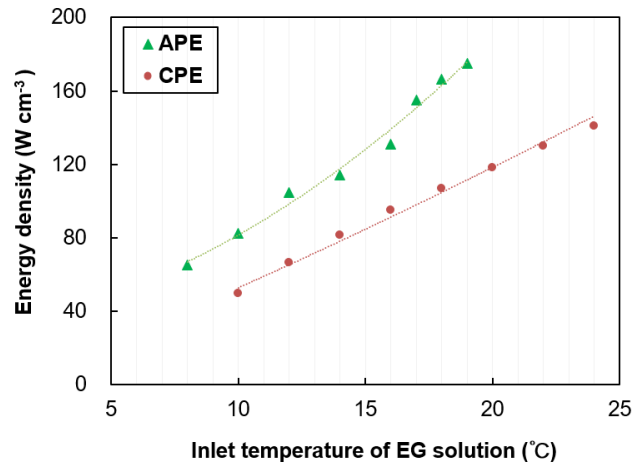


Figure 3: Effect of EG solution inlet temperature on energy density when evaporation temperature is 2°C and EG solution volume flow rate is 50 L/min

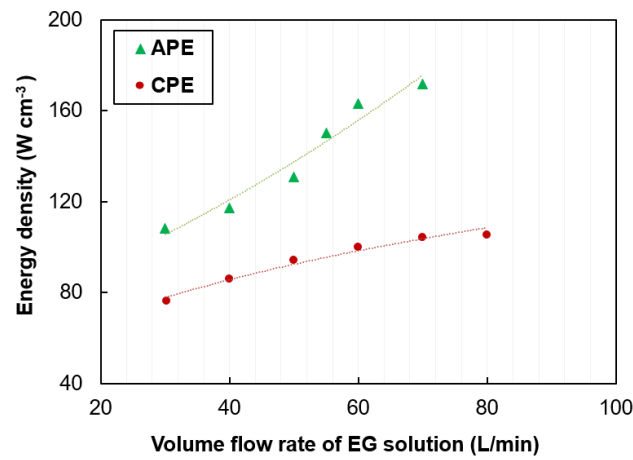


Figure 4: Effect of EG solution volume flow rate on energy density when evaporation temperature is 2°C and EG solution inlet temperature is 16°C

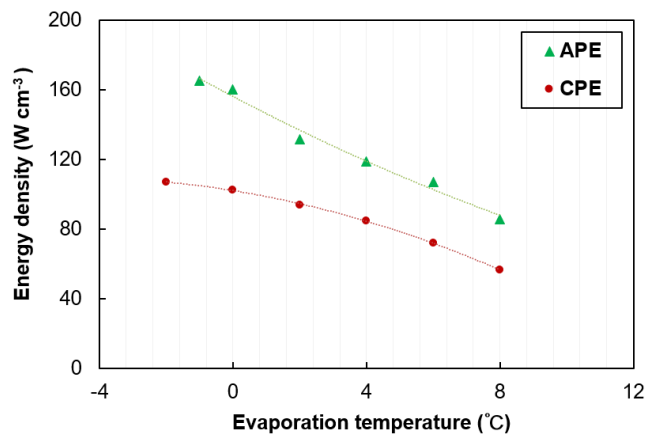


Figure 5: Effect of evaporation temperature on energy density when EG solution volume flow rate is 50 L/min and EG solution inlet temperature is 16°C

Figure 6 shows the effect of mass flux ratio of hot and cold side fluid on the overall heat transfer coefficient for the test plate evaporators. When mass flux ratio varies from 2.8 to 3.6, both the overall heat transfer coefficients of APE and CPE increase. For evaporation, since one side is the sensible heat transfer of a single-phase fluid and the other side is the boiling heat transfer of a two-phase fluid, the formula of the convective heat transfer coefficient of both sides is quite different. In particular, the dependence relationship of mass flux on the heat transfer coefficient is significantly different when PHE or refrigerant changes. The cross sectional area ratio of hot-side channel to cold-side channel of APE proposed in this paper is 1.46, obviously, the optimal mass flux ratio is much larger than this value. Limited by experiment data, there is no optimal point presented. In theory, continue to increase the mass

flux ratio range when the total mass flux is kept constant, an optimum mass flux ratio can be found to maximise the total heat transfer coefficient, which can be realised by further experiment or numerical simulation.

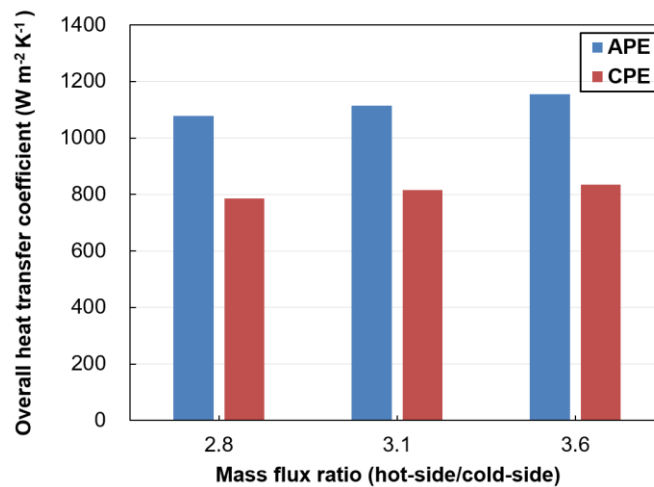


Figure 6: Effect of mass flux ratio of hot side and cold side fluid on the overall heat transfer coefficient

Another reason to explain the good overall heat transfer performance of APE is that the plate geometrical parameters of APE enhance the boiling heat transfer. Figure 7 shows the convective heat transfer coefficient of R410a changes with the equivalent Reynolds number, and six working points obtained by changing EG solution volume flow rate are selected to avoid the effect of the fluid temperature change on the heat transfer coefficient. The range of equivalent Reynolds number is related to R410a mass flow rate, in the same situation, APE can achieve higher heat transfer rate, thus R410a Reynolds number in APE is bigger than CPE when the inlet and outlet status of R410a is fixed.

It can be seen from the Figure 7 that the heat transfer coefficient of R410a of APE is estimated to be around 27% higher than that of CPE in the same Reynolds number, which demonstrates that the unequal depth corrugated structure showed in Figure 1(b) is beneficial for heat transfer.

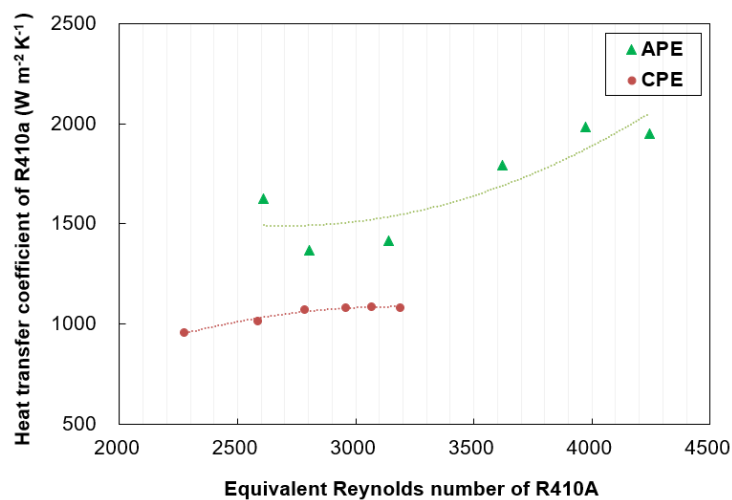


Figure 7: Convective heat transfer coefficient of R410a changes with the equivalent Reynolds number

4.2. Pressure drop

It is acknowledged that the pressure drop mainly affected by mass flux. The high mass flux means high Reynolds number, which tends to increase turbulence. Figure 8 and Figure 9 show the comparison of the frictional pressure drop and fanning friction factor in two types of plate evaporators. It's conventional that the frictional pressure drop increases as the mass flux of R410a increases whereas the friction factor decreases as the equivalent Reynolds number of R410a increases.

Obviously, the frictional pressure drop and fanning friction factor of R410a in CPE is higher than that in APE, and the fanning friction factor of R410a in CPE is almost 2 times higher than that in APE under the same equivalent Reynolds number. The smaller friction factor of APE, which has lower corrugation pressing depths than CPE for half of the plates, can likely be explained by the reason that smaller pressing depths might result in smaller separation regions and lower pressure losses. The corrugation aspect ratio, which is defined as the corrugation pressing depth divided by the corrugation pitch, is a good indicator of the trends since the pressure drop increases with the corrugation aspect ratio. The results reveal that APE has better pressure drop performance than CPE, however, when the refrigerant mass flow rate is constant in practical applications, the narrow channels of APE lead to larger refrigerant mass flux in single channel, thus the pressure drop will increase.

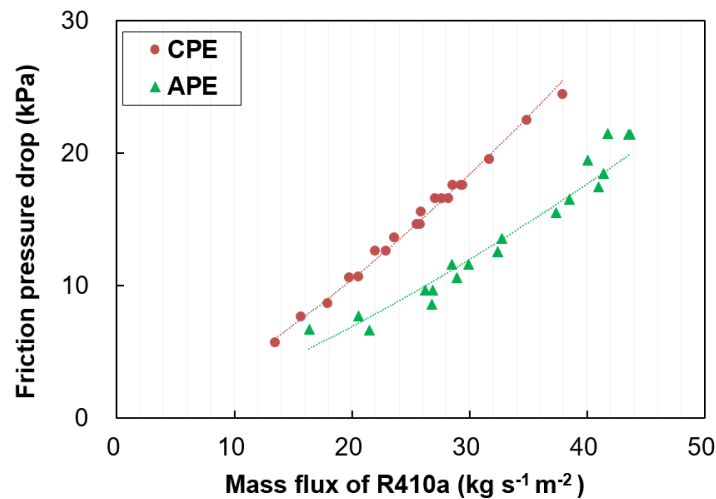


Figure 8: Frictional pressure drop in variation of the mass flux of R410a

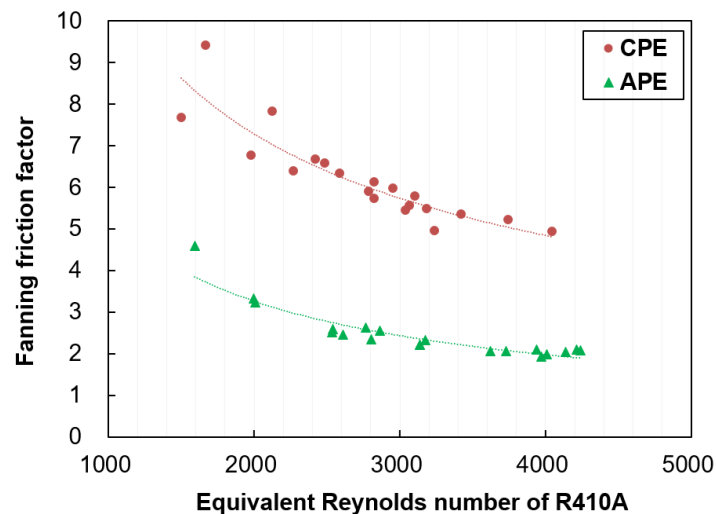


Figure 9: fanning friction factor in variation of the Equivalent Reynolds number of R410a

5. CONCLUSIONS

This paper presented an experiment to study the heat transfer and pressure drop characteristics of APE with R410a as refrigerant and EG solution as secondary refrigerant. For comparison, CPE was also tested under the specific conditions by changing EG solution inlet temperature, EG solution volume flow rate and evaporation temperature. The results show that the APE has better performance both in heat transfer and pressure drop. The energy density of APE is about 20%-40% higher than that of CPE, which means that the APE can make the size of heat exchanger smaller and reduce the charge of the refrigerant when the same heat duty is achieved. Moreover, the R410a friction pressure drop of APE is much lower than that of CPE, which is mainly due to the smaller corrugation pressing depths of APE.

The present work just provides a preliminary exploration of the thermal and hydraulic performance of two-phase flow in an asymmetric plate evaporator, more theoretical and experimental support is needed. For example, the results demonstrate that the unequal depth corrugated structure of APE is beneficial for heat transfer, however,

how the corrugation depth influence the heat transfer mechanism remains unknown. The previous research works only investigated the influence of the chevron angle on two-phase heat transfer, while effects of other geometries such as corrugation pitch and depth were not addressed (Zhang, 2019). More research will be carried out in our project to make up for the gap in this field.

6. ACKNOWLEDGEMENT

This work was supported by the Chinese National Natural Science Foundation (Foundation No.51876185).

7. REFERENCES

- Chang C.M, Yao T.X, 2008. Unsymmetrical plate heat exchanger used for HVAC. *China Construction Heating & Refrigeration*, 09: 48-49. (in Chinese)
- Dae Y.K, Kyung C.K, 2017. Thermal performance of brazed metalfoam-plate heat exchanger as an evaporator for organic Rankine cycle. *Energy Procedia*, 129: 451-458.
- Dahlgren J, Kallrot M, 1998. Gasket for a plate heat exchanger. Patent, DE3468733.
- Dahlberg, Tomas, 2010. Asymmetric heat exchanger, Patent, EP2267391.
- Djordjevic E, Kabelac S, 2008. Flow boiling of R134a and ammonia in a plate heat exchanger. *International Journal of Heat and Mass Transfer*, 51(25-26): 6235-6242.
- Focke W.W, 1985. Asymmetrically corrugated plate heat-exchanger plates. *International Communications in Heat and Mass Transfer*, 12: 67-77.
- Han D.H, Lee K.J, Kim Y.H, 2003. Experiments on the characteristics of evaporation of R410A in brazed plate heat exchangers with different geometric configurations. *Applied Thermal Engineering*, 23: 1209-25.
- Hsieh Y.Y, Lin T.F, 2002. Saturated flow boiling heat transfer and pressure drop of refrigerant R-410A in a vertical plate heat exchanger. *International Journal of Heat and Mass Transfer*, 45(5): 1033-1044.
- JCGM, 2008. Evaluation of measurement data-guide to the expression of uncertainty in measurement. JCGM/WG, 1: 134.
- Kim M, et al, 2013. Numerical study on the cross-corrugated primary surface heat exchanger having asymmetric cross-sectional profiles for advanced intercooled-cycle aero engines. *International Journal of Heat and Mass Transfer*, 66: 139-153.
- Lee H, Hwang Y, Radermacher R, et al, 2013. Experimental investigation of novel heat exchanger for low temperature lift heat pump. *Energy*, 51: 468-474.
- Muhammad I, Muhammad U, Youngmin Y, et al, 2017. Flow boiling of R245fa in the brazed plate heat exchanger: thermal and hydraulic performance assessment. *International Journal of Heat and Mass Transfer*, 110: 657-670.
- Rossato M, Del C.D, Muzzolon A, et al, 2016. Flow boiling of R32 inside a brazed plate heat exchanger. *International Journal of Refrigeration*, 69: 165-174.
- Ulf Vestergren, 2001. Plate heat exchangers. Patent, US6237679.
- Utriainen E., Sunden B, 2002. Evaluation of the cross corrugated and some other candidate heat transfer surfaces for microturbine recuperators. *Journal of engineering for Gas Turbines and Power-Transactions of The ASME*, 124: 550-560.
- Wang L, Sunden B, Manglik R.M, 2007. Plate heat exchangers: design, applications and performance. Ashurst Lodge: WIT press, 27-49.
- Wang Z.Z, Zhao Z.N, Li R.J, 1992. Asymmetric heat exchanger. Patent, CN2119632.
- Yang J, Jacobi A, Liu W, 2017. Heat transfer correlations for single-phase flow in plate heat exchangers based on experimental data. *Applied Thermal Engineering*, 113: 1547-1557.
- Zhang J, Zhu X.W, Maria E.M, Fredrik H, 2019. A review of heat transfer enhancement techniques in plate heat exchangers. *Renewable and Sustainable Energy Reviews*, 101: 305-328.

#283: Adoption of energy efficient buildings with improvement of their windows' aesthetic features

Yusuf Cihat AYDIN¹, Parham A. MIRZAEI²

¹ Department of Architecture and Built Environment, Faculty of Engineering, University of Nottingham, NG7 2RD
University Park, Nottingham, UK, Yusuf.Aydin@nottingham.ac.uk

² Department of Architecture and Built Environment, Faculty of Engineering, University of Nottingham, NG7 2RD
University Park, Nottingham, UK, Parham.Mirzaei_Ahranjani@nottingham.ac.uk

Progress in reducing the energy demand of the building sector through existing measures, such as the development of energy-efficient buildings (EEBs) and stringent building energy regulations, is insufficient to achieve the objectives of the Paris Agreement. Therefore, novel approaches are needed to accelerate the energy demand reduction of the building sector, especially those related to the lack of widespread adoption of EEBs as a result of their marketing failure. Increasing the number of EEBs with better marketability strategies through aesthetic enhancement can accelerate the reduction of energy demand in the building sector.

In this regard, this study aims to investigate the impact of different window features (i.e. position, number, area, width, height, symmetry and proportion) on housings aesthetic, and marketability. It also attempts to develop computational models for their predictions. For this purpose, an artificial neural network (ANN) computational model was developed with the results of a conducted comprehensive survey (n=807). Results show a high level of accuracy (up to 95%) for the performance of ANN models in prediction of individuals' aesthetic appreciation and housing's marketability.

Keywords: aesthetic appreciation; marketability; computational predictive models; artificial neural network

1. INTRODUCTION

Existing global energy demand reduction measures are insufficient to achieve the specified targets of the Paris Agreement (i.e. limiting the global warming to less than 2°C rise). Despite in the last decades energy savings up to 80-85% in energy efficient buildings (EEBs) becoming possible, building sector's energy demand is projected to increase by 48% in 2040 from 2012 levels. The inadequacy of current measures to reduce the energy demand of the building sector was initially conceptualised as the paradox of Inefficiency of Increased Building Energy Efficiency (IIBEE) by authors (Aydin, Mirzaei and Akhavannasab, 2019). The IIBEE paradox stems mainly from the fact that EEBs are not widely adopted as a consequence of several important obstacles known as market barriers (e.g. low market value and high initial cost of EEBs, lack of interoperability between building stakeholders, and unappealing aesthetic of EEBs). As a novel countermeasure strategy, better marketability obtained by aesthetic enhancement of EEBs was proposed to increase the number of deployed EEBs in the previous study. According to a conducted survey among real-estate agencies in 26 UK cities (n=289), strong empirical evidences were found to support the applicability of the proposed strategy (Aydin, Mirzaei and Akhavannasab, 2019).

It is necessary to understand the dynamics of individuals' aesthetic judgment and determine the parameters associated with the aesthetic appreciation to enhance the aesthetic of EEBs. There have been ongoing debates about the subjectivity and universality (objectivity) of aesthetic appreciation since antiquity. Yet, some of the previous studies offer valuable empirical findings for the existence of a common instinctual aesthetic appreciation, being beyond the learning process through cultural transmission. For example, different empirical studies reported that young infants could distinguish the attractive and unattractive faces, which were previously categorised by adults, with expressing a more positive reaction and less withdrawal rate to attractive faces compared to unattractive faces differing in race, gender, and age (e.g. (Langlois, Roggman and Rieser-Danner, 1990)). Similar results were also reported for the reactions of infants to various objects (Langlois, Roggman and Rieser-Danner, 1990). Furthermore, the existence of a common aesthetic appreciation was reported for adults with different demographics (e.g. (Stamps III, 1999)). In addition, according to the numerous magnetic resonance imaging (MRI) experimental studies, the experience of beauty (in general terms) is correlated with activities in a region of the brain that has been generally associated with pleasure and reward (Ishizu and Zeki, 2017), which is in favour of Kant's aesthetics view: "aesthetic judgement is based on feeling pleasure or displeasure".

In addition, computational aesthetic approaches have shown promising results to simulate individuals' aesthetic judgments and perceptions. For example, Marquardt (1997) developed a method on the basis of symmetry and proportional theories called "Phi mask" or "Golden Decagon" to analyse human faces' attractiveness for surgical, cosmetic, and identification purposes (Marquardt, 1997); Phi mask was successful to explain variance in facial attractiveness judgements up to 75% (Bashour, 2006). Advanced non-linear computational approaches such as ANN, decision tree, and machine learning have gained popularity in many different disciplines due to their high performance. In particular, these methods allow processing nonlinear data and handling imprecise and fuzzy information, and they are very successful at providing accurate predictions and generalising a large amount of complex data (Basheer & Hajmeer, 2000). Particularly, better performances of ANNs compared to other models such as regression models and decision tree was reported in previous studies (Tso & Yau, 2007). Previous works have shown promising results to simulate individuals' aesthetic judgments about attractiveness of different visual stimuli such as photographic images (e.g. (Bhattacharya, Sukthankar and Shah, 2010)), and human faces (e.g. (Eisenthal, Dror and Ruppim, 2006)). Although ANN method has become popular in building related studies such as perception of urban environment prediction (e.g. safe, depressing, and beautiful), housing energy consumption, indoor air temperature of buildings, and house price projection, the visual aesthetic of building facades were barely studied with these advanced computational method.

Discovering the dynamics behind the visual aesthetic of building facades can help to prioritise those most influential building components by designers and researchers at design and development process of EEBs and help to improve housing facades design. In addition, being able to simulate individuals' aesthetic appreciation based on certain building parameters with advanced models can help to develop architectural design reviews, which can result in standardised housing aesthetic assessment protocols and achieving a better visual quality in the built environment. Window was identified as one of the most influential building components simultaneously affecting buildings' energy-efficiency, aesthetics, and marketability in previous studies (Aydin, Mirzaei and Akhavannasab, 2019). For example, the data obtained from a comprehensive survey showed that the window position, number, area, width, height and symmetry are key parameters in increasing market demand of residential buildings (Aydin, Mirzaei and Akhavannasab, 2019).

To this end, an ANN, and statistical models were utilised in this study to test the possibility of simulating residential buildings' marketability and individuals' aesthetic appreciation via different window parameters. To validate the practicality of the ANN model, the impact of seven different window parameters (i.e. position, number, area, width, height symmetry and proportion) on the individual's aesthetic judgment and housings' marketability in the UK was investigated with a comprehensive survey (n=807). The window parameters were investigated with thirty-eight different edited building photographs. Then, the relationship between seven window properties, aesthetic appreciation and housings' marketability was investigated.

2. METHODOLOGY

A comprehensive email survey conducted on October 2018 to investigate the impact of seven window parameters on marketability and individuals' aesthetic appreciation about residential building facades in the UK. Then, ANN computational model was trained and developed according to the results of the conducted survey. Except for the demographic questions and benchmark building (the first picture for the calibration purpose), the order of the pictures was randomised to minimise the question order bias while participants could only see one picture at a time to grade the dwellings' beauty and marketability with a bipolar seven-point semantic differential scale. Each question was supported by an optional text box to collect participants' additional comments and to let them express a plausible different answer above the given options. In order to minimise misconceptions and to ensure equal conditions for each participant, they were briefly informed with written instructions about the tasks and working principles of the semantic differential scale.

2.1. Participants

Invitation emails were distributed to home students (native students) from The University of Nottingham (UoN), UK. In order to encourage participants, an opportunity to receive a monetary incentive was offered. 1095 responses were received (288 partially) and fully completed questionnaires were used. The demographic distribution of participants is shown in Table 1.

Table 1: Demographic distribution of participants

Gender		Background		Qualification*		Age		Region ** (SD =1.70)			
(SD = 0.47)	%	(SD =0.48)	%	(SD =1.35)	%	(SD =0.66)	%	%	%	%	%
Male:	32	Architect:	3	Bachelor's degree:	47	Under 18:	0	1:	1	6:	17
Female:	67	Art:	6	Master's degree:	16	18-24:	83	2:	7	7:	18
Other:	1	Other:	92	Ph.D. degree	1	25-34:	11	3:	3	8:	2
				Other:	35	35-44:	4	4:	21	9:	3
						45-54:	2	5:	28	10:	1
						55-64:	1				
						65+:	0				

2.2. Visual stimuli

Extra attention was given to the preference and design of photographic images due to the fact that aesthetic judgement is sensitive to many variables, some of these highlighted in the previous studies (e.g. (Aydin, Mirzaei and Akhavannasab, 2019)). Hence, efforts have been made to ensure that the variations in the participants' judgements are only a result of the configurations being worked on. For this purpose, only one single building parameter affecting individuals' aesthetic appreciation was focused at a time. All other variables were fixed except the configurations of focused building parameter (i.e. window width, height etc.). A common UK terraced house photograph was adjusted with an open-source photo editing program GIMP 2.1 Software to generate all other studied building photos. In total, thirty-eight different black and white fully controlled and identical photographic images have been generated (see Figure 3 and Table 5). Black and white photographs were particularly preferred to minimise the influence of colours on participants' aesthetic appreciation (e.g. (Cubukcu and Kahraman, 2008)). Parametric details of the applied window configurations can be found in Figure 1.

The generated photos were divided into training and experiment categories. For the training category, thirty-three photos were designed to be utilised for developing ANN model. The parametric details of studied window configurations are illustrated in Figure 1. For photos belonging to the training category, each window parameters were modified under four levels, including a benchmark level (see Figure 1). Efforts have been made to extract the isolated impact of each of seven window parameters. For this purpose, in each image, only one parameter was changed, and all other parameters were not varied. However, window area, height, width, position and number, have resulted in more than one variations (see Table 2). Accordantly those parameters were investigated with two variations to extract the isolated impact of each of seven window parameters. In addition to these photos, five independent photos were designed to test the performance and applicability of the developed computational models as explained in the following sections (see Table 5, photos 34 to 38).

Table 2: Variations caused by the configuration of window parameters

Window Parameters	Variations caused by configurations							
	Area	Height	Number	Position X	Position Y	Symmetry	Width	Proportion
Area	X	X					X	
Height		X					X	X
Height Ver.2	X	X						X
Number		X	X	X			X	
Number Ver.2	X		X	X				
Position X*				X				
Position Y*					X			
Symmetry				X	X	X		
Width		X					X	X
Width Ver.2	X						X	X

*Position X and Y refers to the location of windows' centre on the X and Y axis when a coordinate system located at the centre of the building.

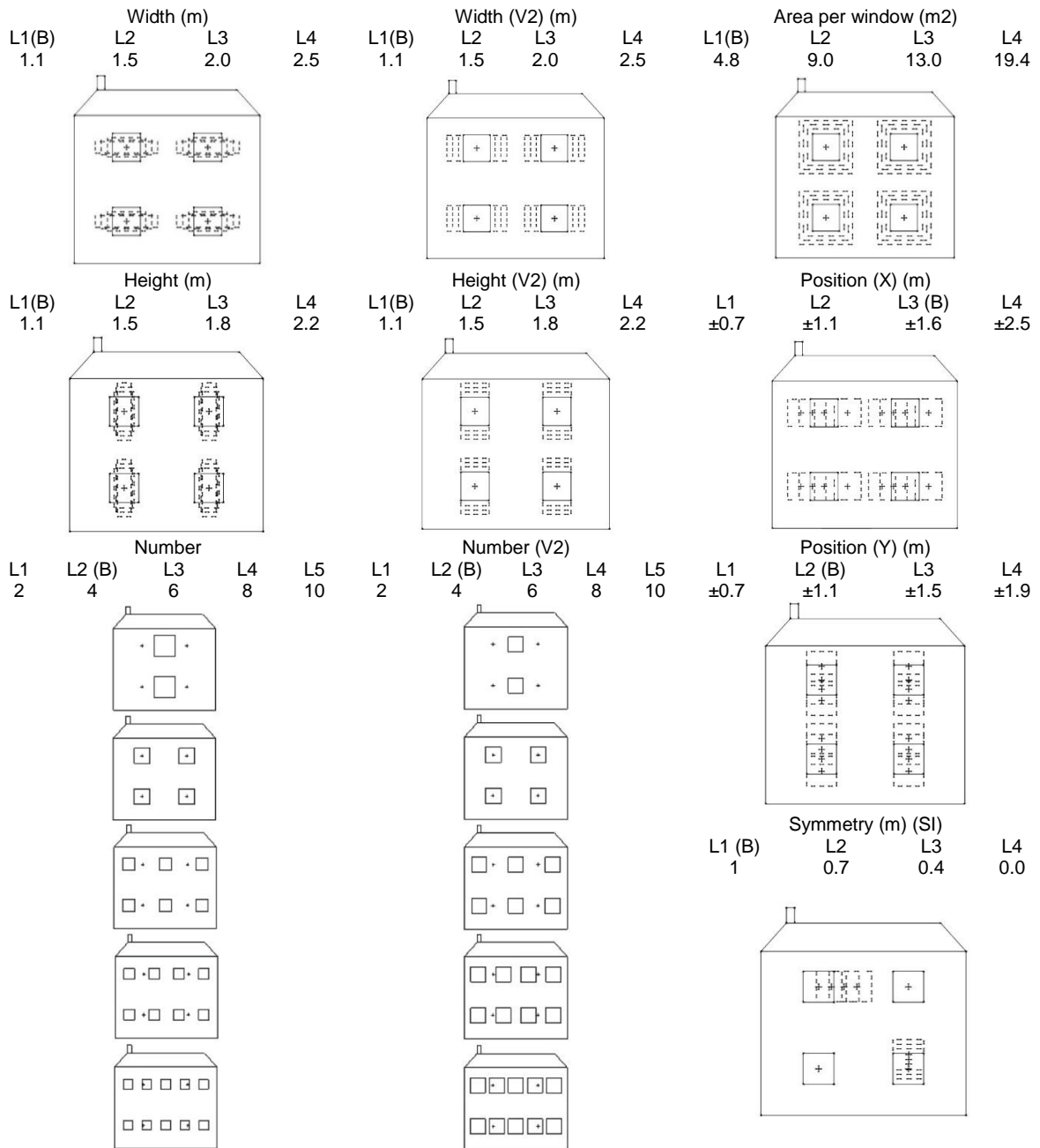


Figure 1: Parametric details of applied window configurations

2.3. Data analysis

Normalisation equation called “feature scaling” or “min-max normalisation” was utilised to standardise the range of independent variables and the results of the questionnaire. Accordingly, values of the bipolar seven-point semantic differential scale (1 as unattractive and unenthusiastic to 7 as attractive and enthusiastic) and the studied parametric window configurations with different units (e.g. m, m2, and SI) were converted to the normalised values between 0 and 1. The forecasting accuracy of the developed ANN model is determined via (1) the total mean square error (MSE), and (2) the consistency percentage when the studied photos are hierarchically ordered; for this purpose, the studied 38 photos were sequenced from the most to the least attractive and marketable ones according to the survey results (means); a similar procedure was applied accordingly to ANN results, and then the percentage of consistency was calculated.

A MATLAB Neural Network Toolbox was utilised to develop the ANN model. Dataset obtained from 33 photos (i.e. training category) was allocated 70% for the training, 15% for the validation and 15% for the testing purposes. Each of the studied photos were defined to ANN as seven parametric variables (i.e. normalised window position, number, area, width, height, symmetry, and proportion). In total, the variations of window parameters that utilised for developing ANN is shown in Table 3. In this study, a supervised feed-forward backpropagation architecture ANN was utilised to develop the predictive model. In addition, different functions, hidden layer numbers and neurons were tested to improve the performance of the developed ANN model. The best performance was achieved with Levenberg-Marquardt backpropagation training function, gradient descent with momentum weight and bias adaption learning function, tangent sigmoid transfer function, two hidden layers, and 13 neurons. The architecture of developed ANN model is illustrated in Figure 2.

Table 3: Number of different window parameters utilised for developing ANN model

Area:	19	Number:	6	Position on Y-axis*:	5	Width:	12
Height:	10	Position on X-axis*:	7	Symmetry:	5	Proportion**:	13

* Window position on X and Y axis was calculated according to the centre of windows, ** Proportion was calculated according to aspect ratios (i.e. width/height).

IBM SPSS Version-23 was utilised for all statistical analysis. The conventional values were chosen for Sig. (2-tailed) value (0.05) with a 95% of confidence interval. As the conducted survey has a normal distribution (skewness: max: 1.534, min: -0.081, kurtosis: max: 1.899 -, min: -0.804) and a large sample size (N = 807), parametric statistical models were utilised. The relationships between the configurations of studied window parameters, aesthetic appreciation, and housings' marketability were determined with Pearson correlation analysis.

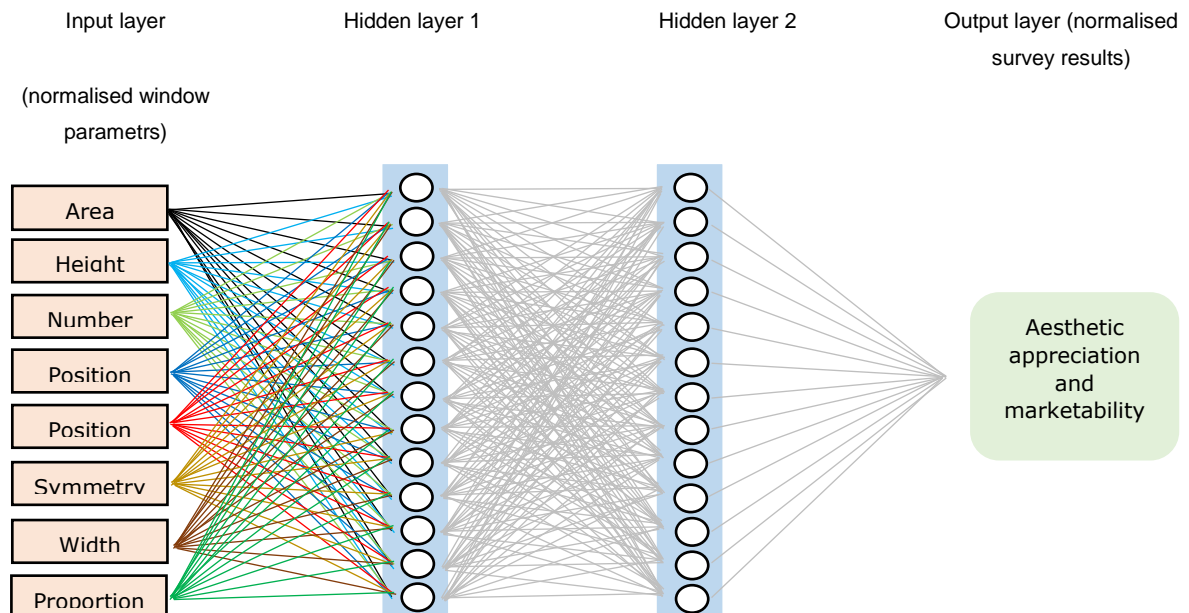


Figure 2: Artificial neural network (ANN) architecture

3. RESULTS AND DISCUSSION

3.1. Survey results

According to Cronbach's alpha (α) criterion a significantly high reliability and internal consistency of the conducted survey was observed ($\alpha = 0.95$). A general outcome of the survey is shown in Figure 3. A clear trend (i.e. upward, downward, and U-shape) can be observed for the impact of each window configuration on housing aesthetic and marketability (see Figure 3). A significantly high positive correlation between individuals' aesthetic appreciation and housings' marketability ($r = 0.876$, $p=0.000$) is also found in this study. This implies that the results of individuals' aesthetic appreciation about the detached house photos can be extended to their marketability. Accordingly, in the rest of the paper, only aesthetic appreciation results will be mentioned.

Housing aesthetic has a downward trend in the window area configurations of level 1 ($M = 4.08$, $Md = 5.00$, $SD = 1.64$) to 3 ($M = 3.22$, $Md = 3.00$, $SD = 1.69$). This implies when the window area was gradually increased, aesthetics of housing was gradually decreased. Yet, in general, the reinforcing effect of the window area on aesthetics of the houses can be observed. The highest aesthetic scores (i.e. around 3 to 4 on a 7-points scale) can be observed in the housing photos that have a relatively higher window area. The area configurations have the highest scores compared to other window configurations. Similarly, the 2nd version (V2) of height, number, and width have relatively higher scores compared to other window configurations although the window area was increased in these cases in order to keep other parameters constant in those 2nd version configurations (see Figure 3). Accordingly, a clear reverse U-shape relationship can be observed between housing aesthetic and window area. As it can be seen in the benchmark housing and window area configuration of level 1 to 3, participants' aesthetic appreciation for the benchmark housing ($M = 2.08$, $Md = 2.00$, $SD = 1.08$) is almost doubled for the window area configuration level 1 ($M = 4.08$, $Md = 5.00$, $SD = 1.64$), and is gradually reduced when the window area is increased in the window area configurations of level 2 ($M = 3.84$, $Md = 5.00$, $SD = 1.67$) and 3 ($M = 3.22$, $Md = 3.00$, $SD = 1.69$) (see Figure 3).

In the window symmetry configurations, the asymmetry of windows is increased at each configuration levels (see Figure 3). The window symmetry configurations are determined as the least attractive housings' parameter, meaning that the most asymmetric housing photo is the least aesthetic one. Participants' aesthetic appreciation for the benchmark housing ($M = 2.08$, $Md = 2.00$, $SD = 1.08$) is gradually reduced when the window asymmetry level is increased in the configurations of level 1 ($M = 1.57$, $Md = 1$, $SD = 0.89$), level 2 ($M = 1.40$, $Md = 1.00$, $SD = 0.77$) and 3 ($M = 1.36$, $Md = 1.00$, $SD = 0.81$). Accordingly, it is reasonable to claim that symmetry has a positive effect on aesthetics. Despite the fact that the window width and height configurations have a downward aesthetic appreciation trend from level 1 to 3, this downward trend evolves to a slight reverse U-shape relationship in 2nd versions of the window width and height configurations. This implies that different window parameters (e.g. window width – height, and width – area) have mutual impact on each other (see Figure 3).

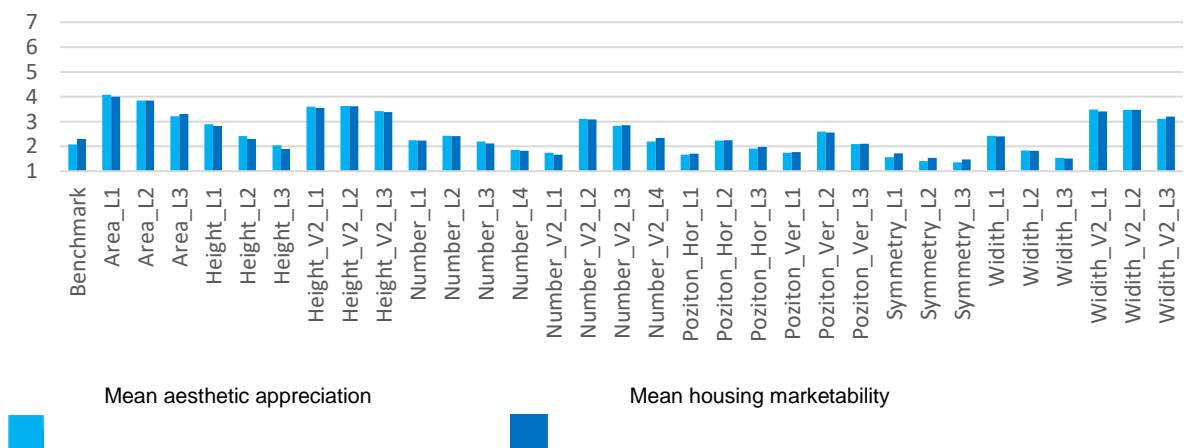




Figure 3: Mean aesthetic appreciation and housing marketability distribution for each housing photos

3.2. Performance of ANN to predict aesthetic and marketability of housings

The comparison of the normalised survey results and ANN predictions are given in Table 4. ANN models predict the aesthetic appreciation for all training housing photos and five additional experimental photos (see photos 34 to 38 in Table 5) with a high accuracy (MSE: $1.73\text{E-}04$, Min: $3.88\text{E-}10$, Max: $5.62\text{E-}03$) (See Table 4). Except for window symmetry configurations, ANN models have a high performance, yet it partially fail to predict the aesthetic appreciation for the photos with asymmetric windows. When the window symmetry configurations are excluded, the difference between the normalised survey results and ANN prediction for training photos is 1.1% (Min: 0.0% on Area_L1, Max: 5.2% on Number_L4), and is 1.2% (Min: 0.7% on Experiment 4, Max: 1.8% on Experiment 5) for the experiment photos. In overall, the percentage of the difference between survey results and predictions of ANN model is 1.2%.












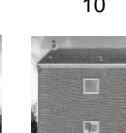

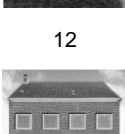




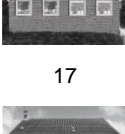




















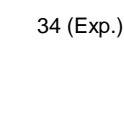
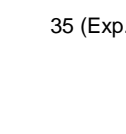
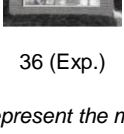
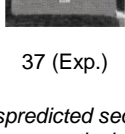
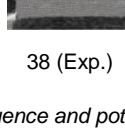
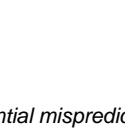
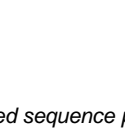
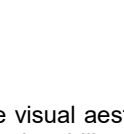
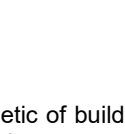
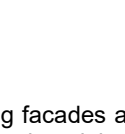
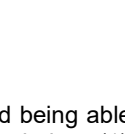
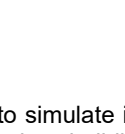
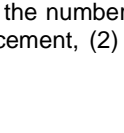
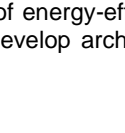
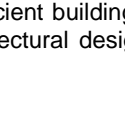
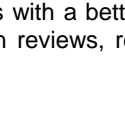
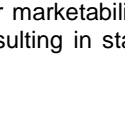





The feasibility of the developed computational models to predict the housing aesthetic was tested and illustrated in Table 5. For this purpose, all studied housing photos are first sequenced from the most attractive to the least one based on the results of the survey and predicted aesthetic values by the ANN model. Then, the consistency of these sequences are compared with the sequence obtained from the survey results. The mispredicted sequences and potential mispredicted sequenced photos are represented with red and blue colours, respectively (see Table 5). The potential mispredicted sequence represents the aesthetic values that have the same aesthetic values with the previous or next housing. For example, according to the normalised survey results, the housing photo of #31 (0.779) is more attractive than #32 (0.776) (see Table 5). However, according to the normalised ANN prediction results, the housing photo #31 (0.780) and #32 (0.780) have a same aesthetic value, so when sequencing the housing photos, the order of the housing photo #31 and #32 can be either mispredicted or accurate.

In general, the ANN model has a consistent performance to sequence the housing photos while their accuracy compared to the survey results vary between %95-63 (see Table 5). It was observed that ANN model is insufficient in determining the minor differences between the aesthetics of some photos and accordingly ANN model compute the same aesthetic appreciation level for those photos (e.g. photo #31 and #32). The developed ANN model predicts the sequence of only two photos mispredicted while ANN is insufficient to determine the minor differences between 12 photos. In general, the ANN model has shown a high performance to predict aesthetic and marketability of detached UK houses.

Table 4: The performance of ANN predictions

Housing No	Housing name	Normalised Survey mean	Normalised ANN prediction	ANN-Survey Squared error (SE)
1	Benchmark	0.262	0.260	3.46E-06
2	Area_L1	1.000	1.000	3.88E-10
3	Area_L2	0.912	0.910	4.41E-06
4	Area_L3	0.681	0.680	1.28E-06
5	Height_L1	0.564	0.560	1.75E-05
6	Height_L2	0.388	0.384	1.61E-05
7	Height_L3	0.251	0.250	1.43E-06
8	Height_V2_L1	0.824	0.820	1.76E-05
9	Height_V2_L2	0.835	0.830	2.37E-05
10	Height_V2_L3	0.754	0.750	1.87E-05
11	Number_L1	0.325	0.320	2.26E-05
12	Number_L2	0.393	0.390	7.79E-06
13	Number_L3	0.306	0.310	1.32E-05
14	Number_L4	0.181	0.190	8.86E-05
15	Number_V2_L1	0.142	0.140	5.44E-06
16	Number_V2_L2	0.644	0.640	1.90E-05
17	Number_V2_L3	0.538	0.550	1.34E-04
18	Number_V2_L4	0.305	0.310	2.25E-05
19	Poziton_X_L1	0.113	0.110	1.07E-05
20	Poziton_X_L2	0.322	0.320	4.74E-06
21	Poziton_X_L3	0.203	0.200	9.10E-06
22	Poziton_Y_L1	0.139	0.140	1.81E-06
23	Poziton_Y_L2	0.455	0.450	2.45E-05
24	Poziton_Y_L3	0.270	0.270	1.02E-07
25	Symmetry_L1	0.075	0.000	5.62E-03
26	Symmetry_L2	0.015	0.000	2.21E-04
27	Symmetry_L3	0.000	0.008	6.21E-05
28	Width_L1	0.392	0.390	5.87E-06
29	Width_L2	0.172	0.170	6.20E-06
30	Width_L3	0.066	0.069	7.84E-06
31	Width_V2_L1	0.779	0.780	1.08E-06
32	Width_V2_L2	0.776	0.780	1.89E-05
33	Width_V2_L3	0.641	0.640	1.99E-06
			Survey-ANN MSE for training photos:	1.69E-04
34	Experiment 1	0.445	0.440	2.52E-05
35	Experiment 2	0.001	0.012	1.11E-04
36	Experiment 3	0.415	0.410	2.36E-05
37	Experiment 4	0.139	0.140	9.57E-07
38	Experiment 5	0.069	0.070	1.50E-06
			Survey-ANN MSE for experiment photos:	4.26E-06
			Overall Survey-ANN MSE:	1.73E-04

Table 5: Comparison of hierarchical order when photos were sequenced from the most attractive to the least one.

Prediction accuracy	Survey	ANN					
		%95-63					
	2	2					
	3	3					
	9	9	1	2	3	4	5
	8	8					
	31	31					
	32	32					
	10	10					
	4	4	6	7	8	9	10
	16	16					
	33	33					
	5	5					
	17	17					
	23	23	11	12	13	14	15
	34	34					
	36	36					
	12	12					
	28	28					
	6	6	16	17	18	19	20
	11	11					
Housing No	20	20					
	13	13					
	18	18					
	24	24	21	22	23	24	25
	1	1					
	7	7					
	21	21					
	14	14					
	29	29	26	27	28	29	30
	15	15					
	22	22					
	37	37					
	19	19					
	25	38	31	32	33	34 (Exp.)	35 (Exp.)
	38	30					
	30	35					
	26	27					
	35	25					
	27	26	36 (Exp.)	37 (Exp.)	38 (Exp.)		

* Red and blue coloured numbers represent the mispredicted sequence and potential mispredicted sequence photos, respectively

4. CONCLUSION

Discovering the dynamics behind the visual aesthetic of building facades and being able to simulate individuals' aesthetic appreciation and housing marketability with computational models can help to (1) reduce building sector's energy consumption with increasing the number of energy-efficient buildings with a better marketability strategy obtained with their aesthetic enhancement, (2) develop architectural design reviews, resulting in standardised

housing aesthetic assessment protocols and achieving a better visual quality in the built environment, (3) facilitate and improve architects building exterior design with building simulation tools.

Impact of seven different window parameters (i.e. position, number, area, width, height symmetry, and proportion) on the individuals' aesthetic judgment and housings' marketability was investigated with a comprehensive survey (n=807). Then, an ANN model was developed to predict aesthetic and marketability of studied housing photos.

According to the results, there is a positive correlation between housings' aesthetic and marketability. Similarly, there is a positive correlation between housings' aesthetic and marketability and window area, height, and position on the X-axis, but no meaningful correlation can be observed for window number, position on the Y-axis, symmetry, width, and proportion. Studied window parameters have mutual impact on each other, accordingly it is not possible to estimate the aesthetic and marketability of residential buildings over a single window parameter. Individuals' aesthetic appreciation was simulated up to %95 accuracy with the ANN model.

5. ACKNOWLEDGEMENTS

The authors would like to express their gratitude to the Faculty of Engineering of University of Nottingham for use of their facilities, and Mehmet Aydin for his financial support.

6. REFERENCES

- Aydin, Y. C., Mirzaei, P. A. and Akhavannasab, S. (2019) 'On the relationship between building energy efficiency, aesthetic features and marketability: Toward a novel policy for energy demand reduction', *Energy Policy*, 128, pp. 593–606. doi: 10.1016/j.enpol.2018.12.036.
- Bashour, M. (2006) 'An objective system for measuring facial attractiveness', *Plastic and Reconstructive Surgery*, 118(3), pp. 757–774.
- Bhattacharya, S., Sukthankar, R. and Shah, M. (2010) 'A framework for photo-quality assessment and enhancement based on visual aesthetics', in *Proceedings of the international conference on Multimedia - MM '10*. Firenze, Italy, pp. 271–280.
- Cubukcu, E. and Kahraman, I. (2008) 'Hue, saturation, lightness, and building exterior preference: An empirical study in Turkey comparing architects' and nonarchitects' evaluative and cognitive judgments', *Color Research and Application*, 33(5), pp. 395–405. doi: 10.1002/col.20436.
- Eisenthal, Y., Dror, G. and Ruppin, E. (2006) 'Facial attractiveness: Beauty and the machine', *Neural Computation*, 18(1), pp. 119–142. doi: 10.1162/089976606774841602.
- Ishizu, T. and Zeki, S. (2017) 'The experience of beauty derived from sorrow', *Human Brain Mapping*, 38(8), pp. 4185–4200.
- Langlois, J. H., Roggman, L. A. and Rieser-Danner, L. A. (1990) 'Infants' Differential Social Responses to Attractive and Unattractive Faces', *Developmental Psychology*, 26(1), pp. 153–159.
- Marquardt, S. R. (1997) 'Method and apparatus for analyzing facial configurations and components', "U.S. Patent No. 5,659,625".
- Stamps III, A. E. (1999) 'Demographic effects in environmental aesthetics: A meta- analysis', *J. Plan. Literature*, 14(2), pp. 155–175.

#284: Experimental measurements of straw drying using flue gases

Wojciech GORYL¹, Mariusz FILIPOWICZ²

¹Faculty of Energy and Fuels, AGH University of Science and Technology, aleja Adama Mickiewicza 30, 30-059 Krakow, Poland, wgoryl@agh.edu.pl

² Faculty of Energy and Fuels, AGH University of Science and Technology, aleja Adama Mickiewicza 30, 30-059 Krakow, Poland, filipow@agh.edu.pl

In many European countries, notably in Poland, there is a significant demand for space heating. This could be largely satisfied by biomass, primarily in rural areas, where biomass is locally available, mainly as agricultural residues. In Poland, this is mainly straw, which is often burnt uselessly in the fields, although it may become an environment friendly fuel for heating the rural holdings, if burnt in dedicated biomass boilers.

One of the main problems of the energy use of biomass is the bulk density as well as the calorific value. One of the most important factors influencing the biomass calorific value is humidity. The higher humidity of the biomass, the lower the calorific value. It should be mentioned that there is a lower and upper limit of humidity, which should not be exceeded in energy use of biomass. This has a negative effect on the biomass combustion process and biomass boiler construction elements.

This paper presents experimental results of the heat and mass transfer in a round bale of straw during straw drying in three different configurations. The experimental measurements were made in a specialized stand of straw driers. Flue gasses from straw combustion in biomass boiler were used as a drying agent. Measurements were made of the humidity and temperature inside the cylindrical straw bale during the drying process. Moreover, the temperature, humidity and flow of the drying agent were measured. In addition, a thermographic analysis of the straw bale surface was made to determine the best method of straw drying in the form of round bales. Finally, the best configuration of straw drying was chosen. It is possible to get a better fuel in a very short time and more energy production during straw combustion in biomass boilers.

Keywords: biomass boilers; straw drying; heat and mass transfer

1. INTRODUCTION

In many European countries, notably in Poland, there is a significant demand for space heating. This could be largely satisfied by biomass, particularly in rural areas, where biomass is locally available, mainly as agricultural residues. In Poland, this is mainly straw. It may become an environmentally friendly fuel for heating rural holdings, if burnt in dedicated biomass boilers. The usefulness of biomass for energy purposes depends on the humidity, type, and composition. However, the basic problem of using biomass as a fuel is moisture content, which is primarily influenced by the period of harvest and the conditions of its storage. Dry biomass can reach a humidity of under 10%, but usually fresh biomass has more than 60% relative humidity, which is very high. This kind of fuel is almost impossible to combust (Goryl, 2016; Goryl, 2017). For the straw combustion in biomass boilers, the humidity of the fuel has to be 10%–20%. This has a favourable effect on the combustion process owing to the catalytic effect of water vapour to the combustion of the excessive amount of volatiles which are in the biomass.

The more compressed the straw (with higher density) and the weather conditions during its storage have a smaller impact on straw quality and the degree of moisture. However, too much compressed straw is very difficult to dry due to problems with the penetration of the drying agent through the straw layers.

Drying biomass for energy purposes could increase the energy efficiency of the combustion process (Verma, 2017; Yi, 2019), but this process is usually quite expensive. It is due to the need to use large amounts of energy for water evaporation (Gebreegziabher, 2013). The most commonly used biomass drying devices are drum dryers, pneumatic dryers, fluid bed dryers, and belt dryers (Li, 2012; Haque 2013). Mostly, in these dryers, the exhaust gases from the fuel combustion or process steam (Song, 2012) are used as the drying agent. Moreover, the drying agent, which is air, is usually used for drying food materials (Ratti, 2001; Lewicki, 2006). Installations for the food industry are much more expensive, relating to investment and operating costs (Jchua, 2003). The above devices are used for drying powdered or crushed materials, so the drying process is faster and, at the same time, it is more energy-efficient (Korn, 2001; Cao, 2010).

If there is a need to dry biomass in the form of bales, for example, straw, hay, or energy willow, drum dryers, pneumatic dryers, fluid bed dryers, and belt dryers cannot be used. For this purpose, other installations should be used and strictly adapted to drying densified cuboidal or cylindrical bales. The literature presents a number of solutions for drying hay bales in the form of cuboidal, as well as cylindrical bales. For straw, there are practically no such dedicated solutions. Owing to the nature of the material, similar solutions may be used.

Hay, as a feed, should have appropriate quality parameters to protect it against mould growth or rotting. Hay should have a moisture content that does not exceed 12%–15% (Descouteaux, 2006a), but straw should have a slightly higher humidity, of 15%–20%. One of the first solutions for drying hay in the form of bales, using forced air circulation, was described in 1947 (Weaver, 1947). A similar drying mechanism has also been described (House, 1988) where the air was used as a drying agent in the process of hay drying in small cuboidal bales. After four months it reached a humidity level of 15%; however, such a long drying time may cause moulding in the outer layers of the hay (Parker, 1992). The lower the material density, the easier it is to dry the material (Descouteaux, 2006a).

In Reference (Descouteaux, 2006b) the design and operation of a prototype hay dryer was described, in which it is possible to dry hay from 30% to 12% moisture content within up to 12 h. It is a batch dryer housing one or two layers of 6 and 12 cuboid bales, respectively, of hay with dimensions of 80 × 90 × 245 cm (width × height × length). The dryer has a propane gas burner with a capacity of 102 kW. It is used to get a hot drying agent. Moreover, the fan of 11.2 kW is used to press the drying agent (at a temperature of approximately 60°C) into the dryer.

The dryer of the same type was used for drying very moist corn straw (Savoie, 2004). In this case, the bales were smaller, so it was possible to put nine bales in one layer and 18 bales in two layers. Drying from 56% to 19% took 52 to 90 hours depends on bales numbers and temperature of drying agent.

In Reference (Misener, 1990), three methods of drying cylindrical hay bales with a diameter of 1.5 m and a length of 1.2 m have been described. The considered dryer could simultaneously dry nine bales of hay on three different air ducts. The first one has a metal rim of 15 cm high and a diameter of 1.1 m, which is placed on plywood with a diameter of 1.8 m. In this plywood, a hole with a diameter of 0.9 m is made, through which hot air is pressed into the bale. The metal rim is designed to minimize the escape of the drying agent outside the bale. The second one has an injected duct at the same diameter as the bale of hay. In addition, the side of the bale is tightly wrapped by foil to avoid the escape of the drying agent through the bale side. The third one had a plywood with a hole of diameter 0.6 m, on which a hay bale is placed. During the drying process of bales in two dryers (on first and third channels) a plate with a diameter of 1.2 m was placed—most probably in order to avoid the flow of the drying agent only along the bale's axis. It was found that the bale wrapped by foil dried much faster than in the first and third cases. It could be caused by forcing the flow of the drying agent along the entire bale of hay.

The article in Reference (Roman, 2014) presents the tests for the possibility of hay drying in cylindrical bales in three different configurations. The hay bales had a diameter of 1.5 m and a height of 1.2 m. The dryer is adapted to dry one bale at a time. The dimensions of the dryer are 1.6 × 1.6 × 0.4 m. After the measurements, it was found that moisture filed in a bale of hay was not homogeneous, but it is possible to dry the bales of hay from 40% moisture content to 12%–15% in 7–12 hours.

It is also possible to combine two or more heat sources to achieve higher efficiency and lower costs of drying. In Reference (Morissette, 2011) the possibility of drying hay in the form of cuboidal bales with a hybrid of a biomass boiler and solar energy is presented. Within 55 days, it is possible to dry almost 6000 small 22.5 kg hay bales from the initial humidity of 18.3%–11.1%, with a net energy consumption of 223.7 GJ, of which 192.4 GJ came from the sun and biomass, and 31.2 GJ is the electricity used to drive fans and circulation pump.

The above installations are used for hay drying but, with some modifications, those installations could be used for bale straw drying for energy purposes. The main problem in the above examples is the drying time, which is too long to be directly used for drying straw for a working boiler installation. For this purpose, several solutions with appropriate modifications should be considered to reduce the drying time. Additionally, in such a modified dryer, there is no need to use heated air as a drying agent, because the purity of the material is not important in this case. Heating the air with gas and liquid fuel burners, or using electric heaters, does not make economic sense. The costs of preparing such a drying agent are very high and could exceed the benefits achieved during the drying process. Owing to the fact that straw used for energy purposes does not have to meet high quality standards (as in the case of hay), it is possible to use direct hot fuel gasses (waste heat), which come from combustion in a biomass boiler. Such utilized waste heat increases the efficiency of the entire system and helps to obtain much more energy fuel. In a further part of the chapter, a unique solution is presented to meet the assumed goals, that is, a straw batch dryer for drying fuel in the shortest possible time. This paper presents experimental results of the heat and mass transfer in a cylindrical bale of straw during the straw drying in three different configurations.

2. DESCRIPTION OF THE INSTALLATION AND MEASUREMENT METHODOLOGY

The main elements of the dryer used in the study include the drying chamber, the transport table, the discharge fan, the fire prevention system, the regulation assembly, the system for the control of operational parameters, the system of pre-extraction and separation of sparks, and the exhaust system. The heat used in the drying process comes from the biomass combustion in the 500 kWth batch straw boiler. In this type of boiler, fuel is manually fed into the combustion chamber. The boiler is a typical straw batch boiler with counter-current combustion. The boiler has two chambers. The first chamber is a primary combustion chamber where fuel undergoes gasification, and the second chamber is a secondary combustion chamber where the products from gasification are burned in the atmosphere of the secondary air. Next, fuel gasses flow through the heat exchanger and leave the boiler.

For safety reasons, the exhaust gases coming from the boiler are pre-dusted in the sedimentation chamber (cyclone) due to the presence of large, sometimes incandescent, stalks of unburned straw. The fuel gasses are divided into two streams. The first stream of flue gasses is directed to the chimney. The second stream is used in the drying process. The gases are transported to a special mixer, where, if necessary, the process of mixing of the exhaust gas with ambient air takes place in order to obtain the desired temperature of the drying agent. It is necessary to control the drying agent temperature owing to the possibility of ignition of dried straw at a high temperature. After the mixing process, the fan presses the previously prepared mixture, using a specially designed nozzle, into the cylindrical bale of straw. A schematic diagram of the system is presented in Figure 1.

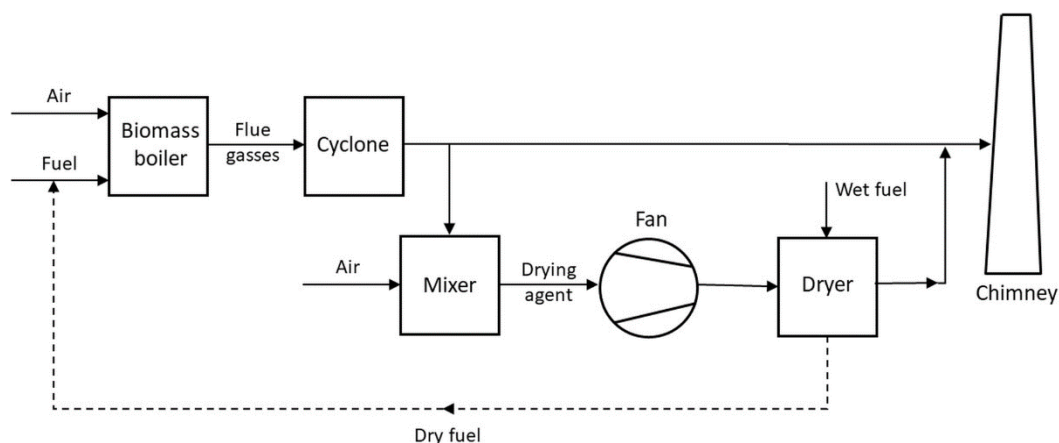


Figure 1: Schematic diagram of the testing site.

The effectiveness of drying cylindrical straw bales by exhaust gasses was measured using a specially manufactured measuring system equipped with eight measuring probes. Each probe was equipped with temperature and humidity sensors. The system collected data every second. First, the probes were calibrated using samples of straw characterized by varying humidity levels. The measuring probes were made of metal, had a diameter of 0.5 cm each, and are of varied lengths: two probes each of 80 cm, 60 cm, 40 cm, and 20 cm. These lengths were matched to the bale diameter (it was 80 cm) so that the longest probes were placed in the bale axis and the two 20 cm probes were placed closer to the surface of the bale. Figure 2 present the drying agent injection nozzle and probes which are used for temperature and humidity measurement. The measurements were carried out 40 cm far from the place where the drying agent was pumped to the bale. Figure 2 presents the modified-3 drying variant (described in Table 1).

Humidity sensors integrated with the measuring probes measure the medium humidity placed in interstalls area. In order to determine the humidity of the material (straw), it was necessary to determine the calibration curve, which could be used to convert the medium moisture to the material moisture. A number of measurements were made to adjust the dependence of medium-straw moisture and using (Hedlin, 1967) an appropriate conversion formula was implemented to obtain straw moisture.

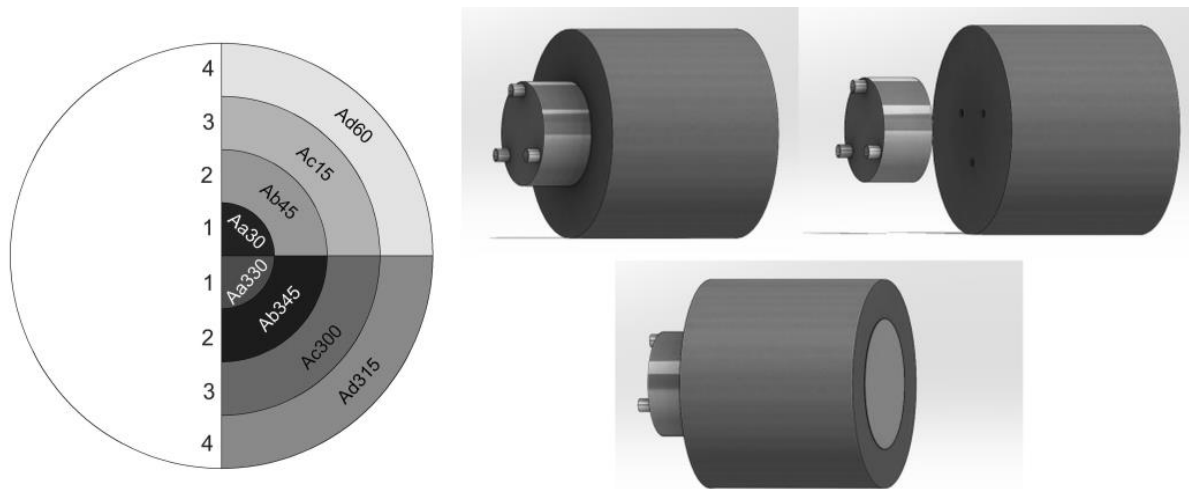


Figure 2: Left: Visualisation of placing probes in measuring layers 1, 2, 3, and 4; Right: visualisation of modified-3 variant of drying (drying nozzle, three holes along the straw bale and metal plate).

In addition, a dedicated measuring device was used to measure the temperature, humidity, and differential pressure of the drying agent. The measuring instruments were installed on a specially made drying agent monitoring channel. The channel is shown in Figure 3.

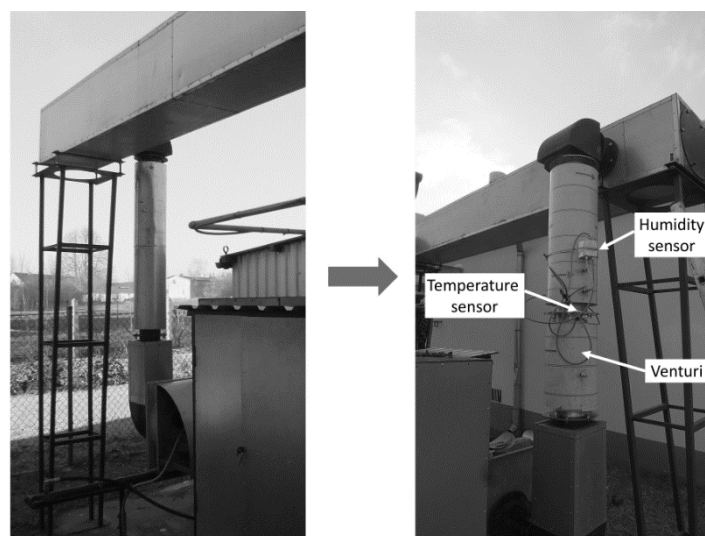


Figure 3: The monitoring channel.

The monitoring channel consisted of two separated channels. In the longer channel at the top, humidity and temperature sensors had been installed. In the shorter channel, the venturi flowmeter was placed. The thermocouple was used for temperature measurement; however, the humidity of the drying agent was measured by the dew point method. The dew point is found by measuring the capacitance of the capacitor placed on the Peltier cell.

The measurement elements were connected to a dedicated data logger, which had been synchronized with the temperature and humidity recorders in the straw bales. The measurement data (temperature, humidity, and flow of drying agent) were recorded on the SD card with an interval of 1 s.

In order to obtain a temperature distribution on the bale surface, which is impossible to visualize with the use of probes, the method of thermography was used. Thermo Tracer H2640 thermal imager from NEC was used. The measuring stand with the camera is shown in Figure 4. Camera is equipped with an uncooled microbolometer matrix with dimensions of 640x480 pixels. The measurement accuracy is 2°C or 2% of the measured value - depending on which value is higher. The thermal resolution of the camera is 0.03°C, which allowed for accurate display of temperature distributions. The measuring range consists of three sub-ranges: 1) from -20 to + 60°C, 2) from -40 to 120°C and 3) from 0 to 500°C. The spectral range of the camera is from 8 to 13 μm. The obtained results from the use of a thermal imaging camera helped to illustrate the effectiveness of bale penetration by drying agent. This method allowed to compare of different drying methods.



Figure 4: Testing stand of thermal imaging camera.

For research purposes, three variants of the straw drying process were selected based on the number of holes along the bale axis and the use of a metal plate blocking the axial flow of the drying agent. These variants are defined in Table 1.

Table 1: Variants of straw drying.

Variant of the drying process	Type of modification	Additional information
Basic	None	None
Modified-1—one hole	One hole with a diameter of 60 mm	Metal plate with a diameter 1000 mm on the opposite side of the bale relative to the location of the drying agent inlet (Figure 2).
Modified-3—three holes	Three holes with a diameter of 60 mm	As above.

Variants of the drying process were selected on the basis of preliminary experiments and analysis of their results. The results led researchers to the decision to introduce the described modifications of the drying process.

Preliminary measurements in a basic drying process showed that the drying agent flows primarily along the bale axis, which caused the heating and drying of only a small part of the straw bale in its axis. This resulted in an under heating of the more external bale layers, wherein the temperature was low and the humidity remained at the same high level. Owing to this problem, modifications of the drying process were applied. Creating a hole along the bale axis helped to better distribute the drying agent in the bale. These modifications were introduced to intensify the drying process and to achieve homogenous temperature field and the smallest possible humidity field within the considered bale.

3. RESULTS

The measurements were carried out in three configurations (basic, modified-1 and modified-3) to examine the effect of the presence of the holes inside the bale of straw on the dynamic of cylindrical straw bales drying. In addition, in each drying process the temperature of the drying agent injected into the bale was recorded. The drying agent temperature is presented in charts in the form of a dash dot curve with the values given on the right axis. The basic and modified process of drying took 140 minutes.

3.1. The basic drying process

Figure 5 presents the variation of humidity and temperature inside the bale of straw in the basic drying process (without the holes). The initial humidity of the bale was in the range of 23%–43%. The internal layers of the bale were drier, and the humidity increased along with the distance from the centre of the bale. This was caused by the fact that the bale had not been covered while storing.

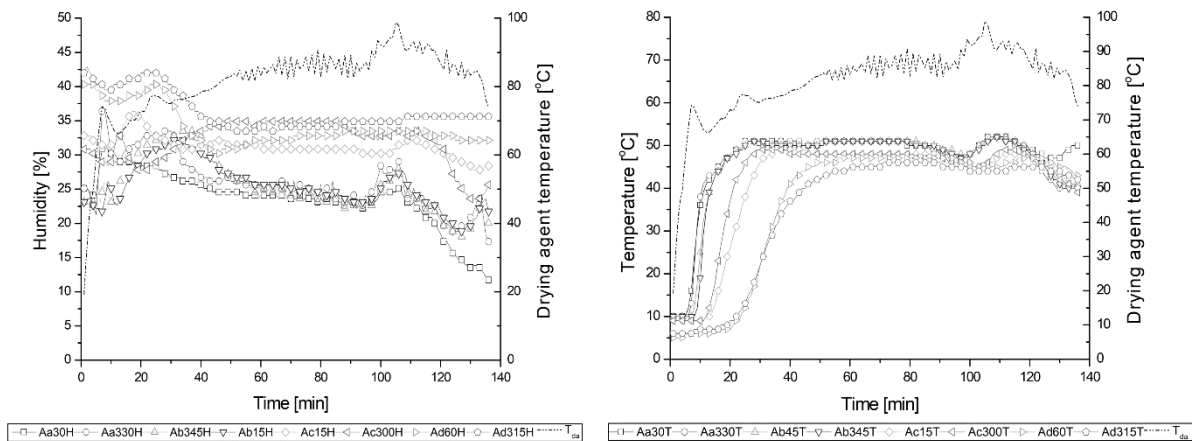


Figure 5: Basic drying process, humidity and temperature measurement.

In the initial drying phase, one could note a sharp increase in the humidity at the inner layer of the bale represented by sensors Aa30H and Aa330H. This was due to the rapid temperature increase in this part of the bale, which contributed to the temporary increase in relative humidity. After the 30th minute of the measurement, a decrease in humidity in the first and second layer (the layers are presented in Figure 10.6) could be observed. This decrease continued until the end of the measurement. In the case of layers 3 and 4, a stable humidity oscillating in the range of 30%–35% was observed. The final humidity value after the measurement reached the value of 12%–35%.

Figure 5 presents the temperature changes inside the bale of straw in a period of 140 minutes of the drying process. Five minutes after the drying process was started, a rapid temperature increase was observed in layer 1. Subsequently, after another 2 minutes passed, rapid heating of layer 2 was observed. Layers 3 and 4, because of their distance from the centre of the bale, heated up much more slowly, and the beginning of the temperature increase in these places could be observed from the 15th and 20th minute, respectively. The maximum temperature for layers 1 and 2 was achieved in the 25th minute of the measurement and its value was approximately 52°C. In the case of layer 3, the highest temperature of 50°C was reached in the 35th minute. The extreme plane was heated at the lowest rate and reached the lowest temperature, reaching a maximum of 46°C at approximately the 60th minute of the measurement. After reaching the temperature of 85°C, the drying agent temperature was maintained until the end of the combustion process.

3.2. The modified-1 drying process

Figure 6 presents the changes in humidity and temperature for the bale with the application of the one hole and the metal plate. The initial humidity of the bale, which was subject to the measurement for the modified drying process with one hole, oscillated within 25-45%.

In the initial phase of drying process, starting from about 10 min it is seen an increase in humidity in all bale layers. This is due to the rapid increase of temperature in the bale, which contributed to temporary exceeding the dew point temperature. After 20 minutes from the start of the measurement, the humidity in the whole bale begin to decrease. The most rapid drop is visible in layer 1 and it lasts up to 40 minutes of measurement. Then, the humidity in this layer stabilizes and at the end of the drying process it reaches the value of approx. 8%. For the second layer

up to 90 minutes, the humidity remains constant at 28-33%. After 90 minutes, the humidity begins to drop rapidly and reaches a value similar to the layer 1. Layers 3 and 4 behave similarly to drying in the basic drying process, i.e. the humidity remains constant at 30-35%.

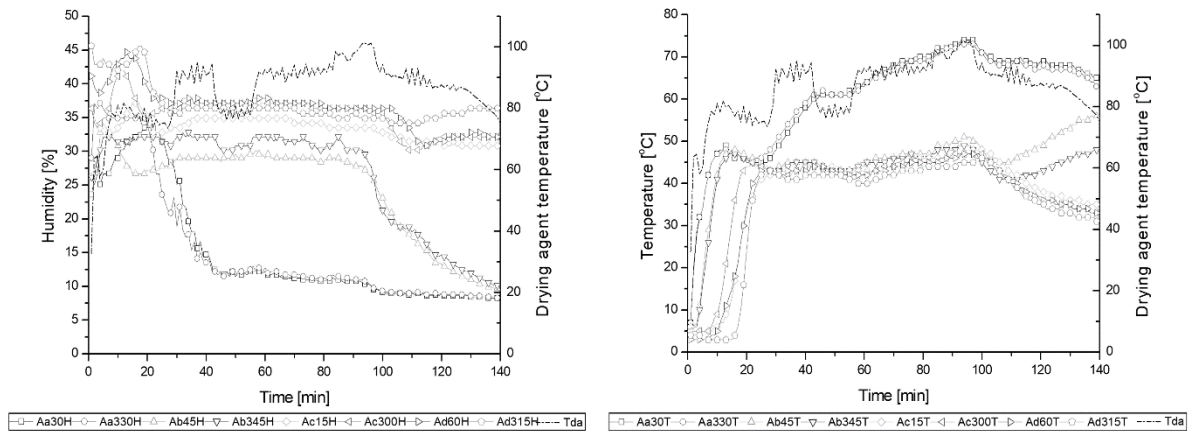


Figure 6: Modified-1 drying process, humidity and temperature measurement.

Figure 6 shows the change in temperature inside the straw bale during the drying process. After 2 minutes from the beginning of the drying process, it is noticed a rapid temperature increase in the layer 1. Then, after another 2 min, the second layer heats up quickly. Layers 3 and 4 due to significant distance from the bale axis heat up much longer, and the beginning of temperature increase in these layers is observed from 10 and 15 minutes, respectively. The maximum temperature for the layer 1 is achieved in 90 minutes of measurement, with its continuous increase during the combustion process, and its value is 74°C. For subsequent layers, the temperature is maintained at a similar level and fluctuates within 40-50°C, and its maximum is achieved similarly to the layer 1, at the 90th minute of the measurement. The temperature of drying agent during the entire combustion process fluctuated within the range of 80-95°C.

3.3. The modified-3 drying process

Figure 7 presents the changes in humidity and temperature for the bale with the application of the three holes and the metal plate.

The initial humidity of the bale, which was subject to the measurement for the modified drying process, oscillated within 30%–45% and was comparable to the bale used in the first and second drying process. The inner layers of the bale were drier and the further from the centre of the bale the higher was the humidity.

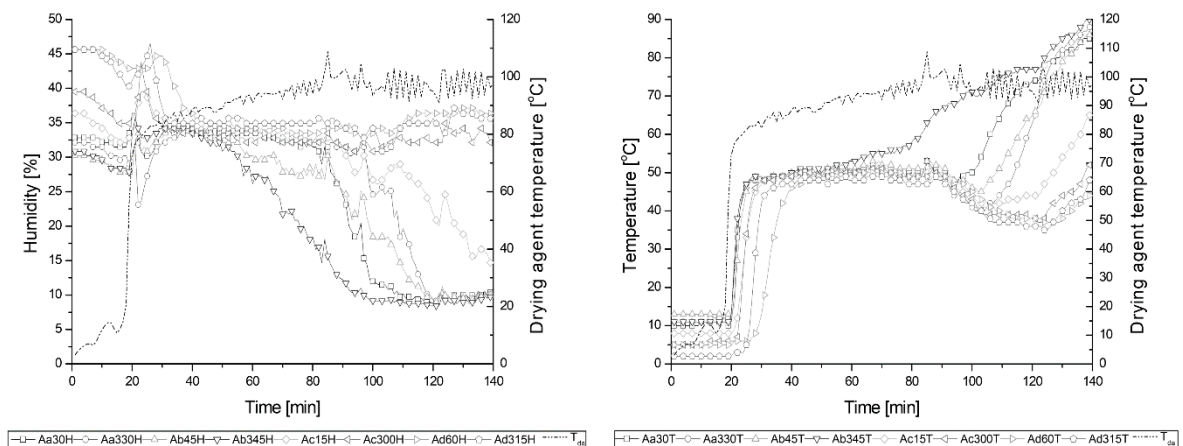


Figure 7: Modified-3 drying process, humidity and temperature measurement.

In this case, problems occurred with igniting the straw in the biomass boiler, and thus the drying agent had a very low temperature. In the 18th minute of the measurement, it was possible to observe a sudden increase of the drying agent temperature, which proved that the fuel started burning in the combustion chamber. After a sudden increase

in the drying mixture temperature, a sudden humidity increase was observed, and after approximately 5 minutes the humidity slowly declined. After 5 more minutes, the humidity in the whole bale was stabilized and reached 35%. Subsequently, until the 120th minute of the measurement, a sudden decrease of humidity was observed, and after another 20 minutes the humidity in layers 1 and 2 was stabilized at the level of 10%. Layers 3 and 4, just as in the previous measurements, were characterized by a similar humidity of approximately 35%.

Figure 7 presents the temperature changes inside the modified bale of straw. Until the ignition of the fuel in the combustion chamber, one may observe a similar temperature value throughout the entire bale of straw. In the 20th–25th minute of the drying process, a rapid rise in temperature in all layers was observed, until the temperature reached 50°C. Subsequently, a stable temperature value may be observed in all layers, until the 90th minute. After this period, the temperature in layers 1 and 2 started to increase and it reached a maximum of 90°C. The maximum temperature reached in layers 3 and 4 was 60°C. The drying agent temperature during the entire period of the drying process varied between 90 and 100°C.

3.4. Thermal imaging

Figure 8 presents thermal images of straw bales, taken from the front of the bale, after the drying process. The thermal imaging camera was set to the same emissivity in each case, which allows to accurately compare the bale heating rate for different drying variants. The ambient temperature was from -8°C to -12°C.

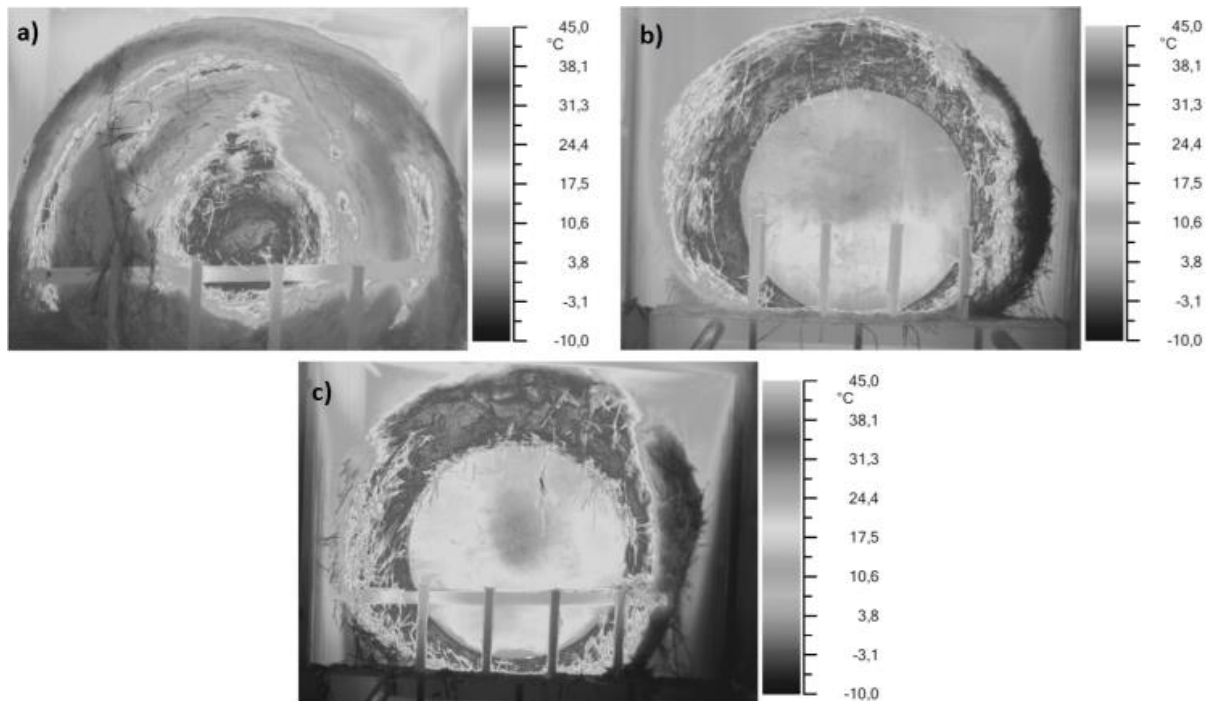


Figure 8: Thermal images, a) basic drying process, b) modified-1 drying process, c) modified-3 drying process.

Thermograms have been calibrated to a temperature range from -10 to 45°C. In the first case (Figure 8a) one can notice the axial flow of the drying agent, which has been confirmed experimentally in Chapter 3.1. Only a small part of the agent is directed to the outer bale areas. The cases modified-1 and modified-3 differ significantly from basic drying process, because the major part of the drying agent is directed radially. In both of these cases, the bales warm up very similarly. Interpretation of temperature distributions may be difficult due to the presence of a metal plate that is well heat conductive.

In the case of basic process, the highest temperatures in the bale axis can be observed and it is 40.9°C maximum. Along the outer layers the average temperature is much lower, oscillated within 0.2°C and 3.6°C. In the case of modified-1, almost the entire surface had the same temperature of about 40°C. In the case of modified-3, in the bale with three holes, the temperature was very similar to those of a bale with one hole. The maximum temperature was around 39°C in entire front surface of the bale. It can be noticed that the use of the modification of drying process could greatly penetrate the straw bale by a drying agent.

4. CONCLUSION

A summary of the drying results for three variants is presented in Table 2. The results of the experimental measurements clearly show that the modified drying process, with one and three holes made along the straw bale axis and with the metal plate on the opposite side of the bale from the drying agent injection site (variant modified-1 and modified-3), is much more efficient solution compared to basic one. However, the modified-3 is the optimal variant of straw drying. In this case, the drying time of the straw can be reduced by more than half compared to basic one.

Table 2: Results of straw drying in different variants.

Variant of drying process	Drying time [min]	Mean weighted humidity		Mass of evaporated water [kg]	Drying rate [kg/h]
		Before drying	After drying		
Basic	140	33.8%	28.1%	8.3	3.56
Modified-1	140	36.9%	25.8%	11.4	4.89
Modified-3	140	39.6%	25.5%	24.8	10.62

In the modified-3 case, with three holes, it was sufficient to dry the straw for about 280 minutes. It should be noted that in the existing system, only part of the exhaust is used to dry the straw. Considering that one cylindrical straw bale is burned in the boiler for about 120–150 minutes, it is able to dry another bale to a satisfactory humidity value using only fuel gases that come from the combustion of one bale. With the maximum possible use of the entire volume of exhaust gas for the fuel drying, it would be possible to shorten the drying time.

During measurements, an increase in humidity in the bales can be observed with a sudden increase in the temperature of the drying agent. The increase in temperature of the drying medium also caused a sudden increase in temperature in the individual bale layers. At a constant temperature of the drying medium, there was a slow process of straw drying only from the outer layers of straw stalk, which is visible in the graphs as a constant humidity value or a slow decreasing in the given measurement point. When the temperature rises rapidly, the water trapped inside the straw stalks begins to release rapidly from its interior after providing the appropriate amount of energy. This moisture went to the interstalks area causing a sudden increase in humidity in the area. Subsequently, the released moisture moved along with the flowing drying agent to subsequent bale layers, and in a given measurement area, the humidity stabilized and returned to the value from before the sudden increase in temperature.

Analysing Table 2, it can be clearly determined that the optimal solution is a modified drying process with three holes, which allows for an increase in straw drying efficiency by approximately 70% compared to the basic process. A dedicated straw dryer installation provides the user enormous financial benefits. Taking into account the results of drying straw in modified variant, it is possible to dry the straw from 40% to 25% humidity, which translates into a change in the heating value from 9 to 12 MJ/kg (Doundy, 2011), that is, producing 30% more heat from a given mass of fuel. Therefore, using a straw dryer for a 250 kg bale (typical bale weight), it is possible to obtain 750 MJ, and considering the efficiency of heat generation in a biomass boiler, 615 MJ more heat.

The analysis of thermographic images confirms the results of the measurements of temperature and humidity inside the straw bale presented in Chapter 3. It shows that the modified drying process (modified-1 and modified-3) is much more effective than the basic one. Thermovision measurements revealed the complex nature of the drying agent flows and the significant impact of local heterogeneities in straw density, porosity or other effects inside the bale. It should be remembered that many factors disturb the bale image as a structure with constant spatial density, porosity, etc.

5. ACKNOWLEDGEMENT

This work was financially supported by the Subvention and Subvention for Young Scientists, 16.16.210.476, Faculty of Energy and Fuels, AGH University of Science and Technology, Krakow, Poland.

6. REFERENCES

- Boundy, B. et al., 2011. Biomass energy data book, Appendix A - The effect of moisture on heating values, Oak Ridge National Laboratory, Tennessee
- Cao, W.F., Langrish, T.A.G., 2010. The development and validation of a system model for a countercurrent cascading rotary dryer, *Drying Technology*, 18(1-2), 99-115
- Descouteaux, S., Savoie, P., 2006a. Bi-directional dryer for mid-size rectangular hay bale, *Applied Engineering in Agriculture*, 22(4), 481–489

- Descoteaux, S., Savoie, P., 2006b. Bi-directional dryer for mid-size rectangular hay bales, *Applied Engineering in Agriculture*, 22(4), 481–489
- Gebreegziabher, T., Oyedun, A.O., Hui, Ch.W., 2013. Optimum biomass drying for combustion – A modeling approach, *Energy*, 53, 67–73
- Goryl, W., Filipowicz, M., 2016. The possibility of using flue gases as a medium for straw drying, *E3S Web of Conferences* 10, 00136
- Goryl, W., Filipowicz, M., 2017. Experimental and numerical analysis of cylindrical straw drying, *EPJ Web of Conferences* 143, 02031
- Haque, N., Somerville, M., 2013. Techno-economic and environmental evaluation of biomass dryer, *Procedia Engineering*, 56, 650–655
- Hedlin, C.P., 1967. Sorption isotherms of five types of grain straw at 70°F, *Canadian Biosystems Engineering*, 1, 37-38,42
- House, H.K., Stone, R.P., 1988. Barn hay drying, *Ontario Ministry of Agriculture and Food*, 88–110
- Jchua, K., Chou, S.K., 2003. Low-cost drying methods for developing countries, *Trends in Food Science & Technology*, 14(12), 519–528
- Korn, O., 2001. Cyclone dryer: a pneumatic dryer with increased solid residence time, *Drying Technology*, 19(8), 1925-1937
- Lewicki, P.P., 2006. Design of hot air drying for better foods, *Trends in Food Science & Technology*, 17(4), 153–163
- Li, H. et al., 2012. Evaluation of a biomass drying process using waste heat from process industries: A case study, *Applied Thermal Engineering*, 35, 71–80
- Misener, G.C. et al., 1990. Drying of large round hay bales, *Canadian Biosystems Engineering*, 32, 263–268
- Morissette, R., Savoie, P., Lizotte, P.L., 2011. Drying baled hay with combined solar and biomass heat sources, *The Canadian Society for Bioengineering*, Paper No. CSBE11-203.
- Parker, B.F. et al., 1992. Forced-air dring of baled alfalfa hay, *American Society of Agricultural Engineers*, 35(2), 607–615
- Ratti, C., 2001. Hot air and freeze-drying of high-value foods: A review, *Journal of Food Engineering*, 49(4), 311–319
- Roman, F.D., Hensel, O., 2014. Numerical simulations and experimental measurements on the distribution of air and drying of round hay bales, *Biosystems Engineering*, 122, 1–15
- Savoie, P., Descoteaux, S., 2004. Artificial drying of corn stover in mid-size bales, *Canadian Biosystems Engineering*, 46, 2.25–2.34
- Song, H. et al., 2012. Influence of drying process on the biomass-based polygeneration system of bioethanol, power and heat, *Applied Energy*, 90(1), 32–37
- Verma, M. et al., 2017. Drying of biomass for utilising in co-firing with coal and its impact on environment – A review, *Renewable and Sustainable Energy Reviews*, 71, 732–741
- Weaver, J.W., Grinnells, C.D., Lovvorn, R.L., 1947. Drying baled hay with forced air, *Agricultural Engineering*, 28(7), 301–304
- Yi, J., Li, X., Duan, X., 2019. Drying efficiency and product quality of biomass drying: a review, *Drying Technology*, Published Online, DOI: 10.1080/07373937.2019.1628772

#285: Insight into the dynamics and performance of vertical-axis turbines with pitch optimisation

Zulfaa MOHAMED-KASSIM¹, Yew Hao LIM², Noorfazreena M. KAMARUDDIN³

¹ School of Aerospace Engineering, Universiti Sains Malaysia, 14300 Nibong Tebal, Penang, Malaysia, zulfaa@usm.my

² School of Aerospace Engineering, Universiti Sains Malaysia, 14300 Nibong Tebal, Penang, Malaysia, steven.lim0403@gmail.com

³ School of Aerospace Engineering, Universiti Sains Malaysia, 14300 Nibong Tebal, Penang, Malaysia, fazreena@usm.my

Vertical-axis hydrokinetic turbines, with their simpler designs and omnidirectional characteristics, have the potential to supply renewable energy cost-effectively from river streams for off-grid remote communities. However, their low performance efficiencies hinder the large-scale applications of these turbines. Previous works have suggested that applying pitch angles on the blades of these turbines can improve their efficiencies. This work aimed to numerically investigate the effects of pitch optimisation on the performance of a straight-bladed vertical-axis turbine, in terms of its torque and power coefficients. Two pitch-optimisation modes, fixed and variable-pitch angles, were employed in addition to the baseline configuration of the turbine at different tip-speed ratios. The dynamics of the turbine were studied in terms of the blade incidence angles and the resultant aerodynamic and rotary forces on the blades. A semi-empirical model was developed herein using to model a simple H-type vertical-axis turbine with three blades, using real aerofoil data to represent the aerodynamic characteristics of the blades. Analyses of the results at a tip-speed ratio of 1 showed that variable-pitch optimisation was far more effective, compared to the fixed-pitch mode, in improving the torque and power coefficients of the turbine. This dynamic mode improved the turbine performance by eliminating, almost entirely, the torque-suppressing drag-induced component of the tangential force throughout the full rotation of each blade. Fixed-pitch optimisation, on the other hand, had competing gains and losses in the downstream and upstream regions, resulting in marginal increments of the turbine performance. This competing effect was eliminated at a higher tip-speed ratio of 2, effectively improving the impact of fixed-pitch optimisation on the turbine performance. In both cases of the tip-speed ratios, positive and negative radial force coefficients on the blades were both unfavourable. Unfortunately, their average values scaled more than eight times higher than those of the tangential force coefficients.

Keywords: vertical-axis turbine; hydrokinetic turbine; turbine dynamics; turbine performance; pitch optimisation

1. INTRODUCTION

Small and micro hydrokinetic turbines offer exciting potentials to generate renewable energy, cost-effectively, from river streams in remote geographical locations to small communities unconnected to power grids linked to large-scale power stations or hydropower plants. Such turbines extract kinetic energy from water streams by being immersed directly into water without adversely affecting the near surrounding. On the contrary, conventional hydropower plants rely on elevated hydraulic heads using dams or reservoirs with sizable land modification or clearing that are detrimental to the local environment, communities, and natural habitats. The hydrokinetic turbines can also potentially replace out-dated diesel or gasoline generators primarily used by residents living in such remote locations. In addition to producing harmful by-products in the form of air pollutants and noise emission, the fuel used to power these generators can be excessively costly due to the transportation costs into remote areas (Anyi et al., 2010).

In Malaysia, the potential for using river-based hydrokinetic turbines is particularly evident for its eastern states in the Borneo Island: Sarawak and Sabah. Their vast networks of river streams, providing ample opportunities for hydrokinetic applications, are supplied by the longest and second longest rivers in Malaysia, the Rajang River (~563 km) in Sarawak and Kinabatangan River (~560 km) in Sabah, respectively (Salleh et al., 2018). Crucially, both states have the poorest electrification in Malaysia where more than 30% of their rural communities do not have access to the electricity supplied by the state governments (Borhanazad et al., 2013). This scenario boosts the need to have alternative sources of renewable electricity, such as that provided by hydrokinetic turbines, for these communities.

Of the two primary types of hydrokinetic turbines, vertical-axis turbines (VAT) offer more cost-effective solutions for rural electrification compared to the horizontal ones, primarily due to their design and manufacturing simplicity as well as generator positioning (Khan et al., 2009). Furthermore, these turbines can receive streams in any direction (i.e., omni-directional) and thus do not need to be equipped with yaw control systems, as is the case for horizontal-axis turbines (Yen, 2012). Their rotors can be equipped with straight blades instead of the twisted- or tapered-blade profiles essential for horizontal-axis turbines; these advanced blade profiles typically require delicate machining. Turbine generators can also be positioned above the water level on one end of the shafts, eliminating the costs to use water-tight containers to house the generators. Other technical benefits of the vertical-axis turbines include manufacturing scalability and low maintenance. These turbines also have the advantages of operating in shallow water with varying or limited flow velocities (Vermaak et al., 2014).

Existing issues of the vertical-axis turbines, nonetheless, prevent large-scale implementations of these turbines in rural and remote locations. A vertical-axis turbine is known to suffer from torque ripple, low performance efficiency, and low starting torque (Kirke and Lazauskas, 2011). Because of the cyclical variation of the incidence angle of the blade (i.e., its angle of attack), each rotor blade experiences large fluctuating aerodynamic loads during each revolution as well as fluctuating tangential forces and torques (hence, torque rippling) produced from these loads. These cyclical effects in turn reduce the mechanical power produced from the rotating blade and thus the performance efficiency of the turbine to generate electricity through the generator. The rippling of the torque also reduces the ability of the turbine to self-start from a resting position. At the same time, the cyclical variation also generates large fluctuating radial forces that can produce shaking on the rotor and strain the rotor arm over a long period of time.

The performance of vertical-axis turbines can be improved to overcome the limitations as described above. For instance, shaking can be reduced using helical and multiple blades (Kirke and Lazauskas, 2011), and turbine efficiency and self-starting ability can be improved using pitch optimisation of the blade angle (Kirke and Lazauskas, 2008) and duct augmentation to increase local flow velocity going into the turbine (Kim and Gharib, 2013; Ponta and Dutt, 2000). Improved blade geometry has also been studied, where a J-shaped profile of a straight-bladed Darrieus turbine was found to improve its self-starting ability by leveraging on drag forces at lower angular speeds of the rotor (Zamani et al., 2016).

Of particular interest to the work herein is the pitch optimisation, which aims to improve turbine efficiency by optimising the incidence angles of the blade as it rotates across different azimuthal positions. Two approaches have been suggested in the literature with regards to pitch optimisation: the addition of either fixed- or variable-pitch angles to the baseline blade orientation with respect to the turbine rotor. Fixed-pitch optimisation requires a reorientation of the blade on its rotor arm that remains unchanged throughout the blade rotation. Various researchers found different improvements to the performance of different configurations of vertical-axis turbines. These improvements were shown in the form of increased power coefficient (C_p). For instance, Fiedler et al. (2009) measured increased performance of up to 29% at negative, or toe-in, pitch angles for H-type vertical-axis turbines tested with NACA 0015 and 0021 blade profiles. Using a straight-bladed Darrieus turbine with a NACA 0015 blade profile, Rezaeiha et al. (2017) computed a maximum increment of 6.6% on C_p at a pitch angle β of -2° .

Variable-pitch optimisation, also referred to as dynamic pitching, offers a more promising solution to improve turbine performance by continuously reorienting, and optimising, the blade incidence angle independently at each azimuthal position of the blade during its rotation. Albeit more complex and costly to implement, the variable-pitch optimisation approach can potentially offer much improved turbine performance compared to the fixed-pitch solution (Kirke and Lazauskas, 2011). Abdalrahman et al. (2017) showed that the percentage improvement exceeds 25% in the power output of an H-type vertical-axis wind turbine using variable-pitch control compared to that using a fixed-pitch. Moreover, the starting torque of a Darrieus turbine in variable pitch mode improved by about three times higher than that in a fixed-pitch mode (Kirke and Paillard, 2017).

The purpose of this work is to analyse the fluctuating dynamics of a straight-bladed vertical-axis turbine operating in different modes of pitch optimisation. The aim of this analysis is to gain insight into the behaviours of the aerodynamic forces on the turbine blades and their influence on the rotary (i.e., tangential and radial) forces and torques of the blades, to highlight key factors that improve turbine performance in the optimised conditions. A semi-empirical numerical model has been developed for this purpose, using actual aerofoil data to represent the aerodynamic characteristics of the blade over one rotor revolution. Correction factors were added using momentum-based models to compensate for the changes in the freestream flow, referred to as the induced velocity, as it moves downstream and interacts with the rotor blades across the turbine. The analogous operations of wind and hydrokinetic VAT rotors permit the use of wind-tunnel-tested aerofoil data to represent the aerodynamic characteristics of the turbine blade in this study. Outcomes of this work are presented in non-dimensional forms and are applicable for both wind and hydrokinetic vertical-axis turbines.

2. METHODOLOGY

2.1. Numerical modelling

A vertical-axis turbine was modelled as a simple H-type three-bladed rotor with a solidity of 0.5, a diameter of 1.03 m, and a height of 1 m. Each blade was straight and untwisted, had a chord of 85.8 mm, with its cross-section represented by the symmetrical NACA 0021 aerofoil. At 9 m/s, the freestream velocity of the flow (V_∞) had a Reynolds number (Re) of 3.82×10^4 , chosen to match the parameters from previous works for comparison. The schematic diagrams of the rotor and its relevant parameters are shown in Figs. 1(a-b), where θ is the azimuthal angle of the blade pivoted at the rotor shaft. V_b is the tangential (or rotational) velocity of the blade. V_a and V_e are the induced and effective (or resultant) velocities of the flow relative to the blade, respectively. F_L , F_D , F_T , and F_R are the lift, drag, tangential, and radial forces on the blade, respectively, with their coefficients labelled accordingly as C_L , C_D , C_T , and C_R , obtained by dividing these forces with the dynamic pressure of the local flow multiplied by the surface area of the blade. In Figure 1(b), β is the pitch angle of the blade, α is the baseline incidence angle of the blade (measured between the chord tangent to the blade path and the vector V_e), and α_e is the effective incidence angle (measured between the pitched chord and the vector V_e). θ covers the full rotation of the blade, ranging from -180° to 180° and discretised with an interval of 0.1° . The incidence angle of each blade changed as it rotated about the rotor shaft, due to its shifting orientation with respect to the freestream flow. The degree of this change depended on how fast the blade rotated, as quantified by its tip-speed ratio (TSR , or λ).

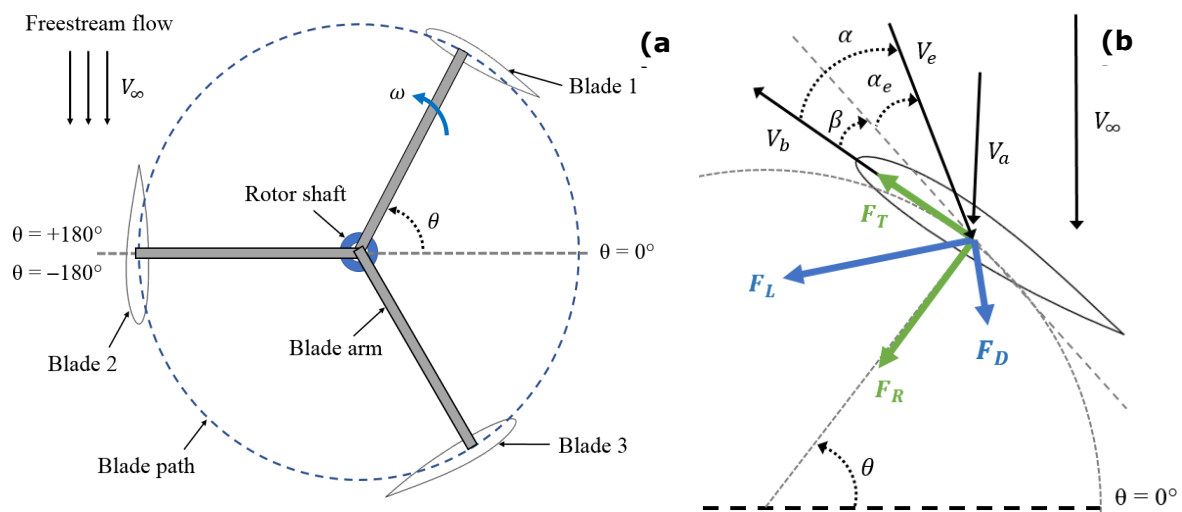


Figure 1: Top-view schematic diagrams of (left) the rotor blades, and (right) the associated flow geometry, forces, and parameters.

Aerodynamic forces on the blades were semi-empirically determined using the experimental data of the symmetrical NACA 0021 aerofoil from the measurements of Sheldahl and Klimas (1981); their coefficients of lift (C_L) and drag (C_D) are shown in Figure 2(a). The corresponding lift-to-drag ratio (C_L/C_D , or simply L/D) of the aerofoil, a standard measure of the aerodynamic performance of the aerofoil, had a maximum value of 35, achieved at a range of α between 8° to 9° . It maintained a large value above 33 for a wider range of α between 8° to 12° (see Figure 2(b)). Formulations to extract the aerodynamic and rotary forces on the blades, based on these empirical data, had been well established and could be referred to elsewhere; ours followed those in the review article by Islam et al. (2008). The equations to transform C_L and C_D onto the tangential and radial force coefficients (C_T and C_R , respectively) on the rotor blade, as shown in Figs. 2(c-d), were particularly important and are shown in Equations 1 and 2. The maximum magnitudes of C_R were larger by about six times than those of C_T , particularly for α between 45° and 135° and between -135° and -45° .

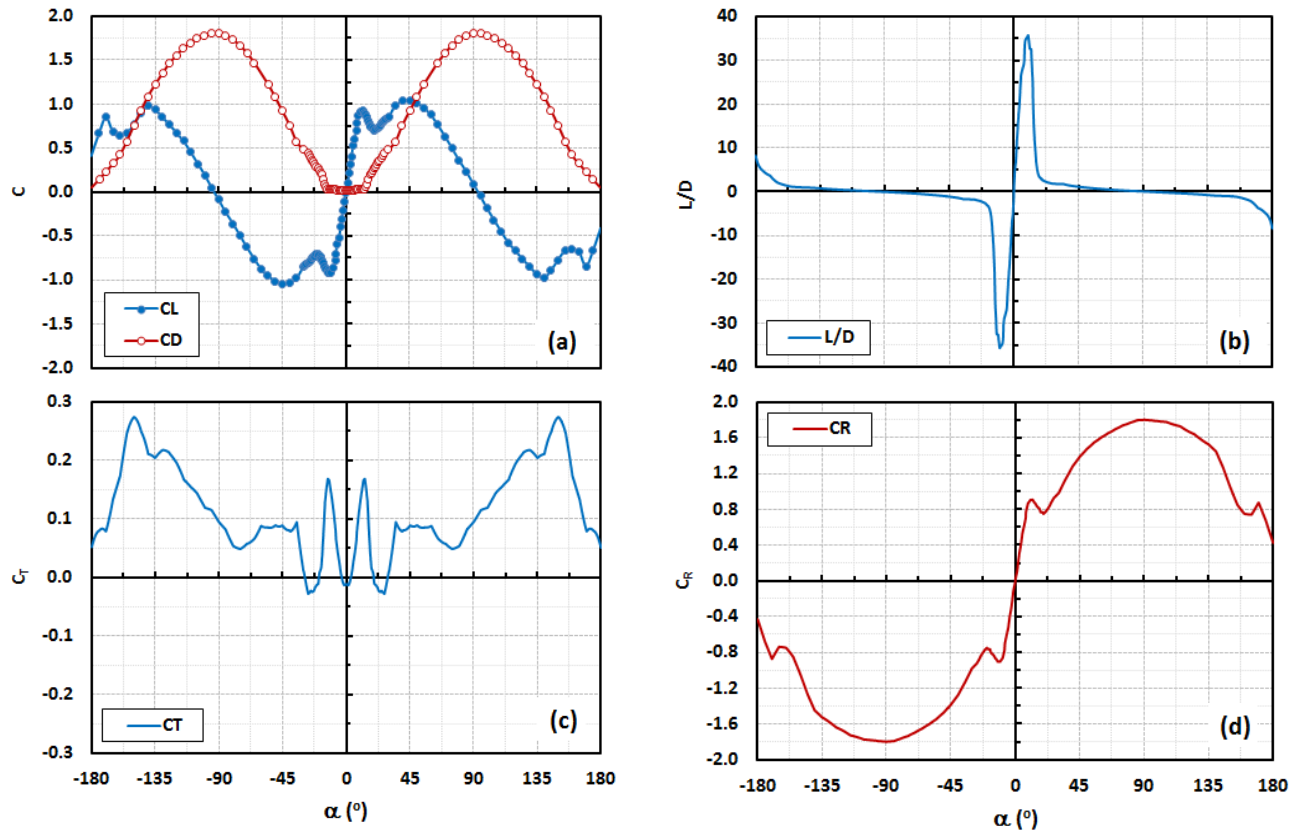


Figure 2: Plotted against the angle-of-attack of the NACA 0021 aerofoil: (a) the experimental data from Sheldahl and Klimas (1981) on the lift and drag coefficients of the symmetric aerofoil and (b) its corresponding lift-to-drag ratio. (c) The tangential force coefficient and (d) the radial force coefficient computed using Equations 1 and 2.

Included in the review by Islam et al. (2008) were the formulations for the average torque (Q) produced by a rotor and its coefficient (C_Q). The average torque was computed by integrating the tangential forces of the rotor blade at all θ over one complete rotation and averaging them, taking into account the total number of discrete θ taken. To account for multiple blades, the tangential forces for each blade were linearly superposed with those of the other blades to obtain the total torque. The turbine power (P) was equal to the total torque multiplied by the angular velocity ω of the rotor. P was based solely on the rotation of the blades without considering any losses. Its coefficient, C_P , is defined in Equation 3, where ρ is the air density and A is the swept area of the rotor.

Equation 1: The tangential force coefficient on the rotor blade

$$C_T = C_L \sin \alpha - C_D \cos \alpha$$

Equation 2: The radial force coefficient on the rotor blade

$$C_R = C_L \cos \alpha + C_D \sin \alpha$$

Equation 3: The power coefficient of the turbine rotor.

$$C_P = \frac{2P}{\rho V_\infty^3 A}$$

The effects of dynamic stall, tip-vortex, vortex-shedding, and curvilinear flow were not accounted for in the simulations herein. Transient effects were neglected as well by analysing blade rotations at fixed tip-speed ratios, equivalent to assuming that the rotor had attained its steady-state rotations. Blade-wake interactions were

approximated in the simulations by using a momentum-based double actuator disk model from the work of Biadgo et al. (2013). They modelled the flow across the turbine with fixed induced velocities, one each for the upstream (i.e., for $0^\circ \leq \theta \leq 180^\circ$) and downstream (for $-180^\circ \leq \theta \leq 0^\circ$) regions of the rotor. Without the induced effects, the flow across the turbine remained identical to the freestream flow prior to reaching the turbine. An improvement to the step-wise model of the induced velocities was proposed in this work, where the induced velocities were assumed to transition linearly across the turbine. Figure 3(a) shows the non-dimensional velocities of these induced flows, normalised against the freestream velocity.

2.2. Validation of the model

The numerical model in this work was validated against results from previous works, with matching turbine and operating parameters. In Figure 3(b), three different cases of the C_p simulated herein (based on different induced flow effects) were compared to the experimental and computational fluid dynamics (CFD) results from Castelli et al. (2011) and the CFD results from Rezaeiha et al. (2018). The simulation compared relatively well across a limited range of λ when the induced flow was assumed to transition linearly across the turbine, but with reduced accuracy at some tip-speed ratios. This linear-transition model was implemented in the remainder of the results computed and presented herein.

The low-order simulations in this study suffered marginally on accuracy, but allowed fast computational time and extended analysis in terms of a wider range of parametric variations. In particular, the optimisation study tested all pitch angles covering the entire 360° range with an interval of 0.1° . This coverage was important in the dynamic-pitch mode where the blade pitch was individually optimised at each θ . The recommended pitch angles to optimise turbine performance in the dynamic-pitch mode comprised of a larger range of angles compared to those in the fixed-pitch mode. Equally important was the extraction of detailed data of the tangential and radial forces, decomposed into separate contributions by the aerodynamic lift and drag forces on the blade. This extracted data provided insight into the main factors that promote, or suppress, the desired tangential forces to produce power, and the impact of pitch optimisation on these factors.

Due to its low computational cost, this model has the potential to be built up into larger system-level codes that includes modelling of the transient mode from rest to steady-state, the mass and moment of inertia of the rotor, incorporating the conversion from the mechanical energy of the rotor up to the final electrical power produced through a generator. The accuracy of this model can be improved modularly to include complex flow effects such as the dynamic stall, curvilinear flow, and better approximation of the wake flow.

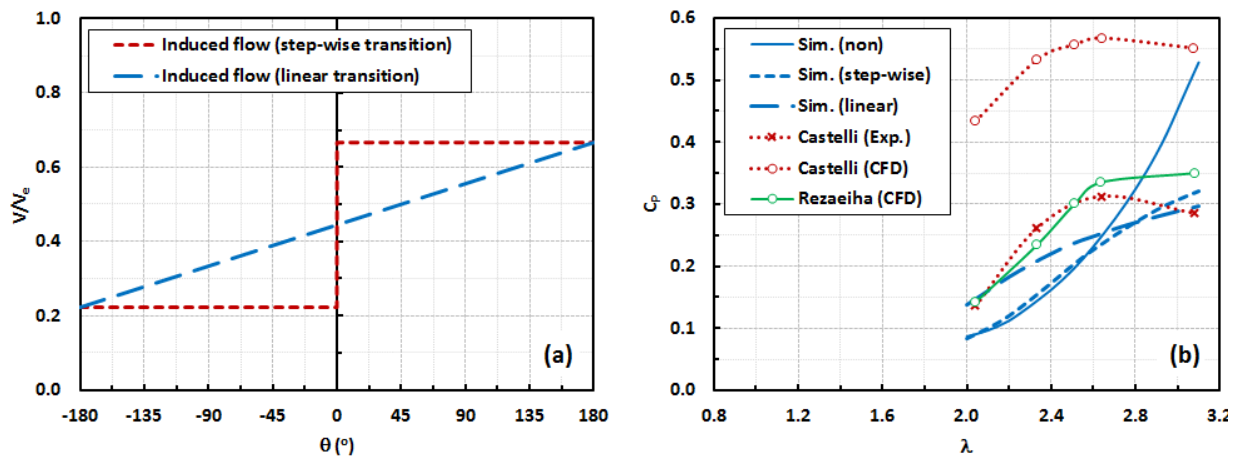


Figure 3: (a) The flow across the turbine with two types of wake-induced effects: step-wise and linear transition of the induced velocities. (b) The simulated C_p for three induced flow cases (no induced flow, step-wise transition, and linear transition) plotted against the experimental and CFD results of Castelli et al. (2011) and the CFD results of Rezaeiha et al. (2018).

3. RESULTS AND DISCUSSION

Two key aspects were focused to gain insight into the complex dynamics of the rotor of the turbine: (1) the dynamics and behaviour of the forces acting on its rotor blades, and (2) the influence of these forces on the turbine performance at different tip-speed ratios. Since the forces on each of the three blades of the turbine at the same θ were identical, subsequent plots and discussions of these forces are presented on one blade only. On the other

hand, the total torque and power based on the forces on the turbine rotor were computed and presented here with all the three blades accounted for.

Three pitching modes were simulated herein: a baseline, fixed-pitch, or variable-pitch mode where the blades were either unpitched or optimised with a fixed or varying β , respectively. For each mode, two cases of λ were chosen to examine the behaviour of the forces on the blades. The smaller $\lambda = 1$ represented the most dynamical, thus unfavourable, fluctuation of the forces as the blades began to operate in the lift-driven mode (i.e., when $\lambda > 1$); the larger $\lambda = 2$ demonstrated that substantial improvement could be achieved by simply doubling the tip-speed ratio.

3.1. Turbine Dynamics

Incidence and Pitch Angles

The complex dynamics of the vertical-axis rotor were primarily governed by the fluctuating effective incidence angles (α_e) of its blades, which in turn were controlled by their pitch angles. When unpitched, and with $\lambda = 1$, the blade incidence angles varied with a sinusoidal-like pattern and bounded between peak and trough values of 37.3° and -18.5° , respectively, as shown in Figure 4(a). The shift in the magnitudes of these bounds were due to the varying degrees of the induced wake effects experienced in the upstream and downstream regions. At $\lambda = 2$, maintaining the sinusoidal pattern, these angles were bounded with a narrower range of peak and trough values of 16.9° and -9.5° (see Figure 4(b)). This narrower range of the bounds was favourable because it confined the blade to operate within large values of its lift-to-drag ratio (see Figure 2(b)) and tangential forces (see Figure 2(c)), while maintaining smaller ranges of the unwanted radial forces (see Figure 2(d)).

When statically optimised, the rotor blades were best pitched at fixed β of -2.1° and 3.1° for the smaller and larger cases of λ (see Figs. 4(c-d)), respectively, to maximise its C_p . Accordingly, α_e shifted with the same amounts, relative to α , throughout all azimuthal positions. In the variable-pitch mode, for both cases of λ as shown in Figs. 4(a-b), the blades were optimised with α_e maintained around 10° to 12° when the blade traversed the upstream path, and around -12° to -10° during the downstream path. These angles coincided with large values of the lift-to-drag ratio of the aerofoil, i.e., $33 < L/D < 35$ (see Figure 2(b)). In this dynamic mode, the pitch angles varied over a larger range between -8.8° and 25.3° when $\lambda = 1$, and a smaller range between -8.8° and 8.8° when $\lambda = 2$. The larger range of pitch angles in the former case was less favourable as it might increase the complexity of building a mechanical system on the turbine to pitch the rotor blades at these large angles.

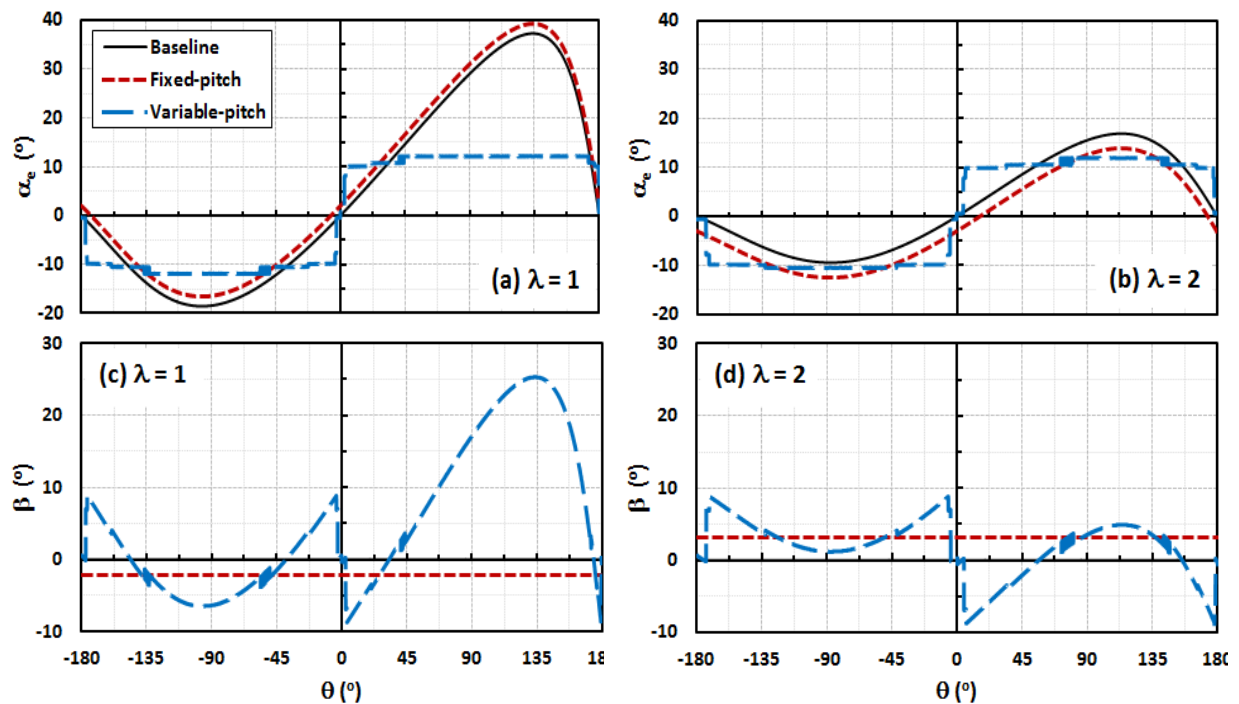


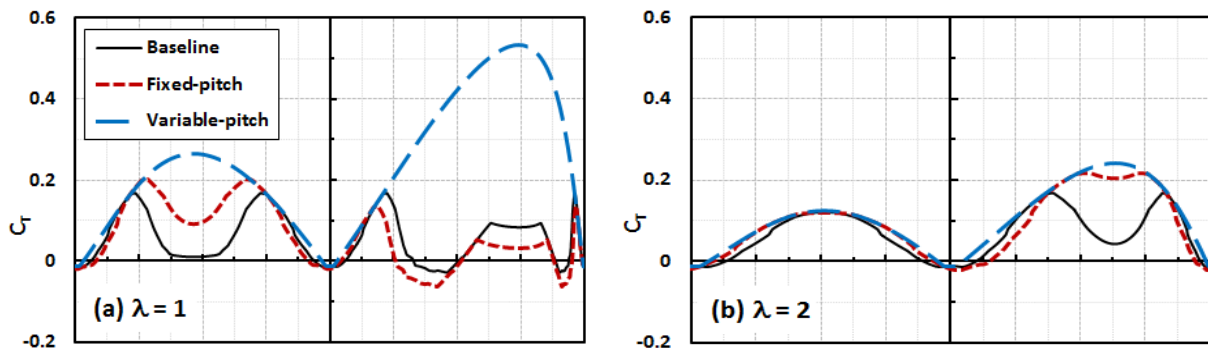
Figure 4: Plotted against θ for the two cases of λ and the three pitching modes: (a,b) the effective incidence angles and (c,d) the optimised pitch angles on the rotor blade. The legend in (a) applies to all the sub-plots in this figure.

Torque-Promoting Tangential Forces

The tangential force coefficients (C_T) acting on the blades for the two cases of λ and the three pitching modes are shown in Figs. 5(a-b). These force coefficients were favourable when they had positive values as these promoted the generation of the desired torque on the rotor. When $\lambda = 1$, the variable-pitch mode demonstrated highly favourable C_T values fluctuating with two peaks of 0.26 and 0.53 at θ of -85° and 134° , respectively. Both peaks were larger in comparison to those of the unpitched or fixed-pitch modes; the upstream peak for the variable-pitch mode was larger by more than three times the peaks of the other two pitching modes. This observation indicated that the performance of the turbine would be significantly improved if its blades were dynamically optimised (as demonstrated below in Figs. 7(a-b)). When $\lambda = 2$, the α_e values for all of the pitching modes became more comparable, resulting in almost similar behaviour and magnitudes of C_T across the blade rotation. This trend broke down, however, when the blade traversed the leading section of the upstream region (i.e., around $75^\circ < \theta < 155^\circ$), where C_T dipped lower, particularly significantly for the unpitched mode. These behaviours could be elucidated further by investigating into the dynamics of the components of the lift and drag forces that contributed in producing the tangential forces acting on the blade.

The tangential forces on the blade, at any θ , could be decomposed into two components: the lift-induced (i.e., the lift force on the blade projected onto its tangential direction) and drag-induced components. These are shown in Figs. 5(c-d) for the two cases of λ and the three pitching modes. An apparent behaviour observed here was that the lift-induced tangential force coefficients (C_{TL}) had almost similar magnitudes, with positive values, across the entire blade rotation for the two cases of λ , owing to the fact that the aerofoil still maintained large values of C_L up to $\alpha = 45^\circ$ (albeit with a local dip of 30% at $\alpha = 20^\circ$ as shown in Figure 2(a)), while the maximum peaks of α_e for both cases of λ were lower than that. The drag-induced components (C_{TD}), on the other hand, had negative values (which meant that they suppressed the production of the desired torque) and were drastically different between the variable-pitch mode and the other two modes. When unpitched with a λ of 1, the aerodynamic drag on the blade fluctuated with large negative values particularly in the upstream side of the traverse. These negative values suppressed the production of torque by cancelling out much of the torque-promoting tangential forces produced by the lift-induced component of the aerodynamic forces. When unpitched with $\lambda = 2$, most of the C_{TD} values were confined to favourably small magnitudes, except near the leading parts of the upstream traverse, resulting in a large dip in C_T in the same upstream region (see Figure 5(b)).

When $\lambda = 1$, pitching the blade with a fixed β had the desirable effect of decreasing the magnitudes of C_{TD} in the downstream traverse, but at the cost of minor increment on their magnitudes across a larger range of θ in the upstream traverse. It was estimated, from the observation of these behaviours, that any gains on the torque and power coefficients of the rotor would be small (as shown below in Figs. 7(a-b)). The situation was more favourable when $\lambda = 2$ because negative C_{TD} mostly occurred during the upstream traverse only (see Figure 5(d)); there was therefore no need to optimise the blade pitch in the downstream region. The fixed-pitch could then be better optimised specifically for the upstream region. As a result, its corresponding C_T values improved significantly, comparable to those of the variable-pitch mode. In the dynamic mode, the C_{TD} values for both cases of λ were almost eliminated, reduced to very small values of about -0.025 at all θ . Judging from the large differences in the scales of these drag-induced components, it can be inferred that the remaining C_{TD} in the variable-pitch mode was primarily due to frictional drag on the surfaces of the blades. The pressure drag (dominant in the other two pitching modes) was entirely eliminated in the variable-pitch mode by streamlining the blades into the direction of the effective flow by varying their pitch angles accordingly. The streamlining of the blade was evident from its constant values of α_e as shown in Figure 4(a).



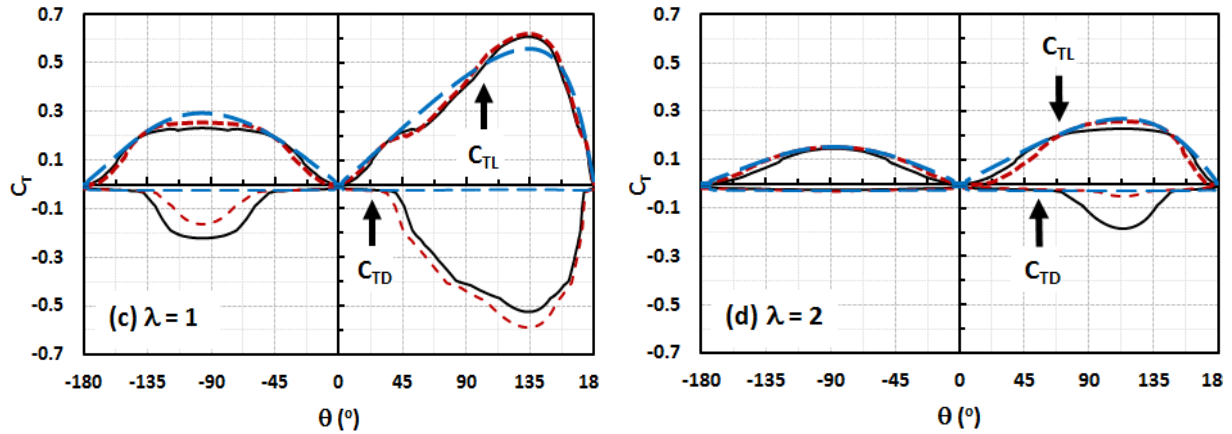
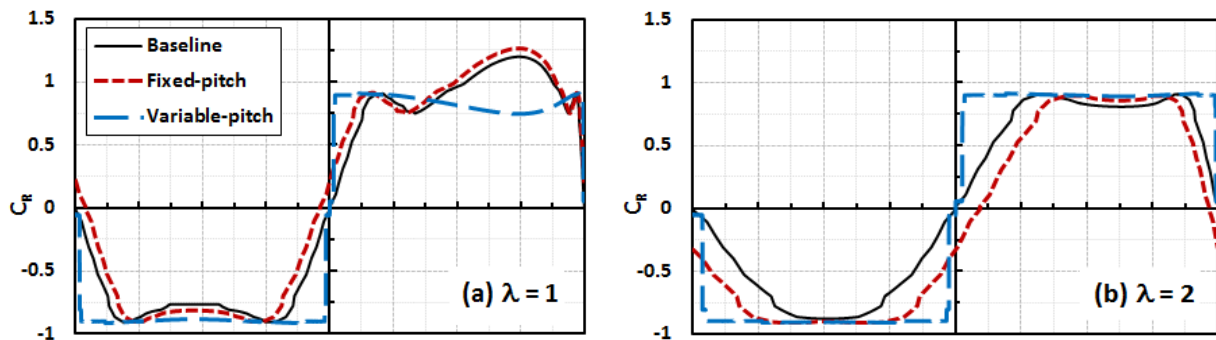


Figure 5: Plotted against θ for the two λ cases and the three pitching modes: (a,b) the tangential force coefficients and (c,d) the lift-induced and drag-induced components of these coefficients on the rotor blade; each arrow points to the group of lines representing the three pitching modes. The legend in (a) applies to all the sub-plots in this figure.

Stress-Inducing Radial Forces

Different from the tangential forces, the radial (or normal) forces acting on the rotor were unfavourable. Positive and negative values of these forces strained the rotor, either by compressing or extending on the rotor arms holding the blades. These unwanted stresses reduced the structural integrity of the turbine over time. Figs. 6(a-b) show these force coefficients (C_R) on the blades for all of the λ cases and the pitching modes. In the variable-pitch mode, the patterns from the two λ cases were similar, showing square-wave patterns with peaks and troughs of C_R close to 0.9 and -0.9 in both cases, and with sudden jumps at the two transition points between the upstream and downstream regions (i.e., when β were 0° and 180°). In the other two pitching modes, their patterns changed more gradually across the upstream-downstream transitions. Beyond these transition points, different λ led to different behaviours: when $\lambda = 1$, C_R had substantial but undesirable positive bulges for the unpitched and fixed-pitch modes, and a slight negative bulge for the variable-pitch mode; when $\lambda = 2$, in the middle segments of the upstream and downstream traverses, C_R plateaued near the square-wave bounds of -0.9 and 0.9 in the variable-pitch mode. Regardless of these differences between the λ cases and the pitching modes, the magnitudes of C_R , on average, were larger (and thus highly undesirable) by roughly more than five times the average of the tangential force coefficients analysed above.

Examining further into the contributing aerodynamic forces, as shown in Figs. 6(c-d), it was observed that the radial forces were highly dominated by their lift-induced components (C_{RL}), for all of the λ cases and the pitching modes studied herein. In particular, when $\lambda = 2$, there was almost no contributions on C_R from their drag-induced components (C_{RD}), except with a minor bulge at the small leading segment of the upstream traverse in the unpitched mode. When $\lambda = 1$, the substantial positive bulges in C_R for the unpitched and fixed-pitched modes during the upstream traverses were contributed by C_{RD} ; smaller negative bulges occurred for these same pitching modes during the downstream traverse that alleviated the extensive stresses. These bulges were eliminated entirely when the blades were dynamically optimised.



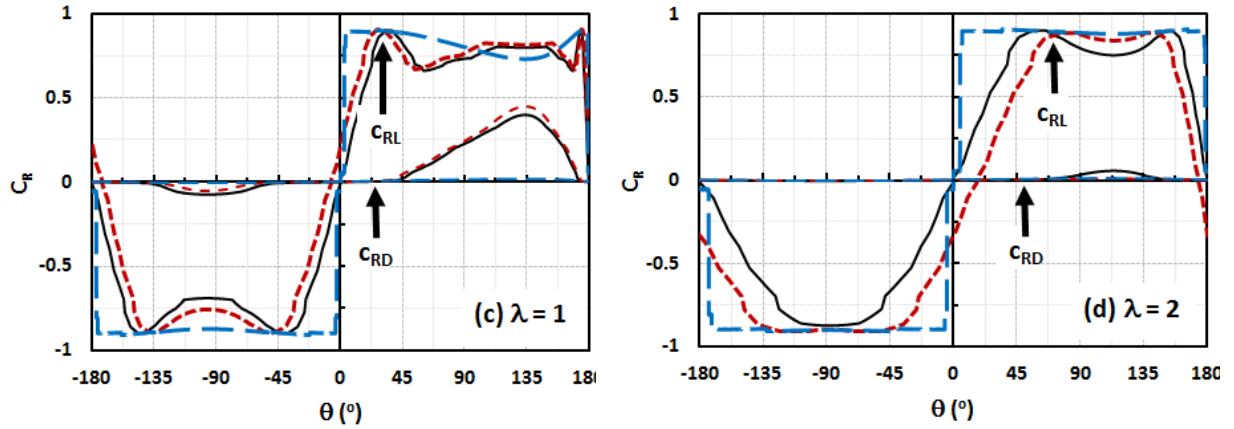


Figure 6: Plotted against θ for the two λ cases and the three pitching modes: (a,b) the radial force coefficients and (c,d) the lift-induced and drag-induced components of these coefficients on the rotor blade; each arrow points to the group of lines representing the three pitching modes. The legend in (a) applies to all the sub-plots in this figure.

3.2. Turbine Performance

The performance of the three-bladed turbine was measured quantitatively and presented herein through two parameters: the total torque coefficient (C_Q) and the turbine power coefficient (C_P). As shown in Figs. 7(a-b), these parameters were analysed herein over a small range of λ from 1 to 2.5 (due to the limited range afforded by the modelling approach and the validation data used here, as discussed in Section 2.2). Both parameters showed similar increasing trends with λ . The dynamic pitch optimisation provided the best improvement on C_Q and C_P , compared to the unpitched rotor blades. The percentages of relative improvement on C_P , relative to its baseline values, reached a high of 263% at $\lambda = 1$, reducing continuously afterward to 51% and 28% at $\lambda = 2$ and 2.5, respectively. The reduction on these values was simply because it was a relative increment, and that the baseline C_P values increased with λ . The absolute increments between the dynamic and baseline modes remained comparable across λ .

Static (or fixed-pitch) optimisation, on the other hand, resulted in varying degrees of improvement on these parameters. From $\lambda = 1$ to about 1.4, the percentages of relative improvement on C_P were marginal at only 5%. The best improvements on C_P for this static optimisation mode occurred over a small range of λ between 1.8 and 2.2, where the percentages of relative improvement on C_P ranged between 15% and 35%, and were about half of those produced through dynamic optimisation. These considerable improvements were possible because the fixed pitch angles could be used to optimise the upstream regions only, without competing optimisation needs from the downstream regions. Beyond this range, the percentages on the relative improvement on C_P continued to reduce, reaching back to 5% at $\lambda = 2.5$.

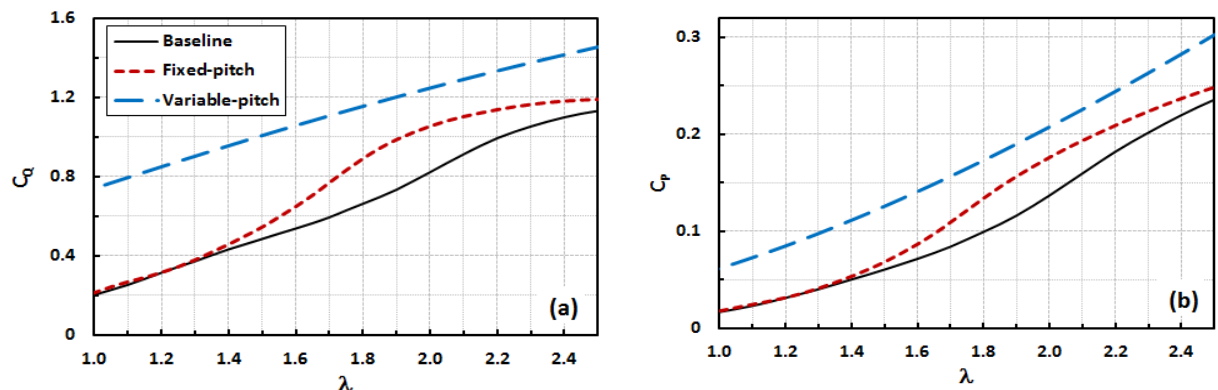


Figure 7: (a) The total torque coefficients and (b) the turbine power coefficients for the three-bladed vertical-axis rotor at various tip-speed ratios. The legend in (a) applies to both sub-plots in this figure.

The static optimisation case was examined further, to analyse the behaviour of the turbine performance when different pitch angles were fixed to the blades. In the case of $\lambda = 1$, desirable pitch angles (i.e., those that produced positive improvements to the baseline mode) existed within a narrow range of about 3° , as shown in Figure 8(a).

With the optimum β at -2.1° , C_P improved almost negligibly from 0.017 (when unpitched) to 0.018 (with the fixed pitch). When $\lambda = 2$, desirable pitch angles were similarly located within a narrow range of about 5° . With the optimum β at 3.1° , C_P improved marginally from 0.16 (unpitched) to 0.18 (pitched).

For each case of λ , the errors in pitching the blades with their optimum β could be tolerated to within narrow bands of β of about 3° to 5° , as discussed above. Beyond these bands, C_P would suffer below the performance levels of the baseline mode. Unfortunately, the sensitivity towards positioning the blades with specific β to optimise C_P were not limited to individual cases of λ only. Across the larger range of λ from 1 to 2.5, optimum fixed-pitch angles varied considerably within small ranges of β , roughly between -2° to 3.5° , as shown in Fig 8(b). Accordingly, the narrow bands of tolerable β for each case of λ would shift together with these optimum β .

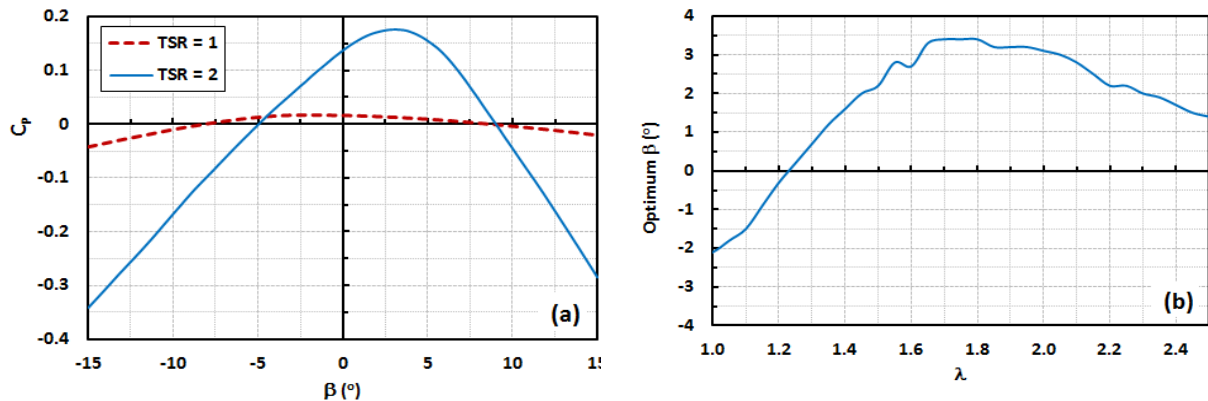


Figure 8: (a) The turbine power coefficients for different fixed-pitch angles applied onto the blades, at $\lambda = 1$ and 2. (b) The optimum fixed-pitch angles for different cases of λ .

4. CONCLUSION

For the straight-bladed vertical-axis turbine studied herein, dynamic optimisation was found to be far more effective, compared to the static optimisation, in improving its power coefficient (C_P). In this mode, at $\lambda = 1$, each blade was well-streamlined into the effective flow direction by dynamically pitching it at every θ with optimised angles. The streamlined blade, in return, prevented pressure-drag from forming, effectively reducing the torque-suppressing drag-induced component of the tangential force coefficients, C_{TD} , to very low magnitudes. When statically optimised at $\lambda = 1$, the overall gains on the power coefficient were marginal because of the competing effect of simultaneously reducing and increasing C_{TD} values in the downstream and upstream regions, respectively. Increasing λ to 2 had the effect of narrowing the effective incidence angles experienced by the blades, thus eliminating the competing effect from the downstream region. The fixed-pitch mode could therefore be made more effective by optimising the upstream region only, as evident in the results discussed above.

Unlike the tangential force, both the positive and negative values of the radial force were unfavourable because they strained the rotor arms either compressively or extensively, thus reducing the operational lifetime of the turbine. Unfortunately, the average values of their coefficients scaled much higher, by more than eight times, than those of the tangential force coefficients in either cases of the tip-speed ratios. Further works in this area could be focused on improving the blade design to significantly reduce these undesirable radial forces.

5. REFERENCES

- Anyi, M., Kirke, B.K., and Ali, S., 2010. Remote community electrification in Sarawak. *Renewable Energy*, 35, 1609-1613.
- Biadgo, A.M., Simonovic, A., Komarov, D., and Stupar, S., 2013. Numerical and analytical investigation of vertical axis wind turbine. *FME Transactions*, 41, 49-58.
- Borhanazad, H., Mekhilef, S., Saidur, R., and Boroumandjazi, G., 2013. Potential application of renewable energy for rural electrification in Malaysia. *Renewable Energy*, 59, 210-219.
- Fiedler, A.J. and Tullis, S., 2009. Blade offset and pitch effects on a high solidity vertical axis wind turbine. *Wind Engineering*, 33(3), 237-246.

- Islam, M., Ting, D.S.K., and Fartaj, A., 2008. Aerodynamic models for Darrieus-type straight-bladed vertical axis wind turbines. *Renewable and Sustainable Energy Reviews*, 12, 1087-1109.
- Khan, M.J., Bhuyan, G., Iqbal, M.T., and Quaicoe, J.E., 2009. Hydrokinetic energy conversion systems and assessment of horizontal and vertical axis turbines for river and tidal applications: A technology status review. *Applied Energy*, 86, 1823-1835.
- Kim, D. and Gharib, M., 2013. Efficiency improvement of straight-bladed vertical-axis wind turbines with an upstream deflector. *Journal of Wind Engineering and Industrial Aerodynamics*, 115, 48-52.
- Kirke, B.K. and Lazauskas, 2008. Variable pitch Darrieus water turbine. *Journal of Fluid Science and Technology*, 3(3), 430-438.
- Kirke, B.K. and Lazauskas, L., 2011. Limitations of fixed pitch Darrieus hydrokinetic turbines and the challenge of variable pitch. *Renewable Energy*, 36, 893-897.
- Ponta, F. and Dutt, G.S., 2000. An improved vertical-axis water-current turbine incorporating a channelling device. *Renewable Energy*, 20, 223-241.
- Rezaeiha, A., Kalkman, I., and Blocken, B., 2017. Effect of pitch angle on power performance and aerodynamics of a vertical axis wind turbine. *Applied Energy*, 197, 132-150.
- Sheldahl, R.E. and Klimas, P.C., 1981. Aerodynamic characteristics of seven symmetrical airfoil sections through 180-degree angles of attack for use in aerodynamic analysis of vertical axis wind turbines. New Mexico: Sandia National Laboratories.
- Vermaak, H.J., Kusakana, K., and Koko, S.P., 2014. Status of micro-hydrokinetic river technology in rural applications: A review of literature. *Renewable and Sustainable Energy Reviews*, 29, 625-633.
- Zamani, M., Maghrebi, M.J., and Varedi, S.R., 2016. Starting torque improvement using J-shaped straight-bladed Darrieus vertical axis wind turbine by means of numerical simulation. *Renewable Energy*, 95, 109-126.

#286: Dynamic simulations of ground-coupled heat pumps using high-resolution analytical models

Min LI¹, Cheng ZHOU²

¹ School of Energy Science and Engineering, Central South University, 410083 Changsha, climin78@gmail.com

² School of Energy Science and Engineering, Central South University, 410083 Changsha, 975571710@qq.com

This paper reports on an algorithm for hourly simulation of ground-coupled heat pump (GCHP) systems. This algorithm integrates the newest analytical models for coefficient of performance (COP) of heat pumps and for heat transfer of ground heat exchangers (GHEs). These analytical models make the algorithm computationally fast and efficient. The algorithm overcomes two limitations restricting the accuracy and precision of the GCHP simulations. First, the simulation studies used analytical models being insufficient for modelling the underground heat transfer. Second, most of the simulations have used empirical approaches to modelling heat pumps. The algorithm comprises seven independent equations for solving seven system variables, thus including $C_{i,4}^7 = 3432$ simulation scenarios. The algorithm is applied to hourly 50-year simulations of a GCHP for illustrating the computation efficiency of the algorithm. The simulation cases show that the COP and seasonal COP of GCHPs depend heavily on the mutual-cause coupling between the ground-side load and the temperature field in the ground. This coupling effect renders the high-resolution simulation highly necessary and this algorithm is compared with an algorithm using a conventional finite line-source model for borehole GHEs. Because conventional finite line-source model neglects the heat capacity of grouting material results in large variations in $T_{f,out}$. Comparison results show that the difference in maximum $T_{f,out}$ during the 50-year is larger than 1.2°C, a temperature difference that may lead to a discrepancy in the design length of GHEs because the length of GHEs is very sensitive to the used extremes of $T_{f,out}$. Thus, in the applications with large-variation load, the effect of heat capacity of grouting material will be more significant

Keywords: ground-coupled heat pumps; ground heat exchangers; hourly simulation; composite-medium line-source model; energy analysis

1. INTRODUCTION

Computer simulation has emerged as an efficient and convenient approach to understanding the complexities of ground-coupled heat pump (GCHP) systems because of the following three reasons

1. The heat transfer in the ground is extremely slow due to the low diffusivity ($\sim 10^{-6}$ m²/s) and large length scale of the ground. The underground thermal process can span 8 time scales (from sub-hour to decades) and accordingly 4 length scales (from centimetre to hundreds of meters) (Spitler, 2011; Li and Zhu, 2016). Such a diverse-scale feature, in conjunction with the increasing size of GCHP systems, almost excludes the possibility of studying the life-cycle performance of GCHP systems in experimental ways.
2. The performance of GCHP systems depends on a large set of influencing factors, e.g., building loads, piping systems, heat-pump performance, automatic control strategies, and the design of ground heat exchangers (GHEs). These factors are significantly correlated because they have a mutual cause rather than a cause-and-effect relationship. Thus, it is also difficult to investigate the influence of these factors by small- or large-scale experiments.
3. Despite these complexities, the major processes involved in GCHPs are governed by the fundamental laws of thermodynamics, heat transfer, and fluid mechanics. These basic laws constitute the theoretical bedrock of the modern refrigeration and heat pump industry, enabling us to confidently simulate GCHPs using these physical laws.

In light of these factors, studies has developed in house algorithms and programs for modelling GCHPs (Bernier, 2001; Zhang and Luo, 2019). Whereas these studies can freely choose models for GHEs and heat pumps, they still suffer from two limitations. First, the simulation studies using analytical heat transfer models have failed to incorporate the newest achievements in the GHE field and used analytical models being insufficient for modelling the underground heat transfer (Michopoulos and Kyriakis, 2009; Zhang and Luo, 2019). These studies cannot evaluate the impacts of the ground surface (Michopoulos and Kyriakis, 2009), the heat capacity of grouting material (Bernier, 2001; Man and Yang, 2008), or the temperature variation along U-shaped channels (Zhang and Luo, 2019). Second, most of the simulations have used empirical approaches to modelling heat pumps, e.g., lookup tables (Bernier, 2001) and simplified curve-fitting equations (Zhang and Luo, 2019). Empirical models are simple to use, but they ignore some key factors and the operating mechanism of heat pumps; thus it is impossible to generalise. The two limitations restrict the accuracy and precision of the GCHP simulations and thus hinder our ability to analyse and design GCHP systems.

To overcome the two limitations, this paper reports on a new simulation algorithm for GCHP systems. The algorithm integrates the newest developments in the GCHP field (Li and Lai, 2015; Li and Zhu, 2016; Ma and Fang, 2017), an integration that makes the algorithm different from all the existing algorithms. First, the algorithm uses a set of theoretical models for the heat transfer in the ground, which can predict the temperature response of GHE fields with time resolution from sub-hour to decades. Second, this algorithm uses a new mechanism-based model for heat pumps, which includes a second-law-based model for the coefficient of performance (COP) and provides a fast approach to the simulation of heat pumps without recourse to equations of state of the refrigerant. As an illustration, this algorithm is used to rate the life-cycle (50-year) performance of a GCHP system and is compared with an algorithm using a conventional finite line-source model for borehole GHEs.

2. MODELS AND ALGORITHMS

2.1. Sub-model for heat pumps

The heat-pump model consists of heat transfer models for heat exchangers and a theoretical equation for COP of the heat pump cycle. The present algorithm uses the ϵ -NTU relationship for the counter-flow evaporator/condenser, where effectiveness, ϵ , is defined as $\epsilon = \Delta T_{\max}/\Delta T_{\text{in}}$, ΔT_{\max} is the maximum temperature difference, and ΔT_{in} is the difference between the inlet temperatures of the heat exchanger. The heat exchangers in a heat pump are used as condenser or evaporator, depending on the operating mode (cooling or heating). For clarity, we named the heat exchanger connected to GHEs ground-loop-side heat-exchanger and that connected to users user-loop-side heat-exchanger. The heat transfer models for these heat exchangers are summarised below.

Ground-loop-side heat-exchanger (Figure 1)

Equation 14: Effectiveness of ground-loop-side heat-exchanger.

$$\epsilon_e = \frac{T_{f,\text{out}} - T_{f,\text{in}}}{T_{f,\text{out}} - T_e} = 1 - \exp(-NTU_e)$$

Equation 2: Heat transfer rate of the ground-loop side.

$$Q_g(t) = c_w m_g [T_{f,in}(t) - T_{f,out}(t)]$$

Where:

- $T_{f,out}$ = temperature of the fluid leaving the GHEs (K)
- $T_{f,in}$ = the temperature of the fluid entering the GHEs (K)
- T_e = phase-change temperature of the working fluid in the ground-loop-side heat exchanger (K)
- NTU_e = number of transfer units (NTU) of the heat exchanger
- Q_g = heat transfer rate of the ground-loop side (W)
- c_w = heat capacity of the circulating working fluid in the GHEs (J/kgK)
- m_g = total mass-flow rate of the circulating working fluid in the GHEs (kg/s)

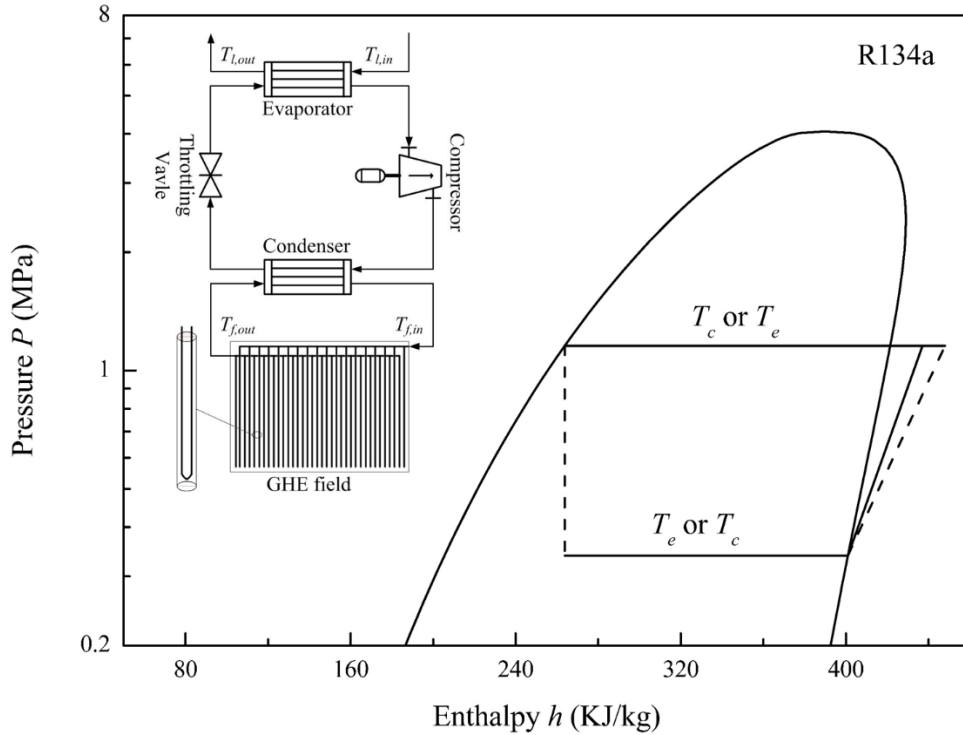


Figure 14: Schematic layout of a GCHP and the pressure-enthalpy diagram of the working fluid R134a

User-loop-side heat-exchanger (Figure 1)

Equation 3: Effectiveness of user-loop-side heat-exchanger.

$$\varepsilon_e = \frac{T_{l,out} - T_{l,in}}{T_c - T_{l,in}} = 1 - \exp(-NTU_c)$$

Equation 4: Heat transfer rate of the user-loop side.

$$Q_u(t) = c_w m_u [T_{l,in}(t) - T_{l,out}(t)]$$

Where:

- $T_{l,out}$ = temperatures of the circulating working fluid leaving the heat pump on the user-loop side (K)
- $T_{l,in}$ = temperatures of the circulating working fluid entering the heat pump on the user-loop side (K)
- T_c = phase-change temperature of the refrigerant in the user-loop-side heat exchanger (K)
- NTU_c = number of transfer units of the heat exchanger
- Q_u = heating or cooling loads (W)
- m_u = mass flow rate of the circulating working fluid in the user loop (kg/s)

Heat-pump cycle

The ground-side load, $Q_g(t)$, depends not only on the heating and cooling load but also on the thermodynamic performance of heat pumps (i.e., COP). This algorithm uses the following second-law-based explicit expression for the heat-pump COP (Ma and Fang, 2017).

Equation 5: The relationship between $Q_u(t)$, $Q_g(t)$ and the coefficient of performance of the vapour-compression refrigeration cycle.

$$Q_g(t) = \begin{cases} \frac{\text{COP}}{\text{COP}+1} Q_u(t), \text{Heating} \\ \frac{\text{COP}+1}{\text{COP}} Q_u(t), \text{Cooling} \end{cases}$$

Equation 6: The definition of coefficient of performance of the vapour-compression refrigeration cycle.

$$\text{COP} = \frac{\eta_m \eta_l \left(\eta_c - \frac{cT_e}{r} \right)}{1 + \frac{1}{2\eta_c} \frac{cT_e}{r} \left(\frac{1}{\eta_c} - 1 \right)}$$

Where:

- COP = coefficient of performance of the vapour-compression refrigeration cycle
- η_m = mechanical efficiency of the compressor
- η_l = isentropic efficiency of the compressor
- η_c = COP of Carnot cycle operating between T_e and T_c ($\eta_c = T_e/(T_c-T_e)$ or $\eta_c = T_c/(T_e-T_c)$)
- r = heat of evaporation of the refrigerant at the evaporating temperature (J/kg)
- c = average specific heat of the saturated liquid refrigerant within the temperature range from T_e to T_c (J/kgK)

Equation (6) is derived from a rigorous entropy-generation analysis, and a further generalised model can be found in reference (Ma and Fang, 2017).

2.2. Sub-model for GHEs

The greatest challenge lies in how to model heat transfer of GHEs in an efficient way. To address this challenge, researchers have attempted to develop various analytical models for the underground thermal process. These models differ from one another mainly in time resolution (Li and Lai 2015). This study used a set of analytical models that are theoretically complete and have enough time-resolution for hourly simulation. This set of models can be referred to as a quasi-3D model for U-shaped GHEs, which formulates $T_{f,out}$ as a function of $T_{f,in}$, T_p , and the dimensionless variable ζ that has a similar implication as NTU for the ordinary heat exchangers (Ma and Li, 2015):

Equation 7: Quasi-3D model for U-shaped GHEs.

$$T_{f,out}(t) = \begin{cases} T_p(t) + [T_{f,in}(t) - T_p(t)] \exp(-2\zeta), \text{Single U-tube} \\ T_p(t) + [T_{f,in}(t) - T_p(t)] \exp(-4\zeta), \text{Double U-tube} \end{cases}$$

Where:

- T_p = average temperature at the interface between the grout material and the outer wall of U-shaped pipes (K)
- L = the total depth of the boreholes (m)
- $\zeta = L/(C_w m_g R_p)$

R_p is the U-pipe thermal resistance consisting of conductive thermal resistance of the U-pipe and convective thermal resistance inside the U-pipe (Li and Lai, 2015)

Equation 8: The U-pipe thermal resistance.

$$R_p = \frac{1}{2\pi k_p} \left(\ln \frac{r_o}{r_i} + \frac{k_p}{ar_i} \right)$$

Where:

- R_p = U-pipe thermal resistance (mK/W)
- K_p = the thermal conductivity of the U-shaped pipe (W/mK)
- α = convective heat transfer coefficient inside the U-pipe (W/m²K)
- r_o = outer radii of the leg-pipe of the U-shaped pipe (m)
- r_i = inner radii of the leg-pipe of the U-shaped pipe (m)

$T_p(t)$ in Equation (7) depends on the time-varying load $Q_g(t)$, which can be tackled by Duhamel's theorem (i.e., the principle of superposition) as follows (Li and Lai 2015) :

Equation 9: Duhamel's theorem.

$$T_p = T_0 + \sum_{j=0}^{N-1} \frac{\Delta Q_g(j\Delta t)}{L} G(t - j\Delta t)$$

Where:

- T_0 = initial ground temperature (K)
- $\Delta Q_g(j\Delta t)$ = step-wise change in Q_g at the beginning of the j th time interval (W)
- Δt = Time step (1 hour)
- $G(t)$ = temperature response to the unit-step ground load (Km/W)

$G(t)$ is the temperature response to the unit-step ground load and has the dimension of thermal resistance (Li and Lai, 2015; Li and Zhu, 2016) . Thermal resistance $G(t)$ is derived from the solutions for heat transfer of GHEs, which is the most complex part of the GCHPs model. There is no single analytical solution applicable to the entire time domain involved in the heat transfer of GHEs. But, a combined composite solution can solve this problem, which yields a composite G-function applicable to time from sub-hour to decades (Li and Li 2014)

Equation 150: Full-scale G-function.

$$G(t) = \underbrace{G_i(t)}_{\text{short-time solution}} - \underbrace{G_m(t)}_{\text{mid-time solution}} + \underbrace{G_o(t)}_{\text{long-time solution}}$$

Where:

- G_i = composite-medium line-source solution (Km/W)
- G_m = infinite line-source solution (Km/W)
- G_o = finite line-source solution (Km/W)

The composite G-function comprises three line-source solutions applicable to three overlapped time domains. First, $G_m(t)$ is the unit-step temperature response on the borehole wall derived from the infinite line-source solution, which is applicable to mid-time domains (several hours to several months) and reads References (Li and Lai, 2015; Li and Zhu, 2016) .

$G_o(t)$ is the unit-step temperature response on the borehole wall derived from a long-term solution. This work used the finite line-source solution developed by Claesson and Javed, (2011). This solution is probably the most efficient long-time model for borehole GHEs because it avoids the double integral for calculating the average temperature of a GHEs field and thus reduces great computational time. For a GHEs field consisting of M boreholes (i.e., $L = M \times H$), G_o reads References (Claesson and Javed, 2011).

For the short-time solution $G_i(t)$, this work used the composite-medium line-source model derived from Jaeger's composite-medium line-source theory (Jaeger, 1944). Readers can find the theoretical development and experimental validation of the model in Refs (Li and Lai, 2012; Li and Zhang, 2019). For single U-shaped tubes, G_i is (Li and Lai, 2012; Yang and Li, 2014).

Equation 161: The composite-medium line-source model for single U-shaped tubes.

$$G_i(t) = \frac{1}{2\pi k_b} \int_{i=-\frac{b}{2}}^{+\frac{b}{2}} \int_0^{+\frac{b}{2}} \dot{q} \exp(-u^2 a_b t) \frac{J_{2i}(ur_A) + J_{2i}(ur_B)}{2} \frac{J_{2i}(uD)(\phi g - \psi f)}{u(\phi^2 + \psi^2)} du$$

Where:

- a_b = thermal diffusivity of the backfilling material (m^2/s)
- k_b = conductivity of the backfilling material (W/m^2K)
- r_A = radial coordinates of point A (m) in Figure 2 (m)
- r_B = radial coordinates of point B (m) in Figure 2 (m)
- D = half-spacing between the legs of U-shaped tubes (m)
- J_n = Bessel functions of the first kind of order n ($n = 2i$)
- u = integral variable

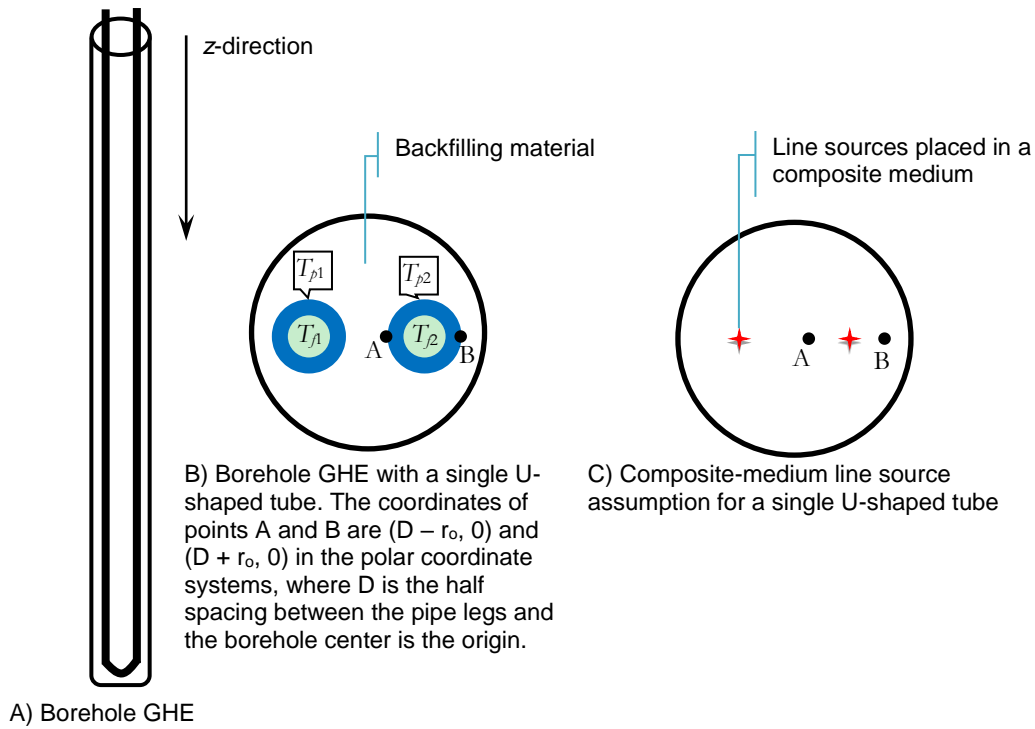


Figure 2: Schematic layout of U-shaped GHEs and the composite-medium line-source model

For double U-shaped tubes, G_i is

Equation 172: The composite-medium line-source model for double U-shaped tubes.

$$G_i(t) = \frac{1}{2\pi k_b} \int_0^{\infty} \int_0^{\infty} \exp(-u^2 a_b t) \frac{J_{4i}(ur_A) + J_{4i}(ur_B)}{2} \frac{J_{4i}(uD)(\phi g - \psi f)}{u(\phi^2 + \psi^2)} du$$

Where:

J_n = Bessel functions of the first kind of order n ($n = 4i$)

The definitions of ϕ , ψ , f and g in Equations (11) and (12) are

Equation 183: The Bessel functions and the derivatives of Bessel functions.

$$\begin{aligned} \phi &= akJ_n(ur_b)J_n'(aur_b) - J_n'(ur_b)J_n(aur_b) \\ \psi &= akJ_n(ur_b)Y_n'(aur_b) - J_n'(ur_b)Y_n(aur_b) \\ f &= akY_n(ur_b)J_n'(aur_b) - Y_n'(ur_b)J_n(aur_b) \\ g &= akY_n(ur_b)Y_n'(aur_b) - Y_n'(ur_b)Y_n(aur_b) \end{aligned}$$

Where:

- $a = a_b/a_s$
- $k = k_s/k_b$
- k_s = thermal conductivity of the ground (W/mK)
- a_s = thermal conductivity of the ground (m^2/s)
- rb = borehole radius (m)
- Y_n = Bessel functions of the second kind of order n , $n = 2i$ in Equation (11) or $n = 4i$ in Equation (12)
- J'_n = derivative of J_n , $n = 2i$ in Equation (11) or $n = 4i$ in Equation (12)
- Y'_n = derivative of Y_n , $n = 2i$ in Equation (11) or $n = 4i$ in Equation (12)

The composite G-function, Equation (10), is built on the idea of matched asymptotic expansion (Li and Li 2014), providing a universal frame of combining different G functions.

2.3. Summary of the simulation algorithm

To conclude, seven equations (i.e., Equations (1) to (7)) constitute the mathematical model of GCHPs, and simultaneously solving these equations provides a general and efficient approach to computer simulation of GCHPs. Equations (8) to (13) are considered as dependent equations because they are substituted for R_p and T_p (t) in Equation (7). Excluding the model parameters (see Figure 3), Equations (1) to (7) comprise 14 design variables. Therefore, we have $C_{14}^7 = 3432$ simulation scenarios, and which seven variables selected to calculate depends on the purpose of computer simulation. In this study, we chose the following rating problem for illustration: given L , m_g , $T_{l,out}$, NTU_e , NTU_c , m_u , and Q_u , calculate $T_{f,out}$, $T_{f,in}$, Q_g , T_e , T_c , $T_{l,in}$ and COP (Figure 3).

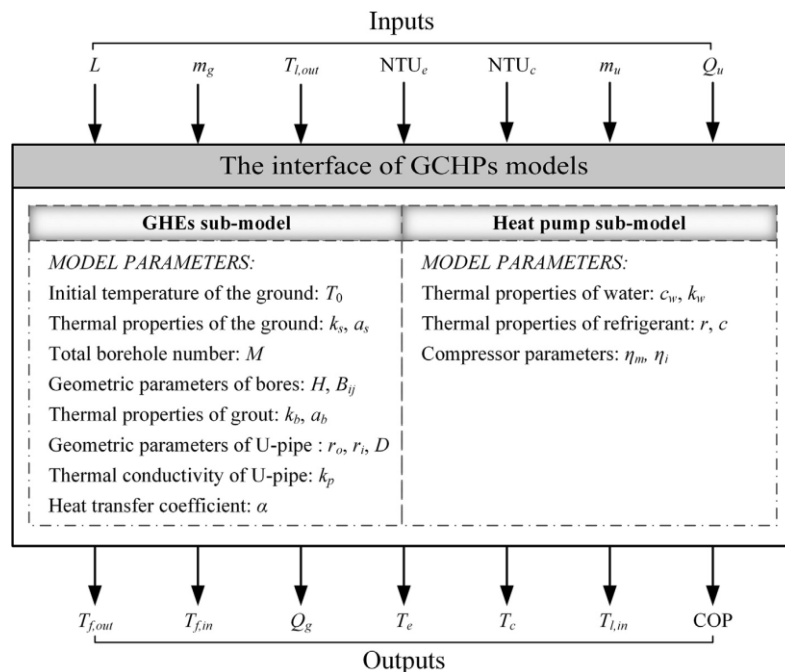


Figure 3: Model interface for the case studies: inputs, outputs, and model parameters

3. RESULTS

3.1. Building

This section presents the results of two case studies to illustrate the application of the simulation algorithm. The first case (i.e. Case 1) used the models and the algorithm presented in Section 2. The second case (i.e. Case 2) differs from Case 1 only in the models used for calculating G and T_p , as explained in Section 3.3. A 3000-m² office building was used in the two cases. The hourly building load was estimated using TRNBuild.

3.2. Results of Case 1

Figure 4 shows the hourly variation of COP within different time ranges, including 50-year, 1-year, and several days. Since the heat pump operated intermittently, the curve of COP is discontinuous (Figure 4B). The peaks and

the low points in Figure 4A are the maximum and minimum COP for cooling in each year on account of the broad spread of cooling COP. The gradual decrease in these extremes reveals that the COP for cooling decreases gradually. This is a result of the gradual increase of the temperature field in the ground. The accumulated heat leads to the yearly increase in T_p , thus causing the COP of the heat pump decreases with time for cooling but increases for heating.

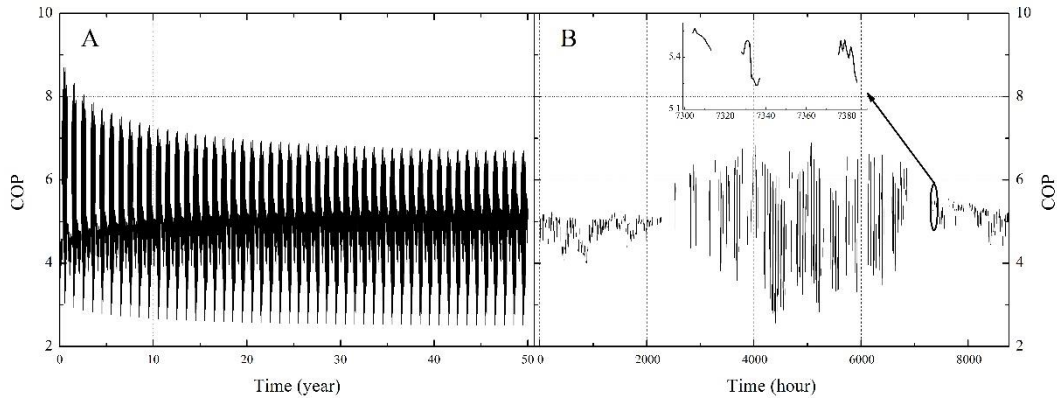


Figure 4: Hourly variation of COP: A. 50-year; B. 1-year

3.3. Comparison study

Short-time solution G_i is essential for hourly simulation of GCHPs because it can tackle the effect of heat capacity of grouting material. To underline this point, we performed one more simulation (Case 2) that ignored the heat capacity of grouting material, that is, using the steady-state thermal resistance R_b for the heat transfer inside the borehole:

$$R_b = R_a + \frac{R_p}{2}$$

$$= \frac{1}{4\pi k_b} \ln \frac{r_b^2}{2Dr_o} + \frac{r_b^4}{D^4} \frac{\sigma}{\sigma} \frac{R_p}{2}$$

Equation 14: The steady-state thermal resistance for the heat transfer inside the borehole.

Where:

- R_b = heat transfer inside the borehole (mK/W)
- R_a = thermal resistance for heat transfer from the U-pipe wall to the borehole wall (mK/W)
- $\sigma = (k_b - k_s)/(k_b + k_s)$

Since the short-time solution was not used, only the finite line-source model was necessary for calculating G function in this case

Equation 15: The finite line-source model.

$$G(t) = G_o(t)$$

long-time solution

Equation 16: Duhamel's theorem.

$$T_p = T_0 + \sum_{j=0}^{N-1} \frac{\Delta Q_g(j\Delta t)}{L} [R_a + G_o(t - j\Delta t)]$$

Therefore, the new simulation still used Equations (1)-(7) as the mathematical model for GCHPs, but Equations (15) and (16) were substituted for G and T_p , instead of Equations (10) and (9).

Figure 5 compares $T_{f,out}$, COP, and SCOP of the two hourly 50-year simulations. For clarity, the outputs of Case 2 are labelled with $G = G_o$ in Figure 5, and those of Case 1 are labelled with $G = G_i - G_m + G_o$. Of particular interest is the effect of heat capacity of grouting material on the amplitude of $T_{f,out}$ (Figure 5A). Neglecting the heat capacity of grouting material results in large variations in $T_{f,out}$. Specifically, in our cases, the maximum difference between $T_{f,out}$ ranges from 2.33 °C (the first year) to 2.48 °C (the fiftieth-year); the difference in maximum $T_{f,out}$ during the 50-year is larger than 1.2 °C, a temperature difference that may lead to a discrepancy in the design length of GHEs

because the length of GHEs is very sensitive to the used extremes of $T_{f,out}$. Using the hourly COP, it is easy to calculate seasonal COP (SCOP) for heating and cooling (Figure 5C). The main trend of SCOP is downwards for cooling but upwards for heating. For cooling, SCOP decreased from about 5.1 to 4.2 (a fall of 20%). SCOP for heating increases from 4.25 to 4.90, a rise of greater than 15% (Figure 5). Although this is only a particular result of the case study, the reflected fact is applicable to most GCHP applications, i.e., the relationship between the variations of SCOP and the ground temperature field (or T_p). As expected, the large amplitude of $T_{f,out}$ results in a decrease in the GCHP performance: hourly COP and SCOP predicted by Case 2 are smaller than those yielded by Case 1 (Figure 5 B and C). It should be noted that the difference between Case 1 and 2 depends heavily on the varying amplitude of cooling and heating load. Thus, in the applications with large-variation load, the effect of heat capacity of grouting material will be more significant.

Finally, and perhaps most importantly, the relationship between the GCHP performance (i.e., COP and SCOP) and the ground temperature field (i.e., T_p) is mutual, not simply cause-and-effect. For instance, a rise in T_p causes a decrease in COP/SCOP for cooling; equally, as COP/SCOP decreases, the work and the ground-side load (Q_g) increase, leading to a further rise in T_p . A similar mutual relation exists in the heating season. These double-way impacts repeat yearly and are coupled to the long-term evolution of the ground temperature, a complication that renders the life-cycle simulation of GCHP systems highly necessary for large-scale engineering applications.

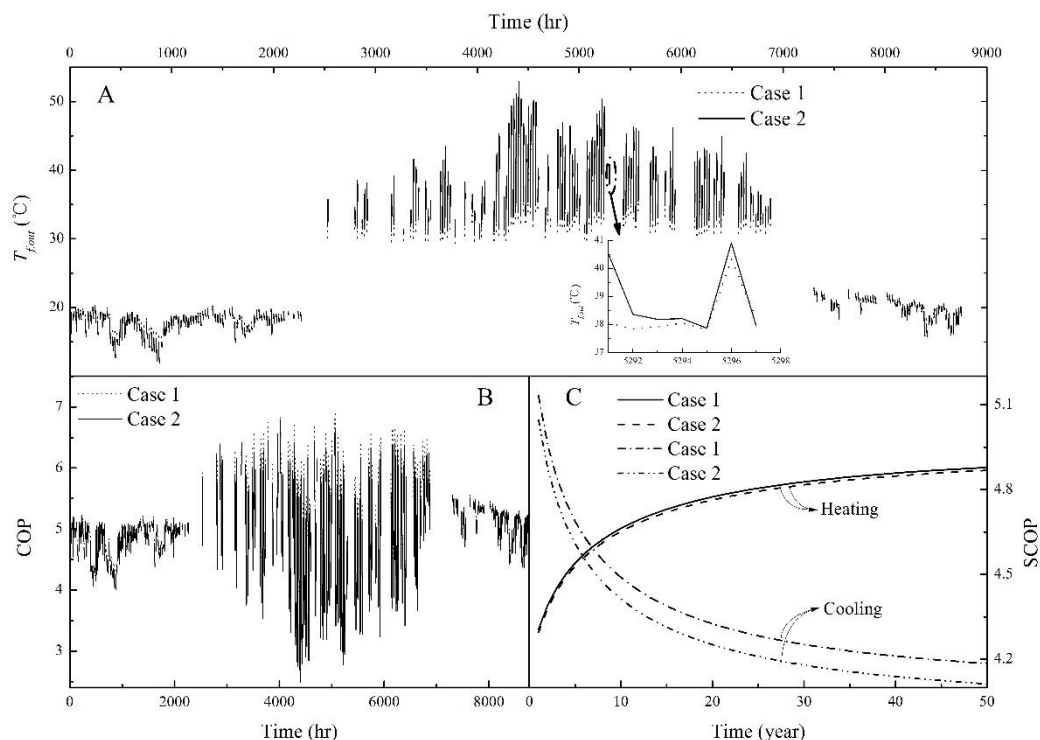


Figure 5: Comparison between the two case studies: Case 1 using full-scale Gfunction, i.e., Equations (9) and (10); Case 2 using Equations (15) and (16). A. The 25th-year hourly $T_{f,out}$; B. The 25th-year hourly COP; C. SCOP for heating and cooling

4. CONCLUSIONS

The purpose of the current study was to present and explain an hourly simulation algorithm for GCHP systems, which uses a mathematical model consisting of 7 independent equations for solving 7 system variables. The new algorithm offers a general and promising framework for the simulation-based analysis and design of GCHPs, embracing totally $C_{14}^7 = 3432$ rating and design calculation scenarios. Different selections of outputs and inputs lead to different engineering problems. The 50-year simulation given here belongs to the group of rating problems, in which the key design variables of the GCHPs are inputs (e.g., NTU_e , NTU_c , and borehole length L). If these variables are used as outputs, the simulation becomes part of the GCHPs design. Since engineering design is essentially an optimisation problem, the algorithm needs to be coupled to an optimisation engine, a study that is our future research focus.

5. REFERENCES

- Bernier, MA, 2001, Ground-coupled heat pump system simulation/discussion, ASHRAE Trans, 107:605-16
- Claesson, J, and Javed, S, 2011, An analytical method to calculate borehole fluid temperatures for time-scales from minutes to decades, ASHRAE Trans, 117(2).
- Jaeger, JC, 1944, Some problems involving line sources in conduction of heat, The London, Edinburgh, Dublin Philos Mag J Sci, 35:169–79.
- Li, M, and Lai, ACK, 2015, Review of analytical models for heat transfer by vertical ground heat exchangers (GHEs): A perspective of time and space scales, Appl Energy, 151:178–91.
- Li, M, and Zhu, K, 2016, Analytical methods for thermal analysis of vertical ground heat exchangers, Advances in Ground-Source Heat Pump Systems Woodhead Publishing, p.157–83.
- Li, M, and Li, P, 2014, Full-scale temperature response function (G-function) for heat transfer by borehole ground heat exchangers (GHEs) from sub-hour to decades, Appl Energy, 136:197–205.
- Li, M, and Lai, ACK, 2012, New temperature response functions (G functions) for pile and borehole ground heat exchangers based on composite-medium line-source theory, Energy, 38(1):255–63.
- Li, M, and Zhang L, 2019, Estimation of thermal properties of soil and backfilling material from thermal response tests (trts) for exploiting shallow geothermal energy: sensitivity, identifiability, and uncertainty, Renewable Energy, 126:3–70.
- Ma, W, and Fang, S, 2017, Second-law-based analysis of vapor-compression refrigeration cycles: Analytical equations for COP and new insights into features of refrigerants, Energy Convers Manage, 138:426–34.
- Ma, W, and Li, M, 2015, New quasi-3D model for heat transfer in U-shaped GHEs (ground heat exchangers): Effective overall thermal resistance, Energy, 90(1):578–87.
- Man, Y, and Yang, H, 2008, Study on hybrid ground-coupled heat pump systems, Energy Build, 40(11):2028-36.
- Michopoulos A, and Kyriakis N, 2009, A new energy analysis tool for ground source heat pump systems, Energy Build, 41(9):937-41.
- Spitler, JD, 2011, Ground-source heat pump systems: the first century and beyond, HVAC & R Res, 6:891–4.
- Yang, Y, and Li, M, 2014, Short-time performance of composite-medium line-source model for predicting responses of ground heat exchangers with single U-shaped tube, Int J Thermal Sci, 82:130–7.
- Zhang, L, and Luo, X, 2019, Comparative analysis of U-pipe location on the sizing of borehole heat exchangers, Appl Thermal Eng, 150:666–73.

#287: Assessing the harmful effects of domestic fuelwood burning on air quality in residential areas within communities: a case study of Kaduna state

Rukaiyatu AHMED¹; Bahijjah ABUBAKAR²; Yasmine DALHATU³

¹Department of. ³Department of Environmental Management and Toxicology, Federal University Dutse, Jigawa State, Nigeria Rukaiyatu.a@fud.edu.ng

²Federal Ministry of Environment, Department of pollution Control and Environmental Health, Maitama Abuja, bahijjah@gmail.com,

³Embassy of Nigeria, 13 Jangmun-RO 6GIL, Yongsan, Seoul, Republic of Korea, dalhatuyasmine@gmail.com

Rural women are custodians of energy for households especially for daily cooking and heating during the cold months of Harmattan. Cooking fuels are very important in every household because most of the food items must be heated, smoked, dried or cooked before consumption. The main source of this energy in most Nigerian households is from burning firewood. This causes indoor air pollution (IAP) due to emissions of black carbon and PM_{2.5}. This paper examines the extent to which air pollution caused by fuelwood burning activities is harmful to the health of people in the study community. It also explores safer and sustainable alternatives, taking a case study of Kaduna state, Nigeria.

Air pollution is one of the leading causes of human mortality in the world; for instance, IAP was reported to have caused 96,000 deaths in 2006 in Sub-Saharan Africa (WHO 2006). In addition, IAP contributes to many morbid conditions (disease) such as pneumonia in children, asthma, tuberculosis, upper airway cancer and catarrh. It was established that there is still over dependency on fuelwood in the study area due to fuel poverty and lack of affordable alternatives. This results in indoor air pollution with serious negative impacts on health.

A review of previous studies has shown that prolonged exposure to MP_{2.5} causes or aggravates several morbid conditions in especially women and children. The health community is on board the health pollution discussion, and the WHO provides technical support to countries in evaluation and scale-up of health promoting fuels and technologies. The achievement of a permanent and sustainable solution to these impending disasters require a multiagency approach involving all stake holders, from local communities, local, state and national governments, national and international agencies, each playing a vital role.

Keywords: fuelwood; air quality; wood burning; fossil fuel; climate change

1. INTRODUCTION

The increasing fuelwood consumption growth being experienced has been ascribed largely to population growth and lack of affordable energy alternatives, especially by poor families. According to a recent Food Agricultural Organization (FAO) findings, there has been a significant shift from “modern” fuels, such as kerosene and LPG back to fuelwood as a result of price increases in the latter (Adu, 2013).

In poor or developing countries, most households burn or cook in open fires, using inefficient cookstoves, responsible for incomplete combustion. This results in the release of Black Carbon (BC) and PM_{2.5}, which are harmful to human lives. In the burden of illnesses and premature deaths, the use of solid fuels (fuel wood) may be responsible for about 3.8 million premature deaths each year (WEO, 2017). Inhaled air pollutants have diverse effects on people that are exposed, depending on body constitution, lifestyle, nutritional status and age. Studies have shown that women and children, who are the most exposed and vulnerable to the pollutants, are two to six times more at risk of contracting serious respiratory infections (Rajbala et al.,2013). Interest in respiratory health impacts of air pollutants from fuel-wood utilization has been increasing rapidly probably as a result of high cases of illnesses recorded.

Building on this mandate, WHO is working to integrate guidance and resources for supporting clean household energy into global health initiatives and decision-support tools, such as the Global Action Plan for Pneumonia and Diarrheal Disease (GAPPD), Global Strategy for Women and Children’s Health, as well as into other aspects of WHO’s own health policy guidance. WHO emphasizes the compelling health arguments for cleaner household energy in a range of global forums addressing maternal and child health issues related to pneumonia as well as forums concerned with noncommunicable diseases. This advocacy can help increase awareness of the importance of providing and scaling up of cleaner household energy as a core preventive public health measure (World Energy Outlook, WEO, 2017).

2. LITERATURE REVIEW

Reductions in air pollution-related disease burden (both for household and outdoor) will be used to monitor the progress towards attaining the Sustainable Development Goal on Health (SDG 3). Ensuring universal access to clean fuel and technologies is a target of the Sustainable Development Goal on energy (SDG 7). Achieving this goal could prevent millions of deaths and improve the health and well-being of the billions of people relying on polluting technologies and fuels for cooking, heating and lighting.

To better assess the health risks of household energy use, as well as differentiated gender impacts from household energy practices, WHO is leading an effort with countries and surveying agencies (e.g. USAID’s DHS, UNICEF’S MICS, World Bank’s LSMS) to enhance, harmonize and pilot questions for national censuses and surveys. The effort will ensure that surveys better capture information on all the fuels and technologies used in the home for cooking, heating and lighting, as well as other impacts like time lost to fuel collection disaggregated by sex (World Energy Outlook, WEO, 2017).

Fuelwood consumption has grown from about 50 million m³ per year in 1990 to about 70 million m³ per year in 2010 which constitutes a higher proportion when compared with other competitive use such as logging (ECN and UNDP, 2018). The Nigerian National Communication to UNFCCC, has also shown deforestation to be the largest source of GHG emissions in the country, being responsible for about 40% of all CO₂ emissions.

The use of fuelwood for cooking and lighting is a major source of air pollution indoor and outdoor. It releases toxic gases such as carbon monoxide, poly aromatic hydrocarbons (PAHs), particulate matter (PM) and other undesirable noxious chemical components. Exposure to these emissions causes an increased risk of several diseases such as chronic respiratory diseases, pneumonia, bronchitis, lung cancer (Bruce, 2002). The smoke from biomass burning has been classified as a probable human carcinogen, and the smoke from coal as a proven human carcinogen (Straif and IARC, 2006). Other physically evident health problems that may be associated with the use of biomass fuels include catarrh, eye irritation, cough, sneezing, dry throat and nausea, shortness of breath, headache, dizziness and skin irritation.

Research reveals that women suffer different types of physical ailments due to the biomass fuel chain. Physical exhaustion, neck aches, headaches, knee aches and back aches. These are reported as the principal health effects associated with the third stage of the biomass fuel chain. Irritation of the mucus membrane of the eyes, nose and throat, coughing, burns, shortness of breath and exacerbation of asthma are identified as principal health effects associated with the fourth stage of the biomass fuel chain (cooking) (Al-Amin, 2014; Ndamase, 2012; WHO, 2005; and Zafar et al, 2002).

In Northern Nigeria where there is a large population, poverty is the most significant parameter that drives extensive traditional use of fuel wood residues (UNDP, 2018). Among rural women and children, it is observed that long periods of exposure to biomass combustion results in chronic obstructive lung diseases, heart diseases, acute respiratory infections, low birth weight, eye disorders such as conjunctivitis, blindness and cancer (Edokpa and Ikelegbe, 2012). Children strapped on their mothers' back while cooking with open cook stoves contracted pneumococcal infections 2.5 times higher than nonexposed ones (WHO, 2005). Epidemiological studies in developing countries have also linked exposure to air pollutants from dirty (biomass) fuel to Acute Respiratory Infection (ARI) in children; chronic obstructive lung diseases such as asthma and chronic bronchitis; lung cancer; still-births and other related problems, which include irritation of the skin, eyes, nose and throat; dizziness, nausea and other long-term chronic health effects (Singh and Parveen, 2010).

The smoke from biomass burning has been classified as a probable human carcinogen, and the smoke from coal as a proven human carcinogen (Straif and IARC, 2006). Other physically evident health problems that may be associated with the use of biomass fuels include catarrh, eye irritation, cough, sneezing, dry throat and nausea, shortness of breath, headache, dizziness and skin irritation.

Furthermore, studies have found strong links between chronic lung diseases in women and exposure to smoke from open cook stoves due to high concentration of NO₂ and SO₂ (Bruce et al, 2002). While another found a strong correlation between the high elemental concentration of aerosol particles, high mortality and high morbidity on fuel wood users (Maloni et al, 2002). In May 2015, the World Health Assembly unanimously adopted a resolution on air pollution and health, calling for the integration of health concerns into national, regional and local air pollution-related policies. Following that in 2016, the World Health Assembly adopted a "Roadmap for Enhanced Action," calling for increased cross-sector cooperation to address the health risks of air pollution.

Interest in respiratory health impacts of air pollutants from fuel-wood utilization has been increasing rapidly probably as a result of high cases of illnesses recorded. Among rural women and children observed that long time exposure to biomass combustion results in chronic obstructive lung diseases, heart diseases, acute respiratory infections, low birth weight, eye disorder, conjunctivitis, blindness and cancer (Edokpa and Ikelegbe, 2012).

3. STATE AND COUNTRY OF REVIEW

Nigeria is a former British colony, which came into existence as a result of the amalgamation of Northern and Southern protectorates, empires and smaller territories (Bello, 2007). Today, Nigeria is made up of 36 states and the Federal Capital Territory (FCT). Nigeria extends from latitude 4°N to 14°N and from longitude 3°E to 15°E (Macmillan Nigeria Secondary Atlas, 2006). Nigeria has a total area of 923,769km² (National Bureau of Statistics, 2009) and its relief is generally divided into lowlands and highlands. Nigeria is drained by two major Rivers, Niger and Benue. The vegetation is also grouped into two (2) main categories - forest and savannah (Bello, 2007). Nigeria's population is currently estimated at about two hundred million (200,000,000) (UNDP: World Population; 2019) of which over 60% engages in agriculture (Bello, 2007).

This review is focused on Kaduna State, which is located in the Northern part of Nigeria's High Plains occupying a total land mass of 46,053km³ with an estimated population of about 7 million people, as a case study. The vegetation cover of Kaduna State is Sudan Savannah type, characterized by scattered short trees, shrubs and grasses. The soil is mostly loamy to sandy type, with some substantial amount of clay (National Human Development Report, 2018). The main stay of the economy in the state is agriculture with about 80% of the people actively engaged in subsistence level farming. The vegetation extends from the Guinea Savannah in the southern part of the state to the Sudan Savannah in the northern part, characterized by scattered short trees, shrubs and grasses.

Over the years, Government at Federal, Regional and Local levels have been discouraging indiscriminate cutting of trees, but this has not yielded the desired result thereby causing desertification in northern Nigeria and deforestation in southern Nigeria partly due to fuel wood consumption which is not only going on unabated but also increasing at alarming rate. The government of Kaduna State has also been actively engaging in different activities and programmes that would ensure environmental sustainability and improve the hitherto destroyed areas over the years from the ravaging impact of global warming and climate change.

Most of the data utilized in this study are secondary data and information on the implication of usage of fuel wood and other biomasses, which were obtained from online resource journals and national statistics database including the National Population Commission, National Bureau of Statistics, etc. They include the percentage distribution of households based on the type

4. STUDY METHOD

There are a number of national and international studies and articles that exist documenting the effect that domestic firewood consumption for fuel purpose affect the health of humans and the air quality of different communities where this occurs. Therefore, this study utilizes secondary data and results from comprehensive studies on the topic of review that have been published in reputable and peer-reviewed journals. The present study examines the effect of dirty fuels (woodfuel) on human health and household health expenditure.

5. RESULTS AND DISCUSSION

Indoor air pollution is a major health problem in the developing world. In sub-Saharan Africa more than 90% of people rely on biomass to meet their domestic energy demands. Pollution from biomass fuel ranks 10th among preventable risk factors contributing to the global burden of diseases. In a recent fuelwood study for the Energy Commission of Nigeria and UNDP in a rural community within Kaduna State, it is shown that the pattern of household energy consumption and supply indicates the use of fuelwood and charcoal in all the households surveyed was 100% (ECN & UNDP, 2018) as shown in the table below.

Table 1: Household Energy Consumption and Supply

S/N	Energy	Fuel Woods	%	Charcoal	%	LPG	%	Kerosene (Paraffin oil)	%	Electricity	%
1	Cooking	25	100	2	8	-	-	5	20	12	48
2	Lighting	-	-	-	-	-	-	3	12	7	28
3	Heating	-	-	10	40	-	-	-	-	-	-
4	Fish smoking	-	-	-	-	-	-	-	-	-	-
5	Garri (cassava flakes) frying	-	-	-	-	-	-	-	-	-	-
6	Others	-	-	-	-	-	-	-	-	-	-
Total		25	100								

Source: ECN & UNDP, 2018

Table 2: Types of Cooking Devices Preferably Used

S/N	Cooking Device	Respondents	%
1	3-stone stove	22	88
2	Kerosene stove	5	20
3	Gas cooker	6	24
4	Tripod iron stove	-	-
5	Half-moon mud stove	2	23
6	Electric cooker	2	23
7	Improved stove	-	-
8	Others		

Source: ECN & UNDP, 2018

Similarly, the results of a study conducted by David et al. (2016) in the south-western part of Nigeria on Indoor Air Pollution (IAP), indicates that 62.2% of the surveyed residents lived in buildings where some form of commercial activities take place. About 6.4% of them admitted to smoking within their living quarters, while 9.2% used generators for generating electricity within their building. However, on fuel type and usage pattern, about 35.2% used kerosene (paraffin oil) stoves for their cooking, while only 4% admitted that they have actual kitchens to do their cooking. Out of the respondents that stated to have a designated kitchen for cooking, only 12% said that their kitchen has proper ventilation. Also, about 18% of the respondents used candle for lighting in closed rooms while 14.4% used palm oil lamps. They concluded that the use of cooking and lighting methods that pollute the air and affect the health of people are informed by poverty, poor ventilation in dwellings and security-related issues.

A household air pollution study conducted by Oluwafemi et al. (2013) where three rural communities in Nigeria were used, targeting a fifty-nine mother-child pairs from the households. The target group was evaluated pre-intervention and then post intervention, one year after distribution of low-emission stoves. It was discovered that the low emission stove intervention caused a significant reduction in indoor PM_{2.5} level and CO level. Also, there was significant reductions in the frequency of respiratory symptoms (such as dry cough, chest tightness, difficulty in breathing and runny nose) in mothers and children. They concluded that cooking with firewood causes household air pollution and compromised lung health, and the introduction of low-emission stoves is effective at improving indoor air quality and reducing exposure-related symptoms.

Finally, Kadafa et al. (2017) assessed the health impact of fuel wood utilization on users in a village at Nasarawa state, Nigeria, where they indicated that poverty and income are the major factors influencing rural households' choice of the domestic energy consumption in the study site and also in Nigeria as a whole. Smoking, exposure to carcinogens, indoor air pollutant (IAP), open cooking practices and dietary factors are major elements that could predispose the health of a human to adverse consequences such as lung cancer (LC) from its causative agents. More than 3 billion people globally practice cooking and room heating by using solid fuel generating IAP, including small soot particles that penetrate deep into the lungs. The problem is more pronounced in the developing countries (Kumlachew et al, 2013).

Currently, the number of people relying on biomass for cooking and heating including wood, animal dung, crop waste is approximately 2.7 billion people and a further 0.4 billion use coal (FAO, 2011). During cooking and heating operations in households, high levels of health-damaging pollutants, including particulate matter and monoxide are released. Particulate Matter (PM) has been classified as aerodynamic diameter as size is critical health determinant. During cooking activities, young children or babies strapped onto their mothers' backs become more exposed to higher levels of the potentially harmful air pollutants from the smoke particles including PM_{2.5} and CO₂. According to Bruce et al, it is estimated that exposure is estimated between 3 – 7 hours per day depending the duration of cooking periods. Furthermore, it was also reported as many as 1 billion people, mostly women and children are regularly exposed to levels of indoor air pollution that are up to 100 times higher than those considered acceptable concentrations (Krassi et al., 2015).

There have been different studies on clean or improved cookstoves intervention projects, but these projects always fail along the line. This is because most of these stoves that are issued to women or householders, especially those in rural communities, are not those that suit the cooking preferences of the particular groups of people. This is why RUWES (Rural Women Energy Security) is currently embarking on a project in collaboration with her implementing partner (Nexleaf Analytics) in a rural community in Abuja, Nigeria funded by the Climate and Clean Air Coalition (CCAC), in order to better understand the cooking preference and experiences of rural women using quantitative and qualitative objective data gathered from stove sensors or monitors and field surveys. The results from this study would significantly add to the body of knowledge for the entire clean cooking sector and help the sector and other stakeholders promote clean cookstoves that are usable and adoptable by different groups of people.

With efficient cookstoves and good fuel management practices, even the indiscriminate consumption of biomass fuels and its attendant emission of gaseous pollutants can be significantly regulated or reduced. However, because of the prevailing economic conditions in the country and poverty in most households, lack of adequate government support for the clean cook sector, inadequate infrastructure, the penetration of such advanced stoves to rural communities for curbing the menace of indiscriminate wood fuel usage has been very slow over the years.

6. CONCLUSION AND RECOMMENDATION

There is no doubt that indiscriminate use of fuelwood as a major energy, results in indoor air pollution with releases of toxic gases and substances which are an environmental and health hazard for population in the communities exposed in Nigeria and in Kaduna State in particular.

Various studies as discussed above, have delineated significant ill effects of indoor air pollution (IAP), such as increased risks of respiratory, skin and eye diseases. IAP has also been associated with increased risk of cancer. It is therefore not surprising that IAP, has become a major area of concern for the world health organisation (WHO) and the entire health community in the world.

The health community is on board the health pollution discussion, and the WHO provides technical support to countries in evaluation and scale-up of health promoting fuels and technologies.

Rural Women Energy Security (RUWES) Nigeria is at the forefront of this effort, showing what is possible, linking climate, energy poverty, air pollution and rural economic stimulation by opening a new sector of the economy.

The achievement of a permanent and sustainable solution to these impending disasters require a multiagency approach involving all stake holders, from local communities, local, state and national governments, national and international agencies, each playing a vital role.

7. REFERENCES

Abalaka J.I and Manu S. 2007. Factors affecting forest bird diversity and recent avifaunal changes in the degrading Kagor-Nindam forest reserves. Kaduna, Kaduna a. *Ostrich*, 78(2): 233-238.

Akut, Y.B. 2008. Some Determinants of House – Hold Energy Consumption in Jimeta. In Mammam, A.B; Chup, C.D; and Mashi, S.A. (eds). *Urbanization, Resource Exploitation and Environmental Stability in Nigeria*. Book of Proceedings of the 49th Annual Conference of the Association of Nigerian Geographers (ANG). Joyce Graphics Printers & Publishers. Pg. 535 & 537.

Al-Amin, M. 2014. "Domestic Energy Crisis and Deforestation Challenges in Nigeria". *J of Environment and Earth Science*, Vol.4, No.2. Pp.74-91

Audu E.B. 2013. Fuel wood consumption and desertification in Nigeria. *International Journal of Science and Technology*; Vol 3, No 1, ISSN 2224-3677

Aweto A.O. 1990. Plantain forestry and forest conservation in Nigeria. *The Environmentalist*, 10: 27-34.

Ayuba, K.H. and Dami, A. 2011. *Environmental Science. An Introductory Text*. A Revised and Enlarged Edition. Published in Nigeria by Apani Publications; No 27, Bagaruwa Road, Costain, Kaduna. Pg. 72, 73 and 76.

Bertrand H.M.N., Emmanuel A., Cyrille C. and Yacouba N.M. 2014. Effects of cooking fuel smoke on respiratory symptoms and lung function in semi-rural women in Cameroon; *International Journal of Occupational and Environmental Health*, Vol.21, No 1.

Bruce, N.; Perez-Padilla, R.; Albalak R. 2002. The Health Effects of Indoor Air Pollution Exposure in Developing Countries. *Protection of the Human Environment*,

Démurger S. and Fournier M. 2011. Poverty and firewood consumption. A case study of rural households in Northern China. Université de Lyon, F-69007, France

ECN and UNDP 2018. Assessment of fuelwood availability and consumption in selected rural communities in Kaduna State; Submitted to Energy Commission of Nigeria and United Nations Development Programme by New Frontier Developments Ltd.

FAO 2011. State of the World's Forests (9th Ed.), Food and Agriculture Organization of the United States, Rome. 2011

Gordon B., Mackay R. and Rehfuess E. 2004. Inheriting the world: the atlas of children's health and the environment. Geneva, World Health Organization.

IEA 2010. Energy Poverty: How to make modern energy access universal? International Energy Agency, World Energy Outlook, Paris.

Kadafa A., Medugu N., Dennis I., Stephen K. and Medan J.D. 2017. The health impact of fuel wood utilization on users in Yelwa Village, Nasarawa State, Nigeria; ISSN 2307-4531; Available online at <http://gssrr.org/index.php?journal=JournalOfBasicAndApplied>

Krassi R., Thet W., Dean B., and Satvinder D. 2015. Prevalence of respiratory symptoms among children in rural Myanmar-disease burden assessment attributable to household biomass smoke; *Indoor Built Environment* 25(5), May 2015, DOI: 10.1177/1420326X15586017.

Kumlachew G., Molla G., Zewdu D. and Dube J. 2013. Current level and correlates of traditional cooking energy sources utilization in urban settings in the context of climate change and health, Northwest Ethiopia: A case of Debre Markos Town; *BioMed Research International*,

Mallo, I.I.Y. and Ochai, B.C. 2009. An Assessment of the Effects of Urbanization on Deforestation in Bwari Council, Abuja – FCT, Nigeria. *Abuja Journal of Geography and Development*. Published by the Department of Geography and Development, University of Abuja, Abuja, Nigeria. Vol. 3, No. 1. January, 2009. Pg.13.

Momodu, I. M. 2013. "Domestic Energy Needs and Natural Resources Conservation: The Case of Fuelwood Consumption in Nigeria". *J of Social Sciences*, Vol 4 No 8, pp.77-97

Miltiadis S., Chalikias and Grigorios Kyriakopoulos and Konstantinos G. Kolovos. 2010. Environmental sustainability and financial feasibility evaluation of wood fuel biomass used for a potential replacement of conventional space heating source. Part I: a Greek case study; Operational research; Vol 10; pgs 43-56.

National Human Development Report. 2018. Jigawa State, Nigeria; Written by the Editors of Encyclopaedia Britannica. Available online at <https://www.britannica.com/place/Jigawa>

Okoye, C.O. and Ezeonyejiaku, D.C. 2010. Desertification in the Drylands of Nigeria: Causes, Consequences and Solutions. *Journal of the Faculty of Environmental Sciences*, Nnamdi Azikiwe University (UNIZIK), Awka, Nigeria. Volume 1, Number 1, 2010. Pg. 49 and 51.

Olanrewaju, R.M. and Ogunleye – Adetona, C.I. 2000. Women in Environmental Degradation. In Jimoh, H.I. and Ifabiyi, I.P. (eds). *Contemporary Issues in Environmental Studies*. First Published in Nigeria by Haytee Press and Publishing Co. LTD. Pg. 149.

Oluwole O., Godson R., Ganiyu A., and Tess W. 2013. Effect of stove intervention on household air pollution and the respiratory health of women and children in rural Nigeria. *Air Quality Atmosphere & Health*; 6(3); article (pdf available) at researchgate.net.

Parrotta, John; Youn Yeo-Chang & Leni D. Camacho 2016. Traditional Knowledge for Sustainable Forest Management and Provision of Ecosystem services, in *International Journal of Biodiversity Science, Ecosystem Services & Management*, Vol.12, 2016, Issue 1-2.

Rajbala S., Rajesh D. and Vikram M. 2013. Indoor air quality index and chronic health disease: A pilot study; *International Journal of Research in Engineering and Technology*; eISSN:2319-1163; pISSN: 2321-7308.

Singh A.L. and Parveen U. 2010. Fuel Choice, Indoor Air Pollution and Women's Health: A Household Level Perspective. In: Singh, A.L. (Ed.), *Environment and Health*. B.R. Publishers, New Delhi, pp: 1-34.

WEO (World Energy Outlook). 2017. Special Report: Energy Access Outlook, International Energy Agency. Available online at <https://webstore.iea.org/weo-2017-special-report-energy-access-outlook>

WHO. 2006. Statistical information system; World Health Organization; Available online at <http://www.who.int/whosis> (August 9, 2007).

WHO. 2005. Indoor Air Pollution and Health. Fact Sheet, No. 292, June, Washington DC.

#290: Vehicle-induced pressure on divider in isolate and tandem

K C TAN¹, K W CHAN², M Z ABDULLAH³

¹School of Mechanical Engineering, University of Sains Malaysia, Engineering Campus, 14300 Nibong Tebal, Penang Malaysia, keacheng@gmail.com

²School of Mechanical Engineering, University of Sains Malaysia, Engineering Campus, 14300 Nibong Tebal, Penang Malaysia, kengwai.chan@usm.my

³School of Mechanical Engineering, University of Sains Malaysia, Engineering Campus, 14300 Nibong Tebal, Penang Malaysia, mezul@usm.my

Roadways provide access and mobility, connecting people in different places. Turbulence induced by moving vehicles on roadways can be potentially used as an energy source. Previous studies have focused on the aerodynamic behaviour of moving vehicles whilst the impact of vehicle-induced turbulence on highway has not been explored. The aim of this study is to investigate the pressure induced by moving cars on the highway divider. Both experimental work and simulation studies were conducted to compare the pressure induced on the divider. Single car (isolate) and car in tandem settings were taken into consideration for this study. The study found that the pressure induced on the highway divider varies with car speed, for both isolate and tandem settings. However, different settings gave slight differences on the pressure induced. The numerical studies conducted verified the experimental data collected. The fluid power induced is theoretically calculated as 303.56W and 275.21W for both isolate and tandem settings respectively.

Keywords: vehicle-induced turbulence; pressure; Ahmed car model; power

1. INTRODUCTION

Roadways are major infrastructure connecting people, providing access and mobility, and traffic volume can be high. When vehicles move along roadways, wind pressure is created, and this pressure varies with different vehicle sizes and speed. The generated wind pressure causes a drag force, a force which is created when solid body moves in fluid medium (Zarkesh and Heidari, 2013). The effect of wind speed and wind direction on the aerodynamic characteristic of moving vehicles (Xiang, Li et al., 2017) and wind profile (Salvadori, Morbiato et al., 2012) have previously been researched.

According to Quinn, total instantaneous force (F) on a flat plate caused by passing vehicles is the sum of wind-induced force (F_w) and vehicle-induced load (F_v) (Quinn, Baker et al., 2001). Wind-induced force is mainly due to inertia flow around the bluff body (Quinn, Baker et al., 2001), or transient pressure field due to unsteady flow (Sanz-Andrés, Santiago-Prowald et al., 2003), whilst vehicle-induced force is caused by the pressure field in the flow region of the vehicle slipstream (Baker, Dalley et al., 2001).

The induced airflow generated has a quantity of mass and velocity, creating energy in the airflow, and the wind energy (pressure) induced is measurable. Vehicles experiencing higher wind energy will lead to a higher aerodynamic force (Wu, Li et al., 2014). In addition, when vehicle type, velocity and distance to road side were known, the expected loading values can be estimated and used for road-side flat element design (Lichtneger and Ruck, 2013).

The objective of this study is to investigate the pressure induced by vehicles on the highway divider, or median barrier. The methodology adopted for this study was presented in section 2, both in terms of experimental methodology (section 2.1) and simulation settings to verified experimental result (section 2.2). Pressure readings and simulations results were presented in section 3 with discussion. The main conclusions were summarised in section 4.

2. METHODOLOGY

2.1. Pressure measurement on divider

An Ahmed model (208.8mm x 57.6mm x 77.8mm, slant angle of 40°) was fabricated from wooden blocks. Together with Perspex (200mm x 200mm, thickness 13mm) with 36 drilled holes (Ø4mm), it were put together as an experimental model.

A pressure difference imposed at 90° on the divider was measured using a digital manometer (Dwyer Series 477-1-FM) at wind tunnel speeds ranging from 7.15m/s to 18.38m/s. This speed range was chosen considering the lowest value of maximum allowed highway speed (19.4m/s) in Malaysia. The car model was placed 50mm from the divider for both isolated and tandem settings; the distance between vehicles was 32mm for the tandem setting.

The experimental setup was scaled at 1:15 compared to actual measurements. Actual experimental setup and schematic diagram are shown in Figure 1 and Figure 2 respectively. The experiments were conducted in an educational open circuit wind tunnel, with test section 0.2m x 0.2m x 0.4m and maximum allowed speed of 37m/s. A pitot tube was used to measure the pressure at both front and rear of the moving vehicle.



Figure 1: Experiment setup showing car model in tandem setting

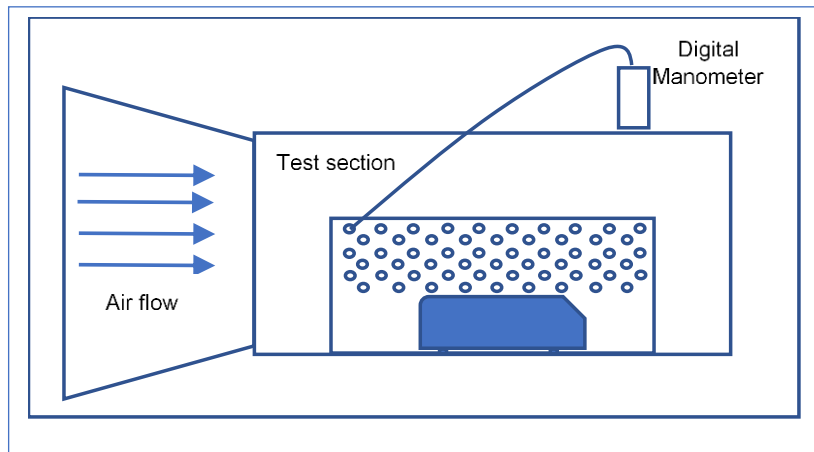


Figure 2: Experiment setup schematic diagram showing car model in isolate setting

2.2. CFD simulation

A numerical approach and modelling method were employed in the present study using ANSYS Aim 18.1 software. The computational domain length was 410mm excluding spacing between two cars, height 200mm and width of 200mm. The coordinate point (0, 0, 0) is at the rear end of the front car.

RANS equations additional closure of $k-\omega$ SST turbulence model was used for this simulation work. The pressure inlet was set as the inlet boundary while the pressure outlet was adopted for the outflow. All the surfaces excluding the inlet boundary and outlet boundary were treated as a no-slip wall.

Results converged at iteration around 200, with default residual tolerance assets set as 0.01. A second order upwind discretisation scheme was used to enhance the calculation accuracy. Simulation results converged based on RMS values, a mesh independent study was carried out to ensure independence of mesh resolution. For the isolate setting, approximately $1.2625E+05$ numbers of elements were meshed with a total number of nodes is 40,019. For the tandem setting, $2.095E+05$ numbers of elements were meshed, and total number of nodes is 65,409.

3. RESULTS AND DISCUSSION

3.1. Experimental and simulation result

From the experiment conducted, the induced pressure on the divider was measurable. Pressure readings at various points on the divider were measured and recorded for different speeds. Pressure readings at selected wind tunnel speeds are presented in Figure 3 and Figure 4.

It was observed that induced pressure increased at higher wind speeds, but there was not much change at different heights (different y-axis value). When a single car was moving, the divider encountered higher pressure (approximately 6.65% - 38.19% higher) at the rear end of the car compared to the front. This is consistent with what has been found in previous studies (Musa, Osman et al. 2012): higher turbulent kinetic energy was produced at vortices behind the car.

In addition, the divider at the side region of the single car also showed pressure readings. This provided evidence indicating that a certain portion of turbulent kinetic energy (vehicle-induced force) was developed.

The car travelling in tandem can be seen at any of the seven selected different inlet velocities, maximum induced pressure occurs at one common position, which is beside the rear car, at about $x = 390\text{mm}$. Based on the experimental data collected, the maximum standard deviation values calculated are 3.12 and 3.21 for isolate and tandem settings respectively.

The experimental data was then compared with simulation results. The computed pressure readings obtained using Ahmed model and ANSYS AIM 18.1 were in good agreement with the experimental results. Both experimental and simulated pressure readings were plotted and are compared in Figure 6 and Figure 7.

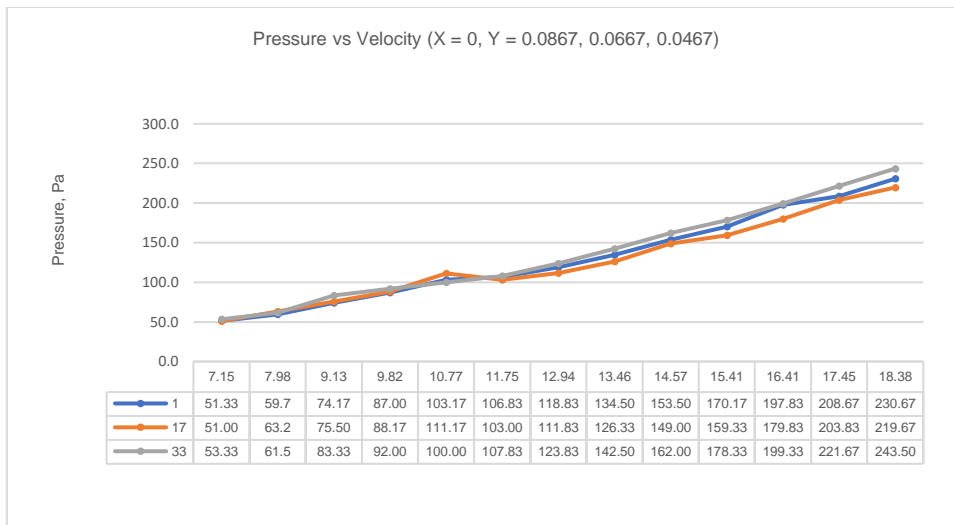


Figure 3: First row pressure reading at different speed – tandem

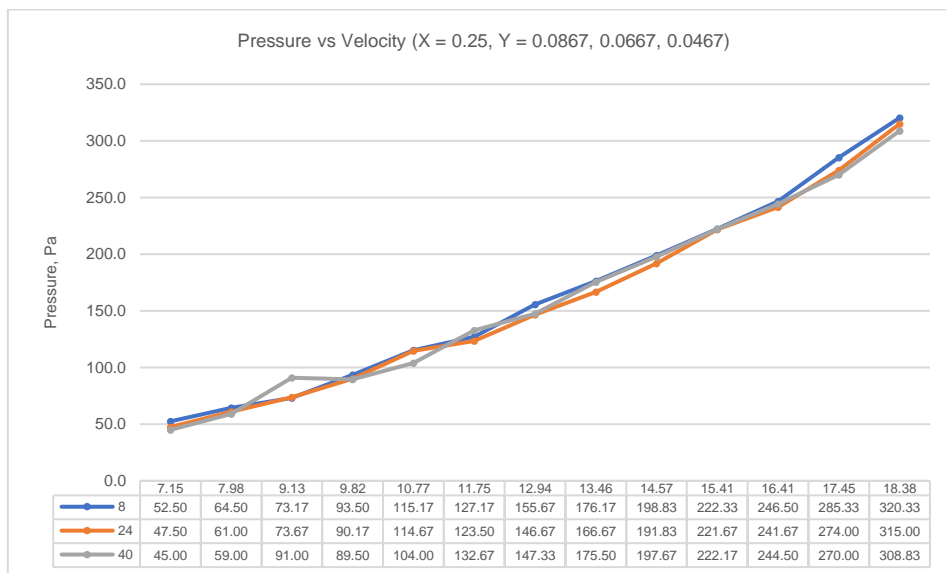


Figure 4: Last row pressure reading at different speed – isolate

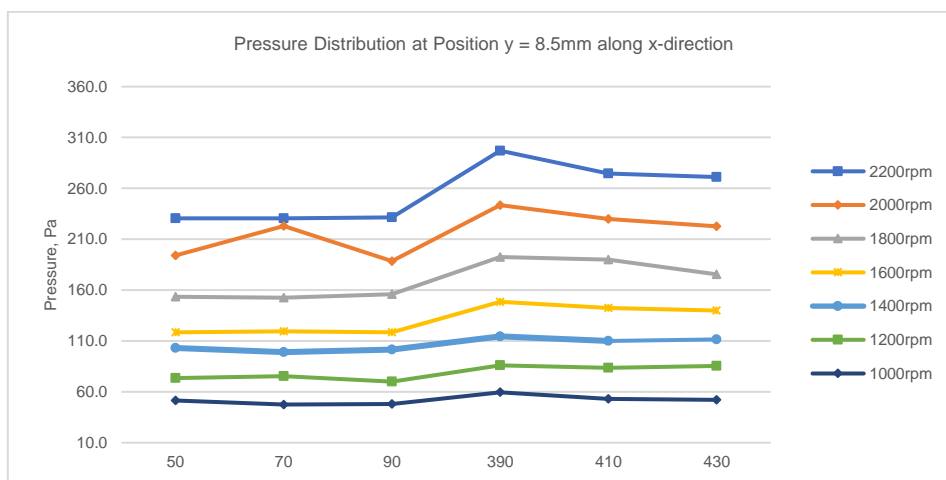


Figure 5: Pressure distribution for different inlet velocities at position y = 8.5mm along x-direction

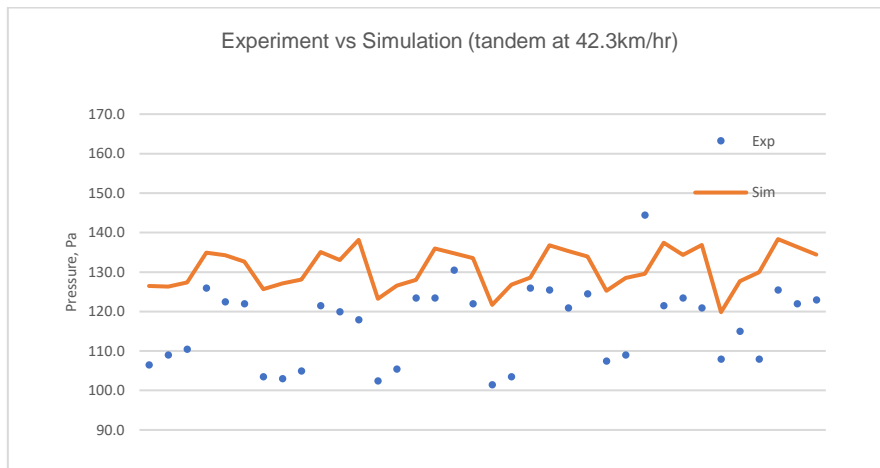


Figure 6: Pressure reading at different point for car moving in tandem at 42.3km/hr

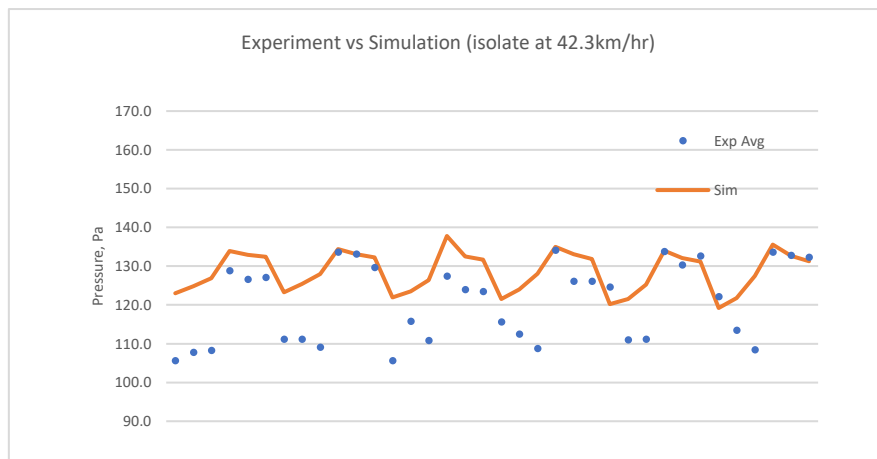


Figure 7: Pressure reading at different point for single car moving at 42.3km/hr

3.2. Fluid Power Calculation

The fluid power is based on volumetric flow and pressure rise, the volumetric flow is calculated from the divider and velocity. For this study, only vehicle speed was calculated; natural wind speed was not taken into consideration.

Equation 1: Fluid power generated from volumetric flow

$$P = Q \cdot \Delta p$$

Equation 2: Area and velocity formed volumetric flow

$$Q = A \cdot V$$

Where:

- P = fluid power (kgm^2/s^3)
- Q = volumetric flow (m^3/s)
- Δp = pressure rise (kg/ms^2)
- A = divider area (m^2)
- V = vehicle speed (m/s)

Overall fluid power imposed on the divider was calculated using Equation 1. The calculated fluid power at different velocities for both settings are presented in Figure 8 and Figure 9. Both isolate and tandem settings showed that fluid power increased as the velocity accelerated.

When a car is moving at 66km/hr, theoretically 287.9W fluid power was received by the divider with an area of 0.0536m². For a car moving in tandem at the same speed with a distance gap of 32mm, 261.01W fluid power was expected.

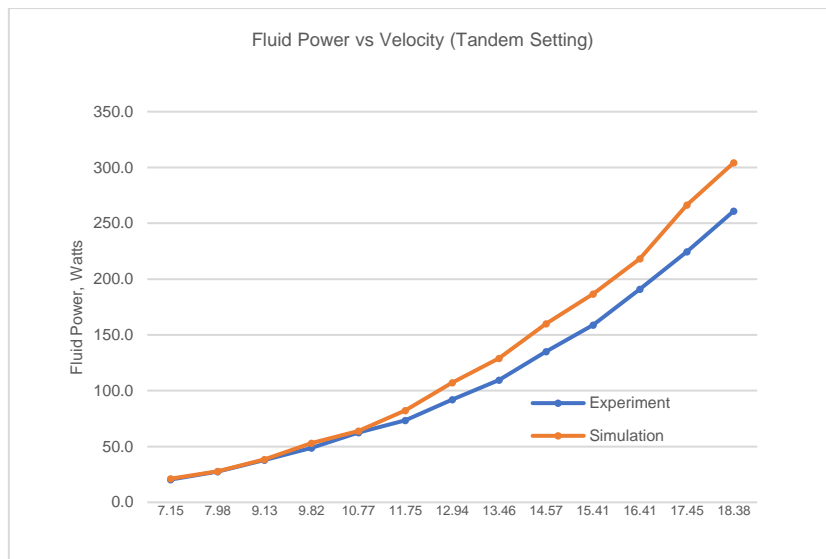


Figure 8: Overall fluid power calculated at different speed

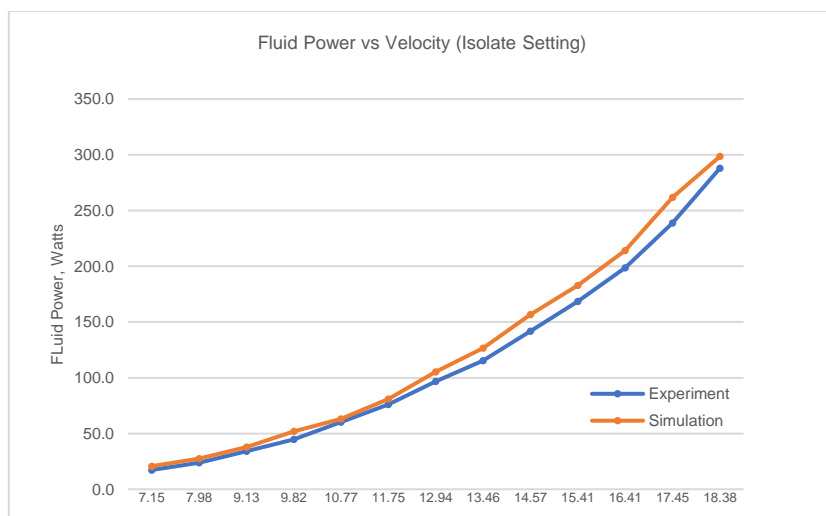


Figure 9: Overall fluid power calculated at different speed

4. CONCLUSION

The conducted experiment showed that pressure was induced on the divider when cars were moving. The pressure increased as the speed accelerated. The computed pressure readings obtained were in line with the experimental results. The fluid power caused by the turbulence was calculated. The theoretical value, 287.9W for isolate setting, 261.01W for tandem setting, provided evidence to further extend the generated power for auxiliary system use.

5. ACKNOWLEDGEMENTS

The author would like to thank the Malaysian Government for awarding *Hadiah Latihan Persekutuan* to support this research study and partial financial support from the Universiti Sains Malaysia (research grant 304/PMEKANIK/60313039).

6. REFERENCES

- Baker, C. J., Dalley, S. J., Johnson, T., Quinn, A. and Wright, N. G. (2001). "The slipstream and wake of a high-speed train." Proceedings of the Institution of Mechanical Engineers, Part F: Journal of Rail and Rapid Transit **215**(2): 83-99.
- Lichtneger, P. and Ruck, B. (2013). Transient wind loads on flat elements induced by passing vehicles Fachtagung "Lasermethoden in der Strömungsmesstechnik" München, Dt. Ges. für Laser-Anemometrie GALA e. V.: 41/41-41/12.
- Musa, N., Osman, K. and Hamat, A. M. A. (2012). "Renewable Energy from Induced Airflow Generated by Cruising Ground Vehicles in Tandem using RANS." Energy Procedia **14**: 1877-1882.
- Quinn, A. D., Baker, C. J. and Wright, N. G. (2001). "Wind and vehicle induced forces on flat plates—Part 1: wind induced force." Journal of Wind Engineering and Industrial Aerodynamics **89**(9): 817-829.
- Quinn, A. D., Baker, C. J. and Wright, N. G. (2001). "Wind and vehicle induced forces on flat plates—Part 2: vehicle induced force." Journal of Wind Engineering and Industrial Aerodynamics **89**(9): 831-847.
- Salvadori, S., Morbiato, T., Mattana, A. and E, F. (2012). On the Characterization of Wind Profiles Generated by Road Traffic. The Seventh International Colloquium on Bluff Body Aerodynamics and Applications (BBAA7), Shanghai, China.
- Sanz-Andrés, A., Santiago-Prowald, J., Baker, C. and Quinn, A. (2003). "Vehicle-induced loads on traffic sign panels." Journal of Wind Engineering and Industrial Aerodynamics **91**(7): 925-942.
- Wu, M., Li, Y. and Chen, X., Peng, Hu (2014). Turbulence Characteristics Relative to Moving Vehicles. World Congress on Advances in Civil, Environmental, and Materials Research, Busan, Korea.
- Xiang, H., Li, Y., Chen, S. and Li, C. (2017). "A wind tunnel test method on aerodynamic characteristics of moving vehicles under crosswinds." Journal of Wind Engineering and Industrial Aerodynamics **163**: 15-23.
- Zarkesh, A. and Heidari, M. (2013). Developing a New Application for Wind Generators in Highways. 2013 Fifth International Conference on Computational Intelligence, Communication Systems and Networks.

#294: A review on green and sustainable technology in protecting honey bees against *Varroa destructor*

Emmanuel TAPIA¹, Hasila JARIMI², Saffa RIFFAT³

¹Department of Architecture and Built Environment, Faculty of Engineering, University of Nottingham, NG7 2RD
University Park, Nottingham, UNITED KINGDOM, b_tapi@hotmail.com

²Department of Architecture and Built Environment, Faculty of Engineering, University of Nottingham, NG7 2RD
University Park, Nottingham, UNITED KINGDOM, hasila.jarimi@nottingham.ac.uk

³Department of Architecture and Built Environment, Faculty of Engineering, University of Nottingham, NG7 2RD
University Park, Nottingham, UNITED KINGDOM, saffa.riffat@nottingham.ac.uk

The greatest ecological impact of bees in nature is pollination. The production of 70% of the 124 main crops for worldwide human consumption depend on pollinators, mainly honey bees. Honey bees are usually subjected to numerous challenges due to their environment. The population of honey bee colonies in the UK has decreased rapidly due to Varroa destructor; parasitic mites that are harmful to bees.

The common methods to control Varroa mites mostly involve a chemical treatment which is potentially dangerous for bees and their products. However, in recent years, the control method is innovating towards thermotherapy method of which thermal energy has been applied to control the mites. Additionally, there are also researchers who have applied green and sustainable technology in the thermotherapy method to control Varroa mites.

This paper summarises the current status of honey bees in the UK and Varroa mites, the life cycle of the Varroa mites inside the beehives, an assessment of its control methods and a description of the thermotherapy treatment using green and sustainable technology.

Keywords: Apis mellifera; Varroa destructor; thermotherapy; hyperthermia; mite control

1. INTRODUCTION

When talking about bees, the species usually referred to is the *Apis mellifera*, the most abundant species. This species of bee and its 28 recognised subspecies (Engel, 1999) can be found in all continents except Antarctica (Mortensen, Schmeihl, and Ellis, 2013). The bees of this species have spread throughout most of the planet due to their great adaptability (Al-Ghamdi *et al.*, 2013). They only require adaptations to the local environment, such as adjustments of the colony cycles to the time of the local floral resources, forming a group in colder climates and migratory swarms (Engel, 1999).

Its reproduction is through eggs. Depending on the type of genetic contribution in their stage of egg and feeding they have in their stage of larva, it will be the caste in which they convert. Each caste has a different function within the colony. The females are born from fertilised eggs and the drones (males) from unfertilised eggs. The female larvae that feed on royal jelly nectar and pollen become queens and those with a standard diet of nectar and pollen develop into adult workers. Among the three castes, the worker bees are the smallest. Their bodies specialise in the collection and transport of nectar and pollen. They are non-reproductive females. They have a stinger that comes off with the poison sac from their abdomen if it is used to sting. This causes the death of the worker bee. The queen has a longer abdomen than the workers, although her head and thorax are similar. It is the only reproductive female in the colony (under regular circumstances). She also has a sting but this does not cause death when she uses it. The drones are the male caste. They are larger than those of the female castes, with a thick blunt abdomen at the end which gives them a bullet appearance. All bees have different stages of development (Figure 1). Between each stage they undergo a metamorphosis, but the times between these vary depending on the caste. The drone has the longest development; however, it is the caste with the lowest life expectancy. The worker bees have a period of intermediate development and the queens are the fastest. These last in optimal conditions reach to live up to 3 years of productive life (Mortensen *et al.*, 2013).

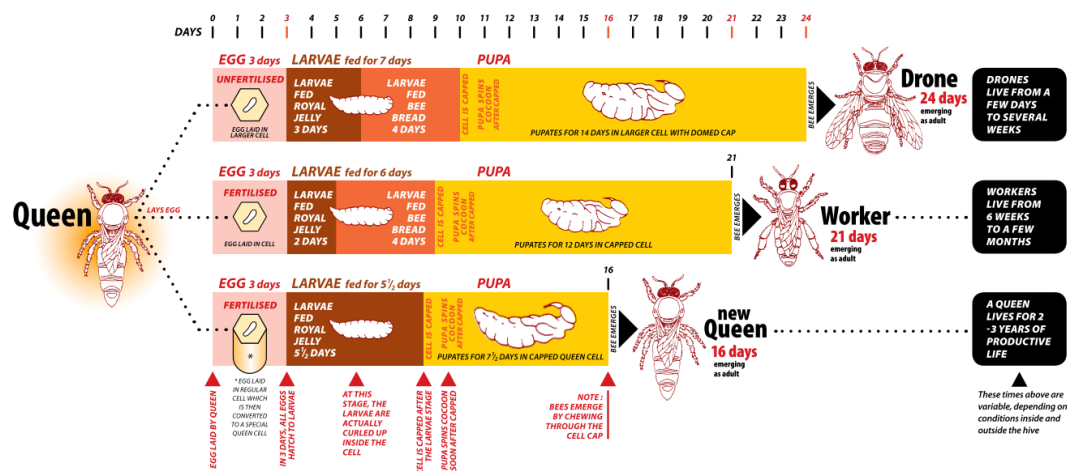


Figure 1: Bee life cycle (Craig 2017)

2. IMPORTANCE OF BEES

It is often thought that bees are only useful for making honey. However, the greatest ecological impact of bees in nature has to do with the pollination of flowers. The bees, during all their life, make approximately ten trips daily transporting the pollen from the stamens to the receptive part of the flowers. In this way, fertilisation and the development of fruits and seeds or fruits take place. Without this process, the plants and trees would stop reproducing. Many plants depend on the help of certain types of bees for their reproduction. As a result, commercial pollination has begun in the agro-food industry on a large scale. The *Apis mellifera* is the most economically valuable species as it does not pollinate plants randomly. It is able to focus on pollinating one specific plant species in every outing. Thousands of flowers daily can be pollinated by a single bee (Thebees.info, 2010). The production of 70% of the 124 main crops for worldwide human consumption depend on pollinators, mainly bees. Similarly, 84% of the food grown in Europe depends directly on pollinators (TAPHA, 2018). The population of bee colonies that lived in the UK has decreased rapidly from 250,000 in 1950s to just under 100,000 in 2015 (Potts *et al.*, 2010). Only 2% of the total bee species found in Great Britain pollinate 80% of the crops. Therefore, the cultivation of fruit is impacted. For example, 45% of the strawberry crops rely on the bees to grow while other crops such as apple depends on up to 85%. In 2012 only those two crops produced £ 200 million to Britain (Knapton, 2015). Bees role is so relevant that the National Audit Office calculated their contribution to the economy of the UK. The value of bee services in 2007 was estimated at £200 million a year. The retail profit of what bees pollinate was valued closer to £1 billion (Holland, 2009). Their overall economic input has increased by 191%, going from £220 million in 1996 to £651 million in 2012 (Knapton, 2015). The impact of bees is constantly trending to continue growing in the coming years.

If it were the man who was in charge of pollinating flower to flower, then the price of the products would rise to unsuspected limits. For example, these insects pollinate the sunflower that gives rise to the oil. They also do the same with coffee, tea and cocoa plants. Also, their work is key to the existence of the forage that animals like cows eat. Therefore, the scenario that we would have if the bees disappear would be devastating. The importance of bees for human beings and the urgent need to take measures to stop their progressive and unjustifiable disappearance are clear. The paradox is that humans continue to plant more and more crops that need bee pollination, although at the same time the critical situation that these insects go through is sometimes ignored.

3. THREATS ON BEES

Nowadays bees are subjected to numerous pressures. They usually faced the natural challenges that their environment provided, for example, temperature, humidity, and predators. However, along with these stressors, there is a decrease in the abundance and diversity of the flowers and the cocktails of agrochemicals to which they are exposed. Behind all the other factors, climate change is also affecting the health of pollinators (Tirado, Simon, and Johnston, 2013). On the other hand, they are also exposed to parasites propagated by human action. None of these stressors is independent and everyone has their contribution against the bees; for example, a bee that has been exposed to pesticides could have alteration to its immune system, causing it to be more susceptible to parasites (Goulson *et al.*, 2015).

3.1. Industrial agriculture

With the technification of large-scale agriculture, monocultures have expanded, fragmenting natural habitats and reducing diversity. All the above, together with practices such as pesticide and herbicide spraying, reduce the bee-nesting capacity, making industrial agriculture one of the main hazards for pollinator communities. Some bees are weakened by contact with pesticides making them more vulnerable to disease and parasite infestation (Tirado *et al.*, 2013). On the insecticides side, are the neonicotinoids those which use has expanded more rapidly in recent years as they are used for a wide spectrum of pests. At the same time, it has been detected that these substances have potential effects on pollinators (Jeschke *et al.*, 2010).

3.2. Climate change

The anticipated consequences of climate change such as increased temperatures, alterations in periods of rain and erratic and extreme climates have a strong impact on pollinators (Tirado *et al.*, 2013). As a result, ineffective pollination of crops could occur. A disturbing scenario is whether bees emerge earlier in the growing season as a strong reaction to climate warming while flowers respond less strongly emerging later. This time phase-out could harm both the bees and the plants and have repercussions on productivity of many crops (New Jersey Institute of Technology, 2014). This change in phenology can happen in the opposite direction, that is, if the spring starts early, the flowers would bloom before and it is unknown if the bees would be able to follow that pace, which would have severe consequences (Fessenden, 2015).

Changes in temperature are also a problem as extreme temperatures are harmful to bees. It is known that despite the temperatures in the environment of its nest, bees regulate the indoor temperature within an optimum range between 33 and 36°C (Arnia, 2013). Bees achieve thermoregulation through some heating or cooling behaviours. So, throughout the year in addition to their regular work, bees devote their energy to maintain freshness in hot season and retain heat during the winter (Abou-Shaara, Al-Ghamdi and Mohamed, 2013). To maintain the optimal temperature, the bees control the internal temperature of the hive and it is the joint action of hundreds or thousands of bees which makes the microclimate thermoregulation (Kridi, de Carvalho and Gomes, 2016).

De Almeida (2008) conducted an experiment in which an increase in temperature led to swarms of bee colonies. It was found that when the outside temperature was such that inside there were 41°C, the bees gave up trying to cool the hive and began to swarm. In this test, the colonies swarmed between 3 and 4 days which means that although the bees can tolerate maximum temperatures is the prolonged exposure to high heat which causes the abandonment (Kridi, de Carvalho and Gomes, 2014). The abandonment is increased by the climatic change due to the changes of weather and temperature. Bees have difficulty adapting because the areas where they can survive have been restricted (Worland, 2015). Kerr *et al.* (2015) compared the activity of pollinators between 1901 and 1974 with the recent decades when climate changed rapidly. Bees in northern countries failed attempting to migrate closer to the North Pole and in the South many populations succumb. Bees lost approximately 200 miles in both Europe and North America (Worland, 2015). Climate change seems to contribute definitively and forcefully to the gradual restriction of the ranges among pollinator species worldwide (Kerr *et al.*, 2015).

3.3. Parasites

There are parasites such as *Nosema ceranae* that are very adverse for bees in some southern European countries. However, in recent years it has been observed that the external parasitic mite *Varroa destructor* is the biggest threat to global apiculture (Tirado, Simon, and Johnston, 2013). In the following section will expand more on this topic.

4. VARROA DESTRUCTOR

Varroa destructor, previously known as *Varroa jacobsoni* is a mite species, an external parasite of bees. Originally it only parasitized the Asian bee but in recent decades it has spread to the western bee *Apis mellifera* (TAPHA, 2018). Being the *Apis mellifera* a recently introduced host for this parasite, it does not have the natural defences to protect itself. This mite can feed on both larvae and adult bees. It feeds on the blood (haemolymph) of the host through perforations in the walls of the body that it makes with sharp parts in its mouth. Female *Varroa* mites have an oval and flat body of reddish colour (1.6 x 1.1 mm). The males are smaller and discoloured, they only exist in brood cells (TAPHA, 2018). (See Figure 2) It is said that a colony that is infested with *Varroa* mite suffers from Varroosis, a disease that between 2 and 3 years can kill the colony if it is not treated (National Bee Unit, 2018).

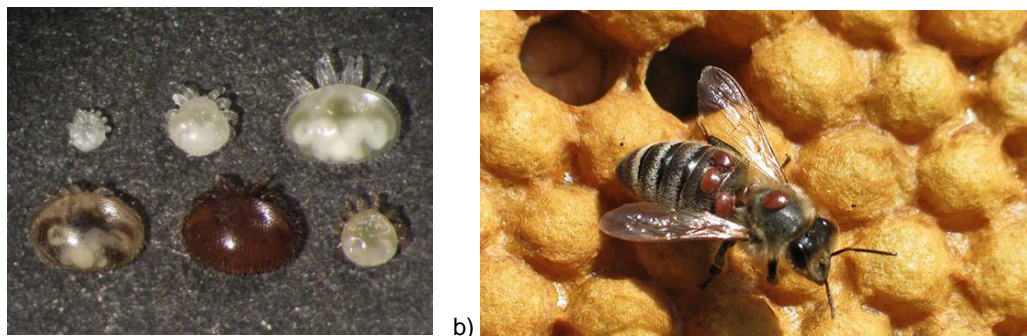


Figure 2: (a) Composition of a "Varroa family" within a honey bee worker brood cell (Reprinted from: Rosenkranz et al., 2010)
(b) A worker bee with four *Varroa* mites. (Reprinted from: Rothamsted Research Ltd 2016)

4.1. Varroosis

To attack, the female mite must find the way to be in contact with a bee that carries it to the honeycomb. Once there, it seeks to enter an open cell. There it hides in the food of the larva. With the cell still sealed, after the larva ends its food, the mite begins its reproduction. Between 1 and 2 days after the mite will have deposited up to seven eggs, of which only two or three become adults. Then the mites feed on pupae in development. It is at this point that the mite can transmit diseases to the pupa. Once the bee has emerged, the mite adheres to it until it is taken to a new open cell with a larva inside (National Bee Unit, 2018).

Currently the *Varroa* mite is present on all continents except Australia. The first reports of its existence in the UK are from April 4, 1992 in Devon (National Bee Unit, 2018). The *Varroa* mite (*destructor*) is considered the most dangerous and harmful pest for beekeeping (Rosenkranz, Aumeier and Ziegelmann, 2010). This threat stands out from others for different reasons:

1. The *Varroa* mite is a relatively new parasite for the honey bee *Apis mellifera*. Particularly in the United Kingdom where it was first found in 1992 (TAPHA, 2018). Therefore, there is no host-parasite balance and beekeepers do not have enough experience to deal with this plague.
2. *Varroa destructor* has spread through the largest beekeeping centres in the world.
3. Due to the action of the *Varroa destructor*, a colony of bees could collapse within 2-3 years in temperate climates.
4. The eradication of the *Varroa destructor* implies extra expenses for the beekeepers and a regular treatment can entail the use of substances that compromise the quality of the products of the bee.
5. Along with the worldwide decrement of pollinators, the *Varroa* mite is a crucial factor in the decline in the number of bee colonies in Europe (De la Rúa et al., 2009). Varroosis can be identified from the autumn when the number of broods being reared is decreased and the number of mites is highest until early spring.

A serious infestation of Varroa can cause general weakening of the colony, atrophied abdomens, deformed wings, or even the total loss of the colony. Varroa is a virus transmission agent for bees, which could affect their health and shorten their lifespan (National Bee Unit, 2018). The transmission of the Deformed Wings Virus (DWV) has been dissipated by human means when transporting bees or some other infected material. The populations of pollinators are connected by the environment in which they develop, which gave favourable conditions for an accelerated dispersion of the Varroa mite (Wilfert *et al.*, 2016).

5. VARROA CONTROL METHODS

To keep the health of the colonies, Varroa mites must be controlled. Mainly there are two categories for their treatment and one that has emerged more recently.

5.1. Biotechnical Controls

These methods seek to reduce the population of mites through physical means. They take advantage of the fact that the mites reproduce in bee brood. The most used is to trap the mites in drone comb and then it is removed and destroyed with the mites inside. Normally these methods can be used during spring and summer (National Bee Unit, 2018).

5.2. Varroacides

This method consists of using substances designed to kill and control the Varroa pest. They are highly effective but potentially harmful to the bee or its products. They are classified in two: those that contain patented chemicals and those that contain naturally synthesised substances (National Bee Unit, 2018.). According to European studies, bees are much healthier by not use pesticides. They also reach longer life cycles and are more resistant to viral attacks (Williams, 2015a).

5.3. Thermotherapy

Also known as hyperthermia, this method is relatively new compared to the previous ones. It consists in the application of heat at different intervals in order to eliminate Varroa. Although it is a risky treatment, it has been effective. Applying temperatures close to 40°C it has been observed that Varroa can be combated, however the risk is that this temperature is close to the temperatures that kill bees (Harbo, 2000). The section 6 of this document elaborates on details of this new method and some of its current applications.

5.4. Incipient techniques

There are other methods that also have a sustainable approach and do not threaten the health of bees or the quality of their product. However, they are still in the development phase. If their effectiveness is proven, they could be used as complementary methods to thermotherapy. Mainly two approaches stand out.

One of them consists of sounds of frequencies between 14,000 and 15,000 Hz with 90 decibels. This acoustic noise affects the feeding of the mites since it is stressful for them. It has been observed that when subjected to this stress, the mites cannot feed and die in about 10 to 20 days. Apparently, this noise does not alter the bees in any way (Krüger, 2017).

The other method seeks to prevent the reproduction of mites through pheromones that cause a disorder in their mating cycle. It involves using a substance that causes male mites to have sexual activity at a wrong time in the reproductive stage of females and causing sexually active females to have less sex activity. Eventually with a poorly achieved reproductive cycle, the mites would perish (Frenkie, 2014).

5.5. Method comparison

Table 1 shows a table of advantages and disadvantages of the use of the three proven methods mentioned above.

Table 10: Advantages and disadvantages of biotechnical methods, varroacides and thermotherapy

	Advantages	Disadvantages
Biotechnical methods	<ul style="list-style-type: none"> ✓ Do not require the use of chemical varroacides ✓ Can be combined with summer management ✓ Inexpensive or free 	<ul style="list-style-type: none"> ✗ Can be time consuming ✗ Some need a high level of beekeeping skill ✗ Generally, not sufficient if used alone ✗ Misuse can harm colonies

Authorised varroacides	<ul style="list-style-type: none"> ✓ Proven efficacy ✓ Proven safety ✓ Convenient to use 	<ul style="list-style-type: none"> ✗ Mites likely to develop resistance ✗ Residue problems in bee products if misused ✗ Can be expensive
Thermotherapy	<ul style="list-style-type: none"> ✓ Proven efficacy ✓ Do not require the use of chemical varroacides ✓ Does not affect the health of the bees nor the quality of their product 	<ul style="list-style-type: none"> ✗ Are laborious to use ✗ Misuse can harm colonies ✗ There are not many commercial offers ✗ Can be expensive

6. THERMOTHERAPY DESCRIPTION AND APPLICATIONS

It has been discovered that *Varroa destructor* is sensitive to temperature raises. It is unable to reproduce in an environment with a high temperature a few degrees higher than the optimum (Linhart, 2015). According to Bičík (2016), it is likely that enzymes responsible for the biosynthesis of proteins, are those that are first affected by the influence of temperature on the mites. For this reason, the *Varroa* mite dies with temperatures higher than 40°C and receives severe damage from 38°C (Linhart, 2015). At even higher temperatures, between 49-50°C, negative effects start to be seen in bees. These begin to regurgitate and experience extreme lethargy and clumping usually occurs. If bees are clumping at the critical moment of warming, they can cause overheating, which would be detrimental to the effectiveness of the treatment and the health of the bees (Cunningham, 1997).

However, if the thermotherapy is conducted properly, it is not very aggressive for bees, much less than a chemical treatment. It could even be a substitute for chemicals due to its high comparable efficiency (Linhart, 2015). When in the brood chamber the temperature is brought to 40-47°C and it is maintained for a period of 2.5 hours, the mites in the sealed brood are eliminated while the bee brood remains unharmed (Bičík, Vagera, and Sádovská, 2016). To achieve a 100% effectiveness over *Varroa* mite in the sealed broods, it is essential to maintain a temperature of 40°C or higher in a period of 150 minutes, but is not recommended to exceed 47°C. It has been proven that to achieve the best results, there must be two sessions of heat therapy. The second heating should be done 7 to 14 days after the first (Bičík, 2015).

Table 2 summarises, on a comparative scale, the temperatures at which bees or *Varroa* mites present significant alterations in their health or behaviour in contrast to the temperature range in which thermotherapy operates.

Table 2: Key temperatures for bees (*Apis mellifera*) and *Varroa* mites (*Varroa destructor*)

Brood box temperature [°C]	Effect on Bees/Varroa	Additional notes	Reference
<10	Bees cannot fly	Honey bees are cold blooded.	(Hiskey 2012)
20	Brood led to higher mortality	If they are submitted for a period greater than 12 hours.	(Wang <i>et al.</i> 2016)
<27	Bees keep inside and thermoregulate the hive	This inner temperature reflects an outside temperature of 9°C.	(Hiskey 2012)
26-33	Varroa is capable of reproduction	It also needs stress less conditions.	(Bičík <i>et.al</i> 2016)
32.5-33.4	Optimal temperature for the development of Varroa	Often found inside the brood nest.	(Arnia 2013)
32-36	Normal temperatures in the brood chambers	Bees keep the brood nest at a constant temperature.	(Burlew 2012)
>36	The reproductive capability of female mites significantly decreases	Synthesis of proteins is affected.	(Bičík <i>et.al</i> 2016)
>38	Varroa die without engaging in reproduction.	Female mites are damaged and become infertile.	(Bičík <i>et.al</i> 2016)
40-47	Thermal conditions for Thermotherapy	It has to last 150 minutes. starting from the moment when the temperature reached 40°C at the floor.	(Bičík <i>et.al</i> 2016)
>40	Increased mortality in adult bees	Bees die exposed to higher temperatures for more than 48 hours.	(Bičík <i>et.al</i> 2016)
>41	Bees start swarming	When they cannot regulate the temperature for a long period (3-4 days).	(Kridi <i>et.al</i> 2016)
43-44	Thermoregulation of bees	Bees heat their bodies to raise the temperature of the beehive. Their thorax achieves up to 44°C.	(Arnia 2013) (Hiskey 2012)
46	Bees still can fly	While their thorax is still at 45°C.	(Heinrich and Esch 1994)

Brood box temperature [°C]	Effect on Bees/Varroa	Additional notes	Reference
>49	Wax loses its mechanical strength	During thermotherapy the structural integrity of the work remains.	(Bičík <i>et.al</i> 2016)
49-50	Bees overheating	They get lethargic and regurgitate if the lapse is prolonged.	(Cunningham 1997)
60-62	Cooling thermoregulation of bees	During thermotherapy no signs of damage to the brood or abnormalities in oviposition by the queens have been registered.	(Bičík <i>et.al</i> 2016)

Throughout the time that thermotherapy has been studied, there have been different types of approaches, of which three stand out. One of them is described by Cunningham (1997), where the bees are temporarily removed from the beehive while the heat treatment is applied to it by a simple cabinet-type heating device. Another approach, presented by Linhart (2015), consisted in a solar thermal hive. This device captures the solar irradiation and uses it to get the mite elimination temperature. Finally, an approach that reached enough standards to become a commercial product such as the Victor (GreenBeehives.com, 2013). They are thermoelectric devices that can be placed some at the base others at the top or even inside the beehive to heat it.

6.1. Cunningham (1997)

The device consists of a portable wooden cabin that contains a conventional "milk house" heater and a metal mesh cylinder to hold the bees inside while they are heated. The cabin has plexiglass windows to ventilate and allow observation. The bees were removed from the beehive and placed in this device for treatment. The device created worked from a 1500 watts conventional electric heater. (Cunningham, 1997)

- **Price:** This device was only used to perform thermotherapy tests on bees but never reached commercial grade.
- **Advantages:** The main advantage is that having such a controlled environment ensured the treatment of all bees. This system helped to verify the effectiveness of thermotherapy.
- **Disadvantages:** Unfortunately, it did not work to treat larvae or eggs and its operation was very laborious since it required transferring the bees.

6.2. Mite Zapper (2001)

The Mite Zapper is a frame that is heated to apply thermotherapy right next to the frames of the brood box (MiteZapper LLC, 2012). It works from a variable electrical resistance installed inside the frame. It requires a battery and has a pre-programmed timer control. This device is shown in Figure 3



Figure 15: Mite Zapper and a battery

- **Price:** The cost of a set of control and two frames is €141.95 EUR
- **Advantages:** It focuses on the brood chamber. It is very compact in relation to the other available options.
- **Disadvantages:** It does not distribute the temperature evenly. It is not compatible with every type of beehive. Its installation requires the removal of a frame inside the brood box.

6.3. Thermosolar Hive (2010)

It is a beehive designed entirely for thermotherapy. It has similar architecture to a conventional beehive but it is made with insulating materials that keep the heat captured. The key factor of this beehive is below the roof, because there is a thermosolar ceiling. A picture of this device is shown in Figure 4.

This device applies thermotherapy using solar thermal windows in each super and below the roof cover of the beehive. To use it the beekeeper must remove the roof and covers from the windows to allow the solar thermal ceiling and windows to capture the heat of the solar radiation. This device has two thermometers that indicate the temperature inside the beehive. When the desired temperature is reached, the beekeeper is responsible for the execution time and the subsequent cooling.



Figure 4: Thermosolar Hive with 2 National boxes (Linhart, 2015).

- **Price:** The most basic model consists of a Thermosolar Hive with the dimensions of a National one and has a cost of \$538.57 USD.
- **Advantages:** This device was evaluated by Bičík (2015) and proven its effectiveness. It also has the advantage of serving not only for thermotherapy but also to favour the working conditions of bees.
- **Disadvantages:** Solar thermal technology can be very stressful for bees. It is also very easy to reach overheating. It also requires a favourable solar environment. In addition, it can be time consuming because the beekeeper should be monitoring the process the whole time.

6.4. The Victor (2013)

The Victor is a wooden box that is placed instead of the roof of a beehive. It distributes the heat from top to bottom. This device consists of an array of electrical resistances that when fed with 12V can generate the necessary heat to raise the temperature of the beehive to that required by the thermotherapy. It also has a set of 4 fans that distribute the heat while ventilating the interior of the hive (Figure 5a). (GreenBeehive.com, 2013)

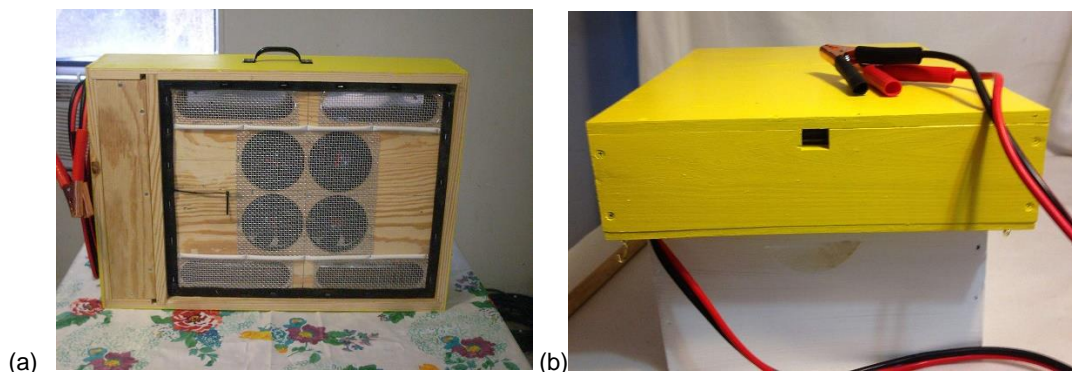


Figure 5: The Victor. (a) Bottom view (b) Front view

- **Price:** This system is sold for hives of 8 or 10 frames. The price for both models is \$195 USD.
- **Advantages:** It is highly transportable and adapts to most commercial beehives. Its use is very simple.
- **Disadvantages:** This device is built mainly on an empirical basis and has

6.5. Mighty Mite Killer (2017)

This is an industrial grade heater blanket with electronic controls which are easily installed and removed on the floor of the breeding box (Williams, 2015b). The Mighty Mite Killer is an electric plate heater that converts alternating current into heat for the hive (Figure 6). It uses a pair of temperature sensors as thermostatic control system. It has an on and off interface; and it switches itself off once the thermotherapy cycle ends.



Figure 6: Mighty Mite Killer

- **Price:** There are 3 models: for 10, 8 and 5 frames. The cheapest is the model for 10 frames and costs \$299.99 USD.
- **Advantages:** It has wide technical support. It is not demanding of time because as it is programmed to reach the desired temperature by itself and to turn off when the necessary time has been fulfilled. Being a plate, it is a compact system. It fits almost any type of commercial vertical beehive.
- **Disadvantages:** It requires to be connected to the electrical grid hence it is not very portable. It does not have a display that allows to monitor the temperature.

6.6. Bienen-Sauna (2017)

This system is inserted in a box additional the regular ones in the beehive. It is placed below the bottom box. Controls internal temperature and humidity. Its main function is to provide a high temperature to favour the production of bees. Additionally, it can be used to apply thermotherapy (Rossa, 2015). Although its principle of operation is not public, it can be inferred that it is an arrangement of resistive plates that convert electrical energy into heat. These plates work along with a system of fans and humidifiers.



Figure 16: Bienen-Sauna

- **Price:** The price for a kit like the one in the figure 7 is €1500 EUR.
- **Advantages:** It is pre-programmed for thermotherapy use. It is capable of regulating the internal humidity of the beehive.
- **Disadvantages:** It uses a battery; therefore, its cycle of use is limited. It is designed to work for long periods of time so it requires large batteries. Its design is not compact.

Table 3 summarises, the commercially available devices for treating beehives against Varroa mites.

Table 3: Commercially available technologies

Technology	Year	Operating temperature (duration)	Cost	Mite mortality rate
Mite Zapper	2001	43 – 45°C (1-5 mins)	~50 USD	100%
Varroa terminator	2010	42°C (180 mins)	€ 362	Kills most Varroa
Thermosolar Hive	2010	40° – 47°C (150 mins)	€ 700 -900	100%
Varroa controller	2010	40° – 47°C (120 mins)	~ € 2388	100%
The Victor	2013	42°C (150 mins)	~195 USD	85 – 95%
Mighty mite killer	2017	43° – 45°C (1-5 mins)	~300 USD	Not known
Bienen-sauna	2017	41° – 42°C (3-4 hours)	€ 1300	75 – 85%

7. CONCLUSIONS

Bees are a fundamental part of human development. However, the natural stressors along with the new threats have reduced its population. Its economic contribution is undeniable and, in the UK, it grows annually contrary to its population decrease. A sensible solution is to mitigate stressors through sustainable farming methods such as incorporating flower-rich habitats into farmland and avoiding the use of pesticides and other substances harmful to bees. Effective monitoring is desirable to have control over the welfare of the bees (Goulson *et al.*, 2015). The methods of sustainable farms favour the development of pollinators, both wild and managed. At the same time, it would be helping to improve the cultivation conditions (Tirado *et al.*, 2013). The same position should be taken with respect to the Varroa mite since the most used control methods are not the most sustainable. The use of varroacides carries potential harm to bees. In such a way that the ideal is implementing a more sustainable and less stressful method such as thermotherapy. This method has to be refined for its application, mainly in areas such as the UK where bees have not yet developed any resistance to that threat.

Despite the fact that thermotherapy has been proven and replicated, there are not enough devices available commercially. The existing thermotherapy methods employ not so convenient devices in practice due to their complexity and laboriousness. On the other hand, for thermotherapy, precise regulation of temperature is needed, which most of these devices do not have. For these reasons, the use of thermotherapy has not spread and remains a rather marginal method. Nevertheless, the potential of this method of Varroa mite eradication can and should be largely explored.

8. ACKNOWLEDGEMENTS

The authors gratefully acknowledge Innovate UK's financial support through Newton Fund (Project reference no:105043).

9. REFERENCES

- Abou-Shaara, H.F., Al-Ghamdi, A.A. and Mohamed, A.A., (2013). Honey bee colonies performance enhance by newly modified beehives. *Journal of Apicultural Science*, 57(2), pp.45-57.
- Al-Ghamdi, A.A., Nuru, A., Khanbash, M.S. and Smith, D.R., (2013). Geographical distribution and population variation of *Apis mellifera jemenitica* Ruttner. *Journal of Apicultural Research*, 52(3), pp.124-133.
- Arnia (Apr. 2013). Temperature and Thermoregulation in the Beehive. [Online]. Arnia. Available at: <https://www.arnia.co.uk/temperature-and-thermoregulation-in-the-beehive/>. [Accessed March 14, 2019]
- Bičák, V., (Sept. 2015). Mite Elimination Thermotherapy 2015. [Online]. Available at: <https://www.beehivethermalindustries.com/resources/studies/mite-elimination-thermotherapy-2015/>. [Accessed March 14, 2019]
- Bičák, V., Vagera, J. and Sádovská, H., (2016). The effectiveness of thermotherapy in the elimination of Varroa destructor. *Acta Musei Silesiae, Scientiae Naturales*, 65(3), pp.263-269.
- Burlew, R., (Apr. 2012). Honey bee eggs in the brood nest. Available at: <https://honeybeesuite.com/honey-bee-eggs-in-the-brood-nest/>. [Accessed March 14, 2019]

Craig, A., (Oct. 2017). The Complete Bee Lifecycle. [Online]. Available at: <https://www.valleybees.org.au/wp-content/uploads/2017/10/HONEYBEE-LIFE-CYCLE-CHART.pdf>. [Accessed March 14, 2019]

Cunningham, J., (Aug. 1997). Evaluating a Heat Therapeutic Control of the Honey Bee Mite Varroa Destructor. [Online]. Available at: https://cdn.sare.org/wp-content/uploads/20180517145428/LNE96_066_Final_Report.pdf. [Accessed March 14, 2019]

De Almeida, G.F., (2008). Fatores que interferem no comportamento enxameatório de abelhas africanizadas (Doctoral dissertation, Universidade de São Paulo).

De la Rúa, P., Jaffé, R., Dall'Olio, R., Muñoz, I. and Serrano, J., (2009). Biodiversity, conservation and current threats to European honeybees. *Apidologie*, 40(3), pp.263-284.

Engel, M.S., 1999. The taxonomy of recent and fossil honey bees (Hymenoptera: Apidae; Apis).

Fessenden, M., (Sept. 2015). How Climate Change is Messing with Bees. [Online]. Smithsonian Institution. Available at: <https://www.smithsonianmag.com/smart-news/how-climate-change-messing-bees-ability-pollinate-180956523/>. [Accessed March 14, 2019]

Frenkie (Oct. 2014). Innovation: Effective Biological Varroa mite Treatment. [Online]. Available at: <https://beetime.eu/innovation-effectivebiological-varroa-mite-treatment/>. [Accessed March 14, 2019]

Goulson, D., Nicholls, E., Botías, C. and Rotheray, E.L., (2015). Bee declines driven by combined stress from parasites, pesticides, and lack of flowers. *Science*, 347(6229), p.1255957.

GreenBeehives.com (June 2013). The Victor - For Varroa Mite Thermal Treatment. [Online]. Available at: <http://www.greenbeehives.com/thevictor.html>. [Accessed March 14, 2019]

Harbo, J.R., (2000). Heating adult honey bees to remove Varroa jacobsoni. *Journal of Apicultural Research*, 39(3/4), pp.181-182.

Heinrich, B. and Esch, H., (1994). Thermoregulation in bees. *American Scientist*, 82(2), pp.164-170.

Hiskey, D., (June 2012). How Honey Bees Keep Their Hives Warm Given That They are Cold Blooded. Available at: <http://www.todayifoundout.com/index.php/2012/06/how-honey-bees-keep-their-hives-warm-given-that-they-are-coldblooded/>. [Accessed March 14, 2019]

Holland, N., (Apr. 2009). The economic value of honeybees. [Online]. BBC News Channel. Available at: <http://news.bbc.co.uk/1/hi/business/8015136.stm>. [Accessed March 14, 2019]

Jeschke, P., Nauen, R., Schindler, M. and Elbert, A., (2010). Overview of the status and global strategy for neonicotinoids. *Journal of agricultural and food chemistry*, 59(7), pp.2897-2908.

Kerr, J.T., Pindar, A., Galpern, P., Packer, L., Potts, S.G., Roberts, S.M., Rasmont, P., Schweiger, O., Colla, S.R., Richardson, L.L. and Wagner, D.L., (2015). Climate change impacts on bumblebees converge across continents. *Science*, 349(6244), pp.177-180.

Knapton, S., (June 2015). Bees contribute more to British economy than Royal Family. [Online]. Telegraph Media Group. Available at: <https://www.telegraph.co.uk/news/earth/wildlife/11679210/Bees-contribute-more-to-British-economy-than-Royal-Family.html>. [Accessed March 14, 2019]

Krüger R., (June 2017). Varroa Sound. [Online]. Available at: https://www.varroa-killer-sound.com/epages/81838618.sf/en_GB/?ObjectPath=/Shops/81838618/Categories/Wirkung. [Accessed March 14, 2019]

Kridi, D.S., de Carvalho, C.G.N. and Gomes, D.G., (2016). Application of wireless sensor networks for beehive monitoring and in-hive thermal patterns detection. *Computers and Electronics in Agriculture*, 127, pp.221-235.

Kridi, D.S., Carvalho, C.G.N.D. and Gomes, D.G., (Sept. 2014). A predictive algorithm for mitigate swarming bees through proactive monitoring via wireless sensor networks. In *Proceedings of the 11th ACM symposium on Performance evaluation of wireless ad hoc, sensor, & ubiquitous networks* (pp. 41-47). ACM.

- Linhart, R., (Aug. 2015). Thermotherapy of the Varroa Mite. [Online]. Available at: <http://modernagriculture.ca/thermotherapy-varroa-mite/>. [Accessed March 14, 2019]
- MiteZapper LLC © (June 2012). Mite Zapper. [Online]. Available at: <https://mitezapper.com/>. [Accessed March 14, 2019]
- Mortensen, A. N., Schmehl, D. R. and Ellis, J. (Aug. 2013). European honey bee. [Online]. Entomology and Nematology Department, University of Florida. Available at: http://entnemdept.ufl.edu/creatures/MISC/BEES/euro_honey_bee.htm. [Accessed March 14, 2019]
- National Bee Unit and The Animal & Plant Health Agency (Aug. 2018). Varroa. [Online]. Available at: <http://www.nationalbeeunit.com/index.cfm?pageid=93>. [Accessed March 14, 2019]
- New Jersey Institute of Technology and Science X - Phys.org. (May 2014). The effects of climate change on the ecological role of bees. [Online]. Available at: <https://phys.org/news/2014-05-effects-climate-ecological-role-bees.html>. [Accessed March 14, 2019]
- Potts, S.G., Roberts, S.P., Dean, R., Marris, G., Brown, M.A., Jones, R., Neumann, P. and Settele, J., (2010). Declines of managed honey bees and beekeepers in Europe. *Journal of apicultural research*, 49(1), pp.15-22.
- Rosenkranz, P., Aumeier, P. and Ziegelmann, B., (2010). Biology and control of Varroa destructor. *Journal of invertebrate pathology*, 103, pp.S96-S119.
- Rossa, R. (Jun. 2015). Die Gerätschaft, [Online] Available at: <https://www.bienensauna.de/handbuch-intern/geraetschaft> [Accessed March 14, 2019].
- Rothamsted Research Ltd (Sept. 2016). Breeding Varroa-Resistant Honey Bees. [Online] Available at: <https://beecare.bayer.com/media-center/beenow/detail/breeding-varroa-resistant-honey-bees>. [Accessed March 14, 2019]
- The Animal and Plant Health Agency (June 2018). Managing Varroa. [Online] Available at: <http://www.nationalbeeunit.com/downloadDocument.cfm?id=16>. [Accessed March 14, 2019]
- Thebees.info (2010). The Economic Importance Of Honey Bees. [Online]. Available at: <http://www.thebees.info/economic-importanceof-honey-bee/>. [Accessed March 14, 2019]
- Tirado, R., Simon, G. and Johnston, P., (2013). A review of factors that put pollinators and agriculture in Europe At Risk. Greenpeace Research Laboratories Technical Report, 44p.
- Wang, Q., Xu, X., Zhu, X., Chen, L., Zhou, S., Huang, Z.Y. and Zhou, B., (2016). Low-temperature stress during capped brood stage increases pupal mortality, misorientation and adult mortality in honey bees. *PloS one*, 11(5), p.e0154547.
- Wilfert, L., Long, G., Leggett, H.C., Schmid-Hempel, P., Butlin, R., Martin, S.J.M. and Boots, M., (2016). Deformed wing virus is a recent global epidemic in honeybees driven by Varroa mites. *Science*, 351(6273), pp.594-597.
- Williams, L., (July 2015a). Bee Hive Thermal Industries Varroa Mites Case Study Temperature vs Pesticides. [Online] Available at: <https://www.beehivethermalindustries.com/resources/studies/bee-hive-thermal-industriesvarroa-mites-case-study-temperature-vs-pesticides/>. [Accessed March 14, 2019]
- Williams, L., (July 2015b). Mighty Mite Killer. [Online] Available at: <https://www.beehivethermalindustries.com/how-it-works/>. [Accessed March 14, 2019]
- Worland, J., (July 2015). Bees Habitat Loss: Study Shows How Climate Change Hurts Pollinators. [Online] TIME USA LLC. Available at: <http://time.com/3951339/bees-climate-change/>. [Accessed March 14, 2019]

#298: Can west-facing PV panels help the grid during the sunset?

A study with Portuguese consumers

José Luís SOUSA¹, Roberto SOLDI², ANTÓNIO G. MARTINS³, Isabele Dal PONT⁴,
André FRIEDRICH⁵

¹School of Technology of Setúbal, Polytechnic Institute of Setúbal, SustainRD; INESC Coimbra, Coimbra, PORTUGAL: jose.luis.sousa@estsetubal.ips.pt

²Federal Institute of Santa Catarina, BRAZIL: roberto.soldi@ifsc.edu.br

³Department of Electrical and Computer Engineering, University of Coimbra; INESC Coimbra, Coimbra, PORTUGAL: agmartins@uc.pt

⁴Federal Institute of Santa Catarina, BRAZIL: isabeledalpont@hotmail.com

⁵Federal Institute of Santa Catarina, BRAZIL: andre.f1997@aluno.ifsc.edu.br

Due to the increase of domestic solar electric energy generation, some utilities, besides facing important reductions in the amount of energy sold during sunlight hours, are requested to satisfy a highly variable load just before sunrise and during the sunset. From the grid point of view, the load diagram is changing to a “duck curve” type. Regarding Portuguese domestic consumers, the evening peak can reach twice or more the value of the morning peak. West oriented solar panels have been proposed as a way of mitigating the impact on the grid of these large variations of demand in very short time periods. This paper analyses the impact on the grid of different Portuguese domestic consumers that produce energy from solar panels. A comparison was made regarding the effects on the grid of facing the solar panels to the south and to the west. Besides the expected reduction in the energy generated, west facing panels can allegedly reduce asymmetries on the grid diagram. Since consumers see no difference in energy prices during the day, solar panels facing west represent a loss of income, followed by an increase in energy expenditure. On the other hand, from the grid point of view, they can be seen as a resource and its interest must be evaluated case-by-case.

Keywords: distributed energy generation; duck curve; PV generation; domestic consumers

1. INTRODUCTION

Renewable energy sources and their share of electricity production have been constantly increasing, mainly driven by energy policies, markets and environmental issues (Anvari *et al.*, 2016) (Kind, 2013). For instance in the European Union, these renewable energies are planned to account for about 20 % of the gross final energy consumption by 2020 and 60 % by 2050 (Anvari *et al.*, 2016: page 1). There are countries with high percentages of electricity from renewable sources, mainly from geothermal and hydroelectric sources (Freitas & Brito, 2019: page 271). However, most countries still depend on non-renewable sources. Among the available renewable energy sources, wind power and photovoltaic (PV) have priority.

Decreasing prices, market availability and technological improvements are the main reasons for the emerging interest in urban PV (Biyik *et al.*, 2017). However, these sources, despite being clean and renewable, are known to be highly intermittent, i.e. they are highly fluctuating on seasonal and daily cycles (Milan, 2013). Although predictable, these fluctuations in the production of PV energy present challenges to network management, in order to guarantee network reliability, which was not built to incorporate a high percentage of variable generation (Tarr, 2018: page 23). Therefore, one of the most important future challenges for the stability of a desired supply grid, based on renewable energies, will be to control or suppress these fluctuations.

On the other hand, the demand is also variable, responding to daily, weekly and seasonal cycles. Throughout the day, several demand levels must be considered. During a business day, there is rapid increase of load between 4 PM and 7 PM. It is a period when office building loads continue, while residential loads increase as residents return home. The late afternoon convergence of residential and commercial loads causes peaks on most utility systems (Lazar, 2016: page 10). This variability was referred to as "The Duck Curve" displaying the "net load" gap between daily forecast electricity load and renewable output, as well as the severe grid transition present in a system with high solar penetration (Lazar, 2016: page 6). The net load is the load served by the electric system minus the load served by variable generation (i.e., wind, solar PV, and solar thermal), which severely fluctuates throughout the day (Tarr, 2018: page 25). Solar energy has an important participation during the day, creating the "belly" shape on the "duck curve". At the end of the day, just as residential demand increases, solar power production fades, creating a "neck" shape on the "duck curve," meaning a rapidly growing ramp-up in energy needs from other sources to compensate the rapidly vanishing contribution of solar energy, adding to the increase in residential demand. The energy system's ability to compensate for this variability is commonly referred to as flexibility (Deason, 2018).

Lazar's recommends some strategies to "soften the duck curve". One of these recommendations is acquiring and deploying west-facing PV. According to the author, these resources could provide power up to two hours later in the afternoon than south-facing panels (Lazar, 2016: page 14). In this paper, the effects that west-facing PV panels can have on the net load profiles of distribution network in Coimbra, Portugal, are analysed. In the next section some references are made to previous works relating to the effects of distributed solar PV on the distribution grids, as well as the solution adopted to overcome possible unwanted situations. The effects of south-facing and west-facing PV panels in a distribution network load profiles are presented and discussed. The paper ends with some conclusions.

2. DISTRIBUTED PV GENERATION IN DISTRIBUTION GRID

Distributed generation technologies are typically defined as small-scale generation (around 10–15 kV) facilities that connect to the electrical distribution network. Among the used technologies, cogeneration, micro-hydro and bio energy have little dependence on climatic conditions, and are therefore able to provide energy in a constant and predictable way. On its turn, wind connected to small-scale networks is not common at the moment and therefore has very little impact on the distribution networks. With PV the situation is different. It is rapidly increasing with almost no energy storage, high intermittency and only partial predictability. As a result, it has significant negative impacts at high penetration levels if appropriate measures are not taken (Passey, 2011: page 1).

In 2013, the California Independent System Operator (CAISO) conducted an analysis to understand how increasing penetrations of renewable resources would impact grid conditions. The analysis examined "net load" and found that at certain times of the year the net load drops at midday and quickly ramps to a late-day peak. More importantly, the forecast finds the drop and ramp of net load becoming more severe each year. This analysis resulted in the iconic "duck curve" chart which shows net load forming the duck's belly during the midday period and the duck's neck during the late-day ramp (Vlahoplus, *et al.* 2016: page 1).

ScottMadden Management Consultants' reviewed the CAISO analysis, and confirmed the duck curve is present and quickly maturing in California. More importantly, they found that significant changes in daily daytime minimum net loads (i.e., the duck's belly) and daily late-day ramps (i.e., the duck's neck) are primarily driven by utility-scale solar in California. The analysis also finds the duck curve is already occurring in other seasons, not just spring months (Vlahoplus, *et al.* 2016: page 5).

Considering the little coincidence between PV supply and residential demand, additional mechanisms will be needed in order to reduce the ramp. Traditional methods such as time-of-use pricing with fixed price intervals will not be enough to redress the variability of solar energy (Denholm, 2015: page 36). To minimise the impact of such fluctuations on the grid, mainly between 4 and 7 pm, Lazar (Lazar, 2016: page 9) suggests among others, the acquisition and deployment of peak-oriented renewable resources, such as solar panels that could be turned to face west rather than south. Majzoobi and Khodaei (2016) also cite orienting solar panels to the west-southwest as a form of increasing the output during afternoon hours, while reducing output during morning hours. In the northern hemisphere most solar panels point south. But west-facing panels are able to generate more even flow of electricity than spikes of energy at noon (Perry, 2014).

The east-west orientation of solar panels effectively results in curtailment in that it generates less energy than a conventional equator-facing orientation. However, with this approach, there is additional generation during the early evening hours, reducing ramping (Doroshenko, *et al.*, 2018: page 375) (Borland & Singh, 2018).

In Portugal the distributed solar PV generation has been increasing in the last few years. However, to the best of the authors' knowledge, its impact on the distribution networks has not been accounted for. In this paper the authors intend to evaluate the impact that distributed PV generation can have in distribution grids, both for south and west-facing panels. The study used data from three electricity substations in the city of Coimbra, in the centre region of Portugal. In the next section the load diagrams (LD) of the three substations are presented and the simulation results from south and west-facing PV panels for both spring and summer days are presented.

3. CASE STUDY

From an analysis of some domestic load profiles, it was possible to verify that electric energy from west-facing panels may reduce some early evening peaks. The load profiles, as seen from the grid, with south and west facing solar PV panels, are presented in *Figure 17*. These load profiles are the result of the subtraction of solar generation diagram from the load diagram of the consumer. Solar generation diagrams were obtained using irradiation hourly diagrams and the area of installed PV panels. For residential LD, the area of PV panels was calculated as the one needed to generate the same energy quantity that is consumed between 7 a.m. and 7 p.m. As can be seen, west facing panels (the dotted light line in *Figure 17*) are more effective than south-facing panels (solid dark line) in reducing early evening peaks.

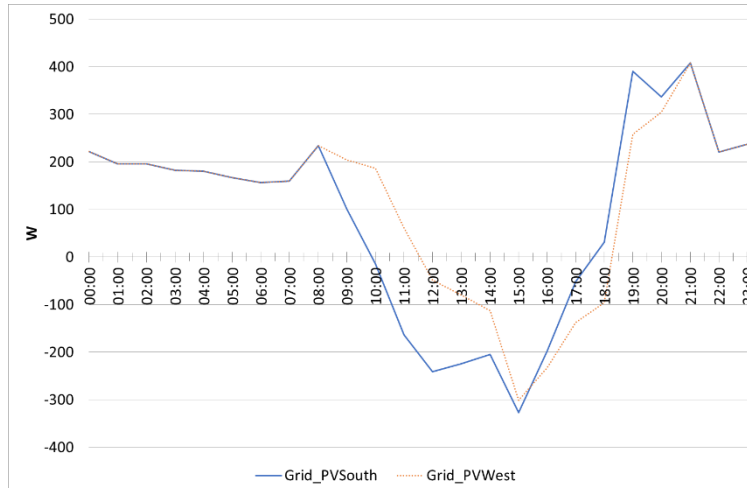


Figure 17: Load diagram of a domestic consumer seen from the grid with PV solar panels.

However, from the grid point of view the aggregated effect of individual consumers can be more important than the effect of a single consumer.

This paper will analyse the effect of increasing PV penetration on three substations' load profiles, which represent an aggregate load level of higher interest to distribution utilities than the individual consumer's load profile. Three different electrical substations (SS) supplying the city of Coimbra were analysed. The three SS are: Alto de São João (ASJ), Relvinha (RV), and Alegria (AL). For each SS, the LD of spring (April) and summer (July) weeks, from Monday to Sunday, in 2018, are presented in the following figures.

As can be seen from *Figure 18(a)*, the ASJ spring LD presents a load pattern influenced by servicing domestic consumers, with an evening peak. Workdays can hardly be differentiated from weekend days. However, in summer the LD loses the evening peak and the LD acquires a more "rectangular" shape (*Figure 18 (b)*).

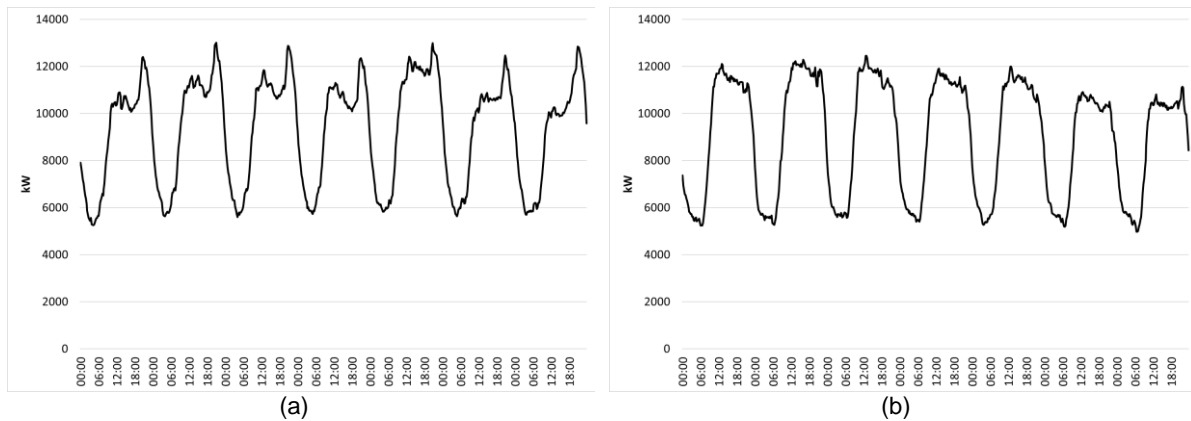


Figure 18: Load diagrams for a (a) spring (April) and (b) summer (July) week of the ASJ substation.

For the AL SS, the morning peak of the spring LD is higher than the evening peak, and the afternoon valley is quite evident (Figure 19 (a)). In weekend days, as expected, the evening peak becomes more relevant due to the absence of the morning peak. On the other hand, the summer daily LD are quite regular with a very significant morning peak and a quite small evening one (Figure 19 (b)). With the absence of the morning peak in weekend days, the LD is quite regular.

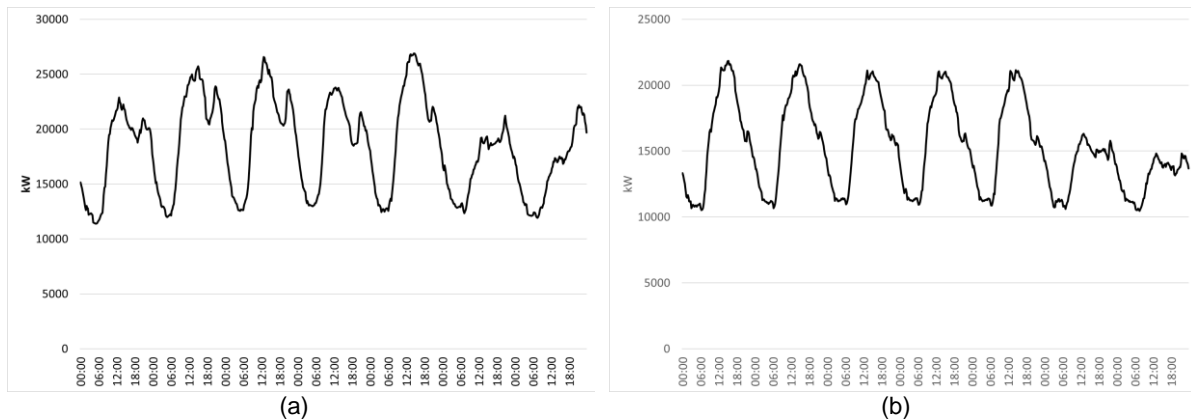


Figure 19: Load diagrams for a (a) spring (April) and (b) summer (July) week of the AL substation.

In Figure 20 the spring (a) and summer (b) LD of the RV substation are presented

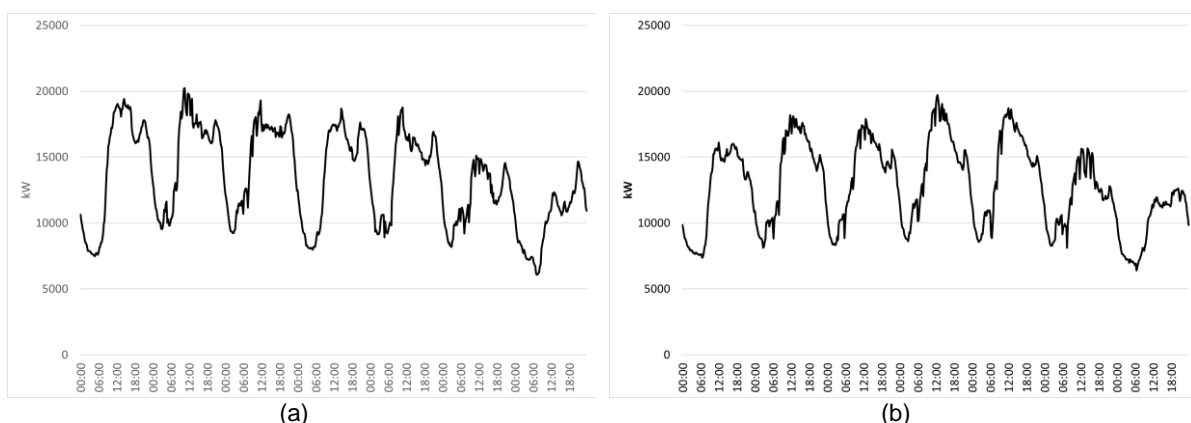


Figure 20: Load diagrams for a (a) spring (April) and (b) summer (July) week of the RV substation.

In order to evaluate the effect of PV solar generation on the LD, only two different daily load profiles were chosen. The results will be presented for both spring and summer days. The base case scenario, referred as No PV, means that no PV was considered in the simulations, given the fact that existing distributed PV installations are only residual, for the time being.

3.1. Solar PV effects on spring load diagrams

The effects of several possible penetration levels of distributed PV solar panels were simulated, leading to the corresponding scenarios, considering that PV solar panels would contribute with a percentage of the peak power of the LD. In this study, the irradiation hourly diagrams were computed using the web platform Photovoltaic Geographical Information System (<https://re.jrc.ec.europa.eu/pvgis/apps4/pvest.php>). With the hourly irradiation diagrams of south-facing panels, the area of PV panels was calculated regarding the area needed to generate a power peak equivalent to a percentage of the LD peak. The generation diagrams of both south and west facing panels were then computed using the irradiance diagrams and the area of PV panels calculated as previously stated.

The studied scenarios considered six solar south-facing PV area values, contributing with 2, 4, 6, 8, 10 and 15% of the LD peak. The effect of orienting these solar panels to the west was also studied.

The spring LD of the ASJ substation that resulted from the simulations with an increasing penetration of south facing PV are presented in Figure 21(a). In Figure 21(b) are presented the LD that resulted from an increasing penetration of west-facing panels.

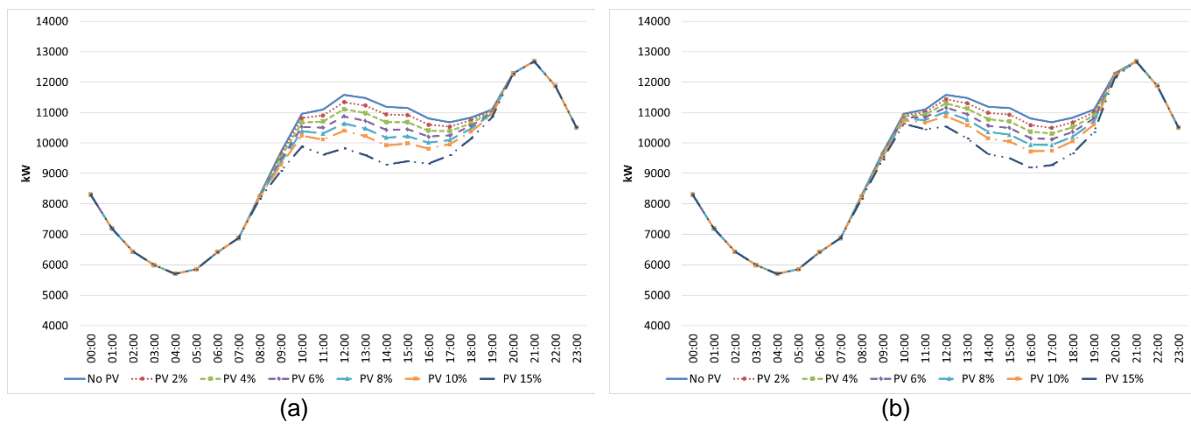


Figure 21: LD for a spring workday of the ASJ substation, with PV contribution from panels facing (a) south and (b) west.

The increase of PV penetration in the ASJ substation leads to a reduction, in spring workdays, of both the LD peak, and the power demand of the afternoon valley, either the solar panels are facing south or west (*Table 11* and

Table 12). Since the peak of this substation LD is at 9 p.m., the electricity output from solar panels has no direct effect on it. The morning peak anticipates two hours, from 12 p.m. to 10 a.m. for the 15% peak reduction scenario. With the increase in PV penetration facing south, the afternoon valley almost disappears due to a flattening of the LD until the evening. The evening rising gradient reflects the higher power value that the grid must incrementally satisfy in an hour, after sunset. These higher incremental power values happen between 7 p.m. and 8 p.m.

For the scenarios with west facing' panels (

Table 12), the morning peak follows the same behavior that was observed for the south facing panels scenarios, although with smaller reductions. West facing panels lead to a deepening of the afternoon valley. In these scenarios two peak periods can still be seen on the resulting LD (Figure 21).

Table 11: Variation of the LD of a spring day of the ASJ substation due to the penetration of PV solar panels facing south.

	No PV	2%	4%	6%	8%	10%	15%
Load diagram peak (kW)	12680	12680	12680	12680	12680	12680	12680
Hour	21:00	21:00	21:00	21:00	21:00	21:00	21:00
Morning peak (kW)	11578	11343	11109	10875	10641	10407	9887
Variation (%)	-	-2.0	-4.0	-6.1	-8.1	-10.1	-14.6
Hour	12:00	12:00	12:00	12:00	12:00	12:00	10:00
Afternoon valley (kW)	10685	10540	10394	10210	10012	9815	9293
Variation (%)	-	-1.4	-2.7	-4.4	-6.3	-8.1	-13.0
Hour	17:00	17:00	17:00	16:00	16:00	16:00	14:00
Evening rising gradient (kW/h)	1188	1218	1248	1278	1308	1339	1414

Comparing the rising gradients at evening hours from south and west-facing panels it can be seen that they are higher with west-facing panels.

Table 12: Variation of the LD of a spring day of the ASJ substation due to the penetration of PV solar panels facing west.

	No PV	2%	4%	6%	8%	10%	15%
Load diagram peak (kW)	12680	12680	12680	12680	12680	12680	12680
Hour	12:00	12:00	12:00	12:00	12:00	12:00	12:00
Morning peak (kW)	11578	11439	11300	11161	11023	10884	10630
Variation (%)	-	-1.2	-2.4	-3.6	-4.8	-6.0	-8.2
Hour	12:00	12:00	12:00	12:00	12:00	12:00	10:00
Afternoon valley (kW)	10685	10497	10309	10121	9933	9728	9190
Variation (%)	-1.8	-1.8	-3.5	-5.3	-7.0	-9.0	-14.0
Hour	17:00	17:00	17:00	17:00	17:00	16:00	16:00
Evening rising gradient (kW/h)	1188	1267	1347	1426	1506	1586	1785

The spring LD of the AL substation, which resulted from the simulations with an increase in PV penetration with south-facing panels, are presented in Figure 22(a) and the ones that resulted from west-facing panels in Figure 22(b). As can be seen, the LD morning peak suffers higher reductions with south facing panels than with west facing ones.

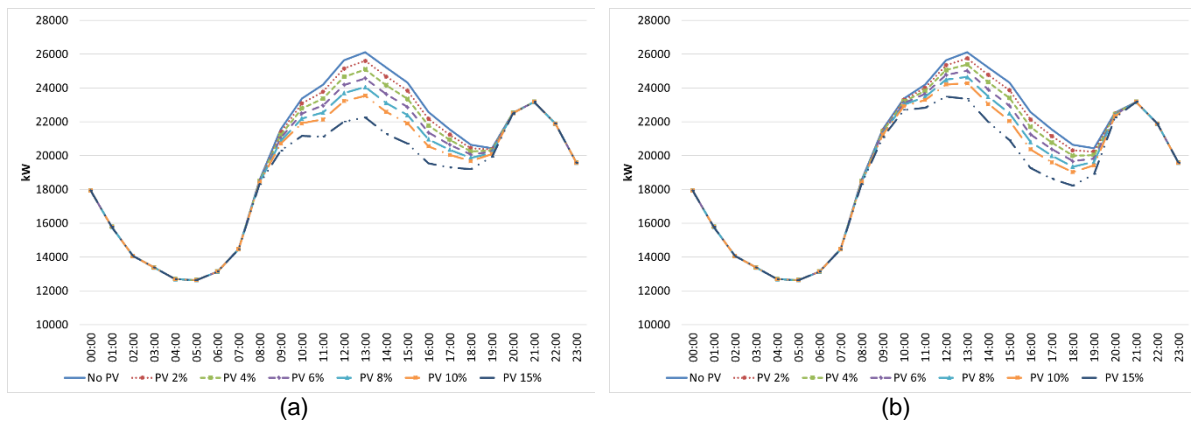


Figure 22: LD for a spring workday of the AL substation, with PV contribution from panels facing (a) south and (b) west.

The increase of PV penetration in the AL substation leads to a reduction, in spring workdays, of both the LD peak, and of the power demand of the afternoon valley, either the solar panels are facing south or west (Table 13 and

Table 14). For the south facing panels and a penetration of 15% of the LD peak, the peak no longer occurs at 1 p.m., but at 9 p.m. The morning peak reduction reaches almost 15% and suffers no change in the hour of occurrence. The variation of afternoon valley is smaller, reaching 6.1% reduction and anticipates one hour, from 7 p.m. to 6 p.m. for the scenarios with 6% or more of PV penetration.

For the scenarios with west-facing panels, the LD peak occurs in the morning. For the 15% scenario, it changes from 1 p.m. to 12 a.m. The west-facing panels lead to a deepening of the afternoon valley, reaching values near 11% reduction for the 15% PV scenario. The valley minimum values have the same behavior that was observed for the south-facing panels: the anticipation from 7 p.m. to 6 p.m. for the scenarios with penetration above 4%.

Table 13: Variation of the LD of a spring day of the AL substation due to the penetration of PV solar panels facing south.

	No PV	2%	4%	6%	8%	10%	15%
Load diagram peak (kW)	26118	25608	25086	24571	24056	23540	23170
Hour	13:00	13:00	13:00	13:00	13:00	13:00	21:00
Morning peak (kW)	26118	25608	25086	24571	24056	23540	22251
Variation (%)	-	-2	-3.9	-5.9	-7.9	-9.9	-14.8
Hour	13:00	13:00	13:00	13:00	13:00	13:00	13:00
Afternoon valley (kW)	20438	20368	20247	20055	19863	19672	19193
Variation (%)	-	-0.3	-0.9	-1.9	-2.8	-3.7	-6.1
Hour	19:00	19:00	19:00	18:00	18:00	18:00	18:00
Evening rising gradient (kW/h)	2098	2160	2222	2284	2347	2409	2565

Regarding the evening rising gradient, they are higher for west-facing panels, when comparing with south-facing ones.

Table 14: Variation of the LD of a spring day of the AL substation due to the penetration of PV solar panels facing west.

	No PV	2%	4%	6%	8%	10%	15%
Load diagram peak (kW)	26118	25750	25383	25015	24648	24280	23484
Hour	13:00	13:00	13:00	13:00	13:00	13:00	12:00
Morning peak (kW)	26118	25750	25383	25015	24648	24280	23484
Variation (%)	-	-1.4	-2.8	-4.2	-5.6	-7.0	-10.1
Hour	13:00	13:00	13:00	13:00	13:00	13:00	12:00
Afternoon valley (kW)	20438	20233	19988	19667	19346	19025	18222
Variation (%)	-	-1.0	-2.2	-3.8	-5.3	-6.9	-10.8
Hour	19:00	19:00	19:00	18:00	18:00	18:00	18:00
Evening rising gradient (kW/h)	2098	2261	2426	2589	2753	2917	3327

3.2. Solar PV effects on summer load diagrams

The summer LD of ASJ substation are characterised by small variations from 9 a.m. to 9 p.m. (Figure 23). The afternoon valley is almost inexistent. The following figures and tables depict the effects of PV generation in a similar way as was used for the case of spring.

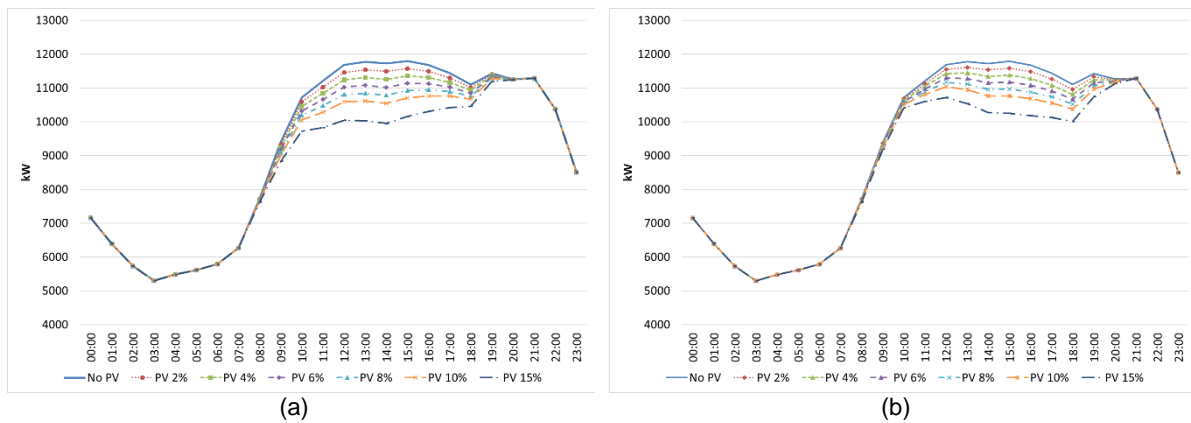


Figure 23: Load diagrams for a summer workday of the ASJ substation, with PV contribution from panels facing (a) south and (b) west.

Regarding summer days, the increase of PV penetration in the ASJ substation leads to a reduction of the LD peak, and of the valley power demand, both when the solar panels are facing south and west (Table 15 and

Table 16). For the south-facing panels an increase in the penetration of PV leads to a shifting of the LD peak from 3 p.m. to 9 p.m. The mid-day peak reduction reaches more than 11% and changes from 3 p.m. to 6 p.m. The variation of the afternoon valley demand, due to an increase in PV penetration, reaches 10.3% reduction and changes from 6 p.m. to 2 p.m. for the scenarios with 10% and 15% of PV penetration.

For the west-facing panels an increase in the penetration of PV leads to the LD peak to shift first from 3 p.m. to 12 a.m. and then to 9 p.m. The mid-day peak reduction reaches more than 9% and changes from 3 p.m. to 12 a.m. The variation of the valley afternoon demand, due to an increase in PV penetration, reaches almost 10% reduction for the 15% of PV penetration scenario.

Table 15: Variation of the LD of a summer day of the ASJ substation due to the penetration of PV solar panels facing south.

	No PV	2%	4%	6%	8%	10%	15%
Load diagram peak (kW)	11793	11575	11365	11334	11303	11288	11288
Hour	15:00	15:00	19:00	19:00	19:00	21:00	21:00
Mid-day peak (kW)	11793	11575	11358	11140	10943	10759	10451
Variation (%)	-	-1.8	-3.7	-5.5	-7.2	-8.8	-11.4
Hour	15:00	15:00	15:00	15:00	16:00	16:00	18:00
Afternoon valley (kW)	11100	11013	10927	10840	10754	10546	9956
Variation (%)	-	-0.8	-1.6	-2.3	-3.1	-5.0	-10.3
Hour	18:00	18:00	18:00	18:00	18:00	14:00	14:00
Evening rising gradient (kW/h)	328	383	438	493	549	604	742

Regarding the evening rising gradient, the west-facing panels lead to values slightly smaller than the ones verified for the south-facing panels scenarios.

Table 16: Variation of the LD of a summer day of the ASJ substation due to the penetration of PV solar panels facing west.

	No PV	2%	4%	6%	8%	10%	15%
Load diagram peak (kW)	11793	11609	11443	11293	11288	11288	11288
Hour	15:00	13:00	13:00	12:00	21:00	21:00	21:00
Mid-day peak (kW)	11793	11609	11443	11293	11164	11035	10712
Variation (%)	-	-1.6	-3.0	-4.2	-5.3	-6.4	-9.2
Hour	15:00	13:00	13:00	12:00	12:00	12:00	12:00
Afternoon valley (kW)	11100	10955	10810	10665	10520	10375	10013
Variation (%)	-	-1.3	-2.6	-3.9	-5.2	-6.5	-9.8
Hour	18:00	18:00	18:00	18:00	18:00	18:00	18:00
Evening rising gradient (kW/h)	328	380	433	486	539	591	723

The summer LD of the RV substation that resulted from the simulations with an increase in PV penetration with south and west-facing panels, are presented in Figure 24 (a) and (b). As can be seen, the LD morning peak suffers higher reductions with south-facing panels than with west-facing ones.

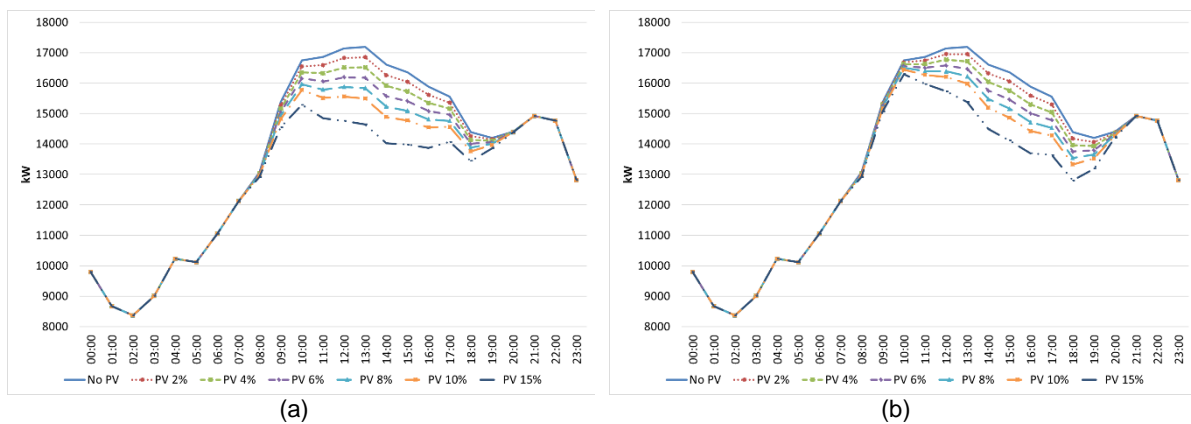


Figure 24: LD for a summer workday of the RV substation, with PV contribution from panels facing (a) south and (b) west.

The increase of PV penetration in the RV substation leads to a reduction, in summer, of both the LD peak, and of the power demand of the afternoon valley, both when solar panels are facing south and west (Table 17 and

Table 18). For the south-facing panels, the increased penetration of PV changes the peak from 1 p.m. to 10 a.m. The mid-day peak is, in fact, the LD peak, and its reduction reaches 11%. The variation of the afternoon valley demand is much smaller, and changes from 7 p.m. to 6 p.m. for the scenarios with 6% or more of PV penetration.

Table 17: Variation of the LD of a summer day of the RV substation due to the penetration of PV solar panels facing south.

	No PV	2%	4%	6%	8%	10%	15%
Load diagram peak (kW)	17195	16856	16516	16193	15966	15772	15287
Hour	13:00	13:00	13:00	12:00	10:00	10:00	10:00
Mid-day peak (kW)	17195	16856	16516	16193	15966	15772	15287
Variation (%)	-	-2.0	-3.9	-5.8	-7.1	-8.3	-11.1
Hour	13:00	13:00	13:00	12:00	10:00	10:00	10:00
Afternoon valley (kW)	14198	14152	14106	14009	13883	13757	13441
Variation (%)	-	-0.3	-0.6	-1.3	-2.2	-3.1	-5.3
Hour	19:00	19:00	19:00	18:00	18:00	18:00	18:00
Evening rising gradient (kW/h)	513	517	522	526	531	535	547

Regarding west-facing panels simulations, the LD peak occurs at 1 p.m. and changes to 10 a.m. as the PV penetration increases. The mid-day peak variations are almost half the ones with the south-facing simulations, west-facing panels lead to a deepening of the afternoon valley, reaching values near 10% reduction for the 15% PV scenario. The afternoon valley minimum values have the same behavior that was observed for the south-facing panels: the anticipation of one hour, from 7 p.m. to 6 p.m. for the scenarios with penetration of 6% or more. The west-facing simulations lead to an increase of the evening gradients, when compared to south facing panels.

From the results, both south and west-facing PV panels can contribute to anticipate morning and mid-day peaks as well as afternoon valleys. However, south-facing panels are more effective than west-facing ones in reducing the morning peak. On the other hand, west facing panels give higher contribution to the afternoon valley.

Table 18: Variation of the LD of a summer day of the RV substation due to the penetration of PV solar panels facing west.

	No PV	2%	4%	6%	8%	10%	15%
Load diagram peak (kW)	17195	957	16769	16581	16504	16444	16295
Hour	13:00	12:00	12:00	12:00	10:00	10:00	10:00
Mid-day peak (kW)	17195	957	16769	16581	16504	16444	16295
Variation (%)	-	-1.4	-2.5	-3.6	-4.0	-4.4	-5.2
Hour	13:00	12:00	12:00	12:00	10:00	10:00	10:00
Afternoon valley (kW)	14198	14063	13929	13753	13542	13331	12802
Variation (%)	-	-0.9	-1.9	-3.1	-4.6	-6.1	-9.8
Hour	19:00	19:00	19:00	18:00	18:00	18:00	18:00
Evening rising gradient (kW/h)	513	539	565	592	618	845	711

3.3. Effects of both south and west facing panels

The possibility of installing west facing panels was considered, as a grid resource, where south facing panels were already installed. In other words, west-facing panels were to be installed in areas of the grid where there already existed south-facing PV panels. The effect on the grid would result from the contribution of both installations. The hypothesis to test was that west-facing panels would eventually mitigate the load demand rising gradient at evening hours caused by south-facing PV generation. For illustrative purposes it was assumed that the south-facing PV panels would contribute to a reduction of 4% of the LD peak, an equivalent area of PV panels was considered to be installed facing west. In Figure 25 two different load profiles (spring workday of AL substation (a) and ASJ substation (b)) are presented with the effect of each panel orientation ("PV 4% south" and "PV 4% west") and the result of the contribution of both options ("PV 4% south and west", meaning the effect of PV 4% south plus PV 4% west).

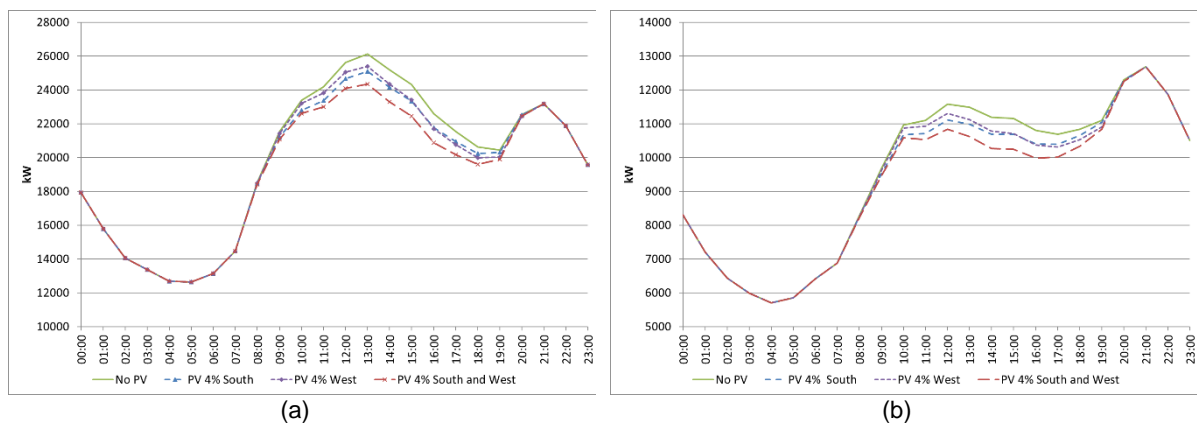


Figure 25: Load diagrams for spring workday with PV contribution from panels facing south and west. : AL substation (a) and ASJ substation (b)

The LD in Figure 25 result from a scenario with 4% of peak load generation from PV panels for each panel orientation, resulting in around 8% peak from the combination of both orientations. For the two cases presented above, the installation of west-facing panels would result in the deepening of the afternoon valley, after 3 p.m.

In these simulations, the area of PV panels facing west was the same as the ones facing south. However, the area of west-facing panels should result from the impact desired by the utility, since those installations are intended to serve the grid.

4. CONCLUSION AND FUTURE WORK

In this work, the authors intended to identify whether distributed PV panels can act as a resource to the grid. To verify the impact that PVs have on the grid, the study tested two orientations of solar panels: south and west. This latter orientation was tested for the impact that its generation could have in the evening load rising ramp. Load diagrams of three different substations in the city of Coimbra, Portugal, were used. In the simulations a full week (Monday to Sunday) was considered in the month of April (spring) and another week in July (summer). In addition, the study considered different scenarios for the contribution of solar energy, from 0% (No PV) to 15% of peak demand. With the increasing penetration of solar energy, the presence of the "duck belly" on the load diagrams was perceived, as well as the rapidly growing load ramp-up in the evening, although they do not make a typical "duck curve".

The results of this preliminary research indicate that both in spring and in summer the afternoon valley tends to disappear due to a flattening of the load diagram with increasing values of solar PV penetrations facing south. On the other hand, west-facing panels tends to contribute to deepening of the afternoon valley. In the evening, west-facing panels do not seem to contribute, as a grid resource, to smooth the evening load gradient caused by the end of solar generation. Admitting that it may be on the interests of the utility, the simulation of installing west-facing panels where there are south-facing panels already installed was considered but was not studied in detail. It should be studied in the future. As a future work, the analysis of feeders, instead of substations, should be considered since it could shed some additional light on the effect of PV generation at a less aggregate load level. It is the authors' opinion that there is no solutions that fit all cases and different alternatives should be considered by distribution system operators.

5. ACKNOWLEDGEMENTS

This work was supported by the Portuguese Foundation for Science and Technology under strategic project grant UID/Multi/00308/2019 and R&D project grant SAICT-POL/23651/2016 | LISBOA-01-0145-FEDER-023651, with the support of FEDER. The authors acknowledge EDP for the access to the load diagrams of the substations.

6. REFERENCES

- Anvari, Mehrmaz, *et al.*, 2016. Short term fluctuations of wind and solar power systems. *New Journal of Physics* 18.6: 063027.
- Biyik, E., Araz, M., Hepbasli, A., Shahrestani, M., Yao, R., Shao, L., ... & Lechón, J. L., 2017. A key review of building integrated photovoltaic (BIPV) systems. *Eng. Sci. Technol. Int. J.* 20, 833–858.
- Borland, J., & Singh, A., 2018. Reducing Morning & Late Afternoon Grid-Buy Demand By Engineering Box-Like Rooftop Solar-PV Generation Profiles Without The High Cost Of Trackers Or Bifacial Panels. In 2018 IEEE 7th World Conference on Photovoltaic Energy Conversion (WCPEC). Waikloa, Hawaii: IEEE.
- Denholm, P., O'Connell, M., Brinkman, G., & Jorgenson, J., 2015. Overgeneration from solar energy in California. A field guide to the duck chart (No. NREL/TP-6A20-65023). National Renewable Energy Lab.(NREL), Golden, CO (United States).
- Doroshenko, M., Keshav, S., Rosenberg, C., 2018. Flattening the Duck Curve Using Grid-friendly Solar Panel Orientation. Proceedings of the Ninth International Conference on Future Energy Systems. Pages 375-377. Karlsruhe, Germany.
- Freitas, S., & Brito, M. C., 2019. Non-cumulative only solar photovoltaics for electricity load-matching. *Renewable and Sustainable Energy Reviews*, 109, 271-283.
- Perry, K., 2014. Most solar panels are facing the wrong direction, say scientists. *The Telegraph*.
- Kind, P., 2013. Disruptive Challenges: Financial Implications and Strategic Responses to a Changing Retail Electric Business. Edison Electric Institute. United States of America. Edison Electric Institute. 1.
- Lazar, J., 2016. Teaching the "Duck" To Fly. (2nd ed.) Montpelier, VT: The Regulatory Assistance Project.
- Majzoubi, A., & Khodaei, A., 2016. Application of microgrids in addressing distribution network net-load ramping. In 2016 IEEE Power & Energy Society Innovative Smart Grid Technologies Conference (ISGT) (pp. 1-5). IEEE.
- Milan, P., Wächter, M., & Peinke, J., 2013. Turbulent character of wind energy. *Physical review letters*, 110(13), 138701.
- Passey, R., Spooner, T., MacGill, I., Watt, M., Syngellakis, K., 2011. The potential impacts of grid-connected distributed generation and how to address them: A review of technical and non-technical factors. *Energy Policy*, 39, 6280-6290.
- Tarr, K. E., 2018. The Energy Imbalance Market: Environmental Benefits of Regional Market. Integration in the West. WWU Honors Program Senior Projects. 74.
- Vlahoplus, C. Litra, G. , Quinlan, P. and Becker, C., 2016. Revisiting the California Duck Curve: An Exploration of Its Existence, Impact, and Migration Potential. ScottMadden Management Consultants. 2016.

#301: Thermal performance assessment of solar box cookers with propolis based latent heat storage and low-cost booster reflectors

Pinar Mert CUCE¹, Sevgi KOLAYLI², Erdem CUCE^{3,*}

¹Department of Energy Systems Engineering, Faculty of Engineering, Recep Tayyip Erdogan University, Zihni Derin Campus, 53100 Rize, Turkey, pinar.mertcuce@erdogan.edu.tr
mertcuce@gmail.com

²Department of Chemistry, Faculty of Science, Karadeniz Technical University, 61080 Trabzon, Turkey, skolayli@ktu.edu.tr

³Department of Mechanical Engineering, Faculty of Engineering, Recep Tayyip Erdogan University, Zihni Derin Campus, 53100 Rize, Turkey, erdem.cuce@erdogan.edu.tr

Solar box cookers are at the centre of interest worldwide as a promising renewable energy application for cooking purposes. Compared to other types available in literature, solar box cookers draw much more attention owing to their simple and low-cost design, emerging thermodynamic performance figures, high durability and reliable cooking processes without any risk of burning food. On the other hand, cooking power and overall thermal performance of solar box cookers are still somewhat challenging for the technology to compete with the conventional cooking systems in areas with low solar radiation potential like the Black Sea Region of Turkey. Within the scope of this research, a novel solar box cooker is devised, fabricated using natural and recycled materials and tested to overcome the said shortcomings of traditional solar box cookers. A double glazed structure having 16mm of air between two 6mm thick thermally resistive clear glass is considered for the aperture glazing with an area of 0.16 m². The oven area has a depth of 350mm, and it is entirely painted matte black for maximum solar absorption. The oven body made of stainless steel sheets is encountered by a latent heat storage medium filled by natural bee product, waste of propolis. Propolis is a resinous mixture that is used for the protection of bee-hives from either climatic changes or diseases. Polyphenols is rich in balsamic and part of the structure is extracted by alcohol than used for many apitherapeutic purposes. The remaining pulp or waste is not considered. In this study, it is used as green chemistry agents.

Keywords: solar box cookers; propolis based latent heat storage; booster reflector; energy and exergy efficiency

1. INTRODUCTION

Cooking is an essential need which constitutes a significant part of the total world energy consumption (Cuce and Cuce, 2013). In most areas of the developing world like Africa, India and China, non-commercial fuels such as agricultural waste, cow dung, firewood and kerosene are usually used by people to meet the cooking demand (Cuce, 2018a). About 36% of primary energy use in India is attributed to cooking, which needs to be noted (Cuce, 2018b). It is emphasised by Pohekar *et al.* (Pohekar and Kumar, 2005) that almost 90% of residents in India still make a fire in rural areas to be able to cook their foods. This can be explained with the abundance of wood in the aforesaid areas. In addition, wood is unequivocally the cheapest energy source in rural areas to meet the cooking demand (Cuce and Cuce, 2015a). However, it needs to be underlined that people may have to walk for hours almost every day to collect the firewood which they need to make a fire for cooking (Cuce and Cuce, 2015b). Excessive use of firewood and other biomass-related energy resources causes serious environmental problems such as deforestation and climate change. Burning of such fuels first of all pollutes the air and negatively affects human health with eye disorders, lung diseases and burns (Geddami *et al.*, 2015). Therefore, intensive efforts are made at global scale to develop renewable and sustainable energy solutions to meet the cooking demand of people in both rural and urban areas. Solar cookers are such devices which are energy-efficient, eco-friendly and low-cost as well as not requiring any skill to operate (Saxena and Agarwal, 2018). In most parts of the world, solar cookers in general have a great potential to reduce total world energy consumption and greenhouse gas emissions owing to the solar radiation potential. Moreover, solar cookers are ideal systems for high nutritional value of food, high durability and almost stable efficiency range over their long lifetimes (Muthusivagami *et al.*, 2010).

In a typical solar cooker, incoming solar radiation is converted into thermal power, which is then utilised to cook food (Saxena *et al.*, 2011). Besides their known function of cooking, solar cookers can be considered for some important processes such as sterilisation and pasteurisation. The overall thermal performance of solar cookers greatly depends on the solar radiation potential of the region. Solar radiation falling on the transparent aperture glazing transmits into the oven area and is absorbed by a surface which is usually made of metallic materials and painted matte black to maximise solar absorption. Material, colour and surface properties are of vital importance for the effectiveness of solar absorption. Foods are put in the cooking pots which are usually made of copper and aluminium, and they are placed on the absorber surface. Through the heat transfer mechanisms of natural convection, conduction and partially thermal radiation, cooking process takes place in solar cookers usually from 1 to 6 hours depending on food. Solar cookers have a wide range of types and applications in market, and they are improved year after year in terms of different performance merits. In other words, classification of solar cookers is a challenge in most cases. However, splitting them into three groups as solar panel cookers, solar box cookers and solar dish/parabolic cookers is approved by most of the researchers.

Solar box cookers, among the three types, can be asserted as the most improved solar cooking devices in terms of thermodynamic performance parameters. Solar box cookers usually have a box shape either cylindrical or prismatic. Aperture glazing which is placed on the top of solar cooker welcomes solar radiation, and transmitted radiative energy is absorbed by a metallic absorber which is painted matte black. Cooking pots are put on the absorber surface directly. Box edges are usually well-insulated to minimise heat losses across the body material, and booster reflectors are considered to enhance the solar intensity thus the efficiency figures (Collares-Pereira *et al.*, 2018). Solar box cookers usually have a lifetime more than 20 years, and thermal performance figures of solar box cookers are promising (good range for energy and exergy efficiency, adequate cooking power for most foods, notably shorter cooking times compared to solar panel cookers) and continuously improved. However, it needs to be noted that solar box cookers have some shortcomings as well especially for hard-to-cook foods. In regions with fair solar radiation potential, solar box cookers might not be sufficient enough for a successful cooking process, and to overcome this handicap, several solutions are considered. Some of them can be listed as improving thermal insulation feature of body, improving incoming radiative power via booster reflectors, enhancing solar absorption effectiveness of absorber surfaces and considering thermal energy storage medium within the body.

Enhancing thermal performance figures of solar box cookers via sensible and latent heat storage materials is in the centre of interest worldwide especially over the last two decades (Nkhonjera *et al.*, 2017). Especially phase change material (PCM) utilisation in solar box cookers to provide late evening cooking draws attention of many researchers, and there are various attempts in this respect conducted with different PCMs. The experimental study carried out by Choudhari and Shende investigates the potential improvements in a solar cooker using PCM (Choudhari and Shende, 2015). The solar cooker system consists of a parabolic dish collector and a cooking pot with PCM. Acetanilide is utilised as PCM and its latent heat value is reported to be 222 kJ/kg. Based on the results, the energy efficiency of the cooker is in the range of 6-8%, and the cooker temperature during the evening period is found to be 78 °C in case of using PCM. Another research based on a parabolic trough collector with PCM (acetanilide) is conducted to investigate the thermal performance of a solar cooker (Saini *et al.*, 2016). The system comprises of absorber tubes, solar cooker and thermosiphon in which thermal energy is transferred from tube to cooking unit. In this experimental setup, water and thermal oil are utilised as working fluids. The findings show that the foods can be cooked two times in a day by using latent heat storage medium and the rate of cooking belonging to the evening time is higher than noon cooking. Compared to water, using thermal oil as a working fluid leads to an increase in the amount of energy stored by PCM in the range of 20-31%. The research conducted by Petela

investigated the changes in energy and exergy efficiency of solar cookers having parabolic shapes (Petela, 2005). Findings of the experimental research indicate that the maximum energy efficiency of the solar cooker is about 19% and the exergy efficiency is nearly 1%. Pyramid solar box cookers are evaluated in another research in terms of several performance figures (Kumar *et al.*, 2011). Depending on the results, the coefficient of heat loss, quality factor and the maximum exergy are found to be 4.09 W/m²K, 0.15 and 7.124 W respectively.

The effective utilisation of PCMs in solar cookers require researchers to have at least fundamental knowledge about latent heat storage materials. PCMs can be split into two groups as organic and inorganic materials. The melting temperatures of organic PCMs are lower than 120°C and it is accepted that this figure is insufficient to cook the foods properly. For greater temperatures over 200°C, nitrate salts are usually considered which are more suitable to be considered in solar cookers as a PCM. According to the numerical and experimental works conducted with PCMs with a melting point lower than 120°C, acetamide and stearic acid are found to be providing better thermal performance than the other options (Chen *et al.*, 2008). It also reported by acetamide is more convenient for aluminium containers than other alternative PCMs like magnesium chloride hexahydrate (El-Sebaili *et al.*, 2009). Coccia *et al.* conduct an experimental study to observe performance of a high-temperature solar box cooker with a solar-salt-based thermal storage unit (Coccia *et al.*, 2018). They design a storage unit which has a double-walled vessel consisting of two stainless steel cylindrical pots assembled concentrically. 4 kilograms of PCM (a mixture of nitrite and nitrate salts) are utilised in the cooking system. It is achieved from the results that PCM thermal storage remarkably enhances the load thermal stabilisation when solar radiation is not available. Saxena *et al.* conducted an experimental study comparing thermal performance of PCM integrated solar cooker and simple solar cooker (Saxena *et al.*, 2013). They studied some of different phase change materials but among them stearic acid (commercial grade) was found to be the best latent heat storage solution which ensured 15 minutes lower cooking time in comparison with box type solar cooker without thermal storage.

Sharma *et al.* investigate thermal performance of a solar cooker based on an evacuated tube solar collector with a PCM storage unit (Sharma *et al.*, 2005). Erythritol is used as a latent heat storage material and their system include two separate parts for energy collection and cooking system coupled by a PCM storage unit. Owing to the PCM utilisation, it is observed that evening cooking takes place faster than noon cooking. Chaudhary *et al.* examine the thermal performance of a solar cooker based on parabolic dish collector with phase change thermal storage unit (Chaudhary *et al.*, 2013). In their experimental setup, acetanilide is used as PCM and they compare three different solar cooker models: ordinary solar cooker, solar cooker with outer surface painted black, and solar cooker with outer surface painted black along with glazing. The experimental results show that PCM in solar cooker with outer surface painted black can store 26.8% more heat compared to PCM in ordinary solar cooker. Buddhi *et al.* design a PCM storage unit for a solar cooker and the system stores energy during sunshine hours (Buddhi *et al.*, 2003). They use acetanilide as a latent heat storage material and the experiments are conducted with different loads and loading times during the winter season. According to the experimental results, it is possible to cook until 20:00 in the evening by using 4 kilograms of acetanilide as PCM.

It is clear through the previous literature that solar box cookers provide better thermal performance figures when they are integrated with latent heat storage materials. However, it is observed that conventional PCMs are usually considered in the previous works, and alternative natural PCMs are almost ignored. Therefore, in this research, a novel latent heat storage material (propolis) is utilised and its potential impacts on thermal performance parameters of solar box cookers are evaluated. Propolis is a resinous mixture usually utilised to protect bee-hives, from climatic changes and diseases. Polyphenols rich in balsamic part of the structure is extracted by alcohol than utilised for various apitherapeutic purposes. The remaining pulp or waste is not used. In this study, it is considered as green chemistry agents.

2. EXPERIMENTATION

Within the scope of this experimental research, thermal performance assessment of solar box cookers with propolis based latent heat storage is done through a comprehensive analysis. A solar box cooker is devised, fabricated and tested in the research for the climatic conditions of Rize, Turkey. The tests are conducted for the typical environmental conditions of July month in the humid temperate climatic conditions in Rize. Specifically, one full day test is carried out in front of Low/zero Carbon Energy Technologies Laboratory at Zihni Derin Campus of Recep Tayyip Erdogan University as shown in Figure 1. The solar box cooker is equipped with a low-cost booster reflector to maximise incoming solar radiation. Aperture glazing is made of two sheets of clear glass with an air gap of 12mm. Total entire thickness of aperture glazing is 20 mm, which is appropriate for such applications in terms of visible light transmittance and thermal resistance. The area of aperture glazing is given to be 0.25 m². In the system, 8 kilograms of propolis are utilised for latent heat storage beneath the absorber surface.

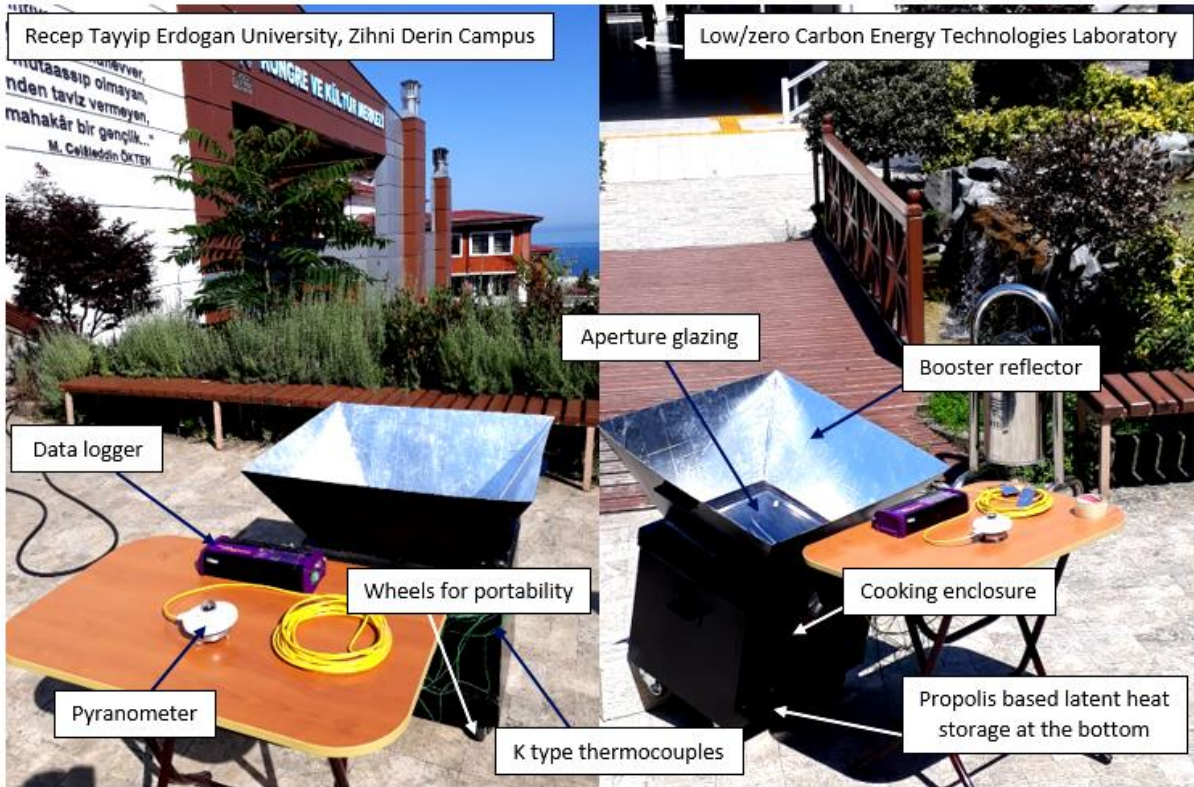


Figure 1: Experimental setup of solar PCM cooker with the measurement systems.

Solar intensity is measured by CMP3 pyranometer from Kipp & Zonen company. The aforesaid device is very sensitive and appropriate enough for such solar thermal applications. Thermal performance assessment is done through a time-dependent data triggering which is provided by DT85 Data logger from DataTaker Company. For the temperature measurements, standard K type thermocouples are utilised. Thermal performance assessment is done through temperature measurements which can be listed as ambient air temperature, oven air and absorber surface temperature, oven wall and PCM temperature, internal and external body temperature, internal and external glazing temperature and water temperature. Internal and external surfaces are painted matte black for maximum solar absorption. Total uncertainty of the measurement system is calculated to be below 1%, which is acceptable.

3. RESULTS AND DISCUSSION

The experimental analysis of novel solar box cooker concept with propolis as latent heat storage material starts at 09:00am in the morning, and lasts until the early morning (06:00am) next day. The propolis utilised inside the solar box cooker has a melting temperature of 47°C, and 8 kilograms of propolis are placed beneath the absorber surface for the heat storage purpose. The tests are conducted under a clear sky. Solar intensity and ambient air temperature during the test period are illustrated in Figure 2. At 09:00am, solar intensity is measured to be 588.2 W/m², and its variation over the test period has a stable tendency except some negligible fluctuations about the sunset. Maximum solar intensity is determined to be 881.1 W/m² during the noontime. The average ambient air temperature during the experiments is observed to be 28.2°C. Oven air and absorber surface temperatures within the solar box cooker are shown in Figure 3. It is firstly understood from the results that oven air temperature rapidly rises compared to absorber surface temperature. This is because of the PCM medium beneath the absorber. Greenhouse effect plays a key role in fast increase of oven air temperature. Some part of the absorbed heat is utilised for phase change process within the propolis mass, and this slows down the temperature rise in metallic absorber. Oven wall temperature has a similar tendency with oven air temperature as expected. It is clear from Figure 4 that oven wall temperature is somewhat lower than oven air temperature. Maximum oven air and oven wall temperature are measured to be 94.5 and 85.2°C, respectively. It is also observed from the findings that PCM temperature is still over 40°C at the end of the test period. This justifies the thermal energy stored within propolis, which can be utilised to keep the foods warm throughout the night time.

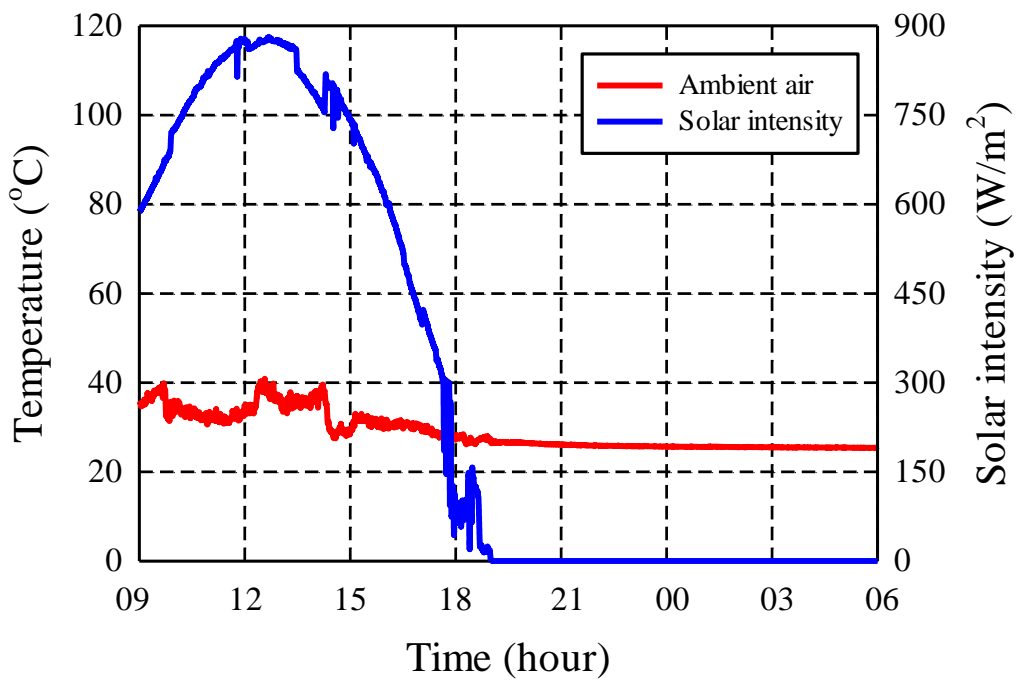


Figure 2: Solar intensity and ambient temperature during the test period of solar PCM cooker.

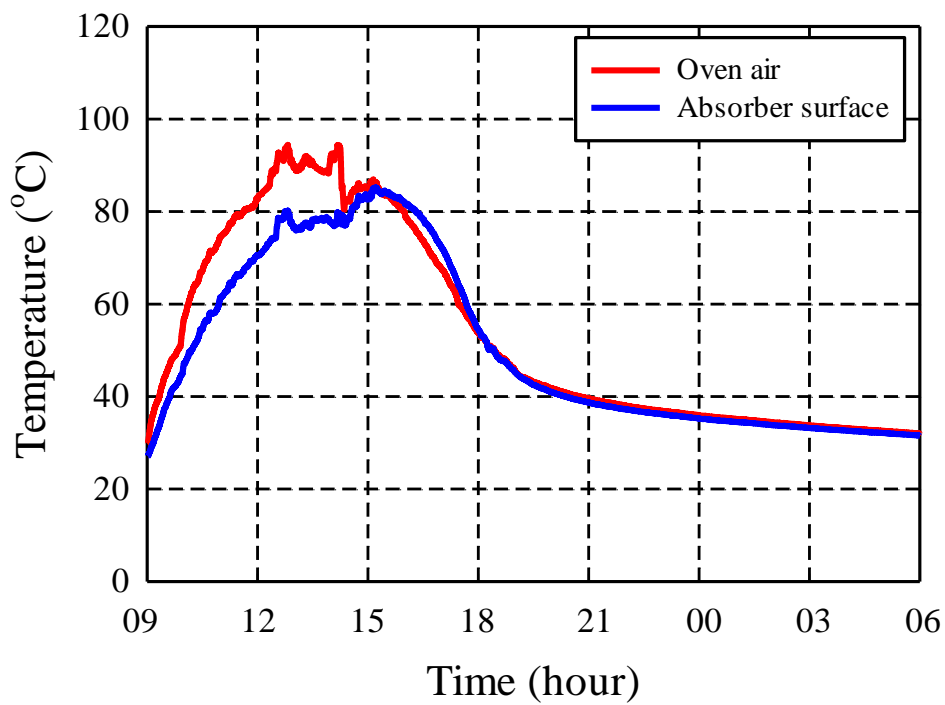


Figure 3: Oven air and absorber surface temperature during the test period of solar PCM cooker.

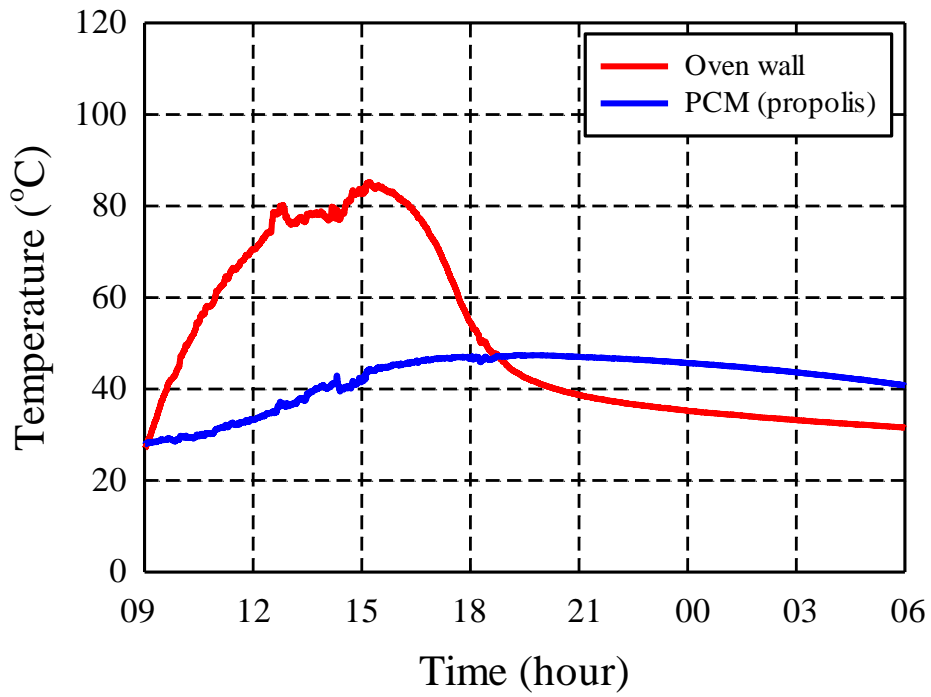


Figure 4: Oven wall and propolis temperature during the test period of solar PCM cooker.

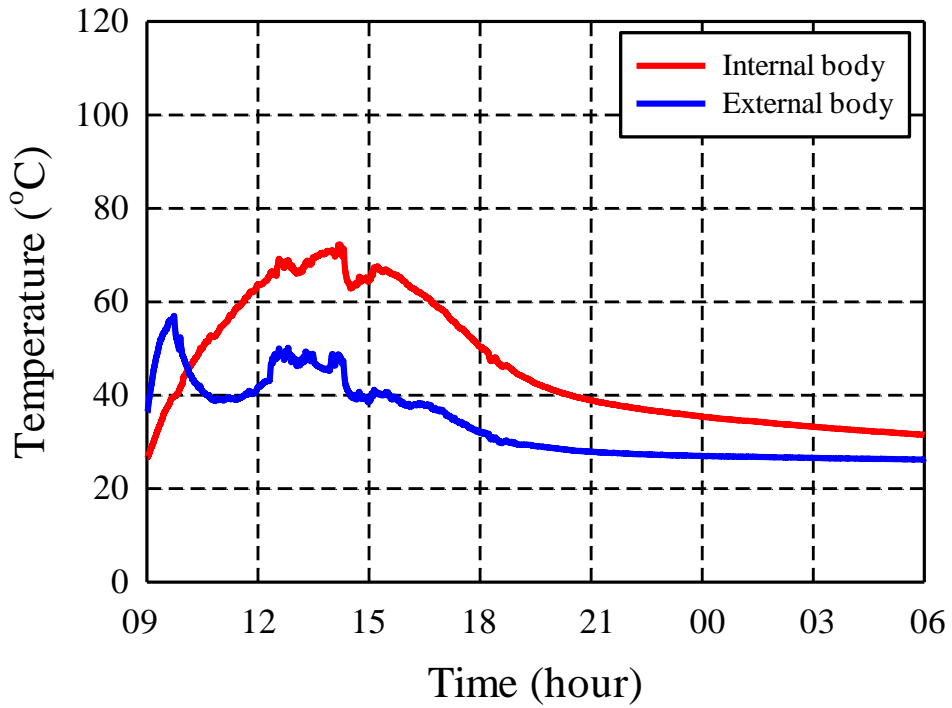


Figure 5: Internal and external body temperature during the test period of solar PCM cooker.

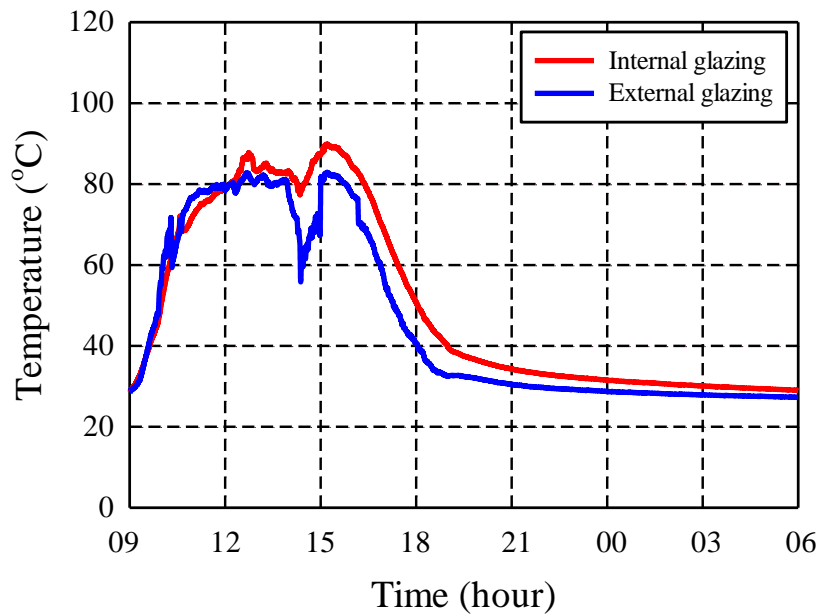


Figure 6: Internal and external glazing temperature during the test period of solar PCM cooker.

Thermal insulation performance of a solar box cooker directly affects the overall performance figures notably energy and exergy efficiency. In this respect, internal and external body temperatures are plotted as shown in Figure 5 to have an understanding about the thermal resistance feature of the present design. At the beginning of the tests, external body temperature gets greater values than the temperature of internal body as it directly absorbs the incoming solar radiation. After a certain period of time, internal body temperature is found to be remarkably higher than external body temperature as expected. Temperature difference is observed to be maximum during the noontime and steadily reduces toward the midnight. Maximum temperature difference is determined to be 27.1°C, which is promising. A similar tendency is obtained for internal and external glazing temperatures. Internal glazing temperature is found to be always greater than external glazing temperature as depicted in Figure 6. Maximum temperature difference is observed to be 21.9°C, which is an acceptable thermal resistance figure. Water temperature is also measured as a function of time as shown in Figure 7. Water mass in the cooking pot is specified to be 0.5 kg. It is clear from the findings that the water temperature reaches 82.5°C within a couple hours, which is in general an ideal temperature to cook vegetable foods. Water temperature is kept over 40°C till very late hours as a consequence of latent heat storage, which needs to be noted as a characteristic output of the research.

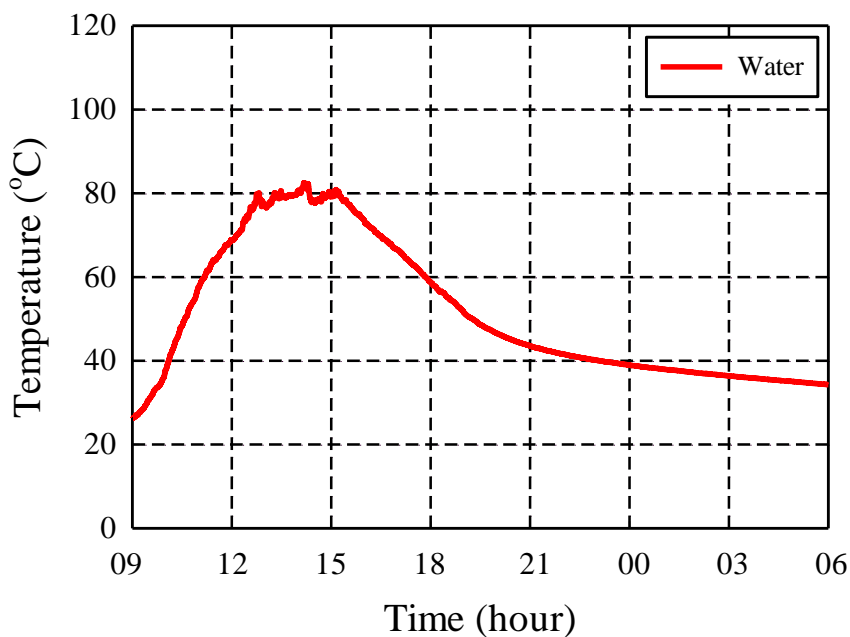


Figure 7: Water temperature during the test period of solar PCM cooker.

4. CONCLUSIONS

A novel solar box cooker integrated with booster reflector and propolis based latent heat storage is devised, fabricated and experimentally analysed for the temperate climatic conditions. It is concluded from the results that propolis, which is a resinous mixture that is used for protection of bee-hives, from either climatic changes or diseases, is also a good PCM solution as a latent heat storage medium. PCM integrated solar box cooker is observed to be thermally resistive enough with 5 cm thick XPS foam insulation. 8 kg of PCM beneath the absorber surface enables the foods to be kept warm throughout the night. The novel design of solar box cooker can provide late evening cooking with a promising energy and exergy efficiency.

5. REFERENCES

- Buddhi D, Sharma SD, Sharma A, 2003. Thermal performance evaluation of a latent heat storage unit for late evening cooking in a solar cooker having three reflectors. *Energy Conversion and Management*, 44, 809-817.
- Chaudhary A, Kumar A, Yadav A, 2013. Experimental investigation of a solar cooker based on parabolic dish collector with phase change thermal storage unit in Indian climatic conditions. *Journal of Renewable and Sustainable Energy*, 5(2), 023107.
- Chen CR, Sharma A, Tyagi SK, Buddhi D, 2008. Numerical heat transfer studies of PCMs used in a box-type solar cooker. *Renewable Energy*, 33, 1121-1129.
- Choudhari KS, Shende MD, 2015. Solar cooker using PCM material. *Journal of Basic and Applied Engineering Research*, 2(17), 1449-1453.
- Coccia G, Di Nicola G, Tomassetti S, Pierantozzi M, Chieruzzi M, Torre L, 2018. Experimental validation of a high-temperature solar box cooker with a solar-salt-based thermal storage unit. *Solar Energy*, 170, 1016-1025.
- Collares-Pereira M, Cavaco A, Tavares A, 2018. Figures of merit and their relevance in the context of a standard testing and performance comparison methods for solar box–Cookers. *Solar Energy*, 166, 21-27.
- Cuce E, Cuce PM, 2013. A comprehensive review on solar cookers. *Applied Energy*, 102, 1399-1421.
- Cuce E, Cuce PM, 2015a. Theoretical investigation of hot box solar cookers having conventional and finned absorber plates. *International Journal of Low-Carbon Technologies*, 10(3), 238-245.
- Cuce E, Cuce PM, 2015b. Energetic and exergetic performance assessment of solar cookers with different geometrical designs. *International Journal of Ambient Energy*, 36(2), 62-69.
- Cuce PM, 2018a. Box type solar cookers with sensible thermal energy storage medium: A comparative experimental investigation and thermodynamic analysis. *Solar Energy*, 166, 432-440.
- Cuce E, 2018b. Improving thermal power of a cylindrical solar cooker via novel micro/nano porous absorbers: A thermodynamic analysis with experimental validation. *Solar Energy*, 176, 211-219.
- EI-Sebaï AA, Al-Amir S, Al-Marzouki FM, Faidah AS, Al-Ghamdi A, Al-Heniti S, 2009. Fast thermal cycling of acetanilide and magnesium chloride hexahydrate for indoor solar cooking. *Energy Conversion and Management*, 50, 3104-3111.
- Geddani S, Dinesh GK, Sivasankar T, 2015. Determination of thermal performance of a box type solar cooker. *Solar Energy*, 113, 324-331.
- Kumar N, Vishwanath G, Gupta A, 2011. An exergy based test protocol for truncated pyramid type solar box cooker. *Energy*, 36, 5710-5715.
- Muthusivagami RM, Velraj R, Sethumadhavan R, 2010. Solar cookers with and without thermal storage—A review. *Renewable and Sustainable Energy Reviews*, 14, 691-701.

Nkhonjera L, Bello-Ochende T, John G, King'ondeu CK, 2017. A review of thermal energy storage designs, heat storage materials and cooking performance of solar cookers with heat storage. *Renewable and Sustainable Energy Reviews*, 75, 157-167.

Petela R, 2005. Exergy analysis of the solar cylindrical-parabolic cooker. *Solar Energy*, 79, 221-233.

Pohekar SD, Kumar D, Ramachandran M, 2005. Dissemination of cooking energy alternatives in India – A review. *Renewable and Sustainable Energy Reviews*, 9, 379-393.

Saini G, Singh H, Saini K, Yadav A, 2016. Experimental investigation of the solar cooker during sunshine and off-sunshine hours using the thermal energy storage unit based on a parabolic trough collector. *International Journal of Ambient Energy*, 37(6), 597-608.

Saxena A, Lath S, Tirth V, 2013. Solar cooking by using PCM as a thermal heat storage. *MIT International Journal of Mechanical Engineering*, 3, 91-95.

Saxena A, Agarwal N, 2018. Performance characteristics of a new hybrid solar cooker with air duct. *Solar Energy*, 159, 628-637.

Saxena A, Varun, Pandey SP, Srivastav G, 2011. A thermodynamic review on solar box type cookers. *Renewable and Sustainable Energy Reviews*, 15, 3301-3318.

Sharma SD, Iwata T, Kitano H, Sagara K, 2005. Thermal performance of a solar cooker based on an evacuated tube solar collector with a PCM storage unit. *Solar Energy*, 78, 416-426.

#304: An exciting opportunity for Zeolite-A/Bentonite adsorbent design as molecular sieve in fuel grade ethanol production through adsorptive distillation

Eny KUSRINI¹, Dwi Aprillia WULANDARI², Anwar USMAN³, Arif RAHMAN⁴, eko adi PRASETYANTO⁵, Muhammad Idiris SALEH⁶

¹Department of Chemical Engineering, Faculty of Engineering, Universitas Indonesia, Kampus Baru UI-Depok 16424, Indonesia, ekusrini@che.ui.ac.id

²Department of Chemical Engineering, Faculty of Engineering, Universitas Indonesia, Kampus Baru UI-Depok 16424, Indonesia, dwi.aprillia@ui.ac.id

³Department of Chemistry, Faculty of Science, Universiti Brunei Darussalam, Negara Brunei Darussalam, anwar.usman@ubd.edu.bn

⁴Department of Chemistry, Faculty of Mathematical and Natural Sciences, Universitas Negeri Jakarta, Rawamangun, Indonesia, arifrahman@unj.ac.id

⁵Faculty of Medicine and Health Sciences, Universitas Katolik Indonesia Atma Jaya, Jl. Pluit Raya 2, Jakarta 14440, Indonesia, prasetyanto@atmajaya.ac.id

⁶School of Chemical Sciences, Universiti Sains Malaysia, Penang, 11800, Malaysia, midiris@usm.my

Dehydration of ethanol using the distillation method is still not optimal, because it will stop at the azeotropic point of 96%. Modification of the distillation method using three processing stages such as distillation, followed by fractionation columns and adsorption using molecular sieve is a new choice in ethanol-water separation above the azeotropic point. Previous studies reported that the use of zeolite powder as molecular sieve requires a complex preparation of equipment and it contaminates ethanol solutions in distillation flasks. In this study, the use of zeolite-A/bentonite (ZAB) adsorbent as molecular sieve to produce fuel grade ethanol through adsorptive distillation has been investigated. ZAB composites were prepared in the form of solid pellets using mixing method. The hydrophilicity properties of ZAB composite was adjusted at pH 10 to obtain zeolite with high hydrophilicity, the alkaline conditions were chosen to prevent a dealumination. ZAB composites were made using a ratio of zeolite-A and bentonite being 6:4 with a thickness of 0.5 mm. Both ZA and ZAB were characterised using X-ray diffraction, Fourier transform infra-red spectroscopy (FTIR), and scanning electron microscopy. The purity of ethanol was analysed using gas chromatography-flame ionization detector. X-ray diffraction patterns of ZA showed sharp peaks of 2θ at 21.63; 24; 27.14; 29.96 and 34.2°, indicating its high crystallinity. FTIR analysis confirmed that ZAB composites were formed. The surface morphology of ZA is in the form of cubic crystals, whereas in ZAB morphology, bentonite coats the cubic surface of ZA. The combination of ZA and bentonite did not significantly change the adsorption properties of ZA and ZAB. By varying the mass of molecular sieve from 10, 20 and 30 g, the optimal condition of adsorptive distillation for ethanol dehydration was obtained at 20 g of ZAB composite with ethanol purity of 98.6%. As for comparison, distillation, distillation fractionation, and adsorption have produced the ethanol purity of 96.2%, 97.3%, and 95.5%, respectively. After the ZAB20 composite is regenerated by heating (120°C), the ethanol purity decreased to 98.3%. Overall, the ZAB20 composite has a potential as molecular sieve to produce fuel grade ethanol in ethanol-water separation through adsorptive distillation.

Keywords: adsorptive distillation, fuel grade ethanol, molecular sieve, kaolin, Zeolite-A/Bentonite composite

1. INTRODUCTION

Ethanol is one of the most desirable fuels for spark-ignition engines and it is an important blend component in the oil refining industry with an estimation of 13.7 billion gallons of ethanol blended with gasoline. Ethanol has a high octane number (RON~109) and a latent heat of vaporisation (HoV) four times greater than gasoline on a stoichiometric basis (Waqas *et al.*, 2017). These characteristics enhance the anti-knock quality of oil-based fuels (Waqas *et al.*, 2017), thereby improving engine efficiency and reducing green house gas (GHG) emissions (Kalghatgi *et al.*, 2017). However, to reach ethanol with purity higher than 96%, known as fuel-grade ethanol, the main problem to be overcome is the difficulty of separating hydrogen bonds (water) in the chemical structure of ethanol. The maximum ethanol produced and distributed in the market is only 95-96%, because an azeotropic point has been reached at this purity. In this condition, the ethanol-water mixture is difficult to be separated further. Some techniques have been proposed for the separation, including adsorption using molecular sieves (Weitkamp & Ernst, 1991), distillation (Widadgo & Seider, 1996), pervaporation (Le *et al.*, 2012) and extraction of ethanol using ionic liquids (Pereiro *et al.*, 2012).

Among the proposed methods, distillation is a simple method for separating ethanol-water based on the boiling points of the both solvents. However, dehydration of ethanol using the distillation method is still not optimal, because it will stop at the azeotropic point. The simple distillation process cannot be used to purify anhydrous ethanol from water (Kiminori *et al.*, 2008). When the ethanol-water mixture at the azeotropic point is boiled, the vapor phase produced has the same composition as a liquid phase. This azeotropic mixture is often called as a constant boiling mixture because the composition is always constant if the mixture is boiled. As shown in Figure 1, the point A mixture was boiled and the steam was separated from the liquid-vapor equilibrium system (point B). This steam is then cooled and condensed (point C). The condensation, boiling, and cooling process were repeated until it reached the azeotropic point. At the azeotropic point, the process cannot be continued because the composition in vapor and liquid is always the same. The azeotropic point is described as an intercepting point between the saturated vapor curve and saturated liquid.

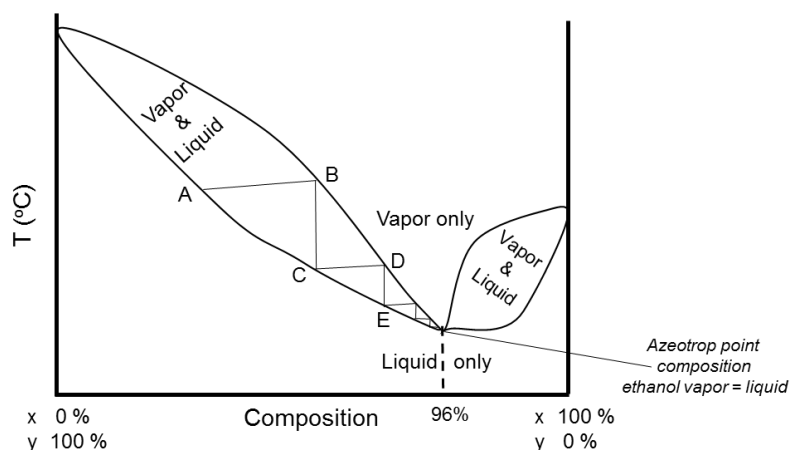


Figure 1: Constant boiling mixture azeotropic point ethanol at composition 96 %

To overcome the above mentioned problem, the use of adsorbents and fractionation columns in the distillation process are introduced. In this case, water vapor in the vapor phase can be absorbed directly onto the surface of the adsorbent, rather than recondensed into a liquid phase. So far, ethanol dehydration process has been carried out using a distillation method with a modification using a fractionation column (fractionation distillation), while a continuous and simultaneous process of distillation, fractional column, and molecular sieve has not been reported. In this study, a modification process of ethanol dehydration was carried out with a three-stage process, including distillation, followed by distillation fractionation and adsorption using molecular sieve (adsorptive distillation) which is a new method in ethanol-water separation above the azeotropic point.

The use of fractionation columns is aimed to increase the purity of ethanol by increasing the surface contact between water vapor and columns, where water vapor which vaporises together with ethanol at distillation will be held back due to the dent curve in the column and fall back into ethanol solution in the distillation flask. In this case, ethanol will continue to evaporate due to the heat conductivity in the column. The stage of adsorption using molecular sieve is expected to increase the purity of ethanol through adsorption mechanisms on the surface of the adsorbent. Morganti *et al.* (2018) has reported a comparison of the additional adsorption processes used to derive ethanol using the dry milling of corn through adsorptive distillation and direct hydration (refining, cracking and hydration). The purity of synthetic anhydrous ethanol from the dry milling of corn using adsorptive distillation was found to be higher than direct hydration (see Figure 2).

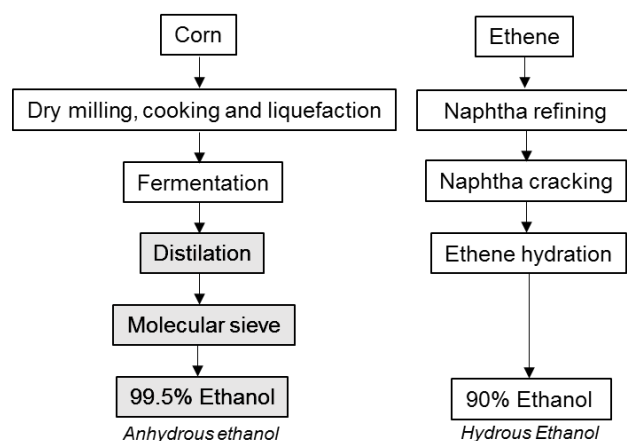


Figure 2: Comparison process used to derive ethanol from the adsorptive distillation of corn and direct hydration of ethene

Recently, Susilawati *et al.* (2018) reported that the use of powder as molecular sieve could contaminate ethanol in distillation flasks and it required further handling to separate the adsorbent from the mixture. To overcome this problem, in this current study, the molecular sieve in the form of a pellet is used. The adsorbent that can play a role as a molecular sieve commonly used for the ethanol dehydration process was types A synthetic zeolite with a uniform pore diameter. This adsorbent has a pore diameter of 3.9 Å, while water and ethanol have a pore diameter of 2.75 Å and 4.4 Å, respectively. Therefore, this adsorbent is selective towards the separation of the ethanol-water mixture (Perry & Green, 1997). Zeolite-A pellets are prepared by the addition of bentonite to enhance the hardness of the adsorbent material and also to increase the surface area of the adsorbent. Thus, the zeolite-A/bentonite (ZAB) composite is expected to possess more active sites readily available to bound with water molecules. This can be rationalised as bentonite has hydrophilic properties (Krisnandi *et al.*, 2013). In this study, zeolite-A was synthesised using the hydrothermal method from Indonesian Belitung kaolin (Simanjuntak & Kusri, 2018), which has a higher potential for long-term production compared to natural kaolin from Kalimantan (Samadhi *et al.*, 2011). An exciting opportunity of ZAB composite used as molecular sieve to produce fuel grade ethanol through adsorptive distillation is explored. The detailed ethanol dehydration (ethanol-water separation) method using distillation, fractionation, and adsorption using ZAB composite as a molecular sieve was reported.

2. EXPERIMENTAL

2.1. Materials

Natural kaolin was obtained from Belitung, Indonesia. Sodium hydroxide (NaOH) and hydrochloride acid (HCl, 37%) were purchased from Merck (Germany). Ethanol absolute with purity of 99.9% (Analytical Grade EMPARTA® ACS) was purchased from Merck (Germany).

2.2. Synthesis of Zeolite A by hydrothermal method

Zeolite-A was prepared by hydrothermal method according to the method that previously reported by Kusri *et al.* (2019). The optimal conditions for the synthesis of zeolite A were consisted of two stages, namely (i) the metakaolinization process, converting kaolin to metakaolin that calcinated with temperature of 750 °C for 3 h, and (ii) zeolitization using 3M NaOH at 90 °C for 7 h. Natural kaolin (300 g) was calcined using a furnace with a temperature at 750 °C for 3 h which is a metakaolinization process from kaolin to metakaolin. Metakaolin is left at room temperature for several hours. The next step is the zeolitization process, reacting metakaolin with 3M NaOH using a magnetic stirrer at 750 rpm, 60 °C, for 3 h, then the temperature was raised to 90 °C for 7 h for crystallisation process. Furthermore, ZA in the form of gel was filtered and washed using distilled water to neutralise the pH of ZA to be about 10. Finally, the solid was dried using an oven at a temperature of 120 °C until the stable mass was obtained.

2.3. Synthesis of Zeolite-A/Bentonite pellets (ZAB)

ZAB composites were prepared by mixing method. Briefly, 16 g bentonite was mixed with 24 g of ZA, then both solid were dissolved in 5 mL of distilled water to form a pasta. ZAB mixture was printed in a diameter size of 0.5 mm. ZAB composite was dried in an oven and kept in a closed container. Schematic of this process is presented in Figure 3.

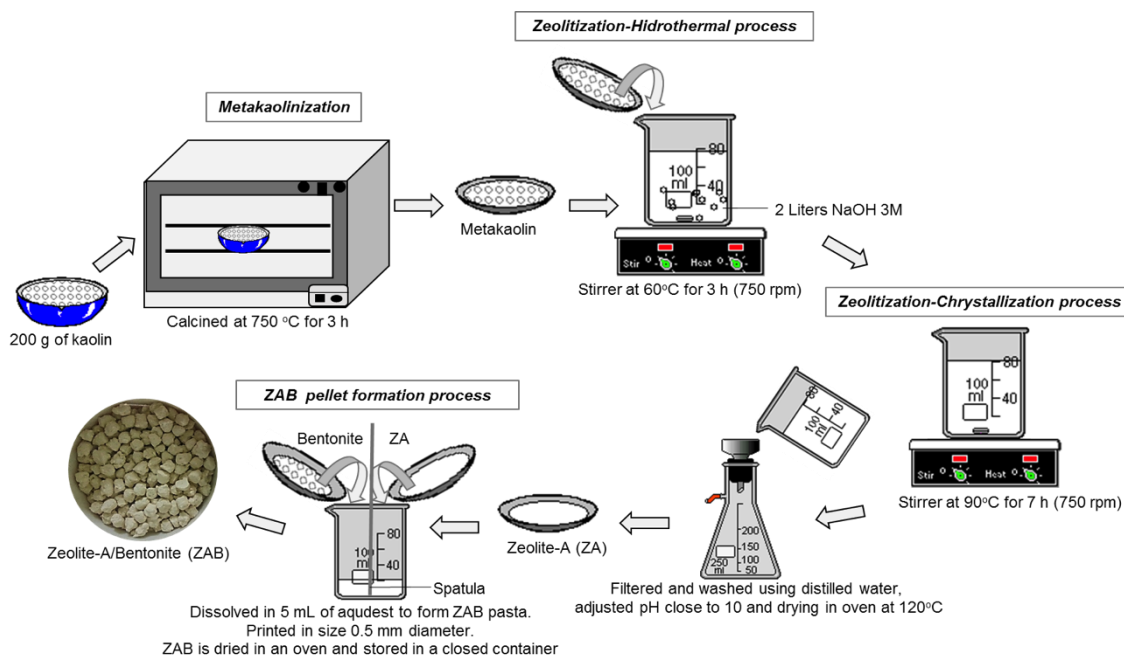


Figure 3: Schematic illustration for synthesis of zeolite-A/bentonite (ZAB) composite as molecular sieve

2.4. Adsorptive distillation process

Schematic experimental setup of adsorptive distillation was set as shown in Figure 4. This arrangement was maintained to prevent the leakage in the distillation. Desiccant container was filled with 10 g of ZAB composite and rearranged to the distillation apparatus. After the tool was assembled, 100 mL of 96% ethanol was put into a distillation flask, the distillation process was carried out at 78 °C and the distillate was kept in the erlenmeyer flask. Distillation was stopped when there is no more ethanol solution in the distillation flask. The ethanol solution was kept and tested using GC-FID to determine the purity. ZAB composite was then removed from the desiccant container and weighed. Finally, the volume of water molecule absorbed was calculated. The same process for distillation, fractionation distillation, and adsorptive distillation were carried out for various mass of ZAB to be 10, 20, and 30 g, and the composites was named as ZAB10, ZAB20 and ZAB30.

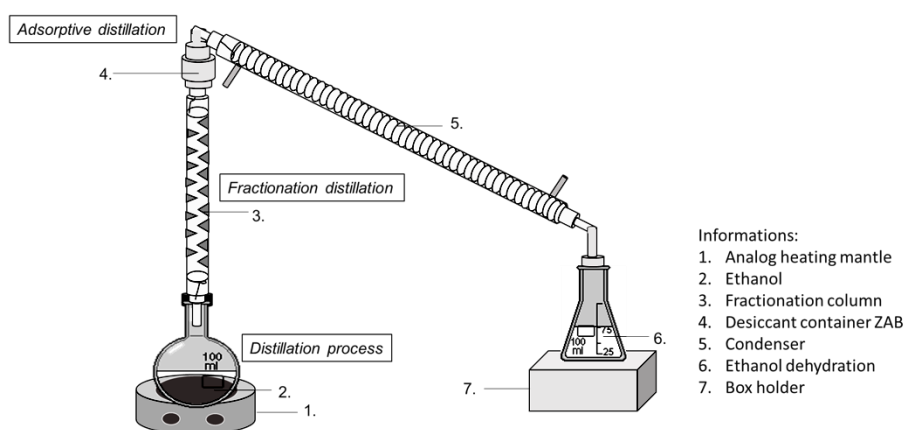


Figure 4: Schematic apparatus of adsorptive distillation

2.5. Characterisation

The functional groups in the ZA and ZAB were characterised by FTIR spectroscopy. The spectrum was recorded using BaSO₄ blank and KBr pellets on a Shimadzu IR 8400S Spectrometer over the range of 400–4000 cm⁻¹. X-ray diffraction (XRD) characterisation was carried out on Rigaku D-MAX 2550 ($\lambda = 1.54184$ nm) with 2θ ranging from 5 to 80° under ambient conditions. Surface morphology and elemental composition of the ZA and ZAB were

evaluated from their scanning electron microscopy-energy dispersive X-ray images (SEM-EDX) (Hitachi, Japan). The purity of ethanol content was determined using gas chromatography-flame ionisation detector (GC-FID).

3. RESULTS AND DISCUSSION

3.1. Synthesis of Zeolite-A/Bentonite (ZAB) composite

Zeolite-A (ZA) has a large ion exchange capacity, mechanical strength and environmentally safe with almost zero loadings of harmful effects on the environment. Among these naturally available raw materials, kaolin has a Si/Al ratio close to 1, thus it can be used as an alternative cheap raw material for the synthesis of ZA (Miao *et al.*, 2009). The synthesis of ZA from Indonesian Belitung kaolin involves two basic steps: (i) metakaolinization, which involves transforming kaolin to metakaolin by chemically activating the natural kaolin, this process can change chemically stable kaolin ($\text{Al}_2\text{O}_3 \cdot 2\text{SiO}_2 \cdot 2\text{H}_2\text{O}$) into a very reactive but amorphous metakaolin ($\text{Al}_2\text{O}_3 \cdot 2\text{SiO}_2$); (ii) zeolitization, treatment of the metakaolin with aqueous alkali solution to form zeolite A.

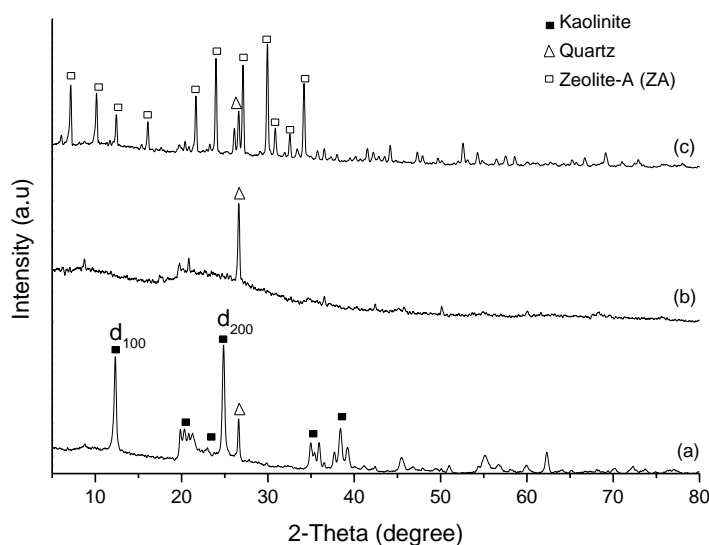


Figure 5: XRD pattern of Indonesian Belitung natural kaolin (a), metakaolin (b), and ZA (c)

The XRD pattern of kaolinite showed a layered structure with d_{100} at 12.34° and d_{200} at 24.64° , which are the characteristic peaks of kaolin and it confirmed its hexagonal structure crystals (see Figure 5a). Kaolinite is the main mineral component of kaolin. Metakaolin is an amorphous material and the highest diffraction peak at 26.59° corresponds to the presence of quartz (SiO_2) (see Figure 5b), which is the crystalline phase in metakaolin. Metakaolin is a calcined product of kaolin with Si/Al ratio of 1. This is a convenient starting material for the synthesis of ZA. The total loss metakaolinization was calculated from the thermogravimetric analysis. The value is similar with that reported by Ayele *et al.* (2015), and it was found to be approximately 12.9%. The XRD pattern of ZA showed a high crystallinity with the highest 2θ peak intensity being 21.63° , 24° , 27.14° , 29.96° , and 34.2° (see Figure 5c). These peaks were confirmed that ZA has been successfully synthesised, as it has been observed and reported by Ayele *et al.* (2015). In the XRD pattern of ZA, the tiny presence of quartz having 2θ of 26.69° was observed. This was caused by unreacted of SiO_2 from the starting raw yet purified (Ayele *et al.*, 2015).

The concentration of NaOH is one of the most important parameters that control the crystallisation of zeolite-A. Increasing in the alkalinity causes an increase in the crystallisation rate via both nucleation and crystal growth as a consequence of the larger concentration of reactive silicate, aluminates and aluminosilicates species caused by the rapid increments of the solubility of the amorphous aluminosilicate precursor. With an increase of alkalinity, the particle size is usually decreased, yielding a narrow distribution of particle size due to an increased nucleation rate and an increased polymerization rate between polysilicate and aluminate anions (Auerbach *et al.*, 2003). The different compositions of the natural clays requires optimisation of NaOH concentration for each source of kaolin, as reported in the literature for preparation of ZA.

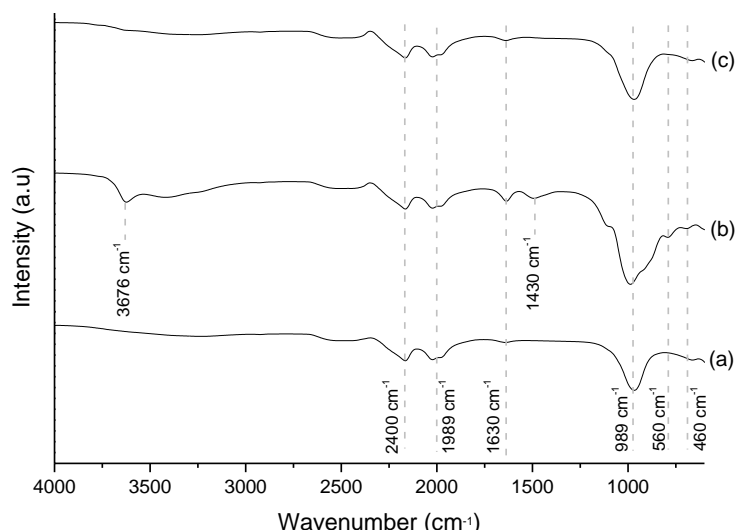


Figure 6: FTIR Spectra of ZA (a), Bentonite (b) and ZAB composite (c)

FTIR spectrum of ZA showed the distinct absorption bands at 2400, 1989, 1630, 989, 560 and 460 cm^{-1} , and these absorption bands are the characteristic of zeolite A (see Figure 6a and c). The absorption band at 989 cm^{-1} corresponds to the internal vibrations of Al–O and Si–O bonds and asymmetric stretching within the tetrahedral zeolite structure. Additionally, the Al–O and Si–O bonds also show internal bendings as indicated by the absorption band at 460 cm^{-1} , while the absorption band at 560 cm^{-1} is caused by external vibration of the cubic units connecting the sodalite cages in the structure of the zeolite. The absorption band at 1630 cm^{-1} indicates that water are bound within the molecular sieves of the zeolite A structure. Additional peaks observed at 1430, 1989, and 2400 cm^{-1} (Figure 6b) are representative of carbon dioxide: the asymmetric stretching of C–O is reflected by the band at around 2400 and 1989 cm^{-1} , while C–O symmetric stretching is 1430 cm^{-1} (Giroux *et al.*, 2016). The use of bentonite did not significantly change the FTIR spectra of ZA and ZAB composite.

The morphology images of ZA and ZAB composite are shown in Figure 7a and 7b. The surface morphology of ZA is in the form of cubic crystals. From Figure 7b, the formation of ZAB composite is confirmed. The EDX elemental composition of ZA and ZAB composite is listed in Table 1. The ratio of Si/Al for ZA is 1.007 and in ZAB composite is 1.24. The use of bentonite in the formation of pellets is aimed to enhance the hardness of the ZAB adsorbent material as well as to increase the surface area of the adsorbent. Thus, they have more active sites are available and can be bound to water molecules.

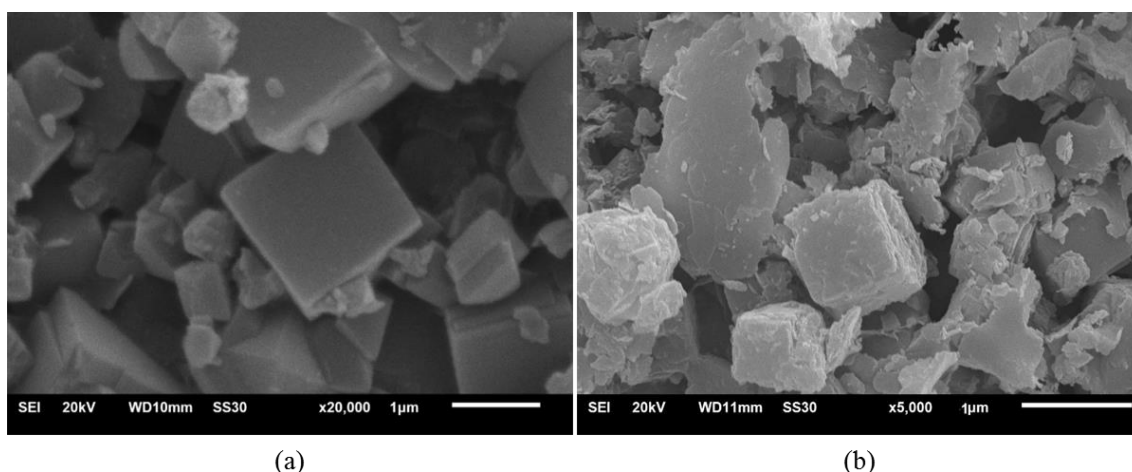


Figure 7: SEM morphology images of ZA (a) and ZAB composite (b)

Table 1: EDX elemental analysis of ZA and ZAB composite

Sample	wt. %						Si/Al ratio
	C	O	Na	Si	Al	Fe	
ZA	-	39.49	9.21	13.55	13.46	1.16	1.007
ZAB composite	9.14	33.5	6.02	17.36	13.95	1.07	1.24

3.2. Adsorptive distillation

Dehydration of ethanol using the distillation method was carried out based on the principle of differences in boiling points of ethanol and water. With a lower boiling point, ethanol will evaporate first and condense into the liquid distillate. The heating temperature must be kept constant. In general distillation, the tools used are only distillation flasks and condensers as ethanol vapor coolers. In this work, additional fractionation column tools were used. This column is installed just above the distillation flask, as shown in Figure 4. The use of fractionation columns is aimed to increase the purity of ethanol through increasing surface contact between water vapor and columns. The presence of a barrier in the fractionation column causes the existence of water vapor which vaporises together with ethanol at the time with distillation and holds back due to the dent curve in the column. The water vapor accumulates in the fractionation column, condenses, and falls back into ethanol solution in the distillation flask. Meanwhile, heat conduction towards the fractionation column increases the ethanol evaporation, causing the ethanol to evaporate to desiccation which has been filled with ZAB composite for the adsorption distillation process.

After the fractionation column, the evaporated ethanol passes through the desiccant containing the ZAB composite. In this case, water vapor is still possible to evaporate with ethanol due to the strong hydrogen bonding between ethanol and water. To increase water vapor adsorption, an adsorbent was modified based on its polarity. The modified ZAB composite becomes very hydrophilic, thus it has a great adsorption capacity for water. There are two ways to modify the hydrophilicity of a zeolite; e.g. changing the silicon-to-aluminum ratio and increasing alkaline condition. Zeolites with a very high silicon-to-aluminum ratio (theoretically up to infinity) are hydrophobic, whereas zeolites with a silicon-to-aluminum ratio fewer than two are hydrophilic. The second method is based on the modification of the pores of the zeolite with a ligand (Giroux *et al.*, 2016). More acidic zeolite causes the structure to undergo a dealumination or alumina release. Loose alumina causes the Si/Al ratio is increased so that zeolites become hydrophobic. Meanwhile, to obtain zeolite with high hydrophilicity, ZA was prepared at pH 10 as the alkaline condition prevents a dealumination.

In this study, the variation of adsorbent mass in the ranges from 10 to 30 g was carried out to determine the optimal amount of ZAB composites in the adsorptive distillation process (see Table 2). In addition, several controlling methods were conducted to compare the ability of dehydration using a distillation method, fractionation distillation using a column, and adsorptive distillation using ZAB composite. The purity of ethanol used in the dehydration process was 96%, which is the azeotropic point of ethanol-water mixture. The results obtained showed that the distillation and adsorption processes did not have a significant effect. The low purity of ethanol using the distillation method is due to the vapor phase and the liquid phase of ethanol being at the azeotropic point. In the adsorption method, the ZAB filtering process after adsorption increased the evaporation of ethanol, thereby the ethanol purity content was reduced. Fractionation distillation produces ethanol with better purity than simple distillation. In the adsorptive distillation, ZAB20 composite can produce the higher purity of ethanol than that found in the ZAB10 composite. However, by using ZAB30 composite, the ethanol purity decreased, because of the ability of an adsorbent to absorb the adsorbate being 20-22% of its total mass (Ayele *et al.*, 2015). Thereby the use of ZAB10 composite has the ability of adsorption only by 2-2.2% or 2-2.2 mL of water in 96% ethanol (96% ethanol: 4% water). Thus, there is still 2% of water that is not absorbed. By using ZAB20 composite, the adsorption capacity of ZAB20 composite is 4-4.4%, the ability to absorb water is more optimal. On the other hand, the adsorption capacity of 6.6% was obtained when ZAB30 composite was used. In other words, the water adsorption ability is much greater, but this causes competition between ethanol and water to fill the pores of the zeolite. Thus, it prevents water molecules from diffusing into the surface of the adsorbent. According to Rakhmatullah *et al.* (2007), water vapor molecules adsorbed by zeolite form circles around the cation (see Figure 8).

Comparison of the fresh ZAB composite and ZAB composite after use in adsorptive distillation is shown in Figure 9. The spent ZAB composite has the same shape as ZAB before adsorption, but has a darker color and more weight (see Table 3). This is due the interaction of the active sites in zeolite A are silica and alumina with oxygen atoms in H₂O molecules as described in Figure 8. Difference color of the fresh ZAB composite and after adsorption was observed. It is because of interaction of H₂O molecules with active sites (silica or alumina cations) on the surface of ZAB.

After the ZAB20 composite is regenerated by heating at a temperature of 120°C in oven, the ethanol purity decreased to 98.3%. The reduction in ethanol content from 98.6% to 98.3% is likely due to the presence of H₂O molecules in the ZAB structure. Further test on the stability of the ZAB20 composite was carried out to determine the optimal regeneration temperature.

Table 2: The GC-FID results of ethanol dehydration using various methods

Ethanol Dehydration Methods	Ethanol purity (%)
Distillation	96.2
Distillation Fractionation	97.3
Adsorptive Distillation – ZAB10	97.8
Adsorptive Distillation – ZAB20	98.6
Adsorptive Distillation – ZAB30	97.5
Adsorption – ZAB20	95.5
Regeneration – ZAB20	98.3

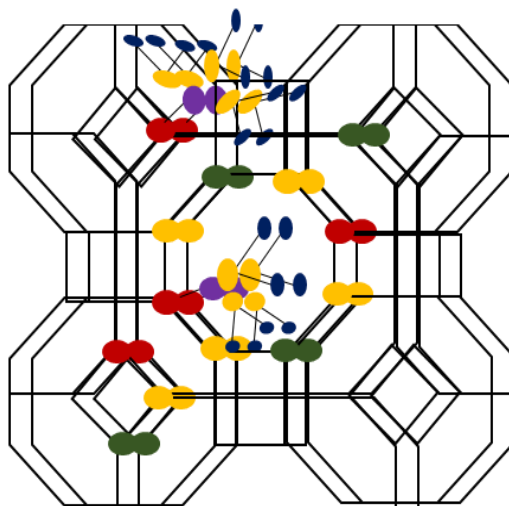


Figure 8: Possible interactions between pore molecules of ZAB composite with H₂O, color codes: yellow = O, red = Si, green = Al, purple = cation Na/Ca/Mg, blue = hydrogen bond

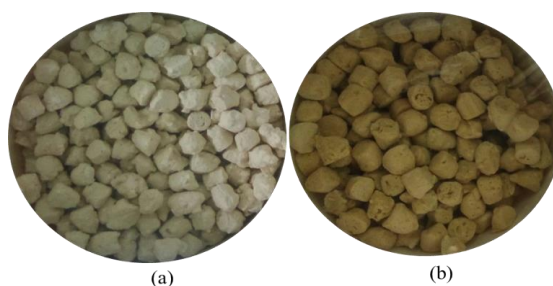


Figure 9: Comparison of the fresh ZAB composite (a) and ZAB composite after adsorption (b)

Table 3: Comparison weight of ZAB composite before and after adsorption

Adsorbent	Weight of fresh (g)	Weight of after adsorption (g)
ZAB10	10.008	12.014
ZAB20	20.003	24.994
ZAB30	30.173	37.462

Comparison of FTIR spectra of the fresh ZAB composite (Figure 10.b) and ZAB after ethanol dehydration showed a significant difference (Figure 10a). It showed distinct absorption bands at 3200-3400 cm⁻¹ and 1630 cm⁻¹ indicated that H₂O molecules are bound within the molecular sieves of the ZAB structure (Giroux *et al.*, 2016; Pavia, 2001). The spectral vibration of O-H alcohol was observed at 3600 cm⁻¹, similar for ethanol reported by Giroux *et al.* (2016). This indicates that ethanol was absorbed into the molecular structure of ZAB composite due to reducing the purity of ethanol.

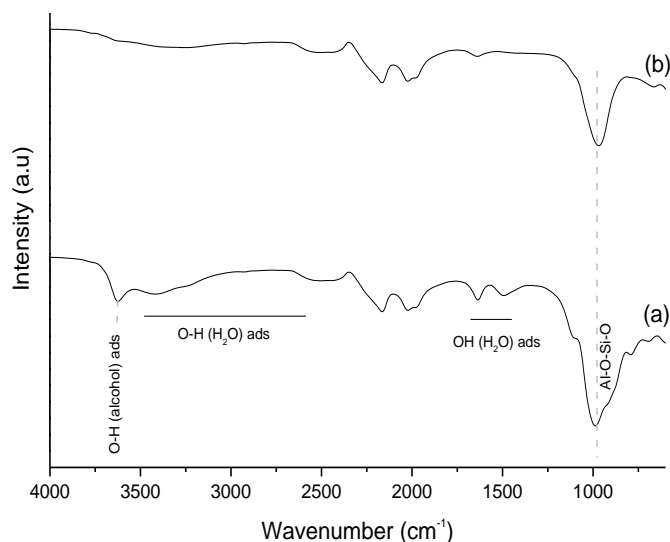


Figure 10: FTIR Spectra of ZAB composite after ethanol dehydration (a), and the fresh ZAB composite (b)

4. CONCLUSION

Zeolite-A/bentonite (ZAB) composite has been successfully synthesised in the form of pellets by mixing method. The hydrophilicity properties of ZAB composite was adjusted at pH 10 to obtain zeolite with high hydrophilicity, the alkaline conditions were chosen to prevent a dealumination. ZAB composites were prepared using a ratio of zeolite-A and bentonite of 6:4 with a thickness of 0.5 mm. X-ray diffraction patterns showed peaks 2θ at 21.63, 24, 27.14, 29.96, and 34.2°, indicating high crystallinity ZA. FTIR analysis shows the complete conversion of ZA to ZAB composite. The surface morphology of ZA is in the form of cubic crystals. The ratio of Si/Al for ZA is 1.007 and in ZAB composite is 1.24. The use of bentonite in the formation of pellets is aimed to enhance the hardness of the adsorbent material and also to increase the surface area of the adsorbent, thus more active sites are available and can bind water molecules. By varying the mass of ZAB composite as molecular sieve, the optimal conditions for ethanol dehydration were obtained at 20 g of ZAB20 composite with ethanol purity of 98.6%. In comparison, distillation, distillation fractionation, and adsorption produced ethanol with the purity of 96.2%, 97.3%, and 95.5%, respectively. Overall, the ZAB20 composite demonstrated its potential as molecular sieves to produce the fuel grade ethanol through adsorptive distillation method.

5. ACKNOWLEDGEMENT

The authors greatly acknowledge to the Ministry of Research and Technology/National Research and Innovation for research grant award through the PTUPT Grant, No. NKB-1733/UN2.R3.1/HKP.05.00/2019 for financial support.

6. REFERENCES

- Auerbach, S.M. Carrado, K.A. Dutta, P.K. 2003. Handbook of Zeolite Science and Technology, Marcel Dekker, New York.
- Ayele, L. Perez-Pariente, J. Chebude, Y. Díaz, I. 2015. Synthesis of zeolite A from Ethiopian kaolin. Microporous and Mesoporous Materials 215. 29-36.
- Giroux, M. Sahadeo, E. Libera, R. Maurizi, A. Giles, I. Marteel-Parrish, A. 2016. An undergraduate research experience: Synthesis, modification, and comparison of hydrophobicity of zeolites A and X. Polyhedron 114. 42–52.
- Kalghatgi, G. Algunaibet, I. Morganti, K. On knock intensity and superknock in SI engines. SAE Int J Eng 10(3).
- Karge, H.G. Verified synthesis of zeolitic materials (2nd revised edition): characterization by IR spectroscopy. DOI: http://www.iza-online.org/synthesis/VS_2ndEd/IR_Spectroscopy.htm.

- Kiminori, S. Katsuhiko, A. Kazunori, S. Kou, I. Soushi, I. Junji, S. Shiro, I. Takashi, N. Kiminori, S. 2008. Dehydrating performance of commercial LTA zeolite membranes and application to fuel grade bio-ethanol production by hybrid distillation/vapor permeation process. *Microporous and Mesoporous Materials* 115. 184–188.
- Krisnandi, Y.K. Sihombing, R. Sunu, M.O. 2013. Bentonit Alam Tapanuli Diinterkalasi Surfaktan Kationik Benziltrimetilammonium Klorida (Btma-Cl) Sebagai Adsorben P-Klorofenol Dan Fenol. FMIPA UI.
- Kusrini, E., M.D. Hans, Putra, N., Usman, A., Gunawan, Y. Synthesis and Characterization of Zeolite-A from Indonesian Belitung Kaolin and Its Application as a Desiccant for Drying of Air in the Corn Drying Process, 2019.
- Le, N.L. Wang, Y. Chung, T. 2012. Synthesis, cross-linking modifications of 6FDA-NDA/DABA polyimide membranes for ethanol dehydration via pervaporation. *J Membr Sci.*415–416:109–21.
- Miao, Q. Zhou, Z. Yang, J. Lu, J. Yan, S. Wang, J. 2009. *Front. Chem. Eng. China* 3. 8-11.
- Morganti, K. Almansour, M. Khan, A. Kalghatgi, G. Przesmitzki, S. 2018. Leveraging the benefits of ethanol in advanced engine-fuel systems. *Energy Conversion and Management* 157. 480–497
- Pavia, D. L., Lampman, G. M., Kriz, G. S., & Vyvyan, J. R. (2001). *Introduction to Spectroscopy Fourth Edition*. Belmont: Brooks/Cole, Cengage Learning.
- Pereiro, A.B. Araujo, J.M.M. Esperança, J.M.S.S. Marrucho, I.M. Rebelo, L.P.N. 2012. Ionic liquids in separations of azeotropic systems – a review. *J Chem Thermodyn.*46:2–28.
- Perry, R.H. and Green, D.W. 1997. *Perry's Chemical Engineers' Handbook*, 7th Edition, Mc Graw-Hill Co, New York, p.1128, 14901497, 1534-1537.
- Rakhmatullah, D.K.A, Wiradini, G. Ariyanto, N.P. 2007. Pembuatan adsorben dari zeolit alam dengan karakteristik adsorption properties untuk kemurnian bioetanol, Fakultas Teknologi Industri Institut Teknologi Bandung.
- Samadhi, T.W. Subagjo, Lismana, K.R. and Fuadi, K. 2011. Synthesis of γ -Al₂O₃ Catalyst Support from Kaolin of Indonesian Origin. *ITB J. Eng. Sci.*, Vol. 43, No. 2, 113-126.
- A.A.Y. Simanjuntak and E. Kusrini. 2018. Feasibility Study for Production of Zeolite A based on Kaolin, *E3S Web of Conferences* 67, 02017.
- Susilawati, Nasruddin, M.N. Chandra, K. Irwan, N. Yuan, A.S. 2018. Ethanol Purification Using Active Natural Pahae Zeolite By Adsorption Distillation Method. *International Conference on Science and Technology 2018*. IOP Conf. Series: *Journal of Physics: Conf*, Series 1116.03203.
- Waqas, M. Naser, N. Sarathy, M. Feijs, J. Morganti, K. Johansson, B. 2017. Blending octane number of iso-stoichiometric blends of gasoline-ethanol-methanol (GEM) in SI, HCCI and CI combustion modes. *SAE technical paper* 2017-01-0726.
- Widadgo, S. Seider, W.D. 1996. Azeotropic distillation. *AIChE J.* 42(1):96–130.
- Weitkamp, J. Ernst, S. 1991. Separation of gaseous water/ethanol mixtures by adsorption on hydrophobic zeolites. *Zeolites* 11(4):314–7.

#306: The indoor climate monitoring using Zigbee wireless network for building thermal comfort application

Waraporn RATTANONGPHISAT¹, Wiriya RUENGYOO², Anantachai SUWANNAKOM³

¹ Energy Technologies Building Laboratory, Department of Physics, Faculty of Science, Naresuan University, Phitsanulok, 65000 Thailand, warapornr@nu.ac.th

² Graduated student, Energy Technologies Building Laboratory, Department of Physics, Faculty of Science, Naresuan University, Phitsanulok, 65000 Thailand, Wiriya_bright@hotmail.com

³ Department of Physics, Faculty of Science, Naresuan University, Phitsanulok, 65000 Thailand, anatachais@nu.ac.th

This paper presents the design and implementation of a wireless sensor network using Zigbee protocol for monitoring the indoor climate of an air-conditioned room. The wireless sensor network included the measuring unit, data transmission unit and data collection unit. The measuring unit consisted of an embedded system module Fio mote-ST (microcontroller), XBee (Zigbee protocol) and HIH6131 (temperature/relative humidity sensors). Gateway and base station were the last two components of the network. The sensor units communicated with the base station and the collection unit via the gateway. Indoor weather was measured then information transmitted to the computer for displaying on the screen in real time whilst at the same time storing the information. The design of the graphical user interface was done using Visual studio, an open source program. The Blockset diagram that came with the hardware was used in the setting up of the Zigbee wireless sensor network. The measured indoor temperature and humidity was displayed in real time. It was found that the Zigbee wireless sensor network for indoor weather monitoring operated effectively and continuously without delay. The temperature sensor provided the measurement value within 2% difference compared to the measurement using Thermocouple type K in the same operating conditions. The occupant comfort calculated by the simple predicted mean vote equation from literature was found during the thermostat temperature setting of between 24°C and 26°C. This temperature setting was slightly low compared to an air-conditioned room in the lower floor as the demonstration test room was located on the top floor of the building with the flat slab roof above, thus higher heat gain could be expected. The advantage of the Zigbee wireless sensor network is that it can operate individually and perform a portable local weather monitoring system.

Keywords: Zigbee wireless sensor network; Thermal Comfort; Air-conditioned room; Tropical climate

1. INTRODUCTION

Increasing global temperature causes significant discomfort when staying outdoors. High temperatures and humidity throughout the year is experienced in tropical climate countries. Economic affordability increases the installation of air conditioners in homes as proved by high installation rates over recent years. Thermal comfort has been used to identify the satisfaction of occupants regarding their dwelling environment relating to temperature and humidity. Physical and human activity are the influencing factors that affect the range of thermal comfort. Monitoring systems becomes necessary to monitor the variation and data collection in order to improve building efficiency. Our previous work employed a wire sensor network, a Controller Area Network (CAN) connected with the microcontroller and temperature/humidity sensors (Rattanongphisat *et.al*, 2016). All 15 sensor nodes wires were connected to the central control unit and a drawback was found when a sensor malfunctioned due to a loose cable. The sensor separated from the microcontroller and caused others in the same line to work unpredictably. Complex wire connections are a feature when installing in a large area requiring a lot of sensors and, because the wiring needs space, it can appear ugly when seeing a mass of wires in the air. However, this wire network is considered a stable operating system. In addition, the power consumption of the air conditioner could be metered by the use of smart current transformer sensors and software platform. The wireless current transformer clamp on the power line to the air conditioner detecting the current use and converted to power for energy consumption. Measured data was used to evaluate the energy performance of the building; particularly, buildings in tropical climate where the predominant energy consumption of the building is the air conditioning system. The study shows a building performance evaluation based on key parameters that are thermal comfort, energy and indoor environment of the monitoring buildings (Oliviaa & Christopher, 2015). Thermal comfort evaluation refer to EN15251, ASHRAE55 and ISO7730 where the predicted mean vote is calculated. The predicted mean vote (PMV) defined in ISO 7730 and the adaptive method are used to design and assess buildings performance. The range of lower and upper temperature levels could be found in the building regulation in some countries.

Recently, the wireless network has been widely used because of their attractive features such as less data cable resulting in cost reduction and convenient installation. Wireless network allows either two individual pieces of equipment or two computers communicating with each other without cable connection between one and another. That also includes the communication among several computers and computer network. In order to do that, the electromagnetic wave sending signal from the sender to the receiver in the air within the limited distant according to the frequency they use. This becomes a benefit of the use of wireless sensor network since the limited distant meant low power requirement thus low cost. The range of frequency in radio wave and infrared is employed. Technology development bring telecommunication to high speed broadband access to the data. Broadband Wireless Access, BWA, can be divided according to the data accessing characteristic. First, Personal Area Network, PAN, send the signal within 10 meter and data rate of 480 Mbps where Zigbee followed the IEEE 802.15.4 standard belong to this category. Second, Local Area Network, LAN, has the range of 100 meter and data rate of 100 Mbps. Third, Metropolitan Area Network, MAN, has the range of between 10 and 50 kilometer and data rate of between 15 to 50 Mbps. Forth, Wide Area Network, WAN, has cover from district to whole country area but with small data rate of 1.5 Mbps. The characteristics of IEEE 802.15.4 protocol includes low power consumption and three frequency band operation as 1 channel 868 MHz in Europe, 10 channels 915 MHz in the United State of America and 16 channels 2.4 GHz worldwide. The use of Zigbee wireless sensor network for temperature and humidity data collection in a laboratory equipped with air conditioner for demonstrating greenhouse was implemented (Yang *et.al*, 2013). The Zigbee wireless sensor network provides an achievement of air conditioner control to the desire setting and also cost reduction compared with conventional system connected by wire. Ambient assisted living for aging community was implemented to monitor indoor air quality, IAQ (Marques & Pitarma, 2016). The indoor monitoring system based on the Internet-of-Things, IoT, that integrated with Arduino, mini Wi-Fi board as ESP8266 and XBee technologies for data transmission and acquisition. It has shown its capability for the real time operation. Home or Office automation employed wireless sensor network for providing the image of indoor environment to occupancy (Abella *et.al*, 2019). The monitoring system consists of a sensor node, microcontroller, radio frequency transceiver and sensors. The study emphasis on supporting the IoT application. On the contrary, the limitation and capabilities of some wireless sensors has been raised according to the experimental results of their accuracy compared with the reference instruments (Mylonas *et.al*, 2019). They found that six types of temperature sensors perform satisfactory measuring results but the relative humidity sensors has a large error range while the CO₂ evaluation found a weak predominant factor. The review of energy metering and monitoring in building practice has shown the challenge of installing meters and sensors in existing buildings where it is not covered with the policies and regulation (Ahmad *et.al*, 2016). They provide inclusive findings on the available technologies and limitation for the use in building energy management systems.

Wireless offer several benefits that are no cable, flexible connection, effective resource sharing, simple installation and mobility. Indoor weather monitoring based on Zigbee IEEE 802.15.4 protocol has several advantages that are low cost and low power consumption. This Zigbee wireless sensor network was selected for the current study. In this study, a wireless sensor network using Zigbee protocol to establish the indoor weather monitoring for the air-conditioned room is presented. The measurement of air temperature and humidity is done by the sensors and collected data were used to evaluate indoor weather condition as well as the thermal comfort.

2. METHODOLOGY

The wireless sensor network was setup for monitoring the indoor weather of air-conditioned room which comprises of wireless XBee module connected with the temperature/humidity sensors in stack and communicate by radio wave at frequency of 2.4 GHz. Testing on this indoor weather monitoring using Zigbee wireless network, measured temperature and humidity data were sent and stored in the personal computer which later was retrieved for thermal comfort analysis. The predicted mean vote method employed in previous study was simplify by multiple regression analysis on the PMV calculation for the air-conditioned slope classroom (Rattanaongphisat et.al, 2016). Two variable sets are physical and personal where the prior variable set includes temperature, velocity, mean radiant temperature, and relative humidity and the latter variable set is clothing insulation and activity level. The model is accepted for air-conditioned buildings. The sPMV index has 7 points thermal sensation scale that ranges between -3 and +3 (-3, -2, -1, 0, 1, 2,3) therefore the closest to zero or the middle of scale would mean comfort preferable as neutral.

2.1. Wireless sensor network

The Zigbee wireless network connects with several nodes that includes one coordinator, routers and end devices. One XBee pro module acted as coordinator is connected to the personal computer while the other eight modules located various positions inside the test room as shown in Figure 1. The network setup is the point to multipoint where one XBee module was used as the coordinator to communicate to other XBee modules as can be seen in Figure 2. A board was designed to include a sensor. The coordinator has been functioned as the bridge to allow data transportation between the Zigbee network and gateway. The USB, Universal Serial Bus, port is used to connect with the router. With Zigbee protocol, these following features could be found as low duty cycle hence long last battery, multiple network topologies supportive for point to point or point to multipoint, the data rate speed of 250 kb per second, Direct Sequence Spread Spectrum (DSSS) thus good performance in the area where interference could be affected, and cost effective. The indoor weather monitoring system is installed in the air-conditioned test room with dimension of 4 meter wide, 11 meter long and 2.6 meter high at Department of Physics, Naresuan University, Phitsanulok.

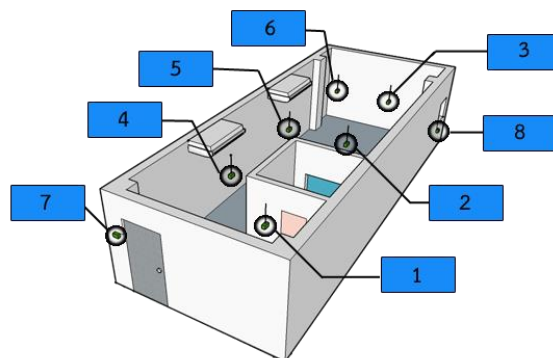


Figure 1: Sensors installation in the air-conditioned test room

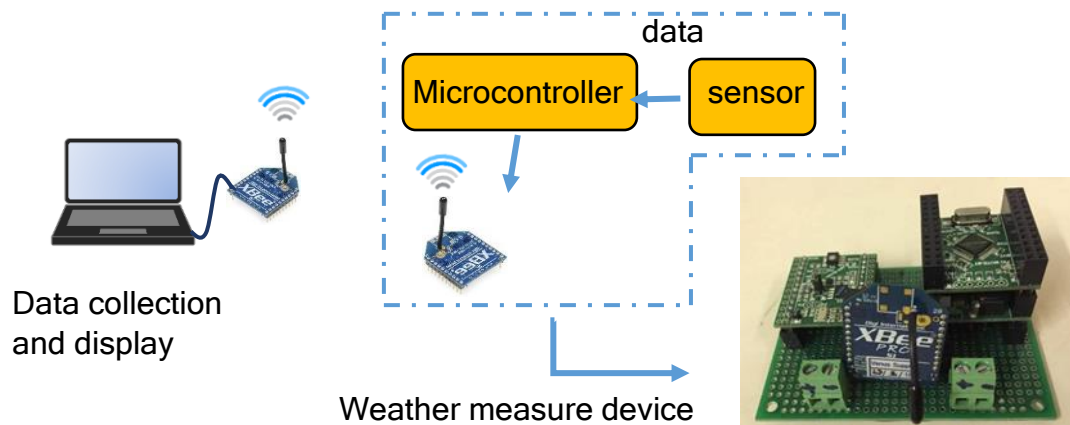


Figure 2: The indoor weather monitoring system

Technical specification of combined humidity and temperature sensor HIH6131 is shown in Table 1.

Table 1: Combined Humidity and Temperature Sensor specification of HIH6131

Characteristic	Condition	Characteristic	Condition
Temperature Accuracy	0.5 °C	Supply Voltage	3.3 Vdc
Operating Temperature	-40°C to 85°C	RH Accuracy	±4 %RH
Hysteresis	±1.5 %RH	Interchangeability	10 %RH to 90 %RH
Output Signal	Digital I ² C	Total Error Band	±5 %RH
Supply Current	650 µA	Response Time	6 s in 20 l/min minimum airflow

2.2. Monitoring system

The graphical user interface of the indoor weather monitoring system is design using Visual studio, an open source, as shown in Figure 3. Eight sensor nodes distribute in the air-conditioned test room and outside. The measured air temperature and relative humidity data were sent to store in the computer at the same time display on the monitor for real time use.

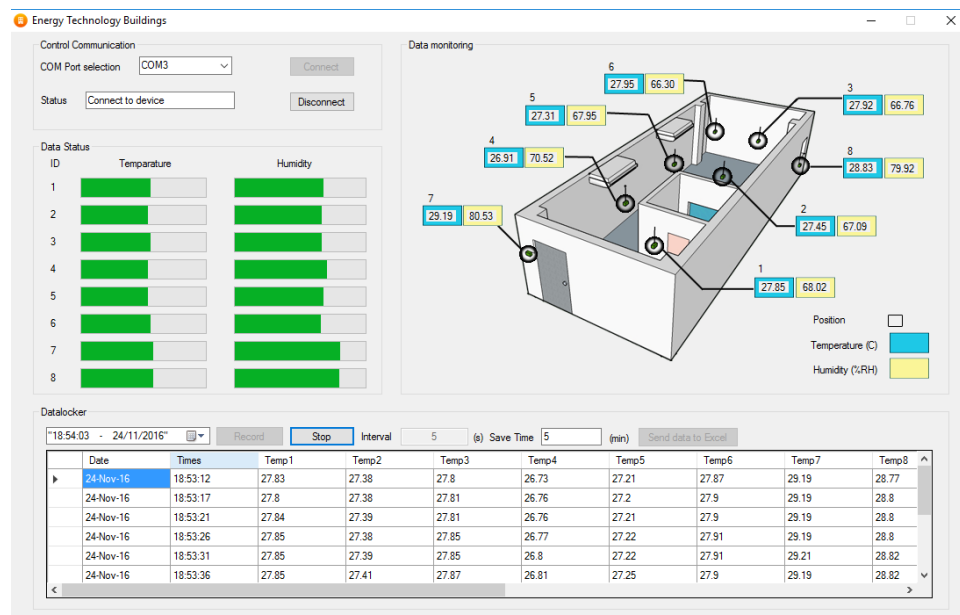


Figure 3: Graphical user interface of the monitoring system

2.3. Thermal comfort

The thermal comfort in the air conditioned environment can be determined using the predicted mean vote index which defines in ISO7730 (ISO7730, 2005). In this study, the simple predicted mean vote related to temperature and relative humidity was setup based on the multiple regression analysis on the PMV index in previous study for the similar occupant activity and outdoor climate (Rattanongphisat, 2017). It could be argued that real time factors included types of clothes wearing by occupants, number of occupants and air velocity should be paid attention when determines the thermal comfort. However, the current finding aims to realise the applicable of wireless sensor network for environmental monitoring on the simplification of thermal comfort evaluation thus reduce the complexity of all that parameters considered in the complete PMV formula with only one study condition. Male students wore short sleeve and trouser and female students wore short sleeve and knee skirt as the student uniform that are the two types of wearing clothes.

The comfort index is show in Equation 1 and Equation 2.

Equation 1: Simple predicted mean vote for male student.

$$sPMV = -4.59 + 0.1759T + 0.00167RH$$

Equation 2: Simple predicted mean vote for female student.

$$sPMV = -5.1948 + 0.19135T + 0.002216RH$$

Where:

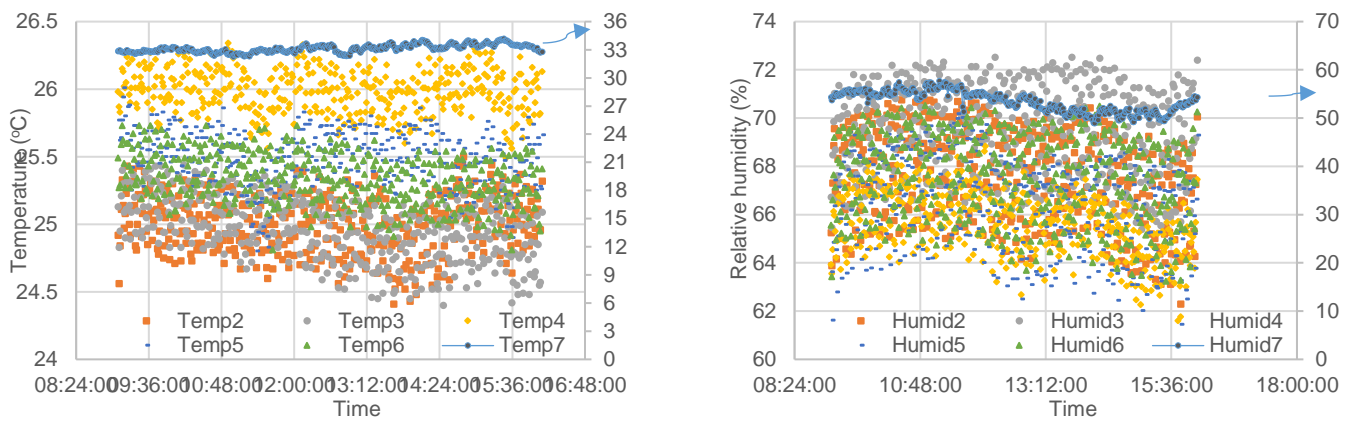
- sPMV = Simple predicted mean vote
- T= Temperature (°C)
- RH= Relative humidity (%)

3. RESULTS AND DISCUSSION

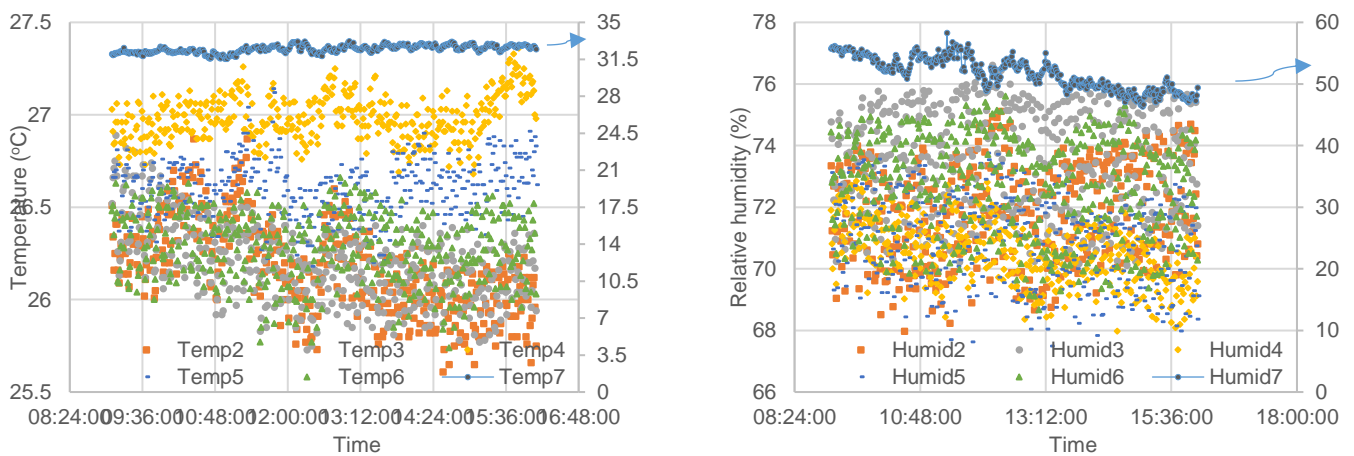
Temperature and relative humidity were collected every 5 minute throughout the time the room was occupied and air-conditioner was switched on. Data has been plot to see the distribution of air temperature and humidity inside the room including the range of upper and lower limit of each thermostat setting up from 24°C to 26°C. In addition, the simple predicted mean vote as a function of temperature and relative humidity from the air-conditioned classroom at Physics building has been employed to evaluate the thermal comfort.

3.1. Indoor weather

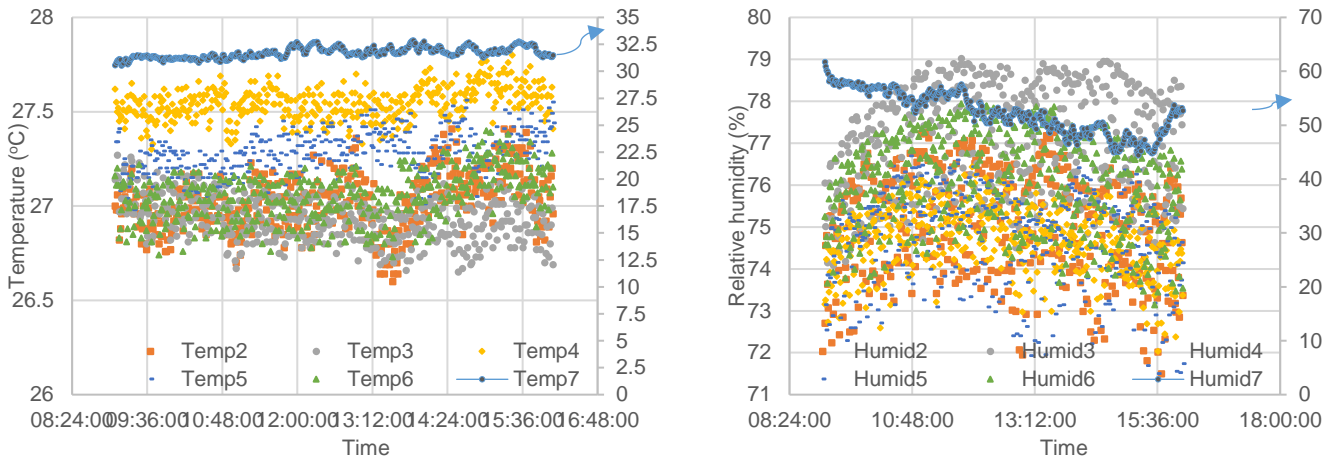
An air-conditioned room was occupied by three students who do the office work on their personal laptop computer in sitting position thus can be classified as low activity similar to sitting in the lecture classroom. Combined temperature and humidity sensors were within 2% different from the thermocouple type K.



(a) 24°C



(b) 25°C



(c) 26°C

Figure 4: Temperature and relative humidity distribution in the air-conditioned test room at thermostat setup of (a) 24°C, (b) 25°C, (c) 26°C

The measured temperature and humidity data plot show the variation of indoor weather at three thermostat setting of 24°C, 25°C and 26°C respectively as shown in Figure 4. Temperature distribution along the test room has shown the variation of indoor temperature from 0.5 to 2°C above the setting temperature for all thermostat setting. The outdoor ambient temperature is varied between 31 and 33°C during the experimental testing. It is found that indoor humidity slightly higher than the outdoor according to high outdoor temperature causes low humidity based on the sensor formula. The monitoring system operates effectively. Measured data were export in excel file that conveniently use for the thermal comfort analysis.

3.2. Thermal comfort

Figure 5 provide the picture of the simple predicted mean vote as a function of the air temperature and relative humidity. The variation of thermal sensation is in the range of existing building in category C that range from -0.7 to 0.7 (ASHRAE, 2007). The upper comfort level is the male student while the lower comfort level is the female student due to higher metabolism rate that has caused male students accepting thermal comfort at slightly lower temperature.

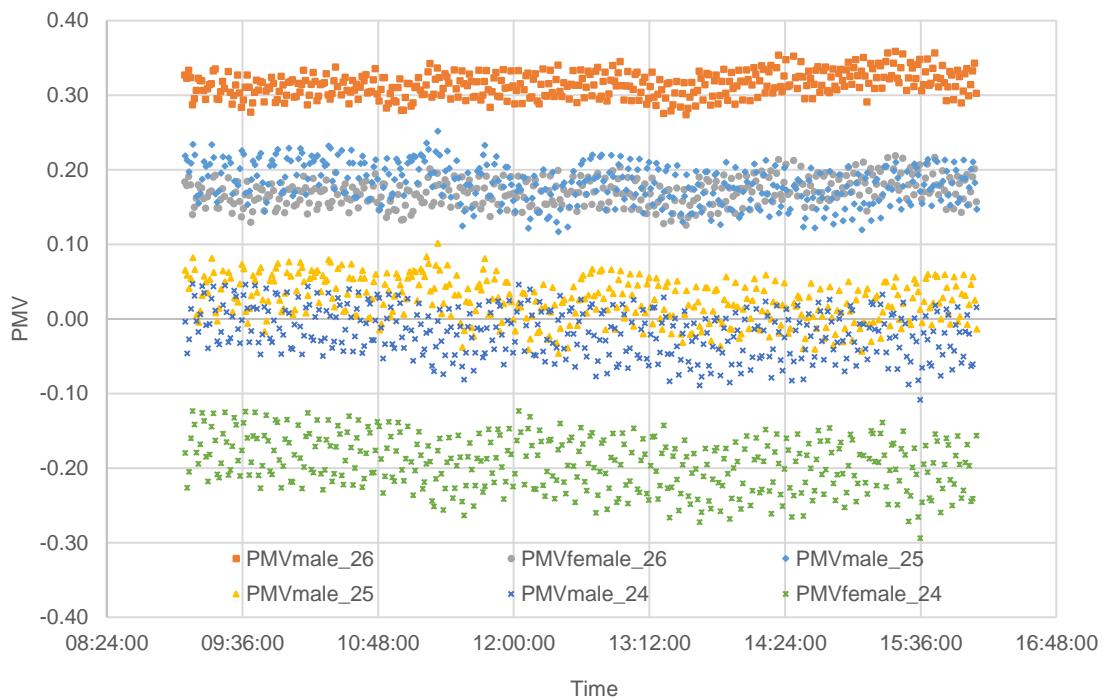


Figure 5: Simple predicted mean vote for the air-conditioned room with thermostat setup of 24°C, 25°C and 26°C respectively

4. CONCLUSION

The wireless sensor network consisted of a microcontroller, XBee module, temperature/relative humidity sensors, collection unit and gateway. The sensor units communicated with the base station and the data collection unit via the gateway. Indoor weather was measured then transmitted to the display monitor and store in the computer using Visual studio, an open source, for the graphical user interface. It has found that the Zigbee wireless sensor network for indoor weather monitoring operate effectively. The occupant comfort calculated by the simple predicted mean vote equation from the previous study was found in the range of -0.3 to 0.35 during the thermostat setting of 24°C, 25°C and 26°C.

5. ACKNOWLEDGEMENT

Thank you Naresuan University for partly financial support to this research.

6. REFERENCES

- Abella, C.S., Bonina, S., Cucuccio, A., D'Angelo, S., Giustolisi, G., Grasso, A.D., Imbruglia, A., Mauro, G.S., Nastasi, G.A.M., Palumbo, G., Pennisi, S., Sorbello, G. & Scuderi, A. (2019) Autonomous Energy-Efficient Wireless Sensor Network Platform for Home/Office Automation. *IEEE SENSORS JOURNAL*. 19(9), 3501-3512.
- Ahmad, M. W., Mourshed, M., Mundow, D., Sisinni, M. & Rezgui Y. (2016) Building energy metering and environmental monitoring – A state-of-the-art review and directions for future research. *Energy and Buildings*. 120, 85–102.
- ASHRAE, Thermal environment conditions for human occupancy, in: ASHRAE Standard 55-2007, ASHRAE, Atlanta, 2007
- HIH 6131-021-001 Sensor. Available from <http://sensing.honeywell.com//HIH6131-021-001-Humidity-Sensors>. [Accessed 13th July 2019]
- Huang, L. C., Chang, H.C., Chen, C.C. & Kuo, C.C. (2011) A ZigBee-based monitoring and protection system for building electrical safety. *Energy and Buildings*. 43 (6), 1418-1426.
- ISO standard 7730, 3rd ed. (En), ISO (2005).
- Mylonas, A., Kazanci, O. B., Andersen, R. K. & Olesen, B. W. (2019) Capabilities and limitations of wireless CO₂, temperature and relative humidity sensors. *Building and Environment*. 154, 362–374.
- Olivia, G.S. & Christopher, T.A. (2015) In-use monitoring of buildings: An overview and classification of evaluation methods. *Energy and Buildings*. 86, 176-189.
- Rattanongphisat, W., Prachaona, T., Harfield, A., Sato, K. & Hanaoka, O. (2017) Indoor Climate Data Analysis Based a Monitoring Platform for Thermal Comfort Evaluation and Energy Conservation. *Energy Procedia*. 138, 211-216.
- Rattanongphisat, W., Suwannakom, A. & Harfield A. (2016) Indoor weather related to the energy consumption of air conditioned classroom: Monitoring system for energy efficient building plan. *IOP Conference Series: Earth and Environmental Science*. 40, 1-8.
- Yang, M.T., Chen, C.C. & Kuo, Y.L. (2013) Implementation of intelligent air conditioner for fine agriculture. *Energy and Buildings*. 60, 364–371.

#308: Energy-economic analysis of a small-scale hybrid trigeneration system including biomass-fired steam cycle and wind turbine

Rafał FIGAJ¹, Mariusz FILIPOWICZ²

¹ AGH University of Science and Technology, Faculty of Energy and Fuels, Mickiewicza 30, 30-059 Cracow, Poland, figaj@agh.edu.pl

² AGH University of Science and Technology, Faculty of Energy and Fuels, Mickiewicza 30, 30-059 Cracow, Poland, filipowicz@agh.edu.pl

In the last two decades, the concept of distributed generation changed the energy generation paradigm, determining a transition from centralised energy generation systems to diffused installations. An example of this transition is outlined by the fact that more and more small-scale energy systems have been installed over Europe in the recent years.

In particular, a special category of such systems consists of hybrid plants where more than one renewable energy is used. In small-scale hybrid applications, the investigation of biomass and wind energy is scarcely addressed in literature with respect to other hybrid configurations, as biomass and solar.

This paper presents a novel small-scale trigeneration system based on biomass combustion, water steam cycle, absorption chiller and wind turbine, suitable for rural areas where biomass resource was diffused and abundant. The system configuration included a bidirectional connection with the electric grid.

The investigation of the system was performed by means of the TRNSYS software and includes the analysis of the dynamic operation of the system and the energy and economic assessment of its performance. The model of the installation was developed using build-in and user developed components based on manufacturer data as well as realistic user demand. In particular, the system was designed to properly manage its energy flows in order to match the user thermal and electrical demand. The dynamic operation of the system was investigated on a daily and monthly basis, while the assessment of the global system performance was performed on a yearly basis. The performance system was investigated for different design parameters (components capacities and set-point temperatures) and in case of a capital investment incentive strategy.

The results show that the system allows one to achieve a significant saving of primary energy compared to a conventional system. However, the cost of the system was the main limit of presented technology in case of an absence of economic incentives.

Keywords: distributed generation; dynamic simulation; hybrid system; TRNSYS

1. INTRODUCTION

The issues concerning the energy production, arising from both world population increase and environmental impact of energy use, and the wide-spreading of renewables are changing dynamically the energy paradigm. In fact, the energy sector is facing new challenges (Jacobsson *et al.*, 2004) and it is adapting to match the concept of sustainable development (Lund, 2007). In the current situation, the conventional fossil fuels are starting to be abandoned in favor of renewable energy sources, being a reliable alternative to conventional sources (York, 2012). Speaking of renewable energy sources it must be considered they intrinsic characteristic, determined by variability and intermittency aspects (Su *et al.*, 2014), which determine that they are less suitable with respect to more programmable and manageable conventional energy sources. In addition to this, renewable energy sources present a relatively low energy density with respect to the area (Twidell *et al.*, 2015), determining a disadvantage for renewable energy use. These above-mentioned characteristics affect the capability of matching the thermal and electrical energy demand of users adopting only renewable energy source without energy storage systems. In fact, a continuous energy production is hardly to achieve with a single source of renewable energy. However, the combination of two or more energy sources in hybrid configurations (Deshmukh *et al.*, 2008) offers the possibility to mitigate the problems related to each renewable energy source. Hybrid renewable energy systems of small-scale are particularly suitable for distributed generation applications (Willis, 2018), especially biomass-based energy systems since they have a high potential of heat generation and limited constraints regarding the energy source availability (Wegener *et al.*, 2018). Therefore, they are suitable for heating/cooling and electrical energy applications. In addition to this, the hybridization of biomass with other renewable energy sources may allow one to achieve operation, environmental, energy and economic advantages (Wang *et al.*, 2016).

In the context of hybrid small-scale biomass-based energy systems, the integration of wind energy is not commonly investigated in literature. In Ref. (Morrone *et al.*, 2018) a biomass fired Organic Rankine Cycle was coupled with a wind turbine in an integrated system, where two sub-systems produced electrical and thermal energy for a domestic application. The sub-systems operated in parallel allowing to match the energy consumption requirements of a low energy consuming residential building. The wind turbine was simulated using real characteristics of five units (16.5 – 49.9 kW) and the weather data of Palermo, Southern Italy. The application of biomass-wind systems was also studied for stand-alone microgrids. In particular, in Ref. (Balamurugan *et al.*, 2011) a biomass gasifier with was integrated with a wind turbine for a case study of a village in India, where the electrification by the connection with the grid was not possible due to installation and economic issues. An electrical energy storage was integrated in the system in order to provide power to the user whatever was the availability of solar energy. In order to perform the analysis and optimisation of the proposed system, HOMER software and measured wind and load data of an Indian village were used. The economic optimisation was performed taking into account initial investment, operation and maintenance costs as function of the components size. For the selected case study, the optimal configuration consisted of 4 25 kW wind turbines, 200 batteries, a 150 kW gasifier and a 100 kW converter. A hybrid biomass-wind system was coupled with solar energy source in Ref. (Gonzalez *et al.*, 2018) in order to produce additional electrical energy. In this case, the hybrid renewable energy system consisted of photovoltaic panels, wind turbine and forest wood biomass gasifier fuelling an internal combustion engine. 265 W modules and wind turbine of a nominal power of 200 kW were selected for the photovoltaic and wind power subsystems, respectively, while, a gasifier/internal combustion system of 500 kW nominal power was considered for the biomass subsystem. In this study, a multi-objective optimisation based on genetic algorithm is carried out, determining a set of optimum solutions from the economic and environmental point of view. In Ref. (Zheng *et al.*, 2018), a microgrid system including biomass combined heat and power system was investigated. In particular, small-scale wind turbines, biomass gasifier, gas storage, photovoltaic modules, battery storage, thermal energy storage and auxiliary boilers were part of the system. The capacities of the system components and system operation schedule were considered in order to achieve the best economic performance. In this case, the authors shown that the optimum system configuration was a function of the electrical energy and natural gas prices, and energy demand magnitude.

As outlined by the analysis of the scientific literature, the investigation of small-scale hybrid biomass-wind systems is scarcely addressed as research topic. Therefore, in order to improve the knowledge about this issue, the authors present the analysis of a novel small-scale trigeneration system based on biomass combustion, water steam cycle, absorption chiller and wind turbine. In the authors' best knowledge, the proposed system is investigated for the first time in literature, since no papers are available dealing with such kind of system for a small-scale application. The novelty of the paper consists also of the implementation of a realistic user thermal demand.

The investigation of the system was performed by means of the TRNSYS software and includes the analysis of the dynamic operation of the system and the energy and economic assessment of its performance. The model of the installation was developed using build-in and user developed components based on manufacturer data.

In the following, the layout and operation strategy of the system is presented, along with the presentation of the case study. Finally, the results are discussed presenting dynamic operation of the system on daily and monthly basis, while a yearly time basis is used to the assessment of the global system performance.

2. LAYOUT OF THE SYSTEM

The proposed hybrid system integrates a water steam power cycle and a wind turbine in order to produce electrical energy, while the thermal energy rejected by the cycle is supplied to the heating system of the user during the winter period, while required during the cooling season it is supplied to an absorption chiller to produce space cooling. The basic system layout has been shown in Figure 1, along with the main components of the system and loops.

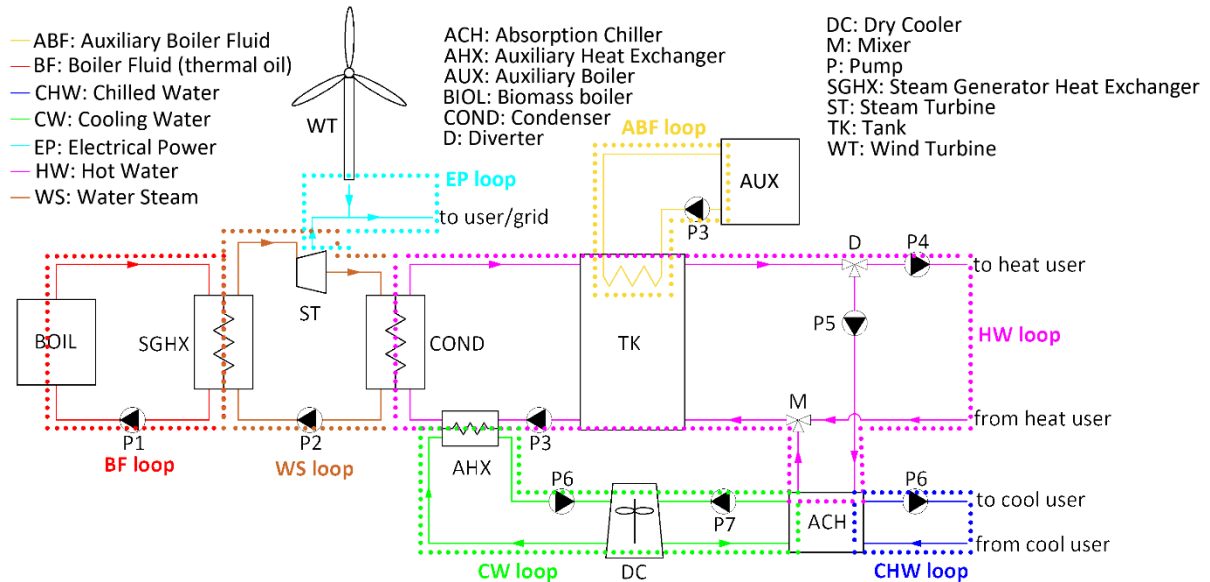


Figure 2: Layout of the proposed biomass-wind hybrid system.

The proposed system consists of several loops: Boiler Fluid (BF), Water Steam (WS), Hot Water (HW), Chilled Water (CHW), Cooling Water (CW), Auxiliary Boiler Fluid (ABF). The main components of the proposed system are as follows:

- biomass boiler, BOIL, consisting of a thermal oil unit powered by wood chips combustion;
- steam generator heat exchanger, SGHX, consisting of a counterflow unit used to produce steam by means of hot thermal oil;
- steam turbine, ST, consisting of a low-pressure unit producing electrical power;
- condenser, COND, used to transfer the waste heat to the user;
- tank, TK, consisting of a stratified thermal storage allowing to buffer the produced heat between the production and utilisation parts of the system;
- auxiliary heat exchanger, AHX, used to dissipate when TK is thermally loaded
- auxiliary boiler, AUX, consisting of a biomass unit producing thermal energy when needed;
- absorption chiller, ACH, a LiBr-H₂O single stage unit;
- dry cooler, DC, used to dissipate the thermal power rejected by AHX and ACH when operating.

The layout of the system was complemented with additional required equipment such as circulation pumps (P), flow diverters (D) and mixers (M). The pumps (P1 – P8) were responsible for the circulation of the fluid within each loop as shown in Figure 1. The operation mode of the system is described as follows. The biomass boiler heats the thermal oil at its outlet to a set point temperature of 200°C. During this operation the thermal power of the boiler varies depending on the required load. The heated BF is supplied to SGHX to produce steam at a pressure of 8.0 bar and a temperature of 185°C. The steam is expanded in the turbine, producing electrical power, then is condensed in COND, supplied with HW stored in TK. The condensed water is supplied by P1 again to SGHX. AHX is activated when the temperature of HW returning from TK rises above 85°C, ensuring proper operation conditions of COND even when TK is thermally loaded. It is crucial to note that the boiler system is equipped with a variable speed pump, allowing to modulate its flow rate. This option was adopted in order control the mass flow of steam and, thus, the electrical power and thermal power rejected by the cycle. In general, such strategy was implemented to allow one a thermally load following operation of the trigeneration system. In particular, a proportional controller sets the flow rate as a function of the tank top temperature: 30% of the nominal flow is set when the temperature is 90°C, while 100% when 85°C is reached. In addition, when the tank temperature drops to 80 °C AUX is activated in order to increase the top temperature of the tank to 90°C. Furthermore, HW is supplied from TK during the heating season to the user, while during the cooling period to the generator side of the absorption chiller, producing chilled water at 7°C which is supplied to the user. In

addition, ACH is connected to DC, in order to dissipate the heat rejected by the condenser and absorber. Alongside with ST, WT produces additional electrical power which is supplied to the user or to the grid depending on the demand of the user.

3. MODEL

The proposed hybrid system was modelled and simulated with Transient System Simulation (TRNSYS) tool (Klein 2006), which is widely adopted in literature in order to simulate dynamic energy systems. The modelling and the simulation of the system in concern were performed using both built-in library components (e.g. pumps, mixers, diverters, valves, controllers, tanks, boilers, etc.) and user defined components (control system, absorption chiller, energy and economic model). The software library components were experimentally validated and/or were based on real operational data; thus, the outcomes of the simulation are highly reliable. In this section, only a description of the energy and economic model used to assess the global performance of the system user has been provided. Other component models are available in the TRNSYS software reference, thus they have been omitted for sake of brevity. Moreover, the implemented user-defined model of the absorption chiller was based on literature (Kohlenbach et al. 2008, Marc et al. 2012), while the wind turbine model was based on manufacturer data (ENAIR 70PRO) (ENAIR 2019).

3.1. Energy and economic model

The analysis of the global energy and economic performance of the proposed system (PS) was based on a comparison with a reference system (RS). In detail, two reference systems were considered:

- NG, consisted of a natural gas boiler, electrical chiller and the electric grid providing heating, cooling and electrical energy, respectively;
- BIO, consisted of a wood chip boiler and the same two components of NG system providing cooling and electrical energy.

In order to perform the analysis, the same amount of final energy provided to the user, in terms of heating, cooling and electrical energy, was assumed for all the systems. RS primary energy (PE) consumption was evaluated adopting a natural gas boiler system efficiency of 0.90, a Coefficient of Performance (COP) of the electrical chiller of 3.0 and a national electric grid efficiency of 0.33 (ABB 2011). Obviously, primary energy consumption of biomass boiler was set to zero. The primary energy consumed by RS and PS was calculated as follows:

$$\text{Equation 1: Primary Energy Consumption of RS.} \quad PE_{RS} = \begin{cases} \frac{E_{th,heating}}{0.9} + \frac{E_{th,cooling}}{3.0 \cdot 0.33} + \frac{E_{el,user}}{0.33} & \text{for NG} \\ \frac{E_{th,cooling}}{3.0 \cdot 0.33} + \frac{E_{el,user}}{0.33} & \text{for BIO} \end{cases}$$

$$\text{Equation 2: Primary Energy Consumption of PS.} \quad PE_{PS} = \frac{E_{el,grid}}{0.33}$$

Where:

- $E_{th,heating}$ = heating demand of the user (kWh)
- $E_{th,cooling}$ = cooling demand of the user (kWh)
- $E_{el,user}$ = electrical energy demand of the user (kWh)
- $E_{el,grid}$ = electrical energy provided by the grid for PS (kWh).

The Primary Energy Saving ratio (PESr) of PS with respect to RS was calculated as:

$$\text{Equation 3: Primary Energy Saving ratio.} \quad PESr = \frac{PE_{RS} - PE_{PS}}{PE_{RS}}$$

In order to evaluate the PS economic performance, investment costs of PS and the operating costs of both PS and RS were considered. In particular, the market cost data were used to determine the capital cost of PS components, in accordance with the procedure adopted in Ref. (Calise et al. 2018, Di Fraia et al. 2018). The specific cost was set to 10.0 and 4.0 k€/kW for the steam turbine trigeneration system and the wind turbine, respectively. The cost of the plant components was included in the total cost of the system and maintenance cost of PS of RS was assumed the same. For the calculation of the operating costs, the natural gas price was assumed to 0.0339 €/kWh for NG system (EUROSTAT 2019), while for the electrical energy a time-dependant tariff was adopted (TAURON 2019). The savings due to the electrical energy supplied to the grid were calculated using a strategy that allows one to (re)buy the electrical energy supplied to the grid at a price 80% lower than the current one. It is worth noting,

that this system is commonly used in Poland for renewable sources. As concerns the biomass price, two scenarios were assumed: BIO1 for which the wood chips were freely available for the user (as local residual biomass), and BIO2 for which the fuel cost was 0.06 €/kg with a lower heating value of 3.7 kWh/kg (Carotenuto et al. 2017). Under these assumptions, savings of PS under three scenarios (NG, BIO1 and BIO2) were calculated. Finally, the profitability of the system was evaluated with the Simple Pay Back (SPB) index as follows:

Equation 4: Simple pay Back calculation.
$$SPB = \frac{C_{PS}}{J_{PS}} \text{ for NG, BIO1 and BIO2}$$

Where:

- C_{PS} = total cost of the proposed system (€)
- J_{PS} = saving of the proposed system in NG, BIO1 and BIO2 scenarios (€/year).

4. CASE STUDY

In order to investigate the system performance, a typical zootechnical farm with household was adopted as case study. The household consisted of sloped roof structure with one floor and an attic, while the farm consisted of two halls. The household had a floor area of 100 m² while both farms halls were 500 m² each. The height of the house was 2.7 m, while for the halls it was between 3.5 to 5.5 m. The climatic conditions were simulated adopting the Meteoronorm weather data for Gdansk, located in Northern Poland. The building structure for the developed case study have been shown in Figure 2.

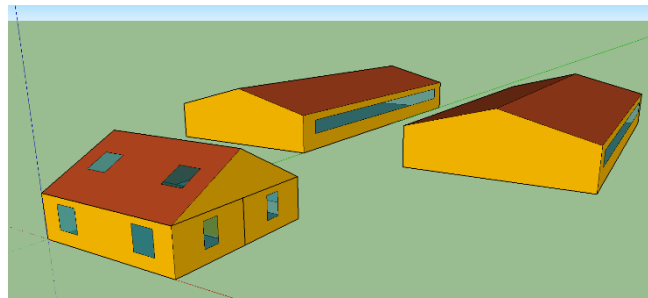


Figure 2: Structure of the buildings used in the case study.

The components of the building, as walls, roofs and floors, were modelled using several series of layers (omitted for brevity), characterised by thermal transmittances reported in Table 1.

Table 1: Thermal transmittances of the building elements in W/m²/°C.

Component	Value	Component	Value
House, external wall	0.400	Window	2.80
House, Adjacent wall	2.20	Hall, external wall	0.540
House, Ceiling	1.78	Hall, roof	0.460
House, Roof	0.320	Hall, ground floor	1.44
House, Ground floor	0.367	-	-

The operation of the space heating and cooling system was set from to October 15th to March 31st and from May 1st to September 15th, respectively, with a 24/24h daily schedule. During that time, air temperature was set to 20°C during winter and 26°C during summer. The building model was developed with Google SketchUP tool and TRNSYS3d plug-in (Klein 2006). Moreover, typical thermal loads of the considered building were implemented to take into account of the building thermal behaviour: equipment, lights, fresh air infiltration, etc. The heating and cooling demand, determined with the building dynamic simulation, was reported in Figure 3. Moreover, the electrical demand was taken from standard profiles available for users as the one here investigated (TAURON 2019). The electrical energy consumption per year of the user was set to 50 MWh, which is common for this kind of utility (OZERISE 2011).

As regards the proposed system, the main design and operating parameters have been reported in Table 2. It is important to note that in this table only the key parameters adopted in the simulations were reported, due to reasons of brevity. The thermal oil properties were taken from manufacturer data (ORLEN 2019).

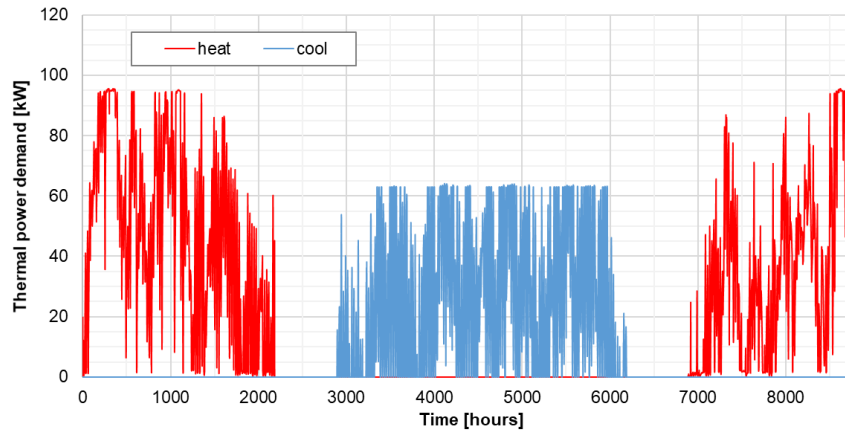


Figure 3: Thermal demand of the buildings.

Table 2: Main parameters of the proposed system (for the component identification see Figure 1).

Parameter	Value	Unit	Parameter	Value	Unit
BOIL capacity	70	kW-	TK, volume	20	m ³
BOIL, outlet temperature	200	°C	P4, mass flow rate	4125	kg/h
P1, mass flow rate	2600	kg/h	P5, mass flow rate	7300	kg/h
Thermal oil specific heat	2.15	kJ/kg/°C	AUX, capacity	100	kW
Thermal oil density	867	kg/m ³	ACH, capacity	70	kW
P2, outlet pressure	8.0	bar	ACH, set-point temperature	7.0	°C
SGHX, pinch point temp. diff.	10	°C	P6, mass flow rate	3600	kg/h
ST, power	6	kW	P7, mass flow rate	18400	kg/h
ST, outlet pressure	0.9	bar	P8, mass flow rate	5500	kg/h
ST, isentropic efficiency	0.75	-	DC, air mass flow rate	64400	kg/h
COND, pressure	0.9	bar	WT, power	4.5	kW
COND, pinch point temp. diff.	10	°C	WT, hub height	15	m
P3, mass flow rate	3600	kg/h	WT, shear site coefficient	0.14	-

5. RESULTS

Temperature and power trends and integrated variable were returned by the dynamic simulation of the developed model. The simulation was carried out with a 0.02 h time step for a one-year basis, from 0 to 8760 h. With these parameters, a large amount of dynamic data was generated by the simulation, thus only the most important results were reported in this paper. In particular, the dynamic operation of the system is shown for a typical summer operation day in terms of temperature trend, while the behaviour of the system during the year was presented adopting a monthly time interval.

The trends of the outlet temperatures of the main system components for the selected representative day of 16th May (from 3268 to 3292 h) are shown in Figure 4. In this figure, it is clearly shown that the boiler system allows one to ensure a stable outlet temperature of the thermal oil (200°C), and, as a consequence, the same trend was registered of the temperature of the steam at the outlet of SGHX (184°C). This was achieved because the boiler control strategy was adequate in order to fix the outlet temperature of the working fluid. The constant operation conditions in terms of temperature was also present for ST, which outlet temperature was 97 °C. It is important note that variable trends of thermal and electrical powers were registered during the selected day, however, they are not reported for brevity (the variability of energy flows are shown in the weekly analysis). This variability was in part shown by the outlet temperatures of TK and cold used. In fact, during the selected day both temperatures oscillated as a function of the cooling thermal load.

The results of the monthly analysis are shown in Figure 5 and Figure 6 in terms of thermal and electrical energy, respectively. The thermal energy provided by BOIL was maximum during the coldest and hottest months of the year, due to the significant thermal demand for heating and cooling during such periods. In fact, the thermal energy provided to the steam cycle is lower during the mid-seasons, when the thermal demand is practically null. This is coherent with the thermal load following control strategy of the trigeneration system. The behaviour of the system determined that a significant part of the thermal energy was dissipated through AHX in order to ensure a proper

operation of COND. In this way, a significant amount of boiler thermal energy was wasted and only electrical energy was usefully generated by ST. Moreover, the analysis of the trends pointed out that BOIL matched the major part of the thermal demand of the user. Nevertheless, AUX must to be activated during almost entire year. This result was achieved because BOIL capacity was undersized with respect to the thermal demand of the user, in order to a reach a high level of heat recovery from the power cycle and to avoid energy waste. It is worth noting that the cooling energy supplied by the evaporator of ACH covers entirely the user demand.

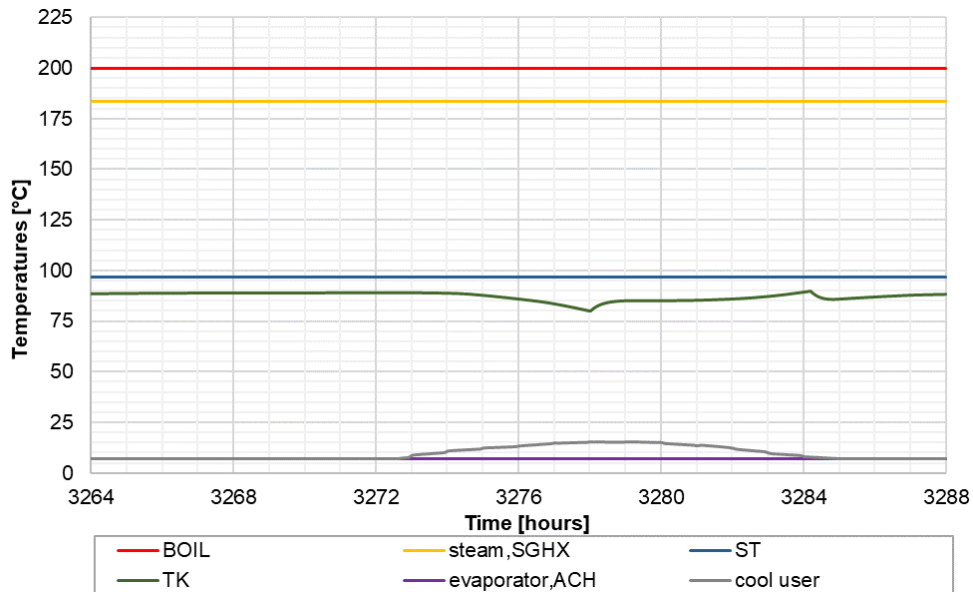


Figure 4: outlet temperatures of the main system components.

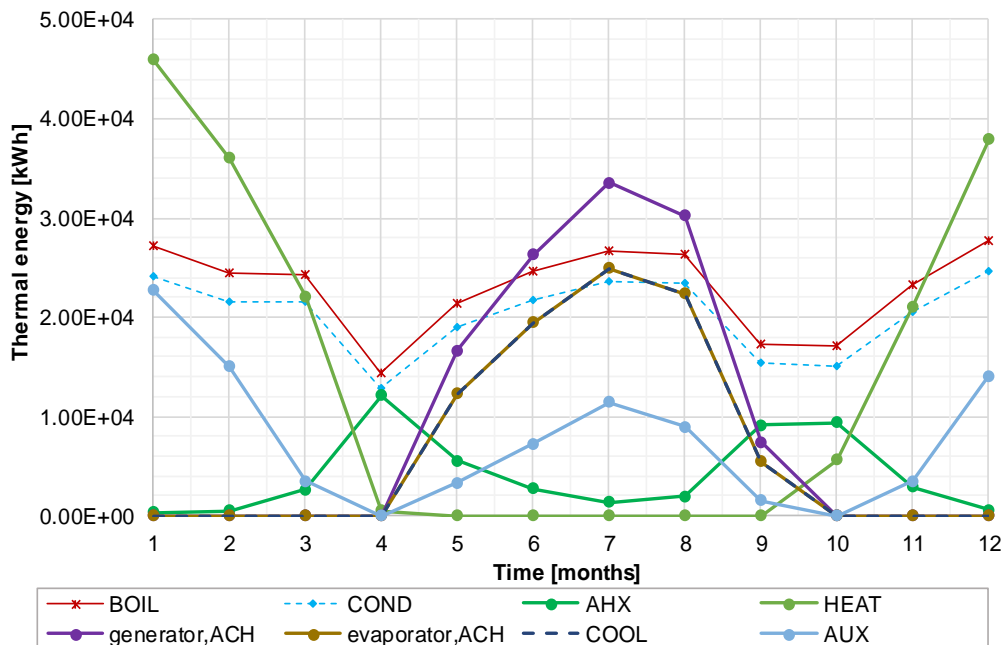


Figure 5: Thermal energy flows of the main system components.

The analysis of the electrical energy flows reported in Figure 6 showed that the electrical energy produced by the system is almost entirely consumed by the user.

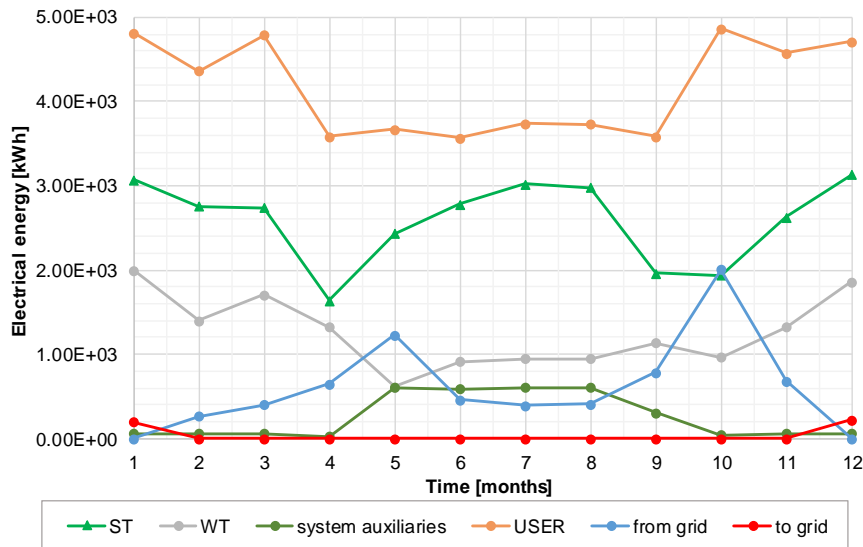


Figure 6: Electrical energy flows of the prosed system.

The electrical energy produced by ST assumed the same trend of the thermal energy produced by BOIL, in fact the higher the thermal input to the steam cycle, the higher was the evaporated mass of water and thus the work produced. The electrical energy by ST produced varied between 1.64 to 3.13 MWh, showing that it operated at partial load especially during the mid-seasons. The wind turbine energy output was higher during the winter due to the availability of wind energy in such period. The maximum energy was achieved in January while the minimum in May. Furthermore, the system auxiliaries had a significant impact on the electrical energy flows during the summer period, since the activation of DC loop for ACH cooling required more power than the one needed to operate only the pump system. Nevertheless, in summer the electrical energy provided by the grid was lower, mainly because ST has run at high load and the used demand was relatively low. The power supplied by the grid was null during December and January due to: i) the significant energy production of ST and WT, and ii) the negligible power consumption of the system auxiliaries. In general, the power provided by the grid was higher when ST operates at reduced load.

The thermal and electrical energies of the main components of the hybrid biomass-wind system have been reported in Table 3. The thermal energy produced by BOIL and transferred to SGHX was higher than the one provided by AUX. This occurred because BIOL operates continuously during the year, while AUX was activated only when needed in order to heat TK. As pointed out by the results, BIOL provided 75.1 % of the thermal input to the system. In the considered steam cycle design configuration, the amount of thermal energy transferred by COND to the cooling medium (HF) was 88.7 % of the one supplied by SGHX to the cycle. This expected result was achieved since the steam cycle operated with relatively small pressure and maximum temperature. Therefore, the amount of produced electrical energy by ST was relatively low. It is also worth noting that the thermal energy dissipated by AHX was not negligible, because it was equal to 49.1 MWh. The ratio between this value and the total heat supplied by COND and AUX was 14.7 %. This occurred because the steam cycle was meant to operate continuously, and even at partial load, a small amount of thermal energy must be dissipated due to a relatively small thermal load and thermally loaded tank. As concerns the electrical energy production, the wind turbine produced 32.5 % of the yearly yield, thus the mayor part was produced by ST, as also pointed out by the monthly results. Moreover, the produced electrical energy allowed one to match 87.1 % of the user demand, with limited electrical energy excess, being less than 1 % of the production. This result occurred due to a proper sizing of the hybrid system components.

Table 3: Thermal and electrical energies of the hybrid system.

Component	Value [kWh]	Component	Value [kWh]
BOIL	2.74E+05	DC	1.94E+05
SGHX	2.74E+05	user,heat	1.69E+05
COND	2.43E+05	user,cool	8.44E+04
AHX	4.92E+04	ST	3.11E+04
AUX	9.12E+04	WT	1.51E+04
generator, ACH	1.14E+05	system auxiliaries	3.09E+03
absorber, ACH	1.06E+05	user,electical	5.00E+04
condenser, ACH	8.81E+04	from grid	6.31E+03
evaporator, ACH	8.45E+04	to grid	4.14E+02

The efficiency and economic parameters have been reported in Table 4. A relatively low efficiency of ST was achieved due to the parameters adopted for the Rankine cycle. This determined a thermodynamic limit for the maximum efficiency achievable by the present steam system. As regards the wind turbine, the wind conditions of the selected locality determined that the equivalent number of operation hours was more than 3300 h. This value highlighted that the availability of wind source was significant, determining favorable conditions for the installation of such kind of system. Moreover, the thermally driven unit achieved a COP of 0,74, which is coherent with the technology of single-stage LiBr-water absorption units. PESr of the proposed system depended on the selected reference system. The hybrid system achieved a remarkable primary energy saving (more than 90 %) in both NG and BIO reference system scenarios. As expected, PESr was higher in case of NG with respect to BIO due to the savings of natural gas generated by the adoption of biomass in the proposed system. The proposed system consumed only the primary energy related to the electrical energy provided by the grid, while in case of NG scenario the reference system consumed a high amount of primary energy due to the adoption of conventional technologies. The proposed system achieved a relatively lower PESr in case of BIO scenario, since the conventional system in this case was based on the utilisation of biomass for space heating purposes. The economic parameters showed that significantly higher savings were achieved in case of NG scenario with respect to BIO1 and BIO2. This is due the cost of the natural gas which was higher than the biomass. Moreover, it is worth noting that the savings of the proposed in case of BIO2 scenario was only due to the avoided consumption of electrical energy. In this economic context, SPB index varied from 6.56 years for NG scenario to 35.0 years for BIO2. Despite a relatively high cost of the system, the economic profitability was affected by the type of fuel used in the reference system; natural gas or biomass. The proposed system in case of NG scenario was fairly feasible from the economic point of view, while it was less attractive for BIO1 scenario. In case of a reference system with a heating system supplied with a not cost-free biomass (BIO2), the proposed system is not feasible from the economic point of view. Finally, in the situation when a capital investment incentive of 50 % was available, the proposed system profitability significantly increased in case of NG and BIO1 scenario, since SBP values were halved.

Table 4: Energy and economic performance parameters of the hybrid system.

Parameter	Value	Unit	Parameter	Value	Unit
efficiency, ST	0.113	-	savings,BIO1	5.83E+03	€/year
equivalent hours, WT	3.36E+03	hours	savings,BIO2	2.29E+03	€/year
COP, ACH	0.740	-	system cost	8.00E+04	€
PESr, NG	0.948	-	SPB,NG	6.56E+00	years
PESr, BIO	0.906	-	SPB,BIO1	1.37E+01	years
savings, NG	1.22E+04	€/year	SPB,BIO2	3.50E+01	years

6. CONCLUSION

The integration of a small-scale biomass (wood chips) steam cycle with a wind turbine in hybrid configuration was investigated from the energy and economic point of view by means of a dynamic simulation model developed in TRNSYS. In order to perform the analysis two reference systems were considered. The first one (NG) consisted of a natural gas boiler, electrical chiller and the electric grid providing heating, cooling and electrical energy, respectively. The second one (BIO), consisted of a wood chip boiler and the same two components of NG system providing cooling and electrical energy. In addition, for BIO two conditions were assumed: i) with cost-free biomass (BIO1) and ii) with market price biomass (BIO2). The analysis of the result of the dynamic simulation showed that:

- the boiler system allowed one to ensure a stable outlet temperature of the thermal oil (200°C), and, as a consequence, the same trend was registered of the temperature of the steam at the outlet of SGHX (184°C);
- the monthly production of electrical energy of steam turbine varied between 1.64 to 3.13 MWh, showing that it operated at partial load especially during the mid-seasons. The wind turbine energy output was higher during the winter due to the availability of wind energy in such period;
- the produced electrical energy allowed one to match 87.1 % of the user demand, with limited electrical energy excess, being less than 1 % of the production;
- the efficiency of the steam turbine was 0.113, due to the relatively low maximum cycle temperature (about 185 °C) and pressure (8.0 bar);
- the wind conditions of the selected locality (Gdansk, Poland) determined that the equivalent number of operation hours of the wind turbine was more than 3300 h.
- SPB index varied from 6.56 years for NG scenario to 35.0 years for BIO2. Despite a relatively high cost of the system, the economic profitability was affected by the type of fuel used in the reference system; natural gas or biomass.

Future development of this study will include a sensitivity analysis and an optimisation aiming at determine the effect of the design and economic parameters on the performance and best configuration for the hybrid system layout.

7. ACKNOWLEDGEMENTS

This work was carried out under statutory research of AGH University of Science and Technology, Faculty of Energy and Fuels, Cracow. The authors acknowledge for the use of the infrastructure of the Center of Energy, AGH UST in Cracow.

8. REFERENCES

ABB, 2011. Poland - Energy efficiency report. *ABB*,

Balamurugan, P., et al., 2011. An optimal hybrid wind-biomass gasifier system for rural areas. *Energy Sources, Part A: Recovery, Utilization, and Environmental Effects*, 33 (9), 823-832.

Calise, F., et al., 2018. Energy and economic analysis of energy savings measures in a swimming pool centre by means of dynamic simulations. *Energies*, 11 (9), 2182.

Carotenuto, A., et al., 2017. A novel solar-geothermal district heating, cooling and domestic hot water system: Dynamic simulation and energy-economic analysis. *Energy*, 141 2652-2669.

Deshmukh, M. and S. Deshmukh, 2008. Modeling of hybrid renewable energy systems. *Renewable and Sustainable Energy Reviews*, 12 (1), 235-249.

Di Fraia, S., et al., 2018. An integrated system for sewage sludge drying through solar energy and a combined heat and power unit fuelled by biogas. *Energy Conversion and Management*, 171 587-603.

ENAIR, 2019. https://www.enair.es/descargas/Ficha_Tecnica/Ficha_Tecnica_E70_en.pdf.

EUROSTAT, 2019. Environment and energy database.

Gonzalez, A., et al., 2018. Environmental and cost optimal design of a biomass–Wind–PV electricity generation system. *Renewable Energy*, 126 420-430.

Jacobsson, S. and A. Bergek, 2004. Transforming the energy sector: the evolution of technological systems in renewable energy technology. *Industrial and corporate change*, 13 (5), 815-849.

Klein, S. A., et al., 2006. Solar Energy Laboratory, TRNSYS. A transient system simulation program. *University of Wisconsin, Madison*,

Kohlenbach, P. and F. Ziegler, 2008. A dynamic simulation model for transient absorption chiller performance. Part I: the model. *International journal of refrigeration*, 31 (2), 217-225.

Lund, H., 2007. Renewable energy strategies for sustainable development. *Energy*, 32 (6), 912-919.

Marc, O., et al., 2012. Assessing performance and controlling operating conditions of a solar driven absorption chiller using simplified numerical models. *Solar Energy*, 86 (9), 2231-2239.

Morrone, P., et al., 2018. Investigation of Integrated Organic Rankine Cycles and Wind Turbines for Micro-Scale Applications. *Energy Procedia*, 148 986-993.

ORLEN, 2019. http://www.ornoil.pl/EN/OurOffer/Products/Pages/produkt.aspx?produkt=ITERM_6_MB.aspx,

OZERISE, 2011. Institute for Renewable Energy, Poland, <https://ozerise.pl/en/>.

Su, W., et al., 2014. Stochastic energy scheduling in microgrids with intermittent renewable energy resources. *IEEE Transactions on Smart Grid*, 5 (4), 1876-1883.

TAURON, 2019. C12a standard load curve, https://www.tauron-dystrybcja.pl/-/media/offer-documents/dystrybcja/uslugi-dystrybcyjne/iriesd/iriesd-teskt/2018-07-16-iriesd_tauron-dystrybcja-tekst-jednolity.ashx.

TAURON, 2019. C12a tariff, <https://www.tauron.pl/dla-firm/prad/taryfa-sprzedawcy/firma-aktywna-c12a>.

Twidell, J. and T. Weir, 2015. Renewable energy resources. 3rd edition. Abingdon, Great Britain: Routledge.

Wang, J. and Y. Yang, 2016. Energy, exergy and environmental analysis of a hybrid combined cooling heating and power system utilizing biomass and solar energy. *Energy Conversion and Management*, 124 566-577.

Wegener, M., et al., 2018. Biomass-fired combined cooling, heating and power for small scale applications—A review. *Renewable and Sustainable Energy Reviews*, 96 392-410.

Willis, H. L., 2018. Distributed power generation: planning and evaluation. 1st edition. Boca Raton, Florida USA: Crc Press.

York, R., 2012. Do alternative energy sources displace fossil fuels? *Nature Climate Change*, 2 (6), 441.

Zheng, Y., et al., 2018. Optimization under uncertainty of a biomass-integrated renewable energy microgrid with energy storage. *Renewable Energy*, 123 204-217.

#312: The implementation of micro hydro power at Diwak River, Semarang, Central Java, Indonesia

Chairiyatul FITRI*, Noah Joel Theofillus WANTAH, Ahmad Farhan NUGRAHA, Abdul NAJIB

*Department of Geological Engineering, Faculty of Engineering, Universitas Diponegoro, 50275, Tembalang, Semarang, Central Java, Indonesia,
Corresponding author: chairyf@gmail.com

Recently, the electrical needs of Indonesia has become a very important sector, but country-wide electrification is still only at 6th position in the Southeast Asia region, therefore in 2019, the government aims to increase electrification to 99.99 percent. However, it must also be balanced by the increase in the use of New and Renewable Energy (NRE). This is in accordance with the target of the Ministry of Energy and Mineral Resources to achieve 23 percent of NRE by 2025. One of the areas in Indonesia that has potential for the utilisation of applied renewable energy is Diwak Village, Semarang, Central Java. The energy in question is micro-hydro power (MHP). This research aims to determine the potential of micro-hydropower in Diwak Village, Semarang. Basically, micro-hydro power (MHP) could be used for an area that has stable water flow discharge and adequate slope. The methods to calculate these include the float method for flow discharge data, Rock Mass Rating (RMR), and calculating the capacity power. As a result, lithologies at the location are the volcanic and autoclastic breccia. The flow discharge in Diwak River is 0.29 m³/sec, and the minimum power that will be generated with its discharge is 40.29 KW. These results sum up that the flow has good potential in utilising MHP in Diwak Village.

Keywords: renewable energy; power; discharge; Micro-hydro; Diwak

1. INTRODUCTION

Nowadays, the electrical needs in Indonesia have become an inseparable aspect of people's daily needs, but the electrification ratio in Indonesia is still at 6th position in Southeast Asia that reached 98.3 percent in 2018 (ASEAN Centre for Energy, 2019). This number implies the fact that there is still enough space to optimise the electrification percentage in Indonesia. Therefore, the government set the target to achieve 99,99 percent at the end of 2019.

The Ministry of Energy and Mineral Resources continues to promote new and renewable energy resources and aims to increase the use of renewables up to 23 percent by 2025 (Patria, 2018). Renewable energy sources, such as solar, wind, geothermal, and hydropower have excellent potential to generate electricity. Among those sources, hydropower is the most reliable source. One form of hydropower-energy is Micro-hydro Power (MHP), a type of hydroelectric power scheme that produces from 5 up to 100 KW of electricity using flowing steam or water flow.

There are several areas in Indonesia which have potential as micro-hydro utilisation areas. One of them is in Diwak River, Semarang, Central Java. Thus, this study aims to find out the potential power generation if micro-hydro power is developed in this area.

2. METHODS

This study used primary and secondary data. The primary data consists of measuring flow data using the float method, slope, and rock strength index using Rock Mass Rating (RMR). The secondary data included the population and the average precipitation data in Diwak Village, Semarang.

2.1. Lithology

Lithology determination used petrological analysis to discover the type of rock, texture, structure, and mineral composition. The outcrop could reflect the base rock characteristic and be useful to help geotechnical assessment (Figure 1).



Figure 1: Field observation to get lithology and geometry of Diwak River

2.2. Geotechnical (Rock Mass Rating)

Geotechnical analysis was required in order to define the ground stability around the researched area, *Rock Mass Rating* (RMR) to be exact. According to Bieniawski (1989), usage of *Rock Mass Rating* (RMR) method is to provide quantitative and qualitative data through certain rock analysis; strength of intact rock material, rock quality designation, spacing of discontinuities, condition of discontinuities, and ground water condition.

2.3. Rainfall in Semarang

According to World Weather and Climate Information 2019, rainy season in Semarang highly falls in January, February, November, and December. Rainfall becomes an important aspect because it will affect the water volume in the river.

3. THEORY AND CALCULATION

Discharge measurements were carried out on the Diwak 1 and Diwak 2 River using the Float method. This method needs two types of information, cross sectional area of the water flowing in the stream and the speed that water is flowing. Normally, this method uses an eggplant which has the same density as water and capped to makes an ideal float as shown in Figure 2.

The Float Method of Estimating Flow

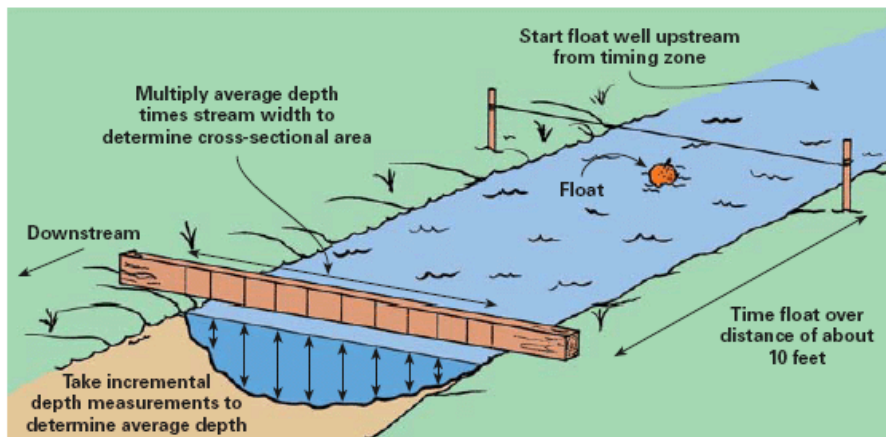


Figure 2: The float method of estimating flow (Suneco Hydro Turbines)

The equation to get the flow rate was:

Equation 19: Quantity of flow rate at Diwak River

$$Q = \frac{V}{t} = \frac{l \times h \times w}{t}$$

Where:

- Q= quantity of the flow rate (m³/s)
- V= Volume (m³)
- l= long (m)
- h= height (m)
- width= (w)
- t= time (s)

The flow rate was calculated in a capacity power calculation. Based on equation (2) below, by using Standard International unit, the power was calculated by:

Equation 2: Quantity of theoretical of the power generation

$$P_{theoretical} = Q \times g \times H \quad (\text{Othman, 2017})$$

Equation 3: Quantity of the power generation (turbine)

$$P_{turbine} = P \times \mu_{turbine} \quad (\text{Arismunandar, 1991})$$

Equation 4: Quantity of the power generation (generator)

$$P_{generator} = P_{turbine} \times \mu_{generator} \quad (\text{Arismunandar, 1991})$$

Where:

- P = quantity of the power generation (kW)
- Q = stream flow (m³/s)
- H = the effective head or the elevation (m)
- G = acceleration due to gravity (m/s²)
- $\mu_{turbine} = 0.7$
- $\mu_{generator} = 0.8$

4. RESULTS

4.1 Geomorphological aspect

The study was conducted at two branches of the Diwak river. The difference between them is on the presence of waterfalls. River 1 has a waterfall, namely Grenjeng waterfall. It is 7 m high, but River 2 does not. However, the waterfalls indicated a steep slope, which is one of the main aspects of micro-hydro power. Based on the field observation, the research location had 25 meters of elevation and a fairly steep slope of 45°.

4.2 Geological and geotechnical aspect

Field observation in Diwak River revealed two kinds of lithology; volcanic breccia, and autoclastic breccia. The determination of this type of lithology was based on petrology analysis. The volcanic breccia was black, had block-sized andesitic fragments (>64 mm) and ash matrix. (Figure 3). Meanwhile, the autoclastic breccia was black, had homogenic fragments and matrix. Its texture was crystalline (Figure 4).



Figure 3: Volcanic Breccia in Diwak



Figure 4: Autoclastic Breccia in Diwak

The lithology related to the geotechnical aspect. This Geotechnical Analysis used the Rock Mass Rating (RMR) method based on Bienawski (1989). The RMR score of volcanic breccia rocks was 61 (Table 1). It implied that volcanic breccia was included in the Good Rock quality (Bieniawski, 1989). So, it was quite resistant and stable, and suitable to be a location for developing micro-hydro power.

Table 19: Rock Mass Rating score of the volcanic breccia (Bienawski, 1989)

Lithology	Parameter					Total Rating
	Compressive Strength	RQD (Palmstrong, 1982)	Spacing of Discontinuities	Condition of Discontinuities	Groundwater Condition	
Volcanic Breccia	Strong Uniaxial Comp. Strength: 50-100 Mpa, Point Load Index: 2-4 Mpa	82	60-200 mm	Slightly rough surface, separation <1mm, highly weathered walls	Damp	
Rating	7	17	8	19	10	61

4.3 Hydrogeological aspect

Flow measurements were carried out at the Diwak 1 and Diwak 2 River using the Floating method. Tables 2 and 3 show the results of measurements of discharge in Diwak 1 and 2. Table 2 is the result of calculating river discharge in the dry season, while Table 3 is the calculation of river discharge in the rainy season.

The results of the calculation show that the Diwak 1 had a greater discharge number, thus the potential for the development of the micro-hydro power is greater to be developed in the Diwak River 1. The discharge generated in Diwak 1 was 0.29 m³/s and 1.33 m³/s.

Table 2: Flow rate on dry season

River	h	w	L	V	t	Q	H
Diwak 1	0.29	2.1	10	6.1	20.74	0.29	25
Diwak 2	0.3	2.2	10	6.6	31.36	0.21	25

Table 3: Flow rate on wet season

River	h	w	l	V	t	Q	H
Diwak 1	0.58	2.1	15	18.27	14	1.33	25
Diwak 2	0.8	2.2	12	21.12	16.5	1.33	25

5. DISCUSSION

The result show that flow discharge of the river is 0.29 m³/s in the Diwak 1 and 0.21 m³/s in the Diwak 2. It reveals that the flow in Diwak 1 is bigger, so, by 0.29 m³/s, the electrical power that can be produced is about 40.29 KW for each operation (Table 4) (sample based on Flow Rate in Dry Season). We assume that the operation system works for three times in a day. As a result, the power will get to 3626.1 KWH per month.

Table 4: Estimation of Micro-Hydro electricity power

River	Q	H	P	Pt	Pg
Diwak 1	0.29	25	71.94	50.36	40.29
Diwak 2	0.21	25	51.57	36.10	28.88

Furthermore, the micro-hydro power plant needs preliminary design for future planning model conceptual design in Diwak Village. In this research, the micro-hydro power plant planning consists of six part. First is the spill point, where the river stream is divided into two with one flow becoming an artificial river. This artificial river flows to a water dam which saves the water before releasing it into the turbine and generator house or powerhouse through pipes. Finally, the water returns to the main river. Based on power plant design, water discharge could be controlled by the water dam and pipes. Meanwhile the elevation difference is controlled by placement of the water dam and the powerhouse (Figure 5).

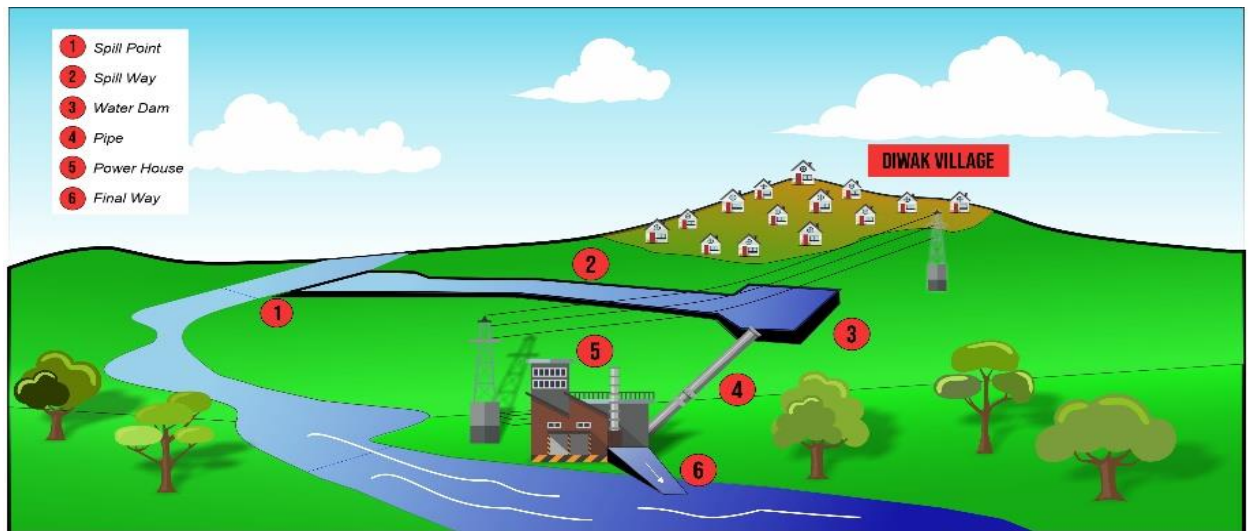


Figure 5: Micro-Hydro planning conceptual model at Diwak River

6. CONCLUSION

In this paper, the necessity of exploring energy from new and renewable sources and the impact of micro-hydro as a new and renewable source has been presented. This electrical energy will be distributed at approximately 3626.1 kWh per month to light up the village. It concludes that Diwak River has huge potential for developing a micro-hydro power. As a result, this energy will help people to have access to reliable and affordable electricity services, not only in Diwak but it also can be applied to other rural areas in Indonesia, as long as there is sufficient elevation and water flow.

7. REFERENCES

Arismunandar, A. 1991. Buku Pegangan Teknik Tenaga Listrik I. Jakarta: PT. Pradnya Paramita.

ASEAN Centre for Energy, 2019. "How Does Renewable Power Generation Capacity Contribute to ASEAN's Grid Interconnection During the First Quarter of 2019?", accessed 30th June 2019, <<http://www.aseanenergy.org/blog/energy-insight/how-does-renewable-power-generation-capacity-contribute-to-aseans-grid-interconnection-during-the-first-quarter-of-2019/>>

Bienawski ZT., 1989. Engineering Rock Mass Classification: A Complete Manual for Engineer and Geologists in Mining, Civil, and Petroleum Engineering.

Othaman, A., Jamel Othman, Wan Mohd Khairudin, Ahmad Shakir, and Abd Gani, 2017. Water Flow Measuring Methods in Small Hydropower for Streams and Rivers-A Study. International Journal of Applied Engineering 2017; 12(24):14484-14489.

Patria, N, 2018. "Indonesia Races Against Time in Renewable Energy", *The Jakarta Post*, 30 May 2018, accessed 30 May 2019.

Suneco Hydro Turbine n.d., "How to Measure Water Flow", accessed 30 June 2019 <<https://www.micro-hydro-power.com/how-to-measure-water-flow.htm>>

World Weather and Climate Information n.d., accessed 20 October 2018. <<https://weather-and-climate.com/average-monthly-precipitation-Rainfall,semarang,Indonesia>>

#319: CFD-based analysis of a battery module with cylindrical lithium cells for automotive

Towards sustainable technologies in automotive

Beatrice PULVIRENTI¹, Emanuele PERSIANO¹, Giovanni SEMPRINI¹, Claudio ROSSI²

¹ Department of Industrial Engineering, University of Bologna, Viale Risorgimento, 2, 40136 Bologna, Italy

² Department of Electric Engineering, University of Bologna, Viale Risorgimento, 2, 40136 Bologna, Italy

The transition to sustainable development of society requires that mobility also moves in this direction. The critical issue in an electric car, in terms of energy consumption and performance, is the battery pack. In the automotive industry, there is a need for batteries with high energy density and large capacity that are safe at the same time. Lithium battery cells fulfill these requirements, if the temperature is controlled. The aim of this study is to simulate the battery thermal management system (BTMS) of a battery pack consisting of a significant number of cylindrical cells (between 1,000 and 10,000), starting from basic modules (bricks). The proposed solution has characteristics of modularity, quality, ease of integration, low cost, passive and active safety, local and remote diagnostic capacity, ease of recovery and reuse at the end of life. The BTMS considered in this paper is an air-cooling system where cold air is conveyed through lithium cells. The temperature distribution within the module of cylindrical Lithium cells is obtained by means of a Computational Fluid Dynamics (CFD) approach, where the conjugate heat transfer approach is adopted in order to find heat transfer convection between air and solid cells. Critical points are detected, where temperature peaks can occur in some conditions, such as during the charge of the battery under extreme external conditions. The sensitivity of various parameters, as the air-flow distribution and temperature, is found on the thermal performance for the proposed BTMS. The optimal air-flow conditions that give the best thermal performances for the brick are obtained. The results are generalised in order to give correlation between battery cells packing density, Nusselt number and air-flow Reynolds number.

Keywords: Electric mobility, Battery thermal management, CFD approach, air-cooling, conjugate heat transfer

1. INTRODUCTION

The quality of life indicators relating to pollution show that, in many cities and mega-cities, urban populations' health is affected by exposure to too high levels of pollutants' concentrations at street level. During the winter months, when the levels of pollutants' concentrations rise above the allowed limits, we often see, especially in the cities of southern Europe, the prohibitions of diesel or petrol vehicles in the municipalities. The greatest measure to overcome this problem would be a change in citizens' habits with a lower use of cars within the city in favour of public transport or bicycles. We think that also a transition from thermal engine vehicles (TEVs) to electric vehicles (EVs) is crucial to lower pollution concentrations within cities. Battery electric vehicles (BEVs) and plug-in hybrid vehicles (PHEVs) are electric vehicles with rechargeable batteries on board with high energy capacity storage. Batteries for electric vehicles are characterised by their relatively high power-to-weight ratio and energy density; smaller, lighter batteries would reduce the weight of the vehicle and improve its performance. Rechargeable batteries used in electric vehicles include lead-acid, Ni-Cd, nickel-metal hybrid, lithium-ion, Li-ion polymer, zinc-air and molten-salt batteries. The most common battery type used in modern electric vehicles are lithium-ion because of their high energy density compared to their weight. Opitz *et al.* (Opitz, 2017) compared the characteristics of different lithium-ion batteries for automotive applications. They compared the characteristics in terms of safety, thermal management systems, lifetime, battery management systems and second life usage. The lithium-ion batteries arranged in battery packs (BPs) have different typologies and sizes, depending on the characteristics of the vehicles where they are mounted. Table 1 shows the specifications of different EV models with lithium-ion batteries (Opitz, 2017).

Table 1: Specifications of different EV models with LIBs (Opitz 2017).

Vehicle Model – Type	Distance range (km)	BP size (kWh)	Power (HP)
Nissan Leaf (2016) – BEV	170	24 – 30	107
BMW i3 (2016) – BEV	130, 250 Range Extender	22	170
Tesla Model S (2015) – BEV	330 – 430	60 – 85	329 – 691
Tesla Model 3 (2017) – BEV	340 – 480	50 – 75	283 – 473
Hyundai Sonata (2016) – PHEV	43 electric, 965 combined	9.8	202
Chevrolet Volt (2016) – PHEV	85 electric, 675 combined	18.4	149
Toyota Prius (2016) – Hybrid	17 electric, 870 combined	0.75	130

The BPs mounted on Tesla models have the greatest energy storage and power. The BPs that appear to be the most suitable for automotive applications are assemblies of modules with cylindrical cells packed together. For instance, the BPs mounted on Tesla S have 16 battery modules with 444 cells each, for a total of 7104 cylindrical cells with format 18650. The cylindrical cells most used in automotive are the formats 18650, 26650 and 21700. Following the BU-301 standard, the code represents the cell size, *i.e.* the first two numbers in the code is the diameter of the cell and the second two are the height of the cell in millimetres. The principal problem connected to these batteries is the thermal management. The temperature change of batteries is usually inevitable because they are affected by environmental conditions and release heat during charging and discharging. Since the performance and life of lithium-ion batteries are very sensitive to temperature, an efficient battery thermal management system (BTMS) is required to maintain the proper temperature range and to minimise temperature gradients to prevent adverse effects from temperature. There are several review papers on BTMSs in the literature. Rao and Wang (Rao, 2011) give a review of the overall thermal energy management of BEVs, HEVs and fuel cell electric vehicles (FCEVs). They show different mathematical models of battery thermal behaviour that are fundamental for a proper design of BTMSs. These authors give a classification of BTMSs, according to the heat transfer mediums, such as liquid and phase change materials (PCMs). Wang *et al.* (Wang, 2016) give a classification of BTMSs according to thermal characteristics of Li-ion batteries and their external thermal management solutions. They examined equivalent circuit models of the Li-ion batteries to understand heat generation and investigated thermal runaway and thermal effects under the sub-zero temperature. Then, they give a classification of BTMS according to medium, such as air, liquid, PCMs, heat pipes and combinations of them. Liu *et al.* (Liu, 2017) reviewed the BTMS according to the phase change process, by distinguishing between the liquid-vapor phase change method and the solid-liquid phase change method as well as air-based and liquid-based BTMSs. Xia *et al.* (Xia, 2017) reviewed the existing BTMSs in terms of cell level and module level. At the cell level, the battery thermal behaviours including the amount of heat generation, heat transfer methods and thermal boundary conditions were investigated, while at the module level, various BTMSs were examined. They compared the efficiency of the air-based BTMSs with the liquid-based BTMSs according to the configuration of the cells (serial, parallel and mixed) and subcategorized the indirect liquid cooling system into tube cooling and plate cooling using mini and micro-channels. Kim *et al.* (Kim, 2019) give a classification of BTMSs according to thermal cycle options. The BTMS with a vapor compression cycle includes cabin air cooling, second-loop liquid cooling and direct refrigerant two-phase cooling. The BTMS without vapor compression cycle includes phase change material cooling, heat pipe cooling and thermoelectric element cooling. Each BTMS is reviewed in terms of the maximum

temperature and maximum temperature difference of the batteries. They propose a novel BTMS to provide an effective thermal management solution for the high energy density lithium-ion batteries.

In this paper, a Computational Fluid Dynamics (CFD) approach is introduced to simulate the thermal behaviour of battery cells in case of air-cooling systems. A conjugate heat transfer approach is adopted in order to find heat transfer convection between air and solid cells. Critical points are detected, where temperature peaks can occur in some conditions, such as during the charge of the battery under extreme external conditions. The sensitivity of various parameters, as the battery spacing, the air-flow distribution and temperature, is found on the thermal performance for the proposed BTMS. The optimal air-flow conditions that give the best thermal performances for the brick are obtained. The results are generalised in order to give a dependence between Nusselt number and air-flow Reynolds number and compared with analogue approaches (Erb, 2017; Wang, 2014; Fan, 2019).

2. A LUMPED PARAMETER APPROACH FOR MODELING THE BMTS

The CFD approach presented in this paper has the scope to provide heat exchange coefficients to lumped parameter approaches to simulate the thermal behaviour of a BP. In this way, a coupled electro-thermal model for cylindrical batteries can describe the transient behaviour of the BP. The terminal voltage is captured by an equivalent circuit model, and a thermal model is adopted to estimate the core and surface temperatures.

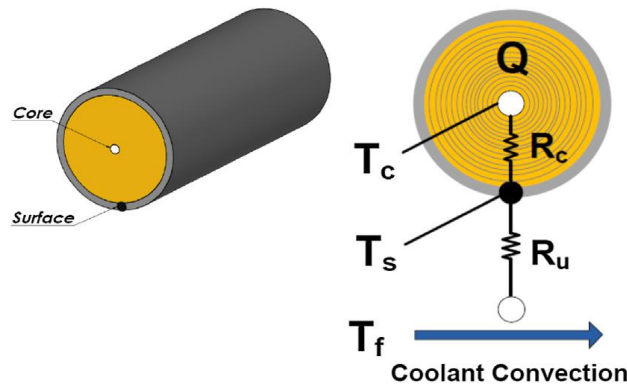


Figure 1: Scheme of the thermal resistances in a cell (Lin 2014).

The cell can be modelled a series of two thermal resistances, as shown by Figure 1 (Lin, 2014), where T_s and T_c are the temperature of the cell surface and the core temperature, respectively, while T_f is the cooling fluid temperature (air). A heat conduction resistance, R_c , is used to model the heat exchange between the core and the surface. Convective cooling through the battery surface is modelled by a convection resistance, R_u , between the cell surface and the cooling fluid. The value of R_u depends on the pack geometry, type of coolant and coolant flow rate. The core of the present paper is the determination of R_c and R_u by means of a CFD approach.

3. COMPUTATIONAL FLUID DYNAMICS (CFD) APPROACH

The geometry of a fundamental unit of the BP, or *brick*, is an arrangement of 16 cells, packed in two lines with 8 cells each. The brick is shown in Figure 2.

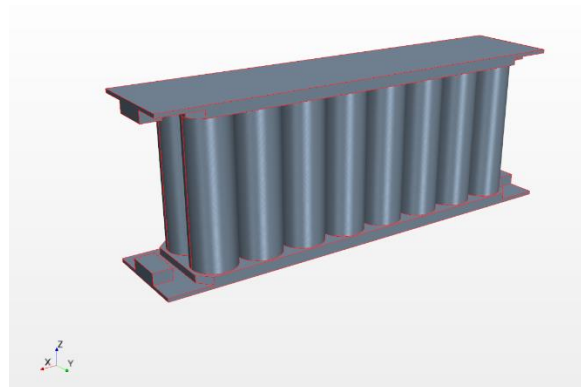


Figure 2: Geometry of a brick

In the present paper, the cells have a format 18650, *i.e.* the diameter is 18 mm and the height is 65 mm. The cells are connected to two electronic boards schematized as a 2.5 mm thick layer of glass-reinforced epoxy laminate material - FR4, with density 1850 kg/m³, thermal conductivity 0.3 W/(m K) and heat capacity 1200 J/(kg K). The horizontal dimensions of the electronic boards are 180 mm x 40 mm. The Li-ion cells have been considered as made by homogeneous material with density 2680 kg/m³, thermal conductivity 3.4 W/(m K) and heat capacity 1280 J/(kg K).

3.1. Computational domain

Two cases have been considered in this paper: a first case with a brick contained within a volume of air and a second case with the brick surrounded by other bricks, in a regular array within a BP. The two computational domains are shown in Figure 3. In the first case, the computational domain includes a volume of air around the solid brick. The volume dimensions in this case are 700 mm x 240 mm x 150 mm (L x W x H), where L is the direction parallel to the airflow, W is the directional perpendicular to the airflow and H is the vertical dimension. For the second case, the computational domain has a size of 180 mm x 40 mm x 70 mm (l x w x h).

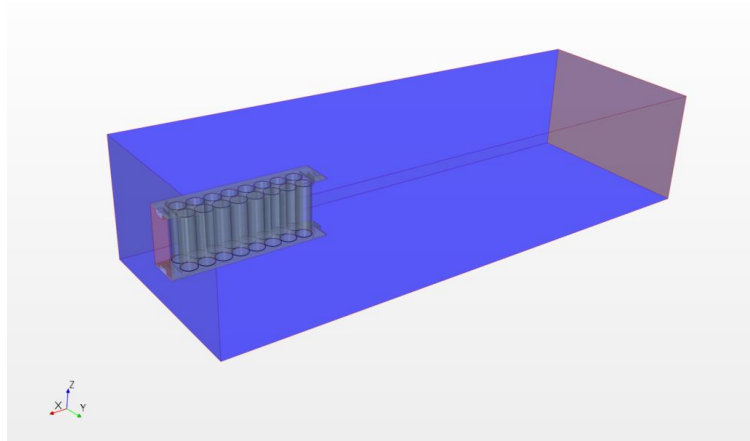


Figure 3: Computational domain for case 1.

In both cases, the inlet airflow condition is imposed on a surface perpendicular to the airflow direction, with the same dimensions of the brick lateral area, *i.e.* 40 mm x 65 mm (w x h), (red in Figure 3).

3.2. Discretization methods and meshes

Different meshes with the same constructive approach have been created for the two cases. The computational domain has been built using unstructured elements with a finer resolution close to the base and the cell walls. Several tests have been performed to verify grid size independence with increasing mesh numbers. For the first case, the smallest dimension of the elements, in the region near the cells, is 0.025 mm in the direction normal to the wall and 0.05 mm in the other directions. For the second case, the smallest dimension of the elements, in the region near the cells, is 0.005 mm in the direction normal to the wall and 0.007 mm in the other directions. The heat sources are modelled as volume sources with the dimension of the cylindrical cells. The final number of the computational cells is about 6.4 million cells for the first case and 8.2 million of cells for the second case. For the first case, symmetry boundary condition has been assigned to the lateral sides and the domain top, a velocity inlet condition was set to the inlet boundary and a pressure outlet condition to the outflow boundary. A no-slip boundary condition was applied at the bases and at the cells' surfaces. For the second case, periodic boundary conditions have been assigned to the lateral sides, while a velocity inlet condition was set to the inlet boundary and a pressure outlet condition to the outflow boundary. A no-slip boundary condition was applied at the bases and at the cells' surfaces.

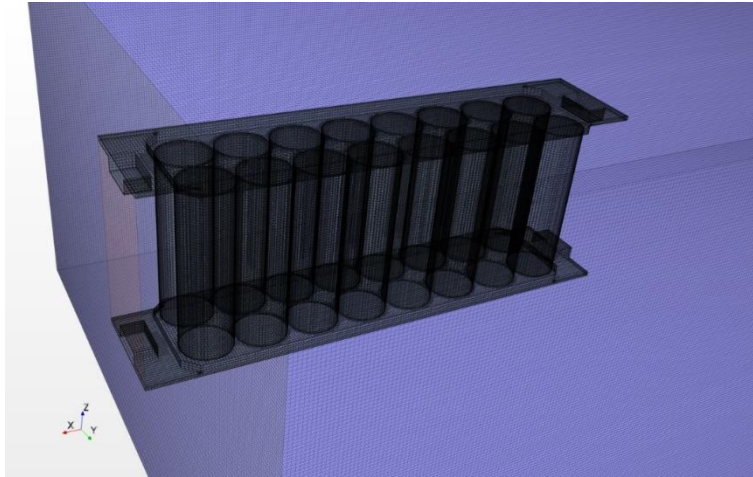


Figure 4: Grid of the brick and the volume occupied by air for the first case.

Figure 4 shows the grid elements within the Li-ion cells and the grid elements in the air for the first case. As in the second case air is forced to flow between the Li-ion cells, smaller grid elements are necessary with respect to the first case.

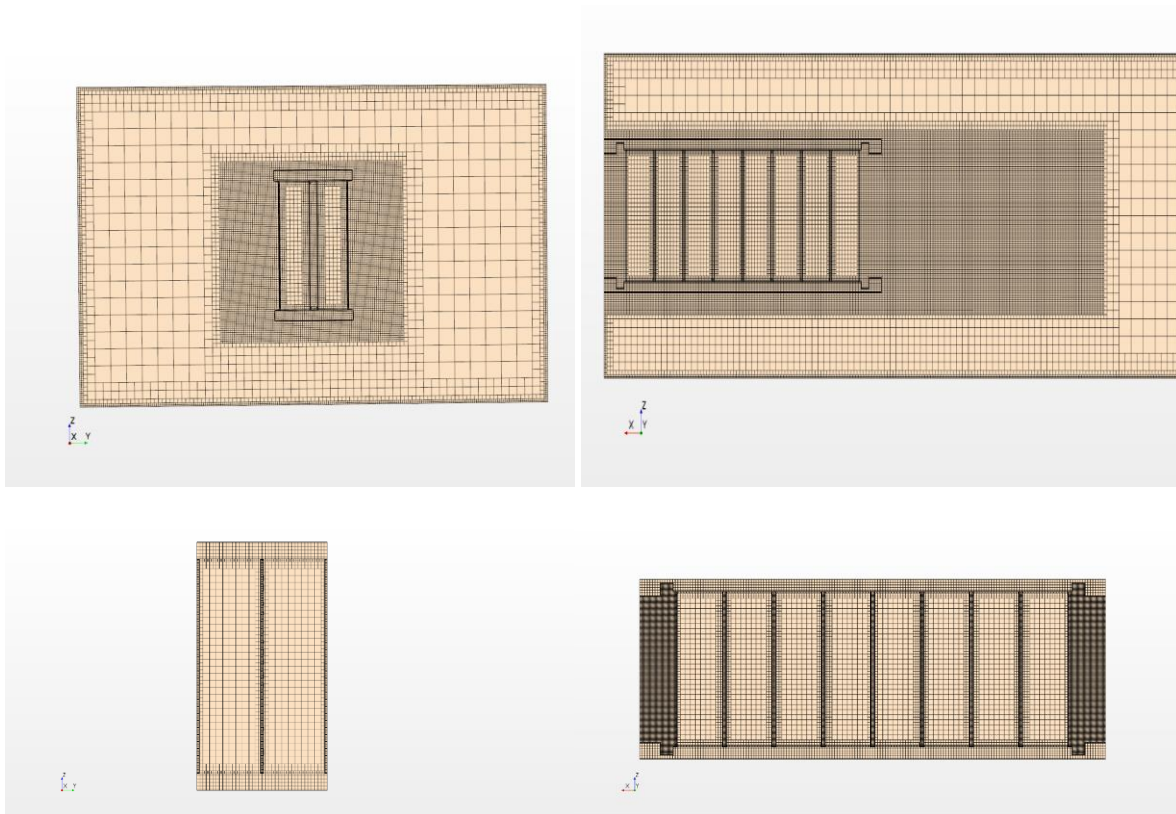


Figure 5: Vertical sections of the brick for the first case (top) and for the second case (bottom).

Figure 5 shows the refinements of the grid elements for the two cases. For case 1, a zone between the cells and in the wake flow

3.3. Numerical models

The CFD code STAR-CCM+ v. 12.02.10 has been employed to solve the steady-state Reynolds-averaged Navier–Stokes (RANS) equations with realisable k - ϵ turbulence model. The transport equations for kinetic energy k and the turbulent dissipation rate ϵ are:

$$\frac{\partial}{\partial t}(\rho k) + \nabla \cdot (\rho k u) = \nabla \cdot \left[\left(\mu + \frac{\mu_t}{\sigma_k} \right) \nabla k \right] + P_k - \rho(\varepsilon - \varepsilon_0) + S_k \quad (1)$$

and

$$\frac{\partial}{\partial t}(\rho \varepsilon) + \nabla \cdot (\rho \varepsilon u) = \nabla \cdot \left[\left(\mu + \frac{\mu_t}{\sigma_\varepsilon} \right) \nabla \varepsilon \right] + \frac{1}{T_\varepsilon} C_{\varepsilon 1} P_\varepsilon - C_{\varepsilon 2} f_2 \rho \left(\frac{\varepsilon}{T_\varepsilon} - \frac{\varepsilon_0}{T_0} \right) + S_\varepsilon \quad (2)$$

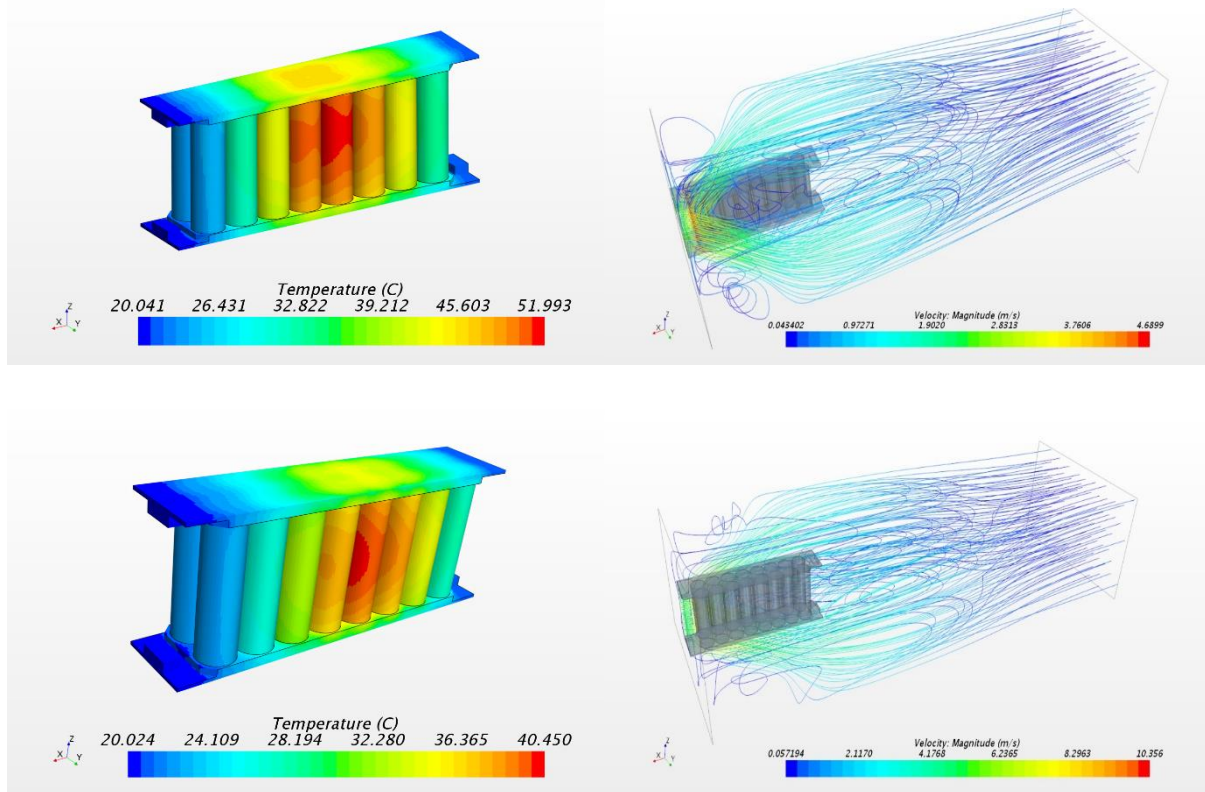
Where u is the average velocity, μ is air dynamic viscosity, σ_k , σ_ε , $C_{\varepsilon 1}$, and $C_{\varepsilon 2}$ are model coefficients, P_k and P_ε are production terms, whose formulation depend on the k - ε model variant, S_k and S_ε are used specific source terms, ε_0 is the turbulent dissipation rate value in the source terms, T_ε is the large-eddy time scale, T_0 the specific time-scale related to turbulent source term.

4. RESULTS AND DISCUSSION

In this section, the two cases with different flow configurations, described in the previous section, are compared and discussed. In both cases, the inlet airflow has a temperature of 20 °C. Different velocity ranges have been considered in the two cases, in order to have similar velocities near the Li-ion cells.

4.1. First case – brick within a boundless space

In this case the cooling airflow partially enters the brick. The inlet velocities considered in this case are $v=2.5$ m/s, $v=5$ m/s and $v=10$ m/s, i.e. the Reynolds number is in the range (3000 ÷ 12000). The characteristic length in the Reynolds number is the diameter of the Li-ion cells, $d=18$ mm. Most of the volume flow rate of the cooling air flows around the brick, as shown by Figure 6 (right column).



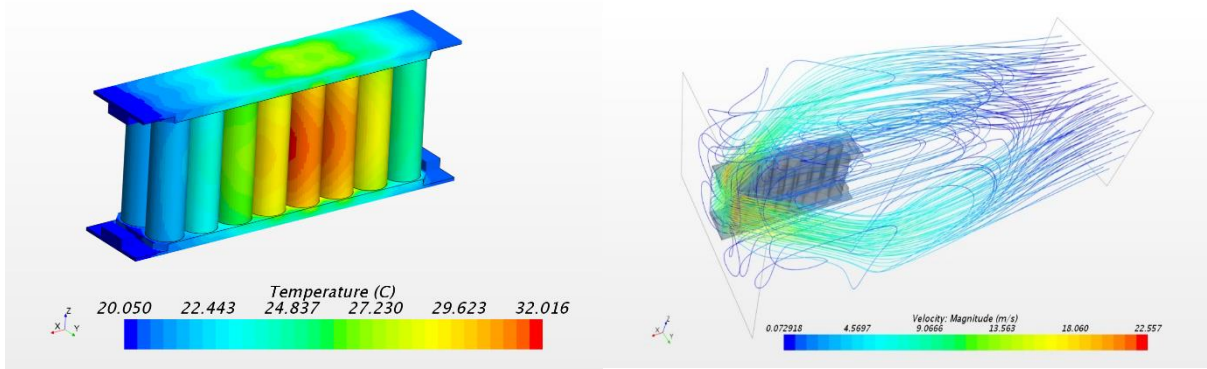


Figure 6: Temperature in the brick for air velocity inlet of 2.5 m/s (top), 5 m/s (middle) and 10 m/s bottom.

Figure 6 shows also that, for all the velocities considered, two symmetric vortices are created downstream the brick and an increase in the heat transfer coefficient between the airflow and the Li-ion cells at the end of the brick. The highest temperatures on the Li-ion cells is observed on the fifth line (counting from the inlet), due to a stagnation zone behind the vortices, as shown by Figure 6 (left column). Table 2 shows the average temperatures obtained on the Li-ion cells in function of the position from inlet. The maximum temperatures ranges from 50.8°C for $v=2.5$ m/s to 31.2°C for 10 m/s. The maximum temperature obtained on the Li-ion cells is plotted in Figure 7 in function of inlet airflow velocity. The temperature of the cells drops as the airflow velocity increases. The average Nusselt number on the Li-ion cell surfaces is plotted against Reynolds number in Figure 8.

Table 2: Temperature on the cells' surface for case 1.

Couple of cells (position from inlet)	Temperature (°C) $v=2.5$ m/s	Temperature (°C) $v=5$ m/s	Temperature (°C) $v=10$ m/s
1	24.2	22.5	21.6
2	31.6	26.2	23.3
3	41.8	31.9	26.2
4	49.6	37.4	29.1
5	50.8	39.5	31.2
6	48.4	38.1	30.9
7	43.1	34.1	28.4
8	33.2	27.5	24.6

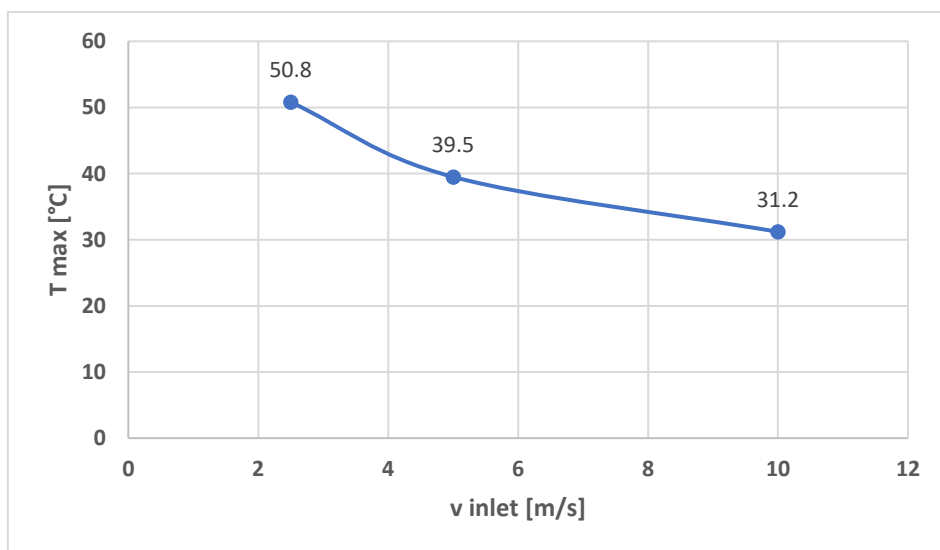


Figure 7: Maximum temperature in the brick versus inlet air velocity for case 1.

Nu is evaluated from the convective heat transfer coefficient h , as $Nu = h d/k$, where d is the Li-ion cell diameter and k the thermal conductivity of air. Figure 8 shows that Nu is an increasing function of Reynolds number in the range $3000 < Re < 12000$.

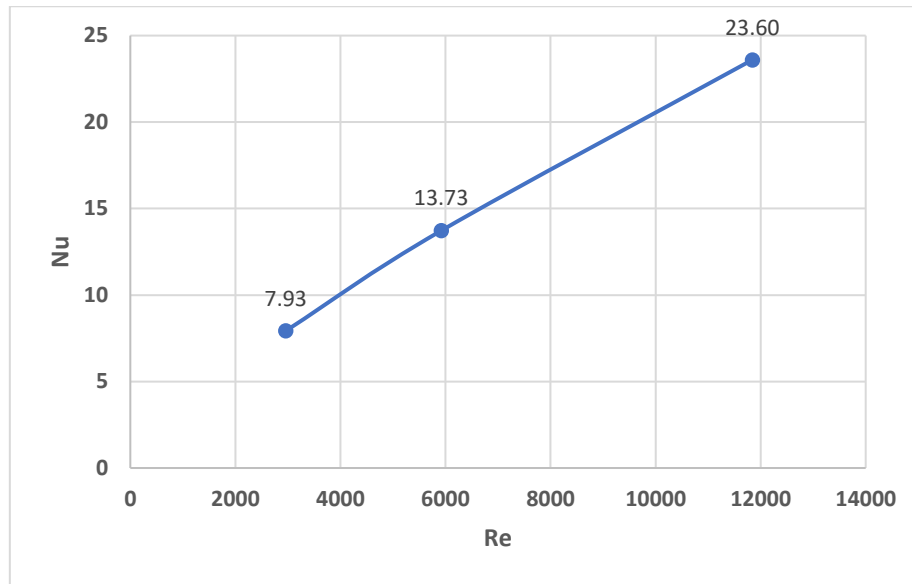
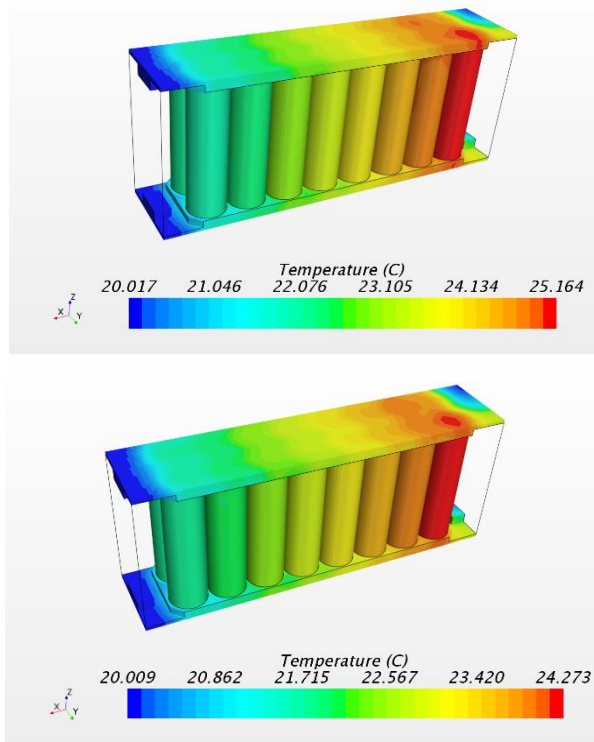


Figure 8: Nusselt number versus Reynolds number for case 1.

4.2. Second case: brick within a confined space

In this case the cooling airflow totally enters the brick. The inlet velocities considered in this case are $v=1$ m/s, $v=1.5$ m/s, $v=2$ m/s and $v=2.5$ m/s, i.e. the Reynolds number is in the range $(1000 \div 3000)$. The characteristic length for the Reynolds number evaluation is the diameter of the Li-ion cells, $d=18$ mm.



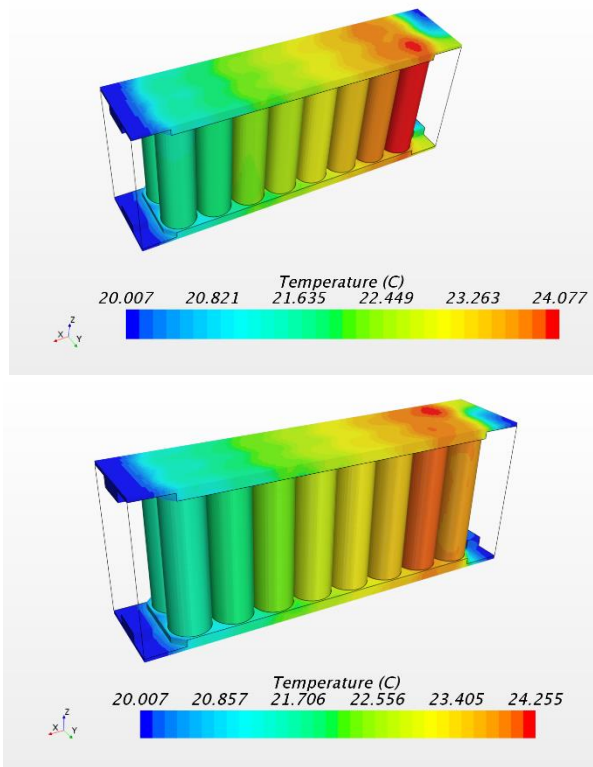


Figure 9: Temperature in the brick for air velocity inlet of 1 m/s (top left), 1.5 m/s (top, right), 2 m/s (bottom, left) and 2.5 m/s (bottom, right).

Figure 9 shows that, for all the velocities considered, the highest temperatures on the Li-ion cells are observed on the last line (counting from the inlet). Table 3 shows the average temperatures obtained on the Li-ion cells' couples as function of the position from airflow inlet. The temperature decreases from 24.9°C for $v=1$ m/s to 23.9°C for airflow inlet velocity of 2 m/s. The maximum temperature obtained on the Li-ion cells is plotted in Figure 10 in function of inlet airflow velocity. The temperature of the cells drops as the airflow velocity increases, reaching a minimum for 2 m/s.

Table 3: Temperature on the cells' surface for case 2.

Couple of cells (position from inlet)	Temperature (°C) $v=1$ m/s	Temperature (°C) $v=1.5$ m/s	Temperature (°C) $v=2$ m/s	Temperature (°C) $v=2.5$ m/s
1	22.1	21.7	21.7	21.7
2	22.4	22	21.9	21.9
3	23	22.5	22.3	22.4
4	23.5	22.9	22.7	22.8
5	23.9	23.3	23.1	23.2
6	24.4	23.6	23.4	23.6
7	24.8	24	23.8	24
8	24.9	24.1	23.9	24.1

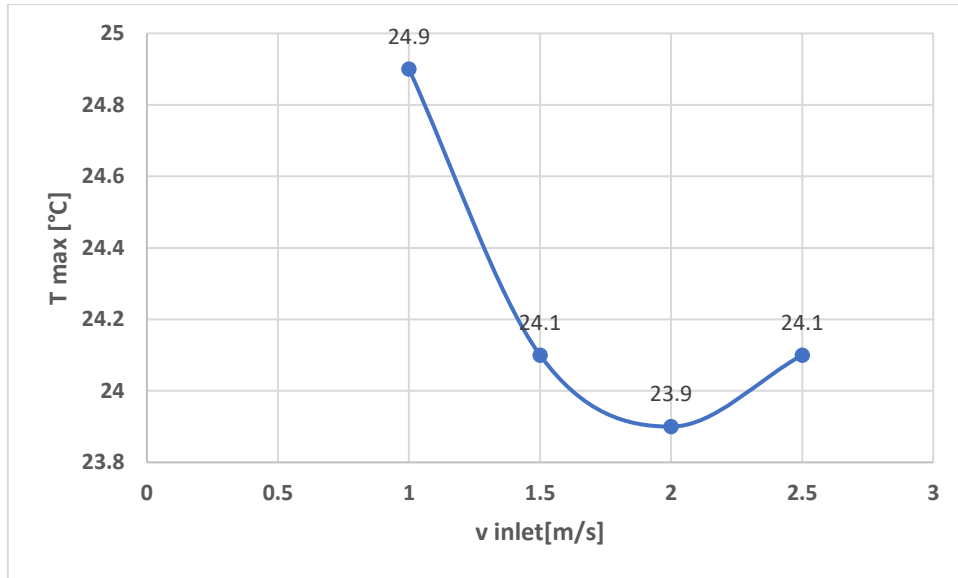


Figure 10: Maximum temperature in the brick versus inlet air velocity for case 2.

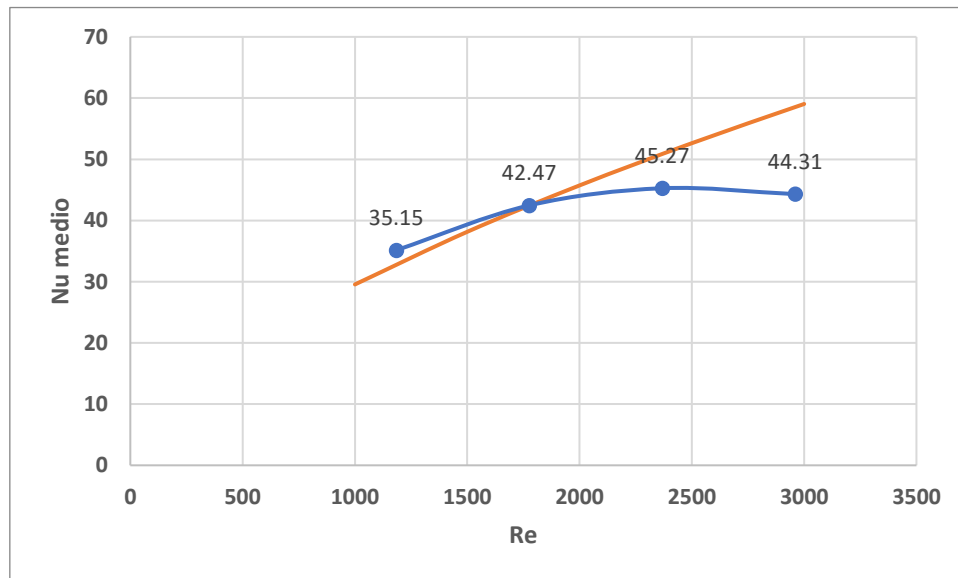


Figure 11: Nusselt number versus Reynolds number for case 2. Orange line represents Zukauskas correlation (Zukauskas 1972).

The average Nusselt number on the Li-ion cell surfaces is plotted against Reynolds number in Figure 11. Figure 11 shows that Nu is an increasing function of Reynolds number, reaching a maximum for $Re \sim 2500$. These results are in agreement with experimental studies like the one by Fan *et al.* (Fan 2019). The Authors study the cooling performances of aligned, staggered, and cross battery packs with cylindrical Li-ion cells by means of experiments. They found temperature differences between the cells and the inlet airflow temperature around 4°C for velocities around 2 m/s. In Figure 11 it is shown the well-known correlation by Zukauskas (Zukauskas 1971): $Nu = c Re^m Pr^{0.36}$, with $c=0.27$ and $m=0.63$ for the Reynolds numbers considered in this work (evaluated with the maximum velocity within the cells). The comparison shows that, for $Re < 2000$, the heat transfer coefficients can be evaluated by means of correlations available in the literature, while for higher velocity regimes we need further investigations.

5. CONCLUSIONS

In this paper, a Computational Fluid Dynamics (CFD) study of the thermal behavior of battery cells with air-cooling systems is presented. The heat transfer convection between air and solid Li-ion cells is obtained by means of a conjugate heat transfer approach. In particular, a module with 16 cylindrical cells, packed in 8 lines of two cells each is considered. The battery packs will be combinations of the modules, or bricks. Two air-cooling systems are

compared: a first case where the brick is not packed with others and a second case with densely packed bricks. In the first case, the airflow partially enters the brick, while two main flows are observed downstream the brick. In the second case, the whole airflow occurs within the channel between cells lines. Then, the inlet airflow velocity ranges considered in the two cases are very different, in order to consider similar velocities near the cells for the two cases. The temperature of each cell in the brick is obtained as a function of the velocity of the inlet airflow for the two cases. The maximum temperature obtained on the cells surfaces obtained for case 1 is 25°C higher than that obtained for case 2. The highest temperature of the cells within the brick is in the middle lines for case 1, while for case 2 the highest temperature is observed in the last line. It is shown that the airflow distribution strongly affects the temperature hotspots within the brick, i.e. the critical zones that can give problems during the battery charge. The heat transfer coefficients are obtained, and the results are generalised in order to give a dependence between Nusselt number and airflow Reynolds number. Per $Re < 2000$, it is shown that the correlations available in the literature, like ad instance the well-known Zukauskas correlation (Zukauskas 1972) can be used to determine the convective heat transfer coefficient on the Li-ion cells' surfaces.

6. REFERENCES

- Erb, D.C., Kumar, S., Carlson, E., Ehrenberg, S.E., 2017. Analytical methods for determining the effects of lithium-ion cell size in air-cooled battery packs, *Journal of Energy Storage*, 10, 39-47.
- Fan, Y., Bao, Y., Ling, C., Chu, Y., Tan, X., Yang, S., 2019. Experimental study on the thermal management performance of air cooling for high energy density cylindrical lithium-ion batteries. *Applied Thermal Engineering*, 155, 96-109.
- Kim, J., Oh, J., Lee, H., 2019. Review on battery thermal management system for electric vehicles. *Applied Thermal Engineering*, 149, 192-212.
- Lin, X., Perez, H.E., Mohan, S., Siegel, J.B., Stefanopoulou, A.G., Ding, Y., Castanier, M.P., 2014. A lumped-parameter electr-thermal model for cylindrical batteries. *Journal of Power Sources*, 257, 1-11.
- Liu, H., Wei, Z., He, W., Zhao, J., 2017. Thermal issues about Li-ion batteries and recent progress in battery thermal management systems: A review, *Energy Conversion and Management*, 150, 304-330.
- Opitz, A., Badami, P., Shen, L., Vignarooban, K., Kannan, A.M., 2017. Can Li-Ion batteries be the panacea for automotive applications? *Renewable and Sustainable Energy Reviews*, 68, 685-692.
- Xia, G., Cao, L., Bi, G., 2017. A review on battery thermal management in electric vehicle application. *Power Sources*, 367, 90-105.
- Wang, T., Tseng, K.J., Zhao, J., Wei, Z., 2014. Thermal investigation of lithium-ion battery module with different cell arrangement structures and forced air-cooling strategies. *Applied Energy*, 134, 229-238.
- Zukauskas, A. 1971. Heat transfer from tubes in crossflow. *Advances in Heat Transfer*, 8, 93-160.

#320: Performance investigation of roof mounted cross axis wind turbine

Mohammed GWANI^{1*}, Wen Tong CHONG², Chin Joo TAN³, Wan Khairul MUZAMMIL⁴

¹Department of Physics, Kebbi State University of Science and Technology, P.M.B 1144 Kebbi State Nigeria.
gwanimohammed@gmail.com,

²Department of Mechanical Engineering, Faculty of Engineering, University of Malaya, 50603 Kuala Lumpur, Malaysia. chong_wentong@um.edu.my,

³Department of Mechanical Engineering, Faculty of Engineering, University of Malaya, 50603 Kuala Lumpur, Malaysia. Tancj@um.edu.my,

⁴Faculty of Engineering, University Malaysia Sabah, Jalan UMS, 88400 Kota Kinabalu, Sabah, Malaysia. khairulm@siswa.um.edu.my

*Corresponding author

Roof mounted wind turbines represent the future outlook of wind energy generation in the urban environment. However, the urban environment is characterised by low wind speed and high levels of turbulence which has a negative effect on the performance of the current wind turbine systems i.e. horizontal axis wind turbine (HAWT) and vertical axis wind turbine (VAWT). These problems can be alleviated by mounting a novel cross axis wind turbine on rooftops of urban buildings to take advantage of the increased wind speed at the top of the roof. The roof mounted cross axis wind turbine (RMCAWT) is designed to operate by interacting with wind speed that is coming from both the horizontal and the vertical directions when mounted on the rooftop. The RMCAWT consists of three main vertical blades, & six horizontal blades arranged in a cross axis orientation. The wind flow on the building rooftop was investigated by using computational fluid dynamics (CFD) simulation software to ascertain the vertical component of the wind at the rooftop. The RMCAWT was tested on a vaulted rooftop and its performance was compared to a bare-CAWT (without rooftop) mounted on an equivalent height as the roof mounted CAWT under similar experimental conditions. The results obtained from the study showed that the RMCAWT outperformed the bare-CAWT. The coefficient of power (C_p) and rotational speed (RPM) of the RMCAWT increases by 37%, and 89% respectively compared to the bare-CAWT.

Keywords: cross axis wind turbine; wind energy; rooftop; renewable energy; urban building

1. INTRODUCTION

Globally, progress in wind energy research continues to be strong with more active countries and players. Wind energy is considered to be a clean source of renewable energy. Wind energy is fast growing all over the world with an increasing trend in worldwide installed wind power capacity since the beginning of the 21st century. The global installed wind capacity at the end of 2016 was around 486 GW (REN 21, 2014). The development of small wind turbines has rekindled hope, and the possibility to harness wind power for on-site energy generation (Casini, 2016). Urban wind turbines have attained approval to a certain extent. Conceptual designs and some examples in reality exist where small-scale wind turbines have been implemented close to buildings or even integrated in the building structure (Beller, 2011). Building rooftops can be an excellent location for wind turbines, both for on-site energy generation, or to take advantage of the faster wind at the rooftop while reducing the cost of support towers (Casini, 2016). The advantage of having power generation close to demand has been proven by integrating wind power in the buildings (Dayan, 2006). However, extracting wind energy in the urban environment has unique challenges due to the complex wind conditions, and the surrounding obstacles of the urban environment (Miles, 2006). There have been major advances in the wind turbine design to adapt to these complex wind conditions and the building itself can be designed to augment the wind speed so that the wind turbine can utilize the higher wind speeds above the rooftop of the building (Chong et al., 2017; Dayan, 2006). To create a reasonable amount of energy from a wind turbine positioned in the urban environments, wind turbines should be able to extract a large amount of energy from the wind (Ayhan & Safak, 2012; Booker et al., 2010). The increased wind speed in the urban environment can be adequately utilized by designing a suitable wind turbine system that will increase the flow velocity which can significantly increase the power output of a wind turbine due to the cubic power of the wind speed (Abe et al., 2005; Ohya et al., 2008).

Wind turbines can be integrated onto the building rooftops as roof mounted wind turbines (Chong et al., 2017; Dutton et al., 2005; Muller et al., 2009; Walker, 2011), or building augmented wind turbine, (Mertens et al., 2002; Peacock et al., 2008; Wang et al., 2015). The majority of installed wind turbines in the urban environment are the horizontal axis wind turbine, HAWT. Ordinarily, HAWT are designed for an open site and mounting HAWT in the urban environment is open to many different challenges like the complex wind conditions of the urban environment, the use of yaw mechanism and the dangers it poses to the surroundings. In view of these issues, many recent studies on the mounting of wind turbine in the urban environment focuses on the vertical axis wind turbine (VAWT). The VAWT is omni-directional, the installation, operation and maintenance are much easier than the HAWT, and it can generate power at lower wind speed. However, the problem associated with the VAWT is that it cannot self-start at low wind speed; this is considered as one of its main set-backs (Ackermann & Soder, 2000; Hau, 2006; Hyun et al., 20012). To overcome these challenges, many researchers have proposed the idea of mounting the VAWT systems on the rooftop of urban buildings to benefit from the increased wind speeds at these points. These systems require either an additional augmentation system (Beller, 2011; Chong et al., 2013; Valsamidis, 1995), or retrofitting onto the building by utilizing the building geometry (Abohela et al., 2013; Ledo et al., 2011; Mertens, 2006).

In this study, the performance of a novel roof mounted cross axis wind turbine (CAWT) has been investigated in an experiment, and the results obtained from the study were compared with a bare-CAWT under similar experimental conditions.

2. WIND TURBINE POWER

Estimating how much energy will be produced by a wind turbine is a very important step in designing a wind turbine. This means that accurate calculations of the energy generated are very important to strike a balance between cost and energy produced at the location. The wind turbine power can be calculated using Equation 1.

Equation 1: Power from the wind turbine

$$P = \frac{1}{2} \rho A U_{\infty}^3$$

Where:

- P = available power in the wind, (W),
- ρ = density (kg/m³),
- u_{∞} = wind speed (m/s)
- A = swept area of the turbine (m²)

The efficiency with which energy is transferred from wind to the wind turbine rotor often determines the actual power produced by a wind turbine. This is called the coefficient of power (C_p) which is the ratio of the actual power developed by the wind turbine to the theoretical power available in the wind. It can be calculated by using Equation 2.

Equation 2: Coefficient of power of wind turbine

$$C_p = \frac{P}{0.5\rho A U_\infty^3}$$

Where

- C_p = power coefficient of the wind turbine

The coefficient of power is the efficiency of the wind turbines. According to the Betz Limit, the theoretical efficiency of a wind turbine is 0.593%. However, practical wind turbines attain lower than the Betz Limit due to the inefficiencies and losses attributed to different configurations, rotor blades profiles, finite wings, friction and turbine design (Ragheb & Ragheb, 2011). The coefficient of power varies with Tip Speed Ratio (TSR). The TSR is the ratio of the mean blade tip speed to the wind velocity. Wind turbines are designed to operate at their optimum TSR in order to obtain maximum and optimal rotor efficiency. The TSR depends on the particular wind turbine design, the airfoil profile, and the number of blades used (Ragheb, 2014). The TSR can be calculated using Equation 3 while the torque coefficient can be calculated using Equation 4.

Equation 3: Tip speed ratio

$$\lambda = \frac{\omega R}{u_\infty}$$

Where:

- ω = angular velocity (rad/s),

Equation 4: Coefficient of torque

$$C_p = \frac{T}{0.5\rho A R U_\infty^2}$$

Where:

- R = radius of the turbine (m)

3. DESCRIPTION OF THE ROOF MOUNTED CAWT

The roof mounted CAWT used in this study was a new design which functions with airflows coming from both the horizontal and vertical direction when mounted on a rooftop. The CAWT comprised of three vertical blades and six horizontal blades which were used as supporting arms. The airfoil supporting struts connected the vertical blades to the drive shaft which in turn was connected to the generator. The lab scale model for the CAWT is shown in Figure 1. The vertical blades were connected to the centre shaft via radial arm supporting struts. The lower and upper parts of the supporting struts were placed at a relative distance of 100mm. The profile of the airfoil used for the CAWT was a symmetrical airfoil NACA 0015 airfoil. The advantage of using NACA 0015 is that this set of airfoil has well-documented lift, drag and pitching moment characteristics thus making validation of theoretical predictions easier (Islam et al., 2008; Kirke, 1998). Additionally, they have the same characteristics of lift and drag on the upper and lower surfaces (Hameed & Afaq, 2013) and have higher power coefficient values compared to the cambered airfoil (Ismail & Vijayaraghavan, 2015), although at positive incidence cambered airfoil have high L/D ratios compared to symmetrical airfoils. However, they perform poorly at negative incidence which can be attributed to the fact that, for each revolution, the angle of attack (α) on a VAWT blade reverses twice therefore making it difficult to avoid negative incidence (Kirke, 1998; Siddiqui et al., 2015). The specifications of the roof mounted CAWT are shown in Table 1.

Table 1: Specification of the Roof mounted CAWT and Bare-CAWT

Parameters	Units	Material
Diameter of rotor, d	50 cm	-
Height of the vertical blade	42 cm	-
Chord length of vertical blade, c	7 cm	-
Length of horizontal blade	25 cm	-
Chord length of horizontal blade	5 cm	-
Wind speed U_∞	4.5 m/s	-
Type of airfoil	-	Symmetrical airfoil
Profile of airfoil	NACA 0015	-
Number of vertical blades, N	3	-
Solidity	0.42	-
Generator	10 W	-
Pitch angle of the vertical blades	0°	-
Vertical blades	-	Carbon fibre
Pitch angle of the horizontal blade	10°	-

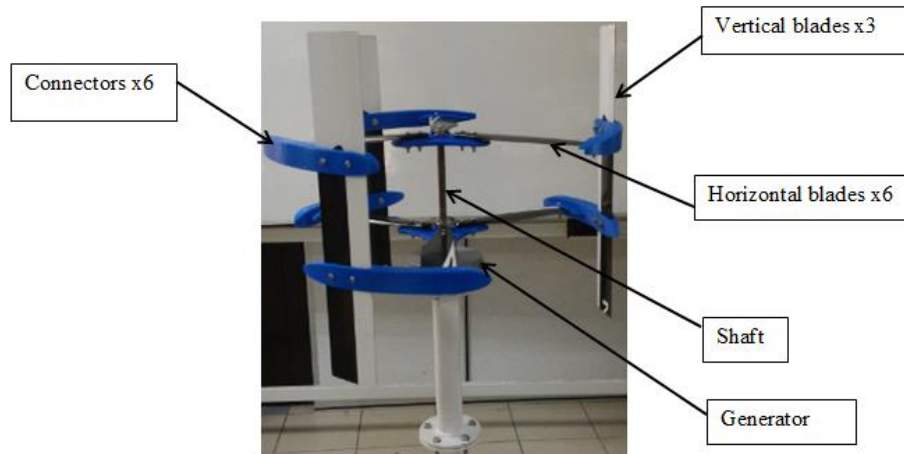


Figure 26: Lab scale model of the CAWT

3.1 Experimental set-up and procedures

A building model with vaulted roof shape was fabricated for the mounting of a CAWT at the rooftop. The height, length and width of building model were 1364mm x 1450mm x 740mm respectively. The experimental set-up and the schematic diagram of the roof mounted CAWT is shown in Figure 2 (a, and b), while the experimental set-up and the schematic diagram for the bare-CAWT is shown in Figure 3 (a, and b). An average wind speed of $4.5 \text{ m/s} \pm 0.2 \text{ m/s}$ was used for this experiment. The wind source was generated from ventilation fans which were arranged at equally-spaced 3×3 grid points. The wind speed measurements were taken downstream of the ventilation fans using a Vane-type anemometer as shown in the experimental set-up in Figure 2.

The rotor of the CAWT was in free-running conditions. Using a controller system, the performance of the roof mounted CAWT was logged. The recorded parameters for the study were the rotational speed (RPM), voltage and the current. The electrical power generated by the wind turbine was calculated by using the values of the current and voltage, also the dynamometer controller system was used to rectify the alternating current voltage from the generator to direct current. The measurement of the rotor rotational speed was taken during free-running conditions where the rotor was subjected to inertia and bearing friction with no external loads applied during this assessment. The rotational speed was measured continuously in second intervals until the stabilized rotational speed of the rotor was achieved

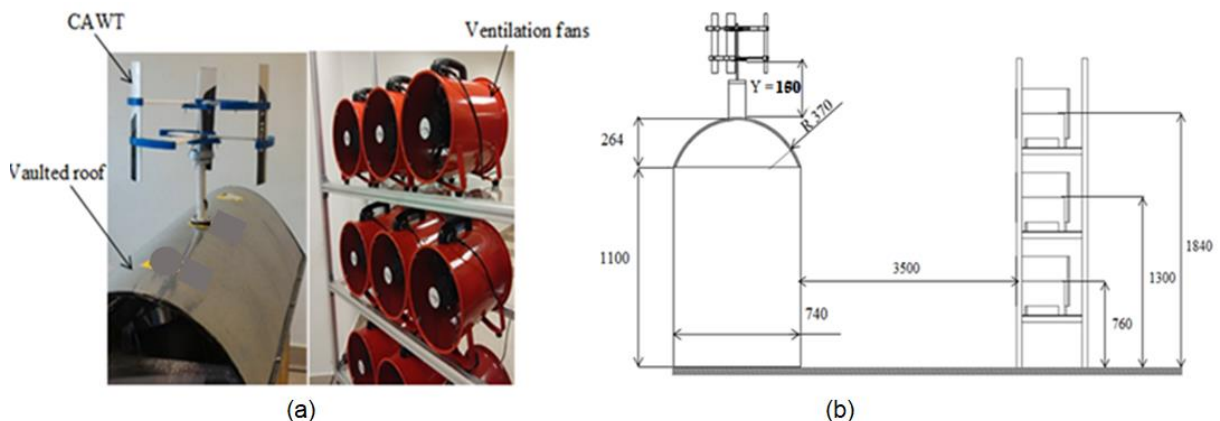


Figure 27: (a) Experimental setup (b) schematic diagram for the bare-CAWT (All dimensions in mm)

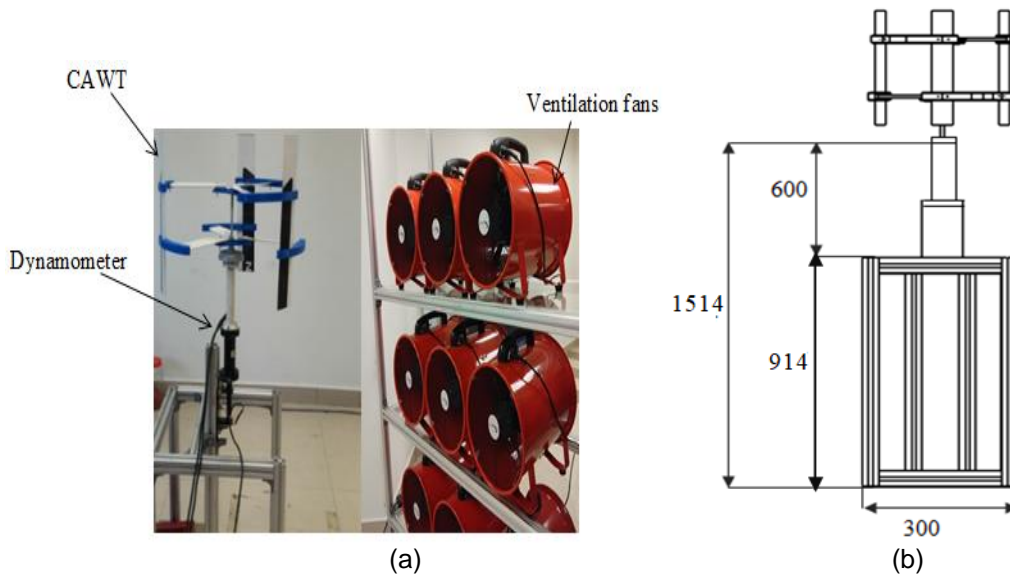


Figure 28: (a) Experimental setup (b) schematic diagram for the bare-CAWT (all dimensions in mm)

4. RESULTS AND DISCUSSION

Initial experiments were conducted to investigate the performance of the roof mounted CAWT. The experiment was conducted for two configurations; (i) CAWT mounted on the rooftop of a building with vaulted rooftop and (ii) bare-CAWT (without rooftop) respectively. The CAWT was placed at a height of $Y = 150\text{mm}$ above the building rooftop and the bare-CAWT was placed at an equivalent height of 1514mm from the ground level. The pitch angle for the horizontal blade of the CAWT was set at 10° , and the averaged wind speed is 4.5m/s . The data obtained from the experiment were used to compare with the performance of the bare-CAWT (without rooftop).

The results obtained from the study were analyzed to ascertain the performance of the CAWT on the rooftop as compared to the bare-CAWT (without rooftop).

4.1. Performance evaluation of the roof mounted CAWT, and bare-CAWT

Figure 4 compares the coefficient of power C_p values against the tip speed ratio (TSR) of the CAWT mounted on a building with vaulted rooftop. The figure shows that the maximum power coefficient, $C_{p,max}$, obtained by the roof mounted CAWT was 0.0781 at TSR of 1.03 while the peak coefficient of power for the bare-CAWT was 0.0569 at TSR of 0.86 . The results indicate that the $C_{p,max}$ value of the roof mounted CAWT was 37% higher than the bare-CAWT, implying that mounting the CAWT on a rooftop will yield 37% more energy than the bare-CAWT as shown in Table 2.

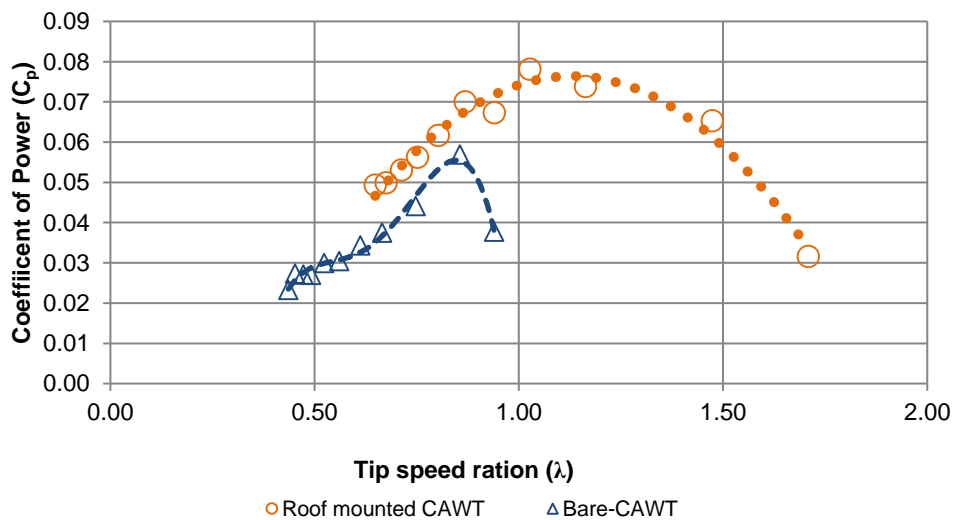


Figure 29: Coefficient of power for the roof mounted CAWT and bare-CAWT

The performance of the roof mounted CAWT and the bare-CAWT in terms of the rotational was also compared. Figure 5 depicts the rotational speed, (RPM) against time for the roof mounted CAWT and bare-CAWT. The free-running conditions of the rotational performance were taken after running for 300 seconds. In this condition the rotors were only subjected to inertia and bearing friction. Figure 5 shows the trends of the rotational speed for the roof mounted CAWT and the bare-CAWT as they increased steadily until reaching a stabilized state. The peak RPM attained by the roof mounted CAWT was 498 RPM while the bare-CAWT attained a 264 peak RPM. In comparison, the rotational speed of the roof mounted CAWT increased by 89% compared to the bare-CAWT.

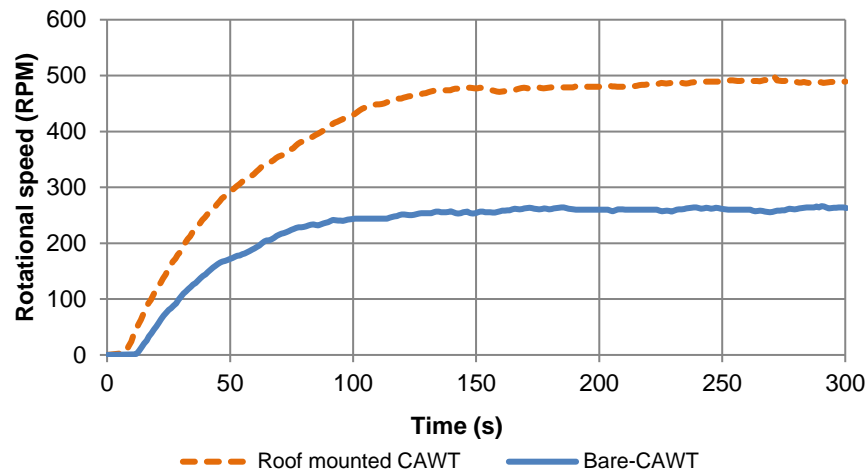


Figure 30: Rotational speed of the roof mounted CAWT and bare-CAWT

Table 2: Summary of the peak values of the experimental results

Parameter	Roof mounted CAWT	Bare-CAWT	Increment (%)
RPM	498	264	89
$C_{p,max}$	0.0781	0.0569	37
Power (w)	0.459	0.273	68
CT	0.0859	0.0591	45
TSR, (λ)	1.03	0.86	30

The power output of the roof mounted CAWT and the bare-CAWT against the TSR is presented in Figure 6. The results showed that the roof mounted CAWT outperformed the bare-CAWT with 68% increase in the power output. This significant improvement in the power output of the roof mounted CAWT can be attributed to the increased wind speed experienced by the CAWT at the rooftop, since the power was directly proportional to the cube of the wind speed. Therefore any slight increase in wind speed can lead to a significant increment in the power output. Furthermore, this increase in wind speed might be an indication that the building induces strong turbulent wind on the leeward side of the buildings and, according to (Cochran, 2002), turbulent wind has a larger energy potential than less turbulent wind with the same average wind speed. Thus high turbulence intensity in wind had significant influence on the performance of the wind turbine.

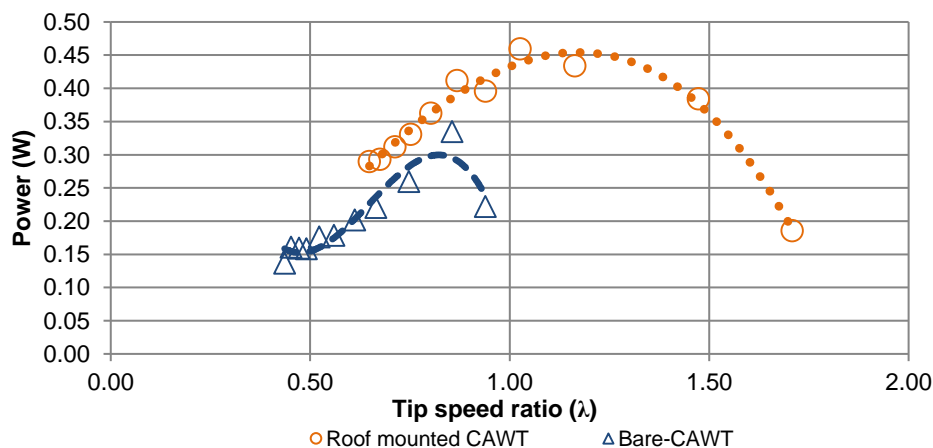


Figure 31: Power against tip speed ratio for the roof mounted CAWT and Bare-CAWT

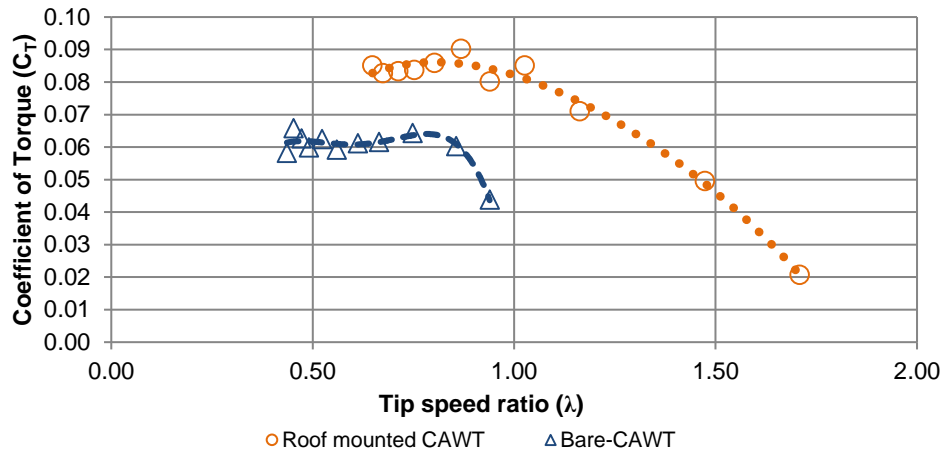


Figure 7: Coefficient of torque against tip speed ration for the RMCAWT and Bare-CAWT

Figure 7 presents the coefficient of torque C_T of the roof mounted CAWT and the bare-CAWT. The figure shows that the roof mounted CAWT had higher torque values when compared to the torque values of the bare-CAWT. The torque values of the CAWT improved significantly when mounted on the rooftop. The peak torque of the roof mounted CAWT increased by 45% compared to the bare-CAWT and the higher torque coefficient produced by the roof mounted CAWT is an indication that the CAWT mounted on the rooftop had a better ability to self-start than the bare-CAWT. The results are summarised in Table 2.

The improved performance experienced by the roof mounted CAWT was due to the accelerating effect at the rooftops. The presence of the horizontal blades as the supporting struts also contributed to the improved performance of the roof mounted CAWT. This was because the horizontal blades of the CAWT interacted with the deflected vertical airflow from the building rooftop, which greatly improved the self-starting capability of the roof mounted CAWT. The case is not the same for the bare-CAWT, there was little or no vertical wind to interact with the horizontal blades due to the lack of deflected wind streams either from the rooftop as in the case of the roof mounted CAWT or guided by a guide van to further direct the deflected wind to the horizontal blades, this necessitates the bare-CAWT to operate only with the wind streams coming from the horizontal directions. In that case, most of the contribution to the performance of the CAWT came from the vertical blades. The building rooftops served as an augmentation device that further increased the wind speed due to the accelerating effect at the rooftop. Moreover, the pitched angle, which was set at 10° , exposed the horizontal blades to a better angle of attack of the vertical wind thereby enhancing the self-starting behaviour and improving the overall performance of roof mounted CAWT. Due to the unique axis of orientation of the CAWT, both the horizontal blades and the vertical blades contributed to the improved performance of the CAWT when mounted at the rooftop. Therefore mounting wind turbines on the rooftop of urban buildings can significantly improve the performance of the wind turbine as asserted by Abohela *et al.* (2013) where the effect of roof shapes on the performance of wind turbines was studied. Their findings revealed that integrating a wind turbine on the roof shape could yield 56% more energy compared to a free standing wind turbine.

A 2D computational fluid dynamic simulation carried out to investigate the flow field around the rooftop (Figure 8) has shown that the wind speed achieved high velocity due to the accelerating effect on the building. The parameters investigated in the CFD simulation were the streamline velocity and the shear stress transport (SST). The k- ω turbulence model was used in the simulation. The wind velocity along the centre line of the roof was found to be 7.05 m/s, which is 56% increment compared with the inlet wind speed, 4.5 m/s, hence the wind speed augmented factor, $f=1.56$. The instantaneous streamlines show that there is a periodic increase in air velocity at the rooftop. This shows that the rooftop can cause an increase in streamwise velocities above the roof. Also from the figure, the boundary layer separated at the windward roof edge of the buildings and the flow formed a separation bubble on the roof. As a consequence, the velocity vector of the flow above the separation bubble made an angle with the horizontal edge of the roof which is referred to as the skewed angle. The skewed angle is largest at the windward roof edge and decreases downwind (Mertens *et al.*, 2003).

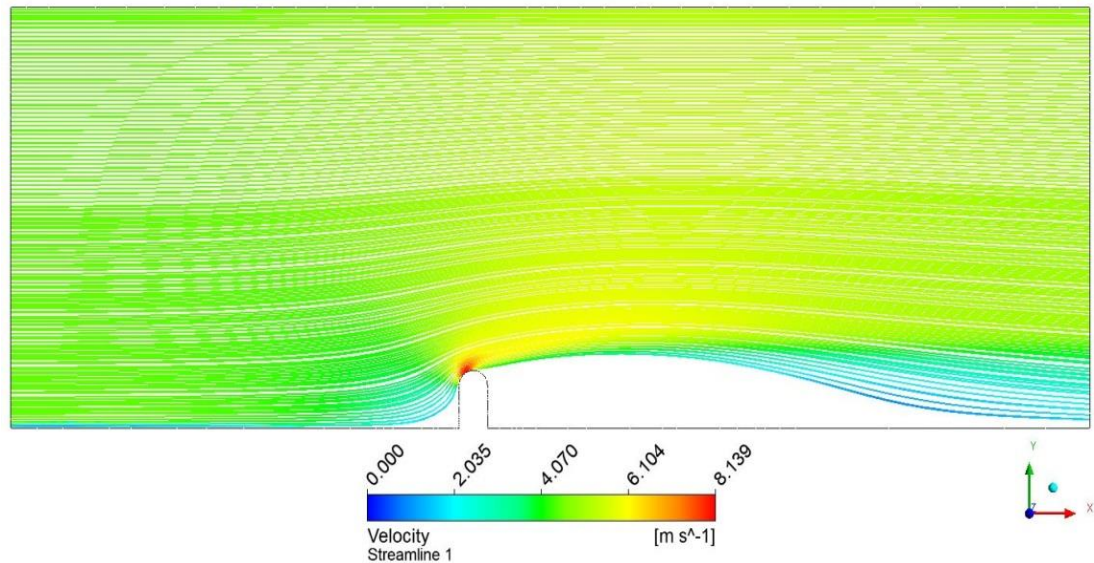


Figure 8: Velocity streamline for the building with vaulted roof shape

5. CONCLUSION

A roof mounted wind turbine is seen as an effective solution for on-site energy generation for buildings with the aim of promoting zero energy buildings in the urban environment. In this study, the performance of a roof mounted CAWT was investigated experimentally and the result obtained from the study was compared with a bare-CAWT (without rooftop) under similar experimental conditions. The results obtained indicates that the roof mounted CAWT outperformed the bare-CAWT. The coefficient of power, rotational speed, power and coefficient of torque of the CAWT improve significantly when it is mounted on the rooftop of the urban buildings compared to the bare-CAWT (without rooftop), and the horizontal blades of the CAWT has positively influence the self-starting behavior and the improved performance of the CAWT due to the interaction with the vertical airflow from the building. The CAWT is considered to be more suitable to be mounted onto the urban building because of the advantages it has over the conventional HAWT and VAWT. The findings from this study will serve as a mile stone towards mounting wind turbine, especially the cross axis wind turbine at the rooftops of the urban buildings for on-site energy generation, which will significantly reduce losses and cost during transmission. However, further research needs to be carried out with large scale CAWT and with different rooftops of the building in order to identify the rooftop that will be more suitable for the mounting of the cross axis wind turbine in the urban environment.

6. ACKNOWLEDGEMENT

The authors would like to thank the University of Malaya for the research grant allocated under the University of Malaya Research Grant (RP015C-13AET), the Centre for Research Grant Management Unit, University of Malaya for the Postgraduate Research Grant (PG098-2014A), and Kebbi State University of Science and Technology through the Tertiary Education Trust Fund for the support provided in carrying out the research work.

7. REFERENCES

- Abe, K., Nishida, M., Sakurai, A., Ohya, Y., & Kihara, H. (2005). Experimental and numerical investigation of flow fields behind a small wind turbine with a flanged diffuser. *Journal of Wind Energy and Industrial Aerodynamic*, 93, 951-970.
- Abohela, I., Hamza, N., & Dudek, S. (2013). *Roof Mounted Wind Turbines: A Methodology for Assessing Potential Roof Mounting Locations*. Paper presented at the PLEA2013 - 29th Conference, Sustainable Architecture for a Renewable Future, Munich, Germany
- Ackermann, T., & Soder, L. (2000). Wind Energy Technology and Current Status: A Review. *Renewable and Sustainable Energy Reviews*, 4, 315-374.
- Ayhan, D., & Safak, S. (2012). A technical review of building-mounted wind power systems and a sample simulation model. *Journal of Renewable Sustainable Energy Review*, 16, 1040-1049.

- Beller, C. (2011). Energy Output Estimation for a Small Wind Turbine Positioned on a Rooftop in the Urban Environment with and without a Duct. *Riso-R- Report*.
- Booker, J., Mellor, P., Wrobel, R., & Drury, D. (2010). A compact, high efficiency contra-rotating generator suitable for wind turbines in the urban environment. . *Renewable Energy*, 35, 2027-2033.
- Casini, M. (2016). Small Vertical Axis Wind Turbines for Energy Efficiency of Buildings *Journal of Clean Energy Technologies*, 4(1).
- Chong, W. T., Gwani, M., Tan, C. J., Muzammil, W. K., Poh, S. C., & Wong, K. H. (2017). Design and Testing of a Novel Building Integrated Cross Axis Wind Turbine. *Applied Sciences*, 7(251), 1-21 doi: 10.3390/app7030251
- Chong, W. T., Pan, K. C., Poh, S. C., Fazlizan, A., Oon, C. S., Badarudin, A., & Nik-Ghazali, N. (2013). Performance investigation of a power augmented vertical axis wind turbine for urban high-rise application. *Renew Energy*, 51, 388-397.
- Cochran, B. (2002). The influence of atmospheric turbulence on the kinetic energy available during small wind turbine power performance testing. . Soria, Spain:: CEDER-CIEMAT.
- Dayan, E. (2006). Wind energy in building: Power generation in the urban environment-where it is need most. *Refocus*, 7, 33-38.
- Dutton, A. G., Halliday, J. A., & Halliday, M. J. (2005). The Feasibility of Building Mounted/Integrated Wind Turbines (BUWTs): Achieving their Potential for Carbon Emission Reductions. *Final Report of Carbon Trust Contract 2002-07-028-1-6, Energy research Unit, Rutherford Appleton Laboratory, Science and Technology Facilities Council, Oxfordshire, United Kingdom* 1-109.
- Hameed, M. S., & Afaq, S. K. (2013). Design and analysis of a straight bladed vertical axis wind turbine blade using analytical and numerical techniques. *Ocean Engineering*, 57, 248–255.
- Hau, E. (2006). *Wind Turbines; Fundamentals, Technologies, Application, Economics* (2nd ed.). Berlin, Germany: Springer.
- Hyun, B., Choi, D., Han, J., Jin, J., & Roo, C. (20012). Performance analysis and design of vertical axis tidal stream turbine. *Journal of Shipping and Ocean Engineering*, 2, 191-2000.
- Islam, M., David, S. K., & Ting, A. F. (2008). Aerodynamic models for Darrieus-type straight-bladed vertical axis wind turbines. *Renewable & Sustainable Energy Reviews*, 12, 1080-1109.
- Ismail, M. F., & Vijayaraghavan, K. (2015). Effect of airfoil profile modification on vertical axis wind turbine performance. *Energy*, 80, 20-31.
- Kirke, B. K. (1998). *Evaluation of Self-Starting Vertical Axis Wind Turbines for Stand-Alone Applications*. (PhD), Griffith Univerisity Gold Coast Campus.
- Ledo, L., Kosasih, P. B., & Cooper, P. (2011). Roof mounting site analysis for micro-wind turbines. *Renewable Energy*, 36(5), 1379-1391.
- Mertens, S. (2006). *Wind Energy in the Built Environment: Concentrator Effects of Building*. (PhD Thesis), Technische Universiteit Delft,, United Kingdom.
- Mertens, S., Delft, T., & Holland. (2002). Wind energy in urban areas: Concentration effects for wind turbine close to buildings. *Refocus*, pp. 22-24.
- Miles, C. (2006). Survey of Urban Wind Energy Technology for Sustainability and the Built Environment. from <https://extension.ucdavis.edu>
- Muller, G., Jentsch, M., & Stoddart, E. (2009). Vertical axis resistance type wind turbines for use in buildings. *Renewable Energy*, 34, 1407-1412.

- Ohya, Y., Karasudani, T., Sakurai, A., Abe, K., & M., I. (2008). Development of a shrouded wind turbine with a flanged diffuser. *Journal of Wind Energy and Industrial Aerodynamic*, 96, 524-539.
- Peacock, A. D., Jenkins, D., Ahadzi, M., Berry, A., & Turan, S. (2008). Micro wind turbines in the UK domestic sector. *Energy and Building*, 40, 1324-1333.
- Ragheb, M. (2014). Optimal Rotor Wind Speed Ratio.
- Ragheb, M., & Ragheb, A. M. (2011). Wind Turbines Theory - The Betz Equation and Optimal Rotor Tip Speed Ratio *Fundamental and Advanced Topics in Wind Power* (pp. 20).
- REN 21. (2014). Renewable energy policy network for 21 century *Renewable energy 2014 global status report*.
- Siddiqui, M. S., Durrani, N., & Akhtar, I. (2015). Quantification of the effects of geometric approximation on the performance of a vertical axis wind turbine. *Renew Energy*, 74, 661-670.
- Valsamidis, M. (1995). Wind turbine cross wind machine. *US Patent No, US 5,380149*.
- Walker, S. L. (2011). Building mounted wind turbines and their suitability for the urban scale- a review of methods of estimating urban wind resource. *Energy and Buildings*, 43, 1852-1862.
- Wang, B., Cotb, L. D., Adolphec, L., Geoffroya, S., & Morchaid, J. (2015). Estimation of wind energy over roof of two perpendicular buildings. *Energy and Buildings*, 88, 57-67.

#323: CFD analysis on operative temperature prediction inside an office equipped with a fan-coil air conditioning system

Giovanni SEMPRINI¹, Beatrice PULVIRENTI¹, Paolo GUIDORZI¹, Aminhossein JAHANBIN¹

¹ Department of Industrial Engineering, University of Bologna, Viale Risorgimento 2, 40136 Bologna, Italy, giovanni.semprini@unibo.it

¹ Department of Industrial Engineering, University of Bologna, Viale Risorgimento 2, 40136 Bologna, Italy, beatrice.pulvirenti@unibo.it

¹ Department of Industrial Engineering, University of Bologna, Viale Risorgimento 2, 40136 Bologna, Italy, paolo.guidorzi@unibo.it

¹ Department of Industrial Engineering, University of Bologna, Viale Risorgimento 2, 40136 Bologna, Italy, aminhossein.jahanbin@unibo.it

An accurate assessment of operative temperature inside a building is essential since it is associated to the human's perception of well-being and comfort. In the present study, a 3D computational fluid dynamic (CFD) code is employed to evaluate the indoor operative temperature for a university office located in a historical building, consisting of thick masonry walls and large single glass windows, using fan coil as an air conditioning system. The experimental measurement was carried out using an innovative system for the sensor localisation (based on acoustic sources and a specific signal processing algorithm) in order to validate the numerical model and to obtain the required initial and boundary conditions for the case under study. The turbulent air flow, the operative temperature, and the local heat transfer characteristics inside the room are presented in typical winter conditions, allowing to identify the best comfort areas. The results show that the operative temperature of the room is significantly affected by surface temperatures of the windows, especially due to the large windows to wall surface ratio, and by the position and operational condition of fan coil. Comfort conditions inside the room are not uniform and big energy consumptions is required to maintain temperature set point. It is concluded that 3D comfort maps on operative temperature and air velocity allow to optimise internal layout of the office room; moreover the possibility to optimise comfort conditions in specific workstation together with control of operating mode of the fan coil (velocity and temperature of air inlet) allows to gain important energy saving results.

Keywords: CFD simulation, Operative Temperature, Thermal Comfort, Energy Saving, HVAC

1. INTRODUCTION

Thermal comfort in office rooms is widely investigated both for increase people satisfaction (Putra, 2017, Maykot, 2018) and to analyse solutions to reduce energy consumption. In many situations the internal layout of HVAC terminal systems and workstations inside a single room are not properly investigated in the design phase causing gradient in temperature and air velocity with different comfort condition for occupants. Moreover, in existing and historical buildings with low thermal performance, also asymmetry of radiant temperature occurs, mainly in winter period and high air temperatures are set inside rooms (Semprini, 2016). CFD analysis could be an important tool in design phase (Shahzad, 2017, Awwad, 2017) for defining the internal layout and the operation mode of terminals (inlet temperature, air flow) and the position of sensor for room control system: the latter plays an important role to maintain internal temperature set-point and position of sensors and temperature set point must be defined according to desired effect.

Accuracy of the CFD results depends mainly on the adopted boundary conditions and convection models. In cases of application of CFD analysis to real buildings and large rooms where many conditions affect the thermo-fluid dynamic behaviour of the air flow, some assumption must be made and a comparison and/or calibration in specified conditions is recommended (Hajdukiewicz, 2013; Shan, 2019). One of main issues comparing experimental measurements and simulations is the uncertainty of measurements of physical properties but also the correct location of measurement positions. In this paper a new methodology based on acoustic signal processing algorithm is presented and adopted for experimental measurements and calibration.

In this paper results of a CFD numerical simulation of an office room have been reported. The case study is an office room located inside a typical historical building built with thick masonry walls and large single glass windows with high thermal transmittance. Spatial distribution of the temperature and air velocity are presented and comfort parameter (operative temperature) for a specific workstation is analysed.

2. NUMERICAL MODEL

The schematic of the computational domain considered is illustrated in Figure 1. It is composed of a 4.73 m × 5.03 m office with 4.24 m height which is equipped with a fan-coil air conditioning system, with an exit surface of the inlet air of 0.08 x 0.65 = 0.052 m². Three different fan speed mode are available and the corresponding mean air velocity at the outlet fan coil were measured, namely 0.8, 2.0 and 3.0 m/s; the air temperature, depending on the centralised water heating system, is 33-34°C. The office domain consists of two external walls with windows, and two internal walls. The boundary surfaces of the office were assumed to be isothermal, except the floor and ceiling surface walls considered as adiabatic.



Figure 1: Schematic of the office under study.

Since the air inside the room is a moist air, the thermophysical properties of moist air were employed in simulations (Tsilingiris, 2008). The values of the thermal properties of dry air at atmospheric pressure (Raznjevic, 1976) and of

the saturation properties of water (Sontag, 2003) were properly taken. The following values of the density, dynamic viscosity, specific heat capacity at constant pressure and thermal conductivity of moist air were obtained for $T = 20^\circ\text{C}$: $\rho_m = 1.153 \text{ kg m}^{-3}$, $\mu_m = 1.82 \times 10^{-5} \text{ kg m}^{-1} \text{ s}^{-1}$, $c_{pm} = 1020 \text{ J kg}^{-1} \text{ K}^{-1}$, and $k_m = 0.0253 \text{ W m}^{-1} \text{ K}^{-1}$.

In analogy with recent literature on CFD simulations of HVAC inside rooms (Sevilgen, 2011; Jahanbin, 2016) the flow was assumed turbulent and the effects of turbulence were considered by a κ - ε model. The governing equation, i.e. the mass, momentum and energy balance equations can be written as:

$$\text{Equation 1:} \quad \nabla \cdot \vec{v} = 0$$

$$\text{Equation 2:} \quad \rho \left[(\vec{v} \cdot \nabla) \vec{v} \right] = \rho \vec{g} - \nabla p + \nabla \cdot \tilde{\tau}_{\text{eff}}$$

$$\text{Equation 3:} \quad \nabla \cdot (\vec{v} (\rho E + p)) = \nabla \cdot \left[(k + k_t) \nabla T + \tilde{\tau}_{\text{eff}} \cdot \vec{v} \right]$$

In Equations 1 – 3, \vec{v} is the velocity vector, p is pressure, $\tilde{\tau}_{\text{eff}}$ is the effective stress tensor, $E = h - p/\rho + v^2/2$, h is specific enthalpy, v is the magnitude of \vec{v} , k is the thermal conductivity, k_t is the turbulent thermal conductivity. The effective stress tensor is given by

$$\text{Equation 4:} \quad \tilde{\tau}_{\text{eff}} = \tilde{\tau} + \tilde{\tau}_t$$

Among common turbulence models, the κ - ε model is the most widely used and validated model. It applies to a wide range of flows, which occur in many technical applications. Due to higher precision and stability for internal flows, the RNG (Renormalisation Group) κ - ε model was chosen for this study (Choudhury D, 1993). The RNG κ - ε model is quite similar to the classic κ - ε model but includes some refinements such as: enhanced accuracy for swirling flows, an analytically derived differential formula for effective-viscosity that accounts for low-Reynolds numbers effects, and an additional term in ε to improve accuracy. The RNG κ - ε model's governing equations are (Yakhot, 1992):

$$\text{Equation 5:} \quad \frac{\partial(\rho \kappa)}{\partial t} + \nabla \cdot (\rho \kappa \vec{v}) = \nabla \cdot (\alpha_\kappa \mu_{\text{eff}} \nabla \kappa) + 2\mu_t E_{ij} E_{ij} - \rho \varepsilon$$

$$\text{Equation 6:} \quad \frac{\partial(\rho \varepsilon)}{\partial t} + \nabla \cdot (\rho \varepsilon \vec{v}) = \nabla \cdot (\alpha_\varepsilon \mu_{\text{eff}} \nabla \varepsilon) + C_{1\varepsilon}^* \frac{\varepsilon}{\kappa} 2\mu_t E_{ij} E_{ij} - C_{2\varepsilon} \rho \frac{\varepsilon^2}{\kappa}$$

In Equations 5 and 6,

$$\text{Equation 7:} \quad \mu_{\text{eff}} = \mu + \mu_t; \quad \mu_t = \rho C_\mu \frac{\kappa^2}{\varepsilon}$$

where $C_\mu = 0.0845$.

$$\text{Also } \alpha_\kappa = \alpha_\varepsilon = 1.39; \quad C_{1\varepsilon} = 1.42; \quad C_{2\varepsilon} = 1.68 \quad \text{and} \quad C_{1\varepsilon}^* = C_{1\varepsilon} - \frac{\eta(1-\eta/\eta_0)}{1+\gamma\eta^3}$$

$$\text{where } \eta = \sqrt{2E_{ij}E_{ij}} \frac{\kappa}{\varepsilon} \text{ and } \eta_0 = 4.377; \quad \gamma = 0.012.$$

The enhanced wall treatment near-wall modeling was employed. This model combines a two-layer model (viscosity-affected layer and fully turbulent region) with enhanced wall functions. It is based on a turbulent Reynolds number, Re_y , defined as [N], $Re_y = \rho y \sqrt{\kappa} / \mu$ where y is the normal distance from the wall.

Radiation heat transfer was considered by applying the surface-to-surface radiation model (Siegel, 1992). In this model, the air inside the room is considered as a transparent medium and all surfaces are assumed to be diffusive

and gray. The following values were considered for the emissivity of surfaces: 0.88, 0.89, 0.88, and 0.9 for fan coil, window (glass), door (glass), and walls, respectively (ASHRAE, 2009).

In order to calculate the operative temperature, T_{opr} , the equation recommended by ISO 7730 (ISO, 2005) was employed, namely

Equation 8:
$$T_{opr} = \psi T_a + (1 - \psi) T_r$$

where T_a is the air temperature, T_r is the mean radiant temperature, and ψ is a factor depending on the air velocity, which in this study was considered equal to 0.5.

The mean radiant temperature of the room surfaces with respect to a virtual person inside the room is given by

Equation 9:
$$T_r = \sum_1^n F_j T_{sj}$$

where T_{sj} is the temperature of the j -th surface and F_j is the angular factor between the person and the j -th surface. The operative temperature is calculated inside the office for 5 different positions (at 4 working desks + central point of the room) as reported in Figure 1, for 3 different values of the fan coil speed.

The CFD code ANSYS Fluent was employed for a 3D fluid flow and heat transfer analysis. The governing differential equations were solved by means of the control volume approach, which converts the governing equations to a set of algebraic discretized equations. Second-order discretization method was used for the pressure, momentum and energy terms, and the well-known SIMPLE (Semi-Implicit Method for Pressure-Linked Equation) was used to solve the pressure-velocity coupling.

A 3D *TGrid* unstructured mesh composed of tetrahedral elements was generated by employing the Gambit software. The computational domain contains 2799219 tetrahedral cells. The mesh independence of the results was assured by performing preliminary computations with different meshes. For the sake of brevity, the corresponding results are not reported here.

3. MODEL VALIDATION BY EXPERIMENTAL TEMPERATURE MEASUREMENT

The determination in the three-dimensional space of measurement positions of the temperature is carried out by measuring the distance of the temperature sensor (a thermocouple) from some known points and is similar in principle to the GPS. To understand the principle of operation we can initially consider the problem in 2 dimensions: if the distance of the target (yellow point in Figure 2a) from another known position point "1" is measured, the target position can be on a circumference centred in point "1". Knowing the distance also from the point "2", there are two possible solutions, intersection of the circles centred in "1" and "2". Finally knowing the distance also from the point "3", there is a unique univocal solution. By extending the same reasoning to a target point located in three-dimensional space, as shown in Figure 2b, if the distance from a single known position point is measured, the position of the target can be anywhere on a sphere. Measuring the distance of the target from two known points, its position can be on the intersection circumference of the two corresponding spheres. Measuring the distance of the target from three known points, there are two possible solutions, intersection of three spheres and finally measuring the distance from four known points there is one and only one solution. Analytically, the problem is addressed by solving, through a specific algorithm, a system of 4 equations with 4 unknowns, which include the four distances of the target from four known points and the three spatial coordinates of each of the four known points (Thompson, 1998). The 4 distances are measured by acoustic waves: 4 different MLS (Maximum Length Sequence) signals, orthogonal to each other are emitted simultaneously by 4 small loudspeakers placed on a grid, all in a known position, as shown in Figure 3a (Rife and Vanderkooy, 1989). The microphone, fixed very close to the thermocouple as shown in Figure 3c, samples these 4 MLS signals, which, despite being emitted at the same time, can be discriminated, being orthogonal to each other, and through the Fast-Hadamard Transform algorithm, are converted into 4 distinct impulse responses, as shown in Figure 5b. From the peak of each of these impulse responses, the flight time of the sound from the respective loudspeaker to the single microphone is calculated. Knowing the speed of sound, corrected according to the average air temperature for more accuracy, the 4 distances from the microphone to the 4 known points (loudspeakers) are obtained and with the algorithm described above, the position in the three-dimensional space of the microphone and thermocouple is found (Guidorzi, 2017). The idea of the position detection system was born from the need to correctly position microphones during measurements on road noise barriers (Garai and Guidorzi, 2015).

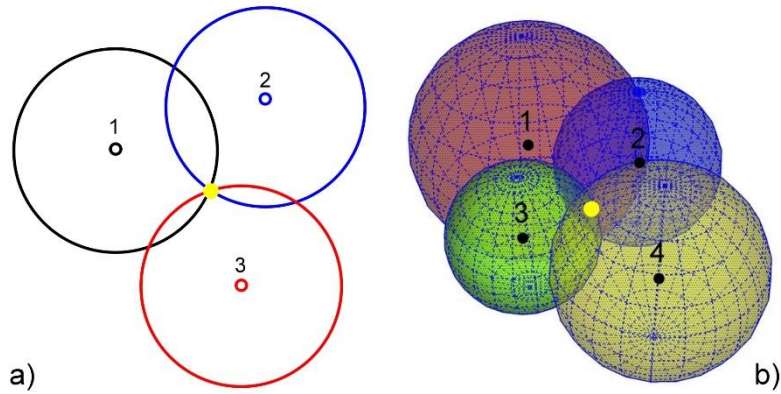


Figure 2: a) Example of trilateration in a 2D plane; b) example of trilateration in 3D space.

The temperature from the thermocouple is detected by an Arduino system, as shown in Figure 3b, interfaced directly with the software for measuring the position on the computer, visible in Figure 5a. The temperature measurement sub-system allows a resolution of 0.25 degrees. Type K thermocouple readings made using Arduino were previously compared and validated with measurements taken with a thermal imaging camera, obtaining a very good agreement, with differences less than 1 degree. The accuracy of the position measurement system is not easy to calculate directly because it depends on many factors, such as the sampling frequency of the measurement system, the size and geometry of the grid with the four speakers, the microphone-speakers grid distance and the air temperature. The measurement of the distance between each of the four speakers and the microphone is calculated by multiplying the time instant of the first peak (see Figure 5b), which provides the flight time of the acoustic wave from the corresponding speaker to the microphone, for the speed of sound in the air. The discrete step between two samples along the time axis defines the resolution in terms of measured distance. Setting the sound card at a sampling frequency of 44.1 kHz, the time interval between two samples is 0.01041667 ms and this implies a resolution on the calculated distance of about 7.8 mm, considering an average sound speed of 343 meters per second. At 96 kHz sampling rate the spatial resolution is about 3.6 mm. These calculations are valid for the measurement of a single distance; in the presented system four distances (not just one) are measured and processed by the spatial trilateration algorithm. Therefore, it is not easy to theoretically determine the accuracy of the 3D measurement system. For this reason, a statistical analysis was performed, measuring the exact length of 1m at various distances from a 1m x 1m square speaker grid. It has been found that with this configuration the system works correctly with an extension of about 10 m in each spatial direction, from the loudspeaker grid. A statistical analysis of these measurements was carried out, finding an average percentage uncertainty of $\pm 1.99\%$ at the sampling frequency of 96 kHz and $\pm 3.5\%$ at the sampling frequency of 44.1 kHz. In Figure 7 the percentual errors on the measurements at 96 kHz are shown, depending on the distance from the loudspeaker grid.

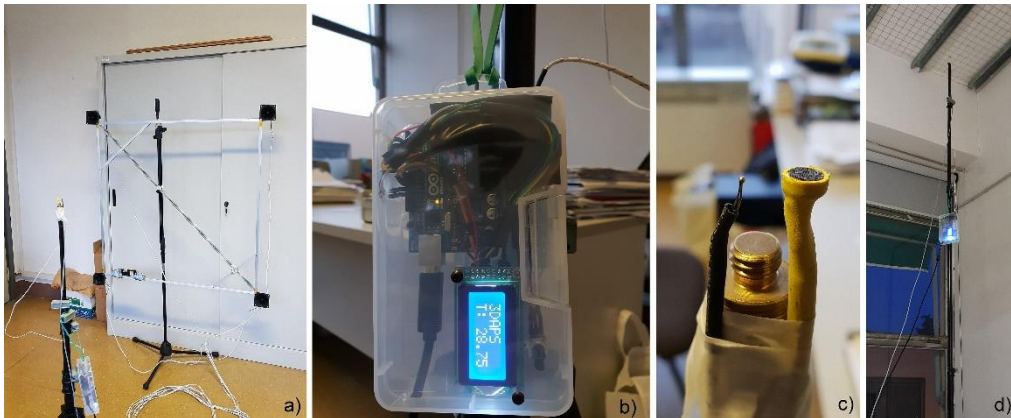


Figure 3: Measurement system: a) loudspeaker grid and microphone/thermocouple; b) detail of the Arduino system for reading the temperature from the thermocouple, interfaced with the measurement software on the computer; c) detail of the microphone and thermocouple; d) example of measurement in a high position.



Figure 4: Panoramic view of the room being measured; in the box the measured points are visible in 3D.

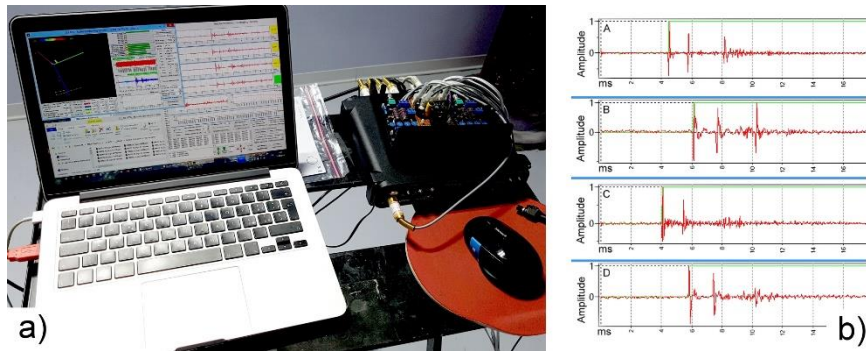


Figure 5: a) Measurement system: software and hardware components (microphone preamplifier, loudspeakers power amplifiers, multi-channel soundcard); b) example measurement of the four impulse responses sampled by the microphone.

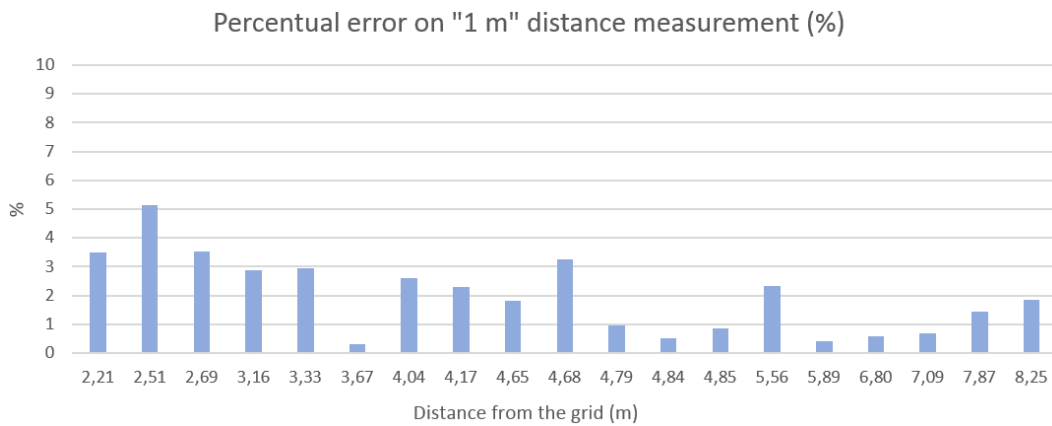


Figure 6: Percentual error on three-dimensional position measurements.

The CFD model was validated by means of experimental temperature measurement explained above. In order to evaluate correct calibration of the numerical model, 32 room positions randomly spread inside the volume were considered. For each position, the value of temperature measured by experimental test was compared with that obtained by CFD results. For the sake of brevity, the corresponding point-to-point comparison results are not presented here. The average reported error of temperature evaluation was 3.6% with reference to experimental data, with a range of variation from 0.1 to 9.5 %. This can be considered a satisfying result.

4. RESULTS AND DISCUSSION

In following images, the maps of air temperatures and air velocity are displayed for 2 air speed of fan coil ($V_1=0.8$ m/s and $V_2=3$ m/s). Temperature map at the height 1.5 from the floor (Figure 7) and in vertical section (Figure 8) show the effect of forced convection, with a general uniform distribution in the room from 22 to 24°C and a zone in front of the fan coil with high temperatures.

The high values of air temperature up to 25°C in some positions (Table 1) result from lack of thermal control in the room where the water temperature was set at high values to allow to balance low radiant temperature in cold winter periods. The increase of air velocity (Figure 9) reduce the uniformity of temperature with a lower air temperature in positions near the window (bottom side), a bigger vertical gradient, and making a general increase of discomfort. The habit to use high speed fan, especially in the beginning of day to reduce the heating period to reach the desired temperature and the lack of room thermostat, leads to a bigger energy consumption with lower comfort condition.

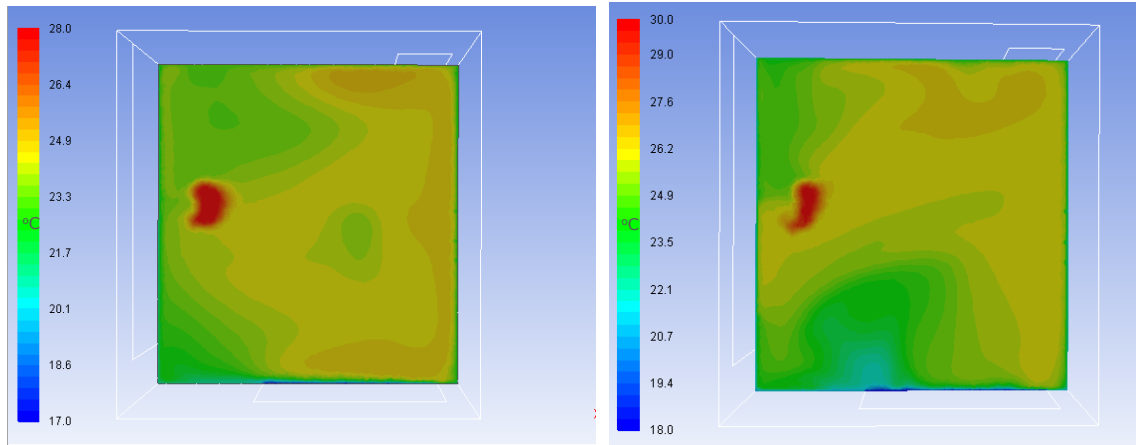


Figure 7: temperature horizontal distribution at height 1.5 m.

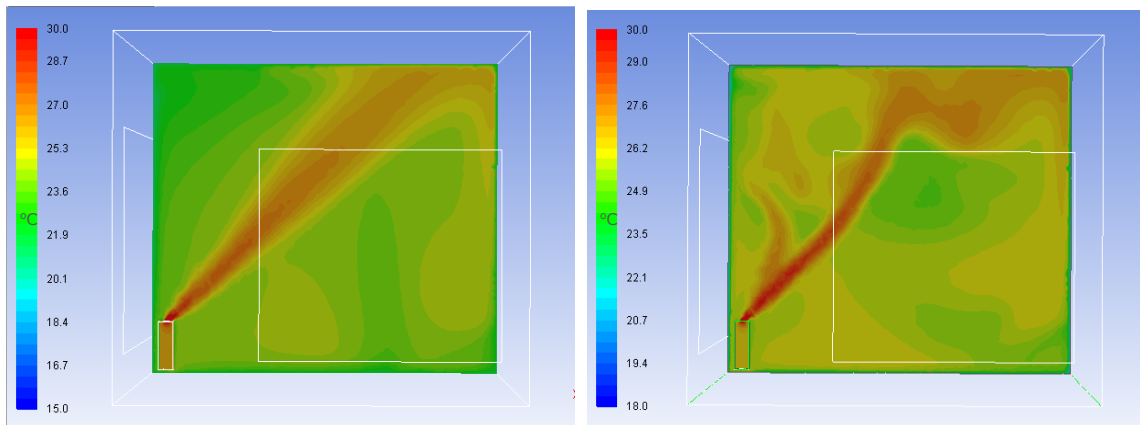


Figure 8: temperature vertical distribution.

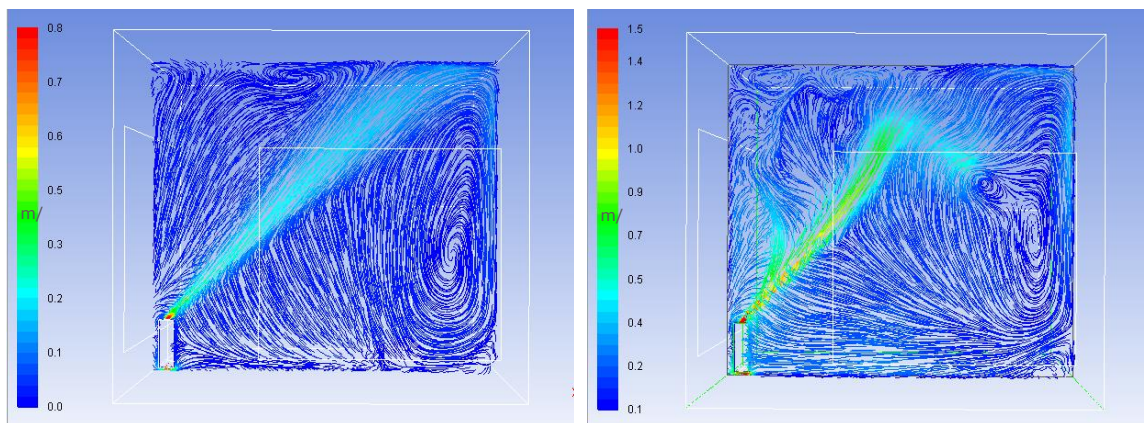


Figure 9: air velocity vertical distribution.

Comfort conditions are then evaluated considering the operative temperature in five position in the room, as indicated in Figure 1. Table 1 reports the air temperature, radiant temperature and operative temperature (according to equation 8). In general, operative temperatures assume values between 22.5°C and 24.0°C thanks to high values of air temperature with an overheating of the room. Radiant temperature is lower at workstation 1 due to the proximity of cold window surface and consequently also the operative temperature assumes minimum value. Considering the boundary conditions of envelope surfaces and the temperature of inlet air of fan coil (65°C) the comfort conditions can be obtained with the fan coil speed in mode 1 (V₁).

The analysis of numerical results gives important information on the possibility to improve the operating mode of the HVAC system in order to reduce energy consumptions: air temperature can be reduced by 2-3°C avoiding to control comfort at workstation 1.

Table 20: Comfort conditions for the three different air flows of fan coil.

	V_1			V_2			V_3		
<i>position</i>	T_{air} (°C)	T_{rad} (°C)	T_{opr} (°C)	T_{air} (°C)	T_{rad} (°C)	T_{opr} (°C)	T_{air} (°C)	T_{rad} (°C)	T_{opr} (°C)
1	24,54	20,45	22,49	24,77	20,66	22,72	25,28	20,79	23,03
2	24,37	21,20	22,78	24,64	21,46	23,05	25,78	21,60	23,69
3	23,84	21,35	22,60	23,94	21,58	22,76	23,96	21,71	22,84
4	23,29	21,99	22,64	24,74	22,26	23,50	25,50	22,40	23,95
5	24,34	21,65	23,00	25,64	21,95	23,79	25,72	22,11	23,92

5. REFERENCES

- Awwad A, Mohamed M, Fatouh M, 2017, Optimal design of a louver face ceiling diffuser using CFD to improve occupant's thermal comfort, Journal of Building Engineering, 11, 134-157
- Choudhury D., 1993, Introduction to the Renormalization Group Method and Turbulence Modelling. Technical Memorandum TM-107, Fluent Inc. Lebanon NH
- Garai M, Guidorzi P, 2015. Sound reflection measurements on noise barriers in critical conditions. Building and Environment, 94(2), 752–63
- Guidorzi P, 2017. Patent Application nr. 102017000066160, filed on 14/06/2017 by the University of Bologna, inventor: Paolo Guidorzi
- Hajdukiewicz M, Geron M, Keane MM, 2013, Calibrated CFD simulation to evaluate thermal comfort in a highly glazed naturally ventilated room, Building and Environment, 70, 73-89
- Jahanbin A, Zanchini E., 2016, Effects of position and temperature-gradient direction on the performance of a thin plane radiator. Applied Thermal Engineering, 105, 467-473
- Maykot J K, Rupp R F, Ghisi E, 2018, A field study about gender and thermal comfort temperatures in office buildings, Energy and Buildings, 178, 254-264
- Putra J C P, 2017, A study of thermal comfort and occupant satisfaction in office room, Procedia Engineering, 170, 240-247
- Raznjevic K., 1976, Handbook of Thermodynamic Tables & Charts. McGraw-Hill
- Rife DD, Vanderkooy J, 1989. Transfer-function measurement with maximum-length sequences. J. Audio Eng. Soc., 37(6), 419–444
- Sevilgen G, Kilic M., 2011, Numerical analysis of air flow, heat transfer, moisture transport and thermal comfort in a room heated by two-panel radiators, Energy and Buildings, 43, 137-146
- Shahzad S. et al., 2017, A user-controlled thermal chair for an open plan workplace: CFD and field studies of thermal comfort performance, Applied Energy, 207, 283-293
- Shan X, Xu W, Lee Y, Lu W, 2019, Evaluation of thermal environment by coupling CFD analysis and wireless sensor measurements of a full-scale room with cooling system, Sustainable Cities and Society, 45, 395-405

Semprini G, Marinosci C, Ferrante A, Predari G, Mochi G, Garai M, Gulli R, 2016, Energy management in public institutional and educational buildings: the case of the school of engineering and architecture in Bologna, *Energy and Buildings*, 126, 365-374

Siegel R, Howell JR., 1992, *Thermal radiation heat transfer*. Taylor & Francis, Washington, DC.

Sontag RE, Borgnakke C, Van Wylen GJ., 2003, *Fundamentals of Thermodynamics*. 6th edition John Wiley & Sons

Thompson RB, 1998. Global Positioning System: The Mathematics of GPS Receivers. *Mathematics Magazine*, 71(4), 260-269

Tsilingiris P T., 2008. Thermophysical and transport properties of humid air at temperature range between 0 and 100°C. *Energy Conversion and Management*, 49, 1098-1110

Yakhot V, Orszag SA, Thangam S, Gatski TB, Speziale CG, 1992, Development of turbulence models for shear flows by a double expansion technique. *Physics of Fluids A*, 4, 1510-1520

ASHRAE Handbook, 2009, *Fundamentals – IP Edition*, Atlanta.

ISO 7730, 2005, *Moderate thermal environment – Determination of the PMV and PPD indices and specification of the conditions for thermal comfort*

#328: A case study of a small wind turbine integrated with the building of AGH Centre of Energy, Krakow

Mariusz FILIPOWICZ

AGH University of Science and Technology, Faculty of Energy and Fuels, Department of Sustainable Energy Development, Mickiewicza Av. 30, 30-059 Krakow, Poland, mariusz.filipowicz@agh.edu.pl

Nowadays, various methods of increasing total energy generation from renewable energy sources (RES) are being considered and applied. Various types of RES installations, characterised by different size, location, performance, etc. are widely spread all over the world. Among them wind energy sector is undergoing the most dynamical growth, currently achieving the generation capacity of about 600 GW.

This is the effect of the construction of big wind turbine farms, where huge megawatt-turbines are commonly installed. However, this policy is not without some drawbacks, such as area usage, location problems and environmental impact.

Therefore, the policy of installing many small wind turbines in densely populated areas would be beneficial in terms of obtaining more power from wind. This also creates an opportunity to develop integrated systems of small energy sources located directly in cities. Such distributed generation systems could include small wind units, building integrated photovoltaic, waste heat conversion, power storage etc. Wind systems with the potential ability of night generation can be a complementary element to photovoltaic.

In built-up areas, the application of building integrated wind energy generators seems to be worth considering. The paper presents the case study of a small wind turbine integrated with the Centre of Energy AGH building. The data from the turbine monitoring gathered by a dedicated registering system were analysed. The analysis includes: wind parameters (velocity, direction, power spectra), power generated in different conditions, environmental impacts of the turbine, like noise and vibrations.

Due to the wind interaction with the building structure, the behaviour of BIWT is much more complex compared to wind turbines in open terrain. Distortions of the wind pattern by the building cannot be neglected and define new conditions for wind energy harvesting.

The performed analysis provides data for elaborate specific location conditions and supports CFD analysis. The aim of the future analysis will be the selection of buildings located in complex built-up areas, fit for the integration with wind turbines.

Keywords: wind energy; integrated wind turbine

1. INTRODUCTION

Most of the energy consumed in the world is used for buildings' needs. Therefore, architectural trends have recently appeared to introduce systems of energy generation within buildings. These may be solar systems (e.g. solar roof, facades, etc.), wind systems (e.g. buildings with wind turbines) and cogeneration systems based on renewable and non-renewable energy sources. An example of such a solution is a building supplied by energy generated from wind by turbines located in the vicinity or on/in an urban building (Sengupta, 2017; Haase, 2015).

Studies have shown that such wind turbine installations may satisfy up to 20% of the building's energy needs (Yang, 2016). The main problem with the implementation of this technology is designing a suitable building shape to get an area with appropriate wind parameters. In Haase (2015) it was shown that wind speed could be increased by up to 40% only by design and optimal building geometry. Further, CFD analyses carried out in Sengupta (2017) proved that the appropriate roof structure on which the wind turbine is located may allow an increase of power density by up to 86%.

There are two basic types of turbines used in those applications – with vertical and horizontal rotation axis. Each of these have advantages and disadvantages. In Toya (2013) it was shown, that horizontal axis wind turbines have a higher performance in flat terrain applications. The main advantage of those turbines is their efficiency, but their disadvantage is that they only operate under unidirectional wind conditions, so its application is limited in urban environments. Vertical axis wind turbines are more suitable for built-up areas as they easily accommodate to multidirectional and turbulent conditions. Flat roofs are more desirable to install wind turbines due to the lack of effect of wind velocity decrease. However, as stated in Ramenah (2016) the determination of the ideal position for the wind turbine in a complex urban area requires long time and very detailed onsite measurements.

In order to strengthen the wind flows near buildings, mounting wind turbines in a special way is required. There are many factors which affect wind flow. The geometry of buildings, their height, width, location, construction etc. have to be analysed. A proper shape of a building is an important way to increase the wind speed near a wind turbine. It has been argued that rectangular and concave buildings, as opposed to round ones, are capable of causing strong vertical air movements that can be successfully used by turbines. It is also possible to adapt the form of the building to get the channel flow (e.g. through the tapered arrangement of buildings, causing the flow increase due to the Bernoulli effect) (Cho, 2011).

For turbines placed near the edge of the roof, consideration of the variable direction of air flow is indispensable (Haase, 2015). Such turbines require a special shape of blade. It is also important to ensure that the installed turbine is not located in a turbulent zone caused by surrounding obstacles. An economical analysis made in Grieser (2015) showed the potential of mounting small wind turbines under different urban location settings. Small wind turbines in Germany could be economically feasible in exposed areas with an average wind speed higher than 4.5 m/s. Inclusion of an energy storage system increases the NPV of small wind turbines investments in most cases.

Analysis of application of vertical axis wind turbines together with solutions presentation and creation of new concept for data delivered by CFD simulations in aim of optimisation of the building shape and turbine integrated with it was presented in Casini (2016). Dilimulati (2018) presented a concept of power augmentation by using a building rooftop turbine installed inside the diffuser which re-directs the airflow over the casing, as well as accelerates the flow, thus augmenting wind power. The concept was validated in a real urban test site with real wind data using CFD. An interesting way to achieve strengthened wind flow is the formation of building façade elements. The solutions described in Cochran (2008) illustrated advanced technologies of wind energy resources exploitation for urban environment. For example, the use of dedicated guide vanes connected with small wind turbines allowed one to multiply power generation due to redirection of wind flow.

To determine possible wind resources, some of the research has focused on estimating wind potential in urban areas, as presented in Sunderland (2013), reporting observations in Dublin. Wind flow channelling, terrain roughness, turbulence or wind blasts were the most important factors. Meteorological data collected for a minimum 10 years is required to carry out such an analysis (Grieser, 2015). An interesting case study was presented in Laiola (2017) and referred to the city of Taranto in the South-East of Italy, where urban wind energy was emerging as a technology popularizing smart grids for sustainable energy development. Gusty and turbulent nature of the urban wind (Emejeamara, 2015) requires creating some opportunity for energy capture as well as extending measurements and developing some models. The measurements described in Karthikeya (2016) for Singapore were done using two measurement systems - rooftop wind measurement systems and remote sensing, mobile wind profiler based on a LiDAR device.

The aim of this work is the case study presentation for a horizontal axis wind turbine - not optimised for urban winds. The location of the building was not considered in terms of wind energy harvesting. Some basic data for period August 2017-July 2018 are presented and discussed.

2. INTEGRATED WIND TURBINE INSTALLATION

The building was located in the city of Krakow, Poland (N50.066598, E19.921297). It was very close to the City center and the building ran along one of the City main streets in the WNW direction (293°). The visualisation is presented in Figure 1.

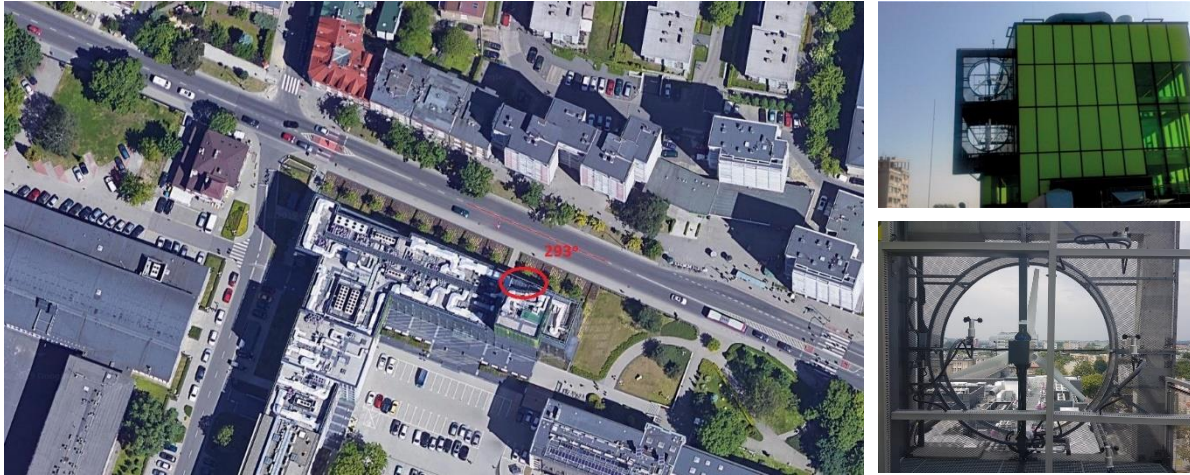


Figure 32: Visualisation of the building and turbine location, the turbine location is in the red circle

The street and the building formed something like a “street canyon”, so some increase in the wind velocity could be expected. The turbine was placed ca. 29 meters above ground level (204.6 m) on the top platform as visible in Figure 1. Unfortunately Krakow has an unfavourable location in terms of wind penetration – it is located in a river basin and surrounded from three sides by hills over one hundred meters high. This creates poor wind conditions, therefore this location was not favourable. Of course it was reflected in the obtained results.

The experimental facility consisted of a double-level platform with turbines (horizontal and vertical), electronic equipment and registering software. The diagram of anemometers location and visualisation of the electronic equipment is presented in Figure 2.



Figure 2: Visualisation of the anemometers location and the electric part of the experimental rig

The turbine under consideration in the paper was a 1kW 3-blade horizontal axis wind turbine (Ventus Swind 1000), the nominal power was reached for the wind velocity equal 10 m/s, the induction generator was 3-phase AC brushless with permanent magnet, the rotor diameter was equal 2.2 m, the starting wind velocity was 2.3 m/s. There was possibility of blade adjustment (mechanical) and gondola adjustment (remote) in range +/- 10°. The turbine was equipped with a rectifier and a grid inverter connected directly to the grid. It was also possible to connect the turbine to a battery load system and to the electronic load for some testing. The turbine was equipped with a clutch for connecting the rotor shaft with the generator, it also had a torque sensor and some other equipment. Generally the facility was equipped with two turbines, meteo station and some sensors (totally 87 signal channels) and the time step of data registration was one second. More information about the system can be found in Filipowicz 2018 and Filipowicz 2019.

3. DATA ANALYSIS

The aim of this section is to characterise wind properties for analysed location.

3.1. Basic wind correlations

The aim of this subsection is to show a correlation between velocities measured by selected anemometers to illustrate the effect of the anemometer position and wind pattern change caused by the presence of the building envelope. Data from anemometers in front of the turbine (V_1, V_2) and behind (V_3, V_4, V_5) are shown in Figure 3.

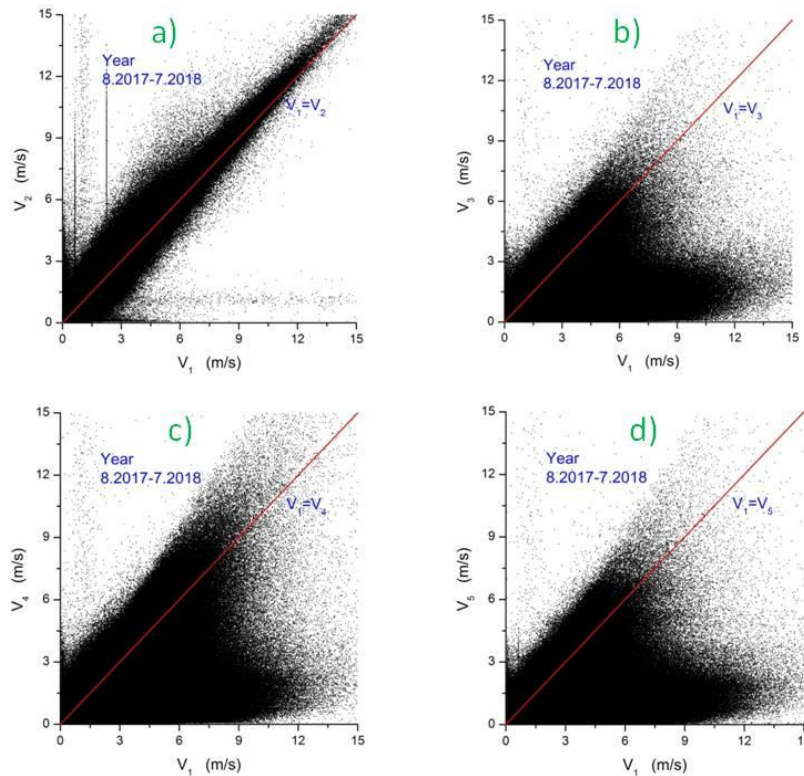


Figure 3: Scatter plot of wind correlations a) V_1 - V_2 , b) V_1 - V_3 , c) V_1 - V_4 , d) V_1 - V_5

It is visible that the correlation between inlet wind velocities (V_1 and V_2) was linear in trend. The points were located with some spread around line $V_1 = V_2$, however this spread was not uniform. More points were placed above this line, which means that case $V_2 > V_1$ was more common. This may be caused by some effect of a small increase in wind velocity caused by the building. Correlations for V_3 - V_5 anemometers were generally similar, however some differences were visible in the shape of the plots. All the time points with higher than V_1 velocities were visible. It confirms a complex wind flow near the turbine and the building.

3.2. Wind velocities

Wind histograms presented for particular months and the whole year are presented to illustrate wind energy potential and its monthly variation. In conditions of Polish climate, those variations are strong and worth emphasising. Also the averaged monthly values are presented. The wind velocity histograms for anemometer V_1 are presented in Figure 4. It is visible that for summer month the calm period (velocity less than 0.5 m/s) was significant, the same for almost half of the year 2018. For the months October 2017, December 2017 and January 2018, a higher fraction of high speed winds was observed. Especially poor wind conditions are visible for February 2018 and for a few months in 2018. The whole year histogram is presented in Figure 4 left. Unfortunately, the big fraction of calm winds (~30%) is visible.

A fitting procedure was applied to find the statistical distribution describing the data in a best way. The typical statistical distribution like Weibull, Gamma (2 and 3 parameters), Square-normal, Generalised Extreme Valued and Double-exponential (4 parameter) were checked. Graphical results are presented in Figure 4 right. Due to a high fraction of the calm period, a double-exponential distribution describes the data in the best way.

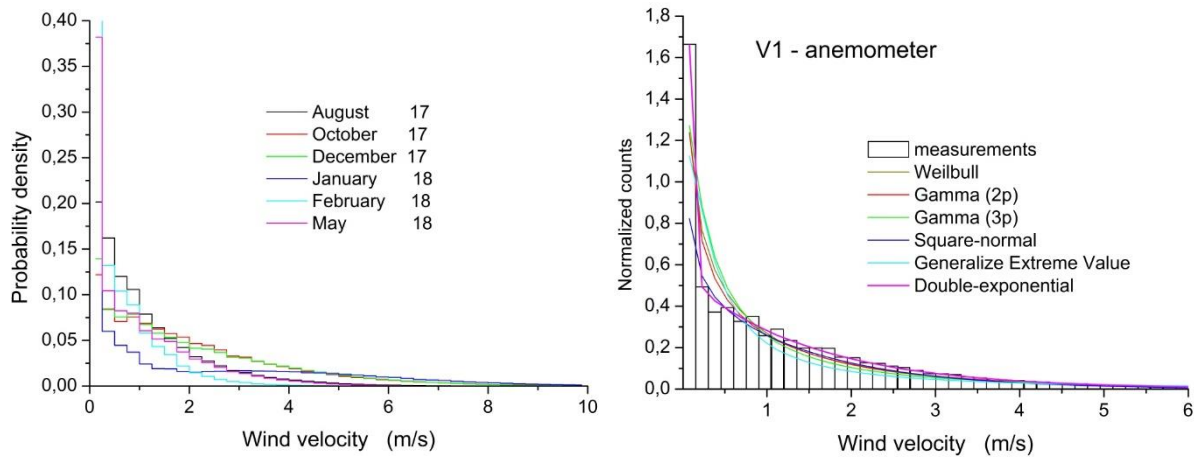


Figure 4: Wind velocity histogram (V_1 anemometer) for selected months and whole year with fitting distributions

The wind profiles for months and hours are presented in Figure 5.

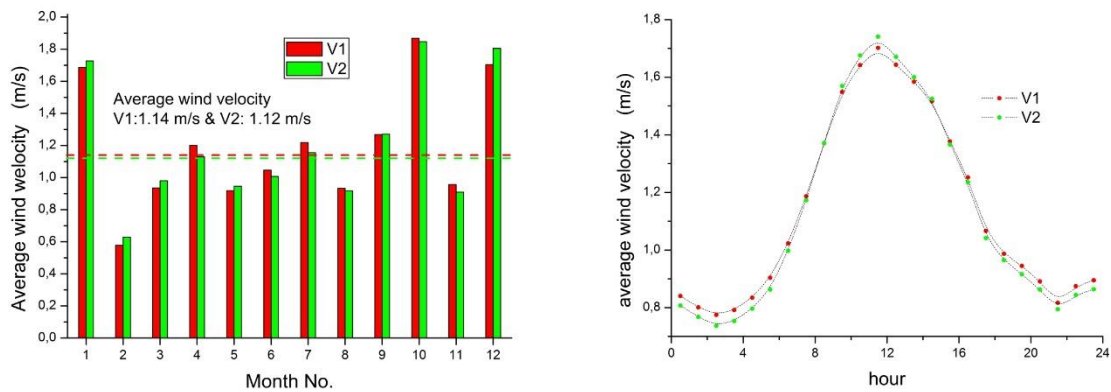


Figure 5: Monthly (right) and diurnal (left) wind velocity profiles for V_1 and V_2 anemometers.

It is well visible that the highest averaged velocities are for some months in autumn and spring (Figure 5 left), the weakest winds were observed in February and in the summer months. The months with strongest winds were October 2007, December 2017 and January 2018. The yearly average wind velocity was only 1.12 (1.14) m/s. This illustrated very weak wind conditions, mainly as a result of extended calm periods. The highest reported velocities (see Figure 5 right) were for midday hours (between ~10-15h), with the maximum near 12-13h. The velocities were twice that of the period of weakest winds (~20-5h), i.e. night winds. In this case, the turbine cannot be a good solution as a night power source. This diurnal profile was rather the opposite to that observed in open terrain where night winds are often considerably stronger than day winds. It can be explained as a result of the accumulation of solar radiation energy in the city area causing an increase of pressure differences during day-hours. However, a built-up area is also responsible for an increase of calm period as illustrated in Figures 4 and 5.

3.3. Wind direction

Figure 6 presents a wind rose for the whole period. It is visible that the predominating direction was SW. Generally, there was a big difference between autumn-winter and spring-summer periods. The unfavourable building orientation was confirmed by the rose. The fraction of winds from the exact WNW direction was only ca. 3% and its velocity was mostly low. The optimal building orientation was then SW.

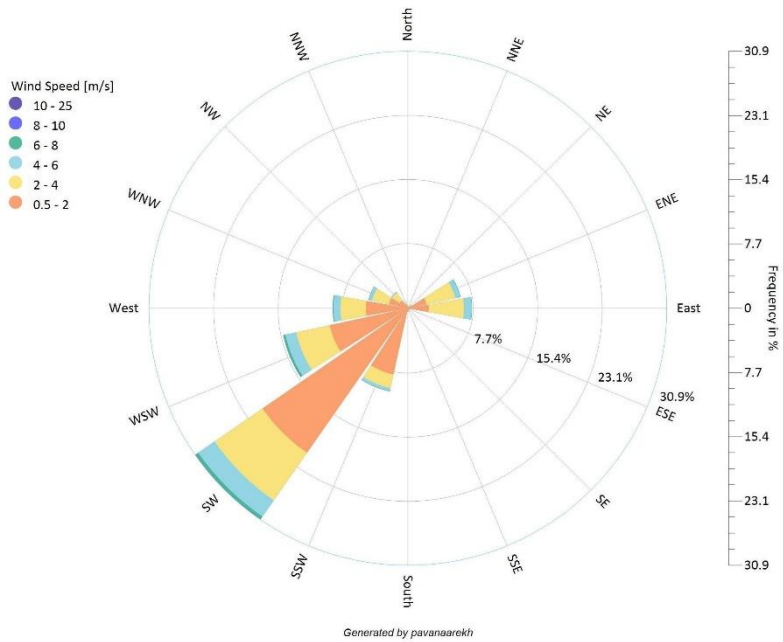


Figure 6: Wind rose for the whole year

3.4. Power spectra

The power spectra for selected cases are presented in Figure 7 which illustrates some characteristic periods.

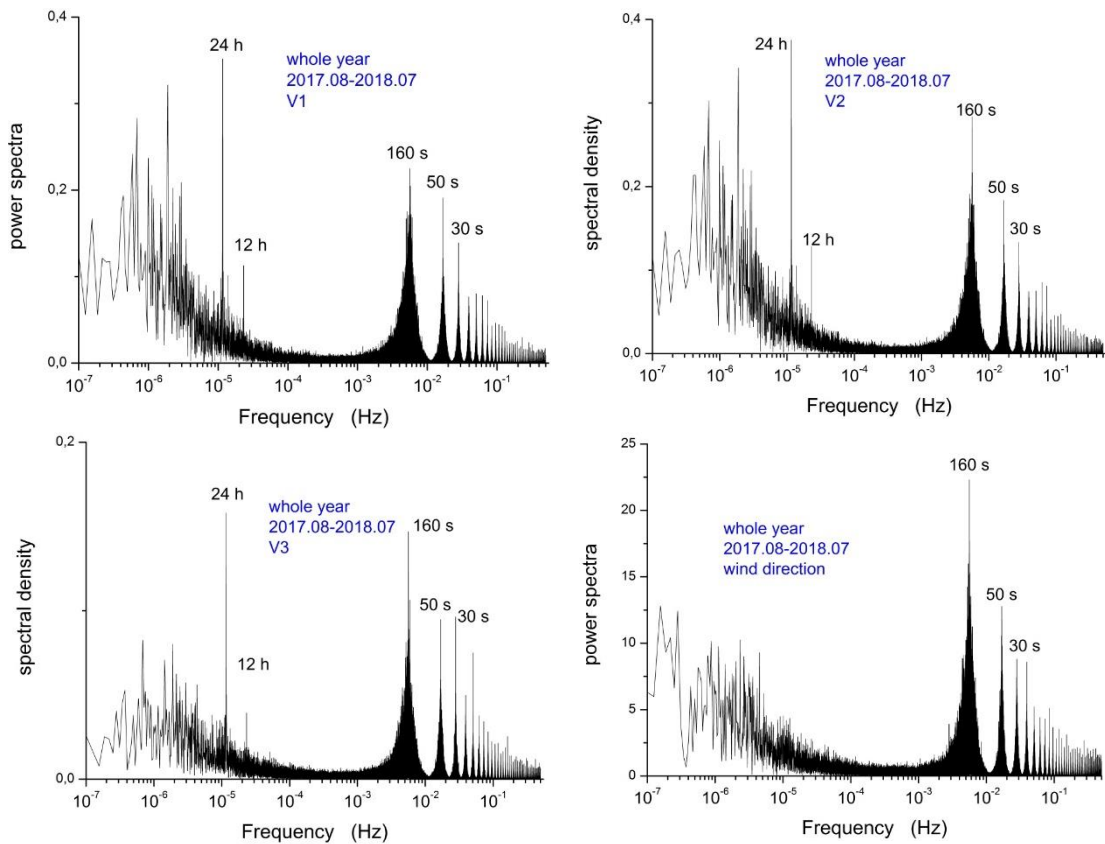


Figure 7: Whole-year power spectra for V_1, V_2, V_3 anemometers and for wind direction

Two peaks - diurnal (24h) and half-diurnal (12h) are visible for all plots except the wind direction. Turbulence power spectra with peaks for 160s, 50s, 30s, 20s, 16s, etc are visible. Comparing spectra for anemometers V_1, V_2 and V_3 - spectra are similar but for V_2 and V_3 turbulence peaks were stronger. For V_3 spectra, the half-diurnal peak was

weaker compared to the V_1 and V_2 spectra, confirming literature data. The existence of the synoptic peak (frequencies around 10^{-6} Hz), diurnal peaks and the turbulence region, generally confirms the literature data, however the turbulence region is more visible here, turbulence peaks are stronger than the synoptic peak.

3.5. Mechanical interaction

The influence of building environment and structure on the wind turbine was checked by analysing noise and vibrations generated by the turbine. The effect can be illustrated by scatter plots presenting level of noise and vibration depending on wind speed and the turbine rotations (RPM). Figure 8 illustrates those dependences.

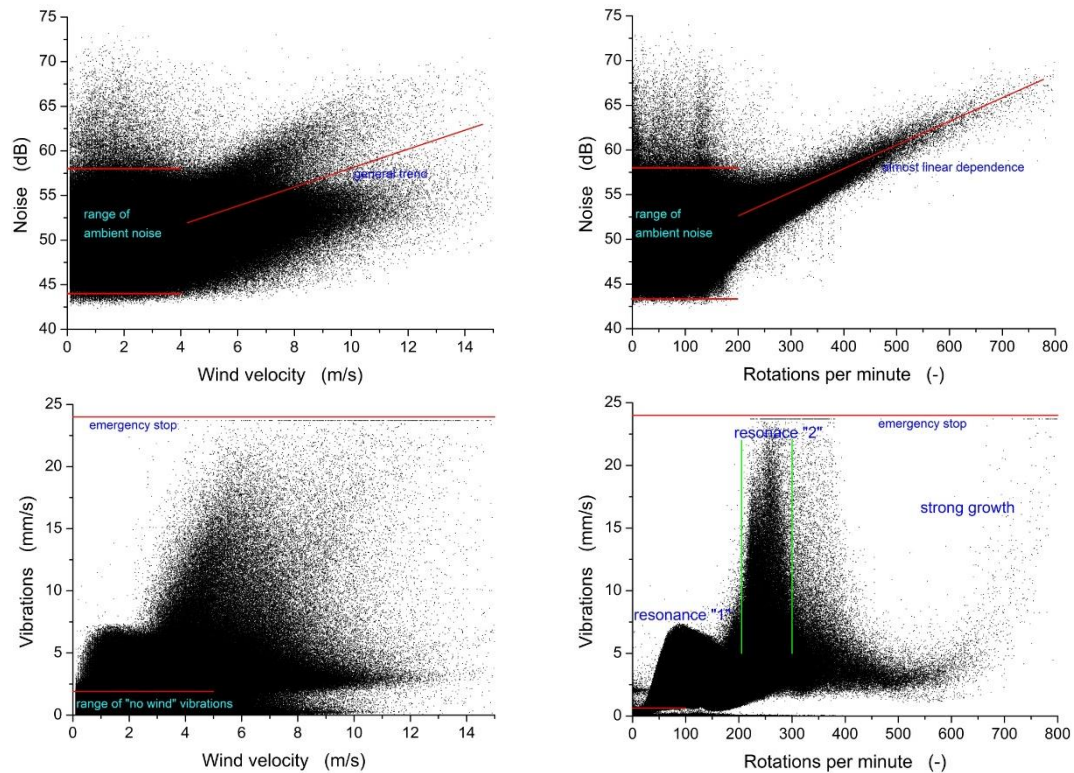


Figure 8: Noise and vibrations scatter plots for V_1 anemometer and rotations per minute

The effect of wind speed and the number of rotations per minute is visible in the noise and vibrations. The noise was almost constant in the range ca. 45-60 dB and a wind speed lower than ~ 4 m/s had no influence on it. Some growth was visible above this speed and was equal to ca. 1dB/(m/s), however the spread around the mean value was quite big. The noise dependence on RPM was similar: up to ~ 200 RPM there was no visible dependence, then growth equal ca. 2dB/100RPM with definitely smaller spread around the mean value can be observed.

The behaviour of vibration was in some way different. For wind velocities larger than ~ 4 m/s, a significant growth of vibrations was observed, the maximum (for safety reason 20 mm/s was the emergency stop criterion) was reached for wind velocity ca. 6 m/s and then generally falls. This shows the existence of the resonance for wind velocity equal ~ 6 m/s. Similar, a stronger resonance peak exists for RPM equal ca. 250. Non resonance growth of vibrations level starts from ~ 600 RPM.

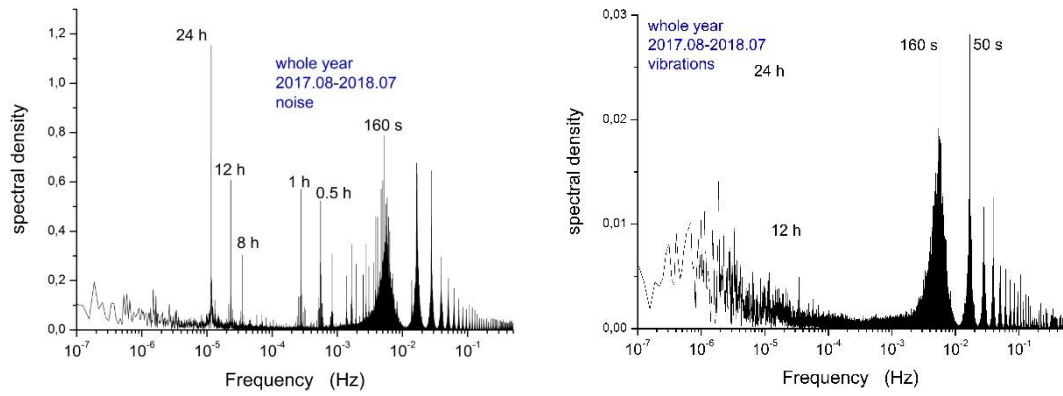


Figure 9: Power spectra for noise and vibrations

Power spectra for noise and vibrations are presented in Figure 9. For noise, it is visible that there is no peak from long-term correlation (the synoptic peak) but strong peaks for 24h, 12h, 8h, 1h, 0.5 h, etc. are visible. This resulted from the diurnal activity of the building and other periodical activities (e.g. street traffic, air conditioning system). For vibrations, long-term correlation was more visible meaning that vibrations have a stricter connection with wind compared to noise. Generally, the noise and vibrations spectra are similar and reproduce the structure of wind spectra (see Figure 7).

4. PERFORMANCE OF WIND TURBINE

In this section, data related to the wind turbine operations – electric power and the torque - are presented (Figure 10). The data was collected for conditions when wind speed was greater than zero (to exclude calm period) as well as the RPM generated power also being greater than zero.

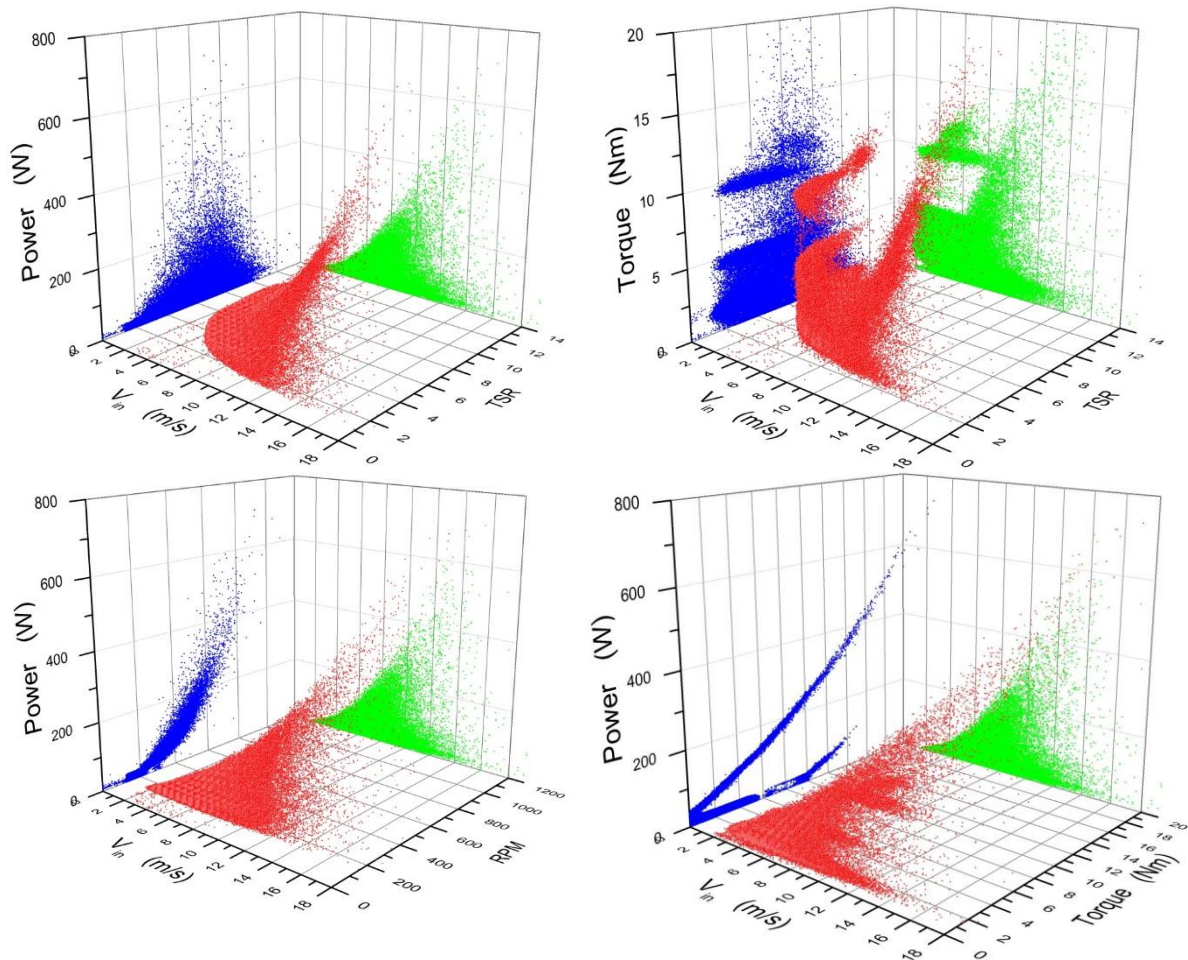


Figure 10: Power spectra for noise and vibrations

Maxima for power generation are visible – the maximum power was generated for inlet wind velocity V_{in} in equal ~ 10 m/s. It was visible that in most cases power falls for higher wind velocities, but sometimes higher power was observed for higher wind velocities, but again, for wind speed larger than 15 m/s, less power was generated. For the TSR parameter, the optimal range was 8-10. This confirms turbulence characteristic wind in the vicinity of the building.

The torque was highest for wind speed region 12-15 m/s and TSR for 8-10 m/s, reaching and exceeding the value of 20 Nm. However, behaviour of the torque was strange – there was a gap between 5-10 Nm for wind weaker than ca. 6 m/s. This is worth further detailed examination as it is the region of strong vibrations – therefore maybe some part of mechanical energy was converted to vibrations.

Electric power in the function of RPM had a simple shape – there was no power for inlet wind velocity less than 2 m/s (no rotations) and for RPM less than 120 RPM (the clutch settings). For RPM up to 200, the generated power did not exceed 30 W (the power inverter setting).

5. CONCLUSION

The facility described in the paper can be treated as a source of quite useful data in terms of the study and optimization of small wind turbines working in built-up area. In this paper, one year of the HAVT elevation wind turbine operation was described. The wide range of observation data was summarised in a compact way and some of the processed data was analysed. The following observations are supported by the performed analysis:

- It was visible that wind in the building vicinity had strong fluctuations of wind velocity and direction can be observed. It affected the performance of the turbine: the inlet wind velocity was often not correlated with the outlet wind; the outlet wind velocity can be higher than the inlet. This meant that the classical analysis of the turbine power and torque curve was difficult, the power and torque coefficient were difficult for interpretation;
- the wind speed histograms show that there existed a big fraction of calm period (velocity less than 0.25 m/s), annually it was ca. 25-30%; there was some difference between months – e.g. the average month velocity varies in range from 1.0 - 2.0 m/s. Generally it was a very low value but some optimisation existed – another turbine location and building orientation might improve the situation;
- the diurnal wind profile has a big variation – the wind speed maximum was registered at midday and the minimum in night hours (from 8pm to 4am), which is not a favourable situation for hybrid systems with PV;
- the wind direction was mostly from the SW, therefore buildings with integrated elevation turbines should be oriented approximately in such direction;
- the power spectra show that there was a weather component and peaks for diurnal breezes, also a high frequency turbulence component was visible. It shows that strong turbulence existed and a special turbine optimisation should be applied;
- the noise and vibration generation was not high, however this parameter should be controlled and in case of danger (especially the resonance vibrations) some emergency systems (brakes) should be applied. The exact turbine noise seems to be smaller than ambient noise, however the generated noise depends on the turbulence wind component;
- the turbine output shows that generated power and turbine torque depended on wind velocity, TSR and RPM but analysis of those relations was commonly not so easy as for a standalone turbine in the open area.

Generally, gathered data shows that such systems are worth further considerations. It is believed that more gathered data and more sophisticated CFD analysis validated by the data will lead to design of more customised devices.

6. ACKNOWLEDGEMENTS

The work has been completed as part of the statutory activities of the Faculty of Energy and Fuels at the AGH UST in Krakow (no. 16.16.210.476). The scientific infrastructure of the Center of Energy (Czarnowiejska 36, 30-054, Krakow, Poland, www.ce.agh.edu.pl) was used. This research was supported in part by PLGrid Infrastructure.

7. REFERENCES

- Casini M., 2016. Small Vertical Axis Wind Turbines for Energy Efficiency of Buildings, *Journal of Clean Energy Technologies*, Vol. 4, No. 1, 56-65
- Cho K., Jeong S., Sar D., 2011. Harvesting wind energy from aerodynamic design for building integrated wind turbines, *International Journal of Technology* 3, 189-198
- Cochran B.C., Damiani R.R., 2008. Harvesting wind power from tall buildings, *WindPower 2008*, Houston, Texas June 2-4, 2008
- Cho K., Jeong S., Sar D., 2011. Harvesting wind energy from aerodynamic design for building integrated wind turbines, *International Journal of Technology* 3, 189-198
- Dilimulati A., Stathopoulos T., Paraschivoiu M., 2018. Wind turbine designs for urban applications: A case study of shrouded diffuser casing for turbines, *Journal of Wind Engineering & Industrial Aerodynamics* 175, 179–192
- Emejamara F.C., Tomlin A.S., Millward-Hopkins J.T., 2015. Urban wind: Characterization of useful gust and energy capture, *Renewable Energy* 81, 162e172
- Filipowicz M., Żołądek M., Goryl W., Sornek K., 2018. Urban ecological energy generation on the example of elevation wind turbines located at Center of Energy AGH, *E3S Web of Conferences* 49, 00023
- Filipowicz M, Goryl W., Żołądek M., 2019. Study of building integrated wind turbines operation on the example of Center of Energy AGH, *IOP Conf. Series: Earth and Environmental Science* 214, 012122
- Grieser B., Sunak Y., Madlener R., 2015. Economics of small wind turbines in urban settings: An empirical investigation for Germany, *Renew Energ.*, 78, 334-350
- Haase M., Lofstrom E, 2015. Building augmented wind turbines - BAWT, SINTEF Academic Press, 2015
- Ishugah T.F., R.Z. Wang Y. Li, Kiplagat J.K., 2014. Advances in wind energy resource exploitation in urban environment: A review, *Renew. Sust. Energ. Rev.*, 37, 613-626
- Karthikeya B.R., Negi P.S., Srikanth N., 2016. Wind resource assessment for urban renewable energy application in Singapore, *Renewable Energy* 87, 403e414
- Laiola E., Giungato P., 2017. Wind characterization in Taranto city as a basis for innovative sustainable urban development, *Journal of Cleaner Production* 172, 1e11
- Ramenah H., Tanougast C., 2016. Reliably model of microwind power energy output under real conditions in France suburban area, *Renewable Energy* 91, 1e10
- Sengupta, A.R., Biswas A., Gupta, R., 2017. Vertical Axis Wind Turbines in the Built Environment-A Review, *ISESCO Journal of Science and Technology* 12, 11-16
- Sunderland K.M., Mills G., Conlon M.F., 2013. Estimating the wind resource in an urban area: A case study of micro-wind generation potential in Dublin, Ireland, *J. Wind Eng. Ind. Aerodyn.* 118, 44–53
- Toja-Silva F., Colmenar-Santos A., Castro-Gil M., 2013. Urban wind energy exploitation systems: Behavior under multidirectional flow conditions. Opportunities and challenges, *Renew Sust Energ Rev* 24, 364-278
- Yang A.S., Su Y.M., Wen C.Y., Juan Y.H., Wang W.S, Cheng C.H., 2016. Estimation of wind power generation in dense urban area, *Applied Energy* 171, 213–230

#329: A comprehensive numerical simulation of a sustainable power and heat generation cycle using CO₂

Onder KIZILKAN¹, Hiroshi YAMAGUCHI²

¹Department of Mechanical Engineering, Faculty of Technology, Isparta University of Applied Sciences, 32200, Isparta, Turkey, onderkizilkan@isparta.edu.tr

²Department of Mechanical Engineering, Doshisha University, Kyo-Tanabeshi, 610-0321, Kyoto, Japan, hyamaguc@mail.doshisha.ac.jp

A comparative numerical analysis of an organic Rankine cycle using supercritical CO₂ and assisted by evacuated solar collectors is presented in this study. In the system, natural working fluid CO₂ is used which is non-flammable, non-toxic and environmentally friendly. The proposed system consists of 15 sets of evacuated solar collectors for heating up the working fluid to a supercritical stage, a turbine for power generation, a feed pump for circulating the fluid and two heat exchangers. The first heat exchanger is a high-temperature heat exchanger used for recovering heat to be used for applications such as absorption refrigeration cycles, hot water preparation, etc., while the second heat exchanger is a low-temperature heat exchanger used for condensation of the CO₂. The characteristics and the specifications of the proposed system are based on an experimental setup which was previously constructed in Doshisha University. The numerical analysis of the organic Rankine cycle for power and heat generation is carried out using the meteorological data of two cities for comparison purposes, Kyoto, Japan and Isparta, Turkey. The performance characteristics of the proposed system are investigated under different working conditions. The analysis is made for the whole year in order to simulate the performance for different climate conditions. The results of the study show that the proposed system has great potential for green and sustainable power and heat generation.

Keywords: sustainable energy, solar energy, power generation, ORC, CO₂

1. INTRODUCTION

The world population and industrial activity increased considerably during the 20th century and, consequently, energy consumption during this period has risen almost exponentially. This increased energy consumption, largely satisfied by fossil fuels, has had significant environmental effects. While the energy demand is continuously increasing in all over the world, as a consequence, the number of new power plants is also increasing. This situation illustrates the necessity of developing new clean energy sources and of decreasing the energy intensity in all sectors of the economy (Cayer et al., 2009; 2010).

In recent years, due to global warming and projected fossil fuel depletion in reserves the utilization of renewable energy got more attention. In this regard, solar energy is projected as one of the most reliable alternative energy sources due to its abundant availability and environment friendliness. So it becomes imperative to upgrade the performance of solar thermal power plants. In order to utilize solar energy in the most efficient way, several possible technologies have been explored over the last three decades. Today, solar energy is converted to useful heat energy by using solar collectors such as flat plate, evacuated tube, parabolic trough, dish collectors, etc. Great interest was given to increase the performance of these collectors. Several research and companies send effort and money for that. Evacuated tube solar collectors (ETSC) are considered an important type of solar collector. ETSC is a device which is generally used to deliver heat for several applications such as water heating, air conditioning, etc. This collector can achieve a higher temperature range of above 120°C, due to their combining effects of highly selective surface coating and vacuum insulation (Naik et al., 2016; Singh and Mishra, 2018; Sharafeldin and Grof, 2018.).

The use of transcritical organic Rankine Cycle (ORC) has recently been studied with low-temperature heat sources such as geothermal sources, solar energy, and vehicle exhaust gases. Because these are sources of sensible heat, a variable temperature is obtained when exchanging heat with the working fluid of the power cycle. The liquid to vapour transformation of the transcritical cycle being also at variable temperature, the match between the two temperature curves provides a high recovery potential. This cycle is then well suited for solar-assisted systems at low temperatures (<350°C) (Cayer et al., 2009; 2010). Conceptually, the ORC is similar to a steam Rankine cycle in that it is based on the vaporization of a high-pressure liquid which is in turn expanded to a lower pressure thus releasing mechanical work. The cycle is closed by condensing the low-pressure vapour and pumping it back to the high pressure. Therefore, the ORC involves the same components as a conventional steam power plant. However, the working fluid is an organic compound characterized by a lower ebullition temperature than water and allowing power generation from low heat source temperatures. These assets make the ORC technology more adapted than steam power to the conversion of renewable energy sources whose availability is generally more localized than that of fossil fuels, and whose temperature (e.g. in a solar collector or in a geothermal well) is lower than that of traditional fuels (Quoilin et al., 2003).

Since the signing of the Kyoto protocol to reduce greenhouse gas emissions by about 5%, the technologically developed countries have had a motivation to switch-over to the ecologically safe chlorine-free refrigerants. The growing ecological concern over the use of working fluids renewed the interest in utilizing environmentally benign natural fluids, such as water, air, ammonia, silicon oil, propane and carbondioxide (CO₂) (Islam and Sumathy, 2013). For instance, while water is potentially the most commonly used working fluid of all due to its availability, stability, environmental compatibility, etc., technically speaking; it might be somewhat unpractical for the applications of relatively low temperatures. Among the natural fluids, CO₂ has been identified as a promising working fluid with many advantages, such as its environmental compatibility and the anomalous behaviour of certain thermo-physical properties (Cardemil and da Silva, 2016). Due to its supercritical condition, CO₂ is attracting interest in solar power applications because it has excellent thermal properties. The critical state can be reached easily due to its moderate critical pressure (7.38 MPa) and low critical temperature (31.1°C). Among other advantages, CO₂ is abundant, inexpensive, non-explosive and non-combustible. Higher efficiencies are possible using supercritical CO₂ because it can withstand high temperatures without degradation, and requires less compression work close to the critical point. Moreover, the change in fluid properties such as density and specific heat close to the critical point offers potential benefits in terms of compact systems (Osorio et al., 2016). Additionally, it has a strong potentiality to be used as an alternative refrigerant as it has a very low GWP and neutral effect on the depleting ozone layer (Islam and Sumathy, 2013).

In the present study, a numerical analysis of a solar-assisted ORC working with CO₂ was presented comparatively. For the modelling of the investigated system, the specifications of the experimental system which have been already constructed in Doshisha University, Kyoto, Japan were used. The system consisted of 15 sets of ETCSs for heating up the CO₂ to a supercritical temperature, a turbine, a mechanical feed pump, a heat recovery system (HRS) and a condenser. For power and heat generation, the numerical analysis of the ORC was carried out for two cities comparatively, Kyoto, Japan, and Isparta, Turkey. The performance of the ORC was assessed for the two cities using the meteorological data for the whole year.

2. SYSTEM DESCRIPTION

2.1. Solar-assisted ORC

As mentioned previously, the investigated solar-assisted ORC was adapted from the experimental setup which was first proposed by Yamaguchi and his research group (Zhang et al., 2005). Figure 1 shows the schematic representation of solar-assisted ORC working with CO₂. The actual experimental prototype of the ORC was designed and constructed at the Energy Conversion Research Centre at Doshisha University. In the first prototype, there was no turbine mounted on the system, instead of the turbine, an expansion valve was used for simulating the turbine operation (Yamaguchi et al, 2006; Zhang et al., 2006; 2007).

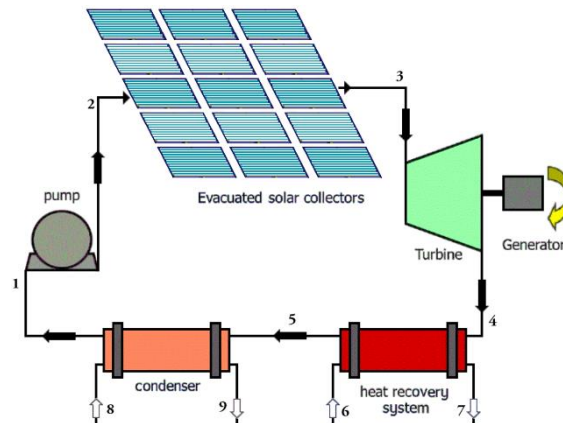


Figure 1: Schematic representation of the proposed system (Adapted from Pumaneratkul, 2018)

In the solar-assisted system ORC, CO₂ is heated up in the ETSC while it is flowing through the serially connected collectors. After passing ETSC, CO₂ becomes supercritical fluid at high temperature and pressure before the inlet of the turbine. After, it enters the turbine and electric power is generated during it is expanded to lower pressure. The CO₂ expelled from the turbine with lower pressure is then cooled in the HRS. The HRS is used to provide heat energy to be used in thermal processes such as hot water preparation, absorption refrigeration, etc. At the exit of the HRS, the supercritical CO₂ is still at a higher temperature; therefore it has to be cooled down to a saturated liquid state in the condenser. After leaving the condenser, CO₂ is pumped by the pump again to a higher-pressure condition (Zhang and Yamaguchi, 2008; Niu et al., 2011).

2.2. Evacuated tube solar collectors

Solar collectors are the major component in solar thermal systems, with flat plate and evacuated solar tube collectors the most common forms. Compared with the flat plate collector, the evacuated solar tube collector generally works better in cold climates (Gao et al., 2017). The ETSCs provide the combined effects of a highly selective surface coating and vacuum insulation of the absorber element so they can have high heat extraction efficiency compared with flat plate collectors. At present, the glass evacuated tube has become the key component in solar thermal utilization (Ma et al., 2010). Also, they are cost-effective, most reliable and have reasonably longer lifetime (Naik et al., 2016). The U-tube solar collector is the heart of the CO₂-based ORC. Its characteristics play an important role in the successful operation of such systems. For the proposed system, the modelling of the ETSC was made using the actual properties of the collectors used in the experimental system. The actual ETSCs was developed and provided by Showa Denko. K.K. as a commercial product (Figure 2). There are 15 units of collectors which can be connected in parallel and/or in series by adjusting the valves. Each collector unit is made of 13 collector tubes. The collectors can stand temperature up to 250°C (Niu et al., 2013).

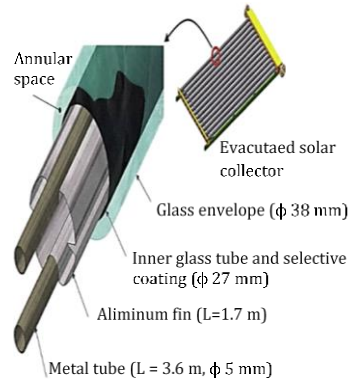


Figure 33: Evacuated tube solar collectors and cross-section of evacuated tube (Yamaguchi et al., 2006)

2.3. Solar energy potentials of Kyoto and Isparta

Turkey's geographical location is highly favourable for the utilization of solar energy. The yearly average solar radiation is 3.6 kWh/(m²day) and the total yearly insolation period is approximately 2460 hours, which is sufficient to provide adequate energy for solar thermal applications. The southeast Anatolian region is the most favourable region for solar energy use (Balat, 2005). However, due to its geographical conditions, Japan is generally a rainy country with high humidity. Because of its wide range of latitudes and seasonal winds, it has a variety of climates. In accordance with Japan's uniformly heavy rainfall, sunshine is generally modest in quantity. According to the Solargis (2019), many parts of Turkey have a great solar energy potential with a maximum yearly direct normal irradiance of 2337 kWh/m² while Japan has a maximum potential of 1500 kWh/m². As seen from Figure 3, many parts of Turkey are available for solar energy due to its geographical position (Solargis, 2019).

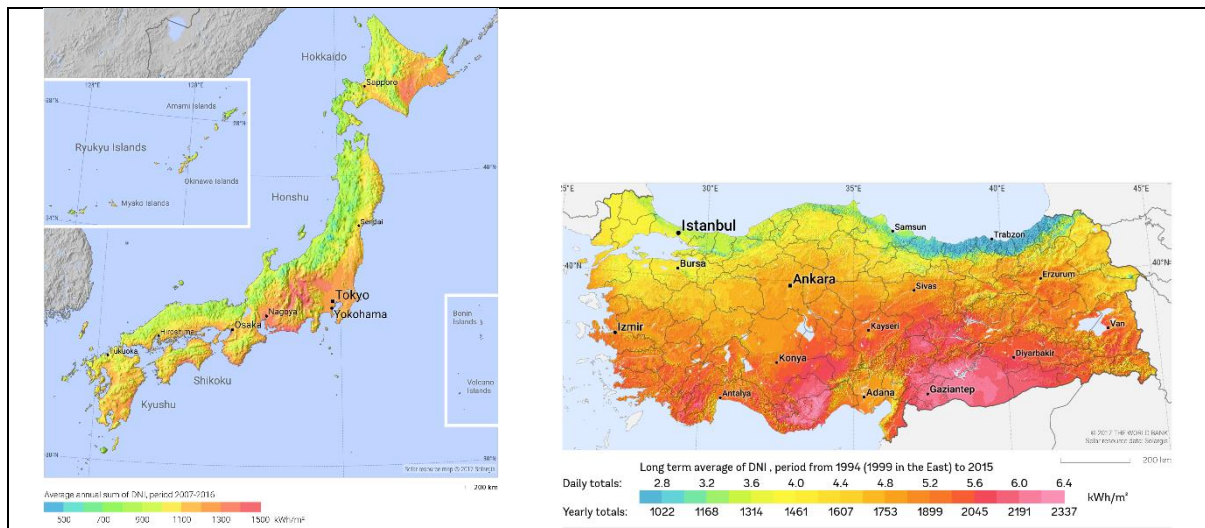


Figure 34: Direct normal irradiance maps for Japan and Turkey (Solargis, 2019)

3. MATHEMATICAL MODELLING

Figure 4 shows the cross-sectional of the evacuated solar U-Tube with the thermal network. The U-tube is heated by the solar radiation across the evacuated space and effective incident solar irradiance is then absorbed by the selective coating. The big amount of absorbed solar energy is conducted aluminium fin to U-tube and then transfer to the working fluid. In order to determine the radiation heat transfer coefficient between the outer glass tube and the sky, the equation given by Kalogirou (2009) is used:

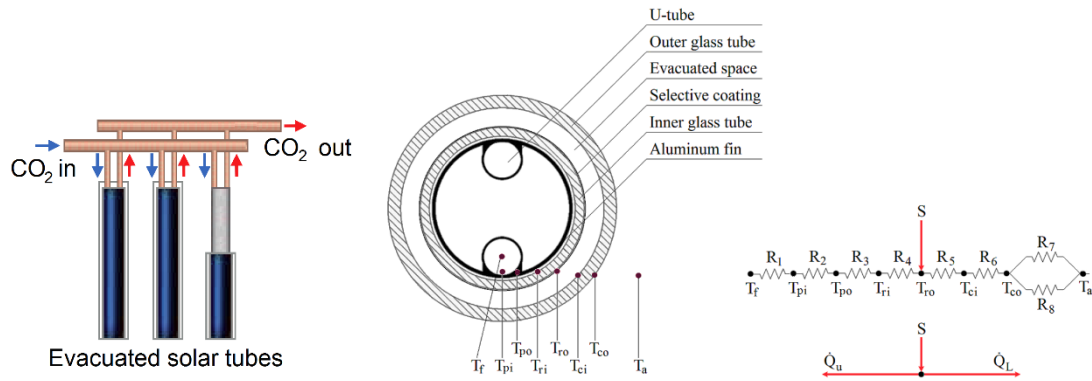


Figure 35: Thermal network of the evacuated solar U-Tube (adapted from Li, et al., 2013; Islam and Sumathy, 2013)

Equation 20: Radiation heat transfer coefficient between the outer glass tube and the sky

$$h_{r,co sky} = \epsilon_c \sigma (T_{co} - T_{sky}) / (T_{co}^2 - T_{sky}^2)$$

Where:

- σ = Stefan–Boltzmann constant (W/m^2K^4)
- ϵ_c = emittance of the glass cover (-)
- T_{co} = temperature of outer glass cover ($^{\circ}C$)

The sky temperature is calculated from $T_{sky} = 0.0552T_{air}^{1.5}$. Convection heat transfer coefficient between outer glass tube and the environment is given below.

Equation 21: Convection heat transfer coefficient between the outer glass tube and the environment

$$h_{c,co a} = Nu_a k_a / D_{co}$$

Equation 22: Nusselt number

$$\text{for } 0.1 < Re < 1000 \quad Nu_{air} = 0.4 + 0.54 Re^{0.52}$$

$$\text{for } 1000 < Re < 50000 \quad Nu_{air} = 0.3 Re^{0.6}$$

Where:

- k = thermal conductivity (W/mK)
- D = diameter (m)
- Re = Reynolds number (-)
- Nu = Nusselt number (-)

The conduction heat transfer coefficient through the outer glass tube can be expressed as:

Equation 23: conduction heat transfer coefficient through the outer glass tube

$$h_{d,co ci} = \frac{k_c}{r_{ci} \ln(r_{co} / r_{ci})}$$

Where:

- r_{ci} = radius of inner glass cover (m)
- r_{co} = radius of outer glass cover (m)

Since the place between inner and outer glass tubes is evacuated, the convection heat transfer is assumed to be zero, thus, the heat transfer occurs only by radiation. The radiation heat transfer coefficient between the absorber surface and the outer glass tube is defined as (Kalogirou, 2009):

Equation 24: Radiation heat transfer coefficient between the absorber surface and the outer glass tube

$$h_{r,ro ci} = \frac{\sigma}{1/\epsilon_r + r_{ro}/r_{ci}(1/\epsilon_c - 1)} (T_{ro} - T_{ci}) / (T_{ro}^2 - T_{ci}^2)$$

Where:

- ϵ_r = emissivity of the selective absorbing coating (-)
- r = inner glass tube
- c = outer glass tube

For the inner tube, the conduction heat transfer through the absorber wall can be expressed as:

$$\text{Equation 25: Conduction heat transfer through the absorber wall} \quad h_{d,ro,ri} = \frac{k_r}{r_{ri} \ln(r_{ro}/r_{ri})}$$

Referring to Figure 2, the overall heat loss coefficient can be determined by:

$$\text{Equation 26: Overall heat loss coefficient} \quad \frac{1}{U_L} = \frac{r_{co}}{h_{r,ro,ci} r_{ro}} + \frac{r_{co}}{h_{d,cl,co} r_{ri}} + \frac{1}{h_{c,co,a} + h_{r,co,sky}}$$

Also, from Figure 2, the heat loss coefficient of the evacuated U-tube tube can be expressed as;

$$\text{Equation 27: Heat loss coefficient of the evacuated U-tube tube} \quad U_L = (T_{ro} - T_a) = h_{c,co,a}(T_{co} - T_a) + h_{r,co,sky}(T_{co} - T_{sky})$$

Absorber temperature, T_{ro} , can be easily calculated iteratively by using Equation (7). The overall heat transfer coefficient from the environment to the fluid inside the U-tube is calculated by;

$$\text{Equation 28: Overall heat transfer coefficient} \quad \frac{1}{U_o} = \frac{1}{U_L} + \frac{r_{co}}{h_{d,ro,ri} r_{ro}} + \frac{r_{co}}{2h_{d,pipe} r_{ro}} + \frac{r_{co}}{2h_i r_{pipe}}$$

After determining heat transfer coefficients, the useful collected solar energy has to be determined:

$$\text{Equation 29: Useful collected solar energy} \quad \dot{Q}_u = F_R A (S - U_L (T_{in} - T_a))$$

Where:

- S = solar irradiance (W/m²)
- FR = heat removal factor (-)
- A = collector area (m²)
- T_{in} = inlet temperature of CO₂ (°C)

The heat removal factor F_R is described by (Kalogirou, 2009):

$$\text{Equation 30: Heat removal factor} \quad F_R = \frac{\dot{m}C_p}{AU_L} (1 - \exp(-\frac{AU_L F'}{\dot{m}C_p}))$$

Where:

F' = collector efficiency factor (-)

$$\text{Equation 31: Collector efficiency factor} \quad F' = U_o / U_L$$

For determining the CO₂ temperature at the collector exit, the useful solar energy collected by evacuated solar tubes can be also written as:

$$\text{Equation 32: Useful solar energy collected by evacuated solar tubes} \quad \dot{Q}_u = \dot{m}C_p (T_{out} - T_{in})$$

For the energy analysis of the supercritical ORC, general energy balance equations are used from the literature (Kizilkan, 2018).

4. RESULTS AND DISCUSSION

ETSC assisted ORC working with CO₂ was analysed comprehensively based on the system characteristics and employing the mathematical model previously described. The analyses were carried out for Kyoto and Isparta for comparison purposes using the actual dimensions and the properties of ETSC mounted at in an experimental setup. Calculations were made utilizing monthly solar radiation data. During all analyses, the system parameters given in Table 1 were used.

Table 21: System parameters

High pressure	9000 kPa
Low pressure	6500 kPa
Mass flow rate of CO ₂	0.007 kg/s
Mass flow rate of cooling water (HRS)	0.01 kg/s
Mass flow rate of cooling water (condenser)	1.1 kg/s
HRS area	0.1 m ²
Condenser area	0.2 m ²
Inlet water temperature (HRS)	35 °C
Inlet water temperature (condenser)	15 °C
Turbine isentropic efficiency	0.94
Pump isentropic efficiency	0.90
Total effective collector area	9.6 m ²

The monthly average solar radiation data for Kyoto and Isparta are given with the average temperatures in Figure 5a. These data were taken from Japan Meteorological Agency for Kyoto (2019) and Turkish State Meteorological Service for Isparta (2019). In Figure 5b, the CO₂ temperature at the outlet of ETSC is given for the whole year. It can be seen from the figure that there is an obvious influence of incident solar radiation on the cycle temperatures. As the average solar radiation increases gradually from January to July, the cycle temperature values increase and vice versa from July to December for Kyoto. This increment trend is from January to August for Isparta. Also, the exit temperature of T₃ is higher for Isparta than the calculated results of Kyoto. The maximum exit temperature achieved for Isparta is 223.9 °C while 207.6°C for Kyoto. The annual average temperature of CO₂ at the exit of the ETSC is calculated as 188.16 °C and 172.09°C for Isparta and Kyoto, respectively. The results of CO₂ temperatures at the exit of the turbine is also given. According to the results, the CO₂ temperature is still high and this leads the utilization of this heat energy for heat recovery purposes.

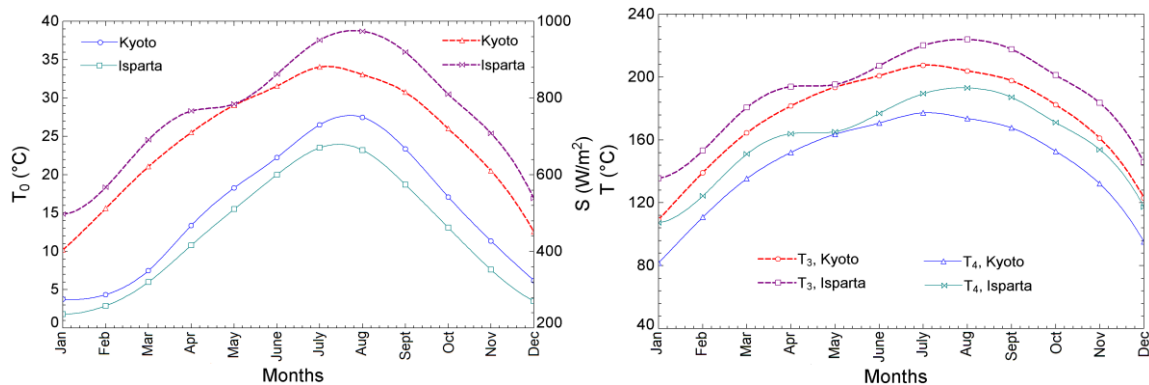


Figure 36: a) Monthly average temperatures and radiation data for two cities b) CO₂ temperature at the inlet (T₃) and outlet of the turbine (T₄)

Figure 6a shows the variations of useful solar energy absorbed by the ORC system with solar collector efficiency for the different months of the year. As seen from the figure, the absorbed solar energy increases from January to July for Kyoto and to August for Isparta with the increase of solar radiation. On contrary to this, the solar collector efficiency is decreasing with the increase of solar radiation as displayed on the right-hand side of the figure. This is because with the increase of solar radiation, the heat loss to the ambient environment is increased which affects the absorbed solar energy. Variation of net power generation and ORC efficiency are given in Figure 6b for both cities. From Figure 6b, it is obvious that the power generation of ORC increases with the solar radiation. The reason is that the turbine inlet temperature effectively raised by from January to July and August for Kyoto and Isparta, respectively. It can also be seen from the figure that, the higher solar radiation leads to an increase in cycle efficiency. With the comparison of the result for two cities, it can be observed that net power generation is obviously higher for Isparta conditions than Kyoto.

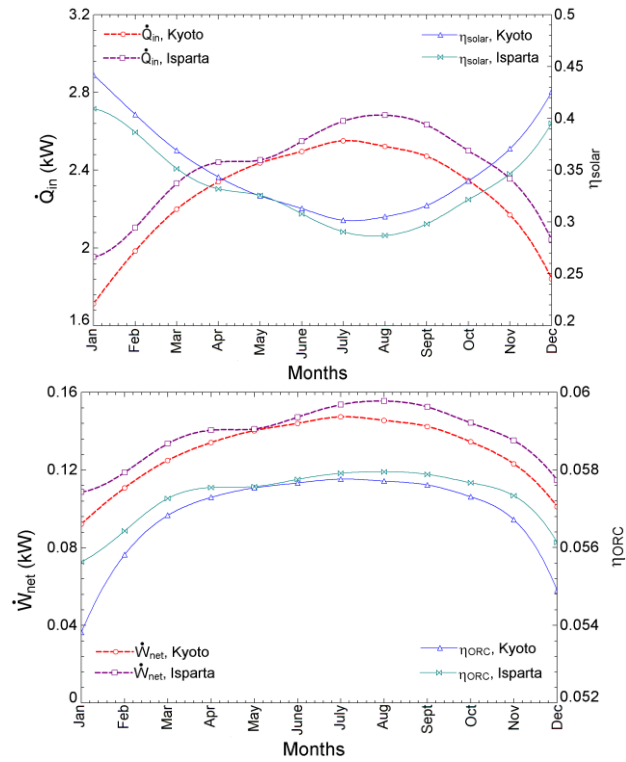


Figure 37: a) Absorbed solar energy and collector efficiency b) Net power generation and ORC efficiency

The variation of recovered heat energy by HRS and the water temperature at the exit of HRS are given according to the months in Figure 7a. With the assumed parameters given in Table 1, the hot water temperature increases with solar radiation and it reaches to a maximum value of 54.87°C for Isparta and 52.91°C for Kyoto. Also, the amount of recovered heat energy can be seen at the left-hand side of the figure. With changing the parameters, such as mass flow rate, heat exchanger area, etc., the temperature of hot water can be increased for utilization in absorption refrigeration cycles since the CO₂ temperature is suitable for such application. Figure 7b shows the overall system efficiency for the months of the year. It is obvious from the figure that the overall efficiency is slightly higher for Isparta than that of Kyoto. Also from the figure, the overall efficiency increases till to July for Kyoto and August for Isparta, after these months, it starts decreasing due to the decrement of solar radiation. It must be noted that, for the calculations of the overall efficiency, net power generation and heat recovery capacity were taken as gained energy. For Kyoto, the minimum overall efficiency was calculated as 20.81% for January, while it was calculated as 25.74% for Isparta. The highest efficiencies were found to be 36.76% and 35.12% for Isparta and Kyoto, respectively.

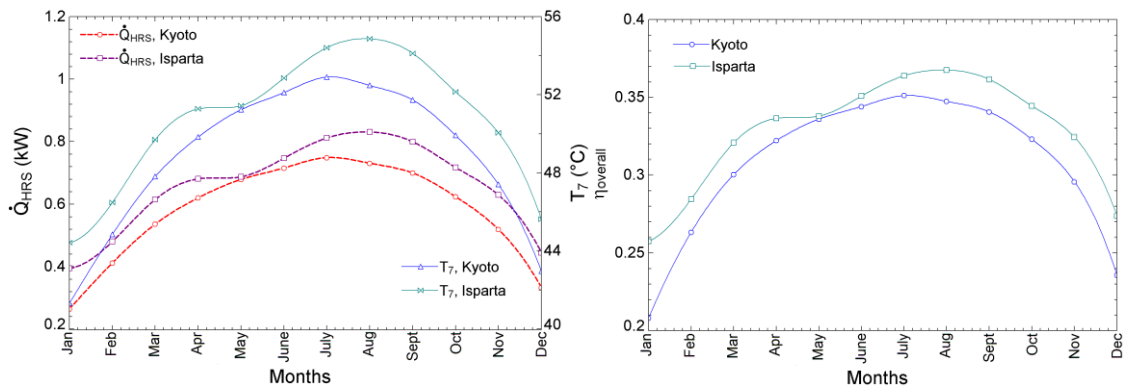


Figure 38: a) Recovered heat energy and hot water temperature at the exit of HRS b) Overall efficiency

The CO₂ temperature variation while passing throughout the ETSC is given in Figure 8, for both cities. The result was given here for July conditions. Symbols on the figure represent the temperature of CO₂ at each collector outlet and there were 15 collectors as mentioned previously. According to the results, the CO₂ temperature increment is higher in the first collectors. After the 8th collector, the increment ratio decreases and in the final collectors, the temperature nearly remains constant. This is mainly because of the temperature difference between the solar

collector and the CO₂ since at the end of collector arrays, the CO₂ temperature approaches collector temperature. The second reason may be the increasing heat losses at high temperatures.

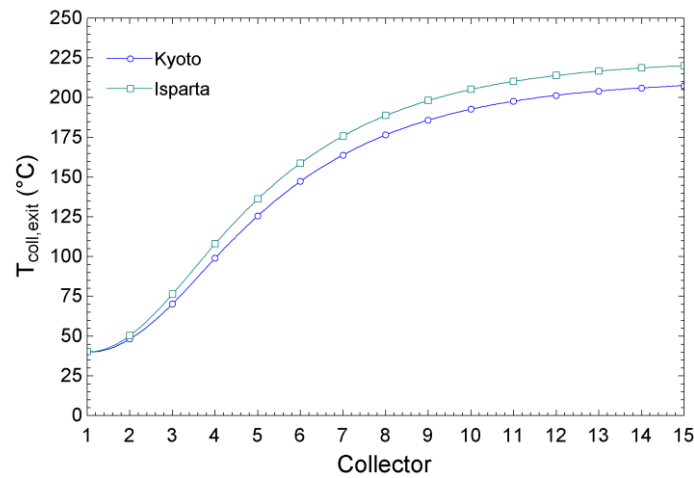


Figure 39: CO₂ temperature variation in the collector arrays

5. CONCLUSION

A numerical investigation has been carried out of a solar-assisted ORC working with CO₂ for power and heat generation. The analyses were done for two cities, Kyoto and Isparta. According to the results, the followings were concluded:

- The solar radiation values of Isparta were higher than the Kyoto due to geographical locations of the cities.
- According to the data, the highest average solar radiation for Kyoto was 881 W/m² in July while it was 971 W/m² for Isparta in August.
- The maximum CO₂ temperatures at the exit of ETSC were 223.9°C and 207.6°C for Isparta and Kyoto, respectively.
- The annual average net power generation was calculated as 128.39 W for Kyoto and 137.13 W for Isparta.
- The mean annual ORC efficiencies were calculated as 5.72% for Isparta and 5.67% for Kyoto while the overall efficiencies were found to be 32.74% for Isparta and 30.56% for Kyoto.
- Isparta's solar potential is obviously higher than that of Kyoto. Furthermore, Turkey has got great potential for solar energy utilization. Kyoto's climatically conditions is rainier than Isparta and the total sunshine is generally modest in quantity.

6. REFERENCES

- Balat, B, 2005. Solar Energy Potential in Turkey. *Energy Exploration & Exploitation*, 23(1), 61–69.
- Cardemil, JM, da Silva, AK, 2016. Parametrized overview of CO₂ power cycles for different operation conditions and configurations – An absolute and relative performance analysis. *Applied Thermal Engineering*, 100, 146-154.
- Cayer, E, Galanis, N, Desilets, M, Nesreddine, H, Roy, P, 2009. Analysis of a carbon dioxide transcritical power cycle using a low temperature source. *Applied Energy*, 86, 1055–1063.
- Cayer, E, Galanis, N, Nesreddine, H, 2010. Parametric study and optimization of a transcritical power cycle using a low temperature source. *Applied Energy*, 87, 1349–1357.
- Gao, Y, Fan, R, Zhang, XY, An, YJ, Wang, MX, Gao, YK, Yu, Y, 2014. Thermal performance and parameter analysis of a U-pipe evacuated solar tube collector. *Solar Energy*, 107, 714–727.
- Islam, MR, Sumathy, K, 2013. Carbon Dioxide driven Solar-assisted Heat Pump Water Heating System: A Theoretical Analysis. *International Research Journal of Environment Sciences*, 2(10), 77-92.
- Japan Meteorological Agency, 2019. Monthly mean air temperature [online]. Available at: https://www.data.jma.go.jp/obd/stats/etrn/view/monthly_s3_en.php?block_no=47759&view=1 [Accessed 15 May 2019]

- Kalogirou, SA, 2009. *Solar Energy Engineering: Processes and Systems*, Academic Press, Oxford.
- Kizilkan, O, 2018. Exergetic performance assessment of solar driven combined CO₂ power and refrigeration system, *International Journal of Exergy*, 27(2), 147-164.
- Li, X., Dai, Y.J., Li, Y., Wang, R.Z., 2013. Comparative study on two novel intermediate temperature CPC solar collectors with the U-shape evacuated tubular absorber. *Solar Energy*, 93, 220–234.
- Ma, L, Lu, Z, Zhang, J, Liang, R, 2010. Thermal performance analysis of the glass evacuated tube solar collector with U-tube. *Building and Environment*, 45, 1959-1967.
- Naik, BK, Varshney, A, Muthukumar, P, Somayaji, C, 2016. Modelling and Performance Analysis of U Type Evacuated Tube Solar Collector Using Different Working Fluids. *Energy Procedia*, 90, 227 – 237.
- Niu XD, Yamaguchi H, Iwamoto Y, Zhang XR, 2013. Optimal arrangement of the solar collectors of a supercritical CO₂-based solar Rankine cycle system. *Applied Thermal Engineering*, 50, 505-510.
- Niu XD, Yamaguchi , Zhang XR, Iwamoto Y, Hashitani N, 2011. Experimental study of heat transfer characteristics of supercritical CO₂ fluid in collectors of solar Rankine cycle system. *Applied Thermal Engineering*, 31, 1279-1285.
- Osorio, D, Hovsopian, R, Ordonez, JC, 2016. Dynamic analysis of concentrated solar supercritical CO₂-based power generation closed-loop cycle. *Applied Thermal Engineering*, 93, 920-934.
- Pumaneratkul C, 2018. *Basic Characteristics of Rankine Cycle with Functional Elements, using Supercritical Carbon Dioxide*. PhD Thesis, Doshisha University, Kyoto, Japan; 115p.
- Quoilin, Q, Van Den Broek, M, Declaye, S, Dewallef, P, Lemort, V, 2013. Techno-economic survey of Organic Rankine Cycle (ORC) systems. *Renewable and Sustainable Energy Reviews*, 22, 168–186.
- Sharafeldin, MA, Grof, G, 2018. Evacuated tube solar collector performance using CeO₂/water nanofluid. *Journal of Cleaner Production*, 185, 347-356.
- Singh, H, Mishra, RS, 2018. Performance analysis of solar parabolic trough collectors driven combined supercritical CO₂ and organic Rankine cycle. *Engineering Science and Technology, an International Journal*, 21, 451–464.
- Solargis, 2019. Solar resource maps of Japan and Turkey [online]. Available at: <https://solargis.com/maps-and-gis-data/download/japan> [Accessed 15 May 2019]
- Turkish State Meteorological Service, 2019. Seasonal climate normal [online]. Available at: <https://www.mgm.gov.tr/veridegerlendirme/il-ve-ilceler-istatistik.aspx?k=undefined&m=ISPARTA> [Accessed 15 May 2019] [In Turkish]
- Yamaguchi H, Zhang XR, Fujima K, Enomoto M, Sawada N, 2006. Solar energy powered Rankine cycle using supercritical CO₂. *Applied Thermal Engineering*, 26, 2345–2354.
- Yamaguchi H, Zhang XR, Fujima K, Enomoto M, Sawada N, 2006. Solar energy powered Rankine cycle using supercritical CO₂. *Applied Thermal Engineering*, 26, 2345–2354.
- Zhang XR, Yamaguchi H, 2008. An experimental study on evacuated tube solar collector using supercritical CO₂. *Applied Thermal Engineering*, 28, 1225-1233.
- Zhang XR, Yamaguchi H, Fujima K, Enomoto M, Sawada N, 2007. Theoretical analysis of a thermodynamic cycle for power and heat production using supercritical carbon dioxide. *Energy*, 2007, 32, 591–599.
- Zhang XR, Yamaguchi H, Fujima K, Enomoto M, Sawada N, 2006. Study of solar energy powered transcritical cycle using supercritical carbon dioxide. *International Journal of Energy Research*, 30, 1117–1129.
- Zhang XR, Yamaguchi H, Fujima K, Enomoto M, Sawada N, 2005. A Feasibility Study of CO₂-Based Rankine Cycle Powered by Solar Energy. *JSME International Journal*, 48(3), 540-547.

#333: Trends on sustainability in Saudi building industry: advances and challenges

Mana ALYAMI¹, Siddig OMER², Saffa RIFFAT³

¹*Department of Architecture and Built Environment, Faculty of Engineering, University of Nottingham, NG7 2RD
University Park, Nottingham, UNITED KINGDOM*

²*Department of Architecture and Built Environment, Faculty of Engineering, University of Nottingham, NG7 2RD
University Park, Nottingham, UNITED KINGDOM*

³*Department of Architecture and Built Environment, Faculty of Engineering, University of Nottingham, NG7 2RD
University Park, Nottingham, UNITED KINGDOM*

In developing countries like Saudi Arabia, the experience of a rapid rate of urbanization and infrastructure expansion, especially with respect to buildings, is immense. In Saudi Arabia, the role of buildings is even more important as they account for around 80 percent of the total national electricity consumption. The issue of energy efficiency is not given serious consideration regarding Saudi building designs, even though sustainability has been a major focus in recent years of the Saudi government; achieving sustainable development has become one of the main goals of Saudi Arabia's economic and social development plan. Based on the local energy consumption trends, forecasts indicate an increase in domestic energy consumption with a growth rate which could reach 4 to 5 percent annually until 2030. This growth in demand is partially attributed to the industrial growth and growing economic prosperity in the Kingdom. A rather significant portion of this energy consumption growth results from the inefficient use of energy and the absence of coordinated enforcement and stakeholder engagement. In order to support sustainable development in the country, it is therefore crucial to improve the energy and environmental performance of buildings. This can be achieved not only by reducing the demand for building energy, but also by integrating renewable and sustainable energy technologies into buildings. This paper provides a brief review of the initiatives, advances, and challenges in the sustainability issues within the Saudi Arabian building sector, and proposes a framework for effective implementation of sustainability in the building sector.

Keywords: energy efficiency; hot climate; sustainable building design; building performance; trends

1. INTRODUCTION

Saudi Arabia, as compared with other developing countries in the Middle East, has experienced dramatic growth in urbanisation at the period of 1990- 2010. Reasons such as substantial rural-urban migration, high fertility rates, concentration of economic activity in urban areas, and international labour migration are the main drivers for this increase of urbanisation levels. Energy consumption is taking place at a rate whereby resource depletion is inevitable (Jamaludin et al, 2014). The increase in global temperature is due to high rates of greenhouse gas (GHG) emissions for which the building sector is perceived to be the largest single cause (Häkkinen et al, 2015). In Saudi Arabia, the role of buildings is even more important as they account for around 80 percent of the total national electricity consumption, exceeding the world average, as stated by Al Rashodi (2014). A breakdown of the consumption rates indicates that residential, commercial and government buildings account for 51.2 percent, 13.6 percent and 13.4 percent respectively. Demand for electricity in the residential sector is expected to double between 2009 and 2025. HVAC (heating ventilation and air conditioning) systems alone are responsible, as Alrashed and Asif (2012) point out, for over 50 percent of the total domestic electricity making it the single largest consumption source. Recently, energy and environmental performance of buildings have become a major focus since buildings are responsible for consuming over 40 percent of the world's total primary energy and releasing over one third of the total CO₂ emissions as mentioned in UNEP-SBCI report, 2009. Hence, sustainability has been a major focus in recent years of the Saudi government and achieving sustainable development has become one of the main goals of Saudi Arabia's economic and social development plan (United Nations Development Group, 2012). In order to support sustainable development in the country, it is therefore crucial to improve the energy and environmental performance of buildings. This can be achieved not only by reducing the demand for building energy, but also by integrating renewable energy technologies and sustainable solutions into buildings. For the aim of improving building energy performance, it is also important to investigate the climatic conditions of the region (Alrashed and Asif, 2015).

2. CLIMATE INFLUENCE ON ENERGY DEMANDS

One of the key characteristics of the desert climate is the high temperature during day that drops sharply during the night. The average temperature in the Kingdom of Saudi Arabia during summer is approximately 45°C, and it is usual for Saudi Arabian summer ambient temperatures to go higher than 46.1°C with mean monthly temperatures ranging between 27.3°C and 37.1°C. Between April and October, relative humidity is low and ambient temperatures are high. The extremely high summer ambient temperatures require suitable cooling systems to ensure thermal comfort for building occupants (Phillip and Lau, 2013). The average temperature in Riyadh throughout the year of 2018 is shown in Figure 1 where clear unpleasant conditions are experienced most of the year.

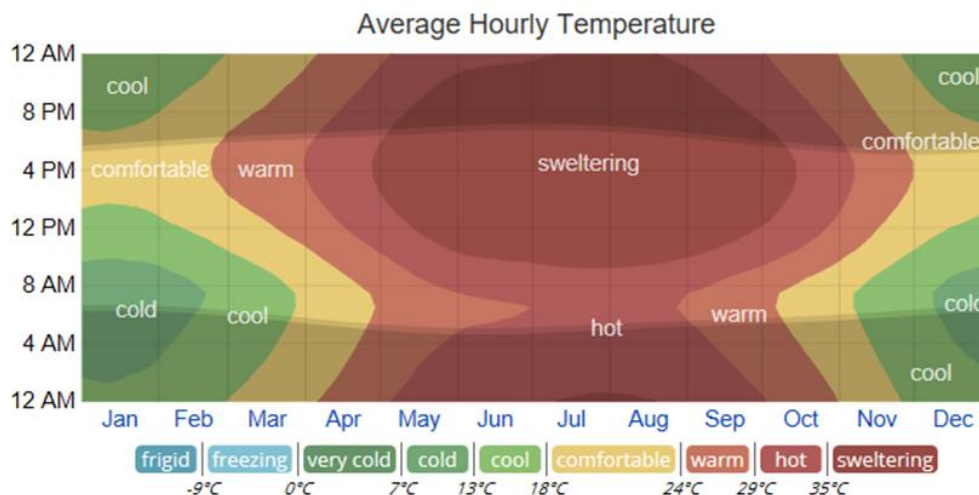


Figure 1: Average temperature in Riyadh throughout the year (Source: Weather spark, Online)

According to the Saudi Electricity Company (SEC), when considering electricity consumption rates in 2014, the residential sector led in total consumption amongst all other sectors by a considerable margin as shown in the chart in Figure 2. In 2014, the residential sector alone was responsible for nearly half of the total consumption in Saudi Arabia. An analysis of the monthly consumption during the same year shows how the monthly total electricity consumption in Saudi Arabia closely follows the average ambient temperatures, reflecting the importance of air conditioning in the summer months when electricity demand is double of that in the winter, shown in Figure 3.

2014 Electricity Consumption

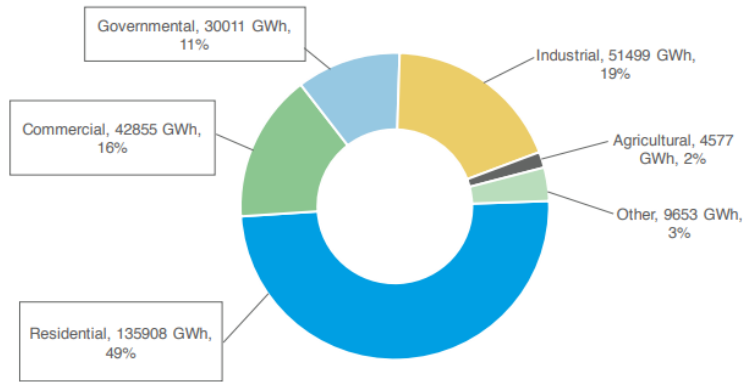


Figure 2: Electricity consumption in KSA during 2014. (Source: SEC, 2015)

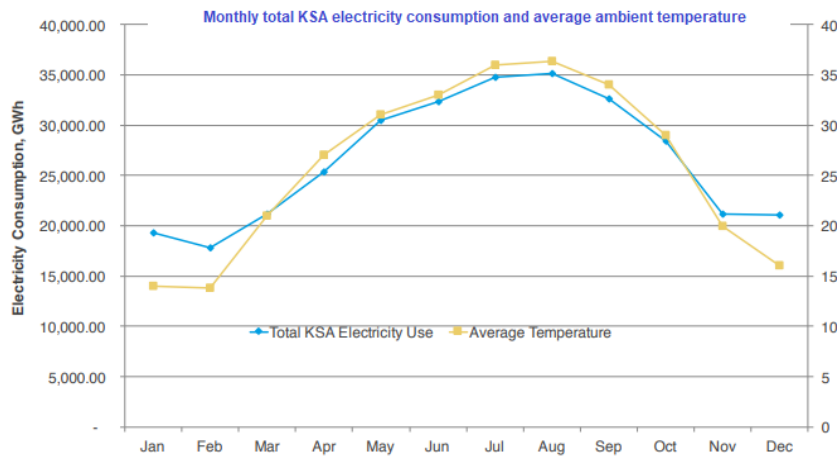


Figure 3: Monthly total KSA electricity consumption and average ambient temperature during 2014 (Source: SEC 2015)

3. CURRENT TRENDS

The volume of construction work in the GCC (Gulf Cooperation Council) countries is dramatically increasing, which poses challenges on energy demand and the environment. The building construction sector in the Kingdom of Saudi Arabia is the largest and fastest in the GCC states. It is estimated that 2.32 million new homes will be built by 2020 in order to meet the demand of a growing population. An analysis of Saudi construction by the Ministry of Municipal and Rural Affairs (MoMRA) showed that over the last decade the number of licenses issued for buildings has increased dramatically, with most of these licences for residential and commercial buildings as shown in Figure 4.

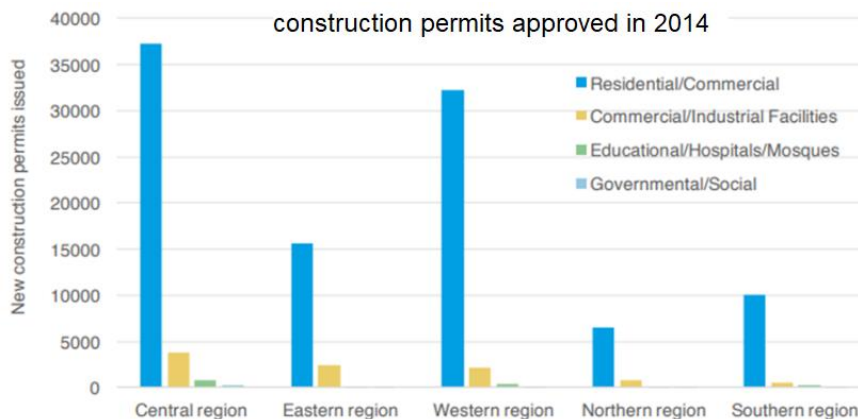


Figure 4: New construction permits approved in 2014 (source: MOMRA)

Urbanisation and industrial revolution, as faced in current times, lead to a number of profound changes, which as a result pose several serious issues at environmental, social, and economic levels. These issues are exacerbated

mainly by the conjugation of three critical factors: growth in population, excessive consumption of resources, and high rates of pollution. The building industry has experienced a considerable amount of development following economic growth causing exploitation of natural resources. These developments are due to the activities in the extraction of a substantial amount of raw materials as well as consumption of large quantities of energy. Therefore, this situation has been one of the key contributing factors for the increased interest in buildings sustainability, which is even more significant for developing countries and hot climate regions like Saudi Arabia.

Taleb and Sharples (2011) illustrate building performance by analysing the sustainability of the Saudi building sector. While identifying the key components of sustainability, namely environmental, economic, and social, they point to the fact that these components are absent in the development of current Saudi buildings. Such buildings remain heavily dependent on air conditioning, a factor that results in high energy consumption because of a large amount of electricity that is used. This situation has resulted in more than half of household electricity being applied for air conditioning given the climate of this region. In addition, building performance has been further diminished in Saudi Arabia due to the high dependence on the burning of fossil fuels as a source of electricity (Taleb and Sharples, 2011). This situation has resulted in detrimental environmental effects that have influenced air, water, and land.

3.1. Energy trends

An inspection of buildings today reveals that high energy consumption is caused by the need for cooling and heating of these buildings. This is even more exaggerated in hot climate regions, where a large amount of energy is utilised in an effort to make buildings more comfortable for occupants. Figure 5 shows that the building sector alone was responsible for about 80 percent of the total energy consumption in Saudi Arabia, 70 percent of this rate is a result of the operation of HVAC systems (KACARE, 2012). Alsurf (2014) mentions that this example of unsustainable practice poses a high pressure on the energy consumption in Saudi Arabia as the increasing future projections of energy consumption depict an alarming image of the country. The situation implies that there is an urgent need to raise awareness on the use of sustainable practices within the building sector.

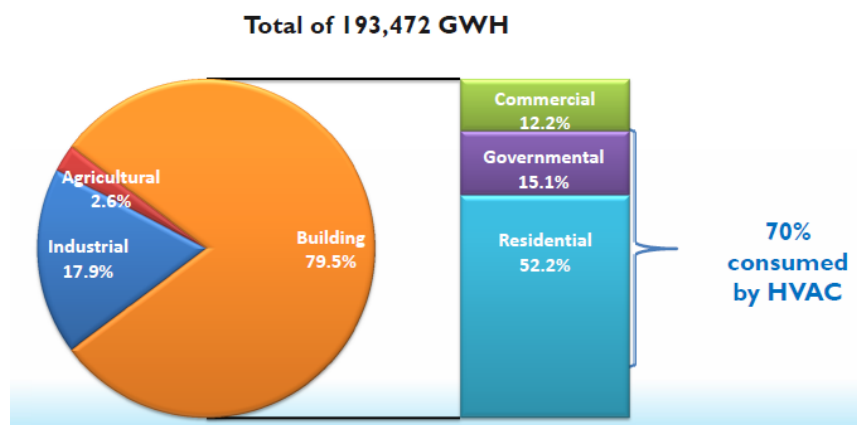


Figure 5: Energy Consumption Patterns in Saudi Arabia (Source: KACARE 2012)

Figure 6 shows the annual electricity peak demand, power generation capacity, and the annual growth in total electricity use consumed and generated from 2000 to 2014 in the KSA. In 2014, Saudi Arabia had a combined power generation capacity of 65,506 MW with peak demand at 56,547 MW (SEC, 2015). The average annual growth rate of peak demand over 2000-2014 was 7.1 percent. Transmission and distribution losses are justifications for the difference between generated and consumed electricity. Projections for the year 2019 include 68,694 MW for generation capacity, 352 TWh for total generation, and 324 TWh for net consumption (BMI Research, 2015).

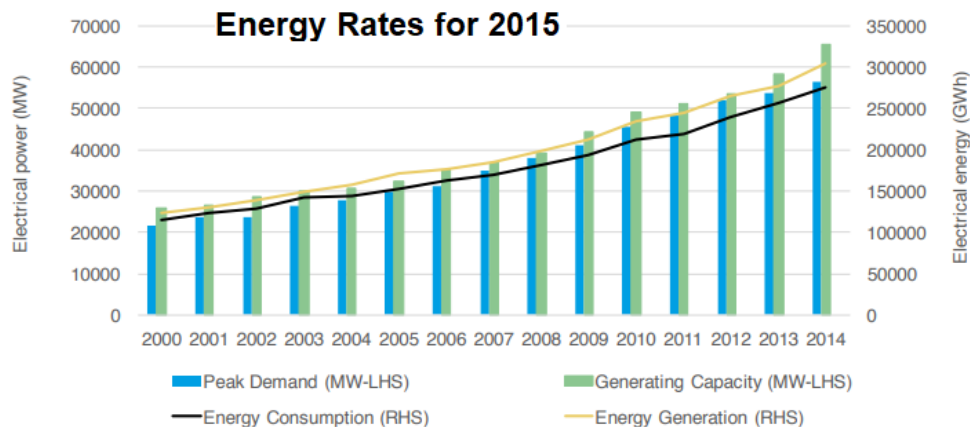


Figure 6: Peak demand, generating capacity, electricity generated, and electricity consumed in Saudi Arabia (SEC, 2015)

According to the British Petroleum (BP) World Energy Statistical Review 2017, Saudi Arabia produced 330.5 billion kWh of electricity in 2016, a 7 percent increase. This implies that Saudi Arabia is faced with a sharply rising demand for power. According to King Abdullah Centre for Atomic and Renewable Energy (KACARE), power demand is driven by population growth, a rapidly expanding industrial sector led by the development of petrochemical cities, high demand for air conditioning during the summer months, and heavily subsidised electricity rates. The country's electric generating capacity in 2016 was approximately 66 gigawatts (GW) with an expansion plan to increase this capacity to 120 GW by 2032, the largest electric power generation expansion plan in the Middle East (KACARE, 2017). Saudi Arabia is the largest producer of crude oil in GCC region with a production of 3.7 billion barrels (bbl) and exportations of 2.6 billion bbl in 2015. However, Saudi Arabia currently is not exporting or importing natural gas and the entire 2.9 QBtu (Quadrillion British Thermal Units) produced is either reinjected into oil fields or consumed by industries such as power, water, and petrochemicals (Saudi Aramco, 2015). By 2021, Saudi Arabia aims to reduce peak demand for electricity by 14 percent and reduce total consumption of electricity by 8 percent.

3.2. Movement toward sustainability

As the KSA is now experiencing a transformation stage, known as Saudi 2030 Vision, the government intends to adopt sustainability measures and apply them to all future projects and encourage such concepts in all sectors. The recent trends in the GCC region suggest that there is a considerable degree of realisation to move towards sustainability in the building sector. In recent years and in terms of green buildings, the GCC countries have made significant progress. The United Arab Emirates (UAE) and Qatar are leading the sustainability trends amongst the GCC countries, also having the highest share of green buildings in the whole Middle East and North Africa (MENA) region. The number of LEED (Leadership in Energy and Environmental Design) registered buildings has increased rapidly across the region, especially in GCC, in the past few years (Asif, 2015). In 2014, there were around 1170 buildings in the GCC region that had a LEED accreditation (Asif, 2015). Of these buildings, 70 percent were located in the UAE. Qatar and KSA are ranked 2nd and 3rd with a respective share of 15 percent and 12 percent, as stated by Asif (2015). The Saudi Green Building Council was established in 2015 to promote and facilitate the green building practice in Saudi Arabia by raising public awareness, helping the construction industry convert to the green building requirements providing training and education, encouraging building materials manufactures and suppliers to produce and supply environmentally responsible products, promoting green labelling, adapt, develop and operate local green building rating system that meet the local environmental requirements while considering the international experience (Alsarf et al, 2014).

Even though, the KSA is trying to build smart and sustainable buildings and "has announced its intention to spend about US\$ 39.9 billion over a period of eight years beginning 2010 for the construction of smart buildings across the Kingdom" (Ventures Middle East, 2011), the novelty of the Saudi Building Code is yet to be applied on all construction projects, especially residential buildings, where it can be seen and assessed in the near future. In this regard, a very forward step towards sustainability was taken when the government issued the executive regulations of the SBC application by the Royal Decree on Jan 2017 that explicitly states the SBC must be applied and implemented as described in the following table:

Table 1: Government plan to implement the SBC (Source: SBC)

Phases of SBC implementation			
Phase	Description	Implementation	
		From	To
1	The code is applied to the following buildings: government and administrative buildings, high buildings (towers - more than 23 m), hospitals, hotels.	Royal Decree issue date	End of Aug 2019
2	The code is applied In addition to what was applied in the first phase on the following buildings: mosques, sport buildings, educational buildings, Commercial buildings, Communication towers, Industrial buildings, Buildings less than 23 m, high-risk buildings	End of 1st Phase	Aug 2020
3	in addition to the above buildings, the code is applied to Wedding lounges, Cinemas, theatres, medical centres, rental apartments, residential and recreational buildings	End of 2nd Phase	Aug 2021
4	in addition to previous buildings, the code must be applied to airports, banks, post, TV and broadcasting buildings	End of 3rd Phase	End of Jul 2022
5	At this phase , the code must be applied to all types of buildings	End of 4th Phase	Jul 2023

Whereas the vast majority of countries have managed to lower the energy intensity of their economies, the Kingdom's energy intensity increased significantly over the last two decades. Hence, it is a strategic imperative for the Kingdom that energy efficiency becomes a major topic for all decisions related to an increase in demand for fuel and feedstock.

The first National Energy Efficiency Program (NEEP) was launched in 2003 as a three-year temporary programme to improve the management and the efficiency of electricity generation and consumption in the Kingdom. This programme ended in 2006. To build on the experience gained from the previous programme and to sustain and unify energy efficiency efforts under one permanent roof, in 2007 the Ministry of Petroleum and Mineral Resources, supported by other government entities in the Kingdom, recommended the creation of a permanent national entity. As a result of this recommendation, the Saudi Energy Efficiency Centre (SEEC) was established in 2010. Since then, SEEC has been responsible for the demand-side energy efficiency effort in the Kingdom, with the mission to improve domestic energy consumption efficiency, and coordinate all related activities between governmental and non-governmental stakeholders (Oxford Energy Forum, 2014). In 2012, SEEC launched the Saudi Energy Efficiency Program (SEEP) with the objective of improving the Kingdom's energy efficiency by designing and implementing initiatives and their enablers. The government intends to have a Saudi Energy Efficiency Law and it has been working with an international law firm and the legal representatives from the stakeholder government entities to draft it (Oxford Energy Forum, 2014). The subcommittee focused the Program's scope of work on three main sectors (buildings, transportation, and industry) representing more than 90 per cent of the Kingdom's energy consumption, and five enablers (regulations, Energy Services Companies, funding, governance, and awareness).

Given the increased concern about the direct impact of population dynamics on sustainable development and the economy, the Council of Ministers established a National Population Committee in 2007 to advise the Government on issues related to population and how they should be reflected in various policies and strategies in different sectors. In 2007, the General Housing Authority was established with the aim of increasing home ownership, increasing the supply of housing and residential land, building adequate housing for the needy, developing a comprehensive housing strategy, and proposing regulations, systems, policies and organisations pertaining to housing. In order to enhance the Government's role in housing policy and provision, the Ministry of Housing (MoH) was established in 2011 (MoMRA, 2016). Clearly, the key strategic objectives under the Saudi housing plan are to increase productivity and efficiency in the housing construction sector, make the sector increasingly reliant on local content in line with saudisation, and ultimately transform the country, strategically located at the intersection of Africa, Asia, and Europe, into a global hub for construction innovation. MoH is looking to cutting edge technology, public-private partnerships (PPPs), and operating models to better target regional and international markets by using technology-led housing delivery that can serve as a model for fast construction (MoMRA, 2016). PPP facilitation is a critical part of the MoH's operating model that seeks to leverage new technologies that can speed up housing requirements sustainably. The government has dedicated a budget of US\$15 billion towards housing development for the next five years, with more than one million housing units expected to be built during that period. As well as growing demand, investment opportunities are also being driven by the private sector's contribution to the sector. Saudi Arabia aims to raise the contribution of approved real estate developers towards new housing development from 10 percent to 30 percent by 2020 (MoMRA, 2016).

In 2013, the Ministry of Municipal and Rural Affairs and other line ministries developed "Sustainable Urban Planning Guidelines for Urban Growth" in the Kingdom of Saudi Arabia, which address these key issues to achieve sustainable urban planning and community design and thereby aims to reduce the consumption of critical resources. The guidelines, once adopted by the government, are intended to ensure future urban development in

Saudi Arabia matches, if not leads, world's best practice for sustainable urbanisation, especially in desert environments (MoMRA, 2016). The guidelines specifically aim to reduce energy consumption at the municipal level through district cooling, water conservation and building energy efficiency. The Sustainable Urban Planning Guidelines for Urban Growth will be integrated into the standards on planning permission and development control, which is under the review by the MoMRA. A number of relevant planning manuals are now in preparation to help planners and decision-makers to apply the recommended guidelines addressing building urban energy consumption as a subset of climate change concerns. These guidelines propose to introduce new standards for thermal insulation, district cooling and energy efficient buildings to reduce energy consumption and greenhouse gas emissions ((MoMRA, 2016). District cooling involves the provision of cooling to multiple buildings or facilities from one or more central cooling plants that are interconnected to the cooling users via networks of supply and return piping. This system helps to protect the environment as it increases energy efficiency and reduces greenhouse gas emissions and air pollution (MoMRA, 2016). Guidelines also introduced building energy codes, which set a minimum level of energy efficiency for buildings. The Government will update existing building codes and adopt new codes, expecting to achieve substantial energy and financial impact. Given that energy consumption is expected to rise in the residential sector by 2020, enacting new building codes is a key strategy for reducing energy consumption and tackle climate change across the buildings sector (MoMRA, 2016). The Kingdom's recently formed Green Buildings Council and the Green Buildings Forum, which each will act as non-government organisations bringing expertise and advice to government and the private sector on modern, environmentally sound building practices (MoMRA, 2016).

3.3. Sustainability assessment and examples

Recently, there has been some research on sustainability assessment and solutions in Saudi Arabia. One example is the work done by Alyami and Rezgui for developing sustainable building assessment tool called Saudi Environmental Assessment Method (SEAM). SEAM is the first developed tool to assess the level of sustainability in the Saudi built environment. It includes exclusive criteria and categories originally designed to suit the Saudi climatic condition and social and economic aspects. SEAM is delivering a new, applicable weighting system to prioritise the Saudi national plan in accordance with sustainability principles (Alyami and Rezgui, 2012). Others (Bannani et al, 2016) have focused on the concept of sustainability in non-domestic buildings since these construction rates are expanding throughout the country. In this study, the most influential elements were identified and the Analytical Hierarchy Process (AHP) has been adopted to assess the weight of the criteria for Saudi Arabia leading to the Saudi Sustainable Assessment Criteria Framework. Nine criteria and 36 sub-criteria were defined in this framework for inclusion as the most appropriate assessment criteria for sustainable non-residential construction in Saudi Arabia. These criteria include water efficiency and energy efficiency, IEQ, materials selection, effective management, land and waste, whole-life cost, quality of service and cultural aspects (Bannani et al, 2016).

There are some mega construction building projects with proven or attempted sustainable and energy conscious solutions in Saudi Arabia such as the King Abdullah City for Atomic and Renewable Energy (KACARE), which was planned using the Sustainable Built Environment Tool (SuBET) framework to achieve a high sustainable urban design standard (Alwaer and Clements-Croome, 2010). Another example is King Abdullah Financial District (KAJD) project, which adopted an applied sustainability design approach to deliver a number of key objectives, such as minimising water use and energy consumptions, improving indoor air quality, and reducing greenhouse gas emissions (Bannani et al, 2016). Another distinct and well-known example is King Abdullah University of Science and Technology (KAUST) which was one of the winners of the American Institute of Architects' Top 10 Green Buildings awards for 2010. KAUST's new campus is Saudi Arabia's first LEED certified project and represents the world's largest LEED Platinum project. The Project's design brief included clear instructions to create a low-energy, efficient, and highly sustainable campus that must be understood in its local and regional contexts (Elgendy, 2010). Sustainable strategies incorporated into the design included, but were not limited to, bringing buildings closely together to minimise the areas of the buildings facades exposed to the sun and encourage passive ventilation between them; mitigating solar gain by using appropriate orientation and shading, incorporating low energy cooling techniques such as chilled beams, heat recovery wheels, and displacement ventilation to reduce the cooling and ventilation loads; covering the campus's roofs with large solar photovoltaic arrays for electricity generation; and implementing sustainable operations plan which includes using green cleaning materials and extensive recycling programs (Elgendy, 2010).

3.4. Challenges

Saudi Arabia so far has no mandatory building regulations, which would require the incorporation of sustainable technology applications and energy efficiency principles into the design of buildings (Alsurf, 2014). Hence, due to rapid population growth and economic development, attention must be given to ensuring sustainable building performance and avoiding further energy demands with consequential economic and environmental costs. Coordinated enforcement of the regulations and standards ought to be optimised by developing a unified enforcement approach and coordinating the various government entities' enforcement efforts in order to ensure high levels of compliance. Lack of engagement of government and private sector stakeholders to ensure practical initiative design and buy-in for smooth implementation has a significant influence on sustainable building industry

in Saudi Arabia (Oxford Energy Forum, 2014). Moreover, the absence of enforcement of these regulations and requirements from the policy side, in addition to the lack of energy policies or strategic plans that determine benchmarks for energy reductions, may hinder the efficiency of such requirements. For example, the SBC has mandated thermal insulation against heat for all new buildings since 2010 as this has been proven to reduce energy demand for buildings by 30 to 40 percent. However, new buildings continue to be erected without proper insulation (Lahn et al, 2013). One of the main challenges in Saudi Arabia is the lack of property tax. This is the reason why large pieces of land can still be found in the inner suburbs of the city. This stands in the way of development. In the last few years, there has been an increase of more than 50 percent of the price of land in Saudi Arabia (Alsurf et al, 2014). As a result, the cost of land generally constitutes half of the cost of erecting a building while in Europe this ratio is about one third (Fattah, 2013). This is why authors like Ferris-Lay (2011) argue that the cost of land is a leading constraint, which makes it a challenge for developers in Saudi Arabia to build affordable and sustainable housing.

Sustainability has been identified worldwide as a necessity and the application of sustainable construction is vital for the conservation of natural resources for future generation needs. In the KSA, the application of sustainability techniques and measures to building construction is still mostly considered as a luxurious option and mainly provided for parties and people who have the financial capacity to afford it (Al surf, 2014). This is the result of lack of public awareness of the benefits of sustainable construction. Sustainable measures should not only be applicable at the design stage of the building, but also during the in-use stage of buildings, the operation and maintenance. In fact, government bodies and building professionals should pay more attention to the in-use stage in a sustainable way.

Saudi Arabia is also trying to position itself to make use of the emerging sustainability trends in the building sector. The Saudi Building Code development and mandatory thermal insulation for all new buildings are positive indications for sustainable development (Asif, 2015). There is, however, a lack of appreciation by some stakeholders of the construction industry. For example, in a recent Saudi Electric Company (SEC) survey, only 580 out of 15000 new commercial buildings (15 percent) have applied the compulsory thermal insulation (Asif 2015). The situation is even worse in some parts of the country. Jeddah city, for example, is the poorest in its compliance with thermal insulation where only 52 out of 5200 buildings are having compulsory insulation (Asif, 2015). According to SEC (2015), contractors have failed to abide by the regulations despite repeated warnings by the SEC.

In developing countries, including the KSA, the design of buildings does not usually take into account the prevailing climate of the areas. In such regard, human thermal comfort is affected by the indoor thermal environment of a building and is responsible for a majority of the building energy consumption. Also, important factors such as the surrounding and site characteristics, building materials selection, architectural design, and orientation are not given serious consideration (Ghabra et al, 2017). This leads to buildings whose indoor climate is poor, which has a negative impact on comfort, efficiency, and health (Madhumathi and Sundararaja, 2014). Mandatory energy efficiency regulations for buildings, if enforced properly, can constitute a strong driving force for the construction industry; including architects, real estate developers, and construction companies, to start integrating sustainable and energy efficient solutions into buildings. However, at present, national standards apply only to new buildings and are often voluntary or poorly enforced so a mandatory regulatory framework is required to ensure that all buildings implement sustainable practices (Myrsaliev and Barghouth, 2015). Current responsibility for enforcement usually lies with municipalities, which often lack financial and human capacity (Ghabra, 2017). Designing, constructing and renovating buildings according to energy efficient specifications will require an upgrading of skills, knowledge and expertise of professionals in the construction sector – including architects, designers, contractors, installers and others – to properly inspect and review site plans, building designs and construction sites, capabilities which are still lacking in most of the Gulf Region in general and Saudi Arabia specifically (Ghabra, 2017).

Investigating building materials and the related embedded energy has been an essential part of sustainable building development. The main concern has been on whether these materials have a high thermal mass (Sinha et al, 2013). In Saudi Arabia, almost all types of building constructions have been built by reinforced concrete, which contributes considerably in building shapes (Marzouk et al, 2014). Unquestionably, this material was a revolution in the field of building industry where building structure was concerned. However, this material does not enjoy the same performance when it comes to the thermal properties. Reinforced concrete construction has poor thermal behaviour in hot climates making it a weak barrier in front of heat flow (Marzouk et al, 2014). The effect of the building envelope depends on the thermophysical properties of materials affecting the rate of heat flow in and out of building, hence affecting the indoor thermal conditions and comfort of occupants (Marzouk et al, 2014). These thermophysical properties of materials used in the building industry in Saudi Arabia have not been given serious attention. In addition, it was thought until recently that the embodied energy content of a building was small compared to the energy used in operating the building over its life. Therefore, most effort was put into reducing operating energy by improving the energy efficiency of the building envelope. Research has shown that this is not always the case. Embodied energy can be the equivalent of many years of operational energy (Milne, 2013). Research by CSIRO has found that the average house contains about 1,000 GJ of energy embodied in the materials used in its construction. This is equivalent to about 15 years of normal operational energy use. For a house that lasts 100 years this is over 10 percent of the energy used in its life (Milne, 2013).

Table 2 highlights the barriers hindering the utilisation of these resources in the Saudi residential sector aiming to promote Low Energy Houses.

Table 2: Barriers to promote LEHs in Saudi Arabia - source: (Alrashed and Asif, 2012)

Type	Barrier
Energy efficiency measures	<ul style="list-style-type: none"> - Lack of awareness about the energy-efficiency measures such as the glazing system, the thermal insulation, the energy-saving lighting fixtures, and energy-efficient appliances and its rating - Cheap electricity tariff - Personal passiveness to buy the energy-saving fixtures - Unclear maintenance responsibility - Lack of expertise in efficient-buildings
Sustainable design features	<ul style="list-style-type: none"> - Lack of acceptability of sustainable design features due to aesthetic aspects and safety issues - Perception that it wastes necessary space and money - Disturbance in terms of noise, as well as, attracting insects and dusts - Concerns about maintenance - Perception that it may affect the lifestyle of users - Uncertainty of the adaptability of these solutions in the Saudi climate - Some of the solutions are not applicable in all regions and kind of residential buildings in Saudi Arabia - Technical issues and faults - Perception that some of the solutions are old style and does not meet the current user's aspiration - Lack of awareness about most of sustainable design features - Non-suitability for Saudi families as some of the features may constrain future expansion and penetrate user's privacy - Regulatory and policy related challenges from the local authorities - Not in line with existing style of typical residential buildings in Saudi Arabia - Lack of expertise in the sustainable design
Renewable energy applications	<ul style="list-style-type: none"> - Non-suitability in residential buildings due to safety issues - Uncertainty of the applications performance in the Saudi climate - Regulatory and policy related challenges from the local authorities - Enormous subsidies on fossil fuel based energy including oil and gas - Lack of public awareness on renewable energy - High capital cost of renewable technologies - Lack of policy initiatives in terms of government targets for renewable technologies and absence of due subsidies/financial incentives on renewable technologies - Lack of information concerning performance, durability, reliability and cost effectiveness of renewable technologies - Lack of private sector stakeholders/renewable entrepreneurs - Capacity issues with micro-renewable systems - Lack of reliable weather data - Lack of acceptability of renewable energy applications due to aesthetic aspects Lack of government subsidy on renewable energy applications - Lack of interest in the renewable energy from the national media and the relevant agencies - Lack of expertise in the field of renewable energy application

4. CONCLUSION

This review reveals that even though there are promising research activities, policy supports and growing public awareness, the Kingdom has wide scope for further developments in order to ensure (through the utilisation of its resources at their fullest potential) that all the viable state-of-the-art technologies for energy conservation and management in buildings are implemented. Even before the Saudi 2030 Vision that outlined a future for the Kingdom beyond oil and gas, the government considered it "a strategic imperative that energy efficiency become a major topic for all decisions related to the increase in demand for fuel and feedstock" (Oxford Energy Forum, 2014). Al Surf et al (2013) have further discussed the issue of rapid urbanisation and have explained that fuelling this exploding urbanisation rate is the lack of regulation to control the current and future urbanisation rate. Assaf et al (2010) elaborate on the causes of housing shortage and state that "It has become a challenging task for the government as well as private real estate sector in the kingdom to provide affordable housing to lower and medium income group families in urban areas mainly due to high demand, escalating prices and non-preference to vertical expansion apartments". Overall, AbdulSalam et al (2014) conclude that the housing sector is driven or influenced not only by development, but also by geographical region, climatic condition, environmental considerations, and cultural requirements. According to Taleb and Sharples (2011), building performance generally in Saudi Arabia lacks the application of energy efficient and sustainable technologies. In the last two decades, energy consumption in Saudi Arabia has sharply increased, specifically, peak load which approximately reached 24GW in 2001 and it is expected to reach 60GW by 2023 (Fasiuddin and Budaiwi, 2011). Also, according to the Saudi Arabia General Authority of Statistics, the population of Saudi Arabia reached 29,994,272 in 2013 and is likely to reach 37,610,985 by 2025 (AbdulSalam et al, 2014). Yet, an energy conscious attitude continues to be virtually absent in the developing world, and this also pertains to Saudi Arabia, as mentioned by Al Surf (2014). The housing sector is in need of stronger governmental regulation. Lack of suitable land to be developed, citizens not being able to have

adequate financial and material support to acquire housing, and inefficient housing market have contributed to the housing shortage in the Kingdom. Generally, the main building design challenges in the region can be categorised into two levels: regulatory and climatic. This implies that there is a need to develop and implement a compulsory regulatory framework with the aim of delivering energy efficient buildings. Moreover, if energy efficiency is to be achieved in residential buildings in particular, an integrated holistic cross-disciplinary design approach should be adopted in local building energy efficiency practices in the Gulf Region in general and in Saudi Arabia in particular (Ghabra, 2017). Finally, while the industry has used tools specific to sustainable construction, to date no assessment tools has been developed that broadly considers Saudi Arabia's specific climatic, societal and cultural contexts. Hence, there is a need to develop a building sustainability assessment tool to measure the extent to which the sustainability agenda are implemented in buildings in Saudi Arabia (Bannani et al, 2016).

"...to improve the sustainability standards in the building sector it is important to increase awareness on the subject amongst various stakeholders including regulatory bodies, building industry and residents. Besides introduction of new policies and regulations, energy efficient technologies and solutions, it is also critical to improve energy consumption habits and lifestyle. In the wake of low electricity tariffs and cheap conventional energy prices in GCC countries, it is important to have strongly supportive government policies to promote sustainable buildings. Government subsidy to enhance the thermal performance of building envelopes and feed-in-tariff schemes, for example, could be of help in this respect" (Asif, 2015)

5. REFERENCES

- AbdulSalam, A., Elsegaey, I., Khraif, R., and Al-Mutairi, A. 2014, *Population Distribution and Household Conditions in Saudi Arabia: Reflections from The 2010 Census*, Springer Plus 2014 3:530
- Al Rashodi, H. (2014) "*Maskan Arabia Urges Use of Thermal Insulation in Houses to Rationalize Power Consumption.*" [online] Available from: <http://saudigazette.com.sa/article/101011> (Accessed February 6, 2019)
- Al Surf, M. S., 2014, *Challenges Facing the Application of Sustainability to Housing in Saudi Arabia*
- Al Surf, M., Susilawati, C. and Trigunarsayah, B. 2013, *Integration of Saudi Arabia's Conservative Islamic Culture in Sustainable Housing Design CIB World Building Congress Construction and Society*. Brisbane Convention & Exhibition Centre Queensland, Australia.
- Al Surf, M., Susilawati, C. and Trigunarsayah, B. 2014, *The Role of the Saudi Government and the Saudi Building Code in Implementing Sustainable Housing Construction in Saudi Arabia*, 20th Annual PRRES Conference, Christchurch, New Zealand, 19-22 January 2014
- Alrashed F., and Asif M., 2012, *Prospects of renewable energy to promote zero-energy residential buildings in Saudi Arabia*. Energy Procedia 18:1096–105
- Alrashed, F. And Asif, M. (2012), *Challenges Facing The Application Of Zero-Energy Homes In Saudi Arabia: Construction Industry And User Perspective*, ZEMCH International Conference.
- Alrashed, F. and Asif, M. 2015. *Climatic classifications of Saudi Arabia for building energy Modelling*, Energy Procedia 75
- Alwaer, H., and Clements-Croome, D., 2010. Building sustainability awards 2010- sustainable innovation of the year. Hilson Moran.
- Alyami, S. H., and Rezgui, Y., 2012. Sustainable building assessment tool development approach. Sustainable Cities and Society. 5(0), 52-62.
- Asif, M. 2015. *Growth and sustainability trends in the buildings sector in the GCC region with particular reference to the KSA and UAE*, Renewable and Sustainable Energy Reviews 55 (2016) 1267–1273.
- Assaf, S. A., Bubshaitr, A. A. and Al-Muwasheer, F. 2010. *Factors affecting affordable housing cost in Saudi Arabia*. International Journal of Housing Markets and Analysis, 3, 290 - 307.
- Bannani R., Vahdati M. M., Shahrestania M., and Clements-Croome D., 2016, *The development of building assessment criteria framework for sustainable non-residential buildings in Saudi Arabia*, Sustainable Cities and Society, July 2016, DOI: 10.1016, j.scs.2016.07.007

BMI Research. 2015. *Saudi Arabia Power Report Q1 2016*. BMI Industry Report and Forecasts Series, Fitch Group Company, London: BMI Research

BP, British Petroleum. 2017. "Statistical Review of World Energy 2017."

Elgendy, K., 2010, *KAUST: A Sustainable Campus in Saudi Arabia*, Carbone Middle East Sustainable Cities.

Fasiuddin, M. and Budaiwi, I. 2011. *HVAC system strategies for energy conservation in commercial buildings in Saudi Arabia*. *Energy and Buildings*, 43, 3457-3466.

Fattah, Z. 2013. *Saudi Arabia's Affordable Housing Shortage*. Businessweek.

Ferris-Lay, C. 2011. *High land prices crimp plans for low-cost homes*. *Arabian Business*

Ghabra, N., 2017. "Energy Efficient Strategies for the Building Envelope of Residential Tall Buildings in Saudi Arabia", Available online on:

http://eprints.nottingham.ac.uk/51738/1/Noura%20Ghabra_4198436_Final%20Thesis.pdf

Ghabra, N., Rodrigues, L. and Oldfield, P., 2017. The impact of the building envelope on the energy efficiency of residential tall buildings in Saudi Arabia. *International Journal of Low-Carbon Technologies*, Volume 12, p. 411–419.

Häkkinen, T., Kuitinen, M., Ruuska, A. and Jung, N., 2015. Reducing embodied carbon during the design process of buildings. *Journal of Building Engineering*, Volume 4, pp. 1-13.

Jamaludin, N., Khamidi, M. F., Wahab, S. N. A. and Klufallah, M. M. A., 2014. *Indoor thermal environment in tropical climate residential building*. Les Ulis, France, EDP Sciences.

KACARE 2012, King Abdullah Centre for Atomic and Renewable Energy, "Building the Renewable Energy Sector in Saudi Arabia".

KACARE 2017, King Abdullah Centre for Atomic and Renewable Energy, *Energy Sustainability for Future Generations*, [online] Available from <https://www.kacare.gov.sa/en/FutureEnergy/Pages/vision.aspx> (Accessed February 6, 2019)

KAPSARC, The King Abdullah Petroleum Studies and Research Centre, 2017, *Evaluating Building Energy Efficiency Investment Options for Saudi Arabia*, October 2016 KS-1655-DP049B

Lahn, G., Stevens, P., Preston, F., 2013. *Saving Oil and Gas in the Gulf*. London: Chatham House (The Royal Institute of International Affairs).

Madhumathi, A., and Sundarraja, M.C (2014), "Understanding Climate For Sustainable Building Design –A Case Study In Warm Humid Region In India", *Journal Of Applied Sciences Research* 10(2), Pages: 69-87

Marzouk, M., Metawie, M., Hisham, M., and Al-Sulahi, I., 2014; "Modeling Sustainable Building Materials in Saudi Arabia", *Computing In Civil And Building Engineering ASCE* 2014

Milne, G., 2013, "Materials Embodied Energy; Your Home- Australia's Guide to environmentally sustainable homes", Available Online at: <http://www.yourhome.gov.au/sites/prod.yourhome.gov.au/files/pdf/YOURHOME-Materials-EmbodiedEnergy.pdf> (accessed 20 March 2019)

Ministry Of Municipal And Rural Affairs MoMRA (2016), "National Report: Third United Nations Conference On Housing And Sustainable Urban Development", , UN HABITAT III, January 2016.

Myrsaliev, N., Barghouth, A., 2015. Arab Future Energy Index (AFEX) Energy Efficiency 2015. [pdf] The Regional Centre for Renewable Energy and Energy Efficiency (RCREEE).

Oxford Energy Forum (2014), "A Brief On Saudi Arabia's Energy Efficiency Program (SEEP)", *Future Energy Challenges In The GCC Region*, May 2014: Issue 96

Phillip, T., and Lau, B., 2013, "PASSIVE DOWNDRAUGHT EVAPORATIVE COOLING: The Applicability for residential space cooling in Riyadh, Saudi Arabia", 29th Conference, Sustainable Architecture for a Renewable Future, Munich, Germany 10-12 September 2013

Sahebzadeh, S., Heidari, A., Kamelnia, H. and Baghbani, A., 2017. Sustainability features of Iran's vernacular architecture: A comparative study between the architecture of hot–arid and hot–arid–windy regions. *Sustainability*, 9(749), pp. 1-28.

Saudi Aramco. 2015. "Annual Report."

SEC Saudi Electricity Company. 2015. "Annual Report." Riyadh

Sinha, A., Gupta, R. and Kutnar, A., 2013. Sustainable development and green buildings. *Drvna Industrija*, Volume 64, pp. 45-53.

Taleb, H. M. and Sharples, S., 2011. Developing sustainable residential buildings in Saudi Arabia: A case study. *Applied Energy*, Volume 88, pp. 383-391.

UNEP SBCI United Nation Environmental Programme, Sustainable Buildings and Climate Initiative, 2009. *Buildings and climate change: A summary for decision-makers 1st ed*, Paris.

United Nations Development Group, 2012 "United Nations common country strategic Framework: Kingdom of Saudi Arabia 2012-2016"

Ventures Middle East 2011. *The Saudi Construction Industry Ventures Middle East*

#334: Dosimetric and performance analysis of *Rhizophora* spp. particleboards as phantom material for SPECT/CT imaging

Puteri Nor Khatijah ABD HAMID¹, Mohd Fahmi MOHD YUSOF², Abd Aziz TAJUDDIN³, Rokiah HASHIM⁴, Rafidah ZAINON

¹School of Physics, Universiti Sains Malaysia, 11800 Penang, Malaysia
pnkah14_phy063@student.usm.my

²School of Health Sciences, Universiti Sains Malaysia, 16150 Kota Bharu, Kelantan, Malaysia,
mfahmi@usm.my

³Albukhary International University, 05200 Alor Setar, Kedah, Malaysia
draat@usm.my

⁴School of Industrial Technology, Universiti Sains Malaysia, 11800 Penang, Malaysia
hrokiah@usm.my

⁵Advanced Medical and Dental Institute, Universiti Sains Malaysia, 13200 Penang, Malaysia
rafidahzainon@usm.my

*The aim of this study is to investigate the dosimetric performance of the fabricated *Rhizophora* spp. particleboards as phantom for the in-vivo imaging of single photon emission computed tomography (SPECT/CT). The phantom made of the particleboards was fabricated based on the external dimension of the readily available Jaszczak phantom. Six vials made of Perspex® with diameters between 1.3 and 3.5 cm were also constructed to simulate the localization of radiopharmaceuticals of different volumes in conjunction with the ^{99m}Tc radiopharmaceuticals of 1.6 µCi/ml activity concentration. The SPECT/CT images of the particleboard phantoms were obtained based on the abdominal scanning protocols. The contrast at different SPECT filters and recovery coefficient, RC of the particleboard phantoms were determined and compared to that in the Perspex® and modified Jaszczak phantoms. The results showed that the contrast of the *Rhizophora* spp. particleboard phantom was in good agreement with that in the Jaszczak phantom. The contrast also increased linearly at higher cut-off frequency of SPECT filters. The evaluation of apparent to the actual size of the *Rhizophora* spp. particleboard phantom was also in agreement within 4.4 and 5.95% to the Perspex® and Jaszczak phantoms respectively for all vial sizes. The RC measured in the *Rhizophora* spp. particleboard phantom was also in good agreement to the Jaszczak with p-value of 0.185. A spill-over effect was also observed at larger vial diameters with values between 4.2 and 6.7%. The overall results indicated the suitability of particleboards made of *Rhizophora* spp. as an alternative phantom material for in-vivo imaging.*

Keywords: Rhizophora spp.; particleboards; phantom material; SPECT/CT

1. INTRODUCTION

Water has been used as standard phantom material to simulate human soft tissues for dosimetric measurements and diagnostic imaging involving ionizing radiations in many available international dosimetric protocols due to its attenuation properties including mass density and interaction with ionizing radiations that is similar to soft tissues (Khan and Gibbons, 2014). The use of water as however is not always practical due to its physical properties of liquid form and incompatibility of many radiation dosimeters to be used in water. Therefore, several solid-type phantoms were introduced to substitute water such as Perspex® and acrylic to overcome the limitations of water. These solid phantoms however still failed to provide accurate dosimetric properties when compared to water and soft tissues.

Previous studies indicated the potential use of *Rhizophora* spp. wood as phantom due to its density and attenuation properties close to that of water. Unfortunately, the density of untreated solid raw wood was not uniform throughout the wood volume and the wood has the tendency to bent and cracked over a period of time. Shakhreel et al., (2006) suggested raw wood to be ground into smaller particle sizes and compressed into particleboards. The fabrication of particleboards has the advantages over the solid raw wood including better density uniformity. The particleboards also can be fabricated at any particle size ranges, desired sizes and shapes and predetermined mass densities. The fabrication of particleboards also can be made by adding other extra materials or adhesive to enhance the physical and mechanical properties of particleboards. The use of the synthetic based adhesive such as the formaldehyde based adhesives increased the strength of the fabricated *Rhizophora* spp. particleboards but significantly reduced their attenuation properties towards ionizing radiations (Ngu et al., 2015). The use of several biological-based adhesives on the other hand showed better physical and mechanical strength of the fabricated *Rhizophora* spp. particleboards without sacrificing their attenuation properties (Abuarra et al., 2014; Tousi et al., 2014; Ababneh et al., 2016; Yusof et al., 2017).

Starch is the carbohydrate-based compound that with elemental compositions that match to *Rhizophora* spp. wood and human soft tissues. Starch is abundant, biodegradable, renewable, economic and widely used in industrial applications in the paper, textile and adhesive industries (Imam et al., 1999; Richardson and Gorton, 2003). Several studies indicated the suitability of starch as wood adhesive and providing better physical properties of particleboards (Moubarik et al., 2010; Moubarik et al., 2013; Liu et al., 2012). The starch used as adhesive in the present study was the commercialized corn starch in the form of fine white powder with 692.661 g/mol of molecular weight and 1.45 g/cm³ of density. The corn starch used in the present study having molecular formula of C₂₇H₄₈O₂₀ and calculated effective atomic number, Z_{eff} of 6.88 which is close to the value of water at 7.42 (AAPM-21, 1983). The corn starch in the present study was used without treatment and addition of hardener to retain the elemental compositions and Z_{eff} of *Rhizophora* spp. wood and starch.

2. METHODOLOGY

2.1. Sample preparation and construction of phantom

The *Rhizophora* spp. particleboards were fabricated by using wood particles of ≤ 74 μm size ranges based on the previous work by Hamid et al., (2018). An amount of 10% corn starch was added into the wood particles based on the dry weight of the wood particles required for the fabrication of the particleboards. A number of 30 particleboards were fabricated each with target density similar to water at 1.0 g/cm³ and 1.0 cm thickness by using the hot pressing method. Each particleboard was measured for its mass density by using the gravimetric method based on the external dimension given by the equation.

Equation 1:
$$density = \frac{thickness \times length \times width}{mass}$$

A phantom set was constructed based on the external dimensions of the available Jaszczak phantom used in the QC of SPECT imaging as shown in Figure 1(a). A number of 6 circular holes were made on several particleboards with diameter between 1.9 and 4.1 cm. The particleboards were then stacked together at fixed into position by the mean of locking to simulate external dimension of Jaszczak phantom commonly used in the quality control and image studies for SPECT/CT as shown in Figure 1(b). A sets of 6 cylindrical-shaped radionuclide containers vials with approximate length of 6 cm were constructed by using acrylic material for the constructed *Rhizophora* spp. particleboard phantom and Jaszczak phantom as shown in Figure 2. The vials were constructed with six different diameters according to the diameters of solid spheres within Jaszczak phantom tank and equipped with cap made of rubber material to avoid spillage of the inserted radionuclide. One set of vials were attached and fixed on a circular-shaped plastic plate for water (Jaszczak) phantom as shown in Figure while another one set of vials were prepared for fabricated *Rhizophora* spp. particleboard phantom. A ^{99m}Tc unsealed source produced from the Mo – Tc generator was used as radionuclide to obtain the SPECT/CT images. The radionuclide had the activity concentration of 59 200 Bq/ml was calibrated using a dose calibrator. The time of the radionuclide calibrating was recorded to determine the current activity of the radionuclide. The radionuclide was injected into vials using a

syringe to prevent the presence of air bubbles. The vials containing ^{99m}Tc radionuclide were positioned in its inserts within the constructed corn starch-bonded *Rhizophora* spp. particleboard phantom according to the number of drilled holes. A set of radionuclide vials were also injected with ^{99m}Tc radionuclide with 59 200 Bq/ml activity concentration. The vials were fixed and locked at the base of the Jaszczak phantom tank. The phantom was filled with distilled water and closed by using an acrylic end plate on top of the phantom. The cover plate was secured with twelve plastic screws around the edge to prevent leakage of water. The remaining space within the tank was completely filled with water through the holes on the top end plate by using a syringe to prevent air bubbles within the phantom.

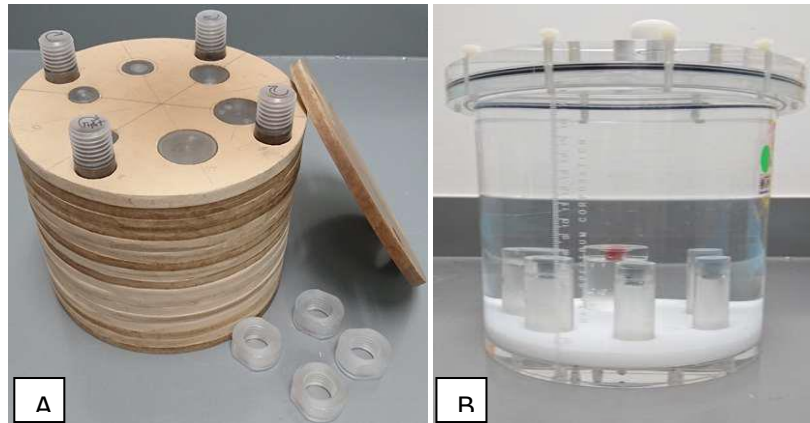


Figure 1: (a) The constructed phantom set made of the fabricated *Rhizophora* spp. particleboards and (b) The commercially available Jaszczak phantom for the quality control for SPECT imaging.

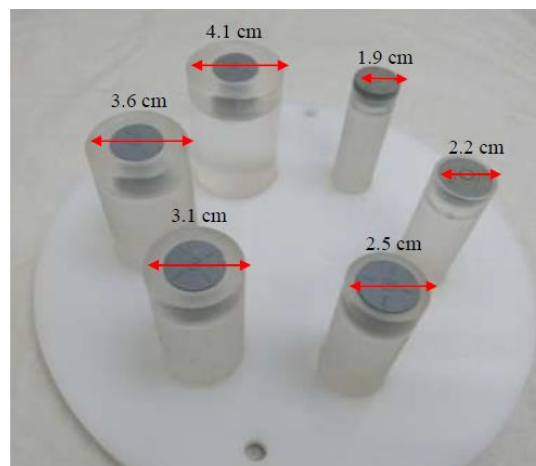


Figure 2: The constructed vials of various diameters for the localization of radionuclide.

2.2. Evaluation of contrast

The SPECT/CT imaging of the constructed corn starch-bonded *Rhizophora* spp. particleboards phantom was performed in the Nuclear Medicine Department, Advanced Medical and Dental Institute (AMDI), Universiti Sains Malaysia. An integrated Discovery SPECT/CT system model NM/CT670 (General Electric Healthcare, USA) equipped with Xeleris software for image analysis was used to obtain and to analyze the SPECT/CT images. The regions of interest (ROI) were drawn at the centre of the 'hot spot' area within the circular regions of vial on the SPECT images defined by using the CT images. Another ROI with similar size was also drawn on the background region that outside the region of vial images in the middle region of the phantom. The similar area size of ROI for each vial was used on all image slices. The image contrast of each vial was calculated by using the equation

Equation 2:
$$\text{Contrast} = \frac{C_{cyl} - C_{bgd}}{C_{bgd}}$$

with C_{cyl} is the average count per pixels in the cylindrical region and C_{bgd} is the average count per pixels in the background region (Cherry et al., 2012). The contrast values were measured at all SPECT filters of Gaussian, Hanning and Butterworth.

2.3. Evaluation of recovery coefficient

A calibration of SPECT imaging system volume sensitivity typically obtained by a correlation of the SPECT results with a calibrated well counter. A derived calibration factor was used for conversion counts per second (cps) to the apparent activity concentration (Bq/ml). A 20 cm diameter large cylindrical phantom with a known and uniform activity concentration, C_{vol} (Bq/ml) of the ^{99m}Tc radionuclide was scanned using SPECT imaging. Attenuation and scattered photons corrections were applied in reconstruction process. The system volume sensitivity value as a calibration factor was derived according Equation 3.24 (Ritt et al., 2011):

$$\text{Equation 3: } \text{Volume Sensitivity, } S_{vol} = \frac{R}{V_{vol}C_{vol}} \times \exp\left(\frac{T_0 - T_{cal}}{T_{1/2}} \ln 2\right) \times \left(\frac{T_{acq}}{T_{1/2}} \ln 2\right) \times (1 - \exp(-\frac{T_{acq}}{T_{1/2}} \ln 2))^{-1}$$

with R is counting rate (cps) in drawn volume of interest, V_{vol} is volume of interest (ml) in SPECT images, C_{vol} is activity concentration (Bq/ml) of phantom, T_0 is the imaging start time, T_{cal} is the time of activity calibration, $T_{1/2}$ is the half-time of the radionuclide and T_{acq} is the duration of the acquisition. The determined value of the conversion factor is 0.00032 cps/Bq. The SPECT images of *Rhizophora* spp. particleboards, Jaszczak and Perspex® phantoms were reconstructed using Butterworth filter with scatter and attenuation correction applied. An ROI was drawn over the area of radionuclide distribution of each vial in the SPECT image and the average counts per pixel were measured. The activity concentration of apparent image were calculated by using Equation 3.25 (IAEA, 2014):

$$\text{Equation 4: } \text{Apparent Activity Concentration, } A_a = \frac{R_{ROI}}{S_{vol}} \times \frac{VS}{T_{acq}}$$

with R_{ROI} is the count per pixel (counts/pixel) in drawn ROI, VS is the voxel size with the values of $4.42 \times 4.42 \times 4.42 \text{ mm}^3$ given by the manufacturer and T_{acq} is the total scanning time (s). The actual activity of ^{99m}Tc source was calculated according radioactive decay law by taking into account the elapsed time of the measurement and the decay constant of the radionuclide by using Equation 3.26:

$$\text{Equation 5: } \text{True Activity Concentration, } A_t = A_0 e^{-\lambda t}$$

with A_t and A_0 is the current and initial activity of the radionuclide source (Bq) respectively, λ is decay constant of the radionuclide (^{99m}Tc) with the value of $3.21 \times 10^{-5} \text{ s}^{-1}$ and t is the time elapsed from the initial activity (s). The RC of SPECT images of the radionuclide measured in the constructed corn starch-bonded *Rhizophora* spp. particleboards phantom therefore was calculated by using Equation 3.27 (Cherry et al., 2012):

$$\text{Equation 6: } \text{Recovery Coefficient, } RC = \frac{A_a}{A_t}$$

with A_a and A_t is the apparent and actual activity concentration of the radionuclide respectively.

3. RESULTS

3.1. Image Contrast at different SPECT filters

The SPECT images of the constructed *Rhizophora* spp. particleboards phantom and the Jaszczak phantom are illustrated in Figure 3. The results showed that the SPECT images in the *Rhizophora* spp. phantoms were comparable to that in the Jaszczak phantom filled with water as medium. Both images showed the similar 'hot spot' and 'cold spots' indicating the high and low activity distributions of the radionuclide within the phantoms at all diameter sizes of the radionuclide localizations. The results were in good agreement to the previous work by Abuarra (2014) on the in-vivo study of *Rhizophora* spp. particleboards by using the positron emission tomography (PET) imaging.

The contrast of SPECT images reconstructed using different filters of Butterworth, Hanning and Gaussian were observed for *Rhizophora* spp. particleboards and Jaszczak phantom as shown in Figure 4. The results showed that post-filtering using a Butterworth filter with cut-off frequency of 0.5 cm^{-1} and order value of 10 resulted in higher contrast compared to reconstruction without filtering and others filters for the Jaszczak phantom and *Rhizophora* spp. particleboards. This result in agreement with Groch and Erwin (2000) study that found Butterworth filter application using 10 and 0.5 cm^{-1} of order and cut-off frequency respectively is the optimum filter for brain SPECT imaging using ^{99m}Tc -HMPAO radiopharmaceuticals. A SPECT imaging of ^{99m}Tc -DMSA renal cortical study for the detection of renal parenchyma focal defect by Brenner et al. (2009) also performed the similarly reconstruction parameter. Raeisi et al., (2007) also suggested the usage of Butterworth filter in image reconstruction to produce the best image quality in SPECT imaging. Dong et al., (2017) also reported that Butterworth filter produce the best balanced image quality between the needs of high contrast, low noise and accurate tumour size. Image filtering is

an important factor that affects the quality of clinical SPECT images. Filtering is a post-processing step in iterative reconstruction to reduce noise, improve the image resolution and limit the degradation of the image (Groch and Erwin, 2000).

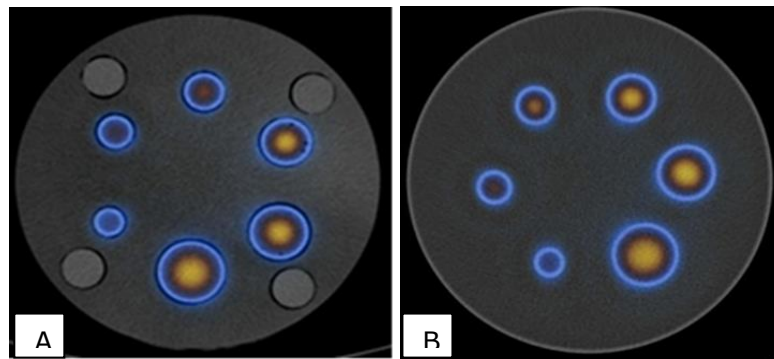
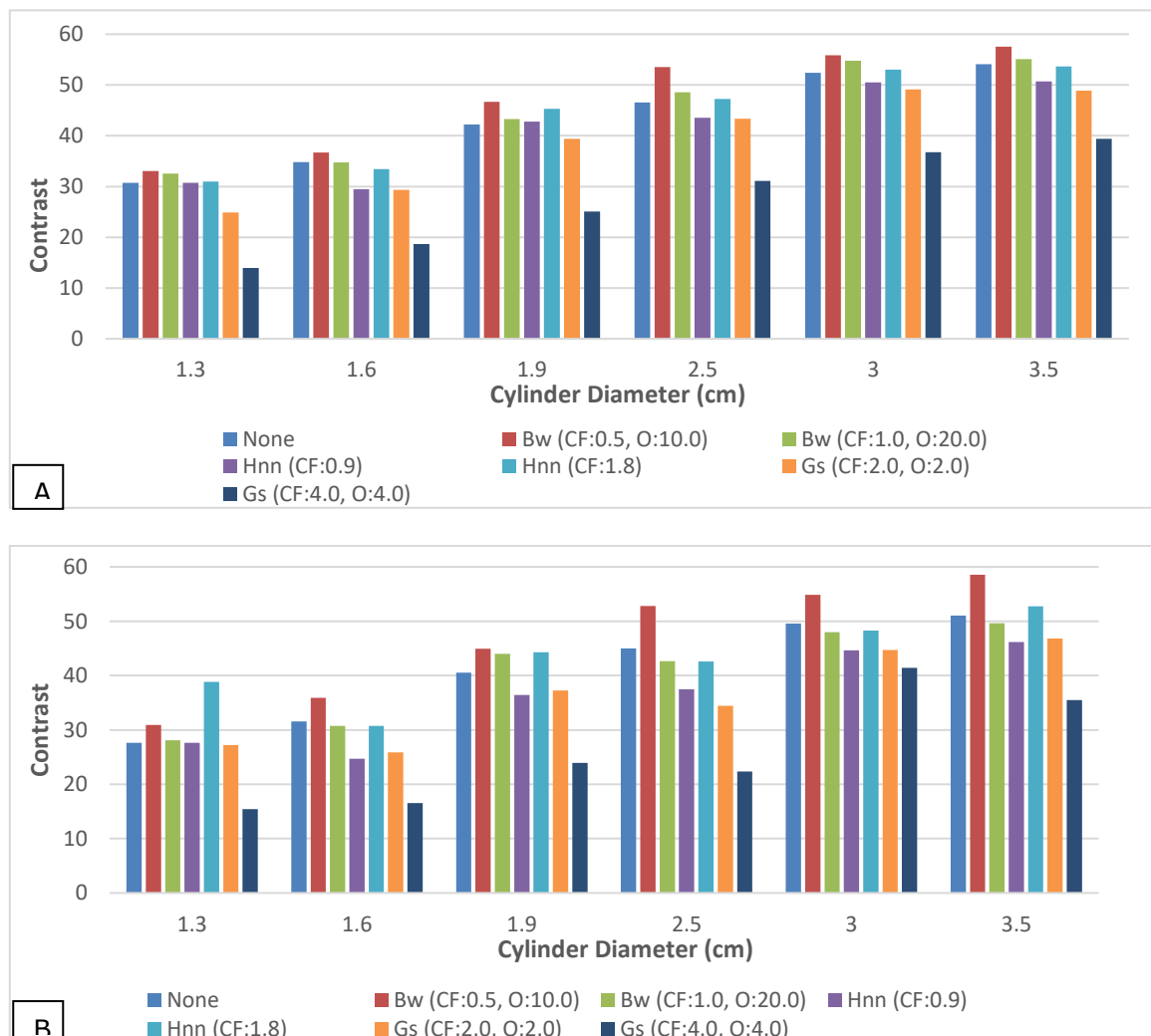


Figure 3: The SPECT images of radionuclide at different diameter sizes by (a) *Rhizophora spp.* particleboards and (b) Jaszczak phantom.



Bw = Butterworth, Hnn = Hann and Gs = Gaussian filter type.
 CF = Cut-off frequency and O = Order of filter parameters setting

Figure 4: The contrast of the SPECT images for (a) *Rhizophora spp.* particleboards and (b) Jaszczak phantoms reconstructed using different SPECT filters.

The SPECT images reconstructed using Butterworth filter were used for evaluation of full width half maximum (FWHM) of the SPECT images. The average FWHM of plotted intensity profile in each cylinder in *Rhizophora* spp. particleboards and Jaszczak phantoms are illustrated in Figure 5. The result showed a good correlation between FWHM and diameter size of cylinder for both Jaszczak and *Rhizophora* spp. particleboards indicated by R^2 values of 0.9530 and 0.9623 respectively. Table 1 shows the ratio of apparent diameter to actual diameter of cylinder size for corn starch-bonded *Rhizophora* spp. particleboards, Jaszczak and Perspex® phantoms. The nearest apparent size to actual size was obtained by 2.5 cm of cylinder diameter for all SPECT phantoms shown by the lowest value of ratio (1.35, 1.40 and 1.30) followed by cylinder diameter with 3.0 cm. The smallest actual size diameter of cylindrical radionuclide vial give about double the apparent size on the SPECT images for all phantoms with ratio value of 2.00 to 2.11. The ratio of dimension for corn starch-bonded *Rhizophora* spp. particleboards and Perspex® phantom were in agreement to values of Jaszczak phantom within 4.44 and 5.95% of differences respectively.

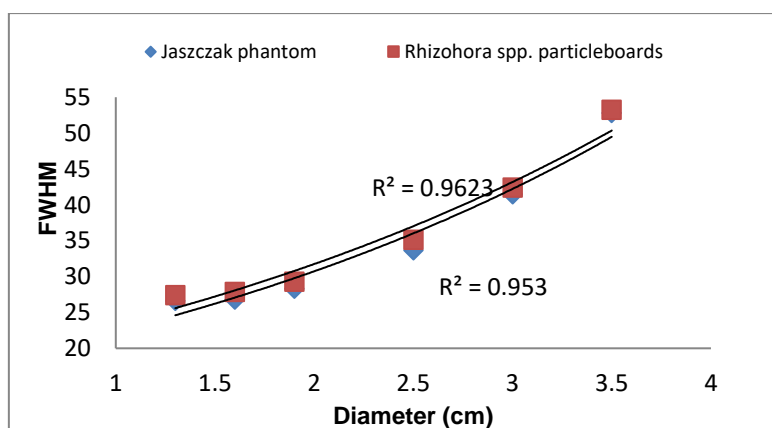


Figure 5: The full width half maximum (FWHM) of radionuclides at different diameters measured in *Rhizophora* spp. Particleboards and Jaszczak phantoms.

Table 1: The ratio of apparent to actual source dimensions for each cylinder diameter for *Rhizophora* spp. particleboards and Jaszczak phantom.

Cylinder diameter (cm)	Jaszczak phantom	<i>Rhizophora</i> spp. particleboards	Percentage difference (%)
1.3	2.05	2.11	2.93
1.6	1.68	1.74	3.57
1.9	1.49	1.54	3.36
2.5	1.35	1.41	4.44
3.0	1.38	1.42	2.90
3.5	1.51	1.51	0

The measured recovery coefficient values are drawn versus the diameter of cylinder as illustrated in Figure 6. The RC curve of the constructed *Rhizophora* spp. particleboards was in excellent agreement to that in the Jaszczak phantom. The result showed the rapidly improvement of recovery coefficients to the value of 1.0 at increasing diameter of cylinder between 1.3 and 2.5 cm. The recovery coefficients of the SPECT images at cylindrical diameter sizes of 2.5, 3.0 and 3.5 cm on the other hand were greater than 1.0 for both *Rhizophora* spp. particleboards and Jaszczak phantom. A paired sample *t*-test calculation showed no significant difference between recovery coefficient values of Jaszczak phantom and *Rhizophora* spp. particleboards with *p*-values of 0.185. An ideal RC value for any SPECT image would be not more than 1.0. The RC values of more than 1.0 would indicate the presence of 'spill over' effect due to contamination of activity from the neighbouring tissue or spot to these hot areas (Gopal, 2010). The spill-over effect is more significant at larger size of radionuclide localizations. In this study, the spill-over feature in the constructed *Rhizophora* spp. particleboards were comparable to that in Jaszczak phantom indicated the similar attenuation properties on *Rhizophora* spp. particleboards to water for *in-vivo* detection of SPECT imaging. The overall results indicated the similar attenuation properties of the fabricated *Rhizophora* spp. particleboards to water for *in-vivo* detection of radionuclide to be potentially used as alternative water equivalent phantom for SPECT and SPECT/CT imaging.

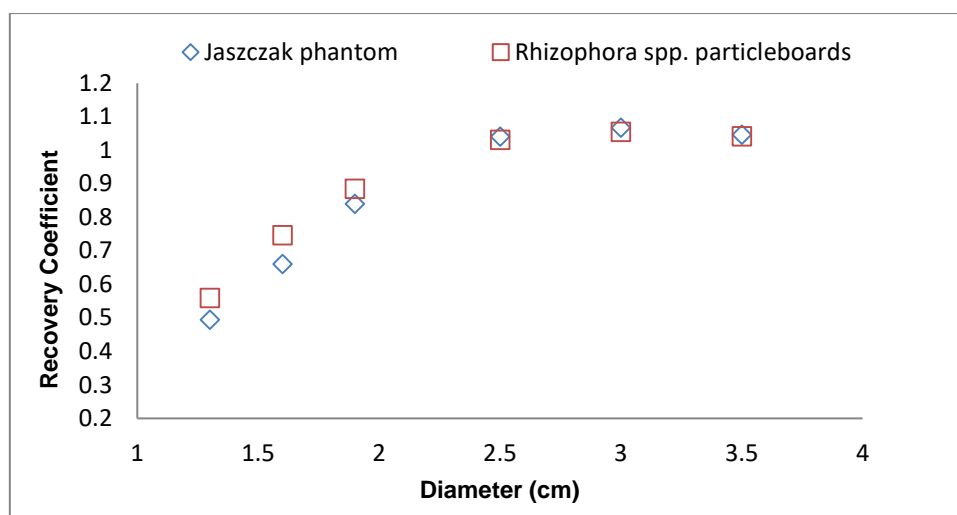


Figure 6: Recovery coefficient (RC) versus diameter of cylinder for SPECT images of *Rhizophora* spp. particleboards and Jaszczak phantom.

4. CONCLUSION

The fabricated *Rhizophora* spp. particleboards constructed as the phantom for SPECT/CT imaging showed similar attenuation characteristics to that in Jaszczak phantom commonly used for QC in SPECT/CT. The contrast values in *Rhizophora* spp. particleboards showed good agreement to Jaszczak at all SPECT filters at all diameter sizes of radionuclide localizations. The measurement of ratio between apparent and actual size of radionuclide localizations showed and excellent agreement to Jaszczak phantom within 4.5% percentage difference. The evaluation of recovery coefficient in *Rhizophora* spp. particleboard also showed an excellent agreement to Jaszczak phantom especially in larger diameter sizes of radionuclide localizations. The overall results indicated the suitability of the fabricated *Rhizophora* spp. particleboards to be developed as an alternative phantom material for in-vivo imaging such as SPECT and SPECT/CT.

5. ACKNOWLEDGEMENT

The author would like to acknowledge the financial support of USM Bridging Grant no. 304.PPSK.6316324 for the study.

6. REFERENCES

- AAPM-21 (1983). Protocol for the determination of absorbed dose from high energy photon and electron beams; Task Group 21. *Medical Physics*, 10(6), 741-771.
- Ababneh, B., Tajuddin, A. A., Hashim, R., & Shuaib, I. L. (2016). Investigation of mass attenuation coefficient of almond gum bonded *Rhizophora* spp. particleboard as equivalent human tissue using XRF technique in the 16.6-25.23 keV photon energy. *Australasian Physical & Engineering Science in Medicine*, 39(4), 871-876.
- Abuarra, A., Bauk, S., Hashim, R., Kandaiya, S., Tousi, E. T., & Aldroobi, K. (2014). Microstructure examination, elemental composition analysis of Gum Arabic bonded *Rhizophora* spp. particleboards and their potential as tissue equivalent material. *International Journal of Chemical, Environment & Biological Sciences*, 2(1), 71-75.
- Brenner, M., Bonta, D., Eslamy, H., & Ziessman, H. A. (2009). Comparison of ^{99m}Tc-DMSA dual-head SPECT versus high-resolution parallel-hole planar imaging for the detection of renal cortical defects. *American Journal of Roentgenology*, 193, 333-337.
- Cherry, S. R., Sorenson, J. A., & Phelps, M. E. (2012). *Physics in Nuclear Medicine*. (4th ed.). PA: Saunders Elsevier Philadelphia.
- Dong, X., Saripan, M. I., Mahmud, R., Mashohor, S., & Wang, A. (2017). Determination of the optimum filter for ^{99m}Tc SPECT breast imaging using a wire mesh collimator. *Pakistan Journal of Nuclear Medicine*, 7(1), 9-15.

- Gopal, B. S. (2010). Basics of PET Imaging (2nd edition). Springer, New York, London.
- Groch, M. W., & Erwin, W. D. (2000). SPECT in the year 2000: Basic Principles. *Journal of Nuclear Medicine Technology*, 28(4), 233–244.
- Hamid, P. N. K. A., Yusof, M. F.M., Hashim, R. & Tajuddin, A. A. (2018). Characterisations and attenuation properties of corn starch-bonded *Rhizophora* spp. as water equivalent phantom material at 16.59 – 25.26 XRF photons and 99mTc gamma energies. *International Journal of Environmental Engineering*, 9(3/4), 254-270.
- Imam, S. H., Lijun, M., Liang, C., & Greene, R. V. (1999). Wood adhesive from crosslinked poly (vinyl alcohol) and partially gelatinized starch: preparation and properties. *Starch-Starke*, 51(6), 225-229.
- Khan, F. M. & Gibbons, J. P. (2014). Khan's The Physics of Radiation Therapy. (5th ed.). Lippincott Williams and Wilkins, Philadelphia.
- Liu, J., Jia, C., & He, C. (2012). Rice straw and cornstarch biodegradable composites. *AASRI Procedia*, 3, 83-88.
- Moubarik, A., Allal, A., Pizzi, A., Charrier, F., & Charrier, B. (2010). Preparation and mechanical characterization of particleboard made from maritime pine and glued with bio-adhesives based on cornstarch and tannin. *Maderas-Ciencia Y Tecnologia*, 12(3), 189-197.
- Moubarik, A., Pizzi, A., Charrier, F., Allal, A., Badia, M. A., Mansouri, H. R., & Charrier, B. (2013). Mechanical characterization of industrial particleboard panels glued with corn starch-mimosa tannin-urea formaldehyde resins. *Journal of Adhesion Science and Technology*, 27(4), 423-429.
- Ngu, K. T., Bauk, S., Hashim, R., Tajuddin, A. A., & Shukri, A. (2015). Fabrication of formaldehyde-based particleboards and their mass attenuation coefficients at 15.77, 17.48, 21.18 and 25.27 keV photon energies. *Journal of Physical Sciences*, 26 (1), 27-33.
- Richardson, S., & Gorton, L. (2003). Characterisation of the substituent distribution in starch and cellulose derivatives. *Analytica Chimica Acta*, 497, 27-65.
- Ritt, P., Vija, H., Hornegger, J., & Kuwert, T. (2011). Absolute quantification in SPECT. *European Journal of Nuclear Medicine and Molecular Imaging*, 38, 69-77.
- Shakhreet, B. Z., Bauk, S., Tajuddin, A. A., Shukri, A. (2009). Mass attenuation coefficients of natural *Rhizophora* spp. wood for X-rays in the 15.77 to 25.27 keV range. *Radiation Protection and Dosimetry*, 135(1), 47-53.
- Yusof, M. F. M., Hashim, R., Tajuddin, A. A., & Bauk, S. (2017). Characterization of tannin-added *Rhizophora* spp. particleboards as phantom materials for photon beams. *Industrial Crops and Products*, 95, 467-474.
- Raeisi, E., Rajabi, H., Aghamiri, M. R., Hajizadeh, E., Seifollahi-Asl, S., Yaghobi, N., & Firozabadi, S. H. (2007). Qualitative evaluation of filter function in brain SPECT. *Iranian Journal of Nuclear Medicine*, 15(27), 1–8.

#338: Thermal performance of a novel thermoelectric refrigerator with a water to air heat exchanger and SiO₂, TiO₂ and Al₂O₃ nanofluids

Pinar Mert CUCE^{1,*}, Saffa RIFFAT², Erdem CUCE³

¹Department of Energy Systems Engineering, Faculty of Engineering, Recep Tayyip Erdogan University, Zihni Derin Campus, 53100 Rize, Turkey, pinar.mertcuce@erdogan.edu.tr

²Department of Architecture and Built Environment, Faculty of Engineering, University of Nottingham, University Park Campus, NG7 2RD Nottingham, UK, saffa.riffat@nottingham.ac.uk

³Department of Mechanical Engineering, Faculty of Engineering, Recep Tayyip Erdogan University, Zihni Derin Campus, 53100 Rize, Turkey, erdem.cuce@erdogan.edu.tr

*Corresponding author

Thermoelectric refrigeration is an eco-friendly and cost-effective cooling method, basically defined as the process of pumping thermal energy out of an insulated medium for reducing the temperature of the medium below that of the surrounding air. Thermoelectric refrigeration is based on a phenomenon called Peltier effect to pump the said heat from one layer to another. Thermoelectric coolers (TECs) are usually utilised for electronics cooling today, however, there are several attempts to expand their application areas like in space cooling. In this research, a novel TEC system was devised, fabricated and experimentally analysed for a potential alternative to conventional refrigerators in the built environment. The novel TEC unit consisted of a heat absorbing and heat dissipating part, which represented the evaporator and the condenser of the system, respectively. Optimum heat sinks were considered for the aforesaid parts, and additionally, a water to air heat exchanger was integrated to the heat dissipating section for the thermal regulation of the hot surface. The water to air heat exchanger was so effective that only 1°C temperature difference between the heat exchanger fins and the surrounding air was observed in all tests. The tests were carried out for a constant surrounding air temperature in the range of 20-21°C with pure water. Moreover, some further tests were conducted with SiO₂, TiO₂ and Al₂O₃ nanofluids at a certain mass fraction. The results revealed that the coefficient of performance (COP) of the novel TEC system was 0.23 for without load condition whereas it was 0.09 with load. The COP was enhanced by about 1.2, 3.7 and 9.6% via the nanofluid integration of SiO₂, TiO₂ and Al₂O₃, respectively for the case of without load.

Keywords: thermoelectric coolers; refrigeration; water to air heat exchanger; thermal performance; COP

1. INTRODUCTION

Thermoelectric coolers (TECs) are in the centre of interest at global scale since they run with no vibration and noise while providing sustainable energy conversion. TECs are lightweight and solid state units with no moving parts (Cuce and Guclu, 2019). TECs have a wide range of applications from electronics cooling to space research which can be attributed to rising tendency of current coefficient of performance (COP) range of TECs (Guclu et al., 2017a). Thermoelectric devices in general can be split into two parts as thermoelectric generators (TEGs) and thermoelectric coolers (TECs). TEGs convert heat into electricity through the Seebeck effect. The Seebeck effect justifies the generation of a voltage difference between two different electrical conductors or semiconductors when they are subjected to a temperature difference (Guclu et al., 2017b). On the contrary to TEGs, TECs are based on the phenomenon of heat dissipation from a medium through the Peltier effect. Peltier effect is expressed as the dissipation or absorption of heat when an electric current is applied to a junction between the aforesaid two substances (Huang et al., 2013).

It is clearly underlined in literature that conventional cooling systems (air, water or liquid cooling applications) already reach their theoretical limits. As a consequence of this shortcoming, TECs draw attention day after day to be an alternative cooling technology in different sectors (Du and Wen, 2011). TECs have a wide range of advantages when compared to other cooling technologies. As an example, TECs do not include any refrigerant or mechanical operation, and they can be devised and fabricated for a certain cooling capacity or dimension. Simplicity, high reliability, quiet operation, compact structure, and lightness are the other characteristic features of TECs. These advantages enable TECs to be considered in various areas such as microelectronic systems, laser diodes, telecommunications, aerospace industry, superconductor systems, food industry and medical devices. The inadequate COP figures in high temperature applications can be asserted as the main handicap of TECs (Yu and Wang, 2009). A typical TEC unit comprises of N-type and P-type element pairs as shown in Figure 1, and these are connected as thermally parallel and electrically series among two ceramic plates (Cheng and Huang, 2012). When a current flow is applied to one side, electrons in the N-type semiconductor and holes in the P-type semiconductor gain mobility as shown in Figure 2. The said movements are related to the current direction as expected. As a consequence of this current flow, heat is transferred from cold side to hot side which yields to cooling process (Zhu et al., 2013).

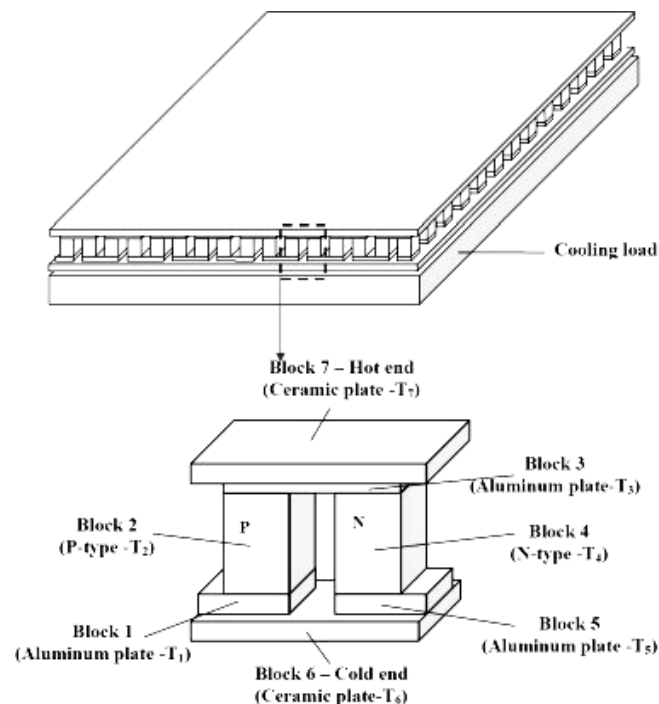


Figure 1: Physical model of a TEC unit (Cheng and Huang, 2012).

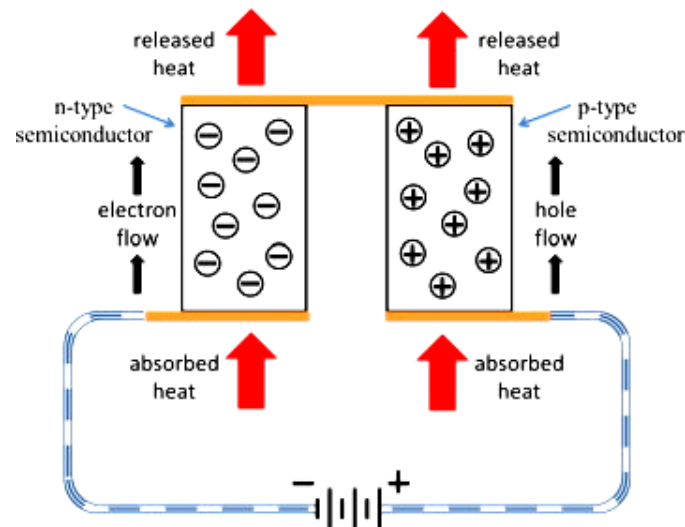


Figure 2: Working principle of TECs (Zhu et al., 2013).

For an optimum system performance and maximum thermal efficiency, two optimised heat exchangers are usually utilised in TEC units. The first heat exchanger, which is fixed on the hot side of TEC unit aims at dissipating heat generated on the hot surface to the surrounding ambient so to decrease the hot side temperature. The second heat exchanger, on the other hand, absorbs heat from cold medium and transports to the cold surface which results in the rise of cold surface temperature of TEC unit. Thermal performance figures of TECs are highly affected by the overall efficiency of the aforesaid heat exchangers. COP of a TEC unit notably improves when the temperature difference between cold and hot side is minimised, which can be secured of course with highly efficient heat exchangers. On the other hand, for the greater temperature differences between cold and hot surfaces, COP of a TEC unit remarkably reduces as expected.

There are numerous works in literature regarding the thermal performance assessment of TECs. Zhang proposes a general approach for optimising and analysing TECs through a case study of microprocessors cooling (Zhang, 2010). Lin et al. evaluated the cooling performance of two-stage TEC unit for the case of current pulse operation (Lin et al., 2016). It is reported that the duration of pulse current and the amplitude are effective parameters on the cold side temperature. In order to achieve maximum temperature reduction across a two-stage TEC unit, a novel design concept was presented by Lv et al. (Lv et al., 2016). Greater holding time of super cooling state and lower temperature overshoot was obtained via the novel design. Two-stage TECs provide better thermal performance figures than single-stage TECs, and they were comprehensively analysed by Ma and Yu (Ma and Yu, 2014). Rao and Patel develop a novel method based on a teaching-learning optimisation algorithm for a two-stage TEC unit (Rao and Patel, 2013). Performance optimisation of TECs was also investigated by Manikandan and Kaushik through the impacts of Thomson effect (Manikandan and Kaushik, 2016). The results reveal that energy efficiency and cooling power were enhanced with Thomson effect. Multi-stage TECs were also analysed by Hwang et al. through a micro TEC using thermal network model (Hwang et al., 2009).

Air conditioning systems and refrigeration play a key role in climate change and global warming issues. About 30% of total ozone layer depletion is ascribed to the aforesaid systems. Traditional cooling technologies such as absorption and vapour compression systems in general have a high COP range, and usually their operation process is safe. However, they have some shortcomings such as noisy operations, costly periodic maintenances and complex structures. Moreover, such systems are not eco-friendly in most cases (Riffat et al., 2001). As a consequence of growing importance of environmental issues, TECs are believed to be a promising alternative to conventional cooling systems owing to their characteristic benefits such as vibration-free and quiet operation, being free of moving parts, notably lightweight system details and eco-friendly structure (Rawat et al., 2013).

There were numerous attempts in literature regarding the numerical and experimental investigation of TECs as space cooling applications. As an example, Jugsujinda et al. carry out an experimental research for thermal performance analysis of a TEC refrigerator (Jugsujinda et al., 2011). It was observed from the tests that the cold surface temperature drops from 30 to -4.2°C in only one hour with an average COP of 0.65. Hermes and Barbosa compare the thermodynamic performance figures of three cooling technologies: Stirling, thermoelectric, and vapour compression using two different compressors (linear and reciprocating) (Hermes and Barbosa). The aforesaid refrigeration technologies were experimentally analysed for identical conditions. It was observed from the results that the efficiency of TEC refrigeration system (COP = 0.69) was lower than the other technologies. However, TECs were found to be promising especially for the low cooling demands with good response time and low energy consumption.

Within the scope of this research, a novel TEC system was devised, fabricated and experimentally analysed. For the first time in literature, an optimised water to air heat exchanger was developed for the said TEC system to regulate the hot surface temperature of TEC unit. The tests were firstly conducted with pure water and reference performance figures were achieved for comparison. Then, three different nanoparticles (SiO_2 , TiO_2 and Al_2O_3) were utilised to produce nanofluids for the novel TEC system. The tests were conducted for a certain mass fraction of 0.1 for each nanofluids, and the enhancements in COP figures were evaluated in comparison with the case of pure water. Each test was carried out inside an environmental chamber with an ambient temperature of 20°C .

2. EXPERIMENTATION

In this study, a novel TEC system was devised, fabricated and experimentally analysed in order to investigate the impacts of various nanofluids on thermal performance figures notably COP. An optimised water to air heat exchanger was developed for the said TEC system illustrated in Figure 3 to be able to regulate the hot surface temperature. The refrigerator was fabricated with thermally resistive 10 mm particleboards reinforced by 50 mm PUR insulation to be able to achieve the adiabatic conditions at the edges. Internal volume of refrigerator was devised to be 80 litres. Two low energy consuming fans were considered at cold and hot side for forced convection of air. Pure aluminium heat sinks were utilised at both sides for efficient heat dissipation and absorption. Water flow was provided by a DC pump running at 12 V and 1 A. a single-stage 40 W Peltier module was used in the system. The TEC system was powered by a DC power source. For the temperature measurements, standard K type thermocouples were utilised. The tests were firstly performed with pure water and reference performance values were obtained for comparison. Afterwards, three different nanoparticles (SiO_2 , TiO_2 and Al_2O_3) shown in Figure 4 were utilised to produce nanofluids for the novel TEC system. The tests were carried out for a certain mass fraction of 0.1 for each nanofluids, and the enhancements in COP figures were assessed in comparison with the case of pure water. Purity of nanoparticles was reported to be over 98%, which was appropriate for such a research. Particle sizes of SiO_2 , TiO_2 and Al_2O_3 nanoparticles were given to be 55-75, 38 and 78 nm, respectively. Each test was conducted inside an environmental chamber with an ambient temperature of 20°C . The chamber was conditioned by an air conditioner at a power of 24000 BTU. Thermal performance assessment was done through a time-dependent data triggering which was provided by DT85 Data logger from DataTaker Company. The measurements were repeated until the steady-state conditions were achieved. The tests were conducted for both without load and with load conditions. For both cases, nanofluids integration to the TEC system was experimentally analysed in terms of its potential effects on COP figures. Total uncertainty of the measurement system was calculated to be below 1%, which was acceptable. COP was calculated by the following equation:

$$\text{Equation 1: } \quad \text{COP} = (m c_p \Delta T / t) / W_{\text{in}}$$

Where:

- m = mass of air and mass of water in without and with load tests, respectively,
- c_p = specific heat capacity,
- ΔT = temperature difference between time intervals,
- t = time interval
- W_{in} = input power to the system.

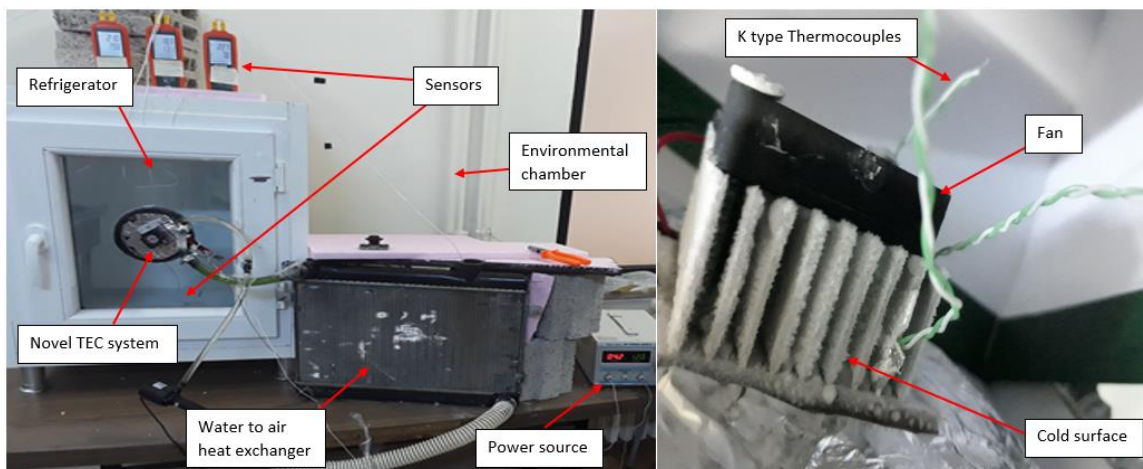


Figure 3: Experimental analysis of novel TEC unit.

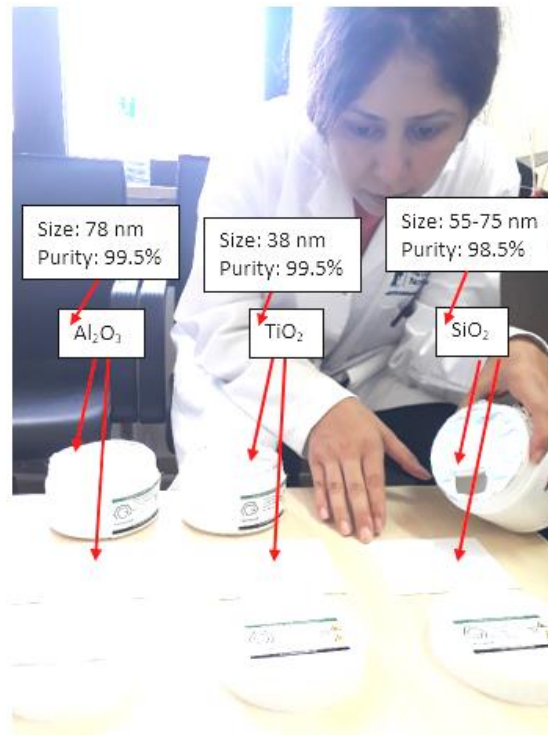


Figure 4: SiO_2 , TiO_2 and Al_2O_3 nanoparticles considered in the research.

3. RESULTS AND DISCUSSION

The demonstration of the results starts with the time-dependent temperature figures for surrounding ambient, hot surface, cold surface, fan outlet air, internal body, external body and cooled space. The experiments were first conducted for without load condition as shown in Figure 5. The average surrounding ambient temperature was determined to be 19.6°C for the tests of without load condition. The cold surface temperature was observed to drop from 21 to -13.8°C within 800 seconds, which needs to be noted. On the other hand, average hot surface temperature was calculated to be 20.6°C . In other words, water to air heat exchanger utilised for the thermal regulation of hot side was capable of providing only about 1°C temperature difference between hot surface and ambient, which was outstanding. It was also observed from the without load tests that internal body temperature was very close to the cooled space temperature. Similarly, there was negligible difference between the temperatures of external body and surrounding ambient. This justifies adiabatic boundary conditions take place at the edges of the refrigerator.

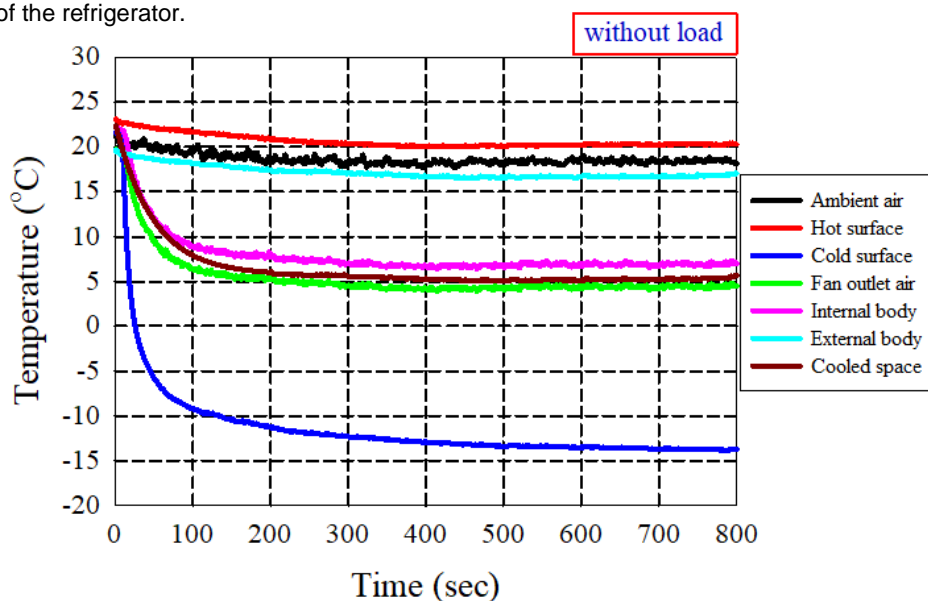


Figure 5: Thermal performance assessment of novel TEC system for without load condition.

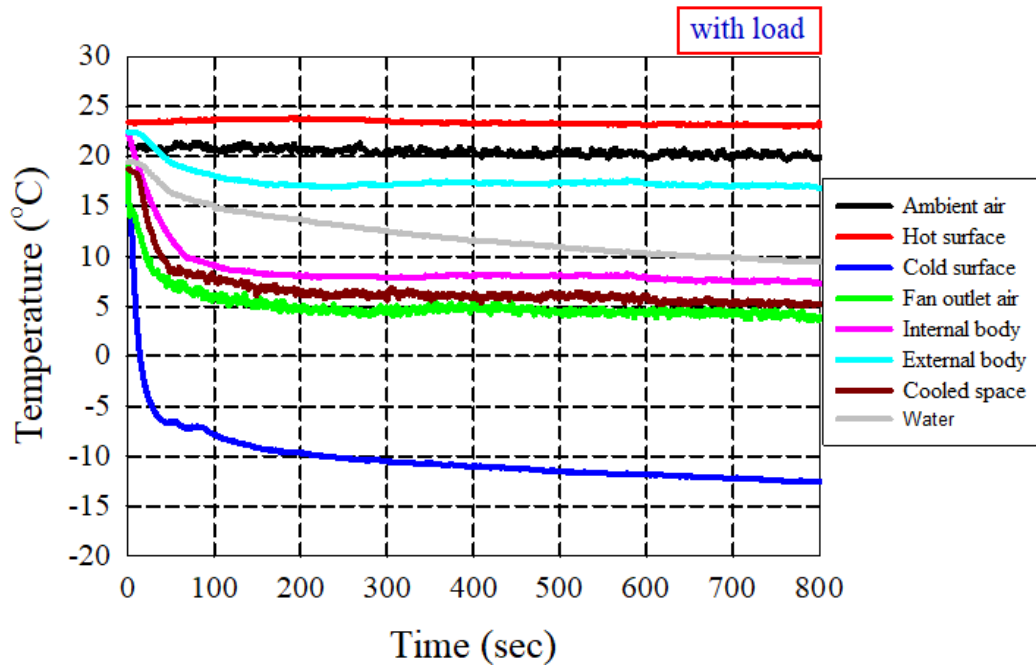


Figure 6: Thermal performance assessment of novel TEC system for with load condition.

Similar to the tests for without load condition, the novel TEC unit was experimentally analysed for the case of with load. Water was considered for these tests with a volume of 0.2 litre. The experimental results were demonstrated in Figure 6. The average surrounding ambient temperature was determined to be 21.1°C for the tests of with load condition. The cold surface temperature was noticed to decrease from 20.9 to -13.7°C within 800 seconds, which needs to be underlined. On the other hand, average hot surface temperature was found to be 22.8°C. In other words, water to air heat exchanger used for the thermal regulation of hot side was capable of providing only about 1.7°C temperature difference between hot surface and ambient, which was promising. It was also observed from the with load tests that internal body temperature was very close to the cooled space temperature. Similarly, there was negligible difference between the temperatures of external body and surrounding ambient. This verifies adiabatic boundary conditions occur at the edges of the refrigerator.

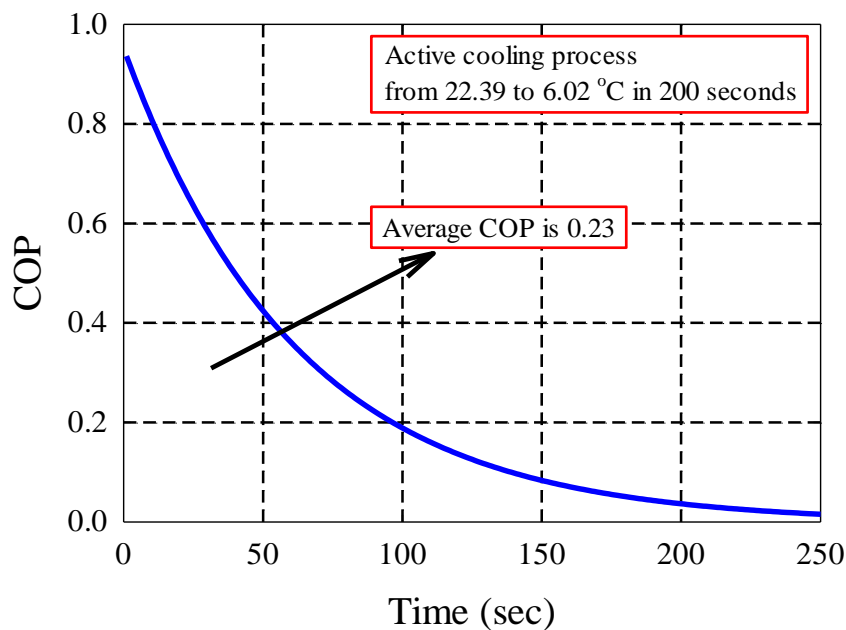


Figure 7: COP of novel TEC system for without load condition.

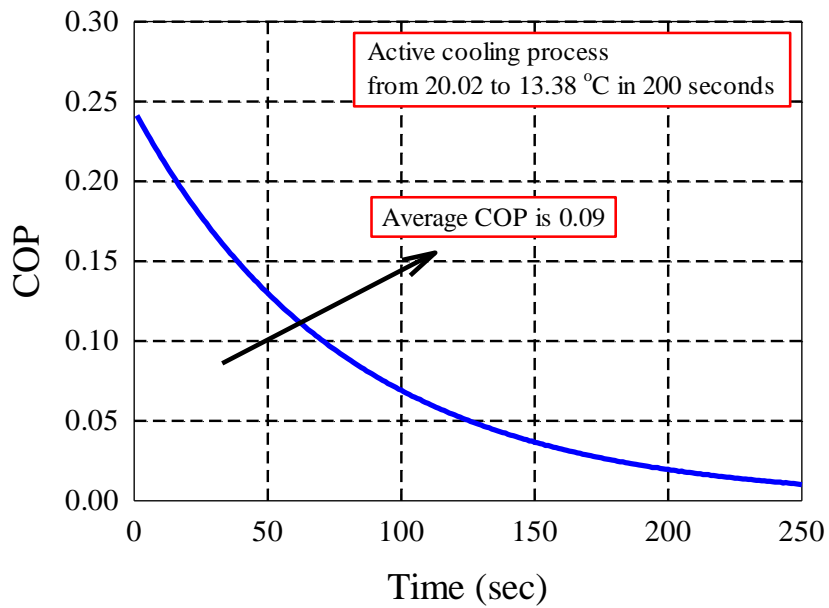


Figure 8: COP of novel TEC system for with load condition.

COP of novel TEC unit was experimentally determined for without load condition as illustrated in Figure 7. Within 800 seconds, air was cooled from 22.39 to 6.02°C, which corresponds to a COP of 0.23 for an air volume of 80 litres. In the calculation of COP, thermophysical properties of air were taken at reference average temperature. Similarly, COP of novel TEC unit was determined for with load condition as depicted in Figure 8. Because of notably higher specific heat capacity of water, temperature reduction in water takes more time compared to air. Water was cooled from 20.02 to 13.38 °C, which corresponds to a COP of 0.09.

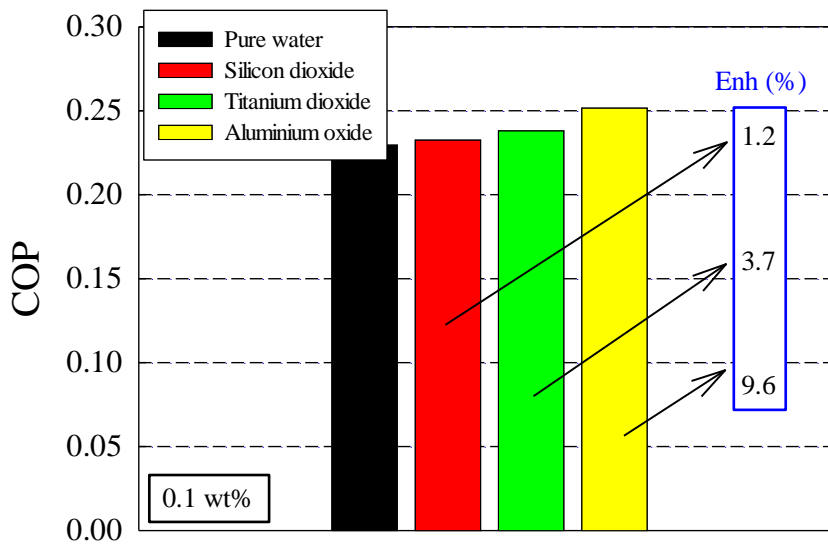


Figure 9: Enhancement in COP of novel TEC system via nanofluids for without load condition.

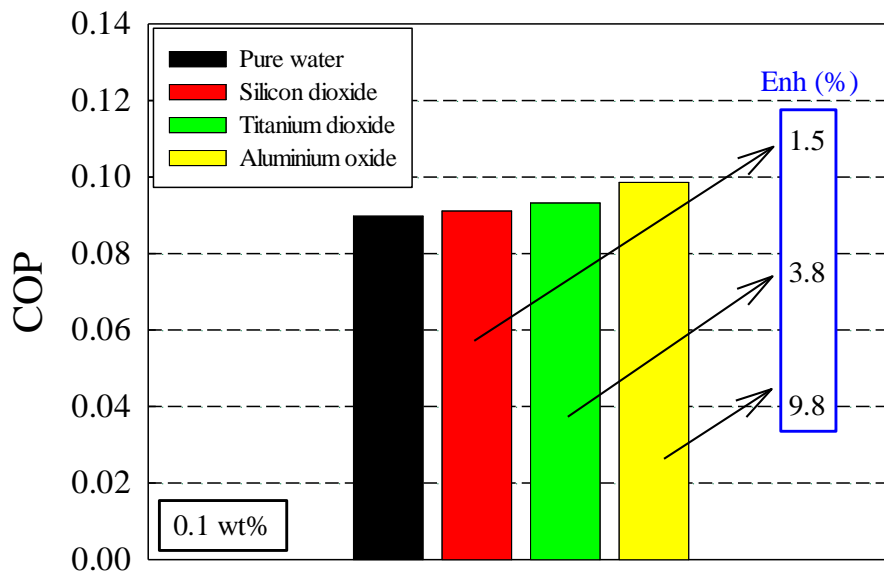


Figure 10: Enhancement in COP of novel TEC system via nanofluids for with load condition.

After the reference tests conducted with pure water, nanofluids were prepared with three different nanoparticles (SiO_2 , TiO_2 and Al_2O_3) at a constant mass fraction (0.1 wt%). The tests were repeated for without load and with load conditions as shown in Figure 9 and Figure 10. The COP was enhanced by about 1.2, 3.7 and 9.6% via the nanofluid integration of SiO_2 , TiO_2 and Al_2O_3 , respectively for the case of without load. Similarly, COP was improved by 1.5, 3.8 and 9.8% for the case of with load. It was understood from the data that even small mass fractions of nanoparticles were capable of improving COP of TECs remarkably compared to the reference tests conducted with pure water.

4. CONCLUSIONS

Three different nanoparticles (SiO_2 , TiO_2 and Al_2O_3) at a certain mass fraction (0.1 wt%) were considered in a TEC refrigerator, and the impacts of nanofluids on the thermal performance figures of TECs were experimentally evaluated. The enhancements were assessed over a reference research conducted with pure water. The tests were repeated for both with and without load conditions. The results indicate that The COP was improved by about 1.2, 3.7 and 9.6% via the nanofluid implementation of SiO_2 , TiO_2 and Al_2O_3 , respectively for the case of without load. Similarly, COP was enhanced by 1.5, 3.8 and 9.8% for the case of with load. It was concluded from the data that even small mass fractions of nanoparticles (0.1 wt%) were capable of improving COP of TECs considerably compared to the reference tests carried out with pure water.

5. REFERENCES

- Cheng CH, Huang SY, 2012. Development of a non-uniform-current model for predicting transient thermal behavior of thermoelectric coolers. *Applied Energy*, 100, 326-335.
- Cuce E, Guclu T, 2019. Thermoelectric coolers (TECs): From theory to practice. *Journal of Electronic Materials*, 48(1), 211-230.
- Du CY, Wen CD, 2011. Experimental investigation and numerical analysis for one-stage thermoelectric cooler considering Thomson effect. *International Journal of Heat and Mass Transfer*, 54, 4875-4884.
- Guclu T, Cuce PM, Besir AB, Cuce E, 2017a. Thermoelectric coolers (TECs) for potential air-conditioning applications in buildings. *First International Symposium on Multidisciplinary Studies and Innovative Technologies*, 2-4 November 2017, Tokat, Turkey.

- Guclu T, Cuce E, Besir AB, 2017b. A systematic overview of thermoelectric coolers (TECs). *International Conference on Advanced Engineering Technologies*, 21-23 September 2017, Bayburt, Turkey.
- Hermes CJ, Barbosa JR, 2012. Thermodynamic comparison of Peltier, Stirling, and vapor compression portable coolers. *Applied Energy*, 91, 51-58.
- Huang YX, Wang XD, Cheng CH, Lin DTW, 2013. Geometry optimization of thermoelectric coolers using simplified conjugate-gradient method. *Energy*, 59, 689-697.
- Hwang GS, Gross AJ, Kim H, Lee SW, Ghafouri N, Huang BL, Lawrence C, Uher C, Najafi K, Kaviany M, 2009. Micro thermoelectric cooler: Planar multistage. *International Journal of Heat and Mass Transfer*, 52, 1843-1852.
- Jugsujinda S, Vora-ud A, Seetawan T, 2011. Analyzing of thermoelectric refrigerator performance. *Procedia Engineering*, 8, 154-159.
- Lin S, Ma M, Wang J, Yu J, 2016. Experiment investigation of a two-stage thermoelectric cooler under current pulse operation. *Applied Energy*, 180, 628-636.
- Lv H, Wang XD, Meng JH, Wang TH, Yan WM, 2016. Enhancement of maximum temperature drop across thermoelectric cooler through two-stage design and transient supercooling effect. *Applied Energy*, 175, 285-292.
- Ma M, Yu J, 2014. An analysis on a two-stage cascade thermoelectric cooler for electronics cooling applications. *International Journal of Refrigeration*, 38, 352-357.
- Manikandan S, Kaushik SC, 2016. The influence of Thomson effect in the performance optimization of a two stage thermoelectric generator. *Energy*, 100, 227-237.
- Rao RV, Patel V, 2013. Multi-objective optimization of two stage thermoelectric cooler using a modified teaching-learning-based optimization algorithm. *Engineering Applications of Artificial Intelligence*, 26, 430-445.
- Rawat MK, Chattopadhyay H, Neogi S, 2013. A review on developments of thermoelectric refrigeration and air conditioning systems: a novel potential green refrigeration and air conditioning technology. *International Journal of Emerging Technology and Advanced Engineering*, 3, 362-367.
- Riffat SB, Omer SA, Ma X, 2001. A novel thermoelectric refrigeration system employing heat pipes and a phase change material: an experimental investigation. *Renewable Energy*, 23, 313-323.
- Yu J, Wang B, 2009. Enhancing the maximum coefficient of performance of thermoelectric cooling modules using internally cascaded thermoelectric couples. *International Journal of Refrigeration*, 32, 32-39.
- Zhang HY, 2010. A general approach in evaluating and optimizing thermoelectric coolers. *International Journal of Refrigeration*, 33, 1187-1196.
- Zhu W, Deng Y, Wang Y, Wang A, 2013. Finite element analysis of miniature thermoelectric coolers with high cooling performance and short response time. *Microelectronics Journal*, 44, 860-868.

#340: Microwave air heater: experimental investigation of a green heat transfer approach in helical coil

Peter Nai Yuh YEK¹, Mohammad Shahril OSMAN¹, Tiew Wei TING¹, Sebastian DAYOU¹, Sie Yee LAU¹, Su Shiung LAM², Rock Keey LIEW²

¹University College of Technology Sarawak, Department of Engineering, No.1, Jalan Universiti, 96000, Sibu, Sarawak, Malaysia. peter.yek@ucts.edu.my,

¹Department of Engineering, University College of Technology Sarawak, Malaysia drshahril@ucts.edu.my,

¹Department of Engineering, University College of Technology Sarawak, dr.ting@ucts.edu.my, ¹Department of Engineering, University College of Technology Sarawak, sebastian@ucts.edu.my,

¹Department of Engineering, University College of Technology Sarawak, lau.sie.yee@ucts.edu.my

²Pyrolysis Technology Research Group, School of Ocean Engineering, Universiti Malaysia Terengganu, 21030 Kuala Terengganu, Terengganu, Malaysia. lam@umt.edu.my,

²Pyrolysis Technology Research Group, School of Ocean Engineering, Universiti Malaysia Terengganu, 21030 Kuala Terengganu, Terengganu, Malaysia. Irklrk1991@gmail.com

Heat transfer to a helical coil induced by microwave heating was performed in this study. Microwave radiation provided indirect and volumetric heating to the activated carbon (microwave absorbent) to store and transfer heat energy to the helical coil and heat up the air indirectly. The helical coil caused centrifugal force and induced a secondary flow to significantly enhance the heat transfer. Microwave radiation provided a high heating rate of 50°C/min to heat the activated carbon and the heat energy that was retained by activated carbon showed low heat loss of 10°C/min during cooling down. Then, the convective heat transfer between helical coil and air in non-isothermal conditions was performed. The overall heat transfer coefficient of the helical coil was evaluated under the condition of curvature ratios of 0.083, 15-25 L/min airflow rate and activated carbon temperature reduced from 300°C to 100°C. Dimensionless number of Reynolds number, Nusselt number and Dean Number were then analysed to evaluate the airflow and heating performance in the helical coil. The experimental results showed good agreement with literature whereas convective heat transfer in the helical coil is more efficient at the high-temperature region as well as higher flow rate applied.

Keywords: microwave; heat transfer; helical coil; heater

1. INTRODUCTION

Food drying is vital for preservation in order to extend the storage period and secure the food supply chain with minimum losses of food after harvest (Aktaş *et al.*, 2017). Hot air drying that involves convective heating and airflow can speed up the removal of moisture contents from food products. Generation of heat for the drying application could represent one of the most significant aspects. Conventional drying is usually performed via the hot air created from solar energy, electric heating or fuel combustion to remove the moisture from the food. These heat generation methods are time and energy consuming with high energy loss and causing a negative impact to the environment (Yahya *et al.*, 2016). Thus, alternative hot air generation, which is green and environmentally friendly, is required to perform an efficient drying process. Microwave heating is able to offer clean and green heat energy generation without producing hazardous gases.

The mechanism of the heat transfer can be explained in the following: activated carbon is used as a microwave absorbent material to convert microwaves into heat energy with a high and controllable heating rate. Hot activated carbon is used to heat the helical coil through conduction heat transfer. Hot air is generated when air is passed through the hot helical coil through convection heat transfer. The helical coil used as a heat exchanger has been used to accommodate a large heat transfer area in a small space with high heat transfer coefficients. The secondary flow is induced by the fluid that flows through curved tubes and improves the transfer of heat due to better fluid mixing (Misurati *et al.*, 2017). Centrifugal force induces the secondary flow in the circular cross structure of helical coils, which is normal to the primary flow direction. The level of centrifugal force in the flowing fluid is determined by the local axial velocity of the fluid particle and the radius of the coil curvature. The secondary flow field intensity increases as the flow rate increases (Pawar and Sunnapwar, 2014). This phenomenon is known as forced convection in which the heat exchanger transfers the heat through the pipe wall from one moving stream to another. The rate of heat transfer and the friction factor are significantly increased by the centrifugal force in the curved tube structure (Austen and Soliman, 1988).

The fluid particles flowing near the wall exhibit lower centrifugal force than those flowing in the core of the tube. Thus, the fluid of the core region is pushed to the outer wall. This stream bifurcates at the wall and causes secondary flows towards the inner wall along the tube's periphery, resulting in additional fluid transport across the pipe. This additional convective transport increases the heat transfer coefficient compared to a straight tube. Because of lower wall resistance and higher process side coefficient, the helical coil offers better heat transfer performance than common shell and tube type heat exchanger. The curved pipe's entire surface area is exposed to the moving fluid, where there is no issue with dead zones. In a relatively smaller volume of the reactor and occupied lower floor area, a helical coil also gives a larger surface area. Fouling problems are comparatively less in the helical coil due to more significant turbulence created inside the curved pipes (Zakrzewska-Trznadel *et al.*, 2009).

In this project, a microwave air heater (MAH) with helical coil was constructed using air as a test fluid to evaluate the heat transfer coefficient. The MAH comprised of the magnetron (microwave source), activated carbon (microwave absorbent) and the helical coil (heat exchanger) to produce hot air in a more economical way. The MAH had utilised radiation, conduction and convection heat transfer mechanisms to offer effective heating and hot air generation.

2. METHODOLOGY

2.1. Materials preparation

The activated carbon from oil palm shell was used as a microwave absorbent due to its high dielectric loss tangent ($\tan \delta$) between 0.1 and 0.8. Activated carbon was produced via microwave steam pyrolysis at a temperature of 700°C for 15 minutes and the characterisation of activated carbon was reported (Yek *et al.*, 2019). Activated carbon was further ground and sieved into 75-120 μm and stored in desiccator.

2.2. Microwave air heater design and setup

Figure shows the major parts of the microwave air heater (MAH): microwave generator, cavity, quartz reactor filled with activated carbon, air compressor, temperature logger and helical coil. An air-cooled magnetron operated at a frequency of 2.45 GHz, and 1000 W was used as a microwave generator in the MAH system. The magnetron transferred the microwave to the cavity through the waveguide. A metal square cavity (250mm L X 200mm H X 300mm W) was used to house the quartz reactor with helical coil and activated carbon. A quartz reactor of 130mm height and 100mm diameter with 3mm wall thickness was constructed to house the helical coil that was surrounded with activated carbon. Quartz reactor was chosen for its capability of high thermal application as well as its superiority in thermal stability and thermal shock resistance. An air compressor with 2.5hp was used to maintain the constant airflow rate.

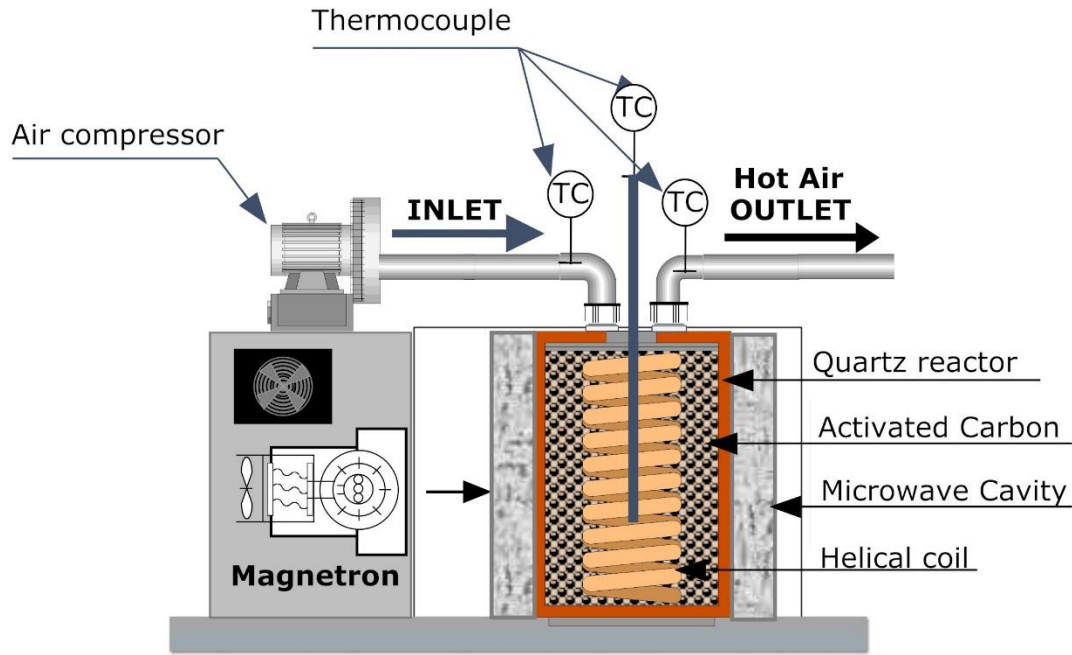


Figure 1: schematics diagram of microwave air heater

The temperature was measured using type-K thermocouples with stainless steel probe of scale up to 1200 °C. Three thermocouples were attached to measure temperatures of the test fluid and activated carbon at three different locations. These three thermocouples were inserted to depth holes that were designed to the size of the thermocouple probe. The first thermocouple, T_1 , was located at the airflow inlet to measure the inlet air temperature. The second thermocouple, T_2 , was inserted into activated carbon to measure the temperature of activated carbon and the third thermocouple, T_3 , was responsible to measure the outlet air temperature. A four channels thermometer with a data logger (OMEGA RDXL4SD) was used to record the temperatures with a sampling rate of 2 seconds. Temperature readings of activated carbon, inlet airflow and outlet airflow were recorded. Details of the helical coil is stated in Table 1.

Table 1: Specification of the helical coil

Parameters of helical coil	Detail
Materials	Stainless steel
Thermal conductivity	16.3 W/m.K
Height	130 mm
Outside diameter of inner tube (d_o)	7 mm
Inside diameter of inner tube (d_i)	5 mm
Wall thickness	1 mm
Outside diameter of outer tube (D_o)	60 mm
Radius of curvature of helical coil	30 mm
Pitch	8 mm
Number of Turns	10

2.3. Experimental design of hot air generation

The experimental design focused on a few key parameters such as airflow rate, the temperature of inlet air, the temperature of activated carbon and temperature of outlet air under non-isothermal conditions. Non-isothermal conditions referring to the temperature of activated carbon varied from 300°C to 100°C. The temperature profile of activated carbon was recorded up to 300°C to observe the heating rate of microwave heating and the heat loss to the environment. The microwave heating stopped when the activated carbon reached 300°C and cooled naturally to 100°C. The airflow rate was manipulated by a valve control throughout the experiment to obtain different flow rates. The air compressor was adjusted to obtain flow rates of 15, 20 and 25 L/min into the helical coil to produce hot air. The temperature of the outlet air was recorded with the data logger every second. With the data collected, the overall heat transfer efficiency and dimensionless numbers were calculated. From the calculations, the heat transfer behaviour of the MAH system was studied and the efficiency of convection heat transfer determined and analysed.

2.4. Reynolds number (*Re*)

The Reynolds number is the ratio of inertial forces to viscous forces and is a convenient parameter for predicting the flow condition, whether laminar, transitional or turbulent. The Reynolds number (*Re*) is defined in Equation 33:

$$\text{Equation 33: Reynolds number} \quad Re = \frac{\rho u d_i}{\mu}$$

Where:

- ρ is = density of air (kg/m³)
- u = velocity of air (m/s)
- d_i = inner diameter of the coil (m)
- μ = dynamic viscosity of air at inlet temperature (Ns/m²).

2.5. Nusselt number (*Nu*)

Equation 34 defines the Nusselt number of the coil which is the ratio of convective to conductive heat transfer in the helical coil:

$$\text{Equation 34: Nusselt number} \quad Nu = \frac{U_i d_i}{k}$$

Where:

- d_i = inner diameter of the coil
- k = thermal conductivity of air.

2.6. Dean number (*De*)

Dean number shown in Equation 35 characterizes the flow in a helical pipe as the ratio of viscous force to centrifugal force acting on a fluid flowing in a curved pipe. For the same flow, the Dean number will never be greater than the Reynolds number. The effects of centrifugal force dominates the flow as the Dean number approaches the number of Reynolds. When the Dean number is close to the Reynolds number, the secondary flow intensity increases.

$$\text{Equation 35: Dean number (De)} \quad De = Re \sqrt{\frac{d}{D}}$$

Where:

- Re = Reynolds number
- d = inner tube diameter
- D = diameter of the coil.

2.7. Calculation of overall heat transfer coefficient

Equation 36 shows the heat transfer of air through the helical coil, which is considered as internal forced convection.

$$\text{Equation 36: Convection heat transfer} \quad Q_m = C_p \rho V (t_{out} - t_{in})$$

Where:

- Q_m = heat transfer of the medium,
- c_p = specific heat
- ρ = density of air.

The calculation of overall heat transfer coefficient, U_o is according to Equation 37. The inside heat transfer coefficient, U_i is defined as:

Equation 37: Overall heat transfer coefficient
$$U_o = \frac{Q_m}{A\Delta T}$$

Where:

- A = inside surface area of a helical coil
- ΔT_o = average temperature differences between the average inlet and outlet temperatures and the temperature of activated carbon (Pawar and Sunnapwar, 2013).

3. RESULTS ANALYSIS

3.1. Temperature profile of activated carbon

Figure (a) shows the microwave heating profile of activated carbon (AC) from room temperature to 300°C and cooled naturally to 100°C in the cavity. Figure (b) shows the temperature difference between AC and outlet air at 15, 20 and 25 L/min. The average heating rate of the microwave was achieved at around 50°C/min and cooling rate of 10°C/min till 100°C. The AC is in graphitized carbon structure with better electric conductivity and working as a microwave absorbance materials to convert the electromagnetics wave into heat energy with higher efficiency (Zhou *et al.*, 2016). The indirect microwave radiation to the AC, in turn, caused a rapid increase in heating rate. Moreover, AC was cooled at a rate of 10°C/min, which is relatively low compared to another medium. The AC was working as an energy storage to preserve the heat within it and continuously heat up the helical coil. Following by the heat transfer from the helical coil to generate hot air to about 200 - 100°C. Microwave air heating can be claimed to be a green and highly efficient hot air generator as 5 minutes of microwave heating was able to produce hot air for another 20 minutes at a temperature range of 100-200°C.

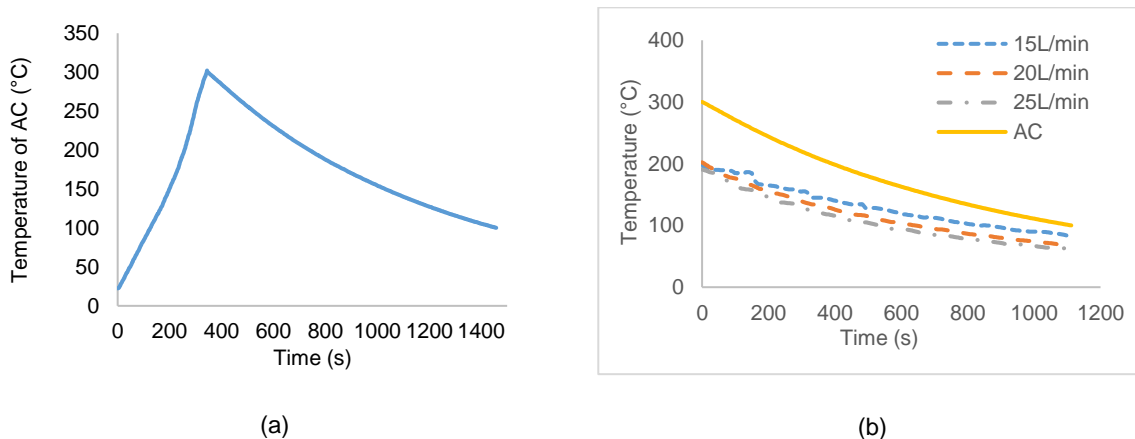


Figure 2: temperature profile of (a) activated carbon (b) outlet hot air

3.2. Overall heat transfer coefficient

Figure 3 shows the overall heat transfer coefficient of the helical coil conducted for air under a non-isothermal unsteady state. This shows that the convective heat transfer was more significant at a higher temperature and a higher flow rate. Increasing the inflow rate produced a higher Nusselt number (Table 2) which indicated that increasing the flow rate enhanced the convective heat transfer due to the increase in turbulence effect on the fluids in the system (Kumar *et al.*, 2006).

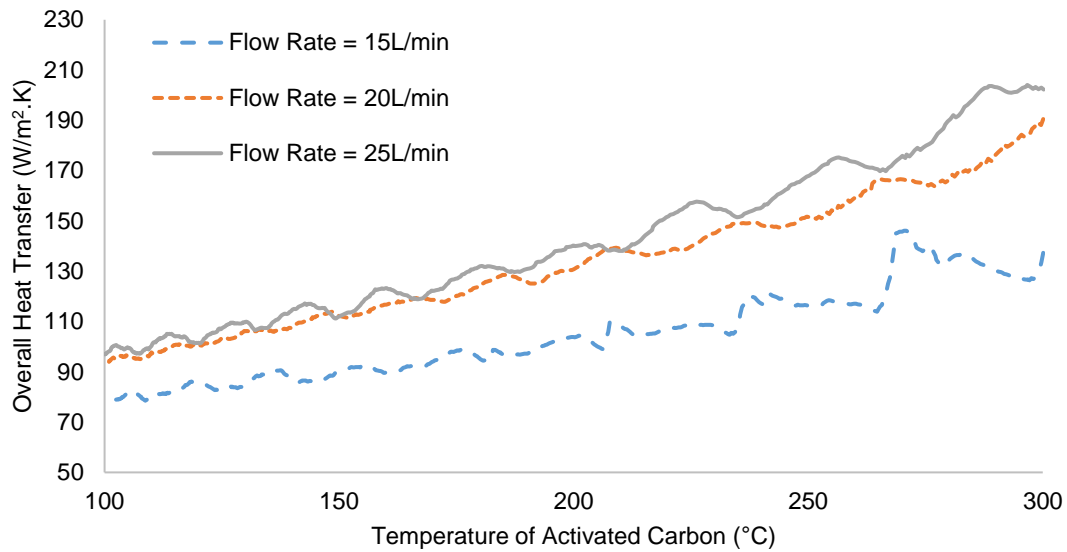


Figure 3: overall heat transfer coefficient of air in the helical coil

Table 2: relationship between heat transfer coefficient and Nusselt number

Temperature of Activated Carbon (°C)	Flow Rate (m³/s)	Heat Transfer Coefficient, (U_o)	Nusselt Number (Nu)
100	0.00025	76.9	10.1
	0.00033	92.9	13.9
	0.00042	96.9	16.5
	0.00025	103.7	13.5
200	0.00033	130.9	19.7
	0.00042	140.1	24.0
	0.00025	137.3	18.2
300	0.00033	190.5	29.1
	0.00042	202.3	35.0

3.3. Reynolds number and Dean number

Table 3 shows the Dean number increased with the Reynolds number. While the higher flow rate caused the increase of the Reynolds number and Dean Number to enhance the heat transfer coefficient. As the Dean number approached the Reynolds number, the significance of secondary flow or dean vortices inside the helical coil increased.

Table 3: Relationship between Reynolds number and Dean Number

Flow Rate (L/min)	Flow Rate (m³/s)	Reynolds Number (Re)	Dean Number (De)
15	0.00025	4256	1304
20	0.00033	5618	1739
25	0.00042	7150	2174

3.4. Uncertainty or error analysis

Probable uncertainties are taken into consideration when measuring different parameters such as inlet airflow rate and inlet and outlet temperature readings. There were four runs repeated for each flow rate to verify the repeatability of the experiments, which yielded better results. Also, the location of thermocouples in activated carbon and outlet air had to be measured precisely for each run to obtain the same temperature readings location for different flow rates. Any change in the location of thermocouples led to distinct temperature readings. The rebound of the microwave cannot be predicted or controlled, thus, the formation of hotspots can neither be controlled nor avoided. Hotspots caused an excessive heating throughout the experiments and led to inaccurate temperature readings especially when hotspots were formed near to thermocouples.

4. CONCLUSION

A highly efficient microwave air heater has utilised helical coil, activated carbon and microwave radiation to conduct a green heat transfer approach. Microwave was heat up the activated carbon to 300°C in 5 minutes and heat energy stored within it. When the temperature of activated carbon dropped from 300 to 100°C, the microwave air heater was able to produce hot air for 20 minutes continuously at a temperature range of 100-200°C. Airflow rates of 25 L/min achieved a higher overall heat transfer of 100-200 W/m².K compared to lower airflow rates of 15 and 20 L/min. Maximum overall heater transfer of 202.3 W/m².K was achieved at activated carbon of 300°C and airflow rate of 25 L/min. Nusselt number. Reynolds numbers and Dean numbers increased with higher flow rates.

5. ACKNOWLEDGEMENT

The authors thank the technical support provided by University College of Technology Sarawak and Universiti Malaysia Terengganu, The authors acknowledge the financial support by the University College of Technology Sarawak for the conduct the research under the University Grant Scheme: (Project No. UCTS/RESEARCH/4/2018/18>(01)).

6. REFERENCES

- Aktaş, M., Khanlari, A., Amini, A. and Şevik, S. 2017. Performance analysis of heat pump and infrared–heat pump drying of grated carrot using energy-exergy methodology. *Energy Conversion and Management*, **132**: 327-338.
- Austen, D. S. and Soliman, H. M. 1988. Laminar flow and heat transfer in helically coiled tubes with substantial pitch. *Experimental Thermal and Fluid Science*, **1**(2): 183-194.
- Kumar, V., Saini, S., Sharma, M. and Nigam, K. D. P. 2006. Pressure drop and heat transfer study in tube-in-tube helical heat exchanger. *Chemical Engineering Science*, **61**(13): 4403-4416.
- Misurati, K. A., Quan, Y., Gong, W., Xu, G. and Yan, Y. 2017. Contrastive study of flow and heat transfer characteristics in a helically coiled tube under uniform heating and one-side heating. *Applied Thermal Engineering*, **114**: 77-84.
- Pawar, S. S. and Sunnapwar, V. K. 2013. Experimental studies on heat transfer to Newtonian and non-Newtonian fluids in helical coils with laminar and turbulent flow. *Experimental Thermal and Fluid Science*, **44**: 792-804.
- Pawar, S. S. and Sunnapwar, V. K. 2014. Experimental and CFD investigation of convective heat transfer in helically coiled tube heat exchanger. *Chemical Engineering Research and Design*, **92**(11): 2294-2312.
- Yahya, M., Fudholi, A., Hafizh, H. and Sopian, K. 2016. Comparison of solar dryer and solar-assisted heat pump dryer for cassava. *Solar Energy*, **136**: 606-613.
- Yek, P. N. Y., Liew, R. K., Osman, M. S., Lee, C. L., Chuah, J. H., Park, Y. K. and Lam, S. S. 2019. Microwave steam activation, an innovative pyrolysis approach to convert waste palm shell into highly microporous activated carbon. *Journal of Environmental Management*, **236**: 245-253.
- Zakrzewska-Trznadel, G., Harasimowicz, M., Miśkiewicz, A., Jaworska, A., Dłuska, E. and Wroński, S. 2009. Reducing fouling and boundary-layer by application of helical flow in ultrafiltration module employed for radioactive wastes processing. *Desalination*, **240**(1–3): 108-116.
- Zhou, F., Cheng, J., Liu, J., Wang, Z., Zhou, J. and Cen, K. 2016. Activated carbon and graphite facilitate the upgrading of Indonesian lignite with microwave irradiation for slurryability improvement. *Fuel*, **170**: 39-48.

#341: 3-D simulation of submicron particle filtration on an elliptical fibrous surface

Ming DONG*, Yan SHANG, Sufen LI

¹ Dalian University of Technology, Dalian 116024, China, dongming@dlut.edu.cn.
*Corresponding author

In this paper, the technology of the computational fluid dynamics coupling discrete element method, enhanced with in-house subroutines was applied to study the deposition behaviour of micro-particles. We use a particle interaction model to simulate the particle deposition behaviour on the surface of the elliptical fibre. The model well predicts the formation of the dendrites and the dynamic progression of the deposition. The deposition structure and the collection efficiency with different angles of orientation relative to the incoming flow, particle diameters, inlet fluid velocity and fibre diameters were explored. For the smaller-size particles which are mainly dominated by the diffusion, the different angles of orientation relative to the incoming flow increases have little influence. It is more obvious on larger particle diameter. There is the higher collection efficiency for relative smaller fluid velocity and bigger particle diameter. The normalized pressure drop and the velocity gradient on both sides of the fibre increase as SVF increases. The collection efficiency increases gradually as SVF increases.

Keywords: Single elliptical fibre; Filtration performance; Collection efficiency; CFD simulation

1. INTRODUCTION

Fibrous filters successfully reduce emissions of airborne particles in indoor environments. They are used in air-conditioning, ventilation and air purifiers to reduce airborne particle levels in the indoor environment, and in respirators to protect humans from airborne particle pollution (Beth, 2009). Fibrous filters are also used in chemical engineering processes and coal-fired industries to remove aerosol particles from carrier gases or flue gas. In most applications, the role of fibrous filter is carried out by the collision or near-contact relative motion between an incoming particle and the filter fibre wall, or with deposited particles on the fibre.

With the fast development of materials technology, fibrous filters composed of noncircular fibres have been used in practical applications to meet different requirements.

Extensive works on fibrous filtration composed of the traditional cylindrical fibres has been carried out. Kasper *et al.* (2009) studied the deposition of monodisperse polystyrene particles on thin metal wires by the way of experimental research. The collection efficiency of single fibres at different packing densities and fibre spacings under the inertia-interception regime was investigated and compared. Hosseini and Tafreshi (2010) used Fluent CFD with customized C++ subroutine to study aerosol filtration in disordered 2-D fibrous media, comparing with the existing 2-D semi-analytical model and previous simulation data obtained from 3-D simulations. Rafał Przekop *et al.* (2003), Lantermann *et al.* (2007) and Wang *et al.* used the Lattice-Boltzmann method to describe the dynamics transport and deposition process of small particles during the flow of aerosol particles through fibrous filters. In addition, the discrete-element method (DEM) which was developed by Cundall and Strack (2008), could be used to model particle systems, such as micro fluidics, particle filtration and blood flow problems. Li and Marshall (2007), Cai *et al.* (2016) and Yue *et al.* (2017) used the DEM approach to investigate the interactions between particles, fibres and fluid to simulate the particle deposition process on fibres. Additionally, the filtering efficiency and pressure drop of the filtration process were obtained.

It should be noted that the mentioned studies mainly focus on the cylindrical fibres. However, more and more non-circular fibres, like the elliptical, trilobal and square or rectangular form, are widely used, which have been proved to perform better than the traditional circular fibres (Zhu, 2000; Wang, J. 2009; Huang; Jin, 2017; Haokai, 2017). Among these non-circular candidates, the elliptical fibre is more streamlined, which may result in a lower drag force. Besides, the specific area per unit volume of elliptical fibre is bigger than the circular one, thus the elliptical fibre performs well for the submicron particles. Although the elliptical fibres have some potential advantages, the related investigations are relatively limited. Besides the models reviewed above, fibres with elliptical cross sections have recently drawn attention of many researchers due to their high surface area per unit volume and low drag force. Raynor (2002a) developed the equations to predict the drag and velocity field around an elliptical fibre by developing analytical expressions. Raynor (2002b) predicted the diffusion efficiency for a single elliptical fibre by using an empirical equation and studied the effect of fibre aspect ratio, filter solidity and fibre orientation. Later, Raynor's research team (Regan, 2009) developed the expressions for predicting single fibre efficiency by the interception mechanism by using a velocity field for flow around an elliptical fibre. Starting with the Zhukovsky conversion, Wang *et al.* further presented an exact solution for the interception efficiency of a particle onto elliptical fibres. The influence of fibre geometric properties such as size, aspect ratio, the orientation angle of the incoming flow, and the particle diameter were considered. Wang *et al.* used the LB-CA model to simulate the filtration process of elliptical fibres and calculated the pressure drop of the system with different fibre orientation angles and aspect ratios and capture efficiency due to various capture mechanisms, then compared them with these of the circular fibres. Huang *et al.* used a lattice Boltzmann-cellular automata model to research the growing process of particle dendrites on elliptical fibres.

In our recent work (Dong *et al.*, 2019), the dynamic collision model of particles is established to simulate the deposition process of the micro-particles on a single cylindrical fibre. The particle interaction model is originally proposed by Brach and Dunn (1995), and extended to more complicated situations. This model (BD model) was extended to include the effects of adhesion on the interaction between particles, and the interaction between particle and fibre surface, and can be incorporated readily into a CFD software package. We predicted the filtration performance of sub-micron particles (0.5 μm -1 μm). The reason is that the intermediate particles (between 0.5 μm -1 μm) are captured by fibres due to the two important filtration mechanisms, Brownian diffusion and interception impaction. The effects of inlet flow velocity, particle diameter as well as fibre diameter on the deposition morphology and the collection efficiency were investigated comprehensively.

Compared with the traditional cylindrical fibres, the noncircular fibres have the advantage of larger specific surface area. Thus the noncircular fibres are likely to enhance particle loading capacity and capture efficiency. Considering the outstanding performance of elliptical fibres on the effective removal of fine and intermediate particles, our current idea is to utilize the particle interaction model to investigate the non-steady-state filtration processes of elliptical fibres. Section 2 gives a summary of the numerical methods of fluid flow, particle motion, and both particle collision. The physical model, mathematical model as well as the numerical approach are described in Section 3. The effect of the particle diameter, the flow velocity, fibre properties such as the orientation of the cross-section to the incoming flow, filter solidity is presented in Section 4. Finally, Section 5 summarizes the conclusions. This

document explains how to prepare a full manuscript submission for SET 2019. We request that all authors follow this template in order to be included in the conference proceedings. These instructions apply for all papers.

2. NUMERICAL METHODS

2.1. Flow field calculations

The fluid flow through the calculation domain is assumed to be laminar as the Reynolds number is very small ($0.144 < Re < 1.441$), defined based on the elliptical fibre diameter D_f (the diameter of circular fibre with the same volume fraction). $D_f = \sqrt{ab}$, where a and b are the major axis length and minor axis length. The finite volume method implemented in the Fluent is used to solve the continuity and momentum equations. Second order upwind schemes the values of pressure and velocity at the boundary of each discrete volume. These methods are state of the common and require no further discussion here.

2.2. Particle motion equations

The particle trajectory is modelled by using the discrete phase model (DPM) in FLUENT, based on a Lagrangian approach. Under the influence of fluid flow, particles were mainly subjected to drag force and Brownian force. Therefore, the particle motion equation can be written as

$$\text{Equation 1:} \quad \frac{du_p}{dt} = F_D(u - u_p) + \zeta_i \sqrt{\frac{\pi S_0}{\Delta t}}$$

Where:

- u = the fluid velocity at the particle location (m/s)
- u_p = the particle velocity (m/s)

$$\text{Equation 2:} \quad F_D = \frac{18\mu}{\rho_p d_p^2 C_c}$$

Where

- μ = the fluid viscosity (Pa•s)
- d_p = the particle diameter (μm)
- ρ_p = the particle density (kg/m^3)
- C_c = the Cunningham slip correction factor, $C_c = 1 + K_n [1.257 + 0.4 \exp(-\frac{1.1}{K_n})]$
- K_n = the Knudsen number ($K_n = 2\lambda/d_p$)
- λ = the molecular mean free path.

The second term on the right-hand side of Equation 1 represents the Brownian force. Where ζ_i is a Gaussian random number chosen from a normal distribution with a zero mean and a unit variance S_0 is the corresponding

spectral intensity of the noise given by Li and Ahmadi (1992)

$$S_0 = \frac{216\nu k_B T}{\pi^2 \rho d_p^5 \left(\frac{\rho_p}{\rho_f}\right)^2 C_c}$$

Where

- ρ_f = the fluid density (kg/m^3)
- ν = the fluid Kinematic viscosity (Pa•s)
- k_B = the Boltzmann constant

Dimensionless parameters are used here in for simplification of the particle-laden flow analysis. The Peclet number, which defines the contribution of convective and diffusional effects on deposition. ($Pe = \frac{3\pi\mu d_p u D_f}{k_B T C_c}$)

The Stokes number (St), which measures the interplay between the travel of particles and fluid flow, is defined

as: Equation 3:
$$St = \frac{\rho_p d_p^2 u C_c}{18\mu D_f}$$

2.3. Particle collision equations

The particle normal collision equation was proposed by Brach and Dunn (1995) (BD model) as

$$\text{Equation 4: } m \frac{\partial^2 \delta}{\partial t^2} = -F_H \left(1 + C_H \frac{d\delta}{dt} \right) - F_A \left(1 + C_A \frac{d\delta}{dt} \right)$$

Where

- F_H and F_A = the Hertzian and adhesion forces(N)
- C_H and C_A = the damping coefficients of F_H and F_A
- δ = the amount of overlap between two particles
- t = the period of contact(s)
- m = the particle mass(kg)

In the BD model, F_H is the classical Hertzian restoring force, which can be given

$$\text{Equation 5: } F_H = K \sqrt{r} \delta^{3/2}$$

Where $K = \frac{4}{3\pi(k_1 + k_2)}$, $k_i = \frac{1 - \nu_i^2}{\pi E_i}$

- r = the particle radius (μm)
- ν_i = the Poisson's ratio
- E_i = Young's modulus

The adhesion force can be expressed as

$$\text{Equation 6: } F_A = -2\pi a f_o$$

Where

- a = the contact radius (μm), $a^2 = \delta r$
- f_o = the circumferential tension of the adhesion force per unit length, $f_o = (9W_A r K / 2\pi)^{1/3}$.
- W_A = the combined surface energy between the particle and surface material (the energy required to separate the materials)

This energy can be obtained through Dupre's equation, $w_A = 2\sqrt{\gamma_1 \gamma_2}$, Where 1 and 2 are the surface-free energies of bodies 1 and 2. The specific surface energy equation is $\gamma = E / y_o (a_o / \pi)^2$,

Where

- y_o = the normal separation distance between two internal surfaces of a crystal (μm);
- a_o = the range of the attractive forces, which was given by Gilman (1960).

Thus, Equation 5 can be rearranged to express the normal motion equation of particles in the BD model as

$$\text{Equation 7: } m \frac{\partial^2 \delta}{\partial t^2} = -K \sqrt{r} \delta^{3/2} \left(1 + C_H \frac{d\delta}{dt} \right) + 2\pi a f_o \left(1 + C_A \frac{d\delta}{dt} \right).$$

The values of C_H and C_A are obtained with Young's modulus of the surface by Kim and Dunn (2007). When C_H and C_A are obtained, the BD model can be numerically solved when discretizing it in a dimensionless motion using Equation 11.

The above derivation provides a dimensionless motion equation of the BD model, which is needed to use numerical methods (such as the Runge-Kutta method) for a discretized solution; however, the number of calculations is very large when using a numerical method. In this regard, Kim and Dunn (2007) derives the BD model further to simplify the calculations. Thus, an explicit expression for calculating the particle restitution coefficient is as follows:

$$\text{Equation 8: } e = \sqrt{1 - (e_A + e_H)} = \sqrt{1 - \Psi_A (1 + C_A v_n) - \Psi_H C_H}$$

Where $\Psi_A = \frac{W_A}{m v_n^2 / 2} = 2C_R f_o \left(\frac{4}{3\pi} \right) \left(\frac{5}{4K} \right)^{3/5} \left(\frac{r}{m^2} \right)^{1/5} v_n^{-4/5}$, $\Psi_H C_H = \frac{\delta F_{HD}}{m v_n^2 / 2} = 2 \frac{a_m^5}{m r^2} K (2/3)^{5/2} \left(\frac{C_H}{v_n} \right) = e_H$

,and $e_A = (\delta F_{AD} + W_A) / (m v_n^2 / 2)$

- V_N = the normal velocity (m/s)
- F_{HD} = the dissipative Hertzian force (N)
- F_{AD} = the dissipative adhesion force (N)
- a_m = the maximum contact radius (μm)

C_R = the surface roughness influencing factor, which is used to balance the energy loss owing to the surface roughness, which is related to the surface roughness of the material.

3. NUMERICAL PROCEDURE

3.1. Specifications

Figure 1 presents the simulation domain and boundary conditions. The dimension is $100\mu\text{m}$, long, $60\mu\text{m}$ wide and $30\mu\text{m}$ high, respectively. The fluid enters the computational domain with a constant velocity and leaves with pressure outlet boundary condition. Particle are injected randomly from the projected image of the fibre on the inlet boundary. The symmetry boundary condition is assumed for the lateral sides of the domain. The stationary wall boundary condition is considered on the fibre's surface. For the surface of the fibre, a user-defined function (the DEFINE_DPM_BC command) representing the interaction model between particle and surface is run in the Fluent environment.

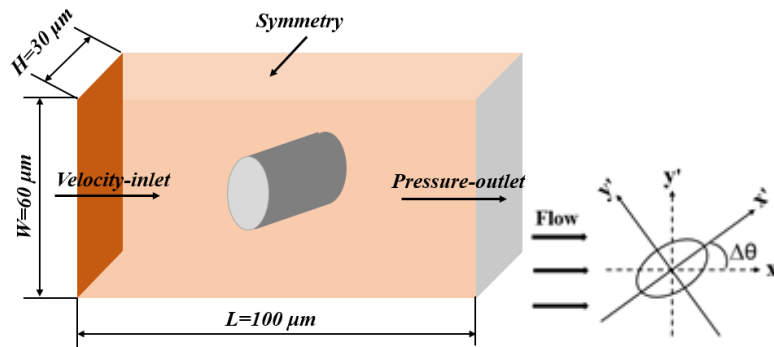


Figure 1: Schematic of fluid flow domain

In this work, the materials of particle and fibre are set as ammonium fluorescein and silicon, respectively. Kim and Dunn relate the C_H and C_A values to Young's modulus values of the surface by using microsphere-surface impact models validation experiments. The values of C_H and C_A approach zero under the given material of particle and fibre based on a microsphere-surface impact model. The parameters used for the various simulations are given in Table 1. The other significant parameters are shown in Table 2.

Table 22: The model parameters of simulation

d_p (μm)	a (μm)	b (μm)	v_{in} (m/s)	SVF(%)	Pe	St
0.5					15056	0.026
0.6					18962	0.038
0.7					22508	0.051
0.8					26795	0.067
1.0	24	16	0.5	5.0	34727	0.105
			0.1		5359	0.013
			0.3		16077	0.040
0.8	24	16	0.5	5.0	26795	0.067
			0.8		42872	0.107
	18	12		2.8	20096	0.089
	24	16		5.0	26795	0.067
0.8	30	20	0.5	8.2	33494	0.054

Table 2: The other significant parameters of simulation

Viscosity of fluid	Density of fluid	Density of particle	Density of fibre	Poisson ratios of particle	Young's modulus of particle	Poisson ratios of fibre	Young's modulus of fibre
/ pa*s	/ kg*m-3	/ kg*m-3	/ kg*m-3		/ GPa		/ GPa
1.79x10-5	1.29	1350	2330	0.33	1.2	0.28	166

3.2. Modelling of particle captured and deposited on fibres

The calculations of particle trajectory have been conducted by integrating the force balance on the particle (Lagrangian method). We have considered both fluid drag and Brownian force in our simulations. Brownian force is programmed in the form of a UDF for the Fluent code. At the beginning of each time step, the DPM model in Fluent will generate a particle in each computational cell of the inlet boundary by loop function. With the increase of the time step, a large number of particles remain in the computational domain, which will increase the calculation load. To improve this, the initial conditions of the particle injection was recompiled by DEFINE_DPM_INJECTION_INIT command. In our simulations, a random computational cell is selected within the projected image of the fibre on the inlet boundary, which has been selected by using random function, and then the particle is injected from this cell under this time step. Meanwhile, the production of other particles is terminated in the other computational cell by loop function.

During the non-steady-state filtration process, the particles can deposit or rebound on the surface of the fibre (or the deposited particles). For detecting a particle deposited on the fibre (or the deposited particles), the particle collision model is programmed in the DEFINE_DPM_BC and DEFINE_DPM_SCALAR_UPDATE command. This model can be used to calculate the coefficient of restitution after the particle collision. If the coefficient of restitution is zero, the particle can deposit on the surface of the fibre (or the deposited particles), flow fields will be recalculated, and if it is larger than zero, the particle can rebound from the surface of the fibre (or the deposited particles). To simulate particle dendrite formation, the document has to save the coordinates of deposited particles. The document is the memories that can be accessed via a UDF program in the solution code. If the coordinate value is one, the particle is deposited, and the computational cell is occupied, and if it is zero, fluid can flow through the cell. This procedure is shown in the flowchart, which is given in Figure 2.

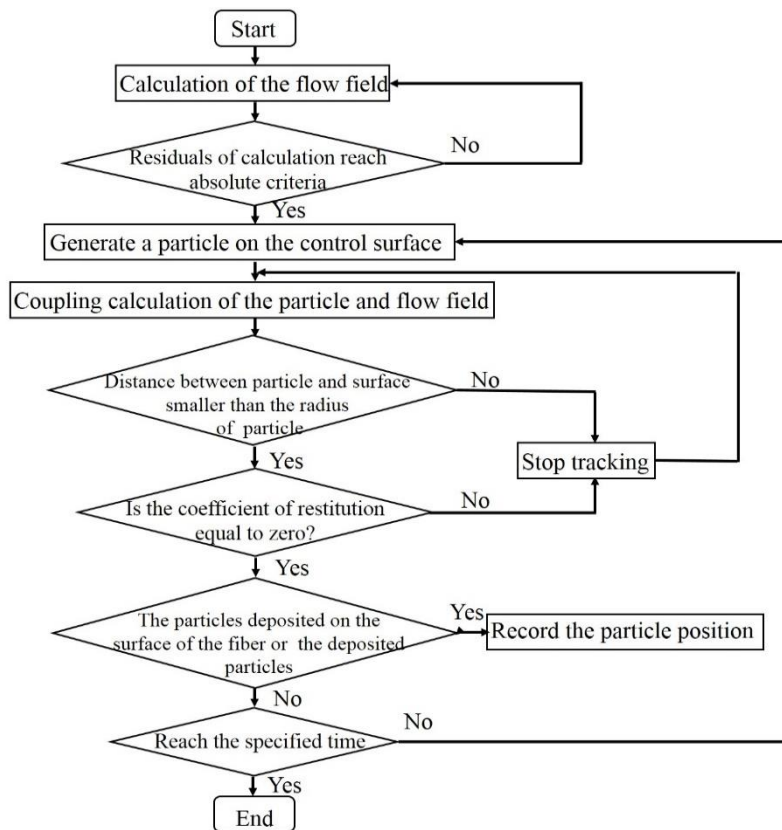


Figure 2: Flowchart of the whole simulation.

The variation of pressure drop through the fibrous medium with the different grid numbers during loading is shown in Figure 3. To study the effect of mesh density, we consider an elliptical fibre with an equivalent diameter of 20 μm , and mesh it with four mesh densities, resulting in 72, 85, 103 and 124 mesh nodes around the fibre. The inlet velocity is 0.5 m/s, and particles with a diameter of 0.8 μm are injected into the domain. Pressure drop caused by the fibre before and after particle deposition is monitored and plotted in Figure 3. It shows that with the increase of the mesh density, pressure drop tends to reach a plateau, indicating that the result is independent of mesh density. Therefore, 85 mesh nodes around the elliptical fibre is adopted for numerical simulation. For other fibre diameters in our simulation, the number of mesh nodes can be chosen proportionally according to above method.

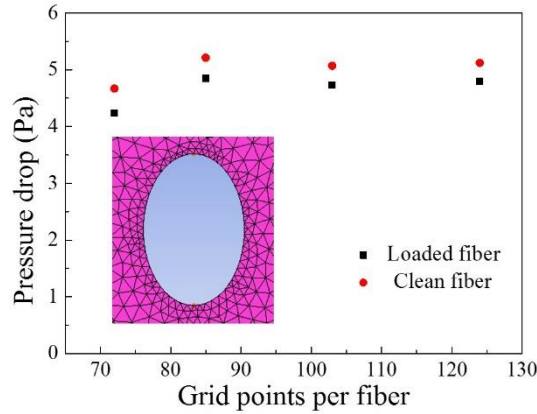


Figure 3: The effect of mesh density on the pressure drop before and after loading with particles having a diameter of 0.8 μm .

4. RESULTS AND DISCUSSION

4.1. Effect of the angle of orientation relative to the incoming flow

Figure 4 and Figure 5 show the effect of the angle of orientation relative to the incoming flow ($\Delta\theta$) on the particle dendrites structure with the time under the different particle diameters. When the particle diameter changes from 0.5 to 0.8 μm , the Peclet number Pe increases from 15056 to 26795 accordingly, the deposition pattern changes from uniform distribution to branched dendrites as shown in the following figures. Because of the instability of the flow field, we do not inject particles into the flow field at the beginning of the simulation. Particles are injected from the entrance at about $T=0.8\text{s}$. Figure 4 shows that the particles are deposited around the fibre uniformly with different $\Delta\theta$. There are more particles distributed on the leeward surface and the sides of the fibre for $Pe=15056$. We can see that the angle of orientation relative to the incoming flow has little influence on the smaller particles. However, there are more particles are deposited on the windward surface and the particle dendrites grow up more obviously in Figure 5 for $Pe=26795$. Meanwhile, the particles may be captured more easily as $\Delta\theta$ increases. This is because inertial impaction is the dominant capture mechanism, the particles do not follow their streamlines and tend to deposit on the front side of fibre instead. Also, the particle dendrites grow up gradually on the sides of fibre, which can affect the pressure drop because the fibre's cross-sectional area normal to the flow direction increases rapidly.

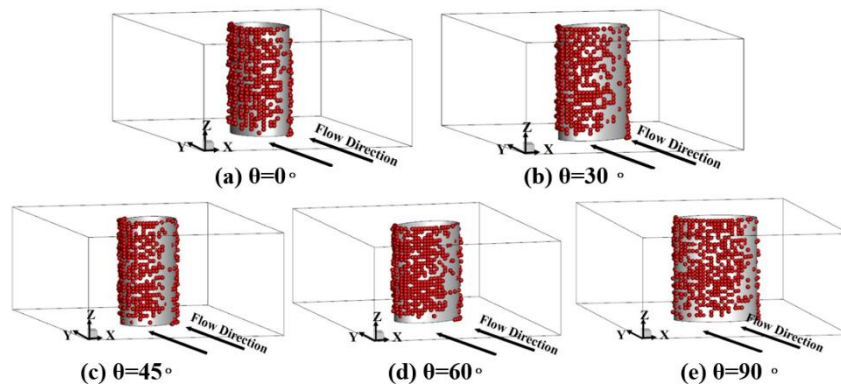


Figure 4: The dendrites structure of the deposited particles for $\Delta\theta$ equal to (a) 0° , (b) 30° , (c) 45° , (d) 60° and (e) 90° . In all cases, $d_p=0.5\mu\text{m}$, $v_{in}=0.5\text{m/s}$ and $a=24\mu\text{m}$, $b=16\mu\text{m}$.

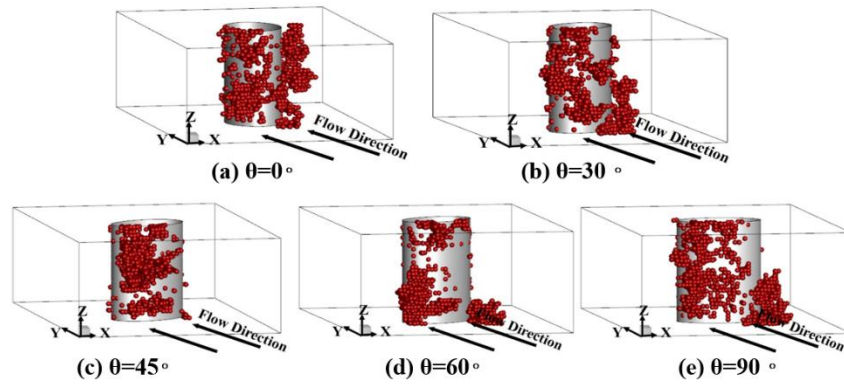


Figure 5: The dendrites structure of the deposited particles for $\Delta\theta$ equal to (a) 0° , (b) 30° , (c) 45° , (d) 60° and (e) 90° . In all cases, $d_p = 0.8\mu\text{m}$, $v_{in} = 0.5\text{m/s}$ and $a = 24\mu\text{m}$, $b = 16\mu\text{m}$.

4.2. Effect of particle diameter

Figure 6 shows the effect of particle diameter on the dendrites structure loaded on the single elliptical fibre. Similarly, particles are injected from the entrance after the flow field is stable ($T > 0.8\text{s}$). In all cases, we set $v_{in} = 0.5\text{m/s}$, $\Delta\theta = 90^\circ$ and $a = 24\mu\text{m}$, $b = 16\mu\text{m}$. It is clearly shown that the deposition dendrites change obviously on the surface of the elliptical fibre when the particle diameter increases from 0.5 to $1.0\mu\text{m}$. When the particle diameters are relatively small ($d_p = 0.5\mu\text{m}, 0.6\mu\text{m}$), the corresponding Peclet number is smaller ($Pe = 15056, 18962$), the particles are mainly captured by the fibres and uniformly deposited on the surface of a fibre under the influence of Brownian diffusion. As particle diameter increases ($d_p = 0.7\mu\text{m}, 0.8\mu\text{m}, 1.0\mu\text{m}$), the corresponding Stokes number is bigger ($St = 0.051 - 0.105$), the particles are primarily deposited on the windward side of the fibre, and the deposited particles grow up to branched dendrites under the influence of inertia. Also, there is a small number of particles in the local region of the side of the fibre.

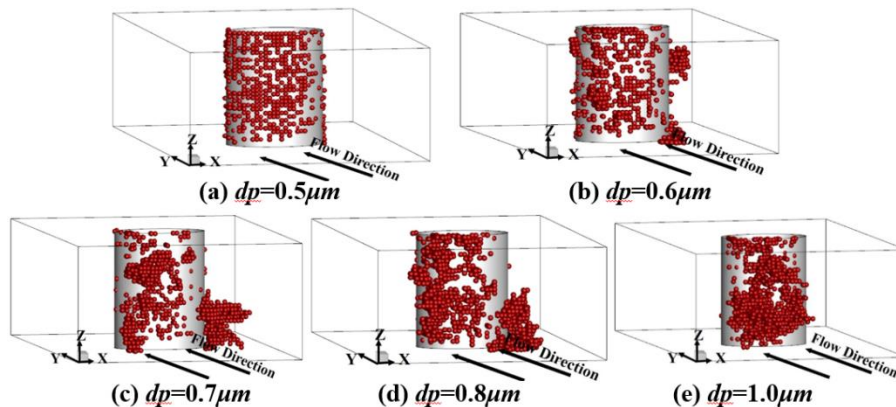


Figure 6: The dendrites structure of the deposited particles for different particle diameters. In all cases, $v_{in} = 0.5\text{m/s}$, $\Delta\theta = 90^\circ$ and $a = 24\mu\text{m}$, $b = 16\mu\text{m}$.

Figure 7 shows the effect of particle diameter on the collection efficiency of the elliptical fibre for different particle diameters with the time. It is evident that, the collection efficiency gradually increases as particle diameter increases from 0.5 to $1.0\mu\text{m}$. It can be explained that the deposited particles on the surface of the fibre relatively uniformly when the particle diameter is relatively smaller ($d_p = 0.5\mu\text{m}, 0.6\mu\text{m}$). When the particle diameter increases to $0.7\mu\text{m}$, $0.8\mu\text{m}$ and $1.0\mu\text{m}$, the particles tend to be deposited on the windward of the fibre, and the deposited particles are practically captured by the dendrites. Thus in turn leads an increasing in collection efficiency of fibre capture due to interception and impaction mechanism effect.

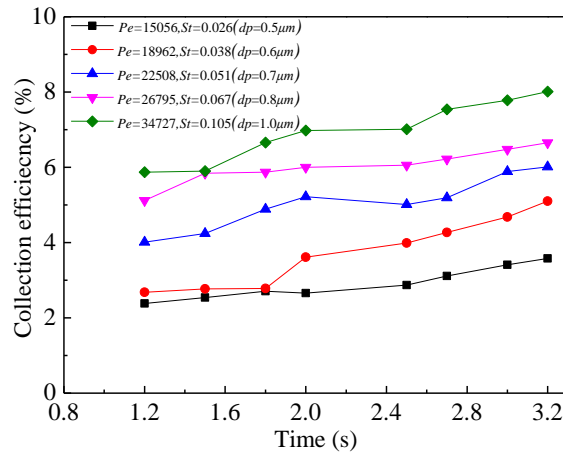


Figure 7: Dynamic changes of collection efficiency under different particle diameters.

4.3. Effect of the inlet fluid velocity

In this section, we examine the effect of inlet fluid velocity on the particle capture for the elliptical fibre. In all cases, $d_p=0.8\mu\text{m}$, $\Delta\theta=90^\circ$ and $a=24\mu\text{m}$, $b=16\mu\text{m}$. When the inlet fluid velocity increases from 0.1 to 0.8 m/s, the Peclet number Pe increases from 5359 to 42872, the Stokes number St increases from 0.013 to 0.107 accordingly. The deposition pattern changes from uniform distribution to branched dendrites as shown in Figure 8. At the beginning of the simulation, we do not inject particles into the flow field due to the instability of the flow field. Particles are injected from the entrance at about $T=0.8\text{s}$. When the inlet fluid velocity is relatively smaller, the particles are deposited around the fibre uniformly, there are more particles distributed on the sides of the fibre. With the increase of inlet fluid velocity, there are fewer particles distributed on the leeward surface, and more particles are deposited on the windward surface; meanwhile, the particle dendrites grow up more obviously. Because of the increase of the corresponding Stokes number, inertial impaction is becoming the dominant capture mechanism. Thus the particles don't follow their streamlines and tend to deposit on the front side of fibre instead. Also, the particle dendrites grow up gradually on the sides of fibre, which can affect the pressure drop because the fibre's cross-sectional area normal to the flow direction increases rapidly.

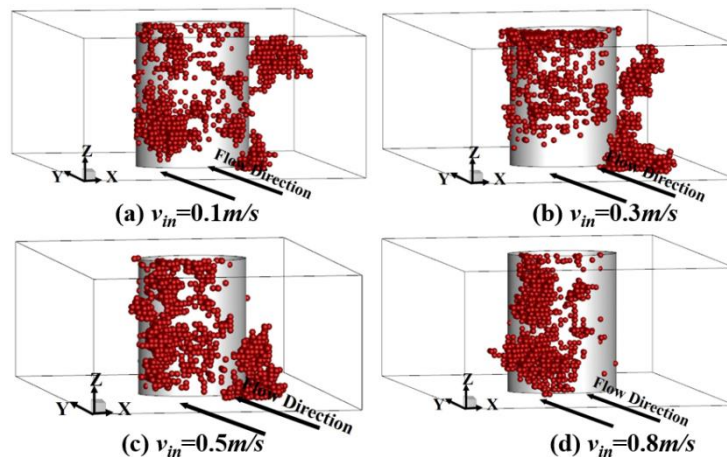


Figure 8: The dendrites structure of the deposited particles for different particle diameters. In all cases, $d_p=0.8\mu\text{m}$, $\Delta\theta=90^\circ$ and $a=24\mu\text{m}$, $b=16\mu\text{m}$.

The effect of inlet fluid velocity (v_{in}) on the collection efficiency with the increasing simulated time is shown in Figure 9, in which v_{in} is set to 0.1m/s, 0.3m/s, 0.5m/s and 0.8m/s while d_p is held 0.8 μm . It is shown that the collection efficiency gradually decreases with increasing inlet fluid velocity. As we all know, diffusion mechanism is dominant for the sub-micron particle, which is more evident under smaller Peclet number. However, the diffusion mechanism has gradually weakened when the inlet fluid velocity increases from 0.1 to 0.8 m/s. In this case, the Stokes number increases from 0.013 to 0.107 accordingly. It implies that the particle deposition mechanism has gradually transformed from diffusion mechanism to interception and inertial impaction mechanism.

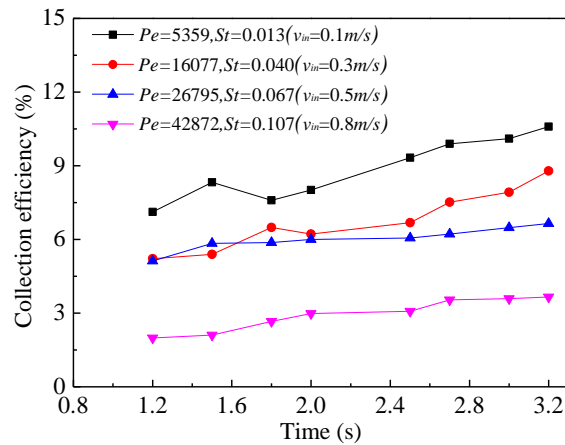


Figure 9: Dynamic changes of collection efficiency under different inlet fluid velocities.

4.4. Effect of fibre diameter(SVF)

Figure 10 shows the effect of fibre diameter on the particle dendrites structure of the elliptical fibre. The corresponding solid volume fractions (SVF) are 8.2%, 5% and 2.8% for the equivalent diameters of the elliptical fibre $D_f=25, 20$ and $15\mu\text{m}$, respectively. The Stokes number increases from 0.086 to 0.143 accordingly. Particles are injected from the entrance after the flow field is stable ($T>0.8\text{s}$) likewise. It can be seen that the deposited particles are concentrated on the windward side for $\text{SVF}=2.8\%$ more obviously, which allows the air to flow through more easily. The number of deposited particles grow up on the sides of fibre gradually with increasing SVF. Also, the deposited particles are distributed on the fibre surface for larger SVF, so the fibre's cross-section is increased.

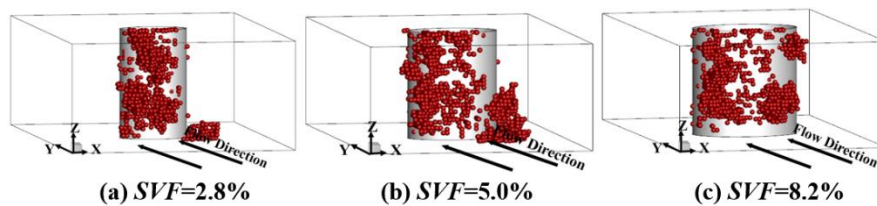


Figure 10: The dendrites structure of the deposited particles for different particle diameters. In all cases, $d_p=0.8\mu\text{m}$, $\Delta\theta=90^\circ$ and $v_{in}=0.5\text{m/s}$.

Here, we also explore the effect of the fibre diameter on the collection efficiency. The simulations are conducted with three equivalent diameters of elliptical fibre, $15, 20$ and $25\mu\text{m}$, respectively. As shown in Figure 11, the collection efficiency increases with increasing fibre diameter. Furthermore, with the increase of the simulated time, there was a rising trend of collection efficiency in these conditions. The collection efficiency of the fibre increases gradually as fibre diameter further increases. The larger SVF leads to an increased effective collision area and enhances the capture performance for micron particles at this point. Moreover, the pressure drop at the SVF of 8.2% is conspicuously higher than that at the SVF of 5% and the SVF of 2.8%.

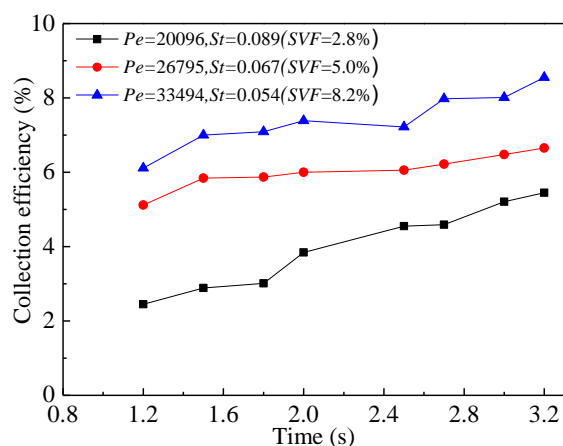


Figure 11: Dynamic changes of collection efficiency under different fibre diameters.

5. CONCLUSIONS

In this paper, we present a case study of simulating the deposition process of the micro-particles on the surface of the elliptical fibre. The ultimate goal of this study is to investigate the dynamic evolution processes of particle dendrites and collection efficiency with the increase of deposited particles. The main conclusions are drawn as follows :

- For the elliptical fibre, the different angles of orientation relative to the incoming flow increases have little influence on the smaller particle diameter ($d_p=0.5\mu\text{m}$) due to the dominant diffusion mechanism. It is more obvious on larger particle diameter ($d_p=0.8\mu\text{m}$).
- As inlet fluid velocity increases from 0.1 to 0.8 m/s, the deposition pattern changes from uniform distribution to branched dendrites. Because of the Peclet number and Stokes number are increasing, the particle deposition mechanism has gradually transformed from diffusion mechanism to impaction mechanism. The collection efficiency gradually decreases with increasing inlet fluid velocity, with the minimum collection efficiency occurring at $v_{in}=0.8\text{m/s}$.
- As particle diameter increases from 0.5 to $1.0\mu\text{m}$, the deposition dendrites significantly change due to different particle capture mechanisms. The collection efficiency increases with increasing particle diameter for the simulated time, with the maximum collection efficiency occurring at $d_p=1.0\mu\text{m}$.
- As the SVF increases from 2.8% to 8.2%, the collection efficiency and the normalized pressure drop increase gradually with the increasing SVF for the simulated time. The solid volume fraction has a significant impact on the particle deposition and dendrites.

6. REFERENCES

- Brach, R. M., & Dunn, P. F. (1995). Macrodynamics of Microparticles. *Aerosol Science and Technology*, 23(1), 51-71.
- Biryukov, D. G., & Kadomtsev, I. G. (2002). Dynamic Elastoplastic Interaction between an Impactor and a Spherical Shell. *Journal of Applied Mechanics and Technical Physics*, 43(5), 777-781.
- Cheng, W., Brach, R. M., & Dunn, P. F. (2002). Three-Dimensional Modeling of Microsphere Contact/Impact with Smooth, Flat Surfaces. *Aerosol Science and Technology*, 36(11), 1045-1060.
- Cundall, P. A. . (2008). A discrete numerical model for granular assemblies. *Geotechnique*, 29(30), 331-336.
- Cai, R. R., & Zhang, L. Z. (2016). Modeling of dynamic deposition and filtration processes of airborne particles by a single fiber with a coupled lattice boltzmann and discrete element method. *Building and Environment*, 106, 274-285.
- Dong M, Li J Y, Shang Y, Li S F.(2019).Numerical investigation on deposition process of submicron particles in collision with a single cylindrical fiber. *Journal of Aerosol Science*,129,1-15.

- Gilman, J. J. (1960). Direct Measurements of the Surface Energies of Crystals. *Journal of Applied Physics* , 31(12), 2208-2218.
- Hosseini S A , Tafreshi H V. (2010). Modeling particle filtration in disordered 2-D domains: A comparison with cell models[J]. *Separation and Purification Technology*, 74(2):160-169.
- Huang, H. ,Wang, K. , & Zhao, H. . (2016). Numerical study of pressure drop and diffusional collection efficiency of several typical noncircular fibers in filtration. *Powder Technology*, 292, 232-241.
- Haokai, H. , & Haibo, Z. . (2017). Numerical study of pressure drop and diffusional collection efficiency of rectangular fibers in filtration. *Journal of University of Chinese Academy of Sciences*.
- Huang, H., Zheng, C., & Zhao, H. (2017). Numerical investigation on non-steady-state filtration of elliptical fibers for submicron particles in the "greenfield gap" range. *Journal of Aerosol Science*, 114,263-275.
- Masliyah, J.H. (1975). Aerosol removal by diffusion and interception in mats of elliptic fibres, *Can. J. Chem. Eng.* 53 568–571.
- Jin, X., Yang, L., Du, X., & Yang, Y. (2017). Modelling filtration performance of elliptical fibers with random distributions. *Advanced Powder Technology*, 28(4),1193-1201.
- Kim, O. V., & Dunn, P. F. (2007). A microsphere-surface impact model for implementation in computational fluid dynamics. *Journal of Aerosol Science*, 38(5), 532-549.
- Kasper G , Schollmeier S , Meyer J , *et al.* (2009).The collection efficiency of a particle-loaded single filter fiber[J]. *Journal of Aerosol Science*, 40(12), 993-1009.
- Li, A., & Ahmadi, G. (1992). Dispersion and Deposition of Spherical Particles from Point Sources in a Turbulent Channel Flow. *Aerosol Science and Technology*, 16(4), 209-226.
- Lantermann, U., & HäNel, D. (2007). Particle monte carlo and lattice-boltzmann methods for simulations of gas–particle flows. *Computers & Fluids*, 36(2), 407-422.
- Li, S. Q., & Marshall, J. S. (2007). Discrete element simulation of micro-particle deposition on a cylindrical fiber in an array. *Journal of Aerosol Science*, 38(10), 1031-1046.
- Ounis, H., Ahmadi, G., & McLaughlin, J. B. (1991). Brownian diffusion of submicrometer particles in the viscous sublayer. *Journal of Colloid & Interface Science*, 143(1), 266-277.
- Raynor. P.C. (2002a).Flow field and drag for elliptical filter fibers, *Aerosol Sci. Technol.*36 :1118–1127.
- Raynor, P.C. (2002b). Single-fiber interception efficiency for elliptical fibers, *Aerosol Sci. Technol.* 42: 357–368.
- Rafał Przekop, Moskal, A., & Leon Gradoń. (2003). Lattice-boltzmann approach for description of the structure of deposited particulate matter in fibrous filters. *Journal of Aerosol Science*, 34(2), 133-147.
- Regan BD, Raynor PC. (2009)Single-fiber diffusion efficiency for elliptical fibers. *Aerosol Sci Technol* ;43:533–43.
- Wang, J. , & Pui, D. Y. H. . (2009). Filtration of aerosol particles by elliptical fibers: a numerical study. *Journal of Nanoparticle Research*, 11(1), 185-196.
- Wang W, Xie M, Wang L.(2012). An exact solution of interception efficiency over an elliptical fiber collector. *Aerosol Sci Technol* ;46:843–51.
- Wang, H., Zhao, H., Guo, Z., & Zheng, C. (2012). Numerical simulation of particle capture process of fibrous filters using lattice boltzmann two-phase flow model. *Powder Technology*, 227, 111-122.
- Wang K, Zhao H.(2015). The influence of fiber geometry and orientation angle on filtration performance. *Aerosol Sci Technol* ;49:75–85.
- Yue, C., Zhang, Q., & Zhai, Z. (2016). Numerical simulation of the filtration process in fibrous filters using CFD-DEM method. *Journal of Aerosol Science*, 101, 174-187.
- Zhu, C., Lin, C. H., & Cheung, C. S. (2000). Inertial impaction-dominated fibrous filtration with rectangular or cylindrical fibers. *Powder Technology*, 112(1–2), 149-162.

#342: The study on the heat transfer characteristics of the double U-tube pipes underground

Yan SHANG*, Xiaowan HUANG, Ming DONG, Sufen LI, Xiaohua LIU

Key Lab. of Ocean Energy Utilization and Energy Conservation of Ministry of Education, Dalian University of Technology, Dalian 116024 P. R. China,

**Corresponding author: shangyan@dlut.edu.cn*

One of the main deployment forms of geothermal energy is the soil source heat pump system. In this paper, the variation of the heat transfer characteristics of the double U-tube heat exchanger underground are analysed based on the soil source heat pump system (SSHP) experimental system, which was installed with six temperature measuring cables with a total of 117 DS18B20 soil temperature measuring points. Based on the same working conditions (the initial soil temperature was 14.5°C, the initial inlet water temperature of the U-tube pipe was 3°C, the flow rate was 120L/h and the corresponding flow velocity was 1.7m/s), the thermal interference of the double U-tube pipes underground was studied during the operation of the soil source heat pump, the soil heat transfer characteristics between single and double U-tube pipes were compared. Furthermore, the effects under different seepage velocity on soil temperature field were studied, the heat transfer rate underground analysed and the variation regulation of heat interference explained. It can be concluded that the thermal radius of the single U-tube system was greater than that of the intersection area of the double U-tube pipes field of the system. The greater the seepage velocity, the greater the radius of action of the buried pipe on the soil along the direction of seepage. The thermal radius was smaller than normal at the direction of vertical to the seepage, and the greater the seepage velocity, the smaller the thermal radius applied by the buried pipe to the soil.

Keywords: double-U-tube pipes; soil source heat pump; performance; heat transfer characteristics

1. INTRODUCTION

Geothermal energy is a renewable energy with huge reserves which far exceeds those of fossil fuel energy. One way to use geothermal energy is the SSHP system, which is an energy-saving and high-efficiency heat pump system that uses the soil as a heat/cold source to take heat/cool capacity by inputting a small amount of electric energy (Omer, 2008; Yang et al., 2010; Lund et al., 2011; Sarbu and Sebarchievici, 2014). In order to study the underground thermo-osmotic coupling heat transfer characteristics in depth, an experimental system is more flexible, convenient for controlling and changing experimental conditions.

Foreign scholars (Mohamed and Horoshenkov, 2009; Mohamed et al., 2015) have carried out related experimental research on the thermodynamic characteristics of shallow soil surface. The influence of the flow rate of the heat exchange medium on the heat transfer performance of the U-tube pipe were mainly studied in the experiment, and the effect of the rainwater seepage on the temperature recovery characteristics of the shallow surface soil were also studied. In order to simulate and predict the performance of the soil source heat pump system in the Akita Plain in northern Japan, a numerical model of underground heat and mass transfer with vertical U-tube pipes in the presence of groundwater seepage was set up according to local geological conditions (Fujii et al., 2005; Fujii et al., 2007). The underground heat transfer characteristics of a single U-tube pipe under the condition of seepage through self-made soil tank experiments has been studied by domestic scholars (Shao et al., 2016; Gao et al., 2017). Meanwhile, the thermal interference problem between underground well groups was studied through numerical simulation, and the Zeng et al. (2015) analysed the reasonable arrangement of heat transfer in vertical U-tube pipes.

In this paper, a SSHP experimental system was set up to study the underground heat transfer problem of double U-tube pipes. Based on this experiment, with or without the seepage, underground heat transfer characteristics of the double U-tube pipes heat exchanger and the thermal interference between the pipes were investigated.

2. EXPERIMENTAL SYSTEM

According to the similarity theory, the underground U-tube pipe size was scaled down based on the actual soil source heat pump system, and an experimental platform for the double U-tube SSHP system was built. The experimental system mainly includes soil tank, seepage device, heat pump unit and data acquisition module. The schematic is shown in Figure.1.

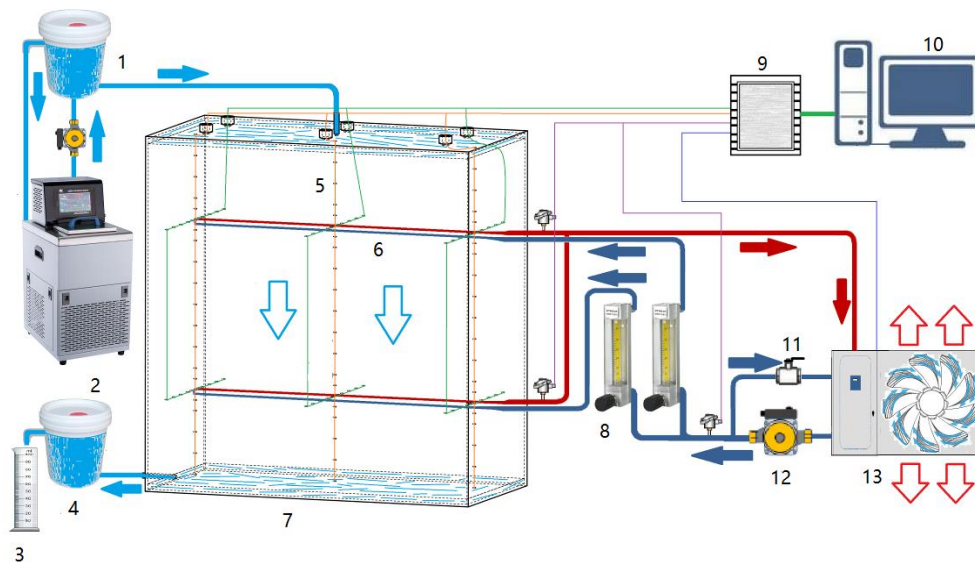


Figure 1: Schematic of the experimental configuration: 1-Water-tank (top) 2-Constant temperature water tank 3-Measuring cylinder 4-Water-tank (bottom) 5-Temperature measuring cable 6-U-tube 7-Soil tank 8-Flow meter 9-Data acquisition module 10-Computer 11-Regulating valve 12-Water pump 13-Heat pump

The circulating medium in the underground heat exchanger was water pumped out from the heat pump water tank by the circulating water pump and flowing to two rota meters. The total flow to the flow meter was adjusted by a regulating valve. The water flowing through the regulating valve returned to the heat pump, avoiding water waste.

Two flow meters operated independently, the water flowing through the flow meter and into the U-tubes buried in the soil to exchange heat with the soil. In winter operating conditions, the soil temperature was higher than the water temperature, so the circulating cooling water in the U-tube pipe absorbed heat from the soil. The water flowed out of the U-tube heat exchanger and back to the heat pump water tank, then the heat in the water was extracted by the heat pump and re-entered into the circulation.

The up-and-down moving water tank was connected with the soil tank, and the momentum of horizontal seepage in the soil aquifer was simulated by gravity potential [12], and the seepage speed was controlled by moving the upper and lower water tanks. Both the temperature measuring cable and the thermocouple were connected to their respective temperature acquisition modules.

The soil temperature measurement points were arranged in three layers along the direction of the U-tube pipe. Each layer was composed of two customized DS18B20 temperature measurement cables. The distance between the temperature measurement points is shown in Figure 2.

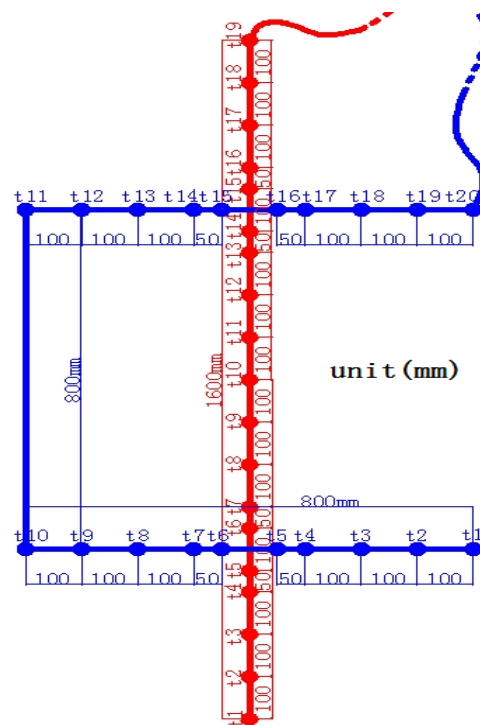


Figure 2: The form of temperature measuring point and cable decorate

3. EXPERIMENT AND RESULTS

Analysis of underground heat transfer characteristics of the double U-tube pipes heat exchanger without seepage. The working conditions mentioned in this section were the same, with the initial soil temperature of 14.5°C, the initial inlet water temperature of the U-tube pipe was 3°C, the flow rate was 120L/h, the corresponding flow velocity was 1.7m/s, and the running time was 12 hours.

3.1. The characteristics in saturated soil

In this section, the difference of underground heat transfer between single and double U-tube pipe during the operation of the SSHP system was studied when there was no seepage in saturated soil. Under the premise that the working conditions were the same, the difference of the underground heat transfer between the two operation modes was reported by comparing the soil temperature fields in two operation modes.

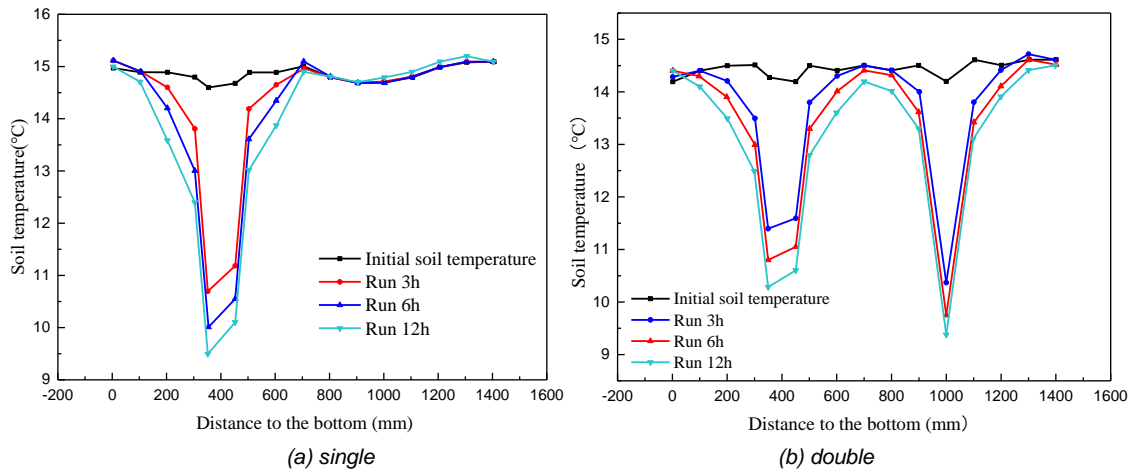


Figure 3: The distribution of soil temperature along the plane of the depth of 800mm and perpendicular to the bottom during the operation of the heat pump system in saturated soil.

It can be seen from Figure 3(a) that when the system was operated with a single U-tube pipe, the temperature field was basically symmetrical about the U-tube pipe, and the thermal radius of action was 400 mm. As can be seen from Figure 4(b), when the system was operated with a double U-tube pipes, the temperature field was symmetric about the centre position of the two U-tube pipes. In a double U-tube pipes system, the temperature field of one of the pipes was symmetrical about the centre line of the pipe, but the thermal radius of a single pipe temperature field in the temperature field overlap zone was 300mm, less than 400mm.

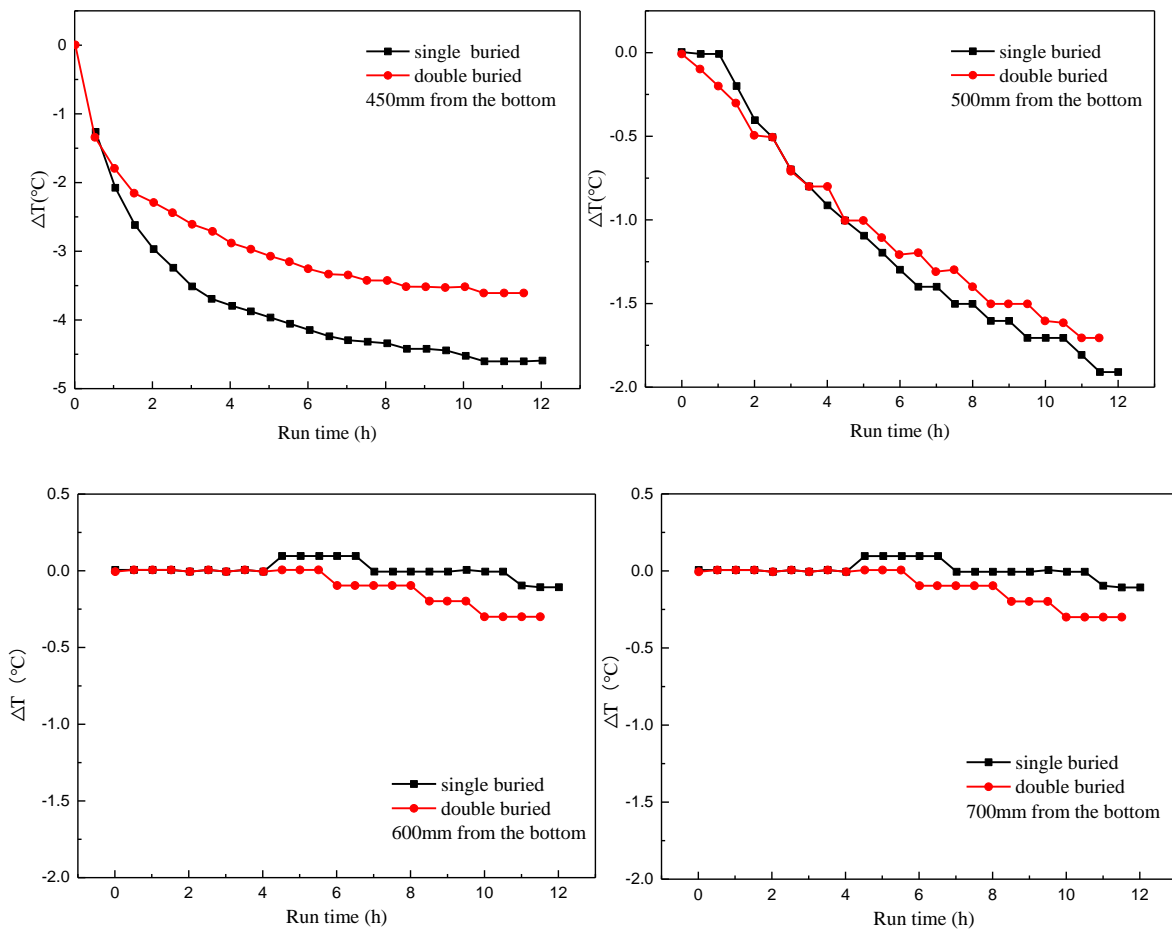


Figure 4: Curve of soil temperature difference with time on different depth plane

Figure 4 shows the relationship between the temperature difference between the soil temperature and the initial soil temperature over time. It can be seen that when the system was operating in double U-tube mode, the temperature gradient of the soil between the buried pipes was significantly lower than when the system was operated with a single U-tube pipe. This can be explained as the soil was affected by two U-tube pipes at the same time, resulting in the temperature gradient in the soil between the two buried pipes being reduced, and the temperature difference increased, so that the average temperature of the soil was lower. This effect was not a simple superposition of the soil temperature field around the two buried pipes.

3.2. The characteristics in unsaturated soil

In this section, in the unsaturated soil with a volumetric water content of 11.2%, the operating conditions were the same under the two operating modes of the single and double U-tube pipes of the system, the difference of the underground heat transfer characteristics between the two operation modes was studied. The distribution of soil temperature along the depth of the well under the condition of the system operated in two modes are shown in Figure 6. When the system was operated with single U-tube pipe, the soil temperature field was nearly symmetrical about the centre of the U-tube pipe, and the thermal radius was 350 mm. When the system was operated with double U-tube pipes, the temperature field was symmetrical about the centre of the two pipes, meanwhile the temperature field of one of the pipes was symmetrical about the centre line of a single U-tube pipe, but the thermal radius of a single pipe temperature field in the temperature field overlap zone was 300mm, less than 350mm.

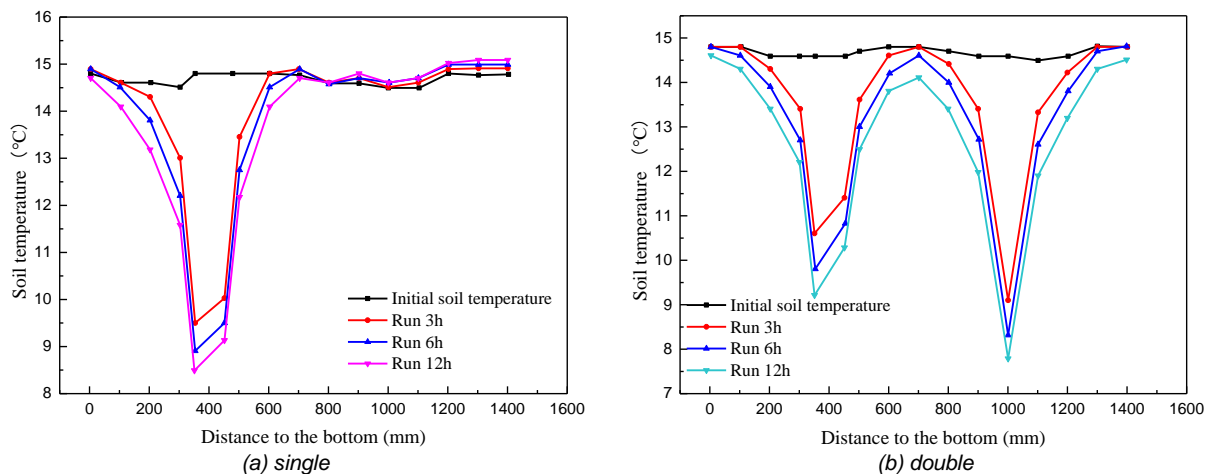


Figure 5: The distribution of soil temperature along the plane of the depth of 800mm and perpendicular to the bottom during the operation of the heat pump system in unsaturated soil

Figure 5 shows the curve of the temperature difference between the soil temperature and the initial soil temperature when the system operated in the unsaturated soil with a volumetric water content of 11.2% in double U-tube pipes mode. Because the soil temperature field of the double pipes was symmetrical about the centre line of the double pipes (700mm from the bottom of the box), only the soil between 450mm and 700mm from the bottom of the box was studied.

Comparing the two figures in Figure 6, it can be seen that the closer to the buried pipe, the higher the rate of change of temperature, the greater the temperature difference after the system reached equilibrium (when the running time exceeded 4 hours). It meant that the closer to b-U pipe, the larger the soil temperature difference was, and the larger the temperature gradient was. The variation of the temperature gradient with time in this part is shown in Figure 7.

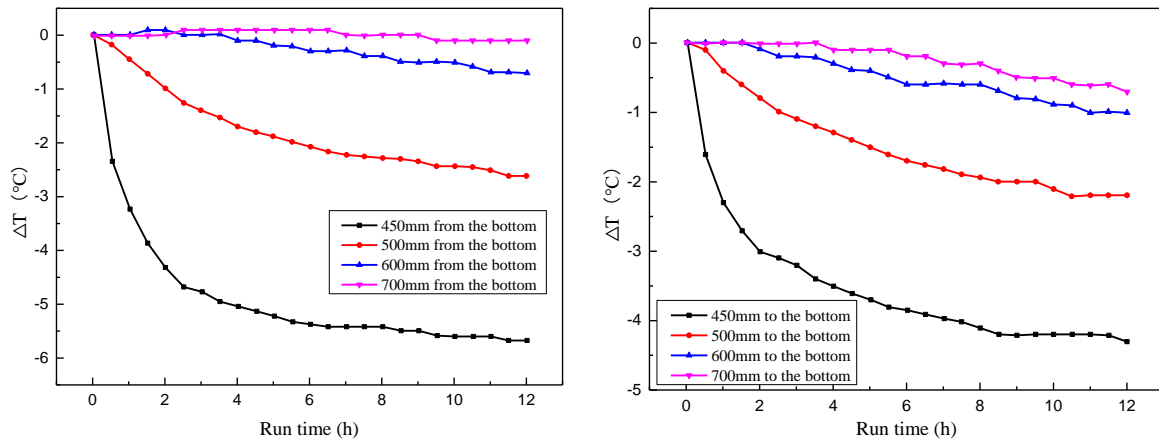


Figure 6: Curves of soil temperature in double U-tube pipes during the operation of unsaturated soil.

Figure 7 shows the change of temperature gradient over time in the operation modes of single and double U-tube pipes. It can be seen the double buried pipe operation when the system ran for 6 hours. The temperature gradient in this part (450mm~700mm) of the soil was stable in both modes of operation.

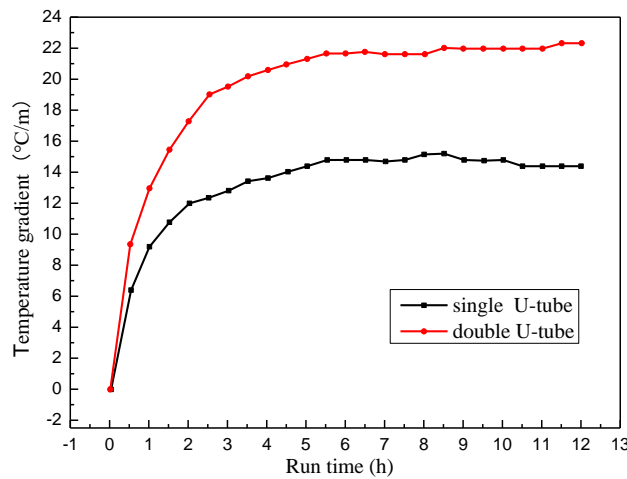


Figure 7: Curve of temperature gradient over time.

By comparing the operation of single and double buried pipes in two soil environments, the analysis showed that the radius of thermal action of saturated soil was greater than unsaturated soil, the reason was the difference in soil water content. Saturation was determined by the ratio of water to gas in the soil pores, while the thermal conductivity of water is much higher than that of gas. Because the water content in saturated soil is greater than that of unsaturated soil, the thermal conductivity of saturated soil was greater than that of unsaturated soil, and the thermal conductivity was stronger, so the thermal radius was larger.

The thermal action radius of the system when the single buried pipe was running was greater than that of the intersection of the two buried pipes' temperature field of the system. The reason for the analysis was that the distance between the two buried pipes was small and thermal interference problems were due to the superposition of temperature field interactions.

3.3 Comparison of heat transfer characteristics of single and double buried pipes

In order to further study the heat transfer characteristics of the system when operating in single and double buried pipes, a comparative analysis of heat exchange capacity and heat pump performance coefficient (COP) was performed, as shown in the following figure:

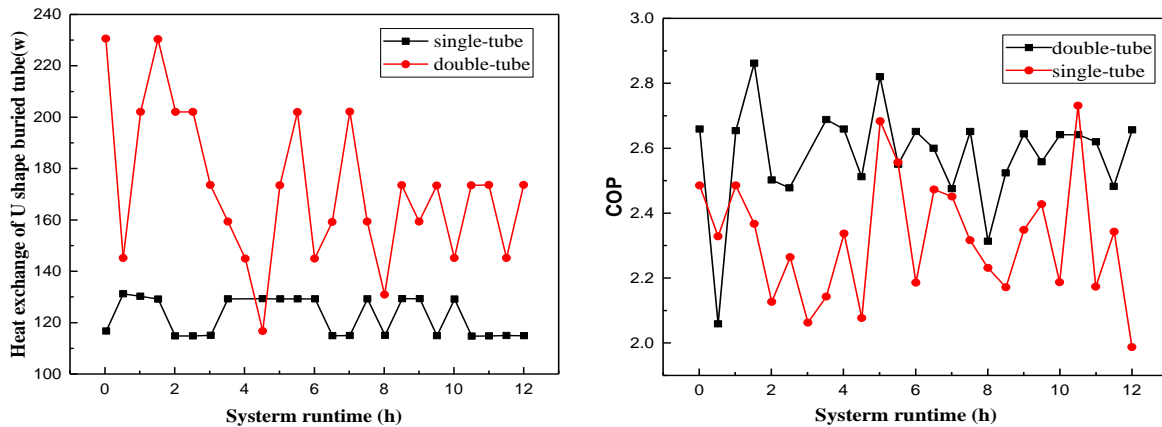


Figure 8: Heat exchange and COP comparison of single and double buried pipes in saturated soil

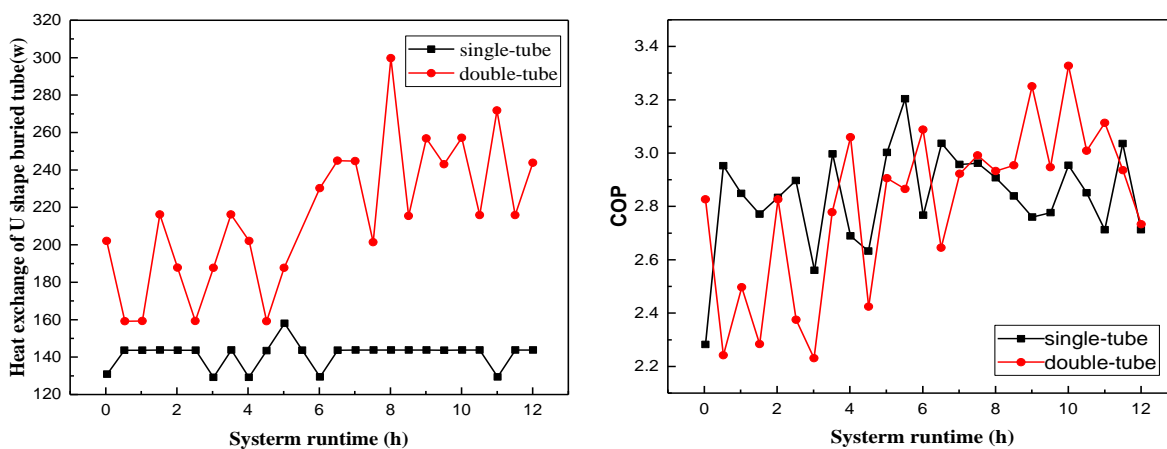


Figure 9: Heat exchange and COP comparison of single and double buried pipes in unsaturated soil

It can be seen from Figure 8 and Figure 9 that whether it was saturated soil or unsaturated soil, the heat exchange of the double pipe operation was significantly higher than that of the single pipe operation. Under the condition that the heat pump power was basically fixed, the COP mainly depended on the amount of heat exchange of the buried pipe, the distribution characteristics and heat transfer of the COP curve. The distribution characteristics of the quantity curves were basically the same.

Comparing the two figures, it can be seen that the heat exchange capacity and COP of unsaturated soil were generally higher than saturated soil. The reason was in the soil, the increase of soil water content in the dry soil will increase the effective thermal conductivity of the soil. After the soil water content reaches a certain level, the continuous increase of the soil volumetric water content reduced the effective thermal conductivity of the soil, so in the unsaturated soil. The effective thermal conductivity was large, which made the heat transfer characteristics in unsaturated soil better.

Therefore, it can be concluded that in practical engineering applications, the buried pipe had a higher heat exchange capacity and better heat transfer performance in the form of well groups.

4. CONCLUSION

The thermal radius of saturated soil was greater than that of unsaturated soil. In two soil environments, the thermal radius of the single U-tube system was greater than that of the intersection area of the double U-tube pipes' temperature field of the system. The reason for the analysis was that the distance between the two pipes was too close, thermal interference problems due to the superposition of temperature field interactions.

When there was seepage in saturated soil, and the system operated in double U-tube mode, the temperature field of the soil along the seepage direction was not symmetrical about any position and it was significantly offset along the direction of seepage; the greater the seepage velocity, the more obvious the offset, the greater the radius of action of the buried pipe on the soil along the direction of seepage. Vertical to the direction of seepage, the thermal

radius was smaller than normal, and the greater the seepage velocity, the smaller the thermal radius applied by the buried pipe to the soil.

When the system was operated as a double buried pipe, the heat exchange amount was much larger than that of the single buried pipe, and the heat pump performance coefficient COP was higher than that of the single buried pipe. Therefore, the buried heat exchanger worked better in the form of a well group.

5. ACKNOWLEDGEMENTS

It is gratefully acknowledged that this work is sponsored by National Science Foundation for Young Scholars of China (51706034).

6. REFERENCES

Fujii H, Inatomi T, Itoi R, 2007. Development of suitability maps for ground-coupled heat pump systems using groundwater and heat transport models. *Geothermics*, 36 (5), 459-472.

Fujii H, Itoi R, Fujii J, 2005. Optimizing the design of large-scale ground-coupled heat pump systems using groundwater and heat transport modeling. *Geothermics*, 34 (3), 347-364.

Gao Y, Guo H.B, Hu X.Lei, Zhang W.N, 2017. Soil heat and moisture properties under thermal effect of heat transfer of horizontal ground-coupled heat exchanger. *HV&AC*, 47(6), 113-116.

Lund J W, Freeston D H, Boyd T L, 2011. Direct utilization of geothermal energy 2010 worldwide review. *Geothermics*, 40 (3), 159-180.

Mohamed M, El Kezza O, Abdel-Aal M, 2015. Effects of coolant flow rate, groundwater table fluctuations and infiltration of rainwater on the efficiency of heat recovery from near surface soil layers. *Geothermics*, 53, 171-182.

Mohamed, M., Horoshenkov, K.V, 2009. Airborne acoustic method to determine the volumetric water content of unsaturated sands. *ASCE J. Geotech. Geoenviron.Eng.* 135 (12), 1872–1882.

Omer AM, 2008. Ground-source heat pumps systems and applications. *Renew Energy*, 12(2), 344–71.

Sarbu I, Sebarchievici C, 2014. General review of ground-source heat pump systems for heating and cooling of buildings. *Energy Build*, 70, 41–54.

Shao J.P, Hu X.J, Liao S.M, Rao Z.H, 2016. Experimental study of a ground coupled heat exchanger under infiltrative condition. *Building Energy & Environment*, 35(6), 6-9.

Yang H, Cui P, Fang Z, 2010. Vertical-borehole ground-coupled heat pumps: a review of models and systems. *Appl Energy*, 87(1), 16–27.

Zeng Z.T, Lv H.B, Zhao Y.L, Ge R.D, 2015. Numerical simulation of effect of ground water seepage on vertically buried tubular heat exchanger. *Acta Energiae Solaris Sinica*, 36(12), 3007-3014.

#343: Experimental studies of a new design of biogas burner for gas-fired wall-mounted boilers

Xiaomei HUANG¹, Mengxiao SUN², Yi ZHAO³, Pengyuan ZHANG⁴, Yang ZHOU⁵

¹ School of Civil Engineering, Chongqing University, 400044 Chongqing, China, hxm1980@cqu.edu.cn

² School of Civil Engineering, Chongqing University, 400044 Chongqing, China, shimianmengyouzhe@163.com

³ School of Civil Engineering, Chongqing University, 400044 Chongqing, China, 20135943@cqu.edu.cn

⁴ School of Civil Engineering, Chongqing University, 400044 Chongqing, China, 1010338216@qq.com

⁵ Foshan Gas Group Co., Ltd, Foshan City, 52800 Guangdong, China, zhouyanghit@126.com

Biogas is deemed to be one of the most promising renewable fuels to have emerged in the past several decades. At present, biogas is mainly applied to cooking as a substitute for fossil fuels. Biogas is rarely reported to be used for space heating. In this paper, we describe a new design of biogas-fired partially premixed burner for a gas-fired wall-mounted boiler, which has a heat input of 25 kW and can be used for spacing heating and fermentation tank heating. 60% of CH₄ and 40% of CO₂ was the reference gas, and the jet diameter and burner port area were designed as 2.0mm and 4744.5mm² respectively, according to the calculation. Then, experiments were conducted to study the performance of the burner. Jet diameters were modified in order to investigate their effects on heat input, primary air ratio and flame stability of the burner. The results indicated that the burner showed superior performance when the jet diameter was set to 2.0 mm whilst the primary air ratio (α') satisfied the design requirement. Moreover, the experiments of the gas-fired wall-mounted boiler were performed to explore the influence of different biogas compositions on exhaust emissions and thermal efficiency when this burner was installed inside. It was concluded that the content of CO met the national standard when methane content varied from 40% to 60%. However, with the increase of methane content, the thermal efficiency of the gas-fired wall-mounted boiler reduced greatly.

Keywords: biogas; burner; jet diameter; heat input; thermal efficiency

1. INTRODUCTION

Due to the depletion of fossil fuels and the increase of polluting emissions, finding environmentally-friendly alternative fuels has become a priority to guarantee the reliable energy provision and health of inhabitants (Hosseini and Wahid, 2013). Therefore, biomass fuels may be an alternative solution to the future shortage of fossil fuels and it is possible for many countries to produce energy from domestic renewable resources (Colorado, Herrera & Amell, 2010). In China, there are two critical issues in meeting the rising energy demand, especially in rural areas (Yu, Duan, Du, Xue and Sun, 2017; Yang, Zhou and Jackson, 2014). Many areas are short of clean energy, such as natural gas (NG) and it is difficult to have complete coverage of natural gas pipeline networks in rural areas. Moreover, almost all gas-fired wall-mounted boilers are designed for natural gas, so these boilers are difficult to popularise in the countryside. Fortunately, biogas, which is generated from landfills, agricultural waste and other sources of biomass, has been widely used as an important source of rural renewable energy with the financial support of the Chinese government (Ministry of agriculture of China, 2007). Because of adequate biogas resource, designing gas-fired wall-mounted boilers for biogas has long-term significance in those areas. Not only can the boilers supply heating and hot water, but they can also heat the biogas fermentation tanks.

Biogas is mainly composed of 50-70% (by volume) methane (CH_4) and 25-40% (by volume) carbon dioxide (CO_2). Furthermore, it may also contain traces of other gases (1-5%) such as hydrogen sulfide (H_2S), ammoniac (NH_3), water vapour, and volatile organic compounds (Tsai, 2007; Rajendran, Kankanala, Martinsson and Taherzadeh, 2014). Due to the high CO_2 content, the combustion characteristics of biogas are inferior to those of natural gas which is almost all methane, resulting in reduced burning velocity, lower flame temperature and a narrower range of flame stability (Lee and Hwang, 2007; Kalghatgi, 1981).

Bearing in mind the aforementioned biogas shortcomings, the flame characteristics of biogas have been studied and some methods to avoid blowout, lifting and yellow tipping have been proposed. It has been observed that, unlike other fuel gases, flashback was not prone to occur in biogas flame due to decreased burning velocity, but lifting and blowout were the most common conditions of flame instability (Zhen, Leung, Cheung and Huang, 2014). With an increase of the primary air ratio, the lifting limits decreased, while the yellow tipping limits increased (Dai, Qin, Chen, Tong, and Liu, 2012). Chao and *et al.* studied the effects of dilution (e.g. CO_2 and N_2) within the blowout limit and established a blowout limit database (Chao, Wu and Lee, 2003). They found that the blowout velocity was determined by the jet diameter and gas flow rate when the flame extinguishes.

Following theoretical analysis, various methods of biogas utilisation have been proposed, which can be divided into two categories. One is to convert low-quality raw biogas into high-quality fuel through biogas purification or blending it with a higher grade fuel (e.g. H_2 , LPG). For example, Lee and *et al.* proposed raising the heating value of biogas by adding LPG. They observed both higher heating values and higher burning speeds of the biogas-LPG mixed fuel in comparison with raw biogas and suggested that the mixed fuel could be used as an interchangeable gas of liquefied natural gas (Lee, Hwang and Lee, 2008). Leung and Wierzbza studied the stability of a diffusion flame burning biogas blended with a small amount of hydrogen (Leung and Wierzbza, 2008). While the initial 10% hydrogen addition to the biogas led to a tremendous boost to the blowout limits, the extent of blowout limit enhancement diminished with a continuous increase from 10% to 25%.

Another method of biogas utilisation is to alter the way of biogas combustion, for instance, adopting new techniques such as flameless combustion and porous media combustion. In recent years, flameless combustion has attracted more attention being one of the best feasible strategies for biogas utilisation. Studies in this field have indicated that flameless combustion modes could contribute to fuel consumption reduction, stability of combustion, temperature uniformity and low pollutant formation (Kozarac, Taritas, Vuilleumier, Saxena, and Dibble, 2016; Ilbas, Sahin and Karyeyen, 2016). Porous media combustion constitutes a particularly attractive technology, which allows operation in ultra-lean combustion regimes with excellent fuel interchangeability and reduces pollutant emissions (Keramiotis and Founti, 2013).

However, when biogas is applied to burners of household heating boilers, it is not practicable to utilise hydrotreaters and new combustion techniques, which are very expensive and complicated, so they are mainly applied to industrial boilers. Compared with NG, there are some problems with combustion in the conventional natural gas burners using biogas due to the higher content of CO_2 . Therefore, some researchers have focused on the modifications of conventional burners, however, to our knowledge, there are few studies on partially premixed burner (PPB) modifications in domestic cookers reported. As pointed out by Grima (Grima-Olmedo, Ramirez-Gomez, and Alcalde-Cartagena, 2014), when biogas was burnt in PPB, wider jet diameters were required since the biogas had a lower calorific value, partly because of the lower CH_4 content. Moreover, the lifting curves move up when the port size becomes wider (Dai, Qin, Chen, Tong, and Liu, 2012).

In addition, in actual applications, the biogas composition is not single and stable, but changes with the internal fermentation environment and external environment. Meanwhile the change of biogas composition has a greater impact on the heat input of the burner, primary air coefficient, flame conditions and other parameters. Therefore, it is necessary to study the working condition of burners and the range of adaptation of burners to the change of biogas composition under different biogas compositions.

This paper focuses on modifying a natural gas-fired burner to a biogas-fired one, using mixed gases of pure CH₄ and CO₂ to simulate typical biogas. The PPB which was applied to gas-fired wall-mounted boilers was studied and the jet diameter and burner port area of this burner were determined through relevant calculations under the rated heat input (25kW). In order to verify the predicted jet diameter, a series of jet diameters were designed for the experiment to study their effects on primary air ratio, heat input and flame shape systematically. Finally, the effects of different biogas components on the thermal efficiency and emissions of NO_x and CO were investigated.

2. DESIGN OF THE BIOGAS BURNER

In China, PPBs are extensively applied to all kinds of domestic gas appliances (e.g. gas stoves, gas water heaters and gas-fired wall-mounted boilers). Customarily, PPB is called atmospheric gas burner, which is one of the most promising gas appliances and has lots of advantages (Ozdemir, 2017; Rashwan, Ibrahim, Abou-Arab, Nemitallah and Habib, 2016), including significantly reducing polluting emissions (e.g. CO and NO_x), improving flame temperature and shortening flame length. As shown in Figure 1, it is a typical PPB of the gas-fired wall-mounted boiler that consists of 15 bar burners. The intervals between bar burners must be appropriate, for it is prone to ignite and obtain secondary air. Once the flammable mixture nearest to the igniter (mid-point position in Figure 1) starts burning, the flame rapidly propagates from port to port over the entire burner until a proper flame is anchored and stabilised at each bar burner. Figure 2 shows a bar burner which mainly comprises the ejector device, premixing chamber and burner head. According to previous studies (Ozdemir, 2017), the sizes of the jet diameter of the ejector and burner port are the most important parts for PPBs' design, which control the characteristics of the partially premixed flame. Therefore, in our study, the modifications in original jet diameter and burner port were strictly carried out.



Figure 1: The burner for the gas-fired wall-mounted boiler

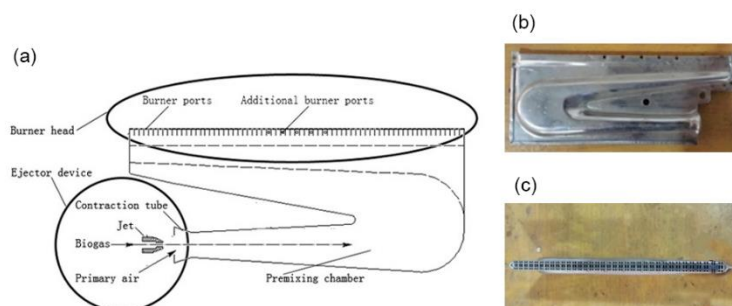


Figure 2: a modified bar of the burner. (a) schematic diagram; (b) side-view; (c) vertical-view.

2.1. Jet diameter of the ejector

The core part of an ejector is the jet diameter because it directly influences the amount of primary air which determines the characteristics of the flame. Generally, for a proper operation, it is crucial that the percentage of primary air should be held constantly at all burning states. It is generally achieved by a proportional pre-mixer utilising the Bunsen concept (Ozdemir, 2017). In this research, an appropriate jet diameter was provided for the conversion of gas-fired wall-mounted boilers commonly used for NG to these for biogas. Therefore, in the

experiments, a series of jet diameters was designed by trial and error at rated pressure of 1600 Pa. To verify the correctness of the experiment results, the jet diameters were compared with those obtained by calculations using Equation 1, which was extensively applied to define the flow rate or jet diameter of the PPB for the type of fuel (Fulford, 1996). Biogas was regarded as ideal gas for its relatively low pressure (< 2000 Pa) in the calculation.

Equation 1: Jet diameter of the ejector.

$$d_0 = \sqrt{\frac{l}{0.0036\mu}} \sqrt{\frac{S}{p_g}}$$

Where:

- d_0 = quantity of cooling or heating energy delivered (kW)
- l = gas flow rate at the jet of ejector (m^3/h)
- μ = coefficient of discharge for the jet
- S = relative density of gas
- p_g = gas pressure at the jet (kPa)

2.2. Burner ports

In order to obtain stable flame and uniform thermal intensity of burner port (q), problems arising from the combustion of biogas must be taken into account in designing the burner ports. The flame remains stable only when the exit velocity of the mixture matches the burning rate. When the velocity of the mixture through the burner port is higher than the flame burning rate, the flame starts lifting from the ports and eventually blows out. On the contrary, when the velocity of the mixture becomes too slow, the burning towards the mixture inside the burner head causes flashback and quenching. Biogas has extremely low flame speed with the result that flame lifting, rather than flashback, is really a problem (Dai, Qin, Chen, Tong, and Liu, 2012).

The key geometrical parameter of flame stability is the burner port, because it affects the mixture exit velocity. Hence, the way of avoiding lifting is to choose a bigger burner port. Additionally, the distance between burner ports determines the characteristics of the ignition and flame. The stronger the interaction between the flame of the burner ports, the better the stability of flame is. Therefore, the total area of the burner ports was optimised as shown in Figure 2(b) and (c) to prevent flame lifting due to lower burning rate when utilising biogas in the conventional burner. As shown in Figure 2(b), it is noteworthy that there are 5 additional burner ports of 2 mm diameter drilled on either side of every bar burner, and the total area (A) of burner ports is increased to 4744.5mm^2 . On one hand, the additional burner ports decrease the pressure of gas mixture inside the bar burner, which results in a decreased exit velocity of the gas mixture. On the other hand, these ports make the ignition more continuous and flame retention more effectively (Ozdemir, 2017). Therefore, the thermal intensity of modified burner port is $5.28\text{W}/\text{mm}^2$ calculated by Equation 2. This value lies in the middle of the stable flame zone as plotted by Dai (Dai, Qin, Chen, Tong, and Liu, 2012). Besides, this value also meets the design requirement of the biogas burner (Fulford, 1996), which makes combustion state preferably being within the range of stability region.

Equation 2: Thermal intensity.

$$q = \frac{Q}{A}$$

Where:

- q = thermal intensity (kW/mm^2)
- Q = heat input of gas-fired wall-mounted boiler (kW)
- A = total burner port area (mm^2)

3. EXPERIMENT AND METHODOLOGY

3.1. Experimental biogas in the tests

In the experiment of optimising the jet diameter, biogas was prepared by blending pure CH_4 and CO_2 at a constant volume ratio where the volume fraction of CH_4 and CO_2 were 60% and 40%, respectively to simulate the biogas supplied typically in practice. To investigate the influence of different biogas components on exhaust emissions and thermal efficiency of the gas-fired wall-mounted boiler, five groups of the gas mixture with different properties

are shown in Table 1. In addition, component experiments were conducted on the jet diameters of 2.0 mm in each group. Pure gases of CH₄ and CO₂ were taken from corresponding high-pressure cylinders. All gases were of commercial grade with over 99% purity to avoid any change of the mixture composition during the experiments.

Table 1: Components and properties of biogas

Group	CH ₄ (%)	CO ₂ (%)	H _i (MJ/Nm ³)	Relative density
1	40	60	14.361	1.393
2	50	50	17.951	1.042
3	60	40	21.541	0.945
4	70	30	25.131	0.847
5	80	20	28.722	0.750

3.2. Experimental apparatus

Figure 3 schematically illustrates the gas blending system and the experimental apparatus for testing PPBs. NG and CO₂ were controlled by the regulating needle valves, with the flow rate metered by gas flow meters, and then entered a wet storage tank alternately. After the gases in the tank reached the expected volume, they were stirred by the built-in fan for at least 30 minutes to make the components mixed. A U-gauge was used to measure the biogas pressure before PPBs. Thereafter, biogas and primary air were mixed evenly in the premixing chamber of PPBs and the mixture finally supplied to the burner head. Additionally, there was a small hole drilled on the premixing chamber, where a gas sampling probe was inserted. The probe was connected to a one metre stainless steel pipe, through which the gas samples were delivered to a gas chromatography and the O₂, CO₂, CH₄ and N₂ were analysed. The test platform of the whole experiment was set up, as shown in Figure 4, where the PPB installed into the gas-fired wall-mounted boiler was chosen for the tests of thermal efficiency and exhaust emissions.

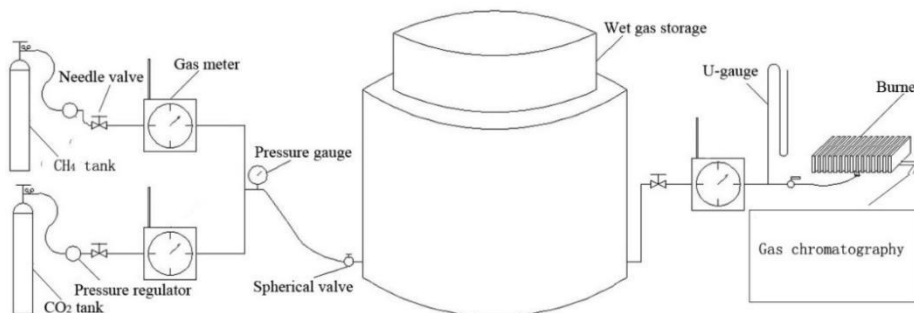


Figure 3: Schematic diagrams of the experimental system



Figure 4: Photo of the test platform for the boiler experiments.

3.3. Experimental procedure

The experiment aimed to investigate the impacts of various jet diameters and biogas composition on the primary air coefficient, heat input, and flame shape. The operational parameters for the current experiments are listed in Table 2. Biogas pressure was typically 1600Pa and the burner port area was 4744.5mm². During the experiments,

the designed operating condition was achieved by regulating the jet diameter of the ejector. All tests were carried out under the same condition. When the flame temperature remained stable, it reached the thermal/chemical equilibrium. Then measurements were carried out at each test individually.

Table 2: Operational parameters for the experiment

Case	Biogas pressure, P (Pa)	Jet diameter, d_0 (mm)	Total burner port area, A (mm ²)
1	1600	1.5	4744.5
2	1600	1.6	4744.5
3	1600	1.7	4744.5
4	1600	1.8	4744.5
5	1600	1.9	4744.5
6	1600	2.0	4744.5
7	1600	2.1	4744.5
8	1600	2.2	4744.5
9	1600	2.3	4744.5

4. RESULTS AND DISCUSSION

4.1. Experiments of the jet diameter

The jet diameter is one of the most important structure parts of PPBs, and it has great influences on the heat input, primary air ratio and flame shape. By comparing the corresponding heat input, primary air coefficient as well as flame shape for different jet diameters listed in Table 2, the optimal jet diameter can be obtained. Meanwhile the accuracy of Equation 1 may be also properly validated.

Effects of jet diameter on heat input

Heat input is the essential assessment criteria for most domestic gas appliances and it reveals the ability of heat release of a burner. However, the jet diameter has a significant impact on gas flow rates which affects the heat input. Generally at standard state, the predicted heat input (Q_0) can be calculated from Equation 3 derived from Equation 1. In fact, under the restriction of experimental conditions, the experiment process cannot be conducted in standard state, so Equation 4 can be obtained after correction.

Equation 3: Heat input at standard state.

$$Q_0 = \frac{15H_l}{3600} = \frac{15 \times 0.0036 \mu d_0^2 H_l \sqrt{\frac{P}{S}}}{3600}$$

Equation 4: Heat input after correction.

$$Q_1 = \frac{L_1 H_l}{3600} \times \frac{P + P_a}{P_0} \times \frac{T_0}{T_1}$$

Where:

- Q_0 = heat input at standard state (kW)
- H_l = lower heating value (MJ/m³)
- L_1 = actual biogas flow rate (m³/h)
- P = biogas pressure (kPa)
- P_a = actual atmospheric pressure (kPa)
- P_0 = standard atmospheric pressure (101.325kPa)
- T_0 = standard temperature (288.15K)
- T_1 = actual biogas temperature (K)

The comparison of measured and calculated heat inputs are shown in Figure 5. The predicted results coincided with the experimental data well, indicating that Equation 3 could calculate the heat input relatively accurately. The reason why there was relative deviation between the predicted and measured heat inputs might be due to the imprecision of jet processing or the interference of some experimental apparatus. Furthermore, the heat input increased with the increase of jet diameter because the fuel flow rate rose along with the increase of the jet diameter. When the jet diameters were bigger than 1.9 mm, the heat input could meet the design requirement (25KW).

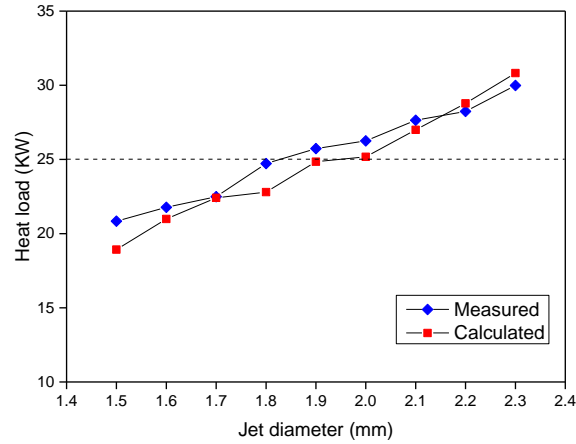


Figure 5: The comparisons between the computed and measured heat input for different jet diameters.

Effects of jet diameter on primary air ratio

The primary air ratio (α') is a crucial design parameter for PPBs. The amount of primary air added to the gas before the flame varies depends on the design of burner, but it is usually around 50% to 75% of the total air requirement (Tumwesige, Fulford and Davidson, 2014). Moreover, the flame height at the flame ports is affected by the primary aeration. The low value of α' means that gas needs to be supplied with more secondary air for combustion and results in long flames and burning imperfectly. Meanwhile, poor combustion generates carbon monoxide (CO), which is poisonous, and carbon particles, which show up as red flashes in the flame. The high value of α' explains that the gas can burn under the primary air, so the flames are much shorter. However, larger primary aeration is inadvisable, as flashback can occur. The predicted primary air ratio can be calculated by Equation 5, and the entrainment ratio is given by Priggs in Equation 6 (Fulford, 1996). In order to validate the predicted α' value calculated by Equation 5, the measured α' value can be obtained by Equation 7 based on the data from the experiment. The corresponding experimental results are shown in Figure 6.

Equation 5: primary air ratio.
$$\alpha' = \frac{rS}{V_0}$$

Equation 6: Entrainment ratio.
$$r = \sqrt{S \left(\frac{d_t}{d_0} - 1 \right)}$$

Equation 7: Measured primary air ratio.
$$\alpha' = \frac{O_2}{(21 - O_2)V_0}$$

Where:

- α' = primary air ratio
- r = entrainment ratio
- V_0 = theoretical air volume required (m^3/h)
- d_t = throat diameter (mm)
- O_2 = O_2 molar fraction in gas (%)

The primary air ratio was inversely proportional to jet diameter: primary air ratio increased with decreasing jet diameter as shown in Figure 6. The narrower the jet diameter was, the higher the biogas pressure at the jet was, so that the more primary air will be injected. Besides, Figure 6 indicated that the predicted values calculated by Equation 5 were basically accurate and consistent with the experimental data especially when the jet diameter was between 1.7 and 2.1mm. As mentioned previously, when the value of α' was between 0.5 and 0.75, the partly premixed flame was relatively stable. Hence, when the values of jet diameter ranges from 1.8mm to 2.2mm, which was corresponding to the primary air ratio ranges from 0.7 to 0.52, the burner could meet the design requirement of PPBs.

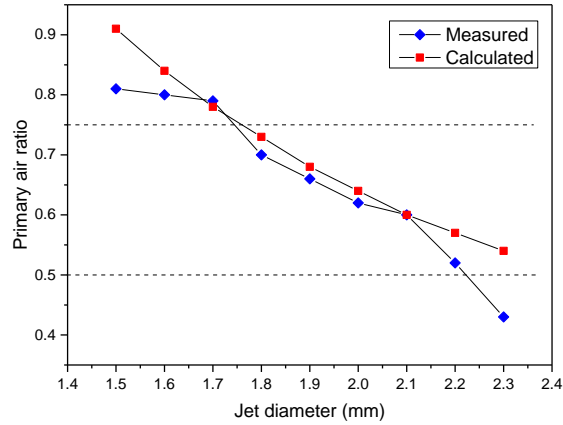


Figure 6: Comparison between calculated and measured primary air ratio (α') under different jet diameters.

Effects of jet diameter on flame shape

The stable flame meant that no flash-back, yellow tipping and lifting were observed. The flame became stabilised and attached to the burner rim when the burning velocity and flow speed of the flame were matched with each other. For a PPB, it usually runs under small excess of air to avoid the danger caused by rich flame. If too much air is supplied, the flame cools off, thus prolonging the working time and increasing the fuel demand.

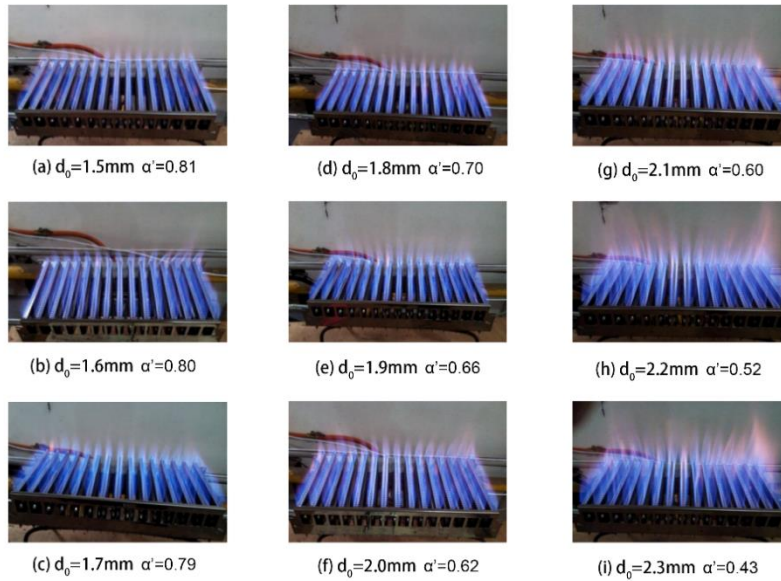


Figure 7: Flame status under different jet diameters.

In the experiment, flame shapes in different jet diameters were observed under rated conditions where the biogas supply pressure maintained 1600Pa and two components of pure biogas were 60% CH₄ and 40% CO₂. The flame heights increased with the increase of the jet diameter and the colour of inner cone in the flame changed from light blue to mazarine, meanwhile the “outer mantle” of the flame became increasingly yellow. It can be interpreted that the hydrocarbon in the flame was converted into aldehyde and ethyl alcohol inside the reaction zone of flame because the primary air ratio decreased with increasing jet diameter especially when the primary air ratio remained higher than 0.7 ($\alpha' > 0.7$). So the outer mantle was nearly transparent, as shown in Figure 7(a)-(c). On the contrary, when the primary air ratio remained lower than 0.7 ($\alpha' < 0.7$), the hydrocarbon was converted into carbon particles inside the reaction zone of flame because of lower temperatures. The outer flame became bright, as shown in Figure 7(d)-(i). In addition, lower primary air ratio caused the shortage of air required for biogas burning, resulting in richer, longer, and softer flames which damaged the chamber walls and increased emissions. Particularly, when the jet diameter was more than 2.1mm, the yellow tipping was fairly distinct, as shown in Figure 7(g)-(i). If the jet diameter was less than 1.9mm, the heat input cannot satisfy the design requirement (25 kW). Therefore, the optional jet diameter was between 1.9mm and 2.1mm.

4.2. Performance experiments of wall-mounted boiler with the designed burner

The composition of biogas varies with the change of external conditions, so the gas-fired wall-mounted boiler of biogas is required to have a good adaptability to different composition of biogas. As biogas composition changes, the combustion characteristics of PPBs will change. Therefore, we installed the PPB in a gas-fired wall-mounted boiler, and tested its exhaust emissions and thermal efficiency. The burner ($d_0=2.0\text{mm}$) was chosen as the test burner and the primary air ratio was 1.7.

Effects of exhaust emissions

CO and NOx are often regarded as the important indices of pollutant emissions. The effects of different biogas composition on the variation of CO and NOx emissions were investigated in this section. According to Equation 8 and 9, the converted CO and NOx contents can be calculated from the original data to the data where the excess air coefficient (α) is equal to 1 and the calculation were presented in Figure 8.

Equation 8: CO content when α is 1.

$$CO = CO' \times \frac{21}{21 - O_2}$$

Equation 9: NOx content when α is 1.

$$NO_x = NO_x' \times \frac{21}{21 - O_2}$$

Where:

- CO = CO content when α is 1 (ppm)
- CO' = measured CO content (ppm)
- NOx = NOx content when α is 1 (ppm)
- NOx' = measured NOx content (ppm)

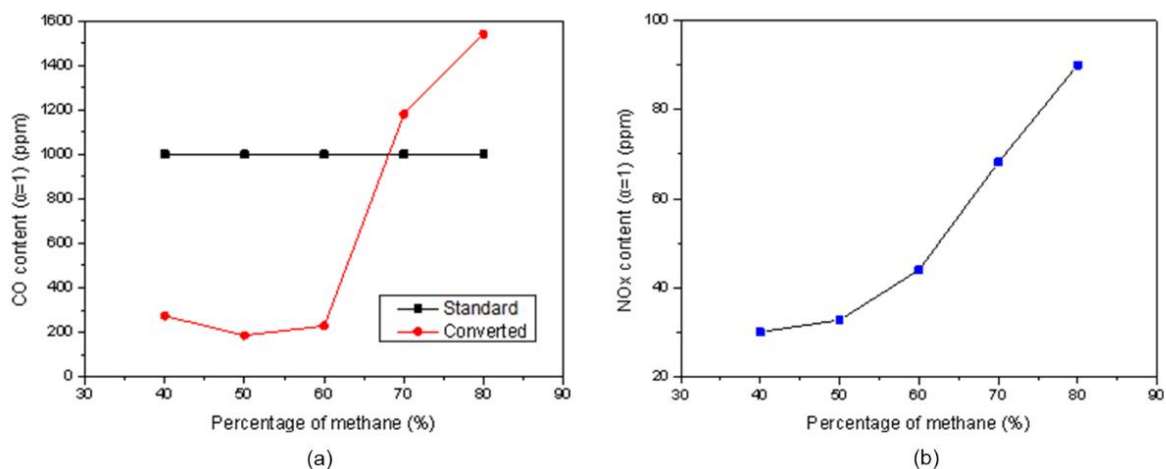


Figure 8: Exhaust emissions under different percentage of methane in biogas. (a) CO content ($\alpha=1$), (b) NOx content ($\alpha=1$).

It was found that with the increase of the volume fraction of methane in the biogas, the amount of CO in flue gas also increased as shown in Figure 8(a). A reasonable explanation for this can be given by the limitation of the burner structure, which led to decreased primary air coefficient when the methane content increased. However, the excess air coefficient remained unchanged and the burner arrangement was tight, so the air and gas were not fully mixed, resulting in increased CO. When the content of methane was less than 60%, the emission met basic requirements of the standard. But when the content was less than 40%, the flame in the combustion chamber began to show strong fluctuations, combustion instability, and even flameout. Therefore, the gas-fired wall-mounted boiler is suitable for the biogas containing 40%~60% of methane when the excess air coefficient is 1.7. As can be seen from Figure 8, as the content of methane increased, the emission of NOx also increased because the generation of NOx was closely related to the combustion temperature whose rise can promote the former. The combustion temperature went up with the increase of methane, so NOx was on the rise as shown in Figure 8(b).

Effects of thermal efficiency

It is illustrated in Figure 9 that the thermal efficiency of the gas-fired wall-mounted boiler decreased with the increasing of methane. When the methane content in biogas was higher than 60%, the thermal efficiency changed dramatically and was lower than the standard value 84%. The main reason for this condition was that when the size of the burner remained unchanged, the methane content increased and the primary air coefficient decreased, resulting in poor combustion condition and increased heat loss from incomplete chemical combustion, thereby reducing the thermal efficiency.

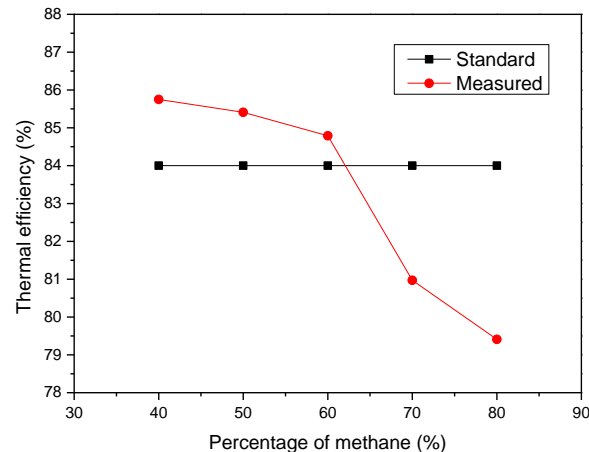


Figure 9: Thermal efficiency under different percentage of methane in biogas.

5. CONCLUSION

The main aim of this research was to investigate the effects of jet diameter on heat input, primary air ratio and flame shape, as well as the influence of different biogas composition on exhaust emission and thermal efficiency. Additionally, the appropriate burner port area was defined as 4744.5mm². According to the calculated and experimental results, the measured results were in good agreement with the predicted values. In order to meet the design requirement of heat input (25 kW), the jet diameter should be more than 1.9mm. Besides, when the jet diameter ranged from 1.8mm to 2.2mm, the primary air ratio (α') satisfied the design requirement of ejecting ability. However when the jet diameter was more than 2.1mm, the combustion characteristic worsened, so the jet diameter must be less than 2.1mm. Generally, the heat input should have a little margin, therefore the optimised jet diameters should be 2.0mm or 2.1mm. These results coincided with calculated values fairly well. Moreover, it was concluded from the whole experiment of the gas-fired wall-mounted boiler that the content of CO met the national standard when methane content was within 40% to 60%. However, with the increase of methane content, the thermal efficiency of the gas-fired wall-mounted boiler fluctuated greatly.

6. REFERENCES

- Chao, YC., Wu, CY. and Lee, KY., 2003. Effects of dilution on blowout limits of turbulent jet flames. *Combustion Science and Technology*, 176(10), 1735-1753.
- Colorado, AF., Herrera, BA. and Amell, AA., 2010. Performance of a Flameless combustion furnace using biogas and natural gas. *Bioresource Technology*, 101(7), 2443-2449.
- Dai, WN., Qin, CK., Chen, ZG., Tong, C. and Liu, PJ., 2012. Experimental studies of flame stability limits of biogas flame. *Energy Conversion and Management*, 63, 157-161.
- Fulford, D. 1996. Biogas Stove Design. Kingdom Bioenergy Ltd.
- Grima-Olmedo, C., Ramirez-Gomez, A. and Alcalde-Cartagena, R., 2014. Energetic performance of landfill and digester biogas in a domestic cooker. *Applied Energy*, 134, 301-308.

- Hosseini, SE. and Wahid, MA., 2013. Biogas utilization: Experimental investigation on biogas flameless combustion in lab-scale furnace. *Energy Conversion and Management*, 74, 426-432.
- Ilbas, M., Sahin, M. and Karyeyen, S., 2016. 3D numerical modelling of turbulent biogas combustion in a newly generated 10 KW burner. *Journal of the Energy Institute*, 91(1), 87-99.
- Kalghatgi, GT., 1981. Blow-out stability of gaseous jet diffusion flames. *Combustion Science and Technology*, 26, 233-239.
- Keramiotis, C. and Founti, MA., 2013. An experimental investigation of stability and operation of a biogas fueled porous burner. *Fuel*, 103, 278-284.
- Kozarac, D., Taritas, I., Vuilleumier, D., Saxena, S. and Dibble, RW., 2016. Experimental and numerical analysis of the performance and exhaust gas emissions of a biogas/n-heptane fueled HCCI engine. *Energy*, 115, 180-193.
- Lee, CE. and Hwang CH. 2007. An experimental study on the flame stability of LFG and LFG-mixed fuels. *Fuel*, 86, 649-655.
- Lee, CE., Hwang, CH. and Lee, HY., 2008. A study on the interchangeability of LFG–LPG mixed fuels with LFG quality in domestic combustion appliances. *Fuel*, 87, 297-303.
- Leung, T. and Wierzba, I., 2008. The effect of hydrogen addition on biogas non-premixed jet flame stability in a co-flowing air stream. *International Journal of Hydrogen Energy*, 33, 3856-3862.
- Ministry of agriculture of China, 2007. Agricultural biomass energy industry development plan (2007–2015). Beijing.
- Ozdemir, IB., 2017. Simulation of turbulent combustion in a self-aerated domestic gas oven. *Applied Thermal Energy*, 113, 160-169.
- Rajendran, K., Kankanala, HR., Martinsson, R. and Taherzadeh, MJ., 2014. Uncertainty over techno-economic potentials of biogas from municipal solid waste (MSW): A case study on an industrial process. *Applied Energy*, 125:84-92.
- Rashwan, SS., Ibrahim, AH., Abou-Arab, TW., Nemitallah, MA. and Habib, MA., 2016. Experimental investigation of partially premixed methane–air and methane–oxygen flames stabilized over a perforated-plate burner. *Applied Energy*, 169, 126-137.
- Tsai, WT., 2007. Bioenergy from landfill gas (LFG) in Taiwan. *Renewable and Sustainable Energy Reviews*, 11, 331-344.
- Tumwesige, V., Fulford, D. and Davidson, GC., 2014. Biogas appliances in Sub-Saharan Africa. *Biomass and Bioenergy*, 70, 40-50.
- Yang, CJ, Zhou, YP. and Jackson, RB., 2014. China's fuel gas sector: History, current status, and future prospects. *Utilities Policy*, 28, 12-21.
- Yu, HW., Duan, JH., Du, W., Xue, S. and Sun, JH., 2017. China's energy storage industry: Develop status, existing problems and countermeasures. *Renewable and Sustainable Energy Reviews*, 71, 767-784.
- Zhen, HS., Leung, CW., Cheung, CS. and Huang, ZH., 2014. Characterization of biogas-hydrogen premixed flames using Bunsen burner. *International Journal of Hydrogen Energy*, 39, 13292-13299.

#344: Synthesis of carbon nanotube-MgO composite by chemical vapour deposition for thermal energy storage

Sebastian DAYOU¹, Abdul Rahman MOHAMED²

¹ School of Engineering and Technology, University College of Technology Sarawak, 96000 Sibu, Sarawak, Malaysia, sebastian@ucts.edu.my

² School of Chemical Engineering, Universiti Sains Malaysia, Engineering Campus, Seberang Perai Selatan 14300 Nibong Tebal, Penang Malaysia, chrahman@usm.my

The aim of this study was to synthesise a nanocomposite structure to be used together with phase change materials (PCMs) for thermal energy storage (TES) applications. This structure is composed of the thermally conductive carbon nanotubes (CNT) connected to MgO, i.e. a ceramic material known to have good compatibility with PCMs. Such interconnection is developed by growing CNT directly on MgO by chemical vapour deposition (CVD) with the aid of a small amount of Co nanoparticles deposited on the surface of MgO that acts as a catalyst for the growth. The deposition of Co on MgO was carried out using a wet impregnation method. A scanning electron microscope (SEM) and energy-dispersive x-ray spectrometer (EDS) were utilised to observe the dispersion of Co on MgO. CVD growth of CNT was conducted at 800°C under the flow of methane (50 mL/min) and nitrogen (100 mL/min) for 30 min. From the study, the interconnection between CNT and MgO was clearly seen under SEM and uniform dispersion of CNT in the composite structure was observed. The approach used in this work would be crucial to minimise the thermal contact resistance due to the established interconnection between CNT and MgO, thus can bring about enhancement to the thermal conduction in TES.

Keywords: thermal energy storage; thermal conductivity; carbon nanotube; MgO; chemical vapour deposition

1. INTRODUCTION

Today, power generation from conventional fossil fuels dominates the global energy market but utilisation of renewable energy sources is expected to grow in the years to come due to great concern over global warming and emissions of greenhouse gases associated with the burning of fossil fuels. Among the renewable energy alternatives, solar energy offers great potential due to its abundance and worldwide accessibility (Kannan and Vakeesan, 2016). In recent years, solar-thermal systems have attracted great interest due to its efficiency for solar energy harvesting and conversion (Lewis, 2016). The deployment of this system is, however, facing a great challenge since solar energy is intermittent in nature. In this regard, solar-thermal energy storage (STES) technology plays a crucial role in providing a solution to this intermittency problem and brings forth practical applications of solar-thermal systems.

In the search for suitable storage materials for STES technology, phase change materials (PCMs) stand out among other candidates due to high thermal storage density and cost-effectiveness (Alva et al., 2017). However, they suffer from low thermal conductivity which hinders the heat charging and discharging efficiency required for STES. A logical solution to this problem would be through the incorporation of thermal conductive fillers into PCMs. Various types of carbon-based nanofillers have been investigated in the past for the purpose of enhancing the thermal conductivity of PCMs (Cui et al., 2011; Tao et al., 2015). Among these carbon allotropes, carbon nanotube and graphene are the most promising nanomaterials for this application. This is due to their intrinsically high thermal conductivity; K that can go to more than 3000 W mK^{-1} at room temperature, which is associated with strong sp^2 lattice (Balandin, 2011).

Despite showing improvement to the heat transfer performance of PCM by the addition of these high- K fillers, the straightforward mixing method leads to another problem. On the one hand, due to the difference in density, and on the other, due to high propensity of aggregation caused by van der Waals interactions, these carbon allotropes are poorly dispersed in liquid PCMs, hence they would be separated from the bulk liquid PCMs (Ge et al., 2014a). To overcome this problem, several researchers have proposed the inclusion of MgO ceramic into the mixture of PCM and high- K filler due to its good compatibility with liquid PCM (Li et al., 2019; Ye et al., 2014; Ge et al., 2014b). However, the disconnection between MgO and CNT from this method can become a barrier for effective heat conduction within the composite. Such a problem is identified as thermal contact resistance, which is known to be a hindrance to thermal conduction effectiveness of CNT-based nanocomposite (Yang et al., 2011; Lahiri et al., 2010; Qiu et al., 2017). Therefore, it is imperative to find a solution to the interconnection issue between MgO and high- K filler in order to maximise the heat transfer rate of PCM. In this work, we report on the synthesis of CNT grafted on MgO by chemical vapour deposition (CVD), which established an interconnection between them. By using this strategy, the thermal contact resistance will be minimised, hence paving the way for high thermal conduction performance in STES material.

2. EXPERIMENTAL

The detail of experimental works involved in the present study is described in this section. Firstly, the experimental rig system for CVD reaction is presented, followed by the procedure for catalyst preparation and CNT growth. Finally, the techniques and related instruments for the characterisation of samples are delineated.

2.1. Experimental rig for chemical vapour deposition (CVD)

The CVD reaction for the synthesis of CNT was conducted in a horizontal tubular furnace (Figure 1a). The schematic representation of the experimental rig system is given in Figure 1b. The system was divided into two main parts: gas mixing and reaction section. The gas mixing section consisted of gas tanks, mass flow controllers and gas mixer. Methane was used as the carbon feedstock while nitrogen was used as the protective inert gas to dilute methane during CVD reaction and purge the reactor after completion of the reaction. The flow rate of the gases was regulated by two mass flow controllers (one for each gas) connected to a 4-channel control panel. These pipelines were merged and flowed through a gas mixer so that a well-mixed gas was obtained before entering the tubular reactor for the CVD growth of CNT.

The main component in the reaction section was the horizontal tubular furnace where the CVD reaction took place. The furnace was equipped with temperature controllers to regulate the temperature inside the furnace. The furnace was assembled with a thermally stable quartz tube. A quartz boat was used to place the catalyst powder in the middle of the furnace reactor. In order to measure the actual temperature inside the furnace, a type K thermocouple was placed at the centre of the reactor, close to the location of the reaction.

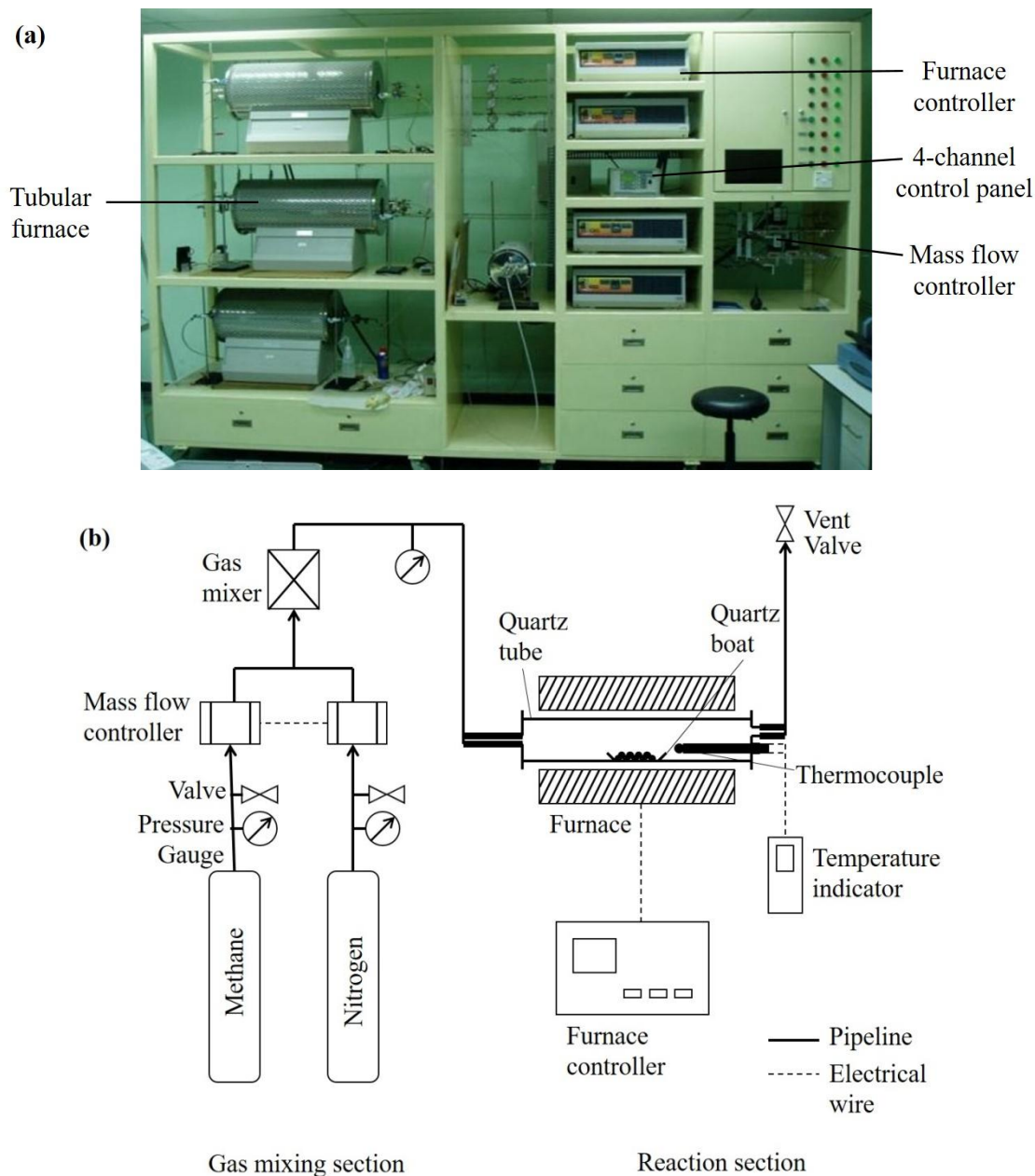


Figure 1: (a) Photographic view and (b) schematic representation of the CVD experimental rig system

2.2. Preparation of catalyst and CNT growth

For the growth of CNT, cobalt was utilised as a catalyst. The catalyst was prepared by depositing it on the surface of MgO by a wet impregnation method. Ethanol solution of $\text{Co}(\text{NO}_3)_2$ (Riedel-de Haën) was used for the preparation of 1 mol.% Co-MgO. 10 g of MgO (HmbG Chemicals) was added to the ethanol solution (50 mL) and then sonicated for 60 minutes. The solution was evaporated to dryness at 85°C under continuous agitation, then the leftover solids were heated at 130°C for 12 hours before being ground into fine powder. The Co-MgO were calcined at 700°C (2 hours) before being used to catalyse the growth of CNT.

For the CVD process, a quartz boat containing 0.4g of the prepared Co-MgO powder was placed into the quartz tube inside the furnace reactor. The furnace was then heated at a rate of 10°C/min under nitrogen flow (100 mL/min). When the temperature reached 800°C, methane (50 mL/min) was introduced to begin the reaction for CNT growth. The reaction was stopped after 30 minutes. The furnace was then allowed to cool down to ambient temperature under the flow of nitrogen (100 mL/min) prior to removal of the quartz boat from the furnace. Dissolution of Co-MgO substrate from the sample was performed by dissolving the samples in a nitric acid solution (2 M), stirring at room temperature for 30 minutes. The harvested powder was then washed with de-ionized water under filtration on a 0.22 μm porosity of polyvinylidene fluoride (PVDF) membrane and then dried at 100°C in an oven. Finally, the powder was heated at 500°C for 60 minutes in a nitrogen atmosphere.

2.3. Characterisation techniques

The powder was dispersed in ethanol using a low-power sonication bath for a few minutes before being deposited on a holey carbon grid (200 mesh size) for characterisation under transmission electron microscopy (TEM). The TEM analysis was carried out using a FEI Tecnai G2 F20 S-TWIN with field emission apparatus at an operating voltage of 200kV. The surface of as-prepared Co-MgO substrate and post-CVD material were observed under scanning electron microscopy (SEM) using FEI Nova NanoSEM 450 and FEI Verios 460L tool under extreme high resolution (XHR), respectively; both occupied with field emission. The former was equipped with Energy Dispersive X-ray Spectrometer (EDS) for elemental mapping analysis to investigate the deposition of cobalt on the surface of MgO particles. Raman spectra of the as-synthesised product after CVD were measured with a Renishaw inVia Raman microscope using an excitation line of 632.8 nm argon laser. The laser power output of 50 mW was focused on the sample with 50X objective lens and no filter was used. A range from 100 cm^{-1} to 3200 cm^{-1} of Raman shift was scanned.

3. RESULTS AND DISCUSSION

Observation of the as-prepared catalyst under SEM showed particles with sizes of 200 – 300 nm. A weak intensity of Co element and intense presence of Mg and O elements were seen from the EDS mapping that correspond to the SEM image (Figure 2). The Co particle was expected to be formed by the wet impregnation method in the form of cobalt oxide with the size range of 5 – 20 nm (Zhang *et al.*, 2010) and due to its very small size, it was not detectable in the SEM image. The strong intensity of Mg and O certainly comes from MgO, which was the dominant compound used in the sample and the particles seen in the SEM image definitely belong to MgO. The wet procedure used in the impregnation method assured the presence of cobalt on the surface of MgO, which was in contrast to other deposition methods such as physical vapour deposition where only the exposed parts may be covered. This finding demonstrated the successful deposition of evenly distributed Co on the surface of MgO.

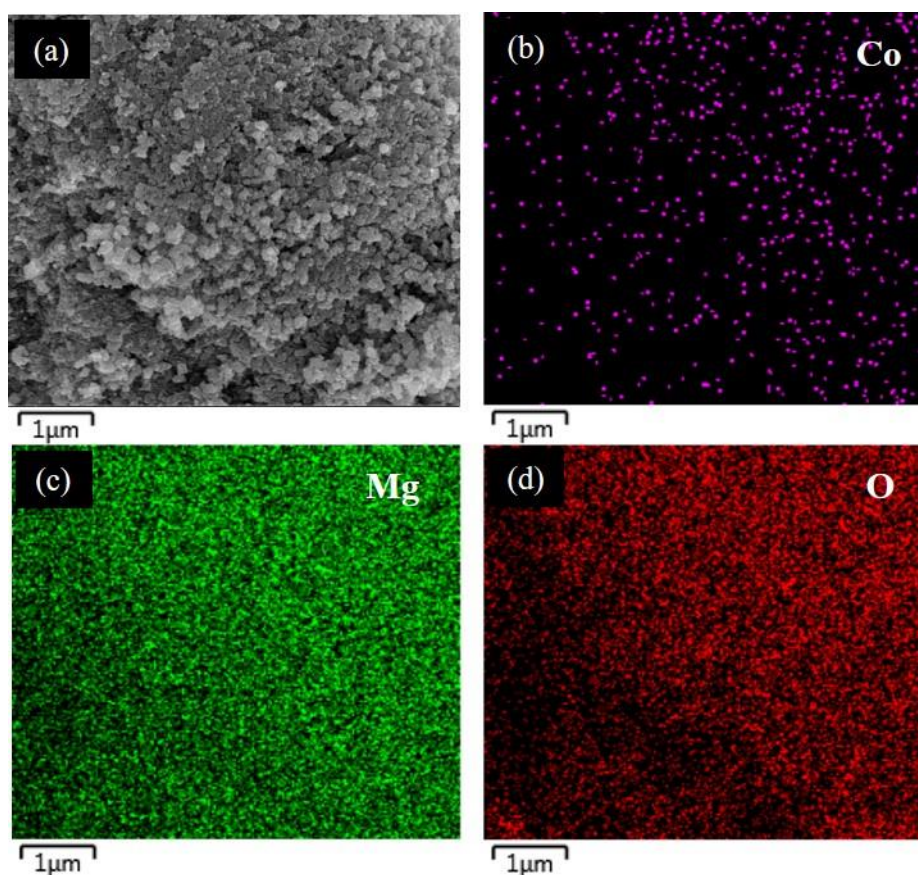


Figure 2: EDS elemental mapping of Co-MgO: (a) SEM image, (b) Co map, (c) Mg map and (d) O map

After CVD, the sample was removed from the furnace and the change in colour of the sample inside the quartz boat was first observed before further examination. The change in colour of the sample from whitish Co-MgO prior to CVD into black powder after CVD can be an early indication of the successful formation of CNT. In order to confirm the role of Co on the growth of CNT, a CVD experiment under similar operating conditions with those used for Co-MgO was also conducted on MgO without Co deposition. It was observed that the sample of bare MgO

turned from white to grey after the CVD process. Raman resonance in both samples show similar spectrum which gave peaks of RBM band, D band, G band and G' band in the region of $\sim 100 - 300 \text{ cm}^{-1}$, $\sim 1328 \text{ cm}^{-1}$, $\sim 1591 \text{ cm}^{-1}$ and $\sim 2625 \text{ cm}^{-1}$, respectively. This is a signature of a single-walled or a double-walled CNT (Li *et al.*, 2005). Hence, the disparity in the darkness level in colour appearance post-CVD between bare MgO and Co-MgO could imply the difference in the amount of grown CNT, by which greater quantity was expected in the darker sample. Observation under SEM further confirmed this manifestation where presence of CNTs were clearly seen in both sample with greater proportion was observed in Co-MgO (Figure 3b). The small amount of CNT found in bare MgO sample (Figure 3a) can be ascribed to the presence of Fe impurities (Dayou *et al.*, 2017b) considering the 98% purity of the commercially obtained raw MgO used in the present work. Previous works had also shown the capability of Fe to catalyze the growth of CNT by CVD (Nishimura *et al.*, 2004; Seah *et al.*, 2012). Further observation under high-resolution TEM in samples with and without the dissolution of MgO revealed a mixture of SWCNT and MWCNT (Figure 3c and 3d). The different type and size of the grown CNT is attributed to the nanoparticle size of the metal catalyst, whereby SWCNT and MWCNT were normally produced by small ($\leq 5 \text{ nm}$) and large-sized particles ($\geq 8 \text{ nm}$), respectively (Moisala *et al.*, 2003; Huang *et al.*, 2012).

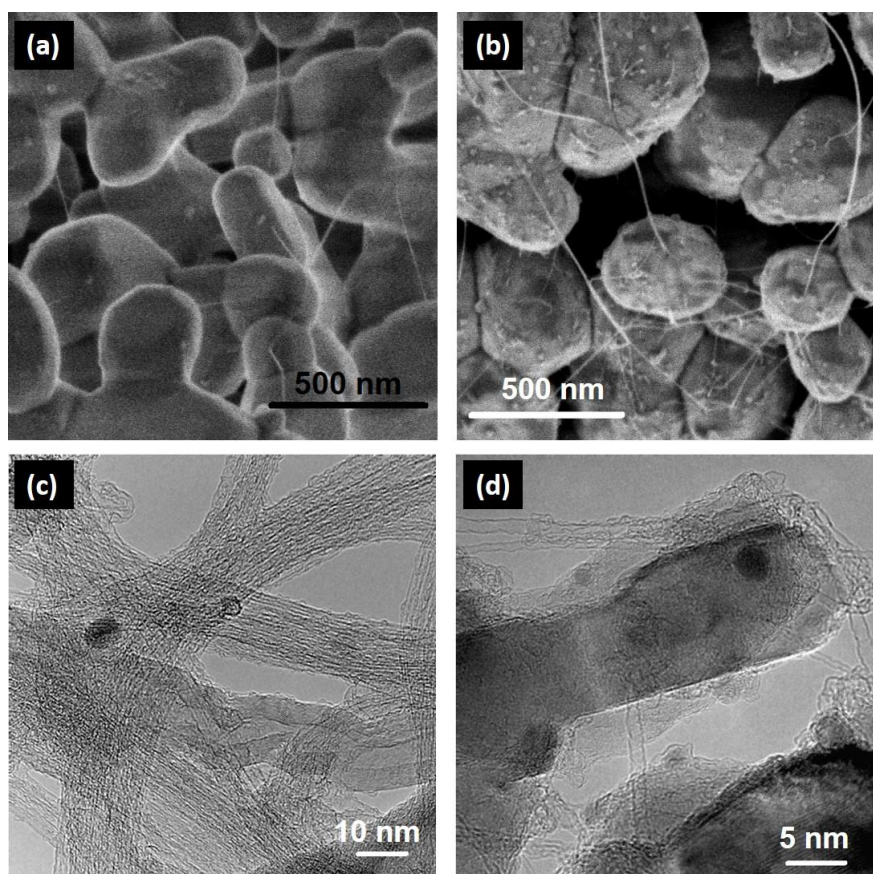


Figure 3: SEM images of post-CVD samples using (a) bare MgO and (b) Co-MgO catalysts; and high-resolution TEM images (c) with MgO solubilization and (d) without MgO solubilization after CVD

The surface morphology of the post-CVD samples clearly show a direct linkage between the CNT tube-end onto the MgO surface (Figure 3b). In addition, the CNT are homogeneously dispersed on the surface of MgO, which could be attributed to the uniform distribution of Co. The growth of CNT can be explained by the vapour-liquid-solid model, i.e. the widely accepted mechanism for CNT growth from the decomposition of carbon feedstock by the CVD reaction (Jourdain and Bichara, 2013). In short, this model describes that carbon dissolution into the catalyst takes place first until supersaturation, which then leads to precipitation of carbon atoms on the catalyst surface before elongation of the tube to form CNT.

In our previous work, the interconnection between MgO and graphene formed by the CVD method produced an 8% increase in thermal conductivity as compared to a non-interconnection state (Dayou *et al.*, 2017a). Compared to graphene, a higher enhancement to the overall conductivity of composite PCM was expected from the grafting of CNT to MgO as it enabled better heat distribution due to its brush-like construction. This allowed heat conduction in the radial direction due to high- K in the axial direction of the columnar CNT. This is in contrast to the localised heat flow pattern in the circumferential direction that can be produced in the composite PCM when using sheet-structured graphene due to its high- K property in planar orientation (Pathak, 2013). The schematic diagram shown in Figure 4 illustrates the comparison related to the aforementioned heat distribution in the composite PCM between

the interconnected CNT-MgO and graphene-MgO system produced by CVD. Furthermore, the fibrous CNT can provide linkage from one to another MgO surface of different particles, which would be unlikely to occur in the case of graphene as far as growth by CVD on the catalyst surface is concerned. This inter-particle contact provided by the grown CNT creates a percolating network, which definitely favours better heat conduction within the bulk composite. Previous work has also shown that multi-walled CNT produced a more effective heat conduction link in composite PCM than graphene, which accounts for 38.41% of the difference in the thermal conductivity enhancement (Tao *et al.*, 2015). Our future work will address the measurement of thermal conductivity of the CNT-MgO composite produced from this work. Although the close interconnection between MgO and CNT produced from the present work may not reduce the thermal contact resistance to a negligible level, the presence of this interconnection would certainly be crucial in enhancing the effective heat conduction for STES material.

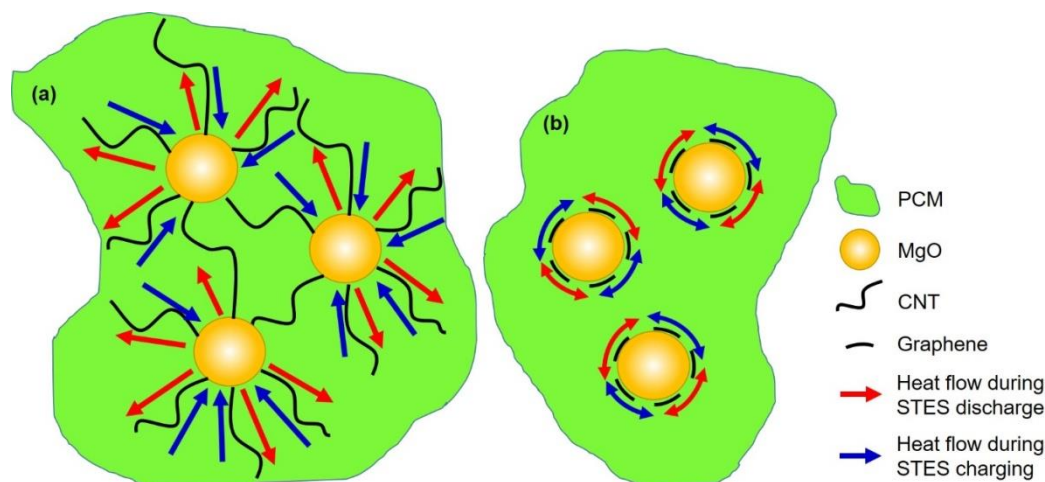


Figure 4: Schematic representation of the comparison between the heat distribution of (a) CNT-MgO and (b) graphene-MgO composite during heat charging and discharge in STES system

4. CONCLUSION

The grafting of CNT on MgO was carried out using the CVD method with the aid of cobalt nanoparticles as catalyst. A wet impregnation method was used to deposit the cobalt nanoparticles evenly on the surface of MgO. The establishment of close interconnection between MgO and CNT in the present work certainly would minimise the thermal contact resistance in the composite PCM. The method presented in this work would be crucial in enhancing the effectiveness of heat conduction, paving the way for the development of high performance STES technology.

5. ACKNOWLEDGEMENT

The present work was supported by Ministry of Science, Technology and Innovation (MOSTI) of the Malaysian Government under ScienceFund grant (Project No.: 03-01-05-SF0659).

6. REFERENCES

- Alva, G., Liu, L., Huang, X. & Fang, G. 2017. Thermal energy storage materials and systems for solar energy applications. *Renewable and Sustainable Energy Reviews*, 68, 693-706.
- Balandin, A. A. 2011. Thermal properties of graphene and nanostructured carbon materials. *Nature Materials*, 10, 569.
- Cui, Y., Liu, C., Hu, S. & Yu, X. 2011. The experimental exploration of carbon nanofiber and carbon nanotube additives on thermal behavior of phase change materials. *Solar Energy Materials and Solar Cells*, 95, 1208-1212.
- Dayou, S., Vigolo, B., Ghanbaja, J., Kairi, M. I., Mohd Zuhan, M. K. N. & Mohamed, A. R. 2017a. Direct growth of graphene on MgO by chemical vapor deposition for thermal conductivity enhancement of phase change material. *Materials Chemistry and Physics*, 202, 352-357.

Dayou, S., Vigolo, B., Ghanbaja, J., Medjahdi, G., Ahmad Thirmizir, M. Z., Pauzi, H. & Mohamed, A. R. 2017b. Direct Chemical Vapor Deposition Growth of Graphene Nanosheets on Supported Copper Oxide. *Catalysis Letters*, 147, 1988-1997.

Ge, Z., Ye, F., Cao, H., Leng, G., Qin, Y. & Ding, Y. 2014a. Carbonate-salt-based composite materials for medium- and high-temperature thermal energy storage. *Particuology*, 15, 77-81.

Ge, Z., Ye, F. & Ding, Y. 2014b. Composite Materials for Thermal Energy Storage: Enhancing Performance through Microstructures. *ChemSusChem*, 7, 1318-1325.

Huang, J., Zhang, Q., Zhao, M. & Wei, F. 2012. A review of the large-scale production of carbon nanotubes: The practice of nanoscale process engineering. *Chinese Science Bulletin*, 57, 157-166.

Jourdain, V. & Bichara, C. 2013. Current understanding of the growth of carbon nanotubes in catalytic chemical vapour deposition. *Carbon*, 58, 2-39.

Kannan, N. & Vakeesan, D. 2016. Solar energy for future world: - A review. *Renewable and Sustainable Energy Reviews*, 62, 1092-1105.

Lahiri, I., Seelaboyina, R., Hwang, J. Y., Banerjee, R. & Choi, W. 2010. Enhanced field emission from multi-walled carbon nanotubes grown on pure copper substrate. *Carbon*, 48, 1531-1538.

Lewis, N. S. 2016. Research opportunities to advance solar energy utilization. *Science*, 351, aad1920.

Li, C., Li, Q., Cong, L., Li, Y., Liu, X., Xuan, Y. & Ding, Y. 2019. Carbonate salt based composite phase change materials for medium and high temperature thermal energy storage: A microstructural study. *Solar Energy Materials and Solar Cells*, 196, 25-35.

Li, L., Li, F., Liu, C. & Cheng, H.-M. 2005. Synthesis and characterization of double-walled carbon nanotubes from multi-walled carbon nanotubes by hydrogen-arc discharge. *Carbon*, 43, 623-629.

Moisala, A., Nasibulin, A. G. & Kauppinen, E. I. 2003. The role of metal nanoparticles in the catalytic production of single-walled carbon nanotubes—a review. *Journal of Physics: Condensed Matter*, 15, S3011-S3035.

Nishimura, K., Okazaki, N., Pan, L. & Nakayama, Y. 2004. In Situ Study of Iron Catalysts for Carbon Nanotube Growth Using X-Ray Diffraction Analysis. *Japanese Journal of Applied Physics*, 43, L471-L474.

Pathak, S. V. 2013. Enhanced Heat Transfer in Composite Materials. Ohio University.

Qiu, L., Scheider, K., Radwan, S. A., Larkin, L. S., Saltonstall, C. B., Feng, Y., Zhang, X. & Norris, P. M. 2017. Thermal transport barrier in carbon nanotube array nano-thermal interface materials. *Carbon*, 120, 128-136.

Seah, C.-M., Chai, S.-P., Ichikawa, S. & Mohamed, A. R. 2012. Synthesis of single-walled carbon nanotubes over a spin-coated Fe catalyst in an ethanol-PEG colloidal solution. *Carbon*, 50, 960-967.

Tao, Y. B., Lin, C. H. & He, Y. L. 2015. Preparation and thermal properties characterization of carbonate salt/carbon nanomaterial composite phase change material. *Energy Conversion and Management*, 97, 103-110.

Yang, J., Yang, Y., Waltermire, S. W., Gutu, T., Zinn, A. A., Xu, T. T., Chen, Y. & Li, D. 2011. Measurement of the Intrinsic Thermal Conductivity of a Multiwalled Carbon Nanotube and Its Contact Thermal Resistance with the Substrate. *Small*, 7, 2334-2340.

Ye, F., Ge, Z., Ding, Y. & Yang, J. 2014. Multi-walled carbon nanotubes added to Na₂CO₃/MgO composites for thermal energy storage. *Particuology*, 15, 56-60.

Zhang, W., Tay, H. L., Lim, S. S., Wang, Y., Zhong, Z. & Xu, R. 2010. Supported cobalt oxide on MgO: Highly efficient catalysts for degradation of organic dyes in dilute solutions. *Applied Catalysis B: Environmental*, 95, 93-99.

#345: Study on controllable electrical nucleation of sodium acetate phase-change material based on anode surface powder-embedded treatment

Hong YU¹, Lizhi ZHANG², Chuanshuai DONG³

¹Key Laboratory of Enhanced Heat Transfer and Energy Conservation of Education Ministry, School of Chemistry and Chemical Engineering, South China University of Technology, Guangzhou 510640, China, hohoyuhong@163.com

²State Key Laboratory of Subtropical Building Science, South China University of Technology, Guangzhou 510640, China, lzzhang@scut.edu.cn

³Key Laboratory of Enhanced Heat Transfer and Energy Conservation of Education Ministry, School of Chemistry and Chemical Engineering, South China University of Technology, Guangzhou 510640, China, dongcs@scut.edu.cn

To provide a stable energy supply from a solar heat pump heating system under different solar radiation intensities, this paper aims at developing a controllable nucleation method using a type of controlled phase-change energy storage material to improve the operating efficiency of the system. Sodium acetate trihydrate is a promising phase-change energy storage material, but it has a serious supercooling effect during solidification. The addition of nucleating agents is a common way to reduce the supercooling degree of sodium acetate trihydrate. The effect of electrode types and activating voltage on the nucleation of supercooled sodium acetate is investigated. The results showed that the copper anode, the silver anode and the silver-plated anode could trigger the nucleation of supercooled sodium acetate solution without adding any nucleating agents. The thickness of metal demonstrated a poor effect on the nucleation of supercooled solution. The rapid nucleation of supercooled solution was achieved by applying a voltage of 1.0 V to 1.8 V to the electrode. When the voltage exceeded 2.0 V, the anode resistance increased with the increasing number of operations, with the surface silver oxide, the trigger efficiency was decreased. This research is very useful to improve the operating performance of the solar heat pump heating system.

Keywords: Sodium acetate trihydrate; copper anode; silver anode; silver-plated anode; solidification process

1. INTRODUCTION

With the increasing global energy crisis, the development of richer, cleaner and more sustainable energy has become the focus of attention in the world. Solar energy is one of the most promising clean energy sources for its immeasurable reserves and wide distribution.

China is abundant with solar energy. About two-thirds of China's land area has an annual average solar radiation of more than $5,000 \text{ J/m}^2$ and an annual average sunshine time of about 2,000 hours (Chyng, Lee *et al.*, 2003). At present, photothermal power generation, photovoltaic power generation, photochemical reaction and direct utilisation of photothermal are the major ways of developing solar energy. Among them, the technology of direct utilisation of photothermal effect can be used for solar heating, as it can directly convert light into heat and collect solar energy through a solar vacuum tube. However, solar energy utilisation is affected by the intermittent and the seasonality of solar illumination. In order to effectively and continuously carry out heating, it is necessary to store heat and release it to make up for the lack of energy when the light is insufficient (Aziz, Chaturvedi *et al.*, 1999). It is obvious that the heat storage technology is the key part for storing heat. Phase-change material has high heat storage density and relatively constant and easily controllable phase transition temperature, thus the application prospect of phase-change material in solar energy storage technology is very broad. Research in phase-change material has become a research hotspot at present (Sharma, Tyagi *et al.*, 2009, Dannemand, Kong *et al.*, 2015).

Inorganic phase-change energy storage material is widely used in solar energy storage technology, industry, agriculture, construction and other fields due to their high heat storage density, low price, wide sources and moderate phase transition temperature (Zalba, Marín *et al.*, 2003). However, because of the inherent supercooling effect of the inorganic phase-change energy storage material, the nucleation of the material in its supercooled solution is hard to control (Johansen, Dannemand *et al.*, 2015). The key to solving this problem is the triggering technique, which is to control the nucleation exotherm timing in the supercooled solution. There are two primary conditions for the controllable nucleation crystallisation of phase-change material. One is the sufficient subcooling degree for material which requires the material to remain as liquid state at low temperature; the second is a fast and effective triggering technique. At present, the methods for triggering the phase change crystallisation of supercooled salt solution mainly include adding nucleating agents, mechanical vibration (Rogerson & Cardoso, 2003a; Rogerson and Cardoso, 2003b), ultrasonic nucleation (Miyasaka, Ebihara *et al.*, 2006; Seo, Suzuki *et al.*, 2012), and applying voltage (Ohachi, Hamanaka *et al.*, 1990).

Kashchiev (Kashchiev, 1972) believed that the promotion or inhibition of the nucleation process by the electric field depended on the ratio of the dielectric constant of the new phase to the old phase. When the dielectric constant of the nucleation phase is less than that of the solution, the electric field promotes the nucleation process. Yoshii and Kuraoka (Yoshii, Kuraoka *et al.*, 2002) studied the effects of sodium hydroxide concentration on the electrical nucleation mechanisms and electrical nucleation induction time of sodium acetate trihydrate by using copper amalgam electrode and silver electrode. The electrical nucleation induction time is an important factor in initiating SAT nucleation in the system after electrical stimulation is triggered. However, there are few systematic studies on the optimised voltage range, the silver electrode specifications and other parameters for electrical nucleation. Sakurai and Yoshinaga (Sakurai, Yoshinaga *et al.*, 2018) sprinkled sodium acetate trihydrate crystals into the surface of the Ag anode in supercooled aqueous solution of sodium acetate (45wt%-54wt%) to make a latent heat storage device. Their experimental results showed that the fast response voltage range of electrical nucleation was 1.4 ~ 1.8 V, and the optimised surface roughness of Ag anode was 0.6 ~ 1 μm . Munakata and Nagata (Munakata and Nagata, 2010) studied the effect of growth direction of electric nucleation crystal on its growth rate. The results showed that the growth rate of crystal growing from bottom to top was higher than that growing from top to bottom in a certain range of supercooled temperatures.

In this paper, the thermodynamic properties of sodium acetate solution and its supercooled stable state are studied. In addition, a technique for controlling the rapid nucleation of supercooled sodium acetate solution is introduced, which used a surface treated anode to investigate the effects of voltage and the size of anode on the electrical nucleation of sodium acetate trihydrate. The influence of different voltage conditions and types on electrical nucleation was also studied.

2. EXPERIMENTAL PROCEDURERE

Figure 1 shows the schematic diagram of the experimental apparatus. The experimental apparatus consists of 25 ml glass bottle, data logger, direct-current power supply, digital display constant temperature water bath, K type thermocouple, power cord and switch. The anodes used in the experiment were polished by sandpaper with a grit of P80 and the sodium acetate trihydrate (SAT) powder was sprinkled onto the surface of the anodes, and then polished by sandpaper with a grit of P360 and the SAT powder was sprinkled onto the surface of the anodes again. Finally, the anodes were polished by sandpaper with a grit of P1200. After that, the anodes were placed in 75°C sodium acetate trihydrate solution for 2 hours to remove the excess SAT powder.

In this paper, a small amount of distilled water was added into the crystal of sodium acetate trihydrate to prepare sodium acetate solution with concentrations of 45wt%, 50wt%, 55wt%, 50wt%+1wt% CMC (cellulose glycolate), 55wt%+1wt% CMC. Then the glass bottle was put into the constant temperature water bath with the water temperature at 75°C. After the crystal of sodium acetate trihydrate was completely melted, the sodium acetate solution was kept warm for 2 hours then air-cooled to room temperature. A voltage of 0.2 ~ 1.8 V was applied to the electrodes to observe the effects of voltage on the nucleation and crystallisation of supercooled sodium acetate solution.

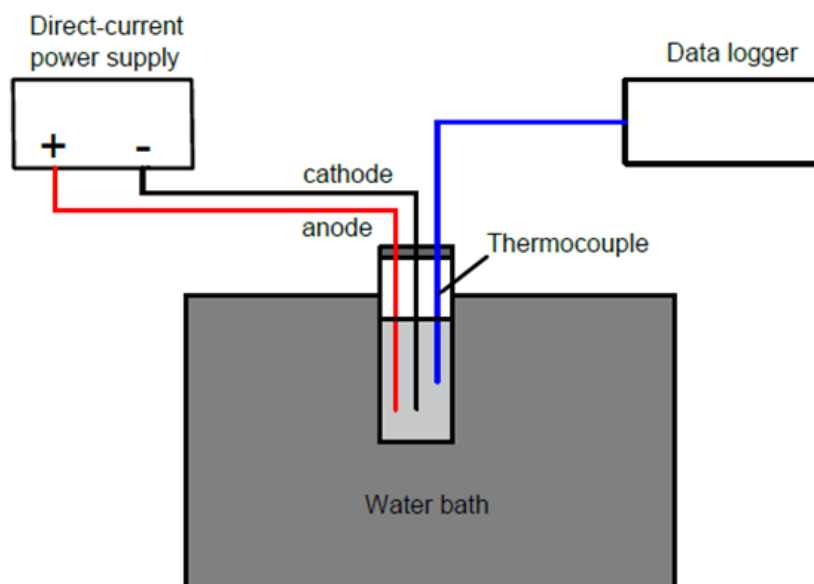


Figure 1: Schematic of the experimental apparatus

3. RESULTS AND DISCUSSION

3.1. Cooling curve of sodium acetate trihydrate solution

Due to the supercooling phenomenon of sodium acetate solution, it did not spontaneously turn into crystals at low temperature. Therefore, SAT crystal were used to induce nucleation when the temperature dropped to 36°C or so. The change curve of temperature with time is shown in the Figure 2.

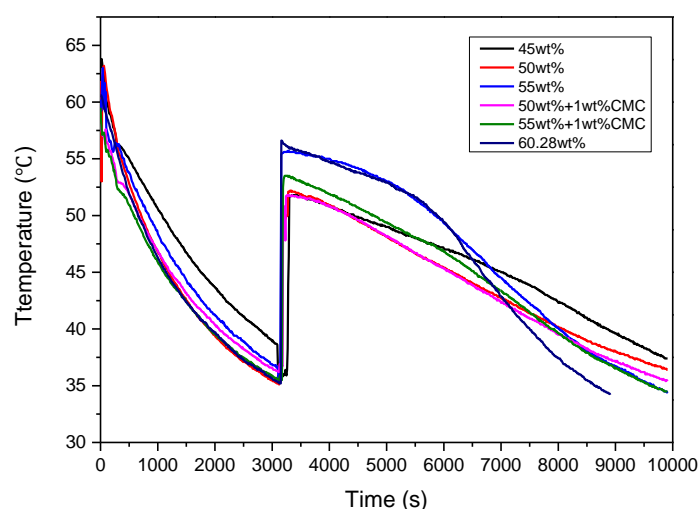


Figure 2: Cooling curve of sodium acetate trihydrate solution in different concentration

It can be seen from Figure 2 that, under the same concentration, the maximum temperature with the thickener addition decreased. The maximum temperature of the supercooled solution of sodium acetate in 50wt%+1wt% CMC was 51.8°C, which was 0.4°C lower than that of solution of 50wt%. The maximum temperature of the

supercooled solution of 55wt%+1wt% CMC was 53.5°C, which was 2.2°C lower than that reached by 55.7°C in 55wt%. Even though the highest temperature reached by exothermic solution of sodium acetate trihydrate (60.28wt%) without additional water was 56.6°C, 0.9°C higher than the 55wt% dose, the sodium acetate trihydrate without additional water had a serious phase separation phenomenon even at the first melting time, as show in Figure 3. Therefore, sodium acetate solutions with concentrations of 50wt% and 55wt% were selected in this paper to investigate the controlled electrical phase-change of supercooled sodium acetate solution.



Figure 3: solution of 60.28wt% has serious phase separation at the first time melting

3.2. Effect of anode types on electrical nucleation

The key to the nucleation of supercooled sodium acetate solution induced by an electric field is the surface condition of the electrode and the applied voltage. Several common electrodes were selected to study the influence of electrode surface condition on electrical nucleation, as shown in Table 1.

Table 1: Effect of electrodes on the electrical process

Electrode (+) – (-)	Treatment for electrode	Nucleation
Cu – Graphite	None	No
Ag – Graphite	None	No
(Ag-plated) – Graphite	None	No
Cu – Graphite	polishing	No
Ag – Graphite	polishing	No
(Ag-plated) – Graphite	polishing	No
Cu – Graphite	Polishing and sprinkling powder	Yes
Ag – Graphite	Polishing and sprinkling powder	Yes
Ag – Cu	Polishing and sprinkling powder	Yes
Ag – (Ag-plate)	Polishing and sprinkling powder	Yes
(Ag-plated) – Graphite	Polishing and sprinkling powder	Yes

As shown in Table 1, the smooth surface anode electrodes without any treatment did not trigger the nucleation of the supercooled sodium acetate solution, nor did the polished anode electrodes without powder on the surface. However, the polished anode electrodes with powder did trigger the phase-change of supercooled liquid quickly and effectively. It was also found that the choice of cathode electrode material had little effect on the electrical nucleation process.

We also observed that the thickness of the electrodes with powder demonstrated poor effect on the nucleation of supercooled solution as shown in Figure 4. In the experiment, we applied 1 V voltage to different sizes of silver anode, silver-plated anode and copper anode, and found that the nucleation of supercooled sodium acetate solution could be induced.

As the corrosion of copper electrode in the sodium acetate solution was serious, the silver anode and silver-plated anode was selected in this study to investigate the effects of applied voltage on the electrical nucleation process of supercooled sodium acetate solution.

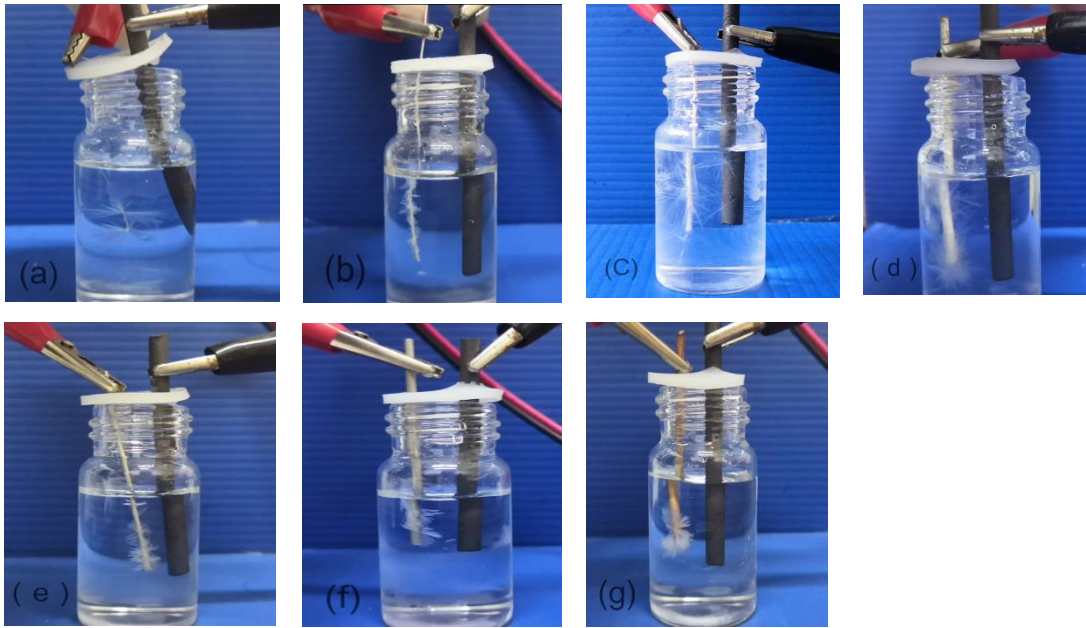


Figure 4: the nucleation process of supercooled solution triggered by different anodes with different sizes at a voltage of 1 V. (a) silver anode with diameter of 0.2 mm, (b) silver anode with diameter of 0.5 mm, (c) silver anode with diameter of 1 mm, (d) silver anode with diameter of 1 mm, (e) silver anode with diameter of 2 mm, (f) copper anode with diameter of 2 mm.

3.3. Effect of applied voltage on electrical nucleation process

According to the theory of Kashchiev (Kashchiev, 1972), when the dielectric constant of crystal phase is lower than that of solution, the electrical nucleation process occurs easily. Once the crystals begin to grow without any interruption, they will not stop until they are fully crystallised. There exists a trigger time between the application of voltage and the beginning of crystallisation. The trigger time is affected by the applied voltage and the size of electrode, as shown in Figure 5 and Figure 6.

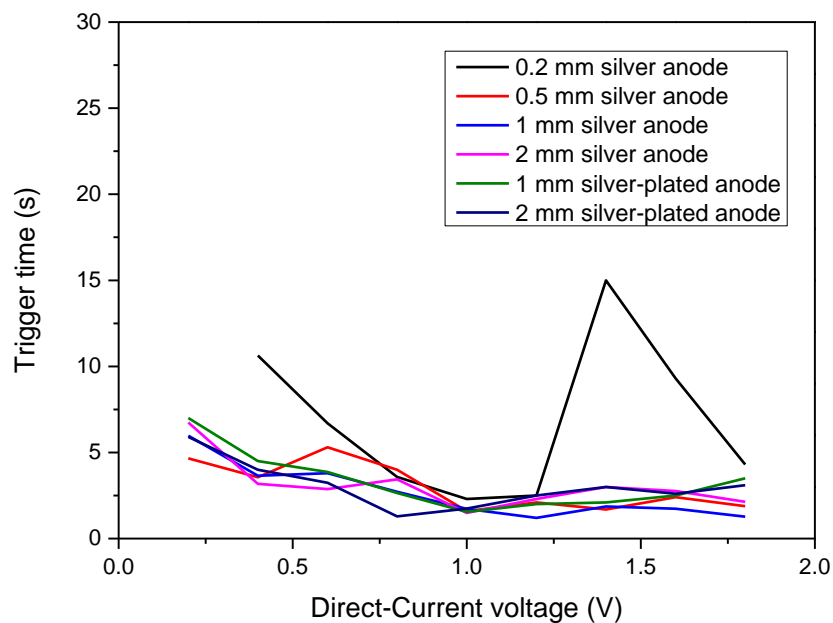


Figure 5: The trigger time for 50 wt% sodium acetate solution with different applied voltage values and electrode diameters

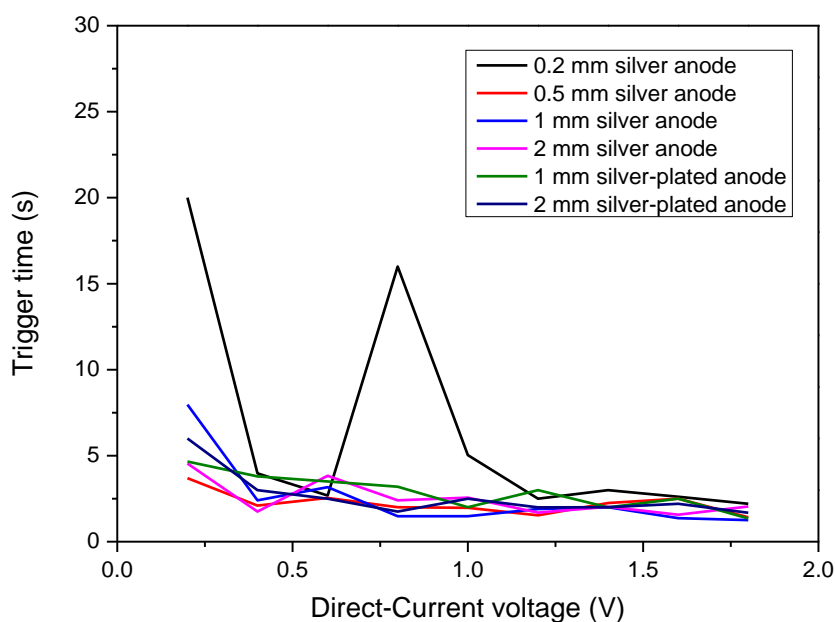


Figure 6: The trigger time for 55 wt% sodium acetate solution with different applied voltage values and electrode diameters

The experimental results show that the applied voltage could quickly and effectively trigger the nucleation of supercooled solution. The anodes with diameter of 0.5mm to 2mm can trigger the nucleation within 10 seconds. While the silver electrode with a diameter of 0.2 mm can also trigger the nucleation, but the effect was very unstable. For the systems with anodes diameter of 0.5mm to 2mm, with the increase of applied voltage, the trigger time decreased, and at the voltage of 0.5 V to 1.8 V, the trigger time was stable within 5 seconds. We observed that the crystal growth rate of the supercooled solution with a voltage of less than 0.8 V was slow, while the crystal growth rate of the supercooled solution with a voltage of more than 1 V was relatively fast. When the applied voltage was more than 1.8 V, the anodes started to oxidise on their surface after being used many times, and then the electrical nucleation did not easily happen.

4. CONCLUSIONS

A new electrical nucleation technology was developed in this study. The effect of anode types, triggering voltage as well as the anode thickness were extensively investigated. The main achievements are as follows:

- The solution of sodium acetate with a concentration of 50wt%-55wt% had a stable supercooling degree and a good phase transition temperature range.
- Without the addition of nucleating agent, the powder-embedded copper anode, silver anode and silver-plated anode triggered the nucleation of supercooled sodium acetate solution, while the trigger of silver anode and silver-plated anode was more effective and stable.
- The supercooled solution can rapidly response to nucleation when the anode diameter was 0.5 to 2 mm, and the voltage was 1 to 1.8 V.

5. REFERENCES

- Aziz, W., Chaturvedi, S.K. and Kheireddine, A. (1999). "Thermodynamic analysis of two-component, two-phase flow in solar collectors with application to a direct-expansion solar-assisted heat pump." *Energy* **24**(3): 247-259.
- Chyng, J.P., Lee, C.P. and Huang, B.J. (2003). "Performance analysis of a solar-assisted heat pump water heater." *Solar Energy* **74**(1): 33-44.
- Dannemand, M., Kong, W., Fan, J., Johansen, J.B. and Furbo, S. (2015). "Laboratory Test of a Prototype Heat Storage Module Based on Stable Supercooling of Sodium Acetate Trihydrate." *Energy Procedia* **70**: 172-181.
- Johansen, J.B., Dannemand, M., Kong, W., Fan, J., Dragsted, J. and Furbo, S. (2015). "Thermal Conductivity Enhancement of Sodium Acetate Trihydrate by Adding Graphite Powder and the Effect on Stability of Supercooling." *Energy Procedia* **70**: 249-256.

- Kashchiev, D. (1972). "Nucleation in external electric field." *Journal of Crystal Growth* **13-14**: 128-130.
- Miyasaka, E., Ebihara, S. and Hirasawa, I. (2006). "Investigation of primary nucleation phenomena of acetylsalicylic acid crystals induced by ultrasonic irradiation—ultrasonic energy needed to activate primary nucleation." *Journal of Crystal Growth* **295**(1): 97-101.
- Munakata, T. and Nagata, S. (2010). Electrical initiation of solidification and preservation of supercooled state for sodium acetate trihydrate. 2010 14th International Heat Transfer Conference, IHTC14, August 8, 2010 - August 13, 2010, Washington, DC, United states, American Society of Mechanical Engineers (ASME).
- Ohachi, T., Hamanaka, M., Konda, H., Hayashi, S., Taniguchi, I., Hashimoto, T. and Kotani, Y. (1990). "Electrical nucleation and growth of NaCH₃COO·3H₂O." *Journal of Crystal Growth* **99**(1): 72-76.
- Rogerson, M.A. and Cardoso, S.S.S. (2003a). Solidification in heat packs: II. Role of cavitation.
- Rogerson, M.A. and Cardoso, S.S.S. (2003b). "Solidification in heat packs: III. Metallic trigger." *AIChE Journal* **49**(2): 522-529.
- Sakurai, K., Yoshinaga, N., Yagi, R., Tomimatsu, N. and Sano, K. (2018). "Effect of embedding sodium acetate trihydrate on the Ag anode in an electrical nucleation cell of a supercooled latent heat storage material." *Solar Energy* **173**: 1306-1314.
- Seo, K., Suzuki, S., Kinoshita, T. and Hirasawa, I. (2012). "Effect of Ultrasonic Irradiation on the Crystallization of Sodium Acetate Trihydrate Utilized as Heat Storage Material." *Chemical Engineering and Technology* **35**(6): 1013-1016.
- Sharma, A., Tyagi, V.V., Chen, C.R. and Buddhi, D. (2009). "Review on thermal energy storage with phase change materials and applications." *Renewable and Sustainable Energy Reviews* **13**(2): 318-345.
- Yoshii, Y., Kuraoka, M., Sengoku, K. and Ohachi, T. (2002). "Induction time and three-electrode current vs. voltage characteristics for electrical nucleation of concentrated solutions of sodium acetate trihydrate." *Journal of Crystal Growth* **237-239**: 414-418.
- Zalba, B., Marín, J.M., Cabeza, L.F. and Mehling, H. (2003). "Review on thermal energy storage with phase change: materials, heat transfer analysis and applications." *Applied Thermal Engineering* **23**(3): 251-283.

#348: Energy performance of venetian blinds in south-oriented residential spaces in Cairo

Impact of three parameters: location, reflectivity and slat angle

Khaled EL-DEEB

Alexandria University, Egypt, km_eldeeb@yahoo.com

The Egyptian capital, Cairo, has a massive building stock and it is currently experiencing mega-scale urban extension projects that will lead to a significant increase in the city's built-up area, and consequently, in the energy needed to run those buildings, making it a necessity to rationalise energy use.

Although window shading can help reduce energy consumption, it is rarely implemented in both existing and newly proposed residential building designs. End-users, then, usually install internal shading devices either to achieve privacy and indoor aesthetics or to block the sun. However, inappropriate shading may cause an increased use of artificial lighting and, in turn, an increase in internal loads on the HVAC (Heating, ventilation and air conditioning) system. Thus, a careful selection and adjustment of shading devices becomes crucial.

Venetian blinds (VBs) are a type of adjustable shading device that can be installed to the interior, exterior or in between glass panes of a window and that can be easily employed in both new and existing buildings. VB attributes are expected to affect the blind's energy performance. This study investigated the impact of three VB parameters: location, slat angle and reflectivity on the overall energy consumption of a residential space with a south-facing facade in the climate of Cairo.

A test room was modelled for energy simulation with a 20% window-to-wall ratio. A venetian blind was assigned with alternatives being located to the indoor, outdoor or in between double glazed panes. High, medium and low reflectivity values were applied at each location at slat angles of 15°, 30°, 45°, 60°, 75° and 90°.

Results showed VB performance across slat angles, where up to 22% energy savings were achieved by mid-pane high reflectivity VBs, while the value exceeded 33% where they were externally located.

Keywords: Venetian blinds; slat attributes; window shading; energy consumption; building performance simulation

1. INTRODUCTION

Residential Buildings are responsible for 50.5% of the total energy consumption in Egypt (Ministry of Energy and Renewable Energy, 2017). Currently, a number of mega-scale projects of cities and urban settlements are being constructed in the country. Some of these projects are wide extensions to the highly-populated capital, Cairo. Energy consumption is, therefore, anticipated to significantly increase in response to both the existing building stock and the under-construction projects which both include a majority of residential buildings. Thus, the need to rationalise energy use and minimise consumption is now more demanding.

Window shading is rarely considered in residential building designs, despite its potential to minimise energy consumption. Occupants usually install internal shading devices either to achieve privacy and indoor aesthetics or to block the sun. However, inappropriate shading may decrease daylight availability indoors to the extent that increases the need for artificial lighting and its consequent energy consumption. In addition, the more artificial lighting is used, the more internal thermal loads are placed on the HVAC system, also resulting in more energy consumption. Thus, a careful selection and adjustment of shading devices becomes crucial in order to minimise the overall consumed energy.

Venetian Blinds (VBs) with horizontal slats represent one type of adjustable easily installable shading device which can be placed either to the inside or outside of a window, or between the panes of a double glazed window. As with any other shading device, VBs have an impact on the daylighting, thermal and energy performance of a building which occurs in response to properties of the device and to the climate and solar profile in the place it is used in. In the case of VBs, a group of attributes and parameters are expected to affect the performance such as the blind's location in the window-blind composition, optical properties, slat-angle (SA), dimensions, proportions and type of blind control. VBs are assumed to be of benefit - in terms of energy consumption - for use in Cairo, however, the properties of the blind that will lead to a better performance are a matter of question.

Literature shows that a wide range of VB aspects and parameters have been investigated. A number of studies approached VBs in terms of daylighting, energy and thermal performance and solar heat gain. Some research work focused on developing detailed methods for the calculation of optical and visible properties (transmittance, reflectance and absorptance) of the slats and the window-blind system as a means for reducing solar gain, whilst others addressed VB dimensional properties such as slat tilt angle, slat-to-slat vertical distance, thickness, geometry, proximity to glass. In addition, some research work was applied to blind control effect and methods, while other work investigated the potential of VB in energy harvesting. Some of these efforts are summarised below.

Cho *et al.* (1995) developed an analytical model for heat transfer through a double-pane window with a mid-pane VB, and quantified the effect of slat tilt angle on heating and cooling loads for buildings in Seoul, South Korea. Tzempelikos (2008) estimated the impact of slat geometry, tilt angle and reflectance on the window-blind effective reflectance and developed an analytical method for calculation of view fractions and direct-to-direct transmission. The impact of slat angle was also investigated by Popovici *et al.* (2016) in relation to dynamic insulation efficiency of a double skin façade and by Simmler and Binder (2008) along with colour and reflectivity on total solar energy transmittance of multiple glazing with outdoor-located VBs. Collins and Harrison (2004) presented a method for predicting convective, radiative and total heat transfer from the inner surface of a window with a VB and a method for predicting solar heat gain coefficient for a window and VB combination. Gomes *et al.* (2014) described a net radiation method for determining solar optical and visible properties of glazing systems with VBs, while the effect of VB attributes on U-value and SHGC of the glazing system was studied by Ariosto and Memari (2014).

Chaiyapinunt and Khamporn (2013 and 2014) investigated heat gain due to the shortwave part of solar radiation for windows with curved VBs and studied the effect on heat transmission for VB parameters including slat angles 0° and 45°, curvature, spacing and proximity to glass as well as slat optical properties. Proximity of indoor-placed VB to glass was also explored by Shahid and Naylor (2005) for its effect on energy performance, while the influence of proximity to the exterior skin was investigated by Parra *et al.* (2015) for the case of a double skin façade along with the effect of differentiated surface treatment for the exterior and interior faces of the VB louvers on thermal performance. The potentials of using VB for energy harvesting was explored by Velasco *et al.* (2017) by means of using blind slats as thermal collectors through circulating water in the void of hollow aluminium slats implemented in nitrogen-filled gap of a double-skin system, where a large reduction in solar heat gains was achieved.

A slat angle control strategy was developed by Kim *et al.* (2007) for VBs in office buildings to adjust the solar radiation for improving both energy efficiency and visual comfort. Another strategy for both slat angle and up/down controls was presented by Oh *et al.* (2013) for minimising energy consumption and removing glare in an office building in Daejeon city, South Korea. Kwon *et al.* (2018) developed a VB control algorithm according to change in orientations and window-to-wall ratios for minimising energy consumed. Eltaweel and Su (2017) proposed a parametric method for individual control of each VB slat to harmoniously distribute reflected daylight to the ceiling

of an office building in Cairo. Karjalainen (2018) developed a strategy to control VBs in a way that takes into account the effect on both solar transmission and heat loss through windows in European climates.

Despite the fact that Venetian blinds are available for use in residential buildings just as they are in office buildings, most of the literature addressed the latter type. Literature also showed that the impact of VB parameters on energy performance in residential buildings, especially for the case of Cairo, was hardly quantified. This research aimed to investigate the impact of three VB parameters on the overall energy consumption of both HVAC and artificial lighting systems, for a South-oriented residential space in the hot arid climate of Cairo. The examined parameters included: slat angle, reflectivity and location. The study explored and quantified the potential energy savings that could be achieved through appropriate selection of VB parameters by examining a matrix of alternatives of VB parameters.

2. METHODOLOGY

A test room of 4.2 x 4.2m representing a residential space with one side exposed to external climatic conditions was modelled for energy simulation using the DesignBuilder tool. The south-oriented wall included a window with window-to-wall ratio 20%, while the other three walls were considered adiabatic. A base case with no shading device was simulated for energy performance, then a matrix of VB alternatives representing the three investigated parameters were assigned to the window and simulated. The matrix was developed as shown in Figure 1.

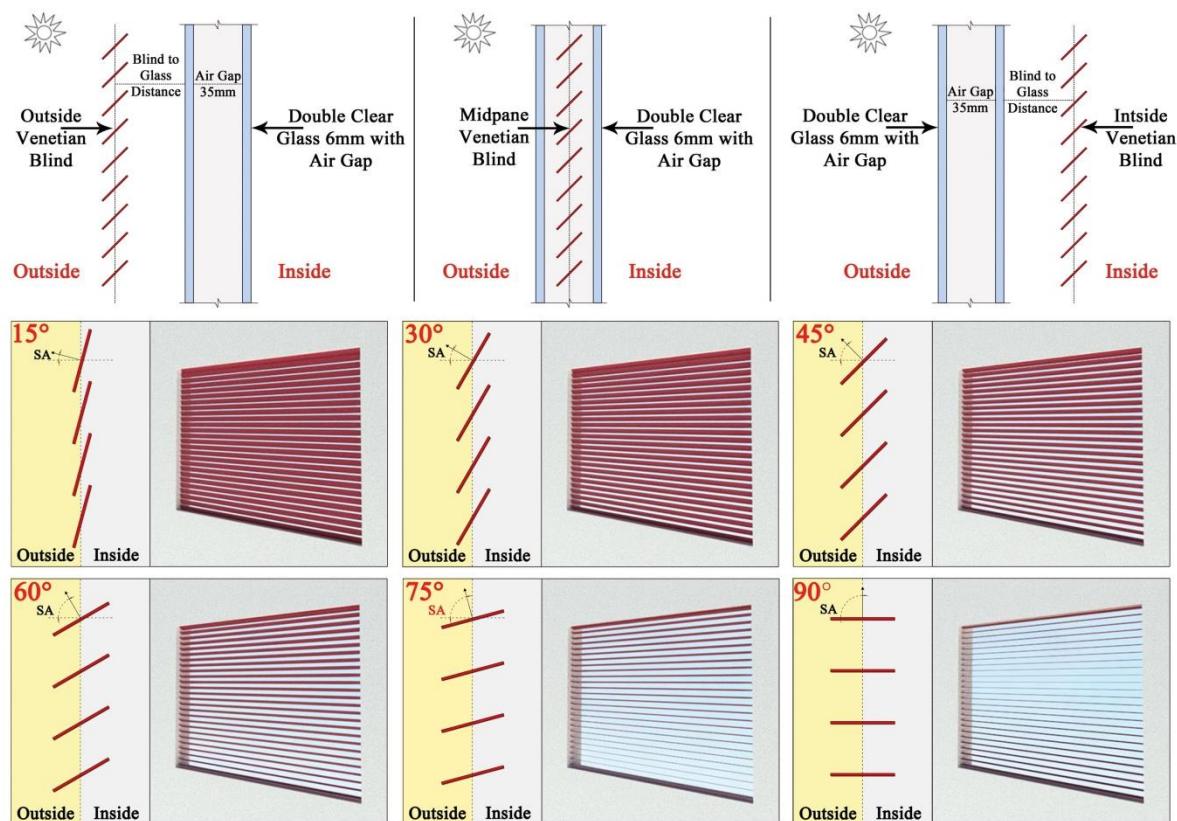


Figure 1: Geometry of studied parameters (VB positions and slat angles).

An occupancy schedule that accounted for the presence of 50% of occupants during day time was assigned to consider the common practice of presence of housewives and/or elderly people at home in the morning, as presented in Figure 2. A light sensor was placed in the middle of the room to measure the amount of indoor illuminance achieved by natural lighting; meanwhile a dimmable artificial light controlled by the sensor was conditionally used in case illuminance fell below the threshold. For that, the artificial lighting schedule was kept "ON" during daytime as it would be turned off when the threshold was naturally maintained. Using a split HVAC unit, the room was air-conditioned to ensure maintaining thermal comfort.

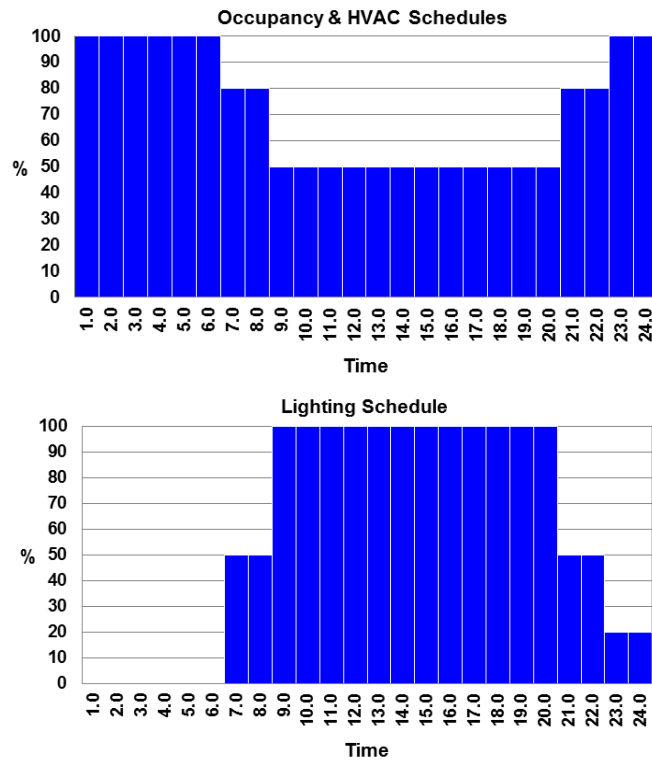


Figure 2: Shows occupancy and HVAC schedules (left) and lighting schedule (right).

A double glazed window was used for all cases in order to neutralise the effect of the number of glass layers when comparing the performance of VBs despite the possibility to install indoor and outdoor-located VBs on single glazed windows. A detailed model description and simulation parameters are presented in Table 1.

Table 1: Simulation parameters of the model.

SIMULATION PARAMETERS			
Test Room		Construction	
Dimensions	4.2 X 4.2 m	Walls	20cm concrete block + 2cm cement plaster each side
Occupancy	0.0566 person/m ²	Infiltration	0.500 (ac/h)
Activity	Residential	Lighting	
Windows		Type	Suspended Fluorescent
Glazing	Double Clear 6mm/35mm Air	Daylighting Control	Illuminance: 150 lux Dimming: On/off Sensor Height: 0.8m
WWR	20%	HVAC	
Shading	Fixed Venetian Blinds	Cooling	23
Slat Angles	15°, 30°, 45°, 60°, 75° & 90°	Heating	21
Locations	Inside, In the middle of double glass panes (Mid-pane) & Outside	Type	Split
Slat Reflectivity	High (80%), Medium (50%) & Low (20%)		

Simulations were performed under the climate of Cairo, classified by Köppen Geiger classification (Kottek *et al.*, 2007) as hot arid. Figure 3 shows monthly mean high and low temperatures in the city, demonstrating that mean high air temperatures rise above comfort level most of the year, reaching up to 32-34°C from June to September.

3. BASE CASE RESULTS

The base case showed a high domination of cooling energy consumption for both artificial lighting and heating. The energy use intensity (EUI) was 80.57kwhr/m² of which cooling energy consumption was 70.9kwhr/m², equivalent to approximately 88% of the overall consumed energy, followed by artificial lighting EUI 9.7kwhr/m², representing approximately 12%, while heating consumption was very small and nearly negligible, Figure 4. Heat gain (HG) and transmitted solar radiation (TSR) through the south-facing window are presented in Figure 5.

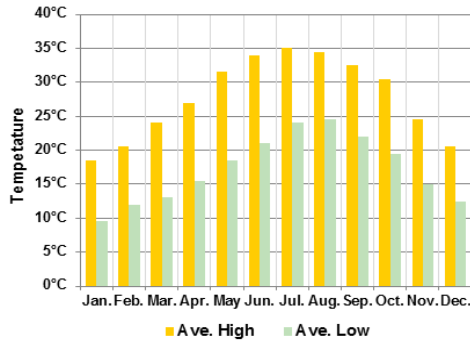


Figure 3: Monthly mean high and low temperatures in Cairo.

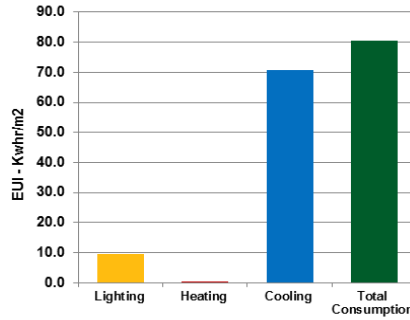


Figure 4: Base case: Annual EUI.

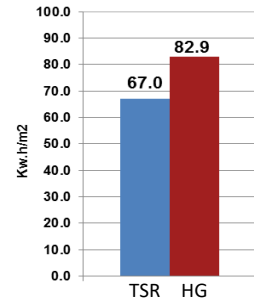


Figure 5: Base case: Annual TSR & HG.

4. VENETIAN BLIND PARAMETERS RESULTS

The examined parameters showed a mutual impact on the thermal, daylight and energy performance. The magnitude of slat angle effect differed across the three reflectivity values, while the impact of both parameters was different across the investigated VB locations. The amount of solar radiation transmitted through the window-VB composition depended on both slat angle and reflectivity, which both affected daylight availability and indoor illuminance levels. Heat gain through the composition depended on both parameters, as well as on the location of the blind, where solar radiation was reflected or absorbed. The combined effect of the three parameters created the overall impact on energy performance.

4.1. Transmitted solar radiation (TSR)

Transmitted solar radiation decreased by installing a shading device on the window. The values of TSR varied depending on two of the three examined parameters (slat angle and reflectivity) while the location parameter did not show any considerable effect and its values nearly coincided. Figure 6 shows the amount of solar radiation transmitted through the window-VB composition at each case as a percentage of the base case. The more closed the SA, the lower the TSR value and the narrower the difference between the three reflectivity cases was. Significantly higher values and differences were recorded at more opened SAs. At SA 15° – the most closed angle – all TSR values were below 10% compared to the base case, with less than 6% difference between the high reflectivity (HR) and low reflectivity (LR) cases. This difference increased to reach more than 21% at SA 90° as TSR increased in a quasi-linear form directly proportional to slat angle but not with the same slope. The increase in TSR compared to the base case between SAs 15° to 90° reached 19.8% at LR case and 35.7% at HR one, while the medium reflectivity (MR) case came in between. These results directly impacted artificial lighting energy consumption that is discussed later in the energy section.

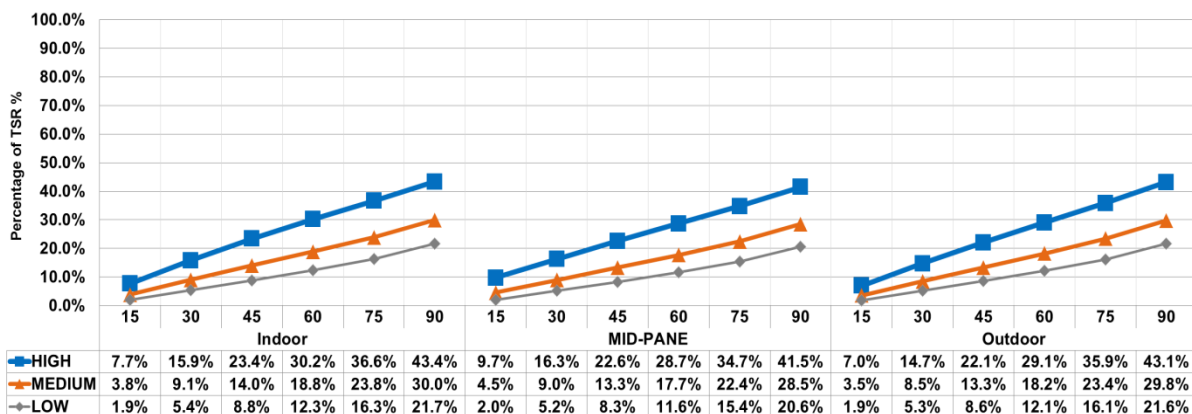


Figure 6: Percentage of transmitted solar radiation compared to base case.

4.2. Heat gain (HG)

All shaded cases led to a decrease in HG, whose values were influenced by the three parameters: slat angle, reflectivity and location. Figure 7 demonstrates the percentage of HG compared to that of the base case for all examined alternatives.

Slat angle effect

The more opened the SA was, the more heat was gained. However, the magnitude of change in the amount of heat gained due to change in SA was not constant in all cases as it was affected by both reflectivity and location of the blind. This magnitude was traced by subtracting values demonstrated in Figure 7 at SA 90° minus those at SA 15°. The resulting values are presented in Table 2, which showed that the impact of SA increased both as reflectivity increased and as the blind was moved a step to the outside. For example, at the LR blind case, the magnitude of change in HG increased from 8.4% for the indoor-located blind to 12.2% for the blind positioned in between the glass panes, then further increased to 16.8% for the outdoor location. The same occurred for MR and HR cases. On the other hand, for the same indoor-location, for example, the magnitude increased from 8.4% for LR blind to 17.1% for MR and further to 25.8% for the HR one. Similar results were achieved at mid-pane and outdoor locations.

Reflectivity and location effect

Heat gain decreased as the VB was located to the outside. The best performance was for outdoor-placed VBs followed by mid-pane cases then by those placed indoors. Figure 8 shows the relation between reflectivity and location regarding their impact on heat gain. HG performance of the blind depended on the place where the solar radiation was absorbed or reflected. For that, LR blinds, which were the most absorbing ones, were the highest in heat gain when located indoors and as the radiation was absorbed after passing through the double layered glass, and re-emitted as long-wave radiation which was trapped inside the glass by greenhouse effect. On the other hand, when located outdoors, these LR blinds changed to be the lowest in heat gain as the radiation was mostly absorbed and re-emitted before reaching the window and with minimum reflected radiation. The opposite occurred with HR cases. For that reason, HR blinds performed best at indoor and mid-pane locations where shortwave radiation was reflected to the outside through the glass, whilst they had the worst heat gain performance when placed outdoors as more radiation was reflected towards the indoor compared to lower reflectivity blinds. The blinds' HG performance directly impacted the cooling energy needed by the HVAC system.

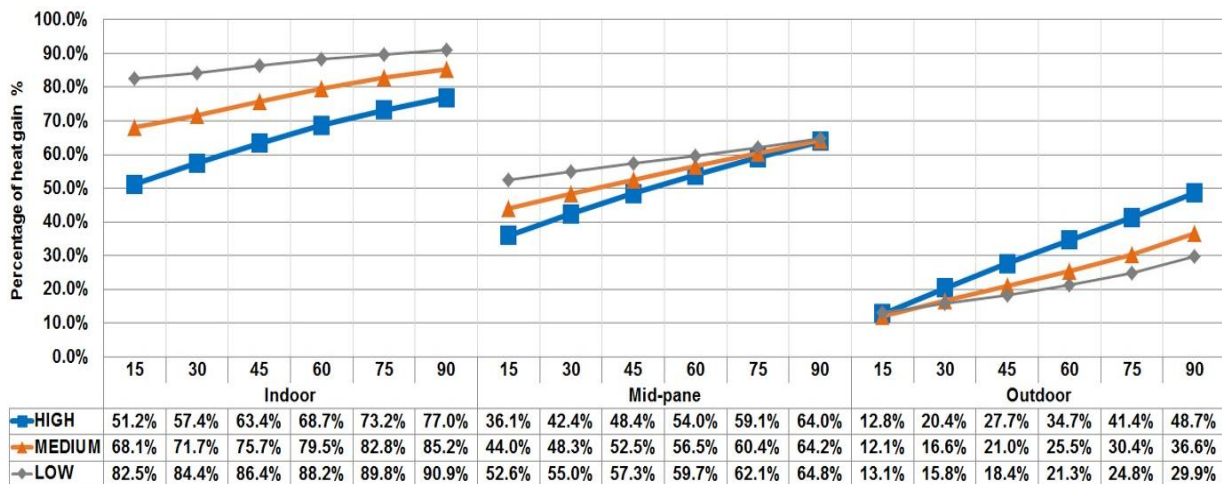


Figure 7: Percentage of heat gain compared to the base case showing impact of SA and reflectivity at each location.

Table 2: Magnitude of change in HG due to change in SA for different blind location and reflectivity cases.

Difference between SA 90° and SA 15° in percentage of heat gain compared to base case			
	Indoor	MID-pane	Outdoor
Low Reflectivity (LR)	8.4	12.2	16.8
Medium Reflectivity (MR)	17.1	20.2	24.5
High Reflectivity (HR)	25.8	27.9	35.9

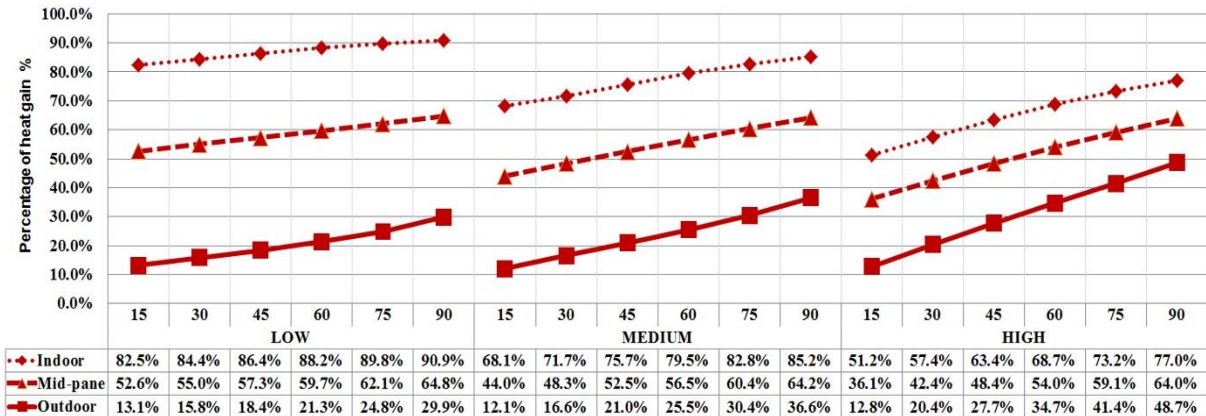


Figure 8: Percentage of heat gain compared to base case showing the impact of VB location at each SA and reflectivity value.

4.3. Energy consumption (EC)

The VB shading device led to an increase over the base case in the energy needed for artificial lighting whose amount depended on natural daylight availability as lighting was controlled based on illuminance levels reaching the light sensor. This amount was inversely proportional to TSR, previously presented in Figure 6, and thus to both SA and reflectivity parameters: as the SA and reflectivity increased, TSR and illuminance levels increased, decreasing the need for artificial lighting. The location parameter did not significantly affect lighting energy consumption where its values were nearly constant for each SA and reflectivity case across the three locations, similar to TSR results. On the other hand, internal loads from occupancy and the radiant fraction of artificial lighting in addition to the heat gained through the window-VB composition were the main contributors to cooling energy consumption. While occupancy was constant for all cases, the amount of artificial lighting and HG were not, and both were affected by the investigated parameters. The inverse relation between heat gain and artificial lighting consumption shaped the amount of cooling energy consumed. The increase in SA and reflectivity led to more heat gain that tended to increase the energy needed for cooling, while in the meantime, leading to a decrease in the need for artificial lighting, and thus, a decrease in its radiant fraction eliminating part of the cooling load. The magnitude of increase or decrease defined the amount of energy consumed for cooling.

Figures 9, 10 and 11 show the percentage of energy consumed in cooling and lighting for each case compared to their corresponding values in the base case. Positive values indicate energy savings while negative ones indicate an increase in consumption. As heating energy was minimal, it was not included separately in the chart yet it was included in the overall consumption values as shown in Figure 12.

Low reflectivity VBs

Figure 9 shows that lighting energy consumed was more than the base case by approximately 28% at the most closed SA 15° and decreased to slightly more than 6% at the most open SA 90° for all VB locations in a nearly linear pattern. The radiant fraction leading to internal cooling loads consequently followed the same pattern. Located indoor, low-reflectivity blinds showed the minimum reduction in HG, shown in Figure 7. As this was accompanied by internal loads from both fixed occupancy loads and an increase in the radiant fraction of lighting, cooling energy consumed showed an increase over the base case by a small range from approximately 6% to 0% as the SA increased, indicating that the internal loads due to both occupancy and radiant fraction of lighting exceeded the expected reductions due to shading. For mid-pane-located VBs, the HG curve significantly improved, reduced by around 40% compared to that of the indoor location, shown in Figure 7, resulting in significant energy savings in cooling energy ranging from approximately 10% to 15%, as illustrated in Figure 9. Outdoor-located VBs achieved about 26% to 30% further reductions in HG curve, shown in Figure 7, leading to more savings in cooling energy that ranged from 32% to 35%, see Figure 9, and to a decrease in the relative weight of the minimised internal loads across SAs. However, these savings increased along with the increase in SA, while the heat gain pattern showed the opposite direction as more heat gain occurred as SA increased. The values in Table 2 show that differences in HG due to changes in SA were minimum in the case of low-reflectivity blinds. This reasoned the pattern as in the meantime of small HG difference across SAs occurred, a significant decrease in the internal loads due to the decrease in artificial lighting took place as SA opened.

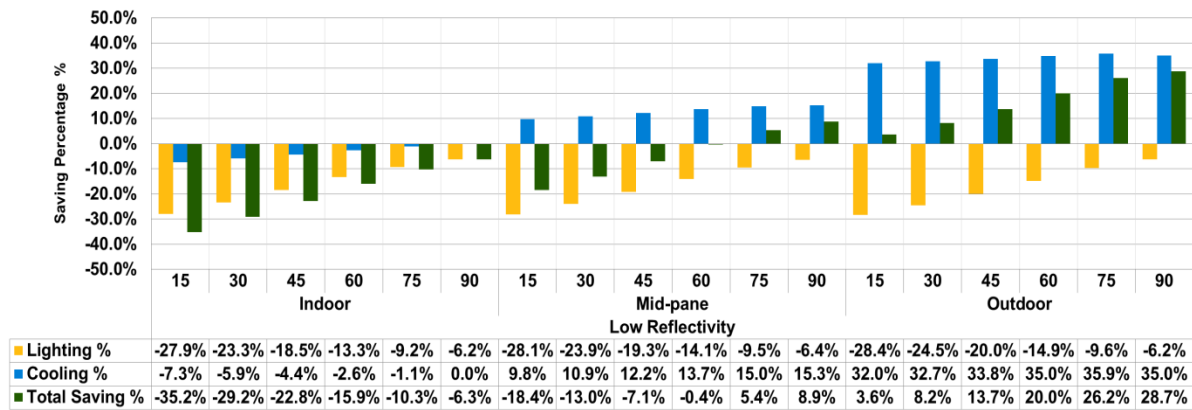


Figure 9: Percentage change in energy consumption at low reflective blind

The resulting overall energy performance of LR VBs showed an increase in energy consumption over the base case for indoor location of all SAs and for mid-pane VBs of SAs less than 60°. Starting from SA 75° mid-pane VBs achieved energy savings ranging from 5.4-8.9%. For outdoor VBs savings were achieved at all SAs starting from 3.6% at SA 15°, becoming more significant as SA increased reaching up to 28.7% at SA 90°.

High reflectivity VBs

High reflectivity VBs achieved the lowest values of energy consumed for artificial lighting among the examined reflectivity cases, as shown in Figure 10. Only 2% to approximately 5% increase over its corresponding value in the base case was achieved for nearly all SAs except for the most closed SA 15° at which the increase reached approximately 12%. These low values resulted in minor cooling loads due to artificial lighting. In the meantime, the difference in HG between the most opened and the most closed SAs was the highest at HR blinds reaching 25.8%, 27.9% and 35.9% for indoor, mid-pane and outdoor-located VB respectively, shown in Table 2. This led cooling energy consumption patterns across SAs to follow that of HG, where the highest savings were achieved at the more closed SAs. The highest cooling energy savings were achieved at SAs 15° and 30°; more than this, the savings decreased continuously in response to the increasing HG. At both SAs 15° and 30° the increase in HG was balanced by a significant decrease in internal loads of the decreased artificial lighting, leading to nearly a similar cooling value.

HR blinds were the highest among the examined reflectivity values in terms of savings in cooling energy for indoor and mid-pane located blinds. For outdoor located blinds, HR achieved higher savings up to SA 45°, which were exceeded by LR and MR blinds starting from SA 60°. The overall energy consumption showed energy savings compared to the base case at all angles and locations. Savings were higher at outdoor locations followed by mid-pane then indoor locations.

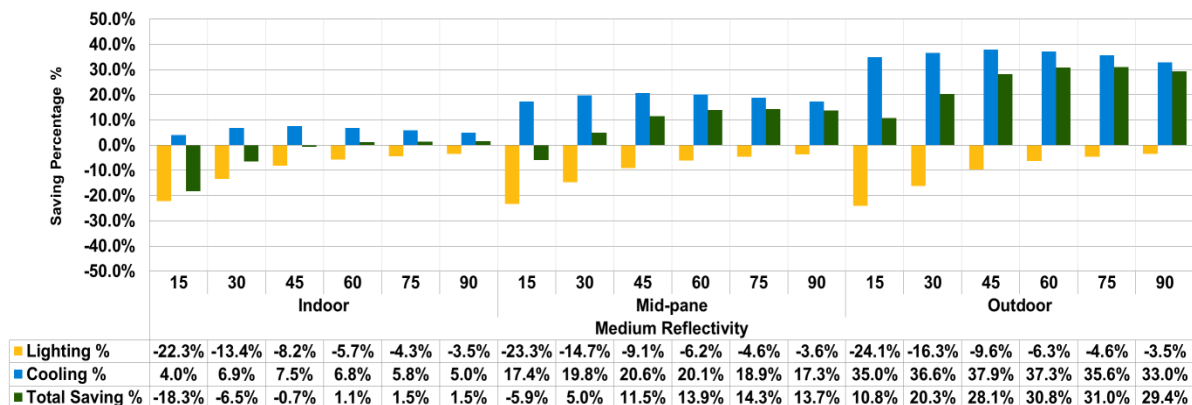


Figure 10: Percentage change in energy consumption at high reflective blind

Medium reflectivity VBs

Results for MR blinds always sat between those of LR and HR in regards to HG, TSR, artificial lighting and cooling energy consumption. The artificial lighting pattern was similar to both LR and HR cases with intermediate values, seen in Figure 11. The cooling energy pattern across SAs was also between that of LR and HR cases, as savings increased till SA 45° then started to decrease till SA 90° reflecting the intermediate values presented in Table 2. Minor cooling energy savings were achieved at the indoor location case, while significant savings reaching 20% and nearly 38% were achieved at mid-pane and outdoor locations respectively.

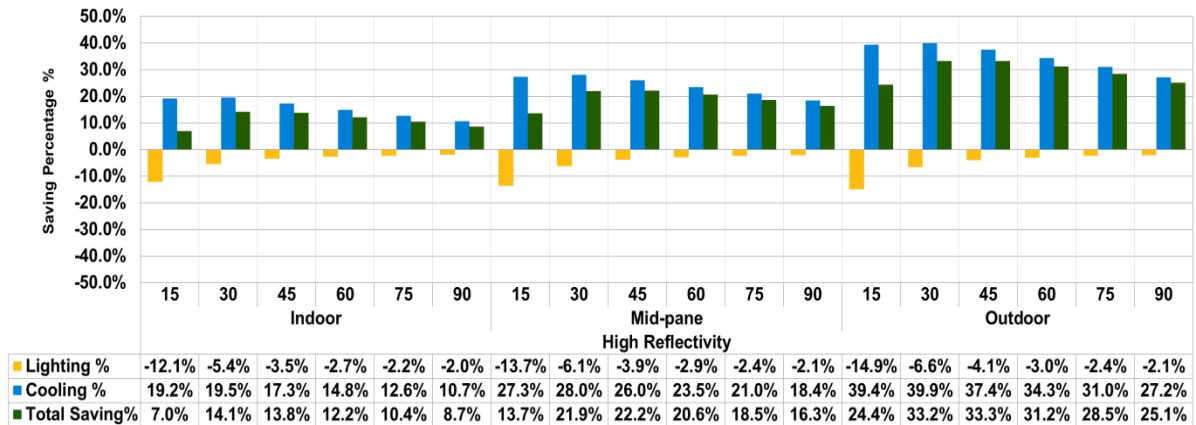


Figure 11: Percentage change in energy consumption at medium reflective blind

Comparison of overall energy consumption

Percentage change in total energy consumption of all heating, cooling and lighting compared to the base case is presented in Figure 12.

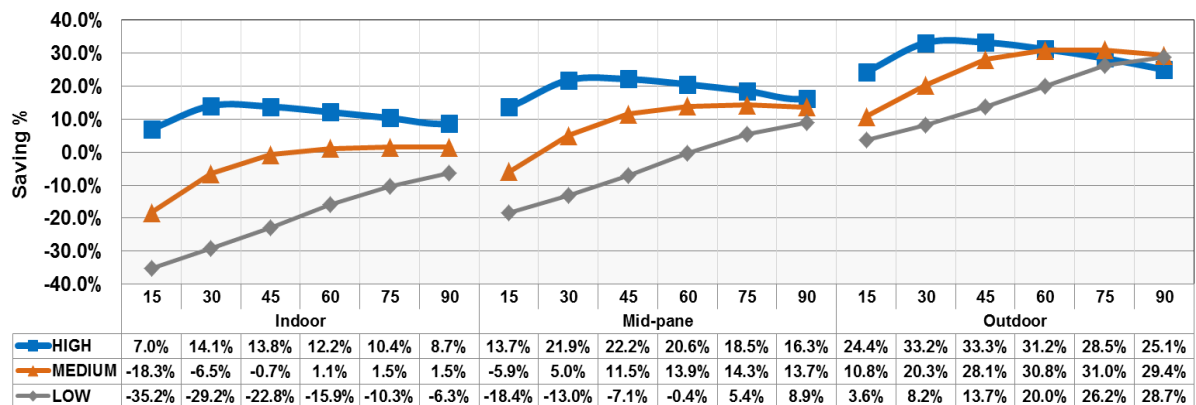


Figure 12: Percentage of change in annual EUI due to reflectivity, slat angle and position.

Results showed that highest savings in performance were achieved at outdoor-placed VBs, followed by mid-pane position, while the lowest cases were at those placed indoors. Results also showed that HR blinds achieved the highest total energy savings at all locations. Maximum savings were achieved at SAs 30° and 45° reaching 14.1%, 22.2% and 33.3% for the inside, mid-pane and outside locations respectively. At each slat angle, they were also of the highest savings except for the most opened angles of outdoor blinds, where savings achieved by both MR and LR blinds were higher.

MR blinds were of no benefit when located indoors as they were either of nearly the same consumption as the base case - at larger SAs - or even exceeded its consumption - at smaller SAs. Significant savings were achieved in cases of mid-pane and outdoor- located blinds, with maximum savings values at SAs 60° to 90°.

LR blinds showed savings at the most opened angles of mid-pane-located VBs and at all cases of outdoor-located VBs, with the maximum savings values at SA 90°. At this angle the minimum differences in overall consumption occurred among all reflectivity values. LR blinds were not of benefit at all indoor-located cases nor at the more closed SAs of mid-pane locations where an increase over the base case occurred.

As an opened view to the outdoor is usually preferred, a VB with SA 30° or 45° might not be visually as favoured as more opened angles. From the graph in Figure 12, it can be noticed that HR blinds of SA 60° can provide more of a view to the outdoors with less than 2% sacrifice in energy savings at all locations. It can also be seen that the savings achieved at the most opened SA 90° of the HR blind located in the middle of glass panes were more than the maximum savings of indoor located VBs which were achieved at SA 30°. The same thing occurred at outdoor-located HR, MR and even LR blinds at SA 90° whose energy savings exceeded the maximum savings recorded at SA 45° by HR blinds located in the middle of glass panes. This indicated that more potential of openness can be available by locating the blind a step outdoors.

Table 3 shows the overall performance of VBs categorised according to the amount of energy savings achieved.

Table 3: results categorised in terms of the amount of energy savings compared to the base case.

Slat Angle	Indoor-placed blind			Mid-pane-placed blind			Outdoor-placed blind		
	HR blind	MR blind	LR blind	HR blind	MR blind	LR blind	HR blind	MR blind	LR blind
15	7.0%	-18.3%	-35.2%	13.7%	-5.9%	-18.4%	24.4%	10.8%	3.6%
30	14.1%	-6.5%	-29.2%	21.9%	5.0%	-13.0%	33.2%	20.3%	8.2%
45	13.8%	-0.7%	-22.8%	22.2%	11.5%	-7.1%	33.3%	28.1%	13.7%
60	12.2%	1.1%	-15.9%	20.6%	13.9%	-0.4%	31.2%	30.8%	20.0%
75	10.4%	1.5%	-10.3%	18.5%	14.3%	5.4%	28.5%	31.0%	26.2%
90	8.7%	1.5%	-6.3%	16.3%	13.7%	8.9%	25.1%	29.4%	28.7%



5. CONCLUSION

Venetian blinds were investigated for energy performance for a South-oriented residential space in Cairo. A test room was modelled with a façade of WWR 20%. The effect of three parameters were investigated: reflectivity, slat angle and location. High, medium and low reflectivity blinds were examined at slat angles from 15° to 90° at three locations: indoor, between glass panes and outdoor. Energy performance can be concluded as follows:

Reflectivity and SA: High reflectivity blinds achieved the highest energy savings in all locations, which occurred at slat tilt angles of 30° and 45°. As SA increased and slats became more horizontal, the performance curve of HR blinds started to decline while the curves of both MR and LR blinds continued to improve, and thus the difference in savings between reflectivity values was minimised. In spite of the decline, HR blinds were still of better performance in indoor and mid-pane locations but were exceeded by MR and LR blinds at the outdoor locations. The curve of energy savings of LR blinds increased in a nearly linear form, while that of MR blind showed an increase until SA 60° then flattened to be nearly horizontal, indicating that for both types, a larger SA is recommended.

Location: For indoor-placed blinds, energy savings reaching 14.1% were achieved by HR blinds at SA 30°, while the use of lower reflectivity blinds were of no benefit. Savings with mid-pane-located blinds were higher, reaching 22.2% for HR blinds at 45°, while the best results of MR and HR blinds were only 13.7% and 8.9% respectively achieved at SA 90°. Outdoor-located blinds achieved the highest savings of 33.3% for HR blinds at SA 45°, while MR and LR blinds were close with 31% and 28.7% respectively but at the more opened SAs 75° and 90°. The performance of outdoor-placed medium and even low reflectivity blinds exceeded those of high reflectivity placed a step to the inside. Where the blind is not located outdoors, it is highly recommended to be of high reflectivity and to be placed in the middle of glass panes rather than to be placed indoors.

6. REFERENCES

- Ariosto, T. and Memari, A. (2014). Evaluation of venetian blind attributes for energy efficiency, Proceedings of the 2nd Residential Building Design & Construction, Penn State, University Park, pp. 64:81.
- Chaiyapinunt, S. and Khamporn, N. (2013). Shortwave thermal performance for a glass window with a curved venetian blind, Solar Energy, 91, pp. 174–185.
- Chaiyapinunt, S. and Khamporn, N. (2014). Heat transmission through a glass window with a curved venetian blind installed, Solar Energy, 110, pp. 71–82.
- Cho, S., Shin, K. and Zaheer-Uddin, M. (1995). The effect of slat angle of windows with venetian blinds on heating and cooling loads of buildings in South Korea, Energy, 20 (12), pp. 1225-1236.

- Collins, M. and Harrison, S. (2004). Estimating the Solar Heat and Thermal Gain from a Window with an Interior Venetian Blind, *ASHRAE Transactions*, 110, ProQuest pp. 486-500.
- Eltaweel, A. and SU, Y. (2017). Controlling venetian blinds based on parametric design; via implementing Grasshopper's plugins: a case study of an office building in Cairo, *Energy and Buildings*, 139, pp. 31–43.
- Gomes, M., Santos, A. and Rodrigues, A. (2014). Solar and visible optical properties of glazing systems with venetian blinds: Numerical, experimental and blind control study, *Building and Environment*, 71, pp. 47-59.
- Karjalainen, S. (2018). Be active and consume less—the effect of venetian blind use patterns on energy consumption in single-family houses, *Energy Efficiency*, 12, pp. 787-801.
- Kim, J., Yang, K., Park, Y., Lee, K., Yeo, M. and Kim, K. (2007). An Experimental Study for the Evaluation of the Environmental Performance by the Application of the Automated Venetian Blind, *Proceedings of Clima 2007 WellBeing Indoors*.
- Kottek, M., Greicer, J., Becck, C., Rudolf, B., Rubel, F. (2006). World Map of the Köppen-Gieger Climate Classification Updated. *Meteorologische Zeitschrift* 2006; 15(3), pp. 259-63.
- Kwon, H., Yeon, S., Lee, K. and Lee, K. (2018). Evaluation of Building Energy Saving Through the Development of Venetian Blinds' Optimal Control Algorithm According to the Orientation and Window-to-Wall Ratio, *International Journal of Thermophys*, pp. 39:30.
- Ministry of Electricity and Renewable Energy, Annual report 2016-2017, p61, available online: http://www.moee.gov.eg/test_new/PDFReports/REP2016-2017.pdf
- Oh, M., Lee, K. and Yoon, J. (2013). Automated Slat Angle Control Of Venetian Blind Considering Energy And Visual Comfort, 13th Conference of International Building Performance Simulation Association, Chambéry, France..
- Parra, J., Guardo, A., Egusquiza, E. and Alavedra, P. (2015). Thermal Performance of Ventilated Double Skin Façades with Venetian Blinds, *Energies*, 8, pp. 4882-4898.
- Popovici, C., Cirlan, V., Mateescu, T., Chereches, N. and Hudisteanu, S. (2016). Influence of various angles of the venetian blind on the efficiency of a double skin façade, *Sustainable Solutions for Energy and Environment, EENVIRO - YRC 2015*, 18-20 November 2015, Bucharest, Romania, *Energy Procedia* 85, pp. 416 – 424.
- Shahid, H. and Naylor, D. (2005). Energy performance assessment of a window with a horizontal Venetian blind, *Energy and Buildings*, 37, pp. 836–843.
- Simmler, H. and Binder, B. (2008). Experimental and numerical determination of the total solar energy transmittance of glazing with venetian blind shading, *Building and Environment* 43, pp.197–204.
- Tzempelikos, A. (2008). The impact of Venetian blind geometry and tilt angle on view, direct light transmission and interior illuminance, *Solar Energy*, 82, pp. 1172–1191.
- Velasco, A., García, S., Guardo, A., Fontanals, A. and Egusquiza, M. (2017). Assessment of the Use of Venetian Blinds as Solar Thermal Collectors in Double Skin Facades in Mediterranean Climates, *Energies*, 10, pp. 1825.

#352: The city of emergence: Urban design strategies for Sejong Smart City

Jieun KIM¹, Doo-Won YOON²

¹Planning and Coordination Division for Multifunctional Administrative City, Korea Planning Association,
238-3 Gareum-ro, Sejong, jiniejuno@gmail.com

² Planning and Coordination Division for Multifunctional Administrative City, Korea Planning Association,
238-3 Gareum-ro, Sejong, zuzic@happycity2030.or.kr

With the development of ICT and the expansion of digitalisation, new social media and services are being created in various ways. People are becoming more connected globally and it has changed the city dweller's way of life. In this paradigm shift, planners need to consider the diversity of urban life and to reflect this into the way new neighbourhoods are designed.

In the traditional way of urban design and master planning, decision making is linked to old customs and planner's intuition to arrive at the final plan. However, because of the complex characteristics of Smart Cities and the future of urban living, planners are now experiencing difficulties in anticipating the optimum result. Therefore, the design process needs to be more legible and analytically linked together to work out the embedded logic.

Consequently, this study looks at the urban design strategies which are working as a performance-based design tool for Sejong Smart City. After planning purposes and multiple design targets are established, various architectural structures are generated. Finally, the best case is selected through a goal-oriented evaluation procedure.

Keywords: smart city; form finding; goal-oriented design

1. INTRODUCTION

1.1. Sejong and Multifunctional Administrative City (MAC)

The city of Sejong is being established to achieve the goals of decentralising population currently concentrated around the capital city. In addition, the government intends that Sejong will encourage a balanced regional economic development in South Korea. To provide equitable physical treatment, the location of Sejong was carefully chosen to make people from every city be able to reach the city within about two hours.

The core part of Sejong is currently being developed, named “Multifunctional Administrative City (MAC)”. (Figure 1) To build the MAC, the Korean government established a new government agency, “Multifunctional Administrative City Construction Agency (MACCA) in 2006, and several of Korea’s ministries and executive offices were relocated from Seoul to Sejong city in 2012.

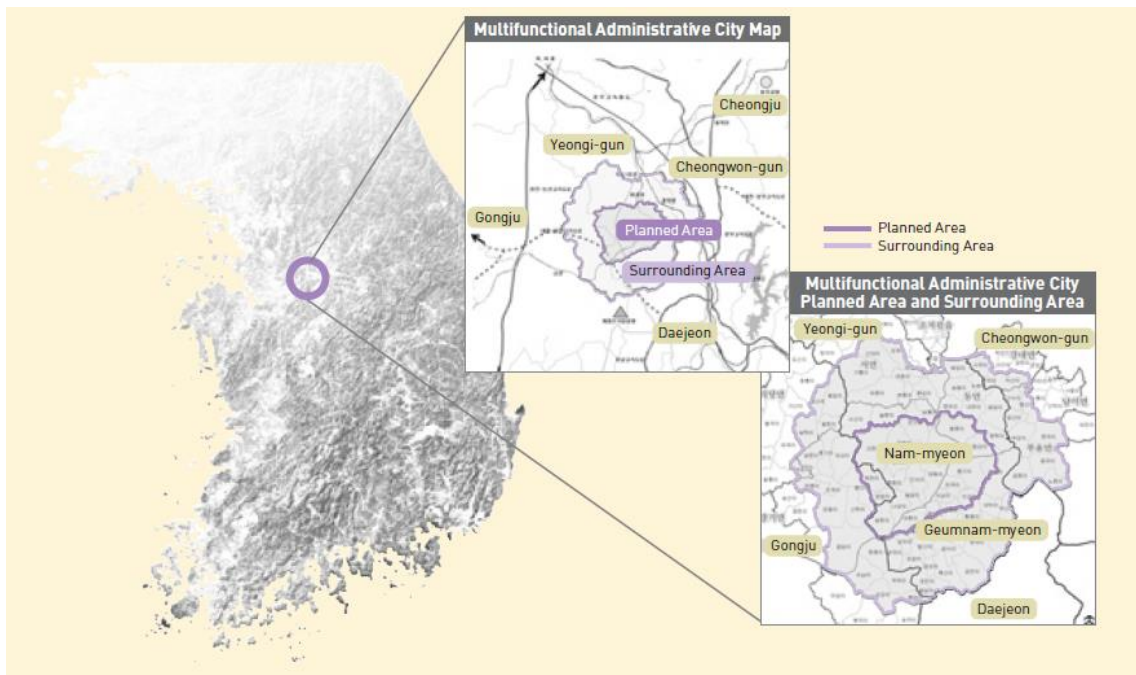


Figure 1: The Location of MAC (Source: Multifunctional Administrative City Construction Agency, 2007)

As illustrated below in Figure 2, the site of MAC is divided into six parts and each one has a main function in accordance with the characteristics of nearby regions. The site of each part is allocated evenly along the ring-shaped urban development axis and they are interconnected by public transportation, such as the BRT. Central green land is planned as a public space to symbolize the importance of environmentally friendly development and to increase sustainability of the city by preserving its central area. (Multifunctional Administrative City Construction Agency, 2007) Therefore, the ratio of green coverage of MAC is higher than any other cities in South Korea.

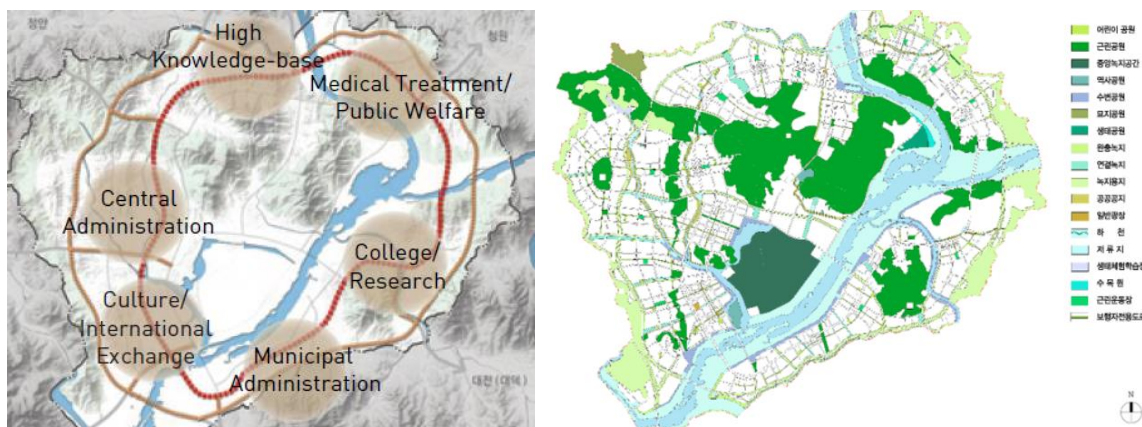


Figure 40: Layout of Major Urban Functions and the distribution of Green Area (Source: <https://www.happycity2030.or.kr>)

1.2. The 5-1 Area in MAC: as a test bed for Smart Cities

The MAC 5-1 Area was selected as a test bed for The National Pilot Project of Smart City by the Ministry of Land, Infrastructure and Transport in January 2018. As the 5-1 Area is an unexploited site, newly developed infrastructures and technologies can be applied with less issues and shorter administrative procedures. In addition, because the site is located near natural environment such as Guem and Miho River, people feel healthy and enjoy the environmental-friendly characteristics. (Figure 3)

By the “Smart City Act” which was amended from “Ubiquitous City Act” in 2018, the MAC 5-1 Area is being developed as a neighbourhood unit that integrates smart services and technologies into physical urban spaces to promote intelligent urban management and innovative industries. Currently Land Use Planning is being made for the establishment of Development and Execution Plans.

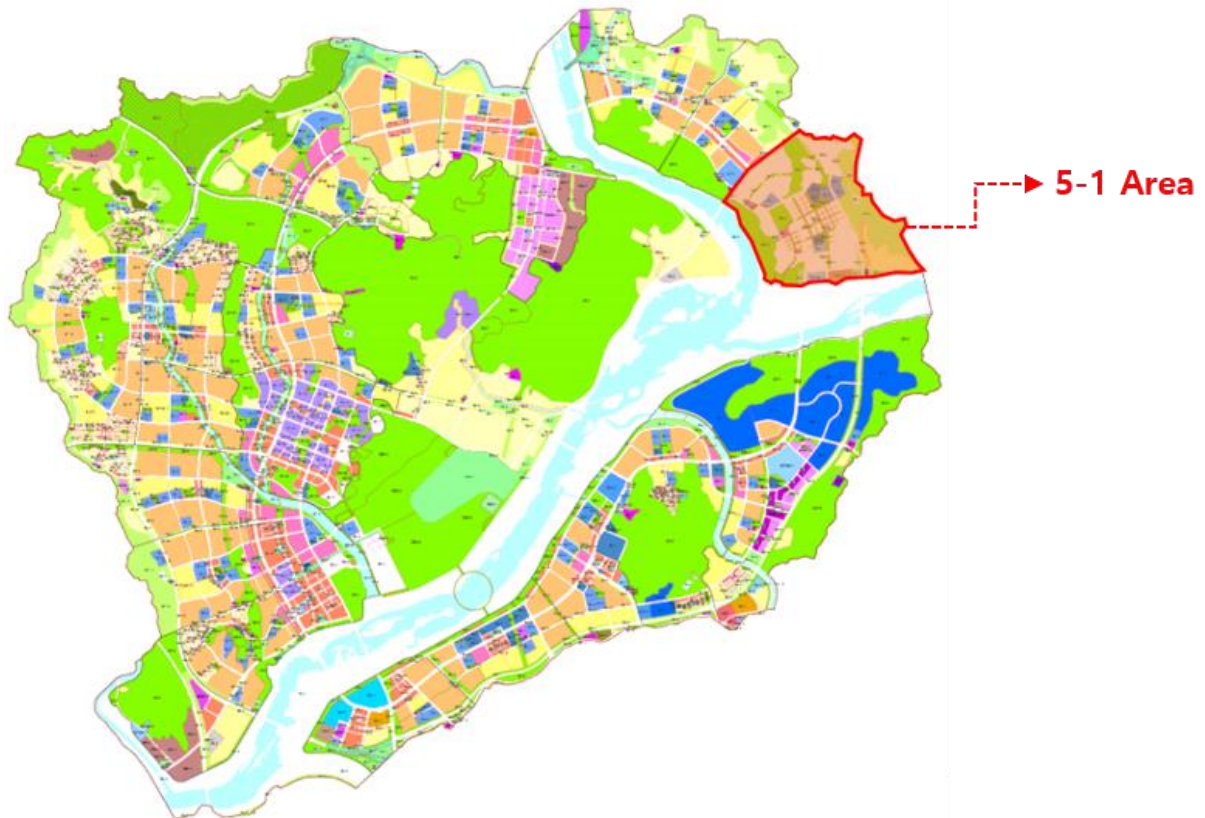


Figure 3: The Location of 5-1 Area in MAC (Source: MAC City Development Plan Map: Version 50th, 2019)

This National Pilot Project aims to create a smart city that changes citizens' daily lives, and it is based on Artificial Intelligence (AI), operational data and block chain etc. All the related services and technologies are categorised according to the seven fields of urban innovation; Mobility, Healthcare, Education, Energy/Environment, Governance, culture and jobs. The purpose of each field is explained in Table 1 below.

In particular, the spatial structure is designed to provide optimised mobility services with the advanced means of state-of-the-art transportation based on self-driving and carpooling. The private vehicle restricted area is under planning for MAC 5-1 Area (Figure 4).

Table 1: 7 Innovation-Components for Smart City








Components	Goals
 Mobility	Gradually reduce the number of cars by introducing a variety of mobility services such as shared transportation and self-driving
 Health Care	Individual hospitals are networked to provide rapid medical information and respond quickly to ensure the citizens' safety (City as an extended hospital)
 Education	Promote critical and creative thinking for teenagers and provide lifelong education for adults
 Energy/Environment	Improve the quality of citizens' lives and create a sustainable city by introducing environmentally friendly energy innovation technologies
 Governance	Provide a 'System for Decision Making' and promote citizen participation with various methods using incentives and block chains
 Culture	Providing citizens with customised cultural services and providing smart shopping services for convenient shopping
 Jobs	Creating a key hub for innovative industries initiatives that provide new opportunities



Figure 4: 5-1 Area Land Use Plan (Source: MAC City Development Plan Map: Version 50th, 2019)

2. OBJECTIVE

2.1. Issues

As urban planning has a wide range of design elements and is difficult to predict, seven smart city innovation components and prototypes that reflect all their services are hard to come up with. In addition, there is no certain media to communicate and to share everybody's knowledge in various fields. Thus, it is difficult to reach a satisfactory agreement (Figure 5).

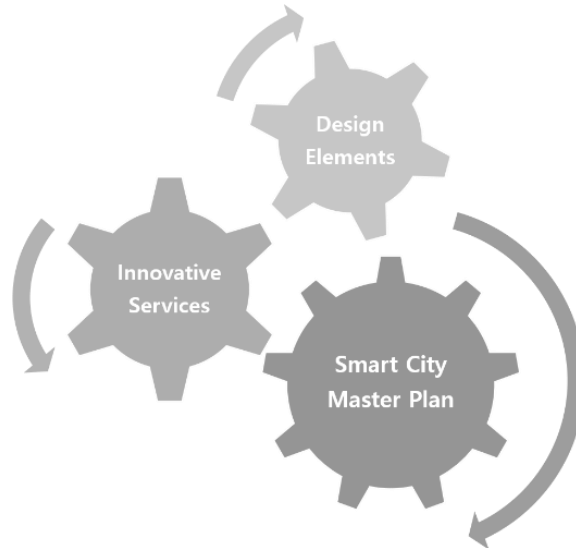


Figure 5: The complex Interactive system

2.2. Aim of the study

The purpose of this study is to develop a performance-based model that reflects the smart city services presented in the Master Plan of MAC 5-1 Area. It is particularly focused on the environmental performance to evaluate its sustainability. It will be useful to generate prototypes and physical models to assess the optimum results (Figure 6).

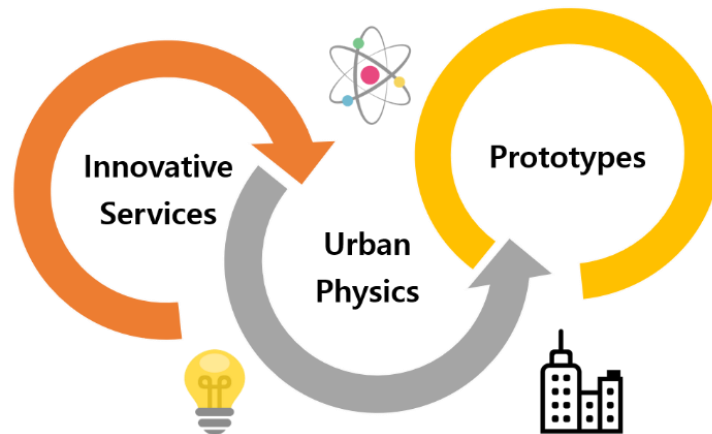


Figure 6: The heuristic model for optimisation

3. METHODOLOGY

3.1. Digital morphogenesis

The term computational morphogenesis is used to describe a form-finding process which manages building form and performance at the same time (Richards, 2011). Kostas (2003) defined that the use of the computer in architectural design is undergoing a shift from “computerisation” to “computation”. Computerisation is the act of processing things that are already conceptualised in the designer’s mind in a computer system. However, computation is not manipulated by the designer but generated by the computer itself. This “computerisation” plays an important role in design practice at present but there will be more demand for “computation” in a new design era which goes beyond the limitations of given standard CAD-software. This means that the computer is increasingly going to be used not only as a drafting or modelling tool, but as a tool for helping designers think and estimate performance in a practical way. To invent intelligent architectural design methods with these computer technologies, the biological approaches are necessary based on their multidisciplinary characteristics (Roudavski, 2006). Recent discourse on digital morphogenesis links to several concepts which include emergence, self-

organisation and form-finding (Hensel et al., 2004). This approach has led designers to actively engage in design in any given circumstance.

3.2. Holistic design approaches

Very carefully designed urban forms are required to respond to Sejong Smart City innovation components and listed services. Therefore, this system is developed to achieve the aim for the synthesis of Smart City performance and mathematical mechanisms in the process of urban form generation. For the physical form generation and the assessment of Smart City performance, design methods are linked with the environmental analysis of computer simulations. In this research, Cellular Automata (CA) are used as a generative design method and the design results are evaluated by researched Sejong Smart City design criteria for decision-making.

In the given circumstances, this system works with parametric and visualisation tools; Rhino and Grasshopper. In addition, the Ladybug and Honeybee, which offers a direct link between 3-dimensional models in Rhino and Energy Plus, is used as an environmental simulation tool. Specific parameters such as block size, building volume, width of road etc. are adjusted through the Rabbit components in Grasshopper.

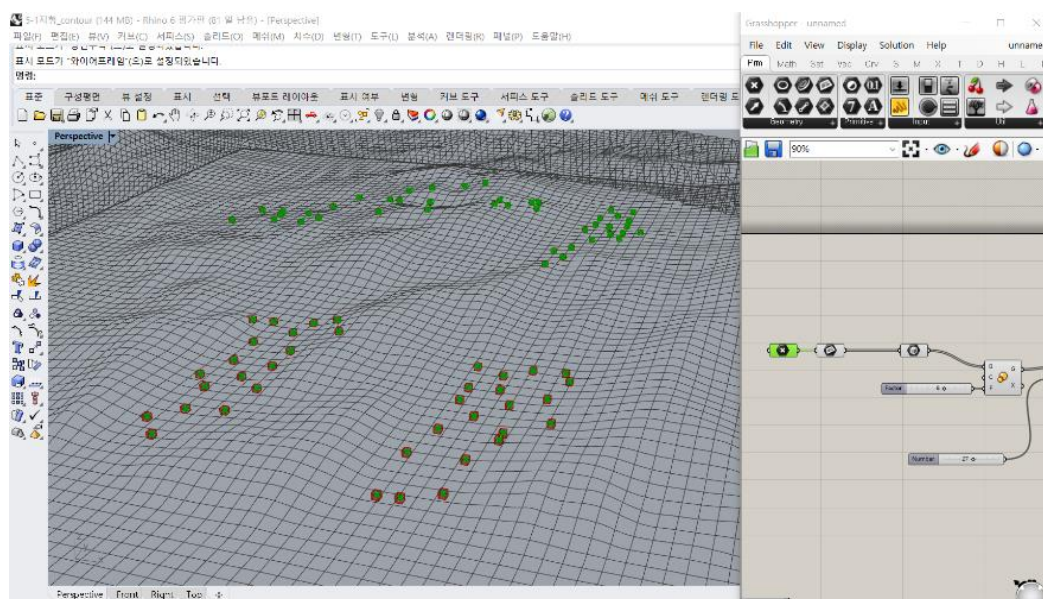
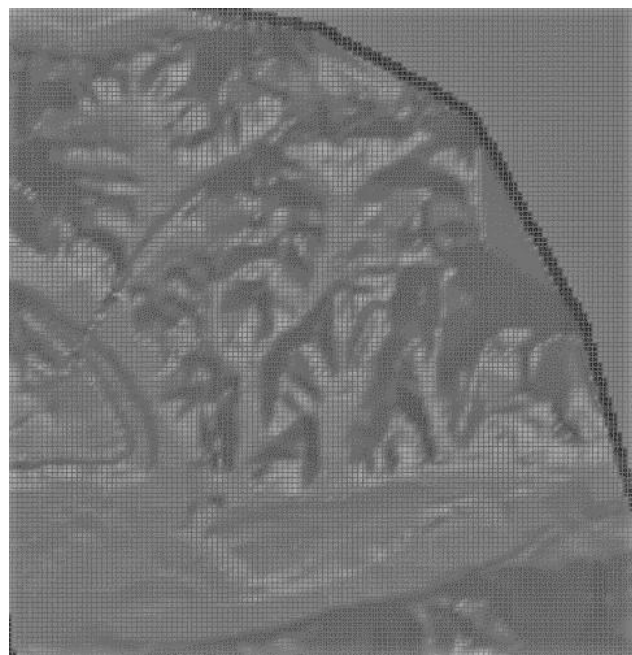


Figure 7: The concept of Generative Model for MAC 5-1 Area

4. CONCLUSION

Because of the wide and inclusive characteristics of urban design, many experts and specialists in various fields are involved. It leads to complicated workflow and increased difficulties of mutual communication. In the case of Smart City, many more people working in different areas participated in the project, albeit in small portions. Thus, understanding other areas of need and expertise is a basic preparation for finding the best way to satisfy a wide variety of people. In addition, planners need to consider the state-of-the-art and experimental technologies which are newly invented and tested in everyday urban life. Therefore, the design methods need to be well-organised especially in the initial stage of the design process.

In this study, the performance-based form-making system is expected to make the working process fast and accurate. However, this on-going project is still developing performance evaluation methods and the practical mechanisms are being extensively researched in terms of its accuracy, connectivity and agile characteristics for Sejong Smart City.

5. REFERENCES

Daniel, R., 2011, Towards morphogenetic assemblies, evolving performance within component-based structures, Proceeding of the 16th International Conference On Computer-Aid Architectural Design Research in Asia, P.515-524

Hensel, M., Menges, A., Weinstock, M., 2004, Emergence: Morphogenetic Design Strategies, Architectural Design Vol. 74 No. 3, London: Wiley Academy

Huang, H. J. Et Al., 2019, Innovative Platform and Joining Smart City, Seoul: The Committee of 4th Industrial Revolution

Kostas T., 2003, Expressive Form a Conceptual Approach to Computational Design, Routledge

Multifunctional Administrative City Construction Agency, 2007, Happycity Sejong the Global Model City Where Everyone Desires to Live, Sejong

Multifunctional Administrative City Construction Agency, 2014, A Prestige city Of Korea Sejong, Sejong

Stanislav, R., 2006, Towards Morphogenesis in Architecture, International Journal of Architectural Computing, Issue 03, Volume 07, P.345-374

#353: Comparison of cascade PCM storage with single-phase sensible or latent heat storage for solar thermal energy

Yongliang SHEN¹, Shuli LIU^{2,*}, Xiaojing HAN¹, Liu YANG¹, Yanjun ZHANG¹, Xiue YANG¹

¹ School of Mechanical Engineering, Beijing Institute of Technology, Beijing 100081, China

² School of Energy, Construction and Environment, Coventry University, Coventry, CV1 2FB, UK

*Corresponding Author: Shuli.Liu@coventry.ac.uk

Solar water heating (SWH) systems have a wide range of applications in the domestic and industrial sectors. Although the optimisation of design is carried out for each part of the device, the system's own defects cannot be avoided. In periods of low solar radiation density, the heat transfer fluid cannot continue to heat the hot water in the tank, resulting in a loss of heat. According to published literature in 2013, the solar collector temperature drops lower than that of the hot water in the storage tank after 15:00, when any remaining solar energy gathered will not be able to be stored resulting in considerable energy loss, as for the single-phase PCM storage. Hence, the authors suggest the use of cascade PCM storage to maximise the energy absorbed and stored for off-radiation use. Different PCMs with various melting temperature were used to storage the energy along the solar collect surface temperature curve. The results of the cascade PCM heat storage were compared with the single-phase sensible and latent heat storage. The results show that the combination of cascade PCM technology and SWH system can improve system efficiency and solar energy fraction, and the more PCM's used, the better heat storage performance can be obtained. For a single-phase PCM storage mode, if the melting point of PCM is too high, the liquid fraction is too low and the PCM cannot store much energy; if the melting point is too low, the energy can only be obtained in the low temperature range. This paper provides reference for the application of cascade PCM heat storage technology in the field of solar thermal storage.

Key words: solar water heating, cascade PCM, heat storage, solar energy

1. INTRODUCTION

Although SWH technology has undergone development since the 1960s, there are still opportunities to further increase efficiency and reliability. In order to solve the problems of overheating, corrosion and heat transfer fluid (HTF) freezing, the structure of the HTF, the collector and the hot water tank have been studied (Hussein, Mohamad, & El-Asfour, 1999). In order to ensure the stability of SWH system, protection from freezing of the heat transfer fluid is necessary. Common antifreeze methods include adopting antifreeze recirculation using an automatic drainage device, and reversing flow from the water tank to reheat the collector in the night (Kalogirou, 2004; Smyth, Eames, & Norton, 2001; Zhou, Ji, Yuan, Zhao, & Huang, 2019). There are many types of antifreeze, such as alcoholic aqueous solutions like ethanol, ethylene glycol, and glycerin, and organic oils such as silicone oil, aromatic hydrocarbons, and hydrocarbon oils. When using antifreeze, in addition to considering the freezing temperature, it should also consider that the antifreeze medium is non-toxic, low in cost, have good thermal properties and be non-corrosive with collectors and heat exchanger materials (Pandey & Chaurasiya, 2017; Shukla, Sumathy, Erickson, & Gong, 2013). A solar collector is the core component of the SWH system. Most of the research on collectors has focused on absorber plate design and glazing materials. A parabolic shape is one of the most efficient among different absorber profiles because the heat output per unit volume is higher than other geometries (Hollands & Stedman, 1992). In addition, rectangular and recto-trapezoidal profiles also showed good heat collecting performance and heat transfer efficiency (Kundu, 2002). The addition of transparent insulation can further increase the efficiency of the collector. Glass and plastic with a solar transmittance of over 90% are commonly used glazing materials (Kalogirou, 2004). By applying a reflective coating and designing the glazing material into different shapes, including rectangular, circular and hexagonal, increased solar transmittance and reduced heat loss coefficient can be achieved (Abdullah, Abou-Ziyan, & Ghoneim, 2003; Furbo & Shah, 2003). Hot water tanks are usually used to store collected solar energy to provide the required hot water at the final temperature of use. One of the main problems with storage tank is the heat loss due to the mixing of hot and cold water. Good thermal stratification can reduce collector inlet temperature and heat transfer losses to increase collector efficiency (Zurigat, Liche, & Ghajar, 1991). A large number of studies have shown that changing the shape of the inlet of the water tank, setting baffles and reducing the inlet velocity and temperature can effectively enhance the thermal stratification (Andersen, Furbo, & Fan, 2007; Shah, Andersen, & Furbo, 2005).

In this paper, based on the published literature (Ayompe & Duffy, 2013) in 2013, the problem of thermal energy loss due to the mismatch between supply and demand of solar radiation in the solar water heating system during the charging process is addressed. Different PCMs were used to compensate for the heat loss in the system when the hot water generated by the collector cannot meet the heat storage requirements. The results of the PCM cascade heat storage were compared with the original experiments, and the system's heat storage capacity and heat storage efficiency were improved.

2. ANALYSIS OF ORIGINAL EXPERIMENTAL RESULTS

2.1. System description

The SWH system in the literature (Ayompe & Duffy, 2013) was built in Dublin, Ireland. The system schematic diagram is shown as Figure 1. The system consisted of a hot water storage tank, control unit, pump and flat plate collector. The heat collecting system consisted of two K420-EM2L flat plate collectors, each with a total area of 2.18 m² and a hole area of 2 m² connected in series with a total area of 4 m². The stainless steel hot water tank (Mode HM 300L D / coil U44332) was 1680 mm high, 580 mm in diameter and with a working pressure of 3 bar. An automatic hot water distribution device was designed and integrated into SWH system to extract water from a hot water tank in a simulated household operation. The hot water demand profile was based on the average European household hot water use standard EU M324EN. Since this paper mainly focuses on the energy storage process, it pays little attention to the specific materials and control unit of the system. Figure 1 shows a schematic diagram of the position of the experimental setup and thermocouple sensor of the SWH system components. $T_{c,o}$ was the temperature of the solar fluid at the outlet of the collector, $T_{b,t}$ the temperature of the water at the bottom of the hot water tank.

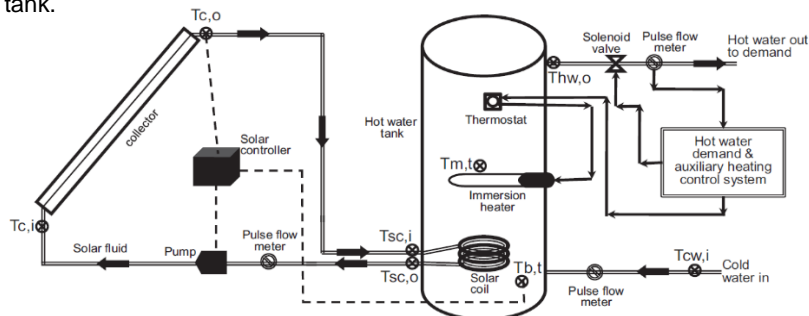


Figure 1: Schematic diagram of the experimental setup (Ayompe & Duffy, 2013)

2.2. Original result analysis

The original experimental results contained temperature changes at each measurement point under three weather conditions (Overcast day: 04/02/2010, clear sky day: 24/05/2009 and intermittent cloud-covered day: 13/10/2009). The experimental results on overcast days and intermittent cloud-covered days have been ignored. The measured parameters on the clear sky day are analysed in this paper. Figure 2 shows the temperature of the collector outlet $T_{c,o}$ and the temperature at the bottom of the hot water tank $T_{b,t}$ as a function of time. The maximum temperature at the collector outlet and the bottom of the hot water tank appeared at 13:00 and 15:00, respectively, reaching 68°C and 56°C. After 16:00, $T_{c,o}$ was always less than $T_{b,t}$, which made the solar fluid unable to exchange heat with the water in the tank. Considering the heat loss between the collector outlet and the tank inlet, the solar fluid was not able to provide heat to the hot water in the tank after 15:00. According to meteorological data, the average temperature in Dublin, Ireland, was only 6-14°C in May, but it had a longer period of sunshine, as shown in the red shaded part of Figure 2. Therefore, hot water with a temperature above 35°C can be considered as useful domestic hot water. Correspondingly, the energy from the solar collector between 15:00 and 18:00 in Figure 2 is considered as useful energy. Therefore, it was necessary to use phase change materials to collect solar energy only in the evening. The function of radiation with time can be obtained by fitting curve, where $y = -5 \times 10^{-6} \cdot x^2 - 0.0184 \cdot x + 941.7$. The total energy from the collector was 11196.4 kJ in 15:00-18:00 by numerical integration.

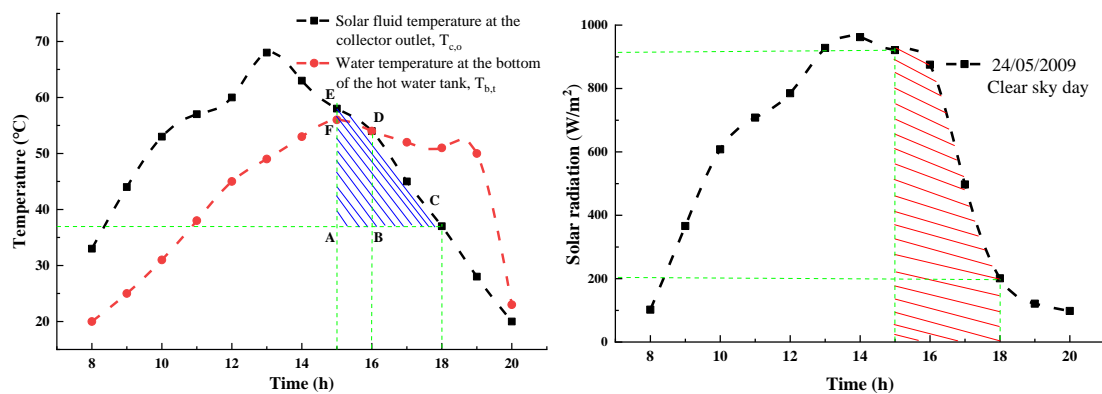


Figure 2: Daily variation of $T_{c,o}$, $T_{b,t}$ and solar radiation on clear sky day-24/05/2009 (Adapted from [19])

3. PCM CASCADE HEAT STORAGE TECHNOLOGY APPLIED IN SWH SYSTEM

For the accuracy of the calculation, ANSYS 16.0 was used to establish two-dimensional physical Modes to study the storage performance of excess heat in the PCMs after 15:00. The performance of cascade (2 and 3 PCMs) and single PCM heat storage Modes were compared.

3.1. The selection of PCMs

Considering the temperature change of the solar collector outlet after 15:00, three PCMs were selected to store the excess heat of the SWH system. The properties of the PCMs are listed in Table 1 (Sharma, Tyagi, Chen, & Buddhi, 2009). Paraffinic organic phase change materials have different transition points and heat of fusion because of their different numbers of carbon atoms.

Table 1: Properties of paraffin heat storage materials

Number of carbon atoms	Density (kg/m ³)	Melting point T_m (°C)	Heat of fusion (kJ/kg)	Specific heat capacity (kJ/kg·K)	Thermal conductivity W/(m·K)	Viscosity (kg/(m·s))
20 (PCM 1)	780	51.5	253	2.12	0.2	0.00324
22 (PCM 2)	780	44.4	249	2.12	0.2	0.00324
24 (PCM 3)	780	36.7	247	2.0	0.2	0.00324

3.2. Theoretical

Physical modes and boundary conditions

The authors assume that the collector outlet fluid no longer exchanges heat with the hot water in the tank after 15:00 but was used to heat PCMs. Three kinds of PCM heat storage modes were established. As shown in Figure 3, HTF flowed through a circular tube for heating PCMs with cylindrical radial distribution. The diameter of the

circular pipeline was 100mm and the outer diameter of PCMs was 300mm. The total height of the cylinder was 600mm, which was divided by PCMs on average. A past study (Seeniraj & Narasimhan, 2008) showed that PCMs were loaded into the corresponding cells in descending order of melting temperatures, which facilitated the melting during the initial stage. Mode 1 only used a single PCM for heat storage while Mode 2 and Mode 3 utilised 2 PCM and 3 PCM respectively, which were cascaded PCM heat storage modes. The fluid inlet was set to the velocity inlet, which was consistent with the original experiment, 0.006m/s. The inlet fluid temperature y (K) was a function of time (s) and was fitted to the *Origin 2018* software by the data of 15:00-18:00 in Figure 3, which was: $y = -0.0667 \cdot x/60.0 + 58 + 273.15$. The temperature of the inlet fluid was set by programming the UDF. Two-dimensional and transient solvers, energy and melting/solidification modes were adopted. The time step size of SIMPLE algorithm was 1 second and the number of time steps were 12,000, which completely met the heat storage process between 15:00 -18:00.

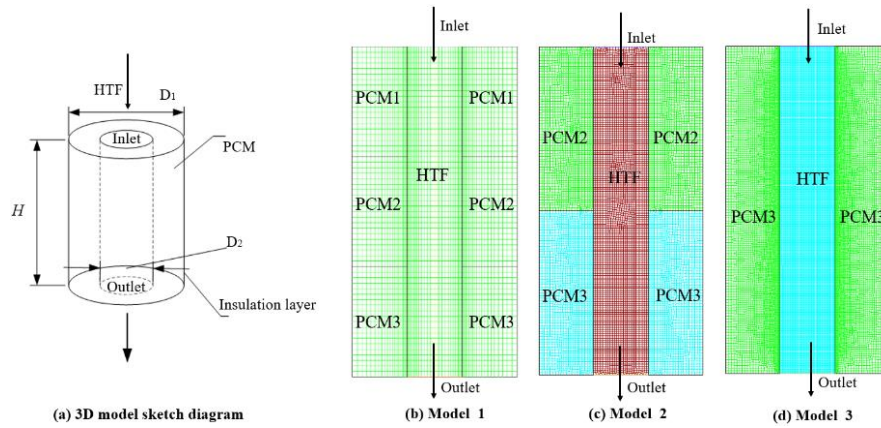


Figure 3: Physical modes and mesh of three heat storage systems

In order to obtain effective results, the following assumptions are also used:

- Flow was transient and two-dimensional.
- Heat transfer from water tank, collector and other fittings were neglected.
- Viscous dissipation and thermal radiation were neglected.
- PCM in liquid state and HTF were incompressible fluids.
- The influence of temperature on the PCMs properties was neglected.
- Heat loss in the whole heat storage process were neglected.
- The outer layer of the PCM was an insulation layer, and the PCMs were insulated from each other.

Mathematical Mode

The melting/solidification mode in *ANSYS Fluent 16.0* software was based on the enthalpy-porosity method, which treated the molten region as a mushy zone of the porous medium.

Equation 1: liquid fraction of PCM

$$\beta = \begin{cases} 0 & T \leq T_s \text{ Solid} \\ (T - T_s)/(T_l - T_s) & T_s < T < T_l \text{ Mushy} \\ 1 & T_l \leq T \text{ Liquid} \end{cases}$$

Equation 2: continuity equation.

$$\nabla \cdot (\rho \vec{u}) = 0$$

Equation 3: momentum equation.

$$\rho \frac{\partial \vec{u}}{\partial t} + \rho (\vec{u} \cdot \nabla) \vec{u} = -\nabla P + \mu \nabla^2 \vec{u} + \rho \vec{g} + \vec{F}$$

Equation 4: energy equation.

$$\frac{\partial}{\partial t} (\rho H) + \nabla \cdot (\rho \vec{u} H) = \nabla \cdot (k \nabla T) + \vec{S}$$

Equation 5: total enthalpy

$$H = h + \Delta H$$

Equation 6: sensible enthalpy

$$h = h_{ref} + \int_{T_{ref}}^T C_p dt$$

Equation 7: latent enthalpy

$$\Delta H = \beta L$$

Equation 8: The source term

$$\vec{S} = A_{mush} \vec{u} \frac{(1-\beta)}{\beta^3 + \chi}$$

Where:

- A_{mush} = mushy zone constant, the constant is a small number to prevent division by zero.
- ρ = density of PCM, kg/m³;
- k = thermal conductivity of PCM, W/(m·K);
- u = velocity of HTF, m/s;
- μ = viscosity, kg/(m·s).

Energy performance analysis

Equation 9: The total energy delivered by the solar HTF to the PCM tanks

$$Q_p = mC_{ps}(T_m - T_i) + \beta mL + mC_{pl}(T_\tau - T_m)$$

Equation 10: The energy storage efficiency of PCMs

$$\eta_s = \frac{Q_p}{A_c \eta \int_{T_i}^{T_\tau} G dt}$$

Equation 11: The energy storage efficiency of system

$$\eta_s = \frac{Q_p + Q_w}{A_c \eta \int_0^\tau G dt}$$

Equation 12: The solar fraction

$$SF = \frac{Q_s}{Q_s + Q_{aux}}$$

Where:

- C_{ps} , C_{pl} , T_i and T_τ = specific heat in solid and liquid phase (kJ/(kg·K)), initial temperature (K) and terminal temperature (K) of PCMs, respectively;
- Q_w = energy storage by water tank in the original experiment.

4. RESULTS AND DISCUSSION

4.1. Variation of PCMs' temperatures with flow time

Figures 4, 5, and 6 show the transient temperature contours and temperature distribution in the X direction with flow time in 3 Modes ((a) 30 minutes, (b) 60 minutes, (c) 90 minutes, (d) 120 minutes, (e) 150 minutes, (f) 180 minutes). The maximum temperatures in the PCMs regions gradually decreased in the three heat storage modes because of the decreasing inlet temperature. As the heat transfer proceeded, the high temperature region diffused to both sides of the PCMs zone.

In Mode 1, the temperature of PCM 1 near HTF exceeded the phase transition point of 51.5°C at the initial stage of charging. With the decrease of inlet temperature and the progress of heat transfer in PCMs, PCM 1 had no zones where the temperature was higher than melting point after 90 minutes. For PCM 2 and PCM 3, the zones width with temperature above melting point were from 4mm to 4.2mm (PCM 2) and from 5mm to 6.5mm (PCM 3). At 180 minutes, the zones widths over 315K (37°C) were 30mm (PCM 1), 28mm (PCM 2) and 12mm (PCM 3), respectively. In Mode 2, zones with temperatures higher than melting point of PCM 2 and PCM 3 existed in the whole charging process. The width of melting zones in PCM 2 was always about 6mm, while increasing gradually from 7mm to 15mm in PCM 3. At 180 minutes, the zones widths over 315K (37°C) were 27mm (PCM 2) and 16mm (PCM 3) respectively. In Mode 3, PCM 3 absorbed heat from HTF throughout the charging process and the melting zone width was always increasing. At 180 minutes, the zone width over 315K (37°C) was 32mm (PCM 3).

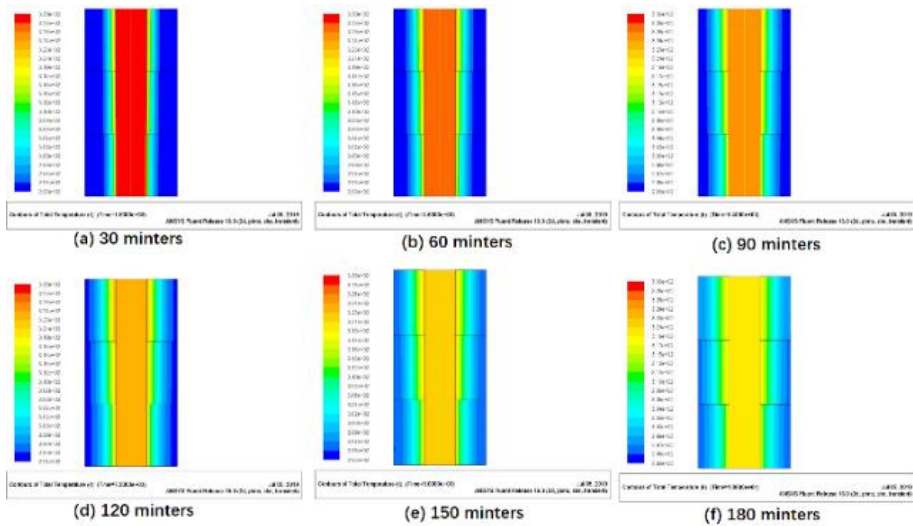


Figure 4(a): The transient temperature contours of Mode 1 ((a) 30 minutes, (b) 60 minutes, (c) 90 minutes, (d) 120 minutes, (e) 150 minutes, (f) 180 minutes)

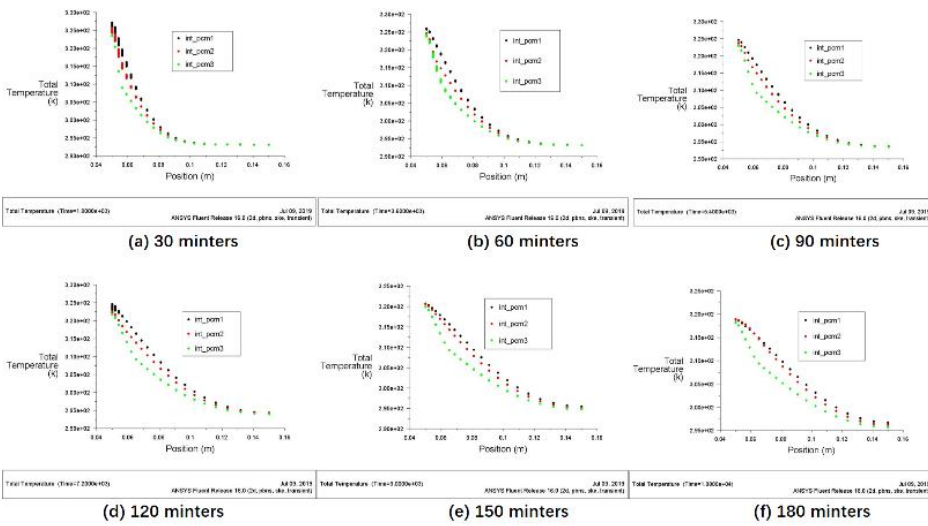


Figure 4(b): Temperature distribution in the X direction with flow time in Mode 1 ((a) 30 minutes, (b) 60 minutes, (c) 90 minutes, (d) 120 minutes, (e) 150 minutes, (f) 180 minutes)

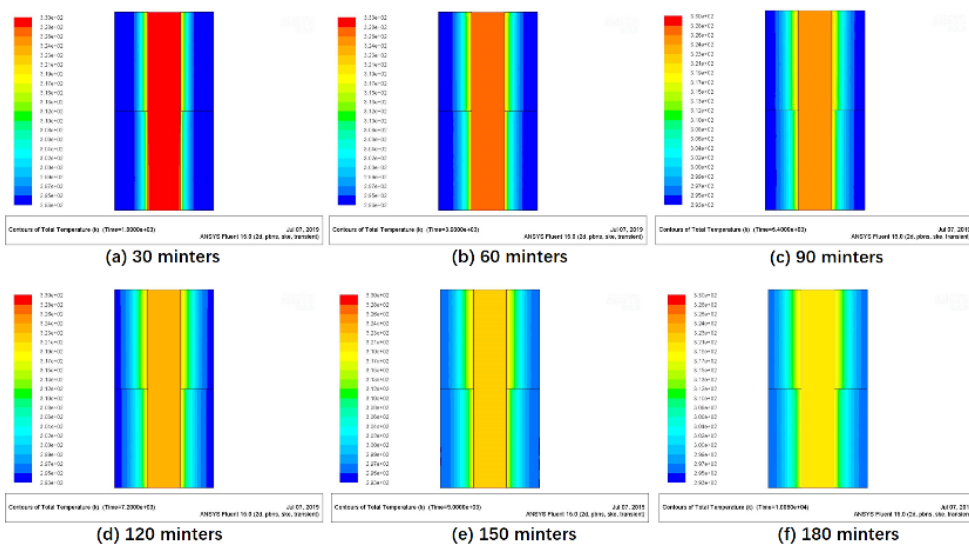


Figure 5(a): The transient temperature contours of Mode 2 ((a) 30 minutes, (b) 60 minutes, (c) 90 minutes, (d) 120 minutes, (e) 150 minutes, (f) 180 minutes)

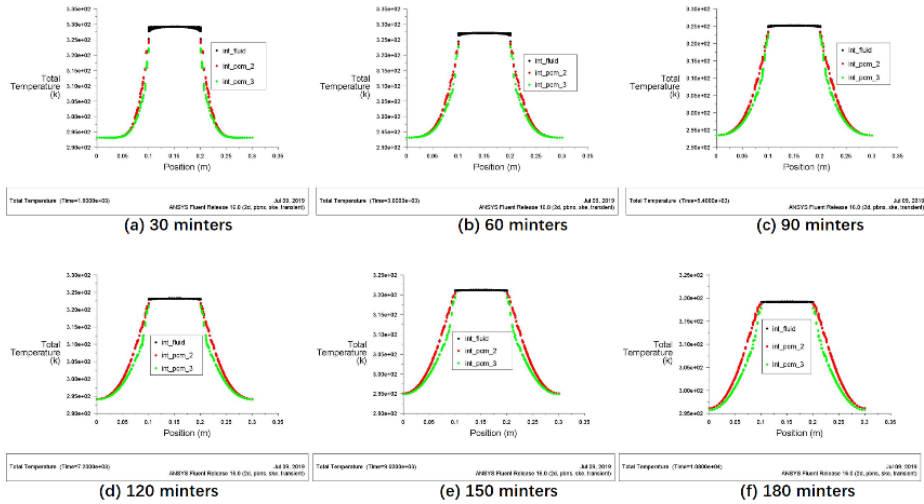


Figure 5(b): Temperature distribution in the X direction with flow time in Mode 2 ((a) 30 minutes, (b) 60 minutes, (c) 90 minutes, (d) 120 minutes, (e) 150 minutes, (f) 180 minutes)

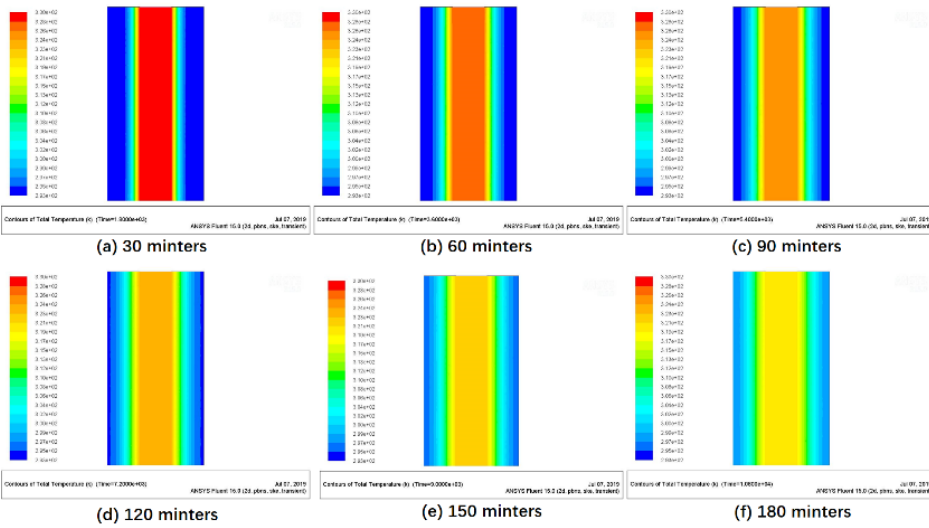


Figure 6(a): The transient temperature contours of Mode 1 ((a) 30 minutes, (b) 60 minutes, (c) 90 minutes, (d) 120 minutes, (e) 150 minutes, (f) 180 minutes)

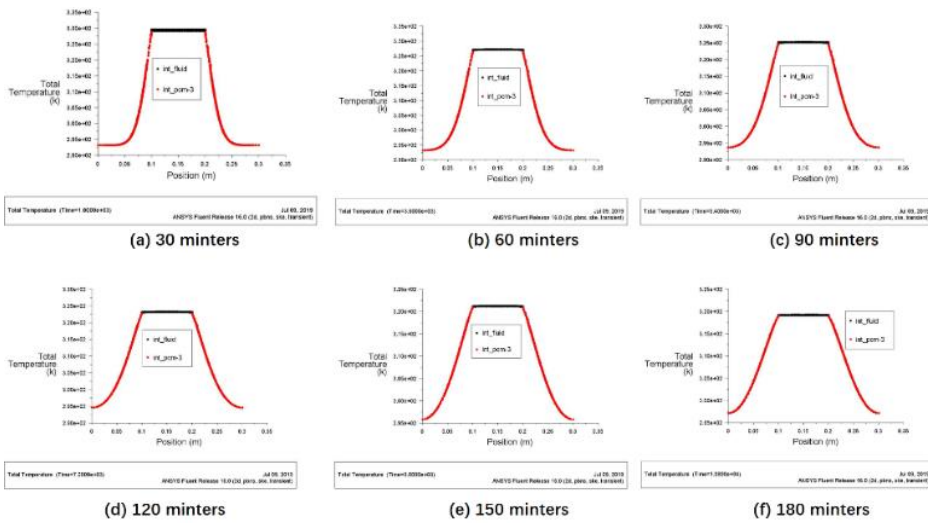


Figure 6(b): Temperature distribution in the X direction with flow time in Mode 3 ((a) 30 minutes, (b) 60 minutes, (c) 90 minutes, (d) 120 minutes, (e) 150 minutes, (f) 180 minutes)

Table 2: The width (mm) and volume (m^3) of PCMs in the corresponding temperature range

Mode	PCM	20-30°C	30-40°C	40-50°C	More than 50°C
Mode 1	PCM 1	50 mm (7.85e-3)	30 mm (3.2028e-3)	20mm (1.5072e-3)	0
	PCM 2	54 mm (8.3423e-3)	26 mm (2.7105e-3)	20 mm (1.5072e-3)	0
	PCM 3	54 mm (8.3423e-3)	38 mm (3.6751e-3)	8 mm (0.5426e-3)	0
Mode 2	PCM 2	54 mm (12.5135e-3)	28 mm (4.3257e-3)	18 mm (2.0008e-3)	0
	PCM 3	60 mm (13.5648e-3)	32 mm (4.4613e-3)	8 mm (0.8139e-3)	0
Mode 3	PCM3	45 mm (21.6189e-3)	33 mm (11.0044e-3)	22 mm (5.0567e-3)	0

Table 2 shows the width of PCMs in the corresponding temperature range when heat storage processes were completed in 3 Modes. In all three modes, the width decreased with the increase of temperature range. In addition, the temperature range of 20-30°C occupied the largest part, and there was no PCM with temperature higher than 50°C. In the later stage of heat storage, the inlet temperature was lower than that of the PCM in the initial stage, which led to reverse heat transfer.

4.2. Variation of PCMs' liquid fraction with flow time

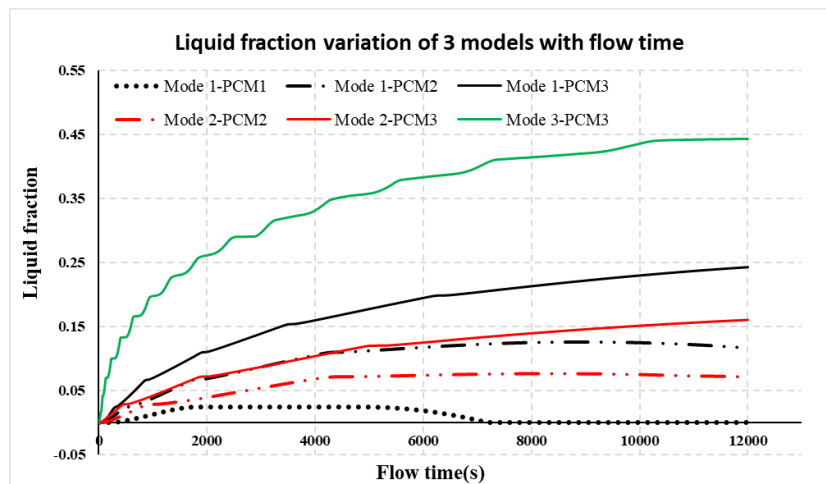


Figure 7: Liquid fraction variation in 3 Modes with flow time

Figure 7 presents the liquid fraction variation in 3 modes with flow time. On the whole, the liquid fraction increased along the flow direction of HTF, which was contrary to the order of the melting point of PCMs. In addition, in the later stage of thermal storage, the upstream PCMs with higher temperatures released a certain amount of heat for the downstream PCMs with lower temperatures.

PCM 3 in Mode 1 had the highest liquid fraction in the whole charging stage and reached 0.44 because of its lower transition point and single heat storage material. Similar to the results shown in Figure 6, the liquid fraction of PCM 3 in Mode 1 showed a tendency to increase first and then decrease, and eventually became 0 at about 2 hours. Therefore, a single PCM (with high melting point) mode could not realise latent heat storage and the heat storage capacity was small.

4.3. Energy performance

PCMs heat storage capacity

Table 3 and Figure 8 present the heat storage capacity in various temperature ranges of three modes. From the perspective of the first law of thermodynamics, the single PCM 3 in Mode 3 stored the most total energy 3828.12kJ including 622 kJ sensible heat and 3206.12 kJ latent heat. While multiple PCMs in Mode 1 and Mode 2 stored 1446.21 (579.04kJ sensible heat and 867.17 kJ latent heat) and 1325.84 kJ (495.4 kJ sensible heat and 830.44 kJ latent heat), respectively. Therefore, a single PCM with a lower transition point heat storage mode can store more total energy because of greater heat transfer temperature difference. The reason for this result is that the insulation

between different PCMs in the cascade heat storage mode caused the heat transfer process to be hindered, while the single PCM heat storage mode did not have this problem, and the single PCM with low transition point completed the storage of huge latent heat.

From the perspective of the second law of thermodynamics, the energy stored in the multiple PCMs in Mode 1 and Mode 2 was in the higher temperature range. PCMs in Mode 1 and Mode 2 stored 424.84 kJ and 382.25 kJ in the temperature range of 40-50°C, compared with 195 kJ in Mode 3. More than 90% of the energy stored in PCM 3 in Mode 3 was within the temperature range of 30-40°C. In contrast, 30% of the total energy of Mode 1 and 28.83% of Mode 2 was within the temperature range of 40-50°C. Therefore, cascade PCMs heat storage modes stored more energy in higher temperature range.

Table 3: Heat storage capacity in various temperature ranges of three modes

Modes	PCMs	Sensible heat (Latent heat)/kJ			Liquid fraction	Total energy (kJ)
		20-30°C	30-40°C	40-50°C		
Mode 1	PCM 1	64.66	79.5	63.6	0	207.76
	PCM 2	68.90	66.78	63.6 (297.64)	0.1220	496.92
	PCM 3	65	87 (569.53)	20	0.2353	741.53
	Total energy	198.56	802.81	424.84		1426.21
Mode 2	PCM 2	102.82	66.78	84.8 (267.45)	0.0731	521.85
	PCM 3	106	105 (562.99)	30	0.1551	803.99
	Total energy	208.82	734.77	382.25		1325.84
Mode 3	PCM 3	169	258 (3206.12)	195	0.4415	3828.12
	Total energy	169	3464.12	195		3828.12

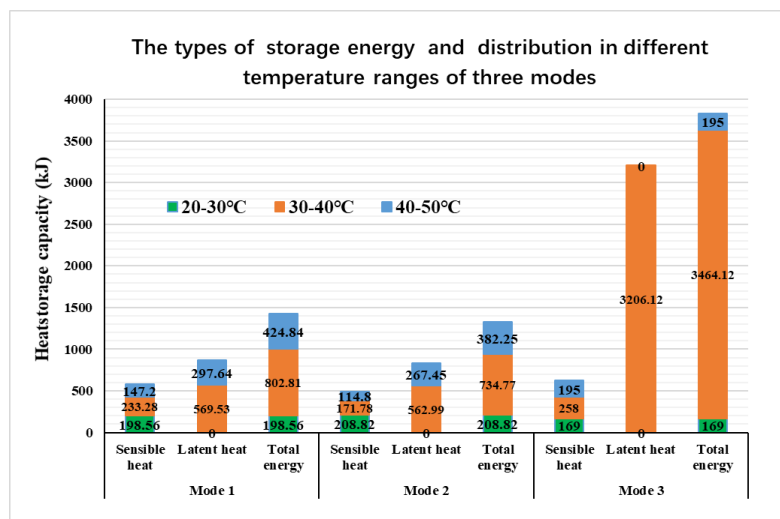


Figure 8: The types of storage energy and distribution in different temperature ranges of three modes

PCMs heat storage efficiency

The total energy from the collector was 11196.4 kJ in 15:00-18:00 by numerical integration. The PCMs heat storage efficiency can be calculated by Equation 9, being 12.74% of Mode 1, 11.84% of Mode 2 and 34.19% of Mode 3. Considering only the amount of energy, mode 3 had higher heat storage efficiency because it had larger heat transfer temperature difference and smaller heat transfer resistance compared with mode 1 and mode 2.

The effect of PCM heat storage on system efficiency and solar fraction

Figure 9 presents the system efficiency and solar fraction in different heat storage modes. In the original experimental results of the literature (Ayompe & Duffy, 2013), the energy from solar collector, energy storage in water tank, auxiliary energy and energy extracted from tank were 59.79 MJ, 22.6 MJ, 31MJ and 53.6 MJ, respectively. Therefore, the system efficiency and solar fraction of the original experiment were 37.8% and 42.16%, respectively. As can be seen from Figure 9, the system efficiencies were 40.18% (Water + Mode 1), 40.02% (Water + Mode 2) and 44.2% (Water + Mode 3), increasing by 2.38%, 2.22% and 6.4% respectively. The solar fractions were 44.82% (Water Mode 1), 44.64% (Water Mode 2) and 49.31% (Water Mode 3), increasing by 2.66%, 2.48%

and 7.15% respectively. Therefore, the system efficiency and solar fraction were improved by integrating PCM heat storage mode into the water tank heat storage mode in the period of low solar radiation density (15:00-18:00).

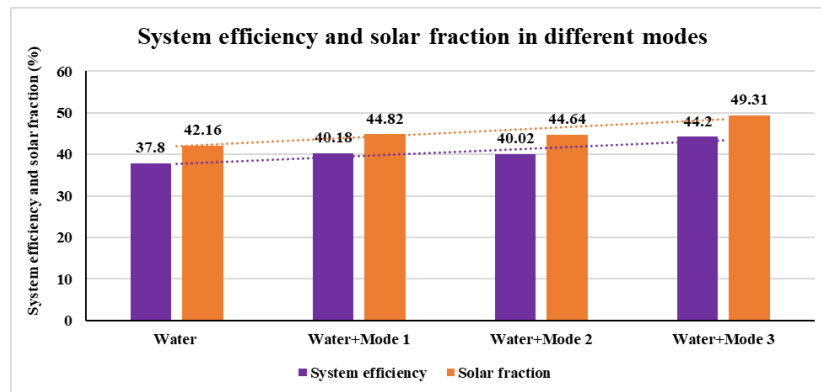


Figure 9: System efficiency and solar fraction in different modes

5. CONCLUSION AND OUTLOOK

Following on from the experimental results of published literature (Ayompe & Duffy, 2013), PCM heat storage modes were integrated into traditional SWH system in low solar radiation intensity period to improve heat storage capacity, system efficiency and solar fraction. There were three modes of PCM heat storage: cascade heat storage mode with three PCMs (Mode 1), cascade heat storage mode with two PCMs (Mode 2) and single PCM heat storage mode (Mode 3). By comparing these results with the original experimental results, the following conclusions can be drawn:

- As the inlet temperature decreased gradually, the melting point of PCMs should be lower than the initial temperature, otherwise it is difficult to store a large amount of latent heat.
- Single PCM with low transition point can store a large amount of latent heat, but 90% is in the low temperature range. The cascade PCM heat storage mode can get more heat in the high temperature range, and mode 1 is better than mode 2.
- Single PCM (with high melting point) mode cannot realise latent heat storage, and the heat storage capacity is small.
- The combination of SWH system and cascade PCM heat storage technology can improve system efficiency and solar energy fraction, and has a good application prospect.

In order to stored more heat in the high temperature range, the following improvements can be made in the cascade PCM physical model of the system:

- Increasing the heat transfer area and reducing the radial heat transfer gradient by appropriately reducing the external diameter and increasing the height of PCM tank.
- Increasing the number of PCMs to reduce the melting point difference between different PCMs.
- Increasing the mass ratio of PCM corresponding to melting point in the required temperature range to store more heat in that temperature range.

6. REFERENCES

- Abdullah, A. H., Abou-Ziyan, H. Z., & Ghoneim, A. A. (2003). Thermal performance of flat plate solar collector using various arrangements of compound honeycomb. *Energy Conversion and Management*, 44(19), 3093-3112. doi:10.1016/S0196-8904(03)00013-X
- Andersen, E., Furbo, S., & Fan, H. (2007). Multilayer fabric stratification pipes for solar tanks. *Solar Energy*, 81(10), 1219-1226. doi:10.1016/j.solener.2007.01.008
- Ayompe, L. M., & Duffy, A. (2013). Analysis of the thermal performance of a solar water heating system with flat plate collectors in a temperate climate. *Applied Thermal Engineering*, 58(1-2), 447-454. doi:10.1016/j.applthermaleng.2013.04.062

- Furbo, S., & Shah, L. J. (2003). Thermal advantages for solar heating systems with a glass cover with antireflection surfaces. *Solar Energy*, 74(6), 513-523. doi:10.1016/S0038-092x(03)00186-5
- Hollands, K. G. T., & Stedman, B. A. (1992). Optimization of an Absorber Plate Fin Having a Step-Change in Local Thickness. *Solar Energy*, 49(6), 493-495. doi:Doi 10.1016/0038-092x(92)90157-6
- Hussein, H. M. S., Mohamad, M. A., & El-Asfour, A. S. (1999). Optimization of a wickless heat pipe flat plate solar collector. *Energy Conversion and Management*, 40(18), 1949-1961. doi:Doi 10.1016/S0196-8904(99)00082-5
- Kalogirou, S. A. (2004). Solar thermal collectors and applications. *Progress in Energy and Combustion Science*, 30(3), 231-295. doi:10.1016/j.pecs.2004.02.001
- Kundu, B. (2002). Performance analysis and optimization of absorber plates of different geometry for a flat-plate solar collector: a comparative study. *Applied Thermal Engineering*, 22(9), 999-1012. doi:Pii S1359-4311(01)00127-2. Doi 10.1016/S1359-4311(01)00127-2
- Pandey, K. M., & Chaurasiya, R. (2017). A review on analysis and development of solar flat plate collector. *Renewable & Sustainable Energy Reviews*, 67, 641-650. doi:10.1016/j.rser.2016.09.078
- Seeniraj, R. V., & Narasimhan, N. L. (2008). Performance enhancement of a solar dynamic LHTS module having both fins and multiple PCMs. *Solar Energy*, 82(6), 535-542. doi:10.1016/j.solener.2007.11.001
- Shah, L. J., Andersen, E., & Furbo, S. (2005). Theoretical and experimental investigations of inlet stratifiers for solar storage tanks. *Applied Thermal Engineering*, 25(14-15), 2086-2099. doi:10.1016/j.applthermaleng.2005.01.011
- Sharma, A., Tyagi, V. V., Chen, C. R., & Buddhi, D. (2009). Review on thermal energy storage with phase change materials and applications. *Renewable & Sustainable Energy Reviews*, 13(2), 318-345. doi:10.1016/j.rser.2007.10.005
- Shukla, R., Sumathy, K., Erickson, P., & Gong, J. W. (2013). Recent advances in the solar water heating systems: A review. *Renewable & Sustainable Energy Reviews*, 19, 173-190. doi:10.1016/j.rser.2012.10.048
- Smyth, M., Eames, P. C., & Norton, B. (2001). Evaluation of a freeze resistant integrated collector/storage solar water-heater for northern Europe. *Applied Energy*, 68(3), 265-274. doi:Doi 10.1016/S0306-2619(00)00049-0
- Zhou, F., Ji, J., Yuan, W. Q., Zhao, X. D., & Huang, S. J. (2019). Study on the PCM flat-plate solar collector system with antifreeze characteristics. *International Journal of Heat and Mass Transfer*, 129, 357-366. doi:10.1016/j.ijheatmasstransfer.2018.09.114
- Zurigat, Y. H., Liche, P. R., & Ghajar, A. J. (1991). Influence of Inlet Geometry on Mixing in Thermocline Thermal-Energy Storage. *International Journal of Heat and Mass Transfer*, 34(1), 115-125. doi:Doi 10.1016/0017-9310(91)90179-1

#354: Courtyard buildings in desert climates: are they energy efficient when air-conditioned?

Khaled EL-DEEB¹, Ahmed SHERIF², Abbas EL-ZAFARANY³

¹ Faculty of Fine Arts, Alexandria University, Egypt. Km_eldeeb@yahoo.com

² School of Sciences and Engineering, The American University in Cairo, Egypt. asherif@aucegypt.edu

³ Faculty of Urban and Regional Planning, Cairo University, Egypt. elzafarany@hotmail.com

Courtyard buildings are typically recommended as a passive solution for compact desert architecture. However, an increasing number of desert buildings are becoming air-conditioned and isolated nowadays. In these cases, the performance of such a form becomes a matter of question, as the prospected goal becomes minimisation of energy consumption as means for achieving thermal comfort.

This paper questions the validity of using courtyard building shapes when air-conditioned in the desert environment. The performance of courtyard buildings is compared to that of other solid building forms. Also, the effect of form, proportions and orientation on energy consumption in the moderate and extreme hot desert conditions is detected. The paper also addresses the climatic conditions in which courtyard buildings likely to be recommended.

A base case of a two-storey squared residential building was simulated using the Energy-Plus software in three cities: Jeddah, Cairo and Alexandria. To this base case, three courtyard buildings of 1:1, 1:2 and 1:5 courtyard aspect ratios were compared. Solid rectangular forms having the same built area and nearly the same proportions as the courtyard buildings were also compared. The forms were tested under three cases of urban fabric: free-standing buildings, linear fabric and compact fabric. For comparison with a contrasting colder climate, all cases were also simulated under the temperate climate of Berlin.

Results showed that a free-standing courtyard building was not a preferred building form, as it resulted in the lowest energy efficiency in all tested cities. A better performance occurred when arranged in a linear pattern, nevertheless, it consumed more energy in comparison to solid building forms. When set in a compact urban pattern it proved to be more efficient than the solid building forms of the same fabric only in the moderate climates, while still less efficient in the extreme hot or cold climates. However, even when located in a compact fabric, air-conditioned courtyard buildings could not be recommended as they achieved less energy savings than solid rectangular forms set in a linear fabric.

Keywords: courtyard building, building form, urban fabric, energy efficiency, simulation, desert building

1. INTRODUCTION

Courtyard buildings were traditionally used in the desert as a passive approach for improving thermal comfort inside buildings in compact urban fabrics. They were typically recommended for desert climates as they provide self-shading and enhance natural ventilation. But nowadays, an increasing number of desert buildings are becoming mechanically air-conditioned and detached. It seemed intuitive to use the same passive approaches for minimising the energy consumption of these buildings.

However, this traditional building approach may not yield the anticipated energy reduction in all desert conditions. The self-shading effect of these buildings might not serve its purpose in very hot desert climates where heat gain through conduction largely supersedes that of radiation. The benefits of natural ventilation become irrelevant as buildings are fully air-conditioned. The large exposed surface area of courtyard buildings increases the liability to heat transfer between the outdoor and the indoor, especially with the commonly adopted detached urban fabrics nowadays.

This paper raises the following questions: does the shading effect of a free-standing courtyard house make it an efficient design alternative despite having a large exposed surface area? Is it affected by the building orientation and, if so, to what extent? Does the same effect apply for all desert climates? All these questions reflect the need for evaluating the validity of the commonly known assumptions and for quantifying the effects of courtyard building form and orientation as passive techniques when applied to air-conditioned buildings located in desert climates.

2. LITERATURE REVIEW

Review of recent literature demonstrated that the performance of a courtyard as a passive cooling strategy was discussed in numerous publications. However, the above raised research questions were hardly addressed in a quantitative systematic analysis. This is especially the case for the effect of using courtyards in two-storey residential air-conditioned located in desert climates.

The effect of a naturally ventilated courtyard on thermal performance was studied in hot arid climate (Al-Hemiddi and Al-Saud, 2001), tropical climate (Sadafi et al, 2011) and warm humid tropical climate (Rajapaksha et al., 2003). Results showed that a courtyard building with controlled natural ventilation, of specified opening time improved thermal performance. However in hot arid climate, the thermal performance resulting from continuous day and night natural ventilation was worse than keeping the building closed without natural ventilation (Al-Hemiddi and Al-Saud, 2001). The effect of courtyard morphology on thermal and luminous environment in hot arid regions was monitored for non-air conditioned buildings and showed that deep and protected courtyard tended to optimise daylight, solar exposure and thermal comfort (Guedouh and Zemmouri, 2017). The shading effect of different courtyard forms and that of courtyard proportions were studied by (Muhaisen and Gadi, 2006, a,b). It was found that in Rome, courtyards with deep proportions were recommended over shallow ones. However, in both studies the tested buildings were solid with no windows, and thus both the effect of transmitted solar radiation and the energy needed for artificial lighting were not considered. The passive effect of courtyard with plants and water pool on energy consumed for heating and cooling was studied, (Safarzadeh and Bahadori, 2005). It was found that passive features alone could not maintain comfort during hot summer times in Tehran, and that similar effects could be obtained through envelope components such as insulation and double glazing. However, the energy needed for artificial lighting that compensates for the effect of shading was not accounted for.

A study of energy performance of courtyard buildings in different climatic conditions showed that better performance was achieved in hot-dry and hot-humid climates rather than in cold and temperate ones (Aldawoud, 2008). The study was limited to zones overlooking the courtyard and ignored the influence of the external perimeter walls and zones. The impact of integrating deep courtyards in mid-rise housing buildings in Dubai was evaluated, showing that a six-storey courtyard building achieved up to 6.9% savings (Al-Masri and Abu-Hijleh, 2012). The addressed heights ranged from 4 to 10 stories high, while two-storey low-rise residential buildings that are common in some countries like Saudi Arabia and in new urban settlements in Egypt were not considered. A seasonal courtyard/atrium mode strategy was proposed by Tabesh and Sertyesililik (2016) for cities in Turkey where energy savings were achieved when courtyard mode was used in summer while atrium mode used in winter. Almhafdy et al. (2019) explored the impact of courtyard geometrical configurations on energy performance in the hot humid tropical climate of Kuala Lumpur, Malaysia.

Some studies addressed the effect of orientation on thermal performance for non-air-conditioned buildings in a hot-humid tropical climate (Al-Tamimi et al., 2011) and the implications of orientation on thermal energy efficiency of passive buildings in mild temperate climate (Morrissey et al., 2011). The former found that an east facing room was higher in temperature compared to a corresponding west facing room for window-to-wall ratios up to 25% where they became nearly similar. The latter found that smaller houses and higher performance designs can retain their performance better across a wider range of orientations in comparison to houses over 250m² area or houses designed for base level of energy-efficiency compliance.

The impact of building form and urban pattern on energy consumption was studied by El-Deeb et al. (2012) for different forms including one squared courtyard building of 1:1 proportions, while courtyard buildings of other length-to-width ratios were not studied. The performance of the examined courtyard form was surpassed by that of other forms. This raised a question of whether different courtyard length-to-width as well as height proportions would provide better results. The effect of building height proportions and that of thickness surrounding a courtyard were investigated for a building with also a squared courtyard of fixed dimensions (El-Deeb et al. 2014). In the current study, courtyard forms of different length-to-width proportions are investigated.

3. OBJECTIVE

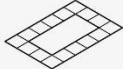
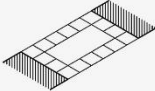
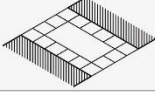
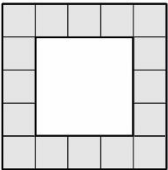
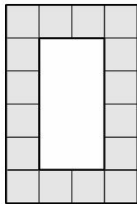
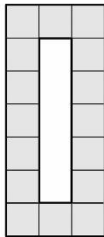
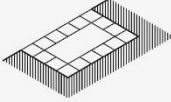
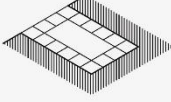
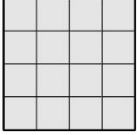
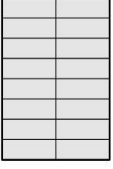
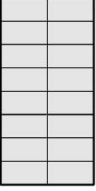
This paper questions the validity of using courtyard building shapes when air-conditioned in the desert environment, and investigates the impact of different courtyard length-to-width proportions on energy consumption. The study compares performance of courtyard buildings to those of solid forms of similar proportions and addresses the climatic conditions in which courtyard buildings likely to be recommended.

4. METHODOLOGY

To evaluate the effect of courtyard, three courtyard buildings of 1:1, 1:2, 1:5 courtyard length-to-width proportions - named Court A, B and C respectively - were examined to represent a variety of courtyard aspect ratios. Each of these forms was simulated for energy performance in different orientations and climates, and in three scenarios of attachment representing alternatives of urban fabric configurations: free-standing, linear (attached from 2-sides) and compact (attached from 3-sides). In linear and compact configurations, rectangular shapes were either attached / exposed from the short or long side. Both cases were investigated.

The performance of courtyard buildings were then compared to that of corresponding solid forms of the same area and similar proportions. The solid square form, Solid A, was considered as a base case for comparisons and analysis. The examined forms and fabric types are presented in Table 1.

Table 1: Simulated building forms

FABRIC TYPE	SIMULATED BUILDING FORMS		
	COURT (A)	COURT (B)	COURT (C)
FREE-STANDING 			
LINEAR (A)  (B) 	 Court 1:1 Form 1:1	 Court 1:2 Form 1:1.5	 Court 1:5 Form 1:2.3
COMPACT (A)  (B) 	 Form 1:1	 Form 1:1.5	 Form 1:1.2

Each of the six building forms was tested in the four principal orientations: North, East, South and West. Significant differences for each shape were displayed in the results. When the tested building was symmetrical in all directions, only North results were displayed as they represent those of all orientations. As East and West in most of the cases did not have significant differences; the average of their results were displayed. When buildings were set in a linear or a compact fabric, differences in the sides attached resulted in differences in performance. The case of higher impact on energy performance was analysed and discussed.

The aforementioned forms were modelled for energy simulation as two-storey height buildings with fixed total floor and window areas. Residential building schedules were assigned. Model details and simulation parameters are presented in Table 2.

Table 2: Simulation parameters for tested building forms.

SIMULATION PARAMATERS					
BUILDING		CONSTRUCTION			
Area/floor	256 m ²	External walls	20cm concrete block + 2cm cement plaster each side		
Total Area	512 m ²	Internal walls	10cm concrete block + 2cm cement plaster each side		
No. of zones/floor	16	Roof	Insulated with 10cm polystyrene foam		
No. of people	7	Internal slab	20cm concrete + 10cm flooring + 2cm plaster		
Ground floor activity	Living	Windows	Area	Fixed for all forms = WWR 20% of "Solid A".	
First floor activity	Bedroom		Type	Double glazed clear	
HVAC	Setpoint	Setback	LIGHTING	Fluorescent	Suspended
Cooling	23	28	Daylighting control		
Heating	21	12	Illuminance:	Dimming:	Sensor height
Type	Split		200 LUX	200 lux	On/off
URBAN FABRIC	Free-Standing		Linear		Compact

Simulation was performed under the climates of Jeddah in Saudi Arabia and both Cairo and Alexandria in Egypt. Despite all of them being classified as hot-arid desert according to Köppen-Geiger climate classification (Kottek et al., 2007), there are differences in temperature ranges across the three cities. Jeddah is generally higher in temperature than all other cities, followed by Cairo then by Alexandria. For comparison with a city of a different climate, simulations were also performed for Berlin, Germany, classified as warm temperate fully humid warm summer (Kottek et al., 2007), and whose temperature ranges fall far below those of the addressed desert cities, Figure 1.

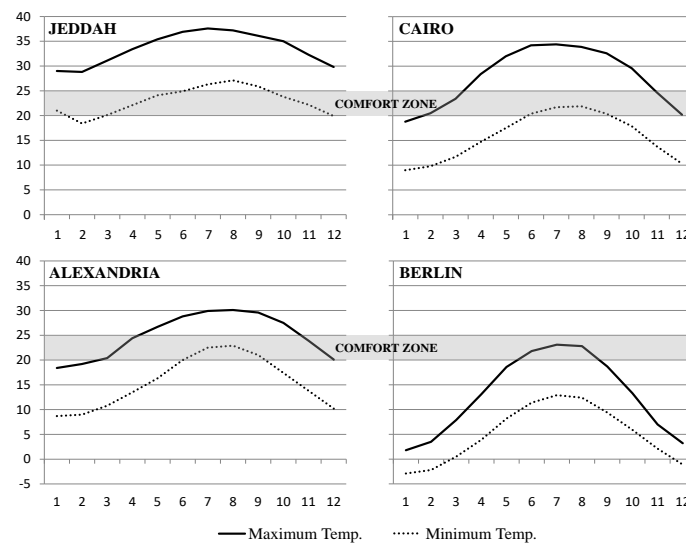


Figure 1: Monthly mean dry-bulb temperatures in tested cities.

5. RESULTS AND DISCUSSION

Results were responsive to the climatic conditions of the tested cities. Tables 3, 4 and 5 show the values of annual energy consumption of all tested cases, in addition to the percent change from the solid square base-case in each of the tested cities.

5.1. Base-case results

Figure 2 illustrates that the energy use intensity (EUI) was highest in Jeddah city. It reached an annual total of 133 Kwhr/m², dominated by a cooling energy of 112 Kwhr/m², no heating and 21 Kwhr/m² for lighting. Cairo and Berlin were of a nearly similar total consumption: 79 and 80 Kwhr/m² respectively, but with a difference in load distribution. Cairo was cooling dominated with minimal heating: only 3 Kwhr/m². To the contrary, the heating loads were

dominant in Berlin, while cooling energy reached only 7 Kwhr/m². The Annual EUI in Alexandria was the lowest among all cities. It reached only 66 Kwhr/m², with most of the energy was consumed for cooling.

Lighting energy consumption of the base-case showed similarity across the tested cities, where its EUI values were 21, 22, 23 and 24 Kwhr/m² in Jeddah, Cairo, Alexandria and Berlin respectively. However, it reflected a minor increase in artificial lighting in cities of higher latitudes.

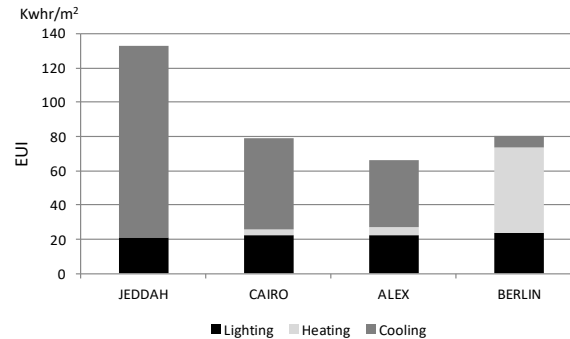


Figure 2: Energy performance of base case across tested cities

5.2. Energy performance of courtyard buildings

Free-Standing

The free-standing square courtyard building (Court-A) was simulated and compared to the base-case (Solid-A). Results demonstrate that the courtyard building lead to an increase in energy consumption by 15% in Jeddah, 8.4% in Cairo and 4.8% in Alexandria, while reached 45% in Berlin Figure 3 and Table 3. The energy consumption of rectangular courtyard forms (Court-B and Court-C) varied according to orientation. With their longer sides facing North and South, their energy consumption was lower than that of the square-shaped courtyard building, but when they faced the East and West they consumed more. However in both cases, energy consumption was also significantly higher than that of the base-case in all cities except for north-oriented cases in Alexandria, where a minor increase of less than 2% occurred at Court-B and nearly similar performance as the base case was achieved by Court C.

The difference between orientation cases for Court-B and Court-C forms ranged from 8.7% to approximately 17% higher than the base-case in Jeddah and 4.5% to 15.8% in Cairo. In Alexandria, the range started from a value close to that of the base case and reached 9% higher, Figure 4. In Berlin, the difference in consumption due to orientation was relatively small, but the consumption itself was very high with a range of 45.5% to 48% of increase in EUI.

On the other hand, solid rectangles of proportions similar to that of courtyard buildings achieved savings in desert cities when oriented to North, Figure 5. Compared to the base case, the North-oriented Solid-B form resulted in 2.6%, 5.3%, and 4.7% energy savings in Jeddah, Cairo and Alexandria respectively, while the Solid-C form of the same orientation achieved 4.4%, 8.7% and 7.5% energy savings in the three cities respectively. Compared to the corresponding courtyard building, the Solid-B form resulted in 14.7%, 12.1%, 6.3% more savings than the Court-B form in Jeddah, Cairo and Alexandria respectively. Also the Solid-C form with the same North orientation achieved 13.1%, 13.2% and 7.8% more savings than its corresponding Court-C form in these cities respectively. It can be noticed that the difference between corresponding courtyard and solid forms of similar proportions were lower in the mild climate of Alexandria than in other desert cities.

Table 3: Annual energy consumption of free-standing building forms in tested cities.

Free-Standing	Orientation	JEDDAH						CAIRO					ALEXANDRIA					BERLIN				
		% form Base Case	Annual Energy consumption Kwahr/m ²				% form Base Case	Annual Energy consumption Kwahr/m ²				% form Base Case	Annual Energy consumption Kwahr/m ²				% form Base Case	Annual Energy consumption Kwahr/m ²				
			Heating	Cooling	Lighting	TOTAL		Heating	Cooling	Lighting	TOTAL		Heating	Cooling	Lighting	TOTAL		Heating	Cooling	Lighting	TOTAL	
Free-Standing	COURT (A)	N	15.1%	0	137	16	153	8.4%	11	59	17	86	4.8%	13	39	17	69	45.8%	93	4	19	117
	COURT (B)	N / S	12.1%	0	133	16	149	6.8%	8	60	17	85	1.6%	12	38	17	67	45.5%	93	4	19	116
		E / W	16.9%	0	140	15	155	14.0%	9	64	17	90	7.3%	14	40	17	71	46.4%	93	4	19	117
	COURT (C)	N / S	8.7%	0	128	16	144	4.5%	8	57	17	83	0.3%	13	36	18	66	46.5%	94	4	20	117
		E / W	16.9%	0	139	16	155	15.8%	10	65	17	92	8.9%	15	40	18	72	48.0%	94	4	20	118
	SOLID (A)	N	0.0%	0	112	21	133	0.0%	3	54	22	79	0.0%	4	39	23	66	0.0%	50	7	24	80
	SOLID (B)	N / S	-2.6%	0	110	20	129	-5.3%	3	51	21	75	-4.7%	4	38	21	63	0.6%	50	6	25	81
		E / W	1.9%	0	116	20	135	1.7%	4	56	21	81	1.4%	5	41	22	67	2.6%	50	7	25	82
	SOLID (C)	N / S	-4.4%	0	109	18	127	-8.7%	4	49	19	72	-7.5%	4	37	20	61	1.8%	53	5	23	82
E / W		3.1%	0	118	19	137	1.2%	4	56	20	80	0.5%	5	41	21	66	4.1%	53	7	24	83	

These results indicate that, in all cities, both square and rectangular free-standing courtyard buildings consumed more energy than the base-case and also more energy than their corresponding solid forms. Only in Alexandria, north-oriented rectangular courtyard forms were of values close to the base case, however, they still consumed more energy than the corresponding solid forms.

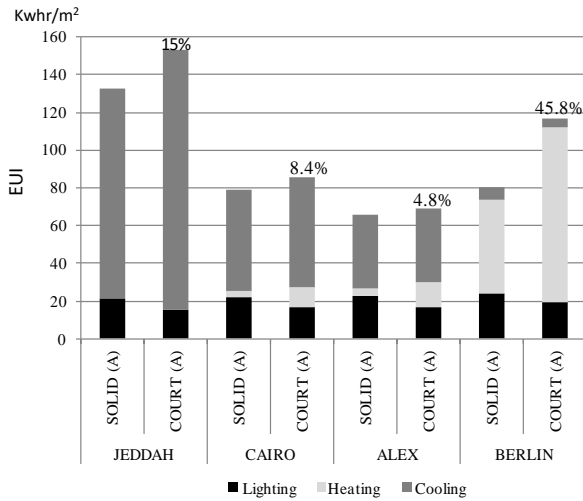


Figure 3: Energy use intensity of Court-A compared to Solid-A base-case in each city, indicating the percent of increase in total energy consumption.

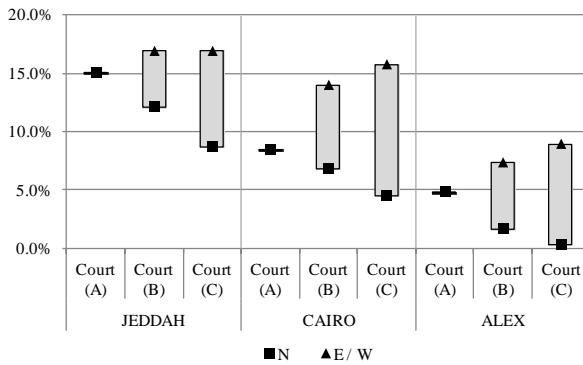


Figure 4: Range of percent change in EUI due to difference in orientation for courtyard buildings in desert cities.

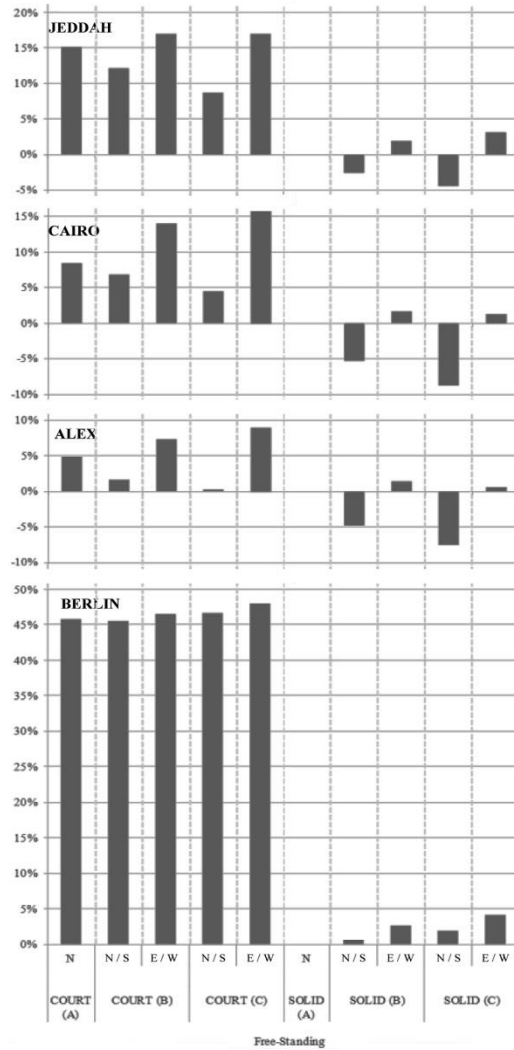


Figure 5: Percent change in energy consumption of tested free-standing forms compared to the base case.

Compact Fabric

Historically, courtyard buildings were used in compact urban fabrics; thus a small surface area was exposed. To check their performance in this case, Court-A, B and C forms were set in a compact fabric in which they were attached from 3 sides - as shown in Table 1 - and simulated for energy performance, Table 4. As a result, each North-facing building was backed by an identical South-facing one. Performance of these two buildings was definitely different. Therefore, their average value of consumption was used for analysis in order to represent the overall effect of using such an urban fabric. The same was applied to East and West-oriented cases.

Results showed that attachment Type A – in which the longer side of the form was exposed – was of better performance than Type B in desert cities, Figure 6. In this attachment, Type A, the averaged North and South orientation results were also of better performance than those of East and West for both courtyard and solid forms. This indicated that the more the surface area oriented to North and hardly subjected to direct solar radiation, the better. The contrary occurred in Berlin, as the less exposed surface and the more solar access is preferred due to the climate's low temperatures in most of the year.

In desert cities, courtyard buildings in compact fabric showed energy savings compared to the free-standing base case. The highest percentage of energy savings was 12.3% achieved in Alexandria by Court-B form with minor increase over Court-A and B cases, while the corresponding solid forms of the same urban fabric, attachment type and orientation lead to an increase in consumption that ranged from 3.5% to 12.9%. A wide range of difference between the corresponding cases was, thus, noticed. The Court-B achieved 15.8% more savings than the Solid-B form of the same settings. This difference reached 16.6% between Court-C and Solid-C, and 24% between Court-A and Solid-A cases.

In Cairo, courtyard buildings were also of better performance than solid forms, but with a narrower range of difference between both building types. The Court-A form achieved the highest savings of 11.2% followed by Court-B, then by Court C that achieved 9.3% and 8% savings respectively. Both Court-B and Solid-B cases achieved the same averaged energy saving values. Court-C was of slightly better performance than Solid-C with only 1.3% difference. Court-A showed a higher difference from Solid-A of the same settings reaching 10.2%, which was less than the difference between both cases in Alexandria.

On the other hand, in Jeddah, all solid forms proved to be of better performance than all cases of courtyard forms. Despite the latter forms achieved energy savings reaching 11.5%, 11.3% and 10.7% for Court-A, B and C cases respectively, they were vastly exceeded by savings achieved by solid forms that reached its highest value at Solid-B form by 22.7% savings, followed by Solid-C, 20%, then Solid-A 18.8%. This indicates solid forms achieved nearly double the savings of courtyard cases, and thus indicated that courtyard buildings were not as efficient in such a hot climate. In Berlin, solid forms achieved more than 27% savings, while courtyard forms – in general - lead to an increase in consumption.

From these results, it was clear that, courtyard buildings in a compact urban fabric achieved more savings than those achieved by free-standing solid forms in all desert cities, while increased consumption in the temperate climate of Berlin. In the moderate climate of Alexandria, courtyard buildings were more efficient than solid forms in the same compact fabric. The same was in Cairo, but with a smaller difference between the corresponding courtyard and solid forms. In contrast, courtyard forms were far less efficient than solid forms in the severe hot climate of Jeddah, even when set in a compact fabric.

Table 4: Annual energy consumption of building forms set in a compact fabric in tested cities.

	ORIENTATION	JEDDAH					CAIRO					ALEXANDRIA					BERLIN					
		% form Base Case	Annual Energy consumption Kwahr/m ²				% form Base Case	Annual Energy consumption Kwahr/m ²				% form Base Case	Annual Energy consumption Kwahr/m ²				% form Base Case	Annual Energy consumption Kwahr/m ²				
			Heating	Cooling	Lighting	TOTAL		Heating	Cooling	Lighting	TOTAL		Heating	Cooling	Lighting	TOTAL		Heating	Cooling	Lighting	TOTAL	
Compact Fabric	COURT (A)	N	-17.4%	0	91	19	110	-13.4%	7	42	20	69	-12.3%	9	29	20	58	4.7%	58	3	22	84
		E / W	-5.7%	0	106	19	125	-3.6%	6	51	20	76	-4.9%	7	35	20	63	4.2%	56	5	22	83
		S	-5.6%	0	106	19	125	-9.0%	3	49	20	72	-10.0%	4	36	20	59	0.9%	54	5	22	81
	COURT (B)	N	-18.3%	0	90	18	108	-13.3%	6	43	20	69	-13.9%	9	28	20	57	7.5%	62	3	21	86
		E / W	-2.0%	0	112	18	130	2.6%	5	57	20	81	-3.0%	8	37	20	64	7.1%	60	5	21	86
		S	-4.3%	0	109	18	127	-5.3%	2	54	20	75	-10.7%	3	36	20	59	2.7%	56	5	21	82
	COURT (C)	N	-15.9%	0	93	19	112	-9.0%	5	46	21	72	-10.9%	8	30	20	59	2.3%	56	3	22	82
		E / W	-8.1%	0	103	19	122	-2.2%	4	52	21	77	-6.2%	6	35	20	62	1.7%	54	5	22	81
		S	-5.7%	0	106	19	125	-3.7%	2	54	20	76	-9.0%	4	36	20	60	-0.7%	52	5	22	80
	SOLID (A)	N	-17.7%	0	88	21	109	-10.2%	7	41	23	71	-10.8%	10	26	22	59	13.9%	64	3	24	91
		E / W	-0.7%	0	111	21	132	5.2%	5	56	22	83	-0.4%	8	36	22	66	12.3%	62	4	23	90
		S	-3.7%	0	108	20	128	-5.8%	2	52	21	75	-11.4%	3	35	21	59	7.3%	59	5	22	86
	SOLID (B)	N	-14.1%	0	90	24	114	-5.4%	5	45	25	75	-5.9%	7	30	25	62	3.7%	53	3	27	83
		E / W	-8.8%	0	97	25	121	-0.8%	4	49	25	79	-3.9%	6	33	25	64	3.6%	51	5	27	83
		S	-5.7%	0	101	24	125	0.0%	2	52	25	79	-3.6%	4	35	25	64	2.0%	50	5	27	82
	SOLID (C)	N	-34.8%	0	56	31	87	-20.4%	1	31	31	63	-12.3%	2	25	31	58	-28.8%	20	6	31	57
		E / W	-2.3%	0	99	31	130	15.2%	0	60	31	91	17.1%	0	46	31	77	-21.1%	17	15	31	63
		S	-2.8%	0	98	31	129	18.3%	0	63	31	94	38.0%	0	60	31	91	-22.0%	13	19	31	62
	SOLID (A)	N	-39.2%	0	56	25	81	-28.2%	2	29	26	57	-21.1%	2	24	26	52	-29.2%	25	5	27	57
		E / W	-6.0%	0	100	25	125	7.8%	0	59	26	85	8.3%	0	45	26	72	-22.9%	21	13	27	62
		S	-6.1%	0	100	25	125	10.7%	0	62	26	88	28.1%	0	59	26	85	-26.1%	16	17	27	59
	SOLID (B)	N	-35.5%	0	53	32	86	-19.9%	1	30	32	63	-11.4%	1	25	32	59	-30.9%	16	6	32	55
		E / W	-5.6%	0	93	32	125	12.3%	0	56	32	89	18.1%	0	45	32	78	-22.7%	14	15	32	62
		S	-5.6%	0	93	32	125	18.4%	0	61	32	94	36.5%	0	58	32	90	-21.9%	11	19	32	63
SOLID (C)	N	-37.2%	0	58	26	83	-26.0%	2	30	26	59	-18.8%	3	24	27	54	-25.8%	28	4	27	59	
	E / W	-2.8%	0	103	26	129	10.4%	0	61	26	87	10.3%	0	46	26	73	-19.8%	24	13	27	64	
	S	-2.7%	0	104	26	129	12.7%	0	63	26	89	29.8%	0	59	26	86	-23.4%	18	16	27	61	
SOLID (B)	N	-37.6%	0	50	33	83	-21.3%	1	28	33	62	-12.7%	1	23	33	58	-32.3%	15	6	33	54	
	E / W	-11.2%	0	85	33	118	6.9%	0	51	33	85	12.4%	0	41	33	74	-25.2%	13	14	33	60	
	S	-11.2%	0	85	33	118	12.3%	0	56	33	89	29.5%	0	52	33	86	-24.6%	10	17	33	60	

Linear Fabric

In order to investigate the performance of courtyard buildings in a linear urban fabric, all forms were examined in case of being attached from two sides as presented in Table 1. For that, two orientations cases were examined, as in each case the form faced two directions in the meantime: North/South (N/S) or East/West (E/W), Table 5.

Results showed that all forms were of better performance of in N/S orientation than in E/W one, Figure 7. Attachment types A and B resulted in nearly similar values in case of Court-B in each city. Both attachment types also showed similarity of results in Court-C case in Jeddah and Berlin, while larger differences occurred in Cairo and Alexandria, in which the attachment case A achieved more savings.

All N/S-oriented courtyard building forms in linear fabric achieved savings compared to the base case in desert cities, however, in E/W orientation most of the cases caused an increase in consumption. Court-B achieved the highest energy savings. Reaching 9.7%, 7.8% and 10.7% in Jeddah, Cairo and Alexandria respectively. In general, the energy savings achieved by courtyard buildings ranged from 4%-9.7% in Jeddah, 6.4%-7.9% in Cairo and 8.7%-10.7% in Alexandria.

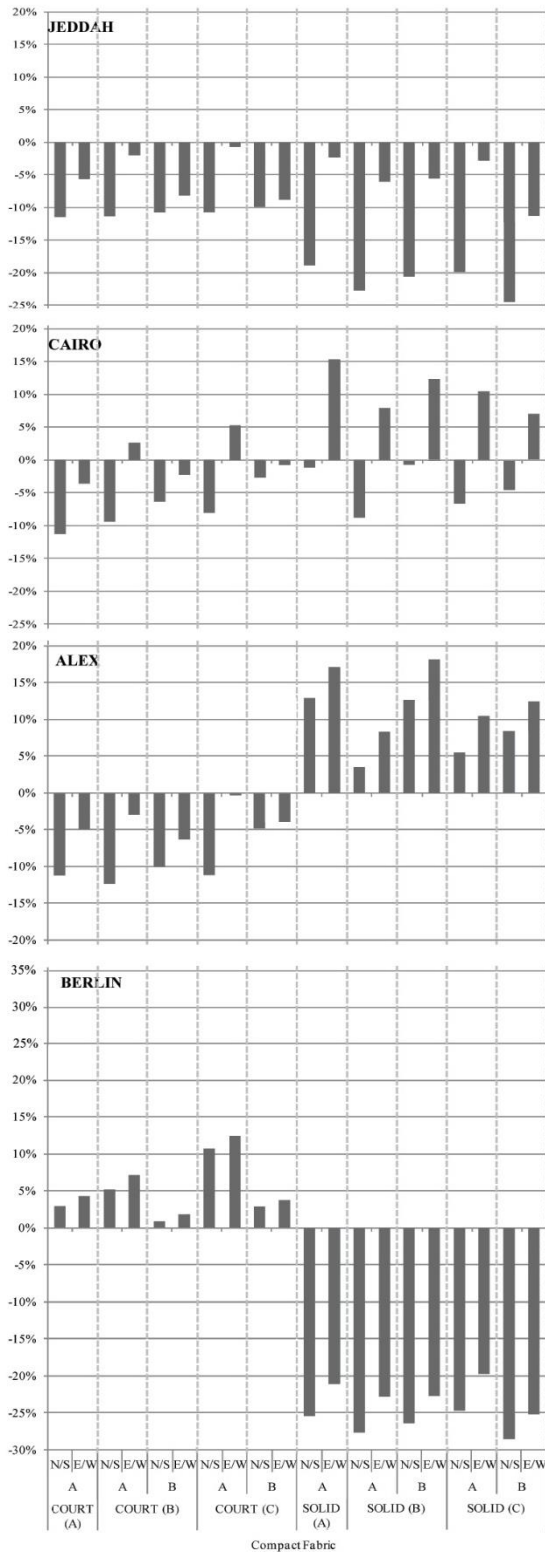


Figure 6: Percent change in energy consumption of tested forms in a compact urban fabric compared to the base case.

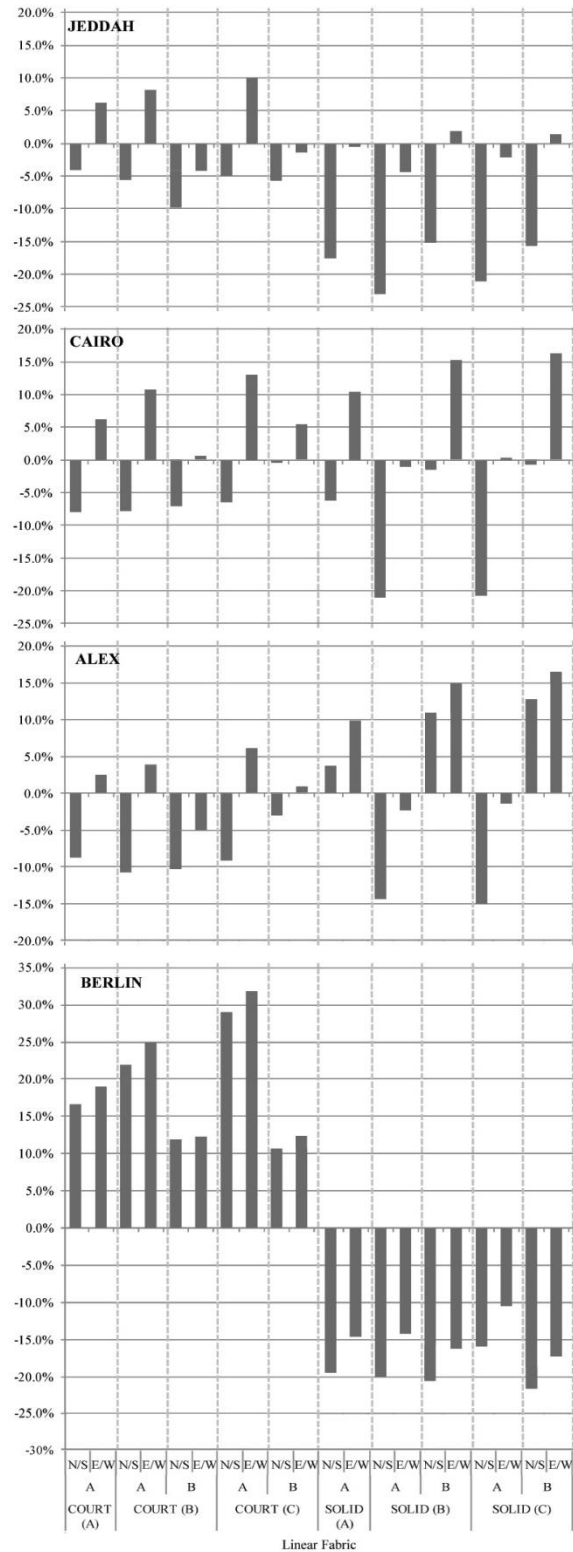


Figure 7: Percent change in energy consumption of tested forms set in a linear fabric compared to the base case.

Nevertheless, these savings were vastly exceeded by those of solid forms. The Solid-B form achieved the highest savings in Jeddah and Cairo, reaching 22.9% and 21%, while Solid-C form achieved the highest savings in Alexandria reaching 14.9%. These values indicate that solid rectangular forms in a linear fabric resulted in more than double the amount of energy savings achieved by courtyard buildings in Jeddah and Cairo, and were of significant additional energy savings in Alexandria. Moreover, they significantly exceeded the amounts of energy

savings achieved by courtyard buildings located in a compact urban fabric in Jeddah and Cairo, while achieved minor additional savings over those in Alexandria. In Berlin, all courtyard cases lead to a significant increase in consumption.

Thus, although courtyard buildings proved to be more efficient than solid forms when used in compact urban fabrics in desert cities, they cannot be recommended because the savings they achieved were exceeded by those of rectangular solid forms that are set in a linear fabric.

Table 5: Annual energy consumption of building forms set in a linear fabric in tested cities.

	ORIENTATION	JEDDAH					CAIRO					ALEXANDRIA					BERLIN					
		% form Base Case	Annual Energy consumption Kw/hr/m ²				% form Base Case	Annual Energy consumption Kw/hr/m ²				% form Base Case	Annual Energy consumption Kw/hr/m ²				% form Base Case	Annual Energy consumption Kw/hr/m ²				
			Heating	Cooling	Lighting	TOTAL		Heating	Cooling	Lighting	TOTAL		Heating	Cooling	Lighting	TOTAL		Heating	Cooling	Lighting	TOTAL	
Linear Fabric	COURT (A)	N / S	-4.0%	0	110	17	127	-7.9%	6	48	18	73	-8.7%	7	34	19	60	16.5%	68	4	21	93
		E / W	6.1%	0	123	18	141	6.1%	7	58	19	84	2.6%	9	40	19	68	19.0%	69	5	21	95
	COURT (B)	N / S	-5.6%	0	109	17	125	-7.8%	5	50	18	73	-10.7%	8	32	18	59	21.9%	74	3	20	98
		E / W	8.2%	0	127	17	144	10.7%	7	62	19	88	3.9%	11	39	19	69	24.8%	74	5	21	100
	COURT (C)	N / S	-9.7%	0	101	19	120	-7.0%	5	49	20	74	-10.3%	8	32	20	59	11.8%	63	4	22	89
		E / W	-4.1%	0	110	18	127	0.4%	6	54	19	80	-4.9%	9	35	19	63	12.2%	64	5	21	90
	SOLID (A)	N / S	-4.9%	0	109	17	126	-6.4%	6	50	18	74	-9.1%	10	32	18	60	29.0%	79	3	21	103
		E / W	10.1%	0	129	17	146	12.9%	8	62	19	89	6.1%	12	39	19	70	31.7%	80	4	21	105
	SOLID (B)	N / S	-5.6%	0	103	23	125	-0.4%	4	51	24	79	-2.9%	7	34	24	64	-14.2%	59	4	26	89
		E / W	-1.3%	0	108	23	131	5.4%	5	55	24	84	1.0%	7	36	24	67	12.3%	59	5	26	90
	SOLID (C)	N / S	-17.5%	0	84	26	110	-6.2%	2	46	27	74	3.7%	2	40	27	69	-19.4%	29	9	27	64
		E / W	-0.4%	0	106	26	132	10.4%	1	60	27	87	9.9%	1	45	27	73	-14.6%	29	12	27	68
	SOLID (A)	N / S	-22.9%	0	85	18	102	-21.0%	2	42	19	63	-14.3%	2	35	19	57	-20.0%	35	6	23	64
		E / W	-4.3%	0	109	18	127	-1.0%	1	58	19	78	-2.3%	2	43	20	65	-14.2%	35	10	24	69
	SOLID (B)	N / S	-15.2%	0	83	30	113	-1.4%	1	47	30	78	10.9%	2	41	30	73	-20.6%	23	10	31	64
		E / W	1.8%	0	105	30	135	15.1%	1	60	30	91	15.0%	1	45	30	76	-16.2%	24	13	31	67
	SOLID (C)	N / S	-20.9%	0	87	18	105	-20.6%	2	42	19	63	-14.9%	3	34	19	56	-15.9%	39	5	23	67
		E / W	-2.0%	0	113	17	130	0.1%	2	59	19	79	-1.4%	3	43	20	65	-10.5%	40	9	23	72
	SOLID (C)	N / S	-15.5%	0	82	31	112	-0.5%	1	47	31	79	12.6%	1	42	31	74	-21.6%	21	11	31	63
		E / W	1.4%	0	104	31	135	16.3%	0	61	31	92	16.5%	0	45	31	77	-17.2%	21	14	31	66

6. CONCLUSION

Three courtyard building forms of 1:1, 1:2 and 1:5 courtyard length-to-width proportions were examined for energy performance and compared to solid building forms of the same area and similar building proportions, in order to investigate the validity of using air-conditioned courtyard building forms in desert climates. The buildings were examined in three cases of urban fabric configurations: free-standing, linear and compact.

Free-standing courtyard buildings proved to consume more energy than all free-standing solid forms in all cities.

In a compact fabric, well-oriented courtyard buildings achieved significant energy savings reaching 11.2%, 11.5% and 12.3% in Jeddah, Cairo and Alexandria respectively. Their performance was better than all solid forms of the same urban fabric in case of Cairo and Alexandria. While in Jeddah, they were surpassed by the performance of solid forms that reached more than 22% of energy savings. In Berlin, all courtyard forms lead to an increase in consumption while all solid forms achieved significant savings.

In a linear fabric, well-oriented courtyard forms achieved energy savings in all desert cities but with lower values than those achieved in a compact fabric. The savings reached 9.7%, 7.8% and 10.7% in Jeddah, Cairo and Alexandria respectively, however, solid forms of the same urban fabric achieved much more savings reaching 22.9%, 21% and 14.9% for these cities respectively. These savings exceeded those achieved by courtyard forms located in a compact fabric, with significant differences in Jeddah and Cairo, and minor differences in Alexandria. In Berlin, courtyard forms in a linear fabric also lead to an increase in consumption.

From these results, it can be concluded that courtyard buildings, when air-conditioned, could be more liable for use in cities of moderate desert climates such as Alexandria and Cairo rather than in extreme hot cities as Jeddah or the cold ones as Berlin. They were more efficient in a compact fabric. But even though, they cannot be recommended even if they existed in a compact fabric configuration as they were exceeded by the performance of rectangular solid forms of a linear fabric.

From these results, it can be concluded that courtyard buildings, when air-conditioned, could be more liable for use in cities of moderate desert climates such as Alexandria and Cairo rather than in extreme hot cities as Jeddah or the cold ones as Berlin. However, although these forms proved to achieve savings in desert cities, they cannot be recommended even if they existed in a compact fabric configuration as they were less efficient than rectangular solid forms in a linear urban fabric. This paper demonstrated that the commonly known belief that courtyard

buildings were more effective in desert environments does not hold anymore in today's modern buildings that depend on mechanical air-conditioning for achieving thermal comfort.

7. LIMITATIONS

The limited floor area, resulted in rather 'thin' courtyard forms, in which several zones were exposed to external climatic conditions from two sides. A larger building area would have included fewer zones exposed from multiple directions, possibly resulting in a different performance.

8. REFERENCES

- Aldawoud, A. (2008). Thermal performance of courtyard buildings. *Energy and Buildings*; 40(5): 906-10.
- Al-Hemiddi, N. A. and Al-Saud, K. A. (2001). The effect of a ventilated interior courtyard on the thermal performance of a house in a hot-arid region, *Renewable Energy*; 24: 581-95.
- Al-Masri, N. and Abu-Hijleh, B. (2012). Courtyard housing in midrise buildings: An environmental assessment in hot-arid climate. *Renewable and Sustainable Energy Reviews*; 16: 1892-8.
- Almhafdy, A., Ibrahim, N. and Ahmad, S. S., (2019), Impacts of Courtyard Geometrical Configurations on Energy Performance of Buildings, *Environment-behaviour proceedings journal*; 4(10); 29-36.
- Al-Tamimi, N., Fadzil, S. and Harun, W. (2011). The effects of orientation, ventilation, and varied WWR on the thermal performance of residential rooms in the tropics. *Journal of Sustainable Development*; 4 (2) 142-9.
- EL-Deeb K., El Zafarany A. and Sherif A. (2012). Effect of building form and urban pattern on energy consumption of residential buildings in different desert climates. *Proceedings of the 28th conference on Passive and Low-energy Architecture PLEA 2012, Lima, Peru.*
- EL-Deeb K., Sherif A. and El Zafarany A. (2014). Effect of courtyard height and proportions on energy performance of multi-storey air-conditioned desert buildings. *Proceedings of the 30th conference on Passive and Low-energy Architecture PLEA 2014, Ahmedabad, India.*
- Kottek, M., Greicer, J., Beccck, C., Rudolf, B. and Rubel, F. (2006). World Map of the Köppen-Gieger Climate Classification Updated. *Meteorologische Zeitschrift*; 15(3): 259-63.
- Morrissey, J., Moore, T. and Horne, R. E. (2011). Affordable passive solar design in a temperate climate: An experiment in residential building orientation. *Renewable Energy*; 36: 568-77.
- Marouane Guedouh, Noureddine Zemmouri (2017). Courtyard Building's Morphology Impact on Thermal and Luminous Environments in Hot Arid Region, *Energy Procedia*; 119: 153-162.
- Muhaisen, A. S. and Gadi, M. B. (2006) (a). Shading performance of polygonal courtyard forms. *Building and Environment*; 41: 1050-9.
- Muhaisen, A. S., Gadi, M. B. (2006) (b). Effect of courtyard proportions on solar heat gain and energy requirement in the temperate climate of Rome. *Building and Environment*; 41: 245-53.
- Rajapaksha, I., Nagai, H., Okumiya, M. A. (2003). ventilated courtyard as a passive cooling strategy in the warm humid tropics. *Renewable Energy*; 28: 1755-78.
- Sadafi, N., Salleh, E., Haw, L.C. and Jaafar, Z. (2011). Evaluating thermal effects of internal courtyard in a tropical terrace house by computational simulation. *Energy and Buildings*; 43: 887-93.
- Safarzadeh, H. and Bahadori, M. (2005). Passive cooling effects of courtyards, *Building and Environment*; 40(1): 89-104.
- Tofigh Tabesh, Begum Sertyesililsik (2016). An investigation into Energy Performance with the Integrated Usage of a Courtyard and Atrium, *Buildings*; 6; 21 doi:10.3390/buildings6020021

#355: Regulatory and policy framework for the uptake of renewable energy in the United Kingdom

Current challenges in a time of mutability of the energy sector

Juan SALAZAR¹, Julie WALDRON², Lucelia RODRIGUES³

¹ University of Nottingham, NG7 2RD University Park, Nottingham, UK, juanjossl@yahoo.com

² University of Nottingham, NG7 2RD University Park, Nottingham, UK, julie.waldron@nottingham.ac.uk

³ University of Nottingham, NG7 2RD University Park, Nottingham, UK, lucelia.rodrigues@nottingham.ac.uk

Energy policies and regulations are regularly introduced to reflect current developments of the energy system. The introduction of sustainable energy technologies created a demand for alternative sources of energy and economic incentives which were widely adopted. This paper presents the panorama of the energy regulatory system in the UK and the range of new policies and regulations required to promote the trade of energy from the perspective of small-scale self-consumers and exporters of renewable energy; specially, the operation of feed-in tariffs and their proposed replacement, the Smart Export Guarantee, and its application within energy storage technologies. The paper also looks into the European market and the implications of the exit of the UK from the European Union. It also identifies uncertainties of the current UK regulatory framework from the perspective of small-scale self-consumer and highlights future challenges regarding the generation and consumption of renewable energy after the exit of the UK from the European Union.

Keywords: renewable energy; policy; regulation; smart export guarantee; Brexit

1. INTRODUCTION

Energy policies play an important role in setting the path to follow in terms of budgets from the public sector perspective and investment from the private sector. Energy is a dynamic and currently evolving sector due to climate change predictions which require an imminent change in the way we produce, store and distribute energy in order to limit the global warming to 1.5°C (Allen et al., 2018). In the case of the United Kingdom, the renewable energy strategy aimed to ensure that 30% of energy generation was from renewable sources by 2020 (Government, 2009). Moreover, current developments on the components of the energy system are looking to optimise generation, storage, distribution and consumption (Rodrigues et al., 2018). The cost of renewable energy is a concern that is starting to recede (Liebreich, 2016), giving rise to possibilities of mass production and access to the market to the public in general. This means that there is a crisis in terms of migration of technologies from carbon-based to renewable technologies due to the unprecedented magnitude. This crisis is reflected in today's regulatory framework for renewable energy, the current needs of new regulation and the pace at which technologies change which may not allow the regulatory body to act within an appropriate timeframe in order to keep up with the expectations of the market.

What this means in real terms is that there is a need to determine what regulatory tools are available for the parties in the electricity market to make use of existing technology and what is the stimuli granted by public policy in terms of cost and benefit to make use of them. This will also have to be contrasted with the reality, though in terms of offer and demand of products, business models, and efficacy of the policies introduced to promote renewable energy.

Along with this mutability, a further aspect must be considered: the exit of the United Kingdom from the European Union. The UK's renewable energy policy is primarily guided by the renewable energy directive 2018/2001/EU (European Union, 2018) which entered into force in December 2018 and there is no certainty as to what will be the effect of EU regulations over UK domestic law after the departure from the European Union.

This paper will assess the United Kingdom's regulatory framework from the renewable energy perspective, starting to outline the main aims of the energy market and then advancing through regulations within the UK which address the uptake of renewable energy. Subsequently, a review of the current policies for renewable energy will be conducted.

2. EUROPEAN UNION REGULATION

According to article 194(1) of the Treaty on the Functioning of the European Union (TFEU) (European Union, 2012), one aim of the Union energy policies is to promote renewable forms of energy.

European Union Directive 2009/28/EC on the promotion of the use of energy from renewable sources established a framework policy regarding this type of energy (Article 1) (European Union, 2009). It sets up a target for the UK to increase the share of final consumption from renewable energy sources to 15% of the gross final consumption of energy by 2020. In addition, it ensured the adoption of policies by member states to increase this percentage over time (Article 3). The directive also facilitated and regulated the creation of joint projects with the participation of member states for the production of electricity from renewable energy sources (Article 7 and 9). Directive 2009/28/EC will be repealed from 1 July 2021 (EUR-lex, 2009).

Now, the recently issued renewable energy directive 2018/2001/EU (European Union, 2018), which entered into force in December 2018, revised the renewable energy policies taking into account that the threshold for the previous target is fast approaching and established a new binding renewable energy target for 2030. The objective of the directive is to achieve a collective target of at least 32% share of the gross final consumption from renewable energy between all the Union members (Articles 1 and 3).

Crucially, Directive 2018/2001/EU (European Union, 2018) introduced regulations about individually or jointly acting renewables self-consumers not previously regulated in Directive 2009/28, and more importantly, the electricity generated can be included in the calculation of the gross final consumption of electricity from renewable sources towards the accomplishment of the targets imposed individually to the Member state or collectively to the Union (Article 7(2)).

Regarding small-scale installations, the preamble in paragraph 17 of the directive states the following: "Small-scale installations can be of great benefit to increase public acceptance and to ensure the rollout of renewable energy projects, in particular at local level. In order to ensure participation of such small-scale installations, specific conditions, including feed-in tariffs, might therefore still be necessary to ensure a positive cost-benefit ratio, in accordance with Union law relating to the electricity market. The definition of small-scale installations for the

purposes of obtaining such support is important to provide legal certainty for investors. State aid rules contain definitions of small-scale installations” (European Union, 2018, p. 84).

Article 21 (European Union, 2018) indicates that consumers should be allowed to become self-consumers, but in addition that they, individually or through aggregates, are entitled to generate renewable energy and store and sell their excess production without being subject to discriminatory or disproportionate treatment, including network charges which are not cost-reflective (Article 21(2,a,i)). Conversely, there is a statement that they should receive remuneration for the self-generated renewable energy they feed into the grid reflecting the value of that electricity, including “long term value to the grid, environment and society” (Article 21(2, d)). In addition, it clarifies that by being small-scale producers, their rights as final consumers should not be disregarded (Article 21(2, c)). The same Article specifies cases where it is appropriate to make non-discriminatory and proportionate charges and fees to renewables self-consumers:

1. When they have been supported through schemes and these fees and charges do not undermine the viability of the project;
2. After 1 December 2026, member states may argue, in case the overall share of self-consumers exceed 8% of the installed electricity capacity, that paying charges or fees to self-generated electricity constitutes a disproportionate burden on the long-term financial sustainability of the electric system;
3. If the self-generated electricity is produced in installations with a total capacity of more than 30kW.

Finally, Member States must put in place a regulatory framework to enable renewables self-consumption, removing unjustified financial or regulatory barriers and granting incentives and support schemes, but also ensuring that renewables self-consumers contribute with the overall cost sharing of the system when the electricity is fed into the grid (Article 21(6)) (European Union, 2018).

About renewable energy communities, paragraph 26 of the preamble states: “Member States should ensure that renewable energy communities can participate in available support schemes on an equal footing with large participants. To that end, Member States should be allowed to take measures, such as providing information, providing technical and financial support, reducing administrative requirements, including community-focused bidding criteria, creating tailored bidding windows for renewable energy communities, or allowing renewable energy communities to be remunerated through direct support where they comply with requirements of small installations” (European Union, 2018, p. 86)

According to article 2 “‘renewable energy community’ means a legal entity: (a) which, in accordance with the applicable national law, is based on open and voluntary participation, is autonomous, and is effectively controlled by shareholders or members that are located in the proximity of the renewable energy projects that are owned and developed by that legal entity; (b) the shareholders or members of which are natural persons, SMEs or local authorities, including municipalities; (c) the primary purpose of which is to provide environmental, economic or social community benefits for its shareholders or members or for the local areas where it operates, rather than financial profits;” (European Union, 2018, p. 103).

Concerning Renewable Energy Communities or jointly acting self-consumers, Directive 2018/2001/EU (2018) grants rights to households to participate in such schemes while maintaining their rights as final consumers and not being subject to unjustified or disproportionate barriers, as long as that participation is not their primary commercial or professional activity. They also have rights to produce, consume, store and sell renewable energy, as well as share the energy within the community or access energy markets. The Member States must provide a regulatory framework to remove unjustified or disproportionate barriers and set transparent procedures to function and facilitate transfer of energy through the distributor system operator, ensuring they contribute to the cost sharing of the system (Article 22).

3. REGULATIONS OF RENEWABLES SELF-CONSUMERS

The regulatory framework of the renewable energy policies is largely contained within the Climate Change Act 2008, the Energy Act 2008 (UK Public General Acts, 2008a), the Energy Act 2013 (UK Public General Acts, 2008b), the Energy Act 2016 (UK Public General Acts, 2013) and the renewable energy directive 2018/2001/EU (European Union, 2018) already outlined.

3.1. Climate Change Act 2008

This regulation sets up the United Kingdom’s policies to measure and reduce greenhouse gas emissions.

Provision 1 of the climate change act 2008 (UK Public General Acts, 2008a) sets up the United Kingdom's target for 2050 to reduce the net carbon emissions by at least 80% compared to 1990. Following an advise by the Committee on Climate change, the target was amended by the Climate Change Act 2008 (2050 Target Amendment) Order 2019 (UK Statutory Instruments, 2019a), which made legally binding a new target to reduce in 100% the greenhouse gas emissions by 2050. It introduced a method to measure greenhouse gas emissions by setting 5 year caps or "Carbon Budgets". However, the Act does not set up specific policies or targets regarding renewable energy.

3.2. The Energy Act 2008

Renewables Obligation

This statute amends sections 32 to 32C of the Electricity Act 1989 (UK Public General Acts, 1989) which introduced the Renewables Obligation (RO). It consisted in a legal requirement imposed to electricity suppliers to supply a minimum amount of electricity from renewable sources (Section 37). This is accounted in the form of Renewable Obligation Certificates (ROCs) which are tradable instruments. The suppliers had to produce the required amount of certificates which represent the amount of renewable electricity supplied. However, as mentioned, these certificates could have been obtained through the secondary market. The RO closed for new applications on 31 March 2017.

This mechanism is oriented for big-scale renewable generators only; regarding small generators, the Energy Act 2008 (UK Public General Acts, 2008b) introduced the Feed-in Tariffs (Section 41), by allowing the authorities to grant licenses to distribute or supply energy and encourage low-carbon generation of electricity by small producers. They are defined in subsection 4 of section 41 as an "owner of plant used or intended to be used for small-scale low-carbon generation, whether or not the person is also operating or intending to operate the plant". Crucially, subsection 3 of Section 41 allows requiring the holder of a supply licence to make payments to small-scale low-carbon generators in specified circumstances.

Feed-in Tariffs

Feed-in Tariffs were introduced on 1 April 2010 (UK Statutory Instruments, 2010) to promote the uptake of renewable low-carbon small-scale generation of energy. It allowed payments for generation or export into the grid of renewable energy, which are made to the generators by licensed energy suppliers called FIT Licensees. The scheme is regulated in the Feed-in Tariffs Order 2012 (UK Statutory Instruments, 2012). The maximum capacity of eligible installations is 50 kilowatts (Section 3) as installations over this are eligible to receive accreditation under the ROO (Section 6). The eligible low-carbon energy source may be anaerobic digestion, hydro generating stations, combined heat and power, solar photovoltaics and wind. Community Energy Installations can also register for the Scheme (Section 11).

The installation must use MCT-FIT Technology and the generator must have a grid connection agreement with the FIT Licensee if the installation is to be connected to the grid. The tariff depends on the type of renewable energy generated for the period during which it falls and other relevant information (Section 13). The tariffs are published by the Authority before 1st of February each year regarding generation and export of renewable energy by accredited FIT installations, for the following FIT year commencing on the 1st of April and ending on the 31st of March of the following year (Section 16). The FIT payment rates must be determined by the Authority in accordance with schedule A to Standard condition 33 Of the Electricity Supply License. The FIT Licensee must take reasonable steps to review the meter readings and make payments at least quarterly during the eligibility period according to the rates determined in accordance with subsection 3.3. of the Schedule A. For example, for FIT year 1 or 2 in a Solar Photovoltaic eligible installation, the payment must be made in accordance with the FIT payment rate table in force at the time of the export or generation of energy. For FIT year 3 with tariff date from 1st April 2010 to 31st January 2013 the FIT Licensee had to follow the FIT payment rates in tables 1 and 3 of Annex 2 of the Schedule A, and so on.

Finally, Section 7 of the Schedule A specified again the obligation for the FIT Licensee to purchase FIT Export from the accredited FIT installation and make the export payments according to meter readings.

The scheme closed for new applicants on 1 April 2019, and a new scheme called Smart Export Guarantee is due to start operating in January 2020.

3.3. The Energy Act 2013

Regarding the Renewables Obligation, Section 55 (UK Public General Acts, 2013) brought an amendment to section 32L of the Electricity Act 1989, introducing a renewables obligation closure order to be made by the

secretary of State, after which no Renewables Obligation Certificates were to be issued in respect of electricity generated after a given date.

Regarding Feed-in tariffs, Section 146 (UK Public General Acts, 2013) increased the Maximum capacity of plant by small-scale low-carbon generators, from 5 megawatts to 10.

This statute also contains the Electricity Market Reform (EMR), which introduced the Contracts for Difference as the main scheme proposed by the government in replace of the Renewables Obligation, to promote low-carbon electricity generation, including renewable energy.

Contracts for Difference

According to the Financial Services and Markets Act 2000 (Regulated Activities) Order 2001/544 (UK Statutory Instruments, 2001), Contracts for Difference has the purpose of securing a profit or avoid a loss caused by fluctuations in the value or price of property or an index or other factor designed for that purpose in the contract (Section 85). In the Energy Market, they are contracts with standard terms between a CFD counterparty and an eligible generator (Sections 6(1), 7, 11 in: UK Public General Acts, 2013). Its purpose is to protect the renewables generators and the consumers from the fluctuations of the prices of energy, by establishing an indexed flat rate consisting in the difference between a “strike price” which includes the costs of investing in a low-carbon technology and the “reference price” which is the average of the market price for electricity in the energy market (BEIS, 2019). If the reference price is lower than the strike price the generator pays the difference to the CFD counterparty, whilst if the reference price is lower than the strike price, the CFD counterparty pays this difference to the generator, “this means that, provided the generator is paid close to the reference price by its offtaker, it should receive a predictable and stable revenue for its energy” (Fairley and Andrews, 2016). One of the factors that affect price is the inclusion of costs associated with the risks of purchasing renewables, and having to balance them, as this type of sources often present intermittent generation of energy (Fairley and Andrews, 2016).

3.4. The Energy Act 2016

This act is mainly concerned with the regulation of the Oil and Gas Authority Limited; however, it also includes an amendment to Part 1 of the Electricity Act 1989 with an order not to issue Renewables Obligation Certificates in respect of electricity generated after the onshore wind closure date, but excludes from this prohibition the energy generated under the circumstances described in 32LD to 32LL (UK Public General Acts, 2016).

4. THE UK'S CURRENT RENEWABLE ENERGY POLICIES

White papers are documents prepared by the Government to set out proposals for future legislation. They reflect the policies of the government in a given area of interest (UK Parliament, n.d.). Regarding energy, the UK Government produces a significant number of white papers and consultations through time which ensure that the actions taken are appropriate to meet the requirements and obligations acquired through previous policies and statutes or to update policies according to current developments in technology.

The renewable energy policies are contained within the Clean Growth Strategy and the Industrial Strategy.

4.1. The Industrial Strategy

The white paper “Industrial Strategy building Britain fit for the future” (Government, 2017a), introduced in July 2016, contains the policies regarding industry and productivity so it is relevant in terms of generation and distribution of energy, as well as the application of new technologies in the field of renewable energy in the public and private sector. For example, in terms of infrastructure, the Industrial Strategy aims to support the electric vehicles infrastructure by investing £400 Million in charging infrastructure and £100 Million to extend the plug-in car (Government, 2017, p. 15). According to this report, around 40% of the UK's total final energy use is spent in transport, therefore, the policy is focused partially in investing in innovation of low-carbon transport technologies. One of the challenges mentioned is “the Faraday Battery Challenge to design, develop and manufacture batteries for the electrification of vehicles and efficient use of renewable energy” (p. 73).

In addition, another ‘grand challenge’ is to promote clean growth by supporting low-cost low-carbon infrastructure systems to the service of industrial opportunities (p. 142). Therefore, one new industrial strategy programme was introduced in energy, and there will be support of innovation in low carbon economy as well as aims to increase private investment and promote market growth (p. 144). Interestingly, there is mention of a ‘whole system approach’ to tackle decarbonisation of energy infrastructure, and this is going to be applied in three important systems which interact constantly with each other: energy generation, transport and heat (p. 145). Some technologies are

mentioned as important synergy-makers between these three systems which will help the growth of the market, they are: energy storage, heat networks, smart meters, vehicle-to-grid and smart charging (p. 145).

Another factor to consider is the aim to minimise energy costs for households and businesses, through innovation and system efficiency. An example of this are the results obtained through innovation in the improvement of the efficiency of offshore wind energy generation (p. 147).

4.2. Clean Growth Strategy

The white paper “The Clean Growth Strategy Leading the way to a low carbon future” (Government, 2017b), was laid before parliament pursuant to Sections 12 and 14 of the Climate Change Act 2008 and amended in April 2018. It sets the strategy to achieve the target imposed in the Climate Change Act 2008 and has two objectives: the first is “To meet the domestic energy demand at the lowest possible net cost to UK taxpayers” and the second one “To maximise the social and economic benefits for the UK from this transition” (p. 10).

In order to achieve a clean growth, three challenges were identified: “1. Ensuring we deliver affordable energy for households and businesses; 2. Decarbonising “harder to reach” parts of the UK economy and 3. Establishing a post-EU emissions and environmental framework that is at least as beneficial as current arrangements”. The “harder to reach” parts of economy in terms of decarbonisation are transport, business and industry, as well as heating across key sectors in the economy (p. 39). The affordability of energy was already mentioned and the Post-EU challenges are addressed further on.

Regarding renewable energy, there is a commitment to invest up to £557 million for Contracts for Difference auctions and to work with the private sector to promote the generation of offshore wind energy.

In addition, for self-consumers, a need has been identified to invest in innovation to promote the efficiency of “key technologies systems and processes” such as batteries and electric vehicles. One of the programs from the BEIS is called Energy Innovation Programme, which has funds to support clean technology to accelerate its deployment.

4.3. Smart Export Guarantee (SEG)

Now, regarding small-scale low-carbon generation, the consultation outcome “the future of small-scale low-carbon generation: Smart Export Guarantee” (BEIS, 2019) was published to set out the policy and propose secondary legislation. As a result of this consultation, a new scheme called the Smart Export Guarantee is being introduced as a mechanism to promote small-scale low-carbon generation. According to the government, the scheme was created to guarantee a payment by the suppliers to homes and businesses who generate and export energy to the grid (HM Government, 2019).

The government decided to implement the policy through secondary legislation: the Smart Export Guarantee (SEG) order 2019 (UK Statutory Instruments, 2019b). This order introduced the SEG Licensee in accordance with section 6(d) of the Electricity Act 1989 and stated the specified maximum capacity as 5 megawatts (Section 3). It also sets the functions for the Authority regarding compliance of SEG Generators of the criteria to receive SEG Payments (Section 4), and requires the Authority to publish guidance to SEG Licensees and Generators (Section 5) as well as a report to show, among other things, the export tariffs that have been offered by SEG Licensees (Section 7(a)).

There is also currently a draft to modify Standard Conditions 57 and 58 of the Electricity Supply Licenses to incorporate the SGE arrangements. The draft specifies that the SEG Licensee must make SEG payments to SEG generators in accordance to Schedule A (Condition 57.3). Crucially, the provisions in Condition 57 are considered “relevant conditions” according to which non-compliance by SEG Licensee will be subject to sanctions by the Gas and Electricity Markets Authority (Condition 57.4).

As mentioned, Schedule A of the Draft to modify Conditions 57 and 58 of the Electricity Supply Licenses regulates the Payments under the Smart Export Guarantee. Section 5 of Part B of the Schedule establishes that the SEG Licensee must provide confirmation of the Export Tariff determined by the SEG Licensee in respect of the SEG Generator. The SEG Licensee has an obligation to ensure the information provided “is otherwise fair, transparent, and appropriate and delivered in a professional manner...” (Section 5.3.1.(d)), and additionally, “when making SEG payments to a SEG Generator, the SEG Licensee shall ensure that it does not materially discriminate without objective justification between SEG Generators” (Section 5.3.2.).

The scheme will come into force on the 1st of January 2020.

5. EXIT OF THE UNITED KINGDOM FROM THE EUROPEAN UNION

“The exact nature of the UK’s future relationship with the EU and the long-term shape of our involvement in areas like the EU Emissions Trading System are still to be determined” (Government, 2017b, p. 10) .

It has been however stated that: “There is also no need to change our domestic targets under the Act as a result of leaving the EU, as these targets are rooted in climate science. The UK remains strongly committed to the Paris Agreement and whatever the form of our future partnership with the EU we will satisfy our international obligations under the Agreement.” (Government, 2017b, p. 44).

According to the Clean Growth Strategy, the government identified four areas where the EU regulations are currently operating in terms of energy and carbon emissions. Accordingly, the UK’s policies are currently relying on this EU mechanisms: 1. The EU Emission Trading System (EU ETS) regarding power, heavy industry and intra EEA aviation sectors; 2. “New car and van CO₂ regulations, and EU fluorinated gas quotas”; 3. “EU products policy which sets minimum standards for a range of products such as white goods and lighting, which improve energy efficiency”; and 4. Non-Energy and climate EU frameworks and policies which affect the UK, such as the Common Agricultural Policy” (p. 44 & p. 45).

It must be additionally considered that the current proposed date for the UK’s departure of the European Union is the 31st of October 2019 and at the moment there is no indication of what rules will apply for the leave of the European Union and what rules will govern the future relationship with this bloc. The European Union (Withdrawal) Act 2018 (UK Public General Acts, 2018) contemplates in its section 2(1) that the EU-derived legislation with effects in domestic UK law before the date of exit, continues to have effect in domestic law. By virtue of this, EU directives implemented before the exit day, such as Directive 2018/2001/EU (European Union, 2018) will continue to have effects in domestic law. Now as has been mentioned, some mechanisms are not part of domestic law and are still being used as reference by the private sector. This would have to be incorporated into the UK’s regulatory framework in order to be legally binding. Now, any agreement to leave the bloc and regulate the future relationship will have to be assessed as it may change how EU law will operate in the UK in the future.

6. DISCUSSION

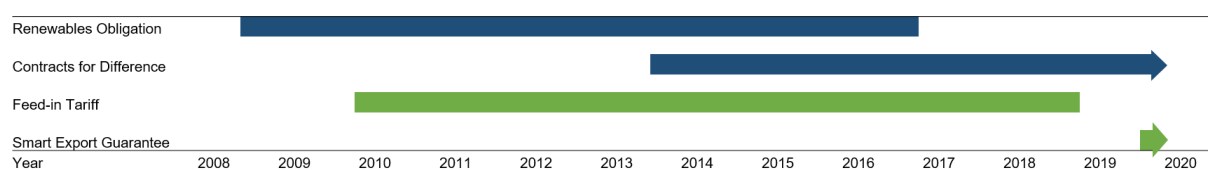
The speech given by Business Secretary Greg Clark (BEIS, 2018) “after the trilemma 4 principles for the power sector”, highlights four principles that are relevant for this review of the policy and regulatory status of the UK renewable energy market: 1. *The market principle*: “we must wherever possible use market mechanisms that take full advantage of innovation and competition”, 2. *The insurance principle*: “given intrinsic uncertainty about the future, government must be prepared to intervene to provide insurance and preserve optionality”, 3. *The agility principle*: “energy regulation must be agile and responsive if it is to reap the great opportunities of the smart, digital economy” and 4. *No free-riding principle*: “all consumers should pay their fair share of system costs”.

This review showed that the schemes for self-consumers and exporters of renewable energy, the FIT and flat rate export tariff, closed to new entrants from March 2019. This policy changed because of the “Steady fall in the cost of low-carbon generation, a move towards cost-reflective pricing, and a continued desire to minimise the costs of support schemes to consumers” (BEIS, 2019, p. 5). This suggests a sense of an unachieved target by the Feed-in Tariff, mechanism which was in the earlier stages reported of not benefitting adequately the self-consumer of energy, due to inefficiency of the business model (Muhammad-Sukki et al., 2013).

Conversely, the design of the tariff of the Smart Export Guarantee is being left for the individual supplier, as this allows flexibility and adaptation to new technologies. However, there is a concern that this freedom was also given to suppliers in the Feed-in Tariff and this eventually did not allow the business model to perform adequately, and instead the mechanism became a barrier for self-consumers contradicting the regulations in the European Directive 2018/2001/EU (European Union, 2018). It appears however, that non-compliance by the SEG Licensee in aspects relating to SEG payments to SEG generators will lead to sanctions by the authority, which may reflect an intent by the government to control and secure the retribution of the scheme. There is also a concern reflected in the policies and proposed secondary legislation to provide clear information to the SEG Generator and protect them against discrimination, which goes in line with the regulations of the European Directive 2018/2001/EU (European Union, 2018) regarding small-scale self-consumers of renewable energy.

According to this, it appears that the previous schemes (i.e. the Feed-in Tariff) did not reflect the fast-paced decrease of the costs of renewable energy for self-consumers and increasing integration of renewable energy sources to the grid due to the developments in technology. In some way, this has been compensated by introducing the Smart Export Guarantee, however, the state of the implementation of the secondary legislation and its entry into force shows a gap in the availability of schemes for small-scale low-carbon self-consumers between march 2019 and January 2020, as can be seen in Table 23.

Table 23: Schemes for small-scale low-carbon self-consumers



As it would seem, at the moment there is no scheme or system to pay for the energy that would inevitably go into the grid from the renewable energy small-scale installation, since the Feed-in tariff closed for new applicants in March 2019 and the Smart Export Guarantee is only available from the 1st of January 2020. In addition, the SEG Licensees are obliged to provide an Export Tariff to the SEG generator before this date, however, the operation of this scheme will be unknown by the small-scale generators despite the obligation by the authority to provide guidance and reports, due to the complexity and newness of the system.

Regarding the targets to decarbonise the economy and the political circumstances of the UK and the European Union, it would seem that the United Kingdom already possess domestic regulations which set ambitious targets and has policies to achieve the proposed targets. According to the United Kingdom's Energy Statistics, 2018 & Q4 2018 (BEIS, 2019b), the share of renewable energy in the United Kingdom increased to 33.3% in 2018. Therefore, it would seem that an eventual departure of the United Kingdom from the European Union would not affect the policies and targets of renewable energy, considering it has already achieved the European proposed target and the local regulations have already included more ambitious targets.

Moreover, in the Clean Growth Strategy is stated: "Leaving the EU will not affect our statutory commitments under our own domestic Climate Change Act and indeed our domestic binding emissions reduction targets are more ambitious than those set by EU legislation" (Government, 2017b, p. 10).

7. CONCLUSION

This paper presented the current panorama of the European Union Regulation, Regulation of Renewables of Self-consumers, the UK's current renewable energy policy, and explored these policies and regulations considering the exit of United Kingdom from the European Union.

There is a need of protecting the small scale self-consumer and exporter, since new technologies represent opportunities to decentralise and make flexible the supply of energy. The pace at which technologies move offer new opportunities in terms of business models to make more affordable the renewable energy, however, the regulations do not seem to catch up on time to avoid a discriminatory treatment or the imposition of disproportionate barriers to small-scale self-consumers. The current gap in the schemes to allow payments for the uptake of renewable energy is evidence of this. Currently there is no operative scheme since the Feed-in tariff closed applications in March 2019 and the Smart Export Guarantee will only start to operate since 1 January 2020.

It was evidenced that the target to decarbonise the economy won't be affected by the exit of the United Kingdom from the European Union as the UK targets to reduce carbon emissions are aligned with the Paris Agreement. However, mechanisms on which the private sector are relying on which are not implemented in domestic law, such as the EU Emissions trading System will need to be include within the UK's legislative framework.

8. REFERENCES

Allen, M., et al., 2018. IPCC, 2018: Summary for Policymakers. In: Global Warming of 1.5°C. An IPCC Special Report on the impacts of global warming of 1.5°C above pre-industrial levels and related global greenhouse gas emission pathways, in the context of strengthening the global, World Meteorological Organization. Geneva.

BEIS, 2019a. THE FUTURE FOR SMALL-SCALE LOW-CARBON GENERATION Response to consultations on policy proposals for a Smart Export Guarantee, and on proposed amended licence conditions.

BEIS, 2019b. PRESS NOTICE STATISTICAL PRESS RELEASE UK Energy Statistics.

BEIS, 2018. After the trilemma - 4 principles for the power sector - GOV.UK [WWW Document]. URL <https://www.gov.uk/government/speeches/after-the-trilemma-4-principles-for-the-power-sector> (accessed 7.29.19).

Department for Business, Energy and Industrial Strategy, B., 2019. The future for small-scale low-carbon generation: part A - GOV.UK.

Department for Business, E.& I.S., 2019. Contracts for Difference.

EUR-lex, n.d. EUR-Lex - 32009L0028 - EN - EUR-Lex [WWW Document]. Eur. Union Law. URL <https://eur-lex.europa.eu/legal-content/EN/ALL/?uri=celex%3A32009L0028> (accessed 7.29.19).

European Union, 2018. DIRECTIVES DIRECTIVE (EU) 2018/2001 OF THE EUROPEAN PARLIAMENT AND OF THE COUNCIL of 11 December 2018 on the promotion of the use of energy from renewable sources (recast) (Text with EEA relevance).

European Union, 2012. Consolidated Version of the Treaty on the Functioning of the European Union.

European Union, 2009. DIRECTIVE 2009/28/EC OF THE EUROPEAN PARLIAMENT AND OF THE COUNCIL.

Fairley, R., Andrews, E., 2016. Electricity market reform: an update on contracts for difference. The In-house Lawyer.

Government, H., 2017a. Industrial Strategy: building a Britain fit for the future.

Government, H., 2017b. The Clean Growth Strategy Leading the way to a low carbon future.

Government, H., 2009. The UK Renewable Energy Strategy.

HM Government, 2019. New laws to guarantee payment for solar homes providing excess electricity - GOV.UK [WWW Document]. Press release. URL <https://www.gov.uk/government/news/new-laws-to-guarantee-payment-for-solar-homes-providing-excess-electricity> (accessed 7.29.19).

Liebreich, M., 2016. BLOOMBERG NEW ENERGY FINANCE SUMMIT In search of the miraculous.

Muhammad-Sukki, F., Ramirez-Iniguez, R., Munir, A.B., Mohd Yasin, S.H., Abu-Bakar, S.H., McMeekin, S.G., Stewart, B.G., 2013. Revised feed-in tariff for solar photovoltaic in the United Kingdom: A cloudy future ahead? Energy Policy. <https://doi.org/10.1016/j.enpol.2012.09.062>

Rodrigues, L., Gillott, M., Waldron, J.A., Cameron, L., Tubelo, R., Shipman, R., 2018. Community Energy Networks in the Making: Project SCENE, Nottingham.

THE EUROPEAN PARLIAMENT AND THE COUNCIL OF THE EUROPEAN UNION, 2018. DIRECTIVE (EU) 2018/2001 OF THE EUROPEAN PARLIAMENT AND OF THE COUNCIL of 11 December 2018 on the promotion of the use of energy from renewable sources (recast) (Text with EEA relevance).

UK Parliament, n.d. White Papers - Glossary page - UK Parliament [WWW Document]. URL <https://www.parliament.uk/site-information/glossary/white-paper/> (accessed 7.29.19).

UK Public General Acts, 2018. European Union (Withdrawal) Act 2018. Queen's Printer of Acts of Parliament.

UK Public General Acts, 2016. Energy Act 2016. Statute Law Database.

UK Public General Acts, 2013. Energy Act 2013. Statute Law Database.

UK Public General Acts, 2008a. Climate Change Act 2008. Statute Law Database.

UK Public General Acts, 2008b. Energy Act 2008. Statute Law Database.

UK Public General Acts, 1989. Electricity Act 1989. Statute Law Database.

UK Statutory Instruments, 2019a. The Climate Change Act 2008 (2050 Target Amendment) Order 2019.

UK Statutory Instruments, 2019b. The Smart Export Guarantee Order 2019. Queen's Printer of Acts of Parliament.

UK Statutory Instruments, 2012. The Feed-in Tariffs Order 2012. Statute Law Database.

UK Statutory Instruments, 2010. The Feed-in Tariffs (Specified Maximum Capacity and Functions) Order 2010 (revoked). Statute Law Database.

UK Statutory Instruments, 2001. The Financial Services and Markets Act 2000 (Regulated Activities) Order 2001. Queen's Printer of Acts of Parliament.

#356: Emission analysis for 1.6L turbocharged CamPro engine using electric turbocompounding as exhaust energy recovery

Mohd Hanif MAT MUHAMMAD¹, Aman Mohd Ihsan MAMAT², Wan Saiful-Islam WAN ISMAIL³, Alessandro ROMAGNOLI⁴

¹Automotive Research and Testing Centre (ARTEC), Faculty of Mechanical Engineering, Universiti Teknologi MARA Shah Alam, Selangor, Malaysia

²Automotive Research and Testing Centre (ARTEC), Faculty of Mechanical Engineering, Universiti Teknologi MARA Shah Alam, Selangor, Malaysia, amanihsan@salam.uitm.edu.my

³Faculty of Mechanical and Manufacturing, Universiti Tun Hussein Onn Malaysia, Batu Pahat, Johor, Malaysia

⁴Nanyang Technological University, 50, Nanyang Ave, Singapore 639798, Singapore

This paper presents the emission analysis of a 1.6L turbocharged CamPro engine installed with an electric turbocompounding (ETC) unit. The computational model was accomplished by using a validated 1D engine simulation GT Power. Initially the 1D engine simulation was run with the baseline engine, a 1.6L turbocharged CamPro engine. Then, the ETC unit was located downstream of the main turbocharger. The exhaust energy was recovered by a bespoke high speed Low Pressure Turbine (LPT) which drove the electric generator using a common shaft. The electric energy produced by the high speed electric generator was recorded from the engine simulation that was run from 1000 RPM to 6500 RPM with the increment of 500 RPM. The brake-specific emission, $bsGas_i$, was used to analyse the effect of the ETC on the NO_x , CO_2 , CO and HC . This paper found that the application of the ETC reduced the $bsGas_i$. The maximum reduction of the $bsGas_{NO_x}$ and $bsGas_{HC}$ was found at a higher RPM: $\Delta_{NO_x} = 28.8\%$ at 6500 RPM and $\Delta_{HC} = 9.9\%$ at 4500 RPM respectively. Additionally, the highest reductions for the $bsGas_{CO_2}$ and $bsGas_{CO}$ were found at 3500 RPM where the $\Delta_{CO_2} = 6.9\%$ and the $\Delta_{CO} = 7.2\%$.

Keywords: energy recovery; electric turbo-compounding; emission; internal combustion engine

1. INTRODUCTION

In 2016 the European Economic and Social Committee declared an aim to achieve 60% fewer greenhouse gas emissions from vehicles by 2050 compared to 1990. This has led car manufacturers to increase the efficiency of their vehicles. Despite many automotive manufacturers shifting their attention to electric vehicles (EVs), new infrastructure development to support EVs is still under developed (Poultney, 2018). Therefore, spark ignition (SI) engines are still seen as a viable option for short to mid-term improvement. One of the new trends for reducing exhaust emissions from SI engines is to downsize the engine by adding a highly boosted turbocharging system. The turbocharged engine has better exhaust emissions than the Naturally Aspirated (NA) engine. Movahed (Movahed et al., 2014) found that the Nitrogen oxides (NO_x) emission for a boosted engine was reduced by up to 66% compared to the NA engine. Engine boosting also reduced carbon dioxide (CO₂), carbon monoxide (CO) and unburned carbon (HC) (Pakale and Patel, 2015; Silva et al., 2009). Despite the lighter weight, lower engine speed, less friction and higher engine performance, the highly downsized engine had a turbo lag problem that limited the turbocharging system to maintain high efficiency at certain engine speeds. Variable geometry turbo (VGT) has been used to expand the operating pressure by varying the turbine geometry and increasing the turbocharger efficiency. Although the VGT setup is complex, the wastegating loss can be reduced and the fuel efficiency can be increased by as much as 7% (Hawley et al., 1999).

A dual stage turbocharger can be used to increase engine boosting and achieve a higher engine efficiency. Zhao et al. tested a dual stage turbocharger, a high pressure and low pressure turbocharger, and they found that the brake specific exhaust gas emission was reduced by as much as 7.83% (Zhao et al., 2015). A study by Saulnier and Guilain (Saulnier, 2004) has deduced that the dual stage turbocharger helped in closing the gap of power peak between high pressure and low pressure. The other method to employ the dual stage turbocharging system is by including an Electric Turbo-compounding (ETC) unit. In this system, a secondary turbine is attached to an electric generator. The recovered energy is converted into the electrical current and stored in the energy storage system to be used on demand. The stored energy can be used to assist the transmission through torque assist by an electric motor or through an electric supercharger to provide boost into the engine cylinder and eliminating turbo lag. A preliminary study showed that an increase in BSFC by 2.28% is possible by using a 1kW generator and had better thermal efficiency (Muhammad et al., 2018). Due to the presence of a secondary turbine, the dual stage setup increased the backpressure and affected the combustion process and the exhaust emission. This paper analyses the effect of the electric turbocompounding on the exhaust emission for the turbocharged CamPro engine.

2. SIMULATION SETUP

The emission analysis for the ETC waste heat recovery system was made through 1D engine simulation. The Proton 1.6L CamPro CFE turbocharged engine was used in this particular study. Table 1 shows the specification of the engine. The engine was modelled in GT-POWER software based on the model developed by Ismail et al. (Ismail et al., 2015) with two main modifications. The first modification carried out was to change the combustion model to include NO_x formation calculation. The SI Wiebe Combustion Model was used with NO_x Reference Object that was turned on. The number of temperature zones was set to two in order to have better prediction of NO_x formation. Specifications of the fuel is also presented in the Table 1. The air properties were set to standard atmosphere.

Table 1: Proton 1.6L CamPro CFE engine specifications

Attribute (Engine)	Value	Attribute (Fuel)	Value
Combustion system	4-stroke, in-line, gasoline PFI	Carbon Atoms per molecule	7.93
Capacity	1.6 litres	Hydrogen Atoms per molecule	14.8
Compression ratio	9.0	Lower Heating Value	4.4x10 ⁴ kJ/kg
Bore x stroke	76mm x 86mm	Critical Temperature	56.8 K
Induction system	Single-stage turbocharger	Critical pressure	24.9 bar
Maximum torque	205 Nm @ 2000-4000 rpm	Absolute Entropy	3.64 kJ/kg.K
Maximum power	103 kW @ 5000 rpm		
Intake cam profile	≤ 220° (duration) / 7.51 mm (valve lift)		
Exhaust cam profile	2° BTDC @ 0.15 mm lift		

The Electric Turbo-Compounding (ETC) unit was included downstream of the catalytic converter in the second engine's architecture modification. Figure 1 shows the layout of the engine. The performance maps of the ETC turbine were based on the data from Mamat et al. (Mamat et al., 2016). The ETC was directly connected to an electric generator without any wastegate. The recovered energy was not fed back into the engine. The final engine model layout is shown in Figure 2. The engine model was run at full-load condition. The electric generator was modelled based on the "MotorGenerator" from the library of GT-POWER using "voltage-rpm" as the controller to

comply with the DC electric generator specification. Detailed specifications of the electric generator was as shown in Table 2.

Table 2: Electric generator specifications

Attribute (Electric Generator)	Value
Inverter voltage	15 V
Motor voltage	15 V
Shaft Speed	50,000 RPM
Power	1 kW
Current	44 A

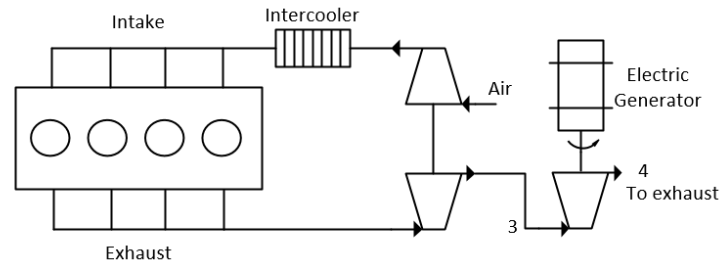


Figure 1: Waste heat recovery using turbocharger and ETC

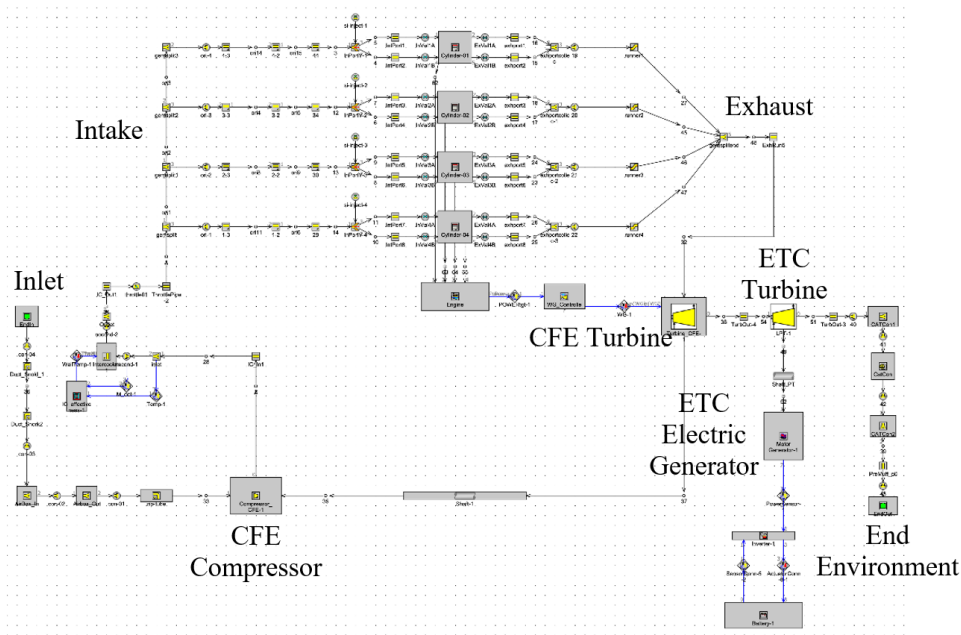


Figure 2: GT-Power ETC model layout.

Since the power obtained from the exhaust recovery was not looped back into the CFE engine, the brake-specific emission for NO_x, CO₂, CO and HC needed to be calculated separately outside the GT-Power solver by including the power generated by the ETC. Equation 1 was used to recalculate this value. As the $bsGas_i$ decreased, the engine performance increased.

Equation 38: Brake-specific gas emission

$$bsGas = \left[\frac{m_{gas,i}}{bkw} \right] \left[\frac{60000 \times rpm}{n_r} \right]$$

Where:

- $m_{gas,i}$ = mass of the gas calculated for (1) NO_x, (2) CO₂, (3) CO and (4) HC
- bkw = engine power
- n_r = revolutions per cycle (=1 for 2-stroke, =2 for 4-stroke)

3. LAYOUT AND SPECIFICATIONS

3.1. Engine model

The modified engine model was compared to the baseline engine model to make sure that the output was similar after changing the updating the combustion model. Data comparison between the brake power output and the BSFC of the two model is shown in Figure 3. Maximum error recorded was 0.1% for brake power and 0.01% for BSFC between the two models.

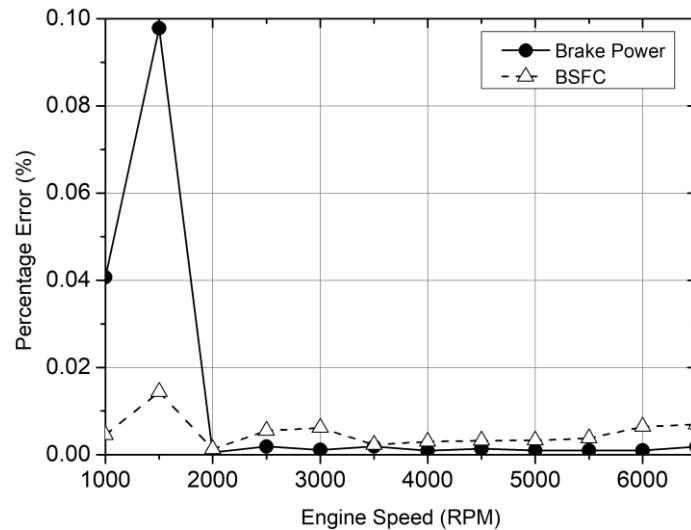


Figure 3: Percentage error of GT-Power model due to different combustion model

3.2. Emission

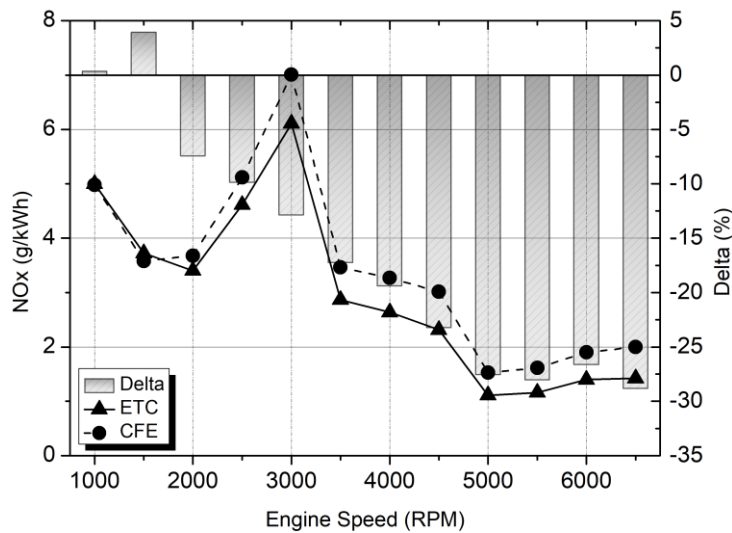


Figure 4: Comparison of brake specific NOx between standard CFE engine and inclusion of ETC

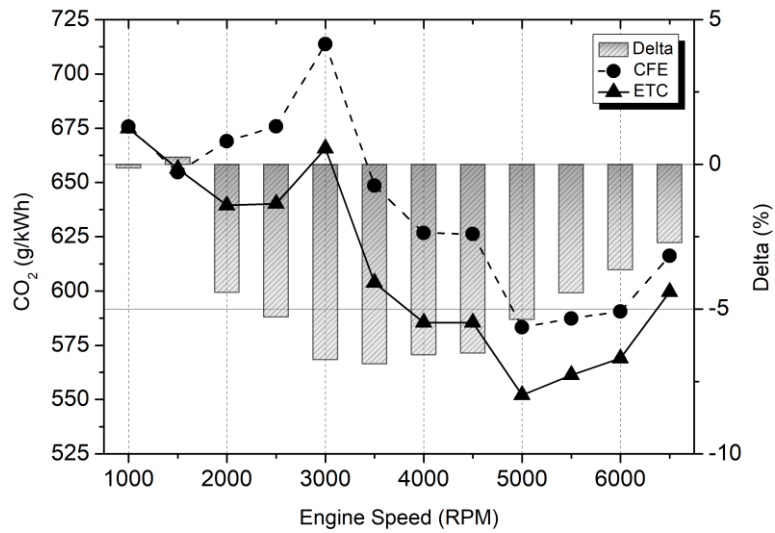


Figure 5: Comparison of brake specific CO₂ between standard CFE engine and inclusion of ETC

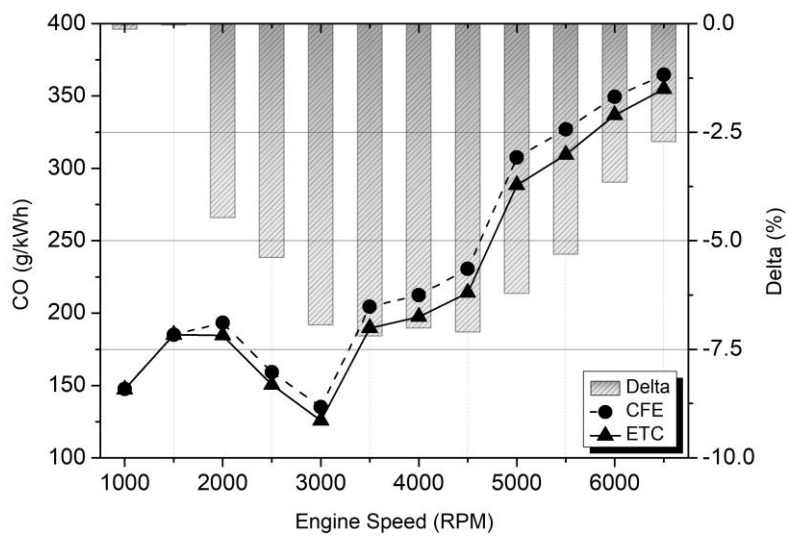


Figure 6: Comparison of brake specific CO between standard CFE engine and inclusion of ETC

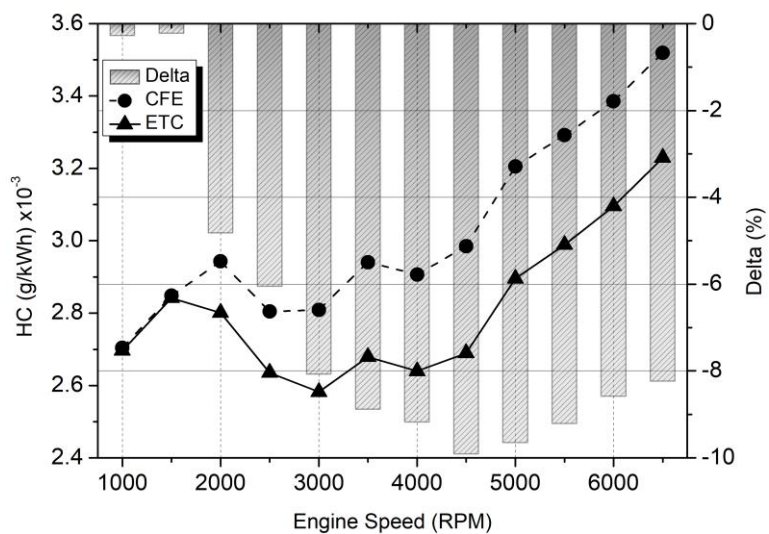


Figure 7: Comparison of brake specific HC between standard CFE engine and inclusion of ETC

The analysis for the brake-specific emission $bsGas_i$ is given in Figures 4 to 7. The x-axis represents the engine RPM, the primary y-axis is the $bsGas_i$ and the secondary y-axis is the difference of $bsGas_i$ estimation between the CFE engine and that with the inclusion of ETC. The NO_x emission was produced due to high temperature combustion in the cylinder. The NO_x can react with the water to produce nitric acid and acid rain and it is dangerous to the environment. Figure 4 shows the brake-specific NO_x, $bsGas_{NO_x}$, for the CFE engine and engine model with ETC. Between 1000 to 2000 RPM, the NO_x formation through $bsGas_{NO_x}$ measurement decreased. Then the $bsGas_{NO_x}$ increased until it achieved maximum value at 3000 RPM; thereafter the $bsGas_{NO_x}$ decreased again as the engine RPM increased. This happened because the flow pressure in the exhaust gas was small at the lower RPM and not recovering much energy. The most $bsGas_{NO_x}$ reduction was found at a higher RPM. The average reduction was found at 16.17% and the maximum reduction was recorded at 6500 RPM with 28.8%. This was expected since the ETC recovered more energy at higher RPM due to the increase of exhaust gas pressure. There was a slight increase in NO_x formation after 5000 RPM due to the increase of peak cylinder temperatures.

CO₂ emissions contribute directly to greenhouse effect. The concentration of CO₂ (ppm) also showed similar trends where it increased at the mid RPM and diminished at the higher end of the engine speed range. Figure 5 shows that the brake specific CO₂, $bsGas_{CO_2}$, decreased as the engine speed increased. The overall $bsGas_{CO_2}$ reduced by 4.37% and the maximum reduction was located at 3500 RPM at 6.9%. Most of the reduction happened between 2500 and 5500 RPM. This was advantageous because the engine cruising speed was expected at this particular range.

The CO formation was due to lack of air during the combustion. CO was odourless and tasteless, thus the CO leakage into the vehicle cabin was considered hazardous and life-threatening. Figure 6 shows that the brake-specific CO, $bsGas_{CO}$, increased as the engine speed increased, which was consistent with the decrease of CO₂. At higher engine speeds, the concentration of CO was higher. Even so, with the addition of ETC, the overall reduction trend was the same as the brake specific CO₂ with an average value of 4.68%. The maximum gain was 7.2% at 3500 RPM.

The HC was formed due to misfired combustion in the cylinder. Due to lack of oxygen, some of the hydrocarbon particles did not react with oxygen and left the combustion chamber as HC. Figure 7 shows that the brake-specific HC, $bsGas_{HC}$, increased at lower RPM until it achieved first peak value at 2000 RPM, then the $bsGas_{HC}$ decreased to the minimum value at 3000 RPM and thereafter the $bsGas_{HC}$ increased at higher RPM. The maximum reduction of the $bsGas_{HC}$ was found at 4500 rpm where the presence of ETC reduced it by as much as 9.9%. The overall reduction of brake specific HC was 6.92%.

4. CONCLUSION

This paper studied the effect of the ETC on the gas emission of the CamPro turbocharged engine by using 1D engine modelling. The maximum reduction of the $bsGas_{NO_x}$ and $bsGas_{HC}$ was found at higher RPM which was $\Delta_{NO_x} = 28.8\%$ at 6500 RPM and $\Delta_{HC} = 9.9\%$ at 4500 RPM respectively. Additionally, the maximum reduction for the $bsGas_{CO_2}$ and $bsGas_{CO}$ were located at 3500 RPM where the $\Delta_{CO_2} = 6.9\%$ and the $\Delta_{CO} = 7.2\%$. In conclusion, the application of the ETC reduced the brake-specific emission, $bsGas_i$, and increased the engine performance.

5. ACKNOWLEDGEMENTS

The authors gratefully acknowledge the help of the Universiti Teknologi MARA, Malaysia, in providing the BESTARI Fund (600-IRMI/MYRA 5/3 BESTARI (14/2017)).

6. REFERENCES

Hawley, J., Wallace, F., Cox, A., Horrocks, R. & Bird, G. 1999. Variable geometry turbocharging for lower emissions and improved torque characteristics. *Proceedings of the Institution of Mechanical Engineers, Part D: Journal of Automobile Engineering*, 213, 145-159.

Ismail, M. I., Costall, A., Martinez-Botas, R. & Rajoo, S. 2015. Turbocharger Matching Method for Reducing Residual Concentration in a Turbocharged Gasoline Engine. SAE Technical Paper.

Mamat, A. M. B., Martinez-Botas, R. F., Rajoo, S., Hao, L. & Romagnoli, A. 2016. Design methodology of a low pressure turbine for waste heat recovery via electric turbocompounding. *Applied Thermal Engineering*, 107, 1166-1182.

Movahed, M. M., Tabrizi, H. B. & Mirsalim, M. 2014. Experimental investigation of the concomitant injection of gasoline and CNG in a turbocharged spark ignition engine. *Energy Conversion and Management*, 80, 126-136.

Muhammad, M. H. M., Mamat, A. M. I. & Salim, W. S.-I. W. 2018. Exergy Analysis of Organic Rankine Cycle and Electric Turbo Compounding for Waste Heat Recovery. *International Journal of Engineering & Technology*, 7, 152-156.

Pakale, N. & Patel, S. 2015. Performance analysis of IC engine using supercharger and turbocharger-A review. *IJRET: International Journal of Research in Engineering and Technology*, 4, 17-22.

Poultney, L. 2018. *The 2018 Nissan Leaf is charming, practical and fun* [Online]. wired.co.uk. Available: <https://www.wired.co.uk/article/nissan-leaf-2018-review> [Accessed 13.09.2018].

Saulnier, S., And Guilain, S. 2004. Computational Study of Diesel Engine Downsizing Using Two-Stage Turbocharging. *SAE Paper*.

Silva, C., Ross, M. & Farias, T. 2009. Analysis and simulation of "low-cost" strategies to reduce fuel consumption and emissions in conventional gasoline light-duty vehicles. *Energy Conversion and Management*, 50, 215-222.

Zhao, R., Zhuge, W., Zhang, Y., Yang, M., Martinez-Botas, R. & Yin, Y. 2015. Study of two-stage turbine characteristic and its influence on turbo-compound engine performance. *Energy Conversion and Management*, 95, 414-423.

#357: Global energy transition: A review of status and future challenges

Selfa Johnson ZWALNAN^{1*}, Yousif Abdallah ABAKR¹, Anandang SHANMUNGAM²,
Mustapha, Danladi IBRAHIM², Su YUEHONG³

¹Department of Mechanical, Materials and Manufacturing Engineering, University of Nottingham Malaysian Campus

²Department of Electrical Engineering, Faculty of Engineering, University of Nottingham Malaysian Campus

³Department of Architecture and Built Environment, University of Nottingham, United Kingdom

*Corresponding author: edxsz1@nottingham.edu.my

As the world population keeps increasing and the standard of living keeps improving, energy systems are bound to face several challenges. At present, there is a need to meet increased energy demands whilst limiting the carbon content of the energy mix to a level that will keep the global temperature rise to well below +2 °C above pre-industrial level before the middle of the 21st century. Many routes have been proposed to keep this target. For the Sustainable Development Scenario (SDS), greenhouse gas emissions are expected to be brought down to zero before the end of 2080. One way is to cut down the carbon content of energy resources by at least 4% per year of its present value if the projected growth in the GDP of 2.1% per year is kept constant. Ironically, the available carbon-free energy technologies have not yet been fully developed to be competitive enough to replace fossil fuel technologies. The transition to carbon-free technologies will take a longer time to evolve. Consequently, the fossil fuel power technologies will continue to dominate the energy mix. However, many roadmaps and technological options have been proposed and adopted at global and regional levels to transform energy systems to low carbon to achieve zero emissions before the end of the 21st century. This paper reviews historical trends, assessing the gains of different climate change adaptation options and roadmap scenarios to achieve a carbon free energy system before the end of the 21st century. It also looks at the implications of the global energy transition. Finally, the paper suggests the need for a holistic approach to the global energy transition as the transition has political and socio-economic implications.

Keywords: energy transition; energy efficiency; global warming; climate change

1. INTRODUCTION

As the world population keeps increasing and the standard of living keeps improving, energy systems are bound to face several challenges (BP, 2018). The biggest challenge will be the need to increase energy production to match increasing demand while at the same time keeping the global greenhouse gas emitted by energy generation within the target required to mitigate climate change. As energy consumption continues to increase due with population rise (Datta and Krishnamoorti, 2019; Faisal *et al.*, 2017), the challenge of air pollution and a global rise in temperature also increases. Consequently this will result to a bigger challenge of mitigating greenhouse gas emissions at an accelerated rate in order to stay within the framework of the Paris roadmap of achieving a low carbon energy mix in the near future (Datta and Krishnamoorti, 2019). At present, one major challenge associated with the energy scenario is global warming and localised pollution caused by greenhouse gases emitted into the atmosphere as fossil fuels are burnt to produce power. Fossil fuel combustion accounts for more than 80% of the carbon dioxide emissions responsible for two-third of global warming. Global warming increases global temperatures leading to extreme weather events that will force humans to migrate and change towards adaptable habitat. To avoid the worst effects of a changing climate, all major players and stakeholders to the Paris Agreement must remain committed to their greenhouse gas reduction targets as set out in the 2015 Paris agreement (IPCC, 2018). To avert the worst effects of climate change, energy systems must evolve from the present predominantly fossil-based energy systems to carbon-free or low carbon energy system to limit global warming to below +2°C above pre-industrial level (European Commission, 2016). The +2°C limit is considered acceptable by the Intergovernmental Panel on Climate Change (IPCC); a body assessing the risk associated with global warming (IPCC, 2018).

To achieve the central aim of the Paris Agreement of limiting global temperature rise to below +2°C before the middle of the 21st century based on the *kaya* model (Wang *et al.*, 2014; Ma *et al.*, 2018), greenhouse gas emissions must be cut by at least 4% every year (IRENA, 2019) from now to the middle of 21st century assuming that the projected growth in the GDP of 2.1% per year will be kept constant (PWC, 2017). Ironically, to cut the carbon content of the energy mix does not imply the end of fossil fuel since, to date, fossil fuels are still the cheapest means of meeting the world's energy needs. Renewable energy technologies, despite producing far less carbon dioxide, are still not being fully exploited to be competitive with fossil fuels and their development will take time to evolve. Consequently, fossil fuel power technologies will continue to dominate the energy mix for a while.

Since demand for fossil fuel will continue to rise, the option will be to de-carbonise the present energy mix by imposing measures like Carbon Capturing and Storage (CCS) where carbon is captured and stored underground (Datta and Krishnamoorti, 2019), complemented by structural reduction methods which aim to convert small inefficient energy projects to bigger concepts with better energy efficiency, and also measures to reduce air pollution and manage the greenhouse gases produced (Gu *et al.*, 2018). The use of negative emission measures like afforestation and the rapid deployment of renewable energy into the energy mix offers better mitigation and is at the forefront of possible solutions (Singh and Dhar, 2019).

2. RECENT GAINS AND THE FUTURE IMPLICATION OF ENERGY TRANSITION

Fossil fuel has been the foundation of world modernisation and civilisation (IRENA, 2019) and it has been the predominant source of primary energy since 19th century to date. However, there are now environmental concerns associated with the use of fossil fuels. Global transition towards more environmentally friendly fuels is now the trend. According to the United Nations Framework Convention on Climate Change (UNFCCC), the goal of achieving the Paris Agreement is achievable if energy system and consumption pattern of all parties and non-members countries alike undergoes rapid transformation (Keramidas *et al.*, 2018). Energy efficiency has equally improved over the year leading to reduction of energy input of the GDP and hence breaking the direct link between population growth and energy demand (IEA, 2018). Interestingly, recent advancements has proved that energy input of the GDP can be significantly reduced (Ma *et al.*, 2017) and China, for example, reduced the energy input of its output progressively and notably by more than twice that of its previous year in 2017 (BP, 2018; Zhang *et al.*, 2019).

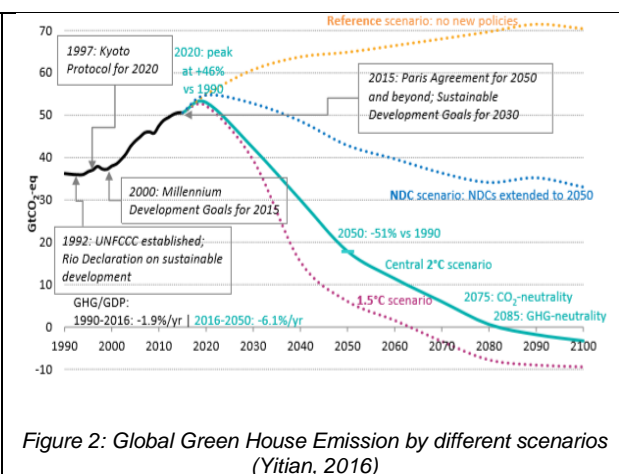
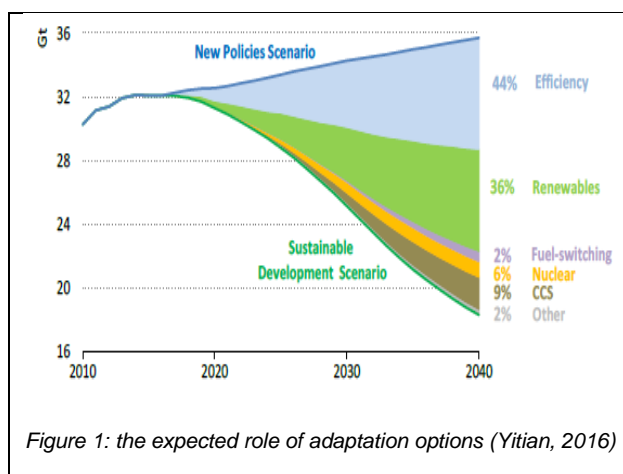
The predominant use of fossil fuel as a major source of energy is primarily driven by its low cost and high energy density (Rodgers, 2019). However, recent environmental concerns and the extraordinary growth of renewable energy has led to the choice of renewable energy systems as economical and sustainable options for most locations around the globe (Keramidas *et al.*, 2018; REN21, 2018). The transition to renewables is not only driven by environmental and climate concern, but the technology is now becoming competitive with conventional energy in many locations today, adding business lookouts to the energy transition (Jung *et al.*, 2018).

3. CLIMATE CHANGE ADAPTATION OPTIONS AND ROADMAP SCENARIOS

The Paris roadmap to low carbon energy in the future relies heavily on the application of technologies to remove huge amount of carbon dioxide and other greenhouse gases to make up for the inadequacy of present measures

(Keramidas *et al.*, 2018; EASAC, 2018). The pathway is largely driven by accelerated effort to shift to low or carbon-free energy sources with a dramatic shift of energy requirement to the power sector (IEA, 2018). For example, the substantial development of electrical mobility (Lah & Lah, 2019) and technological improvements in heat pumps has the potential to shift the demand of primary energy for transport and heat to the power sector.

Many routes have been proposed to the ambitious target of less than +2°C temperature rise above pre-industrial level. For the Sustainable Development Scenario (SDS), greenhouse gas emissions are expected to be brought down to zero before the end of 2080 or even sooner with more persuasive efforts based on the 1.5°C scenario. Figures 1 and 2 explain the role of some technologies and the expected growth of the technical pathways and scenarios to staying on track respectively. Figure 2 explains the length of time it will take to achieve the targeted zero emissions based on the different policies and efforts, starting with the United Nations Framework Convention on Climate Change (UNFCCC) in 1992 and followed 5 years later by the Kyoto protocol in 1997. This transition to zero emission before the end of the 21st century foresees Carbon Capture, Utilisation and Sequestration (CCUS) methodologies as an integral option playing a significant role in climate mitigation (Datta and Krishnamoorti, 2019). According to the IPCC roadmap, CCS is seen to contribute about 24% to the global effort of zero-emission and therefore, attending the zero emission target without CCS is an expensive venture (García and Torvanger, 2019).



Despite the many work and great successes that have been made over the years on the use of CCS to reduce CO₂ emissions, the huge financial investment and the long term risk associated with such technologies still remains a major barrier to the wide application of the technology for carbon capturing and this is an area for more research (Singh and Dhar, 2019). At the moment, CCS is still expensive and the fear of possible leakage in the future has been the focus of many studies (García and Torvanger, 2019; Gasparini *et al.*, 2016; Espinoza *et al.*, 2018; Vielstädte *et al.*, 2019).

Energy efficiency and renewables are expected to be the major drivers, growing to about 44% and 32% respectively in the global effort by the end of 2040 as shown in Figure 1 (IEA, 2017). Nuclear and fuel switching are considered complimentary to renewables and energy efficiencies, providing less than 9% to global effort to limit global warming (IEA, 2017; Dutta, 2018). The decreasing acceptance of the use of fossil-base fuel for energy production arising from public awareness is also key to supporting the energy transition. The existence of cheap technologies to handle the effect of non-CO₂ gases is an added advantage (Winiwarter *et al.*, 2018). The building sector will also change, increasing its electricity demand from 31% in 2015 to 46% in 2050 (Figure 3). Cumulatively, the road map foresees renewable power generation growing from 23% in 2015 to about 71% in its share of power generation in 2050.

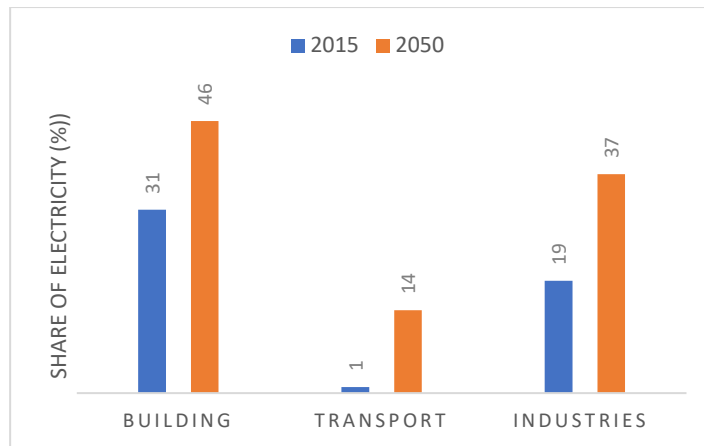


Figure 3: The global share of electrify in three sectors

Interestingly, the building sector will also witness the highest transition moving from 33% of its share of renewable in 2015 to 65% in 2050 (Figure 4a). Policy directions considering climate change will be the main catalyst to accelerating the share of renewables in the power energy mix rising sharply from 50% in 2030 to about 71% of its share of renewable in 2050. Figure 4 (a & b) shows the expected impact and trend in the deployment of renewable energy as a mitigation option in three energy sectors.

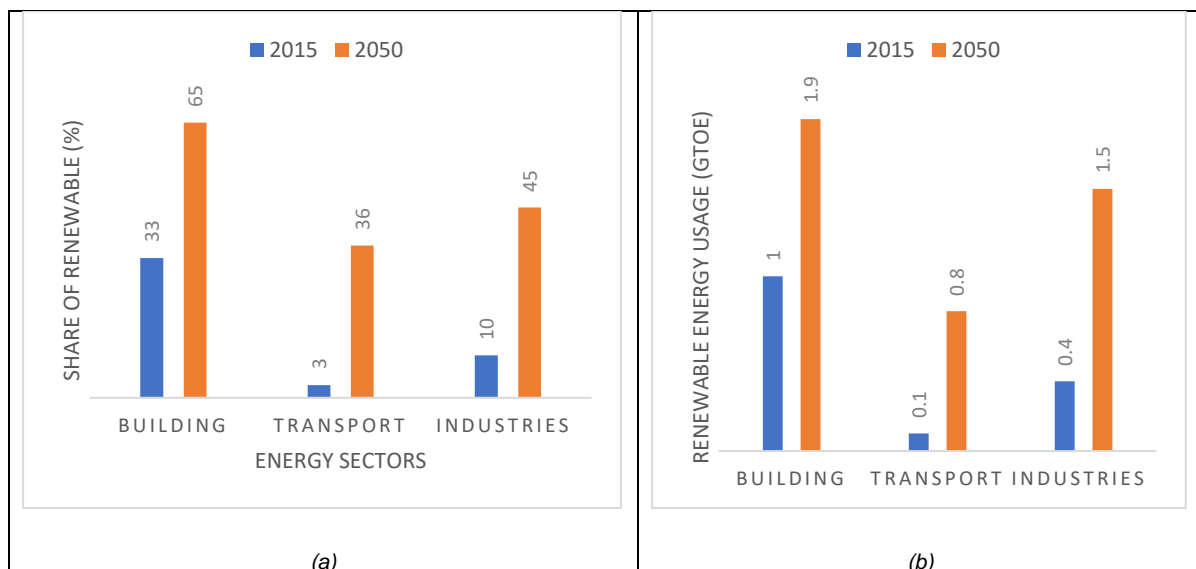


Figure 4: Global Share (a) and usage (b) of renewables in three sectors

4. FACTORS SUPPORTING THE GLOBAL ENERGY TRANSITION RENEWABLE ENERGY

4.1. Falling cost of technologies

The cost of solar and wind technologies has fallen dramatic since 2010, dropping by over 73% and 22% respectively. The cost is projected to further reduce by 59% for solar and about 26% for onshore wind turbines (IRENA, 2016), taking renewable technologies to a competitive edge in terms of cost with conventional energy system. This development has created a good business-case for power generation with renewable technologies especially solar and wind as many investors and individuals invest in the business of renewable power generation. Renewable technologies now have a competitive edge with conventional energy in top markets around the world even without subsidy (IRENA, 2018a). Interestingly, the price of batteries, which was the major reason for the high cost of wind and solar systems, has also declined by about 80% from its 2010 level. The cost reduction in batteries is projected to further decrease by 60% before 2025 (IRENA, 2016). The business model and profit motive will become the new driver as power production from solar and wind reaches parity with conventional energy sources (IRENA, 2019).

4.2. Contaminated air and climate change

Air pollution by products of combustion such as particulate matter (PM) and carbon dioxide from the burning of oil or coal for the production of energy have been reported to be main reason for the gradual reduction in health of air-polluted communities. In particular, Nitrogen dioxide has been linked to decreased function of the lungs resulting to asthmatic conditions causing the death of millions of people around the globe (Eisenman *et al.*, 2019; World Health Organisation, 2019; Lee *et al.*, 2019). The threat posed to human existence due to climate change is another major concern that is playing a key role in shaping the global energy transition. According to Rafaj *et al.*, (Rafaj *et al.*, 2011), the World Health Organisation (WHO) consider that about 6.5 million deaths worldwide are attributed to air pollution. Since renewables and energy efficiency are adjudged to provide the most cost-effective solutions, offering about 90% solution to reduction of carbon emission and strengthened by the profitable business case of renewables, most policy directions in most countries should be directed towards more investment in energy efficiency and renewable innovations (IRENA, 2018b). In recent times, there have been different commitments at regional level and even at national level to transform power production to emission-free sources (Kazimierczuk, 2019). For example, the United Arab Emirate has set the target to increase its renewable and nuclear power by 50%, the target is to reach the SDG objective of delivering an affordable and clean energy for its citizens by 2050 (Trichakis *et al.*, 2018). This development will be a catalyst for the growth of renewables.

4.3. Improved Technological Innovation

Public awareness and the general acceptance of renewable technologies will change the present trajectory towards irreversible climate change, and more scholarly work is dedicated towards studying renewable technologies innovation than fossil fuel technologies (Trencher & van der Heijden, 2019; Irandoust, 2018; van der Meijden & Smulders, 2018). For example, there has been massive improvements in efficiencies of PV modules and solar water heaters (Alam *et al.*, 2015; Gautam, *et al.*, 2017). Evolutional innovations and much research in biofuels, electric cars and the electrolytic generation of hydrogen is opening up new possibilities to extend renewables into new areas, expanding the penetration of renewables especially in the transportation sector (Çabukoglu *et al.*, 2019).

4.4. Global Warming

Since every location has experienced effects of climate change ranging from the most common of air pollution to flooding, draught and heat-waves, public awareness as to the causes are now evident and public knowledge is almost global (Hsiang *et al.*, 2019). Consumers of energy are now more worried of the effect of the energy they consume than the cost of the energy. Awareness and public opinion are now drivers of the energy system toward a lower carbon footprint. Civil society and even religious bodies are now at the forefront of adding to the argument for a change towards fewer carbon-based sources. People are aware of their right of a clean environment and many governments even integrated the climate laws into many sectors of economy (Nachmany & Setzer, 2018).

5. THE IMPLICATION OF THE TRANSFORMATION

The dangers and irreversible implications of global warming has woken global realisation of the need to have a global approach to energy consumption. Technology has evolved in the power sector bringing a significant breakthrough of the inflow of smart energy systems that deliver digital solutions that allows for the smart control of energy demand; greatly eliminating waste and subsequently reducing the net energy demand along with its associated emissions (IRENA, 2018b).

Overall, the global transformation of energy has great impact on the declining cost of PV and wind energy technologies. The cost of battery electricity storage declined dramatically from a global average of 540 USD/KWh in 2014 to USD 210/KWh in 2017. The resulting effect of the fall in cost of solar energy system components led to higher use of PV and wind energy systems in the power section. The capacity of solar photovoltaics grew from 15GW in 2007 to 400GW in 2018 (IRENA, 2018b). Wind energy grew from 50 GW in 2005 to 590GW in 2018. This trend is predicted to continue, and the cost of renewable energy technologies is predicted to fall even further with the consequent effect of motivating large economies to shift their power demands to renewables. At present Germany and Spain have reached 40% in their transition of the power sector to renewables.

Considering the gigantic volume of air pollution from the aviation sector, the sector will have to undergo transformation leading to efficient design of aircraft that uses fuels with less effect on the environment to meet the climate target. The design of new aircraft will have to change to reduce the associated emissions. For example, by 2011, planes were successfully flown on bio-jet fuel even at commercial level and in 2016 the first solar plane was tested (IRENA, 2018b). The Paris target of ending the use of fossil fuel-based energy resources before the end of the 21st century has gradually weakened demand for coal and oil for power production. This implies that a huge quantity of the world's reserves of oil, coal and natural gas will still be left under the ground by the end of the century

(Monasterolo & Raberto, 2019). This scenario will open up new trends in investment forcing countries who initially depend on coal or oil to move towards the new global energy front of non-carbon-based energy systems. This transformation has implications in future investment. Countries and companies who use fossil fuel either for production of some products or sources of energy, could suffer losses from stranded assets due to future regulation that will limit the use of fossil fuel and shifts to renewables due to lower cost (Marques *et al.*, 2018). Losses due to stranded assets are estimated to be between 1 to 4 trillion US Dollars (Marques *et al.*, 2018). Most investors will gradually shy away from fossil-based power-related technologies to investment in renewables. This development will open up new job opportunities in areas of renewables and increase investment in renewables. However, the transition will also lead to job losses in the oil sector. This again has socio-economic implications. Therefore, in order to prevent the occurrence of one problem by solving another, an approach that merges the socio-economic factors into the roadmap for the global energy transformation will be a more holistic approach (European Commission, 2016; IRENA, 2018b; Caetano *et al.*, 2017; Davies *et al.*, 2018).

6. THE NEED FOR MONITORING AND EVALUATION OF THE PROGRESS OF KEY CLIMATE MITIGATION OPTIONS

To boost ambition and increase efforts towards achieving the worldwide target of limiting global warming and rise of temperature to below 2°C and with more effort to reach 1.5°C, it is necessary to put in place a system that tracks and assess the climate change adaptation policies either at global or regional level. This is essential to evaluate the impact of each options to the roadmap in order to quantify the impact and changes that are needed to continue to be on the right path to climate mitigation. A yearly or quarterly meeting of each country and key emission sectors is also a necessary tool for monitoring and evaluating the progress made and a demonstration of a serious support for the Paris Agreement. As a matter of ensuring compliance to countries obligations, the mechanism of systematic review was initiated in Articles 3 and 7 of the Paris Agreement which demands a review of progression periodically (Yitian, 2016; Tompkins *et al.*, 2018). A systematic review at UNFCCC level enables a precise understanding of the current gains and the prediction of future trends with considerable certainty (Sun, 2015) creating healthy competition and best practice (Hönle, Heidecke & Osterburg, 2018). It will also send a strong political signal to countries and sectors which may need to wake up to their individual or regional commitments. Notably, there has been a call at local and regional level for more monitoring and actions through policies that will boost efforts towards the fight to limit global warming within the framework of the UNFCCC (Kamperman & Biesbroek, 2017). Individual assessment by countries and regions provides avenues where countries record their progress, especially now, considering evidence that there has been rise in emissions in 2017 after a steady progress of keeping it low for about 4 years (Olhoff & Christensen, 2018; Le Quéré *et al.*, 2018).

One major concern with most climate change policies is the absence of a large-scale common assessment tool to evaluate the actual extend of the adaption of the policies. For example most advanced countries who are party to the UN framework on climate change pay attention to hazard analysis and rarely is any focus given to evaluating the extent to which the climate adaptation policies are practised (Tompkins *et al.*, 2018). Looking at the critical role of each party to climate change mitigation, it is important that all parties evaluate progress in their Nationally Determined Contributions (NDC) with strong inclination towards the global commitment and more emphasis on the actual adaptation on the ground before the 25th submit of the conference of parties (COP 25). This is the meeting point where parties to the Paris Agreement will collectively take stock and asses the post-Paris climate progress. Before this conference, each member is expected to assess their progress for onward submission.

Previous investigations by the UNFCCC have shown that the aggregate gains made on both compulsory and non-compulsory Nationally Determined Contributions are usually far from what is expected to meet the goal of limiting global warming to below 2°C. For instance, India, being among the highest emitters of greenhouse gas (GHG) and a party to the Paris Climate summit, accepted the more ambitious target of 1.5°C scenario and it has equally taken a commitment with policy direction to reduce its carbon content of GDP by 33%–35% by 2030 with reference to 2005 levels. India will have to concretise its gains for what it has achieved (Mohan & Wehnert, 2019) before the COP 25 meeting. China, another huge emitter, equally made a national commitment to increase its non-fossil energy consumption by 20% in 2030 (Li *et al.*, 2019). It is therefore key that parties appraise their post-Paris achievement. Countries who are not on track are likely to encounter global attention and strong pressure to link their internal policies strongly with global climate commitments (Mohan & Wehnert, 2019). For vulnerable countries, the 2°C scenario may be too relaxed with major implications as much of their land may be submerged under water, forcing them to migrate to habitable areas (Yitian, 2016). British Petroleum (BP, 2018), the IRENA (2019) and other editions of the global energy transformation appraisals track progress of major indicators to achieving the goal of limiting global warming to below 2°C above pre-industrial levels. Table 1 shows the progress of the key indicators in the climate adaptations roadmaps.

Interestingly, from the review, renewable electrification has received much attention. The yearly addition of renewable energy system to the power sector improved from a 17GW/year level in 2010 to 109GW/year in 2018 in comparison to 31GW/year of wind in 2010 and 54GW/year in 2018. By this reckoning, the share of renewable energy in the global power sector increased to 25% in 2018. This is considered significant and on track with the goal of clipping global temperature rise to below 2°C. The share of renewables in global power generation is to

reach 57% by 2030. On the other hand, improvement in global energy efficiency is considered unimpressive, growing by an average of 1.2% per year in 2010 increasing slightly to about 2.3% per year in 2018. This development is considered to be off-track for the role of energy efficiency in the global effort to fight climate change. At the regional or sectional level, countries like China, despite being one of highest emitters of greenhouse gases, has dedicated huge resources into research to reduce energy intensity of its output through improvement in energy system efficiency (Li *et al.*, 2019).

Table 1: Tracking the global progress of key indicators in the climate change adaptation options.

Indicators	Years			Remark (2018/2019)	Reference
	2010	2017	2030		
Renewable share in Power (%)	20	25	57	On-track	(IRENA, 2018b)
solar PV addition (GW/yr)	17	109	194.7	On-track	[(IRENA, 2018b; Pursiheimo <i>et al.</i> , 2019).
Wind Energy additions (GW/yr)	31	51	200	On-track	(IRENA, 2018b).
Energy intensity rate (%/yr)	1.2	2.3	3.3	Off-track	[(IRENA, 2018b).
Oil consumption (Mtoe/yr)	4077.6	4557	2988	Off-track	(BP, 2018; IRENA, 2018b; BP, 2017).
Coal demand (Mtoce/yr)	4936	5357	3190	Off-track	
Emissions per capita (ton)	4.3	4.6	2.6	Off-track	(IRENA, 2018b).
Fossil fuel share of primary energy (%)	About 85	About 84	< 77	----	(BP and B.P.E.Outlook, 2019; Peters <i>et al.</i> ,2017)

The increase of energy-related emissions from 4.3t of carbon dioxide per capita in 2010 to 4.6t of carbon dioxide per capita in 2018 was mainly attributed to an increase in demand for oil and coal as seen in Table1. The demand for oil and coal increased from 87 million barrels and 4963 million barrels per day in 2010 to 89 million barrels and 5357 million barrels per day in 2018 respectively. The share of fossil fuels in primary energy consumption remains almost constant at a global average of about 84% since 2010.

7. CONCLUSION

Overall, the primary goal of the energy transition is exemplified in efforts to reduce air pollution and limit global warming to below +2°C above pre-industrial before the end of this century. The objective is to prevent the catastrophic effect of temperature rise and air pollution in the near future.

The declining cost of renewable technologies has led to more investment in PV and wind for power generation than in oil, gas and coal power technologies. This development has positive benefits not only in reducing the carbon content of the world energy consumption, but also in opened up new job opportunities in areas of renewables. However, there will also be a loss of jobs in the oil, gas and coal industrials. This again has socio-economic implications. Therefore, to prevent the occurrence of one problem by solving another, an approach that merges the socio-economic factors into the roadmap for the global energy transformation will be a more holistic approach

Analytical evidence and available global reviews of historical trends, tracking the progress of key indicators in the climate adaptation roadmap and current status shows that there is a need to increase effort in the global fight against climate change. Monitoring mechanisms should not only ensure strict compliance of developed countries but also emerging economies since they are mainly responsible for huge emissions due to rapid industrialisation which heavily rely on fossil fuels.

8. REFERENCES

Alam, M.S., Alouani, A.T., and Azeem, M.F. "Efficient prediction of maximum PV module output power through dynamic modelling," *Sustain. Energy Technol. Assessments*, vol. 11, pp. 27–35, 2015.

BP and B. P. E. Outlook, "BP Energy Outlook 2019 edition The Energy Outlook explores the forces shaping the global energy transition out to 2040 and the key uncertainties surrounding that," BP Energy Outlook 2019, 2019.

British Petroleum (BP), "British Petroleum Statistical Review of World Energy 2018," 67, 2018.

British Petroleum (BP), "British Petroleum Statistical Review of World Energy June 2017." 2017.

Çabukoglu, E., Georges, G., Küng, L., Pareschi, G. and Boulouchos, K. "Fuel cell electric vehicles: An option to decarbonize heavy-duty transport? Results from a Swiss case-study," *Transp. Res. Part D Transp. Environ.*, vol. 70, no. March, pp. 35–48, 2019.

Caetano, T., Merven, B., Hartley, F. and Ahjum, F. "Decarbonisation and the transport sector: A socio-economic analysis of transport sector futures in South Africa. Energy Research Centre Working Paper." *J. Energy South Africa*, vol. 28, no. 4, pp. 9–18, 2017.

Datta, A. and Krishnamoorti, R. "Opportunities for a Low Carbon Transition-Deploying Carbon Capture, Utilization, and Storage in Northeast India," *Front. Energy Res.*, vol. 7, no. March, 2019.

Davies, M., Swilling, M. and Wlokas, H.L. "Towards new configurations of urban energy governance in South Africa's Renewable Energy Procurement Programme," *Energy Res. Soc. Sci.*, vol. 36, no. November, pp. 61–69, 2018.

Dutta, P. "Role of carbon capture and storage in meeting the climate mitigation target," *Green Energy Technol.*, no. 9789811083921, pp. 87–103, 2018.

EASAC, Science Advice for the Benefit of Europe Negative emission technologies: What role in meeting Paris Agreement targets? no. 35. 2018.

Eisenman, T.S. et al., "Urban trees, air quality, and asthma: An interdisciplinary review," *Landsc. Urban Plan.* vol. 187, no. April 2018, pp. 47–59, 2019.

Espinoza, D.N. et al., "CO₂ charged brines changed rock strength and stiffness at Crystal Geysers, Utah: Implications for leaking subsurface CO₂ storage reservoirs," *Int. J. Greenh. Gas Control*, vol. 73, no. May 2017, pp. 16–28, 2018.

European Commission, "The Road from Paris: assessing the implications of the Paris Agreement and accompanying the proposal for a Council decision on the signing, on behalf of the European Union, of the Paris agreement adopted under the United Nations Framework Convention on Cl," 2016.

Faisal, F., Tursoy, T. and Ercantan, O. "The Relationship between Energy Consumption and Economic Growth: Evidence from non-Granger Causality Test," in *Theory and Application of Soft Computing, Computing with Words and Perception*, 2017, pp. 671–675.

García J.H. and Torvanger, A. "Carbon leakage from geological storage sites: Implications for carbon trading," *Energy Policy*, vol. 127, no. November 2018, pp. 320–329, 2019.

Gasparini, A., Sainz-García, A., Grandia, F. and Bruno, J. "Atmospheric dispersion modelling of a natural CO₂ degassing pool from Campo de Calatrava (northeast Spain) natural analogue. Implications for carbon storage risk assessment," *Int. J. Greenh. Gas Control*, vol. 47, pp. 38–47, 2016.

Gautam, A., Chamoli, S., Kumar, A. and Singh, S. "A review on technical improvements, economic feasibility and world scenario of solar water heating system," *Renew. Sustain. Energy Rev.*, vol. 68, no. September 2016, pp. 541–562, 2017.

Gu, A. Teng, F. and Feng, X. "Effects of pollution control measures on carbon emission reduction in China: evidence from the 11th and 12th Five-Year Plans," *Clim. Policy*, vol. 18, no. 2, pp. 198–209, 2018.

Hönle, S.E., Heidecke, C. and Osterburg, B. "Climate change mitigation strategies for agriculture: an analysis of nationally determined contributions, biennial reports and biennial update reports," *Clim. Policy*, vol. 3062, 2018.

Hsiang, S., Oliva, P. and Walker, R. "The Distribution of Environmental Damages," *Rev. Environ. Econ. Policy*, vol. 13, no. 1, pp. 83–103, 2019.

I. - International Energy Agency, "WEO-2017 Special Report: Energy Access Outlook," 2017.

IEA, "World Energy Outlook 2018, New Policies Scenario," 2018.

IPCC, "An IPCC Special Report on the impacts of global warming of 1.5°C above pre-industrial levels and related global greenhouse gas emission pathways, in the context of strengthening the global response to the threat of climate change, sustainable development," Switzerland., 2018.

Iranoust, M. "Innovations and renewables in the Nordic countries: A panel causality approach," *Technol. Soc.*, vol. 54, no. March, pp. 87–92, 2018.

IRENA, "Renewable Power Generation Costs in 2017," Abu Dhabi., 2018a.

IRENA, "The Geopolitics of the Energy Transformation," Abu Dhabi., 2019.

IRENA, *Global energy transformation: A roadmap to 2050*. 2018b.

IRENA, *The Power to Change: Solar and Wind Cost Reduction Potential to 2025*, no. June. International Renewable Energy Agency, 2016.

Jung, T.Y., Kim, D., Moon, J. and Lim, S.K. "A scenario analysis of solar photovoltaic grid parity in the Maldives: The case of Malahini resort," *Sustain.*, vol. 10, no. 11, pp. 1–14, 2018.

Kamperman, H. and Biesbroek, R. "Measuring Progress on Climate Change Adaptation Policy by Dutch Water Boards," *Water Resour. Manag.*, vol. 31, no. 14, pp. 4557–4570, 2017.

Kazimierczuk, A.H. "Wind energy in Kenya: A status and policy framework review," *Renew. Sustain. Energy Rev.*, vol. 107, no. March, pp. 434–445, 2019.

Keramidas K. et al., *Global Energy and Climate Outlook 2018 : Sectoral mitigation options towards a low-emissions economy*. Luxembourg, 2018.

Lah, O., and Lah, B. *Pathways Towards Decarbonising the Transportation Sector*. Switzerland: Springer International Publishing, 2019.

Le Quéré, D. et al., "Global Carbon Budget 2017," *Earth Syst. Sci. Data*, vol. 10, pp. 405–448, 2018.

Lee, D., Robertson, C., Ramsay, C., Gillespie, C. and Napier, G. "Estimating the health impact of air pollution in Scotland, and the resulting benefits of reducing concentrations in city centres," *Spat. Spatiotemporal. Epidemiol.*, vol. 29, pp. 85–96, 2019.

Li, Y., Chiu, Y. and Lu, L.C. "New Energy Development and Pollution Emissions in China," *Int. J. Environ. Res. Public Health*, vol. 16, no. 10, p. 1764, 2019.

Ma, M., Cai, W. and Cai, W. "Carbon abatement in China's commercial building sector: A bottom-up measurement model based on Kaya-LMDI methods," *Energy*, vol. 165, pp. 350–368, 2018.

Ma, M., Yan, R., Du, Y., Ma, X., Cai, W. and Xu, P. "A methodology to assess China's building energy savings at the national level: An IPAT–LMDI model approach," *J. Clean. Prod.*, vol. 143, pp. 784–793, 2017.

Marques, A.C., Fuinhas, J.A. and Pereira, D.A. "Have fossil fuels been substituted by renewables? An empirical assessment for 10 European countries," *Energy Policy*, vol. 116, no. November 2017, pp. 257–265, 2018.

Mohan, A. and Wehnert, T. "Is India pulling its weight? India's nationally determined contribution and future energy plans in global climate policy," *Clim. Policy*, vol. 19, no. 3, pp. 275–282, 2019.

Monasterolo, I. and Raberto, M. "The impact of phasing out fossil fuel subsidies on the low-carbon transition," *Energy Policy*, vol. 124, no. April 2018, pp. 355–370, 2019.

Nachmany, M. and Setzer, J. "Policy brief Global trends in climate change legislation and litigation: 2018 snapshot," no. May, p. 8, 2018.

Olhoff, A. and Christensen, J.M. *Emissions Gap Report 2018*. 2018.

- Peters G.P. et al., "short Key indicators to track current progress and future ambition of the Paris Agreement," *Nat. Clim. Chang.*, vol. 7, no. 2, pp. 118–122, 2017.
- PricewaterhouseCoopers International Limited (PWC), "Is Paris Possible? The Low Carbon Economy Index." p. 27, 2017.
- Pursiheimo, E., Holttinen, H. and Koljonen, T. "Inter-sectoral effects of high renewable energy share in global energy system," *Renew. Energy*, pp. 1119–1129, 2019.
- Rafaj, P. et al., "Outlook for clean air in the context of sustainable development goals," *Glob. Environ. Chang.*, vol. 53, no. August, pp. 1–11, 2018.
- REN21, "RENEWABLES GLOBAL STATUS REPORT: A comprehensive annual overview of the state of renewable energy," 2018.
- Rodgers, M., Coit, D., Felder, F. and Carlton, A. "Assessing the effects of power grid expansion on human health externalities," *Socioecon. Plann. Sci.*, vol. 66, no. July 2018, pp. 92–104, 2019.
- Singh, J. and Dhar, D.W. "Overview of Carbon Capture Technology: Microalgal Biorefinery Concept and State-of-the-Art," *Front. Mar. Sci.*, vol. 6, no. February, pp. 1–9, 2019.
- Sun, F., He, X., Rummy, P. and Lauzon, K. "Global progress in climate change adaptation policies and its implication for China," *Chinese J. Popul. Resour. Environ.*, vol. 13, no. 1, pp. 21–31, 2015.
- Tompkins, E.L., Vincent, K., Nicholls, R.J. and Suckall, N. "Documenting the state of adaptation for the global stocktake of the Paris Agreement," *Wiley Interdiscip. Rev. Clim. Chang.*, vol. 9, no. 5, pp. 1–9, 2018.
- Trencher, G. and van der Heijden, J. "Contradictory but also complementary: National and local imaginaries in Japan and Fukushima around transitions to hydrogen and renewables," *Energy Res. Soc. Sci.*, vol. 49, no. October 2018, pp. 209–218, 2019.
- Trichakis, P., Carter, N., Tudhope, S., Patel, I., Sgouridis, S. and Griffiths, S. "Enabling the UAE's Energy Transition - Top Ten Priority Areas for Renewable Energy Policymakers," 2018.
- van der Meijden, G. and Smulders, S. "Technological Change During the Energy Transition," *Macroecon. Dyn.*, vol. 22, no. 4, pp. 805–836, 2018.
- Vielstädte, L. et al., "Footprint and detectability of a well leaking CO₂ in the Central North Sea: Implications from a field experiment and numerical modelling," *Int. J. Greenh. Gas Control*, vol. 84, no. April, pp. 190–203, 2019.
- Wang, W., Kuang, Y., Huang, N., and Zhao, D. "Empirical Research on Decoupling Relationship between Energy-Related Carbon Emission and Economic Growth in Guangdong Province Based on Extended Kaya Identity," *Sci. World J.*, no. 1, 2014.
- Winiwarter, W., Höglund-Isaksson, L., Klimont, Z., Schöpp, W. and Amann, M. "Technical opportunities to reduce global anthropogenic emissions of nitrous oxide," *Environ. Res. Lett.*, vol. 13, no. 1, 2018.
- World Health Organisation, "World health statistics 2016: monitoring health for the SDGs, sustainable development goals," 2016.
- Yitian, H. "Climate Mitigation Efforts After the Paris Agreement : Achievements, Remaining Debates, and New Challenges ," *China Q. Int. Strateg. Stud.*, vol. 02, no. 03, pp. 383–400, 2016.
- Zhang, P., Shi, X.P., Sun, Y.P., Cui, J. and Shao, S. "Have China's provinces achieved their targets of energy intensity reduction? Reassessment based on nighttime lighting data," *Energy Policy*, vol. 128, no. September 2018, pp. 276–283, 2019.

#358: Experimental study on thermal performance of novel trapezoidal reactor

Xiaojing HAN¹, Shuli LIU^{2,*}, Yongliang SHEN¹, Liu YANG¹, Xiue YANG¹, Yanjun ZHANG¹

¹School of Mechanical Engineering, Beijing Institute of Technology, Beijing, China, xiaojing910105@163.com

²School of Energy, Construction and Environment, Coventry University, Coventry, CV1 2FB, UK

*Corresponding author: Shuli.Liu@coventry.ac.uk

This paper experimentally researches the thermal performance of a thermochemical reactor for the zeolite 13X-water. It aims to improve the poor thermal conductivity of the zeolite 13X with a novel thermochemical reactor design using added copper strips (Case 2) or fins (Case 3). For all cases of the thermochemical reactor with and without copper strips or fins, the influences of the relative humidity and flow rate of inlet air on outlet temperature and water temperature lift were recorded. Results reveal that 1) the copper strips reactor achieved a higher water temperature than copper fins or smooth tube; 2) copper fins increased the outlet reactor temperature than the other two cases; 3) the whole energy efficiency of the reactors gradually increased from 0.48-0.53-0.78 in the order of Case 1 to Case 3. During the whole discharging process, it was concluded that the outlet temperature of the copper strips reactor was approximately 10°C higher than that of the copper strips or smooth tube, however, its water temperature lift was 4.34°C lower than Case 2 and 0.87°C higher than Case 1. Moreover, the copper fins reactor presented the highest energy efficiency of 0.78. A simplified methodology is proposed for the analysis of the zeolite 13X-water working pairs discharging process through the identification of the critical points as result of the thermal performance of the reactor.

Keywords: thermochemical reactor, zeolite 13X, copper strips, fins, thermal performance

1. INTRODUCTION

Currently, more than 90% of the world's primary energy generation is consumed or wasted in the form of thermal energy (Li et al., 2017, p.383). Among all the energy-consuming contents, the domestic building sector accounts for the highest energy consumption with air conditioning and electrical energy as more people aspire to higher comfort living standards (Aydin et al., 2015, pp.356-357). It is reported that 71% of the final energy demand in Chinese residential sectors results from water and space heating (IEA, 2013). In the United Kingdom, approximately 80% of the energy for domestic buildings, of which direct gas use delivers 72%, and electricity contributes 22%, is for space heating (UK Government, 2013). Additionally, heating, cooling, air conditioning and domestic hot water account for more than half of the energy consumption in buildings (Parameshwaran et al., 2012, p.2397). Therefore, urgent energy management solutions are needed to increase the share of renewable sources and to reduce the reliance on fossil fuel-driven systems (Utlu et al., 2014, p.312).

Thermal energy storage (TES) plays a broad and critical role in making energy available for space heating and cooling, solar energy utilisation, solar thermal power generation, and other applications (Gur et al., 2012, p.1454). In particular, adsorption thermochemical energy storage technology attracts scholars' and researchers' attention due to its high energy storage density, high efficiency and low heat loss during the storage process (Yu et al., 2013, p.489; André et al., 2016, p.703). The increasing energy demands for renewable energy has replaced conventional fossil fuels and electricity consumption, and has been successfully applied to space heating and domestic hot tap water. Thermal energy storage technology can alleviate the mismatch between supply and demand (Zhang et al., 2017, p.2421), a promising novel solution for reducing carbon emission and environment pollution. Thermochemical energy storage technology can store excess thermal energy at off-peak hours and release it during the peak period, effectively achieving rational utilisation of energy. Solar energy, based on clean and easily-accessible properties, is usually regarded as a heat source and stored in thermochemical materials. As solar energy is a diurnal cyclic resource, storing excess energy for long or short-term periods will both increase the use of solar energy systems and reduce fossil fuel consumption (Aydin et al., 2015, p.1214). Moreover, depending on the thermochemical heat storage medium, its storage density can reach as high as 1000-2000 MJ/m³ (Xu et al., 2018, p.98).

Despite the superior properties of thermochemical energy storage technology, innovative reactor design, material and system selection are key issues for the thermal performance enhancement in further development. To fulfil it, efficient thermochemical storage systems should include (Aydin et al., 2016, pp.322-323):

- Good heat and mass transfer properties inside the reactor during the whole charging-discharging process;
- Low pressure drop loss;
- High energy storage density;
- Good cyclic ability;
- High thermal conductivity of material;
- Low regeneration temperature;
- Environment friendly.

Many studies on material and reactor design have been used to improve heat and mass transfer properties, achieving a close combination between sorbent and sorbate and good kinetics performance. Extended surfaces have become a hot topic in heat and mass transfer issues: pipes with conventional fins are employed to enhance the heat transfer rate and are especially preferred in various sorption energy storage systems. The adsorption bed reactor usually consists of a solid sorbent and heat exchanger, the size and shape of the heat exchanger strongly affects the heat and mass transfer inside the reactor. Riffel et al. simulated the heat and mass transfer of an adsorber with a finned-tube heat exchanger, taking into consideration the geometry of the heat exchanger and the diffusion in the adsorbent medium (Riffel et al., 2010, p.1473). The thermal behaviour of the adsorber mainly related to the conductivity of the adsorbent and the heat-transfer coefficient between metal and solid sorbent, finned-tube heat exchanger aimed to enhance the heat-transfer area. Cuypers et al. carried out an experimental test on two lab-scale reactors; one is a glass zeolite reactor containing copper heat exchanger and the other had copper fins with the TCM glued on it (Cuypers et al., 2012, p.207). Based on good results of heat exchanger enhancement and reactor optimisation, high output power (0.6 kW/kg active material) and short reaction times (5 minutes) were obtained due to the heat and mass transport.

A preferred material should be non-toxic, non-corrosive and stable with fast reaction kinetics and high storage density (Zondag et al., 2008). In this study, zeolite 13X can be used as a hydrophilic adsorbent for storing thermal energy. It is characterised by a high porosity and therefore has the advantage of a large adsorption capacity between 0.25-0.45 g_{H₂O}/g_{zeolite}, thus resulting in a high energy density (Köll et al., 2017, p.389, Tatsidjoudong et al., 2013, p.341). However, its high regeneration temperature above 200°C is also the main drawback due to the relatively strong bonds with vapour molecules. Table 1 summarises open systems using zeolite as a storage material. Shigeishi et al. studied the energy storage properties of molecular sieves 4A, 5A, 13X, activated alumina and silica gel. They found that zeolite 13X demonstrated the best adsorbent among these material (Shigeishi et al., 1979, p.489). Based on the porous zeolite 13X, various experimental investigations for the thermochemical

energy storage system have been analysed in recent years. Dawoud et al. studied a closed zeolite 13X-water system charged by a hot fluid with energy efficiency of 0.43-0.67, and gained a high energy storage density of 91.76 kWh/m³ (Dawoud et al., 2007, p.135). They also achieved a temperature lift of 30°C during a 5 hour charging period. Tatsidjodoung et al. built an open solar heat storage system based on zeolite 13X-water for buildings, with an average temperature lift of 38°C was gained with 80kg thermochemical material (Tatsidjodoung et al., 2016, p.488). Christian Finck et al. built a 41kg zeolite thermochemical heat storage module to supply space heating at the temperature of 40°C in a house system (Christian et al., 2014, p.320). The experimental results showed a zeolite temperature lift 31.2°C under the adsorption temperature of 20°C and evaporation temperature of 15°C. Casey et al. also demonstrated that zeolite 13X had the highest temperature lift of all samples due to its high amount of vapour adsorption and fast reaction kinetics (Casey et al., 2015, p.128). However, its high regeneration temperature (>180°C) is prerequisite for the desorption research. So the zeolite 13X and charging temperature of 180°C is used in this paper.

Table 1: Open system prototypes with different zeolite and operating conditions

Year	Mass	Zeolite	Conditions	Max power(kW)	Ref.
2006	70 kg	4A	$T_{\text{charge}}=170^{\circ}\text{C}$, $T_{\text{discharge}}=20^{\circ}\text{C}$	1.5	Bales et al., 2008, p.55
2014	150 kg	13X	$T_{\text{charge}}=185^{\circ}\text{C}$, $T_{\text{discharge}}=25-60^{\circ}\text{C}$	0.4	Boer et al., 2014, p.28
2015	80 kg	13X	$T_{\text{charge}}=120-180^{\circ}\text{C}$, $T_{\text{discharge}}=20^{\circ}\text{C}$	2.25	Johannes et al., 2015, p.80
2018	62.5 L	13X	$T_{\text{charge}}=180^{\circ}\text{C}$, $T_{\text{discharge}}=10-55^{\circ}\text{C}$	4.4	Alebeek et al., 2018, p.325

The thermochemical materials used as well as the reactor design influences the good heat and mass transfer properties. This paper experimentally investigates the thermal performance of a novel trapezoidal reactor with zeolite 13X-water as working pairs. The aims of this research is to improve heat and mass transfer rates, gain preferred outlet reactor temperature and water temperature lift. A reference reactor integrated with smooth tubes (Case 1) is studied to evaluate its thermal performance, through comparison analysis of the results achieved in both rigs (Case 2: copper strips, and Case 3: fins) and operating conditions (relative humidity and airflow rate). There are currently very limited experimental studies investigating novel trapezoidal reactor with different heat exchangers in existing literature and it is envisaged that this innovative concept may act as a model for future short/long-term development of these reactors.

2. METHODOLOGY

2.1. Experiment system

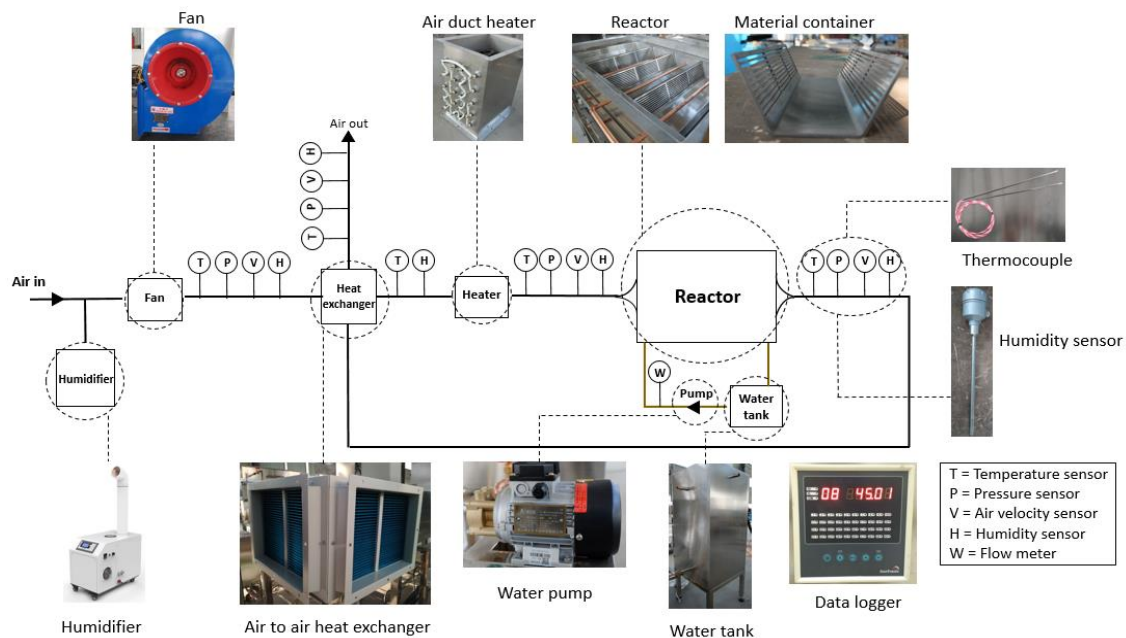


Figure 1a: Schematic diagram of experimental test rigs

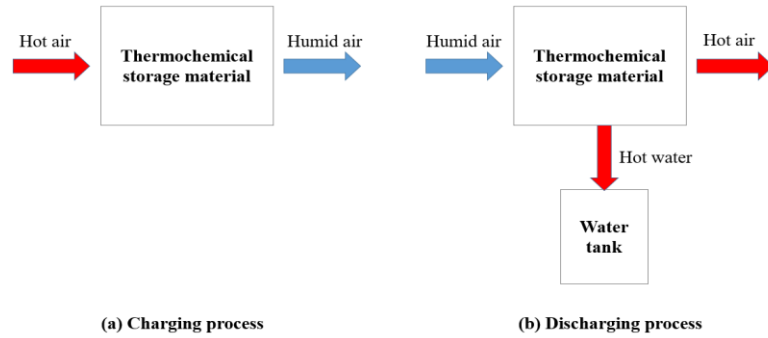


Figure 1b: basic principle of reversible charging-discharging process

Figure 1 introduces the built experimental test rig of the smooth tube reactor and its basic principle. An electric heater and an ultrasonic humidifier were used to achieve charging and discharging processes for heat and moisture supply, respectively. The regeneration temperature of zeolite 13X was easily achieved by an electrical heater which simulated a solar collector. During the charging period, a hot fluid of 180°C was transported to the reactor and the sorbent subsequently released high humidity water vapour and adsorbed heat energy during the 6 hours operating process. While the humid air was passed away from the reactor, the released heat energy was blown into the outlet, the partial one can be used for heating water of copper tubes in the form of convective heat transfer. The obtained outlet temperature and hot water can be supplied for space heating and domestic hot water respectively.

2.2. Reactor design

A thermochemical reactor was built at the Beijing Institute of Technology, in Beijing China, as shown in Figure 2. The reactor was structured in a trapezoid container with openings at the sides. The reactor supported the thermochemical material Zeolite 13X and also provided an air flow path. The side opening width was 4mm, achieving the opening rate at 42% (ratio of air opening areas and trapezoid container side area). The novel reactor design achieved good heat and mass transfer properties. Each container supported 5kg of zeolite 13X. Additionally, to extract the heat, copper tubes 16mm in diameter were distributed across the reactor containers, represented by the red lines of Figure 2 (c). During the charging process, ambient air was heated by the electric heater and blown across the reactor. The temperatures were measured by thermocouples as illustrated in Figure 2 (c). A total of 24 thermocouple sensors measured the temperature of the four containers. Additionally, 5 thermocouples were fixed on the copper tubes to measure the water temperature. All data collected was automatically recorded in a PC through a data logger at an interval of 30 seconds.

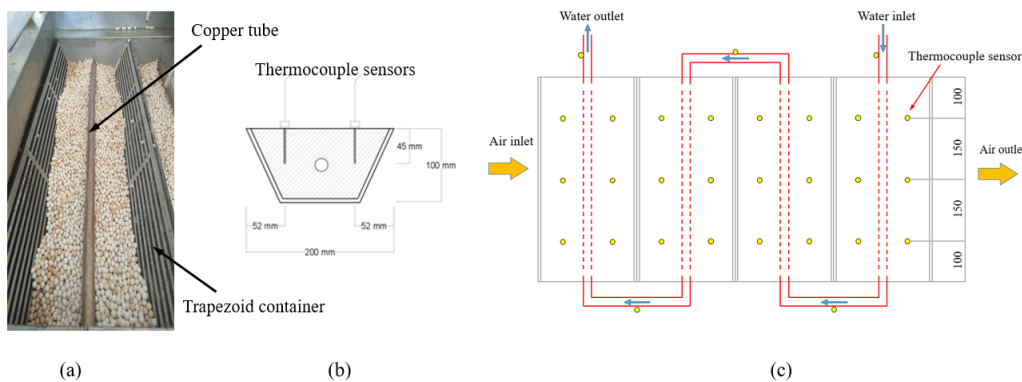


Figure 2: Trapezoidal container with zeolite 13X and thermochemical reactor and locations of thermocouples: (a) trapezoidal container, (b) cross section view, (c) top view

2.3. The details on the copper strips and fins heat exchanger

This section depicts novel heat exchangers with copper strips and fins inside the thermochemical reactor, as shown in Figure 3. The novel design of heat exchanger can enhance the heat transfer between the zeolite particles and it can also enhance the heat transfer from the zeolite to the water flow. The welded copper tube was connected to the water tank with 500*500*900 mm³ which was to collect the recycled water and supply for residents. The water

pump was set for 10 Hz and gained steady water flow rate at 0.08 m³/h. In order to evaluate the stored heat energy in the material with a proper temperature for domestic hot water production and space heating, the inlet temperature was increased from ambient temperature (22°C) to 35°C by a heat recovery unit. Table 2 introduces some basic parameters including particle zeolite 13X, copper tube, strips, fins and reactor.

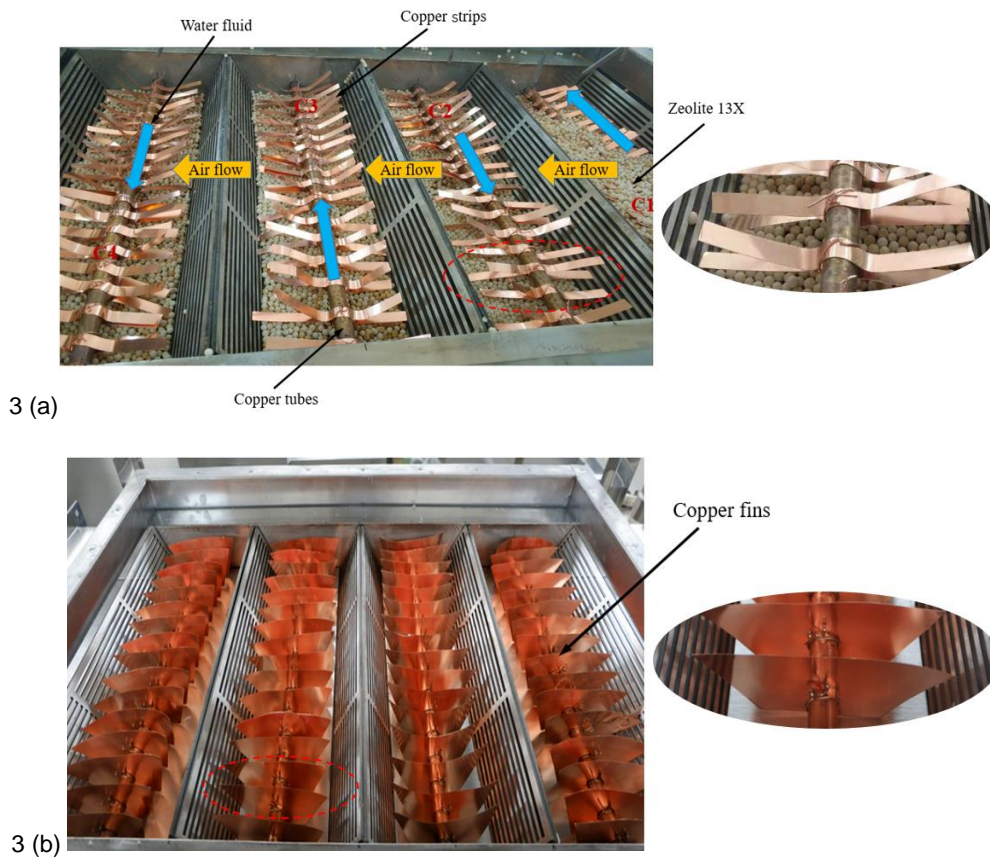


Figure 3: The picture of creative heat exchangers: (a) copper strips, (b) copper fins

Table 2: Properties of the zeolite 13X, characteristics of copper tube, strips, fins and reactor

Name	Parameters	Value
Zeolite 13X (Helaly et al.,2019, P.12)	Thermal conductivity	3.3 (W/m·K)
	Volume density	730 kg/m ³
	Specific heat capacity	1080 (J/kg·K)
	Porosity	0.395
Copper strips	Thermal conductivity	386.4(W/m·K)
	Number of each tube	19
	Thickness	0.3 mm
	Length	120 mm
Trapezoidal fins	Distance between them	25 mm
	Number of each tube	16
	Top side size	100 mm
	Bottom side size	80 mm
	Inclination angle	110°
Copper tube	Distance between them	29.4 mm
	Inner diameter of tube	14 mm
	Outer diameter of tube	16 mm
Reactor	Length	600 mm
	Width	500 mm
	Height	100 mm
	Insulation thickness	30 mm

2.4. Thermal energy analysis

In this experimental research, the thermal performance of the thermochemical reactor focused on the energetic analysis based on the collected experimental data. The cumulative thermal energy output over a t_d (discharging) and energy input over a t_c (charging) period is calculated with the Equation (1) and Equation (2) below:

$$E_{dis} = m \cdot c_p \cdot \int_0^{t_d} (T_o - T_i) dt \quad (1)$$

$$E_{char} = m \cdot c_p \cdot \int_0^{t_c} (T_i - T_o) dt \quad (2)$$

The ratio of the energy gain in discharging cycle to the energy input to the sorbent in charging cycle, defines the heat storage energetic efficiencies:

$$\eta = \frac{E_{dis}}{E_{char}} \quad (3)$$

2.5. Experimental uncertainty analysis

The uncertainty of the experimental test relating to temperature, pressure, flow and relative humidity, is calculated by using Equation (4) (Zhou et al., 2011, p.973). According to the instrumentation specifications listed in Table 3, the overall uncertainty is $\pm 5.29\%$.

$$U = \pm \sqrt{\left(\frac{\Delta T_{TC}}{T_{TC}}\right)_{reactor}^2 + \left(\frac{\Delta T_{TC}}{T_{TC}}\right)_{air}^2 + \left(\frac{\Delta RH}{RH}\right)_{air}^2 + \left(\frac{\Delta P}{P}\right)_{air}^2 + \left(\frac{\Delta V}{V}\right)_{air}^2 + \left(\frac{\Delta V}{V}\right)_{water}^2} \times 100\% \quad (4)$$

Table 3: Instrumentations and related technical information

Parameter	Accuracy	Quantity
Airflow rate	3%	2
Reactor/air/water temperature	3%	31
Air humidity	3%	2
Air pressure	1%	2

3. EXPERIMENTAL RESULTS AND DISCUSSIONS

To investigate the influence of the copper strips and fins on the outlet temperature and water temperature at the discharging period, three sets of experimental tests were carried out. The first one was to study the temperature lift of outlet and water during the whole discharging process (Case 1); the Case 2 and Case 3 for the thermochemical reactor with copper strips and fins, respectively. The experimental operation conditions are shown in Table 4.

Table 4: Typical operation parameters of experimental test

Operation parameters	Charging test	Discharging test
Inlet air temperature	180°C	22-32°C
Vapour pressure	460-480 Pa	200-220 Pa
Relatively humidity of the inlet air	0%	95-99%
Airflow rate	57-300.6 kg/h	57 kg/h
Water flow rate	0 m ³ /h	0.08 m ³ /h

3.1. The influences of copper strips and fins on the charging process

For the charging process, ambient air passed through the electrical heater and formed a hot air steam at 180°C, which was blown through the sorbents with a flow rate of around 250 kg/h. The air was directed to the reactor inlet

for dehydrating the zeolite 13X. After complete regeneration, the thermochemical reactor was hermetically sealed to prevent the adventitious penetration of moisture to the sorbent. Figure 4 (a) illustrates the temperature variations of the reactor with the charging process of the three different cases being run for 6 hours. Figure 4 (b) and (c) depict the reactor pressure drop and airflow rate during the test. Statistically, air pressure ranged from 460 Pa to 480 Pa and airflow rates varied from 57kg/h to 300 kg/h. From the experimental results, some steps can be seen in the temperature curves, the average thermal power and total energy transferred to the reactor during the 6 hours were 2.36 kW and 14.15 kWh for the smooth tube reactor, 2.02 kW and 12.11 kWh for the copper strips one, 2.15 kW and 12.91 kWh for the copper fins one, respectively.

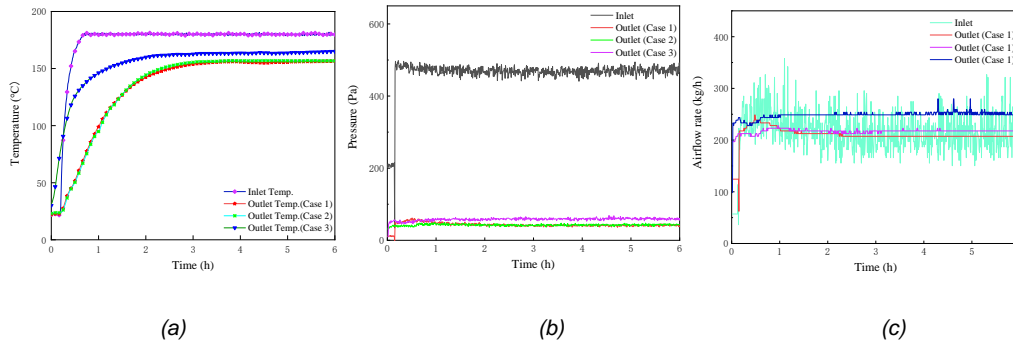


Figure 4: The temperature variations, pressure drop and airflow rate of three cases during 6 hours charging period: (a) temperature (b) pressure (c) airflow rate

In addition to the charging tests under Case 1, the tests were conducted for Cases 2 and 3. The temperature comparison between them were evaluated and are summarised in Table 5. Obviously, for the reactor temperature, Cases 2 and 3 achieved relatively higher peak temperatures than that of Case 1. Overall, the tests show that the integration of copper strips and fins sufficiently lifted the reactor charging performance.

Table 5: The details on the temperature profiles of different areas during the charging period

Case	Temperature (°C)							
	Container 1		Container 2		Container 3		Container 4	
	Max	Min	Max	Min	Max	Min	Max	Min
1	178.52	22.32	175.72	22.55	172.09	23.18	169.65	23.91
2	179.64	27.14	180	26.39	176.74	26.51	174.67	26.7
3	180	32.72	179.62	32.97	178.27	33.05	174.24	33.19

3.2. The influences of copper strips and fins on the reactor temperature distributions at the discharging period

With respect to discharging performance, tests were conducted according to the operation conditions in Table 4 for three different cases. For the cases of the thermochemical reactor with and without copper strips or fins, Figure 5 and Figure 6 depict temperature distributions of four containers and the reactor pressure drop, airflow rate and relative humidity during the tests, respectively. The low humidity air was transported to the reactor, thus resulting in the quick temperature lift and heat transfer. The four containers reached peak subsequently in a short time, especially the copper fins reactor temperature where values were the highest among the three different cases. The difference values become increasingly smaller in the order of the 1st to 4th container. The whole discharging process ran for 5 hours, the inlet pressure and airflow rate kept relatively stable at about 220 Pa and 57 kg/h, respectively, while relative humidity gradually increased.

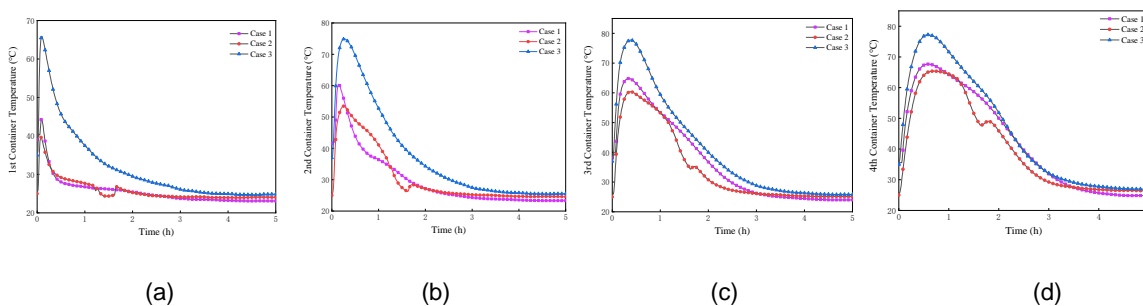


Figure 5: The temperature profiles of four containers inside the thermochemical reactor during 5 hours discharging period: (a) 1st container, (b) 2nd container, (c) 3rd container, (d) 4th container

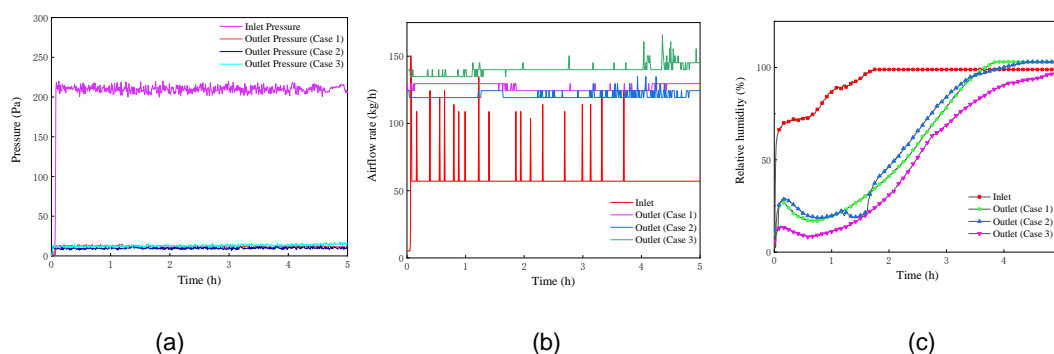


Figure 6: The air flow parameters during 5 hours discharging period: (a) pressure drop, (b) airflow rate, (c) relative humidity

3.3. The influences of copper strips and fins on the outlet temperature

In the discharging process, the fan was set for 57 kg/h to provide stable airflow, the ultrasonic humidifier was placed in the air inlet of the fan and continuously provided 100% RH for inlet of the reactor. From the results in Figure 6, relative humidity of the inlet gradually reached 99.98%, its corresponding pressure and airflow rate kept at about 220 Pa and 57 kg/h, respectively. The dried sorbents gradually sorb the moisture. With respect to the outlet temperature of reactor, as shown in Figure 7 (a), Cases 1 and 2 have almost similar values at the inlet temperature of 23°C, whilst Case 3 achieved over 60°C under the inlet temperature of 31°C. During the discharging process, all the sorption heat released by the thermochemical reactor was used to heat the flowing air. The outlet air temperature reached 50°C, which is suitable for space heating. The maximum outlet temperature of copper fins reactor reached 65.19°C, around 10°C higher than the first two cases. The copper fins reactor in this paper may be suitable for achieving high outlet temperatures, which results from air flow path and limited contact area between tube and zeolite 13X, while that with copper strips optimised its contact area to increase water temperature but kept the same value with Case 1.

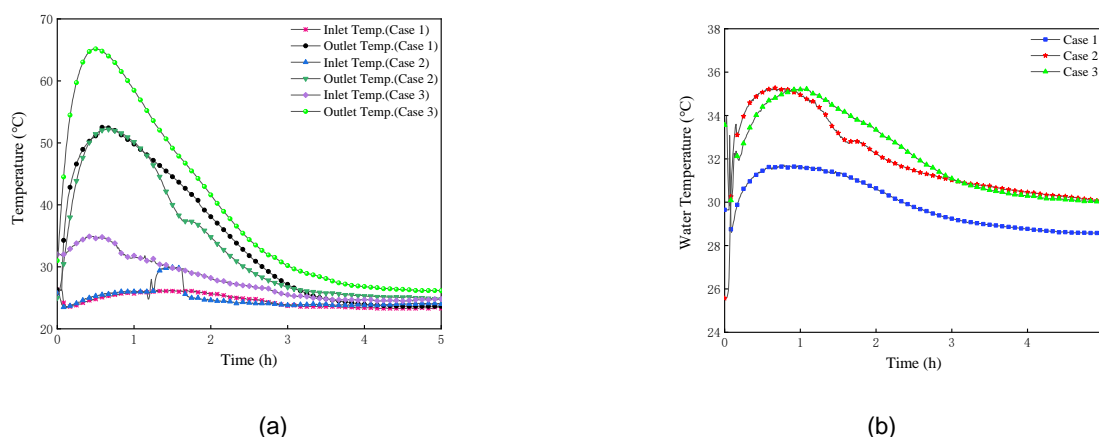


Figure 7: The temperature variations of (a) reactor at the outlet, (b) water temperature

3.4. The influences of copper strips and fins on the water temperature

With respect to the water temperature, as shown in Figure 7 (b), compared with Case 1, Cases 2 and 3 achieved over 35°C. This indicated that additions of copper strips and fins enhanced the heat transfer rate greatly and helped to obtain higher water temperatures.

Table 6: The temperature variations during the whole discharging process

Case	Average Reactor Temperature (°C)												Water Temp. Lift (°C)
	Inlet		Container 1		Container 2		Container 3		Container 4		Outlet		
	Max	Min	Max	Min	Max	Min	Max	Min	Max	Min	Max	Min	
1	26.3	23.3	44.54	23.08	60.45	23.3	64.82	23.98	67.65	24.81	52.57	23.63	4.52
2	30	23.4	39.625	23.92	53.52	24.57	60.35	25.11	65.38	25.75	52.17	24.78	9.73
3	35	24.5	65.91	24.70	74.92	25.44	77.78	25.8	77.23	26.91	65.19	26.14	5.39

Table 6 summarizes the average reactor container temperature and water temperature lift for three different cases. In Case 1, the average maximum reactor temperature was slightly higher than Case 2, but lower than Case 3. For instance, container 1 achieved peak container temperature of 44.54°C quickly (Case 1), with 39.625°C and 65.91°C for Cases 2 and 3, respectively. Among the three different cases, container 4 reached the highest temperature during the discharging process, 67.65°C for Case 1, 65.38°C and 77.23°C for Case 2 and 3, respectively. Additionally, the outlet temperature of Case 3 was approximately 10°C higher than that of the Case 1 and 2, however, its water temperature lift was 4.34°C lower than Case 2 and just 0.87°C higher than Case 1. These indicate that copper strips and fins sufficiently improved water temperature and tackled the poor thermal conductivity issues.

During the discharging process, humid ambient air brought water molecules to zeolite 13X particles which released heat energy. Some was transferred to the copper tubes and heated up the water flow, while the rest was taken away by airflow and heat loss to the environment. Due to the poor thermal conductivity of zeolite 13X, the reactor with smooth copper pipes presented a great need to improve the heat transfer. According to the experiments, the integration of the copper strips proved that water temperature was greatly improved, which met residents' needs for hot tap water production. Similarly, the copper fins reactor presented the highest outlet temperatures and the reactor was suitable for space heating in buildings. Based on Equations (1), (2) and (3), from the results of Table 7, the average thermal power during the 5-hour discharging process were calculated to be 1.35, 1.28 and 2.02 kW in the order of the Case 1 to Case 3, respectively. Case 1 achieved slightly higher value than Case 2 due to low sensible loss in the reactor. Case 3 had the highest values in average power output and energy efficiency, which resulted from good heat and mass transfer properties of the reactor.

Table 7: The information on the power input, output and efficiency

Case	Average power Input(kW)	Average power Output(kW)	Efficiency
1	2.36	1.35	0.48
2	2.02	1.28	0.53
3	2.15	2.02	0.78

4. CONCLUSION

This paper experimentally investigated the thermal performance of a thermochemical reactor for the zeolite 13X-water, a novel thermochemical reactor design aligning with copper strips or fins influenced the outlet temperature and water temperature lift at the discharging period. Through the experimental tests, comparison analysis was made to study with and without the copper strips or fins. Some highlights are presented as follow.

- Compared to the reference reactor, the copper strips reactor had slightly lower outlet temperature but higher water temperature lift; the copper fins reactor presented outlet reactor temperature of over 60°C. For the case of copper fins, the water temperature lift was lower than with copper strips but 0.87°C higher than the reference reactor.
- Among three different cases, the copper fins reactor showed the highest efficiency of 0.78, which verified the feasibility of space heating.
- The optimal reactor design sufficiently improved the heat and mass transfer properties, acting as a new model for future research.

5. REFERENCES

André, L., Abanades, S. and Flamant, G. Screening of thermochemical systems based on solid-gas reversible reactions for high temperature solar thermal energy storage. *Renewable and Sustainable Energy Reviews*, 2016. 64: p. 703-715.

van Alebeek, R., Scapino, L., Beving, M.A.J.M., Gaeini, M., Rindt, C.C.M. and Zondag, H.A. Investigation of a household-scale open sorption energy storage system based on the zeolite 13X/water reacting pair. *Applied Thermal Engineering*, 2018. 139: p. 325-333.

Aydin, D., Casey, S.P. and Riffat, S. The latest advancements on thermochemical heat storage systems. *Renewable and Sustainable Energy Reviews*, 2015. 41: p. 356-367.

Aydin, D., Utlu, Z. and Kincay, O. Thermal performance analysis of a solar energy sourced latent heat storage. *Renewable and Sustainable Energy Reviews*, 2015. 50: p. 1213-1225.

Aydin, D., Casey, S.P., Chen, X. and Riffat, S. Novel “open-sorption pipe” reactor for solar thermal energy storage. *Energy Conversion and Management*, 2016. 121: p. 321-334.

Bales, C., Gantenbein, P., Jaenig, D., Kerskes, H., Summer, K., Van Essen, M. and Weber, R. Laboratory tests of chemical reactions and prototype sorption storage units, A Rep. IEA Sol. Heat. Cool. Program. - Task 32 Adv. Storage Concepts Sol. Low Energy Build, 2008: p. 55.

Casey, S.P., Aydin, D., Riffat, S. and Elvins, J. Salt impregnated desiccant matrices for ‘open’ thermochemical energy storage—Hygrothermal cyclic behaviour and energetic analysis by physical experimentation. *Energy and Buildings*, 2015. 92: p. 128-139.

Cuypers, R., Maraz, N., Eversdijk, J., Finck, C., Henquet, E., Oversloot, H. van’t Spijker, H. and de Geus, A. Development of a Seasonal Thermochemical Storage System. *Energy Procedia*, 2012. 30: p. 207-214.

Dawoud, B., Amer, E. H. and Gross, D. M. Experimental investigation of an adsorptive thermal energy storage. *International Journal of Energy Research*, 2007. 31(2): p. 135-147.

DECC. Estimates of heat use in the United Kingdom in 2012: Department of Energy & Climate Change, The UK Government. 2013.

Finck, C., Henquet, E., van Soest, C., Oversloot, H., de Jong, A-J., Cuypers, R. and van’t Spijker, H. Experimental Results of a 3 kWh Thermochemical Heat Storage Module for Space Heating Application. *Energy Procedia*, 2014. 48: p. 320-326.

Gur, I., Sawyer, K. and Prasher, R. *Searching for a better thermal battery* Science, 2012. 335: p. 1454-1455.

Helaly, H.O., Awad, M.M., Ibrahim I, E-S. and Hamed, A.M. Theoretical and experimental investigation of the performance of adsorption heat storage system *Applied Thermal Engineering*, 2019. 147: p. 10-28.

IEA Transition to Sustainable Buildings: Strategies and Opportunities to 2050: International Energy Agency (IEA). 2013.

Johannes, K., Kuznik, F., Hubert, J-L., Durier, F. and Obrecht, C. Design and characterisation of a high powered energy dense zeolite thermal energy storage system for buildings. *Applied Energy*, 2015. 159: p. 80-86.

Köll, R., van Helden, W., Engel, G., Wagner, W., Dang, B., Jänchen, J., Kerskes, H., Badenhop, T. and Herzog, T. An experimental investigation of a realistic-scale seasonal solar adsorption storage system for buildings. *Solar Energy*, 2017. 155: p. 388-397.

Li, T.X., Wu, S., Yan, T., Wang, R.Z. and Zhu, J. Experimental investigation on a dual-mode thermochemical sorption energy storage system. *Energy*, 2017. 140: p. 383-394.

Parameshwaran, R., Kalaiselvam, S., Harikrishnan, S. and Elayaperumal, A. Sustainable thermal energy storage technologies for buildings : A review. *Renewable and Sustainable Energy Reviews*, 2012. 16: p. 2394-2433.

Riffel, D.B., Wittstadt, U., Schmidt, F.P., Núñez, T., Belo, F.A., Leite, A.P.F. and Ziegler, F. Transient modeling of an adsorber using finned-tube heat exchanger. *International Journal of Heat and Mass Transfer*, 2010. 53: p. 1473-1482.

Shigeishi, R.A., Langford, C.H. and Hollebone, B.R. Solar energy storage using chemical potential changes associated with drying of zeolites. *Solar Energy*, 1979. 23(6): p. 489-495.

Smeding, S., de Boer, R., Zondag, H.A., Krol, G. Development of a prototype system for seasonal solar heat storage using an open sorption process,. 2014: in: Eurotherm Seminar# 99, Advance in Thermal Energy Storage. p. 28-30.

Tatsidjodoung, P. Le Pierrès, N. and Luo, L. A review of potential materials for thermal energy storage in building applications. *Renewable and Sustainable Energy Reviews*, 2013. 18: p. 327-349.

Tatsidjoudong, P., Le Pierrès, N., Heintz, J., Lagre, D., Luo, L. and Durier, F. Experimental and numerical investigations of a zeolite 13X/water reactor for solar heat storage in buildings. *Energy Conversion and Management*, 2016. 108: p. 488-500.

Utlu, Z., Aydin, D. and Kincay, Comprehensive thermodynamic analysis of a renewable energy sourced hybrid heating system combined with latent heat storage *Energy Convers Manage*, 2014. 84: p. 311-325.

Xu, S. Z., Lemington, Wang, R.Z., Wang, L.W. and Zhu, J. A zeolite 13X/magnesium sulfate–water sorption thermal energy storage device for domestic heating. *Energy Conversion and Management*, 2018. 171: p. 98-109.

Yu, N., Wang, R.Z. and Wang, L.W. Sorption thermal storage for solar energy. *Progress in Energy and Combustion Science*, 2013. 39(5): p. 489-514.

Zhang, Y.N., Wang, R.Z. and Li, T.X. Experimental investigation on an open sorption thermal storage system for space heating. *Energy*, 2017. 141: p. 2421-2433.

Zhou D. and Zhao, C.Y. Experimental investigations on heat transfer in phase change materials (PCMs) embedded in porous materials. *Applied Thermal Engineering*, 2011. 31: p. 970-977. Gur I, Sawyer K, and Prasher R, Searching for a better thermal battery *Science*, 2012. 335: p. 1454-1455.

Zondag, H., Kalbasenka, A., van Essen, M., Bleijendaal, L., Schuitema, R., van Helden, W. and Krosse, L. First studies in reactor concepts for thermochemical storage. *Proc.Eurosun*, 2008.

#361: Stimulation of continuous variable transmission (CVT) gear box with Single Input Rule Modules (SIRMs) connected fuzzy based actuator for wind energy harvesting

Chian Haur JONG¹, Peter Nai Yuh YEK², Henryson UNJAH³

¹University College of Technology Sarawak, Department of Engineering, 96000, Sibul, Sarawak, Malaysia.
chian.haur@ucts.edu.my,

²University College of Technology Sarawak, Department of Engineering, 96000, Sibul, Sarawak, Malaysia.
peter.yek@ucts.edu.my,

³University College of Technology Sarawak, Department of Engineering, 96000, Sibul, Sarawak, Malaysia.
henrysonunjah@gmail.com

The paper describes a continuously variable transmission (CVT) device, in which torque transmission and variable gear ratio is actuated by a Single Input Rule Modules (SIRMs) connected Fuzzy Inference System (FIS) controller based on the feedback of the sensory devices. A CVT is a stepless gearbox which can change seamlessly through a continuous range of effective gear ratios. A Fuzzy Inference System (FIS) is a popular computing framework, which is a synthesis of fuzzy set theory, fuzzy if-then rule, and fuzzy reasoning. Nevertheless, conventional FIS models (i.e., Mamdani FIS and Takagi-Sugeno FIS models) are suffer from the "curse of dimensionality" issue, i.e., the number of fuzzy rules required increases in an exponential manner as the number of input increases. To overcome the shortcomings, a SIRMs-connected FIS model is proposed in this study. The SIRMs-connected FIS model is chosen because of its simplicity. Moreover, SIRMs-connected FIS model can reduce the number of fuzzy rules required in an FIS modelling problem. The proposed CVT model will be integrated with 3 phase electromagnetic machine (3-phase EMM) to develop a wind turbine generator. A MATLAB stimulated wind turbine generator model was developed to analyse the efficiency of the fuzzy actuator. In short, the study contributes toward developing a new fuzzy actuator for energy harvesting in the wind turbine generator.

Keywords: continuously variable transmission (CVT); Single Input Rule Modules (SIRMs); connected fuzzy inference system; wind energy

1. INTRODUCTION

A continuously variable transmission (CVT) is not a new technology. Indeed, the first gasoline-engine-powered vehicles with rubber V-belt CVT was reported at 1886 (Rahman et al., 2012). In the last decade, CVT has gaining popularity in the Japanese automobile industry (Heath, 2007). A CVT system has the advantage of varying the gear ratio seamlessly to optimise the power transmission from the car's power plant and its wheels (Rahman et al., 2012, Mantriota, 2005). Moreover, smooth gear ratio changing also provides a comfortable driving experience for the driver (Mantriota, 2005). Over the years, research has been conducted to improve the CVT system using fuzzy relevant techniques. For example, adaptive neuro-fuzzy was used to optimise the CVT performance for power extraction from wind turbines (Petković, 2014). Fuzzy inference systems (FIS) based controller was used by Rahman et al., (2012) to improve the electromagnetic actuation mechanism in CVT systems for power transmission efficiency.

Fuzzy inference systems (FIS), as one of the earliest applications of fuzzy sets theory, has become one of the most successful applications of fuzzy sets theory (Feng, 2010). Examples of FIS models are Mamdani FIS (Feng, 2006; Mamdani, 1976) and Takagi-Sugeno FIS (Takagi et al., 1985) models. Regardless of the popularity of Mamdani and Takagi-Sugeno FIS models, they suffer from the "curse of dimensionality" issue (Kosko, 2015), i.e. the number of fuzzy rules required increases in an exponential manner as the number of inputs increases. Indeed, it is a tedious task to gather a complete set of fuzzy rules in practical applications (Kosko, 2015). Instead of including all input items as the antecedents of fuzzy rules, which is a general practice for the Mamdani and Sugeno FIS models, SIRMs-connected FIS exploits the idea that each SIRM is a single input FIS model. Various SIRMs-connected FIS models have been developed and applied to a variety of application domains. From the literature, SIRMs-connected FIS has been successfully applied to fuel cell power management (Tong et al., 2013), medical diagnosis systems (Seki et al., 2010) and risk assessment (Jong et al., 2014).

In this study, the SIRMs-connected FIS actuator (i.e. SIRMs actuator) was developed to optimise the performance of the CVT. The proposed CVT model was integrated with 3-phase permanent magnet synchronous generator (PMSG) to develop a wind turbine generator. The wind turbine was designed to have 3-phase 400V, 50Hz power output when the generator rotor was operated at 1000RPM. This paper analyses the functionality and efficiency of the SIRMs-connected FIS actuator to keep the generator operating at 1000RPM to ensure a safe and stable voltage supply to DC and AC load connected to the system.

2. MODELLING OF WIND ENERGY CONVERSION SYSTEM

2.1. System description

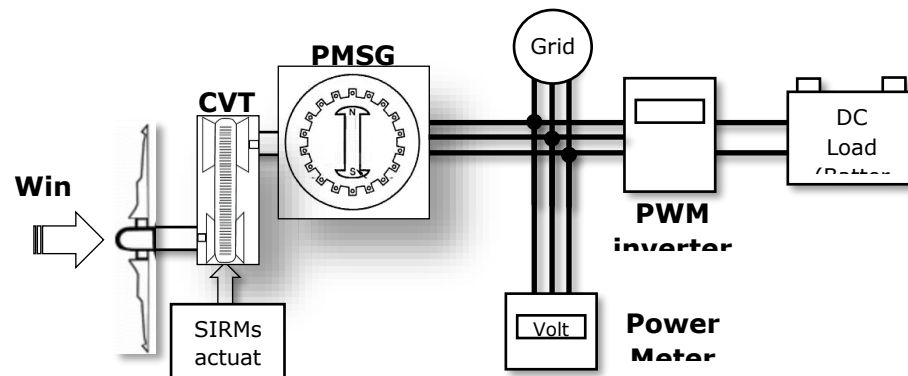


Figure 41: Flow of the working principal of the system

The flow diagram of the working principal of the designed system is shown in Figure 41. The rotor of the wind turbine was coupled to a base (i.e., input) driveshaft of CVT and the gear ratio was controlled by the SIRMs actuator base on the measured rotational speed of follower (F) and base (B) driveshaft of CVT. The follower (i.e. output) driveshaft of the CVT was connected to a unit of 3-phase PMSG. At the ideal wind speed, the SIRMs actuator maintained the rotor speed of PMSG at 1000 RPM to ensure 3 phase 400V, 50Hz power output supply to the grid and also PWM inverter.

2.2. Turbine modelling

The mechanical output power of a wind turbine (P_m) depending on turbine swept area (A), performance coefficient of the turbine (c_p), air density (ρ), and wind speed (v_w). In general, P_w can be defined by Equation 1.

Equation 39: Mechanical output power of a wind turbine

$$P_w = \frac{1}{2} c_p(\lambda_w, \beta) \rho A v_w^3$$

The turbine swept area (A) is depending of the radius of wind turbine (R) which can be calculated with $A = \pi R^2$. The $c_p(\lambda_w, \beta)$ values depend on the blade aerodynamics defined by a function of tip speed ratio (TSR) of the rotor blade tip speed to wind speed (λ_w) and blade pitch angle (β). A turbine model of Siegfried Heier (1998) was used in the simulation and the blade pitch angle was set to zero (i.e., $\beta = 0$). In general, $c_p(\lambda_w, \beta)$ can be modelled with Equation 2.

Equation 40: Performance coefficient of the turbine

$$c_p = 0.5176 \left(\frac{116}{\lambda_w} - 5 \right) e^{-21/\lambda_w} + 0.0068$$

with $\frac{1}{\lambda_{wi}} = \frac{1}{\lambda_w} - 0.035$

In this paper, the parameters of the wind turbine from Ramji et al. (2016) (as summarises in Table 1) was used as the reference parameter for designing the wind turbine model in the Matlab Simulink simulation. The turbine power characteristic is illustrated in Figure 1.

Table 24: Parameter of wind turbine

Nominal Mechanical Output Power	8.5kW
Base Wind Speed	12m/s
Radius of wind Turbine	1.001m
Air Density, ρ	1.225kg/m ³
Pitch Angle, β	0°

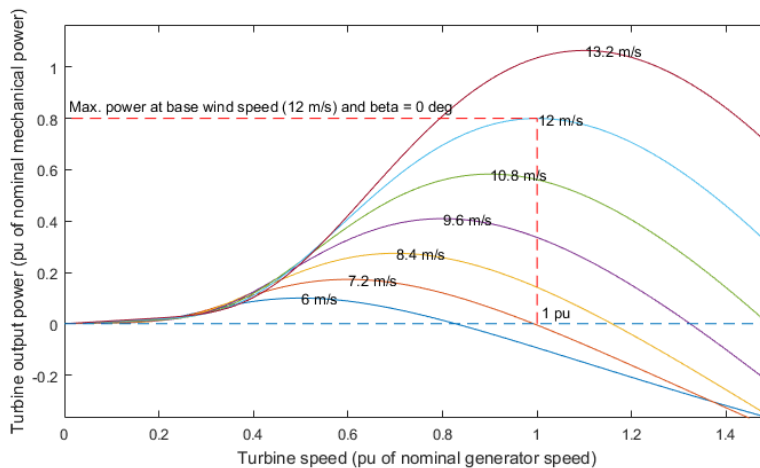


Figure 42: Turbine power characteristic ($\beta = 0^\circ$)

2.3. Modelling of PMSG generator

The used of PMSG is widely reported for stand-alone small wind turbines for the reason of high efficiency and less maintenance (Baroudi et al., 2007). Thus, a sinusoidal PMSG machine was used in the Simulink simulation where the flux established by the permanent magnets in the stator and the electromotive forces were sinusoidal. The PMSG was modelled in rotor reference frame (qd frame). The induced current of d-axis and q-axis of a rotor was determined by Equations 3 and 4 respectively, represented by a second-order state-space model.

Equation 41: Induced current of d-axis
$$\frac{d}{dt}i_d = \frac{1}{L_d}(V_d - Ri_d + L_q p \omega_m i_q)$$

Equation 42: Induced current of q-axis
$$\frac{d}{dt}i_q = \frac{1}{L_q}(V_q - Ri_q + L_d p \omega_m i_d - \lambda_m p \omega_m)$$

Let denote $a \in [q, d]$ where d and q are axis of a rotor. L_a and L_α are the inductance of rotor axis and resistance of the stator windings, respectively. The rotor axis current and voltage are denoted by i_a and V_a , respectively. Angular velocity of the rotor is denoted by ω_m and p is number of pole pairs of the PMSG machine. The electromagnetic torque, T_e of the PMSG machine can be determined by Equation 5.

Equation 43: Electromagnetic torque of the PMSG
$$T_e = 1.5p[\lambda_m i_q + [L_d - L_q]i_d i_q]$$

The parameter of PMSG used for the study purpose in this work is presented in Table 2. The PMSG was designed to generate 400V with 50Hz at 1000RPM.

Table 25: Parameter of PMSG machine

Rated Power	8.5kW
Stator Phase Resistance	0.425Ω
Armature Inductance	0.835 mH
Friction Factor	0.001189 Nms
Pole Pairs	6
inertia	0.01197 kg.m2
Voltage Constant	400 Vrms/Krpm

2.4. Modelling of the CVT gearbox

A variable ratio transmission model was implemented in the simulation where ideal torque transfer with no transmission losses was considered between base (B) and follower (F) driveshaft shaft. In the simulation, relative compliance ϕ between the axes was considered absent, the CVT model was equivalent to a gear with a variable ratio $g_{FB}(t)$. Such a gear imposed a time-dependent kinematic constraint on the motions of the two driveshaft, expressed with Equations 6 and 7

Equation 44: Rotational speed on B driveshaft in unit RPM
$$\omega_B = \pm g_{FB} \cdot \omega_F$$

Equation 45: Rotational speed on F driveshaft in unit RPM
$$\tau_F = \pm g_{FB} \cdot \tau_B$$

3. DESIGN OF THE SIRMS ACTUATOR

3.1. A zero-order SIRMs-connected FIS model

A zero-order SIRMs-connected FIS model with n inputs, (i.e., $y = f(\bar{x})$), where $\bar{x} = (x_1, x_2, \dots, x_n)$ was considered. Each rule modules consisted of m_i fuzzy rules are defined as follows:

$$SIRM - i: \quad \{R_i^{j_i}: \text{if } x_i \text{ is } A_i^{j_i} \text{ then } y_i = c_i^{j_i}\}_{j_i=1}^{m_i}$$

Note that x_i is the sole variable in the antecedent part of fuzzy rule in i -th rule module (i.e, SIRM- i). $R_i^{j_i}$ is the j -th rule in SIRM - i , where $j_i = 1, 2, \dots, m_i$. $A_i^{j_i}$ is a fuzzy set expressed in membership function as $\mu_i^{j_i}(x_i)$. A fuzzy rule $R_i^{j_i}$ is explained as a mapping from $A_i^{j_i}$ to $c_i^{j_i}$, i.e. $R_i^{j_i}: A_i^{j_i} \rightarrow c_i^{j_i}$, where $c_i^{j_i}$ is a fuzzy singleton.

The output of SIRM - i , i.e. $y_i(x_i)$, is obtained with Equation 8. A zero-order SIRMs-connected FIS model further combined the output for each rule module with a weighted addition, as in Equation 8, whereby w_i is a numerical value that reflects the relative importance of the i -th rule module.

Equation 46: Output of SIRM – i

$$y_i(x_i) = \frac{\sum_{j_i=1}^{m_i} [\mu_i^{j_i}(x_i) \times c_i^{j_i}]}{\sum_{j_i=1}^{m_i} [\mu_i^{j_i}(x_i)]}$$

Equation 47: Output of zero-order SIRMs connected FIS model

$$y = \sum_{i=1}^n [w_i y_i(x_i)]$$

3.2. Proposed SIRMs actuator

The SIRMs actuator was a zero-order SIRMs-connected FIS model with 2 inputs, (i.e., $r = f(\bar{e})$), shown in Figure 43, was considered, where $\bar{e} = (e_F, e_B)$. Note that SIRM-1 and SIRM-2 were the rule modules for e_F and e_B respectively. The output of the actuator (i.e., $\in [0.5, 2.0]$) was CVT gear ratio between base (B) and follower(F) driveshaft. e_F and e_B were the differences between the reference rotational speed (1000RPM) and measured rotational speed on F and B driveshaft, respectively.

SIRM – 1:	$\{R_1^{j_1}: \text{if } e_F \text{ is } A_1^{j_1} \text{ then } r_1^{j_1} = c_1^{j_1}\}_{j_1=1}^{m_1}$
SIRM – 2:	$\{R_2^{j_2}: \text{if } e_B \text{ is } A_2^{j_2} \text{ then } r_2^{j_2} = c_2^{j_2}\}_{j_2=1}^{m_2}$

Figure 43: Fuzzy rules for the SIRMs actuator

Gear ratio (r) is obtained with Equation 10. The inference outputs of SIRM – 1, and SIRM – 2, r_1 and r_2 respectively, are unified. Note that w_F and w_B are the important degree of each of the rule modules to r .

Equation 48: Gear ratio output from SIRMs actuator

$$r = w_F \times r_1 + w_B \times r_2$$

$$r = w_F \frac{\sum_{j_1=1}^{m_1} [\mu_1^{j_1}(e_F) \times c_1^{j_1}]}{\sum_{j_1=1}^{m_1} [\mu_1^{j_1}(e_F)]} + w_B \frac{\sum_{j_2=1}^{m_2} [\mu_2^{j_2}(e_B) \times c_2^{j_2}]}{\sum_{j_2=1}^{m_2} [\mu_2^{j_2}(e_B)]}$$

3.3. The monotonicity property of the SIRMs actuator

In this section, the proven theorem by Seki et al. (2008, 2010a) was simplified and adopted as a set of useful governing equations to construct the fuzzy rule of the SIRMs actuator. The approach was to ensure monotonicity property fulfilment of the SIRMs actuator. A fuzzy rule comprises of two parts, antecedent (fact, premise and hypothesis) and consequent (conclusion) (Ross, 2009). For instance, an FIS model, $y = f(\bar{x})$ was considered, where $\bar{x} = (x_1, \dots, x_n)$, a fuzzy rule is written as:

If x_1 is A_1 AND ... x_n is A_n Then y is B

where A_i and B are the fuzzy sets of input and output domains, respectively. “If x_1 is A_1 AND ... x_n is A_n ” is the antecedent, and “ y is B ” is the consequent.

In this project, the triangular fuzzy set in the antecedent parts were designed to fulfil the fuzzy ordering as defined in Definition 1 and 2. To distinguish the fuzzy set order in the antecedent parts, **Error! Reference source not found.** depicts two convex fuzzy sets, A and B, in X domain, with the universe of discourse ranges from \underline{x} to \bar{x} .

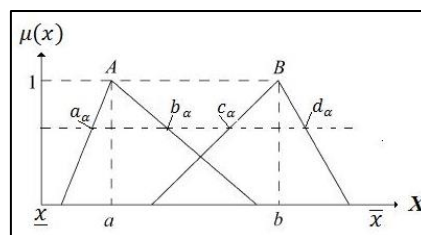


Figure 44: Comparable fuzzy sets with a fuzzy ordering $A \leq B$

Definition 1 (Seki et al., 2008, 2010a; Seki and Tay, 2012; Zadeh, 1965): The α -level sets of A and B are defined in Equation 9.

Equation 49: α -level sets of A and B

$$[A]^\alpha = [a_\alpha, b_\alpha], [B]^\alpha = [c_\alpha, d_\alpha]$$

Definition 2 (Seki et al., 2008, 2010a; Seki and Tay, 2012): A fuzzy ordering $A \preceq B$ exists and there are comparable, if the conditions in Equation 10 are satisfied.

Equation 50: Conditions for A fuzzy ordering $A \preceq B$ exists $a_\alpha \leq c_\alpha, b_\alpha \leq d_\alpha, \alpha \in [0,1]$

Let $f(\bar{x})$ denote an n -input function, where $\bar{x} = (x_1, x_2, \dots, x_n) \in X_1 \times X_2 \times \dots \times X_n$. The i -th input in \bar{x} is represented by x_i where $x_i \in X_i$ and $i = 1, 2, \dots, n$. A sequence, \bar{s} denotes a subset of \bar{x} where x_i is excluded from \bar{s} , i.e. $\bar{s} \subset \bar{x}; x_i \notin \bar{s}$. Then, the monotonicity property of $f(\bar{x})$ is defined by Definition 3.

Definition 3: For a SIRMs-connected FIS model is said to fulfill the monotonicity property between its output, y , with x_i , when y monotonically increases as x_i increases, i.e. $f(\bar{s}, x_i) \geq f(\bar{s}, x'_i)$ where $x_i > x'_i \in X_i$.

A theorem proposed by Seki et al. (2008, 2010a) is summarised in Theorem 1. The theorem was simplified and adopted as a set of useful governing equations for constructing SIRMs connected FIS.

Theorem 1 (Seki et al., 2010): A zero-order SIRMs-connected FIS model (as in Section 3.1) fulfilled the monotonicity property if the following conditions are satisfied.

Condition 1: Fuzzy membership functions for the x_i domain are comparable, i.e., $A_i^{j_i} \preceq A_i^{j_i+1}$, where $j_i = 1, 2, \dots, m_i - 1$.

Condition 2: $c_i^{j_i} \leq c_i^{j_i+1}$, where $j_i = 1, 2, \dots, m_i - 1$.

3.4. Fuzzy membership functions design

Theorem 1 in Section 3.3 was adopted as governing equations to preserve the monotonicity relationship between inputs and output of the SIRMs actuator. The fuzzy membership functions for e_F and e_B are shown in Figure 45 and Figure 46 respectively. Lower and upper limits of input domain of e_F and e_B were -1000RPM and 2000RPM, respectively. Each rule module for e_F and e_B were framed in 7 triangular fuzzy set, namely Extremely Very Slow (EVS), Very Slow (VS), Slow (S), Zero (Z), Fast (F), Very Fast (VF) and Extremely Very Fast (EVF). These membership functions were designed in such that they are comparable, and satisfy Condition 1. For example, for SIRM - 1 in Figure 45, membership functions were designed to satisfy the fuzzy order $EVS \preceq VS \preceq S \preceq Z \preceq F \preceq VF \preceq EVF$.

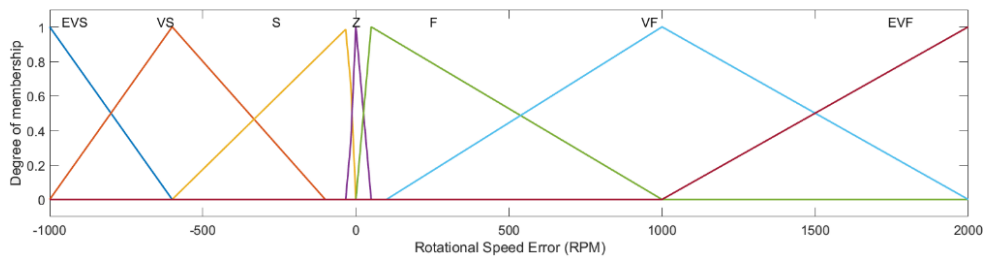


Figure 45: The membership functions of SIRM-1 (i.e., e_F)

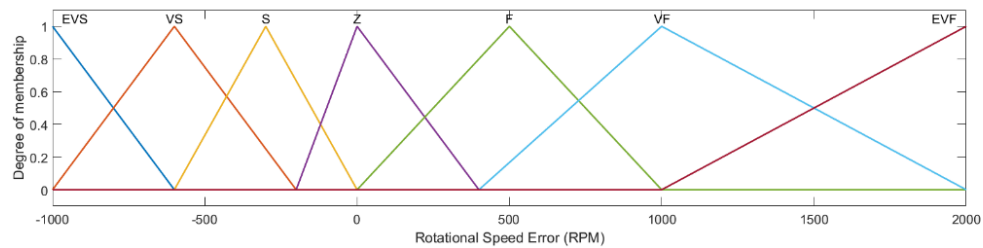


Figure 46: The membership functions of SIRM-2 (i.e., e_B)

3.5. Fuzzy Rule Gathering

The fuzzy rules were designed in such a way that *Condition 2* was satisfied. To evaluate the effectiveness of the proposed approach, a set of fuzzy rules, as summarised in *Figure 47* was used. The fuzzy singleton is 2 (*IncVVF*), 1.67 (*IncVF*), 1.33 (*IncF*), 0 (*NoChange*), 0.75 (*DecF*), 0.6 (*DecVF*), and 0.5 (*DecVVF*) for each of the fuzzy rules, respectively. An *SIRM – 1* satisfied *condition 2* with the $IncVVF \geq IncVF \geq IncF \geq NoChange \geq DecF \geq DecVF \geq DecVVF$ i.e., $2 \geq 1.67 \geq 1.33 \geq 0 \geq 0.75 \geq 0.6 \geq 0.5$

SIRM – 1	$\{R_1^1: \text{ If } e_F \text{ is } EVS \text{ then } r_1^1 \text{ is } IncVVF \}$	SIRM – 2	$\{R_2^1: \text{ If } e_B \text{ is } EVS \text{ then } r_2^1 \text{ is } IncVVF \}$
	$\{R_1^2: \text{ If } e_F \text{ is } VS \text{ then } r_1^2 \text{ is } IncVF \}$		$\{R_2^2: \text{ If } e_B \text{ is } VS \text{ then } r_2^2 \text{ is } IncVF \}$
	$\{R_1^3: \text{ If } e_F \text{ is } S \text{ then } r_1^3 \text{ is } IncF \}$		$\{R_2^3: \text{ If } e_B \text{ is } S \text{ then } r_2^3 \text{ is } IncF \}$
	$\{R_1^4: \text{ If } e_F \text{ is } Z \text{ then } r_1^4 \text{ is } NoChange \}$		$\{R_2^4: \text{ If } e_B \text{ is } Z \text{ then } r_2^4 \text{ is } NoChange \}$
	$\{R_1^5: \text{ If } e_F \text{ is } F \text{ then } r_1^5 \text{ is } DecF \}$		$\{R_2^5: \text{ If } e_B \text{ is } F \text{ then } r_2^5 \text{ is } DecF \}$
	$\{R_1^6: \text{ If } e_F \text{ is } VF \text{ then } r_1^6 \text{ is } DecVS \}$		$\{R_2^6: \text{ If } e_B \text{ is } VF \text{ then } r_2^6 \text{ is } DecVS \}$
	$\{R_1^7: \text{ If } e_F \text{ is } EVF \text{ then } r_1^7 \text{ is } DecVVF \}$		$\{R_2^7: \text{ If } e_B \text{ is } EVF \text{ then } r_2^7 \text{ is } DecVVF \}$

Figure 47: Fuzzy rules embedded in SIRMs Actuator

4. SIMULATION RESULTS AND DISCUSSIONS

4.1. Simulation of SIRMs actuator

The outputs for rule module SIRM-1 and SIRM-2 based on the measured rotational speed error (e_F and e_B) are shown in *Figure 48* and *Figure 49* respectively. The fuzzy set Zero (Z) in SIRM-1 (as shown in *Figure 45*) were designed with narrow triangular base range from -25RPM to 25RPM to ensure the fast respond to the e_F . Thus, more drastic change of gear ratio can be observe in *Figure 48* for e_F input range from -25RPM to 25RPM.

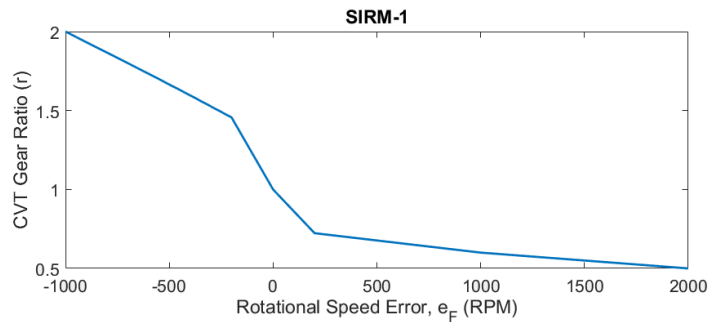


Figure 48: Gear Ratio (r) output from SIRM-1 to drive CVT gearbox

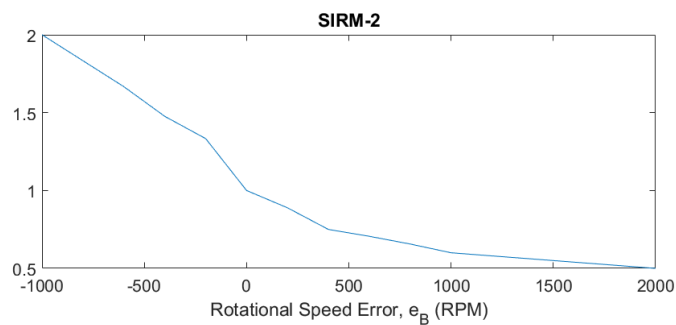


Figure 49: Gear Ratio (r) output from SIRM-2 to drive CVT gearbox

4.2. Simulation Simulink block diagram of wind turbine generator

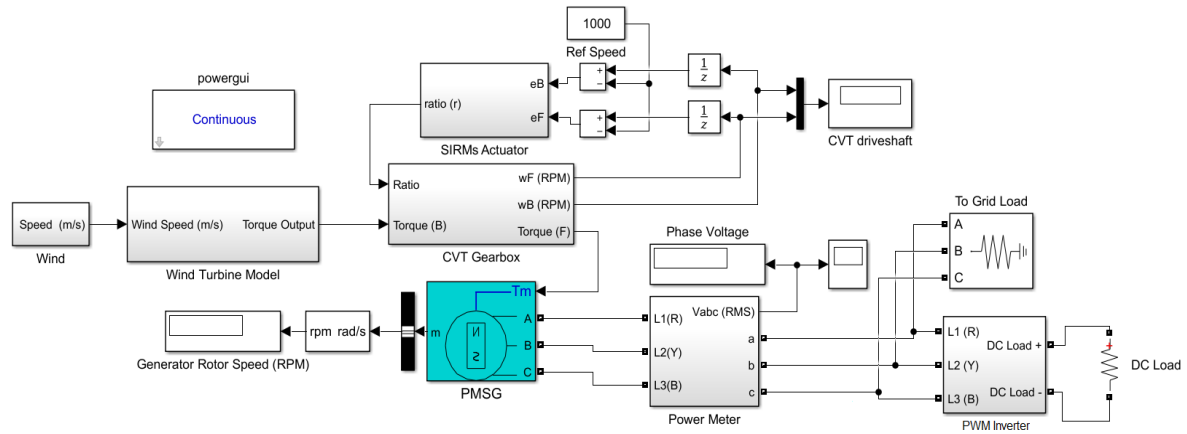


Figure 50: MATLAB/ Simulink block diagram of proposed wind turbine generator

The MATLAB/ Simulink block diagram of the wind turbine generator with CVT gearbox and SIRMs actuator is shown in Figure 50. The SIRMs actuator was stimulated with important degree $[w_F, w_B] = [0.5, 0.5]$ for the rule module SIRM-1 and SIRM-2. A balanced parallel RLC load was attached to the PMSG to simulate the load on the grid. The active power, inductive reactive power and capacitive reactive power was set to 100W, 100VAR and 100VAR, respectively. The wind block stimulated the wind speed in m/s to drive the wind turbine model. The wind speed variation is expressed in the functions as shown in Equation 13, where t is time in seconds.

Equation 51: Wind speed

$$v_w = 7.5 + 2.5 \sin(0.2\pi t)$$

Figure 411 shows the rotational speed for both follower and base driveshaft of CVT. Analysing the plotted graph data from Figure 41 shows driveshaft B which was coupled to the wind turbine was running with input rotational speed from 677RPM to 1368RPM. The driveshaft F was in overdrive to a speed of 1800RPM, when the initial signal of 7.5m/s from the wind block was driving the wind turbine. However, the SIRMs actuator quickly responded by adjusting the gear ratio of the CVT and brought down the F driveshaft rotational speed to 1000RPM, with a speed variation error range from +21.6RPM to -28.1RPM (as shown in Figure 52). Similar results were reported in Figure 53 where the PMSG was generating an average phase voltage output of 400V_{rms} with voltage variation error from +8.8V_{rms} to -10.1 V_{rms}.

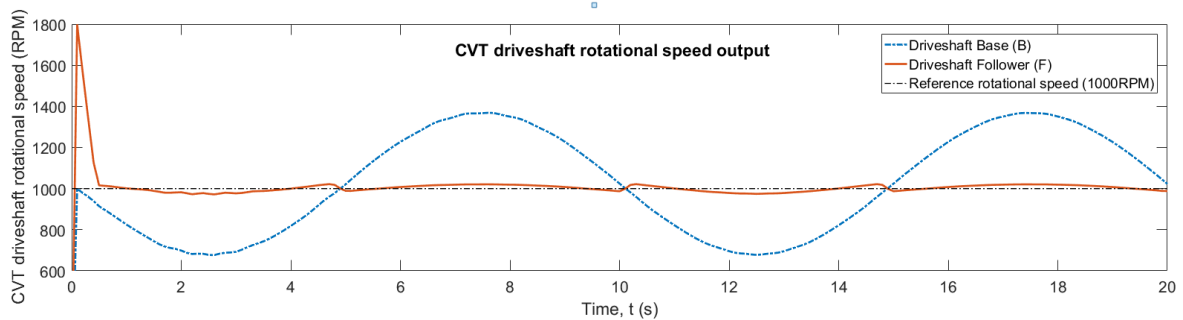


Figure 51: CVT driveshaft rotational speed output

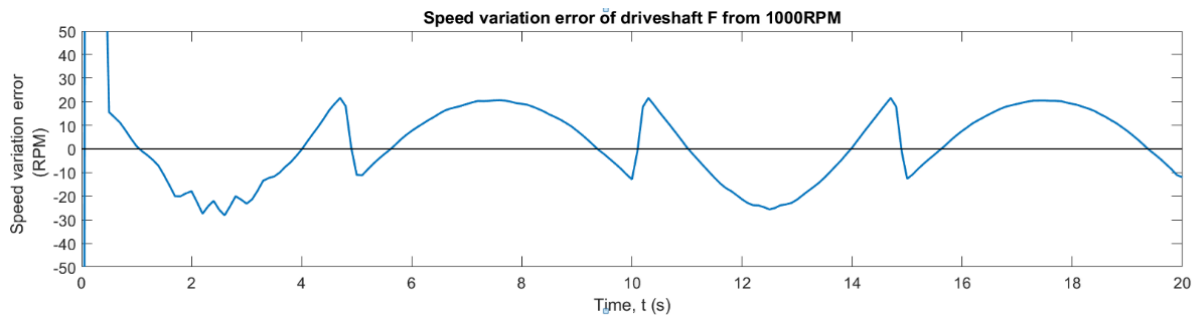


Figure 52: Speed error variation of driveshaft F

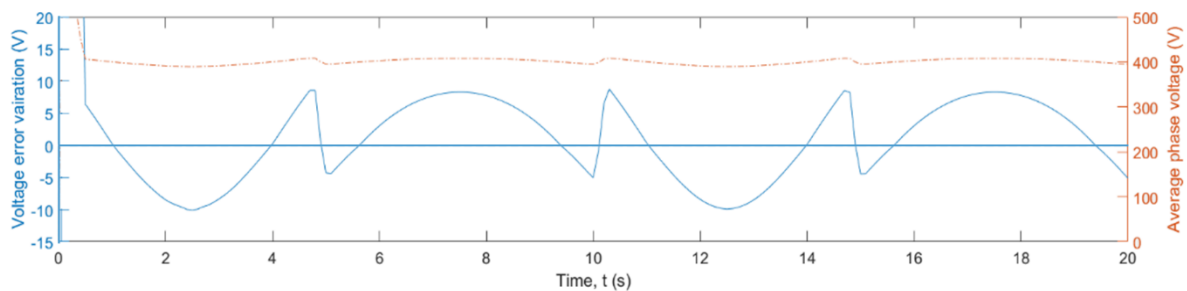


Figure 53: Average phase voltage output and Voltage error variation

5. CONCLUSION

The PMSG wind generator generated 3-phase 400V, 50Hz power output when the generator rotor operated at 1000RPM. A CVT gearbox with SIRMs actuator was adopted in the project to control the gear ratio of CVT and ensure the PMSG rotor was running at a constant 1000RPM rotational speed when the wind speed varied within the operation range of the wind generator. To preserve the monotonicity property of the SIRMs-connected FIS, Seki et al.'s theorem (2008, 2010a) was simplified and adopted as the governing equations for constructing the SIRMs actuator. The designed Simulink wind generator model shown the system was stable with minimum variance when testing the model with ideal wind speed range from 5m/s to 10m/s. Although the results were promising, further study may be required adopting the optimization theory to generate a better fuzzy rule set to operate the SIRMs actuator and minimise the variance.

6. ACKNOWLEDGEMENTS

The project was supported by the research grant UCTS/RESEARCH/3/2016/17 sponsored by Centre for Research & Development from University College Technology of Sarawak (UCTS).

7. REFERENCES

- Baroudi, J.A., Dinavahi, V., and Knight, A.M. (2007). A review of power converter topologies for wind generators. *Renewable Energy*, volume (32), 2369 - 2385.
- Feng, G., (2010), *Analysis and Synthesis of Fuzzy Control Systems: a model-based approach*, CRC Press.
- Feng, G.,(2006). "A survey on analysis and design of model-based fuzzy control systems, *Fuzzy systems, IEEE Transactions on*, 14(5), pp. 676–697
- Heath, R.P.G., (2007), "Seamless AMT offers efficient alternative to CVT", *JSAE Annu. Congr.*, Yokohama, Japan.
- Jong, C.H., Tay, K.M., Lim, C.P., (2014). "A Single Input Rule Modules Connected Fuzzy FMEA Methodology for edible bird nest processing". *Soft Computing in Industrial Applications, Advances in Intelligent Systems and Computing*, 22, pp.165-176, Springer International Publishing.
- Kosko, B., (2015). "Additive Fuzzy Systems as Generalized Probability Mixture Models". In *Fifty Years of Fuzzy Logic and its Applications, Studies in Fuzziness and Soft Computing*, 326, pp.245-265.
- Mamdani, E.H., (1976). "Advances in the linguistic synthesis of fuzzy controllers". *International Journal of Man-Machine Studies*, 8(6), pp. 669-678.
- Mantriota, G., (2005). "Fuel consumption of a vehicle with power split CVT system", *International journal of vehicle design*, 37(4), pp. 327-342.
- Petković, D., Čojbašić, Ž., Nikolić, V., Shamshirband, S., Kiah, M.L.M., Anuar, N.B., Wahab A.W.A., (2014). "Adaptive neuro-fuzzy maximal power extraction of wind turbine with continuously variable transmission", *Energy* 64, pp. 868-874.

Rahman, A., Sharif, S.B., Hossain, A., Mohiuddin, A.K.M., Alam, A.Z., (2012). "Kinematics and nonlinear control of an electromagnetic actuated CVT system for passenger vehicle". *Journal of mechanical science and technology*, 26(7), pp. 2189-2196.

Ramji, T., Ramesh, B.N., (2016), "Fuzzy Logic Based MPPT for Permanent Magnet Synchronous Generator in wind Energy Conversion System", *IFAC-PapersOnLine*, Vo1 49, No 1, pp. 462-467

Ross, Timothy J., (2009), *Fuzzy logic with engineering applications*, John Wiley & Sons Salmeron, J.L., Gutierrez, E., (In press), "Fuzzy Grey Cognitive Maps in reliability engineering", *Applied Soft Computing*

Seki, H., Ishii, H., Mizumoto, M.,(2010). "Nonlinear Identification And Medical Diagnosis System Using Functional-Type SIRMs Connected Fuzzy Inference Method". *International Journal of Innovative Computing, Information and Control*, 6(11), pp.5275-5286.

Seki, H., Ishii, H., Mizumoto, M., (2008), "On the generalization of Single Input Rule Modules Connected Type fuzzy reasoning method", *Fuzzy Systems, IEEE Transactions on*, Vol.16, No.5, pp.1180-1187

Seki, H., Ishii, H., Mizumoto, M., (2010), "Nonlinear Identification And Medical Diagnosis System Using Functional-Type SIRMs Connected Fuzzy Inference Method", *International Journal of Innovative Computing, Information and Control*, Vol 6, No 11, pp.5275-5286

Seki, H., Ishii, H., Mizumoto, M., (2010), "On the Monotonicity of Fuzzy-Inference Methods Related to T–S Inference Method", *Fuzzy Systems, IEEE Transactions on*, Vol.18, No.3, pp.629-634

Seki, H., Tay, K.M., (2012), "On the monotonicity of fuzzy inference models", *Journal of Advanced Computational Intelligence and Intelligent Informatics*, Vol.16, No.5, pp. 592-602

Takagi, T., Sugeno, M., (1985). "Fuzzy identification of system and its applications to modeling and control". *IEEE Trans on Systems, Man, and Cybernetics*, 15(1), pp. 116-132

Tong, S.W., Qian, D.W., (2013). "Control of a fuel cell based on the SIRMs fuzzy inference model". *International Journal of Hydrogen Energy*, 38(10), pp.4124-4131.

#363: Thermoregulation techniques in honey bees' (Apis Mellifera) beehive microclimate and its similarities to our buildings

Hasila JARIMI ^{1*}, Emmanuel-Tapia BRITO² and Saffa RIFFAT ³

¹The University of Nottingham, United Kingdom, Hasila.Jarim@nottingham.ac.uk

²The University of Nottingham, United Kingdom, ezxet4@exmail.nottingham.ac.uk

³The University of Nottingham, United Kingdom, Saffa.Riffat@nottingham.ac.uk

*Corresponding author

Apis mellifera – *Apis*, which is Latin for 'bee', and *mellifera*, which is Latin for 'honey-bearing' – refers to Western or European honey bees. Research shows that regardless of the ambient temperature, the in-hive microclimate of a beehive at the central brood area must be kept at the average optimum temperature of 35°C for the colony to survive. Therefore, to survive both cold winters and hot summers, *Apis mellifera* will employ several heating and cooling strategies to thermoregulate their hives at the optimum temperature. Just like beehives, our buildings are designed with an envelope that is frequently viewed as the barrier that protects the internal occupied space from the impact of the external environment. We also employ similar methodologies to thermoregulate our buildings to reduce the heating and cooling load for lower energy consumption while at the same time providing thermal comfort to the occupants. This paper presents the thermoregulation techniques employed by honey bees and the similarities to our building thermal management systems, of which there are many. However, we can still learn from the thermoregulation management demonstrated by honey bees. Notably, the fact that the temperature stability of the beehive has been consistent and well-maintained regardless of the ambient climate is still something that cannot be accomplished by home builders.

Keywords: thermoregulation techniques; beehives; human buildings; bio-inspired technologies; Apis mellifera

1. INTRODUCTION

A honey bee is an insect that has three main parts to its body: head, thorax and abdomen (Davis and Cullum-Kenyon, 2018). A beehive colony typically consists of a single queen bee; 10,000–60,000 female worker bees that are in charge of cleaning, nursing and serving the broods, foraging, transferring nectar, making the wax, and guarding their colony; and 1000–2000 male bees (drones) whose ‘only’ task is that of mating in the summer with a virgin queen from a foreign colony (Mathis and Tarpy, 2007; Davis and Cullum-Kenyon, 2018). Figure 1 illustrates the three types of bees living in a colony with their average size. The bees’ nest or beehive is where a colony resides or is physically located. In the hive, worker bees construct a honeycomb, which is a mass of hexagonal prismatic wax cells, for the queen bee to lay eggs and for the worker bees to store their honey and pollen. Creating the wax comb is said to be energetically costly. Secreted from the worker bees’ stomach, the production of wax requires at least 6 grams of sugars in the form of honey for every gram of wax secreted (Mathis and Tarpy, 2007). During the process, the worker bees will cluster together to increase their body temperature to 37°C. The secreted wax will be chewed to make the wax ‘workable’ and shaped into the typical hexagon shapes that fit neatly or stick together.

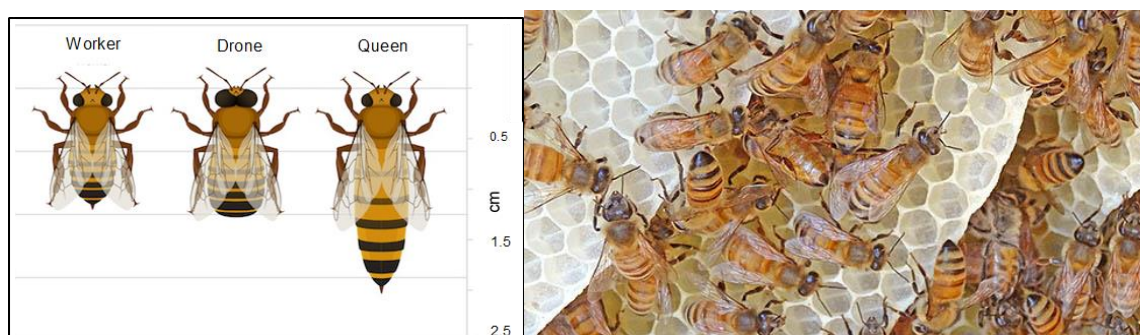


Figure 54: (Left) three types of bee in a colony and their relative size; (right) worker bees constructing honeycomb wax

2. IN-HIVE THERMOREGULATION TECHNIQUES OF THE HONEY BEES AND THE SIMILARITIES TO HUMAN DWELLINGS

Just like beehives, human buildings are designed in such a way that the envelopes are frequently viewed as the barrier that protects the internal occupied spaces from the impact of the external environment, such as sun, wind, rain and snow. We also employ similar methodologies to thermoregulate our buildings to reduce the heating and cooling load to lower energy consumption. A heating, ventilation and air conditioning (HVAC) system is what humans rely on to provide the conditions that we need, such as a certain temperature, relative humidity and ventilation, to ensure the health and thermal comfort of the occupants.

Apis mellifera – *Apis*, which is Latin for ‘bee’, and *mellifera*, which is Latin for ‘honey-bearing’ – refers to Western or European honey bees. Research shows that regardless of the ambient temperature, the in-hive microclimate of a beehive at the central brood area must be kept at the average optimum temperature of 32°C to 36°C for the colony to survive (Seeley, 1981). Therefore, to survive both cold winters and hot summers, just like human buildings, *Apis mellifera* will employ several heating and cooling strategies to thermoregulate their hives to the optimum temperature. Humans have studied honey bees since 7000 BC and it is possible that humans have been inspired by honey bees and learned from them how to create thermal comfort in our buildings in a sustainable way. In this paper, we will explore and discuss various aspects of thermal comfort management of a honey bee colony, including heating, cooling, humidity control, and in-hive air quality. The similarities of the thermal management strategy to human dwellings reflect what humans may have learnt or can learn from honey bees will be discussed.

2.1. Heating in winter or during cold weather

In winter, honey bees do not have a tolerance to freezing temperatures. Table 1 below summarises the temperature ranges and the state of the honey bees when exposed to different temperature ranges. To provide heating in cold conditions, like the honey bees, from an endothermic perspective, buildings consume energy or fuel to create stable thermal comfort. To survive the cold winters, the European bee employs several heating strategies which include air gap sealing, clustering to create insulation, and endothermic heating, to maintain their beehive at its optimal temperature.

Table 26: Temperature range and the state of the honey bees when exposed to different temperature ranges

Cold temperature range	Honey bees' state
Between -2 and 6°C for less than an hour	Honey bees will die
Between 9 and 12°C	Honey bees can survive for several hours provided that they are warmed to room temperature
Outside air temperature of -28°C	A colony of bees in a cluster could maintain a core temperature of 31°C for a short time
Outside air temperature of -25°C	A typical colony of 17,000 honey bees could maintain a core temperature of 31°C for a short time

Air sealing to reduce heat leakage

For millions of years, honey bees have evolved to live in tree hollows which are well insulated by the surrounding wood. Living at a thermally-insulated ambient temperature is very common for honey bees. However, modern beehives do not have such insulation, and therefore the honey bees will instinctively reduce any possibility of heat loss caused by the following: i) an unwanted cavity, ii) air draught heat loss, iii) large entrance or gaps, and iv) unwanted air flow in winter. To do that, as illustrated in Figure 2, honey bees will use propolis, a sticky wax-like resin that acts like superglue, to seal all the cracks and gaps and any forms of opening in the hive. However, since an air flow from the entrance is required for ventilation, honey bees will decide when to close the entrance. Typically, the sealing process takes place in autumn (Hudston, 2017). The propolis at the hive's entrance is also used as a defence against robber bees and mice.



Figure 55: Left – propolis stuck around the edges of a beehive used by the bees to seal two parts of the hive together. Image taken from Just Bee, 2019; right – propolis at the entrance. Image taken from BackYardHive, 2017

Heat loss from buildings can occur through gaps and cracks around windows, doors and roofs through air leakage (see Figure 3). Gaps in insulation and thermal bridging are also a substantial source of heat loss and can cause both draughts and condensation. Regardless of how well a house is insulated to reduce heat loss and heat gain, a proportion of energy is still lost to draughts caused by air leakage. Research shows that building air leakage can cause as much as 15–25% of winter heat loss in buildings and can contribute to a significant loss of coolness in climates where air conditioning is used since the energy used to heat or cool our buildings leaks through unwanted draughts (Reardon, 2013). In addition to heat loss, air leakage can cause condensation that will damage the building materials and reduce indoor air quality. Honey bees use propolis for air sealing, and this technique should sound familiar to any house builders or homeowners. To avoid air leakage, they will use airtight construction while ensuring that junctions and gaps between building components such as at the window and door frames, walls, floors and ceilings, skirting boards, plumbing pipes, exposed rafters and beams, inbuilt heaters and air conditioners, and between dissimilar materials (e.g. masonry walls and timber framing) are sealed with durable, flexible caulks and seals. Larger gaps will be sealed with expandable foam.



Figure 56: Thermal infrared images that show heat leakage from different parts of a house. Image taken from Ahomecheck, 2018

Heat insulation and endothermic heating

When the temperature drops to 15°C, bees will start to cluster (Southwick and Heldmaier, 1987). The bees will form a compact cluster (see Figure 4a) positioning themselves in layers, clumping together oriented inward to reduce the in-hive volume of air for heating. Obeying the principle of heat transfer that increases with the increase in surface area, the cluster formation reduces the bee bodies' surface area exposed to the cold air, thus reducing heat loss via convection by as much as 88% (Southwick, 1983). As the ambient temperature drops, the cluster will become tighter and more compact (less porous), thus further reducing the internal convection current by closing the air channel for ventilation (Southwick, 1983).

Home builders also employ this strategy of reducing the air volume to be heated in a building or house by creating buffer zones (see Figure 5) such as foyers to help reduce heat loss to the outside. The HVAC system was designed to allow for zoning and partial or complete shutdown of supply to minimise the heating area (Mathis and Tarp, 2007). There can also be some utility areas in a building that have lower temperature requirements due to the nature of their functions or the period of their use. Therefore, these zones are suitable for the creation of thermal buffers that would reduce static heat loss in spaces where the maintenance of higher temperatures is important for thermal comfort.

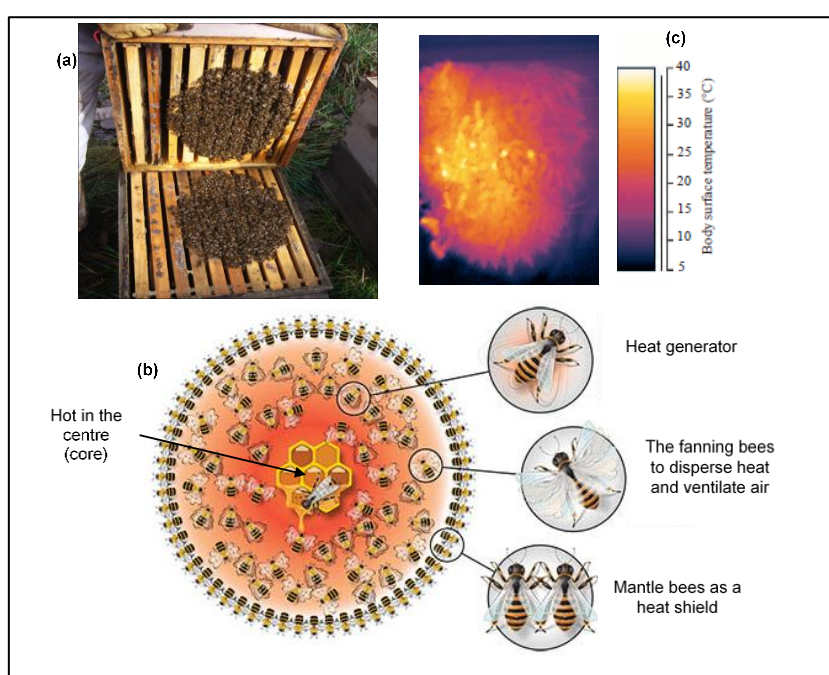


Figure 57: a) Winter clustering in a beehive (scientificbeekeeping.com); b) an illustration of European honey bees clustering together in a mass to generate and conserve heat (Purdue Extension, 2017).; (c) infrared thermogram of the bees on the central comb of a broodless winter cluster (Stabentheiner, Pressl *et al.*, 2003).

Figure 4b illustrates the bees' orientation in the winter clustering. It mainly consists of three layers. In the interior of the cluster, the heater bees perform 'endothermic heating' where an individual bee produces metabolic heat via its thoracic flight muscles due to involuntary muscle contractions (shivering). The heater bees generally remain motionless. To dissipate the heat in the cluster and regulate the amount of CO₂, a group of bees fan their wings to ventilate the heated air. To shield the cluster from heat loss on the external surface of the cluster, other bees connect their legs together to form a shell. Functioning like an insulation layer for a building envelope, this mantle of bees keeps the warmth inside the cluster with their overall heat conductance of approximately 0.10 W/kg °C. As the temperature drops further to below -10°C, the bees increase their endothermic heating to stay warm, which is indeed hard work for the bees. The centre of the cluster basically serves as the central heating system for the colony. The individual bees take turns to perform endothermic heating, fanning, and serving as mantle bees. They rotate in and out of the cluster protecting the queen and keeping the brood nest area warm and safe (Purdue Extension, 2017). Figure 4c shows a thermal infrared image which reflects the temperature variation from the centre of the winter cluster to the surface of the cluster forming a thermal mass wall to the centre of the hives or the brood comb (Stabentheiner, Pressl *et al.*, 2003). Furthermore, the bees' body hairs help to enhance the effectiveness of the insulation of the winter cluster. Just like bird down, a bee's body hairs are not only useful to hold pollen, but also in a winter cluster, the hairs have a heat-retention property, trapping heat to reduce heat escaping from the body.

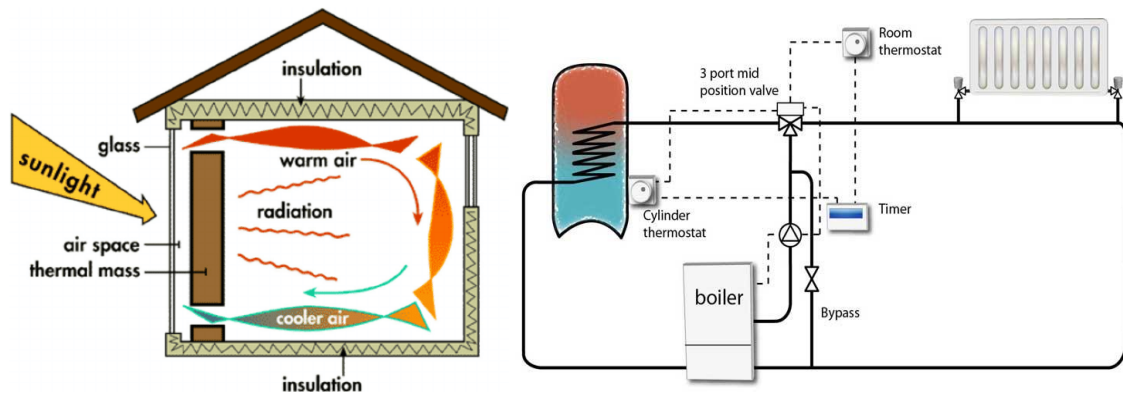


Figure 58: (a) The buffer zone or air space to reduce air space needed for heating; (b) an example of a centralised heating control system

Just like honey bees, humans have employed a building envelope heat insulation strategy to reduce heat loss to the cold. In recent years, high-insulating and fire-safe insulating materials have been actively researched. As mentioned earlier, honey bees will increase their endothermic heating based on the drop in the temperature. We have also incorporated a 'heating' system by installing a single centralised thermostat to monitor a room's temperature, whereby heating will only be introduced when the internal space temperature drops to a certain level. However, unlike honey bees that employ a decentralised control system, human beings have mainly employed a centralised control system like a thermostat to control the HVAC system in a building (see Figure 5b). In a beehive decentralised heating system, collective decision-making based on individual honey bees' assessment of what needs to be done (i.e. heating, fanning or shielding) regarding the immediate local temperature and humidity allows any form of disturbance or perturbations in the in-hive environmental conditions to be addressed very quickly via communication among the bees. This is possible because the bees are not relying only on one single temperature point to respond, but rather on multiple and redundant individual honey bees.

2.2. Cooling during summer or in hot weather

The 35°C in-hive optimum temperature also applies in a warm environment. To survive in warm temperatures, bees have employed a cooling mechanism. Naturally, the bees' cluster disperses at a temperature above 15°C to reduce heat insulation. At a time of high ambient temperature conditions, which happens mainly in the summer during the daytime, overheating due to overcrowding is unlikely to happen because most of the worker bees are out foraging and drones are also outside the colony. Moreover, at night-time, if the hive is overcrowded, the bees will instinctively hang outside in front of their hive's entrance, spending the night outside and staying cool. Nevertheless, to ensure that the brood nest is maintained at its optimum temperature, several cooling strategies have been employed by the worker bees in the beehive.

Ventilation and cooling

To cool the beehive, bees will ventilate the hive by actively fanning their wings. In a research study conducted by Southwick and Moritz (Southwick and Moritz, 1987), when the air temperature inside the brood nest was approaching 35°C, several hundred bees positioned themselves throughout the beehive (i.e. left, right, top and bottom) to take up the fanning position in the ventilation process. These bees, which are called fanners, force air circulation throughout the beehive. However, as the temperature increased to above about 40°C, 20 to 30 bees moved to the outside of the small entrance into the screened landing platform and began fanning activities. These fanning bees also employed a ventilation strategy where they organise themselves into groups and separating regions of continuous inflow and outflow at the hive's entrance. Figure 6a shows a schematic illustrating the path of air through the hive as induced by fanning bees. The warm stale air fanned out from the hive will be replaced/exchanged with cooler fresh air from external ambient air that will enter passively into the hive where fanning bees are absent (Peters, Peleg *et al.*, 2019). It is also very important to note that during the air exchange, sufficient gaseous exchange of oxygen and CO₂ and control of humidity will also take place. Similar to honey bees, in hot weather conditions, the key to cooling a building is removing the built-up heat in the house. This is achievable by using either a natural ventilation system or, like fanner worker bees, a forced mechanical ventilation system introduced to replace the unwanted heat with a cooler fresh air supply. An example very similar to the fanning system introduced by the honey bees at the hive entrance is the window fan that expels hot/stuffy air from an internal space that is then replaced by cooler fresh air from outside (see Figure 6b). Other types of fans and ventilation systems are attic fans, large ceiling air-circulating fans, whole-house fans, and the typical exhaust fans installed in a kitchen, bathroom, etc. to move hot moist air from indoors to outdoors.

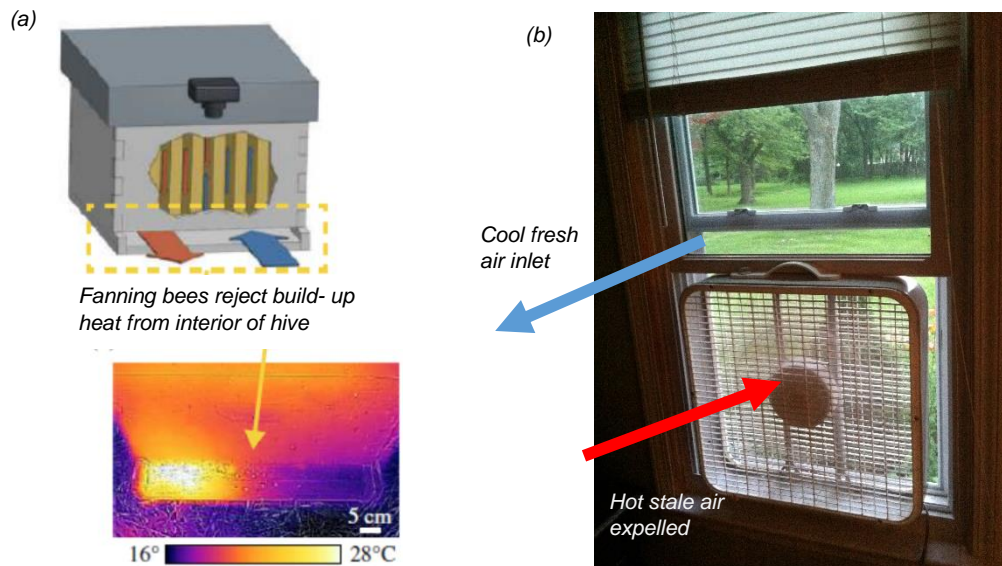


Figure 59: a) The warm stale air fanned out from the hive will be replaced/exchanged with cooler fresh air from the external ambient that will enter passively into the hive where fanning bees are absent (Peters, Peleg et al., 2019) b) a window fan system

Evaporative (swamp) cooler

Another method of cooling employed by honey bees is evaporative cooling with the working principle just like the well-known evaporative cooler or 'swamp cooler'. The working principle of the evaporative cooling system that is very similar to the honey bees in cooling their beehive is shown in Figure 7. To perform evaporative cooling, worker bees will spew the water that they carried to the beehives in their bodies. Other worker bees will then start fanning, actively creating cool humid air that circulates throughout the beehive. Honey bees naturally know that cool air drops, and therefore the water is normally spewed from the top, under the beehive lid.

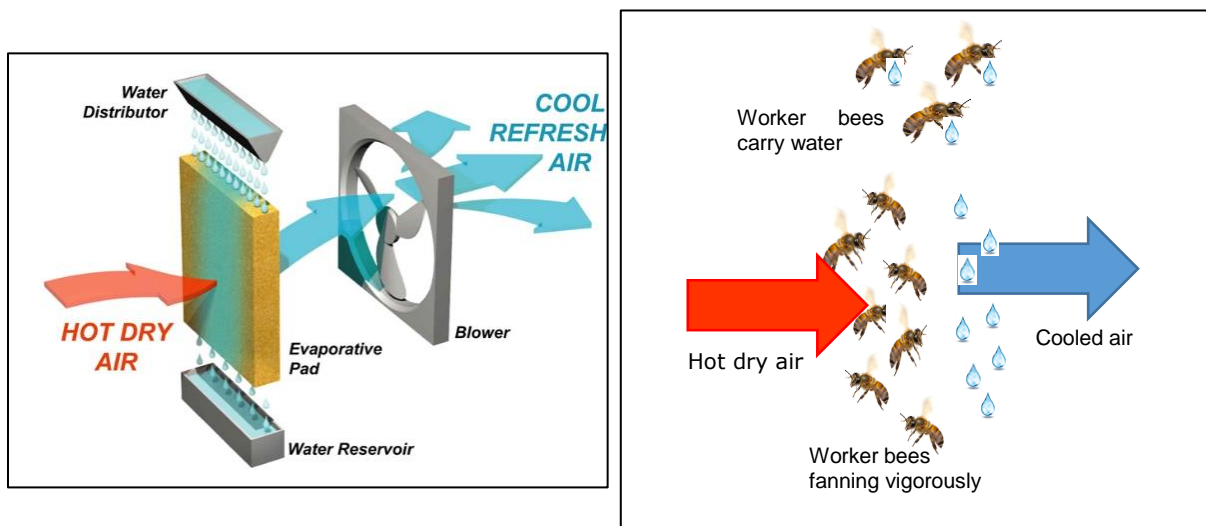


Figure 60: (a) Evaporative (swamp) cooler working principle; (b) an illustration of evaporative cooling performed by the worker bees

2.3. Humidity and air quality control

In addition to manipulating the temperature, the bees team up to maintain different humidity levels in the various parts of the hive mainly via an air ventilation mechanism. Similar to our buildings, air ventilation in a beehive is not only important to expel the heat build-up in a house to avoid overheating as mentioned earlier, but also to reduce the CO₂ concentration and water vapour and to exchange them with a fresh supply of oxygen (Sudarsan, Thompson et al., 2012) for better air quality. A wet and damp beehive, especially with a build-up of condensation due to humid air, can lead to unwanted mould forming in the centre of the brood comb area. It has been concluded

that a honey bee colony has the ability to regulate the humidity in its hive regardless of the weather conditions throughout the year (Eouzan, Garnery *et al.*, 2019). In a research study conducted by Sachs and Tautz (Sachs and Tautz, 2017), in cold weather at an average floor temperature of 10°C, the humidity level is well controlled at a constant temperature. The only possible explanation is that there is a change in the air within the hive with the same temperature but different relative humidity via the active ventilation process performed by the honey bees. In the first step, the bees will fan cold air into the beehive via one of the edges, the cold dry air will warm up and increase in humidity, and then the warm humid air will be fanned downwards. As a result, the cold air from the hive's floor will become humid. However, the bees located above and at the side walls of the centre of the comb act as the heat exchanger. Just like a dehumidifier, the bees will heat the cold humid air and turn it into 'dry' air that is then fanned into the centre of the comb. This temperature and relative humidity control technique is very similar to a mechanical ventilation and heat recovery unit in a building. In addition to ventilation to ensure healthy hives, scientists have discovered that honey bees have sterilised their hives with propolis, which gives the whole colony what is considered to be a form of social immunity. Propolis was found to have certain desirable antibacterial and antifungal properties for colony hygiene (Mathis and Tarpy, 2007). In our buildings, indoor air quality control has recently attracted more interest from researchers. Indoor air qualities involves the control of the CO2 level in a building, as well as other gases such as carbon monoxide, volatile organic compounds, particulates, and microbial contaminants (mould, bacteria). The common indoor air quality system involves filtration and the use of ventilation to dilute contaminants.

3. DISCUSSION AND CONCLUSIONS

Many similarities can be seen between the honey bees' hive and our buildings' thermal management system, as summarised in Table 2. However, we can still learn from the thermoregulation management demonstrated by the honey bees, for example, the fact that the temperature stability of the beehive has been very consistent and well maintained regardless of the ambient climate. This is owing to the decentralised and collective decision-making employed by a honey bee colony. The worker bees in a colony are not being 'allocated' tasks in any way. However, any form of disturbance or changes detected in the hive's environment are individually assessed by each of the worker bees and then immediately passed to the other bees through their special communication technique, 'chemical communication', via the pheromones secreted by the bees and their special dance language, known as waggle dance or wag-tail dance. We can compare this to the heating and cooling control system of a house with tens or hundreds of installed integrated thermostats. A heating or cooling system in a house mainly has a centralised control that has a slow response and feedback and is highly variable but with less energy and capital cost consumption. Nevertheless, human beings have indeed employed several decentralised control strategies in buildings, which include the use of a motion sensor lighting system to reduce lighting loads in non-used space.

Table 27: The similarities between beehives' thermoregulation strategy and our buildings

Thermoregulation techniques	Beehives	Buildings
Increase insulation	Air sealing using propolis, and winter cluster with mantle bees as the heat shield	Seal gaps, cracks at windows, doors, roof area – air tightness testing
Efficient heating	Decentralised control system and endothermic heating only initiated by the bees when the temperature drops further and when clustering can no longer retain heat	Advance heat insulation layer Thermostat to monitor heating system and room temperature
Reduce volume of air for heating	Cluster is formed inward surrounding the central brood area	Buffer zones, thermal buffers
Efficient ventilation and cooling	Honey bees employ fanning by repositioning themselves and employ evaporative cooling by spewing water from the top	Air ventilation system and evaporative cooler technology
Indoor air quality and hygiene control	Efficient ventilation system with honey bees sterilising their beehives with propolis	Air filtration and ventilation system to control indoor air quality
Humidity and temperature control	In certain temperature conditions, the side wall bees perform like a heat exchanger	Efficient heat recovery units

Quoting Albert Einstein, "If the bee disappeared off the surface of the globe, then man would have only four years of life left. No more bees, no more pollination, no more plants, no more animals, no more man". Even losing some honey bees would damage the agricultural industries that depend on them and threaten to make the food we eat more expensive, a situation where the poor are most likely to suffer. Clearly, for over millions of years, honey bees have shown that they employ an excellent thermoregulation strategy for their hives. However, as extreme cold weather conditions and heatwaves have become more and more common due to climate change or global warming, whether *Apis mellifera* can easily adapt themselves to maintain an efficient in-hive thermoregulation technique is questionable. Another question to consider is how climate change will impact on the honey bees'

behaviour, physiology and distribution, and on the evolution of the honey bees' interaction with diseases. Whether they will need extra help us from us is a question that is worth addressing in future research.

4. ACKNOWLEDGEMENTS

The authors gratefully acknowledge Innovate UK's financial support through Newton Fund (Project reference no: 105043).

5. REFERENCES

Ahomecheck. (2018). "Air leakage testing." from <http://ahomecheck.ca/air-leakage-testing>.

BackYardHive. (2017). "Bees add propolis to their hive entrance to winterize and defend from robber bees.", from <https://backyardhive.com/blogs/managing-your-top-bar-hive/propolis-the-defender-of-the-hive>.

Reardon, C. (2013) "Sealing your home ".

Eouzan, I., Garnery, L., Pinto, M.A., Delalande, D., Neves, C.J., Fabre, F., Lesobre, J., Houte, S., Estonba, A., Montes, I., Sime-Ngando, T. and Biron, D.G. (2019). "Hygroregulation, a key ability for eusocial insects: Native Western European honeybees as a case study." *PloS one* 14(2): e0200048-e0200048.

Hudston, S. (2017). "The bees are already sealing their hives for the winter ahead" Retrieved 20 July, 2019, from <https://www.theguardian.com/environment/2017/aug/26/country-diary-bees-sealing-hives-propolis>.

Davis, I. and Cullum-Kenyon, R. (2018). *The BBKA guide to beekeeping*. London, Bloombury Wildlife

Just Bee. (2019). "What is propolis." from <https://www.justbeedrinks.co.uk/propolis-can-help/>.

Peters, J.M., Peleg, O. and Mahadevan, L. (2019). "Collective ventilation in honeybee nests." *Journal of The Royal Society Interface* 16(150): 20180561.

Purdue Extension. (2017). "The complex life of the honey bee." from <https://ppp.purdue.edu/resources/ppp-publications/the-complex-life-of-the-honey-bee/>.

Mathis, R.C. and Tarry, D.R. (2007). "70 Million Years of Building Thermal Envelope Experience: Building Science Lessons from the Honey Bee."

Sachs, R. and Tautz, J. (2017). How Bees (*Apis Mellifera*) Reduce Humidity in the Beehive by Means of Active Ventilation.

Seeley, T.D. and H. B. (1981). *Insects thermoregulation*. New York, Wiley.

Southwick, E.E. (1983). "The honey bee cluster as a homeothermic superorganism." *Comparative Biochemistry and Physiology Part A: Physiology* 75(4): 641-645.

Southwick, E.E. and Heldmaier, G. (1987). "Temperature Control in Honey Bee Colonies." *BioScience* 37(6): 395-399.

Southwick, E.E. and Moritz, R.F.A. (1987). "Social control of air ventilation in colonies of honey bees, *Apis mellifera*." *Journal of Insect Physiology* 33(9): 623-626.

Stabentheiner, A., Pressl, H., Papst, T., Hrassnigg, N. and Crailsheim, K. (2003). "Endothermic heat production in honeybee winter clusters." *Journal of Experimental Biology* 206(2): 353.

Sudarsan, R., Thompson, C., Kevan, P.G. and Eberl, H.J. (2012). "Flow currents and ventilation in Langstroth beehives due to brood thermoregulation efforts of honeybees." *Journal of Theoretical Biology* 295: 168-193.

#372: Numerical simulation on flow characteristics of falling film outside the horizontal tube in low counter-current air flow

Xiaocui ZHANG¹, Qinggang QIU^{2*}

¹Thermal Engineering, School of Energy and Power, Dalian university of Technology, 116024 Dalian China, 1457997450@qq.com

²Thermal Engineering, School of Energy and Power, Dalian university of Technology, 116024 Dalian China, qggang@dlut.edu.cn

*Corresponding author

In this paper, the VOF (volume of fluid) method was used to simulate the thickness and velocity of the falling film in water-air interface at low counter-current air velocity outside the elliptical tube. The elliptical tube had a long semi-axis of 26mm and a short semi-axis of 13mm. The velocity of the air was 0.1 m/s. The Reynolds (Re) number was chosen as the influence factor and the Re numbers were 90, 225, and 311.7, respectively. The three dimensional simulated results showed that the film thickness and the film velocity increased with the increasing of the Re number. The film increased along the axis direction, and the differences of the film thickness in different axis distance increased with the increasing of the Re number.

Keywords: VOF method; Re number; film thickness; film velocity; low counter-current air flow

1. INTRODUCTION

Horizontal tube falling film technology is a highly efficient energy-saving heat transfer technology. It can make full use of phase change latent heat release or absorption and significantly improve the heat transfer performance of the system under conditions of small temperature difference. This technology has a low demand on heat transfer quality and can fully use industrial waste heat and other low grade heat sources. Therefore, it is widely used in industrial development.

Many scholars have studied horizontal tube heat transfer technology and many factors affect the falling film flow and heat transfer effect of the horizontal tube. As early as 1916, Nusselt (Nusselt *et al.*, 1916) proposed the theory of film thickness distribution during the falling film flow of horizontal tubes. He set the momentum effect to have no effect on the film thickness distribution, then the film thickness distribution under the sheet flow pattern was related to the circumferential angle of the round tube and the spray density, and the classical film thickness expression is obtained from Equation 1:

$$\text{Equation 1: classical film thickness} \quad \delta = \left(\frac{3\mu_L \Gamma}{\rho_L (\rho_L - \rho_G) g \sin \theta} \right)^{\frac{1}{3}}$$

Where:

- Γ = one-side spray density of the working fluid outside the heat exchange tube (kg/(m·s))
- μ_L = dynamic viscosity of the external working fluid (kg/(m·s))
- ρ_L = density of liquid phase (kg/m³)
- ρ_G = density of gas phase (kg/m³)
- g = gravitational acceleration (m/s²)
- θ = circumferential angle based on the vertical direction (°)

Many researchers have studied the effect of the elliptical tube. For example, Peng *et al.* (Peng *et al.*, 2018) studied the changes of the film thickness in the semi-elliptical tube under different spray flows, tube pitch and the height of the liquid distributor, and they found that the thickness of the liquid film was stable, when the circumference of the semi elliptical tube was 79.8 mm and the ratio between the long and short axes was 2.1, spray flow rates were around 0.14 L/min, H was 15 mm and tube spacing less than 20 mm, which was beneficial to the full heat transfer. Tan *et al.* (Tan *et al.*, 2017) found that compared to the circular tube, the liquid flow rate in the elliptical tube was faster and they also suggested a heat transfer model for the horizontal tube through the study and analysis of the tube shape. Qi *et al.* (Qi *et al.*, 2016) found that heat transfer coefficient of the system with E = 1.5 elliptical tubes increased by 20-22% compared with circular tubes. Asbik *et al.* (Asbik *et al.*, 2005) numerically studied the boundary-layer transition in flowing film evaporation on a horizontal elliptical tube, and they found great sensitivity of the relationship between turbulent and laminar viscosities to the various pressure gradients, the water flow rate at the entrance, and the temperature difference between the wall and the vapor-liquid interface. The air flow also can affect the falling film behaviour, and Ruan *et al.* (Ruan *et al.*, 2009; Ruan *et al.*, 2011) found that with increasing gas velocity, the stable model disappeared when the steam flow velocity was greater than 3.5 m/s, and they also found that the counter-current gas flow thickened the falling film.

Fiorentino and Starace (Fiorentino & Starace, 2016) studied the temporal change characteristics of the film flow process of flow in the vapour flow, and they found that when the rate of the water was low, the film broke up. Mohamed (Mohamed, 2007) found that the value of the film thickness was slightly decreased by increasing the rotation speed. A reduction of the film thickness was observed at about 12% for water film at Reynolds number 285 and 300 rpm rotating speed.

The flow behaviour and film distribution around the bubbles have a critical role in the heat transfer system. In this paper, depending on the VOF method, the 3-D mode was carried to simulate the flow behaviour and film distribution outside the elliptical tube in different Re numbers.

2. THE NUMERICAL SIMULATED METHOD

2.1. The physical model the grid model

Figure 1 shows a three-dimensional schematic diagram of the falling film flow of a horizontal tube. The schematic diagram intercepts two of the heat exchange tubes of the entire heat exchange tube bundle. The liquid column formed at the bottom of the previous horizontal tube or the liquid droplets detached from the horizontal tube and

then dripped down. A horizontal elliptical tube was placed on top of the tube and the liquid film was spread on the surface of the tube. Affected by many factors, the liquid film of adjacent liquid columns collided and superimposed during spreading, which formed troughs and peaks between two adjacent liquid columns, and finally formed new liquid at different positions at the bottom of the horizontal tube. In the figure, λ represents the distance between adjacent liquid columns.

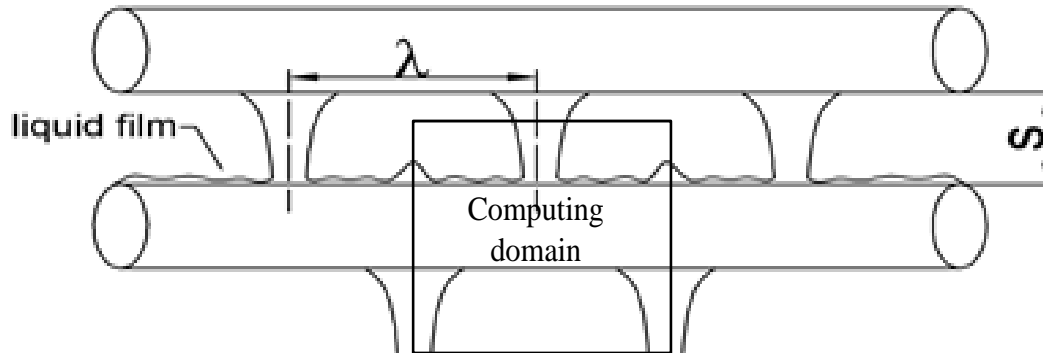


Figure 1: The three-dimensional schematic diagram of horizontal tube fall film

In this paper, the computational region and mesh model of the 3D model were established to simulate the falling film flow behaviour and film distribution outside the horizontal elliptical tube. Figure 2 shows the selection of the calculation region and the established mesh model in the 3D simulation process. As seen in the figure, the velocity inlet was set in a plane section with a diameter of 2mm, and the radius of the concentric plane of the pressure inlet on the outside was 5-10 times larger than that at the velocity inlet to ensure that the calculation area was large enough to not affect the fluid flow. The outer wall of the round pipe was set as a wall boundary. The special boundary conditions and geometry of the model have featured in previous work by the authors (Zhang, Zhu & Qiu, 2019).

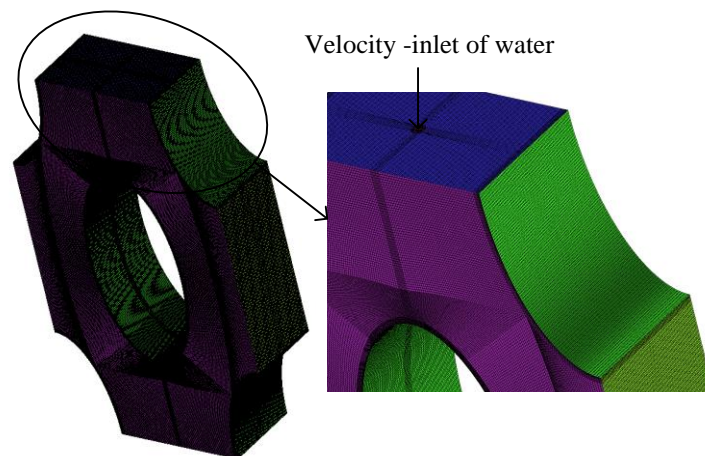


Figure 2: Grids model and a local enlarged view around the inlet of the spray water

In the process of 3D meshing, this paper used the ICEM software to obtain a high-quality mesh by creating blocks and O-sectioning of the fluid inlet area and the outer wall surface of the tube. In addition, the mesh boundary layer needed to be added near the pipe wall to refine the mesh to ensure the calculation accuracy of the falling film flow region. Also, the calculation field needed to be initialised in the numerical calculation, that is, the state at the start of the given calculation. In the simulation of falling film flow, it was assumed that all the gas was filled in the calculation domain at time $t=0$; all the velocity inlets were liquid inflow, corresponding to the flow process after the liquid in the actual flow was ejected from the spout.

2.2. VOF method

In this paper, the VOF (Volume of Fluid) model was selected to dynamically capture the interface between gas and liquid phases to obtain the flow edge of the liquid phase liquid film. The following focuses on the principles and calculation methods of VOF.

The VOF method is a method of defining a gas-liquid interface by calculating a volume fraction F (Volume Fraction) of each phase in each grid cell. The volume fraction of each phase in the grid unit ranges from 0-1, that is, when the volume fraction of a phase was 1, meaning that the grid unit was completely filled with the fluid; when the volume fraction of a phase was 0 indicating that there was no such fluid in the grid unit, and another fluid filled the grid unit. Figure 3(a) shows the meaning of the interface and volume fraction of the two phases in the grid unit in the VOF method. Figure 3(b) and Figure 3(c) show the interface and volume fraction intervals of two phases obtained by rectangular and piecewise linear geometric reconstruction, respectively (Hyman, 1984).

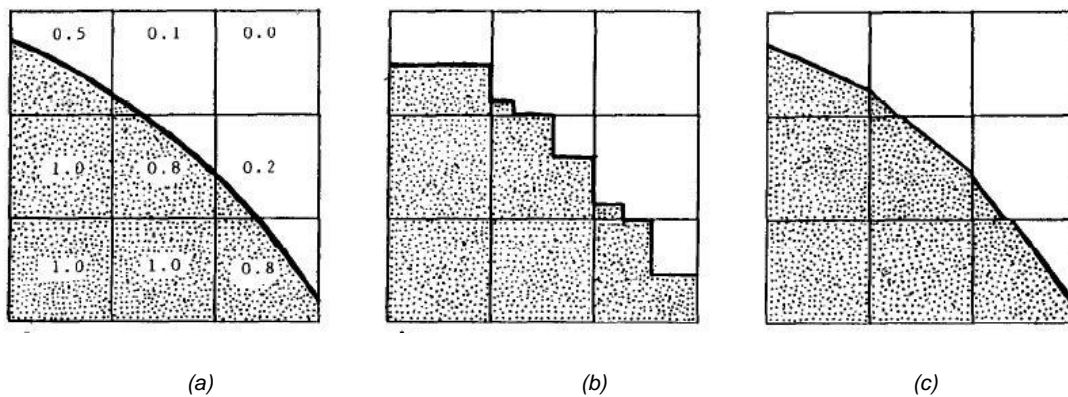


Figure 3: (a) Original interface and volume fractions, (b) The rectangular fractional volume methods to reconstruct the interfaces, (c) The piecewise-linear fractional volume methods to reconstruct the interfaces

As shown in Figures 3(b) and 3(c) above, the interface reconstruction method will lead to certain interface distortion, and the related reconstruction methods such as triangle reconstruction, rectangular reconstruction or linear segmentation were the applications. In this paper, Geo-Reconstruct was used to calculate the volume fraction. The volume fraction of water in all results was 0.5 in this paper.

2.3. Grids number and time steps independence verification

The meshing and time step of the computational domain was critical to the numerical results, and the capture of the two-phase interface also required some grid precision. This simulation selected models with different grid numbers for testing. The number of grid models was 1800 thousand, 3000 thousand, 5000 thousand, 8000 thousand, respectively. The inspection standard for grid accuracy was the shape of the liquid film outside the horizontal tube and the accuracy of the liquid film thickness. Figure 4 shows the variation of the film thickness at a certain point outside the horizontal tube with different grid number models. As the number of grids in the model increased, the thickness of the liquid film gradually decreased until it no longer changed. The grid model was more than 5000 thousand.

The time step also affected the accuracy of the model calculation, so it was necessary to verify that the time step was irrelevant to the calculation accuracy. The simulation tested the same mesh model under different time steps. The time step was selected as 0.1ms, 0.3ms, 0.5ms and 0.7ms. As shown in Figure 5, as the time step decreased, the thickness of the liquid film gradually decreased. When the thickness of the liquid film was less than 0.5ms, the thickness of the liquid film did not change substantially, so the time step selected was 0.5ms.

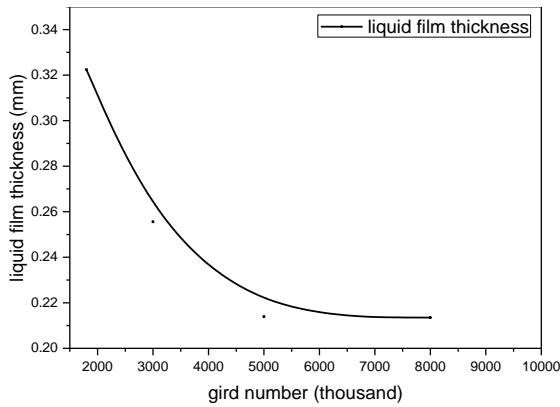


Figure 4: the independence of the grids number

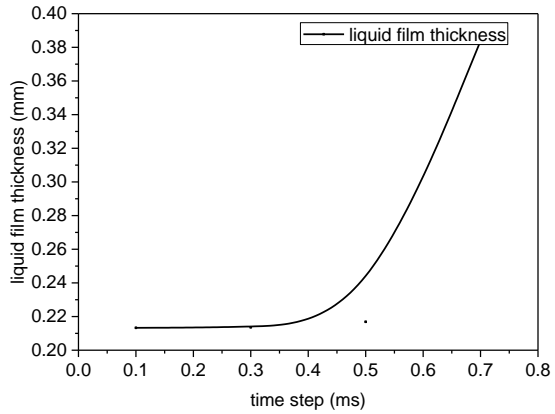


Figure 5: the independence of the time steps

3. RESULTS AND DISCUSSION

3.1. The liquid film thickness distribution along axial and circumferential direction

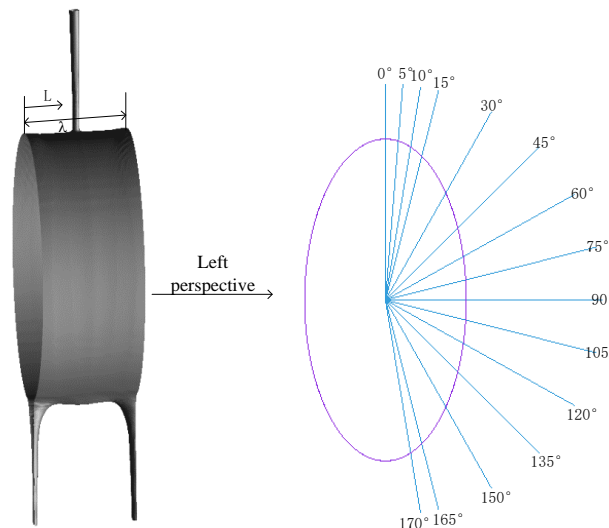


Figure 6: Division of axial dimensionless distance and circumferential angles

In order to study the distribution of the liquid film in the axial direction and the circumferential direction, a plane was selected at the axial distance of the top of the elliptical wall of the research unit. Figure 6 shows the division of axial dimensionless distance and circumferential angles. The circumferential angle was 5°, 10°, 15°, 30°, 45°, 60°, 75°, 90°, 105°, 120°, 135°, 150°, 165° and 170°, respectively. The liquid film thickness distribution was analysed. The dimensionless distance L^* is defined as Equation 2:

Equation 2: dimensionless distance

$$L^* = \frac{L}{\lambda}$$

Where:

- L^* = dimensionless distance
- $\lambda = 20$ (mm)
- L = distance from the measuring point to the leftmost symmetry plane (mm)

Figure 7 shows the film thickness along the circumferential angle in different axial distance and Re numbers. From Figure 7, it can be seen that the circumferential liquid film thickness distribution along the axial direction was the

same at different Re numbers, when the Re number was less than 311.7, and the thickness of the liquid film increases from the centre to two sides. This was because the liquid flow column was on a slice with a dimensionless distance of 1, and the liquid film hit on the top of the elliptical tube spreading to both sides. The thickness of the liquid film from the centre to the sides was gradually thickened due to the surface tension. However, the film thickness increased with the increasing of the dimensionless distance, when the Re number was 311.7. This was due to that the flow pattern changes from a column flow to a sheet-column flow as the Re number increased. Additionally, due to the sweeping action of the counter-current air flow, the liquid film thickness distribution increased along the axial distance.

In the circumferential direction, it was seen that the film thickness distribution generally increased, then decreased and then tended to be gentle, and finally increased. The liquid film thickness increased in the circumferential direction in the range of the circumferential angle of 5° to 30° . This was due to the impact of the liquid film, so that the thickness of the liquid film had a rebound effect at a circumferential angle of 30° , which resulted in liquid accumulation, and finally forming a relatively thick liquid film. In the range of the circumferential angle of 30° to 145° , the thickness of the liquid film first decreased and then gradually increased and the film thickness reached a minimum at 90° . This was because the gravity component in the vertical direction became larger and larger as the circumferential angle increased in the range of the circumferential angle of 30° to 90° , so the liquid film liquid film flow speed increased, and the liquid film thickness became thinner. When the circumferential angle was greater than 90° , the gravity component in the vertical direction became smaller and smaller along the circumferential angle, which caused the accumulation of the liquid film and film thickness to gradually increase. After the circumferential angle of 145° , the film thickness decreased when the Re number was 90, and when the Re number was greater than 90, the change trends of the film thickness were opposite. This was because the counter-current air flow had a large influence on the falling film of the small Re number, so that the liquid film at the bottom of the elliptical tube was blown off, resulting in a decrease in the thickness of the liquid film.

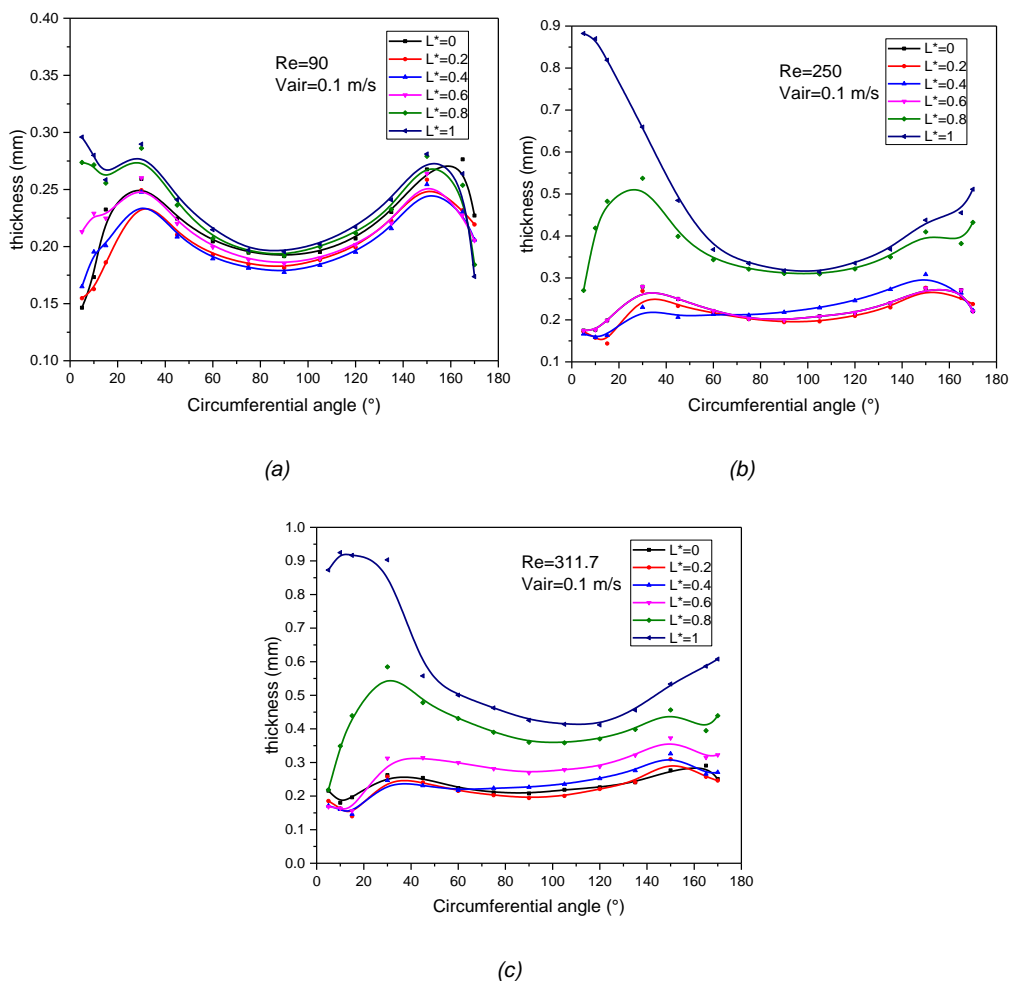


Figure 7: Variation of film thickness with circular angle in different axial distance. (a) Re=90, (b) Re=250, (c) Re=311.7

3.2. The effect of Re number on film thickness

Figure 8 shows variation of film thickness with circular angle in different Re numbers at the slice of $L^*=0$ and 0.2 . From this figure, it can be seen that the film thickness increased with the increasing of the Re number, but the increase was smaller. The reason of the increasing of the film thickness was that the increase in flow velocity caused the liquid to spread over a unit area per unit time, thus causing the liquid film to become thick. However, when the Re number was increased to a certain extent, the liquid film flow accelerated, so that the columnar flow became a curtain-like flow, causing the increase of the liquid film to become small, and even at some positions, the liquid film thickness became small. In the range of the circumferential angle of 5° to 30° , it can be seen that the film thickness first decreased and then increased when the Re was greater than 90, but the film thickness always increased when the Re was 90. This was because when the Re number was small, the impact of the incoming flow was relatively small, the rebounding force was not obvious, so that the thickness of the liquid film was increased, and when the Re number was large, the rebound action caused a vortex to form around the liquid column, so that the liquid film had a minimum value.

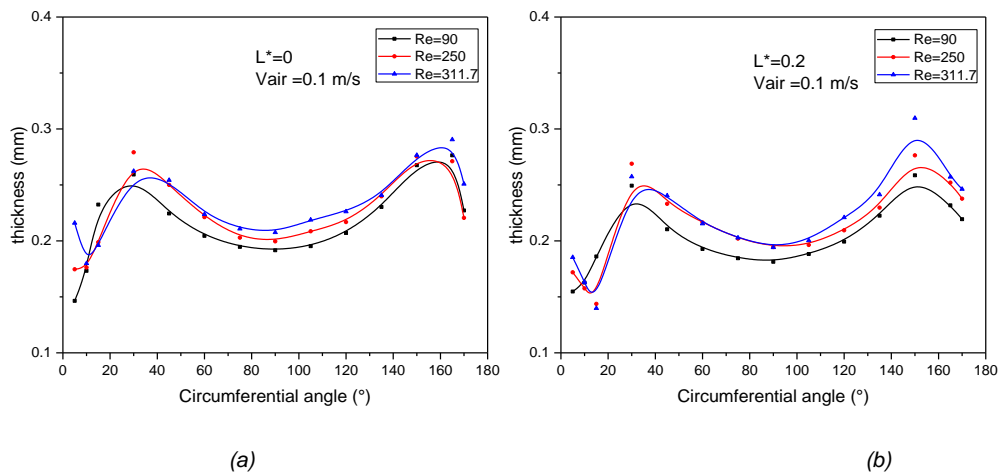


Figure 8: Variation of film thickness with circular angle in different Re numbers (a) $L^*=0$, (b) $L^*=0.2$

3.3. The effect of Re number on film velocity

Figure 9 shows the variation of film velocity in the interface with circular angle in different axial distance and different Re numbers. In the range of the circumferential angle of 5° to 30° , it can be seen that the liquid velocity liquid film thickness varied greatly because the flow velocity was very high. When the liquid column hit the wall surface of the horizontal tube, the reverse force and viscous force of the wall surface were affected in the impact region, therefore, the liquid film flow velocity was rapidly reduced. Outside the impact zone, the liquid film spread from the centre to both sides due to the surface tension, so the flow rate was increased.

After the circumferential angle of 30° , the film velocity tended to be stable and it can be seen that the liquid velocity increased with the Re number. When the Re number was 90, the difference of film velocities was little at different axial distance, and the average film velocity was 0.186 m/s. but with the increasing of the Re number, the difference also increased. As the Re number continued to increase, the difference no longer continued to increase and the average velocity was 0.333 m/s and 0.380 m/s, respectively, which corresponded to Re numbers 250 and 311.7. That was the flow reach balance so that the flow rate did not continue to increase, only the flow pattern had transition.

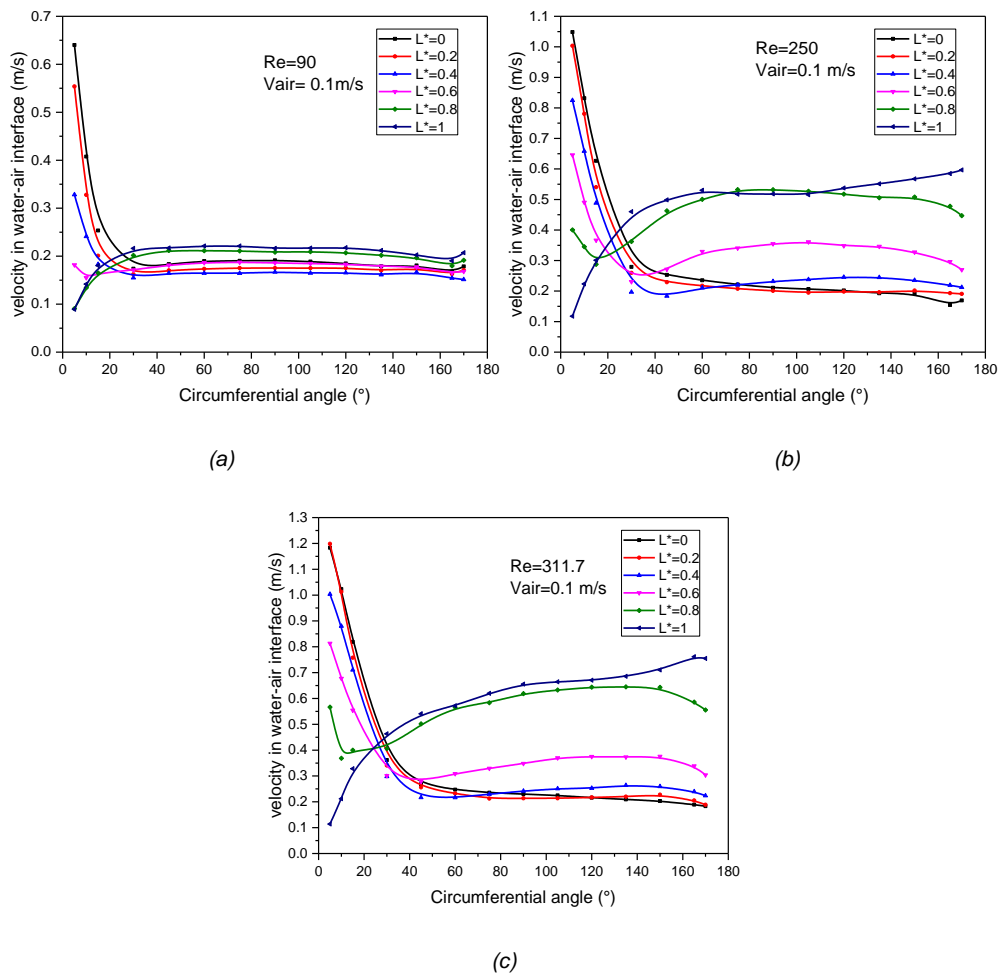


Figure 9: Variation of film velocity with circular angle in different axial distance. (a) $Re=90$, (b) $Re=250$, (c) $Re=311.7$

4. CONCLUSION

In this paper, the three dimension model was used to simulate the film thickness and flow behaviour of the water outside the horizontal elliptical tube in low counter-current air flow. Some conclusions are as follows:

- (1) In the axial direction, the film thickness increased from the centre to two sides. Along the circumferential direction, in the range of 5° to 30° , the film thickness first decreased and then increased when the Re was greater than 90, but the film thickness always increased when the Re was 90, and the minimum value of the film thickness appeared in 90° .
- (2) The film thickness increased with the increasing of the Re number, but the increase was smaller. When the Re number was increased to a certain extent, the liquid film thickness changed little.
- (3) In the range of the circumferential angle of 5° to 30° , the liquid velocity liquid film thickness was rapidly reduced, and after 30° , the velocity of film trend was stable.

5. ACKNOWLEDGEMENTS

The authors gratefully acknowledge the support of the National Natural Science Foundation of China (No. 51876026, No. 51776014). The authors also thank the anonymous reviewers for the helpful comments and suggestions related to this paper.

6. REFERENCES

- Asbik, M., Ansari, O., Zeghamati, B. Numerical study of boundary-layer transition in flowing film evaporation on horizontal elliptical cylinder, *Numer. Heat Tranf. A-Appl.*, 48(2005) pp:645-669.
- Fiorentino, M., Starace, G. Numerical investigations on two-phase flow modes in evaporative condensers, *Appl. Therm. Eng.*, 94(2016) pp:777-785.
- Hyman, J. M. Numerical Methods for Tracking Interfaces [J]. *Physica D Nonlinear Phenomena*, 1984, 12(s 1–3):396-407.
- Mohamed, A.M.I. Flow behavior of liquid falling film on a horizontal rotating tube, *Exp. Therm Fluid Sci.*, 31(2007) pp:325-332.
- Nusselt, W, Die Oberfl achenkondensation des Wasserdampfes *Zeitschr. Ver. Deut. Ing[J]*, 1916, 60(3):541–546, 569–575.
- Peng, T., Zhou, Y., Hu, H., Yan, Z. Research on the Thickness of Falling Liquid Film Outside Horizontal Semi-Elliptical Tubes With Digital Image Processing, *Journal of Engineering Thermophysics*, 39(2018) pp:2040-2047.
- Qi, H., Feng, H.J., Lv, H.Q., Miao, C. Numerical and experimental research on the heat transfer of seawater desalination with liquid film outside elliptical tube, *Int. J. Heat Mass Transfer*, 93(2016) pp:207-216.
- Ruan, B.L., Jacobi, A.M., Li, L.S. Effects of a countercurrent gas flow on falling-film mode transitions between horizontal tubes, *Experimental Thermal and Fluid Science*, 33(2009) pp:1216-1225.
- Ruan, B.L., Li, H., Wang, Q.W. Theoretical analysis on film thickness of intertube falling-film flow with a countercurrent gas flow, *ASME, 2011 International Mechanical Engineering Congress and Exposition. American Society of Mechanical Engineers*, (2012).pp:881-888.
- Tan, Q., Jiang, B. Analysis of Falling Film Flow and Heat Transfer Characteristics outside the Elliptical Horizontal Tube, *Journal of Engineering for Thermal Energy and Power*, 32(2017) pp:20.C.
- Zhang, X.C., Zhu, X.J., Qiu, Q.G. Study on liquid film thickness and flow characteristics of falling film outside an elliptical tube, *Desal. Water Treat*, 157(2019) pp:1-7.

#373: Numerical study on heat transfer of supercritical water in different sub-channels

Shuai ZHAO¹, Qinggang QIU^{2*}, Xiaojing ZHU³

¹Thermal Engineering, School of Energy and Power, Dalian university of Technology, 116024 Dalian China, 1294602935@qq.com

²Thermal Engineering, School of Energy and Power, Dalian university of Technology, 116024 Dalian China, qggang@dlut.edu.cn

³Thermal Engineering, School of Energy and Power, Dalian university of Technology, 116024 Dalian China, zhuxiaojing@dlut.edu.cn

*Corresponding author

In this paper, heat transfer characteristics of supercritical water in vertical tubes with a square cross section, circular cross section and regular triangle cross section, respectively, were studied using ANSYS CFX 14.5 at working conditions of mass flow rate 800 kg/(m²s), pressure from 23, 25 MPa and heat flux from 300-1000 kW/m². The results showed that when the heat flux increased, the heat transfer coefficient decreased, the wall temperature decreased when the heat flux increased. Because of the circumferential heterogeneities of square channels and regular triangle channels, point-to-point simulation from the vertex angle to the midpoint of the edge is necessary. For square channels and regular triangle channels, the midpoint of the edge had the highest heat transfer coefficient and the vertex angle had the lowest heat transfer coefficient, it was necessary to compare the heat transfer coefficients at the vertex angle of the triangular channels and the square channels with the circular channels. For the three channels, there was no difference between the circular channels and other two channels in the low enthalpy region and the high enthalpy region, but it was obvious that the heat transfer coefficients of circular channels was higher than others in the vicinity of the pseudo-critical point. The reason for this was the separation between the boundary layer and the wall.

Keywords: supercritical water; heat transfer; wall temperature distribution; variety of channel type

1. INTRODUCTION

Channel structure has an important influence on flow and heat transfer characteristics. Improving the performance of the original channels (Wang *et al.*, 2000) or addition other cross sectioned coiled-wire inserts in the channels (Keklikcioglu & Ozceyhan, 2018; Gunes, 2009) can increase the heat transfer coefficient of the channels. By changing the shape of the channels, the heat exchange performance can be improved. Compared to conventional large-diameter round tubes, Jige developed a heat transfer model for condensation heat transfer in rectangular mini-channels considering the flow patterns and effects of vapour shear stress and surface tension (Jige *et al.*, 2016). When the shape of the pipe was constant, the change in tube diameter enhanced heat transfer (Lei & Li, 2007). Many scholars have studied the effects of changes in tube structure on heat transfer. Zhang studied numerically laminar convective flow and heat transfer in trapezoidal ducts with a rectangular cross-section (Zhang *et al.*, 2017), and presented the heat transfer and friction characteristics and performance analysis of convective heat transfer through a trapezoidal duct with different slope angles b ($0 \leq b \leq 50$). In the vicinity of the critical point, the fluid density changed drastically, the viscosity and the thermal conductivity decreased rapidly, and the specific heat at constant pressure increased to infinity. Han *et al.* studied the numerical simulation of the flow and heat transfer characteristics of cylindrical, elliptical and rhombic pile-honeycomb spiral heat transfer models, and found the distribution of wall heat transfer coefficient of the cylindrical structure was relatively concentrated, the maximum value was larger but the maximum value was significantly smaller than the other two structures (Han, Wang & Liu, 2017). Hong *et al.* put forward a new design of wavy corrugated tube (WCT) aiming to improve heat transfer by employing multilongitudinal vortices. The main findings were that the WCTs exhibited superior heat transfer rate and PEC compared with the plain tube, due to improved flow mixing and enhanced heat flux by multi-longitudinal vortices induced by corrugations (Hong *et al.*, 2017). By comparing the effects of different channels structures, it was possible to select the channel structure that was more favourable for heat transfer. Aneesh computationally studied the thermo-hydraulic characteristics and performance of Alloy 617 based PCHEs (Printed Circuit Heat Exchanger), working in He-He counter flow loop by using a reduced PCHE unit, considering three different periodic channels, viz., triangular, sinusoidal and trapezoidal configurations (Aneesh *et al.*, 2018). They found the trapezoidal PCHE model was found to offer the highest heat transfer augmentation and pressure drop penalty, and could obtain both maximum heat transfer rates and optimal thermo-hydraulic performance. Enoki examined the characteristics of flow boiling heat transfer and pressure drop of a refrigerant R410A flowing vertically upward in small copper rectangular and triangular tubes with hydraulic diameters of 1.04 and 0.88 mm, for the development of a high-performance heat exchanger using small tubes or mini-channels for air-conditioning systems, and the pressure drop was found to be slightly lower in the rectangular and triangular tubes and the heat transfer was much better than in the circular tube (Enoki *et al.*, 2013). Wang *et al.* studied the flow and heat transfer characteristics of supercritical water in sub-channels with square distribution and triangular distribution. The influence of heat flux, pressure and mass flow rate on the heat transfer characteristics was analysed. The results showed that the quadrilateral pipes were more likely to pass through the pseudo-critical region than the annular channels (Wang *et al.* 2014; Wang *et al.* 2016).

The effect of different runner structures on heat transfer had many factors. Sharabi predicted turbulent convective heat transfer to a fluid at supercritical pressure in square and triangular channels, and the sensitivity analysis performed to evaluate the separate effects of acceleration and buoyancy due to density non-uniformity clearly. Zhouhang Li *et al.* investigated the flow and heat transfer of supercritical CO₂ in helically coiled tubes over a wide range of fluid temperature, mass flux, heat flux and coil geometries, and found that the effect of wall curvature on integral heat transfer was overwhelmed by gravitational buoyancy when $Rig, CT > 8$, and helically coiled tubes presented similar performance to straight tubes. On the other hand, when $Rig, CT < 5$ the curvature effect dominated and helically coiled tubes showed superior heat transfer characteristics to straight tubes.

The research concerning the influence of the cross section profile on supercritical water is less plentiful. In this paper, the flow characteristics of supercritical water in tubes with different cross sectional shapes (circular channels, triangular channels and square channels) was simulated. The circumferential heterogeneities of the heat transfer in the square channels and triangular channels were analysed emphatically, the point-to-point simulation from the vertex angle to the midpoint of the edge was carried out for the two types of channels and compared the point where heat transfer was least favourable with circular channels. What is more, this paper compares the heat transfer coefficient and wall temperature of three kinds of channel from $y+$ and eL/D (L was the distance between the radial point and the vertex, and D was the distance from the centre of the section to the vertex), determining the best heat transfer channels.

2. NUMERICAL APPROACH

2.1. Organisation of the paper

In order to ensure the three kinds of channels had the same heat exchange amount, the three channels had the same heat exchange area, that is, the side area, and the mass flow rate of the supercritical water in the three channels was the same, 0.01634 kg/s. The circumference of the square pipe was 16mm and was used as a

benchmark; the diameter of the circular pipes was 5.1mm, the side length of the regular triangle was 5.34mm, and the length of the three pipes were 1000mm. Because of the circumferential heterogeneities of the heat transfer in the square channels and triangular channels, the pointwise simulation was inevitable. As shown in Figure 1, the distance between the points was 0.5mm in the regular triangular channels and 0.3mm in circular channels.

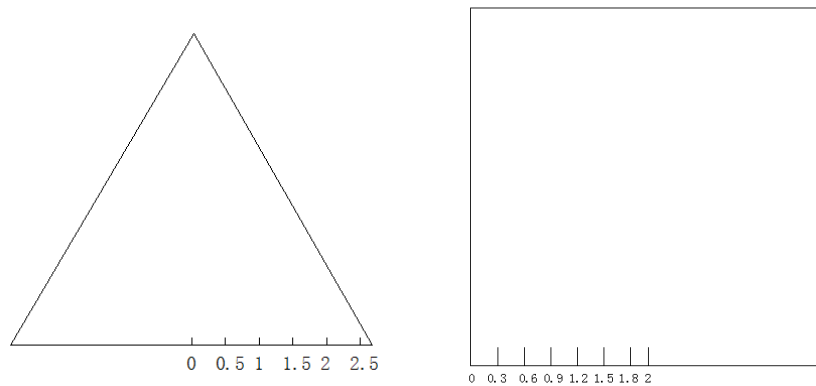


Figure 1: The location of the simulated point.

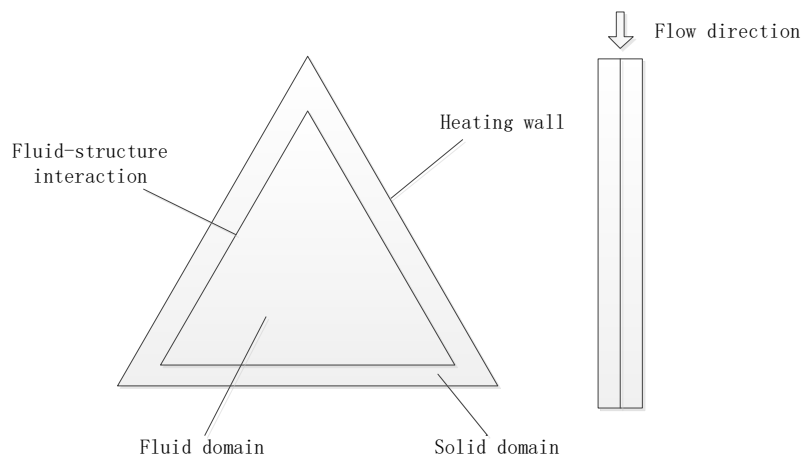


Figure 2: Physical model of channels comparison.

As shown in Figure 2, when comparing the heat transfer coefficients of different channels, due to the circumferential heterogeneities of the heat transfer in the triangular channels and square channels, a wall thickness of 0.5 mm was added to the triangular channels and the square channels. Heating on the outside wall, fluid-solid coupling between the fluid and solid domains increased the dependability of the simulation and the physical model of the square channel was similar to the triangle when compared with different channels.

The properties of supercritical water used the existing type in CFX 14.5, which was the steam 51 defined by International Association for the Properties of Water and Steam. The entrance was set to the quality entrance and mass flux, temperature, and turbulent kinetic energy are also set. The outlet was set to pressure outlet and export pressure was determined. The heat flux of heating surface was uniform, and the surface was smooth and no slip. The convergence criteria for the numerical calculation was set to 10^{-6} , and a monitoring point was set up near the outlet to detect the fluid temperature.

The flow of supercritical water in square tubes were under mass flow rate of 800 kg/(m²s), pressure of 23 MPa, 25 MPa, 28 MPa and heat flux of 300 kJ/m²s, 600 kJ/m²s, 800 kJ/m²s. When comparing the heat transfer of different channels, for the flow in regular triangular channels and square channels, the mass flow rate was 800 kg/m²s and the heat flux was 300 kJ/m²s, 600 kJ/m²s, pressure from 23MPa to 25MPa. The working conditions of the triangular tubes was the same as the square tubes.

2.2. Introduction of turbulence model

Previously, most numerical simulations of flow in sub-channels with grid spacers were solved by solving the RANS (Reynolds-averaged Navier-Stokes) equations and anisotropic two-equation turbulence model (Conner *et al.*, 2010; Gandhir & Hassan, 2011; Zhu *et al.*, 2018). The peak velocity of the cross section obtained by the simulation was much larger than the experimental value. The Reynolds Stress Model originally included the influence of the curvature of streamline, mutation of strain rate, secondary flow or buoyancy. In theory, Reynolds stress was suitable for complex forms of flow. For most flows, the SSG model was more accurate than the LRR model, especially for vortex flow. Therefore, the SSG model was superior to other models which were recommended for use. The standard Reynolds stress model in CFX was derived from the ε equation.

$$\text{Equation 1: } \frac{\partial \overline{\rho u_i u_j}}{\partial t} + \frac{\partial (U_k \overline{\rho u_i u_j})}{\partial x_k} - \frac{\partial}{\partial x_k} \left(\left(\mu + \frac{2}{3} C_S \rho \frac{k^2}{s} \right) \frac{\partial \overline{u_i u_j}}{\partial x_k} \right) = P_{ij} - \frac{2}{3} \delta_{ij} \rho \varepsilon + \Phi_{ij} + P_{ij,b}$$

Where:

- Φ_{ij} = pressure strain coefficient,
- P_{ij} = exact output term, given by the following equation:

$$\text{Equation 2: } P_{ij} = -\overline{\rho u_i u_k} \frac{\partial U_j}{\partial x_k} - \overline{\rho u_j u_k} \frac{\partial U_i}{\partial x_k}$$

The output term produced by buoyancy is following:

$$\text{Equation 3: } P_{ij,b} = B_{ij} - C_{buo} \left(B_{ij} - \frac{1}{3} B_{kk} \delta_{ij} \right)$$

The most important term in the Reynolds stress model is the pressure strain rate coefficient Φ_{ij} .

$$\text{Equation 4: } \Phi_{ij} = \Phi_{ij,1} + \Phi_{ij,2}$$

For the SSG Reynolds stress model:

$$\text{Equation 5: } \Phi_{ij,1} = -\rho \varepsilon \left[C_{S1} a_{ij} + C_{S2} (a_{ik} a_{kj} - \frac{1}{3} a_{mn} a_{mn} \delta_{ij}) \right]$$

$$\text{Equation 6: } \Phi_{ij,2} = -C_{r1} P a_{ij} + C_{r2} \rho k S_{ij} - C_{r3} \rho k S_{ij} \sqrt{a_{mn} a_{mn}} + C_{r4} \rho k \left(a_{ik} S_{jk} + a_{jk} S_{jk} - \frac{2}{3} a_{kl} S_{kl} \delta_{ij} \right) + C_{r5} \rho k (a_{ik} \Omega_{jk} + a_{jk} \Omega_{ik})$$

In our previous work (Zhu *et al.*, 2018) the authors performed the comparison study of five turbulence models (the RNG $k-\varepsilon$ model, shear stress transport model, the SSG model, Launder Reece and Rodi quasi-isotropic model, omega Reynolds stress model) and compared results against the experimental data of Yamagata *et al.* It was concluded that the SSG Reynolds stress model was most suitable to the current numerical simulation. So having already verified the turbulence model, it was not repeated in this paper. In this paper, the SSG Reynolds stress model was used to simulate the flow in the sub-channel.

2.3. Mesh dependency

The quality of the mesh directly affects the accuracy of the numerical simulation results as Katz and Sankaran mentioned in their article (Sankaran, 2013). For complex geometries, the division of mesh was especially important. Due to the physical properties near walls changing dramatically, the mesh structure of the near wall should be reasonable. In this paper, the structured grid of the fluid domain was divided in ICEM software. The grid of the boundary layer and the area that flow field changed needed dramatic densification treatment to ensure the quality of the mesh. This measure can improve the speed and accuracy of the calculation. The three-dimensional geometry grid and its local amplification of the wall-fluid adjacent zone are shown in Figure 3.

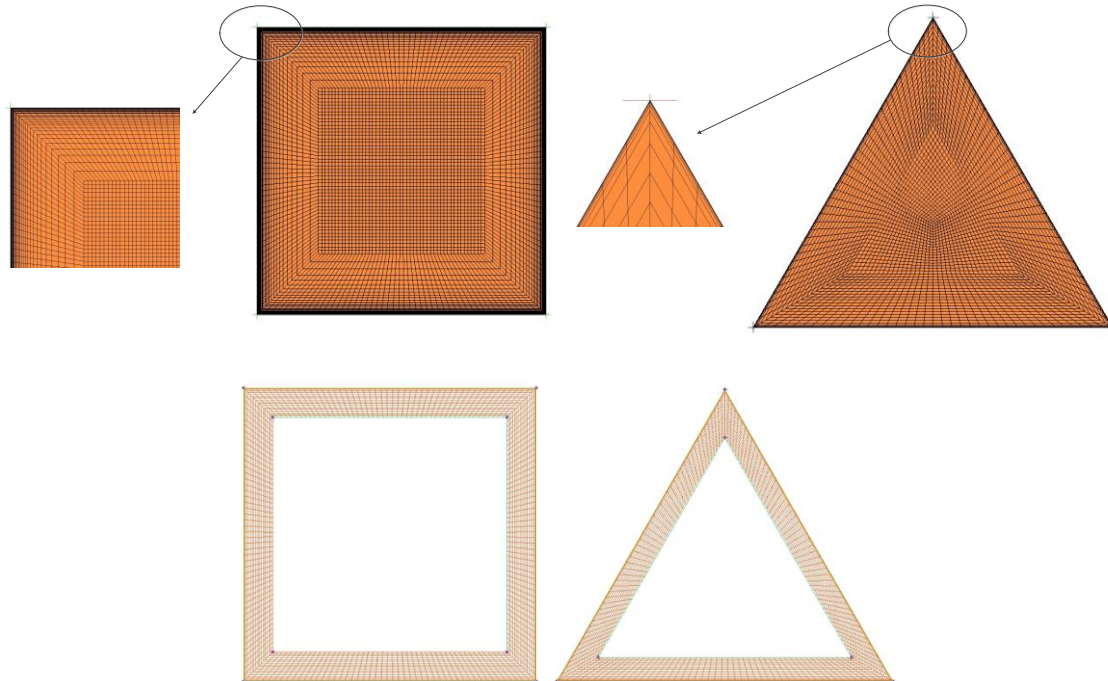
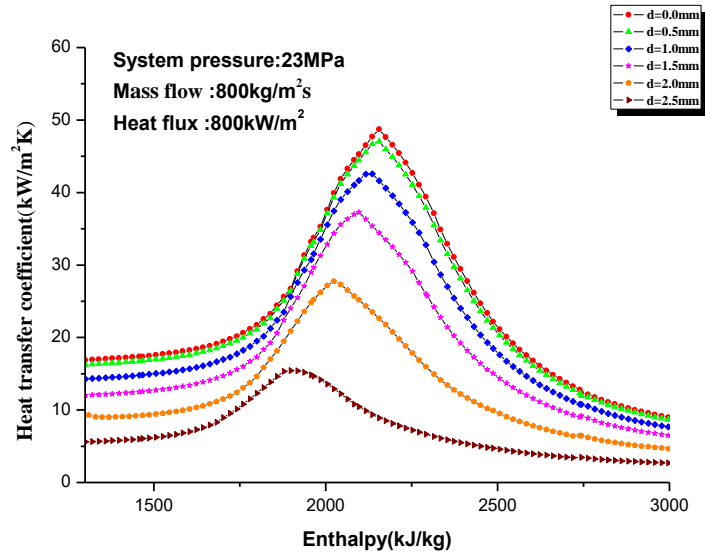


Figure 3: Local volume mesh at inlet cross-section

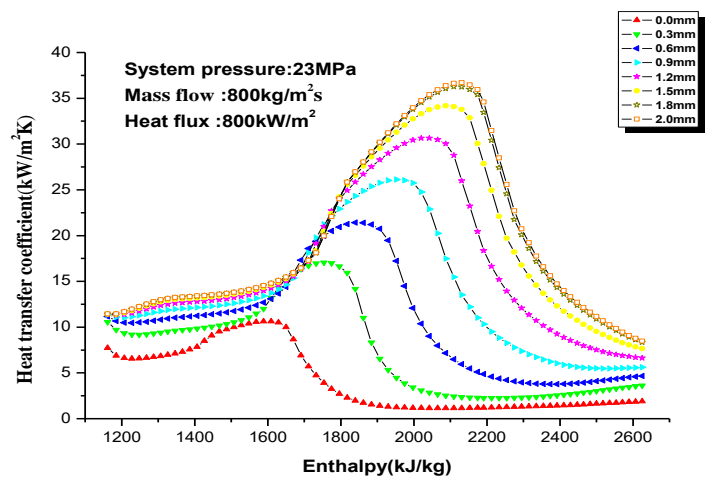
3. NUMERICAL RESULTS AND DISCUSSION

3.1. Heat transfer characteristics of regular triangular and square channels

For the triangle and square channels, the heat transfer coefficient of supercritical water was simulated at heat fluxes under the conditions of 23 MPa and 800 kW/m², the heat flux was 800 kW/m². In this paper, we mainly discuss the heat transfer coefficient at the different positions of the sides of the triangular pipe varying with the enthalpy. No matter what the cross-section of channels was, the heat transfer coefficient gradually became smaller from the midpoint to the vertex of the edge, as seen in Figure 4, that is to say, the heat transfer coefficient was the largest at the midpoint of the triangle and the heat transfer coefficient at the apex position was the smallest, d was the distance from the midpoint of the side to the top corner.



(a) Heat transfer coefficient versus bulk enthalpy at different position in square channels.



(b) Heat transfer coefficient versus bulk enthalpy at different position in regular triangular channels.

Figure 4: Heat transfer coefficient versus bulk enthalpy at different position

For regular triangular channels, the vertex angle was 60° and the vertex angle was 90° for square channels. When the vertex angle was large enough, the separation between the boundary layer and the wall surface was likely to occur, resulting in the reflux of the fluid in the outlet position of computational region, which reduced the thermal current intensity. There was a great resistance at the vertex angle and the above reasons reduced the heat transfer coefficient of the vertex angle.

The fluid at the vertex angle had a lower viscosity and thermal conductivity, resulting in a higher thermal resistance, so the heat transfer coefficient was low.

3.2. Comparison of heat transfer characteristics between different channels

Because the circumferential heterogeneities of the heat transfer in the triangular channels and square channels were evident, the value of the heat transfer coefficient from the midpoint of the side to the vertex angle was different, for the regular triangular channels and the square channels, the heat transfer at the vertex angle was the worst, so comparing the heat transfer coefficients at the vertex angle of the triangular channels and the square channels with

the circular channels. As shown in Figure 5, with the increase of the enthalpy, the heat transfer coefficient increased sharply, reaching the peak value and then decreasing.

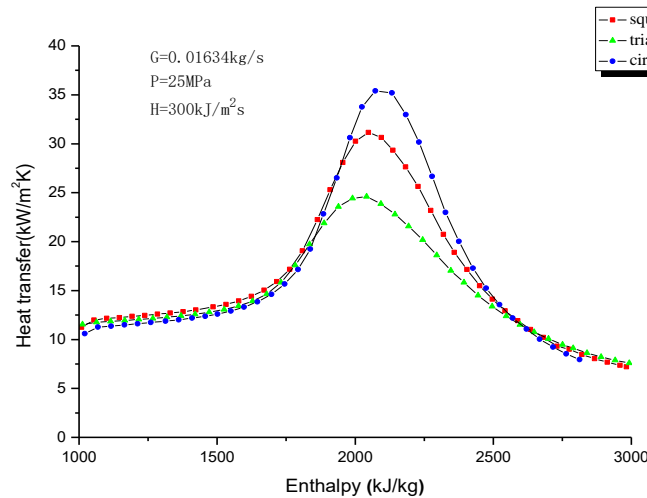


Figure 5: Comparison of heat transfer coefficients between different sub-channels

There was a significant enhancement of heat transfer phenomenon in the pseudo-critical region because here, the specific heat at constant pressure and the dynamic viscosity of the supercritical water increased sharply and then sharply decreased, and the density and thermal conductivity decrease rapidly, so the heat transfer between the tube wall and the fluid was enhanced. The decrease of viscosity and density can increase the buoyancy but Ackermann believed that the reason for the enhancement of heat transfer was that the nucleate boiling occurred near the pseudo-critical point (Ackermann, 1970). For the three channels, there was no difference between the circular pipe and other two channels in the low enthalpy region and the high enthalpy region, but it was obvious that the heat transfer coefficients of circular channels was higher than triangular channels and the square channels near the pseudo-critical point. The heat transfer coefficient of the triangular channels reached the peak first, followed by the square channels, and finally the circular channels reached the peak.

In the condition of the same heat transfer area, the cross-section area of circular channel was the largest, followed by the square, the smallest area of the triangle. Under the condition constant mass flow, the fluid velocity of the triangular channel was the highest, and the high fluid velocity had a strengthening effect on the heat exchange. But the separation between the boundary layer and the wall surface was likely to occur at the vertex angle of the triangular channels and the square channels, resulting in the reflux of the fluid in the outlet position of computational region and there was a great resistance at the vertex angle, which made the flow rate of the supercritical water at the vertex angle decrease and reduce the thermal current intensity. Therefore, heating time was longer and it was easier to reach the peak.

The supercritical water flow velocity in the triangle channel was larger than that of the square pipe, but in the large specific heat region, the heat transfer coefficient in the square was higher than the triangle channel because the friction coefficient decreased with the increase of the inclination angle. The angle of the square (90°) was greater than the triangle (60°) so the resistance at the corners of the triangle was greater. It can be seen from the above that friction was more influential to heat transfer.

Through the above comparison of the three kinds of tubes, it was found that the heat transfer condition of the supercritical water of triangular tubes and the square tubes was worse than that of the circular tubes because the triangular tubes and the square tubes have heat transfer heterogeneity.

3.3. The influence of buoyancy

When the density difference between the mainstream fluid and the near wall fluid reached a certain degree, it changed the flow structure by changing the buoyancy and affecting the turbulent flow. The larger density contrast between the wall and the mainstream area caused buoyancy, the bigger the ratio of wall heat flux to mass flow, the more obvious the buoyancy was.

Jackson *et al.* advanced the use of Bo^* to represent the buoyancy force:

Equation 7:

$$Bo^* = \frac{Gr^*}{Re^{3.425} Pr^{0.8}}$$

Equation 8:

$$Gr^* = \beta g d^4 q_w / (\lambda v^2)$$

Figure 6 shows the variation of Bo^* number with the main enthalpy under different pressures and different heat flux densities. It was observed that under the same enthalpy, the dimensionless parameter Bo^* of the triangular channel was the largest, and the Bo^* of the circular channel was the smallest. The effects of buoyancy produced a non-uniform density distribution; the flow at the top corners of triangular and square channels was disorderly; the lighter fluid with low thermal conductivity gathered near the top wall due to the buoyancy effect, causing the deterioration of heat transfer capacity. Before the critical temperature, the Bo^* number was more dispersed; after the critical temperature, the distribution of Bo^* numbers was concentrated. Before the critical temperature, the change of pressure had little effect on Bo^* , but the heat flux had a great influence on Bo^* . As the heat flux increased, Bo^* became larger and the heat transfer effect worsened. Near the critical temperature, the Bo^* number changed the most and the wall temperature changed the least. This was strongly related to the change in density of supercritical water near the critical temperature.

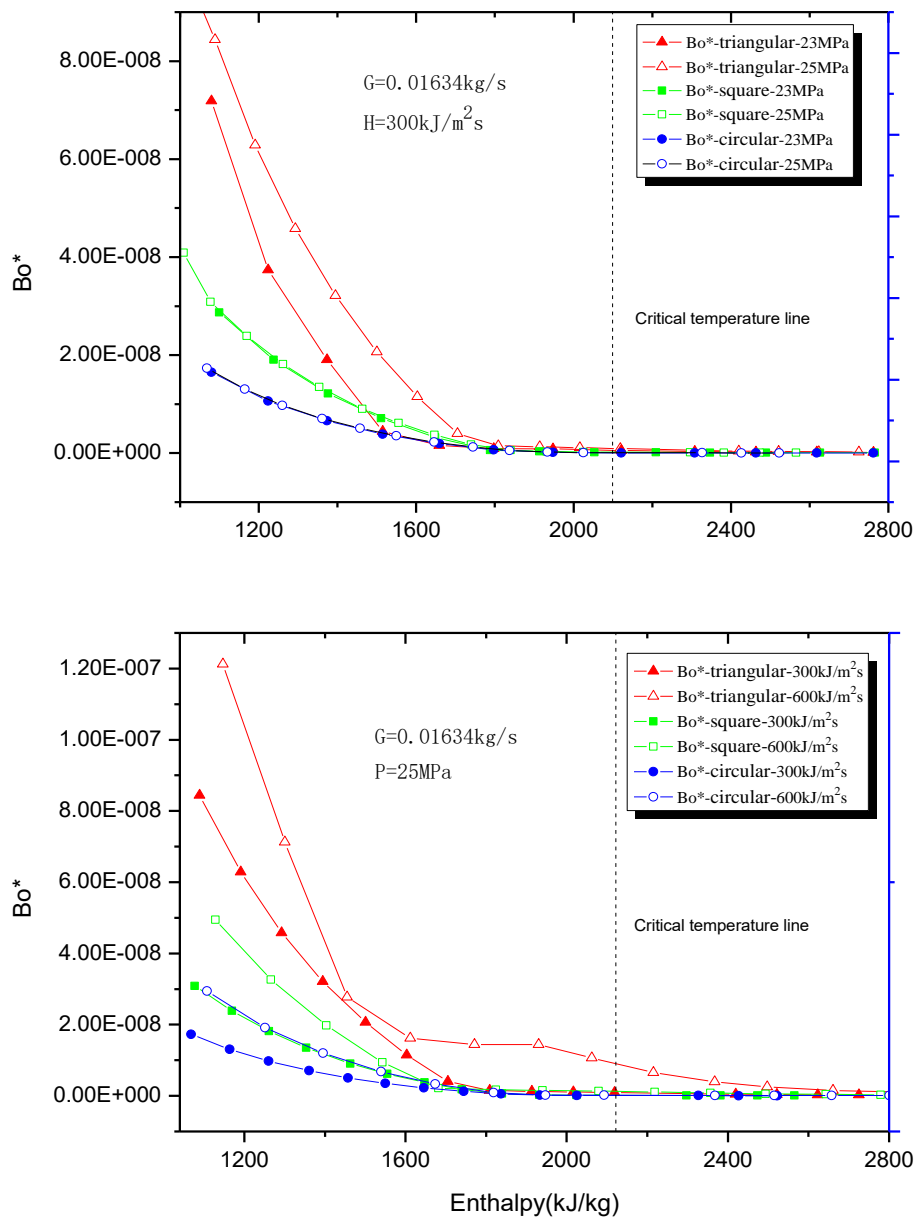


Figure 6: Buoyancy parameter, Bo^* distributions in different operating conditions

4. CONCLUSIONS

Regardless of the cross-sectional shape of the sub-channels, an excessively high heat flux can block the heat transfer between the fluid and the wall, and the increase of heat flux can increase the buoyancy. As the pressure increases, the drastic change of the physical properties of supercritical water in the pseudo-critical region weakened. The increase of heat flux and pressure can weaken the heat transfer, in particular, the influence on the large specific heat region was most obvious. Because of circumferential heterogeneities of the heat transfer in square channels and triangular channels, due to the limitation of the shape of the fluid field (especially the triangular pipe), the vortices around the centre of the channels was large, which increased the disturbance of the fluid and taking away more heat. Meanwhile the vertex angle was far away from the vortex, and with the influence of resistance and backflow, the fluid near the wall could not leave the wall to take away the heat in time, and the temperature kept rising. For triangular channels and the square channels, the heat transfer coefficient was the largest at the midpoint and the heat transfer coefficient at the apex position was the smallest. The heat transfer coefficient at the apex reached its peak first. Because triangular tubes and the square sub-channels have heat transfer heterogeneity, the heat transfer at the vertex angle of the triangular channels and the square channels affected the overall heat transfer. Therefore, comparing the heat transfer coefficients at the vertex angle of the triangular channels and the square channels with the circular channels, the heat transfer of circular sub-channels was the best.

5. REFERENCES

- Ackerman, J.W. 1970, Pseudo-Boiling Heat Transfer to Supercritical Pressure Water in Smooth and Ribbed Tubes[J]. *Journal of Heat transfer*, pp. 490-498.
- Aneesh A.M., Sharma, A., Srivastava, A., Chaudhury, P. 2018, "Effects of wavy channel configurations on thermal-hydraulic characteristics of Printed Circuit Heat Exchanger (PCHE)", *International Journal of Heat and Mass Transfer*, 118, 304-315.
- Conner, M.E., Baglietto, E., Elmahdi, A.M. 2010, CFD methodology and validation for single-phase flow in PWR fuel assemblies[J]. *Nuclear Engineering & Design*. 240(9), 2088-2095.
- Enoki, K., Miyata, K., Mori, H., Kariya, K., Hamamoto, Y., 2013, "Boiling Heat Transfer and Pressure Drop of a Refrigerant Flowing Vertically Upward in Small Rectangular and Triangular Tubes", *HEAT TRANSFER ENGINEERING*, 34,11-12.
- Gandhir, A., Hassan, Y. 2011, RANS modeling for flow in nuclear fuel bundle in pressurized water reactors (PWR)[J]. *Nuclear Engineering & Design*. 241(11), 4404-4408.
- Gunes, S., Ozceyhan, V., Buyukalaca, O. 2009, "Heat transfer enhancement in a tube with equilateral triangle cross sectioned coiled wire inserts", *EXPERIMENTAL THERMAL AND FLUID SCIENCE*, 34, 684-691.
- Han, P-F., Wang, Z-F., Liu, Z-Y. 2017, Research on Flow and Heat Transfer Characteristics Inside Spiral Pile-honeycomb Structures with Different Shapes. *International Journal of Plant Engineering and Management*. 22 (2).
- Hong, Y., Du, J., Wang, S., Huang, S-M. 2017, Heat transfer and flow behaviors of a wavy corrugated tube. *Applied Thermal Engineering*. 126, 151–166.
- Jige, D., Inoue, N., Koyama, S. 2016, "Condensation of refrigerants in a multiport tube with rectangular minichannels", *INTERNATIONAL JOURNAL OF REFRIGERATION-REVUE INTERNATIONALE DU FROID*, 67, 202-213.
- Keklikcioglu, O., Ozceyhan, V. 2018, "Experimental investigation on heat transfer enhancement in a circular tube with equilateral triangle cross sectioned coiled-wire inserts", *APPLIED THERMAL ENGINEERING*, 131, 686-695.
- Lei, X., Li, H. 2007, A study of heat transfer scaling of supercritical pressure water in horizontal tubes. *International Journal of Heat and Mass Transfer* , 114, 923–933.
- Liu, G., Huang, Y., Wang, J. 2016, Heat transfer of supercritical carbon dioxide flowing in a rectangular circulation loop. *Applied Thermal Engineering*. 98, 39–48.

Sankaran, K.V. 2013, Mesh quality effects on the accuracy of CFD solutions on unstructured meshes.[J]. Journal of Computational Physics.

Wang, W., Lu, T., Zhao, P., 2014, Experimental Investigation on Heat Transfer of Supercritical Pressure Water Flowing in the Sub-channel With Square Distribution in Supercritical Water Cooled Reactor. Proceedings of the CSEE, 34(20).

Wang, W., Zhang, B., Lei, J., 2016, Investigation on Flow and Heat Transfer Characteristics of Supercritical Water in Sub-channel with Triangular Distribution of SCWR. Atomic Energy Science and Technology, 50(7).

Wang LJ, Sun DW, Liang, P, Zhuang LX, 2000, "Experimental studies on heat transfer enhancement of the inside and outside spirally triangle finned tube with small spiral angles for high-pressure preheaters", INTERNATIONAL JOURNAL OF ENERGY RESEARCH, 24,309-320.

Xu, W., Wang, W., Du, X., Zhu, X. 2017, Numerical investigation on the secondary flow of supercritical water in a four-head internally ribbed tube. Applied Thermal Engineering. 120, 708–718.

Zhang, X., Wang, Y., Jia, R., Wan, R. 2017, Investigation on heat transfer and flow characteristics of heat exchangers with different trapezoidal ducts[J]. International Journal of Heat and Mass Transfer. 110, 863–872.

Zhu, X J, Du, X, Li, Q, Qiu, Q G. 2018, Study on the effects of system parameters on entropy generation behavior of supercritical water in a hexagon rod bundle. International Journal of Heat and Mass Transfer. 117, pp. 669-681.

#375: Study on the migration and degradation of organic compounds in coal-gasification wastewater with a novel treatment

Wei ZHANG¹, Defu CHE², Suilin WANG³

¹School of Environment & Energy Engineering, Beijing University of Civil Engineering & Architecture, No.1 Zhanlanguan Road, 100044, Beijing, China, zhangwei1@bucea.edu.cn

²School of Energy & Power Engineering, Xi'an Jiaotong University, No. 28 Xianning West Road, Xi'an, China, Albert.820@126.com

³School of Environment & Energy Engineering, Beijing University of Civil Engineering & Architecture, No.1 Zhanlanguan Road, 100044, Beijing, China, suilinwang@bucea.edu.cn

The traditional treatment for coal-gasification wastewater is time-consuming and high-cost due to a great number of organic compounds. In this paper, a novel coal-gasification wastewater treatment is proposed. Pre-filtrated wastewater was sprayed into the gasifier instead of pure steam, and then organic constituents reacted at different temperatures. The migration and degradation of typical hydrocarbon and nitrogen-containing compounds in wastewater were experimentally studied. The release of nitrogenous and carbonous gas products were also analysed during a rapid combustion process. The results showed that the degradation rate of constituents increased with reaction temperature, and most organic constituents were degraded below 800°C. The initial concentration of phenol had a slight effect on the degradation rate, and NH₃ held back the phenol reaction. The removal efficiency of COD and NH₃-N ranked in different atmospheres as follows: oxidative > inert > reductive. The thermal decomposition of organic constituents was enhanced by increasing oxygen concentration and residence time. Furthermore, a simplified kinetic study of COD and NH₃-N removal efficiency was carried out on the hypothesis of pseudo-first order reaction model. The pre-exponential factor and apparent activation energy for COD and NH₃-N removal efficiency were obtained in the range of 3.63×10³-1.62×10⁶, 34.39-58.16 kJ·mol⁻¹ and 1.58×10⁴-8.71×10⁵ s⁻¹, 41.25-61.75 kJ·mol⁻¹, respectively.

Keywords: coal-gasification wastewater; organic compounds; kinetic reaction; migration and degradation

1. INTRODUCTION

With the requirement for high-efficient coal utilisation and stringently-controlled pollutant emissions, coal-gasification technology is a promising industrial application for fossil fuels, gaining increasing attention. However, compared to the fluidised-bed gasifier and entrained-flow gasifier, much wastewater with a high concentration of toxic and refractory contaminants is generated in the moving-bed gasifier, which primarily originates from quenching reaction and raw gas purification (Gao, Lu & Wang, 2010). For instance, 1.1-1.3 m³ wastewater is obtained during the gasification of 1 ton of coal in the moving-bed gasifier. The contaminants in the coal-gasification wastewater (CGW) mainly include phenols, ammonia, fatty acid, and aliphatic hydrocarbon, and the discharge of the contaminants seriously endangers aquatic life and water potability.

Recently, several mature treatment technologies have been widely utilised in gasification industries, including physical, chemical, physicochemical and biological methods, etc. Physico-chemical pre-treatment is mainly adopted to recover the by-products phenol and ammonium, and a series of biological treatments are used for the degradation of contaminants. For decades, scholars have also proposed various treatment methods for coal-gasification wastewater, i.e. solvent extraction, biodegradation and oxidation treatments. The effective reduction of pollutants through solvent extraction is of significance for operation stability of biological treatment. Recent progress has centred upon the process optimisation (Luo *et al.*, 2015), i.e. energy-saving, agent consumption reduction, and the application of new extraction agents (Gai *et al.*, 2016). Physico-chemical technologies are extensively utilised due to high separation efficiency of chemical constituents, but the chemical solvents used for coagulation precipitation (Martínez-Quiroz *et al.*, 2017), adsorption (Erto *et al.*, 2013) and membrane separation (Li, J.F., *et al.*, 2016) have a high adsorption ability coupled with high cost. Currently, different absorption properties of activated carbons and activated coke are being compared to investigate a suitable adsorbent for pre-treatment of CGW (Li, P., *et al.*, 2015). Biological treatments including activated sludge, anoxic-oxic, anaerobic-anoxi-oxic and anaerobic-anoxi-oxic-membrane bioreactor (A²O-MBR), is widely used for wastewater treatment (Romero Pareja *et al.*, 2016; Wang, W., *et al.*, 2011; Wang, Z.X., *et al.*, 2012; Zhao & Liu, 2016). Anaerobic processes have attracted increasing attention due to the biodegradation improvement of CGW. However, wastewater pre-treatment is required for the anaerobic digestion or biological treatment of CGW due to the high toxicity of organic components in CGW to biological system (Zhao & Liu, 2016). As an economic and efficient treatment technology, the biological treatment process is of growing interest and treatment process enrichment, biodegradation improvement, pollutants removal and sludge production reduction are the key issues for the technological innovation of biological treatment. Besides, the selection and optimisation for advanced oxidation processes (cavitation, photocatalytic oxidation and Fenton's chemistry) (Wang, Y.Z., *et al.*, 2014; Zhuang *et al.*, 2015) and chemical oxidation (utilisation of ozone and hydrogen peroxide) (Chang *et al.*, 2015; Xing *et al.*, 2014) is widely investigated to degrade toxic and bio-refractory chemical constituents, etc. In comparison with advanced oxidation processes, chemical oxidation can yield high phenol removal efficiency without secondary pollution, but high operation cost and low NH₃-N removal limits its application (Gogate & Pandit, 2004a). Generally, coal-gasification wastewater is treated with hybrid methods for high treatment efficiency. The combination of these oxidation processes can eliminate the drawbacks of individual techniques and obtain better results compared with individual techniques (Gogate & Pandit, 2004b). Inevitably, energy consumption, reducing pollutant and by-product production should be taken into consideration in oxidation processes.

With ever-increasing population and a decreasing source of available freshwater, it is crucial to exploit new treatment technologies for industrial wastewater through proper management and application of existing technologies (Ji *et al.*, 2016). Considering high solvent and operation costs, secondary pollution and the long processing cycle of existing wastewater treatments, the purpose of this paper was to attempt an alternative approach of wastewater treatment in the coal gasification process. After pre-treatment of tar recapture and impurity filtration, wastewater is applied as a gasification agent to replace total or partial pure steam. With wastewater being heated and sprayed into the gasifier, water participates in the water-gas shift reaction, meanwhile organic constituents in wastewater are thermally degraded in specific conditions and potential chemical energy of organic constituents is recovered. It is desirable that high efficiency of wastewater treatment can be obtained along with recycling water resources, reducing secondary pollution, and saving reconfiguration costs.

The preliminary work indicates that thermal removal of contaminants in coal-gasification wastewater is effective. However, thermal degradation characteristics of contaminants in coal-gasification wastewater remains rarely reported. In the present work, the effects of several representative factors (temperature, reaction atmosphere, oxygen concentration and residence time) on contaminants removal characteristics are investigated. In addition, the kinetic analysis of chemical oxygen demand (COD), ammonia nitrogen (NH₃-N) were further conducted based on pseudo first-order kinetics assumption.

2. EXPERIMENT

In the study, we used one kind of representative coal-gasification wastewater from Lurgi pressurised gasification process in Yima, China. The morphology of the selected wastewater was dark brown and foamy, as shown in Figure 1.



Figure 1: Appearance of original coal-gasification wastewater

The original coal-gasification wastewater contained more than 95% water in weight. The main water quality indices of CGW are shown in Table 1. The contaminants in the wastewater mainly consisted of ammonia, aliphatic, and aromatic hydrocarbons for the dry distillation stage under strong reducing atmosphere. The main organic constituents and proportions of wastewater sample are tabulated in Table 2. Monohydric phenols are shown as the representative aromatic hydrocarbons (Shang & Gu, 2012), phenol and methyl-phenol were the main constituents in coal-gasification wastewater.

Table 1: Main water quality indices of coal-gasification wastewater

Water quality	Unit	Measured value
COD	mg·L ⁻¹	13687
NH ₃ -N	mg·L ⁻¹	8477
Volatile phenol	mg·L ⁻¹	4300
pH	-	11.8

Table 2: Organic constituents of wastewater sample

No	Name	Chemical formula	Retention time/min	Proportion/%
1	Pyridine	C ₅ H ₅ N	2.416	0.3539
2	Phenol	C ₆ H ₆ O	6.142	37.3668
3	Aniline	C ₆ H ₇ N	6.222	0.3607
4	2-methyl-phenol	C ₇ H ₈ O	7.988	10.8054
5	4-methyl-phenol	C ₇ H ₈ O	8.64	34.6026
6	2-ethyl-phenol	C ₈ H ₁₀ O	10.32	0.8557
7	3,5-dimethyl-phenol	C ₈ H ₁₀ O	10.646	4.0126
8	4-ethyl-phenol	C ₈ H ₁₀ O	11.172	1.6633
9	3-ethyl-phenol	C ₈ H ₁₀ O	11.252	5.5033
10	2,3-dimethyl-phenol	C ₈ H ₁₀ O	11.52	0.6342
11	3,4-dimethyl-phenol	C ₈ H ₁₀ O	11.96	1.8472
12	3-(1-methylethyl)-phenol	C ₉ H ₁₂ O	12.961	0.396
13	1-ethyl-4-methoxy-benzene	C ₉ H ₁₂ O	13.269	0.346
14	3-ethyl-5-methyl-phenol	C ₉ H ₁₂ O	13.869	0.8001
15	Others	-	-	0.4522

2.1. Experimental apparatus and procedure

The experiments were performed in an entrained-flow reactor system and schematic diagram of experimental apparatus is shown in Figure 2. The reactor system included gas preparation, wastewater atomisation, thermal degradation and resultant collection sections. Reactant gases were dropped from cylinder pressure to ambient pressure across the regulator. Flow rate was controlled by ServenStar D07-19B mass flow controller (MFC) and calibrated prior to the experiment. The oxidative, inert and reductive atmospheres were supplied through various mixing proportions of N₂, H₂ and CO. The participation of oxygen was represented for oxidative atmosphere, purified nitrogen was used for inert atmosphere and carrier gas, and reductive atmosphere (0.1 N₂+0.25 H₂+0.65

CO) was used. The wastewater was atomised to mist using ultrasonic atomiser in the container, and then the mist was carried by reactant gases into one-dimensional drop-tube furnace. The resultants were collected in gas-washing bottles cooled by an ice bath at 0°C. To completely collect organic constituents in CGW, the resultants and connecting tubes were washed. The tube (length = 1200 mm and inner diameter = 38 mm) in the furnace was made of alumina. The internal temperature of the drop-tube furnace was measured and controlled by four groups of temperature indicator and controller (TIC) connected to a main console, respectively. All the experiments were carried out thrice and the experimental values were averaged.

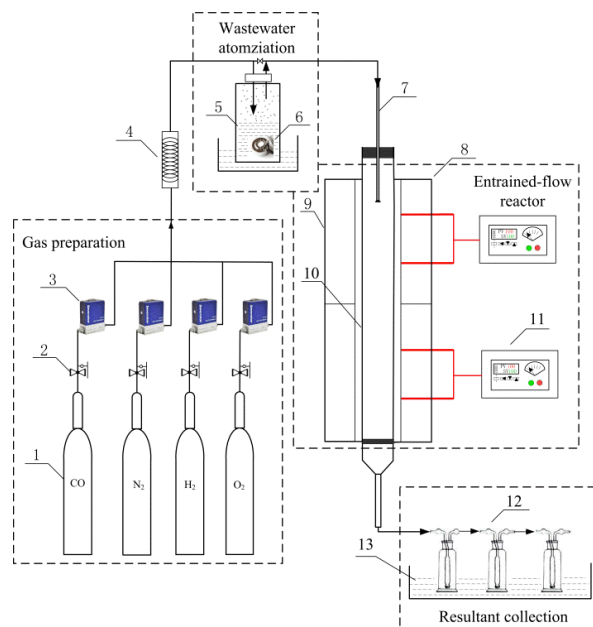


Figure 2: Schematic diagram of entrained-flow reactor system: (1) gas cylinder, (2) pressure gauge, (3) flow controller, (4) gas mixing chamber, (5) container, (6) atomiser, (7) feeder, (8) thermocouple, (9) one-dimensional drop-tube furnace, (10) alumina tube, (11) temperature controller, (12) collection flask, (13) ice bath

The variables including reaction temperature, atmosphere and residence time were considered to investigate thermal removal characteristics of organic constituents. The design of experimental parameters is tabulated in Table 3.

Table 3: Design of experimental parameters

Type	Unit	Value
Gas flow rate	L·min ⁻¹	1.8-10
Temperature	°C	200-1200
CO:H ₂ :N ₂	-	0.65:0.25:0.1
Oxygen proportion	-	5-30 % vol.
Residence time	s	0.34-2.74
Wastewater flow rate	mL·min ⁻¹	0.4

2.2. Analytical methods

The solution measurement of COD and NH₃-N was performed using fast confined catalytic, digestion spectrophotometer and Nessler's reagent colorimetric methods, respectively (SEPAE, 2012). The digestion of organic constituents in experimental sample was conducted on COD digestion device (Merck, Spectroquant Nova 60). The concentrations of COD and NH₃-N were measured by UV-Vis spectrophotometer (Perkin-Elmer, UV320). All chemical reagents used in the experiments were above analytical purity. The organic constituents were analysed by gas chromatograph-mass spectrometer (GC-MS, Agilent, 5973) outfitted with a DB-5MS capillary column (30×0.25 mm×0.25 μm) and using helium as the carrier gas.

2.3. Data interpretation

The residence time of wastewater in the drop-tube furnace was related to the flow rate of gas mixture, which is determined as the tube volume divided by volumetric flow rate of gas mixture at specific temperature and pressure. Considering thermal expansion effect at high temperature, residence time under atmospheric pressure is calculated by

$$\text{Equation 1: } t(\text{s}) = \frac{L \cdot A}{Q} \cdot \frac{273}{T + 273}$$

Where:

- t = residence time (s),
- L and A = length (m) and cross area (m^2) of the tube, respectively,
- Q = flow rate of gas mixture ($\text{m}^3 \cdot \text{s}^{-1}$),
- T = the furnace temperature ($^{\circ}\text{C}$).

COD and $\text{NH}_3\text{-N}$ are two representative indices of water quality. Removal efficiency can quantitatively measure the effects of experimental factors on water quality indices. The removal efficiency of COD and $\text{NH}_3\text{-N}$ can be defined as

$$\text{Equation 2: } X(\%) = \frac{C^0 - C}{C^0} \times 100$$

Where:

- X = removal efficiency (%),
- C^0 and C = initial and final concentration ($\text{mg} \cdot \text{mL}^{-1}$), respectively.

The conversion formula of NO concentration is

$$\text{Equation 3: } c_{\text{NO}} (\text{mg}/\text{m}^3) = \frac{30}{22.4} \times c_{\text{NO}}$$

Regarding the mass equilibrium of element N, the concentration of resultant gas N_2 can be calculated by

$$\text{Equation 4: } c_{\text{N}_2} (\text{mg}/\text{m}^3) = \frac{14 \times 10^3}{17} (C_{\text{NH}_3}^0 - C_{\text{NH}_3}) - \frac{14}{22.4} (c_{\text{NO}} + c_{\text{NO}_2} + 2c_{\text{N}_2\text{O}})$$

Where:

- $C_{\text{NH}_3}^0$, C_{NH_3} = concentration of initial and residual NH_3 , (mg/L),
- c_{NO} , c_{NO_2} , and $c_{\text{N}_2\text{O}}$ = concentration of NO, NO_2 and N_2O (ppm), respectively.

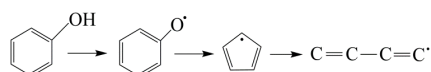
3. RESULTS AND DISCUSSION

In experimental process, wastewater was sprayed into tubular reactor and underwent three stages continuously or concurrently: water evaporation, organic contaminants cracking into small molecules in pyrolysis and combustion (Xiao & Ma, 2012).

3.1. Effect of temperature

Pyrolysis of organic constituents was the primary step in whole combustion reaction. Figure 3 shows the variation of COD and $\text{NH}_3\text{-N}$ removal with reaction temperature (200-1200 $^{\circ}\text{C}$) in inert atmosphere, and the removal profiles of COD and $\text{NH}_3\text{-N}$ passed through three temperature zones. As illustrated in Figure 3(a), the removal efficiency

of COD was slowly increased in the range of 200-600°C, monotonically ascended with reaction temperature in 600-1000°C, and finally nearly approached 97% at 1200°C. This is due to aliphatic and aromatic hydrocarbons being predominantly decomposed below 1000°C, and only a small part of organic matters existed in stable structures when the temperature was above 1000°C. Aliphatic hydrocarbons with C-H bond began with dehydrogenation and chain breakage reactions at low temperature, then further decomposed into CO₂ and H₂O at high temperature. In addition, the benzene-ring opening was enhanced as temperature increased from 600-1000°C, and then transformed into small molecules through dehydrogenation and chain breakage. The results appreciably coincided with Wright's results (Wright, 1960). In addition, coal-gasification wastewater primarily consisted of monohydric and polyhydric phenols. After dehydrogenation reaction, CO and cyclopentadieny were proportionally generated with the benzene-ring opening (Zhong & Bozzelli, 1998).



The variation of NH₃-N removal efficiency with reaction temperature is shown in Figure 3(b). The removal efficiency of NH₃-N was increased slowly in the range of 200-400°C and 800-1200°C, while NH₃-N removal was observed with obvious escalation between 400°C and 800°C. It is explained that radical H· can be yielded from aliphatic and aromatic compounds in the dehydrogenation process, and radical OH· was generated from the breakage of OH bond and aromatic rings (Li & Tan, 2000). In the pyrolysis process, ammonia molecules decomposed into N atoms through the attack of radical H·, and N atoms integrated into N₂ molecules with mutual combination (Liu, H., *et al.*, 2008; Rahinov *et al.*, 2003). Hawboldt *et al.* showed that the removal of NH₃ was below 25% in 850-1050°C, sharply increased to 55% at 1150°C, and considerably jumped to 83% at 1200°C (Hawboldt, 1998). The similar results that NH₃ removal increased from 10% to 75% with rising temperature were obtained by Clark *et al.* (Clark, Dowling & Huang, 1998). However, present results showed that NH₃ conversion was higher than the ones mentioned above at the same temperature. It was probably attributed to the interaction between hydrocarbon radical and N-containing compounds (Liu, C., *et al.*, 2014).

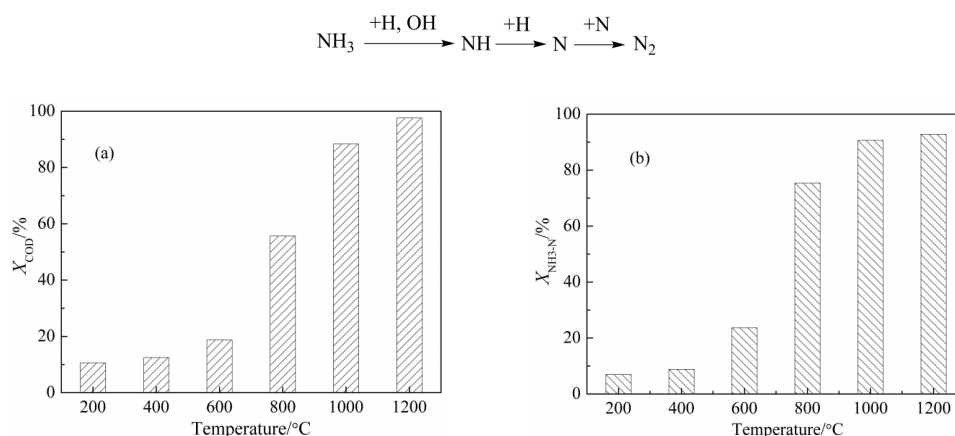


Figure 3: Variation of removal efficiency with temperature in pyrolysis reaction: (a) COD, (b) NH₃-N

The colours of original wastewater and resultant were compared at various temperatures in inert atmosphere, as shown in Figure 4. The colours of resultant water gradually became lighter with the increase of reaction temperature. The resultant at 800°C was nearly as clear as pure water. Therefore, coloured contaminants were easily decomposed at lower temperature and it was proved that the proposed treatment can remove and degrade the constituents in the wastewater.

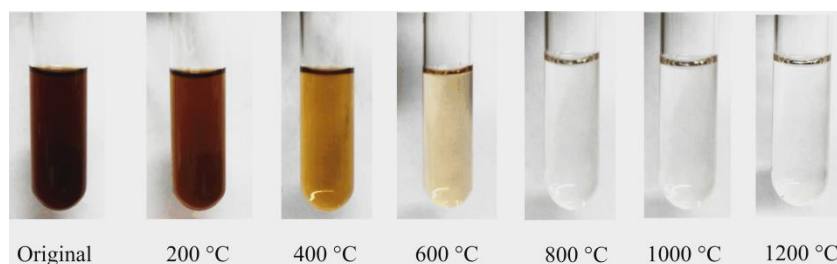


Figure 4: Colours of original wastewater and resultant

3.2. Effect of reaction atmosphere

Figure 5 illustrates the influence of reaction atmosphere on COD and NH₃-N removal. In Figure 5(a), COD removal presented a slow increase under different reaction atmospheres in the lower temperature range of 200-600°C. However, obvious increases were observed in the higher temperature region. The removal efficiency of COD in different reaction atmospheres were ranking as: oxidative > inert > reductive. It was because the addition of oxygen molecule increased the break probability of C-H bond in aliphatic hydrocarbon and benzene-ring of aromatic compounds (Li, J. & Van Heiningen, 1990).

Figure 5(b) shows that NH₃-N removal efficiency rose consistently with increasing reaction temperature. The variation of NH₃ removal in oxidative atmosphere with reaction temperature coincided with that in inert atmosphere. The highest removal efficiency of NH₃-N was obtained in oxidative atmosphere within the whole reaction temperature zone, and NH₃-N removal in reductive atmosphere was almost complete at 1200°C. Based on experimental results and those of Kaul *et al.* (Kaul *et al.*, 1998), we speculate that more radical H· is generated due to the attack of oxygen molecule to relatively weaken the C-H bond in organic constituents, and then enhances the breakage of organic molecule structures and nitrogen transformation from ammonia to other existing forms. Nevertheless, nitrogen transformation was suppressed in reductive atmosphere, which coincides with Lin's research results (Lin, J., Weng & Taketa, 2009). In Clark's study (Clark, Dowling & Huang, 1998), NH₃ conversion was below 10% between 700°C and 1100°C, but increased to 60%-100% as the temperature rose above 1100°C. In comparison to Hawboldt's results (Hawboldt, 1998), NH₃ conversions here were slightly greater at low temperature and smaller at high temperature.

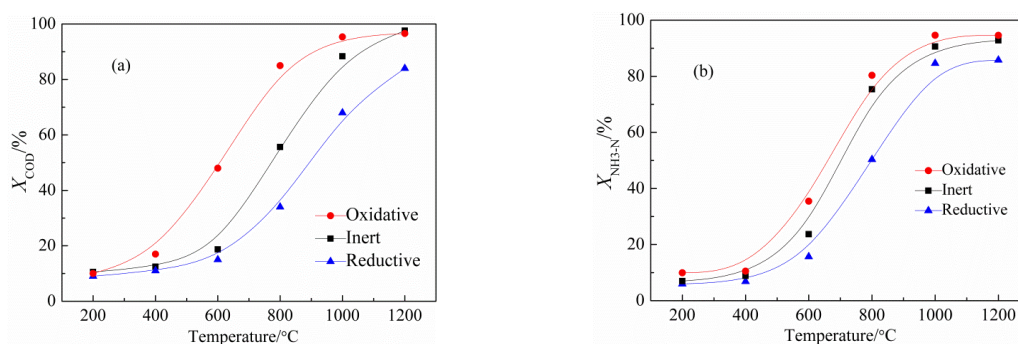


Figure 5: Comparisons of removal efficiency between different atmospheres: (a) COD, (b) NH₃-N

3.3. Effect of oxygen concentration

The effect of oxygen concentration on COD and NH₃-N removal efficiency is illustrated in Figure 6. With the increase of oxygen concentration, the removal efficiency of COD and NH₃-N increased slowly in the range of 200-400°C, but rose considerably between 400 and 1000°C. COD and NH₃-N removals reached 94.1% and 95.2% at 1000°C in ambient atmosphere, respectively. The results were attributed to the participation of more active radicals in the thermal degradation with the rise of oxygen concentration (Wang, Y.Z., *et al.*, 2012). The profiles of COD and NH₃-N overlapped and kept constant above 1000°C in 21% and 30% O₂ atmospheres. The phenomena indicated that stable constituents were independent of temperature and oxygen concentration. Additionally, the polymerisation of aromatic hydrocarbons was inhibited and more small organic molecules were yielded with increasing oxygen concentration (Angeles-Hernández, Leeke & Santos, 2008). Since gasification agents (wastewater and air/oxygen) were sprayed into the reactor from the bottom of the gasifier, the refractory constituents were degraded along with redox reaction through ambient, oxygen-lean and reductive regions. The reaction temperature was reached above 1000°C in the oxidation region. It was noted that high removal efficiency was obtained at an ambient reaction atmosphere and 1000°C. Thus the operation parameters of existing gasification processes are feasible with consideration to removal efficiency and operation cost.

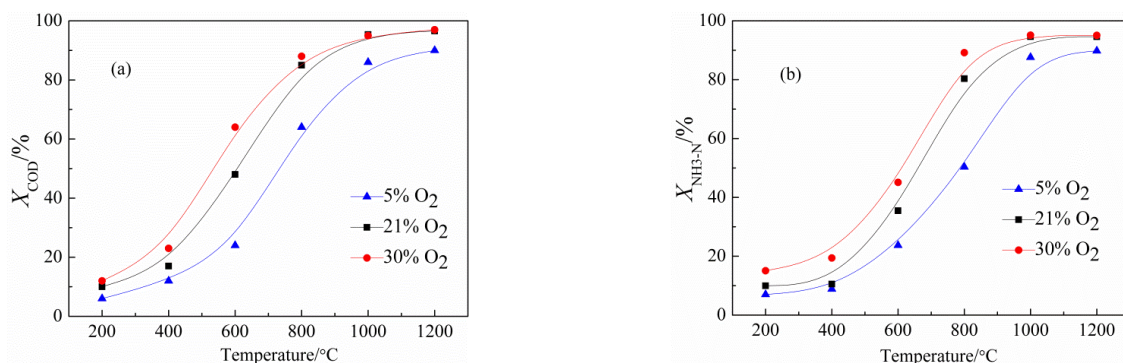


Figure 6: Effect of oxygen concentration on removal efficiency: (a) COD, (b) NH₃-N

3.4. Effect of residence time

The removal efficiency of COD and NH₃-N with residence time in various reaction atmospheres at 800°C is shown in Figure 7. From Figure 7(a), removal efficiency of COD reached 18% in inert atmosphere as residence time was 0.34s. As residence time prolonged, COD removal improved and reached to 97% at 1.37s. Hence, removal efficiency can reach a high value in a short residence time. The removal efficiency of COD in inert atmospheres was higher than that in reductive atmospheres and lower than that in oxidative atmospheres. Figure 7(b) illustrates that the removal efficiency of NH₃-N continuously increased with the increment of residence time. NH₃-N had a remarkable removal efficiency at 0.68 s in oxidative atmosphere. Compared with that in oxidative atmosphere, the removal efficiency of NH₃-N was much smaller at low temperature, while was nearly approached at high temperature in inert and reductive atmospheres. Previous studies indicated that the oxidation of NH₃-N had a much more rapid process than pyrolysis (Clark, Dowling & Huang, 1998; Miller *et al.*, 1983). Removal efficiency of NH₃-N presented a linear rise with increasing residence time in reductive atmosphere. As a consequence, long residence time was required to complete the decomposition of contaminants in inert and reductive atmospheres. From Figure 7, the removal efficiency of COD and NH₃-N were reached above 95% and 90% with the residence time 1.37s.

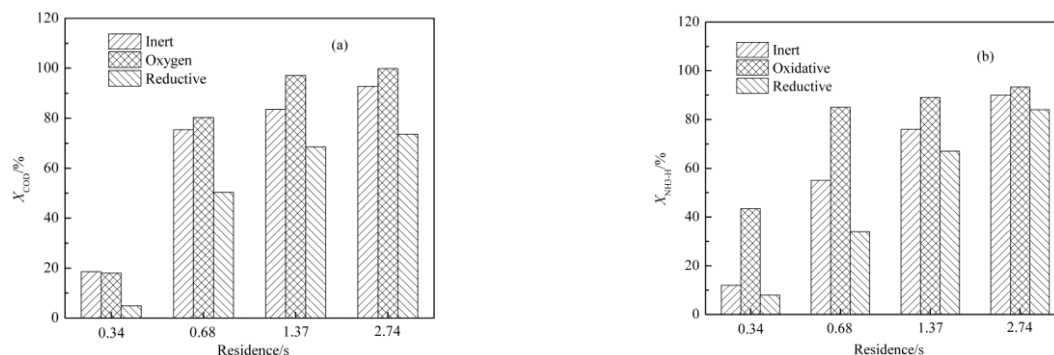


Figure 7: Effect of residence time on removal efficiency at 800°C: (a) COD, (b) NH₃-N

3.5. The formation of NO

The pyrolysis and oxidation of NH₃-N and N-containing heterocyclic compounds yielded N₂ and NO_x, which was mainly composed of NO. Figure 8 illustrates the effects of reaction atmosphere and oxygen concentration on the formation of NO. As shown in Figure 8(a), the formation of NO fluctuated at 20 mg/m³ under reductive atmosphere, and slowly increased to 118 mg/m³ at 1200°C under inert atmosphere. As mentioned in Section 3.1, ammonia decomposed into N-atoms, and then N-atoms combined into N₂ without the participation of oxygen. In addition, less NO was influenced by the presence of CO in reduced atmosphere, which tended to generate additional radicals by the branching CO oxidation and then participated in the reduction process (Błaszczuk, Nowak & Jagodzki, 2013). The formation of NO under oxidative atmosphere differed from that under other atmospheres. NO reached the maximum value 230 mg/m³ at 800°C, then decreased along with reaction temperature, and finally increased up to 187 mg/m³ at 1200°C. Similar tendencies were obtained under 5% O₂ and 30% O₂ atmosphere, as presented in Figure 8(b). As denoted in overall reactions (Mei *et al.*, 2016), more ammonia can be oxidised into NO with the increase of temperature, and NO reduction with ammonia occurred with a narrow temperature window (roughly 800-1000°C) without any additives, which was in agreement with Ling's work (Liang *et al.*, 2014). Thus, the chemical equilibrium of oxidation reaction and reduction reaction was reached at 800°C. After the depletion of

NO in the temperature window, the formation of NO increased monotonously with elevated temperature in the range of 1000-1200°C.

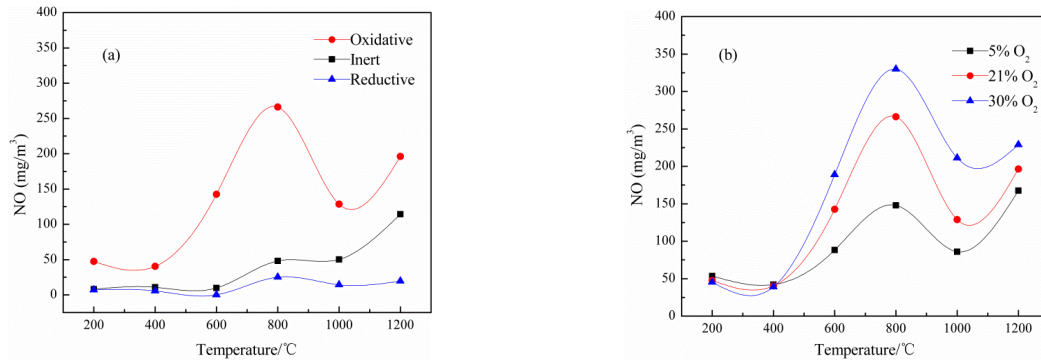


Figure 8: Variation of NO with reaction temperature: (a) reaction atmosphere; (b) oxygen concentration

3.6. Kinetic study

The kinetic analysis was carried out to further understand the thermal degradation characteristics of contaminants in wastewater. This experiment involved a series of pyrolysis and combustion reactions, and COD, NH₃-N removal efficiency were chosen as the representatives of thermal degradation of complex organic contaminants.

Referring to the similar kinetic study of black liquor (Cao *et al.*, 2011) and ammonia (Monnery *et al.*, 2001), the reaction was assumed to be a pseudo-first order reaction in this paper. Therefore, the chemical reaction rate can be shown as follows.

Equation 7:
$$-\frac{d[C]}{dt} = k[C]$$

Where:

- C = concentration of COD or NH₃-N (mg·mL⁻¹),
- t = residence time (s),
- k = reaction rate constant (s⁻¹).

In order to calculate the kinetic parameters, thermal degradation of coal-gasification wastewater was conducted ranged from 400°C to 1000°C and residence time of 0.34-2.74s. The variation of k with temperature T can be expressed with the form of Arrhenius equation

Equation 8:
$$k = A \exp\left(-\frac{E}{RT}\right)$$

Where:

- A = apparent pre-exponential factor (s⁻¹),
- E = apparent activation energy (kJ·mol⁻¹),
- R = universal gas constant (kJ·mol⁻¹·K⁻¹).

Through linear regression, kinetic parameters can be obtained at different atmospheres, as shown in Table 4. The activation energy in different atmospheres was ranking in the order: oxidative < inert < reductive, indicating that thermal degradation of contaminants in wastewater was easiest in oxidative atmosphere. In view of high correlation coefficients, the pseudo-first order reaction assumption was relatively reliable and capable to this study.

Table 4: Kinetic parameters of COD and NH₃-N

Indice	COD			NH ₃ -N		
	oxidative	inert	reductive	oxidative	inert	reductive
$E/\text{kJ}\cdot\text{mol}^{-1}$	34.39	46.99	58.16	41.25	56.08	61.75
A/s^{-1}	3.63×10^3	2.69×10^5	1.62×10^6	1.58×10^4	5.89×10^5	8.71×10^5
R^2	0.9869	0.9876	0.9886	0.9889	0.9867	0.9899

Figure 9 illustrates the Arrhenius plots between experimental and fitting data in different reaction atmospheres. Considering the main content in wastewater, the kinetic parameters of thermal degradation of coal-gasification wastewater was represented by a chemical reaction of phenols and ammonia. Nowadays, scholars worldwide have carried out kinetic analysis of phenols and ammonia. Horn (Horn *et al.*, 1998) measured the Arrhenius expression of dominant initiation reaction of phenol pyrolysis to be $1.0\times 10^{12}\exp(-254.41/RT) \text{ s}^{-1}$. The activation energy for phenol dimerization and dehydroxylation are 88 and 201 $\text{kJ}\cdot\text{mol}^{-1}$, respectively (Huelsman & Savage, 2013). Rahinov *et al.* measured the absolute concentration of NH₂ radicals during the process of ammonia pyrolysis in the temperature of 800-1000 K, and the activation energy obtained for the process was about $125_{-10}^{+20} \text{ kJ}\cdot\text{mol}^{-1}$ (Rahinov *et al.*, 2003). Monnery *et al.* studied the pyrolysis of NH₃ under Claus furnace and obtained activation energy $E_a = 69.05 \text{ kJ}\cdot\text{mol}^{-1}$ (Monnery *et al.*, 2001). The activation energies obtained in our experiments were smaller than the results from the references mentioned above. It is inferred that in comparison with the simple substances in those previous experiments, mixture solutions were used in our experiments and the interactive reaction between hydrocarbon radicals and N-containing compounds were supposed to be considered (Alzueta, Glarborg & Dam-Johansen, 1997; Liu, C., Zhang & Yin, 2014). The high R-square of Arrhenius fitting indicated that the pseudo-first order assumption was reliable for kinetic analysis of COD and NH₃-N removal in the coal-gasification wastewater treatment.

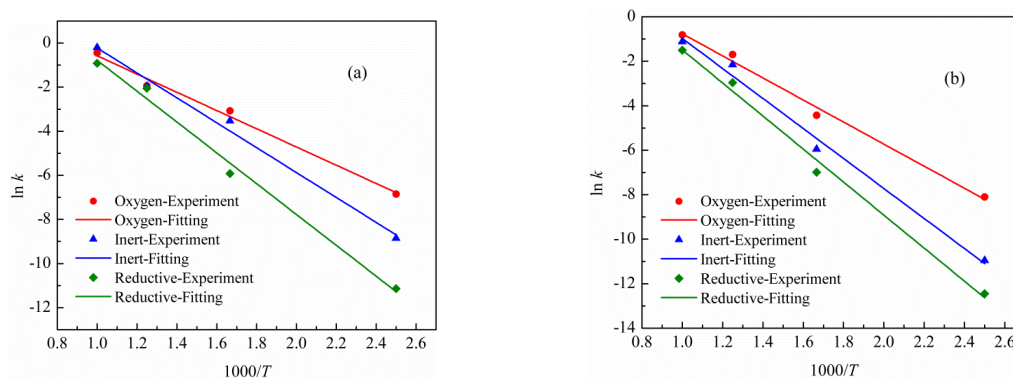


Figure 9: Arrhenius fitting of COD and NH₃-N in different reaction atmospheres: (a) COD; (b) NH₃-N

4. CONCLUSIONS

An alternative approach of wastewater utilisation in coal-gasification process was proposed and evaluated. Coal-gasification wastewater sprayed into the gasifiers as a substitute for pure steam can achieve water savings and contaminants degradation. Thermal removal of COD and NH₃-N was investigated using a lab-scale entrained-flow reactor. The experimental results showed that mainly removal of COD and NH₃-N occurred in the temperature range of 600-1000°C and 400-800°C, respectively. The organic constituents in the wastewater can be more efficiently decomposed in oxidative atmosphere, while less efficiently decomposed in reductive atmosphere. In addition, the removal efficiency of COD and NH₃-N exhibited a rising tendency with the increased oxygen concentration. Longer residence time promoted thermal decomposition of organic matters in different atmospheres. The existing operation process can meet the requirement obtaining high removal efficiencies and the cost of facility reconfiguration will be reduced to a large extent. Furthermore, the apparent activation energy for COD and NH₃-N removal efficiency were obtained in the range of 34.39-58.16 $\text{kJ}\cdot\text{mol}^{-1}$ and 41.25-61.75 $\text{kJ}\cdot\text{mol}^{-1}$, respectively. The

high correlation coefficient indicated that the pseudo-first order assumption was reliable for kinetic analysis of COD and NH₃-N removal.

5. REFERENCES

Alzueta, M.U., P. Glarborg, and K. Dam-Johansen, 1997. Low temperature interactions between hydrocarbons and nitric oxide: An experimental study. *Combustion and Flame*, 109(1-2): 25-36.

Angeles-Hernández, M.J., G.A. Leeke, and R.C. Santos, 2008. Catalytic supercritical water oxidation for the destruction of quinoline over MnO₂/CuO mixed catalyst. *Industrial & Engineering Chemistry Research*, 48(3): 1208-1214.

Błaszczuk, A., W. Nowak, and S. Jagodzik, 2013. Effects of operating conditions on deNO_x system efficiency in supercritical circulating fluidized bed boiler. *Journal of Power Technologies*, 93: 1-8.

Board, S.E.P.A.E., 2012. *Water and wastewater monitoring analysis method*. Beijing: China Environmental Science Press.

Cao, C., et al., 2011. Hydrogen production from supercritical water gasification of alkaline wheat straw pulping black liquor in continuous flow system. *International Journal of Hydrogen Energy*, 36(21): 13528-13535.

Chang, Y., et al., 2015. Rapid nonylphenol degradation in wastewater sludge using microwave peroxide oxidation with nitric acid. *Environmental Progress & Sustainable Energy*, 34(2): 520-525.

Clark, P., N. Dowling, and M. Huang. 1998. Ammonia destruction in the Claus furnace. *Proceedings of the Brimstone 1998 Sulphur Recovery Symposium*. Tucson, Arizona.

Erto, A., et al., 2013. A Comparison Between a Low-Cost Sorbent and an Activated Carbon for the Adsorption of Heavy Metals from Water. *Water, Air, & Soil Pollution*, 224(4): 1-10.

Gai, H.J., et al., 2016. Conceptual design of a modified phenol and ammonia recovery process for the treatment of coal gasification wastewater. *Chemical Engineering Journal*, 304: 621-628.

Gao, J., J. Lu, and J. Wang, 2010. *Pollution and control in coal chemical industry process*. Beijing: Chemical Industrial Press.

Gogate, P.R. and A.B. Pandit, 2004. A review of imperative technologies for wastewater treatment I: oxidation technologies at ambient conditions. *Advances in Environmental Research*, 8(3-4): 501-551.

Gogate, P.R. and A.B. Pandit, 2004. A review of imperative technologies for wastewater treatment II: hybrid methods. *Advances in Environmental Research*, 8(3-4): 553-597.

Hawboldt, K.A., 1998. Kinetic modelling of key reactions in the modified Claus plant front end furnace. *Department of Chemical and Petroleum Engineering*.

Horn, C., et al., 1998. Shock-tube study on the high-temperature pyrolysis of phenol. *Symposium (International) on Combustion*, 27(1): 321-328.

Huelsman, C.M. and P.E. Savage, 2013. Reaction pathways and kinetic modeling for phenol gasification in supercritical water. *The Journal of Supercritical Fluids*, 81: 200-209.

Ji, Q., et al., 2016. A review on the coal gasification wastewater treatment technologies: past, present and future outlook. *Journal of Cleaner Production*, 126: 38-55.

Kaul, S.N., et al., 1998. Application of full-scale evaporation-incineration technology for hazardous wastewater. *Water Science and Technology*, 38(4-5): 363-372.

Li, C. and L. Tan, 2000. Formation of NO_x and SO_x precursors during the pyrolysis of coal and biomass. Part III. Further discussion on the formation of HCN and NH₃ during pyrolysis. *Fuel*, 79(15): 1899-1906.

Li, J. and A.R.P. Van Heiningen, 1990. Kinetics of carbon dioxide gasification of fast pyrolysis black liquor char. *Industrial & Engineering Chemistry Research*, 29(9): 1776-1785.

Li, J.F., et al., 2016. Advanced treatment of biologically treated coking wastewater by membrane distillation coupled with pre-coagulation. *Desalination*, 380: 43-51.

Li, P., et al., 2015. Pretreatment of coal gasification wastewater by adsorption using activated carbons and activated coke. *Colloids and Surfaces A: Physicochemical and Engineering Aspects*, 482: 177-183.

Liang, L., et al., 2014. Influence of mixing, oxygen and residence time on the SNCR process. *Fuel*, 120: 38-45.

Lin, J., Q. Weng, and N. Taketa, 2009. Release of NO_x and its precursors during coal gasification. *Journal of Engineering Thermophysics*, 30: 1593-1596.

- Liu, C., C. Zhang, and R. Yin, 2014. A study on NO reduction by biomass tar-using phenol as a model compound of tar from updraft biomass gasification. *Environmental Progress & Sustainable Energy*, 34: 47-53.
- Liu, H., et al., 2008. Experimental investigation on the conversion of nitrogenous gas products during coal pyrolysis. *Journal of Fuel Chemistry and Technology*, 36(2): 134-138.
- Luo, L., et al., 2015. Experimental determination and correlation of liquid-liquid equilibria for the ternary system 2-methoxy-2-methylpropane β o-cresol β water at 298.15 K and 313.15 K. *Journal of Chemical & Engineering data* 60(5): 1396-1400.
- Martínez-Quiroz, M., et al. Innovative uses of carbamoyl benzoic acids in coagulation-flocculation's processes of wastewater. *Chemical Engineering Journal*.
- Mei, Y., et al., 2016. Selective non-catalytic reduction of flue gas in a circulating fluidized bed. *Energy Sources, Part A: Recovery, Utilization, and Environmental Effects*, 38(7): 921-927.
- Miller, J.A., et al., 1983. Kinetic modeling of the oxidation of ammonia in flames. *Combustion Science and Technology*, 34(1-6): 149-176.
- Monnery, W.D., et al., 2001. Ammonia pyrolysis and oxidation in the Claus furnace. *Industrial & Engineering Chemistry Research*, 40(1): 144-151.
- Rahinov, I., et al., 2003. NH₂ radical formation by ammonia pyrolysis in a temperature range of 800-1000 K. *Applied Physics B*, 77(5): 541-546.
- Romero Pareja, P.M., et al., 2016. Changes in enzymatic and microbiological activity during adaptation of a conventional activated sludge (CAS) to a CAS-oxic-settling-anaerobic (OSA) adapted process. *Desalination and Water Treatment*, 57(6): 2719-2725.
- Shang, B. and L. Gu, 2012. Research progress on wastewater treatment technology of coal gasification. *Chemical Industry and Engineering Progress*, 31: 182-185.
- Wang, W., et al., 2011. Treatment of coal gasification wastewater by a two-continuous UASB system with step-feed for COD and phenols removal. *Bioresource Technology*, 102(9): 5454-5460.
- Wang, Y.Z., et al., 2012. Oxidative degradation of Lurgi coal-gasification wastewater with Mn₂O₃, Co₂O₃, and CuO catalysts in supercritical water. *Industrial & Engineering Chemistry Research*, 51(51): 16573-16579.
- Wang, Y.Z., et al., 2014. Oxidative degradation of Lurgi coal gasification wastewater: Optimization using response surface methodology. *Environmental Progress & Sustainable Energy*, 33: 1258-65.
- Wang, Z.X., et al., 2012. Removal of COD, phenols and ammonium from Lurgi coal gasification wastewater using A₂O-MBR system. *Journal of Hazardous Materials*, 235-236(0): 78-84.
- Wright, F.J., 1960. Gas phase oxidation of the xylenes, General kinetics. *The Journal of Physical Chemistry*, 64(12): 1944-1950.
- Xiao, S. and J. Ma, 2012. Review of the incineration process for the treatment of industrial wastewater. *Industrial Water Treatment*, 32(6): 16-19.
- Xing, Z.-P., et al., 2014. Treatment of antibiotic fermentation-based pharmaceutical wastewater using anaerobic and aerobic moving bed biofilm reactors combined with ozone/hydrogen peroxide process. *Environmental Progress & Sustainable Energy*, 33(1): 170-177.
- Zhao, Q. and Y. Liu, 2016. State of the art of biological processes for coal gasification wastewater treatment. *Biotechnology Advances*, 34(5): 1064-1072.
- Zhong, X. and J.W. Bozzelli, 1998. Thermochemical and kinetic analysis of the H, OH, HO₂, O, and O₂ Association Reactions with cyclopentadienyl radical. *The Journal of Physical Chemistry A*, 102(20): 3537-3555.
- Zhuang, H., et al., 2015. Advanced treatment of biologically pretreated coal gasification wastewater by a novel heterogeneous Fenton oxidation process. *Journal of Environmental Sciences*, 33: 12-20.

#376: Developing an integrated Building Information Management (BIM) guideline for educational campuses facility management:

The case of Jordan University of Science and Technology

Jaser MAHASNEH¹, Mais MOMANI²

¹Jordan University of Science and Technology, Jkmahasneh@just.edu.jo
²Jordan University of Science and Technology, mais.momani@hotmail.com

This research aims to build an integrated Building Information Management (BIM) framework for the campus' facilities management at Jordan University of Science and Technology (JUST) to support improvements in the operation and maintenance practices by lightening the application of BIM in existing buildings' facility management and benefit from all its privileges. A literature review helped to understand generic BIM implementation. Four case studies of educational institutions which have BIM framework and guidelines were investigated and analysed, then a cross comparison between the cases was carried out to determine the baseline and the common outlines. Then the current operation and maintenance practices at JUST was studied and analysed by interviewing the involved personnel and observing the facility management practices. The outcomes were validated and finally BIM guidelines for JUST were proposed. It was found that working with a well-designed BIM framework can support sustainable improvements in the operation and maintenance practices, transform the manual process to be digital, improve the accuracy of data, records and outcomes, and reduce the interoperability cost, time, and resources. It is hoped that this framework will help the Jordanian educational institutions to comfortably adopt BIM.

Keywords: Building Information Modelling; BIM; facility management; educational campuses

1. INTRODUCTION

Implementing a BIM framework for the construction industry is a serious step towards improving the quality of projects and dealing with project development challenges (Ansah and Sorooshian 2017) since the construction industry is recognised in many countries as the most challengeable industry (Haron 2013). It is the first stage to creating a roadmap to developing a more sustainable 3D digital smart city, campus and buildings in Jordan.

BIM has benefits in providing accurate and relevant information in real-time for facility management throughout the lifecycle of a project by filling the gap in communications between the design and the construction phases on the one hand and in the operational phase for the improvement of the effectiveness of the facility management on the other hand (Haines 2016).

The operational phase is the largest fraction of the building lifecycle costs; studies on building estimations confirmed that operation and maintenance costs are five to seven times higher than the initial investment costs (Lee, An et al. 2012), and three times higher than the construction costs (Yalcinkaya and Singh 2014). Thus, the considerable environmental and economic needs provide a necessity for efficient management of both new and existing building facilities (Kassem, Kelly et al. 2015). Even though the industry recognises the great value of BIM in facility management (FM) (Patacas, Dawood et al. 2015), the potential benefits of BIM in operation and maintenance management are still a new area of study (Eastman, Teicholz, Sacks, & Liston, 2011). The use of BIM in the operation and maintenance phases of construction is still limited (Dong, O'Neill et al. 2014).

The implementation of BIM in Jordan is still in the initial phase. In spite of the benefits of applying BIM processes, it confronts critical obstacles like the lack of government encouragement, the absence of BIM knowledge, the absence of BIM implementation strategies and standards, the cost of BIM staff and training, and the fear of change (Matarneh and Hamed 2017).

This study delivers a framework for BIM implementation in JUST campuses by illustrating the application of BIM in facility management and potential advantages in utilising BIM in existing buildings in order to reduce the interoperability costs, maintenance costs and improving the facility management process through the building lifecycle. Having a model with database (data management) for the university buildings would shorten the road for any future studies or extensions.

This study focused on the operation and maintenance phase for creating a building information modelling framework for educational institutions by cultivating the current manual processes of information delivery, which leads to improving the facility management data accuracy. Creating an integrated BIM framework for educational campuses facilities management will allow the facility managers to realise the maintenance records, used materials, and other associated information, which make the operation and maintenance process more effective and efficient.

2. METHODS

In order to achieve the research aims, two types of qualitative research methods were used: the first one was the case study approach (multiple case studies type was used in this research), then a cross comparison between them to determine the baseline and the common outlines. The second approach was through interviews, according to Saunders (Saunders 2009) this approach helps to answer the "what, where, how many and how much" questions. This approach can be a good method for making comparisons between the standards and the current situation by determining a benchmark to rely on. The facility management current practices at JUST were investigated by interviewing the relevant personnel and observing their practices, then the outcomes were validated, and finally the BIM guidelines for JUST were proposed. Figure 61: Research procedure.

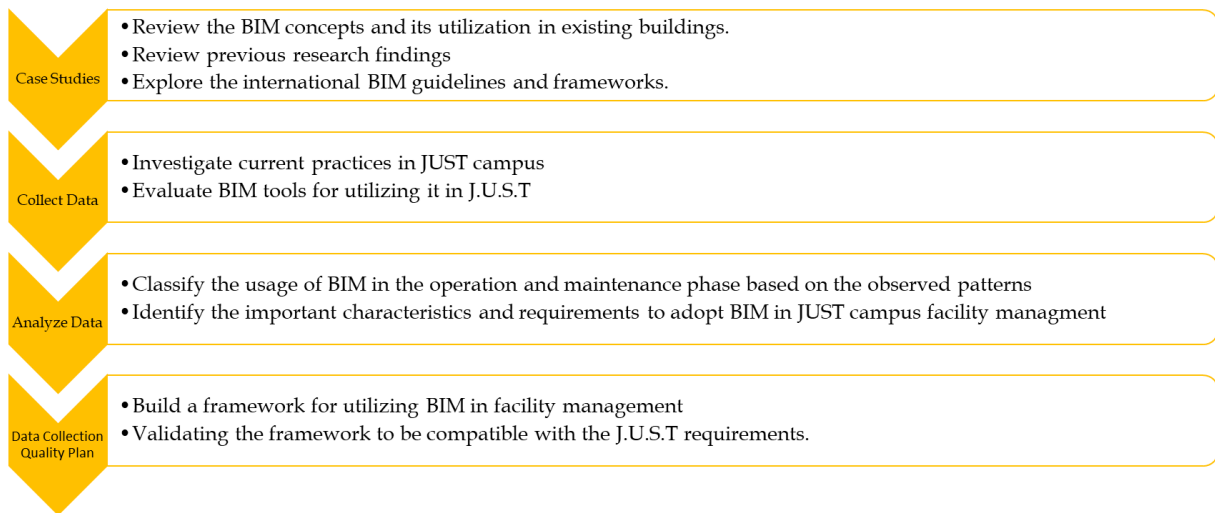


Figure 61: Research procedure

2.1. Case studies

Regarding the lack of protocol and standards in BIM adoption (NBS 2018), the case study analysis was used to set a comprehensive template for using BIM at different phases and stages. This helped to structure a general template to identify the best practices and to demonstrate a baseline for fields of application required data, common elements and keywords, tools and modelling techniques, standards and table of contents for structuring a framework and strategies for adopting BIM in the F.M process at JUST University. Figure 62: Case study procedure.

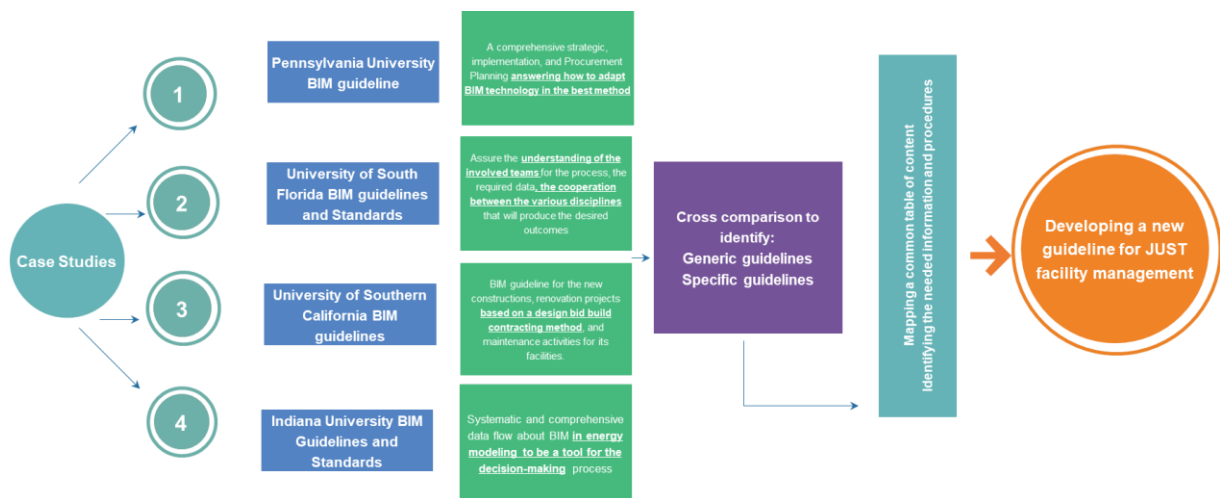


Figure 62: Case study procedure

3. INTERVIEWS AND OBSERVATION

A series of interviews were conducted with key experts (engineers and directors) who managed departments related to facility management in JUST and who had wide experience in the field. The interviews were intended to present and elaborate the proposed guideline and its added value to the facility management practices, discuss the process and take feedback to validate the guidelines. The proposed guidelines received good feedback from the experts, and they agreed on the benefits for integrating BIM into facility management process and for considering this document as a standard for existing facilities and for any new construction project. Figure 63: Data collection steps.

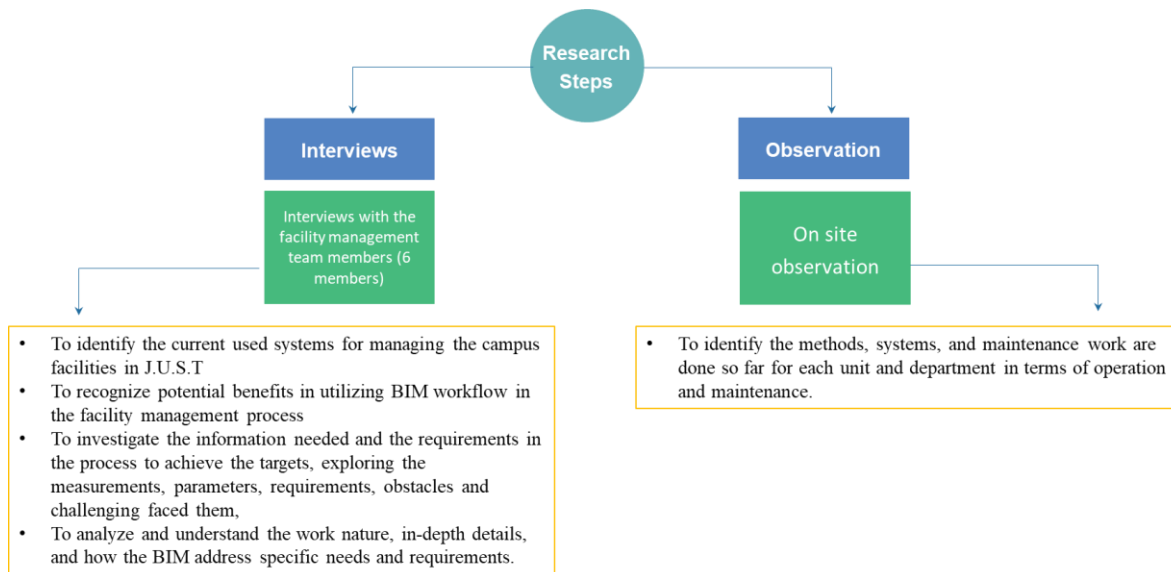


Figure 63: Data collection steps

This research used two main steps as follows:

- *Interviews:* Interviews with the facility management team members (6 members) were conducted to identify the current systems used for managing the campus facilities in JUST; to recognise potential benefits in utilising BIM workflow in the facility management process; to investigate the information needed and the requirements in the process to achieve the targets, exploring the measurements, parameters, requirements, obstacles and challenges facing them; and to analyse and understand the work nature, in-depth details, and how the BIM address specific needs and requirements.
- *Observation:* On-site observation was done to identify the methods, systems, and maintenance work carried out by each unit and department in terms of operation and maintenance.

4. THE ANALYSIS

4.1. Case studies

After investigating the case studies, and for a better implementation of BIM into the facility management practices, a comprehensive BIM guideline for campus planning was developed to assure adopting BIM for the campus' building's lifecycle. The proposed guideline was considered as the first step to implementing BIM into the facility management practices. The guideline contained a common framework for BIM guides and demonstrated the information required to be attached to the model, roles and responsibilities, standards and requirements. Table 28: BIM guideline table of content and chapters.

Table 28: BIM guideline table of content and chapters

Chapter	Name	Content brief	Standards
One	Introduction	This chapter provides a description of BIM, the scope of work, the procedures to be followed to successfully adopt BIM in the campus planning and facility management	Omniclass www.bim.psu.edu
Two	Requirements	This chapter sets the required technical criteria to utilise BIM in JUST campus' projects including: 1. Model Requirements 2. Software authorisation and collaboration: 3. Digital Submissions requirements 4. Geo-referenced model and geographical location 5. The level of development 6. BIM Execution Plan	BIMForum_LOD AIA E202 LOD UI Execution Plan

7. Needed Information

Three	Deliverables	This chapter sets the required deliverables should be submitted after each phase to assure linking all the related data to the BIM model, this chapter includes: <ol style="list-style-type: none"> 1. Milestones and Deliverable Schedule 2. Model and data delivery 3. COBie spreadsheet standards 4. Project phases requirements 	COBie: wbdg.org/resources/cobie.php Omniclass tables
Four	Integration and Coordination Procedures	This chapter defines the coordination between the involved team to assure the proper collaboration and coordination between disciplines to develop the model and model view extraction structure for all the construction document files, this chapter includes: <ol style="list-style-type: none"> 1. Subcontractor Coordination 2. Digital Fabrication 3. Suggested Coordination Process 4. Clash detection process 	Collaborative production of architectural, engineering and construction information – Code of practice – BS USC – Appendix A
Five	Roles and Responsibilities	BIM planning committee: BIM Champion Executive Representation Middle Management Representation Technical Workforce Representation Units and Departments involved in the process	
Sex	Education and Training	This chapter defines the needed steps to pave the road for all the involved member to better understanding BIM and prepare the infrastructure to implement this guideline This chapter includes: <ul style="list-style-type: none"> - Education - Training 	

4.2. Analysing JUST facility management current practices:

After analysing the current practices of facility management, it was found that there were no holistic facility management practices at JUST; there were individual operational and maintenance practices and a lack of updated technological maintenance and management system. Even though there were some new technologies used in some of the campus buildings, there was still a need for a holistic system to cooperate, manage, and control all the working systems under the Building Management System (BMS) to enhance the work environment. Table 29: The facility management used systems.

Table 29: The facility management used systems

System	Buildings	Benefits
Building Management System (BMS)	the medicine major's faculty GYM & Stadium	1. Fire-fighting and fire alarms 2. Monitoring and controlling the electrical and mechanical operations
Ascent Compass system	The presidency building	3. Internal temperature 4. Internal humidity
TAC Xenta system	The lecture halls	5. Switch on/off timer
Firefighting & alarms (Advanced)		6. Real-World workflow
Desigo Insight system	Library Zone	7. Providing visuals

	And others.....
JUST Operation and Maintenance Management System (Working partially)	1. Financial Claims 2. Equipment and tools 3. Work applications 4. Operations 5. Online Maintenance Requests 6. Determine Equipment types and Numbers 7. Materials used and their expiry dates And others....

4.3. Identifying the gaps and the potential to implement BIM in JUST campus facility management

After the completion of a building, the contractor hands over a large amount of information and documents related to the building generated from the previous construction phases, including the as-built drawings and documents, the equipment manuals, the warranties and any other necessary documents. Often, a large amount of time, money, and effort is then spent in winnowing and investigating all these documents to formulate operational and maintenance systems and processes.

At this point gaps emerge where some required information from the O&M perspective is missing or incomplete which leads to inefficient processing due to obsolete technological transformation systems, which in turn leads to delays and time-consuming validation of information (Sattenini A. 2011). Some of the gaps can be bridged by implementing a BIM for FM, mentioned below:

Efficient work procedures and decision-making process.

The process is mainly manual with a large amount of data required in the facility management process, found in papers, documents, or through personnel experience. In emergencies, a prompt reaction is required to solve a problem which can affect the users or the educational process in general. Detecting the problem in an automated and mobile localised system is essential in the maintenance process, which would allow an easy way to point to breakdowns, allow safer and more secure arena for the workers, save effort and extra maintenance costs and be a more sustainable process. Having a database with all this data can help to detect problems faster, recording previous maintenance works, notifying staff about preventive maintenance schedules, and providing full details about the equipment list and the materials used.

Records and as-built data accuracy

There can be a significant difference between original drawings of a building (paper-based documents) and the AutoCAD drawings of the area, with imprecise measurements and huge distortions. This can happen because there is no reference point to rely on when drawing the plans and there are no coordinating systems in general. Also, it can differ in the level of detail shown. This inaccuracy can cause many challenges in maintenance works and Space Management. Therefore, the existence of accurate architectural, structural, mechanical and plumbing plans is something that requires immediate action to unify work processes and reduce maintenance work errors. The existence of previous maintenance work records with full details and attributes helps to determine the breakdown cause and reacting faster for reparations. Having continuous studies on buildings' operations and efficiency can improve efforts, works, and identify the proper, suitable, sustainable budget, materials and supplies.

Some systems work partially

Having facility management systems to monitor and control the operation and sometimes to help detect breakdowns is a good starting point, but some of these systems are only working partially, with not all of the tools and options activated so the process may return to being a manual system again.

Lack of a sustainable and strategic plan

Determining the appropriate plan when a holistic strategic plan is available can enhance the work environment by being more organised through automation.

5. THE CONCLUSION

After understanding the nature of the campus facility management practices and the required data, and through case studies and literature review of guidelines for other universities using BIM, a BIM framework for JUST campus buildings' facility management was developed. This should meet the needs of relevant staff and help to solve

conflicts and be considered as a tool for decision-makers in facility management. Also it will aid successful implementation in the facility management process, highlighting the main uses, deliverables, requirements, roles and responsibilities, and other fundamental outlines and standards which should be taken into consideration.



Figure 64: BIM framework for JUST campus existing buildings' facility management

6. THE FINDINGS

The research revealed that there was great potential and added value in applying BIM to facility management practices at JUST, helping to minimise the post-occupancy costs, optimise time and resources, enhance the work environment, and to coordinate the work process through the building life cycle phases.

The findings for this research demonstrated as follows:

1. Implementing BIM for facility management practices has potential and added value for improving the system
2. Creating a digital campus can benefit the working staff and the academic staff.
3. The facility management system used in JUST is still a manual and paper-based process; BIM can play a significant role in transforming it into a digital process.
4. Data is not fully recorded in one server or database: using a BIM platform can record all the facility management activities, records, and make the data more accessible.
5. There is a difference between the original drawings (paper-based) and the created AutoCAD drawings for the campus buildings. BIM can improve the data flow between the teams and the involved parties, which leads to having an accurate updated data.
6. Integrating a BIM system can improve the order of work in terms of speed, needed data, resources, and visualising the proposed works.
7. The communication between the involved facility management units and departments needs to be enhanced: BIM can improve the workflow and bridge the communication gaps.
8. Using BIM in space management activities, can improve the quality of work, optimise resources, minimise the errors, reduce the post-occupancy costs and speed the process.
9. Using BIM system can be a great tool to analyse different sorts of data, identify breakdowns, and be a decision-making tool for the corrective, predictive, and preventive maintenance management actions.
10. The BMS system contains several operation systems working separately, each system serving one building or two maximum. BIM can unify and integrate the systems to join the platforms.

7. FUTURE STUDIES

The research established a framework or guideline for utilising BIM in facility management practices, however, JUST should steadily transform to BIM in a pilot project (small project), giving an improved opportunity to

successfully implement with quick and easy momentum. Additional work and further research should be carried out to:

1. link the separate operating systems and data and to understand how this data will affect the operation and maintenance system and determine the proper integration method.
2. Investigation in-depth how to integrate BMS with the BIM and choosing the software to fit JUST needs and requirements.
3. Determine how to use new technologies to automate the data process and information exchange
4. Determine the method to measure the existing buildings' dimensions and area (manual process, laser scanner, points to BIM....) to be used in the model-making phase.
5. Skilled personnel must be involved in the process to assure the models' quality so extensive training should be done for the suitable personnel or contracting a third party to assist in creating the models.
6. Explore the values when implementing this guideline in the construction industry firms.

8. REFERENCES

Ansah, R. H. and S. Sorooshian (2017). "Effect of lean tools to control external environment risks of construction projects." Sustainable Cities and Society **32**: 348-356.

Dong, B., Z. O'Neill and Z. Li (2014). "A BIM-enabled information infrastructure for building energy Fault Detection and Diagnostics." Automation in Construction **44**: 197-211.

Haines, B. (2016). The Benefits of Lifecycle BIM for Facility Management.

Haron, A. T. (2013). Organisational readiness to implement building information modelling: A framework for design consultants in Malaysia, University of Salford.

Kassem, M., G. Kelly, N. Dawood, M. Serginson and S. Lockley (2015). "BIM in facilities management applications: a case study of a large university complex." Built Environment Project and Asset Management **5**(3): 261-277.

Lee, S.-K., H.-K. An and J.-H. Yu (2012). An extension of the technology acceptance model for BIM-based FM. Construction Research Congress 2012: Construction Challenges in a Flat World.

Matarneh, R. and S. Hamed (2017). "Barriers to the Adoption of Building Information Modeling in the Jordanian Building Industry." Open Journal of Civil Engineering **7**(03): 325.

NBS (2018). National BIM Report 2018.

Patacas, J., N. Dawood, V. Vukovic and M. Kassem (2015). "BIM for facilities management: evaluating BIM standards in asset register creation and service life planning." Journal of Information Technology in Construction **20**(10): 313-318.

Sattenini A., A., S., & Thuston, J. (2011). "Preparing A Building Information Model For Facility Maintenance And Management." 28th International Symposium on Automation and Robotics in Construction, Seoul, South Korea: 144-149.

Saunders, M., Lewis, P. & Thornhill, A., (2009). "Research methods for business students,."

Yalcinkaya, M. and V. Singh (2014). Building information modeling (BIM) for facilities management—literature review and future needs. IFIP International Conference on Product Lifecycle Management, Springer.

#377: Bioenergy contributions to the renewable energy technology mix: research incursion in South Africa

Andrew C.ELOKA-EBOKA

Discipline of Mechanical Engineering, School of Engineering, University of KwaZulu-Natal, Durban, SOUTH AFRICA. fatherfounder@yahoo.com

Renewable energy from biomass, biofuels and biodiesel encapsulated as bioenergy has become an interesting aspect of clean energy technology and is currently receiving global attention. Bioenergy produced using several technologies derived from renewable feedstocks and sustainable wastes was the focus of this research. In South Africa, bioenergy in the form of solids, liquids and gaseous fuels have been characterised as first, second and third generation (1D, 2D and 3D) systems in order to solve myriads and most critical energy aspects of the sustainable development goals of Africa. The technologies evolved have been directed to specific bioenergy feedstocks and needs for optimal utilisation and application and they include direct combustion (for power generation), anaerobic digestion (for methane-rich gas production), fermentation (of sugars for alcohols as fuels), oil extraction and transesterification (for biodiesel as fuels), pyrolysis (for biochar, gas and oils for fuel and chemicals), gasification (for carbon monoxide and hydrogen-rich syngas as fuels and value added products) and generalised thermo-chemical conversion. The technologies are further driven by arrays of secondary treatments (stabilisation, dewatering, upgrading, refining) depending on specific final products. This article explores these and all such research and development (R&D) strategies and technological packages of bioenergy in South Africa. These have implications in the commercialisation, entrepreneurship, informing policy and direct impact in Africa's energy sustainability.

Keywords: bioenergy, biofuels, biomass, biodiesel, bio-product, bio-processing, bio-refineries.

1. INTRODUCTION

Bioenergy consists of solids, liquids and gaseous fuels. Liquid fuels can be used directly in the existing roads, railroad and aviation transportation network stock, as well as in engines and for power generation. Solid and gaseous fuels can be used for the production of power as well as for other purpose-driven direct or indirect turbine-equipped power plants. Chemical products can also be obtained from all organic matter produced. Additionally power and chemicals can come from the use of plant-derived industrial, commercial, or urban wastes, or agricultural or forestry residues. Biomass resources include primary, secondary, and tertiary sources of biomass. Primary biomass resources are produced directly by photosynthesis and are taken directly from the land (Anjos, 2013; Arts, 2007; Barbanera, 2016). They include perennial short-rotation woody crops and herbaceous crops, the seeds of oil crops, and residues resulting from the harvesting of agricultural crops and forest trees (e.g., wheat straw, corn stover, and the tops, limbs, and bark from trees). Secondary biomass resources result from the processing of primary biomass resources either physically (e.g., the production of sawdust in mills), chemically (e.g., black liquor from pulping processes), or biologically (e.g., manure production by animals). Tertiary biomass resources are post-consumer residue streams including animal fats and greases, used vegetable oils, packaging wastes, and construction and demolition debris. There are various conversion technologies that can convert biomass resources into power, heat, and fuels for potential use in UEMOA countries (Anjos, 2013; Arts, 2007). South Africa has huge potential for bioenergy production with abundant untapped flora, recycled feedstocks, farm produce, biomasses, municipal wastes and so on.

Biomass-derived energy currently accounts for about 3 quads (quadrillion Btu (British thermal units)) of total primary energy use in the United States. Of this amount, about 0.8 quads are used for power generation (Chadwick, 2000). Several biomass energy production technologies exist today which contribute to this energy mix. Biomass combustion technologies have been the dominant source of biomass energy production, both historically and during the past two decades of expansion of modern biomass energy in the US and Europe (Cheng, 2013). As a research and development activity, biomass gasification has usually been the major emphasis as a method of more efficiently utilising the energy potential of biomass, particularly wood. Gasification technology was first commercialised using coal, however biomass resources such as wood have a unique environmental advantage over traditional fossil fuels in that the gasification of biomass has a mitigating effect on global warming, when a renewable biomass fuel is used instead of a fossil fuel. Also, biomass feedstocks are typically lower in sulphur and nitrogen than most coals. Numerous biomass gasification technologies existing today are in various stages of development. Some are simple systems, while others employ a high degree of integration for maximum energy utilisation (De Lary, 2012; Eloka-Eboka, 2017). "Integration" refers in a general way to obtain heat and multiple products, in addition to electricity from the fuel or feedstock used. In a specialised way in gasification power systems, "integration" refers to use of the heat and steam flows from the gasification and gas cleaning steps in the process for enhancement of the other parts of the process. One important example of such integration is the use of steam raised in syngas cooling as part of the steam flow into the steam power section of an IGCC power plant. IGCC is an integrated gasification combined cycle (Hu, 2014; Lam, 2011; Ponnuswamy, 2014). Advanced biomass gasification offers the flexibility of producing a fuel gas with sufficient energy content to be utilised in advanced integrated combined cycle power systems (Lam, 2011). The higher energy content of the advanced biomass gasification processes also improves the capability for the biomass-derived gas to be further processed for chemical production. The purpose of this short communication study is to explore the bioenergy potential of South Africa and their contributions in terms of the various research strategies being conducted in harnessing and tapping them for the direct socio-economic impact on the rural communities. Some economic comparisons of generations of bioenergy are presented, different biomass gasification technologies, including the carbon dioxide emissions reduction and potentials of each. To accomplish this, a literature search was first conducted to determine which technologies were most promising based on a specific set of criteria. The technical and economic performances of the selected processes were evaluated using computer models and available literature. Evaluation methods developed by EPRI (the Electric Power Research Institute) were then used to determine the carbon dioxide reduction potential of the technologies (Kyoto Protocol, 1997).

2. RENEWABLE ENERGY TECHNOLOGIES

The renewable energy capabilities of South Africa employ the integration of one, two and more of the following technologies in different economic applications depending on provinces of abundance. The technologies developed and available for use in South Africa include the following:

- Wind turbines technologies
- Hydroelectric – SH, MH,PH
- Geothermal power
- Solar photovoltaics -Hybrids
- Solar thermal power -Hybrids
- Ocean current power technologies
- Tidal power technologies
- Hydrogen technologies

- Fuel Cells technologies
- Wave power technologies and
- Bioenergy – Biofuels, Biomass, Biodiesel

Bioenergy has been included as the last option as it is currently under development. The Department of Energy has realised the huge potentials available and has made policies and legislations to advance and establish the bioenergy sector including research works on advanced and sustainable biofuels and biofuels from wastes biomasses. Bioenergy consists of solids, liquids, and gaseous fuels. These have been classed as first generation (1G), second generation (2G) and third generation (3G) bioenergy from diverse feedstocks.

- Biomass: bio-diesel, ethanol, bagasse, wood, bark, coconut fibre, straw, hemp, peat, willow, switch grass, charcoal etc.
- Waste: tires, landfill gas, food waste, forest residue, coffee refuse, Christmas trees, poultry litter, packaging waste, Algae etc.

First Generation bioenergy are primary resources produced directly by photosynthesis and are taken directly from the land: woody crops and herbaceous crops, the seeds of oil crops, and residues resulting from the harvesting of agricultural crops and forest trees.

Advanced and sustainable bioenergy are produced from recycled products, sustainable biomasses and from wastes while second generation bioenergy are products of processing of primary biomass resources or secondary products. Third generation bioenergy are post-consumer residue streams. They also include bioenergy produced from wastes, micro-algae, macro-algae and all such tertiary feedstocks and so on.

2.1. Energy from biomass and biogas

Biomass is produced in nature through photosynthesis achieved by solar energy conversion. Biomass means organic matter. In simplest form the reaction is the process of photosynthesis in the presence of solar radiation and can be represented as: $\text{H}_2\text{O} + \text{CO}_2 + \text{Solar energy} \rightarrow \text{CH}_2\text{O} + \text{O}_2$. Biomass can be converted into fuels through a number of different processes including solid fuel combustion, digestion, pyrolysis, and fermentation and catalysed reactions. Electricity is generated in many places through solid fuel combustion (Rahaman, 2011). Biomass resources fall into three categories:

- Biomass in its traditional solid mass (wood and agricultural residue which can burn directly to obtain energy)
- Biomass in non-traditional form (converted into liquid fuels eg ethanol and methanol to be used in engines)
- Fermented anaerobically to obtain a gaseous fuel called biogas (comprising 55% to 65% Methane, 30% to 40% CO_2 and the rest impurities i.e. H_2 , H_2S and some N_2).

The main source for production of biogas is wet cow dung or wet livestock (and even human) waste. Biogas can be captured from marshes, from landfill or wastes such as sewage, and burned to produce electricity. It can also be generated intentionally through anaerobic composting. When refined, it can be used to power vehicles directly. Biogas can be produced from the decomposition of animal, plant and human waste. It is a clean but slow burning gas and usually has a calorific value between 5000 to 5500 kcal/kg. It can be used directly in cooking, reducing the demand for firewood. Moreover, the material from which the biogas is produced retains its value as a fertilizer and can be returned to the soil. Biogas has been popular with the name "Gobar Gas" mainly because cow dung has been the material for its production. It is not only the excreta from cattle but also the piggery waste as well as poultry droppings are very effectively used for biogas generation (Rogner, 1997). A few other materials through which biogas can be generated are algae, crop residues (agro-wastes), garbage kitchen wastes, paper wastes, sea wood, human waste, waste from sugarcane refineries, water hyacinth etc. Any cellulosic organic material of animal or plant origin, which is easily biodegradable, is a potential raw material suitable for biogas production (Shabani, 2016).

Table 1: First generation vs second generation bioenergy - biofuels

	1 st Gen.	2 nd Gen.
Biofuels readily usable in existing petroleum infrastructure	Yes	Yes
Proven commercial technology available today	Yes	No
Relatively simple conversion processes	Yes	No
Markets for by-products of fuel production needed	Yes	Yes/No
Capital investment per unit of production	Lower	Higher
Feedstock cost per unit of production	Higher	Lower
Total cost of production	High*	Lower
Minimum scale for optimum economics	Modest	Large
Land-use efficiency	Low	High
Direct food vs. fuel competition	Yes	No
Feasibility of using marginal lands for feedstock production	Poor	Good
Ability to optimize feedstock choice for local conditions	Limited	High
Potential for net reduction in petroleum use	Good*	Better
Potential for net reduction in fossil fuel use	Modest*	High
Potential for net reduction in greenhouse gas emissions	Modest*	High

* Except for first-generation Brazilian sugar cane ethanol, which would get a more favourable mark.

2.2. Industry standard tests for characterising biomass

Several of the industry standard tests for characterising biomass are described:

- *Total Solids*: A way to determine the moisture content within the sample.
- *Ash Determination*: The amount of inorganic or mineral material present in the sample.
- *Exhaustive Ethanol and Water Extractable*: The removal of non-structural material from the biomass sample to prevent interferences during other analyses, as well as free sugar determination.
- *Structural Carbohydrates*: The determination of glucose, xylose, galactose, arabinose and mannose concentrations in the sample; used to determine cellulose and hemicellulose concentrations in the biomass.
- *Acetyl Content*: Acetic acid concentration in the sample, may also include formic and levulinic acid content depending on the feedstock.
- *Lignin*: Determination of the structural plant material that does not contribute to the sugar content in the sample.
- *Starch Content*: Represents the readily available source of sugar within some feedstock.
- *Ethanol Content*: Analysis of fermentation broths using gas chromatography.
- *Bomb Calorimetry*: The determination of the sample's calorific value

3. BIOMASS PROCESSING TECHNOLOGIES

There are six generic biomass processing technologies based on:

- direct combustion (for power)
- anaerobic digestion (for methane-rich gas)
- fermentation (of sugars for alcohols)
- oil exaction (for biodiesel)
- pyrolysis (for biochar, gas and oils)
- gasification (for carbon monoxide and hydrogen-rich syngas).

These technologies can then be followed by an array of secondary treatments (stabilisation, dewatering, upgrading, refining) depending on specific final products. They are encapsulated on the following schematics in Figure 1

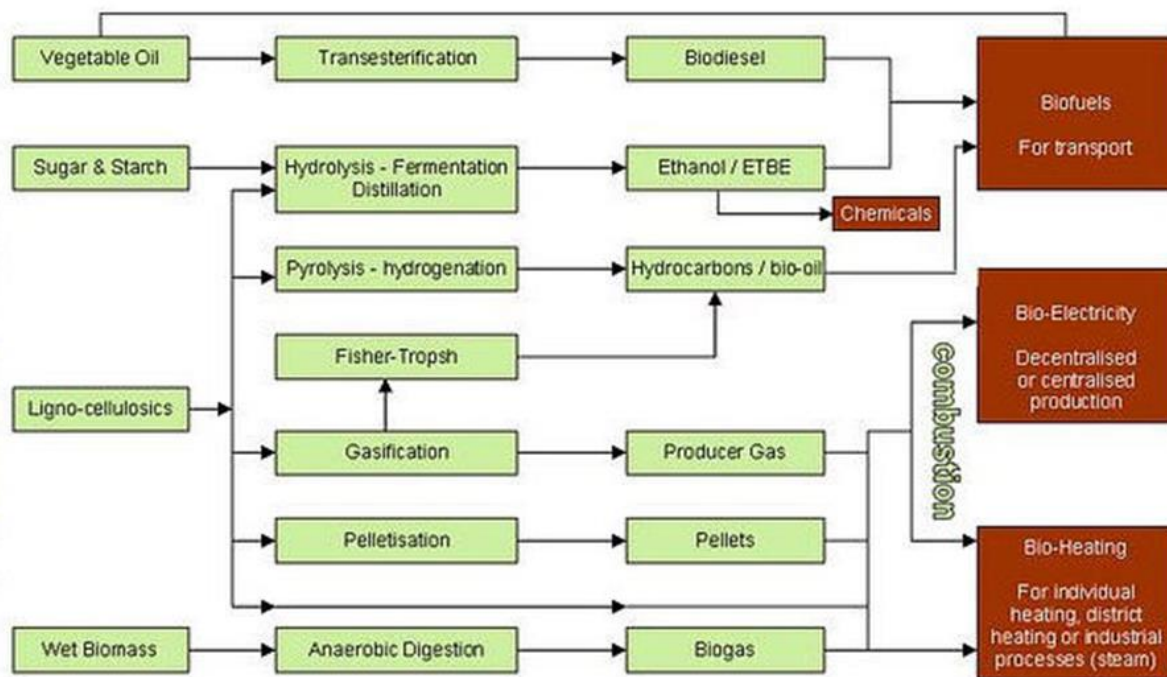


Figure 1: Schematic of bioenergy processing technology – an overview

3.1. Availability of biomass (sources of biomass)

Biomass resources fall into three categories: (i) Biomass in its traditional solid mass (wood and agriculture residue). In this process, the biomass burns directly and gets the energy. (ii) Biomass in non-traditional form (converted into liquid fuels). The biomass is converted into ethanol (ethyl alcohol) and methanol (methyl alcohol) (iii) fermenting the biomass anaerobically to obtain a gaseous fuel called biogas. Terrestrial crops include (1) sugar crops such as sugarcane and sweet sorghum; (2) herbaceous crops, which are non-woody plants that are easily converted into liquid or gaseous fuels; and (3) silviculture (forestry) plants such as cultured hybrid poplar, sycamore, sweet gum, alder, eucalyptus, and other hard woods. Animal and human waste are indirect crops from which methane for combustion and ethylene (used in the plastic industry) can be produced while retaining the fertilizer value of the manure. Aquatic crops are grown in fresh, sea and brackish waters, e.g. Sea weeds, marine algae.

3.2. Available quantity of energy

The available quantities of Energy include:

Calorific value

The heat of combustion (calorific value) is the total energy released as heat when a substance undergoes complete combustion with oxygen under standard conditions. It is measured in units of energy per unit of the substance, usually mass, such as: kJ/kg, kJ/mol, kcal/kg, Btu/lb. Heating value is commonly determined by use of a bomb calorimeter.

High calorific value

The quantity known as higher calorific value (HCV) is determined by bringing all the products of combustion back to the original pre-combustion temperature, and in particular condensing any vapour produced. Such measurements often use a standard temperature of 15°C. This is the same as the thermodynamic heat of combustion since the enthalpy change for the reaction assumes a common temperature of the compounds before and after combustion, in which case the water produced by combustion is liquid. The higher heating value takes into account the latent heat of vaporisation of water in the combustion products, and is useful in calculating heating values for fuels where condensation of the reaction products is practical (e.g., in a gas-fired boiler used for space heat). In other words, HCV assumes the entire water component is in liquid state at the end of combustion and that heat below 150°C can be put to use.

Low calorific value

The quantity known as lower calorific value (LCV) is determined by subtracting the heat of vaporisation of the water vapour from the higher heating value. This treats any H₂O formed as a vapour. The energy required to vaporise the water therefore is not released as heat (Hu, 2014). The LCV assumes that the latent heat of vaporisation of water in the fuel and the reaction products is not recovered. It is useful in comparing fuels where condensation of the combustion products is impractical, or heat at a temperature below 150°C cannot be put to use.

3.3. Biomass characteristics

Ultimate & Proximate analysis

Proximate analysis is used for calculation of chemical composition of the residue including moisture content, ash content, volatile matter and fixed carbon. Moisture content is one of the most important properties of biomass, over which its heating value depends. The moisture content is determined by drying the weighed amount of sample in an open crucible kept at 110°C in an oven for one hour by using standard oven dry method. The biomass sample is first ground to form fine powder, then this powdered sample is kept for determination of proximate analysis. Standard method for moisture determination involves heating of 1 gm biomass sample in a hot air oven to 110°C using the following equation. Moisture (% M) = $(W_1 - W_2) / W_3 \times 100$ W₁ = Weight of the crucible & the air dried sample (g), W₂ = Weight of the crucible & oven dried sample (g), W₃ = Weight of the air dried sample taken (g). The experimentation of moisture content determination is extended for measurement of ash content of biomass. The sample, obtained after determination of moisture content, is then heated to 750°C in a muffle furnace and is kept there for two hours or more till constant weight is recorded.

The weight of residue represents the ash content of the biomass. Ash is defined as the weight of the residue remaining after complete burning of 1gm of the biomass at 750°C. Ash (% A) = $(W_4 - W_5) / W_6 \times 100$ W₄ = Weight of the crucible & the oven dried sample (g), W₅ = Weight of the crucible & residue (g), W₆ = Weight of oven dried sample taken (g) Volatile matter (% VM) is determined by keeping the dried sample in a closed crucible at 600°C for 6 minute and then at 900°C for another 6 minute. The difference in the weight due to the loss of volatiles is taken as the total volatile matter present in the biomass. It is termed as the weight loss due to heating of 1gm of biomass at 900°C in furnace for 6 minutes. Weight loss due to VM = Total loss of weight- loss due to moisture. Fixed carbon (FC) content is found by applying the mass balance for the biomass sample. The carbon content determined through this method is not the actual carbon content present in biomass but only the non-volatile part of carbon content, as some of carbon present in biomass also escape along with the volatiles. The content of fixed carbon is determined by subtracting the sum of A %, VM & % M from total of 100% composition. FC= 100- (% A + % VM + % M). Ultimate Analysis is important for determining the elemental composition (C, N₂, H₂, S, O₂ etc.) of the biomass fuels & is also useful for calculating their heating value. The carbon and H₂ contents are determined by C-H-O analyser by standard method.

Further, knowing the ash content, O₂ is determined by difference. However, the samples must be dried prior to analysis. Nitrogen and sulphur are normally negligible. C-H-O analyser consists of an electric furnace, a sample column and absorbent column. The dry matter is powdered and weighed (w₁) before putting it in the sample column. The absorbent column is filled with a weighed quantity (w₂) of calcium hydroxide (Lam, 2011). Subsequently the furnace is started and O₂ from a separate O₂ cylinder is supplied to the sample column at a pressure of 4 Pa. A temperature of more than 1400°C is maintained for about 20 min. Then furnace is switched off and the fused sample is taken out and weighed (w₃). The calcium hydroxide from the absorbent column is also taken out and reweighed (w₄). From these observations the carbon content of the sample can be determined using the following relationship. The difference (w₄ – w₂) will give carbon dioxide formed. Carbon in absorbent (w₅) = $(w_4 - w_2) \times 12 / w_3$ % carbon in the sample = $w_5 \times 100 / w_1$

4. BIOMASS CONVERSION

Biomass can either be utilised directly as a fuel, or can be converted into liquid or gaseous fuels, which can also be used as feedstock for industries. Most biomass in dry state can be burned directly to produce heat, steam or electricity. On the other hand biological conversion technologies utilise natural anaerobic decay processes to produce high quality fuels from biomass (Ponnuswamy, 2014; Kyoto Protocol, 1997). Various possible conversion technologies for getting different products from biomass is broadly classified into three groups, viz. (i) thermo-chemical conversion, (ii) bio-chemical conversion and (iii) oil extraction. These alternative technologies for biomass conversion offer sound and alternative options for meeting the future fuels, chemicals, food and feed requirements (Rahaman, 2011; Rogner, 1997; Shabani, 2016; Singh & Singh, 2014; Van Den Hende, 2012). Three main approaches can be adopted for generation and utilisation of biomass: (i) Collection of urban and industrial wastes as supplementary fuel in boilers and as a feed stock for producing methane and some liquid fuels. (ii) Collection of agricultural and forest residues to produce fuels, organic manures and chemical feed stock. (iii) Growth of some

specific energy plants for use as energy feedstock and cultivation of commercial forestry, aquatic and marine plants for different products. Energy Resources: Development, Harvesting and Management (Vassilev, 2013)

Thermo-chemical conversion includes processes like combustion, gasification and pyrolysis. Combustion refers to the conversion of biomass to heat and power by directly burning it, as occurs in boilers. Gasification is the process of converting solid biomass with a limited quantity of air into producer gas, while pyrolysis is the thermal decomposition of biomass in the absence of oxygen. The products of pyrolysis are charcoal, condensable liquid and gaseous products. Biochemical conversion includes anaerobic digestion to produce biogas and fermentation to obtain alcohol fuels. The third approach is oil extraction. Edible and non-edible oils can be extracted from a variety of grains and seeds (Zhao, 2014; Zheng, 2012). They can be directly used as fuels by transesterification process to produce bio-diesel, which is a good substitute for conventional diesel oil. Thermal conversion processes for biomass involve some or all of the following processes:

- Pyrolysis: Biomass + heat + charcoal, gas and oil.
- Gasification: Biomass + limited oxygen + fuel gas
- Combustion: Biomass + stoichiometric O₂ + hot combustion products (Zheng, 2012).

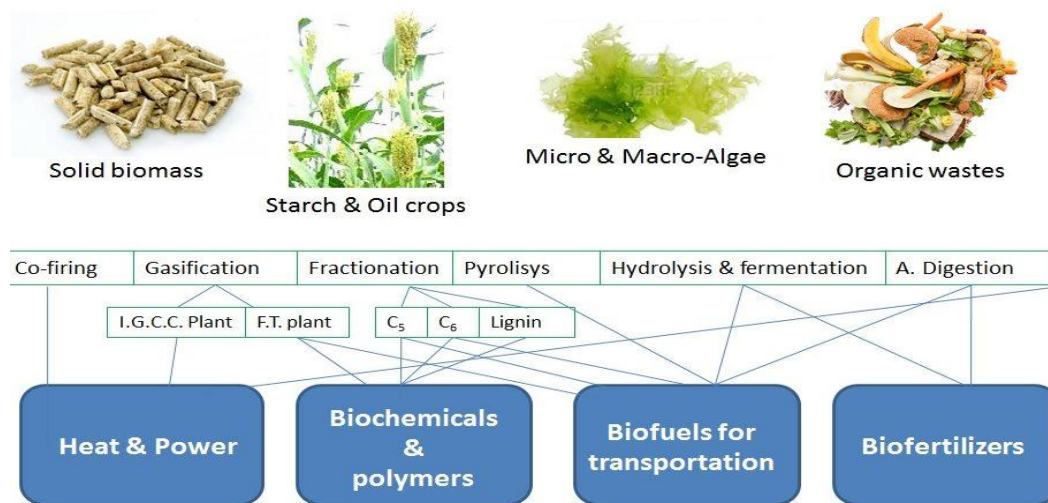


Figure 2: Feedstocks of Bioenergy and by-products and processes

4.1. R&D strategy and technology packages

In our institutions in South Africa, the following are our research strategies in exploring the contribution of research and development in Bioenergy:

- Enhancements to existing biomass resource assessment and management strategies to cover wider biomass resources and period of analysis.
- Advanced research addressing thermo-chemical conversion of biomass — combustion and gasification, with an emphasis on efficiencies and environmental compliance.
- Establishing of standards, best practices and monitoring protocols in the biomass-based projects.
- Development of technology packages for replacing fossil fuels in industries.
- Evolving of specifications and standards for biomass energy devices and providing technical support in establishing test centers.
- Engine research with special reference to Producer Gas Applications and adoption of Natural Gas engines for this.
- Exploring extent of potential for replacement of fossil fuel by biomass in sector-wise industrial and commercial usage.

4.2. Further some research insights

We have expanded our research scope and competencies to include wider research and development needs of the country. The most isolated case is the exploration of the use of sugar cane fibres and pith for producing briquettes and fuels pellets for various industrial, commercial and domestic purposes. They are also to be explored as hybrids briquettes and pellets in mix with existing charcoal briquettes which are so much in need for the braaiing

industry, a huge industry in South Africa. This isolated case of waste to energy from sugar cane bagasse is presented in Figure 3.

- Large Scale algae biomass Integrated Bio-refineries
- Prospects of biofuels and biodiesels from Micro-algal Technologies
- Production of Value-added products from Micro-algal Cultivation
- Modelling and simulation of integrated algal biomass bio-refineries
- Energy Requirement/Exergy of algal biomass integrated bio-refineries
- Integration of Flue gases/effluents for carbon sequestration: Algal biomass production
- Techno-economics of Renewable Energy Technologies
- Bio-Nanotechnology for Thermal/Energy Application
- Energy Efficiency for the South African Power Generating Industry
- Exploring the effectiveness of pith-fibre fractions separation: Sugarcane bagasse briquetting
- Photovoltaic Applications for Rural Electrification
- Integrating Technology and design research in Policy Framework
- Thermo-chemical conversions and valorisation of various biomass in Africa



Figure 3: Bioenergy from Waste: Charcoal and Sugar bagasse in South Africa – isolated examples

5. CONCLUSION

Bioenergy and its technologies have become an interesting aspect of clean energy technology and is currently receiving global attention. South Africa has also woken up to this need and have laid out several research and development strategies to institute this technology. Bioenergy from renewable feedstocks and sustainable wastes research and development were presented. The approach in the forms of solids, liquids and gaseous fuels have been characterised as first, second and third generations (1D, 2D and 3D) feedstocks have been to solve the sustainable development goals of Africa. The technologies evolved have been directed to specific bioenergy feedstocks and there is the need for optimal utilisation and application. This article explored these and all such research and development (R&D) strategies and technological packages of bioenergy in South Africa. These have implications in the commercialisation, entrepreneurship, informing policy and direct impact in Africa's energy sustainability. The exploration of sugar-cane bagasse biomass for use as briquette/pellet fuels are also presented and they have huge potential for one of the world's producers of sugar as second and third generations bioproduct as renewable fuels.

6. REFERENCES

- Anjos, M., Fernandes, B. D., Vicente, A. A., Teixeira, J. A., & Dragone, G. (2013). Optimization of CO₂ bio-mitigation by *Chlorella vulgaris*. *Bioresource technology*, 139, 149-154.
- Arts, R., Chadwick, R., Eiken, O., Trani, M., & Dortland, S. (2007). *Synthetic versus real time-lapse seismic data at the Sleipner CO₂ injection site*. Paper presented at the 2007 SEG Annual Meeting.

- Barbanera, M., Lascaro, E., Stanzione, V., Esposito, A., Altieri, R., & Bufacchi, M. (2016). Characterization of pellets from mixing olive pomace and olive tree pruning. *Renewable Energy*, *88*, 185-191.
- Chadwick, R., Holloway, S., Kirby, G., Gregersen, U., & Johannessen, P. (2000). *The Utsira Sand, Central North Sea—an assessment of its potential for regional CO₂ disposal*. Paper presented at the Proceedings of the 5th
- Cheng, J., Huang, Y., Feng, J., Sun, J., Zhou, J., & Cen, K. (2013). Improving CO₂ fixation efficiency by optimizing Chlorella PY-ZU1 culture conditions in sequential bioreactors. *Bioresource technology*, *144*, 321-327.
- De Lary, L., Loschetter, A., Bouc, O., Rohmer, J., & Oldenburg, C. (2012). Assessing health impacts of CO₂ leakage from a geological storage site into buildings: role of attenuation in the unsaturated zone and building foundation. *International Journal of Greenhouse Gas Control*, *9*, 322-333.
- Eloka-Eboka, A. C., & Inambao, F. L. (2017). Effects of CO₂ sequestration on lipid and biomass productivity in microalgal biomass production. *Applied Energy*, *195*, 1100-1111.
- Hu, Q., Zeng, R., Zhang, S.-X., Yang, Z.-H., & Huang, H. (2014). Production of microalgal lipids as biodiesel feedstock with fixation of CO₂ by Chlorella vulgaris. *Food Technology and Biotechnology*, *52*(3), 285-291.
- Lam, M. K., & Lee, K. T. (2011). Renewable and sustainable bioenergies production from palm oil mill effluent (POME): win-win strategies toward better environmental protection. *Biotechnology Advances*, *29*(1), 124-141.
- Ponnuswamy, I., Madhavan, S., Shabudeen, S., & Shoba, U. (2014). Resolution of lipid content from algal growth in carbon sequestration studies. *Int. j. Sci. adv. technol*, *67*, 23-32.
- Kyoto Protocol. (1997). United Nations framework convention on climate change. *Kyoto Protocol, Kyoto*, *19*.
- Rahaman, M. S. A., Cheng, L.-H., Xu, X.-H., Zhang, L., & Chen, H.-L. (2011). A review of carbon dioxide capture and utilization by membrane integrated microalgal cultivation processes. *Renewable and Sustainable Energy Reviews*, *15*(8), 4002-4012.
- Rogner, H.-H. (1997). An assessment of world hydrocarbon resources. *Annual review of energy and the environment*, *22*(1), 217-262.
- Shabani, M. (2016). CO₂ bio-sequestration by Chlorella vulgaris and Spirulina platensis in response to different levels of salinity and CO₂. *Proceedings of the International Academy of Ecology and Environmental Sciences*, *6*(2), 53.
- Singh, S., & Singh, P. (2014). Effect of CO₂ concentration on algal growth: a review. *Renewable and Sustainable Energy Reviews*, *38*, 172-179.
- Van Den Hende, S., Vervaeren, H., & Boon, N. (2012). Flue gas compounds and microalgae:(Bio-) chemical interactions leading to biotechnological opportunities. *Biotechnology Advances*, *30*(6), 1405-1424.
- Vassilev, S. V., Baxter, D., Andersen, L. K., & Vassileva, C. G. (2013a). An overview of the composition and application of biomass ash. Part 1. Phase-mineral and chemical composition and classification. *Fuel*, *105*, 40-76.
- Xie, Y.-P., Ho, S.-H., Chen, C.-Y., Chen, C.-N. N., Liu, C.-C., Ng, I.-S., . . . Chang, J.-S. (2014). Simultaneous enhancement of CO₂ fixation and lutein production with thermo-tolerant Desmodesmus sp. F51 using a repeated fed-batch cultivation strategy. *Biochemical engineering journal*, *86*, 33-40.
- Zhao, B., & Su, Y. (2014). Process effect of microalgal-carbon dioxide fixation and biomass production: a review. *Renewable and Sustainable Energy Reviews*, *31*, 121-132.
- Zheng, H., Gao, Z., Yin, F., Ji, X., & Huang, H. (2012). Effect of CO₂ supply conditions on lipid production of Chlorella vulgaris from enzymatic hydrolysates of lipid-extracted microalgal biomass residues. *Bioresource technology*, *126*, 24-30.

#378: Chemo-physical and thermal properties of sugarcane bagasse fractions (fibre and pith) technique

Nkosinathi E. MADLALA¹, Andrew C. ELOKA-EBOKA², David LOKHAT³

^{1,3} Discipline of Chemical Engineering, School of Engineering, University of KwaZulu-Natal, Durban, SOUTH AFRICA

² Discipline of Mechanical Engineering, School of Engineering, University of KwaZulu-Natal, Durban, SOUTH AFRICA. fatherfounder@yahoo.com

Good understanding of chemo-physical properties of sugarcane bagasse biomass and its fractions is vital for energy co-generation and briquetting. The present study was conducted on bagasse biomass collected from Tongaat Hullet Maidstone Mill to explore the influence of separating bagasse into pith and fibre fractions on their energy density. Bagasse biomass was separated into component fractions and then milled for characterisation for pre-analysis. Analysis was carried out for: moisture content, bulk density, proximate analysis, elemental analysis, calorific values and thermo-gravimetric analysis (TGA). Pith fraction had a lower energy density of 15.74 MJ/kg as compared to fibre 17.73 MJ/kg and bagasse 16.14 MJ/kg. Also fibre had a high bulk density of 230 kg/m³ as compared to bagasse (190 kg/m³) and pith the least at 77 kg/m³. Bagasse and fibre was milled and demonstrated a similar particle size distribution ranging from 0.39 – 0.48mm whilst pith ranged from 0.52 – 0.68mm at moisture content less than 10% moisture. Results from the proximate analysis and TGA curves indicated a higher ash content for pith than bagasse and fibre, as well as higher decomposition rate for pith than bagasse and fibre. Elemental contents: carbon, nitrogen, and hydrogen were almost similar in bagasse and fibre as compared to the pith fraction with a higher amount of carbon than nitrogen and hydrogen contents. Bagasse, fibre and pith had zero percent sulphur content, which proved that bagasse biomass is environmental friendly. Preliminary results of this study serve to establish a database for the potential of fibre to be used as the feed stock biomass for energy co-generation as compared to bagasse and the pith fraction.

Keywords: bagasse; fibre; pith; chemo-physical; thermo-chemical properties; sugar milling

1. INTRODUCTION

Bagasse is the raw material left from sugarcane after juice extraction for sugar at sugarcane milling (Ganesan *et al.*, 2007). Bagasse as a waste material has the potential to be used as a commercial raw material for value-added products, new products and recycled materials. It constitutes of 43-52 percent fibre, 46-52 percent moisture and the remaining portion of 2-6 percent of soluble solids (Lokhat and Bernhardt, 2017). Fibre is of great interest in material manufacturing because of its relative cheapness, availability and competitiveness in terms of strength to weight of material (Balaji *et al.*, 2014). The chemical composition of sugarcane bagasse which includes cellulose, hemicellulose, pectin, lignin and waxes confers on it certain chemo-physical properties (Sangnark and Noomhorm, 2003). For instance, in the case of fibre, it can gain flexural and tensile strengths, hardness and impact strength if proper alterations and manufacturing procedures are followed (Balaji *et al.*, 2014). Bagasse has many applications: as an energy source, it has been used as a fuel for furnace firing, in boilers or for direct combustion; as an animal feed, the presence of pith and fibre fractions makes it ideal for consumption by humans and other animals; as raw materials for the pulp and paper industry due to its cellulose content; for deployment as a bio-composite material (Balaji *et al.*, 2014); and in the construction/building industry as a reinforcing material due to its mineralogical content of silica (Schettino and Holanda, 2015). The lignocellulosic nature of bagasse as a biomass makes it significantly difficult to digest; the biological and chemical digestion is not very effective. However, a number of biological, chemical, and physical forms of digestion of plant biomass has been explored and improved upon in recent studies. Therefore, sugarcane bagasses chemo-physical properties becomes a crucial determinant on its adoption as a raw material and applicability to various needs and industries, and so its characterisation is quite imperative.

Hydrolysis is a promising and efficient process to digest plant materials for fermentable sugar and chemicals for food and energy production (Sangnark and Noomhorm, 2003). They reported that mechanical shear was also effective to break the complex structure and expose the hydroxyl group to bind with water for bagasse fibre to solubilise. Furthermore, γ -irradiation has been used to extensively degrade and solubilise bagasse biomass in water with no direct production of glucose due to further degradation of glucose. However, Sangnark and Noomhorm reported that the use of hydrogen peroxide improved physical properties of sugarcane bagasse. Also, the particle size reduction of bagasse improved chemical and physical properties. They reported that particle size reduction of < 0.075 mm improved the bulk density of the compressed bagasse biomass by approximately 20 to 25 percent (Sangnark and Noomhorm, 2003). In addition, the particle size reduction and chemical constituency of sugarcane bagasse in the ash formed has also drawn attention for application in the construction sector, being used as a composite pozzolanic material. In the tilling sector, it is also possible that it can partially replace quartz in tile manufacturing, but this is still open to research.

The focus of this study therefore is to explore the chemo-physical and thermal properties in terms of the degree of significant difference of bagasse biomass fractions with the objective to determining the fraction having properties with more potential for use as briquettes to serve as a finished energy fuel source.

2. MATERIALS AND METHODS

2.1. Bagasse preparation

The sugarcane bagasse used on this study was collected at Tongaat Hullet Sugar Maidstone mill in Durban, South Africa. The initial moisture content of bagasse was approximately 25 percent. The bagasse was cleaned by washing it and drying in the sun on top of a roof for two weeks.

2.2. Bagasse separation

Sugarcane bagasse was separated to its fractions of fibre and pith. The separation was done at Tongaat Hullet Sugar Maidstone mill using a mechanical depither with an unknown model number. The fibre and pith exit the depither with approximately 50 percent moisture content.

2.3. Physical properties

Particle size, moisture content and bulk density of bagasse and its fractions of fibre and pith were determined using standard methods and modern methods for particle size analysis. Before physical property characterisation, the bagasse and its fractions of fibre were milled using a hammer milling machine. Thereafter, the characterisation was computed.

Particle size

Particle size reduction of bagasse and its fraction of fibre was achieved by the use of hammer milling machine. Thereafter, SALD-3101 Laser Diffraction particle size Shimadzu analyser was used to determine the particle size analysis of milled bagasse, fibre and pith. Particle size was computed at 0.39 – 0.63 mm range at quantity of 25% - 75%.

Moisture content and bulk density

Moisture content was measured for sugarcane bagasse and its fractions of fibre and pith using moisture analyser (Model: Boeco Germany BM035). Approximately 2g of test samples were placed on the moisture analyser at 105°C for one hour. Percentage moisture and dry content was recorded. The bulk densities of samples were determined by a cylindrical container (100ml beaker). To determine the volume of a beaker, the pre-weighed beaker was filled with water to its maximum capacity (at room temperature). The mass of the container plus water was measured using a mass balance scale (Adventure) with a maximum mass of 310g. The volume of the container was calculated based on the net weight of water and the density of water (1000 kg/m³). A pre-weighed cylindrical container was filled with the test samples of bagasse, fibre, and pith of particle size less than 0.6mm and dropped from a height of 10cm on to a horizontal laboratory patch. The samples material in the container were topped until the maximum capacity was reached, the surplus material was sheared off. The samples plus the beaker were weighted, and net mass of material was divided by the volume of container to obtain the bulk density, bulk density was calculated using Equation (1):

$$\text{Equation 1: } P_b = \frac{F - E}{V}$$

Where:

- P_b = bulk density of the sample (kg/m³)
- F = weight of the container plus sample (kg)
- E = weight of the container (kg)
- V = volume of the container (m³)

2.4. Proximate analysis

Percentage volatile matter (PVM)

2g of powdered bagasse, fibre, pith and 2g of pulverised briquette samples in a crucible were placed in the oven until a constant weight was obtained. The samples were then heated in the muffle furnace at a temperature of 550°C for 10 minutes. The sample was then weighed after cooling in a desiccator. The PVM was calculated using Equation (2):

$$\text{Equation 2: } PVM = \frac{A - B}{A} \times 100$$

Where:

- A = oven dry weight (g) of samples
- B = weight of the samples after 10 min in the muffle furnace at 550°C temperature

Percentage ash content (PAC)

2g of powdered bagasse, fibre, pith and 2g of pulverised briquette samples were also heated in the muffle furnace at a temperature of 550°C for 4 hours. The samples were weighed after cooling in a desiccator to obtain the weight of ash C. The PAC was calculated using Equation (3):

$$\text{Equation 3: } PAC = \frac{C}{A} \times 100$$

Percentage fixed carbon (PFC)

The PFC was calculated by subtraction of PVM, PAC and PMC from 100 as shown in Equation (4):

Equation 4: $PFC = 100 - (PAC + PMC + PVM)$

2.5. Ultimate analysis

Elemental analysis was carried out through ultimate analysis. The elemental composition of carbon C, hydrogen H, nitrogen N, sulphur S was determined using scientific flash 2000, which uses combustion at a temperature exceeding 1400°C, method prescribed by Jittabut (2015). The oxygen O content was calculated by subtraction of CHNS from 100, using Equation (5):

Equation 5: $O\% = 100 - (C\% + H\% + N\% + S\%)$

Determination of High Heat Value

The high heat value of the samples of bagasse and its fractions was determined in accordance with Jittabut (2015). The heat value was determined using bomb calorimeter. Approximately 0.4g of each sample was burnt in the bomb calorimeter until complete combustion was obtained. The temperature difference was used to compute HHV using Equation (6): of the bagasse and its fraction of fibre and pith biomass and its briquettes.

Equation 6: $Q = \frac{(C_{water} + C_{cal})(T_2 + T_1)}{W_f}$

Where:

- Q = calorific value of the bagasse, fibre and pith (MJ/kg)
- C_{water} = heat capacity of water (MJ/kg°C)
- W_f = weight of the biomass material sample (kg)
- C_{cal} = heat capacity of the bomb calorimeter (MJ/kg°C)
- $T_2 - T_1$ = rise in temperature (°C)

2.6. Thermo-gravimetric analysis

A thermogravimetric analyser (TGA) was used to determine the TG of bagasse and its fractions of fibre and pith at the University of Kwa-Zulu Natal, Westville Chemistry laboratory. The TGA unit had a furnace attached with linear heating rate of 10°C/min until it reach a maximum heat of 600°C held for 5 minutes at 600°C. In this study, Nitrogen gas at a flow rate of 100ml/min was used to create the oxygen-free inert atmosphere to avoid combustion of bagasse biomass.

3. RESULT AND DISCUSSION

The result of bagasse and its fraction of fibre and pith demonstrated a significant difference $p < 0.05$ on physical, proximate and ultimate analysis. The significant difference was configured by the use of statistical parameters of F calculated and $F_{critical}$ using excel Microsoft 2013.

3.1. Physical properties

Bulk Density

Figure 1 illustrates that the fibre fraction had a maximum bulk density of 0.23 g/cm³ (230 kg/m³) followed by bagasse which was found to be 0.19 g/cm³ (190 kg/m³) which is in the range as reported by Mashoko *et al.* (2010) for South African sugarcane. Lastly, the pith fraction had a very low bulk density of 0.077 g/cm³ (77 kg/m³) as compared to fibre and pith. Sapariya *et al.* (2013) reported that bagasse had a bulk density of 0.074 g/cm³, which is closer to the density of the pith fraction in this study. The lower bulk density of bagasse and its fractions as compared to that of coal and charcoal encourages densification of this fraction to be used as a solid fuel for better handling, transportation and increasing of energy density per unit mass.

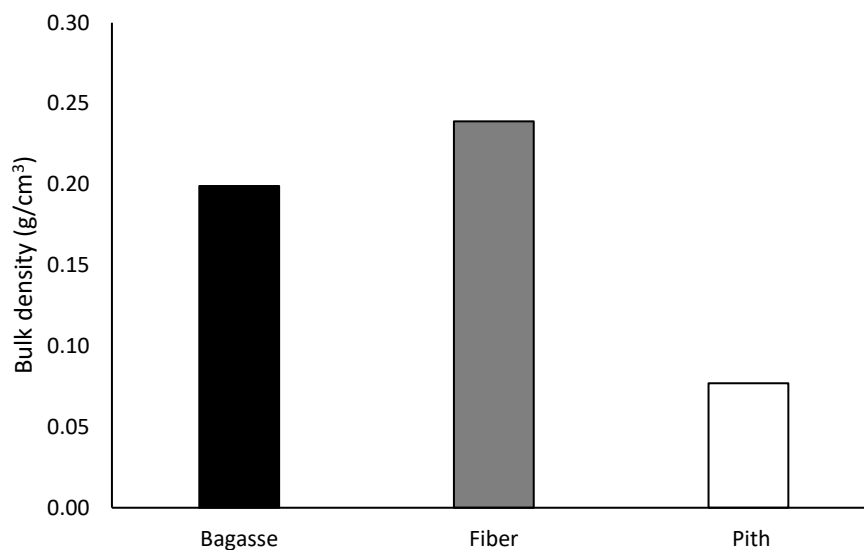


Figure 65: bulk density characterisation of bagasse and its fractions of fibre and pith

Proximate analysis

Statistical results show a statistical significance $p < 0.05$ which indicated that bagasse, fibre, and pith had different percentage volatile, ash, and fixed carbon (Figure 3.2). Fibre indicated a maximum percentage volatility at 89.05% follow by bagasse at 80.55%, with pith the least at 76.77%. Pith had 18.12% of ash after burning while bagasse and fibre yielded very low ash content of 8.01% and 1.75%. Bagasse and fibre demonstrated fewer problems in boilers due to the delay in thermochemical conversion process and corrosion (Sadaka and Negi, 2009). Fibre and bagasse had a potential for gasification and pyrolysis with lower temperatures since indicated high volatile. Fibre had the least fixed carbon of 12.0% where pith had high fixed carbon of 41.3% as presented by Garivait *et al.*, (2006). Pith had great potential to burn slowly without high flame and the by-product of combustion was solids as compared to bagasse and fibre, which can give rise to liquid by-product due to low fixed carbon percentage and high volatiles which normal have a problem of tar and oils (Kamruzzaman and Islam, 2011). Mansaray and Ghaly (1997) reported that the content of volatile, ash, and fixed carbon varied with geographic location.

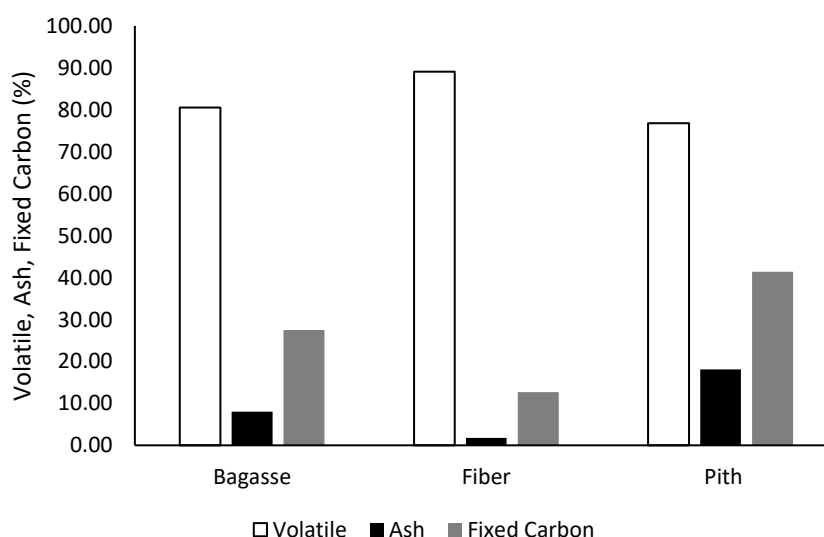


Figure 66: Proximate analysis of bagasse and its fraction of fibre and pith

3.2. Ultimate analysis and calorific value

Fibre had high carbon content of 45.51% as compared to bagasse and pith, followed by bagasse (45.21%) and the lowest was pith at 40.67%. High carbon content in biomass indicated that the biomass had a great use for energy generation through combustion, since carbon enhance long burning time. Bagasse, fibre, and pith demonstrated a very low percentage of hydrogen at 5.34, 5.50, and 5.04 respectively; also, the bagasse and its fraction indicated very low nitrogen percentage of 0.16, 0.16, and 0.35. The results presented in this study are more closely related to the results presented by Garivait *et al.* (2006) in bagasse elemental composition. However, the bagasse and its fractions of fibre and pith had high oxygen proportion as compared to other elements of carbon, hydrogen, nitrogen and sulphur. In addition, bagasse and its fractions had zero percent of sulphur. Results of bagasse and fibre does not show any significant difference $p > 0.05$ in their elemental analysis. Bagasse and fibre had maximum content of carbon, hydrogen, nitrogen, while pith had a low content, but pith had a high content of oxygen due to its sponge-like nature (Figure 3.3a and Table 3.1). Basu (2010) indicated that a lower content of sulphur and nitrogen in fuel biomass, contributed positively to the environment. Elemental analysis is very important since it contributes to calorific value of the biomass. Kamruzzaman and Islam (2011) reported that a high proportion of hydrogen and oxygen compared to carbon reduced calorific value. In this study bagasse, fibre and pith demonstrated a very low proportion of hydrogen as compared to carbon, but a high proportion of oxygen compared to carbon.

Kamruzzaman and Islam (2011) reported that the heating value of agriculture biomass ranged from 10.59-18 MJ/kg. The reported range corresponded with the result presented in this study (Table 3.1), which ranged from 15.74, 16.14, and 17.73 MJ/kg for pith, bagasse, and fibre respectively (Figure 3.3b). Fibre indicated high heat value as compared to bagasse and pith fractions while pith was the lowest in heat value among bagasse and fibre fractions. Fibre had high heat value as compared to other fractions because of its rigid structure and high content of carbon and high volatile matter which made it preferable for gasification at lower temperature (Mansaray and Ghaly, 1997). However, Ahiduzzaman (2011) reported that the removal of ash from the biomass improved biomass heat value.

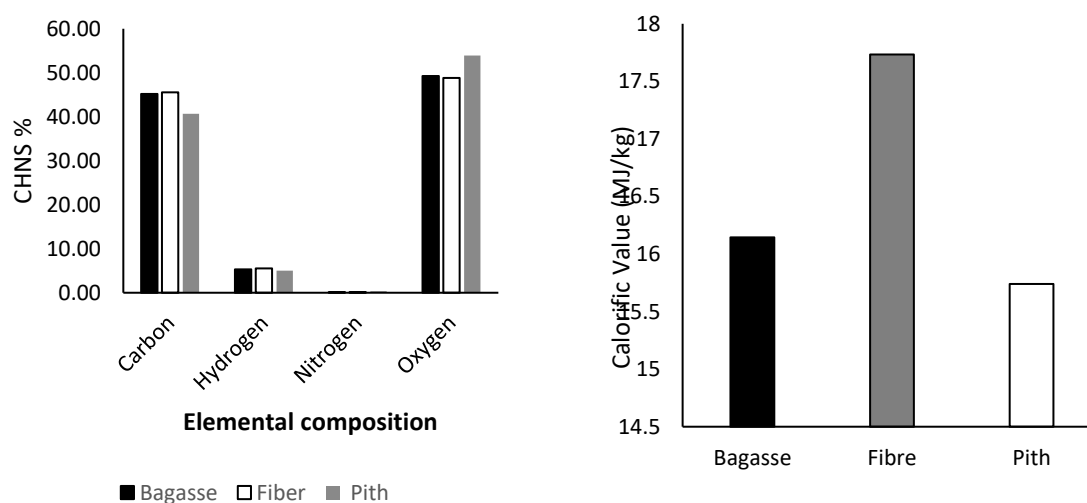


Figure 67: Elemental analysis and heat value of bagasse and its fractions of pith and fibre

Table 30: Characterisation of bagasse and its fraction of fibre and pith

	Bagasse	Fibre	Pith
Moisture %	10	9.6	11.8
Bulk Density (kg.m ⁻³)	199.34	239.19	77.23
Particle Size (mm)			
25%	0.39	0.39	0.52
50%	0.42	0.42	0.6
75%	0.48	0.48	0.683
%V	80.55	89.05	76.77
%Ash	8.01	1.75	18.12
%FC	27.46	12.70	41.35
Carbon%	45.21	45.51	40.67
Hydrogen%	5.34	5.50	5.04
Nitrogen%	0.16	0.16	0.35
Oxygen%	49.27	48.79	53.92
Calorific Value (MJ/kg)	16.14	17.73	15.74

3.3. Thermo-gravimetric analysis

The TGA curves of bagasse biomass and its fractions of fibre and pith show that the maximum decomposition and the weight remains occurred at the same temperature ranges of 250°C to 500°C and 500°C to 600°C. The bagasse indicated a different trend from the range of 30°C to 49°C where gas absorption occurred thereof the moisture reduction took place from all three biomass in the temperature range of 49°C to 100°C through vaporisation (drying zone). The temperature reported by Anukam *et al.* (2016) for the drying zone was determined mainly by the thermal conductivity of the biomass, the temperature for the drying zone reported to be less than 120°C. The mass remaining as ash for all biomass varied from 0 to 3% which was different from the ash result obtained from proximate analysis with the mass varying from 1 to 18.12%. The difference in results was due to the temperature at which the analysis were determined; for proximate analysis the maximum temperature was 500°C while during TGA the maximum temperature was 600°C. The temperature above 600°C was called the secondary pyrolysis zone where char can melt and produce CO, H₂ and CO₂ gas which further increased weight loss remains. Both bagasse, fibre and pith underwent endothermic reaction as reported by Kamruzzaman and Islam (2011) which explains that bagasse biomass required energy from the surrounding to undergo chemo-physical reaction.

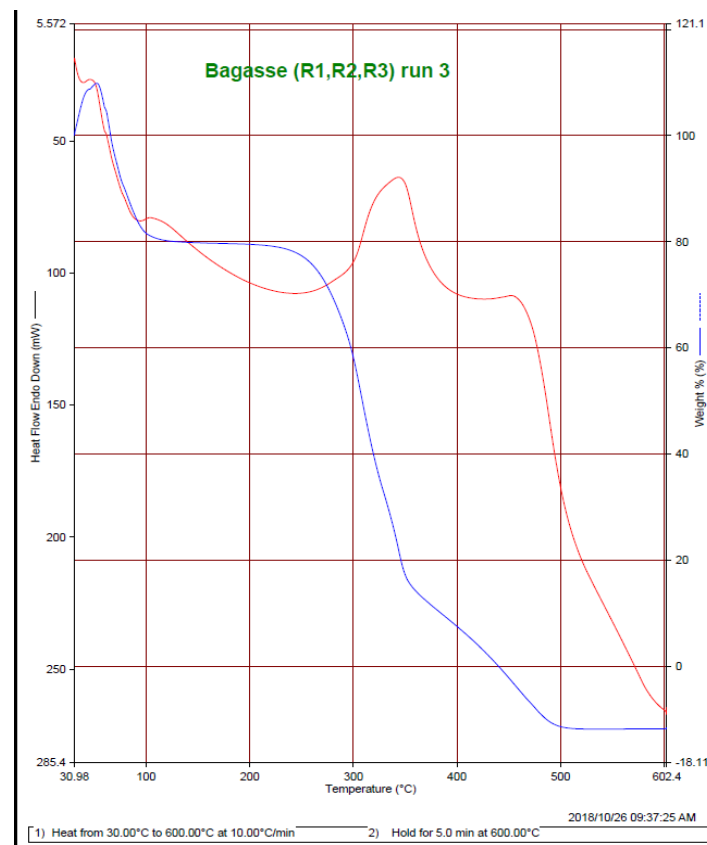


Figure 68: TG curve for bagasse at 10°C/min heating rate in inert media

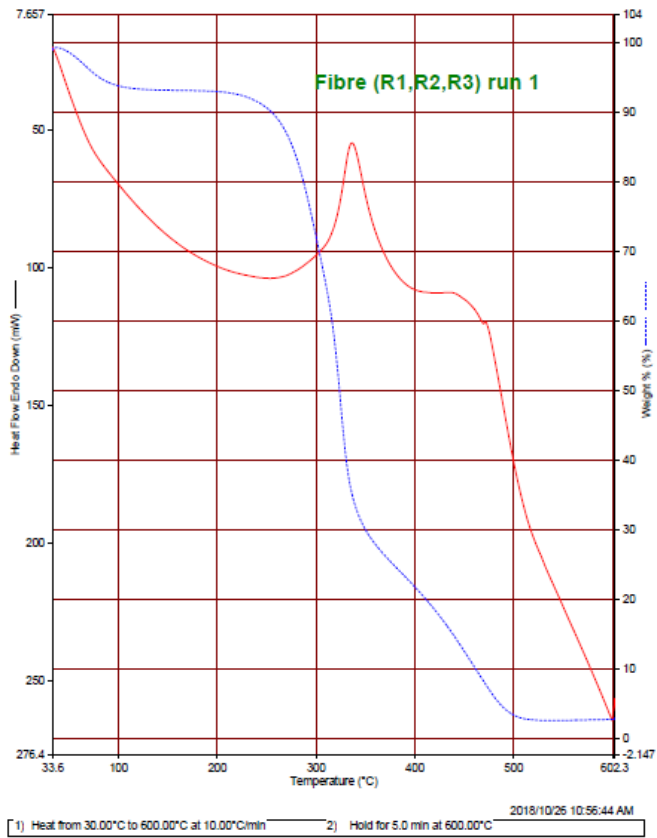


Figure 69: TG curve for fibre at 10°C/min heating rate in inert media

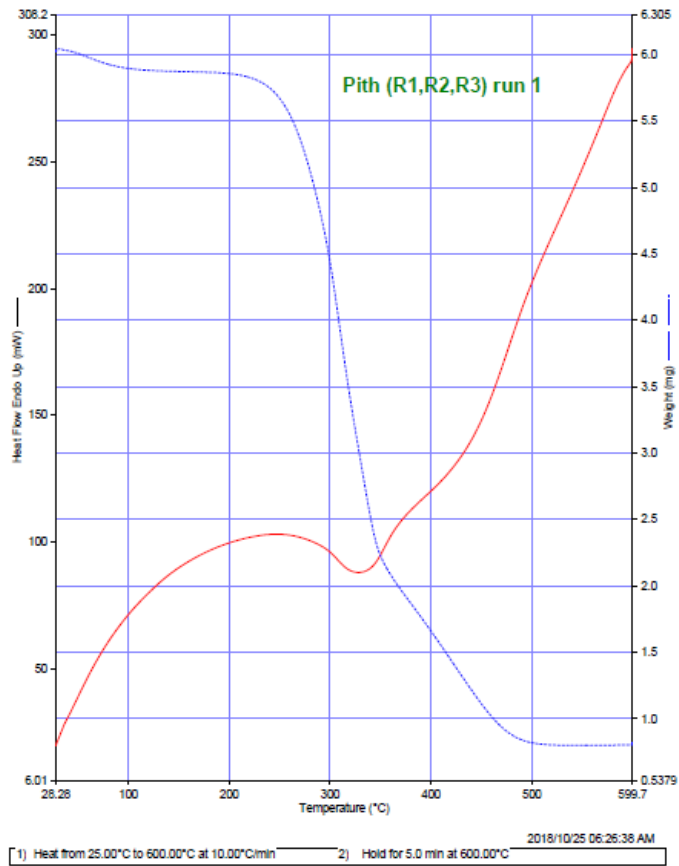


Figure 70: TG curve for pith at 10°C/min heating rate in inert media

4. CONCLUSION

Bagasse and its fractions of fibre and pith demonstrated a significant difference in their characterisation results. Bagasse raw material can be used in many industrial sectors whilst fibre demonstrated an epical result to be used as the energy source both for oxidation and gasification as compared to bagasse and pith. The presence of pith reduced the energy density of the bagasse as demonstrated by the results in this study. However, pith has been used as a raw material for animal feed which opens the opportunity for car manufacturing and the pulp and paper industry to use fibre for value added product. Therefore separation of bagasse fractions seems to be the promising activity for economic development within the sugarcane milling industry.

5. REFERENCES

- Ahiduzzaman, M. 2011. Studies and Investigation on Extraction of Energy and Value Added Product from Rice Husk. *A PhD Dissertation submitted to department of Mechanical and Chemical Engineering, Islamic University of Technology, Gazipur, Bangladesh*
- Anukam, A, Mamphweli, S, Reddy, P, Meyer, E and Okoh, O. 2016. Pre-processing of sugarcane bagasse for gasification in a downdraft biomass gasifier system: A comprehensive review. *Renewable and Sustainable Energy Reviews* 66 775-801.
- Balaji, A, Karthikeyan, B and Raj, CS. 2014. Bagasse fiber—the future biocomposite material: a review. *International Journal of Cemtech Research* 7 (1): 223-233.
- Basu, P. 2010. *Biomass gasification and pyrolysis: practical design and theory*. Academic press,
- Ganesan, K, Rajagopal, K and Thangavel, K. 2007. Evaluation of bagasse ash as supplementary cementitious material. *Cement and concrete composites* 29 (6): 515-524.
- Garivait, S, Chaiyo, U, Patumsawad, S and Deakhuntod, J.2006. Physical and chemical properties of Thai biomass fuels from agricultural residues. *The 2nd Joint International Conference on "Sustainable Energy and Environment (SEE 2006)*, 1-23.
- Jittabut, P. 2015. Physical and thermal properties of briquette fuels from rice straw and sugarcane leaves by mixing molasses. *Energy Procedia* 79 2-9.
- Kamruzzaman, M and Islam, AS. 2011. Physical and thermochemical properties of rice husk in Bangladesh. *BioRes* 11 (6): 35-49.
- Lokhat, D and Bernhardt, H.2017. Inclined perforated drum dryer and separator for cleaning and drying of sugarcane bagasse. *Proceedings of the Annual Congress-South African Sugar Technologists' Association*, 455-465. South African Sugar Technologists' Association,
- Mansaray, K and Ghaly, A. 1997. Physical and Thermo-chemical Properties of Rice Husk. *Energy Sources* 19 989-1004.
- Mashoko, L, Mbohwa, C and Thomas, VM. 2010. LCA of the South African sugar industry. *Journal of Environmental Planning and Management* 53 (6): 793-807.
- Sadaka, S and Negi, S. 2009. Improvements of biomass physical and thermochemical characteristics via torrefaction process. *Environmental Progress & Sustainable Energy: An Official Publication of the American Institute of Chemical Engineers* 28 (3): 427-434.
- Sangnark, A and Noomhorm, A. 2003. Effect of particle sizes on functional properties of dietary fibre prepared from sugarcane bagasse. *Food chemistry* 80 (2): 221-229.
- Sapariya, DD, Sheth, NR and Patel, VK. 2013. Bagasse as an alternative source of energy.
- Schettino, MAS and Holanda, JNF. 2015. Characterization of sugarcane bagasse ash waste for Its Use in Ceramic Floor Tile. *Procedia Materials Science* 8 190-196.

#379: Sustainable waste management by Sri Lankan entrepreneurs

Thesara Vithana P. JAYAWARDANE

Department of Industrial Management, University of Moratuwa, Sri Lanka
[*thesaraj@uom.lk*](mailto:thesaraj@uom.lk)

Waste management is an embryonic issue in Sri Lanka which has become a challenge to not only the government, but also to business owners, academics and urban and rural residents. Over 6,900 tons of waste is generated daily in Sri Lanka whilst the daily waste collection is only around 2,500 tons. Sixty percent of this waste is generated in Colombo, the capital of Sri Lanka while the remaining forty percent is generated by rural municipal council areas. An adequate waste management does not come about on its own. Around the world, all of the sustainable waste management systems have been formed by the interested stakeholders in waste management. In assessing the situation in Sri Lanka, it is evident that the entrepreneurs play a vital role in sustainable waste management. The objective of writing this paper is to identify the techniques adopted by the Sri Lankan entrepreneurs in maintaining sustainable waste management. Another objective is to list the key issues faced by these entrepreneurs related to sustainable waste management in Sri Lanka. The paper will provide some suggestions and recommendations to improve the waste management practices followed by these entrepreneurs in Sri Lanka. This paper is based on secondary research. Existing reports related to waste management and recommendations prepared by scientists, engineers, academics, planners, charitable organisations, consultants, ministries of the government and key industry experts are studied and analysed. This paper recommends that strengthening the national policy framework would be a key for sustainable waste management in Sri Lanka. This paper recognises that Sri Lankan entrepreneurs, who are actively involved in sustainable waste management, contribute positively to the development of the country.

Keywords: Sri Lanka, sustainable, waste management, entrepreneurs

1. INTRODUCTION

As a developing country, Sri Lanka is home to many leading corporate leaders, engineers and entrepreneurs but faces the challenge of increasing amounts of waste, with aggregating toxic components. Even though there is a national strategy formulated for waste management, it is not being implemented efficiently. The governmental bodies organise many environmental awareness and education programs but no significant progress can be witnessed in waste management in Sri Lanka.

Entrepreneurship is identified as the generation of an idea and culminates in realization of the project objectives (Archer et al., 2009). Entrepreneurship in waste management contributes to environment protection, economic restructuring and job creation. Entrepreneurial activities in waste management are observed in the areas of waste collection, handling, sorting, storage, transport, transformation and energy recovery.

Entrepreneurs can not only invest money in waste management sector, but also infuse new ideas, technologies and skills which can transform waste from being a liability into an asset. Involvement of the entrepreneurs will certainly increase the efficiency of waste management (National Strategy for Solid Waste Management, 2002). Entrepreneurial projects related to waste management can be seen in sole proprietor ventures to large-scale projects involving many skilled and unskilled workers. Waste management is a labour intensive process with plenty of opportunities to generate new jobs and such entrepreneurial involvement include waste collection, transportation, reuse and recycling, upcycling and power generation.

According to the World Bank, Sri Lankan municipalities spend 20 to 50 per cent of their annual budget on waste management, but only less than 60 per cent of waste is collected and less than 50 per cent of the population has access to municipal waste collection services (Colombo Environmental Improvement, 2003). Entrepreneurs contributing to waste management should realise that it indeed requires ample amount of resources. Constant flow of revenue is needed to make these waste management projects sustainable. As individuals who are working towards sustainable waste management and environmental protection, they must recognise this and act accordingly. Thus, entrepreneurs must sought revenue from payments made for services offered or through funds from national and international governments, corporate, philanthropy and other welfare organizations under various programs.

2. RESEARCH PROBLEM

Today, waste has become a serious environmental and socioeconomic issue in Sri Lanka. Population growth, migration and rapid urbanisation will certainly accelerate this issue further in the coming years. In many developing countries in Asia, waste is increasingly being used to produce both materials and energy, and recycling now saves more greenhouse gases than it generates (Van der Wel and Post, 2007).

Sri Lanka, being a developing country, is faced with the major challenge of improving its inadequate and unsustainable waste management systems. Sustainable development is a global objective to overcome the economic, environment and society disasters around the world. Therefore, a major requirement has arisen for research to be developed in order to create project ideas for social and environmental entrepreneurship to contribute to the creation of a waste management system which will become a sustainable entrepreneurial development.

Waste management is an obligatory function of all the local authorities in Sri Lanka such as municipal councils, urban councils, and pradesiya sabhas (Fernando, 2006). With the rapid pace of urbanisation, the situation is becoming uncontrollable with time. This research aims to find the relationship between sustainable development, entrepreneurship and waste management. The key requirement of this research is to create awareness transmit a genuine cultural orientation towards sustainable behaviour in waste management.

3. OBJECTIVES

- To identify the techniques adopted by the Sri Lankan entrepreneurs in maintaining sustainable waste management.
- To examine the key issues faced by the Sri Lankans entrepreneurs related to sustainable waste management in Sri Lanka.
- To specify methods that will improve the waste management practices followed by the Sri Lankan entrepreneurs.

4. LITERATURE REVIEW

Most experts in various humanities fields agree that the entrepreneurship plays a main role in the development and growth of social, economic and political fields of a country. The only solution of survival in this changing world is innovation and entrepreneurship in which the improvements of economic performance or growth would be developed (Talebi and Khaksar, 2011).

Around the country, especially in the Colombo District, one may see how waste accumulates without being properly disposed. You will literally see garbage bags simply lying around in front of walls, at the corners of streets, clogging drainage channels, and in many empty lands as piles. Dengue is one of the most common fatal diseases carried by mosquitoes that are bred in the mountains of empty tins, coconut shells and scattered plastic bottles filled with rainwater. Flies move in dozens in the piles of organic waste mixed in with household and industrial waste. Since there is no proper mechanism for waste collection, people tend to leave their garbage in bags in front of their house. This invites scavenging by animals and the scattering of garbage everywhere. "Due to a lack of sufficient land and resources, as well as poor planning and erratic service, most of the waste in the country is unmonitored and is disposed of into unmanaged dumpsites in wetland areas, and along the roads, streams and rivers resulting in leakage of toxins into drinking water. Open burning of mixed wastes is common in both rural and urban settings, contributing to poor air quality and a number of health concerns. Haphazard wild dumping is the most commonly practiced means of waste disposal." (Pilapitiya, 2006).

"The government structure of Sri Lanka is divided into National level (the President, Parliament, Ministries and connected departments, etc.), Provincial level (headed by the Provincial Councils), District level (headed by Government Agents), Division level (headed by Divisional Secretaries), Pradeshiya Sabhas, Municipal and Urban Councils, and the Grama Seva Nildaris which generally have a Public Health Inspector assigned to them and who is responsible for solid waste management. The Ministry of Forestry and Environment and the Central Environmental Authority are responsible for solid waste management policy making." (Van Zonn, 2000).

A National Waste Management Strategy has been drawn up and legislation enacted to effect sustainable solutions to the waste issues in the country. However, implementation has fallen short (Pilapitiya, 2006). Local authorities (Urban Councils and Pradeshiya Sabhas) are responsible for the collection and disposal of solid waste. Currently household, industrial, medical and other wastes are all being disposed of together without precautionary measures (Van Zonn, 2000). Many charitable organisations and non-governmental agencies do contribute to the public and environmental health of Sri Lanka. The Central Environmental Authority which is funded by such foreign organisations works with the government, to find and implement solutions to the sustainable waste management.

In this research, literature on Sri Lanka, Malaysia and Singapore was investigated and compared in order to get a sense of the waste management in countries facing challenges similar to Sri Lanka. Singapore faces similar challenges as far as population and limited land but has access to resources and technology that have enabled it to implement innovative, expensive solutions that can provide insight into what might be possible in the future for Sri Lanka. Malaysia and Sri Lanka are particularly similar in that they have rapidly expanding urban populations, rely on tourism and have unique regional cultures. Sri Lanka is similar to both the above countries as they have experienced economic difficulties and ethnic conflict previously. Sri Lanka has high population density, and a lack of suitable land availability, which has had an enormous impact on the waste management.

According to US and Foreign Commercial Service Report (2003), South Korea incinerates approximately 23% of its solid waste. For Sri Lanka incineration is not considered a viable option due to the high moisture content in the waste and the toxic by-products created by burning of plastics, polythene, etcetra (Sunday Observer, 2004). Many projects have been undertaken in Sri Lanka, with governmental, World Bank, corporate and private funding, specifically targeted to address the growing solid waste issues and entrepreneurs must take an approach that focuses on developing the market for wastes.

A few years ago, open dumping type landfills were the only type of landfill available, but there are now newly developed sites using modern technologies to reduce environmental pollution caused by leachate and gas emissions. Thus entrepreneurs must encourage the involvement of foreign environmental companies to manage the waste issue in a sustainable manner. Landfill gas harvesting and recycling are emerging businesses around the world. According to ISA (2003), Korea has installed 100 methane gas extraction wells into an existing landfill site and uses the captured gas to heat and cool neighbouring households and businesses.

"Sri Lanka has implemented numerous solid waste management projects over the past ten years, with some degree of success but, without a significant shift in the situation. It would appear, actually, that the situation is worsening as the country continues to develop economically" (Bandara, 2003). In addition, "Country wide sustainable waste management infrastructure is weak, equipment is old and ill maintained, absenteeism is extremely high among municipal waste collectors, and resources that are spent are often misspent on duplication of efforts or corruption (Pilapitiya, 2006). Sri Lanka is facing the challenge of lack of financial and human resources to obtain and implement expensive technologies, and has a shortage of skilled experts. Literacy rate in Sri Lanka is extremely high but the graduates are completing higher education without gaining necessary amounts of practical, applicable

skills and experience (Gunawardena, 2006). Well-written, progressive reports are generated and published but do not get implemented.

“Responsible solid waste management is expensive and at present does not offer adequate incentive to encourage people to change their current unsound practices” (Pilapitiya, 2006). There is more money to be made by illegally filling in a wetland area with unmonitored solid waste and selling it as a construction site for homes and businesses than there is in sound solid waste management. In the absence of enforcement of regulations and disincentives for unsound practices, the irresponsible habits tend to be the norm and the public health suffers as a result, particularly the poor and disadvantaged (Pilapitiya, 2006).

Singapore on the other hand has achieved noteworthy success in managing its waste sustainably. This could be, in part, due to the strict penal system that inhibits illegal waste management practices that Sri Lanka may or may not want to replicate. Singapore serves as a model of what is possible when responsible waste management is made a priority with governmental commitment. According to Tan and Khoo (2006), education, economic incentives and disincentives, and thorough research into best practices have also played a role in Singapore’s waste management success. It is ideal to get guidance from that research in order to adopt the decisions taken in Singapore to make future planning for Sri Lanka. In this report Tan and Khoo (2006) mentions various waste management options which includes landfilling, incineration, recycling and composting and concludes stating “incineration imposes considerable harm to both human health and the environment, and landfill gases and leachate generate minimal environmental damage. Composting of horticultural wastes hardly imposes any environmental damage and of all the waste strategies, recycling offers best solution”.

5. METHODOLOGY

The research was done mainly with secondary data obtained from materials from existing reports related to waste management and recommendations prepared by scientists, engineers, academics, planners, charitable organisations, consultants, ministries of the government and key industry experts. This research extracted, studied and analysed those data to obtain the necessary information on entrepreneurs of Sri Lanka and sustainable waste management.

Additionally semi-structured interviews and environmental education and awareness building programs provided data for the inquiry. This research was qualitative in approach and employed formal and informal interviews, focus groups and questionnaires. Data obtained from a survey research was also extracted and analysed for the purpose of this research. The standardized five point’s Likert questionnaire which was used by many researchers with a proven reliability and validity was used in order to respond to the research after the review of related literature and scrutinizing documents and library sources. The questionnaire contains 15 components in which 3 components related to the general demographics of the entrepreneur and 12 components related to sustainable waste management.

Out of that data-base population consisting two hundred (200) interviews and case studies, twelve (12) entrepreneurs were chosen from convenience sampling. Convenience sampling is useful where it is otherwise difficult to elicit a sufficient level of response (Bell and Bryman, 2007). These selected entrepreneurs represented the key characteristics and attributes of the total sample group. They were interviewed face to face at a location of their convenience with similar questions that were raised in the data base interview. They elaborated the responses given in previously to provide a wider understanding to the researcher. All these entrepreneurs shared their experiences with the researcher in terms of garbage disposal, waste reduction, reusing of plastic bottles and bags, recycling of glass, plastic and metal, and composting. Participating entrepreneurs were encouraged to form their own environmental task force responsible for upholding the commitment of environmentally sound waste management in their communities.

6. VALIDITY AND RELIABILITY

Results were also presented for the respondents to see if the answers have been interpreted correctly. Furthermore, the validity of the result has been discussed with the supervisors, academic consultants, experts of the industry with valuable feedback. Cross checking of the information was done with the aid of industry experts and professional bodies. In terms of reliability measurement repetition of the study was conducted. Randomly selected few respondents were asked to do the interviews again with a third person. This was done in order to see if the same results were to be obtained. Because of the lack of time, it was not possible to conduct the study more than once for all the respondents. But the chosen sample reiterated that the findings or the answers were more or less identical.

7. KEY FINDINGS

The research reviewed the existing literature to understand and relate the waste management practices adopted by entrepreneurs of Sri Lanka. It was also analysed to identify if these practices are meeting the techniques and standards of the comparative countries. During the research it was understood that the Sri Lankan government and local authorities do take part actively in tackling the waste management situation but when compared to countries such as Singapore or Malaysia that are well streamlined and established, there is a gap existing.

7.1. Business profile of the entrepreneurs

The chosen entrepreneurs who were further interviewed admitted to actively taking part in sustainable waste management. They were identified as being very dynamic and innovative in developing the strategies and business models in promoting sustainable waste management practices. Out of the 12 chosen participants, 6 were sole proprietors, 4 were running joint ventures or partnerships while 2 had registered their business as companies under the Company Act.

7.2. Techniques adopted by entrepreneurs

The following examples will emphasise the various techniques adopted by the Sri Lankan entrepreneurs in maintaining sustainable waste management.

Dilmah tea recycling

"Dilmah Recycling" was inaugurated as part of Dilmah Tea's commitment to reduce its plastic footprint. This facility converts a significant portion of Dilmah's tea packaging waste materials into reusable items. According to the United Nations Environment Programme about 280 million tonnes of plastic is produced globally each year and only a very small percentage is recycled. Dilmah Recycling hopes to address this global issue by acting as a research and educational centre to spread awareness on the importance of plastic recycling in Sri Lanka. The centre utilises plastic upcycling techniques to develop inventive recycling solutions and products (Dilmah sustainability report, 2018).

During the first stage of production, the waste material goes through a sorting and inspection process to ensure that it is free from materials such as tea debris, plastic tape etc. It is then passed through a shredder to break the material into smaller workable sizes. Following this, the shredded material is subjected to high temperature and pressure in a hot press machine for a fixed period of time during which the original material undergoes transformation yielding a product which has altered composition and properties. The final output resulting from this process is set inside the cold press to speed up the cooling process of the material and later utilized in the production of decorative and construction material.

The objectives of this programme is to implement a process that strives to convert a significant portion of Dilmah's tea packaging waste materials into reusable objects, to achieve a 10% successful upcycling conversion of Dilmah's waste packaging material, to bring Dilmah's waste program into alignment with the company's sustainability schemes, and to serve as an educational/research facility and create awareness on the importance of sustainability and recycling/upcycling.

SLIIT's 'Clean Lanka'

'ICT for Development' research group at SLIIT has attempted to provide an appropriate sustainable solution for modern society employing smart technologies. At present, solid waste is kept in bins or bags by citizens outside their homes which are collected by trucks of the respective municipal councils. At times of special occasions where lot of waste is generated, failing to collect waste on time causes major local issues.

As per the municipal councils, these issues have arisen due to the inability to manage the truck fleet efficiently and poor unawareness of the changing conditions in the area. Furthermore, the municipal council is also solely responsible for categorizing and distribution of solid waste to traders who may be interested in buying certain types of them. As such, the citizens do not have the opportunity to gain any monetary benefits from their solid waste (Daily News, 2019).

The project, by the name 'CleanLanka', is aimed at developing a cost effective, integrated, end-to-end solution that enables efficient and effective collection and management of solid waste produced in urban areas of Sri Lanka. The proposed solution only requires the use of a smart phone per house-hold. The system was developed in relation to the municipal council of Kaduwela as a pilot study. An analysis was carried out prior to the project on the current processes and practices employed by various parties such as municipal councils, waste trading and recycling companies with the aim of identifying critical elements, current issues and inefficiencies.

The Waste collection scheduler is composed of static scheduler and the dynamic scheduler. Static Scheduler is capable of generating the best waste collection plan for a given area considering fixed conditions such as number

of houses, annual calendar events and holidays and geographical maps of the area on a daily, weekly or monthly basis. Dynamic scheduler can alter usual schedules considering day-to-day conditions such as traffic, weather, user feedback and possible locations and dates of upcoming events in the area.

Hayley's waste minimising projects

Hayleys Fabrics provides fabric waste scrap to women in neighboring communities, which is subsequently fashioned into wicks for oil lamps and household rugs. This initiative also supports the empowerment of women through generating an alternative source of income. Sectors have obtained and continue to comply with a host of environmental permits/licenses and certifications, while frequently receiving awards for excellence in environmental commitment (Hayleys, 2019).

Rainforest Alliance and sustainable management

The Rainforest Alliance (RA) Sustainable Agriculture Network Certification Programme ensures sustainable waste management practices through numerous standards encompassing social, environmental and ethical practices. The certification centres on compliance to ten universal principles and the subsequent section will detail the Plantation sector's initiatives and results in complying with the principles pertaining to environmental sustainability.

7.3. Key issues faced by the entrepreneurs

This is a brief summary of key issues faced by the Sri Lankan entrepreneurs related to waste management.

Health and environmental issues

Waste management certainly impact the health and wellbeing of people's and the environment in general. Unplanned and illegal waste dumping creates breeding grounds for various pathogens and other harmful organisms, and exposes people to chemical and mechanical hazards in case of hazardous waste. By polluting the ground, the surrounding air, and water will spread diseases and enhances exposure to harmful chemicals beyond the immediately affected areas. Non-composted organic waste, by its anaerobic decomposition, contributes to greenhouse gas emissions (Solid Waste Management in Sri Lanka, 2007).

Technical issues

- Waste treatment and disposal

Waste, in many (planned and unplanned) areas is frequently just dumped along the wayside, in drainage channels and other water courses. In Sri-Lanka, the highest proportion of waste consists of potentially compostable, and thus valuable, organic waste. Illegal dumpsites, unmanaged and without the minimally required lining and fencing, and equally unmanaged company dumpsites contribute to environmental and social degradation. In many places, municipal authorities have set up large scale mechanised collection systems, using skip buckets or containers at selected transfer stations without, however, coming to grips with the neighbourhood-level waste management. Entrepreneurs should promote the three-R strategy of Reduction, Re-use, and Recycling (Solid Waste Management in Sri Lanka: Policy & Strategy, 2007).

- Collection

Municipal authorities do the collection but it is not simple as collecting waste from transfer stations using expensive trucks, skip buckets, and containers, but instead the entire transport chain from the household level upwards needs to be studied. Can the entrepreneurs contribute or take initiative for transport taking place between the household level and the transfer station and make the process be better regulated, recognised, safe, effective and efficient? Can they encourage their employees to become a part of a socially and economically valuable operation?

Institutional and organisational issues

The various skills and activities required by the entrepreneurs and their respective employees has become an issue when it comes to sustainable waste management. The requirement of formal contracts and licensing agreements, creation of these and implementing has become a key issue. The procedures to follow to be aligned with the financial institutes and government bodies also come as a key issue to these entrepreneurs.

Legal, political, and policy issues

Solid Waste Management in Sri Lanka (2007) states, "governance can be described as the manner in which public and private actors in society interact, democratically and transparently, and the general state of the urban environment is widely regarded to be an excellent indicator of the state of governance. Hence it is safe to assume that in a specific sense, governance means the manner in which laws and regulations structure the waste management policies and laws. But, governance mostly is an intensely political process focusing on power relationships between actors and sector in society and waste management is no exception. Therefore it is vital for the entrepreneurs to understand the manner in which politicians and political candidates value the importance of waste management in their constituencies in order to make it a sustainable venture. It is also essential to realise that the development and sustainability of community-based waste management is better than any formal licence or agreement.

Financial and economic issues

When actively involved in sustainable waste management, the entrepreneurs come across various financial and economic issues. These include analysis of annual budgets, audits, reports, and minutes of the municipal council related to waste management, municipal fee schedules, subsidies, and the political basis for them, permits, fines, and sanctions, taxation policy and records, capital and operating cost as well as recycling proceeds.

Socio-cultural issues

The manner in which people perceive their environment, and the manner in which waste is perceived, is closely related to their cultural background (Ghosh, 2000). Entrepreneurs located in the heart of Colombo, where densely packed, fast growing, slums are present, find it hard to convince the others of sustainable waste management and make it effective.

8. DISCUSSION

Below described are various methods found during the research, which will improve the sustainable waste management techniques followed by Sri Lankan entrepreneurs.

Institutional responsibilities

Even though the waste management is an obligatory function of all the local authorities in Sri Lanka, which includes the municipal councils, urban councils, and pradesiya sabhas, the service they perform in waste management is so poor, which results in problems of health, sanitation and environmental degradation. The entrepreneurs must take action to promote and contribute towards sustainable waste management.

There is an increase in the country's urban population at the rate of 2.5% which is far ahead of the annual population growth rate of 1.5%. With this rapid pace of urbanization, the waste management situation is becoming uncontrollable for entrepreneurs. There needs to be improvement in institutional weaknesses, social responsibility and environmental accountability of each citizen, means to fund for inadequate financial resources, improve technical competency, and create public apathy towards waste management, in order for entrepreneurs to contribute satisfactorily towards this cause.

Waste composition and volume

The total municipal solid waste generated in the country is assumed to be around 6,900 tonnes per day but the daily waste collection by local authorities is only 2700 tonnes. According to the available data, waste composition in Sri Lanka consist of 62% biodegradable waste, 6.5% of paper, 6% polythene and plastic, 6% of wood 2% glass (Colombo Environmental Improvement, 2003). Therefore, it is safe to assume that the average Sri Lankan municipal waste consists of a large proportion of compostable material.

System issues

The waste management practices in Sri Lanka needs a proper technique. Initially, the sorting of waste needs to be more methodical. Domestic, trade and institutional waste including hazardous biomedical/healthcare waste and industrial waste are also disposed mixed with municipal wastes. Garbage is thrown on the streets, footpaths, drains and water bodies treating them as receptacles of waste. Recyclable waste material is also not segregated at the source and is disposed of along with the domestic, trade and other waste.

Construction and demolition wastes also pose serious problems as this waste is deposited on the roadside or open spaces, obstructing traffic and causing nuisance (Solid Waste Management in Sri Lanka, 2007). General public continuously speak ill of the system but do not contribute for handling their waste social responsibly. Since most waste that is found everywhere has resource recovery potential, waste cannot be considered useless. Therefore, entrepreneurs must treat waste at all times as a commodity that has an economic value.

Justification for a National Policy

There is a critical requirement for a national approach to handle the waste management in Sri Lanka. Environmental friendly disposal of waste with special emphasis on prevention of waste generation has to be pursued. This is in order to avoid environmental degradation and negative impacts on the health of all life forms. As far as the country's constitution goes, every citizen in Sri Lanka is obliged to protect nature and conserve its riches. Further, "the National Environment Policy builds upon the polluter pays principle and emphasizes the need to reduce consumption and recycle and reuse materials to the maximum extent possible. It further emphasizes that it is the common but differentiated responsibility of every institution and individual to be involved in all aspects of waste management" (Solid Waste Management in Sri Lanka, 2007). Thus the overall goal of the national policy on waste management is to ensure integrated, economically feasible and environmentally sound waste management practices for the country.

9. RECOMMENDATIONS

The key issues found the entrepreneurs faced while sustainably managing the waste in Sri Lanka and the ways to improve their techniques were discussed above. The following are the recommendations this research presents in terms of methods that will improve for an improved and efficient waste management by entrepreneurs in Sri Lanka.

On waste disposal

- Community and neighbourhood level recycling and composting activities, as much as possible reducing and re-using waste at the source.
- Transfer stations, waste separation facilities, disposal sites and sanitary landfills, to create minimum health and environmental standards by securing and lining of landfills.
- Centralised composting facilities, to deplete nutrients by ever exploding cities.

On national policy

- Discuss the national waste management policy and strategy with relevant parties and contribute to drafting a national policy on waste management.
- Assist in analysing the institutional and legal reforms, transfer of technologies and capacity building, financing mechanisms and promotional campaigns.
- Support discussions on future of the national platform on waste management.

On management

- Waste management should be managed by entrepreneurs, adhering to the waste management hierarchy where the emphasis is on reduction of waste generation, reuse, recycling and resource recovery to the maximum extent possible, followed by appropriate treatment and finally by the disposal of residual waste.
- Adhere to national environmental standards developed under the provisions of the National Environmental Act.
- Resource maximisation should be ensured by promoting sustainable production and consumption and enforcing producer responsibility approach throughout the Product Life Cycle.
- Partnerships to be created in order to encourage efficient and cost effective collection, transportation, storage and treatment of waste and disposal of residues.

On financial mechanisms

- Appropriate resource mobilisation strategies should be followed with sustainable financing mechanisms for waste management.
- Obtain assistance from local authorities to ensure self-financing for waste management by effective revenue generation mechanisms.
- Appropriate financial incentive schemes should be explored and established by entrepreneurs to promote waste management.
- Carbon financing could be promoted as an incentive for promoting waste management practices in line with the existing clean development mechanism policy.

On legal mechanisms

- Entrepreneurs can assist to strengthen the existing regulatory mechanisms through appropriate legal reforms.
- Support effective law enforcement in order to ensure maintaining the accountability of stakeholders.

On research and development

- Awareness, education, training and capacity building on integrated waste management should be promoted among all stakeholders, especially employees and customers of the entrepreneurs.
- Research and development on waste management, should be encouraged and promoted and funded by the entrepreneurs.
- Best environmental practices should be implemented in all areas of their respective business.

10. CONCLUSION

Sri Lanka's current consumption, in the form of various goods, must end up in the waste stream and the responsibility is to either innovate in the field of waste management or to keep continuing the existing polluting methods of waste disposal. However, this field has lot of challenges and it takes persistence and providence to overcome them, as the root of the problem mostly lies in the minds of the people. To solve this ongoing challenge, smart minds need to come up with innovative solutions. Therefore, emerging entrepreneurs have a special task and responsibility towards this objective. An entrepreneur is one who plays significant role in the economic development of a country and the Sri Lankan entrepreneur is regarded as a person who has the initiative, skill and motivation to set up an enterprise of their own and who always looks for high achievement.

- The objectives of this research paper was to identify the techniques adopted by the Sri Lankan entrepreneurs in maintaining sustainable waste management, to examine the key issues faced by the Sri Lankans entrepreneurs related to sustainable waste management in Sri Lanka and to specify methods that will improve the waste management practices followed by the Sri Lankan entrepreneurs.
- The outcome of the study resulted from secondary data obtained from materials from existing reports related to waste management and recommendations. This research extracted, studied and analysed those data to obtain the necessary information on entrepreneurs of Sri Lanka and sustainable waste management. Additionally semi-structured interviews and environmental education and awareness building programs provided data for the inquiry. This research was qualitative in approach and employed formal and informal interviews, focus groups and questionnaires. Data obtained from a survey research was also extracted and analysed for the purpose of this research.

Government, private business, urban and rural residents and foreign organisations all face impressive challenges in arriving at solutions to the ongoing waste management issue in Sri Lanka. Entrepreneurs in Sri Lanka has come forward and started taking positive action in implementing sustainable waste management techniques. The techniques used by these entrepreneurs for sustainable waste management were discussed with the focus on Dilmah's tea recycling, SLIIT's 'Clean Lanka', Hayley's waste minimising projects and Rainforest Alliance.

The key issues identified by these entrepreneurs when implementing sustainable waste management were Health and environmental issues, Technical issues, Institutional and organisational issues, Legal, political, and policy issues, Financial and economic issues, and Socio-cultural issues. They were discussed in this research along with various methods to overcome the said challenges which includes Institutional responsibilities, Waste composition and volume System issues, and Justification for a National Policy. Recommendations were made for future for these entrepreneurs in the areas of waste disposal, national policy, management, financial mechanisms, legal mechanisms, and research and development.

Sri Lankans cannot wait for the government to develop solutions to sustainable waste management. They must take responsibility for their garbage and develop appropriate, community driven solutions to protect their, and their children's, lives and futures. Entrepreneurs can facilitate the necessary shift in consciousness, and behavioral change that has so far failed to occur through other interventions. Today the situation in Sri Lanka has changed to a certain extent and several of the local authorities now indeed recognise their presence. The next stage is that it is seen that working together with entrepreneurs is much more fruitful and efficient than working in isolation of each other.

10.1 Future studies

The Ministry of Environment and Natural Resources has conducted a massive campaign of awareness building in regards to persistent organic pollutants with significant success. Awareness must be created so people understand the connection between burning their garbage, generating persistent organic pollutants and the incidence of illness in themselves and their families. More research needs to be conducted to trace health trends related to the burning of wastes and emissions of pollutants into the environment, and training materials and events need to make these connections clear in tangible ways (Gunawardena, 2006). This would be an excellent research opportunity for medical students and would offer the practical skill building experience that is presently missing in the Sri Lankan educational system.

11. REFERENCES

Archer, G. and Baker, T. & Mauer, R. 2009, Towards entrepreneurial success. *Frontiers of Entrepreneurship Research*, 5

Bandara, N.J.G.J., 2003, Environmental Impacts Associated with Current Waste Disposal Practices in a Municipality in Sri Lanka- A Case Study, Workshop on Sustainable Landfill Management 3-5 December 2003; Chennai, India. pp. 19-26.

Bell, E and Bryman, A., 2007, *Business Research Methods*, second edition, published by Oxford University Press, New York.

Colombo environmental improvement, 2003, document of the world bank, article available: <http://web.worldbank.org/wbsite/external/topics/exturbandevlopment/extuswm/0>

Daily News Paper, 2019, Solid waste management in Sri Lanka article available: <http://www.dailynews.lk/2019/06/13/finance/188189/smart-system-solid-waste-management-sri-lanka>

Dela, J., Wendy G., Dhunmai C., 2006, The role of communication of Sri Lanka: a Biodiversity Hotspot. *Sri Lanka: Environmental Foundation Ltd, Journal Volume 22 (2): April-June 2006.*

Dilmah Tea PLC, 2017, Recycling waste: methods adopted by Dilmah, available at:

<https://www.dilmahtea.com/sustainability/pdf/Dilmah-Sustainability-Report-2017.pdf>

Environmental Unit, 2005, Environmental Assessment in the Democratic Socialist Republic of Sri Lanka Document of Joint UNEP/OCHA Environment Unit article available:

www.reliefweb.int/rw/RWB.NSF/db900SID/VBOL-69EHS9?OpenDocument

Fernando, H., 2006, The wandering collector, *Explore Sri Lanka*, Magazine, Number 42.

Ghosh, N., 2000, One man's crusade cleans up a town, *Sri Lanka Daily News*, August, p. 9.

Gunawardena, C., 2006, Issues Related to Education and Sustainable Development, Handout presented at the SLMA 2006 Issues in Sustainable Development lecture series.

ISA - Korea's Solid Waste Management Market, 2003, U.S. & Foreign Commercial Service, article available: <http://strategis.ic.gc.ca/epic/internet/inimrri.nsf/en/gr109806e.html>. [August 2006].

Hayleys Group PLC, 2019, Sustainable waste management, article available:

<https://www.hayleys.com/sustainability/sustainability-practices>

Jayawardane, V.P.T. 2015, Management Styles of Sri Lankan Women Entrepreneurs towards Empowerment

PhD Thesis

Ministry of Environment and Natural Resources-Sri Lanka, 2007, Caring for the Environment, *Path to Sustainable Development*, 1,

Ministry of Environment and Natural Resources-Sri Lanka, 2002, State of the Environment in Sri Lanka: A National report prepared for the South Asian Association for Regional Cooperation, *Colombo: Environmental Economics & Global Affairs*, Ministry of Environment and Natural Resources

Ministry of Environment and Natural Resources, 2003, Theoretical Manual for Environmental Valuation in Sri Lanka, Economics and Global Affairs Division, The World Bank, article available:

<http://web.worldbank.org/WBSITE/EXTERNAL/TOPICS/EXTURBANDEVELOP>

Moonasinghe, V., 2003, Waste – A Global Problem, article available:

<http://www.sarid.net/archives/sarid-archives.htm>.

National Council for Economic Development of Sri Lanka, 2015, Ensure Environmental Sustainability of Sri Lanka, National Council for Economic Development of Sri Lanka and United Nations Development Programme.

National Strategy for Solid Waste Management, 2002, Government Report, Ministry of Environment & Natural Resources-Sri Lanka

Nuchemy (Pty) Ltd, 2007, Case study carried out for some available landfills in Sri-Lanka, *Energy Forum*, Moratuwa University, Moratuwa

Pilapitiya, S., 2006, Challenges of Solid Waste Management in Sri Lanka: Past, Present and Future, *Environmental Foundation Limited Journal*, Volume 22, Pages 2-6.

Post, V., 2007, Mission Report of Hambantota Sri Lanka, *VNG and Logo South Good Local Government Conference*, Gouda

Senanayake, R.M.B., 2006, Aid: Boon or Bane? Sri Lanka's dependency on aid could lead to economic stagnation, *LMD Journal*, January, pg. 167

Solid Waste Management in Sri Lanka, 2007, Sustainable Waste Management, *Strategies and Policies*, Sri Lanka

Sunday Observer, 2014, Garbage-the reality, Sri Lanka Sunday Observer Environment Section, October

Sustainable Development Board, 2002, Sri Lanka's Middle Path to Sustainable Development in the 21st Century: National Report to the World Summit on Sustainable Development, Sri Lanka

Tan, R.B.H. and Khoo, H., 2006, Impact Assessment of Waste Management Options in Singapore, *Journal of the Air & Waste Management Association*, Volume 56: March, pp.244-254 National University of Singapore, Singapore

Van der Wel, A. and Post, V., 2007, Solid Waste Management in Sri Lanka: Policy & Strategy, *Cordaid Reconstruction*, 4

Van Zonn, L., and Siriwardena, N., 2000, Garbage in Sri Lanka, IRMP, Colombo, article available: <http://environmental.scum.org/sl Waste-main.pdf>

#380: Laboratory testing for the vacuum glazing, double glazing and single glazing

Shihao ZHANG*, Hasila JAMIRI, Qi XU, Saffa RIFFAT

*Department of Architecture and Built Environment, Faculty of Engineering, University of Nottingham, NG7 2RD
University Park, Nottingham, UNITED KINGDOM*

**Corresponding author: Shihao.zhang@nottingham.ac.uk*

*The most common glazing types for domestic buildings is single glazing, insulating glazing (also known as double glazing) and vacuum glazing. Currently, single glazing is becoming a thing of the past and is being replaced with its more durable and efficient counterpart, double glazing or vacuum glazing. Double glazing has been widely used in the EU and China. The unit price of double glazing has improved because of mass manufacturing. This paper describes four types of glazing systems as well as mathematical analyses of the energy transfer process through a computer programme using a computer simulation to analysis performance. The results show that vacuum glazing enjoys the best thermal performance. The overall U-value can achieve about 1.05 W/m²*K, which can have huge commercial potential for vacuum glazing. The carbon emission reduction potential of using vacuum glazing across Wuhan has also been analysed.*

Keywords: vacuum glazing; double glazing; single glazing; carbon reduction potential

1. INTRODUCTION

Nowadays, greenhouse gas (GHG) emissions have become an increasingly severe problem for every government in the world. The building and related industry has become the primary contributor to GHG emissions. In the city, there are the thousands of buildings and during the long life-cycle of them, they need to be constructed, maintained and demolished, which consumes a vast amount of energy, water, materials and so on. With the development of real estate in Asia and the Mideast area, the total GHG emissions will increase greatly in the next 40 years. A survey from the Intergovernmental Panel on Climate Change estimated that 40% of the total non-renewable energy is consumed by the building-related industry (Nakicenovic, 2007). Humans are facing the most serious energy and pollution problem ever seen (Ajanovic & Haas, 2017) and governments are making efforts to develop low-carbon house technologies (Zhao et al., 2015).

As for China, the situation is more urgent. The growth rate of energy consumption in buildings is more than 10% over the past decades (Chang et al., 2014). In fact, Chinese people suffer from the High Emission Economy. So, we should evaluate the negative influence of massive urbanisation and building construction. From the perspective of the Chinese government, they have started to collect macro-level analysis, such as input/output (I/O) analysis and structural path analysis (Chang et al., 2014; Nakicenovic, 2007). On the basis of the industrial and project, previous researchers have proposed a lot of methodology for studying the current status of GHG emission. However, those methodology are not practical because of uncertain statistics (Hong et al., 2016). So, the result of the research above cannot be the theoretical basis for the Chinese market.

Windows are a significant source of transmission heat loss or heat gain at different climate zones. Heat loss through windows accounts for about 20% of the total heat loss from an average home in UK. The energy efficiency of window technology is crucial to energy efficiency and to reduce the fuel energy costs and carbon emissions. Also increasing thermal resistance of window may help to reduce the condensation problem which is a common complaint by residents.

The conventional vacuum glazed window consists of two plane sheets of glass separated by a vacuum and small support pillars. The vacuum provides a high insulating value as heat loss via conduction is virtually eliminated. The pillars are positioned between the glass panes with a gap of 0.2mm. Vacuum glazed windows can eliminate heat transport between the glass sheets due to gaseous conduction and convection.

This research developed experiments to investigate the thermal transmittance (U-value) of the three types of glazing mentioned above. Using testing and economic analysis, the main aim of the research was to find the best technology compatible with the higher levels of the Code for Sustainable Homes and the future requirements of commercial buildings.

2. PROTOTYPE DESCRIPTIONS



Figure 1: Testing Prototype

The testing box was made of four replaceable pieces of window. These four windows consisted of 10mm vacuum glazing window, 28mm normal double-glazing window, 20mm double glazing window and 4mm single glazing window. The size of the window was 30cm by 30cm.



Figure 2: Vacuum glazing



Figure 3: 28mm normal double glazed window



Figure 4: 4mm single glazing



Figure 5: 20mm double glazing

3. MATHEMATICAL ANALYSES OF THE HEAT TRANSFER PROCESS FOR VACUUM GLAZING

BS EN ISO 6946 and CIBSE Guide A quote standard values for the thermal resistance of unventilated cavities as a function of the thickness of the cavity and the direction of heat flow, which are shown in the following tables and figures.

Table 1: surface resistance values

Surface Resistance $m^2 \cdot K / W$	Direction of the heat flow		
	Upwards	Horizontal	Downwards
R_{si}	0.1	0.13	0.17
R_{se}	0.04	0.04	0.04

* R_{si} : internal surface resistance, R_{se} : external surface resistance

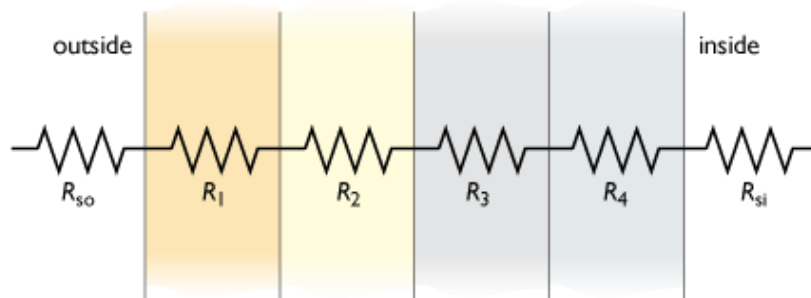


Figure 6: Summing thermal resistances

$$R_G = R_{so} + R_1 + R_2 + R_3 + R_4 + R_{si} \text{ (in } m^2 \cdot K / W \text{)}$$

Table 2: Thermal conductivities $W/m \cdot K$ of unventilated air cavities

Thickness of the air	Direction of the heat flow		
	Upwards	Horizontal	Downwards
5	0.045	0.045	0.045
7	0.054	0.054	0.054
10	0.067	0.067	0.067
15	0.094	0.088	0.088
25	0.156	0.139	0.132
50	0.313	0.278	0.238
100	0.625	0.556	0.455
300	1.875	1.667	1.304

The values in Table 2 above are directly proportional to the thickness of the layer, d in metres, and can be expressed as:

- Upwards heat flow: $\lambda = 0.00511 + 6.227 \cdot d \text{ W/mK}$;
- Horizontal heat flow: $\lambda = 0.00858 + 5.518 \cdot d \text{ W/mK}$;
- Downwards heat flow: $\lambda = 0.0247 + 4.268 \cdot d \text{ W/mK}$;

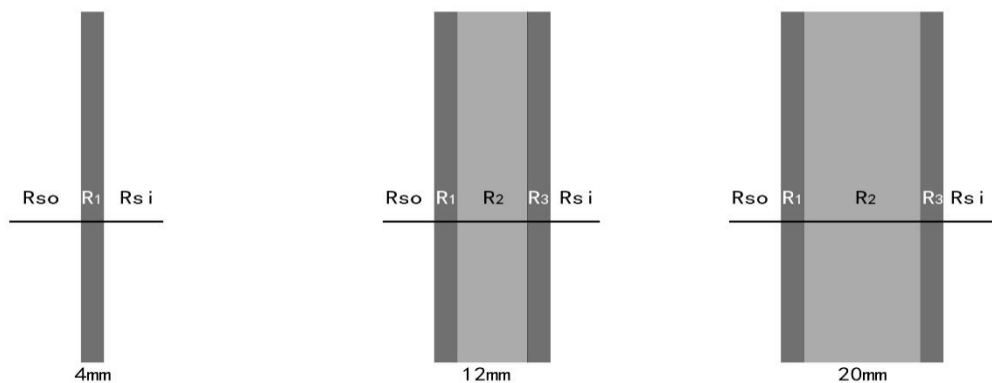


Figure 7: Summing thermal resistances

Based on above references, for single glazing,

- $\lambda_{\text{glass}} = 1.05 \text{ W/mK}$,
- $R_{\text{glass}} = 0.0038 \text{ m}^2\text{K/W}$.
- $R_{\text{so}} = 0.04 \text{ m}^2\text{K/W}$,
- $R_{\text{si}} = 0.13 \text{ m}^2\text{K/W}$.
- $R_A = R_{\text{so}} + R_{\text{GLASS}} + R_{\text{si}} = 0.172 \text{ m}^2\text{K/W}$

Based on above references, for air gap in 20mm,

- $\lambda_{\text{air}} = 0.00858 + 5.518 \cdot 0.012 = 0.12 \text{ W/mK}$,
- $R_{\text{air-20mm}} = 0.17 \text{ m}^2\text{K/W}$. For the glazing,
- $\lambda_{\text{glass}} = 1.05 \text{ W/mK}$,
- $R_{\text{glass}} = 0.0038 \text{ m}^2\text{K/W}$.
- $R_{\text{so}} = 0.04 \text{ m}^2\text{K/W}$,
- $R_{\text{si}} = 0.13 \text{ m}^2\text{K/W}$.
- $R_B = R_{\text{so}} + R_{\text{GLASS}} + R_{\text{air}} + R_{\text{GLASS}} + R_{\text{si}} = 0.34 \text{ m}^2\text{K/W}$

For the developed panel with vermiculite,

- $\lambda_{\text{air-12mm}} = 0.075 \text{ W/mK}$,
- $R_{\text{ver}} = 0.16 \text{ m}^2\text{K/W}$.

For the double glazing with air gap in 12mm,

- $\lambda_{\text{glass}} = 1.05 \text{ W/mK}$,
- $R_{\text{glass}} = 0.0038 \text{ m}^2\text{K/W}$.
- $R_{\text{so}} = 0.04 \text{ m}^2\text{K/W}$,
- $R_{\text{si}} = 0.13 \text{ m}^2\text{K/W}$.
- $R_C = R_{\text{so}} + R_{\text{GLASS}} + R_{\text{ver}} + R_{\text{GLASS}} + R_{\text{si}} = 0.338 \text{ m}^2\text{K/W}$

Therefore, The theoretical U-value of single glazing is:

- $U_A = 1/R_A = 5.8 \text{ W/m}^2\text{K}$

The theoretical U-value of double glazing with air gap in 20mm is:

- $U_B = 1/R_B = 2.88 \text{ W/m}^2\text{K}$

The theoretical U-value of double glazing with air gap in 12mm is:





- $U_C = 1/R_C = 2.96 \text{ W/m}^2\text{K}$

4. EXPERIMENT SET UP

Four glazing sheets were used for the test windows measuring 300mm by 300mm designed for hotbox measurements of the overall U-value. The test rig is shown in Figure 1, with 10mm vacuum glazing window, 20mm normal double-glazing window, 20mm heat insulation bridge aluminium double glazing window and 4mm single glazing window joined together to construct a test box. A well-insulated framing system was made to fix the four glazing pieces in place. The temperature difference across the inside and outside glazing surfaces were measured by K type thermocouples, with $\pm 0.001^\circ\text{C}$ accuracy. The air temperature in the hot box and cold side (laboratory) were also measured. HFP01-05 heat flux sensors were used to measure conductive heat transfer (loss or gain) through the window surfaces and its sensitivity was $61.542 \mu\text{V}/(\text{W/m}^2)$. A 200W mini heater was used as a constant heating power supplied to the hot box. Test data was collected by a DT85 data logger.

Followed the above test conditions and procedures, different types of glazing window were tested in the laboratory condition in the Department of Architecture and Built Environment University of Nottingham.

Table 3: Major measurement tools

Measurement Tools	Images	Details	Description
Datalogger		DT80 series 3 180mm x 137mm x 65mm 110/240Vac to 15Vdc, 800mA	Linearization errors < 0.1°C
Heat Flux sensor		HFP01-05 Temperature range: - 30 to +70oC Accuracy: ±5%0.01m/s	Sensitivity: 63.6µV/Wm-2 and 63.6µV/Wm-2
K-type Thermocouple		K-type 0.2mm diameter Operating temperature reaches up to 250°C	Accuracy: ±1.5°C
Mini Heater		40W Mini Fan Heater	

5. CALCULATION AND EXPRESSION OF RESULTS

The equation of the window thermal transmittance U-values (W/m²K), are calculated as follows,

Equation 1:

$$U = \frac{\varphi}{A(T_{e1} - T_{e2})}$$

Where:

- φ = heat flux though the prototype (in Watt)
- A (in m^2) = total area of the individual glazing.
- T_{e1} = temperature measured inside the box,
- T_{e2} = environmental temperature (in °C).

5.1. Test results and analysis

Vacuum glazing window U-value results with time were calculated and are shown in Figure 8.

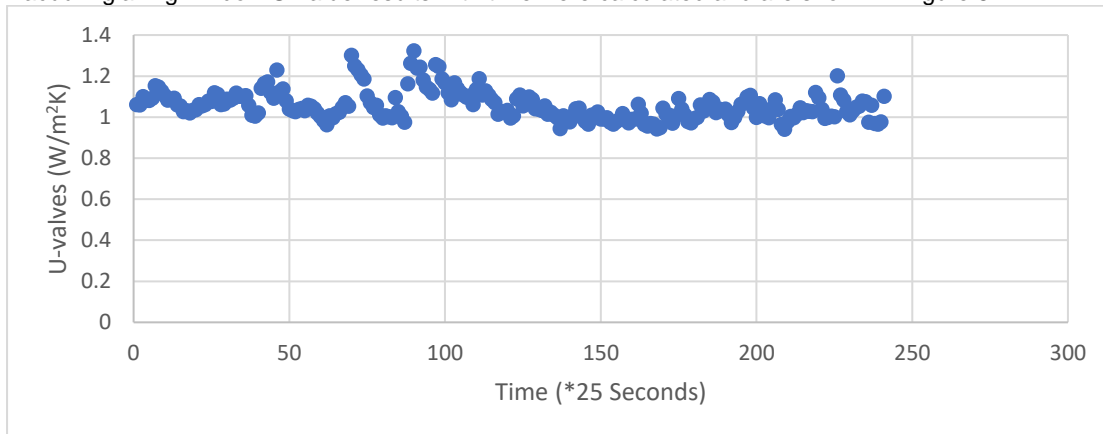


Figure 8: Vacuum glazing window U-values

When the apparatus reached equilibrium with the temperatures and the power supplied being stable without continuously increasing or decreasing, the readings were taken and the test continued for 5 hours. The average U-value of the vacuum glazing was around 1.056 W/m^2K . The same test procedures and conditions were applied to the double-glazing window sheet.

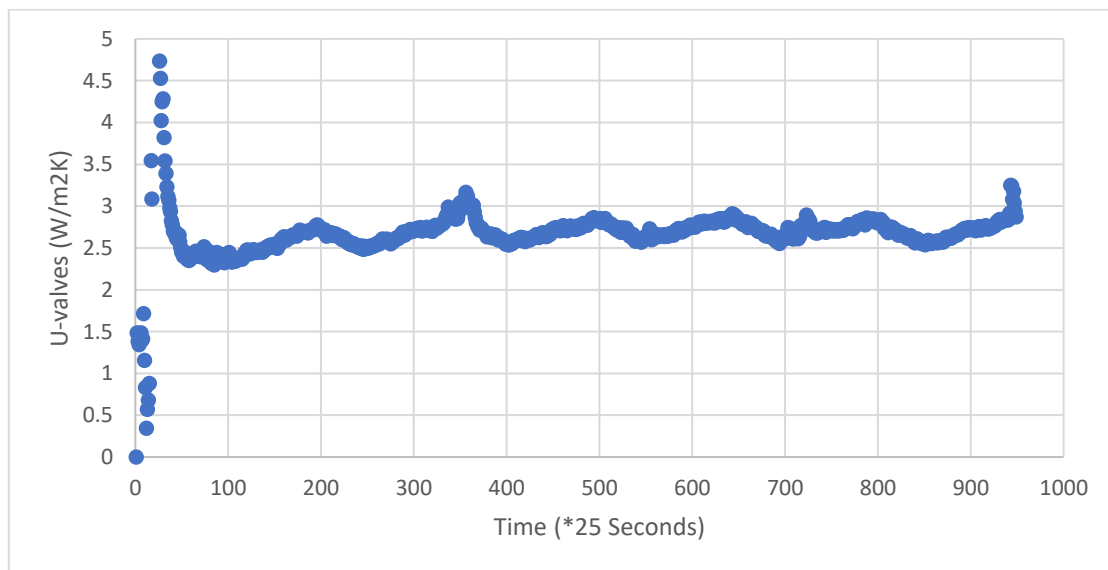


Figure 9: shows U-values results with time of normal double glazing

Average U-value of the 28mm normal double glazing was about 2.675 W/m^2K , which was higher than for vacuum glazing. The heat insulation bridge aluminium double glazing window U-values with time were calculated and shown in the following.

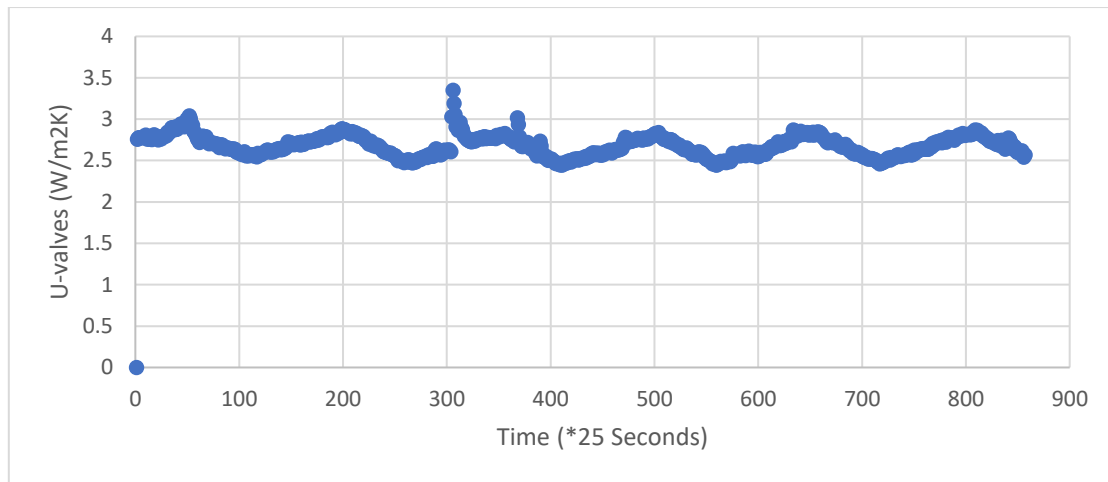


Figure 10: Heat insulation bridge aluminium double glazed window U-values

The average U-value of the 20mm double glazing was about 2.679 W/m²K, which was similar to the standard double glazing. The average U-value of the single glazing was about 10.7245 W/m²K, which is much higher than any other type of glazing.

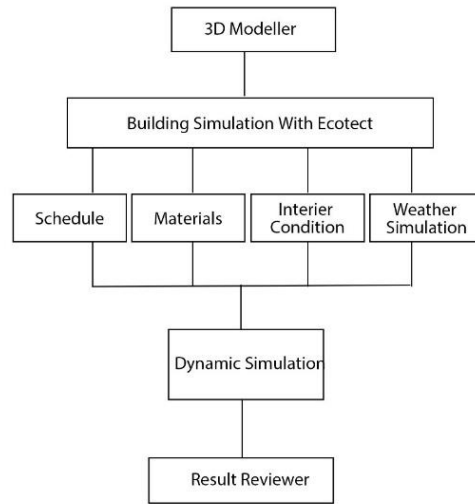
From the above diagrams, it can be seen that vacuum glazing performed best due to its better thermal resistance performance. Normal double glazing and heat insulation bridge aluminium double glazed window also achieved a good U-value, but single glazing window performed worst. However, some issues need to be addressed for vacuum glazing, e.g. high manufacturing cost, difficulty to assemble the glass module, glass is not strong enough and so can easily break, and difficulty maintaining the vacuum seal for an extended period. Further development is still needed to develop pre-fabricated energy-efficient housing including investigation into a novel type of vacuum glazing with better thermal resistance performance.

6. ECONOMIC AND ENVIRONMENTAL ANALYSIS OF THE VACUUM TUBE WINDOW SYSTEM

6.1. Using computer simulation to evaluate the performance of the glazing system

A test house in Wuhan was used to test the actual thermal performance of this seasonal technology system. However, in the design stage, the interior environment situations should be assessed. Using accurate values of annual cooling load and heating load, the system used a variety of materials to obtain results energy performances of several different kinds of glazing systems.

In this stage, Autodesk Ecotect software was applied to simulate the proposed Wuhan House (Figure 11). Autodesk Ecotect is a building thermal analysis software developed by Square One Research. Ecotect provides analysis of a building's energy consumption and assesses summer peak temperatures. Comparing the results of the simulation under different glazing system, we were able to find out the performance gaps between the systems. Table 4 shows the energy consumption & energy gap of different glazing types



Flow Chart on the Ecotect Model Process

Figure 11: Flow chart of an Ecotect model process

Core parameter settings in Ecotect software included a year calendar, local weather, zoning of the house, construction materials, internal conditions of each zone and operation schedules. Figure 12 shows a 3D model of the Wuhan House in Ecotect.

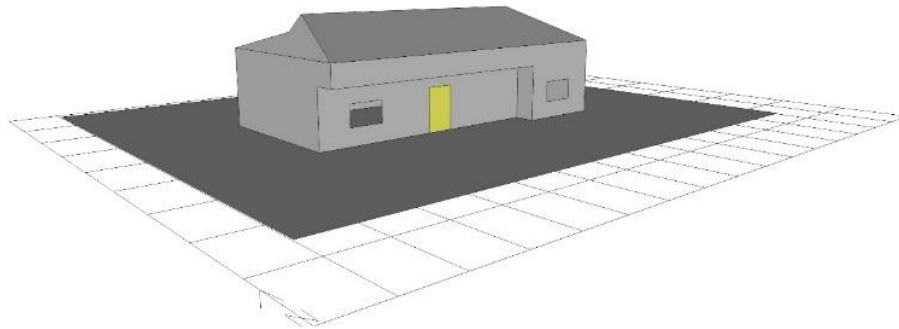


Figure 12: The Wuhan house in Ecotect

Table 4: Energy consumption & energy gap of different glazing types

Type	Energy Consumption-Wh	Energy Gap between Vacuum Glazing-kWh
Single-Glazing	790544	295.403
20mm Double-Glazing	606794	111.653
28mm Double-Glazing	608122	112.981
Vacuum Glazing	495141	0

6.2. Environmental effect

Based on the above information, the annual carbon emission reduction of the conventional 20mm double glazing, 28mm double glazing and single glazing windows compared with vacuum glazing can be worked out in terms of kg per annum. The following equations can be used:

Equation 2:

$$E_{carbon} = f_{c,e} * (Q - Q_{Vacuum})$$

Where E_{carbon} is the carbon emission reduction of vacuum glazing compare with other kind of the glazing system. From the analysis (Gu et al., 2015), the $f_{c,e}$ is about 0.4646 kgCO₂/kWh. Table 5 shows energy gap and annual carbon emissions reduction with four types of glazing.

Table 5: Energy gap of different glazing types & annual carbon emission reductions

Glazing Type	Energy Gap between Vacuum Glazing-kWh	Annual Carbon Emission reduction replaced by vacuum glazing-kg
Single-Glazing	295.403	139.4
20mm Double-Glazing	111.653	51.92
28mm Double-Glazing	112.981	52.54

6.3. Life cycle analysis

Assuming an expected life cycle of 25 years, the total energy and emission savings achieved by replacing other glazing with vacuum glazing can be calculated by multiplying the energy and cost savings per annum by the life cycle time. The calculations are shown below in Table 6. The total extra life-cycle cost of the other glazing systems over vacuum glazing also show below.

Table 6: Energy and emission savings achieved by replacing other glazing with vacuum glazing

Glazing Type	The Life-long extra energy cost over vacuum-£	The initial cost over Vacuum Glazing-£	The extra Life-long cost over the vacuum-£
Single-Glazing	517.5	-119.28	398.22
20mm Double-Glazing	195.35	-79.52	115.83
28mm Double-Glazing	197.5	-68.16	129.34

Due to its low thermal transmittance (U-value), vacuum glazing can reduce heat loss by over 60% compared to single glazed windows. The initial cost of the vacuum glazing is slightly higher than the double glazing. Despite the relatively higher initial cost of the vacuum glazing, the house in Wuhan utilised vacuum glazing and reduced the carbon emissions and increased energy savings were 139.4 kg and £517.50 respectively compared to single glazing. For each square metre of double glazing window compare to the vacuum glazing, the annual energy saving was about £195 and CO₂ reduction was about 52 kg. Vacuum glazing has shown to offer huge potential in energy savings and CO₂ reduction in buildings. It has a low U-value and significant lower heat loss rate than the conventional double glazing and triple glazing windows, therefore heating costs for buildings will be greatly reduced. A replacement of 20% of the three other kind of windows by vacuum glazing can reduce the annual energy bill by £119.28, £79.52, and £68. As for the 28mm double glazing and 20mm double glazing, the thermal performance was similar, showing similar carbon emissions and economic advantage. The gap of energy use and carbon emissions between glazing types is illustrated in Figure 13 below.

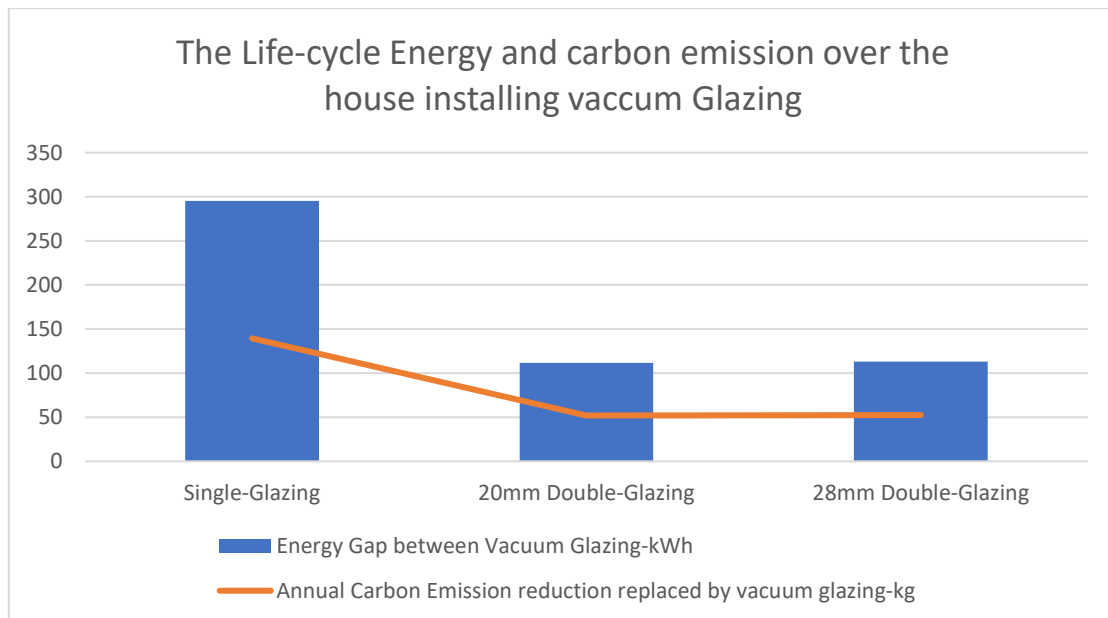


Figure 13: The gap of energy use and carbon emissions between glazing types

7. SUMMARY

This paper described four type of the glazing system as well as mathematical analyses of the energy transfer process through a setup of computer programmer. Using the computer simulation to analysis the performance. The result shows that the vacuum glazing enjoy the best thermal performance. The overall the U-value can achieve

about 1.05 W/m²*K, which have huge commercial potential of vacuum glazing. Carbon emission reduction potential of using vacuum glazing across the Wuhan has also been analysed.

8. REFERENCES

Ajanovic, A. & Haas, R., 2017. The impact of energy policies in scenarios on GHG emission reduction in passenger car mobility in the EU-15. *Renewable and Sustainable Energy Reviews*, 68, pp.1088–1096. Available at: <http://www.sciencedirect.com/science/article/pii/S1364032116002215> [Accessed June 2, 2017].

Chang, Y. et al., 2014. Disaggregated I-O LCA model for building product chain energy quantification: A case from China. *Energy and Buildings*, 72, pp.212–221. Available at: <http://dx.doi.org/10.1016/j.enbuild.2013.12.026>.

Gu, B. et al., 2015. CO₂ Emission Reduction Potential in China's Electricity Sector: Scenario Analysis Based on LMDI Decomposition. *Energy Procedia*, 75, pp.2436–2447. Available at: <http://dx.doi.org/10.1016/j.egypro.2015.07.210>.

Hong, J. et al., 2016. Uncertainty analysis for measuring greenhouse gas emissions in the building construction phase: A case study in China. *Journal of Cleaner Production*, 129, pp.183–195. Available at: <http://dx.doi.org/10.1016/j.jclepro.2016.04.085>.

Nakicenovic, N., 2007. *World energy outlook 2007: China and India insights*, IEA/OECD.

Zhao, D.-X. et al., 2015. Social problems of green buildings: From the humanistic needs to social acceptance. *Renewable and Sustainable Energy Reviews*, 51, pp.1594–1609. Available at: <http://www.sciencedirect.com/science/article/pii/S1364032115007194>.

#381: The impact of shading devices on the visual comfort and energy consumption of office rooms

A case study of the Ingenuity Building, Nottingham, UK

Shayeeka Binte ALAM

Department of Architecture and Built Environment, University of Nottingham, arch08hridita.alam@gmail.com

External shading devices on a building façade is a significant passive design strategy which can decrease direct solar radiation while controlling the direct daylight. While having an immense aesthetic impression, shading devices help to minimize the incident solar radiation and control daylight penetration, hence create a considerable effect on the building's energy performance. As energy conservation and efficiency are fundamental areas of focus in contemporary building design, the effect of shading devices on energy consumptions should be widely explored. The study of this paper evaluated the visual comfort and energy demand of a real case office building, the Ingenuity Centre; which is enveloped by an exceptionally distinct shading device. The purpose of this study was to understand the relation between daylighting and energy consumption of Ingenuity Building considering the impacts of shading device. Quantitative methodologies such as spot measurement and checking the rule of thumbs were undertaken to get a practical idea of the spaces. After analysing the physical model on Heliodon, a digital model was built in IES-VE, to analyse the annual average lux level and Daylight Factor of the office rooms during the active office hours. A significant observation of this study was that the existing shading devices were not providing optimum solutions to daylight inclusion, instead, there was a notable presence of glare causing visual discomfort. Moreover, there was no improvement in the overall energy consumption of the building with the existing shading devices. The proposed shading devices, which were suggested considering the building orientation and climate, improved the daylight level in the office rooms and reduced the energy load as well. The results showed that the annual average lux was increased by 4.5% with a significant reduction in glare with the proposed shading strategy. It was evident that an appropriately designed shading device could achieve higher energy efficiency, providing improved visual comfort. Further exploration is required in this matter with various orientations and building forms, the size and depth of the shading devices as well as materials.

Keywords: shading devices, daylight, office building, visual comfort, energy consumption

1. INTRODUCTION

Shading devices, a fundamental part of the building envelope, function like a hat on a building. While performing as a protector of the inner spaces from the direct solar gain through openings, windows and large glazed surfaces, shading devices also influence positively towards energy efficiency in buildings (*Lee et al., 1998, pp.47-63*). The design and orientation of shading devices change according to different climatic region. For example, buildings in hot-humid climate demand shadings which can reduce the amount of solar radiation and sunlight penetration into the building. On the contrary, for cold climate, it is important to let the sunlight penetrate the building and let the envelope absorb the solar radiation to sustain the heat, hence working as a thermal mass to provide warmth during winter.

Energy efficiency is now considered as one of the fastest and most appropriate approaches to minimize any energy-related emissions associated with air pollution, global warming and climate change (Dincer, 1998, pp.427-453). Buildings all over the world are now expected to achieve energy efficient status by adopting several active or passive design strategies (Iqbal, 2007, pp. 2166-2177). Numerous approaches can be tried to reduce energy consumption in a building. A study in Hong Kong reported that 35% of total cooling demands could be saved by energy efficient envelope design (Chan, 1998, pp. 21-39). Another study confirmed that external shading devices, which can be made of building materials or plants, could reduce the indoor cooling load by 30%. This study also stated that shading devices are more effective in reducing cooling load compared with the use of high-performance glazing (Balaras et al, 2000, pp. 143-54).

2. The Ingenuity Centre, Nottingham

2.1. Building profile

The Ingenuity Centre is the latest addition to the University Innovation Park (UNIP) at Jubilee Campus. Located at the focal point of the UNIP, the Ingenuity Centre is a three-storied building providing office-based accommodation for technology-driven start-up businesses from the local business community and from within the University. Formerly the site of Nottingham's famous Raleigh bicycle factory, it also manufactured ammunition and armaments during World War II (Philpot, 2016, pp.17-21).

Completed in autumn 2016, the works of Ingenuity Building were managed by Robert Woodhead. The architect for the scheme was Bond Bryan, with Arup acting as services and structural engineer. The director of the Bond Bryan Architects, Mathew Hutton, claimed that the building was designed to appear as a hi-tech structure that would not look out of place in a sci-fi movie with a complex array of metal fins configuring a metallic bronze-coloured circular envelope (*Figure 71*). The curtain wall of the central core is glass and a black aluminium cassette cladding, while the support structure behind the blade cladding is also black (Hutton, 2017).



Figure 71: The Ingenuity Building (source: author)

The three-storey building is cylindrical, having a glazed core with an atrium space at the centre. The partitions for the spaces inside can be easily reconfigured to make smaller, cellular space and larger open spaces. There are

mixture of cellular and open-plan spaces at the first and second floors of the building. The ground floor level has more open, shared areas for social and public engagement including the atrium, seminar spaces and collaborative hub space (Hutton, 2017).

2.2. Background context

As stated by Hutton (2017), the main concept behind the architecture of the Ingenuity Centre was to reflect the local industrial heritage of the area surrounding the Innovation Park. The design was based on the shape of a tyre (Figure 72) to honour the Raleigh cycles factory, which dominated the Triumph Road site from the 1930s until the end of the 20th century (Hutton, 2017).

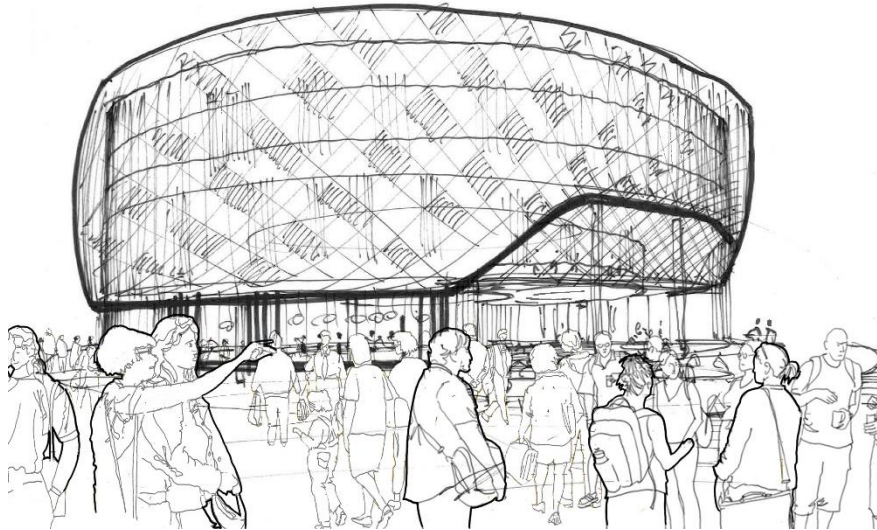


Figure 72: Architects perspective (source: Hutton, 2017)

The building was considered by the architect as a combination of hi-tech with heritage. In order for the building to resemble the Raleigh bicycle, which had its factory on the site, 1218 numbers of 350 mm wide x 50mm deep, angled, aerofoil-shaped fins were presented as shading devices (Philpot, 2016, pp.17-21).

The shading devices were constructed from anodised aluminium fins, with black concentric steel rings (Figure 73). This structure was mounted on vertical, curved hockey blade frames attached to the central cylinder. Each individual aerofoil blade was manufactured off-site but had to be cut to exact size by hand on site before installation (Philpot, 2016, pp.17-21).



Figure 73: Shading devices of Ingenuity building (source: author)

According to Hutton (2017), extensive modelling was carried out by the architects using Building Information Modelling (BIM) to ensure the effectiveness of the blade design. The aim was to design in such way so that the blades were neither obstructive nor oppressive while viewed from the inside and did not restrict the daylight entering the building at different times of year (Hutton, 2017).

2.3. Climate analysis

From Figure 74, it was understood that the average temperatures in Nottingham ranged from 10°C to 21°C in the summer season and from 2°C to 10 °C in the winter season. It was crucial to allow sun rays to get into the building in winter to lower the heating loads, whereas the opposite is required in summer.

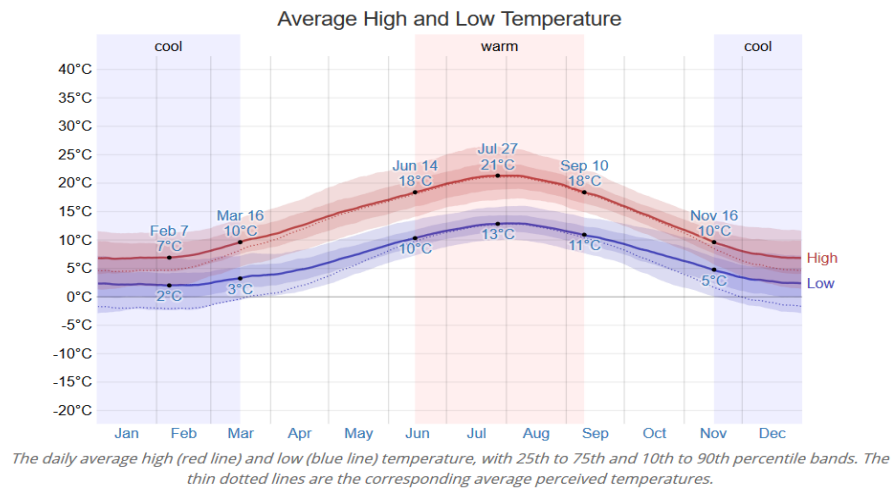


Figure 74: Temperature graph of Nottingham (Source: weatherspark, 2018)

Since summer has longer daylight hours (Figure 75), the building would be subjected to direct sunlight exposure for a long time, resulting in higher indoor temperatures in the building creating thermal discomfort. On the contrary, during winter, sunlight is appreciated, but the sun altitude is lower, increasing the probability of glare.

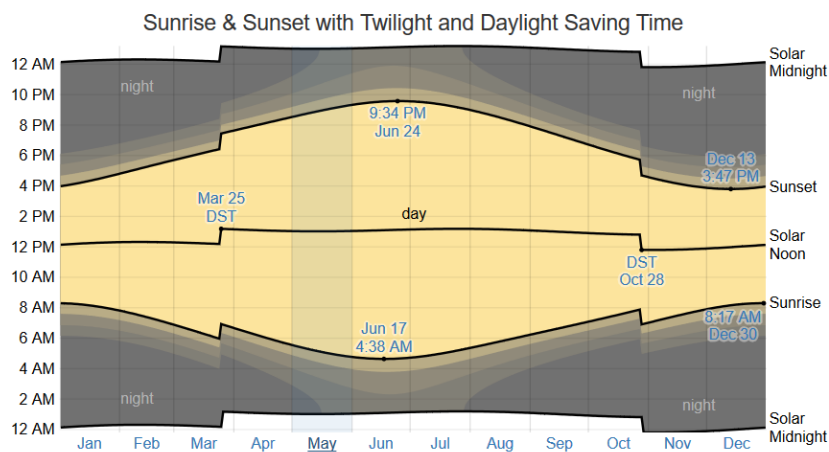


Figure 75: Hours of daylight (Source: weatherspark, 2018)

3. RESEARCH METHODOLOGY

In this paper, the author studied the performance of the shading devices focusing on daylight and energy consumption of the Ingenuity Building. The relationship between daylight and energy consumption was investigated, specifically on how the daylight levels change according to the shading device design and their influence on the performance of the building's energy consumption.

The initial investigation on daylighting and building energy consumption was carried out using Sefaira. Quantitative methodologies such as spot measurement and checking the rule of thumb were undertaken to get a practical idea of the spaces. After analysing the physical model on Heliodon, a digital model was built in IES-VE, to analyse the annual average lux level and daylight factor of the office rooms. Three separate analyses were conducted, comparing existing shading devices with no shading device, and finally proposing a shading strategy that responds to the limitations of the current design. The analyses was focused on two office rooms, both located on the first floor, one room facing the north and the other facing the south (*Figure 76*). Since the east and west sides of the building consisted of service facilities and circulations, there were no office rooms to compare with. Both the office rooms, located in the north and south, were almost identical in size, measuring 6.2m x 5.3m, having a ceiling height of 3.6m. The computer model simulations were run to achieve annual results during office hours, which was 9.00-17.00 from Monday to Friday.

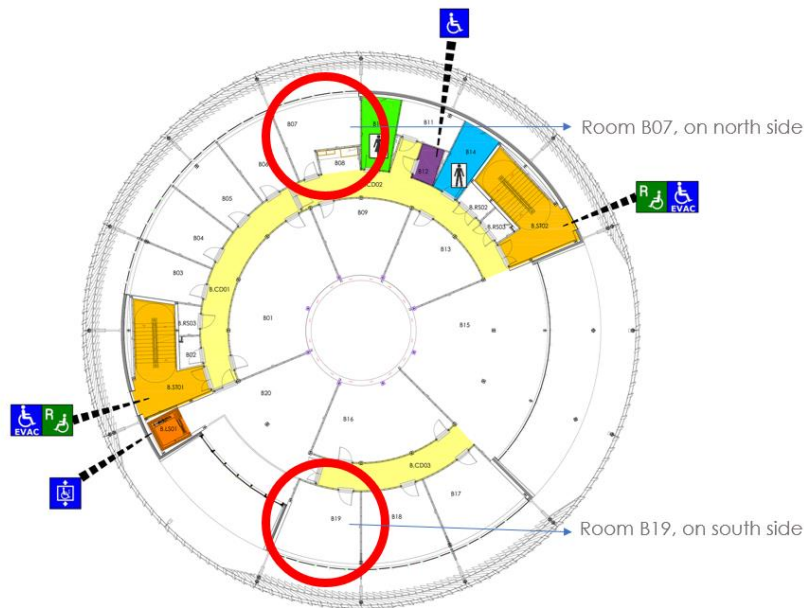


Figure 76: Selected office rooms of Ingenuity Building on the first floor

4. SHADING DEVICE ANALYSIS

The climatic condition and sun altitude play a vital role while designing a shading device. A well-designed shading device, which can be a part of a building or separately placed, can significantly reduce building heat gain and cooling requirements and improve the natural lighting quality of building interiors (Lee, 1995, pp.326-342).



Figure 77: IES model with yearly sunpath diagram for Ingenuity Building (source: author)

The design of effective shading devices depends on the solar orientation of a specific building façade. From Figure 77, we can see the sunpath diagram of Nottingham with reference to the case study building. The sun rotates from east to west at a very low altitude, which indicates there will be no direct sunlight on the north façade. Any shading device on the north façade will only contribute to a reduction in daylight inclusion.

On the other hand, the sun altitude on the south façade varies from 14° to 59° through the year, meaning the shading devices should be designed in a certain way so that they can mitigate the solar radiation at this angle. During winter, when the sun is at a low angle, sunrays should penetrate the rooms, but the effect of glare would be a concern.

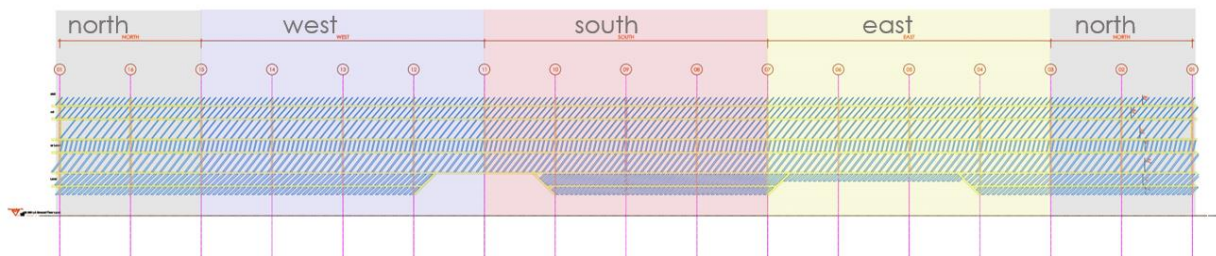


Figure 78: Shading devices of Ingenuity Building

While analysing shading devices of the Ingenuity Building, it was observed that they are all at the same angle all around the building (Figure 78). Since the sun altitude is different according to the sunpath diagram of Nottingham, the shading devices should have been oriented accordingly. After a detailed analysis of the sun orientation, horizontal shading devices were proposed with an inclination of 20°. They were 500mm in depth, also working as light shelves to provide light to the back of the room (Figure 79). The horizontal shades could replace the existing ones, creating the same exterior view from the entry side of the building (Figure 80).

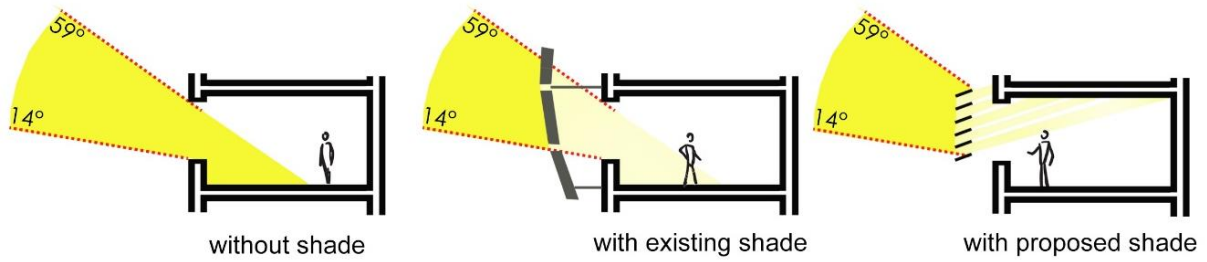


Figure 79: Different shading orientation for the south room



Figure 80: author's proposal of shading devices, adopted from Hutton, 2017

5. VISUAL COMFORT

In every environment, it is necessary for people to be comfortable whilst carrying out their works safely and properly. In an office building, the crucial elements are visual comfort and thermal comfort. The parameters to analyse the visual comfort of space are daylight factor, glare and illuminance. All these parameters were analysed for the two rooms in Ingenuity Building to understand the comfort level with existing shading, without shading and with proposed shading devices.

5.1. Daylight factor

Daylight factor (DF) is the ratio between the actual illuminance at a point inside a room and the illuminance possible from an unobstructed hemisphere of the same sky. DF is a constant, expressed as a percentage and always calculated on an overcast sky. As a rule of thumb, 80% of a floor area should have an average DF of 2% (Rennie, 1998, pp.39-52).

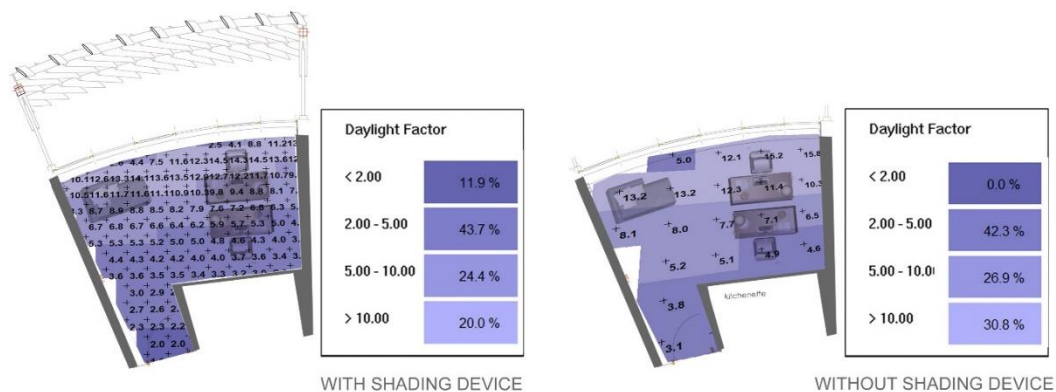


Figure 81: Daylight factor distribution in the north room

While running the simulation with the computer-generated model in IES-VE for the north room, the DF distribution was better without shading than with shading (Figure 81). As discussed in the shading device paragraph, the north side of the building did not require any shading, explaining why the DF level was reducing when shading devices were used (Figure 82).

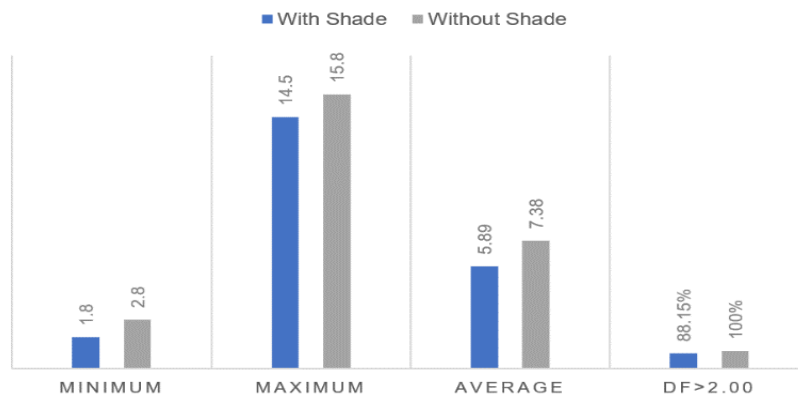


Figure 82: Daylight factor levels of the north room

The simulation of the south room showed that there was no improvement of DF level with the shading, as the room had angled vertical shading, rather than horizontal ones (Figure 83). But the proposed horizontal shading device could provide 92.31% of DF>2.00 which is required for a comfortable office environment (Figure 84).

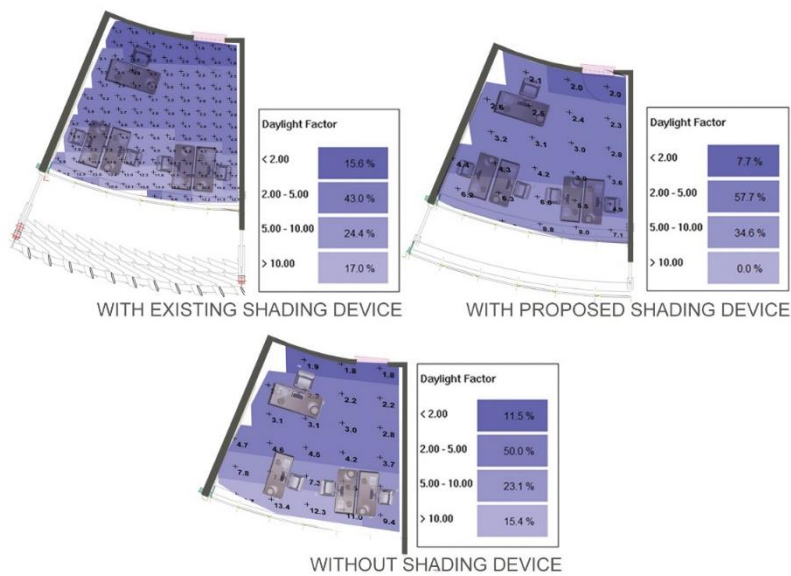


Figure 83: Daylight Factor distribution in the south room

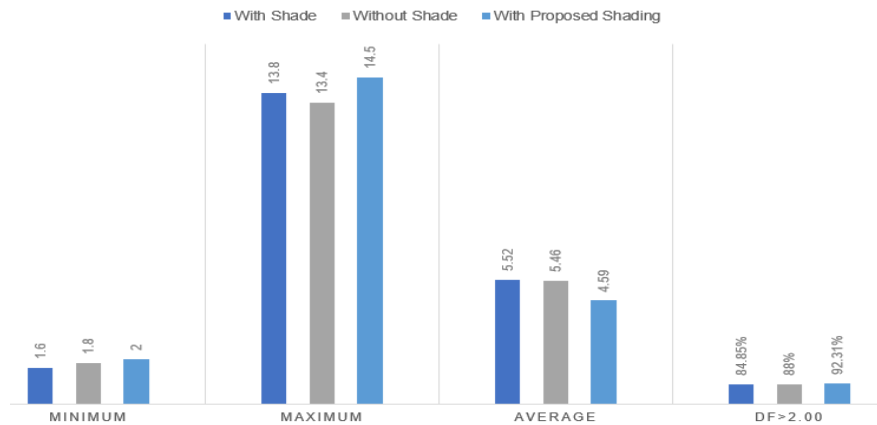


Figure 84: Daylight factor levels of the south room

From Figure 84, it was clear that the DF level improved with the new proposed shading. While the existing situation portrays an uneven distribution of DF, the proposed shading provided more stable DF all over the room.

5.2. Climate based daylight modelling

Climate based daylight modelling (CBDM) is the prediction of any luminous quantity (illuminance and/or luminance) using realistic sun and sky condition derived from standardized climate data. Unlike the conventional daylight factor approach, a climate-based analysis employs realistic, time varying sky and sun conditions and predicts hourly levels of absolute daylight illuminance. With the help of CBDM, the useful daylight illuminance (UDI) was simulated for both rooms. The UDI scheme measured how often in the year daylight illuminance with a range was achieved. According to the CIBSE lighting guide, it is compulsory to have a minimum of 300 lux of illumination for the office visual task lighting (CIBSE, 2006, pp.1-22). The following assumptions were considered while simulating the UDI: work plane height 0.85m, sky condition: overcast sky, occupancy hours: 9.00am-17.00pm, threshold lux level: 500 lux. The simulations were done for the 5 weekdays (Monday-Friday).

Illustrated in Figure 85, it was observed that the band of lux level 500-2500 decreased with the existing shading device for the north room. As there was no specific need for shading on the north façade, the shading was minimising the annual illuminance level. It was evident from Figure 86 that the shading was reducing the illuminance level for the north room.

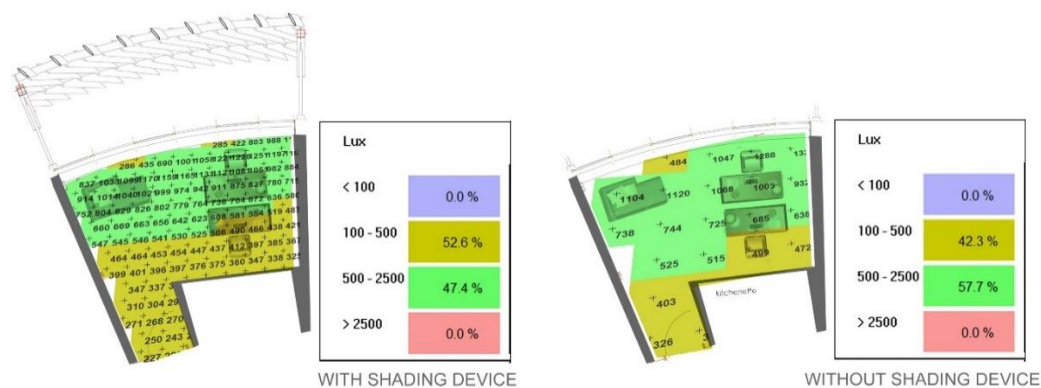


Figure 85: annual illuminance level of the north room

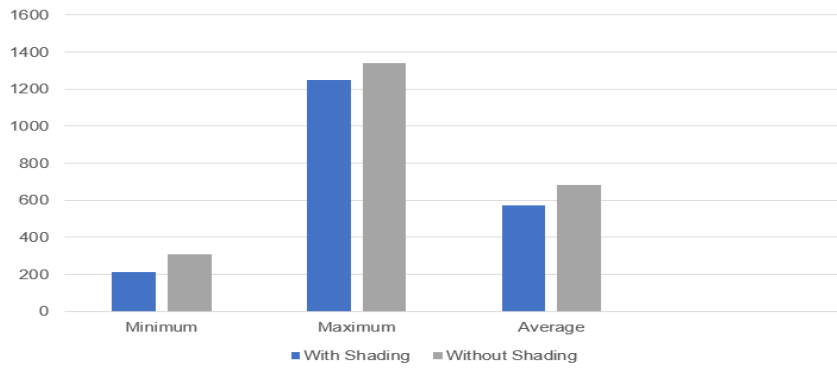


Figure 86: Summary of annual illuminance level for north room

While analysing the UDI for the south room, it was observed that the proposed shading had 6% more illuminance above 2500 lux, which was better than without shading (Figure 87).

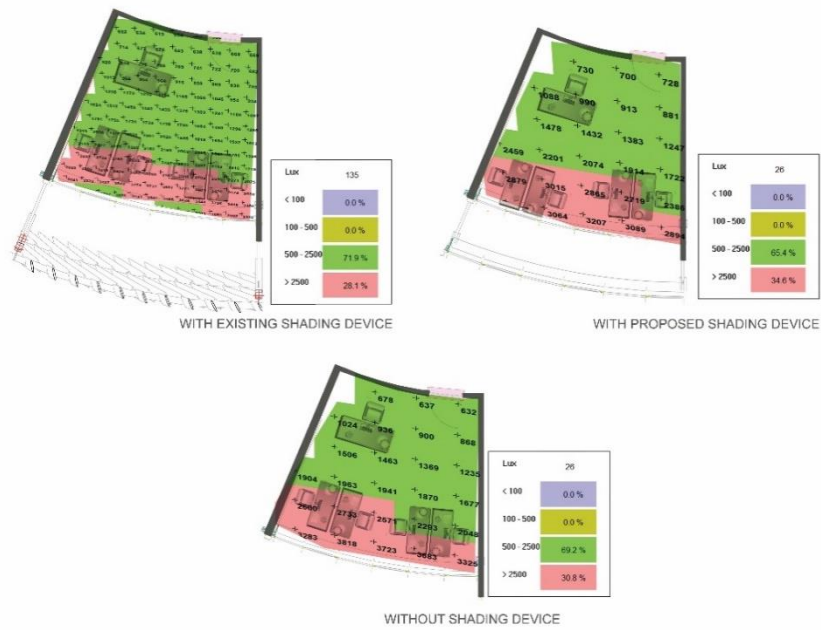


Figure 87: Annual Illuminance level of the south room

Also, from Figure 88, it was clear that, even though the maximum illuminance was lower for the proposed shading, the average illuminance was increased. This provided a better visual condition for the south room.

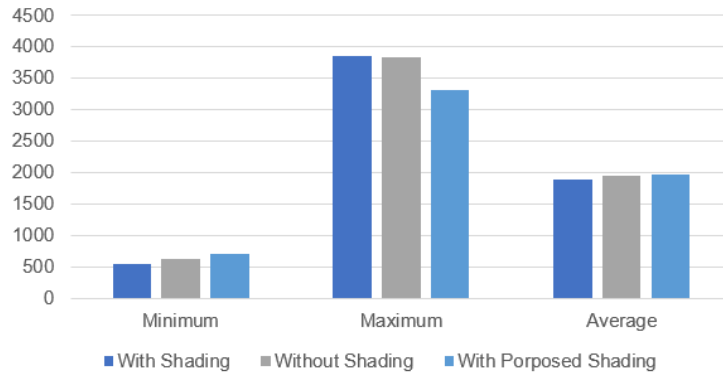


Figure 88: Summary of annual illuminance level for the south room

6. ENERGY CONSUMPTION ANALYSIS

To analyse the energy consumption performance of the Ingenuity Building, a digital energy model was built. All three cases were analysed by Sefaira to compare the simulations. The assumptions used on Sefaira were the following: office building in Nottingham, wall insulation $0.51\text{W/m}^2\text{K}$, floor insulation $0.32\text{W/m}^2\text{K}$, roof insulation $0.18\text{W/m}^2\text{K}$, glazing U factor $1.80\text{W/m}^2\text{K}$, visible light transmittance 0.42 , solar heat gain coefficient 0.4SHGC , infiltration Rate $7.17\text{m}^3/\text{m}^2\text{h}$, ventilation rate 15L/s person , equipment 25W/m^2 , lighting 10W/m^2 . These values are accountable for the ASHRAE 90.1-2013 Baseline.

Surprisingly, the energy use of the whole building was the same as the existing shading and without any shading at $122\text{kWh/m}^2/\text{yr}$. But the energy breakdown showed that the heating load was increased with the shading and the cooling load was decreased (Figure 89), which meant that with the shading devices, less solar radiation could get into the building resulting in a higher heating demand. With the proposed shading devices, the energy consumption of the whole building was reduced to $121\text{kWh/m}^2/\text{yr}$. Though the heating load increased in that case, the cooling load was significantly decreased. As the solar radiation was shaded with better orientation, it resulted in less cooling demand.

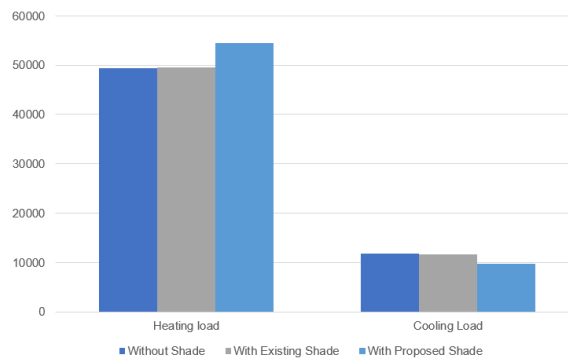


Figure 89: Energy consumption of Ingenuity Building in $\text{kWh/m}^2/\text{yr}$

7. CONCLUSION

The purpose of this study was to understand the relation between daylighting and energy consumption of Ingenuity Building considering the impacts of shading devices. A significant observation of this study was that the existing shading devices were not providing optimum solutions to daylight inclusion; instead, there was a notable presence of glare causing visual discomfort. Moreover, there was no improvement in the overall energy consumption of the building with the existing shading devices.

The proposed shading devices, which were suggested considering the building orientation and climate, improved the daylight level in the office rooms and reduced the energy load as well. The daylight factor above 2.00 of the

south office room was increased to 92.31%, whereas it was 84.95% with the existing shading devices. The annual average lux was increased by 4.5% with the proposed shading devices.

It was evident that appropriately designed shading devices could achieve higher energy efficiency, providing improved visual comfort. Further exploration is required in this matter with various orientations and building forms, with a range of sizes and depths of shading devices as well as materials.

8. REFERENCES

Balaras CA, Droutsas K, Argiriou AA, Asimakopoulos DN, 2000, Potential for energy conservation in apartment buildings. *Energy. Buildings.* 31(2) p.143-54.

Chan KT, Chow WK 1998 Energy impact of commercial-building envelopes in the sub-tropical climate *Appl. Energy.* 60(1) p.21–39.

CIBSE, 2006. *Guide A Environmental Design.* 7 ed. Norwich: CIBSE.

Dincer, I, 1998 Energy and environmental impacts: present and future perspectives. *Energ. Source.* 20(4-5) p.427-453.

Hutton, M., 2017. <https://www.linkedin.com/pulse/hi-tech-meets-heritage-matthew-hutton> [Accessed 25 May 2018].

Iqbal I, Al-Homoud MS, 2007 Parametric analysis of alternative energy conservation measures in an office building in a hot and humid climate. *Build. Environ.* 42(5) p.2166-2177.

Lee, E. S. S., 1995. The design and evaluation of integrated envelope and lighting control strategies for commercial buildings. *ASHRAE Transactions*, Volume 1, pp. 326-342.

Lee, E.S., Di Bartolomeo, D.L., Selkowitz, S.E., 1998. Thermal and daylighting performance of an automated Venetian blind and lighting system in a full-scale private office. *Energy. Buildings.* 29, p47–63.

Philpot, R., 2016. *Architectsdatafile.* [Online] Available at: <http://www.architectsdatafile.co.uk/> [Accessed 25 May 2018].

Rennie, D., Parand.F., 1998. *Environmental Design Guide for naturally ventilated and daylit offices.* 1 ed. s.l: BRE. pp.39-52.

Tzempelikos, A. and Athienitis, A.K. 2002. Investigation of lighting, daylighting and shading design options for new Concordia University engineering building. In: *Proceedings of eSim2002 Building Simulation Conference*, Montreal, Canada, pp. 177–184.

Weatherspark, 2018. *weatherspark.* [Online] Available at: <https://weatherspark.com/y/41783/Average-Weather-in-Nottingham-United-Kingdom-Year-Round> [Accessed 25 May 2018].

#383: Quality improvement of syngas from gasification process of palm kernels using NiO/CaO catalysts on ceramic supporters coupled with biochar absorber from agricultural residues

Suttipong RATTANAHIRUN¹, Wipawee KHAMWICHIT^{2*}, Attaso KHAMWICHIT³

¹Department of Civil and Environmental Engineering, Walailak University, 222 Thai Buri, Tha Sala District, 80161, kwipawee@wu.ac.th,

²Department of Civil and Environmental Engineering, Walailak University, 222 Thai Buri, Tha Sala District, 80161, khamwipawee@gmail.ac.th

³Department of Chemical Engineering, Walailak University, 222 Thai Buri, Tha Sala District, 80161, kattaso@mail.wu.ac.th

In this study, palm kernel shells were utilised in the gasification process to produce syngas. In addition, biochar prepared from pyrolysis of the left-over mangosteen and durian peels were used in the process to enhance the tar removal efficiency. The expected outcomes of this study could result in not only the generation of renewable energy from but also the waste utilisation of agricultural residues. The effect of catalysts and biochars on the syngas quality improvement were particularly studied. Palm kernel shells (PKS) were used as raw materials. The composition and heating values of the biomass were characterised by proximate, ultimate, and bomb analysis. Syngas was produced from a downdraft gasifier connected with catalytic and adsorption units in sequence. The gasification process was operated with 1 kg of PKS per batch at a fixed air flow rate of 25 L/min. The NiO/CaO (10 %wt) catalysts on ceramic supporters with various NiO contents of 2%, 4%, and 8% were synthesised by co-impregnation. Biochars were synthesised by pyrolysis process of durian and mangosteen peels at around 300 - 500°C for 2 hrs. Morphology and compositions of the synthesised catalysts and biochars were analysed. The results of SEM analysis showed that the NiO and CaO were deposited and well dispersed on the porous ceramic ring supporters. The presence of active NiO on the catalyst was also confirmed in FTIR (Fourier transform infrared) results (wavelength of 615 cm⁻¹). Biochars from durian and mangosteen peels, with BET (Brunauer-Emmett-Teller) surface area of 0.9219 - 0.9989 m²/g and adsorption pore size of 11.193 - 11.912 nm, were obtained from a pyrolysis process at 400 - 700°C. The syngas samples were collected from the gasification unit every 15 to 60 minutes. The gas chromatography was used to analyse the syngas compositions. The GC results indicated that increasing NiO contents in the catalysts tended to result in increasing CH₄ composition of the syngas for both systems with and without biochar. With tar filtration unit containing biochar, the ability of tar removal was significantly increased by 2 to 9 times comparing to the system without biochar.

Keyword: NiO/CaO catalysts; palm kernels; biomass; biochar; gasification; syngas improvement

1. INTRODUCTION

Energy demand and consumption has become a crucial global problem for several decades. After the industrial revolution, the energy demand has dramatically increased, however energy supplies from fossil fuels is a non-renewable resource and will become in short supply in the near-future.

Thailand is an important country in terms of food resources. Thailand has abundant areas of agriculture, including rice, corn, sugar cane, and oil palm, etc. In southern Thailand, oil palm is a major economic agriculture leading to a massive amount of biomass residue left from agricultural activities and palm oil refineries. The areas of oil palm agriculture in Thailand was 5.5 million Rai (8,800 km²) in 2017, resulting in 4.77 million Rai (7,632 km²) of oil palm crops and 13.51 million tons of palm oil (Economics, 2017). Biomass residues of palm oil refinery were approximately 78-82% composed of empty fruit bunch, fibre and kernel shells with the heating values of 16.32, 17.25, and 18.53 MJ, respectively. These biomass residues can be used as feedstocks in thermo-chemical processes to produce biofuel or syngas. Syngas, primarily composed of hydrogen, methane, carbon monoxide, carbon dioxide and light hydrocarbons, can be produced by the gasification process of biomass. However, heavy and light tar is also generated. Tar in syngas leads to lower efficiency and gas engine damage because of its high viscosity. There are several approaches to remove tar from the produced syngas, for example through separation processes. However, tar obtained from physical removal is found to be inefficient in energy reuse due to its low heating value. It is more practical to decrease the tar content by thermal cracking reactions with the aid of steam or catalysts to transform tar into high heating value gaseous components (Kuchonthara et al., 2009).

Recently, there have been several research studies concerning an improvement of quality and quantity of syngas using nickel oxide or base oxide in a downdraft gasifier (Mohammed et al., 2011). Nickel oxide is mostly used to enhance tar cracking and hydrocarbon removal in syngas at temperatures higher than 780°C (Sutton et al., 2001). However, nickel oxide is relatively pricey, therefore other oxide catalysts such as calcium oxide is used together with nickel oxide to reduce costs. Phanpruk and Khamichit (Phanpruk and Khamwichit, 2017) found that yields of syngas produced from the gasification process of kernel shells using downdraft gasifier were relatively comparable for nickel oxide and calcium oxide (74.25 and 67.63%, respectively).

The purpose of this research was to study how the use of NiO/CaO-based catalysts together with biochar from agricultural biomass residues improved the quality of syngas obtained from palm kernels using the gasification process. Three different dosage of NiO/CaO (2%, 4%, 8% NiO/10% CaO) doping on ceramic rings were synthesised by co-impregnation sol-gel process. Biochar synthesised from durian and mangosteen peels was utilised to adsorb liquid and gaseous tar.

2. MATERIALS AND METHODS

2.1. Catalyst preparation

Nickel nitrate hexahydrate solution (Ni(NO₃)₂•6H₂O) and Calcium nitrate solution (Ca(NO₃)₂•4H₂O) were used as precursors to prepare 2%, 4%, 8% NiO/10% CaO of the gel solution. Ceramic rings were used as substrate due to their high surface area (Kuchonthara et al., 2009). The ceramic rings were soaked in precursor solutions in the hot basin at 70°C until the gel solution was completely dried. Then they were heated in the oven at 110°C for 24 hours before calcining 950°C for 6 hours. Finally, the calcined ceramic rings were left at room temperature in the desiccator.

2.2. Biochar preparation

Durian and Mangosteen peels were sun-dried and chopped to be approximately 2cm in diameter before putting into an 18L bucket. The bucket was filled with the dried and chopped biomass and placed along with woodchips and palm fibre (used as fuel for synthesis of biochar) into a 100L stainless steel tank. The pyrolysis process of biochar was conducted at 400-600°C for 2 hours.

2.3. Downdraft gasification process

Kernel shells were dried in the oven at 80°C for 24 hours prior to 1kg of them being placed in the gasifier. Air was pumped at a constant rate of 25 L/min to the gasifier to maintain a feed/air ratio of 1:0.6. The process comprised of the gasifier, catalytic reactor, tar condenser, and tar filter. The synthesised ceramic ring doped with catalyst was placed in the catalytic reactor with the ratio of feed/catalyst of 1:0.25. Cracked tar from the catalytic reactor was then condensed in the tar condenser. Syngas was passed to the tar filter unit (filled with biochar with the ratio of feed/biochar of 1:2) for the adsorption of gaseous tar. Figure 1 illustrates the gasification process diagram used in this study.

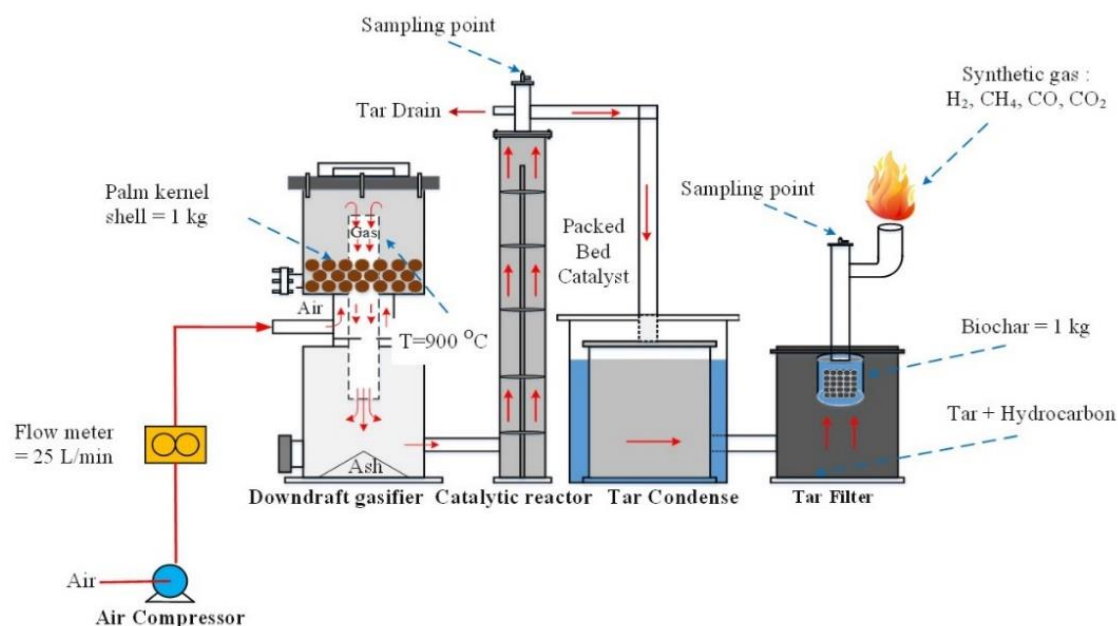


Figure 1: Downdraft gasification process diagram used in this study

2.4. Characterisation of biomass, biochar, and catalytic ceramic ring

Composition and heating value

Compositions of biomass (kernel shell) and synthesised biochar from durian and mangosteen peels in this study were analysed according to the ASTM D3172-3175 standard. Thermo Quest model Flash EA 1112 was used to analyse the elemental composition of both biomass and biochar while the heating value of the kernel shells was analysed using Bomb calorimeter model AC 500.

Morphology

Morphological properties of biomass, biochar, and catalyst were examined by Scanning Electron Microscope (SEM, Model Merlin compact, Zeiss). The specimens were mounted on aluminum stubs, sputter-coated with gold and examined in a Merlin compact scanning electron microscope. Samples were analysed at 1,000x and 10,000x magnifications.

Specific surface area of the synthesised biochar

Specific surface areas and pore diameters of the synthesised biochar were analysed using the Brunauer–Emmett–Teller (BET) technique (Surface Area and Porosity Analyser (BET), ASAP2460, Micromeritics, USA).

Chemical property characterisation of catalyst

Functional groups of chemical structures of doped ceramic ring were analysed by ATR-FTIR Spectrometer (Model Tensor 27, Bruker) using ATR-FTIR technique.

Syngas analysis

Syngas produced from the gasification process of kernel shells was collected at a sampling point of the tar filter unit every 15 minutes from the beginning of the process to 60 minutes. Gas samples were collected into Tedlar bags then were analysed by Gas Chromatography model 7890.

3. RESULTS AND DISCUSSIONS

3.1. Biomass characterisation

The results of proximate and ultimate analysis of the palm kernels used in this study are shown in Table 1. Volatile matter was found to be approximately 71.6%, whereas the fixed carbon and moisture contents were 15.1% and 9.9%, respectively. Since the kernels contained high amounts of volatile matter, the material could be potentially combusted in the gasification process to generate energy. The CHN-O elemental analysis indicated that the combustible kernels consisted of carbon, hydrogen, and oxygen which were suitable to be used as biomass raw material for the purposed gasification. As shown in Table 2, high heating value (HHV) and low heating value (LHV) of the shell obtained from Bomb calorimeter measurements were roughly 4,830 and 4,225 kcal/kg, respectively. In general, the results were in good agreement with past related research studies reported elsewhere in which the biomass materials were successfully utilised to produce syngas.

Table 1: Proximate and Ultimate analysis results for the palm kernels

Proximate analysis (%wt dry basis)				Ultimate analysis (%wt dry basis)				Ref.
Moisture content	Ash	Volatile matter	Fixed carbon	C	H	O	N	
9.94	3.41	71.57	15.08	52.30	52.30	39.17	0.42	This study
12.99	2.73	70.96	13.31	46.61	5.55	35.85	0.20	(Phanpruk, 2016)
11.00	2.10	67.2	19.7	49.74	5.32	44.86	0.08	(Abnisa et al., 2011)
10.23	3.24	85.11	1.42	47.88	5.15	42.69	0.94	(Onochie et al., 2017)
6.33	11.75	62.82	19.10	44.29	9.01	43.13	2.37	(Ahmad et al., 2014)
9.70	4.48	80.81	13.81	48.61	5.70	44.70	1.01	(Shahbaz et al., 2016)

Table 2: Heating values of palm kernels

HHV (kcal/kg)	LHV (kcal/kg)	Ref.
4,830.70	4,225.39	This study
4,512.13	3,996.46	(Phanpruk, 2016)
5,469.57	5,812.96	(Okoroigwe and Saffron, 2012)
4,497.98		(Shahbaz et al., 2016)
3,857.46	N/A	(Samiran et al., 2015)

3.2. Catalyst Characterisation

Morphology of the prepared catalysts containing NiO and CaO on a ceramic supporter was analysed from the SEM results. Figure 2 illustrates the SEM pictures of the (a) NiO (2 wt%)/CaO (10 wt%)/Ceramic ring, (b) NiO (4 wt%)/CaO (10 wt%)/Ceramic ring, and (c) NiO (8 wt%)/CaO (10 wt%)/Ceramic ring catalysts at a magnification around 10,000x magnifications. The micrographs exhibited rough surfaces with uniform distribution of the NiO/CaO catalyst crystals on the porous supporter. At fixed 10 wt% CaO, the size of the disperse agglomerates tended to increase with increasing co-impregnated NiO contents. The porosity of the catalysts was observed to decrease as the NiO increased from 2 wt% to 8 wt%.

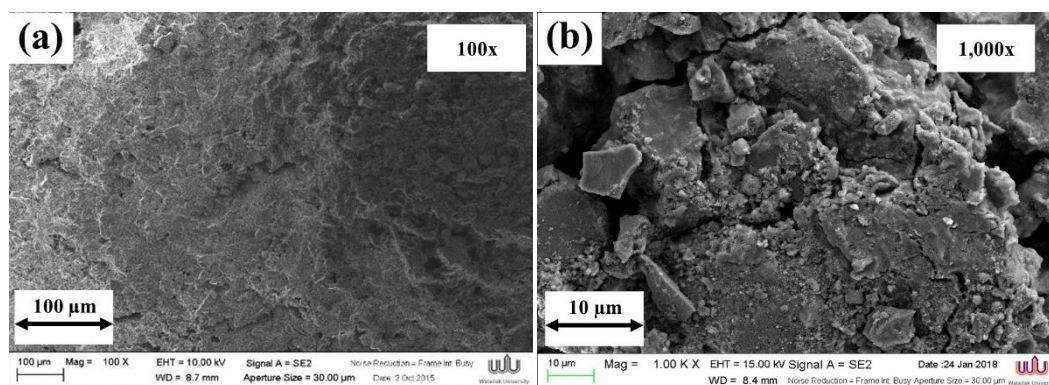


Figure 2: SEM results at 15 kV (1,000x magnifications) of (a) Ceramic ring, (b) 2%NiO/10%CaO/Ceramic ring,

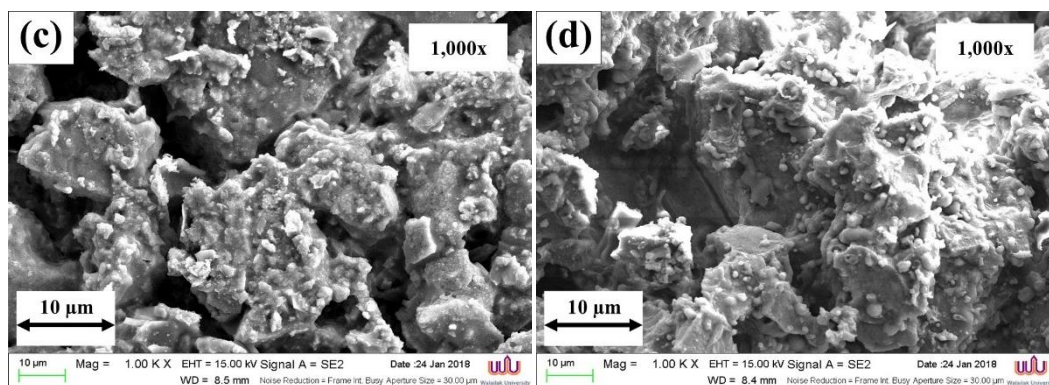


Figure 2: SEM results at 15 kV (1,000x magnifications) of (c) 4%NiO/10%CaO/Ceramic ring, and (d) 8%NiO/10%CaO/Ceramic ring

The NiO and CaO contents were evaluated from element analysis of the EDX results. Figure 3 shows the EDX results of the prepared NiO (x%)/CaO (10%)/Ceramic catalysts with varied NiO contents of 2 wt%, 4 wt%, and 8 wt%. The EDX analysis suggested that active NiO and CaO were successfully co-impregnated. The catalysts contained Ni and Ca contents relatively close to the prepared solution concentrations. The increase in the concentration of $\text{Ni}(\text{NO}_3)_2 \cdot 6\text{H}_2\text{O}$ in the solution generally increased the Ni content in the catalyst. The Ni compositions were found to be 2.86% for the NiO(2%)/CaO(10%), 6.85% for the NiO(4%)/CaO(10%), and 10.52% for the NiO(8%)/CaO(10%), respectively. The presence of NiO and CaO deposited on the ceramic surface as seen from the EDX results was the indicator of effective impregnation of the active compounds. This could be attributed to the interaction between NiO/CaO and the silicate oxide (SiO_2) component of the ceramic supporter, as suggested in Wang's study (Wang et al., 2012). In addition, the presence of active NiO on the catalyst was also confirmed in FTIR result where the peak at the wavelength of 615 cm^{-1} associated with Ni-O stretching vibration band was observed (Segawa et al., 2015), as shown in Figure 4.

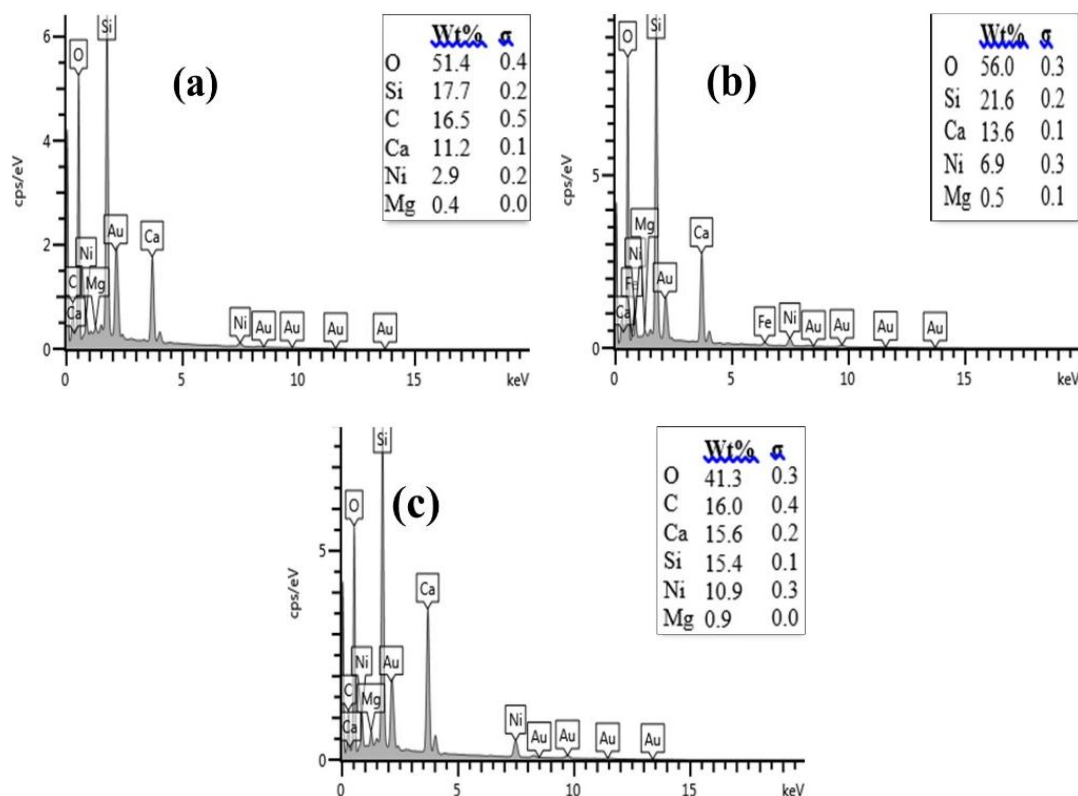


Figure 3: EDX results at 15 kV (1,000x magnifications) of (a) Ceramic ring, (b) 2%NiO/10%CaO/Ceramic ring, (c) 4%NiO/10%CaO/Ceramic ring, and (d) 8%NiO/10%CaO/Ceramic ring

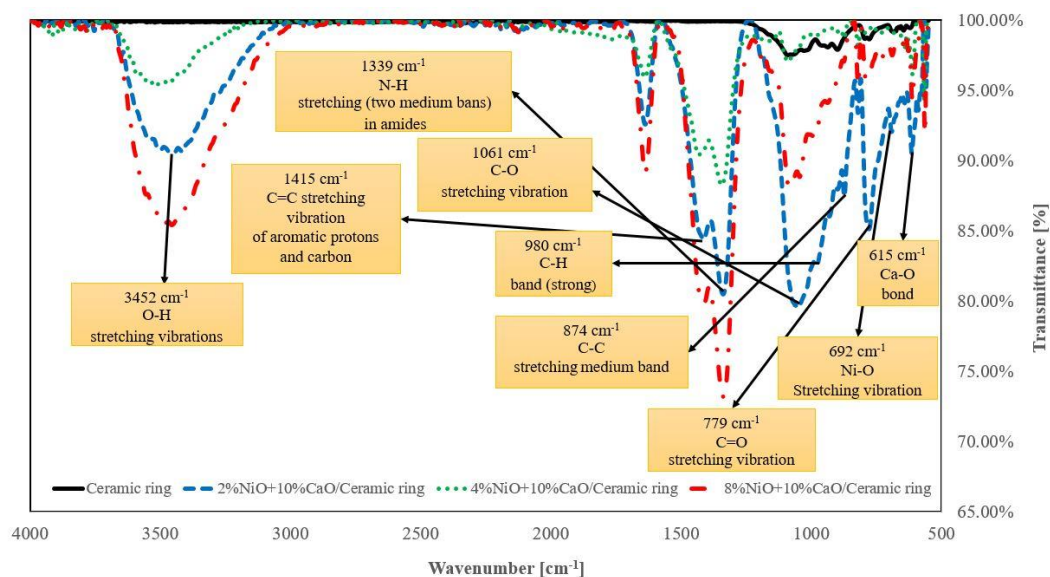


Figure 4: FTIR analysis of Ceramic ring, 2%NiO/10%CaO/Ceramic ring, 4%NiO/10%CaO/Ceramic ring, and 8%NiO/10%CaO/Ceramic ring in the wave range of 500-4000 cm^{-1}

3.3. Biochar Characterisation

Biochar synthesised from durian and mangosteen peel residues was used as the physical absorbent for tar removal in this study at a fixed ratio of 50:50 by weight of durian and mangosteen. Figure 5 illustrates SEM results of biochar at 10 kV with a magnification of 500 and 10k times. The SEM pictures of the sectional fracture surface of both durian and mangosteen show porous structures with various pore sizes. It seemed that the pore size distribution of the biochar made from durian peel appeared to be more uniform than those obtained from mangosteen. Biochar from mangosteen possessed a porous structure with broader pore size distribution across the surface. The SEM results were in good agreement with BET surface analysis.

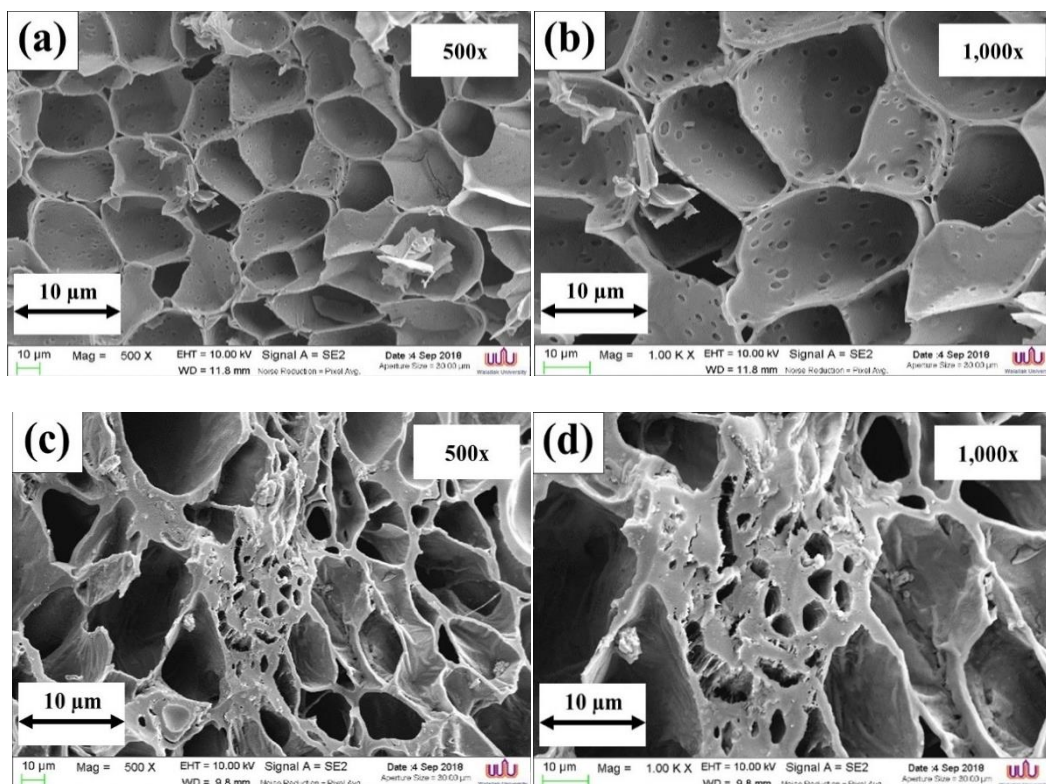


Figure 5: SEM results at 10kV of (a) durian-peel biochar (500x magnifications), (b) durian-peel biochar (1,000x magnifications), (c) mangosteen-peel (500x magnifications), and mangosteen-peel (1,000x magnifications)

The EDS analysis indicated the main elemental compositions of the prepared biochar, as shown in Figure 6. The biochar obtained from durian peels consisted of 75.1% C, 12.4% O, and 11.3% K, respectively. The elemental composition results were typical for biochar which could be used as an adsorbent to physically adsorb tar compounds from syngas in the gasification process (Chaichana et al., 2014)

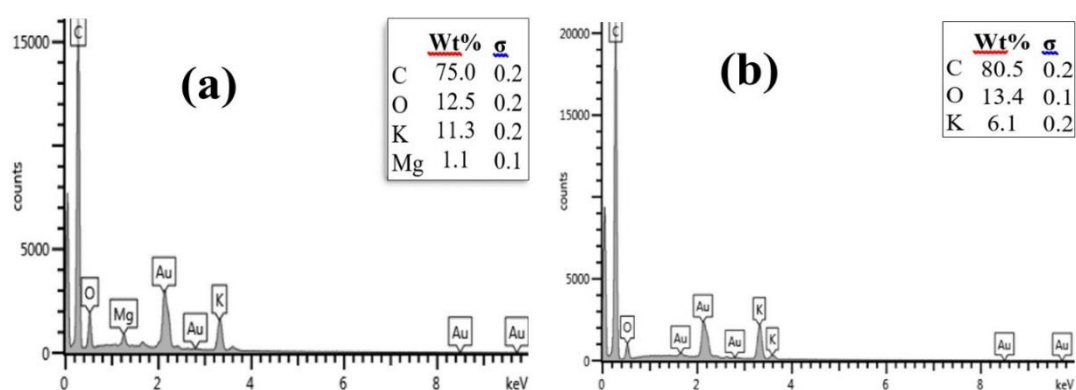


Figure 6: EDX results at 10kV (500xmagnifications) of (a) durian-peel biochar, (b) mangosteen-peel biochar

Table 3 shows the BET analysis results of the synthesised biochar. The specific surface areas (SSF) were found to be 0.9989 m²/g for the durian-peel biochar, and 0.9219 m²/g for the mangosteen-peel biochar. In addition, the average pore diameter of the durian-peel biochar (11.193 nm) was slightly smaller than that of the mangosteen-peel biochar (11.912 nm). It was believed that the mixture of 50:50 ratio between the materials would be capable of adsorbing condensed volatile tar residues with a wide spectrum of molecular sizes. The gasification performance study will be further discussed.

Table 3: BET analysis of the biochar

Biochar Type	BET Surface Area (m ² /g)	Adsorption Average Pore Diameter (nm)	Ref.
Durian-peel	0.9989	11.193	This study
Mango-peel	0.9219	11.912	
Palm oil char	1	N/A	(Kastner et al., 2009)
Peanut hull char	1.54		

3.4. Gasification performance study

Compositions of syngas for each experiment are illustrated in Table 4. The gas chromatography (GC) results of the syngas samples obtained from the gasification process at 15, 25, 35, 45, and 60 minutes were used to analyse the compositions of syngas produced from the process. In this study, CH₄ and CO₂ were detected by GC analysis. From the table, the presence of the catalysts affected the syngas compositions. Increasing NiO contents in the catalysts tended to result in increasing CH₄ composition of the syngas. The analysis of GC for experiments without biochar suggested 8% NiO resulted in the highest maximum percent composition of CH₄ in syngas (4.61%), followed by maximum compositions of CH₄ at 3.01% for 4% NiO, 2.44% for 2% NiO. Maximum compositions of CH₄ for no-catalyst and 2% NiO were insignificantly different. It was believed that the catalysts would facilitate the further chemical cracking reactions of the volatile tar compounds. The results were in good agreement with Phanpruk (Phanpruk, 2016) whose study demonstrated NiO effectively improved the CH₄ yields for the gasification process of palm residues. For the experiment with the use of biochar, the maximum composition of CH₄ for 8% NiO was the highest (3.27%), followed by those of 2% NiO and 4% NiO (2.96%, 1.14%). From the observation of the experiment, the best flames occurred during 25-35 minutes of the processing time when the colour of the flames were light blues, indicating an existence of high syngas and low tar. From the results, the %CH₄ values obtained from the system with biochar filter were slightly lower than those of the system without the filter unit. It is worth mentioning that the back pressure built-up in the system having the packed-bed biochar filter unit installed was relatively high, resulting in decreased flowrate of the syngas product passing the filter. During the process, the rest of the produced gas was released at the bypass outlet. The difference in flow characteristics particularly the pressure drop across the filter unit could affect the physical adsorption of other components of the produced gas besides tar.

Table 4: CH₄ and CO₂ composition of syngas

Sample	15 min		25 min		35 min		45 min		60 min	
	CH ₄ (%vol)	CO ₂ (%vol)	CH ₄ (%vol)	CO ₂ (%vol)	CH ₄ (%vol)	CO ₂ (%vol)	CH ₄ (%vol)	CO ₂ (%vol)	CH ₄ (%vol)	CO ₂ (%vol)
Without Biochar										
No Catalyst	0.75	19.62	0.83	21.74	2.49	35.97	1.18	42.43	0.61	30.68
2%NiO/10%CaO	0.35	3.20	1.37	19.44	2.44	33.40	2.75	41.56	0.64	24.58
4%NiO/10%CaO	0.73	33.55	3.01	50.17	2.41	61.21	1.37	57.86	0.44	50.00
8%NiO/10%CaO	0.63	13.85	1.42	32.95	4.61	59.99	1.74	50.04	0.52	44.35
With Biochar										
No Catalyst	2.30	28.48	1.41	27.94	1.55	32.13	0.89	30.77	0.41	23.94
2%NiO/10%CaO	2.96	50.20	3.70	66.40	1.46	48.42	0.75	42.54	0.68	33.84
4%NiO/10%CaO	1.27	21.07	1.64	29.69	1.14	27.64	0.66	29.68	0.77	24.37
8%NiO/10%CaO	2.84	43.65	3.27	39.48	2.37	30.91	2.43	37.47	1.40	32.43

3.5. Adsorption of Tar

To enhance tar removal efficiency, a filter packed with 1kg of 50:50 (durian/mangosteen) biochar was connected to the system to trap volatile tar compounds prior the gas exit. Table 5 shows the amount of condensed tar in the filter unit after 60 minutes of the gasification process of 1kg kernels. Without the biochar filter, a small amount of the tar, approximately 0.2 kg, was condensed and coated onto the internal surface of the filter unit. However, the amount of tar trapped in the filter having biochar was observed to increase from 2 to 9 times for 0%, 2%, 4%, and 8% NiO content in the catalysts. The results were in good agreement with the study by Kuchonthara et al., (2009) in which the NiO/Al₂O₃ catalysts were used to improve the catalytic reforming performance of the gasification process of rice husks, resulting in a significant amount of tar reduction. When compared to the system with filter units filled with rice husks in Phanpruk (2016) study, it was found that the tar removal efficiency of the biochar filter was significantly improved by almost 100 percent. This may result from the superior adsorption performance of the biochar.

Table 5: Amount of tar remaining in tar filter unit

Sample	Tar Filter Unit	
	Without Biochar	With Biochar
No Catalyst	0.02	0.04
2%NiO/10%CaO/Ceramic ring	0.03	0.03
4%NiO/10%CaO/Ceramic ring	0.02	0.12
8%NiO/10%CaO/Ceramic ring	0.02	0.18

4. CONCLUSION

Co-impregnation of NiO/CaO on a ceramic ring was successfully demonstrated to be effective in improving the quality of the syngas. Increasing in NiO contents tended to increase maximum CH₄ composition for both gasification of kernel shells with and without the use of biochar. With a tar filtration unit containing biochar, the ability of tar removal was significantly increased by 2 to 9 times of that without biochar.

5. ACKNOWLEDGEMENT

This work was financially supported by Research Grant No. WU59113

6. REFERENCES

- Abnisa, F., Daud, W. M. A. W., Husin, W. N. W. & Sahu, J. N. 2011. Utilization possibilities of palm shell as a source of biomass energy in Malaysia by producing bio-oil in pyrolysis process. *Biomass and Bioenergy*, 35, 1863-1872.
- Ahmad, R., Hamidin, N., Md Ali, U. & Abidin, C. Z. A. 2014. *Characterization of Bio-Oil From Palm Kernel Shell Pyrolysis*.
- Chaichana, T., Waewsak, J., Kaew-On, J. & Onthong, U. 2014. Fuel Properties of Mangosteen Pericarp Charcoal. *Thaksin University* 17, 29-36.

Economics, O. O. A. 2017. *Agricultural Statistics of Thailand* [Online]. Available at: <http://www.oae.oae.go.th> [Accessed].

Kastner, J. R., Miller, J. & Das, K. C. 2009. Pyrolysis conditions and ozone oxidation effects on ammonia adsorption in biomass generated chars. *Journal of Hazardous Materials*, 164, 1420-1427.

Kuchonthara, P., Kunsopa, S., Mekasut, L. & Vitidsant, T. 2009. Catalytic Reforming of Biomass-derived Tar using NiO/Al₂O₃ Modified by Base Oxides of Mg and Ca Chulalongkorn University.

Mohammed, M. A. A., Salmiaton, A., Wan Azlina, W. A. K. G., Mohammad Amran, M. S. & Fakhru'l-Razi, A. 2011. Air gasification of empty fruit bunch for hydrogen-rich gas production in a fluidized-bed reactor. *Energy Conversion and Management*, 52, 1555-1561.

Okoroigwe, E. & Saffron, C. 2012. *Determination of Bionenergy Potential of Palm Kernel Shell by Physicochemical Characterization*.

Onochie, U. P., Obanor, A. I., Aliu, S. A. & Ighodaro, O. O. 2017. Proximate and Ultimate Analysis of Fuel Pellets from Oil Palm Residues. *Nigerian Journal of Technology*, 36, 987-990.

Phanpruk, T. 2016. *Gasification of Oil Palm using Downdraft Gasifier and Tar Removal by Catalyst*. Walailak University.

Phanpruk, T. & Khamwichit, W. 2017. The Estimate of Energy Generation Potential of Biomass Residue from Oil Palm Industries in Southern Thailand. *Journal of Engineering and Applied Sciences*, 12, 2795-2801.

Samiran, N., Mohd Jaafar, M. N., Chong, C. T. & Jo-Han, N. 2015. *A Review of Palm Oil Biomass as a Feedstock for Syngas Fuel Technology*.

Segawa, T., Kawaguchi, K., Ishii, K., Suzuki, M., Arimitsu, N., Yoshida, H. & Fukui, K. 2015. Nickel oxide powder synthesis from aqueous solution of nickel nitrate hexahydrate by a microwave denitration method. *Advanced Powder Technology*, 26, 983-990.

Shahbaz, M., Suzana, Y., Inayat, A., Patrick, D., Partama, A. & Fadzil, A. 2016. *Thermal Investigation of Palm Kernel Shell (PKS) with Coal Bottom Ash in Thermo Gravimetric Analyser (TGA) in Inert Atmosphere*.

Sutton, D., Kelleher, B. & Ross, J. R. H. 2001. Review of literature on catalysts for biomass gasification. *Fuel Processing Technology*, 73, 155-173.

Wang, J., Cheng, G., You, Y., Xiao, B., Liu, S., He, P., Guo, D., Guo, X. & Zhang, G. 2012. Hydrogen-rich gas production by steam gasification of municipal solid waste (MSW) using NiO supported on modified dolomite. *International Journal of Hydrogen Energy*, 37, 6503-6510.

#384: Recovery of malic acid using trioctylamine in 1-decanol: equilibrium studies by response surface methodology using Box Behkhen optimisation technique

Victoria INYANG*, David LOKHAT

Discipline of Chemical Engineering, School of Engineering, University of KwaZulu-Natal, Durban, SOUTH AFRICA.

Corresponding author: vickyinyang@yahoo.com

Reactive extraction is a significant technique employed for the removal of organic acids from dilute aqueous solutions. This technique was explored by applying Response Surface Methodology (RSM) in process parameter optimisation for malic acid recovery from aqueous streams using Trioctylamine as the extractant and 1-decanol as the organic diluent. Malic acid, a C4 dicarboxylic acid, has a wide variety of applications in the polymer, food, chemical and pharmaceutical industries. Extraction efficiency was systematically carried out using three process parameters for reactive extraction: temperature, initial malic acid concentration and extractant (Trioctylamine) composition. Response Surface Methodology in combination with Box-Behnken design involving seventeen experimental runs was employed for malic acid reactive extraction in this study. A statistical second order polynomial predicted an extraction efficiency of 97.98%. The optimum conditions of the process variables were found to be: temperature: 308.65 K, acid concentration: 0.711 Kmol/m³, Trioctylamine composition: 21.706% (v/v). Under these optimum conditions, the experimental response of extraction efficiency of 98.35% was obtained. The experimental results obtained were in close conformity with the predicted values by numerical optimisation using Response Surface Methodology. These findings can pave the way for the reactive separation process design for recovery of carboxylic acids from dilute aqueous waste streams as well as a fermentation broth.

Keywords: malic acid, reactive extraction, equilibrium studies, optimisation, Box Behnken design.

1. INTRODUCTION

Carboxylic acids are usually present in low concentrations in aqueous streams. Interest in the recovery of these acids from dilute aqueous solutions with acid concentrations lower than 10% (w/w) has received considerable attention. Most recent research is targeted at carboxylic acid separation process selection with low material consumption and less energy requirement in the downstream processing. An intensified process which satisfies these requirements is reactive separation since significant improvements are achieved in both stages of reaction and separation. Carboxylic acids such as butyric acid, lactic acid, propionic acid and malic acid are useful bulk chemicals for several industries. Malic acid is a C₄-dicarboxylic acid and also an intermediate of the tricarboxylic acid cycle. It has a variety of applications in polymer, food, chemical and pharmaceutical industries. The downstream recovery technique for carboxylic acids accounts for more than 50% of overall production costs (Hulse, 2004) hence the current interest in finding a more cost-effective recovery technique. Reactive extraction is a significant technique for the separation of important carboxylic acids which leads to high solute distribution coefficient as a result of combining physical and chemical phenomena (Datta *et al.*, 2015). The factors that are favourable for carboxylic acids reactive extraction include: an existing functional group which increases capacity and selectivity in solute molecules, high driving force of complexing agents as a result of low concentration and low volatility of the solute (Hong *et al.*, 2001). The application of reactive extraction to different organic acid from dilute aqueous solution has been successfully carried out, for example Lactic acid (Wasewar *et al.*, 2002, Wasewar, 2005); Itaconic acid (Wasewar *et al.*, 2010, Wasewar *et al.*, 2011, Kreyenschulte *et al.*, 2018); Succinic acid (Kurzrock and Weuster-Botz, 2011, Eda *et al.*, 2015); Levulinic acid (Brouwer *et al.*, 2017, Kumar *et al.*, 2010, Eda *et al.*, 2018); pyruvic acid (Marti *et al.*, 2011); tartaric acid (Sharma *et al.*, 2017); propionic acid (Keshav *et al.*, 2008, Keshav *et al.*, 2009b, Keshav *et al.*, 2009a); and 3-Hydroxypropionic acid (Chemarin *et al.*, 2019). The appropriate solvent selection as constituents of the organic phase is an underlining factor for high distribution coefficient and extraction efficiency. High viscous extractants, for example phosphorus bonded, oxygen bearing and hydrocarbon, high molecular weight aliphatic amines with diluents, are often employed in carboxylic acid reactive extraction processes to improve the physical properties such as interfacial surface tension and viscosity (Gorden *et al.*, 2015, López-Garzón and Straathof, 2014). But the most effective and efficient extractant system has been the tertiary amine-based complex. This provides high extraction efficiency (>90%) and is less expensive as compared with the phosphorus based extractants (Wasewar, 2005). The extractants used in the reactive extraction process in organic acid separation can be recycled thus making it an effective and efficient process but the difficulty lies in the identification of cheap and efficient extractants. Generally, the extractants are often used with an organic solvent as a diluent (such as decanol, octanol, butanol and nonanol) to help improve the acid-extractant solvation power, prevents third phase formation which limits the extraction ability thus giving a high distribution coefficient (Wasewar, 2005). Significant research studies have been conducted on the influence diluents have on amine extractant in carboxylic acids recovery (Tamada and King, 1990b, Tamada and King, 1990a, Marinova *et al.*, 2005, Senol, 2004).

Several studies have been conducted on the reactive extraction process on organic acid separation from fermentation aqueous waste streams. However, studies which employ statistical techniques on the experimental design of malic acid recovery from aqueous solution using intensified process such as reactive liquid-liquid separation process is limited in literature. The selection of a suitable technique for evaluating different process parameters is important as well as any interactions involved while minimising the number of experimental runs. This research study is centred on the application of Box Behnken in data analysis, optimising process parameters and exploring appropriate conditions to be employed in the reactive extraction process for optimal extraction efficiency and distribution coefficient.

The study intends to enhance the extraction yield for effective and efficient recovery of malic acid from dilute aqueous solution by employing trioctylamine as the extractant mixed with high polarity solvent 1-decanol as the diluent. Also, the major factor influencing the reactive extraction process includes temperature, concentration of the extractant and acid. This work is also aimed at analysing, optimising and finding appropriate conditions of these process variables using response surface method (RSM) by employing a Box-Behnken design to maximise the efficiency of malic acid reactive extraction process (% E) and distribution coefficient (K_D). The statistical design of the experiment was used for process parameter optimisation for the malic acid extraction to prevent drawbacks obtained from classical methods. The optimum parameters of the intensified reactive extraction process was used to determine the reaction rate kinetics of the extraction process. Response surface methodology (RSM) is an effective tool for statistical design of experiments, model development and for finding complex processes in order to optimise the target yield(s). It is also a statistical tool used to create a link between a set of defined experimental variables and the observed results. The adopted stepwise procedure in this study is given in Figure 1.

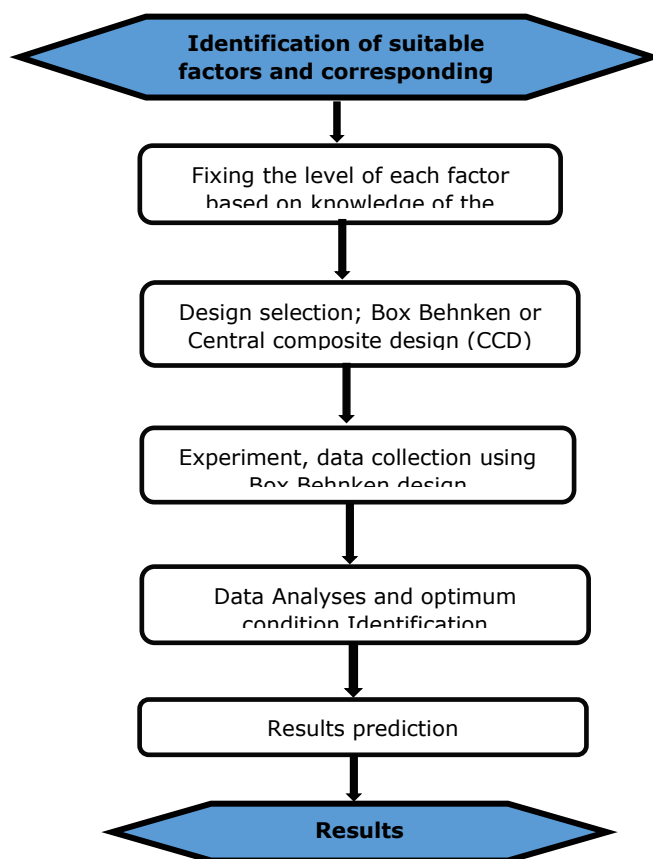


Figure 1: RSM step-wise procedures adopted in the study

2. RENEWABLE ENERGY TECHNOLOGIES

2.1. Materials and methods

Experimental chemicals deployed

All the chemicals, DL-Malic acid ($C_4H_6O_5$), density 1.61g/mL, Trioctylamine (TOA), $[CH_3(CH_2)_7]_3N$, density 0.809g/mL and 1-decanol, density 0.829g/mL deployed in this study at purity of 98% were purchased from Sigma-Aldrich and the experimental water was obtained using an Elga PURELAB Option Q purification system. Distilled water from our laboratory was used throughout the experiment. Phenolphthalein indicator (pH) and 0.1M Sodium hydroxide were also purchased from Sigma-Aldrich. All chemicals were used as supplied with no further purification.

2.2. Methods

Equilibrium studies

Reactive extraction equilibrium studies were conducted by preparing 25mL aqueous solution (0.1 kmol/m³ concentration of malic acid) and 25mL organic phase solution was prepared by mixing 10-30% of Trioctylamine extractant (v/v) i.e. 0.229 kmol/m³ in 1-decanol at temperatures between 298-313K in an orbital shaker which was placed in the oven for 5 hours at 120 rpm, the two phases were left to settle for 2 hours. The aqueous phase analysis was carried out using the titration method with 0.1N NaOH and phenolphthalein as the indicator in order to obtain Malic acid concentration. The organic phase concentration of Malic acid was analysed through mass balance. The experimental runs were done in triplicate to confirm the reproducibility of results. The malic acid recovery process performance was assessed by extraction efficiency (%E) and distribution coefficient (K_D) at equilibrium as the ratio of the concentration of acid in the organic phase $[HA]_{org}$ to the concentration in aqueous phase $[HA]_{aq}$ as shown in Equations 1 and 2

$$\text{Equation 1: } \text{Distribution coefficient} = \frac{[HA]_{org}}{[HA]_{aq}}$$

$$\text{Equation 2: } \text{Extraction efficiency (\%E)} = \frac{K_D \times 100}{1 + K_D}$$

The different experimental cycles were carried out using the design of experiment template obtained using Box-Behnken design (BBD) with three variables at three levels each in the optimisation of the process variables used in the reactive extraction process. The Design Expert version 10.0 (Statease Inc., Minneapolis, USA) was employed in this study. The un-coded (original) value of the different factors and their corresponding coded levels employed in the experimental design are shown in Table 1.

Table 1: Range of different variables for reactive extraction of DL-Malic acid

Factors	Units	Coded Values	Level	
			Low	High
Temperature	K	Factor X ₁	298	313
Solvent Composition (v/v)	%	Factor X ₂	10	0.67830
Acid Concentration	Kmol/m ³	Factor X ₃	0.100	1.000

There are three main stages in Response Surface Methodology which include

- i. Parameter selection and experimental design; finding a suitable estimation between independent process (factors) and the dependent (response) variables. (Marchitan *et al.*, 2010).
- ii. Modelling of the response obtained from experimental results through regression and analysis of variance.
- iii. Response optimisation; the optimum values of the independent process parameters; Malic acid concentration, extractant ratio (%v/v) and temperature (K) were estimated to gain maximum value of the response, Extraction Efficiency (%E).

The relationship established between coded (x_i) and real (X_i) value is represented in equation 4 as

$$\text{Equation 3: } \text{Coded value (x}_i\text{)} = \frac{X_i - X_0}{\Delta X_i}, i = 1, 2, 3, \dots, n$$

Where:

- ΔX = phase change and
- X₀ = real value at the center position

Taking into consideration all interactions of the input parameters (linear to linear and linear to quadratic), the behavior of the system can be described by the following equations;

$$\text{Equation 4: } Y = \beta_0 + \sum_{i=1}^n \beta_i X_i + \sum_{i=1}^n \beta_{ii} X_i^2 + \sum_{i < j}^n \beta_{ij} X_i X_j + \varepsilon$$

Where:

- I and j = linear and quadratic coefficients respectively;
- n = number of experimental parameters (n=3).
- β₀ = constant coefficient,
- β_i = linear outcome or slope of input factor,
- β_{ii}X_i = quadratic outcome of input factor
- X_i and β_{ij} = linear effect interaction between input factors X_i and X_j,
- ε = residual error.

3. RESULTS AND DISCUSSION

The experimental data was analysed using Box Behnken design in Response Surface Methodology (RSM) to analyse the combined effects of temperature, malic acid concentration and TOA composition and the results are reported in Table 2.

Table 2: Experimental design of variables (coded) for malic acid extraction efficiency %E

		Factor 1	Factor 2	Factor 3	Response 1
Std	Run	A:Temperature	B:TOA Concentration	C:Acid Concentration	Extraction Efficiency
		K	%	Kmol/m3	%E
2	1	1.000	-1.000	0.000	96.5285
9	2	0.000	-1.000	-1.000	99.8095
7	3	-1.000	0.000	1.000	95.26
11	4	0.000	-1.000	1.000	94.7867
17	5	0.000	0.000	0.000	98.34
8	6	1.000	0.000	1.000	96.4733
1	7	-1.000	-1.000	0.000	95.1446
14	8	0.000	0.000	0.000	98.3515
3	9	-1.000	1.000	0.000	94.7394
6	10	1.000	0.000	-1.000	99.7714
5	11	-1.000	0.000	-1.000	99.9429
13	12	0.000	0.000	0.000	98.3446
12	13	0.000	1.000	1.000	97.2152
10	14	0.000	1.000	-1.000	99.9429
15	15	0.000	0.000	0.000	98.3273
16	16	0.000	0.000	0.000	98.3481
4	17	1.000	1.000	0.000	98.0024

Analysis of Variance (ANOVA) was employed to predict the correlation between independent process variables and the corresponding responses and a second-order polynomial equation was obtained for extraction efficiency of malic acid and is presented in Equation 5 as;

$$\text{Equation 5: } \%E = 98.34 + 0.71X_1 + 0.45X_2 - 1.97X_3 + 0.47X_1X_2 + 0.35X_1X_3 + 0.57X_2X_3 - 1.16X_1^2 - 1.08X_2^2 + 0.68X_3^2$$

Where:

- X_1 = temperature,
- X_2 = Acid concentration
- X_3 = TOA concentration.

Table 3 presents the regression model and ANOVA of extraction efficiency for reactive extraction of Malic acid using TOA in 1-decanol. From the table, the model F-value of 21.8 indicates the model is significant. There is only a 0.03% chance that an F-value this large could occur due to noise. Values of "Prob>F" less than 0.0500 indicate model terms are significant. In this case, X_1 , X_2 , X_3 , X_1^2 , X_2^2 , X_3^2 are significant model terms. Also, values of "Prob>F" greater than 0.1000 indicate the model terms are measured as significant. The correlation coefficient values (R^2) was adequate (> 0.9644) for the response ($P \leq 0.05$) (Baş and Boyacı, 2007). The plots of the correlation coefficient and the adjusted values for comparing the model fitness is presented in Figure 2. The adequate precision value which measures single to noise ratio was expected to be greater than 4. The model ratio in this work was 13.366 which indicated an acceptable signal and can be employed to pilot the design space. The variation coefficient obtained was relatively low (CV=0.54%), which indicated the accuracy and reliability of the model.

Table 3: Analysis of variance and response surface regression model for malic acid reactive extraction

Source	Sum of Squares	df	Mean Square	F Value	p-value Prob > F	
Model	51.75	9	5.75	21.07	0.0003	significant
<i>A-Temperature</i>	4.05	1	4.05	14.82	0.0063	
<i>B-TOA Concentration</i>	1.65	1	1.65	6.04	0.0436	
<i>C-Acid Concentration</i>	30.94	1	30.94	113.36	< 0.0001	
<i>AB</i>	0.88	1	0.88	3.23	0.1151	
<i>AC</i>	0.48	1	0.48	1.76	0.2266	
<i>BC</i>	1.32	1	1.32	4.83	0.0640	
<i>A²</i>	5.64	1	5.64	20.68	0.0026	
<i>B²</i>	4.92	1	4.92	18.03	0.0038	
<i>C²</i>	1.93	1	1.93	7.08	0.0325	
Residual	1.91	7	0.27			
<i>Lack of Fit</i>	1.91	3	0.64	7196.59	< 0.0001	significant
<i>Pure Error</i>	3.539E-004	4	8.847E-005			
Cor Total	53.66	16				

Std. Dev.	0.52	R-Squared	0.9644
Mean	97.61	Adj R-Squared	0.9186
C.V. %	0.54	Adeq Precision	13.366

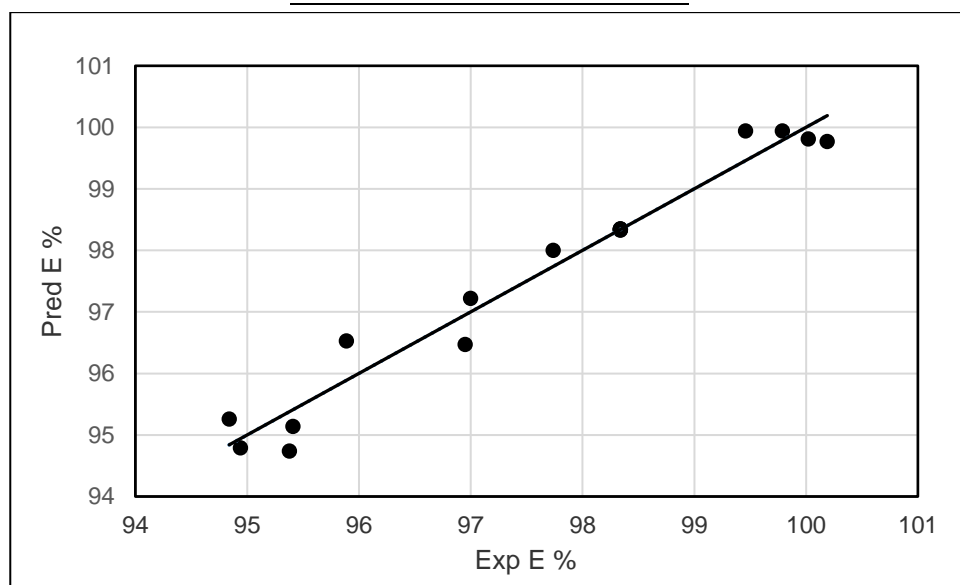


Figure 2: Predicted model plot against experimental extraction efficiency from RSM Model

4. PROCESS VARIABLES OPTIMISATION

The optimisation of process variables was important in order to maximise the yield of extraction and also to make the overall process cost effective. The same software, Design Expert, was employed in the numerical optimisation of the process parameters to maximise the malic acid extraction efficiency. The optimum values obtained for the reactive extraction from the model equation were as follows: the predicted maximum values for the extraction efficiency that can be obtained under these optimised conditions are temperature: 308,65 K; acid concentration: 0.711 kmol/m³; Trioctylamine composition: 21.706% (v/v); and the model prediction for the extraction efficiency under these optimum condition was 97.98%. Experimental verification and validation were conducted in triplicate at the optimised process variables and the results obtained (98.35%) were in good agreement with the predicted model response values.

5. CONCLUSION

In this study, the reactive extraction of malic acid onto a biphasic organic-aqueous system with trioctylamine in 1-decanol as extractant and diluent respectively for determining the extraction efficiency and distribution coefficient was successfully carried out. Box Behnken design was employed to study the interactive effects of different process parameters on the equilibrium studies of malic acid. The regression analysis using ANOVA, experimental design and quadratic model was developed to predict and optimise the functional relationship between the process variables (temperature, malic acid concentration and extractant composition) and the response (extraction efficiency and distribution coefficient). The optimum conditions of the process variables were found to be: temperature: 308,65 K; acid concentration: 0.711 Kmol/m³; and Trioctylamine composition: 21.706 % (v/v). Under these optimum conditions, the highest value for the extraction efficiency (%E) was 98.35%. These findings and results can pave the way for the reactive separation process design for recovery of carboxylic acids from dilute aqueous waste streams as well as a fermentation broth. This can unlock pathways to the recovery of these acids in low concentrations.

6. REFERENCES

- Baş, D. & Boyacı, I. H. 2007. Modeling and optimization I: Usability of response surface methodology. *Journal of food engineering*, 78, 836-845.
- Brouwer, T., Blahusiak, M., Babic, K. & Schuur, B. 2017. Reactive extraction and recovery of levulinic acid, formic acid and furfural from aqueous solutions containing sulphuric acid. *Separation and Purification Technology*, 185, 186-195.
- Chemarin, F., Moussa, M., Allais, F., Trelea, I. C. & Athès, V. 2019. Recovery of 3-hydroxypropionic acid from organic phases after reactive extraction with amines in an alcohol-type solvent. *Separation and Purification Technology*, 219, 260-267.
- Datta, D., Kumar, S. & Uslu, H. 2015. Status of the Reactive Extraction as a Method of Separation. *Journal of Chemistry*, 2015.
- Eda, S., Borra, A., Parthasarathy, R., Bankupalli, S., Bhargava, S. & Thella, P. K. 2018. Recovery of levulinic acid by reactive extraction using tri-n-octylamine in methyl isobutyl ketone: Equilibrium and thermodynamic studies and optimization using Taguchi multivariate approach. *Separation and Purification Technology*, 197, 314-324.
- Eda, S., Parthasarathy, R. & Prathap Kumar, T. 2015. *Reactive Extraction of Succinic Acid from Aqueous Solutions using Tri-N- Octylamine (TOA) in 1-Decanol: Equilibria and Effect of Temperature*.
- Gorden, J., Zeiner, T. & Brandenbusch, C. 2015. Reactive extraction of cis,cis-muconic acid. *Fluid Phase Equilibria*, 393, 78-84.
- Hong, Y., Hong, W. & Han, D. 2001. Application of reactive extraction to recovery of carboxylic acids. *Biotechnology and Bioprocess Engineering*, 6, 386-394.
- Hulse, J. H. 2004. Biotechnologies: past history, present state and future prospects. *Trends in food science & technology*, 15, 3-18.
- Keshav, A., Wasewar, K. & Chand, S. 2008. Reactive extraction of propionic acid using tri-n-butyl phosphate in petroleum ether: Equilibrium study. *Chemical and biochemical engineering quarterly*, 22, 433-437.
- Keshav, A., Wasewar, K. L. & Chand, S. 2009a. Recovery of propionic acid by reactive extraction-1. Equilibrium, effect of pH and temperature, water coextraction. *Desalination and Water Treatment*, 3, 91-98.
- Keshav, A., Wasewar, K. L. & Chand, S. 2009b. Recovery of propionic acid from an aqueous stream by reactive extraction: effect of diluents. *Desalination*, 244, 12-23.
- Kreyenschulte, D., Heyman, B., Eggert, A., Maßmann, T., Kalvelage, C., Kossack, R., Regestein, L., Jupke, A. & Büchs, J. 2018. In situ reactive extraction of itaconic acid during fermentation of *Aspergillus terreus*. *Biochemical Engineering Journal*, 135, 133-141.

- Kumar, T. P., Vishwanadham, B., Rani, K. P., Mallikarjun, M. & Rao, V. B. 2010. Reactive extraction of levulinic acid from aqueous solutions with tri-n-octylamine (TOA) in 1-octanol: equilibria, kinetics, and model development. *Chemical Engineering Communications*, 198, 572-589.
- Kurzrock, T. & Weuster-Botz, D. 2011. New reactive extraction systems for separation of bio-succinic acid. *Bioprocess and biosystems engineering*, 34, 779-787.
- López-Garzón, C. S. & Straathof, A. J. J. 2014. Recovery of carboxylic acids produced by fermentation. *Biotechnology Advances*, 32, 873-904.
- Marchitan, N., Cojocaru, C., Mereuta, A., Duca, G., Cretescu, I. & Gonta, M. 2010. Modeling and optimization of tartaric acid reactive extraction from aqueous solutions: A comparison between response surface methodology and artificial neural network. *Separation and Purification Technology*, 75, 273-285.
- Marinova, M., Albet, J., Molinier, J. & Kyuchoukov, G. 2005. Specific influence of the modifier (1-decanol) on the extraction of tartaric acid by different extractants. *Industrial & engineering chemistry research*, 44, 6534-6538.
- Marti, M. E., Gurkan, T. & Doraiswamy, L. K. 2011. Equilibrium and Kinetic Studies on Reactive Extraction of Pyruvic Acid with Trioctylamine in 1-Octanol. *Industrial & Engineering Chemistry Research*, 50, 13518-13525.
- Senol, A. 2004. Effect of diluent on amine extraction of acetic acid: modeling considerations. *Industrial & engineering chemistry research*, 43, 6496-6506.
- Sharma, H., Singh, K., Wasewar, K. L. & Athankar, K. K. 2017. L (+)-tartaric Acid Separations Using Aliquat 336 in n-Heptane, Kerosene, and 1-Octanol at 300±1 K. *Journal of Chemical & Engineering Data*, 62, 4047-4063.
- Tamada, J. A. & King, C. J. 1990a. Extraction of carboxylic acids with amine extractants. 2. Chemical interactions and interpretation of data. *Industrial & engineering chemistry research*, 29, 1327-1333.
- Tamada, J. A. & King, C. J. 1990b. Extraction of carboxylic acids with amine extractants. 3. Effect of temperature, water coextraction, and process considerations. *Industrial & engineering chemistry research*, 29, 1333-1338.
- Wasewar, K. L. 2005. Separation of lactic acid: recent advances. *Chemical and biochemical engineering quarterly*, 19, 159-172.
- Wasewar, K. L., Heesink, A. B. M., Versteeg, G. F. & Pangarkar, V. G. 2002. Reactive extraction of lactic acid using alamine 336 in MIBK: equilibria and kinetics. *Journal of Biotechnology*, 97, 59-68.
- Wasewar, K. L., Shende, D. & Keshav, A. 2010. Reactive extraction of itaconic acid using quaternary amine Aliquat 336 in ethyl acetate, toluene, hexane, and kerosene. *Industrial & Engineering Chemistry Research*, 50, 1003-1011.
- Wasewar, K. L., Shende, D. & Keshav, A. 2011. Reactive extraction of itaconic acid using tri-n-butyl phosphate and aliquat 336 in sunflower oil as a non-toxic diluent. *Journal of chemical technology and biotechnology*, 86, 319-323.